

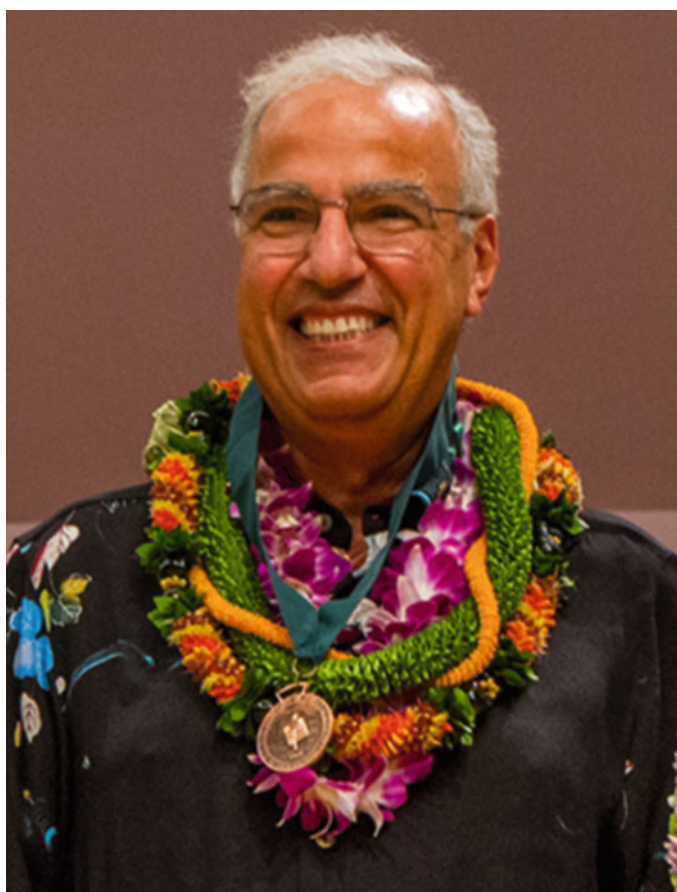
Akhlesh Lakhtakia · Cynthia M. Furse  
*Editors*

# The World of Applied Electromagnetics

In Appreciation of Magdy Fahmy  
Iskander

 Springer

# The World of Applied Electromagnetics



Akhlesh Lakhtakia • Cynthia M. Furse  
Editors

# The World of Applied Electromagnetics

In Appreciation of Magdy Fahmy Iskander

 Springer

*Editors*

Akhlesh Lakhtakia  
NanoMM – Nanoengineered  
Metamaterials Group  
Department of Engineering Science  
and Mechanics  
Pennsylvania State University  
PA, USA

Cynthia M. Furse  
Department of Electrical  
and Computer Engineering  
University of Utah  
Salt Lake City, UT, USA

ISBN 978-3-319-58402-7

ISBN 978-3-319-58403-4 (eBook)

DOI 10.1007/978-3-319-58403-4

Library of Congress Control Number: 2017944136

© Springer International Publishing AG 2018

This work is subject to copyright. All rights are reserved by the Publisher, whether the whole or part of the material is concerned, specifically the rights of translation, reprinting, reuse of illustrations, recitation, broadcasting, reproduction on microfilms or in any other physical way, and transmission or information storage and retrieval, electronic adaptation, computer software, or by similar or dissimilar methodology now known or hereafter developed.

The use of general descriptive names, registered names, trademarks, service marks, etc. in this publication does not imply, even in the absence of a specific statement, that such names are exempt from the relevant protective laws and regulations and therefore free for general use.

The publisher, the authors and the editors are safe to assume that the advice and information in this book are believed to be true and accurate at the date of publication. Neither the publisher nor the authors or the editors give a warranty, express or implied, with respect to the material contained herein or for any errors or omissions that may have been made. The publisher remains neutral with regard to jurisdictional claims in published maps and institutional affiliations.

Printed on acid-free paper

This Springer imprint is published by Springer Nature

The registered company is Springer International Publishing AG

The registered company address is: Gewerbestrasse 11, 6330 Cham, Switzerland

*To everyone who applies Maxwell's  
equations for the benefit of humanity*

# Foreword

This festschrift volume recognizes the long and distinguished career of Magdy F. Iskander as researcher, educator, and leader in his professional and academic communities. His students and colleagues have spoken in great detail through their chapters here of his many contributions to the fields of electromagnetics and wireless technologies, as well as his success in translating his work into effective educational and university-industry interactions. Magdy, himself, has written in this volume the fascinating story of his life and career path over four decades, with detailed chapters on his research in computational electromagnetics, propagation modeling, antennas and antenna arrays, and metamaterials and his entrepreneurial and educational activities.

My own reflection on Magdy's career accomplishments dates to our time together as colleagues at the National Science Foundation when he joined our Division of Electrical and Communications Systems (ECS) in the Engineering (ENG) Directorate as program director, from January 1998 to October 1999. Shortly after his arrival at NSF, he began meetings with colleagues in our Computer and Information Science and Engineering (CISE) Directorate to explore cooperation in the area of wireless communications. These discussions led to the first of several workshops on wireless technologies that Magdy helped organize while at NSF, an area of high importance for ECS. Drawing on community input from these workshops, Magdy led the development of an NSF joint solicitation with ENG, CISE, and the NSF International Office on Wireless Information Technology and Networks. Its intent was to encourage fundamental research that would enable further advances in wireless mobile communications and in their applications and services. Magdy was also a member of the 1999 WTEC panel on Wireless Information Technology formed to assess US competitiveness in wireless communication R&T in Europe and Japan. Prior to leaving NSF, Magdy developed, together with colleagues at ARO, DARPA, and NRL, a well-recognized workshop on RF micromachining and MEMS technology for wireless communication systems.

After returning to his faculty position as professor of electrical and computer engineering at the University of Utah, Magdy was recruited in 2002 to join the faculty of the University of Hawaii at Manoa as professor of electrical engineering in the College of Engineering. There he took on the position he maintains today as director of the Hawaii Center for Advanced Communications. He brought in significant funding for the center from industry and state and federal governments to expand research and education programs in wireless communication technologies and to support hiring of young new faculty. With resources from an NSF Major Research Instrumentation (MRI) grant, he established an indoor antenna range to advance research on digital signal processing and design and optimization of next-generation wireless communication systems. He worked to strengthen collaborative research ties through the center with industry and to build a strong education and workforce-development effort with local school systems, which included an effective NSF- and state-supported Research Experience for Teachers (RET) program. In 2004, Magdy submitted a successful proposal to NSF to establish as co-director a University of Hawaii partnership with the NSF Industry/University Cooperative Research Center (I/UCRC) for Telecommunications Circuits and Systems (Communications One) at Arizona State University. This joint effort continues to support strong industry-university collaborative research and robust education and outreach programs.

Magdy was recognized by the IEEE in 1993 with a fellow award for his “contributions to computational techniques in bioelectromagnetics, near-field dosimetry analysis, and to engineering education.” In 2002, he was elected president of the IEEE Antennas and Propagation Society. Among many awards in his career, he received their prestigious Distinguished Educator Award in 2012 and, similarly in 2013, the award from the IEEE Microwave Theory and Techniques Society. Magdy has a prolific record of lectures, publications, editorships of professional journals, conference proceedings, patents, books, and book chapters. In 2011, he organized an NSF-sponsored US/Ireland research and technology collaboration workshop in Dublin, Ireland, and more recently in 2014 a US/Egypt workshop in Alexandria, Egypt, his childhood home. Magdy has organized and chaired numerous international conferences and workshops. A number of these have been held in Hawaii, thus contributing to the state’s economy and where he, indeed, has been a most gracious host.

With this festschrift and a special session of the 2017 IEEE International Microwave Symposium, many of his students and colleagues in the electromagnetics engineering community are celebrating Magdy’s many career achievements and his enduring friendships.





Magdy F. Iskander and Lawrence S. Goldberg, Maui, Hawaii, 2012

National Science Foundation  
Arlington, VA 22230, USA  
[lgoldber@nsf.gov](mailto:lgoldber@nsf.gov)

Lawrence S. Goldberg

# Acknowledgments

The editors warmly thank Prof. Magdy F. Iskander for inspiring them, mentoring them, guiding them, and encouraging them.

The editors thank Dr. Lawrence S. Goldberg for the gracious and informative foreword and all colleagues who contributed chapters to this festschrift. Not only did they write their own chapters, but they also provided thoughtful peer reviews of chapters written by others.

The editors are grateful to the personnel of Springer Nature for the assistance at critical junctures during the copyediting, proofreading, and production phases. Special thanks are due to Charles Glaser for his enthusiastic reception of the idea of this festschrift, to Murugesan Tamilselvan for coordinating all pre-production activities, and to ArunPrakash Ramasamy for overseeing production activities.

The editors also thank their family members for encouraging them and patiently allowing them the time needed to celebrate and commemorate the successful career of a valued scientist, engineer, mentor, and friend, Prof. Magdy F. Iskander.

# Contents

<b>1</b>	<b>Introduction</b> .....	<b>1</b>
	Akhlesh Lakhtakia and Cynthia M. Furse	
<b>2</b>	<b>Four Decades of Academic Career in Electromagnetic Research and Education</b> .....	<b>5</b>
	Magdy F. Iskander	
<b>3</b>	<b>Millimeter-Wave Endfire Single-Feed Circular-Polarization Antipodal Fermi Tapered Slot Antenna</b> .....	<b>55</b>
	Zouhair Briqech, Abdel-Razik Sebak, and Tayeb A. Denidni	
<b>4</b>	<b>High-Performance Hybrid Smart Antenna Array for Advanced Wireless Communication Applications</b> .....	<b>77</b>
	Nuri Celik	
<b>5</b>	<b>Antenna Arrays for Physical Layer-Based Directional Networking Technology</b> .....	<b>107</b>
	Gui Chao Huang, Magdy F. Iskander, Farhan A. Qazi, Zhengqing Yun, and Galen H. Sasaki	
<b>6</b>	<b>Electrically Small Antennas</b> .....	<b>133</b>
	James M. Baker	
<b>7</b>	<b>Metamaterial-Based Antennas and a Metasurface-Based Terahertz Frequency Splitter</b> .....	<b>159</b>
	Hisamatsu Nakano, Jun Shibayama, and Junji Yamauchi	
<b>8</b>	<b>Electromagnetic Research and Challenges for Tactical Communication</b> .....	<b>183</b>
	Mahbub Hoque and Jeffrey Boksiner	
<b>9</b>	<b>Antenna Miniaturization in Mobile Communication Systems</b> .....	<b>205</b>
	Yue Li, Zhijun Zhang, and Magdy F. Iskander	

<b>10</b>	<b>Making UWB Antennas Unidirectional: Phase Coherence with an Ultra-Wide Band Frequency Selective Surface Reflector</b> .....	227
	Yogesh Ranga, Karu P. Esselle, and Ladislau Matekovits	
<b>11</b>	<b>Radar Cross Sections of Six Different Radar Reflectors Mounted on Power Boats</b> .....	259
	Hsing Yi Chen and Chien Yi Lin	
<b>12</b>	<b>Radio Propagation Modeling and Simulation Using Ray Tracing</b> ....	275
	Zhengqing Yun and Magdy F. Iskander	
<b>13</b>	<b>Radio Propagation Modeling: A Unified View of the Ray-Tracing Image Method Across Emerging Indoor and Outdoor Environments</b> .....	301
	Soo Yong Lim, Zhengqing Yun, and Magdy F. Iskander	
<b>14</b>	<b>Wireless Performance in Dense-Transceiver Scenarios to Enable Context-Aware Scenarios</b> .....	329
	Peio Lopez-Iturri, Leyre Azpilicueta, Erik Aguirre, and Francisco Falcone	
<b>15</b>	<b>Bioelectromagnetic Dosimetry: Simulating Electromagnetic Fields in the Human Body</b> .....	351
	Cynthia M. Furse	
<b>16</b>	<b>Crossed Viewpoints on Microwave-Based Imaging for Medical Diagnosis: From Genesis to Earliest Clinical Outcomes</b> .....	369
	Jean-Charles Bolomey	
<b>17</b>	<b>Real-Time Quantitative Reconstruction Methods in Microwave Imaging</b> .....	415
	Denys S. Shumakov, Daniel Tajik, Alexander S. Beaverstone, and Natalia K. Nikolova	
<b>18</b>	<b>Electromagnetics in Medical Applications: The Cardiopulmonary Stethoscope Journey</b> .....	443
	Ruthsenne R.G. Perron, Magdy F. Iskander, Todd B. Seto, Gui Chao Huang, and Darcy A. Bibb	
<b>19</b>	<b>The Ewald–Oseen Extinction Theorem and The Extended Boundary Condition Method</b> .....	481
	Akhlesh Lakhtakia	
<b>20</b>	<b>Propagator Methods in Electromagnetics</b> .....	515
	Jongchul Shin and Robert D. Nevels	
<b>21</b>	<b>Wave Propagation and Field Manipulation in Non-Hermitian Metamaterials</b> .....	545
	Silvio Savoia, Giuseppe Castaldi, and Vincenzo Galdi	

**22 Unidirectional, Defect-Immune, and Topologically Protected Electromagnetic Surface Waves**..... 569  
 George W. Hanson, Seyyed Ali Hassani Gangaraj,  
 and Andrei M. Nemilentsau

**23 Single-Band and Multiband Angular Filtering Using Two-Dimensional Photonic Crystals and One-Layer Gratings**..... 605  
 Andriy E. Serebryannikov and Ekmel Ozbay

**24 Toward the Construction of Parts of the Universe on Tabletops** ..... 631  
 Tom G. Mackay and Akhlesh Lakhtakia

**25 Electromagnetics Education: Past, Present, and Future Directions** .. 655  
 Cynthia M. Furse and Elene Tiffany Iskander

**26 Curriculum Vitae** ..... 677  
 Magdy F. Iskander

# Chapter 1

## Introduction

**Akhlesh Lakhtakia and Cynthia M. Furse**

Two developments occurred in the last five decades to revolutionize the application of electromagnetism. The first was the proliferation of digital computers from the 1970s that allow rapid calculations to solve a variety of electromagnetic problems. Scattering of electromagnetic waves by a diverse variety of objects can be investigated today. The scattering object can be homogeneous or heterogeneous; isotropic, biisotropic, anisotropic, or bianisotropic; and linear or nonlinear. Its dimensions can be small, similar, or large in comparison to the wavelength. Even though most scattering problems are still solved in the frequency domain, time-domain scattering problems are also very tractable today.

The second development was an explosion in the availability and the capabilities of equipment for electromagnetic measurements. Faster and more complex experimentation was facilitated by miniaturization and computerization of experimental equipment that integrated measurement and computational processing of data for rapidly exploitable understanding of electromagnetic phenomena. Affordable vector network analyzers, spectrum analyzers, high-speed oscilloscopes, power meters, and digital signal generators have become standard lab equipment since the 1980s. Large datasets from experiments on the propagation of electromagnetic signals in complex environments—such as the human body, fogs, urban environments, forests, and the ionosphere—can be analyzed with a rapidity that was perhaps unimaginable in the electromagnetics research community at the beginning of the 1970s.

---

A. Lakhtakia (✉)

NanoMM – Nanoengineered Metamaterials Group, Department of Engineering Science and Mechanics, Pennsylvania State University, University Park, PA 16802, USA  
e-mail: [akhlesh@psu.edu](mailto:akhlesh@psu.edu)

C.M. Furse

Department of Electrical and Computer Engineering, University of Utah, Salt Lake City, UT 84112, USA  
e-mail: [cfurse@ece.utah.edu](mailto:cfurse@ece.utah.edu)

The research career of Prof. Magdy Fahmy Iskander, presently Director of the Center for Advanced Communications at the University of Hawaii, commenced in 1971 at the University of Manitoba. Digital computers had begun to emerge in academic environments just about the same time. Ungainly behemoths by today's standards in size but puny in computational capabilities, these digital computers were quickly adopted by computational electromagnetics. As a young graduate student, Magdy was at the forefront of the use of digital computers for applied electromagnetics. That characteristic of his research career has not changed for more than four decades.

Magdy's initial research in computational electromagnetics was focused on the numerical solution of scattering by objects of complex shapes. At the University of Utah which he joined in 1977 after receiving his PhD in 1975 and a subsequent postdoctoral fellowship for a year in Manitoba, his research branched out in two different directions.

The first direction was computational bioelectromagnetics. Potential adverse effects of microwave radiation on human health and the prospect of designing electromagnetic equipment capable of measuring and even healing medical conditions required critical advances in microwave dosimetry, but early experimentation on humans would be totally unethical as well as impractical. The method of moments (MoM) and the extended boundary condition method (EBCM) were the two computational techniques that appeared both appropriate and tractable. Magdy assisted in the formulation of prolate-spheroidal models of humans and other animals, chose the EBCM for calculations, and participated in the dissemination of dosimetry data through four editions of a handbook. A. Lakhtakia, his first PhD student, used the EBCM for near-field dosimetry and then collaborated in the development of the iterative EBCM (IEBCM). Magdy went on to use the MoM, which provided the basis for the undergraduate and master's research of C.M. Furse, and the then-nascent finite-difference time-domain (FDTD) method for scattering by inhomogeneous objects for which the IEBCM required computational resources that were then simply unavailable.

The second direction was to use microwaves to map human tissue in vivo for diagnostic applications. Magdy participated in experiments to determine the spatial distribution of water in canine lungs as a measure of an animal's health. He devised new kinds of microwave applicators to irradiate deep-seated tissue, tomographic equipment to acquire data from exposure in different directions, and algorithms to process and interpret tomographic data. His interest in microwave-assisted diagnostics has continued unabated, and he has recently invented the microwave cardiopulmonary stethoscope.

Not only was Magdy a pioneer in computational electromagnetics and microwave-assisted diagnostics, but he also recognized much earlier than many of his peers that computers would become an essential tool in the electromagnetic research community. In 1990, he founded the NSF/IEEE Center for Computer Applications in Electromagnetic Education (CAEME), funded by the US National Science Foundation (NSF) and the Institute of Electrical and Electronics Engineers (IEEE) to spearhead development of software and multimedia for undergraduate

students. He became the founding editor of the journal *Computer Applications in Engineering Education*, now in its 25th year of publication. He also founded the University of Utah Engineering Clinic Program which matches groups of five undergraduate students with industrial clinic sponsors to carry out a (funded) project of interest to the industrial sponsor. Originally begun in electrical engineering, this program has expanded to mechanical engineering as well.

In 1998, at a critical time in the early emergence of modern mobile wireless communication systems, Magdy became a Program Director for the Electrical, Communications, and Cyber Systems (ECCS) Division of the US National Science Foundation, to formulate a wireless communication initiative in the Engineering Directorate. Through these efforts to identify basic research needs essential for wireless communication systems, Magdy helped enable an industry that is part of our everyday lives today. One key aspect of this, which Magdy began working on in 1999 at the University of Utah and continued after he moved to the University of Hawaii in 2002, is propagation modeling to predict (and therefore design) how wireless signals propagate, reflect, refract, and attenuate in buildings and cities. Taking the science from simple ray-tracing codes to advanced propagation solvers, Magdy and his research team have enabled the design of next-generation wireless systems.

We would be remiss in not mentioning the distinguished leadership of Magdy in the applied electromagnetics research community. A distinguished lecturer for the IEEE Antennas and Propagation Society from 1994 to 1997, he served as the President of that society in 2002. From 1997 to 1999, he was a Program Director in the Electrical Communications and Cyber Systems Division at the NSF. During his long career, he has organized many conferences, as becomes apparent from his reminiscences in Chap. 2 and his curriculum vitae in Chap. 26.

This festschrift is a celebration of the research and pedagogical accomplishments of a distinguished leader of the applied electromagnetic research community. This collection of chapters written by former and current students, former and current collaborators, and admirers of Prof. Magdy F. Iskander focuses on the diversity and the societal impact of the research streams flowing through his career. As his research remains vibrant even in the fifth decade of a productive research career, he has coauthored five chapters in this festschrift which brings together contributions on microwave circuitry, design and testing of antennas, electromagnetic propagation in novel types of materials, biomedical applications, radiation dosimetry, and engineering education. It raises awareness not only of past contributions but also the future prospects of electromagnetic technologies. We, the editors, sincerely hope that the synoptic view of applied electromagnetics, stemming from the life and times of just one person, will inspire junior researchers in search of fascinating questions still to be answered and spark the creative energy of mid-level and even senior researchers in our research community to carry on the great work of applying electromagnetics for the good of humanity.



# Chapter 2

## Four Decades of Academic Career in Electromagnetic Research and Education

Magdy F. Iskander

### 2.1 Introduction

Four decades of academic career is a long time to highlight, especially when it has all been filled with excitements, challenges, opportunities, and accomplishments that I experienced and have been able to share with colleagues, faculty, and students and enjoy its fruits with family and friends. Surely, my career can be characterized by hard work, dedication to do my best, in whatever I touch, and commitment to succeed and be proud in whatever I produce. Being fair and square is how I operated, telling it like it is is how I communicated, and relying on God's help and the prayers of Saints is what I trusted. In the following sections, I briefly describe my contributions in different scholarly areas in which I was fortunate enough to attract external funding and work on with faculty, colleagues, and students for a sufficiently long and productive time. This includes contributions in research advances and innovation in engineering education. But before we get to this, however, let me start with a brief biographical sketch.

I was born in Alexandria, Egypt, on August 6, 1946. I loved playing soccer and going to church, but early on I found joy and satisfaction in doing well and being recognized for my success at school (Fig. 2.1).

I achieved major success in high school, as a very top student in the country, and graduated with a final grade of "Excellent with First Class Honor" from the College of Engineering at the University of Alexandria in 1969. During my high school and college years, I participated in Sunday school teaching, and during summer I spent time in monasteries praying and recuperating for tough competitions during the school years. Upon graduating from the University, I was appointed as lecturer

---

M.F. Iskander (✉)

Hawaii Center for Advanced Communications, University of Hawaii at Manoa,  
Honolulu, HI 96822, USA

e-mail: [magdy@hawaii.edu](mailto:magdy@hawaii.edu)



**Fig. 2.1** Early years: (a) Magdy at 11 years old, (b) Magdy during high school graduation #1 in Alexandria, and (c) Dr. Iskander graduation with PhD from the University of Manitoba

at the University, and this is where I discovered my love for teaching. I exclusively selected to work with the professor who was teaching quantum mechanics and theory of relativity. Because of the difficulty of these subjects, I organized review sessions for students and was amazed by the huge number of students who attended these extra sessions. This, however, did not last for long. Even before completing my 2-year obligatory teaching services at the University and before being allowed to travel abroad for graduate studies, I received a scholarship from the University of Manitoba, Canada, as in those days Egypt did not have a diplomatic relationship

with the USA and no passports were issued for travel to the USA. So, I joined the University of Manitoba in September 1971. For a boy from Egypt to live in Manitoba, it was really cold, but with focus on studying and competition with students from across the world, it was just fine, and I very quickly learned to enjoy my stay in Canada. I completed my master's degree in 9 months, and my advisor gave me a \$99 Greyhound bus ticket to travel to anywhere in the continental USA and Canada. Wow, this was fun. Soon after my return, I was informed of the acceptance and publication of my first IEEE paper *A Time-Domain Technique for Measurement of Dielectric Properties of Biological Substance*, IEEE Transactions on Instrumentation and Measurements, vol. IM-21, pp. 425–429, 1972. My advisor who offered me the scholarship that facilitated in obtaining my exit visa from Egypt and travel for graduate studies in Canada was Dr. Stan Stuchly. He was a brilliant experimentalist, and with his encouragement and friendly support, I felt at home and very much enjoyed working with him. He also approved my travel to Boulder, Colorado, to attend my first international conference, the 1972 IEEE Conference on Instrumentation and Measurements.

I was very fortunate that after my first year in Canada, I received the National Research Council Fellowship (\$4000 a year, for 4 years), and for my PhD I decided to work more on the theoretical and computational aspects of electromagnetics. This was made possible by the CNRC scholarship as it allowed me to join a university and work on a subject of my choice anywhere in Canada. I stayed on at the University of Manitoba as I knew the professors there and completed my PhD in electrical engineering in 1975. My PhD advisor was Professor Mike Hamid, and working with him was different. Professor Hamid constantly challenged his students, and this was a good thing, and he often returned to his office during evening hours to work with his graduate students and often spent hours of discussion with us on problem formulations and validity of data from computer simulations. So we were always trying to be fully prepared, as we never know who was going to be next on the hot seat. Professor Hamid also loved publications, and I, frankly, loved this environment as well and believe that it played an important role in shaping my academic career. Before finishing my PhD, I applied for the Canadian National Research Council (CNRC) Post-Doctoral Fellowship and was very fortunate to be awarded one full \$10,000 for 1 year. This CNRC Fellowship provided a very critical support during the transitional period between the graduate work and the traditional job hunting effort after graduation. I started on the CNRC Fellowship in 1976 and left to start my postdoctoral/research associate appointment at the University of Utah in March 1977. From there, one can follow my academic career from the attached biography in Chap. 26. I just want to add that upon joining the University of Utah as a postdoctoral fellow and through mentorship by outstanding colleagues including the late Professor Curtis Johnson and my good friend Professor Carl Durney, my academic career started to take shape and quickly grow achieving high research productivity in research and excellent experience in teaching. I never thought I will leave the University of Utah; the environment was simply highly productive, very supportive, and certainly enjoyable particularly with the many friendships we made during an almost 25-year career in Salt Lake City, Utah.

As for sabbatical and other research leaves, I also had a few experiences. I started with leaves in both 1985 and 1986 at the Chevron Oil Field Research Company, La Habra, CA, where I was hired as consultant for 3 months each year. There, we conducted truly pioneering research on the use of RF energy for enhanced oil recovery. I worked with my good friend Dr. Don Anderson, and after encouraging simulation results and the laboratory validation of data, our work shifted to multimillion-dollar field trials. We also arranged for graduate students from the University of Utah to join the research at Chevron. This is where Professor Cindy Furse (then a graduate student) and I worked tirelessly on designing and optimizing designs of multi-section insulated antennas for a borehole enhanced oil-recovery method. New technologies for digging exploration holes with dielectric material casing were developed, and while results from field trials also confirmed simulation and experimental data, it was not possible to move forward with full commercialization of this technology. Enhanced oil recovery using steam technologies was more economically attractive. In 1987, I took a full year of sabbatical leave from the University of Utah, and I spent the fall and spring semesters doing research at University of California at Los Angeles (UCLA) and teaching at Harvey Mudd College. At UCLA, I was hosted by Professor Nick Alexopoulos and late Professor Robert Elliott, in the electrical engineering department. It was also there where I met with Professor Hisamatsu Nakano, from Japan, who was also spending a sabbatical leave at UCLA at that time. While discussing and working on research ideas at UCLA, Professor Nakano had a teaching assignment at UCLA, and I was teaching and learning about the Engineering Clinic Program at Harvey Mudd College. It was one of the most productive times of my career as I was also consulting on my enhanced oil recovery project at Chevron and was reviewing data from the ongoing field trial in Huntington Beach, California. I spent the last 4 months of this sabbatical leave, May–September 1987, at Laboratoire des Signaux et Systèmes, École Supérieure d'Électricité, Plateau du Moulon, Paris, France, where I worked with Professor Jean-Charles Bolomey. During this stay, I witnessed, first hand, the birth of SATIMO, his company for microwave imaging and which is now part of the Microwave Vision Group.

In 1994, I spent 1 month at Universitat Politècnica de Catalunya, Barcelona, Spain, where I worked with distinguished colleagues including Professors Lluís Jofre and Jordi Romero. I gave several lectures on multimedia modules for engineering education, and I was so impressed with the quality of their students that I ended up recruiting 11 of them when I returned back to the University of Utah. Some of them worked on antenna-type research projects, while others joined my CAEME Center for Electromagnetic Education and helped in developing several of the software simulation packages and multimedia modules. Also in 1994, I spent a 1-month visit with Professor Bolomey at École Supérieure d'Électricité where I gave lectures on multimedia modules and the use of technology in engineering education. I visited China for the first time in 1997 where I was hosted for a month by Professor Zhenghe Feng of Tsinghua University. I toured several cities and gave lectures during this period, and this is where I met my longtime colleague, Professor Zhengqing Yun, who was a postdoctoral fellow at Southeast University in Nanjing,

China, at this time. Shortly after, Dr. Yun joined me at the University of Utah, and he has been with our team since then including after moving to the University of Hawaii in 2002. In 1998, I spent 1 month as a distinguished lecturer of the IEEE AP-S at Tokyo Institute of Technology, where I was hosted by Professor Makoto Ando. There I gave several lectures on antenna array technologies and multimedia modules for electromagnetic education. During this period, I also visited several universities in Japan including Hosei University where I was hosted by Professor Hisamatsu Nakano, who was the Dean of Engineering at that time. This visit was another eye-opener for me; I loved Japan so much and thought it would be a perfect place for my retirement.

I took two more short leaves, one in April–May 2008 at Laboratory of Electronics, Antennas and Telecommunications (LEAT), University of Nice Sophia Antipolis, CNRS, Nice, France, while the other was at Department of Electronic Engineering, Tsinghua University, Beijing, China, October–November 2009. At the University of Nice, I was hosted by Professor Christian Pichot, and I gave several lectures on varying topics of electromagnetic research. While there, I also participated in one of the PhD defense committees which happened to be scheduled during my stay in Nice. As for the 1-month stay at Tsinghua University, I was hosted by Professor Zhijun Zhang and Professor Feng. Besides me giving several lectures on a variety of topics in electromagnetic research, my daughter Tiffany, who was working on her PhD at that time, also gave a talk in the department of psychology at Tsinghua. My family and I enjoyed very much the kind and gracious hospitality by Professors Zhang and Feng and were particularly happy as we toured Beijing after the 2008 Olympics and saw the dramatic changes the Olympics made in the city and its surroundings. Actually this visit also presented the kickoff event for launching the long-standing and highly productive relationship between our group at the University of Hawaii and our distinguished colleagues at Tsinghua University. Besides numerous joint research publications, I also taught a graduate course for credits on “Computational Electromagnetics” at Tsinghua, for 2 years, and hosted some of their star postdoctoral fellows in preparation for their anticipated academic careers. Finally, I want to acknowledge with thanks and appreciation the great experience I enjoyed while on leave and working as a program director at the National Science Foundation, Electrical, Communications and Cyber Systems (ECCS) Division. This was in 1998, a critical time that witnessed the early emergence of modern and mobile wireless communication systems. At that time, much of the research work was considered industry-based development with the exception of some advances in software digital signal processing and networking fundamental research issues. These issues, however, were being considered and addressed by the Computer and Information Science and Engineering Directorate (CISE) at NSF. My job description as stated in the NSF Dear Colleague Letter and job ad was to formulate a wireless communication initiative in the Engineering Directorate. But even after being hired to do this job, there was still doubt by some about the engineering role in addressing fundamental research issues associated with this technology, and hence justify NSF funding, I worked very hard with colleagues from CISE and from various defense agencies including DARPA, ARO,

and ONR to help highlight the fundamental engineering research challenges that need to be addressed and solved before the full realization of mobile, reliable, and broadband tetherless communication system. At the end, a collaborative initiative between the Engineering Directorate and CISE was developed, and thanks to the great response from the electromagnetic community, we ended up funding almost half of the projects in engineering. What a great turnaround in research focus, just in a single year of highlighting needs and remaining research challenges. I consider my experience at NSF as one of the turning points in my career, and to my colleagues and friends at NSF, Dr. Larry Goldberg, Dr. Radhakishan Baheti, and Dr. Usha Varshney, who worked with me and supported my wireless initiative against strong domination by a CISE group, my sincere thanks and wholehearted appreciation.

Before I get to the research and educational activities, which are the main topics for this chapter, let me briefly describe my family and share with you a family picture. My Egyptian family consists of my father Fahmy Iskander and my mother Fotna Youssef Farag (wives in Egypt do not change family name after getting married). I have three sisters: Fify, the oldest; then me; followed by Ekhlal, my middle sister; and then Sohair, the youngest. I met my wife Sonia while a graduate student in Canada, and our relationship continued to grow in love and support and got stronger after leaving Canada. We are now married for over 39 years, and we have one daughter E. Tiffany Iskander. Tiffany completed her PhD in psychology in 2013 with Prof. Cindy Furse (coeditor of this book) and now lives with her husband Jason Cox in Des Moines, IA. Figure 2.2 shows a family photo that was recently taken when we all met in Honolulu, Hawaii, to celebrate my 70th birthday.

In the following sections, I briefly summarize some of my work in different research areas and highlight what is different and new in our work in each of these areas.

## 2.2 Research Areas and Contributions

During my 40-year academic career, I worked on and made contributions in several electromagnetic research areas and participated in developing designs in several electromagnetic applications, ranging from material characterizations to antenna designs, computational techniques, metamaterial designs, propagation modeling, and biomedical device development and applications. In all cases, my focus was placed on advancing electromagnetic knowledge, providing innovative solutions, and making contributions that not only distinguish our work from others but also are clearly new and suitable for attracting extramural funding from government organizations like NSF and National Institutes of Health (NIH); US Department of Defense (DoD) sponsors, such as Army Research Laboratory (ARL) and Communications–Electronics, Research, Development and Engineering Center (CERDEC); US Department of Energy (DoE) sponsors such as Oak Ridge and Lawrence Livermore Lab.; as well as from many industries including Raytheon,



**Fig. 2.2** Photo of the Iskander family, from *right to left* (when looking at picture), my sister Sohair (lawyer) with her husband Mounir (mechanical engineer), next my middle sister's husband Aziz (teacher) and my sister Ekhlās (accountant), then my wife Sonia and I, followed to the *left* with my daughter Tiffany (psychologist) and her husband Jason (film maker). My eldest sister Fify passed away several years ago

Motorola, Agilent, Corning, Hewlett–Packard (HP), and Texas Instruments. It may be important at this stage to point out that while we maintained focus on exploiting capabilities and expertise in electromagnetics, changes in application areas were associated with availability of funds in developing existing technologies and in new funding opportunities in federal agencies and industry. It is not quite as simple as following and chasing of funds, but instead it is related to changes in research areas and to delivering innovative solutions to new technologies and associated challenges such as in an emerging wireless communications technology.

In the following sections, a brief synopsis of our research contributions in different areas is provided, leaving details to some of the other chapters, kindly contributed in this book by former students and research colleagues. Highlights of contributions in each of the research areas are presented, references are provided, and focus is placed on novelty and application areas of developed solutions. To help bring out some historical perspective of four decades of research in electromagnetics, I start with contributions made using analytical techniques during the years of my graduate work, and the rest will follow based on topics and the developed research regardless of the time period during which this research was performed.

### 2.2.1 *Green's Functions and Multipole Expansion-Based Analytical Solutions*

In my early graduate work and while still taking courses, I recognized the importance of Green's theorems and their powerful applications in solving a variety of electromagnetics (EM) problems detailed in the classic textbook of Morse and Feshbach [1]. This book and specifically the chapters on Green's function had significant influence on my PhD work as together with Schwartz's iterative procedure of overlapping regions [2], I was able to use Green's function for simple geometries to solve more complex structures including waveguide junctions [3–5], scattering by a polygonal conducting cylinder [6], near-field coupling between sectoral horn antennas [7], and in determining modes in some waveguides of irregular cross sections [8, 9]. Key to this formulation and iterative solution procedure is Green's function  $G$  solution of the Helmholtz equation [1]

$$\nabla^2 G_k(r|r_0) + K^2 G_k(r|r_0) = -4\pi\delta(r - r_0) \quad (2.1)$$

satisfying homogeneous boundary conditions on some surface  $S$ . The reciprocity relation is  $G_k(r|r_0) = G_k(r_0|r)$ , since the equation is self-adjoint. In Ref. [1], it is shown that if  $\psi$  is a solution of  $(\nabla^2 + K^2)\psi = 4\pi\rho$ , having value  $\psi_0(r^s)$  on the surface  $S$  and having outward-pointing normal gradient  $N_0(r^s) = \left(\frac{\partial}{\partial n}\right)_s$  on  $S$ , then within and on  $S$ ,

$$\psi(r) = \int \rho(r_0) G_k(r - r_0) dv_0 + \frac{1}{4\pi} \oint \left[ G_k(r|r_0^s) N_0(r_0^s) - \psi_0(r_0^s) \frac{\partial}{\partial n} G_k(r|r_0^s) \right] dA, \quad (2.2)$$

where the first integral is over the volume enclosed by  $S$  and the second is a normal outflow integral over all of  $S$ . The normal gradients are taken in the outward direction, away from the interior where  $\psi$  is measured.

While the initial use of these techniques was useful in solving a collection of scattering, waveguide modes, and waveguide junction problems during my graduate work [3–9] (see Figs. 2.3, 2.4, 2.5, and 2.6), we continued to use iterative methods to solve different types of problems including determination of resonance absorption by biological objects (human and animal models) [10–16] as well as for the determination of the resonance absorption of branched chains of aerosol particles [17–20]. These problems were truly challenging, and the extended boundary condition method (EBCM) failed to provide much needed specific absorption rate (SAR) values at the resonant frequencies of human and animal models [21].

The aerosol community continued to use the Lorenz–Mie solution for spherical objects as valid approximation for calculating scattering and extension cross sections of branched chains of aerosol particles [22]. The problem with the EBCM



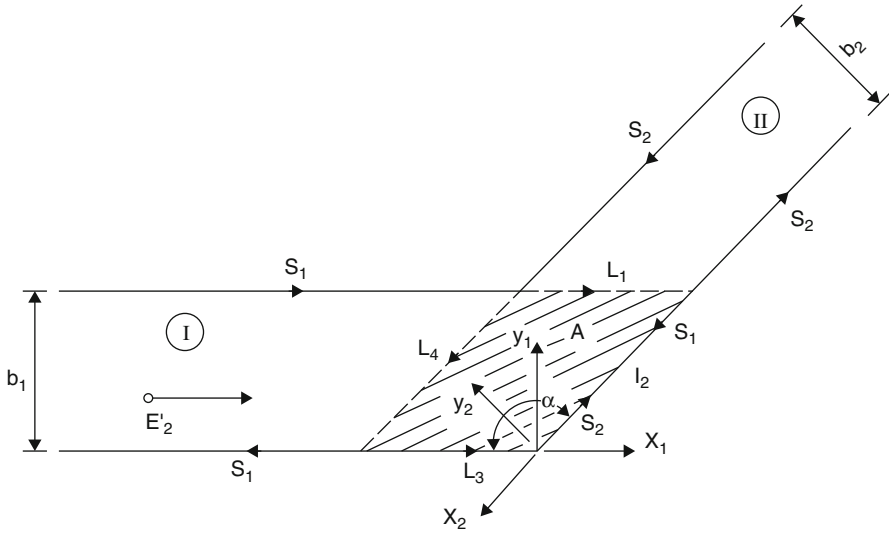


**Fig. 2.3** Longitudinal section of a sharp bend between two asymmetrical H-plane waveguides [3, 4]

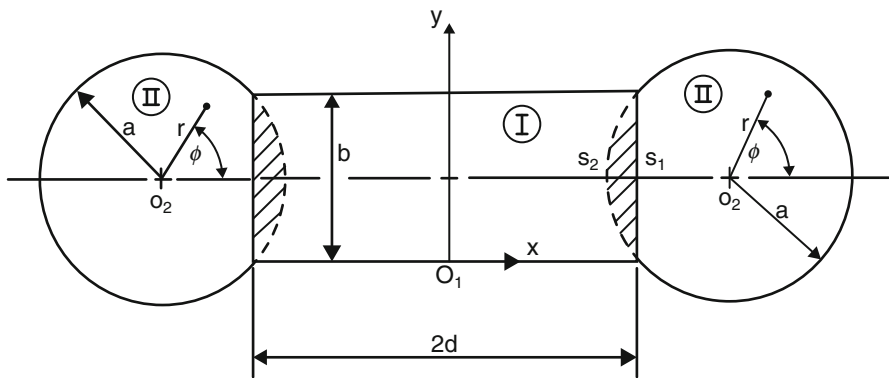


**Fig. 2.4** Cross section of the dumbbell waveguide [3]

was that the developed integral equation was solved by expressing the fields in terms of a single set of spherical functions [1]. This limited the application of the solution to objects of limited axial ratio and was not suitable to elongated objects like human subjects. We developed the iterative extended boundary condition method (IEBCM) which utilizes multiple spherical expansions and also implemented an iterative procedure to help solve for the unknown expansion coefficients in these multiple regions [10–17]. Figure 2.7 shows an example of the multipole spherical expansions utilized and the calculated SAR values at and beyond resonance for biological models [21].

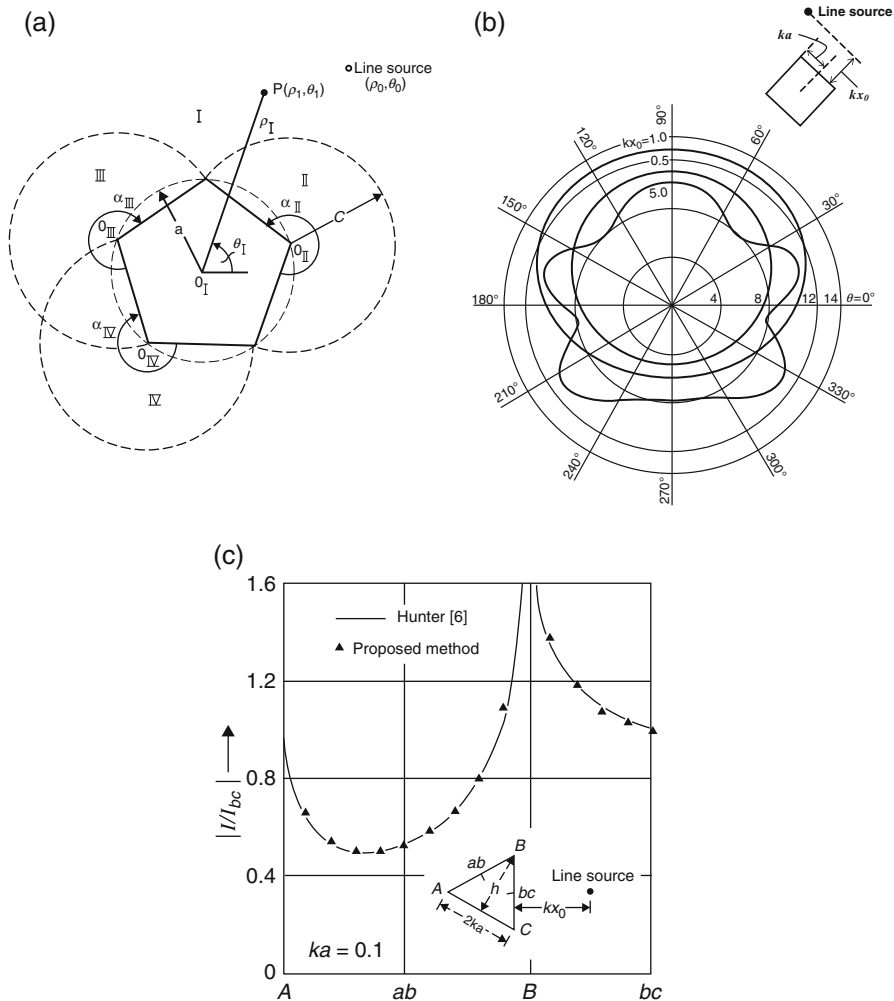


**Fig. 2.5** (a) Geometry of regular polygonal cylinder and overlapping regions; (b) scattering pattern of a square cylinder of  $ka = 0.1$ , with illuminating line source located at  $ka = 0.5, 1.0,$  and  $5$ ; (c) calculated surface current on triangle object illustrating accuracy of calculations [6]

As for the calculations of optical scattering and absorption by aerosol particles, our team initially used IEBCM for these calculations and obtained results at and beyond resonance [17–19, 23]. With funding from the Lawrence Livermore Lab., our interest in the area of “nuclear winter” continued to grow and used a method of moments and volume integral equation method to calculate scattering and absorption by branched aerosol chains of carbon particles [20]. Specific geometries of some of the chains simulated in our calculations were based on realistic carbon

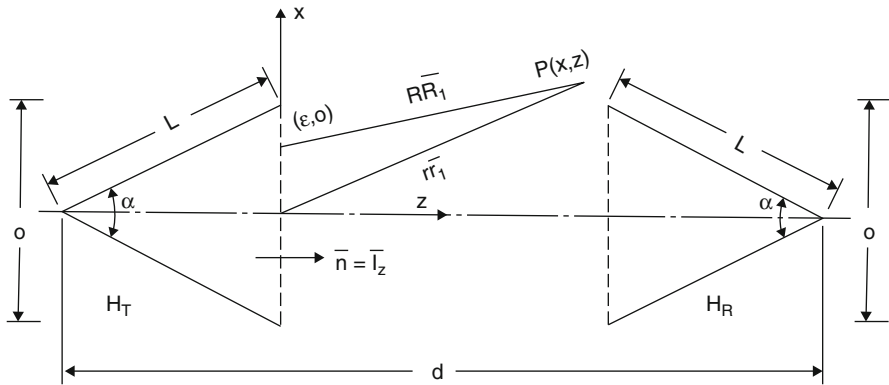


**Fig. 2.6** Schematic diagram for transition between two H-plane sectoral horns with near-field interaction characterized using the method of overlapping regions [7]

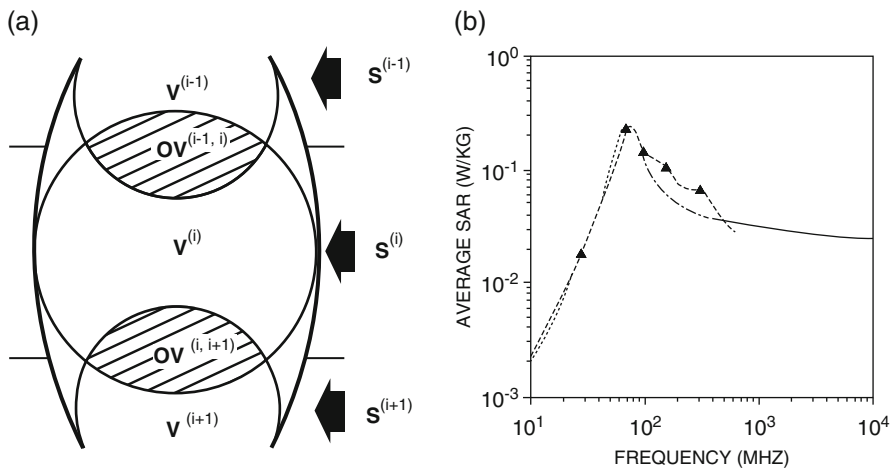


**Fig. 2.7** (a) Multiple spherical field expansions in the IEBCM and (b) an example of calculated SAR for a spheroidal model of man [15]

chains from experimentally simulated fires at the National Bureau of Standards [23]. Figure 2.8 shows the geometries and an example of the obtained results.

At that time, however, the power of personal computers continued to grow, and computational techniques such as the method of moments (MoM) and finite-difference time-domain (FDTD) method continued to show increased popularity as well as effectiveness in solving engineering problems of practical interest. Therefore, many of our research activities during the late 1980s and 1990s were related to the computational techniques area which are discussed in Sect. 2.2.3.

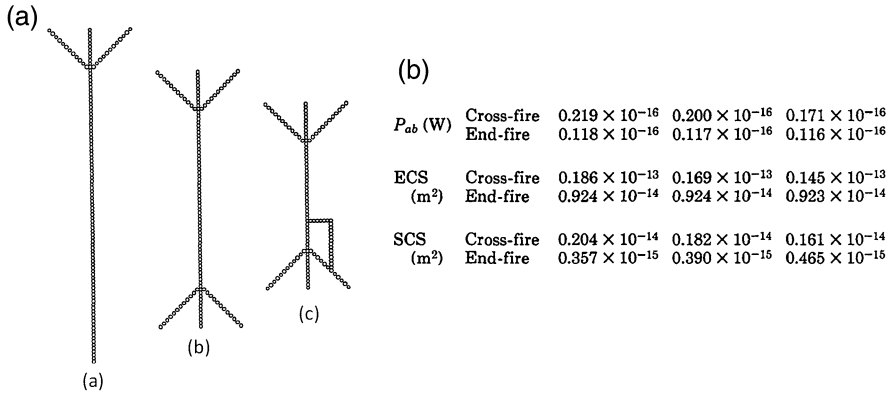


**Fig. 2.8** (a) Geometries of three different branched chains of aerosol particles used in the volume integral equation simulations; (b) results of absorbed power,  $P_{ab}$ , extinction ECS, and scattering SCS cross sections [20]

## 2.2.2 Material Characterization

Measurement of the dielectric properties of small biological samples was the topic of my master's degree research at the University of Manitoba. We used what was new then, a short rise time (picoseconds) time-domain method for the broadband characterization of biological samples [24]. As this was my first IEEE published paper, I am happy to share with you a schematic of the sample holder (see Fig. 2.9) as well as an example of the obtained results (Fig. 2.10) [24]. The paper also included uncertainty analysis and detailed calculations of estimated measurement errors. Follow-up papers used the same analysis for frequency-domain measurements [25].

Besides the development of the time-domain analytical and experimental measurement procedures, much of the work was focused on testing sample materials with known broadband dielectric properties and basically verifying the accuracy of the developed approach. I was distanced from measurement and experimental methods during my PhD studies but certainly kept considerable interest in making these types of dielectric property measurements should a need arise and associated funding is made available.

New opportunities for continuing with this research area arose when we established a collaborative program with colleagues at Oak Ridge National Lab. At that time (mid-1980s to mid-1990s), they were involved in an exciting program on microwave processing of ceramic materials. Claims were made that the fast microwave sintering of ceramics at 28 GHz may result in fine-structured ceramics and hence a stronger and improved quality end product. To help with these studies, along with the simulation work that was a part of this collaborative work, we identified two new research needs that could not be met with available dielectric property measurement methods. This includes performing high-temperature

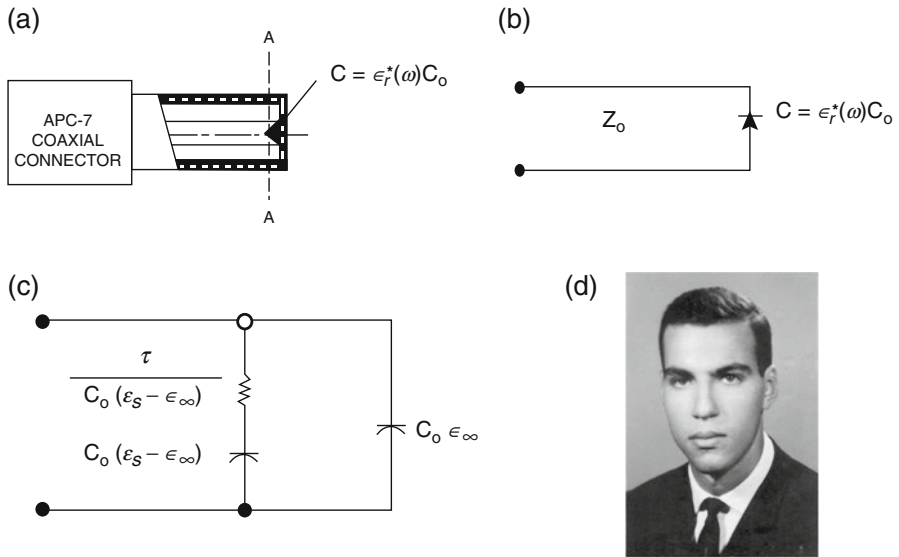


**Fig. 2.9** (a) Coaxial sample holder, (b) its equivalent circuit, and (c) equivalent circuit for sample holder with a dielectric showing Debye dispersion [24]. (d) Magdy Iskander, 1971

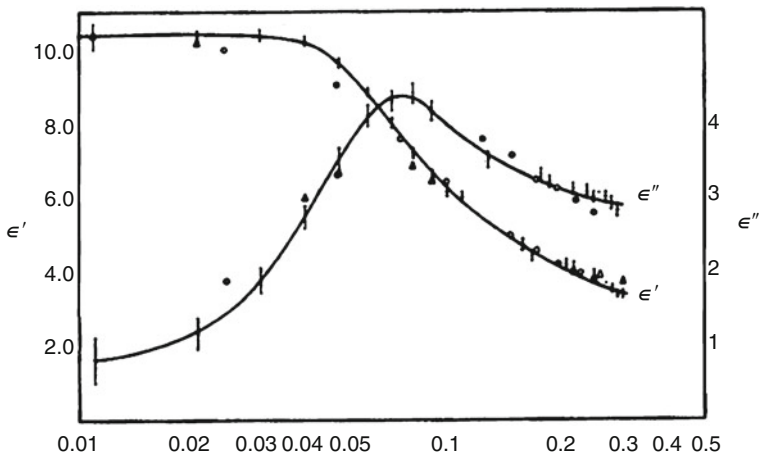


**Fig. 2.10** Experimental results for alkyl alcohol  $C_8H_{17}OH$  at  $16.5^\circ C$  [24]

measurements, up to  $1400^\circ C$ , and also extending the capabilities of the HP dielectric probe for thin-sample measurements. These two tasks were successfully achieved [26], first by developing a high-temperature metalized ceramic dielectric probe [23] and also by developing a FDTD code for calibration and thin sample measurements [27]. Examples of the obtained results are shown in Figs. 2.11 and 2.12.

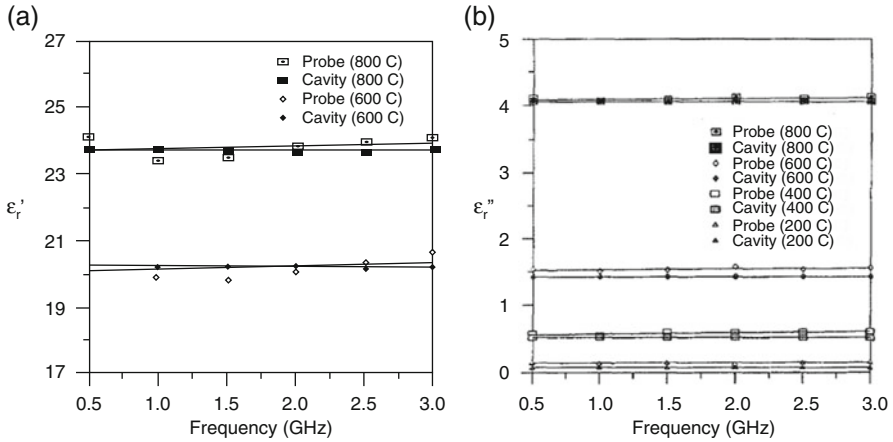


**Fig. 2.11** (a)  $\epsilon_r'$  of  $\text{ZrO}_2$ , 8 mol%  $\text{Y}_2\text{O}_3$  versus cavity results at both 600 °C and 800 °C in the frequency range from 500 MHz to 3 GHz. (b)  $\epsilon_r''$  of  $\text{ZrO}_2$ , 8 mol%  $\text{Y}_2\text{O}_3$  versus cavity results at 200 °C, 400 °C, and 800 °C in the frequency range from 500 MHz to 3 GHz [27]

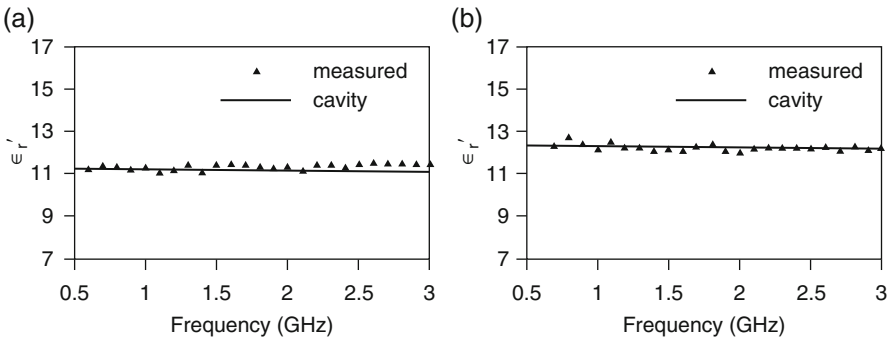


**Fig. 2.12** Measured results of a 0.6-mm thin sample of (a) alumina and (b) sapphire at 800 °C. Results are compared with values from cavity perturbation techniques [26]

More recently we were approached with another set of dielectric and magnetic property measurement problems. We were working on a project for identifying unexploded ordnances in Hawaii. The challenge is related to the fact that we were looking for metallic object buried in soil with a high iron concentration in Hawaii, i.e., looking for metal buried in metal! This clearly required the development of a highly sophisticated digital signal-processing program to support our ground-penetrating radar measurements and identify parameters such as target resonances, elongation factors, etc. These measurements were also supported with a strong program for the dielectric and magnetic characterization of volcanic soil in Hawaii. What was equally challenging was the requirement to make these measurements *in situ* and without disturbing the soil. It is well known that extracting soil samples complicates these measurements as additional parameters such as packing factor,

density, and moisture content affect these highly sensitive dielectric and magnetic characterization results. We developed and patented a new in-situ measurement procedure [28] that not only provided an invaluable database for these properties but also helped in improving the accuracy and certainly the effectiveness of the ground-penetrating radar measurement procedure. We maintain these material characterization capabilities in our labs as they provide invaluable resources for researchers and support for our ongoing projects.

### 2.2.3 *Computational Electromagnetics*

My interest in computational techniques was intensified when we were developing the multiple spherical function expansions and the overlapping region method to extend the frequency range of the EBCM [10]. During the early 1980s, there was a strong interest in calculating the electromagnetic absorption by human models and in particular in extending the frequency range to and beyond resonant frequencies [13]. Our IEBCM intended to achieve this goal [15]. This calculation technique, still using the multipole expansion method, was then extended to calculate near-field scattering and absorption by biological models [11, 14, 16]. More details about these methods can be found in cited references and Chap. 19 of this book.

In parallel with this early work on quantifying and characterizing absorption characteristics of biological models, we were working on another NIH-funded project for using microwave methods for monitoring changes in lung-water content. With the development and the patenting of a unique electromagnetic coupler [29, 30] that effectively couples EM energy to the human body with minimal external leakage, we were able to conduct successful transmission coefficient experiments on planar phantoms and confirm the validity and sensitivity of using the phase of the microwave transmission coefficient for accurate detection of changes in lung-water content. We then needed to take the study beyond simple planar models of cross sections of the thorax and realized the need to better support the animal experiments with simulation work that takes into account realistic and anatomically accurate cross sections of the thorax. While in the medical library looking at anatomy books and trying to select a suitable thorax cross section for our simulations, one medical doctor told me that we can actually get these cross sections using the new computer-aided tomography (CAT) scans. This was in late 1978, and CAT scans were discovered in 1972. Our collaborating medical team, sure enough, was able to obtain CAT scans relevant to our project, and we hand digitized the cross section and solved the electromagnetic field distribution from an aperture source using the MoM [31] [*A Microwave Method for Estimating Absolute Value of Average Lung Water*, Radio Science, vol. 17, pp. 111S–117S, 1982. Paper was submitted August 7, 1978, and accepted May 1980]. After this initial paper, we [32, 33] as well as others continued to use these anatomically correct cross sections to study electromagnetic interactions with the human body.

Attention was then shifted to the use of 3D modeling to characterize EM interactions with biological models. Initially, the MoM with pulse basis functions was used in these calculations, but after considerable excitement for being able to calculate SAR distribution in the human body and identify possible hot spots, in addition to average SAR calculations, significant concerns were raised regarding accuracy of using pulse basis functions and associated results [34]. As was pointed out by Massoudi et al. [34], field distributions from the MoM with pulse basis function expansions violated establish EM boundary conditions between the mathematical cells representing the dielectric object. This prompted a whole new and continued effort of using advanced basis functions such as rooftop, linear expansion, and basis functions for the unknown fields [35], but this effort suffered from the limitation of requiring excess computation time and hence the inability to model large objects. Reference [35] provides an example where the linear expansion functions were used in the MoM to calculate the internal field distributions of arbitrarily shaped, inhomogeneous dielectric object. The formulation of this approach is based on the traditional use of free-space Green's function integral equation but with 3D linear basis functions being used to describe the field variation within each mathematical cell. Polyhedral volume elements are used to realistically model the scatterer's curvature without using excessive number of unknowns. A new testing procedure, called modified Galerkin's method, was developed and used to help reduce computation time. This modified Galerkin's method basically involved carrying out analytical integration of the weighting functions over a spherical volume inside each mathematical cell instead of numerically integrating over the entire cell. With this reduction in computation time, it was possible to model and accurately calculate internal fields inside realistic models of small animals. The development of modified Galerkin's method, therefore, helped in improving the accuracy of using advanced basis functions; it was not without considerable computational challenges (time and memory resources) that limited results to only electrically small dielectric objects and not for human-sized objects. Regular 3D method of moments solutions with cubical mathematical cells were, however, still useful in designing interstitial antennas and in providing practical assessment regarding the effectiveness of using this type of antenna designs [36] in the microwave hypothermia treatment of deep-seated cancer tumors [37].

It became clear, at this point, that an alternative approach was needed to help with accurate determination of field distribution in full-size human models and in particular at some experimentally identified locations in the human body where fields tend to concentrate and hence could pose EM health hazards. With the growing interest in the FDTD method, our team took on the task of developing a multigrid FDTD method [38, 39]. Two papers on the development of the multigrid FDTD method were published by White et al. [38]. Besides the basic development of the multigrid code, the method was applied to calculate EM power distribution in large microwave and radio frequency (RF) engineering systems including commercial systems used in drying and sintering of ceramics. Results were reported for fine to coarse mesh cell dimension ratios up to 11



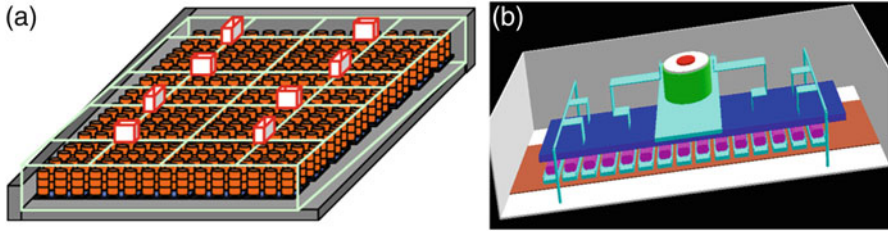


**Fig. 2.13** Microwave kiln and RF dryer sintering and drying honeycomb ceramics at Corning

and saving in computation times up to 80x [39]. In simulating commercial RF ceramic sintering and drying systems, such as those shown in Fig. 2.13, it was necessary to accurately model and determine EM power deposition in delicate honeycomb ceramic ware, while they were being processed in electrically very large production environments. The multigrid FDTD solution provided invaluable results that lead to significant advances in designing and using these large production systems. Additional simulation work by Yun et al. actually leads to the discovery of a new distributed source microwave system for sintering of ceramics that was patented by Corning Inc. [40]. The research support from Corning Inc. continued for over 11 years, and besides publications and graduate research opportunities for our students, it provided researchers and production colleagues at Corning with significant insight into the RF and microwave drying and sintering processes and certainly saved the corporation millions of dollars by improving efficiency and maximizing production quality of its environmental (honeycomb) products [41].

The same multigrid code was also used to evaluate biological effects of cell phones and calculated SAR values in human heads. In this case our team was particularly interested in examining the validity of assessing the biological effects associated with cell phones based on carrying out simulations and even measurements that used an isolated head and neck model [42]. Examination of available data from this earlier simulation work showed that hot spots exist in the neck area, and this suggested that the rest of the body (not included in these simulations) could have significant effect on the level of field intensities in this neck area and possibly throughout the head. The availability of the multigrid FDTD code came to the rescue, and we were able to simulate “human body effects on the microwave absorption in the human head exposed to radiation from handheld devices” [43]. In this case, an anatomically detailed head model (with the eyes, eyeballs, brain, bone, and skin) was included in the fine grid region of the FDTD method, and a coarse FDTD mesh was used to represent the rest of the body as shown in Fig. 2.14 [43]. Results in Fig. 2.15 and Table 2.1 show significant differences (40–50%) in SAR values due to body effects, depending on the separation distance between the phone and the head. What was particularly gratifying is what I saw during a visit to one of the research labs in Taiwan. The researcher was illustrating their new experimental setup for measuring SAR due to cell-phone exposures. He showed

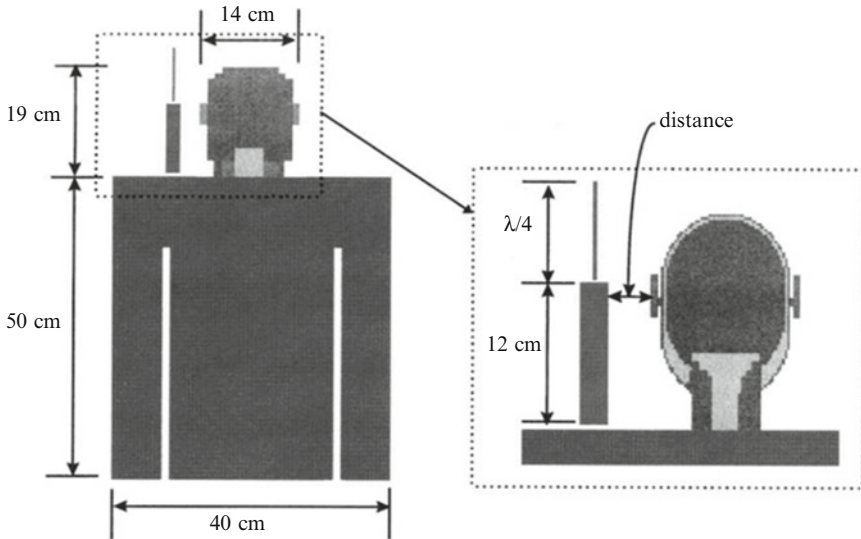


Fig. 2.14 FDTD regions in the multigrad FDTD simulations [43]

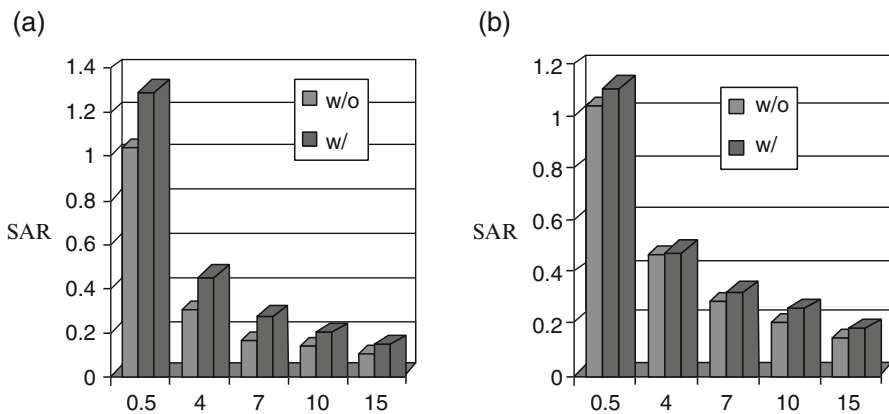


Fig. 2.15 SAR results in human head (a) 900 MHz, (b) 1900 MHz [43]

me the experimental model which included a head attached to the human torso and emphasized that, unlike their earlier work with isolated head only, taking the effect of the human body into account is an important consideration for success.

The other significant contribution that our team made in the area of computational techniques is related to the development of a 3D dynamic model of a human thorax with two RF sensors placed on the chest as in the case of Cardio-Pulmonary Stethoscope (CPS) measurements [44]. The simulation procedure is based on the 3D model using Ansys<sup>®</sup> finite-element high-frequency structure simulator (HFSS) code together with the 3D tissue model of the thorax that is approved by the US Food

**Table 2.1** Total SAR in the human brain, vertical monopole, and vertical polarization [43]

Distance (cm)	Frequency					
	900 MHz			1900 MHz		
	w/o	w/	Increase (%)	w/o	w/	Increase (%)
0.5	1.04	1.29	24	1.03	1.12	8.7
4.0	0.30	0.46	53	0.45	0.48	6.7
7.0	0.17	0.24	41	0.28	0.30	7.1
10.0	0.13	0.16	23	0.18	0.21	17
15.0	0.099	0.12	21	0.11	0.136	24

and Drug Administration (FDA) for simulations related to RF safety compliance. In addition to the use of tetrahedral elements (over half a million tetrahedral) in the finite element method (FEM) and adaptive meshing techniques that significantly helped in improving accuracy of the electromagnetic field calculations, our team adapted a dynamic model that accounted for breathing in the thorax and for varying heart rates. The original objective was to develop such a model to a high level of sophistication so as to be able to model physiological and anatomical changes (e.g., size and shape of the heart, rate of heartbeats, locations and distribution of water in the lungs, etc.) associated with heart failure and pulmonary diseases. While this initial big objective has been difficult to achieve because of lack of physiological data that could support the simulation, the model and obtained simulation results provided very useful data that guided additional development in the CPS technology. This includes the observation that the use of multiple sensors in CPS measurements could lead to the determination of the status of the lung-water content. Therefore, besides the changes in lung-water content which is routinely being monitored using the CPS system, simulation results showed that it is possible to measure the status of lung water (increase or decrease) by measuring the magnitude in addition to phase of the scattering parameters and using one of the multisensor set that has clear view of the lung.

Figure 2.16 illustrates an example of the placements of RF sensors on the human thorax in a simulated multisensor CPS system. Each of the 10 sensors in this figure has an identifiable placement on the thorax. The placements of the ten sensors are shown by anterior, posterior, left lateral, top, and 45° anterior-lateral views of the thorax. As may be seen, a horizontal row of the sensors (1–8) is included, of which three sensors (1–3) are anteriorly located, three (4–6) are laterally located, and two (7–8) are posteriorly located. In addition to the horizontal row of sensors, one sensor (9) is shown located near the lower extent of the lung, and another sensor (10) is shown located near the heart. Figure 2.15 illustrates the case with a ten-sensor arrangement to help cross-examine a variety of output data and fully explore benefits from using the multisensor CPS system. Depending on application and need for data to complement clinical observations, the use of a fewer sensors is possible

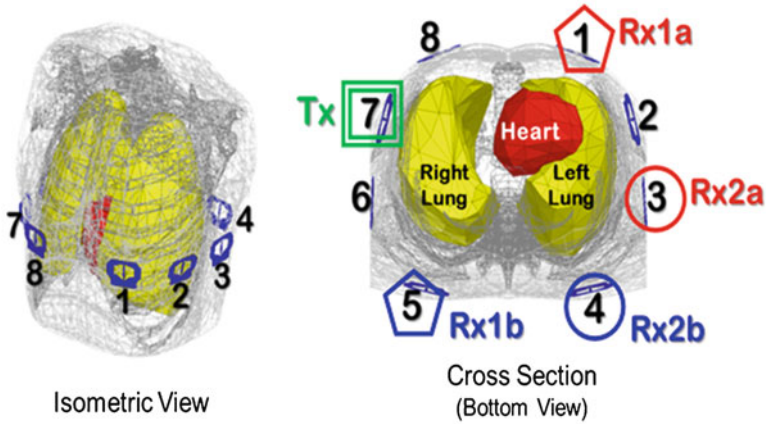


**Fig. 2.16** Finite-element model of a human thorax and illustration of relative placement of sensors around the chest

and clinically preferable in a typical CPS measurement. In these simulations, fluid accumulation in lungs was modeled by adjusting the fractional volume of edema (i.e., replacing air with water in a region of lung tissue) from 15% to 45%. RF sensors were assumed to operate at 915 MHz. Based on the sensor placements illustrated in Fig. 2.16, it may be noted that sensors 5–8 are shown to have the most unobstructed “views” of the lung and can, therefore, provide the magnitude of the scattering parameter which accurately reflects the amount of water content in the lung. Detailed discussion of these results is given in Chap. 18.

Simulation results also showed that the phase changes are larger (number of degrees per change in water content) than the changes in the magnitude (in dB). This means that the phase is more sensitive to changes in lung water, as indicated and well documented from our earlier studies and validation with animal experiments. The magnitude measurements using the multisensor CPS system will be used not only to measure changes but also to assess status (indicate increase or decrease in lung water) of lung-water content. Results from Table 2.2 clearly demonstrate this effect and were actually used as the basis for filing for a new patent application for using the CP Stethoscope measurements not only for measuring changes in lung-water content but also for assessing if such change is associated with an increase or decrease of water in the lungs.

Results from Table 2.2 were used as the basis for submitting our recent patent application [45]. The highlighted cells in Table 2.2 indicate the cross sensor  $S_{21}$  scattering coefficient calculations with magnitude values correlating well (increased attenuation) with the increase in lung-water content, regardless of the direction in the phase change (positive or negative). As will be noted by comparing these sensor numbers with their locations in Fig. 2.16, these highlighted values are obtained from sensors with clear views of the lung across the thorax. Our team is presently working on improving the 3D modeling and simulation capabilities so as to achieve the set goal of developing a fully dynamic model that is sufficiently accurate

**Table 2.2** Three-dimensional simulation results of a complete scan of the scattering coefficient (magnitude and phase results) across pairs of the ten RF sensors

$\Delta$	2		3		4		5		6		7		8		9		10				
	Mag	Phase	Mag	Phase	S	Mag	Phase	Mag	Phase	Mag	Phase	Mag	Phase	Mag	Phase	Mag	Phase	Mag	Phase		
1	-0.14	-1.4	8.23	-16.7	-9.97	-56.8	3.52	-71.3	-14.53	-253.4	13.42	-75.5	-14.75	-96.7	18.77	18.77	-138.8	-2.36	-58.4	-0.65	-15.5
2	8.23	-16.7	0.13	0.7	9.28	28	-7.24	4.4	-3.88	-41	13.29	-227.3	11.71	-273.8	7.3	-318.7	-4.72	7.5	3.91	-52	
3	-9.97	-56.8	9.28	28	0.16	-1.2	-5.89	44.1	8.45	-84.7	-8.15	26.7	11.67	-250.6	-6.86	-288.9	-0.56	-4.2	-4.62	18.8	
4	3.52	-71.3	-7.24	4.4	-5.89	44.1	0.14	0.7	2.55	14.8	-5.66	-20.1	-3.79	-46.7	-5.16	-159.6	-5.42	-10.3	-6.3	7.8	
5	-14.53	-253.4	-3.88	-41	8.45	-84.7	2.55	14.8	-0.16	-0.9	-0.88	-6.2	-2.56	45.8	-1.54	-33.8	-3.88	-58.9	-1.46	-40.7	
6	13.42	-75.5	13.29	-227.3	-8.15	26.7	-5.66	-20.1	-0.88	-6.2	0.09	-1.1	-0.95	3.2	-2.43	43.4	11.33	-187.1	-20.31	-91.4	
7	-14.75	-96.7	11.71	-273.8	11.67	-250.6	-3.79	-46.7	-2.56	45.8	-0.95	3.2	0.1	1.1	-0.33	-6.3	1.84	-32.1	-6.54	38.9	
8	18.77	-138.8	7.3	-318.7	-6.86	-288.9	-5.16	-159.6	-1.54	-33.8	-2.43	43.4	-0.33	-6.3	-0.13	1.5	3.91	29.5	-8.13	53.9	
9	-2.36	-58.4	-4.72	7.5	-0.56	-4.2	-5.42	-10.3	-3.88	-58.9	11.33	-187.1	1.84	-32.1	3.91	29.5	0.18	1.8	2.26	-17.1	
10	-0.65	-15.5	3.91	-52	-4.62	18.8	-6.3	7.8	-1.46	-40.7	-20.31	-91.4	-6.54	38.9	-8.13	53.9	2.26	-17.1	0.09	0.4	

S,S indicates cross sensor transmission coefficient

for analyzing the CPS waveforms as well as for providing detailed physiological features associated with cardiopulmonary disease [46].

### ***2.2.4 Propagation Modeling***

Our team started working on propagation modeling right after I returned from the assignment at NSF in 1999, and we took up the task of developing a computationally efficient ray-tracing approach that is particularly suitable for modeling propagation in urban environments. For these environments, not only did higher-order diffraction terms from corners and sharp edges needed to be taken into account, but it was equally important to find ways and means to eliminate the search algorithms which are used in ray-tracing codes to determine which walls and structures are to be considered for reflection and transmission coefficient calculations. The goal of eliminating the need for search algorithms was achieved when we developed two computer graphic-based procedures for propagation modeling [47, 48]. These approaches are based on digitizing the propagation domain and the use of simple but innovative procedures for determining the ray path and if reflection and/or transmission coefficient calculations are needed. The first approach utilizes rectangular cell and a coding procedure for all cells in the digitized propagation environment [47]. Reflection/transmission coefficients are calculated only when the ray path crosses cells of different codes, thus suggesting change in the propagation environment. The other approach utilized triangle cell in 2D and tetrahedral cells in 3D and relies on a simple calculation of the vector product of two vectors to determine if reflection and transmission parameters need to be calculated [48, 49]. These approaches were evaluated in indoor [50] and outdoor [47] environments. In the specific examples when accuracy of ray-tracing results was validated by comparing with experimental measurements [50, 51], a 40-fold improvement in computational efficiency was reported. At this point, our team received significant funding from NSF and the Army Research Office to study the indoor/outdoor propagation characteristics. For these studies, we used hybrid FDTD and ray-tracing calculations and specifically examined propagation through walls of complex structures and also transmission through windows and metal-framed structures [52, 53]. For complex walls, using the hybrid FDTD and ray-tracing approach, it was shown that the equivalent dielectric constant approach does not provide accurate results particularly when the complex walls involve metal-reinforced concrete structures [52]. In this case, it was shown that the presence of metal rods and with certain spacing between rods may cause resonance effects at certain frequencies, and in fact significant RF transmission could be encountered even through thick concrete walls separating rooms in an indoor propagation environment. This observation was confirmed when conversations were heard across rooms during the Iraq War and when colleagues from Verizon, Inc., indicated experiencing similar observations in some of their field tests.

As for indoor/outdoor modeling of windows and metal-framed structures, our team adopted once again a hybrid FDTD and ray-tracing approach to account for the diffraction effects [53]. Specifically, windows and metal-framed structures were modeled using FDTD, and the resulting radiation pattern was modeled (magnitude and phase) in terms of a large number of rays representing the radiation pattern. This ray representation was then integrated in a regular ray-tracing algorithm for indoor/outdoor propagation modeling in an urban environment. The obtained results were further experimentally confirmed as may be noted in Fig. 2.17 [53]. Clearly, extensive analysis and trade-off studies were conducted to determine the minimum number of rays that is required to represent the resulting diffraction patterns. Furthermore, these studies clearly demonstrated the significant errors that may be encountered when windows were assumed sufficiently large so as to neglect these diffraction effects. Similar to the case of complex walls, window- and metal-framed structure models need to be included in fully developed propagation models that accurately calculate indoor/outdoor propagation and path-loss effects in wireless communication environments.

A new phase of propagation modeling capability emerged when our team decided to use geospatial resources such as Google Earth™ to model propagation characteristics in urban environments [54, 55]. In one of the earlier papers in this area, our team used projective geometry to extract 3D buildings from Google Earth™. This was an important step in developing accurate propagation models taking into account building heights as well as effects of transmitters, heights, and placement arrangements in an urban propagation environment. A summary of much of this work is described in Dr. Yun's recent paper [56] and is also included in Chaps. 12 and 13 of this book. As an example of our recent work in this area, we examined the validity of empirical models (e.g., Hata models) in large urban environments and developed new loss exponent indices for different urban environments, including New York City, Chicago, and also Salt Lake City to account for the presence of mountain ranges [57]. Specifically, a three-dimensional ray-tracing method is used to propose modifications for the Hata model and obtain accurate estimation in large urban cities. The mean propagation path loss and the loss exponent  $n$  values are calculated as a function of length of street, number of side streets, transmitting antenna heights, and in the presence of unique site topologies such as mountainous. It is shown that for large cities and transmitters higher than any building,  $n$  values similar to those of free space propagation may be used for estimating path loss. For transmitters at heights lower than most of the buildings and for streets further away from transmitters,  $n$  values that are three times larger than those from the Hata model are required for accurate path loss estimation. It was shown that reflections from mountains may have minimal effects except when transmitters are placed on them and for routes near or along these mountains. The new propagation models include parameterization that would enable fast local calculations in defined categories of the propagation environment which leads to estimating path loss in streets near or further away from transmitters [57]. Figure 2.18 shows an example of the simulation models used in New York City, and Tables 2.3 and 2.4 show results of path-loss indices together with comparison with those

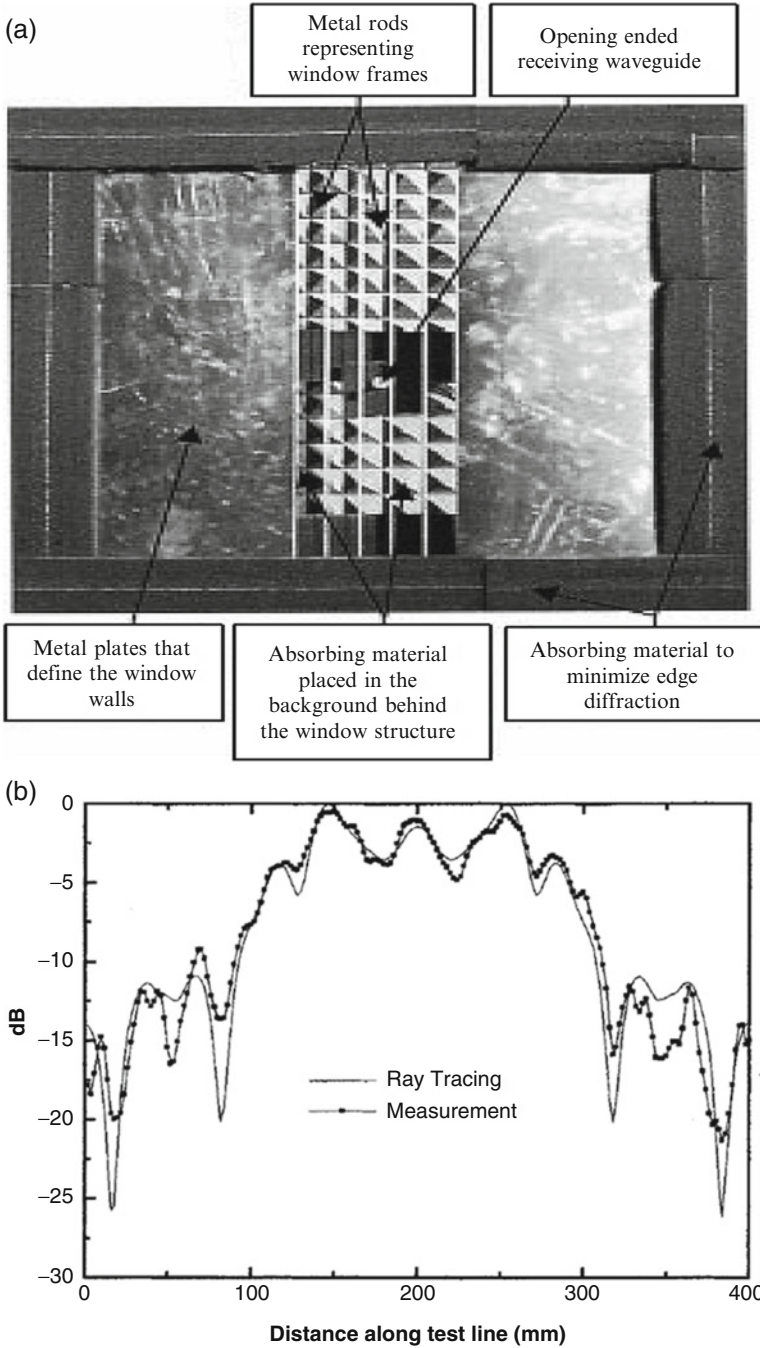


**Fig. 2.17** (a) Photograph of window structure scale model. (b) Comparison of measurement and ray tracing results [53]



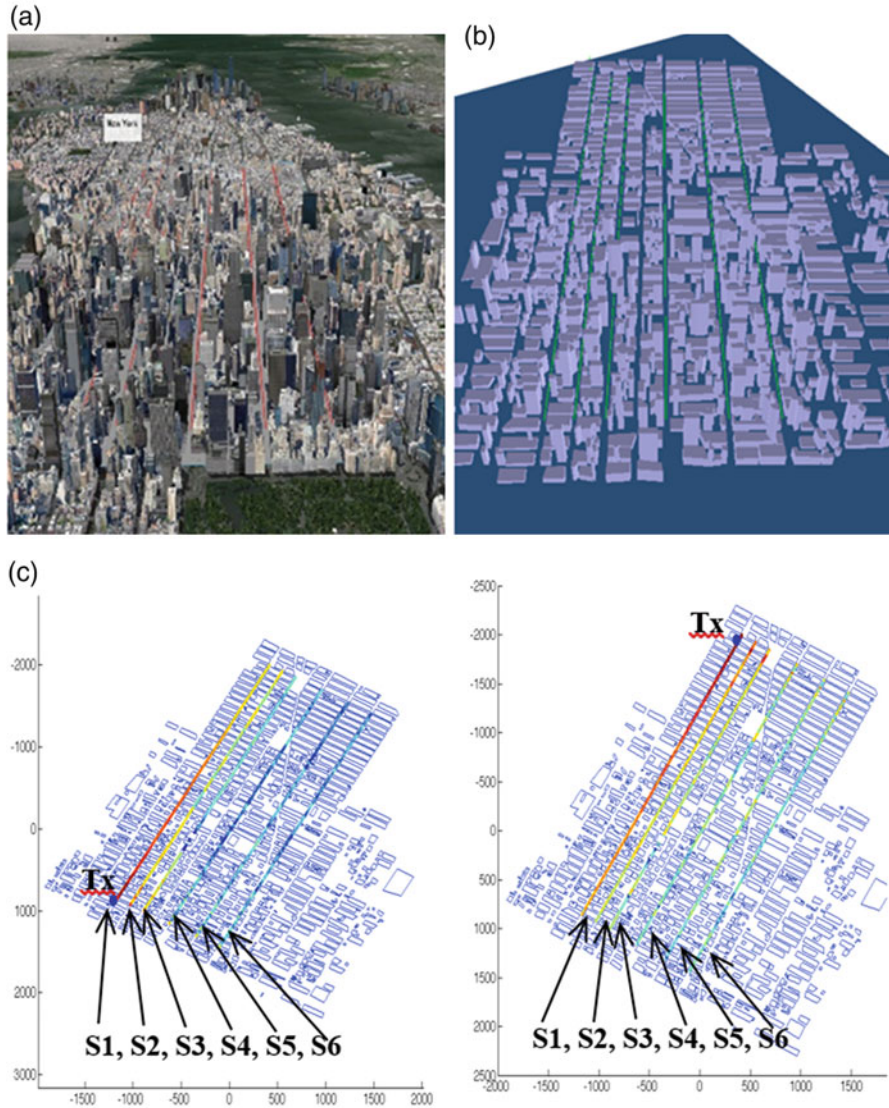


**Fig. 2.18** Modeled blocks in New York City, (a) Google Earth™ view, (b) constructed 3D models, and (c) modeled streets for two scenarios of the transmitter locations [57]

available from the Hata model. In Tables 2.3 and 2.4, S1 to S6 represent marked streets parallel to the transmitter, with S1 the closest and S6 the farthest.

General observations from these simulations show that the path-loss index  $n$  values are near those of free space propagation when transmitter heights are higher than any of the building, while  $n$  values as large as three times estimated

**Table 2.3**  $n$  values for different transmitter heights along six streets in New York, Scenario I [57]

Tx Height (m)	S1	S2	S3	S4	S5	S6	Hata
40	3.10	3.08	5.50	5.38	2.04	6.31	3.44
	3.03	2.80	4.02	4.05	1.06	6.02	
100	4.53	3.41	6.92	7.55	5.77	9.97	3.18
	4.67	1.78	5.70	5.92	5.35	9.43	
160	2.82	3.79	6.72	7.71	7.98	9.67	3.05
	2.71	3.36	5.82	6.08	8.18	9.62	
220	1.82	2.79	5.14	6.74	1.43	7.68	2.96
	1.77	2.55	4.26	5.33	0.50	7.86	
280	1.49	2.49	4.91	5.17	2.06	6.49	2.89
	1.58	2.66	4.14	4.66	1.57	6.13	

**Table 2.4**  $n$  values for different transmitter heights along six streets in New York, Scenario II [57]

Tx Height (m)	S1	S2	S3	S4	S5	S6	Hata
40	3.30	3.08	3.30	1.43	1.32	8.87	3.44
	3.45	2.93	2.42	0.47	0.96	8.71	
100	1.65	3.03	3.94	1.67	6.00	14.9	3.18
	1.85	3.18	3.18	1.22	5.30	14.5	
160	1.82	2.61	4.07	2.12	6.51	9.80	3.05
	1.93	2.80	4.13	1.45	4.89	9.11	
220	1.66	2.20	0.74	3.83	2.84	9.55	2.96
	1.73	2.54	0.10	3.32	2.25	8.61	
280	1.38	2.36	0.79	3.81	3.73	8.99	2.89
	1.45	2.37	0.40	2.84	2.71	7.54	

values based on the Hata model need to be used when transmitter heights are lower than most of the buildings and/or for streets that are further away from the transmitters. Furthermore, results from modeling cities with large mountains such as Salt Lake City showed that effects of mountains on estimated path-loss values are negligible when transmitters are placed on buildings near (but not too close) to the mountains, and relatively larger values of  $n$  will be needed to calculate path loss when transmitters are placed on the mountains and in particular (factor of 2 compared to the Hata model) on streets and routes near or along these mountains.

More recent research is using machine learning together with geospatial resources to enable propagation modeling for accurate determination of source location [58].

### 2.2.5 *Antennas and Antenna Array Research*

As we are doing research in electromagnetics and being involved in a variety of applications, antenna and antenna array designs are a natural part of our research portfolio. As part of my PhD dissertation, I worked on new field coupling between sectoral horn antennas, again with focus on Green's function formulation and the use of the method of overlapping regions to iteratively solve the resulting coupled integral equations [7]. In the medical application area, we developed and patented a unique electromagnetic energy coupler to human tissue and with minimal leakage around the body [59]. An interesting paper in which we described an analytical technique for characterizing the coupling characteristics of a coplanar waveguide to lossy dielectric layer was published in 1986 [60]. It was shown that with contact with lossy dielectric materials, additional electric field components are excited in the lossy dielectric, thus facilitating the strong coupling at area of contact with the body (e.g., chest) and with minimal leakage around the body [59, 60].

Research focus during the 1980s and 1990s was on computational techniques, modeling and simulation of RF drying, and calculation of optical scattering by aerosol particles and agglomerate chains, as described in earlier sections. In the late 1990s, we were introduced to the continuous transverse stub (CTS) technology developed by Hughes Aircraft and were in particular interested in developing a tunable version of this technology using layers of ferroelectric materials [61]. The use of ferroelectric material for developing tunable devices such as phase shifters was gaining attention at that time. The reason for this was simply to take advantage of the recent advances in developing ferroelectric materials with high tunability and less loss tangent. So with funding from the ARL, we pursued the idea of developing tunable CTS antenna arrays with beam-steering capabilities. After significant simulation effort, however, we determined that such an effort while academically interesting is practically limited due to the high ohmic losses associated with such arrangements [62]. It was, however, interesting to see that advances in this technology are not particularly related to the quality of the ferroelectric materials but instead to the ohmic losses as high values of the dielectric constant of ferroelectric materials (particularly those with high tenability) tend to reduce the input impedance of the RF devices and result in significant, and in many cases, very high values of ohmic losses.

Working with CTS antenna array designs, however, was inspiring in a different way. Our team identified a need to extend this technology to lower-frequency applications, and to this end, we invented and patented two new versions of the CTS technology including the coplanar waveguide and the coaxial transmission line versions of CTS [63, 64]. These new designs were not only simulated but were indeed built and tested in our labs [65–67]. Wayne Kim in his PhD dissertation studied the development of a new version of ferroelectric-loaded coplanar waveguide CTS array, and in addition to loading the array with ferroelectric layer to facilitate tenability and provide beam-steering capability, it was suggested that a thin layer of

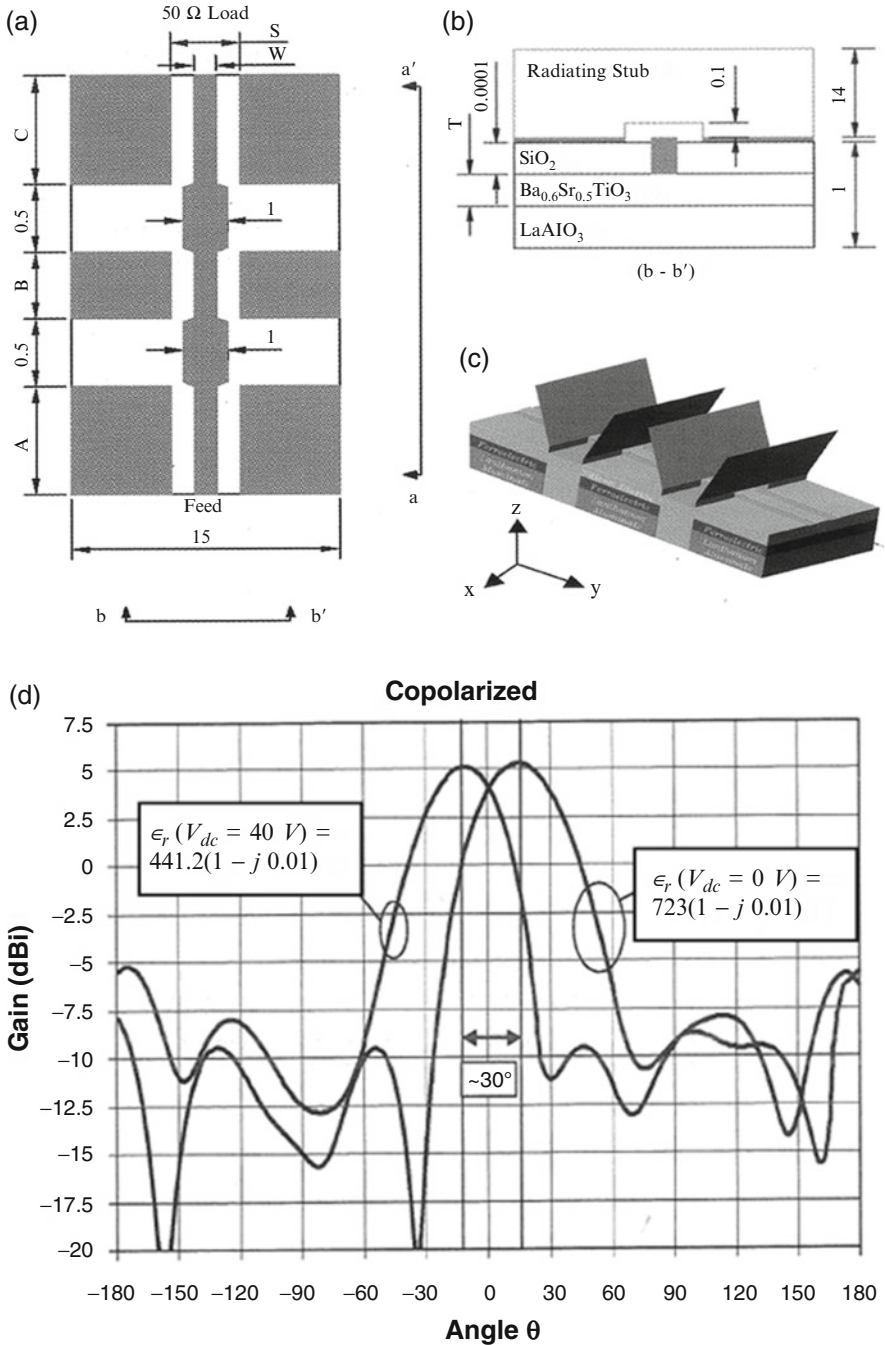
polymer or semiconducting material be inserted between the ferroelectric material and the coplanar waveguide conductors to minimize the ohmic losses [68].

Figure 2.19 shows a possible implementation of the design and example of the simulation results [68]. The figure shows that such an arrangement would indeed result in reducing the overall losses in the structure, but fabrication wise, it is very challenging. Even after having an opportunity to further develop this coplanar waveguide array under an ONR grant, the achieved tenability was modest ( $27^\circ$  max) with gain loss of about 2.5 dB. The fabrication process was also unpredictable, required many trial-and-error fabrications, and also required detailed testing using outside testing facilities to help optimize the material properties. Instead of ferroelectric materials, our team, later on, used lumped-element metamaterials to design a coplanar waveguide-based CTS array with beam-steering capabilities [69]. Figure 2.20 shows the fabricated coplanar waveguide CTS array with achieved simulation and experimental results [69].

With a 2-year grant from Raytheon, Inc., we were asked to develop a perfect magnetic conductor (PMC) ground plane to provide unidirectional radiation from their newly developed ultra-wideband long-slot antenna array [70]. This was the PhD dissertation project for Dr. Jodie Bell who used a hybrid ground plane design approach to meet this ultra-wideband requirement [71, 72]. More about this design is discussed in Sect. 2.2.6, but it is important to mention that this contract from Raytheon helped us get more involved in the long-slot antenna array designs and resulted in new innovations including the cylindrical implementation for omnidirectional applications and the dual polarization designs [73, 74]. An improved simplified input impedance design and impedance transformer circuit were achieved as part of this work [75].

An example of dual polarization antenna arrays is shown in Fig. 2.21, together with simulation and experimental results [75]. In this  $4 \times 8$  dual polarization long-slot antenna array design, slots were introduced on the conducting patches to increase the fringing capacitance and hence facilitate simplified input impedance feed using a 60 ohm microstrip line. Figure 2.21 shows more details of the design parameters and the simplified microstrip line feed. The  $4 \times 8$  long-slot dual polarization antenna array was also fed by a compact Butler matrix design [76], and performance was compared with that of a  $4 \times 8$  dual polarization stacked microstrip antenna array [77]. Figure 2.22 shows results for these beam-steering measurements for both the antenna arrays. It should be mentioned that much of these designs and fabrication effort were done with funding from CERDEC and will be included as part of Mr. Gui Chao Huang's soon-to-be defended PhD dissertation (also see Chap. 5).

As may be noted from the prior sections, the reported beam-steering capabilities were achieved using new  $4 \times 8$  Butler matrix design [77]. In this design, crossed coplanar waveguide designs were used to help reduce size and improve performance of the Butler matrix. Our team was also involved in developing innovative digital beamforming approach, the hybrid smart antenna system [78]. Based on initial simulations, it was shown that by using directional antenna elements, it is possible to use only one third of the receiving elements in an array and still not only have



**Fig. 2.19** (a) Coplanar waveguide CTS phased antenna array; (a) top view illustrating ferroelectric free region between the radiating stubs; (b) front view illustrating the use of via through the polymer layer for biasing the ferroelectric layer; (c) perspective view, all dimensions in mm, and conductor thickness is 1.5  $\mu\text{m}$ ; and (d) radiation pattern at 10 GHz, showing beam steering without gain loss [68]

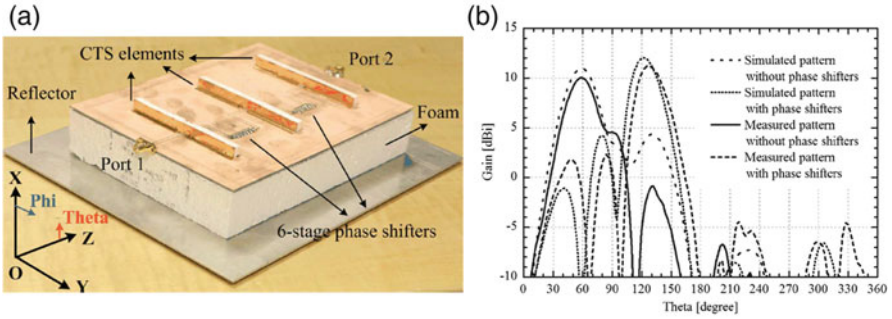


**Fig. 2.20** (a) Photograph of three-element coplanar waveguide CTS antenna array with lumped element phase shifter. (b) Results of simulation and measurements of co-polarization E-plane radiation pattern at 2.4 GHz [69]

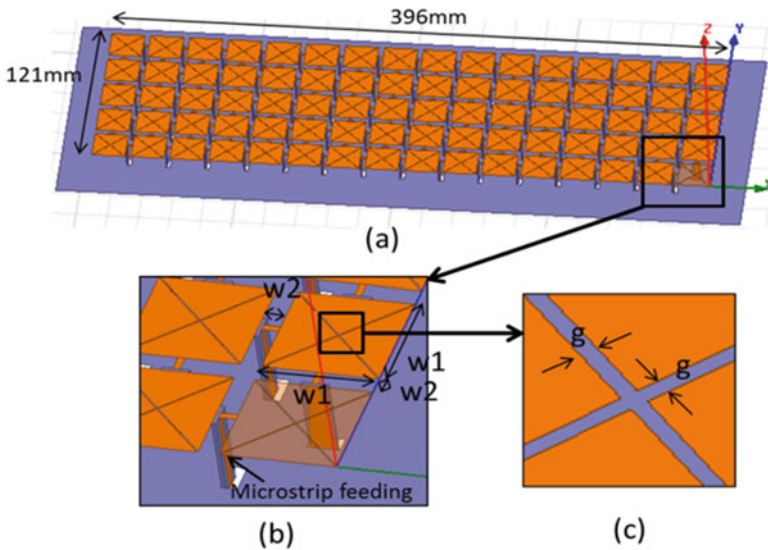


**Fig. 2.21** The  $4 \times 8$  long-slot antenna array design and results. (a) Dimension of the overall antenna; (b) metallic patch width ( $w1$ ) and slot width ( $w2$ ); (c) small slot width,  $g$  on each metallic patch; (d) measured radiation pattern in the  $x$ - $z$  plane in vertical excitation mode; and (e) horizontal excitation mode [75]

active directionality but also obtain similar values of the bit-error rate (BER) [78, 79]. Clearly with fewer elements, there will be broader beam width and reduced gains, but the fact that directionality and similar BER values could be achieved at lower cost (fewer receiving electronic components) was exciting. Dr. Celik for his PhD dissertation constructed an  $8 \times 8$  prototype and experimentally validated this observation [80]. Furthermore, and while attempting to extend these observations and build a prototype system for digital TV (DTV) operation at 60 GHz, he realized

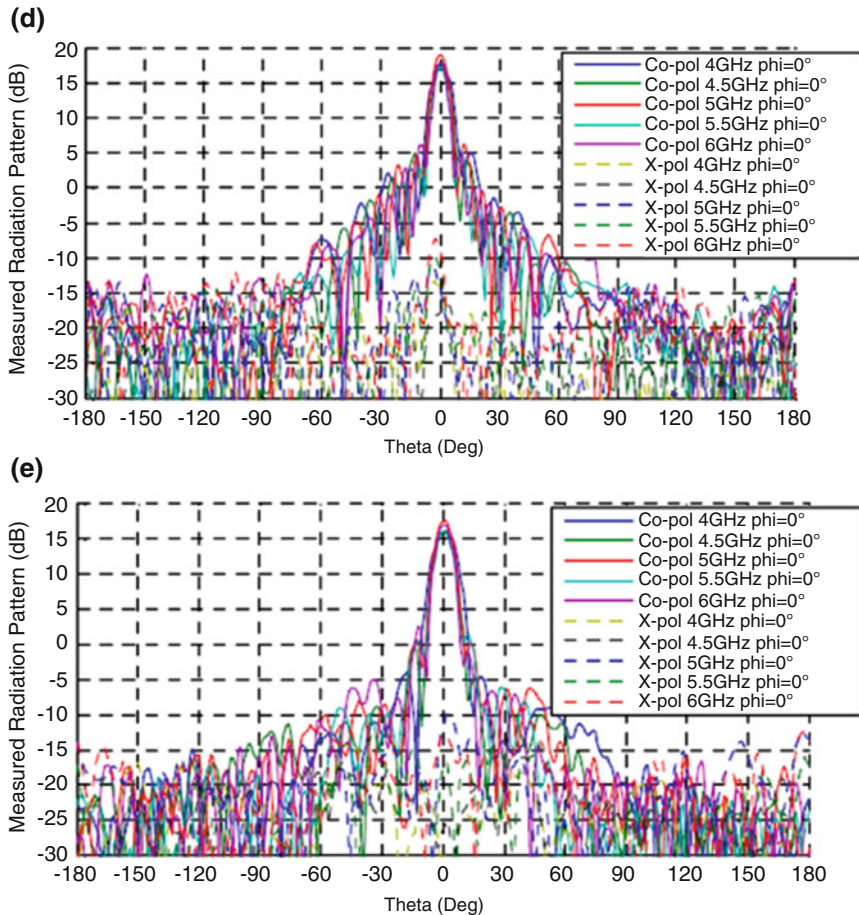
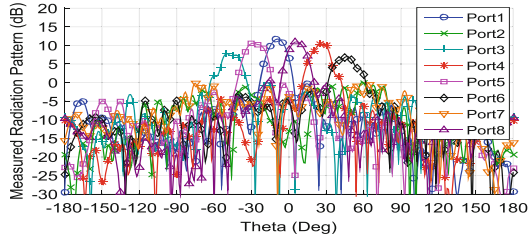
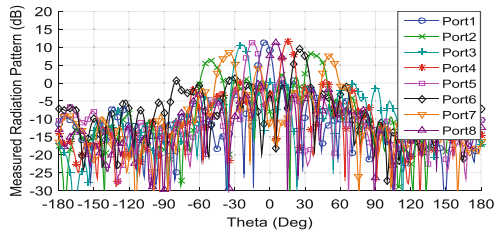


**Fig. 2.21** (continued)

that it is necessary to extend the principle of pattern multiplication to near-field sources [81]. For such a case, it is necessary to take into account directions of rays and further account for the tilt angle of the 60 GHz sources to provide radiation pattern overlap and hence beamforming capabilities [80]. These initial digital beamforming capabilities and prototype system are now being expanded to include transmission channels and develop a fully operational multiple-input multiple-output (MIMO) system for directional networking communication systems. An overview of this work is described in Chap. 4 of this book. Before concluding this antenna section, I would like to also mention the high-frequency (HF) antenna development effort which was part of Dr. James Baker's PhD dissertation. As a part of a broader Department of Homeland Security-funded project, the National Center for Island, Maritime and Extreme Environment Security (CIMES), our team



(a)



(b)

	Long Slot Antenna Array	Stacked Patch Antenna Array
Frequency (GHz)	4-6	4.5-5
Gain (dB)	17	18
Axial Ratio (dB)	< 1.8	< 1
3dB Beam width (deg.)	15	10
Dimension (mm)	250x156x12	355x189x3.8

(c)

**Fig. 2.22** (a) Fabricated  $4 \times 8$  dual polarization long-slot antenna array and measured radiation pattern with beam-steering capability, (b) fabricated  $4 \times 8$  dual polarization stacked patch antenna array and measured radiation pattern with beam-steering capability, and (c) performance comparison [77]

was tasked with the development of a compact high-frequency (HF) antenna system with advanced capabilities [82]. The requirements included small size for portable and fast deployment operations, light weight, suitability for operation on floating platforms and in arctic environments, and the ability to operate over multiple frequencies in the HF band. An example of the developed antenna design is shown in Fig. 2.23 together with results from its simulation and experimental characterization [83, 84]. As may be seen from Fig. 2.23, multiple resonances were achieved in a compact wire antenna design that is 0.85 m high and has 1.2 m diameter. Detailed discussion of these antenna designs and measurements is included in Chap. 6.

Besides the abovementioned examples of our antenna work, it is important to acknowledge the extensive antenna design work by Dr. Dalia Elsheikh which focused on broadband and miniaturization for biomedical applications [85, 86]. The innovative and productive collaborative work with colleagues at Tsinghua University in China has also been a source for inspiration [87, 88]. Some of this work is also presented in Chap. 9 of this book.



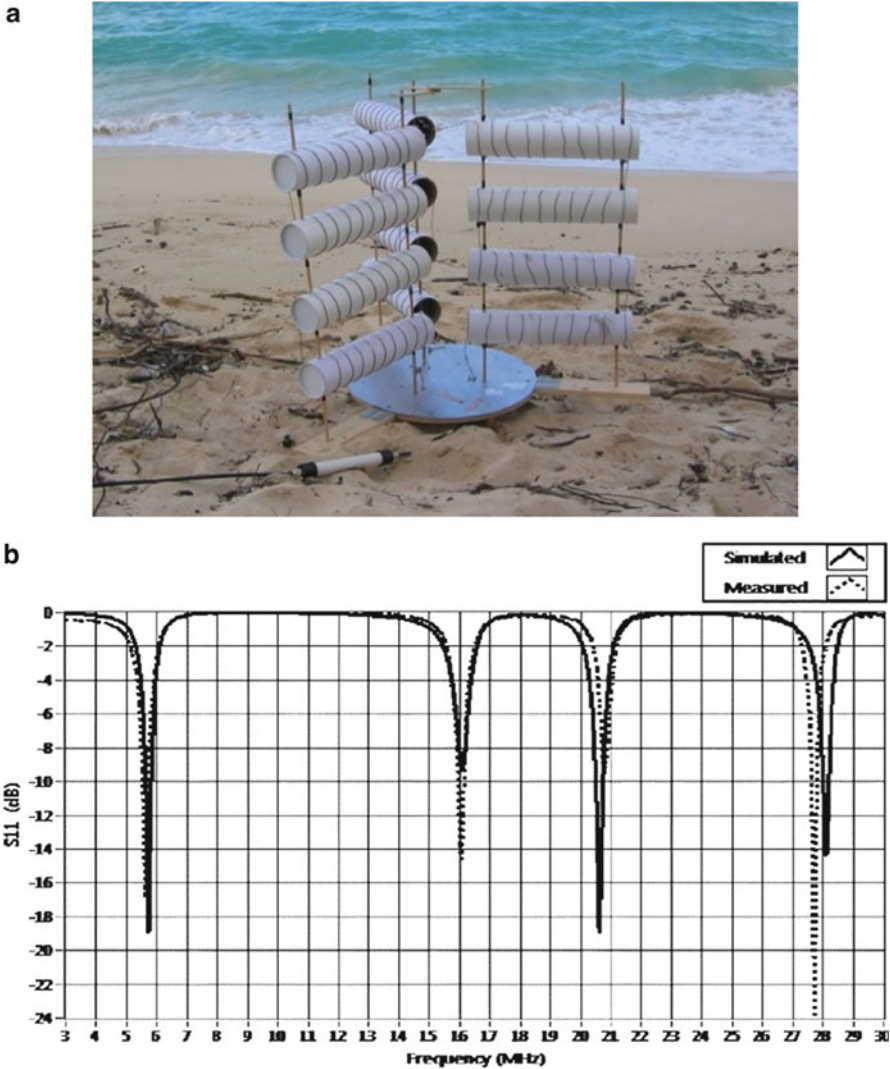


Fig. 2.23 (a) Prototype compact HF antenna and (b) comparison of the simulated and measured reflection coefficients of the compact HF antenna [82, 83]

### 2.2.6 Metamaterial Research

Our team started working on metamaterials when we were tasked by Raytheon, Inc., to develop an ultra-wideband perfect magnetic conducting plane to use with their new ultra-wideband long-slot antenna (LSA) array. The developed LSA had a bandwidth of over 100:1, and what makes this task particularly challenging is the fact that that band starts at 100 MHz [71, 72]. Metamaterials are known for

enabling narrowband designs, and a review of available literature shows that most of the available designs are in the GHz frequency band. To help with achieving the set goal, Jodie Bell in his PhD dissertation explored the development of a hybrid PMC plane that combines ferrite slab to satisfy the PMC design requirement at lower frequencies and a regular mushroom-type PMC design to meet the design requirements at higher frequencies [70]. It was suggested that the magnetic properties of the ferrite slab will continue to decrease at higher frequencies, the effect of the mushroom PMC will start to take effect at higher frequencies, and the overall hybrid structure will satisfy the ultra-wideband requirements. This prediction actually turned out to be true, and what was particularly interesting is that the overall design covered the desired band without frequency gaps [89]. Figure 2.24 shows a schematic of the hybrid PMC ground plane together with simulation results [70]. In particular, it is shown that while the mushroom structure was designed to operate around 3.7 GHz, it influenced results at lower frequencies and provided continued PMC performance starting at about 2.5 GHz all the way to 4.86 GHz [70, 89]. These simulation results were also confirmed experimentally where a prototype of the hybrid PMC was built and tested in a specially designed rectangular TEM cell. The experimental procedure and results are described in several publications by our group [89, 90].

The fact that ultra-wideband performance was achieved using the lossy characteristics at lower frequencies, hence having more loss when used in combination with radiating elements, was unsatisfactory, and our team continued to search for ways and means to design ultra-wideband PMC planes. At that time, we were working on developing reliable procedures for detecting and classifying unexploded ordnates (UXOs), and we noted the superior detection accuracy achieved using genetic programming as compared with neural network approaches [91]. The use of genetic programming (GP) for designing ultra-wideband PMC became the PhD dissertation topic for Dr. Jennifer Rayno who published and presented several papers on this topic [92, 93]. The presence of multitude of possible 3D metamaterial design topologies in 3D space leads to significant complexities in the design process and makes it infeasible to explore this 3D design space manually. A possible solution appeared to be to specify some fundamental building blocks to help create 3D metamaterial designs and let an evolutionary process automatically build and change the designs over time such that the end result meets the design requirements. This is exactly what GP does, and as such, it was used for developing these broadband metamaterial designs [91].

In GP, the solution is represented as a computer program (tree-based data structure), and in the case where GP is being used to build a structure (e.g., a metamaterial unit cell), running the program generates the topology with optimized performance. It is to be noted that GP is different from genetic algorithms (GA) which are often used to optimize parameters in a given design so as to meet set specifications. Through our NSF-funded GP research, we focused on developing GP algorithms for designing challenging broadband PMC metamaterial ground plane at a challenging lower frequency, a few hundreds of MHz. Through true 3D

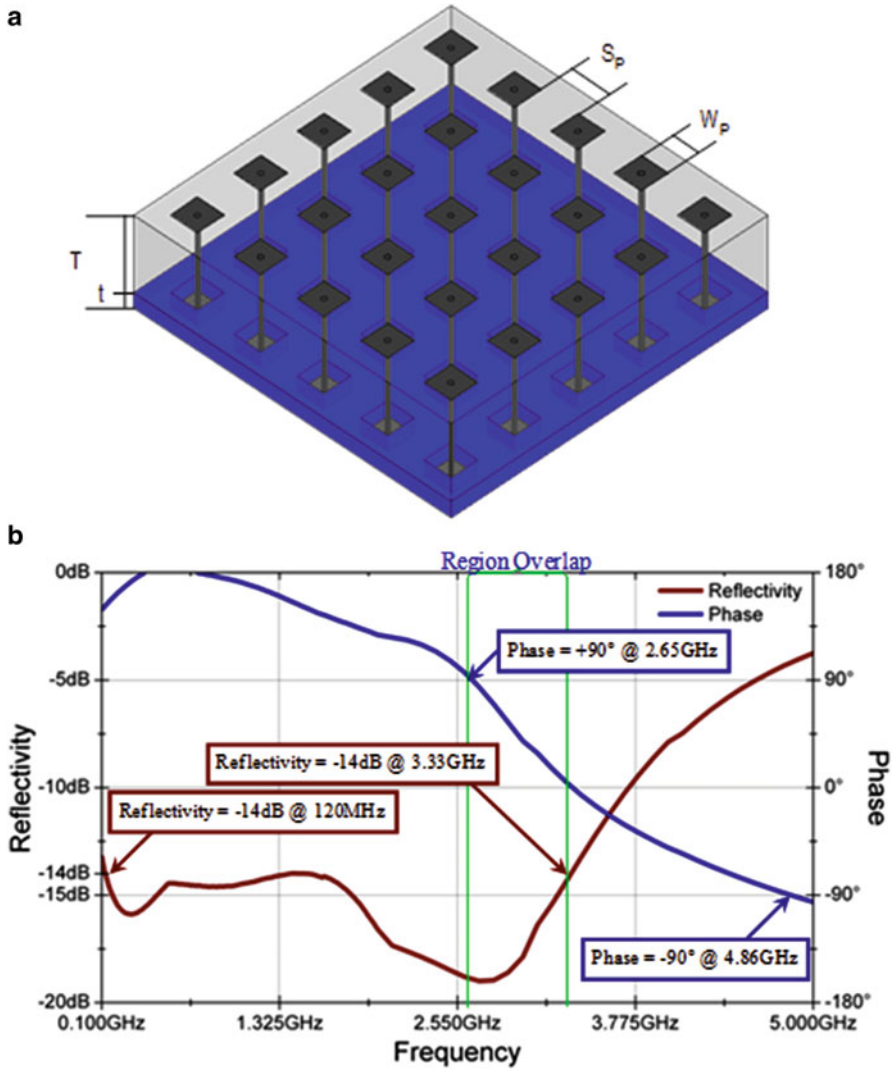


**Fig. 2.24** (a) Geometry of hybrid EBG/ferrite ground plane and (b) simulation results showing phase and reflectivity [70]

patterning, several successful broadband designs were achieved in the “no-man’s” frequency band, and some of the designs were validated by comparing results from two different EM simulation packages [92]. Examples of these designs together with simulation results are shown in Fig. 2.25.

While results from this initial work were very encouraging and successful broadband artificial PMC ground planes were designed, GP in its present form faces several challenges that we intend to overcome in future work. These include

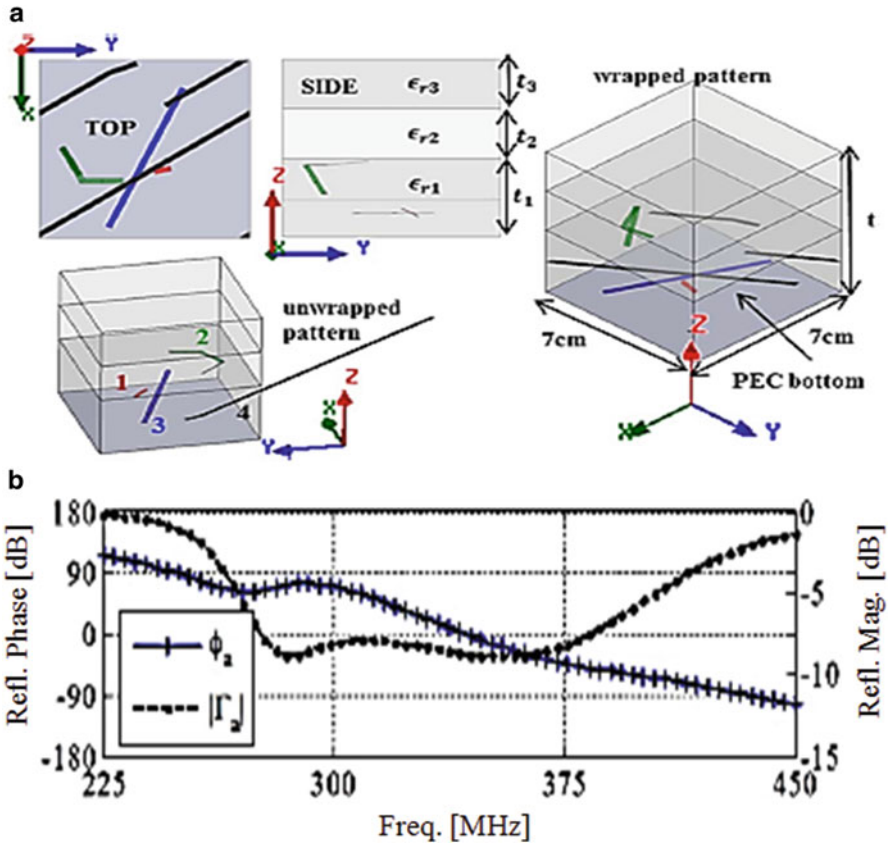


Fig. 2.25 (a) Unit cell for artificial magnetic conductor (AMC) ground plane design. (b) Reflection coefficient magnitudes (black) and phases (blue) using available dielectric [92]

computational efficiency, limited topology options, lack of integration of lumped components and tunable materials, and inability to affordably fabricate simulated designs using presently available 3D printing technologies. Many of these issues are being addressed as part of our ongoing research in this area.

### 2.3 Road to Entrepreneurship

In the remaining two sections of this chapter, I discuss two different topics. The first is on our entrepreneurship effort to develop and commercialize the Cardio-Pulmonary Stethoscope device [94], and the other (described in next section) is focused on educational activities to stimulate interest and enhance the learning

of electromagnetics [95]. A detailed description of the research on the Cardio-Pulmonary Stethoscope is provided in Chap. 18.

My interest in using electromagnetic techniques in medical diagnosis goes back to 1977 when I joined the University of Utah. The initial successes in designing a unique electromagnetic coupler [59] and making successful phantom experiments [31] sparked enthusiasm and led to conducting several successful animal studies [96, 97] and led to continued interest in developing new simulation studies on 2D models of the thorax and the innovative utilization of, what was very new then, CAT scan images [97]. The need to use large and expensive network analyzers for these measurements, and the need to place and align transceiver sensors across a section of the thorax with clear view of the lung, made it difficult to consider any further commercialization of this technology. Our team moved on and continued to attract funding and do research in different applications of electromagnetics. It was only in 2009 and as a result of a visit by my colleague and friend Roger Stancliff from Agilent Technologies, Inc., that we were encouraged to return to this medical application work and consider the commercialization of the microwave method for measuring changes in lung-water content [98]. With Roger's help, we obtained some initial funding from Agilent, followed by additional funding from NSF, and we were on our way to continue our work in this area and develop additional features and measurement capabilities of this technique [99]. Specifically, we used signal processing techniques to extract vital signs including heart and respiration rates, in addition to changes in lung water, from the measured microwave transmission coefficient signals. Our team and through Dr. Ruthsenne Perron's dissertation work also developed textile sensors [100] that could easily be integrated in shirts and bras, hence providing convenient continuous monitoring during daily activities. We were also able to evaluate the biological effects associated with the use of our device by comparing resulting SAR values with those of commercial cell phone using Federal Communications Commission (FCC)-approved facility at Kyocera Wireless Lab.; see results in Fig. 2.26. This leads to the very important step of obtaining an Institutional Review Board (IRB) approval for using the device on human subjects. At this stage, we were able to make measurements on healthy subjects and confirm the adequacy and accuracy of the method in measuring vital signs such as the respiration and heart rates.

The project took a significant leap toward commercialization when we were invited to participate in the NSF I-CORPS program. We had a team that consisted of Dr. Nuri Celik, as the entrepreneur, both Dr. Shirley Danial and Mr. Roger Stancliff as business mentors, and I as the PI on this project. As customer development is a key component in the nine elements of business model canvas [101, 102], we were out in the streets of Washington DC, trying to interview our customers who are mainly MDs in hospitals and medical centers. We interviewed over 106 MDs and were very surprised by the significant need for a technology that could accurately, noninvasively, on a continuous basis, monitor vital signs and measure changes in lung-water content. We worked long and hard on completing our I-CORPS training and were even rewarded by receiving the best in show in our cohort of 21 universities. When we returned back to Honolulu, we decided to participate



Fig. 2.26 Results from SAR measurements on the Cardio-Pulmonary Stethoscope

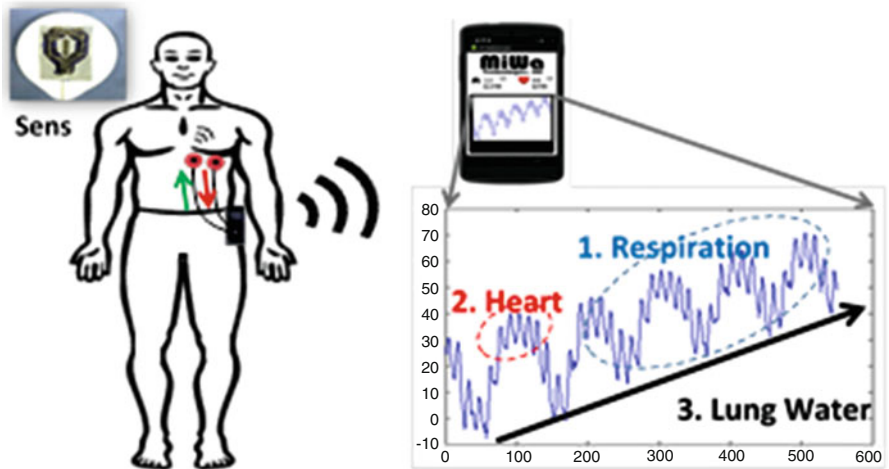


Fig. 2.27 The Cardio-Pulmonary Stethoscope, by MiWa Technologies, LLC

in the Business Plan Competition organized by our business school, so we formed a company, MiWa Technologies, LLC [103], and used the first place prize of \$10,000 to support the development of the microwave technology. Specifically, we developed a small  $2.7 \times 2.7$ -square-inch battery-operated transceiver that is equipped with Bluetooth data transmission to mobile unit and even developed the app for receiving and analyzing the received signal. At this stage, the device looked as may be seen in Fig. 2.27 and seemed to be ready for commercialization.

I also want to mention that during our I-CORPS participation, the instructors disliked the word “Microwave” in the name of our device, and as a result the name “Cardio-Pulmonary Stethoscope” was born. It is now a “chest patch” device [94] with noninvasive and continuous monitoring of vital signs and changes in lung-water content. As a result of a recent NIH grant, our group together with a clinical team from Queen’s Medical Center in Honolulu, HI, led by Dr. Todd Seto, was able to conduct clinical trials on heart failure (HF) and hemodialysis patients (HD). In the case of HF patients, changes in lung water results were compared with Swan-Ganz catheter wedge pressure measurements, while for HD patients, CPS results for changes in lung water were compared with the total amount of fluid loss during the dialysis process. In both cases, heart and respiration rates were compared with those obtained from an FDA-approved commercial device, Propaq LT. Results from clinical trials were very encouraging as a correlation factor for heart rate ( $HR = 0.995$ ) and respiration rate ( $RR = 0.991$ ) was obtained. For changes of lung-water content, results from HD patients are very encouraging, correlation factor = 0.928. Data from HF patients although satisfactory will require additional verification before publication. Several issues need to be reexamined regarding this HF patient population as focus needs to be placed on patient populations that require continuous monitoring. More discussion of clinical trials and results are given in Chap. 18. New NIH proposals with additional clinical trials are being submitted, together with continued exploration of additional information that could be extracted from the measured CPS data. A new US patent application that describes a multisensor CPS system for assessing status of lung-water content in addition to measuring the change has been submitted [45], and it is expected that with the continued use of advanced signal processing algorithms, more cardiopulmonary parameters will be monitored accurately, noninvasively, and continuously for home care patients and in hospitals.

## 2.4 Contributions in Electromagnetic Education

A successful academic career would be incomplete without innovative contributions to engineering education. I believe that leading innovations in engineering education is an integral part of a job in academia, and even with the pressure on faculty to pursue externally funded research, ways and means need to be found to contribute to innovation in education even at the undergraduate level. These innovations can take various forms including textbook writing, initiation of new programs and development of new courses, development of new laboratories, and provision of research opportunities for undergraduate and graduate students. I was fortunate to have some of these opportunities which I pursue with joy and satisfaction even today. I learned about the Engineering Clinic Program from Harvey Mudd College and have successfully implemented it at the University of Utah for 15 years (where it continues today), until I moved to Hawaii. I was also given the opportunity to write and submit the Computer Applications in Electromagnetic Education (CAEME)



**Fig. 2.28** Laboratory facilities for undergraduate research experience and participation in the Engineering Clinic Program

proposal to NSF on behalf of IEEE and the Antenna and Propagation Society, and this is what turned into the CAEME Center that published and distributed books and CDs to universities from all over the world. I am grateful to John Wiley and Sons who approved my proposal to launch a new journal *Computer Application in Engineering Education (CAE)*, which is now in its 25th year of publication and has received an award for excellence in scholarly publishing. At no time, have I felt that these activities were interfering with my ongoing technical research but instead added the joy of contributing to engineering education and helped in maintaining my enthusiasm and commitment to a career in academia.

In the Engineering Clinic Program, for example, we charged \$25,000 for each sponsored project. This provided not only funds to support the project and provide limited stipends to some of the participating students, but it also provided funds to purchase significant equipment and facilities for undergraduate labs. Equally important, it also generated strong commitment on the part of the sponsor to work with faculty and students and ensure successful outcomes from the sponsored projects. Figure 2.28 shows some of the laboratory facilities that were established as a result of the Engineering Clinic Program.

In a way, programs such as the Engineering Clinic are demanding programs as they involve industrial participation and oversight of academic education, with different perspectives. But, on the other hand, the students' learning was unequalled, and this maintained students' interest and continued their strong participation in



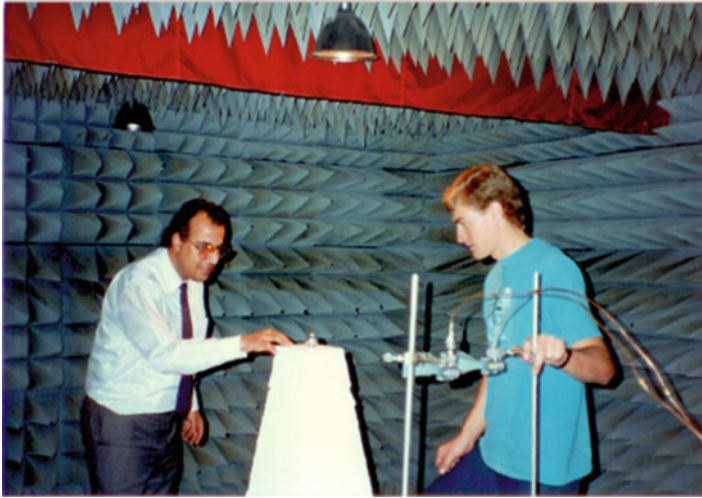


**Fig. 2.29** Iskander working with an undergraduate student on an engineering clinic project

the program throughout the years. Working with students on industry-sponsored projects was simply a joy as may be seen from Fig. 2.29.

Here, I also want to acknowledge with thanks and appreciation the strong support we received from the University of Utah administration, who waived overhead charges on the Engineering Clinic Program and allowed us to secure significant funding that ensures the continued operation of this program – to this day. As a matter of fact, just a year before my leaving the University of Utah, \$640,000 of the Engineering Clinic Program funds was allocated to establish an Engineering Clinic Endowed Chair which I occupied until I left the University.

The development of the CAEME Center was a project that started when we received NSF funding and worked with distinguished colleagues from across the electromagnetic community to develop the Center and achieve its much-anticipated benefits. The organization of CAEME had a Policy Board that includes representatives from IEEE, NSF, and participating IEEE societies and industries and also a Board of Technical Advisors that included truly distinguished members of the EM community including Professor Robert E. Collin and Professor Roger Harrington. There was not a unified vision for the Center's activities at the very beginning, but with the publication of our software book [104] and continued publication of multimedia CDs and other CAEME products [95, 105–112], the Center gained international reputation, and its products were acquired by universities from across the globe. Figure 2.30 shows a group picture of CAEME software products, including two software books, CAEME I and II, two CDs that include software and multimedia modules in electromagnetics, and three CDs for stimulating interest and learning on STEM courses. These three CDs are the Calculus Castle, the Physics Museum, and the CD on the human genetics, shown on the left-hand side of Fig. 2.30. The two electromagnetic CDs are shown at the bottom right of Fig. 2.30.

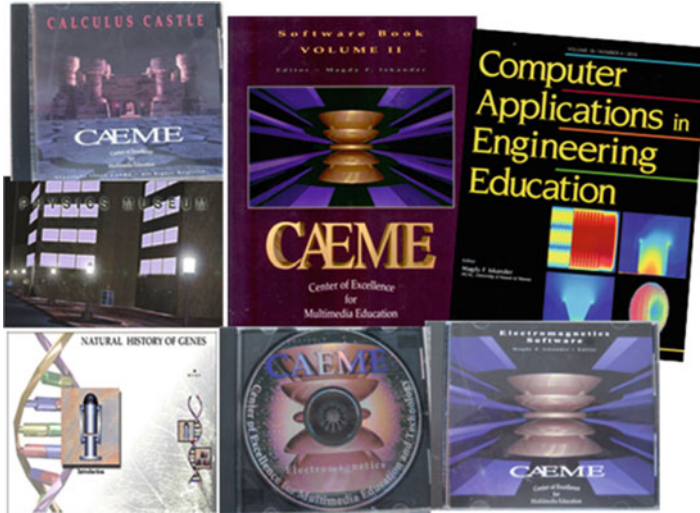


**Fig. 2.30** Educational products from the CAEME Center and the cover of the *Computer Applications in Engineering Education*, By John Wiley and Sons

As may be noted from Fig. 2.30, the establishment of the CAEME Center motivated the publication of the new journal *Computer Applications in Engineering Education (CAE)*, by John Wiley and Sons. This was the most significant commercial product spun off as a result of the CAEME activities. The journal spans all engineering subjects, and this stimulated interest in using computers and software tools across the entire engineering community, in the USA and abroad. During the first few years of publication of CAE, the journal included a diskette with one or more of the developed software, and later on the software was provided online. In other words, we were pioneering the use of software tools in engineering education, and we are happy to report that these tools are still being used now in the USA and across the world. There is now a long list of journals that focus on the use of computers and software tools in education, but CAE started in 1992, won publication excellence award in 1993, and is now in its 25th year of publication – a truly remarkable effort. Congratulations to the Wiley editorial and production staff for a job well done.

Finally, as for course development and textbook writing, I am proud to be among the very first who introduced computational electromagnetics for undergraduates [113], and I hope my textbook, *Electromagnetic Fields and Waves* [114], will encourage more educators to use dynamic fields and interesting applications of time-varying Maxwell's equations in teaching introductory electromagnetics.



**Fig. 2.31** To my family with all my love for support, inspiration, and unconditional love

## 2.5 Concluding Remarks

Recalling this long list of research and educational activities over the period of four decades helped me think of those who inspired this career and facilitated it and those who supported and enabled these accomplishments. It is a long list of family members, friends, colleagues, and dedicated students. It is true that my love for teaching was inspired as a result of my first students' evaluations after teaching a large class at the University of Utah, sometime in 1978. But it goes far beyond this. I am very much indebted to the educational institutions who prepared me for this, the University of Alexandria, Egypt, and the University of Manitoba, Canada, and the educational institutions who helped in nurturing and supporting these activities, the University of Utah and the University of Hawaii at Manoa. Family support clearly played a very important role in developing my career, starting from father Fahmy, mother Fotna, and my three sisters Fify, Ekhlas, and Sohair, who early on in my life expected and insisted on getting the best from me in whatever I do. Then my wife, Sonia, and daughter, Tiffany, who, through their love and support, inspired my enthusiasm, sustained my perseverance, and helped me overcome challenges. No words can express enough my deep gratitude to my family's support. Figure 2.31 is for you, with all my love and wholehearted thanks for your unconditional love and support.

To the hundreds of colleagues from universities I worked at or associated with, from companies I worked or interacted with, and from federal and military agencies who believed in and supported my research, I am most grateful for your friendships and support throughout these years. To my students, graduate and undergraduates, all of this would not have happened without you and through your hard work and belief in electromagnetics. It has been a great journey that you helped lighten it with much needed thousand points of light. Special thanks and appreciation to my first PhD student and colleague, Professor Akhlesh Lakhtakia, who suggested this book idea, did much of the ground work, and also arranged for its publication. I am

most grateful to both Professors Akhlesh Lakhtakia and Cynthia Furse who together championed the cause, believed in the initiative, collaborated with colleagues from across the globe, spent considerable time and effort, and made this publication possible. To all the friends and colleagues who shared their talent and expertise and contributed chapters to this special publication, thank you, and I am most grateful.

## References

1. P.M. Morse, H. Feshbach, *Methods of Theoretical Physics* (McGraw-Hill, New York, 1953)
2. L.V. Kantorovich, V.I. Krylov, *Approximate Methods of Higher Analysis* (Interscience Publishers, New York, 1958)
3. M.F. Iskander, M.A.K. Hamid, Iterative solution of waveguide discontinuity problems. *IEEE Trans. Microwave Theory Tech.* **25**, 763–768 (1977)
4. M.F. Iskander, M.A.K. Hamid, Simplified solutions of a cross-junction and specially truncated bands in parallel plate waveguides. *Radio Electr. Eng.* **47**, 269–273 (1977)
5. M.F. Iskander, M.A.K. Hamid, Scattering coefficients at a waveguide-horn junction. *Proc. IEE* **123**, 123–127 (1976)
6. M.F. Iskander, M.A.K. Hamid, Scattering by a regular polygonal conducting cylinder. *Archiv Elektr. Übertrag.* **30**, 403–408 (1976)
7. M.F. Iskander, M.A.K. Hamid, Numerical solution for the near-field transmission between two H-plane sectoral electromagnetic horns. *IEEE Trans. Antennas Propag.* **24**, 87–89 (1976)
8. M.F. Iskander, M.A.K. Hamid, Analysis of triangle waveguide of arbitrary dimensions. *Archiv Elektr. Übertrag.* **28**, 455–461 (1974)
9. M.F. Iskander, M.A.K. Hamid, Eigenvalues for a trapezoidal waveguide. *Radio Electr. Eng.* **44**, 593–596 (1974)
10. M.F. Iskander, A. Lakhtakia, C.H. Durney, A new iterative procedure to solve for scattering and absorption by dielectric objects. *Proc. IEEE* **70**, 1361–1363 (1982)
11. A. Lakhtakia, M.F. Iskander, C.H. Durney, H. Massoudi, Absorption characteristics of prolate spheroidal models exposed to the near fields of electrically small apertures. *IEEE Trans. Biomed. Eng.* **29**, 269–278 (1982)
12. A. Lakhtakia, M.F. Iskander, C.H. Durney, An iterative extended boundary condition method for solving the absorption characteristics of Lossy dielectric objects of large aspect ratios. *IEEE Trans. Microwave Theory Tech.* **31**, 640–647 (1983)
13. A. Lakhtakia, M.F. Iskander, Theoretical and experimental evaluation of power absorption in elongated biological objects at and beyond resonance. *IEEE Trans. Electromagn. Compat.* **25**, 448–453 (1983)
14. A. Lakhtakia, M.F. Iskander, Scattering and absorption of lossy dielectric objects irradiated by the near fields of aperture source. *IEEE Trans. Antennas Propag.* **31**, 111–120 (1983)
15. M.F. Iskander, A. Lakhtakia, C.H. Durney, A new procedure for improving the solution stability and extending the frequency range of the EBCM. *IEEE Trans. Antennas Propag.* **31**, 317–329 (1983)
16. A. Lakhtakia, M.F. Iskander, C.H. Durney, H. Massoudi, Irradiation of prolate spheroidal models of humans and animals in the near field of a small-loop antenna. *Radio Sci.* **17**(5S), 77–84 (1982)
17. M.F. Iskander, A. Lakhtakia, Extension of the iterative EBCM method to calculate scattering by low-loss or lossless elongated dielectric objects. *Appl. Opt.* **23**, 948–953 (1984)
18. M.F. Iskander, S.C. Olson, R.E. Benner, D. Yoshida, Optical scattering by metallic and carbon aerosols of high aspect ratio. *Appl. Opt.* **25**, 2514–2520 (1986)
19. M.F. Iskander, H.Y. Chen, J.E. Penner, Scattering and absorption of very long aerosol particles. *Aerosol Sci. Technol.* **10**, 172–180 (1989)

20. M.F. Iskander, H.Y. Chen, J.E. Penner, Optical scattering and absorption by branched chains of aerosols. *Appl. Opt.* **28**, 3083–3091 (1989)
21. P.W. Barber, Scattering and absorption efficiencies for non-spherical dielectric objects-biological models. *IEEE Trans. Biomed. Eng.* **25**, 155–159 (1978)
22. T.P. Ackerman, B. Toon, Absorption of visible radiation in atmosphere containing mixtures of absorbing and nonabsorbing particles. *Appl. Opt.* **20**, 3661–2668 (1981)
23. R.D. Mountain, G.W. Mulholland, H. Bawm, Simulation of aerosol agglomeration in free and continuum flow region. *J. Colloid Interface Sci.* **114**, 67–81 (1986)
24. M.F. Iskander, S.S. Stuchly, A time-domain technique for the measurement of the dielectric properties of biological substances. *IEEE Trans. Instrum. Meas.* **21**, 425–429 (1972)
25. S.S. Stuchly, M.A. Rzepecka, M.F. Iskander, Permittivity measurements at microwave frequencies using lumped elements. *IEEE Trans. Instrum. Meas.* **23**, 56–62 (1974)
26. S. Bringham, M.F. Iskander, Open-ended metalized ceramic coaxial probe for high temperature dielectric properties measurements. *IEEE Trans. Microwave Theory Tech.* **44**, 926–935 (1996)
27. S. Bringham, M.F. Iskander, M.J. White, Thin-sample measurements and error analysis of high-temperature coaxial dielectric probes. *IEEE Trans. Microwave Theory Tech.* **45**, 2073–2083 (1997)
28. M.F. Iskander, H. Youn, C. Amazeen, B. Burns, Systems for transverse electromagnetic mode in-situ soil testing. U.S. Patent 8,461,851, 2013
29. M.F. Iskander, Apparatus and method for measuring the permittivity of a substance. U.S. Patent 4,510,437, 1985
30. M.F. Iskander, Apparatus and method for measuring lung water content. U.S. Patent 4,488,559, Dec 1984 (20 claims)
31. M.F. Iskander, C.H. Durney, D.J. Shoff, D.G. Bragg, Diagnosis of pulmonary edema by a surgically noninvasive microwave technique. *Radio Sci.* **14**(6S), 265–269 (1979)
32. M.F. Iskander, R. Maini, C.H. Durney, A microwave method for measuring changes in lung water content: numerical simulation. *IEEE Trans. Biomed. Eng.* **28**, 797–804 (1981)
33. M.F. Iskander, C.H. Durney, D.G. Bragg, B.H. Ovard, A microwave method for estimating absolute value of average lung water content. *Radio Sci.* **17**, 111S–117S (1982)
34. H. Massoudi, C.H. Durney, M.F. Iskander, Limitations of the cubical block model of man in calculating SAR distribution. *IEEE Trans. Microwave Theory Tech.* **32**, 746–752 (1984)
35. C.T. Tsai, H. Massoudi, C.H. Durney, M.F. Iskander, A linear approximation method for solving internal field distribution of arbitrarily shaped inhomogeneous dielectric bodies. *IEEE Trans. Microwave Theory Tech.* **34**, 1131–1139 (1986)
36. A.M. Tumeh, M.F. Iskander, Performance comparison of available interstitial antennas for microwave hyperthermia. *IEEE Trans. Microwave Theory Tech.* **37**, 1126–1133 (1989)
37. C.M. Furse, M.F. Iskander, Three-dimensional electromagnetic power deposition in tumors using interstitial antenna arrays. *IEEE Trans. Biomed. Eng.* **36**, 977–986 (1989)
38. M.J. White, M.F. Iskander, Z. Huang, Development of a multi-grid FDTD code for three-dimensional applications. *IEEE Trans. Antennas Propag.* **45**, 1512–1517 (1997)
39. M.J. White, M.F. Iskander, Z. Yun, A new 3D FDTD multi-grid technique with dielectric traverse capabilities. *IEEE Trans. Microwave Theory Tech.* **49**, 422–430 (2001)
40. C. Araya, M.F. Iskander, J. Brennan, Slotted waveguide antenna array for microwave assisted Gas Kiln. U.S. Patent 6,583,394, 2003
41. M.F. Iskander, R.L. Smith, O. Andrade, H. Kimrey, L. Walsh, FDTD simulation of microwave sintering in multimode cavities. *IEEE Trans. Microwave Theory Tech.* **42**, 793–800 (1994)
42. O.P. Gahndi, G. Lazzi, C. Furse, Electromagnetic absorption in the human head and neck for mobile telephones at 835 and 1900 MHz. *IEEE Trans. Microwave Theory Tech.* **44**, 1884–1897 (1996)
43. M.F. Iskander, R. Quintero-Illera, Z. Yun, Polarization and human body effects on the microwave absorption in a human head exposed to radiation from hand-held devices. *IEEE Trans. Microwave Theory Tech.* **48**, 1979–1987 (2000)

44. R.R.G Perron, Noninvasive electromagnetic sensors for continuous monitoring of human vital signs and assessment of lung fluid content, PhD dissertation, May 2016
45. M.F. Iskander, R.R.G. Perron, Lung water content measurement system and calibration method. U.S. Patent application, submitted 2015
46. M.F. Iskander, Z. Yun, R.R.G. Perron, T.B. Seto, J. Yu, US provisional patent application number 62/431,763 on 12/8/2016 titled "Machine Learning Based Cardiopulmonary Disease Assessment Using CP Stethoscope Measurements"
47. Z. Yun, M.F. Iskander, Z. Zhang, A fast ray tracing procedure using space division with uniform rectangular grid. *Electron. Lett.* **36**, 895–897 (2000)
48. Z. Zhang, Z. Yun, M.F. Iskander, A new ray tracing method for propagation models in wireless communications. *Electron. Lett.* **36**, 464–465 (2000)
49. M.F. Iskander, Z. Yun, Propagation prediction models for wireless communication systems. *IEEE Trans. Microwave Theory Tech.* **50**, 662–673 (2002)
50. Z. Zhang, Z. Yun, M.F. Iskander, 3D tetrahedron ray tracing algorithm. *Electron. Lett.* **37**, 334–335 (2001)
51. Z. Yun, Z. Zhang, M.F. Iskander, A ray-tracing method based on the triangular grid approach and application to propagation prediction in urban environments. *IEEE Trans. Antennas Propag.* **50**, 750–758 (2002)
52. Z. Yun, M.F. Iskander, Z. Zhang, Complex-wall effect on propagation characteristics and MIMO capacities for an indoor wireless communication environment. *IEEE Trans. Antennas Propag.* **52**, 914–922 (2004)
53. Z. Zhang, R. Sorensen, Z. Yun, M.F. Iskander, J.F. Harvey, A ray-tracing approach for indoor/outdoor propagation through window structures. *IEEE Trans. Antennas Propag., special issue on Wireless Communication*, M.F. Iskander and J.W. Mink, Guest Editors, **50**, 742–749 (2002)
54. Z. Yun, M.F. Iskander, S.Y. Lim, D. He, R. Martinez, Radio wave propagation prediction based on 3D building structures extracted from 2D images. *IEEE Antennas Wirel. Propag. Lett.* **6**, 557–559 (2007)
55. Z. Yun, S.Y. Lim, M.F. Iskander, Use of geospatial resources for Radio propagation prediction in Urban areas. *IEEE Antennas Wirel. Propag. Lett.* **8**, 587–591 (2009)
56. Z. Yun, M.F. Iskander, Ray tracing for radio propagation modeling: principles and applications. *IEEE Access.* **3**, 1089–1100 (2015)
57. D. Green, Z. Yun, M.F. Iskander, J.F. Harvey, Propagation modeling for realistic modern urban environments: a comparison with empirical models. *IEEE Antennas Wirel. Propag. Lett.*, submitted, 2017
58. D. Bibb, Z. Yun, M.F. Iskander, Approximate source localization using multi-class classification. *IEEE Antennas Wirel. Propag. Lett.*, submitted, 2017
59. M.F. Iskander, C.H. Durney, Electromagnetic energy coupler/ receiver apparatus and method. U.S. Patent 4,240,445 (8 claims)
60. T.S. Lind, M.F. Iskander, On the coupling characteristics of coplanar waveguides and microstrip lines to multi-layer dielectric media. *IEEE Trans. Electromagn. Compat.* **34**, 117–123 (1992)
61. M.F. Iskander, Z. Yun, Z. Zhang, R. Jensen, S. Redd, Design of a low-cost 2D beam-steering antenna using ferroelectric material and the CTS technology. *IEEE Trans. Microwave Theory Tech.* **49**, 1000–1003 (2001)
62. M.F. Iskander, Z. Zhang, Z. Yun, R. Isom, M. Hawkins, R. Emrick, B. Bosco, J. Synowczynski, B. Gersten, New phase shifters and phased antenna array designs based on ferroelectric materials and CTS technologies. *IEEE Trans. Microwave Theory Tech.* **49**, 2547–2553 (2001)
63. M.F. Iskander, W. Kim, J. Bell, Multiband coplanar waveguide CTS antenna. U.S. Patent 7,079,082, July 2006
64. Z. Zhang, M.F. Iskander, Z. Yun, Coaxial continuous transverse stub element device antenna array and filter. U.S. Patent 6,201,509, Mar 2001

65. M.F. Iskander, Z. Zhang, Z. Yun, R. Isom, Coaxial continuous transverse stub (CTS) array. *Microwave Wirel. Compon. Lett.* **11**, 489–491 (2001)
66. R. Isom, M.F. Iskander, Z. Yun, Z. Zhang, Design and development of single and multiband coaxial continuous transverse stub (CTS) antenna arrays. *IEEE Trans. Antennas Propag.* **52**, 2180–2183 (2004)
67. W. Kim, M.F. Iskander, A new coplanar waveguide continuous transverse stub (CPW-CTS) antenna for wireless communications. *IEEE Antennas Wirel. Propag. Lett.* **4**, 172–174 (2005)
68. W. Kim, M.F. Iskander, W.D. Palmer, Integrated phased array antenna design using ferroelectric materials and continuous transverse stub technology. *IEEE Trans. IEEE Antennas Propag.* **54**, 3095–3105 (2006)
69. Y. Li, M.F. Iskander, Z. Zhang, Z. Feng, A new low cost leaky wave coplanar waveguide continuous transverse stub antenna array using metamaterial-based phase shifters for beam steering. *IEEE Trans. Antennas Propag.* **61**, 3511–3518 (2013)
70. J.M. Bell, M.F. Iskander, J.J. Lee, Ultra-wideband hybrid EBG/ferrite ground plane for low profile Array antennas. *IEEE Trans. Antennas Propag.* **55**, 4–12 (2007)
71. J.J. Lee, S. Livingston, R. Koenig, Wide band long slot array antennas. *IEEE Antennas Propag. Soc. Int. Symp.* **2**, 452–455 (2003)
72. A. Neto, J.J. Lee, “Infinite bandwidth” long slot array antenna. *Antennas Wirel. Propag. Lett.* **4**, 75–78 (2005)
73. H.S. Youn, Y.L. Lee, N. Celik, M.F. Iskander, Design of a cylindrical long-slot array antenna integrated with hybrid EBG/ferrite ground plane. *IEEE Antennas Wirel. Propag. Lett.* **11**, 180–183 (2012)
74. J. Rayno, N. Celik, M.F. Iskander, Dual polarization cylindrical long-slot Array (CLSA) antenna Integrated with compact broadband Baluns and slot impedance transformer. *IEEE Antennas Wirel. Propag. Lett.* **12**, 1384–1387 (2013)
75. G.C. Huang, M.F. Iskander, M. Hoque, S.R. Goodall, T. Bocskor, Antenna array design and system for directional networking. *IEEE Antennas Wirel. Propag. Lett.* **15**, 1141–1144 (2015)
76. W. Liu, Z. Zhang, Z. Feng, M.F. Iskander, A compact microstrip crossover and its application in 4x4 butler matrix design. *IEEE Microwave Wirel. Compon. Lett.* **22**, 254–256 (2012)
77. G.C. Huang, M.F. Iskander, M. Hoque, Circularly polarized antenna array designs for directional networks. *IEEE Antennas Wirel. Propag. Lett.*, submitted, 2016
78. Z. Zhang, M.F. Iskander, Z. Yun, A. Host-Madsen, Hybrid smart antenna system using directional elements – Performance analysis in flat rayleigh fading. *IEEE Trans. Antennas Propag.* **51**, 2926–2935 (2003)
79. M. Rezk, W. Kim, Z. Yun, M.F. Iskander, Performance comparison of a novel hybrid smart antenna system versus the fully adaptive and switched beam antenna arrays. *IEEE Antennas Wirel. Propag. Lett.* **4**, 285–288 (2005)
80. N. Celik, W. Kim, M.F. Demirkol, M.F. Iskander, R. Emrick, Implementation and experimental verification of hybrid smart-antenna beamforming algorithm. *IEEE Antennas Wirel. Propag. Lett.* **5**, 280–283 (2006)
81. N. Celik, M.F. Iskander, R. Emrick, S. Franson, J. Holmes, Implementation and experimental verification of a smart antenna system operating at 60 GHz band. *IEEE Trans. Antennas Propag.* **56**, 2790–2800 (2008)
82. M.F. Iskander, Z. Yun, N. Celik, H. Youn, N. Omaki, J.M Baker, HF and passive radar designs for homeland security applications. *Mar. Technol. Soc. J.* **45**, 111–119 (2011)
83. J. Baker, H.-S. Youn, N. Celik, M.F. Iskander, Low-profile multi-frequency HF antenna design for coastal radar applications. *IEEE Antennas Wirel. Propag. Lett.* **9**, 1119–1122 (2010)
84. J. Baker, M.F. Iskander, A new design approach for electrically small high-frequency antennas. *IEEE Antennas Wirel. Propag. Lett.* **14**, 402–405 (2015)
85. D. Nashaat, H.A. Elsadek, E.A. Abdallah, M.F. Iskander, H. Elhenawy, UltraWide bandwidth 2x2 microstrip patch array antenna using electromagnetic band-gap structure (EBG). *IEEE Trans. Antennas Propag.* **59**, 1528–1534 (2011)

86. D.N. Elsheakh, H.A. Elsadek, E.A. Abdallah, M.F. Iskander, H. Elhenawy, Enhancement of microstrip monopole antenna bandwidth by using EBG structures. *IEEE Antennas Wirel. Propag. Lett.* **8**, 959–962 (2009)
87. H. Wang, Z. Zhang, Y. Li, M.F. Iskander, A switched beam antenna with shaped radiation pattern and interleaving array architecture. *IEEE Trans. Antenna Propag.* **63**, 2914–2291 (2015)
88. Y. Li, Z. Zhang, C. Deng, Z. Feng, M.F. Iskander, 2-D design scalable dual polarized series-fed slot antenna array using single substrate. *IEEE Trans. Antennas Propag.* **62**, 2280–2283 (2014)
89. J.M. Bell, M.F. Iskander, Experimental analysis of an ultra-wideband hybrid EBG/ferrite ground plane. *IEEE Trans. Instrum. Meas.* **58**, 2899–2905 (2009)
90. J.M. Bell, M.F. Iskander, Equivalent circuit model of an ultra-wideband hybrid EBG/ferrite structure. *IEEE Antennas Wirel. Propag. Lett.* **7**, 573–576 (2008)
91. J.S. Kobashigawa, H.-s. Youn, M.F. Iskander, Z. Yun, Classification of buried targets using ground penetrating radar: comparison between genetic programming and neural networks. *IEEE Antennas Wirel. Propag. Lett.* **10**, 971–974 (2011)
92. J. Rayno, M.F. Iskander, N. Celik, Synthesis of broadband true-3D metamaterial artificial magnetic conductor ground planes using genetic programming. *IEEE Trans. Antennas Propag.* **62**, 5732–5744 (2014)
93. J. Rayno, M. Iskander, M. Kobayashi, Hybrid genetic programming with accelerating genetic algorithm optimizer for 3D metamaterial design. *IEEE Antennas Wirel. Propag. Lett.* **15**, 1743–1746 (2016)
94. M.F. Iskander, N. Celik, R. Gagarin, G.C. Huang, D.A. Bibb, Microwave stethoscope for measuring cardio-pulmonary vital signs and lung water content. U.S. Patent 9,526,438, 2016
95. M.F. Iskander, Technology-based electromagnetic education. *IEEE Trans. Microwave Theory Tech.* **50**, 1015–1020 (2002)
96. M.F. Iskander, C.H. Durney, Microwave methods of measuring changes in lung water. *J. Microw. Power* **18**, 265–275 (1983)
97. M.F. Iskander, C.H. Durney, Electromagnetic techniques for medical diagnostics: a review. *Proc. IEEE* **68**, 126–132 (1980)
98. N. Celik, R. Gagarin, H.-S. Youn, M.F. Iskander, A non-invasive microwave sensor and signal processing technique for continuous monitoring of vital signs. *IEEE Antennas Wirel. Propag. Lett.* **10**, 286–289 (2011)
99. N. Celik, R. Gagarin, G.C. Huang, M.F. Iskander, B. Berg, Microwave stethoscope: development and benchmarking of a vital signs sensor using computer controlled phantoms and human studies. *IEEE Trans. Biomed. Eng.* **61**, 2341–2349 (2014)
100. R.R.G. Perron, G.C. Huang, M.F. Iskander, Textile electromagnetic coupler for monitoring vital signs and changes in lung water content. *IEEE Antennas Wirel. Propag. Lett.* **14**, 151–154 (2015)
101. A. Osterwalder, Y. Pigneur, *Business Model Generation: A Handbook for Visionaries, Game Changers and Challengers* (Wiley, Hoboken, NJ, 2010)
102. S. Blank, B. Dorf, *The Startup Owner's Manual, The Step-by-Step Guide for Building a Great Company* (K & S Ranch, Pescadero, CA, 2012)
103. <http://www.miwatechnologies.com>
104. M.F. Iskander, NSF/IEEE CAEME center: an exciting opportunity to align electromagnetic education with the nineties. *Comput. Appl. Eng. Educ.* **1**(1), 33–44 (1992)
105. M.F. Iskander, T. Reed, J. Breen III, Interactive video lessons for electromagnetic education. *Comput. Appl. Eng. Educ.* **1**, 147–158 (1993)
106. M.F. Iskander, Computer-based electromagnetic education. *Special Issue of the ACES J. Comput. Appl. Electromagn. Educ.* **8**, 77–107 (1993)
107. M.F. Iskander, J.C. Catten, R. Jameson, A. Jones, A. Balcells, Development of multimedia modules for education. *Comput. Appl. Eng. Educ.* **3**, 97–110 (1995)
108. M.F. Iskander, E. Jensen, TLine: software for sinusoidal steady-state analysis of transmission lines. *Comput. Appl. Eng. Educ.* **2**, 185–194 (1994)



109. M.F. Iskander, J.C. Catten, R.M. Jameson, A. Rodriguez-Balcells, A.K. Jones, Interactive multimedia CD-ROMs for education. *Comput. Appl. Eng. Educ.*, 51–60 (1996)
110. O. de los Santos Vidal, M.F. Iskander, Multimedia modules for electromagnetics education. *Comput. Appl. Eng. Educ.* **5**(4), 257–267 (1997)
111. S. Sanz, M.F. Iskander, L. Yu, Development of an interactive multimedia application in electromagnetics: antenna theory and design. *Comput. Appl. Eng. Educ.* **8**, 11–17 (1999)
112. J. Fabrega, S. Sanz, M.F. Iskander, New labVIEW-based software packages and multimedia modules for electromagnetics education. *Comput. Appl. Eng. Educ.* **6**, 1347–1364 (1998)
113. M.F. Iskander, M. Morrison, M. Hamilton, A new course on computer methods in electromagnetics. *IEEE Trans. Educ.* **31**, 101–115 (1988)
114. M.F. Iskander, *Electromagnetic Fields and Waves*, 2nd edn. (Waveland Press, Long Grove, IL, 2012)

# Chapter 3

## Millimeter-Wave Endfire Single-Feed Circular-Polarization Antipodal Fermi Tapered Slot Antenna

Zouhair Briqech, Abdel-Razik Sebak, and Tayeb A. Denidni

### 3.1 Introduction

Due to their diverse polarity, microstrip antennas are widely in demand in radar, satellite, navigation, imaging, and wireless communications applications [1–8]. Circular-polarization (CP) antenna types are able to achieve better weather penetration, and no orientations are required between communication terminals unlike linearly polarized antennas. Importantly, in satellite and point-to-point communications, CP antennas are preferred, since they reduce loss caused by polarity misalignment between the transmitting and receiving antennas. Furthermore, CP probes in millimeter-wave (MMW) imaging and detection systems provide additional information about the object’s shape, orientation, and surface material. Polarization diversity increases the intensity of pixel resolution in the target’s images generated by imaging and detection systems [9–11]. Majority of MMW systems require a low-cost, lightweight, and low-profile directive CP antenna with high gain to compensate for the propagation loss at MMW frequencies [12].

---

Z. Briqech

Department of Electrical and Computer Engineering, Concordia University, Montréal, QC, H3G 2W1, Canada

Institut National De La Recherche Scientifique (INRS), Place Bonaventure, Montréal, QC, H5A 1C6, Canada

A.-R. Sebak (✉)

Department of Electrical and Computer Engineering, Concordia University, Montréal, QC, H3G 2W1, Canada

e-mail: [abdo@ece.concordia.ca](mailto:abdo@ece.concordia.ca)

T.A. Denidni

Institut National De La Recherche Scientifique (INRS), Place Bonaventure, Montréal, QC, H5A 1C6, Canada

A planar antenna structure, such as a patch antenna [2–8], is preferable, due to its simple feeding schemes, low cost, and ability to be implemented in standard printed circuit board (PCB) and integrated circuits. Printed CP MMW antennas are investigated thoroughly to enhance short wireless communications in several applications. In Ref. [13], a printed CP helical antenna in a stacked design operating at 60 GHz has been investigated. The  $4 \times 4$ -element antenna implemented using low temperature co-fired ceramic (LTCC) technology achieved a gain of 14.3 dBi. A CP curved leaky-wave slot antenna has been presented in Ref. [14]. This design generates a broadside radiation pattern with a moderate gain of 8 dBiC over a frequency range 4.5–6.7 GHz and a 3-dB axial ratio (AR) of about 53%. In Ref. [15], double-sided patch antennas have generated a CP by controlling the phase between feeding ports, which leads to an omnidirectional pattern covering a narrow bandwidth of 2.4–2.5 GHz with maximum gain of 3.3 dBiC. Lai et al. [16] have introduced a broadside CP pattern generated by dielectric resonator antenna (DRA) which is fed by a pair of cross slots and used a half-mode substrate integrated waveguide feeding mechanism. The antenna provided a 3-dB axial ratio of 4.0% at the V-band. In Ref. [17], a  $2 \times 2$  CP patch with coupled slots in a substrate integrated waveguide (SIW) cavity has provided a gain of 7.5 dBiC for single elements and an average gain of 12.5 dBiC for the  $2 \times 2$  array at 58–64 GHz. Ladan et al. [18] have utilized SIW for feeding a  $2 \times 2$  CP patch array for studying the feasibility of wireless power harvesting and transmission. The CP antenna generated a broadside pattern with a gain of 12.6 dBiC at 24 GHz. In Ref. [19], a CP covering 9–11 GHz leaky-wave lens (LWL) implemented with printed-slot technology has been used to synthesize focused near fields. The majority of these antennas provide broadside or omnidirectional radiation patterns and a narrow bandwidth.

The printed tapered slot antenna provides a directive beam in the endfire direction. It is able to achieve high gain, high efficiency, and wide bandwidth and is easy to fabricate [20]. In comparison, this antenna is compatible with numerous applications, such as MMW imaging and detection systems [21], and phased and scanning arrays [22, 23]. CP waves are achieved when two orthogonal linearly polarized modes with a  $90^\circ$  phase difference and equal amplitude are generated. In the case of TSA antennas, they are excited separately. Guntupalli and Wu [24] have introduced a  $1 \times 4$  CP array formed by microstrip slots exciting antipodal linearly tapered slot antennas (ALTSA) using two ports of a coplanar waveguide to SIW transition. The array provides a gain of 14 dBi over 32–37 GHz band. Karamzadeh and Kartal [25] have designed a  $2 \times 2$  tapered slot antenna array using a feeding network of two rat-race ring couplers, two branch line couplers, and a crossover generating a gain of 13.9 dBiC over 4.81–6.17 GHz band. The CP antenna in Ref. [25] is achieved via two input ports. In Ref. [26] 3-D interconnects of a  $2 \times 2$  CP array ALTSA antenna with a dielectric rod using two-port SIW transition generated a gain of 14 dBi at 60 GHz.

Despite the good performance of these CP TSA antennas [24–26], they use more than one element in an array form and multi-excited ports which increases the unwanted radiation losses from the feeding network resulting in a moderate CP antenna gain. In addition, the overall radiation efficiency may decrease dramatically

with frequency due to ohmic losses in the feeding lines. A significant challenge lies in the development of a single-feed circular-polarization TSA that is related to this work.

This work presents a single-feed circular-polarized AFTSA-SC antenna with a measured gain exceeding 18 dB at 60 GHz. A 55–67 GHz millimeter-wave broadband, high-gain, and high-efficiency CP AFTSA-SC antenna is designed, optimized, and implemented. The circular-polarization wave is generated by a  $50 \Omega$  single-feed microstrip line exciting simultaneously a pair of AFTSA-SC antennas. These two AFTSA-SC antennas are aligned orthogonally to each other in 3D form, as illustrated in Fig. 3.1. The equal amplitude with  $90^\circ$  phase difference line to feed the two AFTSA-SC antennas is implanted using slotted cutouts in the center of each element's substrate to create the two orthogonal waves which leads to a

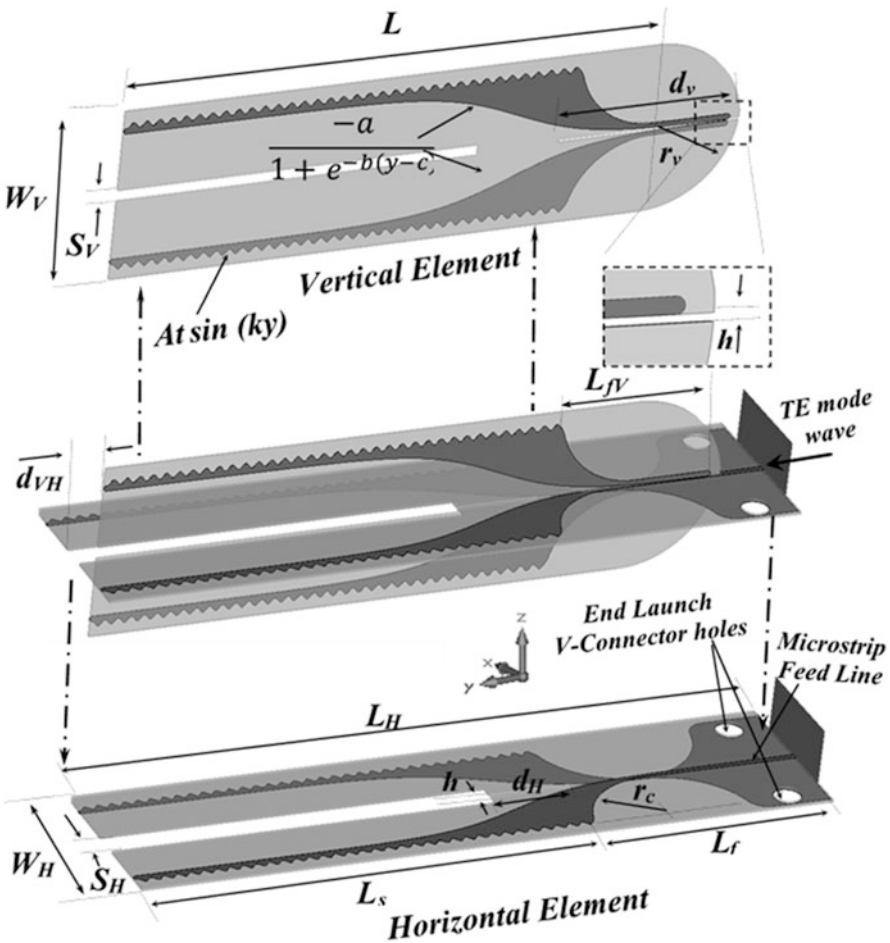


Fig. 3.1 Geometry of the circular-polarization AFTSA-SC antenna

circular-polarization wave. Avoiding an extra feed polarizer reduces the number of ports needed in the CP array structure by 50% which reduces fabrication complexity as well as associated conductor and feeding losses. In addition, this chapter provides the geometrical parameters for optimizing the  $90^\circ$  delay line and the principles for right-hand circular-polarization (RHCP) and left-hand circular-polarization (LHCP) structures. The design procedures for RHCP and LHCP AFTSA-SC antennas are experimentally verified by prototype measurements. An agreement between calculated and measured results is observed.

The proposed CP design presents an ability to receive a diverse polarity wave with the advantages of low profile, low cost, and an endfire characteristic and can replace bulky horn antennas with very close performance. In addition, this design can be scaled up to operate at 77 GHz for automotive radar applications and/or higher MMW frequency such as 94 GHz and 144 GHz and 220 GHz. Furthermore, this high-gain antenna is a good candidate for MMW imaging and detection applications. The proposed antenna, due to its low cost and high efficiency, can be employed as a feed for reflectarray antennas.

In the following sections, the main contributions of this work are presented including the design of a novel state-of-the-art single-feed circular-polarization AFTSA-SC antenna profile. The engineering design aspect is detailed in Sect. 3.2. Analysis and understanding of the behavior of the RHCP AFTSA-SC profile, as well as showing key parameters to obtain a circular-polarization wave at the desired band, are presented in Sects. 3.2.1 and 3.2.2. Details of prototyping process and realization of RHCP and LHCP antenna profiles including measured results to demonstrate circular-polarization performance, return loss, axial ratio, and radiation patterns are given in Sect. 3.3.

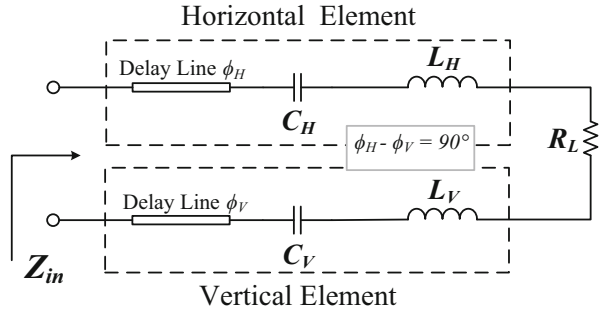
## 3.2 Design Procedure

Figure 3.1 shows the geometry of a circular-polarized antenna element including its main design parameters. It consists of a pair of AFTSA-SC antennas. These two AFTSA-SC antennas are aligned orthogonally to each other. The vertical element on the  $zy$ -plane is inserted through the horizontal element that lies on the  $xy$ -plane. The  $50 \Omega$  input port feeds equally both the horizontal and vertical elements, as shown in Fig. 3.2. Two orthogonal modes are excited along the  $x$ -direction and  $z$ -direction. A  $90^\circ$  phase shift is provided by substrate cuts indicated as  $S_V$  and  $S_H$ , which leads to a CP mode.

The first design guideline involves identifying the desired operating band of the AFTSA-SC antennas as reported by Yngvesson et al. [20] and [27]. The substrate thickness  $h$  of the antenna is

$$0.005 \leq \left( h = \frac{c_0}{f_1 (\sqrt{\epsilon_r} - 1)} \right) \leq 0.03. \quad (3.1)$$

**Fig. 3.2** The equivalent circuit model of the circular-polarization AFTSA-SC antenna



The condition for the aperture width  $W_a$  is given by

$$W_a \geq c_0/2f_1, \tag{3.2}$$

where  $f_1$  is the lowest frequency in the selected band,  $c_0$  is the speed of light, and  $\epsilon_r$  is the relative permittivity of the substrate.

The tapered slot profile is defined by the Fermi-Dirac function, first reported by Sugawara et al. [28] as

$$f(y) = \frac{-a}{1 + e^{-b(y-c)}}, \tag{3.3}$$

where  $y$  is a variable from  $-L_f$  to  $L_s$ . The length from the input feed line to the start point of the corrugation is  $L_f$ .  $L_s$  is the length from the start point of the corrugation to the end of the slot. The constant  $a$  is the asymptotic value of the width of the taper, and  $W_a = 2a$ . The parameter  $c$  is related to the  $y$ -coordinates of the Fermi-Dirac function inflection point, while the parameter  $b$  is related to the gradient at inflection point  $c$ . The variable ranges recommended in Ref. [27] are

$$5\lambda_g \geq a \geq 3\lambda_g, \tag{3.4}$$

$$1.5\lambda_g \geq b \geq 0.8\lambda_g, \tag{3.5}$$

$$2\lambda_g \geq c \geq \lambda_g, \tag{3.6}$$

where  $\lambda_g$  is the guided wavelength.

To enhance the radiation characteristics such as reducing the sidelobes and cross polarization levels, and enhancing the matching impedance [27], sine-shaped corrugations are employed at the edge of the AFTSA, as shown in Fig. 3.1. The sin-corrugation profile is defined as  $A_r \sin ky$ , where  $A_r$  is the amplitude constant, and  $k$  is the period constant. Based on Ref. [27],  $A_r$  and  $k$  have empirical guideline ranges

**Table 3.1** The RHCP-AFTSA-SC optimized parameters

Parameter	$L_H$	$L_f$	$L_s$	$W_H$	$W_V$	$S_H$	$S_V$
Value (mm)	51.5	17.7	34	13	13	2	0.8
Parameter	$d_H$	$d_v$	$d_{vH}$	$h$	$L_{fV}$	$A_f$	$k$
Value (mm)	6.07	13.7	1.7	0.2	11.7	0.2	6.5
Parameter	$r_c$	$r_v$	$a$	$b$	$c$		
Value (mm)	6	7	4.8	0.35	4		

All dimensions are given in mm

of  $\lambda_g/3 \geq A_f \geq \lambda_g/10$  and  $k \geq 1.5 \lambda_g$  which could be optimized to enhance reflection coefficient and antenna gain, as well as to reduce sidelobe level.

After the initial antenna design, the optimization was performed using the full-wave CST Microwave Studio's time-domain solver. The circular-polarization AFTSA-SC is implemented using Rogers RT/Duriod 4003 substrate with  $\epsilon_r = 3.55$ ,  $\tan \delta = 0.0027$  at 10 GHz, with a thickness = 0.2 mm. It is designed and optimized to operate over the 55–65 GHz band. The final dimensions are presented in Table 3.1. CST tools are then used to study the effect of the delay lines (substrate cuts).  $S_V$ ,  $S_H$ , and  $d_{HV}$  are discussed and described with more detail in Sect. 3.2.2.

### 3.2.1 Simulated Results of the RHCP AFTSA-SC Profile

PCB-TSAs are forms of traveling wave antennas, in which the tapering structure topology creates only a linear polarization or dual polarization achieved with a single or dual feed. The circular polarization can be achieved with a dual TSA: one oriented horizontally and the other vertically, with a  $90^\circ$  phase shift required between the feeding ports. However, single-feed circular-polarized TSAs have not been reported anywhere, to the authors' knowledge. This work presents a novel state-of-the-art circular-polarization AFTSA-SC with a single-feed topology implemented design, which has a high gain, high efficiency, low cost, and relatively low profile and is easy to fabricate. Furthermore, the CP AFTSA-SC design can be constructed in RHCP and LHCP, and the antenna is easy to optimize to the desired characteristics.

The simulated RHCP axial ratio (AR) and reflection coefficient ( $S_{11}$ ) of the CP-AFTSA-SC antenna are plotted versus frequency in Fig. 3.3. The bandwidth for a  $-10$  dB return loss covers the axial ratio band, which shows an  $S_{11}$  below  $-15$  dB for the entire 55–65 GHz band. A wide circular-polarization bandwidth of 3.8 GHz is maintained across a band of 59.1–62.9 GHz for an axial ratio of less than 3 dB. Furthermore, Fig. 3.4 shows the results of the RHCP profile's realized gain, and in this case the cross polarization waves are the LHCP realized gain. The CP antenna is RHCP dominant to LHCP with 9 dB in a different range of gain.

In order to further understand the behavior of the CP AFTSA-SC, the electric field distribution was investigated and studied at 60 GHz with the help of the CST-MWS. Figure 3.5 shows snapshots of the RHCP AFTSA-SC electric field

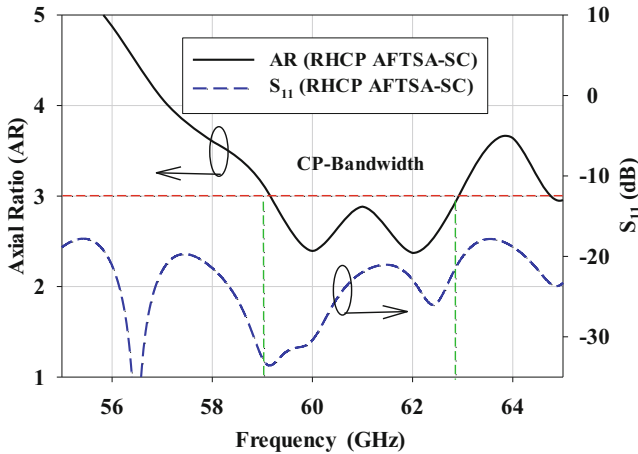


Fig. 3.3 Simulated axial ratio and  $S_{11}$  of RHCP AFTSA-SC antenna

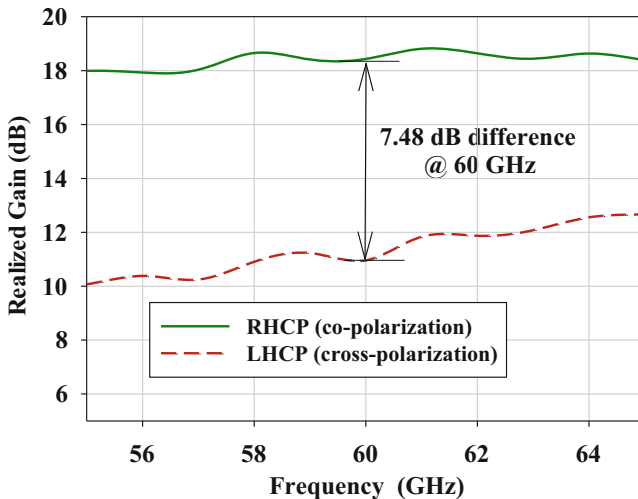
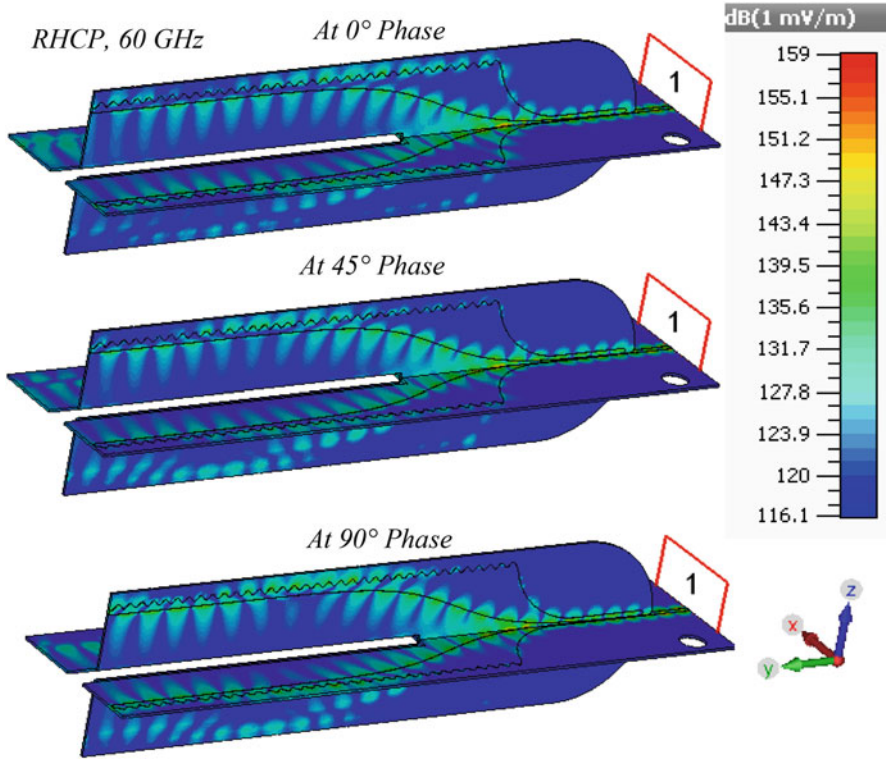


Fig. 3.4 Realized gain of the RHCP FTSA-SC antenna, and cross polarization response expressed as LHCP

at 60 GHz for  $0^\circ$ ,  $45^\circ$ , and  $90^\circ$  phases. The electric field distribution originating at the feed line splits into two pairs in the beginning of the antenna slot. One pair consists of horizontal pear-waves, present in the E-plane propagating on the  $xy$ -plane. Meanwhile, the electric field distribution behavior shows there is less effect of the vertical layer and groove on the vertical element. Likewise, for the H-plane that propagates on the  $zy$ -plane, it is observed the horizontal element has less effect on the electric field distribution that comes from the vertical element, as illustrated in Fig. 3.5.





**Fig. 3.5** A time snapshot of the electric field of RHCP AFTSA-SC at 60 GHz for  $0^\circ$ ,  $45^\circ$ , and  $90^\circ$  phases

The slot width changes the relative permittivity of the substrate, which changes the propagation delay between the slots. An optimized slot width for  $S_H$ ,  $S_V$ , and the inserting distance  $d_{VH}$  leads to a  $90^\circ$  phase difference between the horizontal and vertical elements. As a result, the antenna proves that the horizontal and vertical field components have a circular polarization. The two components have equal magnitude and a  $90^\circ$  time-phase difference between them.

### 3.2.2 CP Parametric Study

As shown in Fig. 3.6, when the cutout width,  $S_H$ , is increased from  $0.07$  to  $1.4 \lambda_g$ , there are slight changes in the antenna AR, when  $S_H$  is varied from  $0.07$  to  $1.1 \lambda_g$ ; however, when  $S_H \geq 1.4 \lambda_g$ , this indicates a phase delay outside the desired bandwidth. The  $S_H$  changes the phase delay from the taper slot to another slot at the horizontal element. In Fig. 3.7, any variation in  $S_V$  also changes the phase

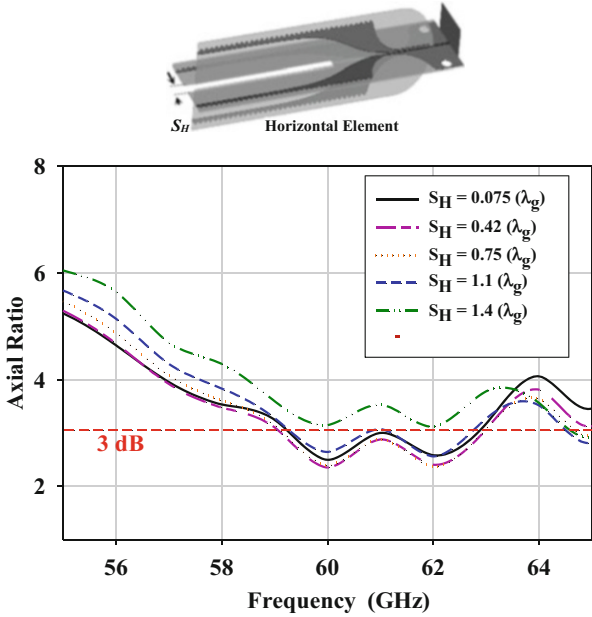


Fig. 3.6 The impact in varying: the width cutout ( $S_H$ ) of the horizontal element

delay from the taper slot to another slot at the vertical element. This parameter influences the circular-polarization bandwidth; optimizing  $S_V$  leads to a downshift in axial ratio response. Figure 3.8 shows the effect of the vertical element’s inserting distance ( $d_{VH}$ ). It can be concluded that adjusting the inserting distance  $d_{VH}$  leads to controlling the circular-polarization bandwidth up and down the resonant frequency and to achieve a desired  $AR \leq 3$  dB bandwidth. Therefore, these three parameters affect the axial ratio level, which can be optimized at certain frequencies to obtain the required CP band. All optimized dimensions of CP AFTSA are listed in Table 3.1.

### 3.3 Measured Results

#### 3.3.1 Prototyping Process

The CP AFTSA-SC prototypes are fabricated using an LPKF etching laser machine. Photographs of the CP AFTSA-SC RHCP design prototypes are shown in Fig. 3.9a and b, which offer a top and bottom view for both the horizontal and vertical elements. The laser machine cuts slots through the substrate, where the vertical element is cross aligned, and slides through the grooved slot of the horizontal elements, and then the feed line of the vertical element is soldered to the horizontal

**Fig. 3.7** The impact of varying: the width cutout ( $S_V$ ) of the vertical element

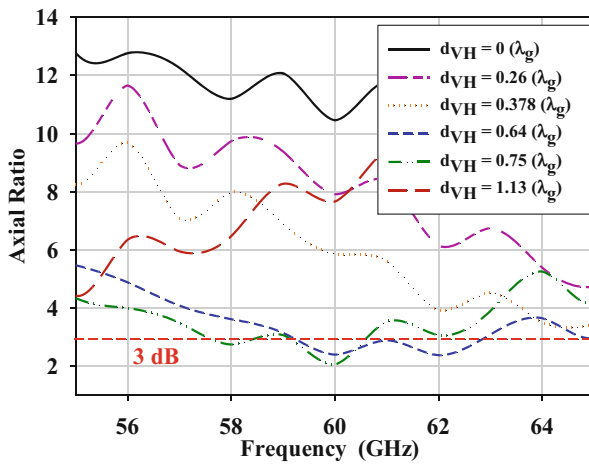
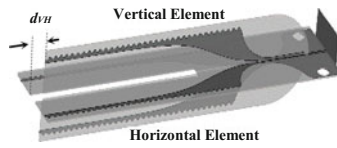
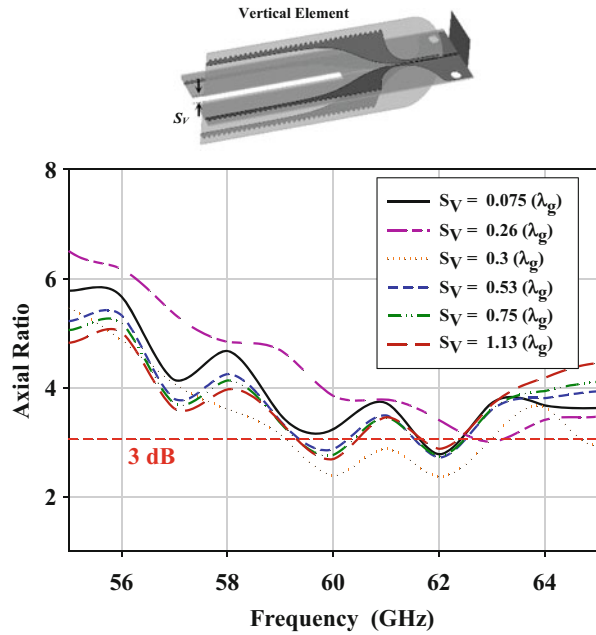


**Fig. 3.8** The impact of varying: the inserting distance ( $d_{vH}$ )

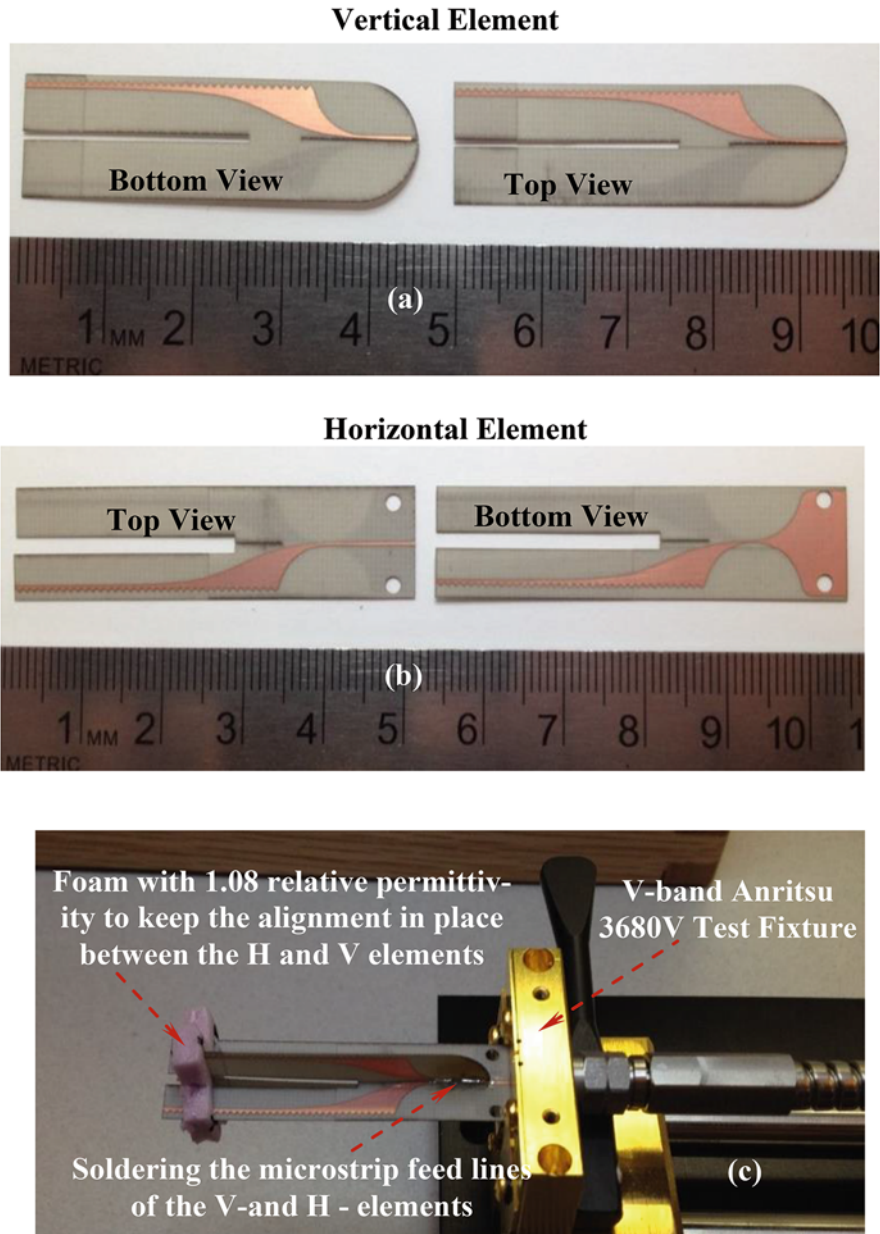


**Fig. 3.9** Photographs of the CP AFTSA-SC prototypes, horizontal and vertical elements RHCP design

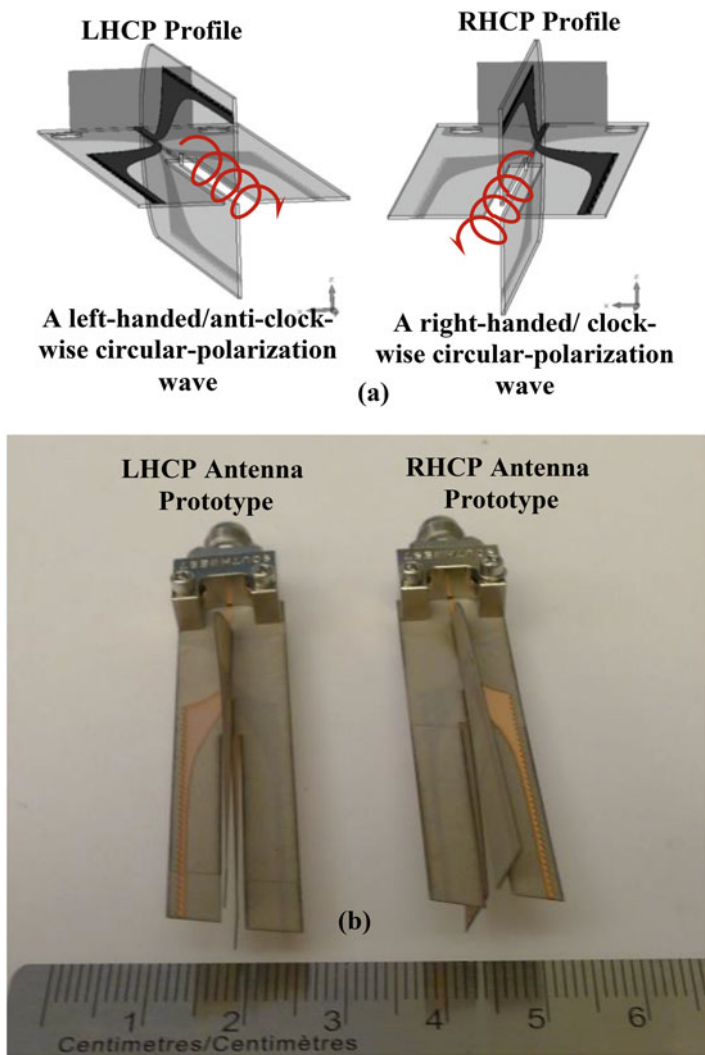
element's feed line. Furthermore, Fig. 3.9c shows the setup of the reflection coefficient measurement for the prototype, the simulated and measured reflection coefficient  $S_{11}$  results of the CP AFTSA-SC, and the linear polarization for AFTSA-SC elements. The reflection coefficient measurement is conducted using an Agilent network analyzer PNA (N5227A) at a band of 55–67 GHz, and the antenna is connected using an Anritsu Test Fixture (3680 V). The vertical antenna element is inserted and soldered at the feed line connection to the horizontal elements, and a piece of foam is attached to the antenna, as indicated in Fig. 3.9c, to maintain alignment of the vertical and horizontal elements. The relative permittivity of the foam is 1.08.

### 3.3.2 RHCP and LHCP Profile Prototypes

The AFTSA-SC antenna can be formed in RHCP and in LHCP profile. The direction of the circular-polarization wave depends on the position of the horizontal and the vertical element's feed line taper slot. In the case of replacing both feed tapered slots on the right side of the aperture (from the perspective of the antenna's front view), the antenna then generates a RHCP, and if both feed tapered slots are replaced on the left side of the aperture, then the antenna generates a LHCP – as shown in Fig. 3.10a. Both RHCP and LHCP profiles are designed accordingly with the dimensions listed in Table 3.1. Both profiles are fabricated and illustrated in Fig. 3.10b.

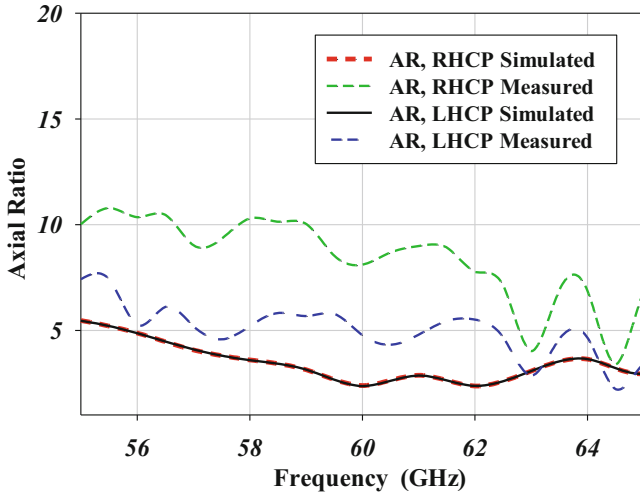
The measured and calculated axial ratio results for the RHCP and LHCP AFTSA-SC profiles are illustrated in Fig. 3.11. The simulated axial ratio results for the RHCP and LHCP are identical to each other, and the performance with AR <3 dB at 3 GHz is about 43% of CP bandwidth. The RHCP and LHCP profile measured results of AR <3 dB are presented around 63 and 64.5 GHz, and the RHCP response is closer to the calculated results, compared to the LHCP response. The difference between the simulated and measured results is due to fabrication errors and to misalignment of the V- and H-elements. The microstrip feed line of the H-elements is attached to the V-elements using hand soldering. It is difficult to achieve a perfect 90° between the elements due to the imperfection of hand alignments during soldering. To keep the aperture of the elements perpendicularly aligned, a foam form is attached to the two elements, as shown in Fig. 3.9c for the  $S_{11}$  measurements, and in Fig. 3.14 for the radiation pattern measurements.

Figure 3.12 shows a comparison between the measured and simulated results of the reflection coefficient and realized gain of the RHCP AFTSA-SC element. The antenna bandwidth is defined as  $S_{11} < -10$  dB covering the entire band of 55–67 GHz, and the measured return loss is better than  $-15$  dB over the entire frequency range of 57–67 GHz. Generally, there is a good agreement between the simulated and measured results. Fig. 3.13 shows the LHCP profile measured and simulated results for the return loss and gain. The  $S_{11} < -10$  dB covers the entire band, and  $S_{11} < -20$  dB is indicated from 58.4 to 63.5 GHz of the measured result. The gain measurements are achieved by replacing the RHCP/LHCP AFTSA-SC



**Fig. 3.10** (a) Sketch of RHCP and LHCP AFTSA-SC antennas; (b) RHCP and LHCP antenna prototypes

(antenna under test) with a V-band standard-gain horn. However, the measured gain shows a slight discrepancy from the simulated results in terms of the rippled performance within the range of 61–67 GHz. This may be due to errors in the prototype alignment between the crossed antenna elements, to waveguide-to-coax adapter mismatch, and/or to measurement errors. This misalignment error can be eliminated by employing a high-precision mechanical soldering machine and alignment unit which has been used for industrial applications.



**Fig. 3.11** Comparison of measured and calculated axial ratios for the LHCP and RHCP AFTSA-SC antennas

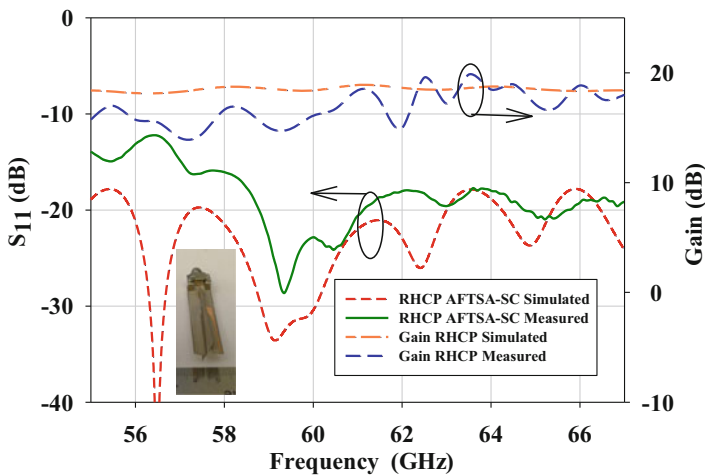


**Fig. 3.12** Comparison of measured and calculated reflection coefficient  $S_{11}$  and gain results for the RHCP AFTSA-SC antenna

Figure 3.14 shows the fabricated prototype for the proposed antenna mounted at the far-field position in the MMW anechoic chamber. The antenna is connected to the End Launch V-band connector and aligned at the testing scanning arm in the anechoic chamber to perform radiation pattern measurements. The E-plane co-polarization component is presented in the  $xy$ -plane, aligned with the horizontal element, and the co-polarization H-plane is presented in the  $zy$ -plane. Furthermore,

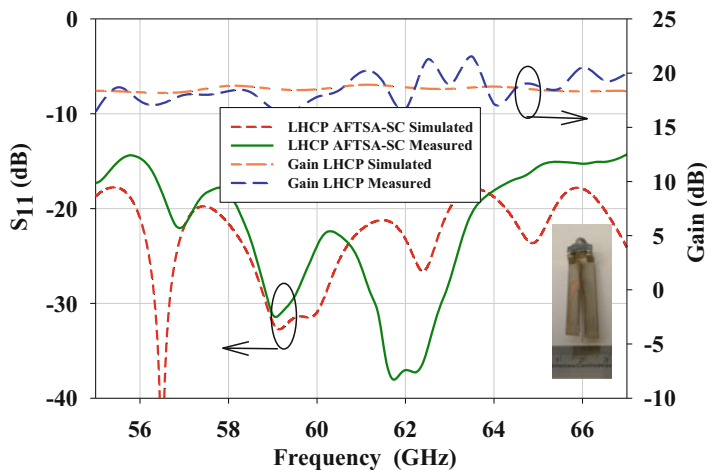


**Fig. 3.13** Comparison of measured and calculated reflection coefficient  $S_{11}$  and gain results for the LHCP AFTSA-SC antenna

during the antenna measurement process, to keep the flatness of the thin substrate, the alignments might be changed slightly with the change of both elements, which is reserved by foam at the antenna's endfire aperture, as shown in Fig. 3.14.

This proposed design can be employed in an array structure. With tapered slot antennas, the spacing between the elements depends on the aperture width between slots. However, this spacing would be more than  $\lambda_0/2$ . In this case, a tapering power destitution can be applied to reduce the grating lobe and the sidelobe level as spacing increases by  $>\lambda_0/2$ . This CP design presents an ability to receive a diverse polarity wave with the advantages of low profile, low cost, and endfire characteristic, which can replace a bulky antenna horn, with very close antenna performance. In addition, this design can be employed in CP phased antenna arrays, which can scale up for 30 GHz and down to operate at 77 GHz for automotive radar applications and/or a higher MMW frequency such as 94, 144, or 220 GHz. Furthermore, this high-gain antenna is a good candidate for MMW imaging detection applications, and due to its low cost and high efficiency, it can be employed as a feed for reflectarray antennas.

Figures 3.15 and 3.16 present the simulated and measured results of E-plane ( $xy$ -plane) and H-plane ( $zy$ -plane) radiation patterns for the LHCP AFTSA-SC at 59, 60, and 61 GHz. Figure 3.15 shows the radiation patterns of the LHCP AFTSA-SC, and Fig. 3.16 illustrates the LHCP AFTSA-SC profile patterns. One can observe that a good endfire axial ratio is obtained for both the RHCP and LHCP antennas. Fortunately, the radiation patterns at the selected frequencies show a good agreement between the measured and simulated results. Furthermore, there is a low sidelobe level of about  $-16.3$  and  $-7.9$  dB in the H- and E-plane, respectively, at 60 GHz. In the selected band, the AFTSA-SC exhibits a HPBW of about  $17$ – $19^\circ$  and  $14$ – $16^\circ$  in the H- and E-plane, respectively. However, one notices a slight difference between



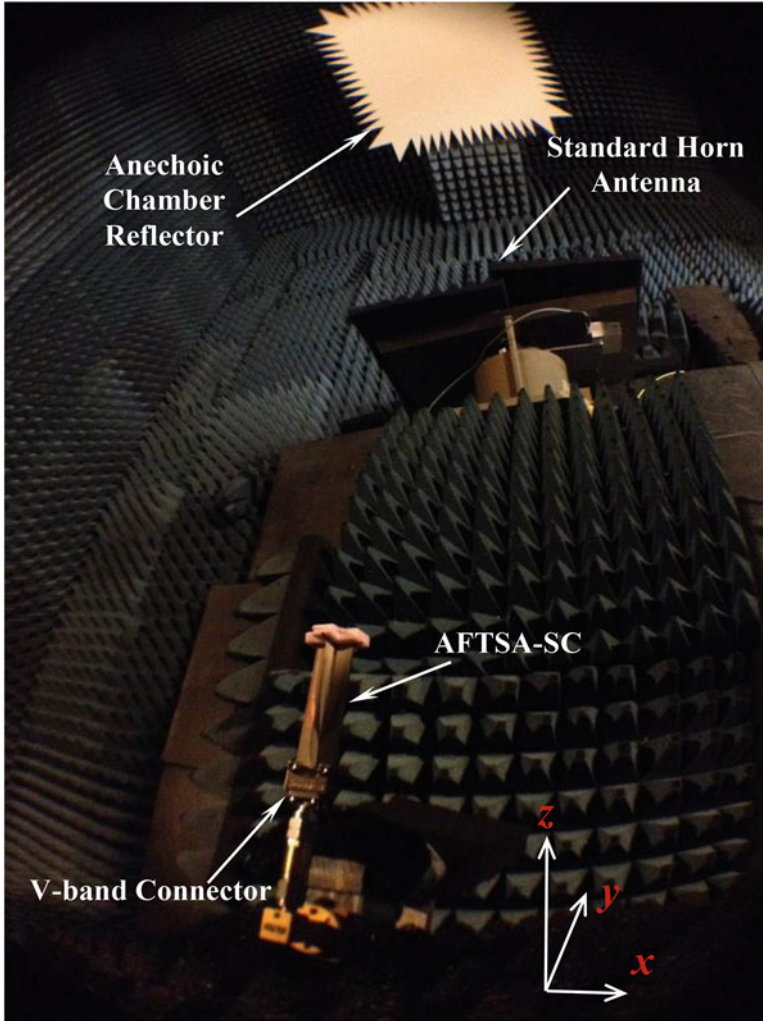


**Fig. 3.14** Radiation patterns measurement setup at the mm-wave anechoic chamber, the CP AFTSA-SC, uses the End Launch 1.85 mm connector

the measured and simulated patterns at some frequencies. This is contributed to by misalignment on aperture cross elements, measurement errors, and mounting antenna setup. Finally, the proposed antenna shows a stability and good radiation pattern for the whole range of the operating bandwidth.

**Fig. 3.15** Comparison of E- and H-plane measured and calculated radiation patterns for LHCP AFTSA-SC profile at 59, 60, and 61 GHz

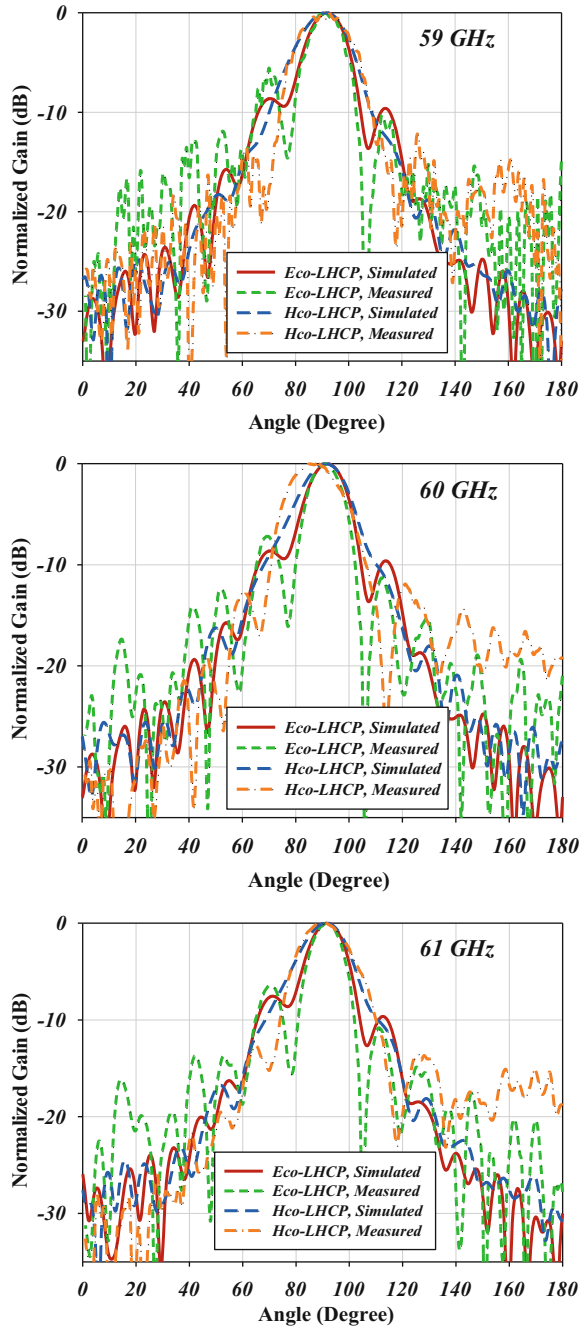
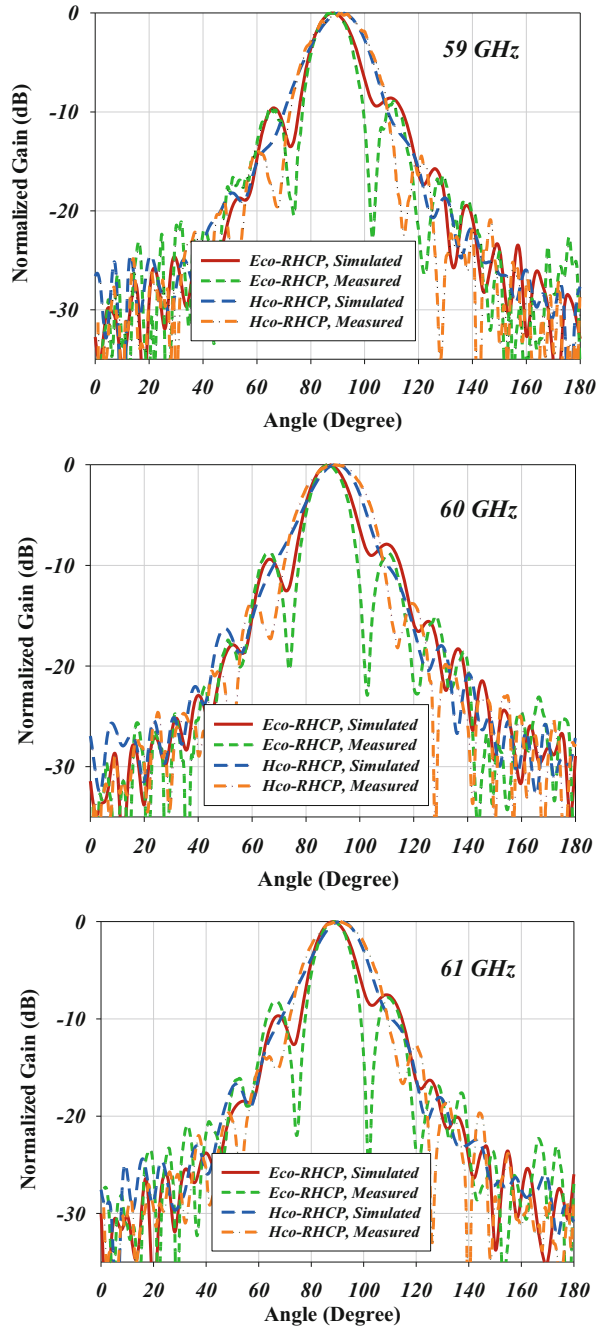


**Fig. 3.16** Comparison of E- and H-plane measured and calculated radiation patterns for RHCP AFTSA-SC profile at 59, 60, and 61 GHz



### 3.4 Future Research Direction and Potential Applications for the MMW Printed Circular-Polarized AFTSA-SC

The circular-polarized AFTSA-SC can be integrated into a beam steering array with an electronics phase shifter or as a low-cost alternative purpose for the piezoelectric transducer (PET) as a controlled phase shifter [29]. A Y-junction-shaped power divider is preferable for the endfire antenna since it reduces the discontinuity caused by the feed line bends, which reduces the reflection coefficient and increases the antenna impedance bandwidth. An electromagnetic bandgap (EBG) structure surrounded feeding network is preferable for increasing the isolation between the output ports and leads to a reduction in mutual coupling and surface waves [30, 31]. Furthermore, an unequal feeding network division is recommended with the Taylor N-bar in order to reduce the sidelobe level ratio (SLR) and associated grating lobes. A wideband circular-polarized beam steering phased array with a 60 GHz circular-polarized AFTSA-SC can be developed for wideband 2D or 3D image detection scanning for security and medical diagnosis applications. This new single-feed circular-polarized AFTSA-SC antenna provides a diverse polarity to enhance the image contrast. This design has a wide bandwidth, high gain, low feeding network loss, low cost, and low profile. It is believed that these features will fulfill MMW scanning sensor requirements and enhance imaging detection system performance.

### 3.5 Summary

A single-feed CP for an AFTSA-SC antenna with a low-cost PCB, high gain, and stable endfire radiation characteristic along the frequency range of 50–67 GHz was developed and implemented. Two CP antenna prototypes have been introduced using AFTSA-SC with an RHCP profile and LHCP profile. A new design procedure using a single excitation port for TSA antenna types has been introduced for obtaining a  $90^\circ$  phase shift between two orthogonal modes using slotted cutouts in the antenna substrate leading to the CP mode. A high-gain and endfire radiation pattern antenna is preferable for millimeter-wave applications especially for imaging detection systems. In addition, a circular-polarization antenna may receive more waves with desirable reflection characteristics from a target to be imaged than the linearly polarized. Further, a linearly polarized antenna receives waves depending on the particular orientation of the scanned target, whereas a circular-polarization antenna receives more uniform reflection characteristics. In this work, the simulated CST results have been validated using measurements for the return loss, gain, axial ratio bandwidth, and radiation pattern performance. The general trend is a good agreement between the measured and simulated results. Fabrication errors caused by misalignments between the orthogonal elements have led to a difference between simulation and measurement in axial ratio results. The proposed single-feed CP

AFTSA shows significant performance as a low-cost, high-gain CP and a highly efficient antenna for potential future research work in millimeter-wave imaging detection system applications.

## References

1. E.E.M. Woestenburg, L. Bakker, M.V. Ivashina, Experimental results for the sensitivity of a low noise aperture array tile for the SKA. *IEEE Trans. Antennas Propag.* **60**(2), 915–921 (2012)
2. D.M. Pozar, S.M. Duffy, A dual-band circularly polarized aperture-coupled stacked microstrip antenna for global positioning satellite. *IEEE Trans. Antennas Propag.* **45**(11), 1618–1625 (1997)
3. A. Perron, T. Denidni, A. Sebak, Circularly polarized microstrip/elliptical dielectric ring resonator antenna for millimeter-wave applications. *IEEE Antennas Wirel. Propag. Lett.* **9**, 783–786 (2010)
4. Y. Dong, H. Toyao, T. Itoh, Compact circularly-polarized patch antenna loaded with metamaterial structures. *IEEE Trans. Antennas Propag.* **59**(11), 4329–4333 (2011)
5. Z. Wang, S. Fang, S. Fu, S. Jia, Single-fed broadband circularly polarized stacked patch antenna with horizontally meandered strip for universal UHF RFID applications. *IEEE Trans. Microwave Theory Tech.* **59**(4), 1066–1073 (2011)
6. H. Chen, Y. Wang, Y. Lin, C. Lin, S. Pan, Microstrip-fed circularly polarized square-ring patch antenna for GPS applications. *IEEE Trans. Antennas Propag.* **57**(4), 1264–1267 (2009)
7. Y. Zhou, C. Chen, J. Volakis, Single-fed circularly polarized antenna element with reduced coupling for GPS arrays. *IEEE Trans. Antennas Propag.* **56**(5), 1469–1472 (2008)
8. S. Yang, K. Lee, A. Kishk, K. Luk, Design and study of wideband single feed circularly polarized microstrip antennas. *Prog. Electromagn. Res.* **80**, 45–61 (2008)
9. W. Kim, N. Moon, H. Kim, Y. Kim, Linear polarization sum imaging in passive millimeter-wave imaging system for target recognition. *Prog. Electromagn. Res.* **136**, 175–193 (2013)
10. A. Duric, A. Magun, A. Murk, C. Matzler, N. Kampfer, The fully polarimetric imaging radiometer SPIRA at 91GHz. *IEEE Trans. Geosci. Remote Sens.* **46**, 2323–2336 (2008)
11. O. Stahli, C. Matzler, A. Murk, N. Kampfer, Sky measurements with the imaging polarimeter SPIRA at 91GHz, in *2010 11th Specialist Meeting on Microwave Radiometry and Remote Sensing of the Environment*, pp. 181–186, Mar 2010
12. E. Altshuler, R. Marr, A comparison of experimental and theoretical values of atmospheric absorption at the longer millimeter wavelengths. *IEEE Trans. Antennas Propag.* **AP-36**(10), 1471–1480 (1988)
13. C. Liu, Y. Guo, X. Bao, S. Xiao, 60-GHz LTCC integrated circularly polarized helical antenna array. *IEEE Trans. Antennas Propag.* **60**(3), 1329–1335 (2012)
14. S. Lin, Y. Lin, A compact outer-fed leaky-wave antenna using exponentially tapered slots for broadside circularly polarized radiation. *IEEE Trans. Antennas Propag.* **60**(6), 2654–2661 (2012)
15. A. Narbudowicz, X. Bao, M. Ammann, H. Shakhtour, D. Heberling, Circularly polarized antenna with steerable dipole-like radiation pattern. *IEEE Trans. Antennas Propag.* **62**(2), 519–526 (2014)
16. Q. Lai, C. Fumeaux, W. Hong, R. Vahldieck, 60 GHz aperture-coupled dielectric resonator antennas fed by a half-mode substrate integrated waveguide. *IEEE Trans. Antennas Propag.* **58**(6), 1856–1864 (2010)
17. A. Guntupalli, K. Wu, 60-GHz circularly polarized antenna array made in low-cost fabrication process. *IEEE Antennas Wirel Propag Lett* **13**, 864–867 (2014)
18. S. Ladan, A. Guntupalli, K. Wu, A high-efficiency 24 GHz rectenna development towards millimeter-wave energy harvesting and wireless power transmission. *IEEE Trans. Circuits Syst. I Regul. Pap.* **61**(12), 3358–3366 (2014)

19. J. Gomez-Tornero, D. Blanco, E. Rajo-Iglesias, N. Llombart, Holographic surface leaky-wave lenses with circularly-polarized focused near-fields—Part I: concept, design and analysis theory. *IEEE Trans. Antennas Propag.* **61**(7), 3475–3485 (2013)
20. K.S. Yngvesson, T.L. Korzeniowski, Y.S. Kim, E.L. Kollberg, J.F. Johansson, The tapered slot antenna—A new integrated element for millimeter wave applications. *IEEE Trans Microwave Theory Tech.* **37**, 365–374 (1989)
21. K. Sawaya, H. Sato, Y. Wagatsuma, K. Mizuno, Broadband fermi antenna and its application to mm-wave imaging, in *Proceedings of 2nd European Conference on Antennas and Propagation (EuCAP)*, Edinburgh, Nov 2007
22. B. Veidt, G.J. Hovey, T. Burgess, R.J. Smegal, R. Messing, A.G. Willis, A.D. Gray, P.E. Dewdney, Demonstration of a dual-polarized phased-array feed. *IEEE Trans. Antennas Propag.* **59**, 2047–2057 (2011)
23. H. Holter, T.-H. Chio, D.H. Schaubert, Experimental results of 144-element dual-polarized endfire tapered-slot phased arrays. *IEEE Trans. Antennas Propag.* **48**, 1707–1718 (2000)
24. A. Guntupalli, K. Wu, Frequency-steered directive beam with dual circular polarization and two-dimensional scan capability for millimeter-wave imaging and sensing systems, in *2014 IEEE 15th Annual Wireless and Microwave Technology Conference (WAMICON)*, 2014
25. S. Karamzadeh, M. Kartal, Circularly polarised MIMO tapered slot antenna array for C-band application. *Electron. Lett.* **51**(18), 1394–1396 (2015)
26. A. Guntupalli, K. Wu, Polarization-agile millimeter-wave antenna arrays, in *Microwave Conference Proceedings (APMC), 2012 Asia-Pacific*, IEEE, 2012, pp. 148–150
27. Z. Briqech, A. Sebak, T.A. Denidni, High gain 60 GHz antipodal fermi tapered slot antenna with sine corrugation. *Microw. Opt. Technol. Lett.* **57**(1), 6–9 (2015)
28. S. Sugawara, Y. Maita, K. Adachi, K. Mori, K. Mizuno, Characteristics of a mm-wave tapered slot antenna with corrugated edges. *IEEE MTT-S Int. Microwave Symp. Digest* **2**, 533–536 (1998)
29. Z. Briqech, A. Sebak, T.A. Denidni, Low-cost wideband mm wave phased array using the piezoelectric transducer for 5G applications. *IEEE Trans. Antennas Propag.*, *intended for the Special Issue on “Antennas and Propagation Aspects of 5G Communications,”* submitted in 2016
30. F. Yang, Y. Rahmat-Samii, *Electromagnetic Band Gap Structures in Antenna Engineering* (Cambridge University Press, Cambridge, 2009)
31. A. Elboushi, Z. Briqech, A. Sebak, 4-elements MMW array with EBG feeding network, in *Antennas and Propagation Society International Symposium (APSURSI)*, IEEE, pp. 162–163, 7–13 July 2013



**Zouhair Briqech** (S’11–M’15) received a Ph.D. in Electrical and Computer Engineering from Concordia University, Montreal, QC, Canada, in 2015. Since 2010, he has worked as a research assistant for the Department of Electrical and Computer Engineering at Concordia University, working on investigating millimeter-wave antenna designs for imaging detection systems, MIMO, and 5G applications. He pursued his postdoctoral fellow work on antennas and system designs for ground-penetrating radars (GPR), with the Electrical and Computer Engineering Department, and the Faculty of Civil Engineering at the Université de Sherbrooke,

Sherbrooke City, QC, as well as a Postdoctoral Researcher with the Institut national de la recherche scientifique (INRS), in Montreal, QC, Canada. He is currently a member of the antenna design team at MacDonald, Dettwiler and Associates MDA, Montreal, QC, Canada. His main research interests include MMW imaging detection systems, novel antenna design/microwave applications, EMI/EMC, DRA, SIW, EBG, ultra-wideband, multiband, RFID, circular-polarized antennas, and small antenna designs. He is a member of the Applied Computational Electromagnetics Society

(ACES). He is also a former member of Space Concordia in the Canadian Satellite Design Challenge (CSDC), which is involved with designing an antenna for the “Alexander” nanosatellite project at Concordia University.



**Abdel-Razik Sebak** (F'10) received a B.Sc. degree from Cairo University, Cairo, Egypt, and M.Eng. and Ph.D. degrees from the University of Manitoba, MB, Canada, all in electrical engineering. Dr. Sebak is a Tier 1 Concordia Research Chair and professor with Concordia University. Before joining Concordia University, he was a professor at the University of Manitoba. He was also with Cairo University and worked with the Canadian Marconi Company on the design of microstrip phased array antennas. His current research interests include phased array antennas, mm-wave antennas and imaging, computational electromagnetics, advanced composite materials for aerospace shielding and antenna applications, and interaction of EM waves with engineered materials and bio-electromagnetics. Dr. Sebak received the 2000 and 1992

University of Manitoba Merit Award for outstanding Teaching and Research, the 1994 Rh Award for Outstanding Contributions to Scholarship and Research, and the 1996 Faculty of Engineering Superior Academic Performance. Dr. Sebak is the General Chair of the 2016 ANTEM Symposium and served as the TPC Co-Chair of the IEEE ICUWB2015. He has also served as the Chair for the IEEE Canada Awards and Recognition Committee (2002–2004) and as the Technical Program Chair for the 2002 IEEE CCECE Conference and the 2006 ANTEM Symposium. He is a member of the Canadian National Committee of the International Union of Radio Science (URSI) Commission B.



**Tayeb A. Denidni** (M'98–SM'04) received M.Sc. and Ph.D. degrees in electrical engineering from Laval University, Quebec City, QC, Canada, in 1990 and 1994, respectively. From 1994 to 2000, he was a Professor with the engineering department, Université du Québec in Rimouski (UQAR), Rimouski, QC, Canada, where he founded the Telecommunications laboratory. Since August 2000, he has been with the Institut National de la Recherche Scientifique (INRS), Université du Québec, Montreal,

QC, Canada. He found RF laboratory at INRS-EM, Montreal. He has a great experience with antenna design, and he is leading a large research group consisting of three research scientists, eight PhD students, and two MSc students. He served as a principal investigator on many research projects sponsored By NSERC, FCI, and numerous industries. His current research areas of interest include reconfigurable antennas using EBG and FSS structures, dielectric resonator antennas, metamaterial antennas, adaptive arrays, switched multi-beam antenna arrays, ultra-wideband antennas, microwave antennas, and development for wireless communications systems. From 2008 to 2010, Dr. Denidni served as an Associate Editor for IEEE Transactions on Antennas and Propagation. From 2005 to 2007, Dr. Denidni served as an Associate Editor for IEEE Antennas Wireless Propagation Letters. Since 2015, he has served as Associate Editor for IET Electronics Letters. In 2004, he was elevated to the grade of Senior Member of the IEEE.

# Chapter 4

## High-Performance Hybrid Smart Antenna Array for Advanced Wireless Communication Applications

Nuri Celik

### 4.1 Introduction

Signals in wireless communication systems are exposed to several environmental effects such as attenuation, reflection, multipath, diffraction, and several other types of amplitude and phase distortion in a more severe way than their wired counterparts [1, 2]. To make matters worse, the wireless medium has to be shared by multiple users, creating significant interference issues and making the frequency spectrum very scarce. For this reason, the wireless communication systems typically have much lower data rates than wired systems. With development of advanced signal processing algorithms, low-power microprocessors, multiple access systems, and multiple antenna systems, the data rate gap between wireless and wired communication systems has been rapidly closing, in a good agreement with Edholm's Law [1].

Multiple access systems such as time division (TDMA), frequency division (FDMA), code division (CDMA), and space-division multiple access (SDMA) have been proposed to increase the wireless resources available to multiple users [2–5]. Combinations of TDMA, FDMA, and CDMA have been widely used in existing wireless communication systems, because their hardware requirements are minimized. On the other hand, SDMA systems, which take advantage of smart antennas, have not been widely adopted at the end-user level due to their size, cost, and hardware/software requirements.

SDMA can be effectively accomplished by enabling narrow beam/highly directive radiation patterns at the user equipment/base stations and adaptively steering the radiation pattern toward the base stations/other users. This way, the interference to the other users of the spectrum can be kept at a minimum, and the same radio resources can be allocated to the other nearby users. Smart antenna systems

---

N. Celik (✉)  
Trimble Inc, Sunnyvale, CA, USA  
e-mail: [nuri\\_celik@hotmail.com](mailto:nuri_celik@hotmail.com)



use multiple antennas to form a very directive radiation pattern, hence the name beamforming, as well as to adaptively steer the peak of this directive radiation pattern in the direction of the intended party, such as the base station, hence the name beamsteering [6].

Smart antenna systems adaptively perform the beamforming/beamsteering operations through the use of multiple antennas as well as additional radio-frequency (RF) hardware/software. These requirements usually limit the use of smart antenna systems in cost-prohibitive applications such as commercial wireless communications. To overcome these issues and enable the wide use of smart antennas in wireless communication systems, especially in commercial applications, the hybrid smart antenna array (HSAA) is introduced in this chapter.

In the first part of the chapter, the principles of the HSAA are described as well as the design/optimization of the antenna array with directional antenna elements. The element tilt angle is introduced as an array design parameter to extend the beamsteering range of the HSAA with directional array elements. Simulation results are provided to show the extended beamsteering range as well as its comparable performance to a fully adaptive smart antenna system. The genetic algorithm (GA) array geometry optimization for determining the best tilt angles is briefly discussed, and the performance of the HSAA with the optimized tilt angles is demonstrated through computer simulations.

In the second part of the chapter, the prototype wireless receiver implementing the HSAA at 2.4 and 60 GHz is described along with the experimental results. These two frequency bands have been intentionally chosen to reflect the advantages and viability of the HSAA for commercial wireless communication systems.

### ***4.1.1 Background on Smart Antenna Systems***

Smart antenna systems can form and steer a high-gain/directional radiation pattern in the direction of the intended party. Because the available power is radiated in a limited angular range, the limited power resources of mobile units are efficiently used. Therefore, an increased communication range for a given transmit power is achieved. For a cellular phone system, extended communication ranges result in a less dense base-station placement, decreasing the initial deployment costs. Additionally, smart antenna systems are capable of placing pattern nulls in direction of interferers. These mechanisms result in less interference received/created in the shared channel, leading to increased system capacity and immunity to intentional jammers.

As shown in Fig. 4.1, there are three main building blocks of a smart antenna system. The antenna subsystem can include multiple transmit or receive antennas. The beamsteering subsystem includes the hardware to handle the beamsteering operation and the control module to provide the beam pattern adaptation capability utilizing the feedback signal. In the following paragraphs, the existing smart antenna mechanisms performing these functions are discussed.

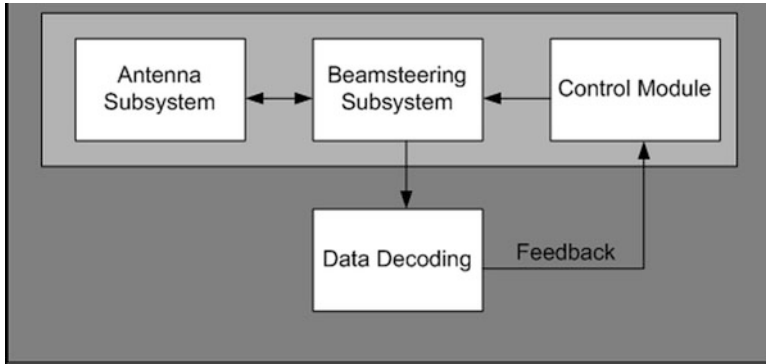


Fig. 4.1 Block diagram of a smart antenna system

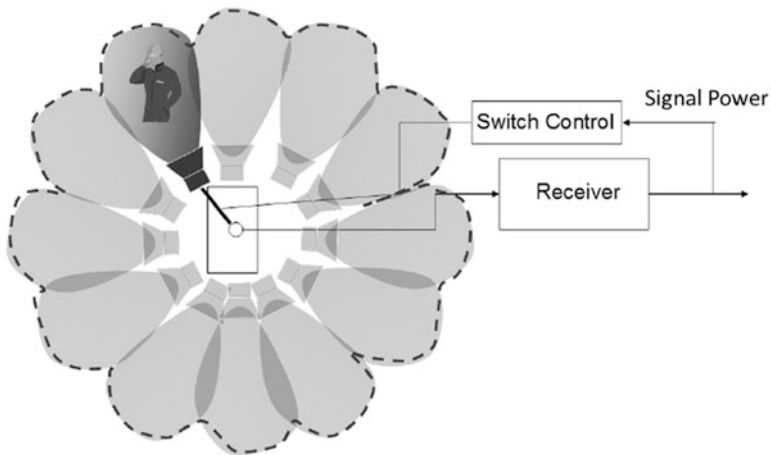


Fig. 4.2 Block diagram of an antenna switching system

Mechanical steering systems are the most common smart antenna systems and use a highly directive antenna connected to a gimbal mechanism. Systems employing this mechanical approach are mostly seen near airports or military sites.

Antenna switching systems employ multiple directional antennas and switch between these antennas depending on the user’s location. As shown in Fig. 4.2, this scheme employs multiple directional antennas, each with a different main beam direction to cover all possible locations of the mobile user.

One of the advantages of antenna switching is its simplicity. The switch controller scans the antennas and selects the antenna with the highest received signal power which corresponds to the darker colored antenna in Fig. 4.2. However, the signal power, illustrated by the dashed lines, fluctuates significantly with the direction of the user, especially when the user falls in between two antenna beams. This variation in the signal power is termed “scalloping” in the literature, and it

is closely related to the roll-off of the antenna pattern as a function of angle [7]. The scalloping is illustrated in Fig. 4.2 by dashed lines, which trace the edges of individual antenna radiation patterns. Also the system is susceptible to interference if the user and the interferer fall into the main lobe of the same antenna.

Mechanical steering and antenna switching systems rely on steering the fixed beam of a single antenna in the desired direction, hence they cannot be considered as beamforming systems. Systems described in the following paragraphs perform both the beamforming and beamsteering functions. These systems achieve beamforming and beamsteering by changing the amplitudes and the phases of the signals received by each antenna and combining them to form a beam in the desired direction and to place pattern nulls in the direction of interferers. In digital systems, this amplitude control and phase shift of signals at each array element can be equivalently described by multiplying the signal by a weight. This way, the signal at the array output can be formulated as a linear combination of the array element outputs with different weights.

Beam switching systems employ multiple preset directional radiation patterns and select the best pattern depending on the user location. Figure 4.3 shows such a beam switching system with a switch that selects between several precalculated antenna combining weights. These weights can be stored in a look-up table or implemented in several ways using specialized hardware. One way to implement these weights in hardware is to use a Butler matrix [9–12]. Butler matrix uses a combination of  $90^\circ$  hybrid couplers and fixed phase shifters to create a set of beams with different directions covering the desired angular region.

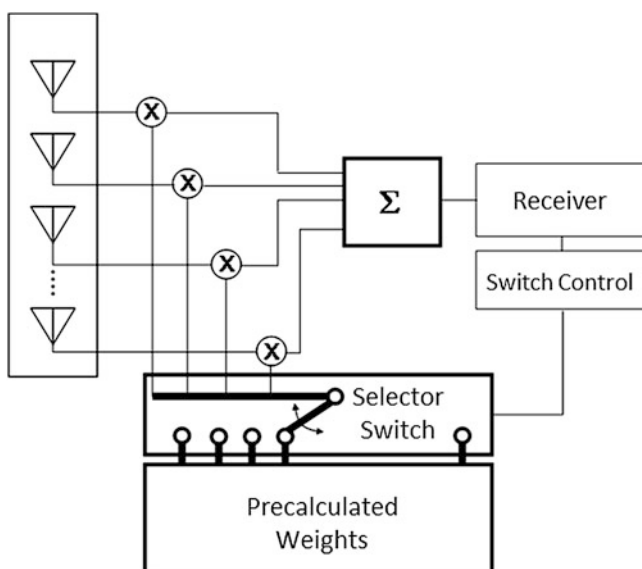


**Fig. 4.3** Block diagram of a beam switching system

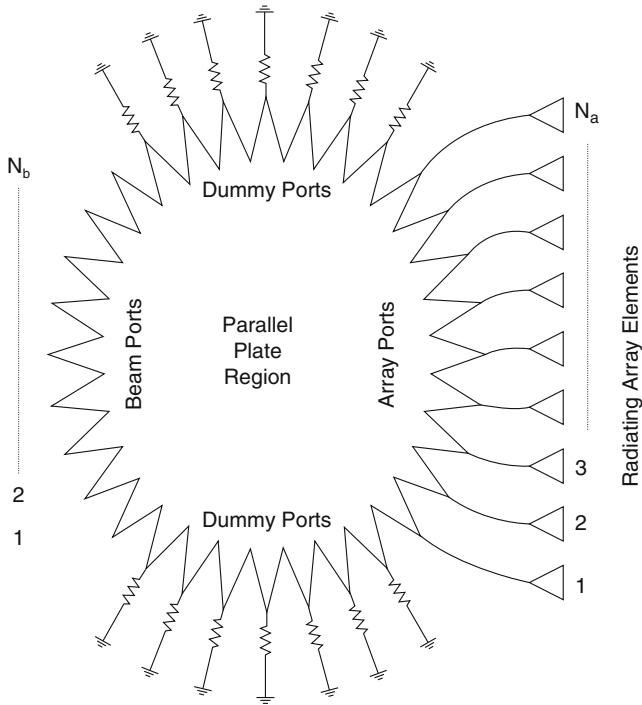
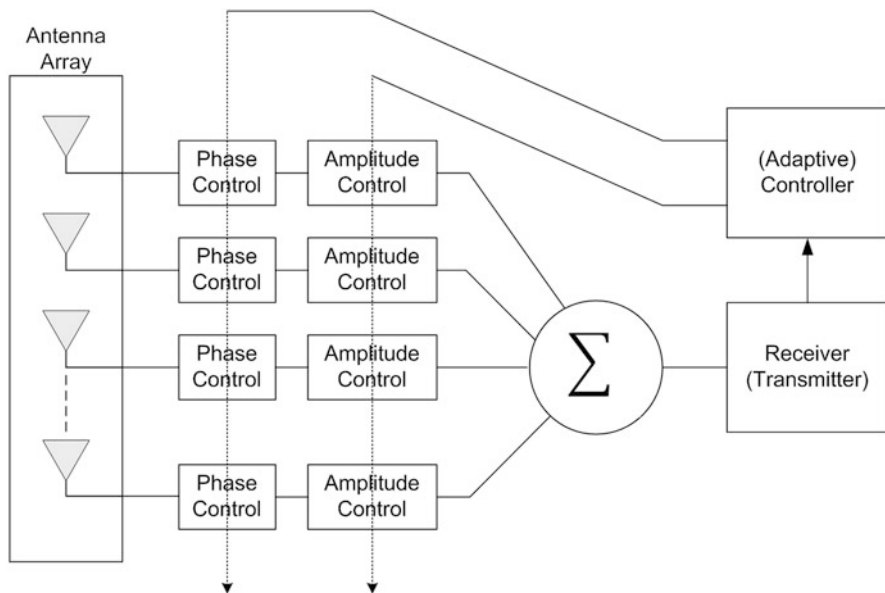


Fig. 4.4 Structure of the Rotman lens [14]

Unlike the Butler matrix, the Blass matrix uses time delays, which makes it more suitable for broadband operation [13]. Similarly, several fixed beams can be obtained using various microstrip structures such as the Rotman lens. The Rotman lens, shown in Fig. 4.4, is a special microstrip geometry acting as a fixed beamforming network to provide several fixed beams [14]. The advantages associated with a Rotman lens are its monolithic construction, ease of manufacturing, low cost, reduced weight, and simultaneous availability of multiple beams [15].

The smart antenna systems presented so far are based on switching between preset configurations; therefore, they have minimal complexity compared to a single antenna system. However, they have limited beamsteering and interference rejection ability. On the other hand, adaptive beamforming systems have the capability of steering the radiation pattern to an arbitrary direction and placing multiple nulls in the direction of the interferers. Adaptive beamforming can take place in the RF domain with the use of phase shifters and amplifiers as shown in Fig. 4.5 or in the digital domain with the help of advanced computer programs and multiple-channel analog-to-digital converters (ADC) as shown in Fig. 4.6.

To receive beamforming with an RF beamformer, the receiver steers its beam by changing the phases and amplitudes of the signals received at each array element while observing the power of the desired signal at the beamformer output. However,



**Fig. 4.5** Block diagram of an adaptive beamformer in the RF domain

as the signal combining is done prior to the receiver, it is not possible to apply adaptive algorithms. Henceforth, the controller has to search all possible steer angles in order to find the direction of the transmitter. The required search time renders this beamsteering scheme inapplicable to highly mobile communication scenarios. This is why beamforming in the RF domain is adopted in radar applications where the search operation is inherent and satellite communications where the relative position of the satellite does not change rapidly with respect to the control station. In spite of its searching time requirements, beamforming in the RF domain can still be attractive, because it avoids the RF hardware costs associated with a multichannel receiver. As beamforming is achieved in the RF domain, only a single-channel receiver is needed, which significantly reduces the hardware costs. Moreover, there are works in the literature focusing on integration of the phase shifters with the array elements, further reducing the system complexity [16–18]. For a detailed formulation of the RF beamformer operation and the description of underlying limitations, please see Ref. [6].

In a digital beamforming system, as illustrated in Fig. 4.6, the beamforming operation is done in the digital domain. Therefore, there must be as many receiver channels as the number of antennas, which results in significant additional costs. The received signals at the array elements are independently frequency downconverted to intermediate frequency (IF) signals, as ADCs have limited bandwidth. A multichannel ADC, included in the receiver, digitizes the IF signals, and then the ADC outputs are multiplied by complex weights and combined. Multiplication by

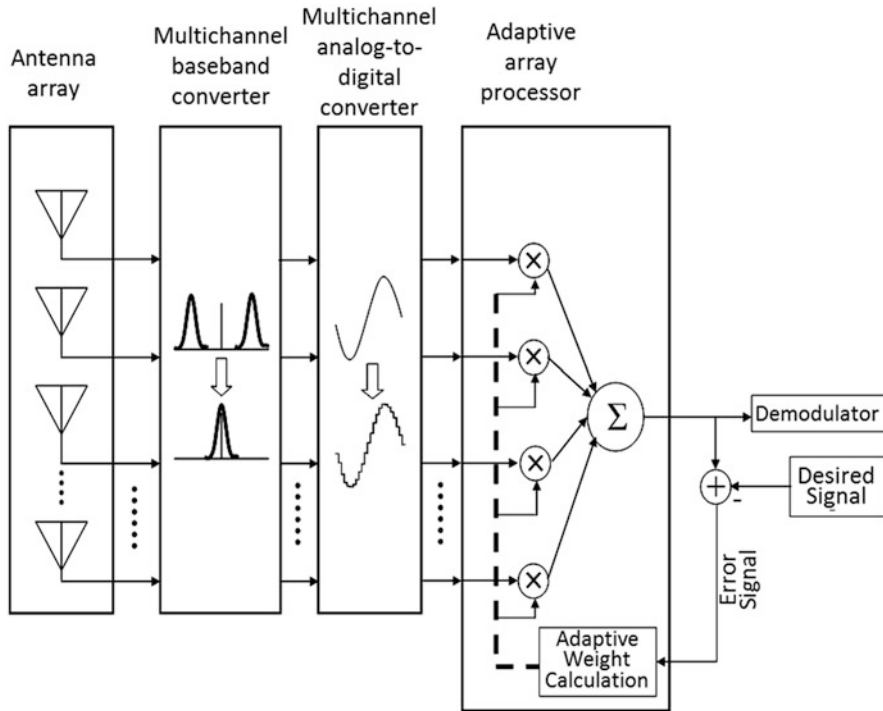


**Fig. 4.6** Block diagram of an adaptive digital beamformer [8] (Reproduced by the permission of John Wiley & Sons Inc.)

a complex weight adjusts both the phases and the amplitudes of the signals to form the desired beam. Unlike a phased array system, the adaptive digital beamforming system is data aided, meaning that the weights are modified according to the error between the desired signal and the beamformer output. The weights are adaptively calculated with the help of the data using several available algorithms such as phase-locked loop [19, 20], Applebaum [21–23], Shor [24], least mean squares (LMS) [25], and recursive least squares (RLS) algorithms [26]. Reference [6] includes a very detailed list of these algorithms and their descriptions.

### 4.1.2 Comparison of Existing Smart Antenna Approaches

In Table 4.1, a performance comparison of the existing smart antenna mechanisms is given. The gray cells in the table denote the desirable properties. With this information, it can be concluded that no single system is perfect, either leading to scalloping effects, high costs, significant computing power requirements, or limited beamsteering resolution. To overcome these problems and limitations, it is

**Table 4.1** Comparison of smart antenna methods

Mechanism Criteria	Mechanical	Antenna Switching	Beam Switching	Adaptive Beamforming in RF	Adaptive Digital Beamforming
Computational Complexity	Low	Low	Low	Low	High
Tracking Speed	Low	High	High	Mediocre	Mediocre
Hardware Cost	Mediocre	Low	Low	High	High
Beamsteering Resolution	High	Low	Low	Mediocre	High
Scalloping Effects	Low	High	High	Mediocre	Low
Interference Cancellation	Low	Low	Low	Mediocre	High

Gray cells denote desirable properties

necessary to come up with a hybrid system combining the advantages of one or more mechanisms while avoiding the associated drawbacks.

In order to come up with a smart antenna system that has low cost, high resolution, low computational complexity, high tracking speed, low scalloping effects, and high interference cancelation capability, a beamforming method combining the advantages of antenna switching and adaptive digital beamforming is proposed. The hybrid smart antenna array (HSAA) is the proposed middle solution between the antenna switching and adaptive digital beamforming approaches. Using highly directive antennas with each array element's main lobe looking in a different direction (tilting), a few of the array elements with the highest received signal powers are selected for the digital beamforming stage, hence decreasing the hardware cost and computational complexity, and leading to high tracking speeds and low scalloping effects with excellent interference cancelation capabilities. The HSAA is described in detail in the following section.

## 4.2 Hybrid Smart Antenna Array (HSAA)

Unlike the traditional adaptive antenna approaches, the HSAA employs several highly directive, high-gain array elements and selects a few of them for the beamforming stage as shown in Fig. 4.7. The HSAA system differs from the adaptive beamformer system of Fig. 4.6 by the inclusion of a smart switch and the use of a selection feedback from the adaptive array processor. The array elements in HSAA have directive radiation patterns with main beams directed to different locations due to element tilting. If the radiation patterns are aligned to look in exactly the same direction, the principle of pattern multiplication will become valid, the smart switch selection will become pointless, and the system will have limited

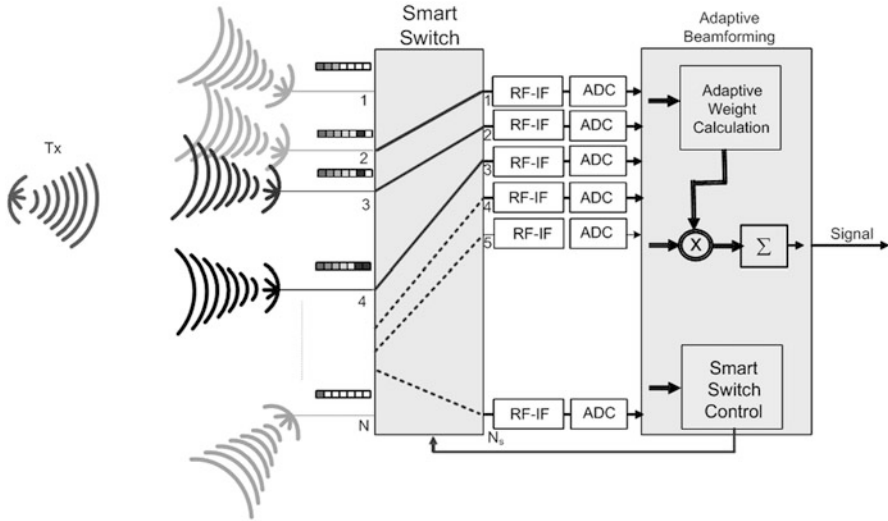


Fig. 4.7 Block diagram of the hybrid smart antenna array (HSAA) [6]

beam scanning range determined by the directivity of the array elements. Therefore, it is essential to have directive radiation patterns adjusted to have different directions for providing a performance gain, hence the tilting proposed in the HSAA.

The HSAA has  $N$  directive elements in the array with radiation patterns pointing to different directions. In order to have patterns pointing to different directions, each element is tilted with respect to the array axis. These tilt angles have to be optimized to provide uniform coverage. With this configuration, each array element will have different received signal power depending on the transmitter direction. The smart switch controller measures the power of the signal received by each array element and instructs the smart switch to connect  $N_s$  ( $N_s < N$ ) of them to the beamforming block. For the case shown in Fig. 4.7, the receive patterns of the 2nd, 3rd, and 4th array elements are well aligned with the transmitter's radiation pattern, so they are selected for the beamforming operation as indicated by the solid lines inside the smart switch.

An important concern in performing the array element selection is keeping the element spacing constant to eliminate beam splitting and grating lobe effects [27]. In order to achieve this, it must be ensured that neighboring elements are always selected for the beamforming operation. For this purpose, the tilt angles have to be monotonically increasing with the element index. In Fig. 4.8, the proposed array element tilting is illustrated for a linear array with uniform element spacing. The tilt angles are optimized using the genetic algorithm (GA) for a given  $N$ ,  $N_s$  and the element radiation pattern, to minimize the scalloping and provide coverage for all desired angular regions. The details of this optimization can be found in Ref. [28].



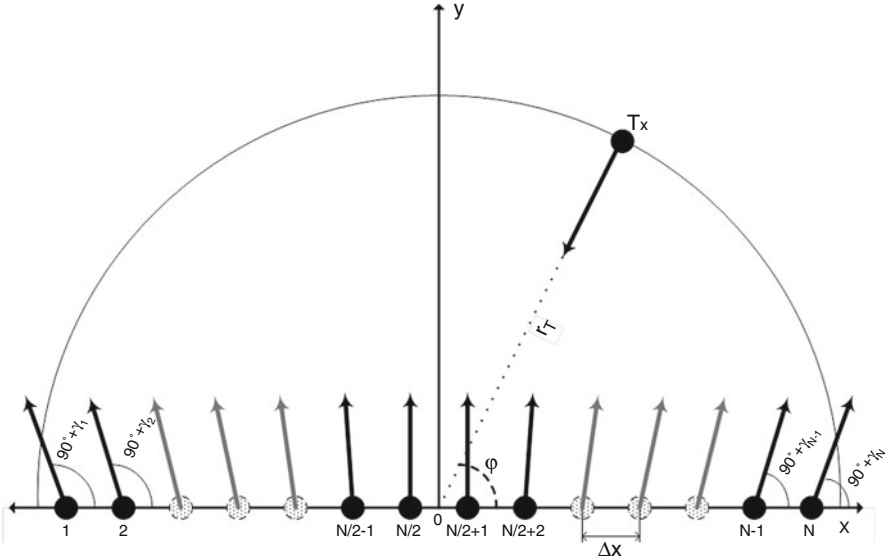


**Fig. 4.8** Array elements in an HSAA system should have monotonically increasing tilt angles [28]

The HSAA with optimized array geometry presents several advantages over the fully adaptive beamforming systems. Some of these are summarized below:

- **Use of high-gain array elements:** The existing smart antenna systems utilize low-gain, wide-beam elements and rely on the array gain component for increasing the overall gain of the system. This significantly increases the required number of array elements and makes the system infeasible for commercial applications. The HSAA can achieve a similar gain with significantly lower number of array elements.
- **Use of highly directive array elements:** The pattern beamwidth is an important performance indicator for smart antenna systems, as it determines the resilience of the system to interferers as well as the amount of environmental noise acquired by the system. By employing array elements that already have narrow beamwidths, the resulting array beamwidth becomes much narrower than arrays with the same number of isotropic elements.
- **Use of a few elements in the beamforming:** When the array elements have high directivity and high gains, the number of array elements required for the beamforming stage to meet the required overall gain will be significantly reduced. As HSAA needs significantly fewer elements in the beamforming stage, it results in significant savings in the system cost, as well as increased tracking ability due to reduced computational requirements.

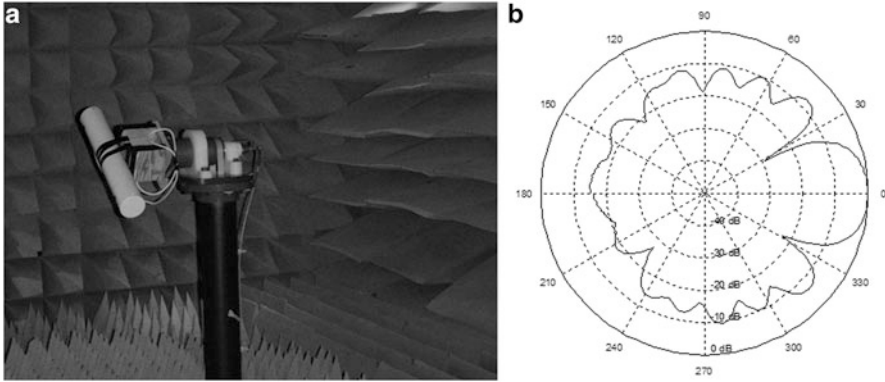


**Fig. 4.9** (a) The measurement setup in the antenna chamber, (b) the measured radiation pattern for the Hyperlink Technologies Yagi-Uda antenna [29]

#### 4.2.1 Performance Evaluation of HSAA Through Computer Simulations with Realistic Antenna Radiation Patterns

In this section, the results of the computer simulation studies implementing the HSAA system are presented. In these computer simulation studies, actual radiation patterns of commercially available antennas are employed. The simulated arrays consist of dipoles for the fully adaptive beamforming system and Yagi-Uda elements for the HSAA operating at 2.4 GHz. The realistic radiation patterns of the commercial antennas are measured in the antenna range as shown in Fig. 4.9.

The selected Yagi-Uda antenna has 15 dBi gain, and the diameter of the circular radome is 76 mm, which corresponds to  $0.6 \lambda$  at 2.4 GHz [29]. Moreover, the antenna is pretty directive with  $30^\circ$  half-power beamwidth (HPBW), promising great sidelobe level reduction performance for an HSAA system. The dipole antenna is a generic 2.4 GHz half-wave element with omnidirectional radiation pattern. In the computer simulations, an element spacing of 80 mm is considered because of the relatively larger radome size for the Yagi-Uda. The received SNR is set to 20 dB. The mutual coupling effects between the array elements have not been considered in the simulations.

In the simulations, it is assumed that part of the transmit signal is known to be able to use data-aided adaptive beamforming algorithms. This is a valid assumption since many communication systems employ predefined signals such as frame headers or training bits for signal processing or synchronization purposes [2]. In beamforming weight calculations, the least mean squares (LMS) algorithm [25] is used. LMS algorithm is adaptive and can be used for beamforming when the transmitter's direction is unknown.

In a very brief form, the LMS algorithm can be formulated as follows:

$$\hat{d}(t) = \mathbf{w}^H \times \mathbf{u}(t). \quad (4.1)$$

In (4.1),  $\hat{d}$  is the estimated signal at the output of the beamformer,  $\mathbf{w}$  is the column vector of beamforming weights, and  $\mathbf{u}$  is the column vector of received signals at each array element. Superscript  $H$  denotes the Hermitian transpose.  $t$  is the time index. The LMS algorithm starts with arbitrary initial weights and calculates the LMS error  $e$  at each time step:

$$e(t) = d(t) - \hat{d}(t). \tag{4.2}$$

In (4.2),  $e$  is the LMS error and  $d$  is the known transmit signal. After the error is calculated, the beamforming weights are updated:

$$\mathbf{w}(t + T_S) = \mathbf{w}(t) + \mu e(t)\mathbf{u}(t). \tag{4.3}$$

In (4.3),  $T_S$  is the sampling period and  $\mu$  is the LMS step size [25].

#### 4.2.1.1 No Interferer Case

Figures 4.10 and 4.11 show the simulated radiation patterns when the angle of arrival (AOA) of the desired signal is equal to  $90^\circ$  and  $120^\circ$ , respectively. The array elements have not been tilted to illustrate the principle of pattern multiplication. For

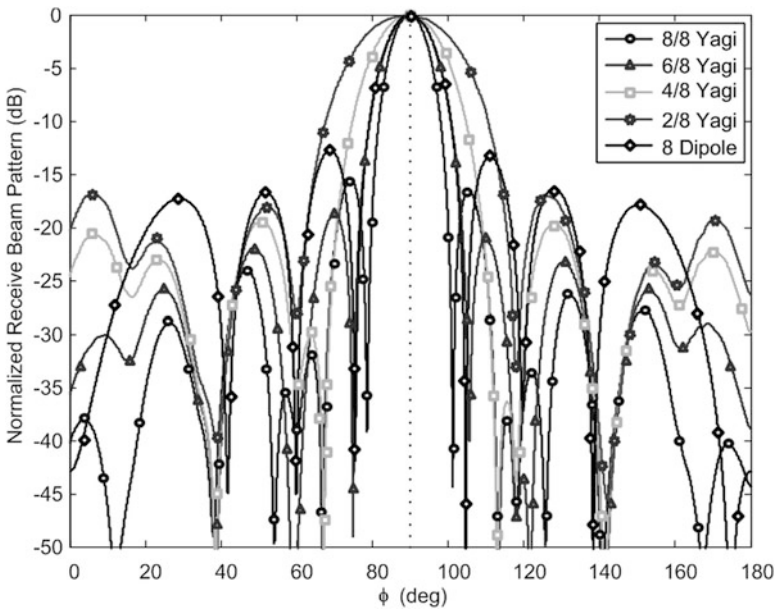


**Fig. 4.10** Normalized beam patterns for various values of  $N_s$  when AOA =  $90^\circ$ . Please note that label format corresponds to  $N_s/N$

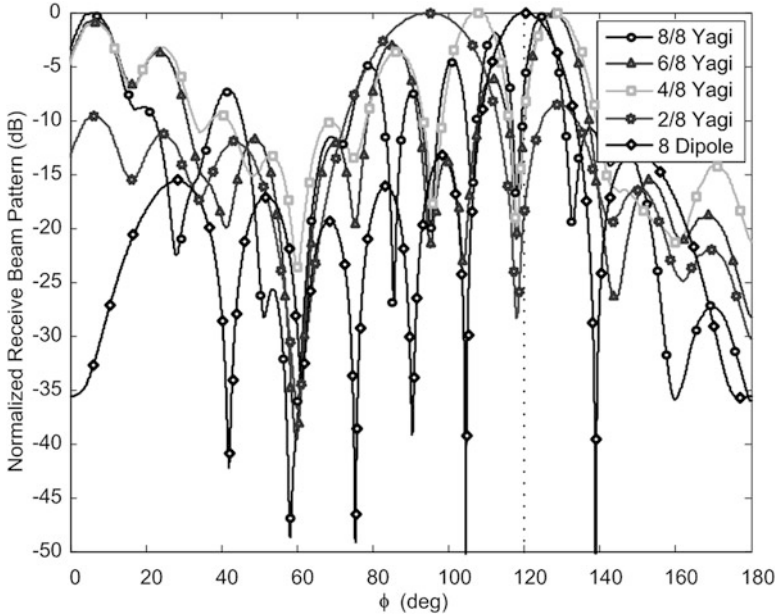


**Fig. 4.11** Normalized beam patterns for various values of  $N_s$  when  $\text{AOA} = 120^\circ$ . Please note that label format corresponds to  $N_s/N$

all the figures in this chapter, if the plot labels include a slash (“/”) sign, the number before the slash sign is the number of elements selected for the beamforming ( $N_s$ ), and the number after the slash sign is the total number of array elements ( $N$ ). The cases with  $N_s < N$  refer to the HSAA performance, whereas the cases with  $N_s = N$  and the ones with dipoles belong to a fully adaptive array.

For the  $90^\circ$  case shown in Fig. 4.10, the HSAA with six Yagi-Uda elements has better performance than the eight dipole case, showing the performance gain with directive elements. This performance gap increases for arrays with larger number of elements (HSAA with 8-element Yagi-Uda array performs similar to a 24-element dipole array) [6]. In Fig. 4.11, to illustrate the principle of pattern multiplication, the AOA has been changed to  $120^\circ$ . Without tilting, this angle corresponds to a null in the element pattern as shown in Fig. 4.9b. Due to this null, the adaptive algorithm fails to place the peak of the radiation pattern in the desired AOA even with eight elements, and the dipole array results in a better performance. This exemplifies why the directional elements have usually been avoided in antenna arrays.

To overcome this limitation and enable beamsteering in a larger angular range with directional elements, element tilting is proposed in the HSAA. To illustrate the advantage of the array with tilted elements, each element is tilted by an incremental tilt angle of  $\varphi = 22.5^\circ$ ; the resulting element radiation patterns are shown in Fig. 4.12.

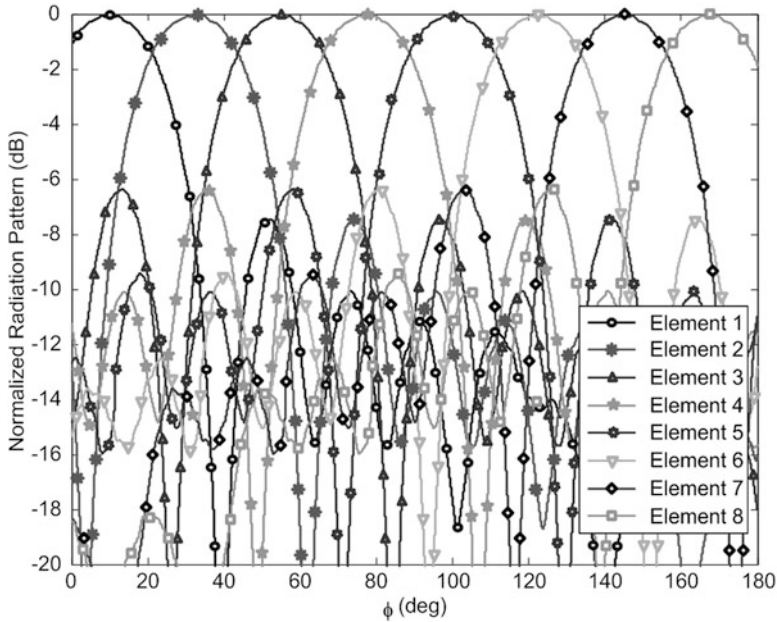


**Fig. 4.12** Tilted element radiation patterns for an eight-element Yagi-Uda array with a tilt angle of  $\phi = 22.5^\circ$

Figures 4.13 and 4.14 show the simulated radiation patterns when the angle of arrival (AOA) for the desired signal is at  $90^\circ$  and  $120^\circ$ , respectively, with tilted array elements. Due to element tilting, the HSAA performs similarly for AOAs of  $90^\circ$  and  $120^\circ$ . The performance difference, when all or half of the array elements used in the Yagi-Uda array is insignificant, shows the advantage of the HSAA in using only a subset of available array elements. Because of the tilting, the additional elements receiving negligible signal do not have a significant contribution to the beamformer performance. The performance of the four-element Yagi-Uda array with HSAA is very close to the fully adaptive array with eight dipoles [6]. The performance will be a lot better with larger antenna arrays having more elements since the overlap between the element radiation patterns is increased. Please see Ref. [6] for more simulation results.

This example shows the increased beam scanning range with the introduction of element tilting. This way, the HSAA can perform beamsteering uniformly in a given angular range with highly directional elements.

#### 4.2.1.2 Single Interferer Case

Unlike the fixed beamforming networks, adaptive smart antennas can place nulls in the interferer directions and continuously move the nulls to track moving interferers. Simulation studies have been conducted to illustrate this capability. For

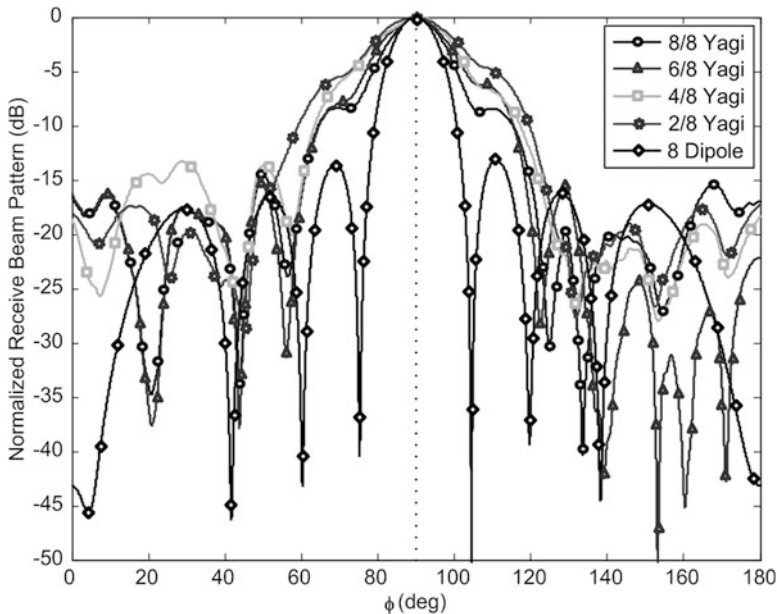


**Fig. 4.13** Normalized beam patterns for various values of  $N_s$  when  $AOA = 90^\circ$  with element tilting. Please note that label format corresponds to  $N_s/N$

all the simulated cases, there is a single interferer at  $110^\circ$  with  $-20$  dB signal-to-interference ratio (SIR). This case corresponds to a strong interferer (jammer) having a hundred times more power than the desired signal.

For distinguishing between the interferer and the desired transmitter, orthogonal codes and binary phase shift keying (BPSK) modulation are employed in the simulator. The BPSK-modulated data waveform has 500 kb/s data rate, and no pulse shaping is applied. The desired transmitter always transmits a data sequence of 1s, whereas the interferer transmits alternating data sequences of 50 1s and 50 0s. The transmitter and the interferer both share the same center frequency of 2.4 GHz, and only the desired signal is known at the receiver. Due to space limitations, convergence of the LMS algorithm will be shown instead of the individual radiation patterns to illustrate the advantages of HSAA.

In Fig. 4.15, absolute value of the LMS error defined in Eq. 4.2 is plotted for different subarray configurations. Since the preambles (known synchronization codes) have limited lengths in real life, the slope of convergence up to a few hundred iterations becomes very important, and having an LMS algorithm run for 6000 iterations is not very realistic. Figure 4.15 shows that the HSAA with 10 and 15 elements chosen out of 60 outperforms the 60-element fully adaptive beamforming system in terms of convergence speed. The HSAA with 10 and 15 elements chooses the antennas which receive negligible interference, hence the increased convergence speed. However, when the number of array elements is increased above 20, the

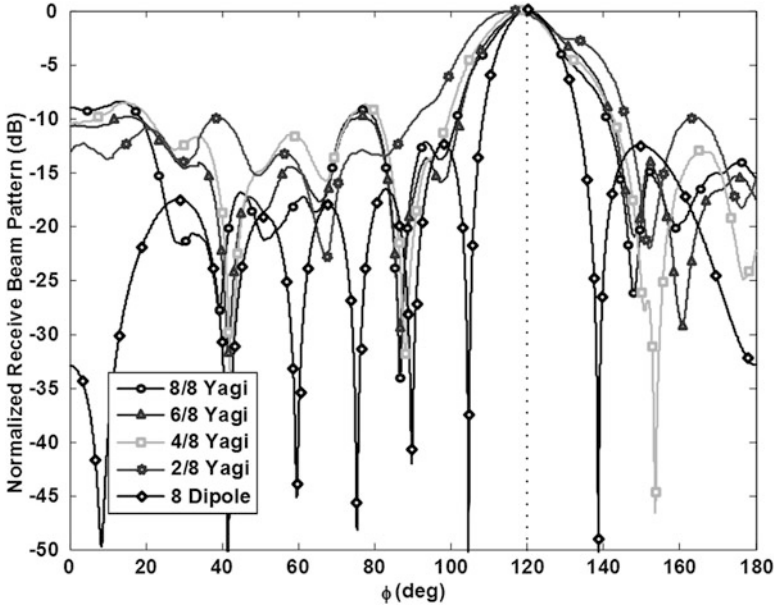


**Fig. 4.14** Normalized beam patterns for various values of  $N_s$  when  $\text{AOA} = 120^\circ$  with element tilting. Please note that label format corresponds to  $N_s/N$

HSAA has to include the array elements which receive some interference, hence the convergence performance is significantly degraded, and the slope becomes similar to that of a dipole array (fully adaptive system). This result shows that the HSAA using only one sixth of the array elements outperforms the fully adaptive beamforming system in the case of a strong interferer.

#### 4.2.2 Array Geometry Optimization Using Genetic Algorithm for 60 GHz Systems

HSAA uses directional elements with individually tuned tilt angles to provide uniform beamsteering with minimal scalloping effects in the desired angular range. To determine these tilt angles, the array design is formulated as an optimization problem. The inputs for this problem are the number of array elements ( $N$ ), the number of receiver channels ( $N_s$ ), the desired beam scanning range, and the element radiation patterns. The output is the set of tilt angles measured with respect to the broadside direction of the array. The genetic algorithm (GA) is used for optimization. GA is a powerful tool for finding the global minimum of functions that have multiple local minima [28, 32]. The objective of the GA is to minimize the fluctuation in the beamformer output power (scalloping) within

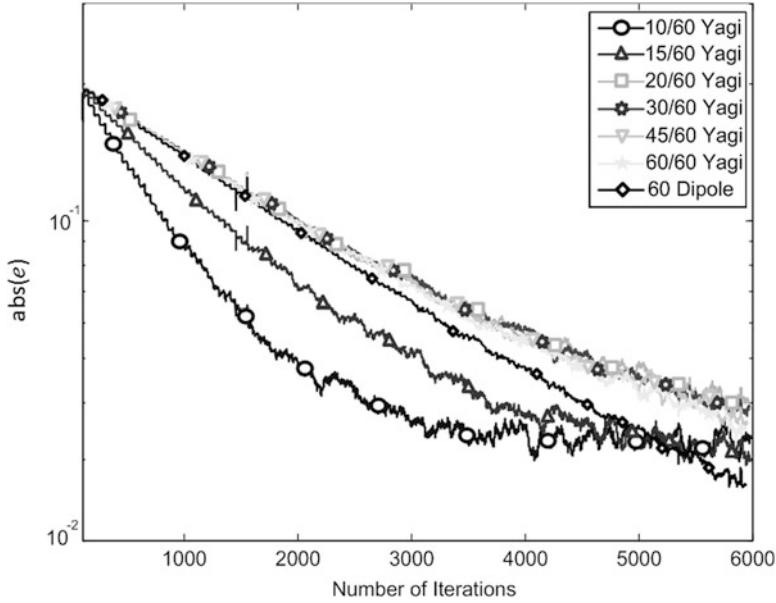


**Fig. 4.15** Absolute LMS error versus the number of iterations for various values of  $N_s$ , when  $\text{AOA} = 90^\circ$ , the tilt angle is  $3^\circ$ , and there is one interferer at  $110^\circ$  with  $\text{SINR} = -20$  dB. Please note that label format corresponds to  $N_s/N$

the desired scan range. An approximation to the LMS algorithm is employed for the calculation of the array output power in GA optimization for reducing the computational complexity, and the performance with the optimized array is evaluated with beamforming simulations to verify the validity of this approach. Only the optimization results will be discussed here. For a detailed derivation of the optimization procedure, please refer to Refs. [6, 28].

In the GA optimization, the measured radiation pattern of a 60 GHz horn antenna with  $6^\circ$  beamwidth is used. The desired scan angle is chosen to be between  $80^\circ$  and  $100^\circ$  where  $90^\circ$  corresponds to the array's broadside direction. In Fig. 4.16, the element radiation patterns with optimized tilt angles (dashed) as well as the estimated array output power (solid) have been plotted for a receiver with two channels ( $N_s = 2$ ) and three channels ( $N_s = 3$ ). The output power fluctuation in the desired scan angle range is 0.31 dB with two channels, and it increases to 1.31 dB with the inclusion of the third channel. This amount of fluctuation is still very small when the high directionality of the array elements is considered. Also notice that in Fig. 4.16a, with two receiver channels, the GA basically distributes the array elements with equal angular intervals over the desired scan range, which is the trivial solution. However, when the number of receiver channels is increased to 3, the resulting solution is more intricate and no longer has equal intervals as shown in Fig. 4.16b.



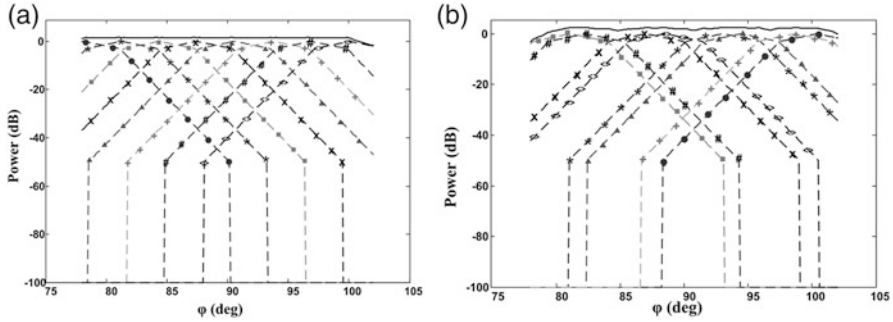


**Fig. 4.16** (a) Resulting element radiation patterns (*dashed*) and receive power pattern (*solid*) for  $N = 8$  and  $N_s = 2$  (b). Resulting element radiation patterns (*dashed*) and receive power pattern (*solid*) for  $N = 8$  and  $N_s = 3$  (From Ref. [28])

**Table 4.2** Array output power fluctuation in dB versus  $N$  and  $N_s$  [28]

		Number of downconversion channels ( $N_s$ )			
		1	2	3	4
Number of array elements ( $N$ )	2	13.7708	12.7919	12.7919	12.7919
	3	5.4227	3.6530	3.4282	3.4282
	4	2.7000	1.2707	1.3003	1.3004
	5	2.129	0.9889	0.8486	0.9167
	6	1.8387	0.8206	0.7290	0.6886
	7	1.5000	0.5067	1.0277	0.4833
	8	1.4516	0.3112	1.3037	0.8627
	9	1.3548	0.4958	1.1819	0.6387
	10	1.3000	0.2357	0.4568	0.4190
	11	1.2581	0.3017	0.7895	0.6235
	12	1.2000	0.1964	0.5568	0.674

In Table 4.2, the resulting output power fluctuation (scaloping) in dB is tabulated for various number of array elements and number of receiver channels. These results show that the GA solution is able to find the best array geometry with very small gain fluctuation ( $<1$  dB for all non-degenerate cases). The solutions get more elaborate with the increased number of receiver channels. As seen in Table 4.2, the HSAA with two to four channels has significantly lower output power fluctuation compared to an antenna switching system ( $N_s = 1$ ).

After the array geometry is optimized using GA, detailed system simulation studies with a full implementation of the LMS algorithm are conducted to evaluate the performance of the optimized array and prove the validity of the LMS approximation used in GA. In Fig. 4.17, three representative beam patterns for AOAs  $80^\circ$ ,  $90^\circ$ , and  $100^\circ$  are plotted for  $N = 10$  and  $N_s = 2$ . These patterns look identical and suggest that there is no fluctuation in the output power of the beamformer with the change in AOA. In Fig. 4.18, the beamformer output power is plotted for all possible AOA values and compared to the values estimated by the GA method. As observed, these values match very closely and validate the GA optimization approach.

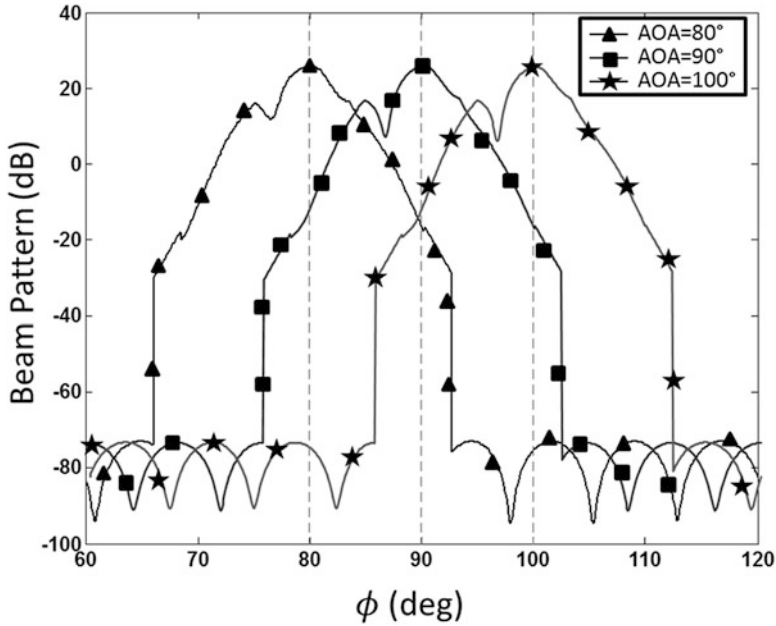


**Fig. 4.17** The non-normalized receive beam patterns for AOAs 80°, 90°, and 100° for  $N = 10$  and  $N_s = 2$  (From Ref. [28])

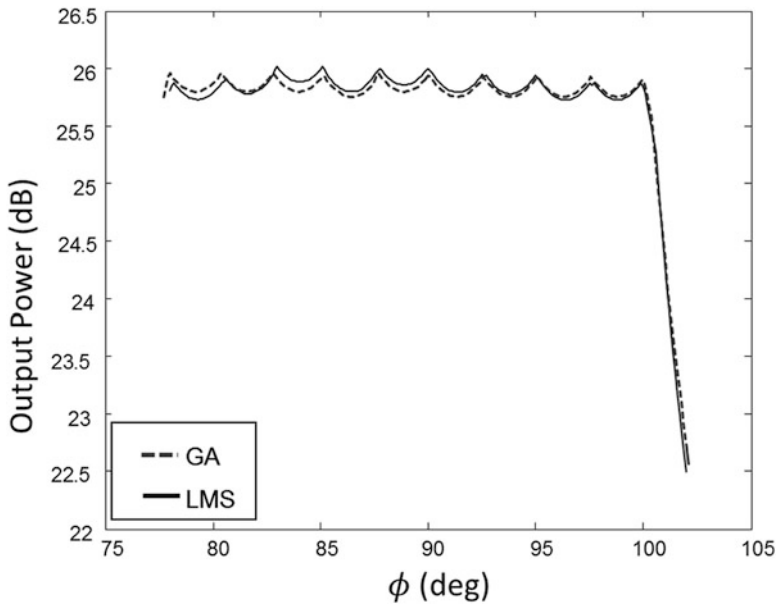


**Fig. 4.18** The beamformer output power versus the AOA (From Ref. [28])

### 4.2.3 *Experimental Verification of the Hybrid Smart Antenna Array at 2.4 GHz*

A digital communication system prototype was built to experimentally verify the accuracy of the proposed HSAA. On the transmitter side, an Agilent E4438C vector signal generator is employed as the signal source. This signal generator can output signals with up to 25 dBm of power and up to 6 GHz including digital modulation capability. Moreover, it has the standardized communication system filters already built in with customization options that permit specification of the individual bits in the transmitted waveform.

On the receiver side, a custom digital receiver with eight independent channels was designed and built using off-the-shelf components for 2.4 GHz operation. This frequency was chosen because of its worldwide adoption for wireless LAN applications and the abundance of inexpensive RF components. The receiver consists of a multichannel frequency downconverter that converts the RF signals to intermediate frequency (IF) signals and a multichannel ADC. The data processing and remaining receiver functionality are implemented in a personal computer using Matlab<sup>®</sup>. All the RF hardware and the personal computer are embedded into a custom-made computer case for compactness and portability, as shown in Fig. 4.19. Reference [6] has the specifics of this test bed as well as the part numbers used in the frequency downconverter.

Due to space limitations, only the experimental results with the directive array elements case are presented here. References [6, 30, 31] have more details for the experiments with dipole antennas as well as with the use of modulated

**Fig. 4.19** A photo of the smart antenna system prototype built in a computer case [8] (Reproduced by the permission of John Wiley & Sons Inc.)





**Fig. 4.20** Photo of the Yagi-Uda antenna array and its setup in the antenna range [6]

communication signals. The results presented here were obtained using continuous wave (CW) transmit signals. Figure 4.20 shows the antenna array geometry with the highly directional Yagi-Uda elements with no tilting.

In the simulation studies presented in Sects. 4.2.1 and 4.2.2, the mutual coupling between the array elements had not been considered. For proper operation of the experimental HSAA prototype, the antenna array must be calibrated with the mutual coupling effects included. This procedure is detailed in Ref. [6]. To illustrate the significance of mutual coupling effects, the gains of each array element were measured simultaneously with all array elements activated. This was done by calculating the total power of the received signal in all channels when a CW signal is transmitted. Figure 4.21 shows the receive power patterns for all the array elements measured simultaneously using the eight-channel HSAA prototype. In this figure, the first plot is the received power pattern for the leftmost array element, and the last plot is for the rightmost element. As observed, the measured patterns are very different from the single element pattern shown in Fig. 4.9b due to severe mutual coupling effects. In summary, the beams of the Yagi-Uda antennas have been widened ( $90^\circ$  half-power beamwidth instead of  $30^\circ$  previously measured), and nulls are introduced in the dipole antenna patterns. Also notice the radiation pattern differences between the edge elements and the center elements.

Since the directional Yagi-Uda antennas have become almost omnidirectional due to mutual coupling, only the case without element tilting has been experimentally verified. The effect of element tilting was verified for 60 GHz systems, the results of which are shown in the next section. In Figs. 4.22 and 4.23, the measured normalized radiation patterns have been plotted for  $\text{AOA} = 90^\circ$  and  $\text{AOA} = 120^\circ$ , respectively. Because the beams of the array elements have been broadened, the HSAA was able to steer the beam peak to  $120^\circ$  without any issues as opposed to the

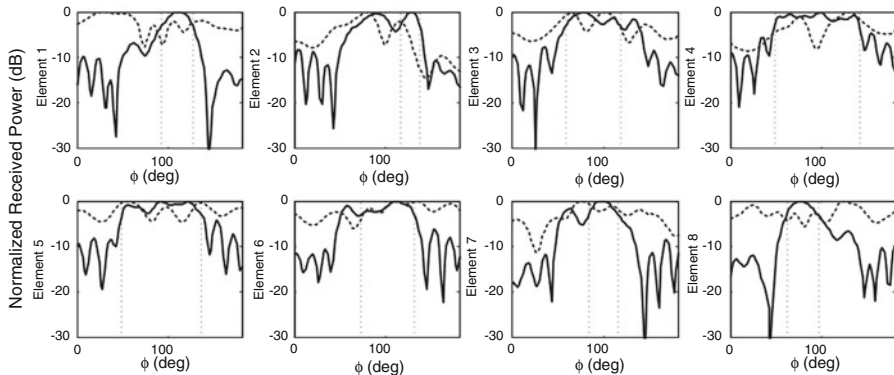


**Fig. 4.21** The measured receive power patterns of the Yagi-Uda (*solid*) and dipole (*dashed*) array elements [6]

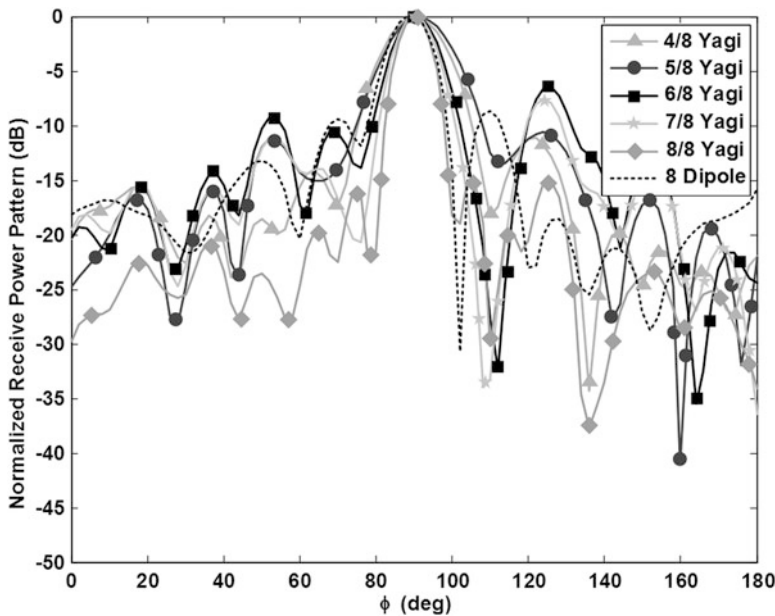


**Fig. 4.22** Normalized beam patterns for various values of  $N_s$  when  $AOA = 90^\circ$ . Please note that label format corresponds to  $N_s/N$

simulated case presented in Fig. 4.11. According to these results, the HSAA system with the Yagi-Uda array has better coverage and lower sidelobe levels than a fully adaptive system that employs a dipole array. Even with six elements selected out of the eight, the HSAA system outperforms the fully adaptive array, promising cost reduction and lower computational complexity.

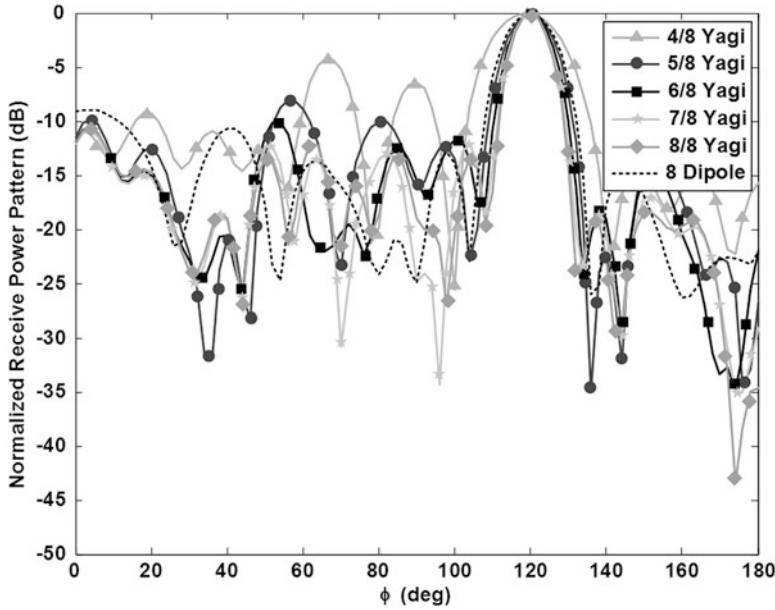


**Fig. 4.23** Normalized beam patterns for various values of  $N_s$  when  $AOA = 120^\circ$ . Please note that label format corresponds to  $N_s/N$

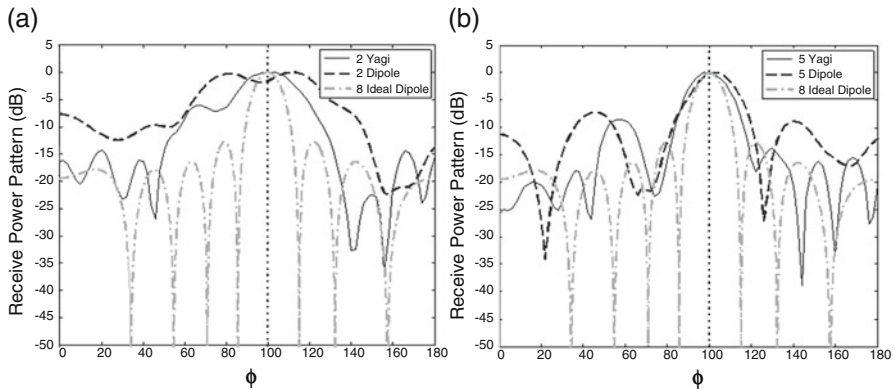


**Fig. 4.24** (a) Normalized beam patterns for  $N_s = 2$  when  $AOA = 100^\circ$ . (b) Normalized beam patterns for  $N_s = 5$  when  $AOA = 100^\circ$

In Fig. 4.24a, the beam patterns when  $N_s = 2$  are shown. It is seen that when omnidirectional array elements are used in the HSAA system, it is not possible to place the beam peak in the AOA direction, whereas the HSAA using Yagi-Uda elements has the peak in the correct place. For comparison, the case when  $N_s = 5$  is plotted in Fig. 4.24b. As observed, both the dipole and the Yagi-Uda array have the peak in the AOA direction, but the Yagi-Uda array results show better

sidelobe performance. Moreover, the measured beam pattern of the Yagi-Uda array has a performance similar to the eight-element fully adaptive array assuming ideal elements. This shows that the HSAA has a clear advantage over the fully adaptive system when the mutual coupling effects are included.

#### 4.2.4 *Experimental Verification of the Hybrid Smart Antenna Array at 60 GHz*

The value of HSAA with directional elements becomes more evident at higher frequencies, since the antenna elements get more directional and the receiver components become more expensive. To verify the effects of tilt angles and optimized array geometry, a two-channel receiver implementing HSAA at 60 GHz was built. Reference [33] has the details of this receiver and the experimental procedure for obtaining the beam patterns.

Because 60 GHz communication systems operate at short distances with high data rates, the distance between the transmitter and receiver may not be enough to satisfy the far-field requirements for the whole array. Because of this, the principle of pattern multiplication may not be valid for these systems, and an alternative derivation of the general beamforming problem is required. In Ref. [33], the general beamforming problem for closer transmitter/receiver separations is derived. In Fig. 4.25, the element patterns for a fictitious two-element array are shown for a short transmitter/receiver separation indicating that beams for the array elements may be

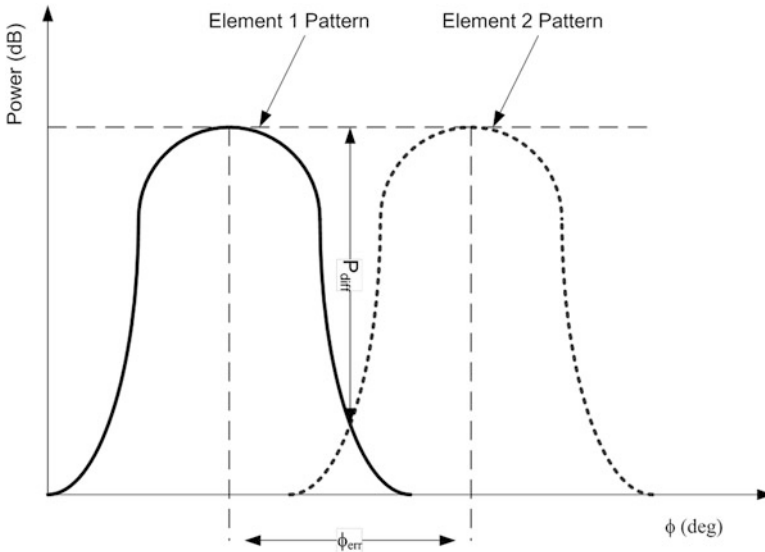


**Fig. 4.25** Illustration of nonoverlapping element patterns for a two-element array without tilting (From Ref. [33])

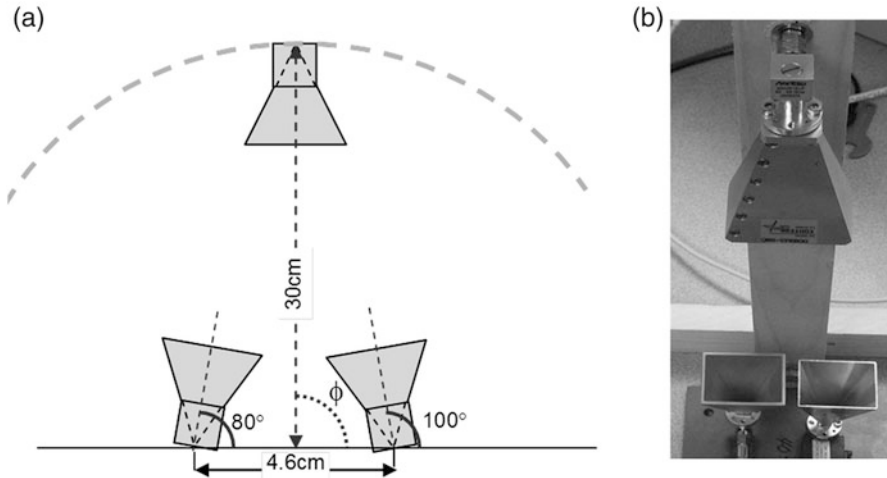


**Fig. 4.26** (a) Tilted array configuration with  $20^\circ$  negative tilt for the 60 GHz experimental system and (b) the photo of the array setup (From Ref. [33])

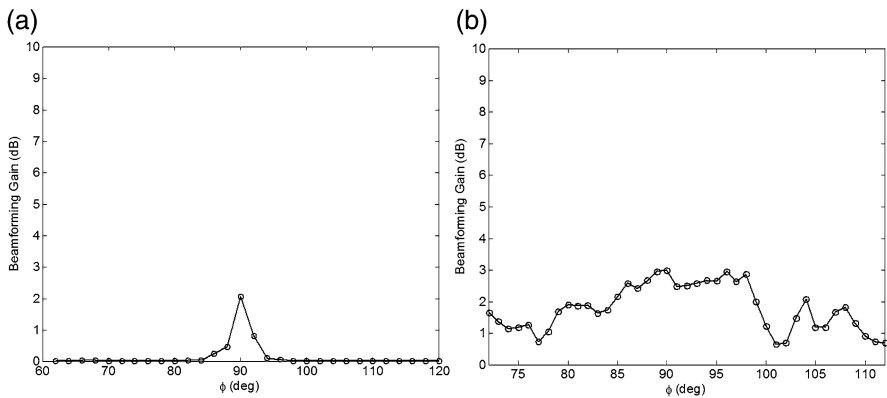


**Fig. 4.27** (a) Gain of the adaptive beamforming system with respect to antenna switching without any tilting. (b) Gain of the adaptive beamforming system with respect to antenna switching with  $20^\circ$  negative tilting (From Ref. [33])

separated even without tilting. In the case of nonoverlapping beam patterns for short separation distances, a negative tilting needs to be applied to ensure that there is enough overlap between the array element patterns for beamforming. This negative tilt angle used in the experimental system is illustrated in Fig. 4.26. Without a negative tilt, the adaptive beamforming system has a limited performance advantage over an antenna switching system as shown in Fig. 4.27a. Figure 4.27b shows about 3 dB gain advantage with adaptive beamforming between the angles of  $85^\circ$  and  $95^\circ$  when a negative element tilting of  $20^\circ$  is introduced.



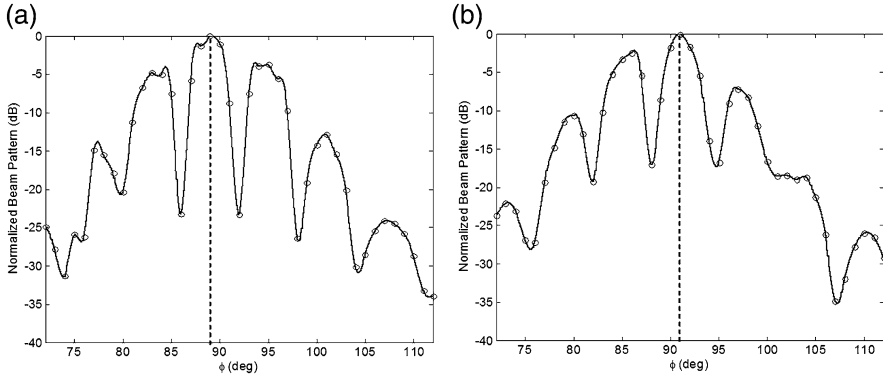


**Fig. 4.28** (a) Measured beam pattern for AOA = 89° with the tilted configuration. (b) Measured beam pattern for AOA = 91° with the tilted configuration (From Ref. [33])

Figure 4.28 shows the measured radiation patterns for the AOA = 89° and AOA = 91°. For these cases, the HSAA correctly steered the beam in the exact direction of the transmitter. However, because the element spacing of the array is much larger than the wavelength (about eight wavelengths), several grating lobes are observed in the radiation patterns. For this reason, the beam scanning range of the system turned out to be between 87° and 93°. Outside this angular range, the grating lobes become comparable to the main lobe. A larger angular range can be covered by designing several two-element subarrays focusing on different sectors of the desired beam scanning range and by selecting the appropriate subarray with the highest total received signal power. With the current prototype, performance analysis of only one subarray is conducted due to high costs of the RF components and lack of availability of an RF switch operating at 60 GHz.

### 4.3 Conclusions

In this chapter, the Hybrid Smart Antenna Array (HSAA) was introduced. Results of computer simulations as well as experimental evaluations were presented to illustrate its advantages over fully adaptive beamforming systems. Practical implementations of the fully adaptive smart antenna systems are often limited because of the hardware costs and the computational burden they add to the system. In order to overcome the limitations of these systems, a hybrid of the antenna switching and adaptive digital beamforming methods was proposed. This is called HSAA. Unlike fully adaptive algorithms which use low-gain elements with low directivity in the array, the HSAA uses highly directive elements with optimized tilt angles and selects few of these elements for the beamforming stage, reducing the hardware cost and the computational complexity. Directive elements have usually been avoided in antenna arrays, since they limit the usable beam scanning range and lead to scalloping effects. In the HSAA, directive array elements were used with each element tilted with respect to the array axis to extend the available beam scanning range.

The computer simulations showed that the HSAA with highly directive array elements and no tilting achieved superior performance compared to a fully adaptive system while having a limited beam scanning range. When element tilting was introduced to increase the beam scan range, the main lobe of the HSAA became larger compared to a fully adaptive system. For a given set of array element patterns and element tilt angles, only a subset of the array elements received significant signal powers. Including the remaining elements in the beamforming did not necessarily increase the system performance. The computer simulation results also indicated that in addition to the computational gains from including fewer antennas in the beamforming algorithm, the convergence was faster since the HSAA eliminated the elements receiving negligible signal power and significant interference prior to the beamforming process. Based on computer simulations, it was shown that three times the convergence speed had been achieved in some cases where the interferer was much more powerful than the desired signal.

A genetic algorithm-based optimization tool was developed for determining the best set of tilt angles for each array element that achieved uniform overall beam pattern in the desired scan range. The optimization results indicated that even with very directive elements, it was possible to obtain uniform coverage in a wide scan angle with minimal scalloping effects. In this process of achieving beamforming with highly directive array elements, the trade-off between the number of elements used in each subarray, the number of switchable subarrays, and the uniformity of the overall beam pattern was identified. It was shown that increasing the number of elements in each subarray reduced the number of switching adjustments; however, it led to higher fluctuations in the beamformer output power. The GA optimization approach was verified by employing the optimized array in the HSAA simulations and comparing the resulting fluctuation with the GA predicted values. Almost perfect agreement of the two results indicated that the approximation for determining the array output power was accurate.

After extensive verification of the HSAA through computer simulations, an HSAA receiver prototype operating at 2.4 GHz was built to verify the algorithm experimentally. This system was used with an array of highly directive Yagi-Uda elements. Although the radiation patterns had significantly changed because of the mutual coupling effects, a significant performance gain and sidelobe level reduction were observed when the directive array elements were used. For example, it was shown that, selecting five elements out of the eight from the Yagi-Uda array, the same performance as a fully adaptive system using eight dipoles was achieved with HSAA. Moreover, through the HSAA, it was possible to determine the correct AOA using only two out of the eight elements for all cases, whereas at least five elements were required to determine the correct AOA with the fully adaptive beamformer.

In practical 60 GHz communication systems with adaptive arrays, the transmitter-receiver separation may not be sufficient to satisfy the far-field conditions as well as the principle of pattern multiplication. For this case, a more general beamforming formulation was developed. In light of this derivation, the negative element tilt angle was also introduced for the first time as a new array design variable.

As the cost of a large 60 GHz array is prohibitive, a prototype consisting of a two-channel array system was built. As the 60 GHz horn antennas used in the experimental verification have  $6^\circ$  beamwidth and their aperture sizes are on the order of eight wavelengths, beam patterns without grating lobes were obtained only in a  $6^\circ$  angular range. With these experiments, the claims about the element tilt angles were also verified, and it was seen that there must be significant overlapping of the element patterns in order to achieve beamforming gains over what could be achieved using an antenna switching system.

It is worth mentioning here that the ADC used in the experiments was not capable of transferring the received signals to the array processor in real time because of the limited data channel bandwidth. Because of this, it was not possible to evaluate the response of the system to changing AOA conditions during the experiments. For practical communication systems, a stand-alone HSAA with several real-time digital signal processors needs to be built to implement the beamforming algorithm in real time. For the 60 GHz band, the prototype was limited to only two channels. This severely limited the beam scanning capability of the HSAA system to a few degrees. For a better evaluation, a prototype with a larger number of array elements needs to be built.

The ultimate goal of the research presented in this chapter is implementing a realistic communication system with HSAA capable of transmitting and receiving data. For this reason, simulation models and prototypes will be developed for not only showing the resulting radiation patterns but also the true communication system performance parameters such as bit error rates and achievable data rates with the HSAA. Moreover, the GA-based array optimization algorithm will be integrated with full-wave electromagnetic structure simulators to take into account the interactions between the array elements for a better estimation of the real-life performance. Achieving these goals is challenging and requires collaboration of several experts with different backgrounds.

## References

1. S. Cherry, Edholm's law of bandwidth. *IEEE Spectrum* **41**(7), 58–60 (2004)
2. J.G. Proakis, *Digital Communication Systems* (McGraw-Hill, New York, 2000)
3. T.S. Rappaport, *Wireless Communications Principles, and Practice* (Prentice-Hall, Upper Saddle River, NJ, 2001)
4. N. Abramson, F.F. Kuo, *Computer Communication Networks* (Prentice-Hall, Upper Saddle River, NJ, 1973)
5. A.J. Viterbi, *CDMA: Principles of Spread-Spectrum Communication* (Addison Wesley, Reading, MA, 1995)
6. N. Celik, High performance hybrid smart antenna array for advanced wireless communication applications, PhD dissertation, University of Hawaii, Honolulu, 2008
7. J.C. Liberti, T.S. Rappaport, *Smart Antennas for Wireless Communications* (Prentice Hall, Upper Saddle River, NJ, 1999)
8. M.F. Iskander, W. Kim, J. Bell, N. Celik, Z.Q. Yun, Antenna array technologies for advanced wireless systems, in *Modern Antenna Handbook*, C. A. Balanis (Ed), (Wiley Interscience, New York, 2008)

9. I. Bahl, P. Bhartia, *Microstrip Antennas* (Artech House, Boston, 1980)
10. J.L. Butler, R. Lowe, Beam forming matrix simplifies design of electronically scanned antennas. *Electron. Des.* **9**, 170–173 (1961)
11. J.L. Butler, Digital, matrix, and intermediate-frequency scanning, in *Microwave Scanning Antennas*, R. C. Hansen (Ed), vol. III, (Academic Press, St. Louis, MO, 1966)
12. J.P. Shelton, K.S. Kelleher, Multiple beams for linear arrays. *IRE Trans. Antennas Propag.* **9**(2), 154–161 (1961)
13. J. Blass, Multidirectional antenna: a new approach to stacked beams. *IRE. Int. Conf. Rec.* **8**(part 1), 48–50 (1960)
14. W. Rotman, R.F. Turner, Wide angle microwave lens for line source applications. *IEEE Trans. Antennas Propag.* **11**, 623–632 (1963)
15. M.S. Smith, Design considerations for ruze and rotman lenses. *Radio Electron. Eng.* **52**(4), 181–187 (1982)
16. T.W. Bradley, Development of a voltage-variable dielectric (VDD) electronic scan antenna, in *Proceedings of the 1997 IEEE International Radar Conference*, Syracuse, 1997, pp. 383–385
17. M.F. Iskander, Z. Yun, Z. Zhang, R. Jensen, S. Redd, Design of a low-cost 2-D beam-steering antenna using ferroelectric material and the CTS technology. *IEEE Trans. Microwave Theory Tech.* **49**(5), 1000–1003 (2001)
18. M.F. Iskander, Z. Zhang, Z. Yun, R.S. Isom, M. Hawkins, R. Emrick, B. Bosco, J. Synowczynski, B. Gersten, New phase shifters and phased antenna array designs based on ferroelectric materials and CTS technologies. *IEEE Trans. Microwave Theory Tech.* **49**(12), 2547–2553 (2001)
19. F.J. Altman, W. Sichak, A simplified diversity communication system for behind-the-horizon links. *IRE Trans. Commun. Syst.* **4**(1), 50–55 (1956)
20. R.T. Compton, *Adaptive Antennas: Concepts and performance* (Prentice-Hall, Upper Saddle River, NJ, 1988)
21. P.W. Howells, Explorations in fixed and adaptive resolution at GE and SURC. *IEEE Trans. Antennas Propag.* **24**(5), 575–584 (1976)
22. S.P. Applebaum, Adaptive arrays. *IEEE Trans. Antennas Propag.* **24**(5), 585–598 (1976)
23. I.J. Gupta, Performance of a modified Applebaum adaptive array. *IEEE Trans. Aerosp. Electron. Syst.* **20**(5), 583–593 (1984)
24. S.W.W. Shor, Adaptive technique to discriminate against coherent noise in a narrow-band system. *J. Acoust. Soc. Am.* **39**(1), 74–78 (1966)
25. B. Widrow, P.E. Mantey, L.J. Griffiths, B.B. Goode, Adaptive antenna systems. *Proc. IEEE* **55**(12), 2143 (1967)
26. S. Haykin, *Introduction to Adaptive Filters* (MacMillan Publishing Company, London, 1984)
27. W.L. Stutzman, *Antenna Theory and Design* (John Wiley and Sons Inc., New York, 1981)
28. N. Celik, M.F. Iskander, Genetic algorithm based antenna array design for a 60 GHz hybrid smart antenna system. *IEEE Antennas Wirel. Propag. Lett.* **7**, 795–798 (2008)
29. Hyperlink Technologies, Hyperlink HG2415Y-SM Yagi Antenna Datasheet, *Hyperlink Technologies* (2016). [Online]. Available: <http://www.l-com.com/productfamily.aspx?id=6312>. Accessed 15 Oct 2016
30. N. Celik, W. Kim, M.F. Demirkol, M.F. Iskander, R. Emrick, Implementation and experimental verification of hybrid smart-antenna beamforming algorithm. *IEEE Antennas Wirel. Propag. Lett.* **5**, 280–283 (2006)
31. N. Celik, M.F. Iskander, Z. Zhang, Experimental verification of the hybrid smart antenna algorithm with modulated waveforms. *IEEE Antennas Wirel. Propag. Lett.* **8**, 236–239 (2009)
32. M. Mitchell, *An Introduction to Genetic Algorithms* (MIT Press, Cambridge, MA, 1998)
33. N. Celik, M.F. Iskander, R. Emrick, S. Franson, J. Holmes, Implementation and experimental verification of a smart antenna system operating at 60 GHz band. *IEEE Trans. Antennas Propag.* **56**(9), 2790–2800 (2008)



**Nuri Celik** (S'2005, M'2009) received the B.S. and M.S. degrees from Bilkent University, Ankara, Turkey, in 2000 and 2003, respectively, both in electrical and electronics engineering. He received his Ph.D. in electrical engineering from the University of Hawaii at Manoa in 2009. From 2009 to 2013, Dr. Celik was an Assistant Researcher at the University of Hawaii at Manoa. He is currently an antenna engineer at Trimble Inc., Sunnyvale, CA. His research interests include antenna array design and associated signal processing, smart antennas, GNSS antennas, broadband antenna and metamaterial ground plane design, bio-inspired optimization of electromagnetic structures, and design of electromagnetic-based medical sensors and associated signal processing.

# Chapter 5

## Antenna Arrays for Physical Layer-Based Directional Networking Technology

Gui Chao Huang, Magdy F. Iskander, Farhan A. Qazi, Zhengqing Yun,  
and Galen H. Sasaki

### 5.1 Introduction

The establishment of a cost-effective, reliable, and broadband wireless communication system in rural areas remains a significant technology challenge that requires a fresh look and innovative solutions. The vast coverage areas, rough terrain, and low node density in these areas often prohibit a cost-effective implementation of a standard wireless network system based on available technologies. The USA has tremendous wireless coverage from a variety of carriers, but the Federal Communications Commission in its 2015 report acknowledged that 55 million Americans – 17% of the population – lack access to an advanced broadband network. Moreover, a significant digital divide remains between urban and rural America: Over half of all rural Americans lack access to broadband service [1]. This has a negative impact on the inhabitants of rural communities and hinders economic developments in these areas.

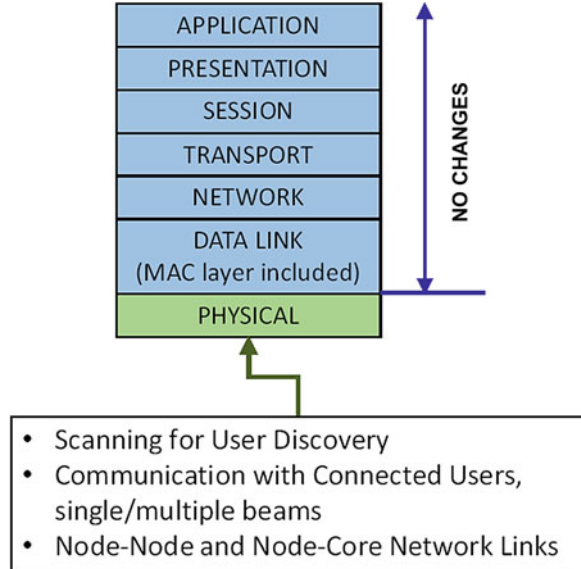
To overcome challenges in communication networks for rural areas, an advanced directional networking technology is being developed by our group [2, 3]. The directional networking system is comprised of interconnected *advanced nodes* which are equipped with enhanced hardware, three antenna arrays, propagation modeling, and digital signal processing (DSP) and network logic capabilities to achieve a physical layer-based implementation (no changes to MAC and upper OSI layers), as shown in Fig. 5.1. Among the critical hardware requirements is the

---

G.C. Huang • M.F. Iskander • F.A. Qazi (✉) • Z. Yun  
Hawaii Center for Advanced Communications, University of Hawaii at Manoa,  
Honolulu, HI 96822, USA  
e-mail: [fqazi@hawaii.edu](mailto:fqazi@hawaii.edu)

G.H. Sasaki  
Department of Electrical Engineering, University of Hawaii at Manoa,  
Honolulu, HI 96822, USA

**Fig. 5.1** Physical layer-based implementation



development of high-gain, narrow beam, directional antennas with digital/analog beamforming, with a separate array for user discovery, six sectoral communication arrays, and an array for node to node connectivity [2]. This set of antenna arrays, thus, enables the nodes to discover new users, communicate with connected users, and maintain node-node and node-core network connectivity all while achieving a vaster coverage area than traditional wireless base stations with omnidirectional antennas. To ensure that full directionality is achieved, algorithms and procedures are developed that enhance logic capability and intelligence to the physical layer and help achieve cost-effective directional networking approach that does not require complex and expensive changes in upper layer of the OSI communication models. Specifically, all the required modifications are carefully chosen to conform to the MAC layer standards of the radio used and, hence, are restricted only to the physical layer of the OSI layer stack (Fig. 5.1).

To examine the feasibility of developing such a system, its overall performance was simulated using MATLAB's WLAN Systems Toolbox for waveform generation, demodulation, and analyses [2]. Simulations were performed to test the ability of advanced nodes to discover and communicate with users and analyze the performance and coverage. Eight-element scanning and communication antenna arrays were used on a communication network setup that included mobile users that communicate with the node using the Wi-Fi standard IEEE 802.11 ac. The waveforms were designed using the MATLAB's WLAN Systems Toolbox occupying 80 MHz bandwidth, centered at 5.25 GHz. Figure 5.2 shows sample simulation result illustrating the multi-beam capability of the advanced nodes as a single mobile user in *sector 1* is tracked within the sector. In Fig. 5.3, sector-to-sector handover is illustrated as the user moves from *sector 2* to *sector 1*.

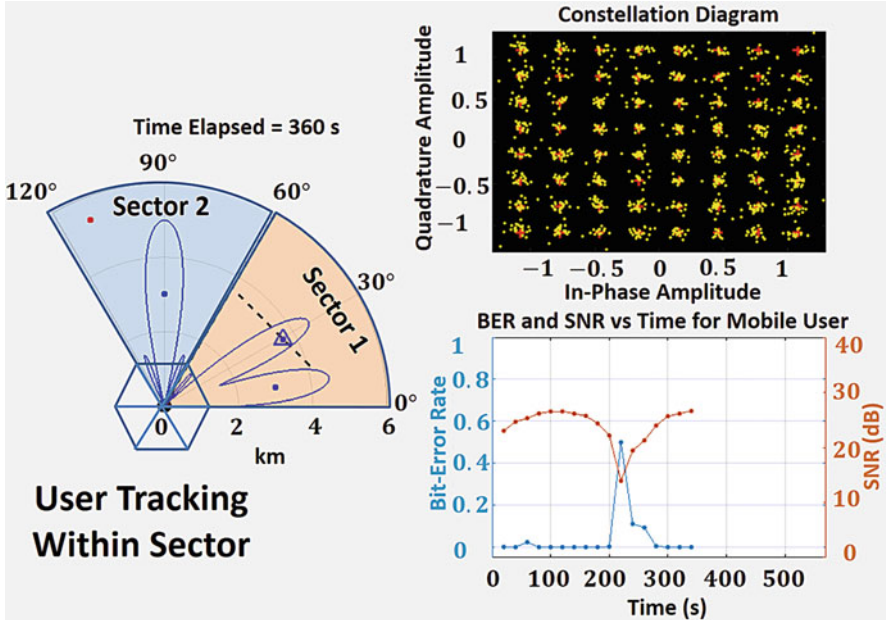


Fig. 5.2 Simulation result based on IEEE 802.11 ac of the proposed system for user tracking

In realizing this new technology, antenna arrays and feeding network were developed. The main focus of this chapter is on the development of low-cost, low-profile, broadband, high-gain, and circularly polarized antenna arrays, as well as a low-cost feed system that enables beam-steering or beam-switching capabilities. Furthermore, alternative antenna designs were simulated, and some of these designs were prototyped and experimentally tested. The remaining sections of this chapter are focused on the antenna array designs, prototyping, and testing.

## 5.2 Antenna Array

The desired requirements of the antenna array for the directional networking are low cost, low profile, broadband, circularly polarized, high gain, and with beam-steering capability. The broadband property allows the system to support faster data rate and more channels. Circularly polarized electromagnetic wave can help mitigate the multipath fading effect and provide stable signal level over long distance. Furthermore, beam-steering capability allows the antenna array to steer the main beam direction without physically moving/reorienting the antenna array.

Circularly polarized antenna arrays have been widely investigated, due to their attractive properties, such as lessened multipath fading effect and insensitivity to transmitter and receiver orientations. However, majority of the published works on circularly polarized antenna array either have less than 30% bandwidth or lack a feeding network to support beam steering [4–7]. Wideband antennas, such as



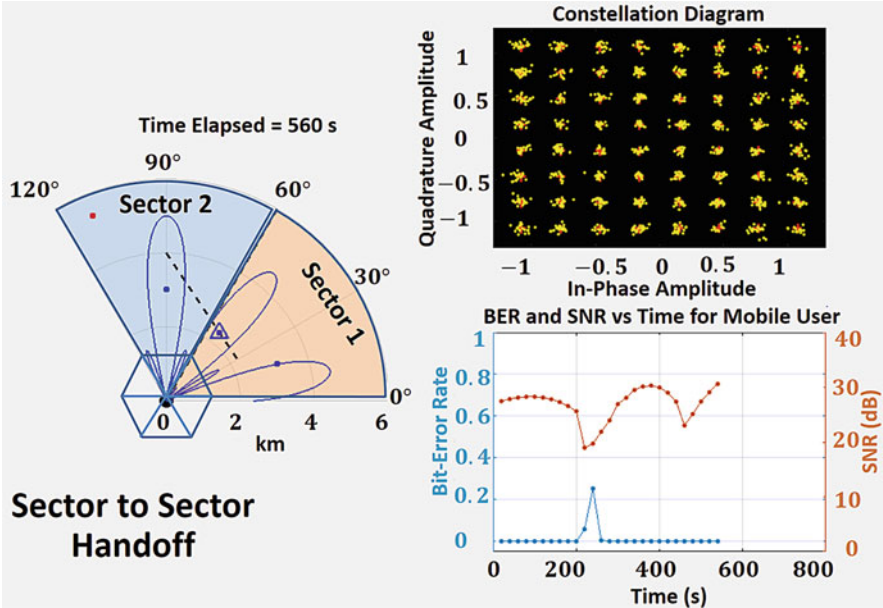


**Fig. 5.3** Simulation result based on IEEE 802.11 ac of the proposed system for sector-sector handover

Vivaldi or Spiral antennas, either have large size or require a broadband balun and impedance transformer [8, 9]. Previously, a broadband cylindrical long-slot array (CLSA) with dual polarization property had been developed by our group [10, 11]. It also had been shown that the CLSA has the capability of beamforming [12]. Thus, a dual-polarized antenna array based on the long-slot array concept was proposed to cover the frequency range of 4–6 GHz for directional networking. To achieve lower profile, two dual-fed stacked-patch-antenna arrays were also developed with the compromise of the wide bandwidth while providing comparable performance in circular polarization characteristics as well as improvements in beamforming and steering characteristic. The radiation characteristics of the arrays were examined and compared in terms of bandwidth, beamwidth, gain, axial ratio, and beam direction. The operating frequencies of the antenna arrays and feed system were specified by the sponsor Communications-Electronics Research, Development and Engineering Center (CERDEC).

### 5.2.1 Long-Slot Antenna Array

The long-slot antenna (LSA) array was originally designed by Raytheon. It is an ultra-wideband linearly polarized structure with input impedance ranging from 150 to 337  $\Omega$  [11, 13, 14]. For the LSA array to be broadband, the feeding port distance

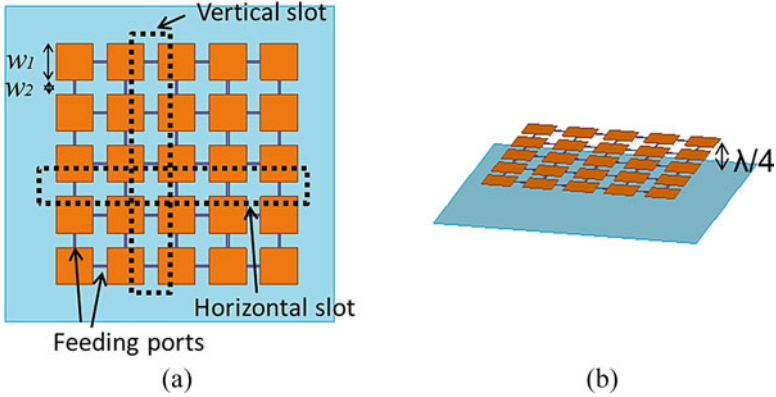


Fig. 5.4 4×4 dual polarized LSA array. (a) Top view. (b) Isometric view

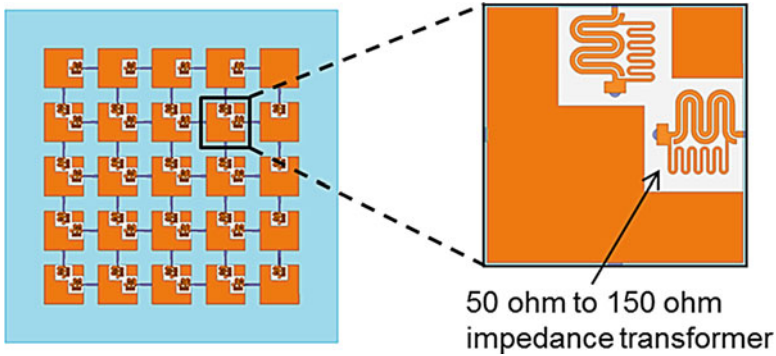


Fig. 5.5 4×4 dual polarized LSA array fed by 50–150  $\Omega$  impedance transformers

needs to be less than or equal to half of the free-space wavelength at the highest operating frequency [14]. To support dual polarization, additional orthogonal slots are fabricated between the feeding ports. Due to the structure of the LSA array, the radiation pattern is bidirectional. To achieve unidirectional radiation, a ground plane is placed a quarter-wave apart from the antenna array. Figure 5.4 shows a dual-polarized 4×4 LSA array.

Since the LSA array has input impedance of 150–337  $\Omega$ , a wideband impedance transformer is needed such as the compact microstrip-couple-line-based impedance transformer [13] shown in Fig. 5.5. However, the impedance transformer is complicated and difficult to fabricate. To simplify the feeding structure, parametric studies on the patch width ( $w_1$ ) and slot width ( $w_2$ ) were performed with a 3D full-wave electromagnetic field simulator (HFSS). In these studies, the patch width and slot width were changed, while the feeding port distance was kept constant. In antenna design, return loss (S11) is usually used to represent the impedance bandwidth of the antenna. For the LSA array, since the antenna elements are connected, the mutual

coupling can be high. It is not enough to just look at individual return loss from each port; thus, overall return loss is used to represent the overall impedance matching of the antenna. The overall return loss is calculated as:

$$\text{Overall Return Loss} = 10 \log \left( \frac{\text{Incident Power} - \text{Accepted Power}}{\text{Incident Power}} \right), \quad (5.1)$$

where *incident power* is the time-averaged power from the source and *accepted power* is the time-averaged power entering a radiation antenna structure.

Figure 5.6 shows the simulation result of the parametric study. Based on the simulation result, larger slot width has broader bandwidth and higher impedance; larger patch width has narrower bandwidth and lower impedance. With large patch width, the capacitance between the slots increased and resulted in smaller impedance. To retain the bandwidth, instead of minimizing the slot width, a new LSA design was proposed in which small slots are created on the patches to introduce additional capacitance on the patches, which results in decreased input impedance of the LSA array [15]. Figure 5.7 shows the proposed 4×8 LSA design.

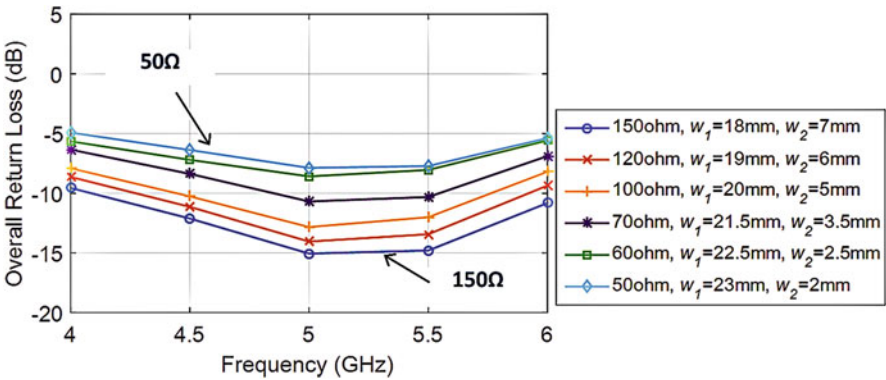


Fig. 5.6 Simulated overall return loss of the 4×4 LSA array in difference slot width and patch width

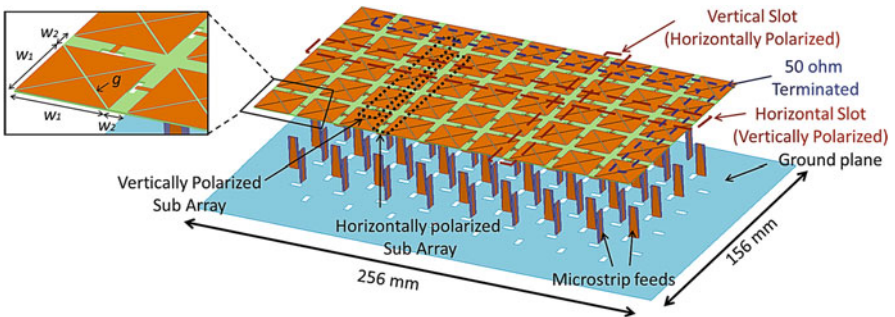
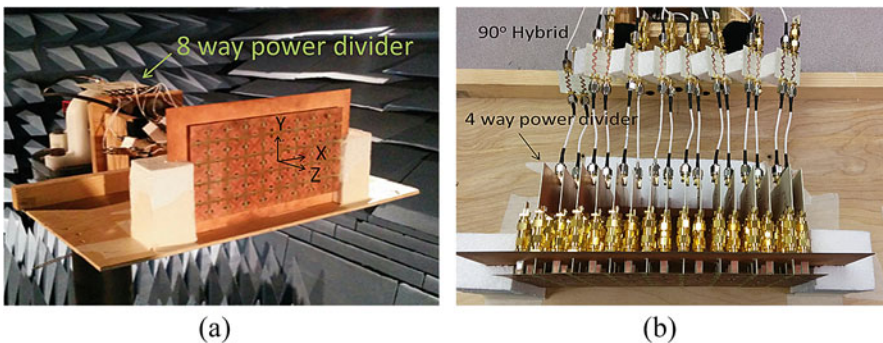


Fig. 5.7 4×8 LSA array design with small slots on the metallic patches and microstrip feeds

As shown in Fig. 5.7, small slots with width  $g = 0.26$  mm were created on each metallic patch. The metallic patches were supported by a 0.4 mm-thick FR4 substrate. The patch width ( $w_1$ ) and slot width ( $w_2$ ) were designed to be 20 and 4 mm, respectively, resulting in a feeding port distance of  $0.48\lambda$  at 6 GHz, where  $\lambda$  is the free-space wavelength. The slots in between each metallic patch were fed by tapered microstrips from the back of the antenna array, which transform  $50\text{--}60\ \Omega$  and are much simpler than the couple-line-based impedance transformer. With the small slots on the metallic patches, the input impedance of the antenna array was reasonably matched to  $60\ \Omega$  over 4–6 GHz. To support right circular polarization (RCP), the horizontal slots must be excited with  $90^\circ$  phase delay relative to the vertical slots. As the antenna array only needs to perform beam steering in the azimuth plane, the feeding ports were combined vertically with four-way power combiners. As shown in Fig. 5.7, four of the horizontal slot-feeding ports were combined vertically with a four-way power divider to form a vertically polarized subarray, and four of the vertical slot-feeding ports were also combined vertically with a four-way power divider to form a horizontally polarized subarray. The vertically polarized and the horizontally polarized subarrays were fed with a 4–6 GHz  $90^\circ$  hybrid coupler to form a RCP subarray. As a result, the antenna array was divided into eight RCP subarrays with 12 extra feeding ports terminated with  $50\ \Omega$  loads.

The  $4\times 8$  LSA array was simulated, fabricated, and measured. Figure 5.8 shows the fabricated antenna array. The antenna array radiation pattern measurement was done in the anechoic chamber at University of Hawaii at Manoa. The broadside radiation pattern of the LSA array was measured. In the measurement system, an eight-way power divider was used to feed the antenna array so that all the subarrays were fed in the same phase. The LSA array was used as a receiver and a linearly polarized horn antenna was used as a transmitter. To measure the RCP gain and axial ratio, two measurements were performed with the horn antenna rotated  $90^\circ$  to obtain the E-field in two orientations,  $E_\theta$  and  $E_\phi$ . The  $E_{\text{RCP}}$ ,  $E_{\text{LCP}}$ , and the axial ratio (AR) are calculated as [9]:



**Fig. 5.8** Fabricated  $4\times 8$  LSA array. (a) Isometric view. (b) Top view

$$E_{RCP} = \frac{1}{\sqrt{2}} (E_{\theta} + jE_{\phi}), \quad (5.2)$$

$$E_{LCP} = \frac{1}{\sqrt{2}} (E_{\theta} - jE_{\phi}), \quad (5.3)$$

$$AR = \left| \frac{|E_{RCP}| + |E_{LCP}|}{|E_{RCP}| - |E_{LCP}|} \right|, \quad (5.4)$$

where  $j^2 = -1$ .

The simulated and measured results of the  $4 \times 8$  LSA array are shown in Figs. 5.9 and 5.10. Figure 5.9a shows the simulated and measured results of the return loss and RCP gain of the LSA array. The simulated overall return loss is less than  $-7.5$  dB across the 4–6 GHz band, while the measured return loss is below  $-10$  dB. The discrepancy between the simulated and measured return loss is due to the  $90^\circ$  hybrid coupler and the feeding network which are not included in the simulation of the LSA array. The  $90^\circ$  hybrid coupler improves the return loss of the antenna array, as most of the reflected energy from the output ports of the hybrid coupler is transmitted to the isolated port of the hybrid coupler. Also, the resonances in the measured data are due to additional cable length in the feeding network. The simulated RCP gain ranges from 17 to 19 dB, while the measured gain ranged from 15.5 to 18 dB. The decreased in the measured gain is due to the insertion loss from the eight-way power divider,  $90^\circ$  hybrid coupler, and the four-way power divider. The axial ratio of the antenna array is shown in Fig. 5.9b. The simulated axial ratio is below 1 dB, where the measured axial ratio is below 1.8 dB which is in good agreement with simulation. The measured RCP and the cross polarization radiation patterns in  $x$ - $z$  plane at different frequencies are shown in Fig. 5.10. The 3 dB beamwidth ranges from  $19^\circ$  to  $13^\circ$  from 4 to 6 GHz. The side-lobe level is less than  $-13$  dB. The cross polarization level is more than 20 dB in the broadside.

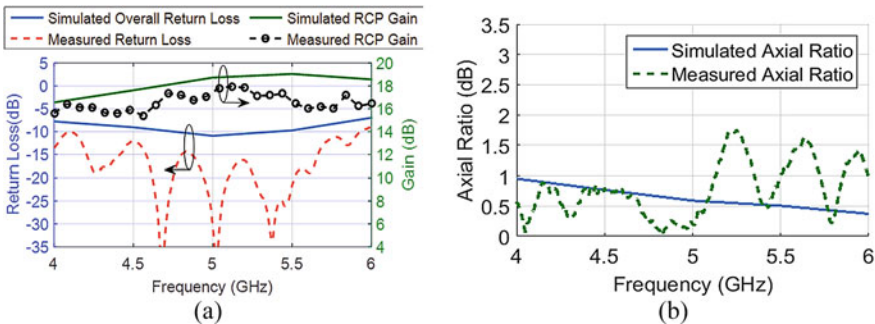


**Fig. 5.9** Simulated and measured results of the  $4 \times 8$  LSA array. (a) Return loss and realized RCP gain. (b) Axial ratio

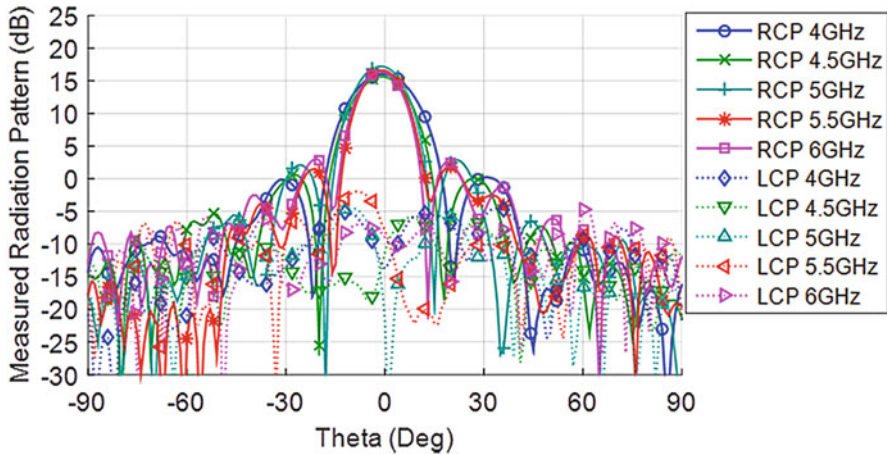


Fig. 5.10 Measured radiation pattern of the  $4 \times 8$  LSA array in x-z plane

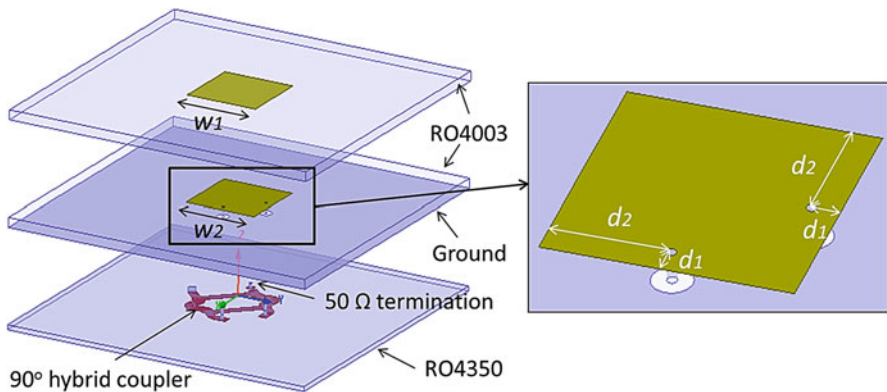
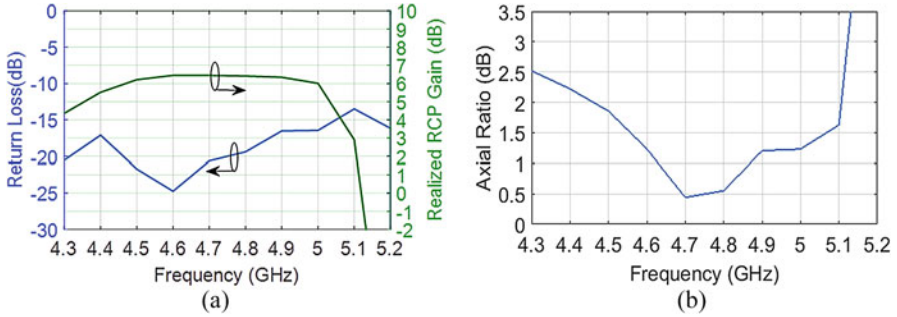


Fig. 5.11 Dual-fed stacked patch antenna single element schematic

### 5.2.2 Stacked-Patch Antenna

For the patch-antenna design, a narrower bandwidth was anticipated. Hence, the design operating frequency of the patch antenna was limited to 4.5–5 GHz. To fulfill the bandwidth requirement, a dual-fed square-patch antenna was chosen, as it is known to provide improved axial ratio values over a broader bandwidth [16–19]. The single-element patch-antenna design is shown in Fig. 5.11. The antenna consists of three layers: parasitic patch layer, driven patch layer, and feeding network layer. The driven patch was fed by two probes from the back of the antenna. The two feeding probes were fed by a  $90^\circ$  hybrid coupler to provide right-hand circular polarization. The  $90^\circ$  hybrid coupler was printed on the feeding network layer, and the isolated port of the  $90^\circ$  hybrid coupler was terminated with a  $50 \Omega$  chip



**Fig. 5.12** Dual-fed single-element stacked-patch antenna. (a) Return loss and realized RCP gain. (b) Axial ratio

resistor. A parasitic patch was added on top of the antenna to broaden the return-loss bandwidth of the antenna. The substrate used on the parasitic and driven patch layers was Rogers RO4003 which has a relative permittivity of 3.55 and thickness of 1.523 mm. The substrate used on the feeding network layer was Rogers RO4350 which has a relative permittivity of 3.66 and thickness of 0.762 mm. As a result, the total thickness of the antenna was 3.8 mm. The antenna was simulated in HFSS, whereby the patch width  $w_1$  and  $w_2$  and the feeding probe position  $d_1$  and  $d_2$  were determined to be 14.68, 14.7, 0.28, and 1.64 mm, respectively. Figure 5.12 shows the simulation results of the single-element patch antenna. In the frequency band of interest, the return loss is below  $-15$  dB, the RCP realized gain is around 6.4 dB, and the axial ratio is below 1.9 dB.

The  $4 \times 8$  patch-antenna array was developed based on the single-element patch antenna in Fig. 5.11, where the spacing between the antenna array elements was  $0.66\lambda$  (at the center frequency of 4.75 GHz). To further improve the axial ratio of the antenna array, sequential rotation technique was applied, whereby  $2 \times 2$  antenna elements formed a square subarray and the elements were sequentially rotated  $90^\circ$  counterclockwise with respect to each other, as shown in Fig. 5.13a. As for feeding the antenna elements, these elements were combined vertically by a branch-line-based feeding network such that there were eight vertical subarrays. The branch-line-based feeding network was designed on the same layer as the hybrid coupler, as shown in Fig. 5.13b.

Thus, the overall size of the antenna array is  $355 \times 189 \times 3.8$  mm including the branched-line-based feeding network. A quarter-wavelength impedance transformer was used to match the impedance at the T-junction of the feeding network. As the antenna polarization was RCP and the elements were rotated counterclockwise, the rotation would cause a phase lead in the antenna element. To compensate for the rotation of the antenna element, the corresponding phase delays were added to the feeding network based on the angle of rotation, so that the directions of the E-field are synchronized in each element.

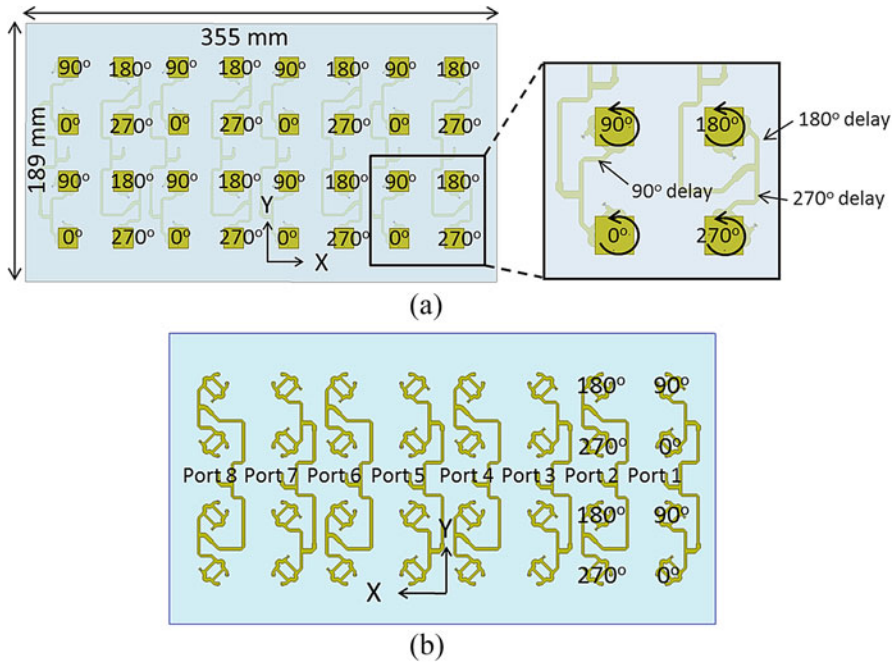


**Fig. 5.13** 4×8 dual-fed stacked-patch-antenna array with sequential rotation. (a) Front view. (b) Back view



**Fig. 5.14** Fabricated 4×8 dual-fed stacked-patch-antenna array. (a) Isometric view. (b) Back view

The 4×8 dual-fed stacked-patch-antenna array was fabricated and experimentally characterized. Figure 5.14 shows the fabricated antenna array. The simulated and measured return loss and RCP gain of the stacked-patch-antenna array are shown in Fig. 5.15a. Both simulated and measured return losses are less than 10 dB from 4.5 to 5 GHz. The simulated RCP gain ranges from 20 to 21.5 dB, while the measured RCP gain ranges from 17 to 19 dB and decreases at higher frequencies as illustrated in Fig. 5.15a. The decrease in gain at higher frequencies could be due to fabrication errors. Specifically, the antenna array, when fabricated, had a very small gap (order



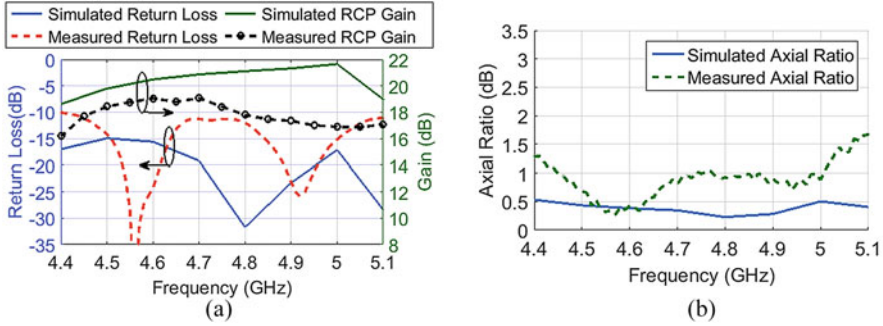


**Fig. 5.15** Simulated and measured results for the 4×8 dual-fed stacked-patch-antenna array. (a) Return loss and realized RCP gain. (b) Axial ratio

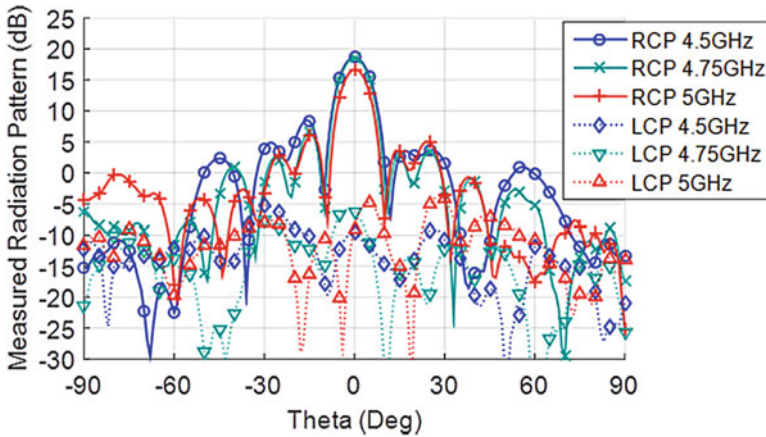


**Fig. 5.16** Measured radiation pattern of the 4×8 dual-fed stacked-patch-antenna array in the x-z plane

of 0.2 mm) in between the stacked substrates (due to the solder on top of the driven patches), which resulted in the aforementioned errors. The simulated axial ratio in Fig. 5.15b is below 0.5 dB and the measured axial ratio is below 1 dB. The measured RCP and the cross polarization radiation patterns in the x-z plane are shown in Fig. 5.16. The 3 dB beamwidth ranges from 10° to 9° from 4.5 to 5 GHz with a side-lobe level of less than -10 dB. The cross polarization level is more than 20 dB.

To improve the gain of the stacked-patch-antenna array, a modified version of it was also designed [20]. Substrates with high relative permittivity can lower the gain and reduce the bandwidth of a patch antenna [21]. Several methods have been introduced to improve the gain of patch antennas, such as perforation of the surrounding substrate of the patch antenna to lower the surrounding effective relative permittivity, implement electromagnetic band-gap structure on the surrounding to block the propagation of the surface wave, and either use substrate material with low

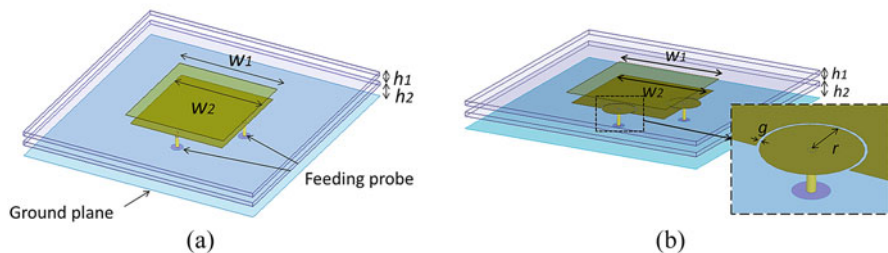


**Fig. 5.17** (a) Dual-fed stacked-patch-antenna design with air gap. (b) Dual-fed stacked-patch-antenna design with air gap and annular gaps

relative permittivity or suspend the metallic patch over air [21–24]. In the modified design, a substrate with quite low relative permittivity was used, and air gaps in between the substrate and the ground plane were introduced. Figure 5.17a shows the initial design of the stacked-patch-antenna element; the design was similar to the patch antenna above except air gaps were introduced between the substrate and the ground plane. The substrate which was used in this antenna design is Rogers RO4725JXR. It has a relative permittivity of 2.64 and thickness of 0.78 mm. The parasitic patch size  $w_1$  and the driven patch size  $w_2$  were decided to be 21.3 and 20 mm, respectively. The distance  $h_1$  between the parasitic patch and the driven patch was 2 mm, and the distance  $h_2$  between the driven patch and the ground plane was 3 mm. The simulated return loss of the antenna is plotted on a Smith chart in Fig. 5.18. Due to the extra height from the air gap, extra inductance is introduced on the feeding probe; hence, the return-loss curve is on the upper part of the Smith chart, which means the impedance is not matched.

To compensate for the inductance caused by the long feeding probe, capacitive annular gaps [25] were introduced on the driver patch for each feeding probe where the center of the annular gaps were laid over the center of the feeding probes, as shown in Fig. 5.17b. The capacitance of the annular gap depends on the gap width  $g$  and the inner radius  $r$ . To ensure the coupling between the feeding probe and the driver patch, the gap width was designed to be small and was equal to 0.2 mm. Thus, to change the capacitance of the annular gap, the inner radius of the annular gap was adjusted so that it shifted the return-loss curve to the center of the Smith chart, as shown in Fig. 5.18. The return-loss curve shifted toward the capacitance side of the Smith chart, and the feeding probe experienced more negative reactance for smaller  $r$ . This is because the capacitive reactance is inversely proportional to the capacitance and less capacitance is induced for smaller  $r$ . The return-loss curve surrounds the center of the Smith chart when  $r = 3$  mm. Figure 5.19 shows the simulation results of the antenna with  $r = 3$  mm. The  $-10$  dB impedance bandwidth is about 16.7% from 4.4 to 5.2 GHz. Within this frequency band, the antenna gain on the broadside is slightly above 8 dB (which is about 2 dB higher than of the stacked-patch antenna described at the beginning of this subsection, i.e., Sect. 1.2), and the axial ratio is below 2.2 dB.

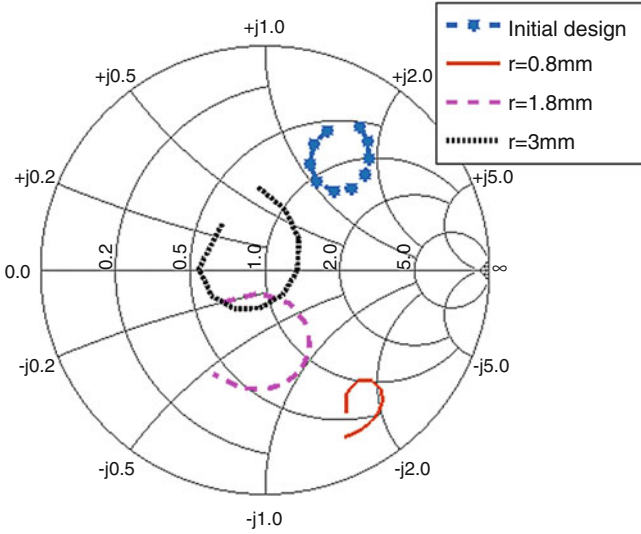


Fig. 5.18 Return loss as a function inner annular gap radius on a smith chart

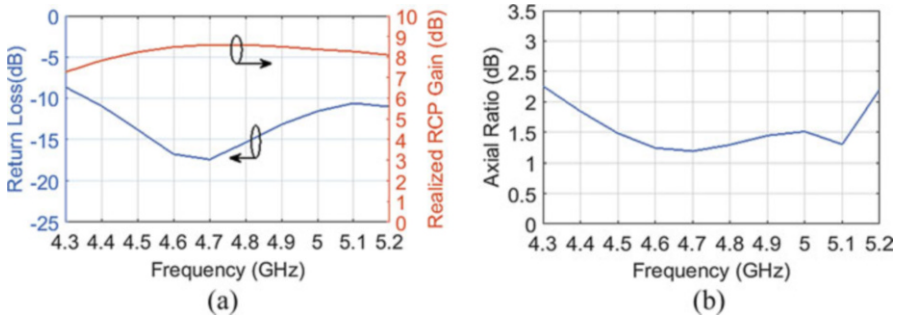
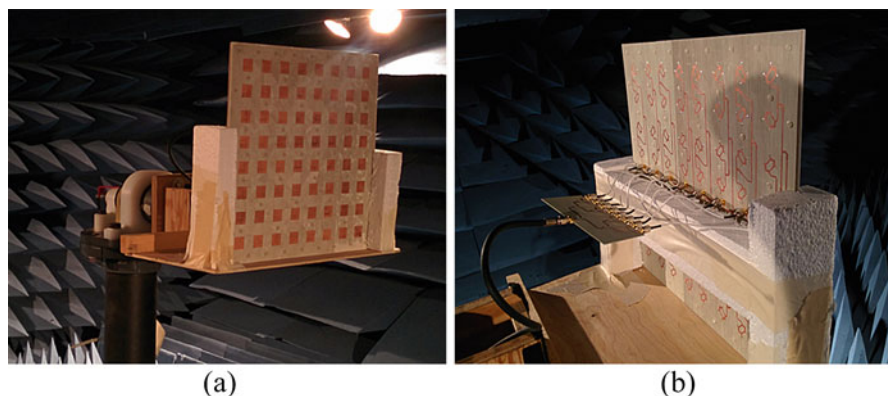
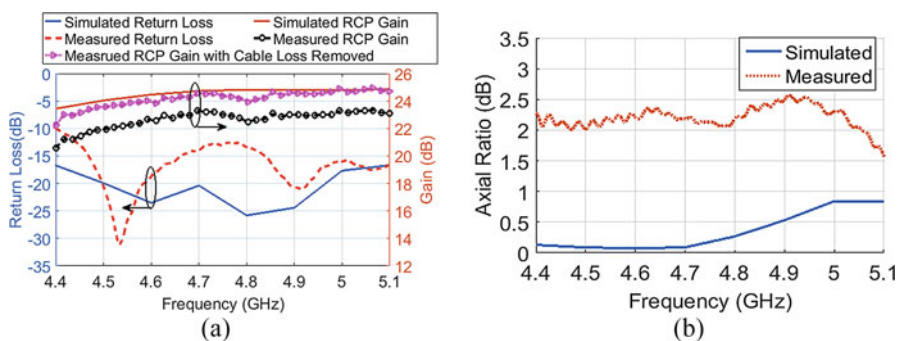


Fig. 5.19 Simulation result of the antenna design. (a) Return loss and realized gain. (b) Axial ratio

An 8×8 antenna array based on the stacked-patch antenna with air gap above was fabricated and experimentally characterized, as shown in Fig. 5.20. A feeding network similar to the one for the 4×8 stacked-patch antenna was built and used to combine the antenna elements vertically to form eight subarrays. The simulated and measured results are shown in Figs. 5.21 and 5.22. The return loss is lower than −10 dB for both the simulation and the fabricated design over the 4.4–5.1 GHz band. The simulated gain ranges from 23.5 to 25 dB, while the measured gain ranges from 20.5 to 23.4 dB. After the post-processing of measured data and removing additional insertion losses due to cable and power divider feeds, the measured gain matched very well with the simulated gain, as shown in Fig. 5.21a. The simulated axial ratio is less than 1 dB, while the measured axial ratio is less than 2.5 dB. The 3 dB beamwidth ranges from 10° to 9° from 4.4 to 5.1 GHz with a side-lobe



**Fig. 5.20** 8×8 stacked-patch-antenna array. (a) Front view. (b) Back view



**Fig. 5.21** Simulated and measured results of the 8×8 dual-fed stacked-patch-antenna array. (a) Return loss and realized RCP gain. (b) Axial ratio

level of less than  $-10$  dB. In comparison to the 4×8 stacked-patch-antenna array, the 8×8 stack patch antenna with air gap has about 5 dB increase in gain, which 3 dB is from doubling of the antenna size and 2 dB is from the gain improvement in the antenna element. The total thickness of the 8×8 stacked-patch-antenna array is 5.8 mm, which also includes the feeding network. This is only 2 mm thicker than the 4×8 stacked-patch-antenna array.

In comparison to the LSA array, the patch-antenna arrays have lower profile and higher gain but narrower operating bandwidth. Excluding the feed network, the 4×8 and the 8×8 stacked-patch-antenna arrays have thickness of  $0.048\lambda_c$  and  $0.079\lambda_c$ , respectively, where  $\lambda_c$  is the free-space wavelength corresponding to the center frequency of the operating frequency band. In comparison, the thickness of the LSA array is  $0.2\lambda_c$ . The LSA array has intrinsically wide bandwidth. The measured return loss of the LSA array covered 4–5.9 GHz for return loss  $< -10$  dB, while the patch-antenna arrays covered 4.4–5.1 GHz. However, to achieve wideband property, the spacing between adjacent feeding ports of the LSA array needs to be less than or

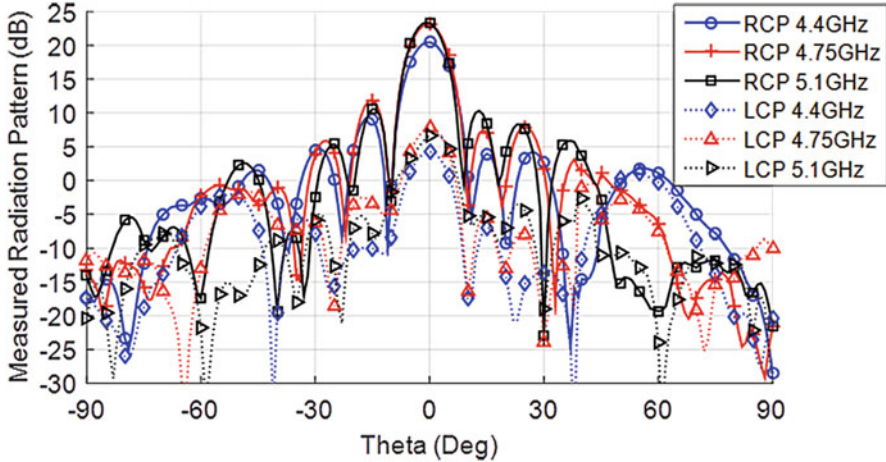


**Fig. 5.22** Measured radiation pattern of the  $8 \times 8$  dual-fed stacked-patch-antenna array in the  $x$ - $z$  plane

equal to half the wavelength corresponding to the highest operating frequency. This design requirement limits the gain of the array. The antenna arrays have comparable circular polarization characteristics (i.e., axial ratio and cross polarization level) over their operating frequency bands.

### 5.3 Beam-Steering/Switching Feeding Network

Beam steering can be done mechanically or electrically. In mechanical beam steering, a positioner is needed to move the antenna or antenna array, which is slow. In electrical beam steering, the phase of the signal going into to each antenna element is modified so that constructive interference of the electromagnetic field occurs in the desired direction. The phase of the signal can be modified in a digital or analog manner. In digital beamforming, the signals are processed digitally; there are more freedoms in controlling the phase and amplitude of the signal, which results in higher accuracy and lower side-lobe level and supports additional features such as calculation of the angle of arrival. However, the computation power requirement and cost of the system are high. In analog beamforming, the signal phase is modified by electrically controlled phase shifters or a passive RF circuit with RF switches such as Rotman lens, Butler matrix, or Blass matrix.

An  $8 \times 8$  Butler matrix beam-switching feed network was chosen to feed the antenna array due to its low-cost and design simplicity [26]. A schematic of the proposed  $8 \times 8$  Butler matrix beam-switching feed network is shown in Fig. 5.23a. It consists of  $22.5^\circ$ ,  $67.5^\circ$ , and  $45^\circ$  phase shifters,  $90^\circ$  hybrid coupler, and crossover. The design includes 12 broadband hybrid couplers and 16 crossover junction. Based

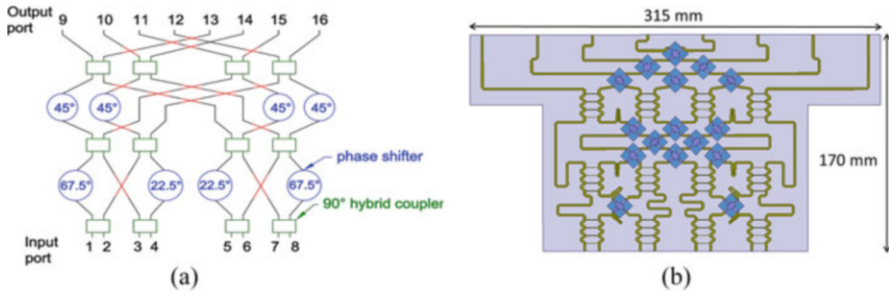


**Fig. 5.23** (a) Schematic of 8x8 Butler matrix beam-switching feed network. (b) Microstrip implementation of the Butler matrix beam-switching feed network

**Table 5.1** Linear phase increment of the output ports for each input port of the Butler matrix beam-switching feed network

Input port	1	2	3	4	5	6	7	8
Phase increment in output ports	$-22.5^\circ$	$157.5^\circ$	$-112.5^\circ$	$67.5^\circ$	$-67.5^\circ$	$112.5^\circ$	$-157.5^\circ$	$22.5^\circ$

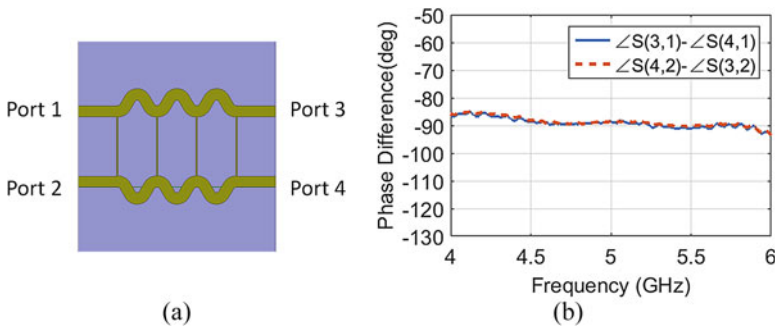


**Fig. 5.24** (a) Schematic of 90° hybrid coupler. (b) Measurement result of phase difference in the output ports of the hybrid coupler

on the schematic, the theoretical phase increment of the output ports for each input port of the Butler matrix beam-switching feed network was calculated, as shown in Table 5.1. The phase increment ranges from  $-157.5^\circ$  to  $157.5^\circ$ , which results in steering angle of  $-60^\circ$  to  $60^\circ$  for antenna array with element spacing of half wavelength. The Butler matrix beam-switching feed network was designed on a Rogers RO4350B substrate with relative permittivity 3.66 and thickness of 0.762 mm. Figure 5.23b shows the final design of the microstrip realization of the 8x8 Butler matrix beam-switching feed network.

The components of the Butler matrix beam-switching feed network were designed separately. Figure 5.24 shows the three-stage 90° hybrid coupler [27] which was designed to cover the 4–6 GHz frequency band. As shown in the figure,

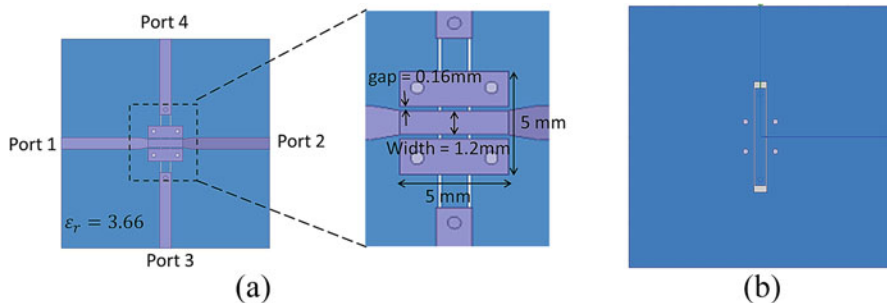


**Fig. 5.25** (a) Crossover top view. (b) Crossover bottom view

the microstrip line of the hybrid coupler was meandered to minimize the size of the hybrid coupler. The measurement result of the phase difference in the output ports of the  $90^\circ$  hybrid coupler is  $90^\circ \pm 5^\circ$  throughout the chosen frequency band.

The traditional way of implementing a crossover junction is to connect two  $90^\circ$  hybrid couplers in series. However, the hybrid-coupler-based crossover dramatically increases the size of the Butler matrix beam-switching feed network as it requires 16 crossover junctions. To reduce the size of the Butler matrix beam-switching feed network, the conductor-backed coplanar waveguide crossover [28] was chosen due to its broadband characteristic and compact size. The crossover allows two radiofrequency paths crossing each other by using two orthogonal coplanar waveguide on top and bottom layers of the substrate. The size of the crossover was further reduced by reducing the number of via holes as well as the center conductor width and gap of the coplanar waveguide. Figure 5.25 shows one of the reduced-size crossovers with the coplanar waveguide portion reduced to  $5 \times 5 \text{ mm}^2$ . The simulated and measured performances of the reduced-size crossover are shown in Fig. 5.26. It has a return loss less than  $-20 \text{ dB}$ , insertion loss less than  $0.7 \text{ dB}$ , isolation more than  $26 \text{ dB}$ , and the phase difference between the two paths less than  $2^\circ$  over the  $0.5\text{--}6 \text{ GHz}$  frequency band.

The phase shifters were designed together with the crossovers to take into account the phase delay of the crossover. The broadband two-section Schiffman differential phase shifter [29] was implemented in the Butler matrix beam-switching feed network to provide  $22.5^\circ$ ,  $45^\circ$ , and  $67.5^\circ$  phase shifts. Figures 5.27a and 5.28a show the simulation setup of the phase shifters integrated with the crossovers. For the simulation setup of the  $45^\circ$  phase shifter in Fig. 5.28a, part of the model was cut out to reduce the simulation time as the schematic is symmetric. Based on the simulated results, the  $22.5^\circ$  phase shifter achieves  $22.5^\circ \pm 0.5^\circ$  phase shift, the  $67.5^\circ$  phase shifter achieves  $67.5^\circ \pm 2^\circ$  phase shift, and the  $45^\circ$  phase shifter achieves  $45^\circ \pm 1.4^\circ$  phase shift, across the  $4\text{--}6 \text{ GHz}$  frequency band.

The components of Butler matrix beam-switching feed network were integrated to form the  $8 \times 8$  Butler matrix network shown in Fig. 5.23b. The Butler matrix beam-switching feed network was fabricated and experimentally characterized.

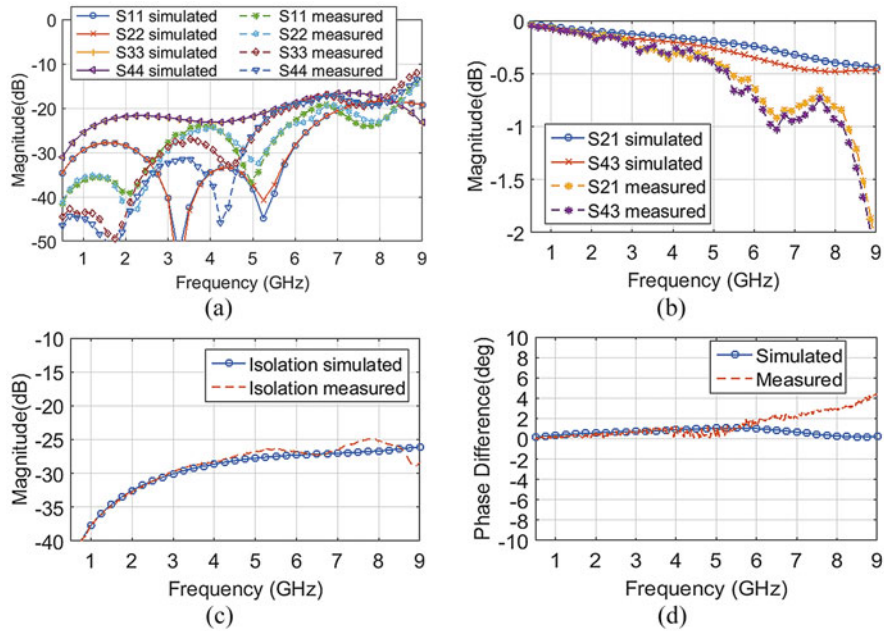


**Fig. 5.26** Simulated and measured result of the crossover. (a) Return loss. (b) Insertion loss. (c) Isolation. (d) Phase difference

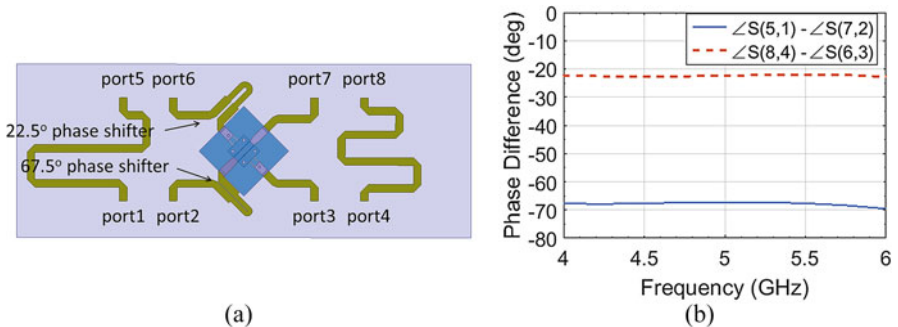


**Fig. 5.27** (a) Schematic of 22.5° and 67.5° two-section Schiffman phase shifter integrated with crossover. (b) Simulation result

The fabricated network and some of the measured results are shown in Fig. 5.29. The return loss is less than  $-10$  dB, insertion loss is  $3 \pm 2$  dB, and output phase variance is  $\pm 15^\circ$ .



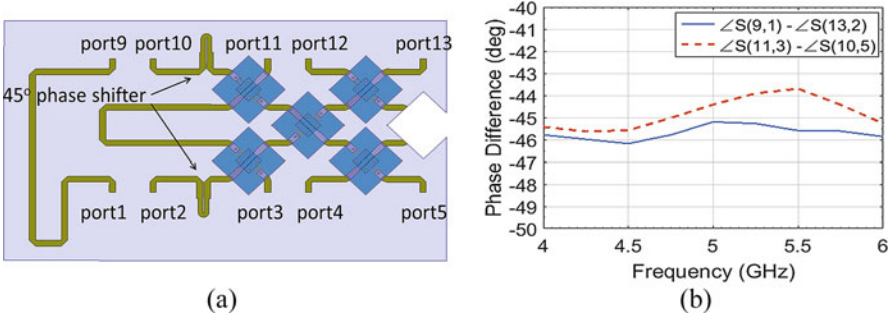


**Fig. 5.28** (a) Schematic of 45° two-section Schiffman phase shifter integrated with crossover. (b) Simulation result

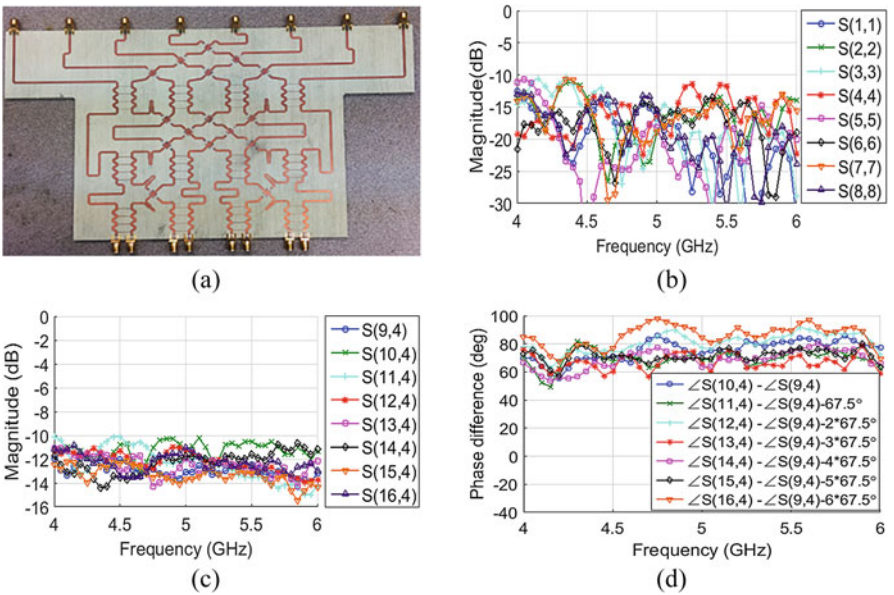


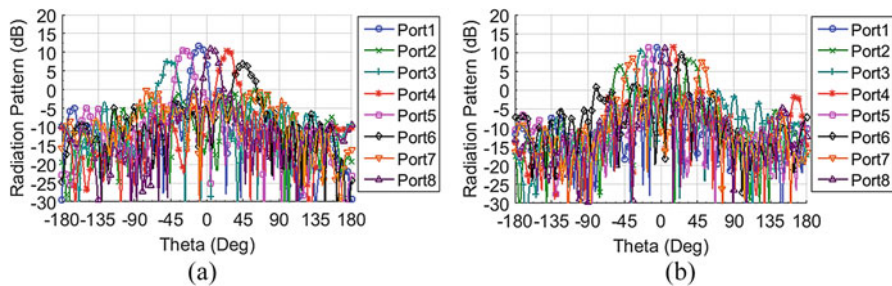
**Fig. 5.29** (a) Prototype of the Butler matrix beam-switching feed network developed. (b) Measured return loss. (c) Insertion loss of port 4. (d) Phase shift in the output port while exciting port 4

### 5.4 Antenna Measurement with Butler Matrix

As the compact 8×8 Butler matrix beam-switching feed network was developed and fabricated, measurements were also conducted on both 4×8 antenna arrays when fed by the Butler matrix beam-switching feed network. Based on the phase increment of the Butler matrix in Table 5.1 and the feeding port or antenna element spacing, the calculated beam directions for both antenna arrays using uniform linear

**Table 5.2** Theoretical beam direction of the antenna arrays at 5 GHz

Input port	1	2	3	4	5	6	7	8
LSA	$-9^\circ$	n/a	$-51^\circ$	$28^\circ$	$-28^\circ$	$51^\circ$	n/a	$9^\circ$
Stacked patch	$-5^\circ$	$39^\circ$	$-27^\circ$	$16^\circ$	$-16^\circ$	$27^\circ$	$39^\circ$	$5^\circ$

**Fig. 5.30** Measured radiation pattern of the antenna array fed by the Butler matrix beam-switching feed network in the x-z plane at 5 GHz. (a)  $4 \times 8$  LSA array. (b)  $4 \times 8$  stacked patch antenna array

array factor equation are shown in Table 5.2 at 5 GHz. For the LSA array, however, beams resulting from feeding ports 2 and 7 of the Butler matrix are not included in Table 5.2. This is because when using the smaller inter-element spacing in the LSA array design, the isotropic source-based array factor equation results in unrealizable angles using the actual directional element of this array. Figure 5.30 shows the measured radiation patterns of the LSA array and the patch-antenna array fed by the Butler matrix in the x-z plane. The measured beam directions agree well with the theoretical beam directions for both antenna arrays. With limited feeding port distance, only six main beams are observed emanating from the LSA array. On the other hand, the patched-antenna array has more design flexibility in terms of element distance (larger element distance), which results in eight main beams. As only one component, i.e.,  $E_\theta$  was measured for each input port, there would be a 3 dB increment in the measured radiation pattern for RCP gain.

## 5.5 Conclusion

Three right-circularly polarized antenna arrays and a broadband Butler matrix beam-switching feed network were developed for directional networking application. The  $4 \times 8$  LSA array covers the frequency band of 4–6 GHz with gain of 17 dB and axial ratio  $< 1.8$  dB. The  $4 \times 8$  low-profile stacked-patch-antenna array covers the frequency band of 4.5–5 GHz with gain of 18 dB and axial ratio  $< 1$  dB. The  $8 \times 8$  stacked-patch-antenna array with improved element gain has gain of 23 dB and axial ratio  $< 2.5$  dB. The three antenna arrays are designed to meet sponsor requirement for the US Army CERDEC.

Future work will include development of designs in Wi-Fi band of 5.17–5.84 GHz for the implementation in the ongoing NSF-EARS-funded directional networking project at HCAC. The feed system will also be redesigned to improve the insertion loss in the desired frequency band. The antenna array and the feed system will be integrated in the directional networking prototype system being developed for the field trial in rural areas. We intend to use the patch-antenna array design as it provided improved gain and beamforming capability. At higher frequencies, larger arrays can be fabricated in order to further improve the gain that would, as a result, cover longer distances.

As for the beamforming, we will continue to explore the trade-offs involved in either analog implementation (e.g., using Butler matrix) vs digital implementations. Butler matrix-based implementation is a low-cost option, hence attractive for rural area implementation, and also requires only one feed and a set of switches for controlling the beam direction. Digital beamforming implementation, on the other hand, requires multiple feeds but has the advantage of flexibility in beamforming options such as the generation of multiple simultaneous beams and adaptive beamforming. This trade-off will be evaluated in a variety of communication environments to clearly identify performance advantages of each.

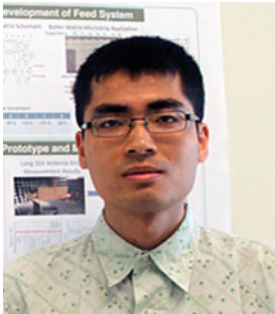
In parallel with the aforementioned comparative study, our team is evaluating the use of an  $8 \times 8$  MIMO digital beamforming system by Sundance [30], which is available in our laboratory. This system mainly consists of multiple digital signal processors and Xilinx Virtex-6 Field Programmable Gate Arrays and is programmable using Texas Instruments Code Composer Studio. This option may facilitate a rapid implementation and field testing for ongoing research in developing a physical layer-based directional networking technology.

## References

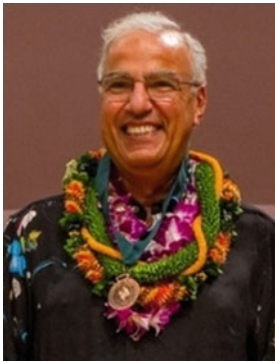
1. T. Wheeler, M. Clyburn, J. Rosenworcel, A. Pai, M. O'Rielly, *2015 Broadband Progress Report and Notice of Inquiry on Immediate Action to Accelerate Deployment* (Federal Communications Commission, Washington, DC, 2015), pp. 14–126
2. M.F. Iskander, Z. Yun, F.A. Qazi, G. Sasaki, A. Das, Physical layer based approach for advanced directional networking, in *Proceedings of IEEE Military Communications (MILCOM) Conference*, 2016, pp. 224–229
3. G.C. Huang, M.F. Iskander, M. Hoque, Advanced antenna array designs for directional networks, in *Proceedings of IEEE Military Communication (MILCOM) Conference*, 2016, pp. 204–207
4. J. Baik, T. Lee, S. Pyo, S. Han, J. Jeong, Y. Kim, Broadband circularly polarized crossed dipole with parasitic loop resonators and its arrays. *IEEE Trans. Antennas Propag.* **59**(1), 80–88 (2011)
5. Y. Hu, W. Ding, W. Cao, Broadband circularly polarized microstrip antenna array using sequentially rotated technique. *IEEE Antennas Wirel. Propag. Lett.* **10**, 1358–1361 (2011)
6. V. Rafii, J. Nourinia, C. Ghobadi, J. Pourahmadazar, B.S. Virdee, Broadband circularly polarized slot antenna array using sequentially rotated technique for C-band applications. *IEEE Antennas Wirel. Propag. Lett.* **12**, 128–131 (2013)

7. S. Yang, R. Chair, A. Kishk, K. Lee, K. Luk, Study on sequential feeding networks for subarrays of circularly polarized elliptical dielectric resonator antenna. *IEEE Trans. Antennas Propag.* **55**(2), 321–333 (2007)
8. Y. Hu, Z. Qiu, B. Yang, S. Shi, J. Yang, Design of novel wideband circularly polarized antenna based on Vivaldi antenna structure. *IEEE Antennas Wirel. Propag. Lett.* **14**, 1662–1665 (2015)
9. C. Liu, Y. Lu, C. Du, J. Cui, X. Shen, The broadband spiral antenna design based on hybrid backed-cavity. *IEEE Trans. Antennas Propag.* **58**(6), 1876–1882 (2010)
10. H.S. Youn, L. Lee, N. Celik, M. Iskander, Dual-polarization cylindrical long-slot array antenna integrated with hybrid groundplane, in *Proceedings of IEEE Antennas Propagation Society International Symposium*, Chicago, 2012
11. J. Rayno, N. Celik, M.F. Iskander, Dual-polarization cylindrical long-slot array (CLSA) antenna integrated with compact broadband baluns and slot impedance transformers. *IEEE Antennas Wirel. Propag. Lett.* **12**, 1384–1387 (2013)
12. H.S. Youn, Y.L. Lee, N. Celik, M.F. Iskander, Design of a cylindrical long-slot array antenna integrated with hybrid EBG/ferrite ground plane. *IEEE Antennas Wirel. Propag. Lett.* **11**, 180–183 (2012)
13. L.Y. Lee, H. Youn, M.F. Iskander, Long slot array (LSA) antenna integrated with compact broadband coupled microstrip impedance transformer, in *Proceedings of IEEE Antennas and Propagation Society International Symposium*, Chicago, 2012
14. A. Neto, J.J. Lee, Ultrawide-band properties of long-slot arrays. *IEEE Trans. Antennas Propag.* **54**(2), 534–543 (2006)
15. G.C. Huang, M. Iskander, M. Hoque, S. Goodall, T. Bocskor, Antenna array design and system for directional networking. *IEEE Antennas Wirel. Propag. Lett.* **14**, 1141–1144 (2015)
16. K. Yang, K. Wong, Dual-band circularly-polarized square microstrip antenna. *IEEE Trans. Antennas Propag.* **49**(3), 377–382 (2001)
17. K.-F. Tong, T.-P. Wong, Circularly polarized U-Slot antenna. *IEEE Trans. Antennas Propag.* **55**(8), 2382–2385 (2007)
18. H.L. Chung, X. Qing, Z. Ning, Broadband circularly polarized stacked patch antenna for UHF RFID applications, in *Proceedings of IEEE Antennas and Propagation Society International Symposium*, Honolulu, June 2007, pp. 1189–1192
19. Z.N. Chen, X. Qing, H.L. Chung, A universal UHF RFID reader antenna. *IEEE Trans. Microwave Theory Tech.* **57**(5), 1275–1282 (2009)
20. G.C. Huang, M.F. Iskander, M. Hoque, A wideband circularly polarized stacked patch antenna array and feed system, in *Proceedings of IEEE International Conference on Wireless Information Technology and Systems (ICWITS) and Applied Computational Electromagnetics (ACES)*, Honolulu, 2016
21. J.S. Colburn, Y. Rahmat-Samii, Patch antennas on externally perforated high dielectric constant substrates. *IEEE Trans. Antennas Propag.* **47**(12), 1785–1794 (1999)
22. H. Boutayeb, T.A. Denidni, Gain enhancement of a microstrip patch antenna using a cylindrical electromagnetic crystal substrate. *IEEE Trans. Antennas Propag.* **55**(11), 3140–3145 (2007)
23. R. Gonzalo, P. De Maagt, M. Sorolla, Enhanced patch-antenna performance by suppressing surface waves using photonic-bandgap substrates. *IEEE Trans. Microwave Theory Tech.* **47**(11), 2131–2138 (1999)
24. H.S. Lee, J.-G. Kim, S. Hong, J.-B. Yoon, Micromachined CPW-fed suspended patch antenna for 77 GHz automotive radar applications, in *Proceedings of the European Conference on Wireless Technology*, 2005, pp. 269–272
25. J.M. Kovitz, Y. Rahmat-Samii, Using thick substrates and capacitive probe compensation to enhance the bandwidth of traditional CP patch antennas. *IEEE Trans. Antennas Propag.* **62**(10), 4970–4979 (2014)
26. G.C. Huang, M.F. Iskander, M. Hoque, S.R. Goodal, T. Bocskor, Implementation of high performance and broadband crossover junction in butler matrix design, in *Proceedings of IEEE Antennas and Propagation Society International Symposium*, July 2015, pp. 1052–1053
27. M. Muraguchi, T. Yukitake, Y. Naito, Optimum design of 3-dB branch-line couplers using microstrip lines. *IEEE Trans. Microwave Theory Tech.* **31**(8), 674–678 (1983)

28. W. Liu, Z. Zhang, Z. Feng, M.F. Iskander, A compact wideband microstrip crossover. *IEEE Microwave Wireless Compon. Lett.* **22**(5), 254–256 (2012)
29. B. Schiek, J. Kohler, A method for broad-band matching of microstrip differential phase shifters. *IEEE Trans. Microwave Theory Tech.* **25**(8), 666–671 (1977)
30. <http://www.sundance.solutions/>



**Gui Chao Huang** received his BS degree in electrical engineering from the University of Hawaii at Manoa, HI, in 2012. He is currently a PhD candidate in the Department of Electrical Engineering at the University of Hawaii at Manoa. He joined the Hawaii Center for Advanced Communications as a student research assistant in 2011. His research interests include antenna design, specifically, broadband antenna and phased array. His research in antenna design has been funded by the US Army CERDEC. He has also designed and developed several prototypes of the CP-Stethoscope system. His work has been published in *IEEE Antenna and Wireless Propagation Letters*. He is a member of Eta Kappa Nu (HKN), the National Honor Society for Electrical and Computer Engineers. He was awarded the Kresser ARCS Award in Engineering in 2015.



**Magdy F. Iskander** is the director of the Hawaii Center for Advanced Communications and professor of Electrical Engineering, University of Hawaii at Manoa. He is co-director of the NSF I/UCRC and a fellow of IEEE (1993). He was the 2002 president of the IEEE AP-S, Distinguished Lecturer, and a program director in the ECCS Division at NSF. Dr. Iskander joined the University of Hawaii in 2002, and prior to that, he was a professor of ECE Department and the Engineering Clinic Endowed Chair Professor at the University of Utah. He received many awards for excellence in research and teaching including the University of Hawaii Board of Regents' Medal for Excellence in Research and Medal for Teaching Excellence, IEEE MTT-S Distinguished Educator Award, IEEE AP-S Chen-To Tai Distinguished Educator Award, Northrop Grumman Excellence in Teaching Award, and others.

He has published over 270 papers in journals and books and holds ten patents. He authored/edited several books including the textbook *Electromagnetic Fields and Waves*. He is the founding editor of *Computer Applications in Engineering Education* published by John Wiley & Sons 1992–present. His research has been funded by NSF, NIH, Army Research Office, US Army CERDEC, Office of Naval Research, and corporate sponsors.



**Farhan A. Qazi** received his BS degree in electronic engineering from Ghulam Ishaq Khan Institute of Engineering Sciences and Technology, Pakistan, in June 2009. He received his MS and PhD degrees in electrical engineering from the University at Buffalo and the State University of New York, in 2012 and 2015, respectively. His concentration during graduate studies was in wireless communications and signal processing with research centered on design and analysis of waveforms for radar and communication applications. Dr. Qazi is currently working as a postdoctoral fellow at the Hawaii Center for Advanced Communications (HCAC) conducting wireless communications and signal processing-based research in HCAC's physical layer-based advanced directional networking project, funded in part by National Science Foundation EARS program. He is also providing biomedical signal processing support for HCAC's Cardiopulmonary Stethoscope project. Dr. Qazi's research interests span around wireless communications (including standards such as IEEE 802.11 and 3GPP's LTE), directional networking (digital beamforming), and signal processing (for communication, biomedical, and radar applications). He has published work in IEEE Transactions on Aerospace and Electronic Systems as well as IEEE Aerospace and Electronic Systems Magazine.



**Zhengqing Yun** received the PhD degree in electrical engineering from Chongqing University, Chongqing, China, in 1994. He was an assistant researcher at the Hawaii Center for Advanced Communications (HCAC) from 2002 to 2005, where he became an assistant professor in 2006. He was involved in a postdoctoral work with the University of Utah and Southeast University, China, before he joined the University of Hawaii at Manoa (UH), Honolulu, Hawaii. He is currently an associate professor at the Hawaii Center for Advanced Communications (HCAC), College of Engineering, UH. Dr. Yun's current research interests include radio propagation in complex environments, such as urban, indoor, and mountainous areas. He served as the technical program co-chair of the IEEE Antenna and Propagation Society International Symposium, Honolulu, in 2007, and the technical program chair of the IEEE International Conference on Wireless Information Technology and Systems, Honolulu, in 2010 and 2016, and Maui, Hawaii, in 2012. He was an associate editor of the IEEE Transactions on Vehicular Technology and the IEEE Transactions on Antennas and Propagation. He is currently an associate editor of the IEEE Access.



**Galen H. Sasaki** received his BS degree in electrical engineering from the University of Hawaii, in 1981, and the MS and PhD degrees in electrical and computer engineering from the University of Illinois, Urbana-Champaign, in 1984 and 1987, respectively. He has been an associate professor at the Department of Electrical Engineering at the University of Hawaii since 1992. He was an assistant professor at the Department of Electrical and Computer Engineering at the University of Texas at Austin from 1987 to 1992. He held visiting positions at the Naval Research Laboratory, IBM Research, Tellabs, Xros, and Nortel Networks. He was an associate editor for the *IEEE/OSA Journal of Optical Communications and Networking*, *IEEE Transactions on Information Theory*, and *IEEE/ACM Transactions on Networking*. His research interests are in communication networks, optimization algorithms, and performance evaluation.

# Chapter 6

## Electrically Small Antennas

James M. Baker

### 6.1 Introduction

The design of electrically small antennas (ESA) presents a wide variety of challenges, primarily due to inherently low impedance and narrow bandwidths. Improving these performance characteristics is especially challenging in the high frequency (HF) band (3–30 MHz) due to the longer wavelengths (10–100 m) and corresponding antenna physical dimensions. These challenges are amplified for applications such as coastal HF surface wave radar (HFSWR) systems, which also require vertical polarization for long-range surface wave propagation over the ocean and military applications that require mobile, rapidly deployable, covert systems.

A typical coastal HFSWR antenna system involves arrays of quarter-wave monopole structures with antenna heights of up to 25 m and even larger ground radial networks. As a result, current HFSWR and over-the-horizon radar (OTH-R) antenna systems tend to be located at fixed sites with extensive infrastructure and site preparation requirements. One solution for these issues is provided by electrically small wire antennas, which better support mobile operations and rapid deployment to remote, desolate, or otherwise unprepared locations. For these types of applications, the primary characteristics of interest (and limiting factors) in antenna design are overall size and weight constraints, lowest achievable operating frequency, input impedance, gain, bandwidth, polarization, and phase stability.

---

J.M. Baker (✉)  
U.S. Marine Corps, Carlsbad, CA, USA  
e-mail: [jmbaker@hawaii.edu](mailto:jmbaker@hawaii.edu)



## 6.2 Electrically Small Antennas

Over the years, there have been many contributors to the theory and design of antennas that are electrically small. Wheeler [1, 2] and Chu [3] pioneered the field by developing fundamental properties of electrically small antennas. The generally accepted criteria for what makes an antenna *electrically small* is based on the free space wave number  $k$  and the radius  $a$  of the spherical volume occupied by the antenna. An antenna is considered to be electrically small when the value of  $ka \leq 0.5$  [4] (where  $k = 2\pi/\lambda$ ,  $\lambda$  is the wavelength at a given frequency, and  $a$  is the radius of the spherical volume enclosing the antenna). This is consistent with Wheeler's definition for small antenna: "... here defined as one occupying a small fraction of one radiansphere in space" [2]. In the early days of radio communications, all antennas were electrically small. Hansen provided a chronology of electrically small antennas beginning in 1889 with the Hertz loop antenna, followed by Marconi's long-wire antennas [5].

It is important to identify the relevant metrics for meaningful comparison of various dissimilar antenna geometries. The following sections review fundamental and practical performance properties that have been well established for antennas in general, the fundamental limitations to these properties for electrically small antennas, and the derivation of practical metrics for characterizing performance of antenna geometries. This is necessary to provide for consistent and practical analysis and comparison for all designs presented herein, as well as any other published designs, regardless of specific geometry.

### 6.2.1 Wheeler's Radiation Power Factor

Wheeler [1] developed radiation power factor (PF) as a figure of merit for electrically small electric and magnetic antennas based on their equivalent circuit parameters: conductance  $G_e$ , resistance  $R_m$ , capacitance  $C$ , inductance  $L$ , and angular frequency  $\omega = 2\pi f$  where  $f$  is the frequency in Hz. Wheeler then expressed these equations in terms of wavelength  $\lambda$  and the cylindrical volume of each antenna (cylinder radius  $a$  and height  $b$ ), showing that the two expressions for radiation PF were equivalent for electric ( $p_e$ ) and magnetic ( $p_m$ ) antennas:

$$p_e = \frac{G_e}{\omega C} = \frac{4 \pi^3 a^2 b}{3 \lambda^3}, \quad (6.1)$$

$$p_m = \frac{R_m}{\omega L} = \frac{4 \pi^3 a^2 b}{3 \lambda^3}. \quad (6.2)$$

Wheeler further developed the concept of a radian sphere with radius  $r$  equal to one radian length ( $r = \lambda/2\pi$ ) [2]. The radian sphere defines the transition between the near-field and far-field regions of an electrically small antenna and is used to

determine the effective antenna volume and its associated effective radius. The spherical volume can then be expressed [2] in terms of radian length ( $\lambda/2\pi$ ) as

$$V_s = \frac{4\pi}{3} \left( \frac{\lambda}{2\pi} \right)^3. \quad (6.3)$$

The relationship between the effective volume  $V_{\text{eff}}$  and the radian sphere volume  $V_s$  is expressed as

$$V_{\text{eff}} = \frac{9}{2^p} V_s, \quad (6.4)$$

and the effective volume in terms of effective radius is expressed as

$$V_{\text{eff}} = \frac{4\pi}{3} (r_{\text{eff}})^3. \quad (6.5)$$

The effective radius ( $r_{\text{eff}}$ ) can then be stated in terms of radiation power factor  $p$  as

$$r_{\text{eff}} = \frac{\lambda}{2\pi} \left( \frac{9}{2^p} \right)^{\frac{1}{3}}. \quad (6.6)$$

This provides a very useful metric for direct comparison of performance improvement for different antenna structures [2]. If the antenna structures being compared are of the same height, the effective radii can be compared directly. If the structures have different heights, the ratio of their respective effective radius to height can be compared. The constraints developed by Wheeler are considered to be practical rather than fundamental in that they were developed for dipole (electric) and loop (magnetic) antennas [6]. It is also worth noting that Wheeler established that the radiation PF is a function of antenna dimensions and resonant wavelength and is the same for electric and magnetic antennas.

### 6.2.2 *Chu's Limit on $Q$*

Chu derived a radiation quality factor  $Q$  for a hypothetical antenna enclosed in a sphere of radius  $a$  using equivalent circuits, describing the electromagnetic fields outside the sphere in terms of infinite series of transverse electric (TE) and transverse magnetic (TM) modes [3]. Chu also defined  $Q$  at the input terminals of an antenna structure based on its equivalent RLC circuit, expressed  $Q$  as a function of stored energy and power dissipated in radiation, and expanded the mode wave impedance into a continued fraction that could be interpreted as a ladder network of capacitors and inductors [3]. Chu's  $Q$  is considered to be a fundamental limitation

for electrically small antennas because it applies to any antenna configuration that fits within a sphere of radius  $a$  and excites a single TM mode [3]. This fundamental limit, established by Chu, was later reexamined by McLean [7] who derived the following exact expression for Chu's  $Q$  based on antenna  $ka$ :

$$Q_{\text{Chu}} = \frac{1}{(ka)^3} + \frac{1}{ka}. \quad (6.7)$$

Chu's  $Q$  did not include stored energy inside the sphere and so is considered the lower bound for lossless antennas. Many papers over the years have refined and modified this expression to increase the value for predicted  $Q$  in search of better agreement with measured antenna performance. One estimate for  $Q$  was developed by Hansen and Collin [6] using numeric methods and curve fitting to better predict measured performance for the lowest-order TM mode as depicted in:

$$Q_{\text{approx}} = \frac{1}{\sqrt{2}(ka)} + \frac{3}{2(ka)^3}, \quad (6.8)$$

which is considered to be accurate within 0.5% for  $ka$  ranging from 0.1 to 0.5 and useful when comparing simulation results for lossless antennas in free space or over a perfect electric conductor (PEC) ground plane. Other versions add an efficiency term to Chu's  $Q$  as in:

$$Q_{lb} = \eta_r \left[ \frac{1}{(ka)^3} + \frac{1}{ka} \right], \quad (6.9)$$

where  $\eta_r$  represents radiation efficiency [8]. Chu's  $Q$  is inversely related to Wheeler's radiation PF and the effective radius, Eq. (6.6), can be reexpressed in terms of  $Q$  as:

$$r_{\text{eff}} = \frac{\lambda}{2\pi} \left( \frac{9}{2Q} \right)^{\frac{1}{3}}. \quad (6.10)$$

Yaghjian and Best [9] developed an expression for  $Q$  derived directly from antenna impedance and angular frequency which provides an additional metric, independent of  $ka$ , for comparing the quality factor of different antenna geometries. This approximation is expressed as

$$Q_Z(\omega) = \frac{\omega}{2R(\omega)} \sqrt{R'(\omega)^2 + \left[ X'(\omega) + \frac{|X(\omega)|}{\omega} \right]^2}, \quad (6.11)$$

with  $R(\omega)$  and  $X(\omega)$  representing the input (feed point) resistance and reactance and  $R'(\omega)$  and  $X'(\omega)$  representing the derivative of the resistance and reactance with respect to the angular frequency ( $\omega$ ). Equation (6.11) is valid for antennas with a

single resonance within the resonant bandwidth. This expression can be calculated and analyzed over ranges including anti-resonant as well as resonant frequencies [8]. It also provides an additional parameter for comparing antenna performance between designs with differing geometries and dimensions as well as for comparing the performance of a specific design to fundamental limitations.

### 6.2.3 Wave Impedance

Chu [3] defined voltage ( $V_n$ ), current ( $I_n$ ), and impedance ( $Z_n$ ) of an equivalent circuit for the spherical waves outside the radian sphere for the  $TM_n$  mode as:

$$V_n = \left(\frac{\mu}{\varepsilon}\right)^{\frac{1}{2}} \frac{A_n}{k} \left(\frac{4\pi n(n+1)}{2n+1}\right)^{\frac{1}{2}} j \frac{d\rho h_n(\rho)}{d\rho}, \quad (6.12)$$

$$I_n = \left(\frac{\mu}{\varepsilon}\right)^{\frac{1}{2}} \frac{A_n}{k} \left(\frac{4\pi n(n+1)}{2n+1}\right)^{\frac{1}{2}} \rho h_n(\rho), \quad (6.13)$$

$$Z_{n, TM} = j \frac{d\rho h_n(\rho)}{d\rho} / (\rho h_n(\rho)), \quad (6.14)$$

where  $h_n$  is the spherical Hankel function of the second kind for mode  $n$ ,  $\mu$  is permeability,  $\varepsilon$  is permittivity,  $k$  is  $2\pi/\lambda$ , and  $\rho = ka$ , where  $a$  is the radius of the spherical volume enclosing the antenna. The notation  $d/d\rho$  indicates the first derivative with respect to  $\rho$ . Chu further expanded these definitions for the  $TE_n$  modes, showing that impedance for the  $TE_n$  mode

$$Z_{n, TE} = \rho h_n(\rho) / \left(j \frac{d\rho h_n(\rho)}{d\rho}\right) \quad (6.15)$$

is equal to the admittance ( $Y_n = I/Z_n$ ) of the  $TM_n$  mode described in Eq. (6.14). These equations for TE and TM mode impedances are normalized with respect to free space impedance  $Z = (\mu/\varepsilon)^{1/2}$ . They are significant as they are only dependent on the  $ka$  of an antenna's geometry and they represent the impedances of the spherical waves that must couple to free space for far-field radiation.

The resistive component of the  $TM_n$  mode, calculated from Eq. (6.14), is presented in Fig. 6.1 where a significant decrease in resistance is readily observed as the value of  $ka$  is decreased from 0.5 toward 0. It is also observed that for  $ka < 0.5$ , only the first mode has any usable resistance for supporting wave propagation. The reactive component of wave impedance is plotted in Fig. 6.2 where the negative reactance increases (in magnitude) significantly as  $ka$  is decreased below 0.5. For comparison purposes the  $ka$  of a quarter-wave monopole,  $ka \approx 1.5$ , is also depicted in the two figures.

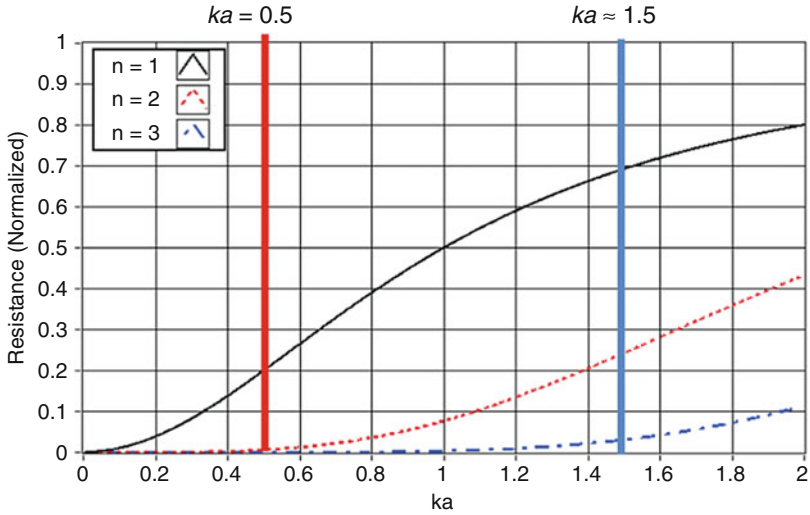


**Fig. 6.1** Resistive component from Eq. 6.13 for  $TM_n$  modes  $n = 1, 2,$  and  $3$

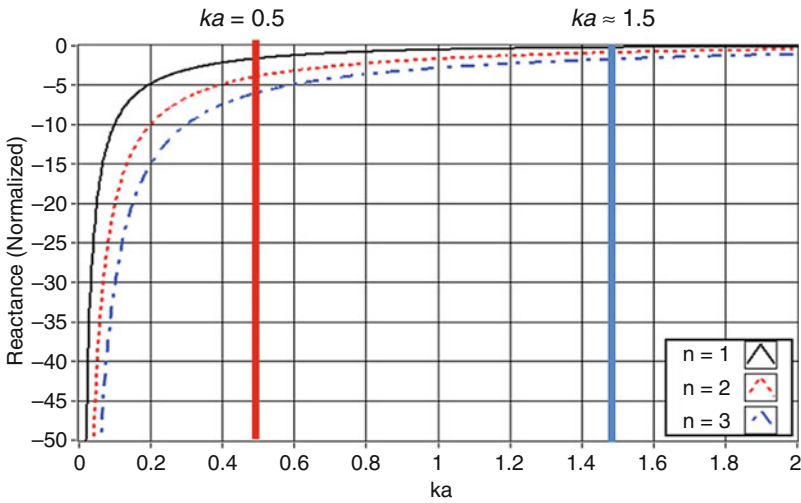


**Fig. 6.2** Reactive component from Eq. (6.13) for  $TM_n$  modes  $n = 1, 2,$  and  $3$

### 6.2.4 Radiation Resistance

The term *radiation resistance* is defined in the IEEE Standard Definition of Terms for Antennas (IEEE Std 145-1993) as “the ratio of the power radiated by an antenna to the square of the RMS antenna current referred to a specified point.” In the general case for arbitrary current distribution on a lossless dipole, radiated power ( $P$ ) can be expressed in terms of average current amplitude ( $I_{av}$ ) and antenna length ( $L$ ) as [10]:

$$P = \sqrt{\frac{\mu_o}{\epsilon_o}} \frac{\beta^2 I_{av}^2 L^2}{12\pi}, \quad (6.16)$$

where  $\beta = 2\pi/\lambda$  and the terms  $\mu_o$  and  $\epsilon_o$  represent free space permeability and permittivity, respectively. For transverse electromagnetic (TEM) modes of propagation (e.g., free space, transmission lines),  $\beta = k$ . The radiation resistance for an electrically small dipole antenna can then be expressed in terms of the ratio of average to peak current and the ratio of physical length to wavelength ( $L_\lambda = L/\lambda$ ) [11] as:

$$R_r \cong 790 \left[ \frac{I_{av}}{I_o} \right]^2 L_\lambda^2. \quad (6.17)$$

This approximation is valid for antennas with  $L \ll \lambda$  [11]. Antennas with dimension  $ka < 0.5$  (equivalently,  $L_\lambda < 0.08$ ) easily satisfy this limitation.

### 6.2.5 Effects of Height, Volume, and Wire Length

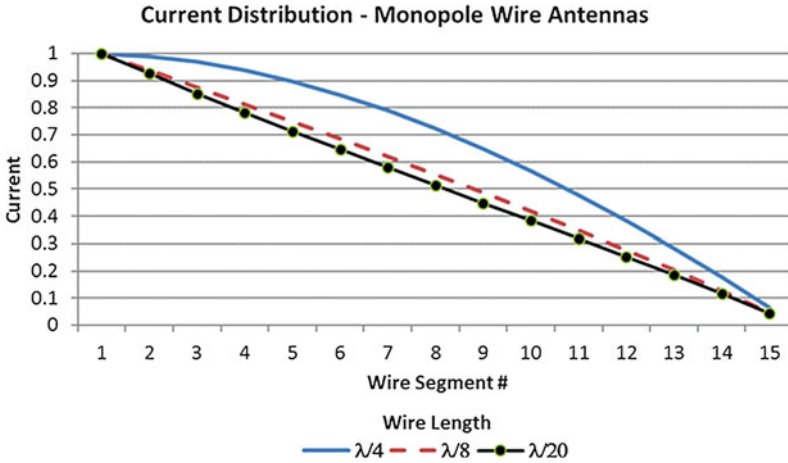
The antenna radiation resistance is proportional to  $(L/\lambda)^2$ ; therefore wire antennas of the same height and resonant frequency generally exhibit the same properties, independent of their geometries. Lower resonant frequencies can be achieved when the geometry effectively utilizes available height and overall volume to meet design goals and requirements. The challenge is to minimize the impact on performance when reducing the height or volume. The length of the wire inside the antenna volume is the dominant factor in establishing resonant frequency. An increase in the wire length will lower the resonant frequency yet will also decrease input resistance and increase  $Q$ . Increasing wire length is also one way to increase antenna inductance, but may also lower the resonant frequency if done indiscriminately. Another method for lowering resonant frequency without increasing wire length is to decrease the wire diameter; this will reduce the antenna's radiation efficiency, which may or may not be an acceptable trade-off.

## 6.3 Design Principles

The key design principles for small wire antennas are to maximize the effective radius at the desired resonant frequency in order to achieve the minimum possible  $Q$  and maximize the input resistance. The impact of the limitations on performance for electrically small antennas was captured by designing a simple quarter-wave ( $\lambda/4$ ) monopole for resonance at 6 MHz. The wire length was progressively reduced from  $\lambda/4$  down to  $\lambda/20$  with the impact on performance analyzed, compared, and results reported in Table 6.1;  $r'/h$  represents the effective radius normalized by the physical

**Table 6.1** Performance at 6 MHz for progressively smaller monopole antennas

Antenna length ( $\lambda$ )	$ka$	Height (m)	Resistance ( $\Omega$ )	Reactance ( $\Omega$ )	$Q_z$	$r'/h$
$\lambda/4$	1.49	11.8	36.0	0	6.4	0.60
$\lambda/8$	0.75	5.9	6.5	-249	50.2	0.60
$\lambda/10$	0.60	4.7	3.9	-322	95.5	0.60
$\lambda/12$	0.50	4.0	2.7	-385	160.0	0.61
$\lambda/20$	0.30	2.4	0.9	-580	657.9	0.63

**Fig. 6.3** Current distribution for  $\lambda/4$ ,  $\lambda/8$ , and  $\lambda/20$  monopole antenna

height. The values for resistance and reactance represent the input impedance of the antenna. The effective radius was calculated using Eq. (6.10) and the quality factor  $Q_z$  was calculated using Eq. (6.11). The notation  $r'$  is equivalent to  $r_{\text{eff}}$ . Both terms are commonly used for describing the effective volume of an electrically small antenna.

This preliminary analysis demonstrates the unavoidable impact on performance characteristics as the height of the monopole is reduced. It can be seen from Table 6.1 that only the antennas of heights of  $\lambda/12$  or less are considered to be electrically small; the input resistance for these antennas is too low for practical applications, and their high capacitive reactance will cause excessive power reflection at the feed point if not properly matched. These smaller antennas also have much higher  $Q$  values, indicating very narrow bandwidths. The geometries were modeled in NEC version 4.2 [12] using 15 wire segments (feed point located at segment #1) and the electric current distribution calculated for each configuration. The current distributions for  $\lambda/4$ ,  $\lambda/8$ , and  $\lambda/20$  configurations are plotted in Fig. 6.3. The sinusoidal distribution for the antenna of length  $\lambda/4$  quickly converges to a triangular distribution as the wire length, relative to wavelength, is reduced.

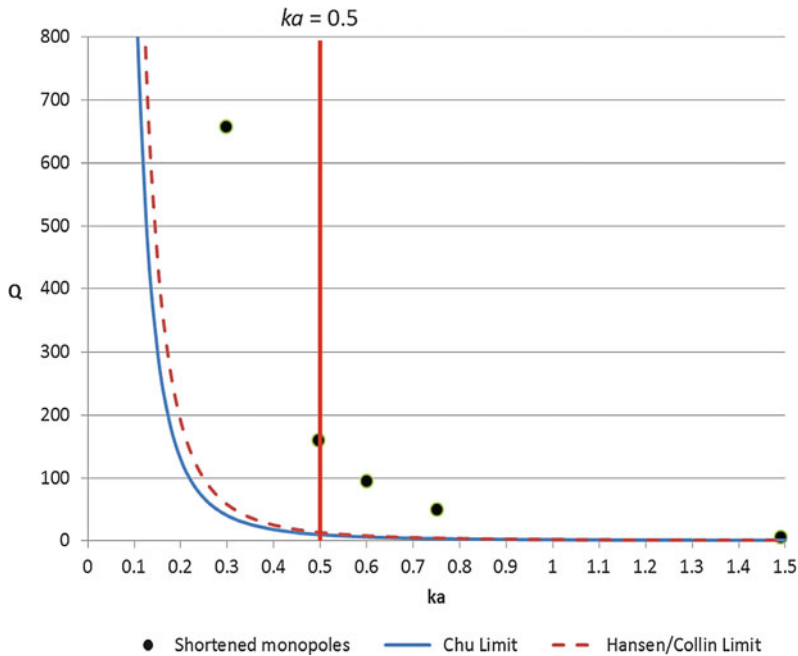


**Fig. 6.4** Chu and Hansen/Collin limits with shortened monopoles from Table 6.1

Specific performance characteristics for the shortened monopole antennas listed in Table 6.1 are depicted in Fig. 6.4, together with Chu's limitation and the Hansen/Collin revision, to highlight the region where  $ka$  is less than 0.5 and to demonstrate the rapid increase in  $Q$  as antenna size (in terms of  $ka$ ) is reduced. The individual monopole configurations may be identified in the figure by their  $ka$  values from Table 6.1.

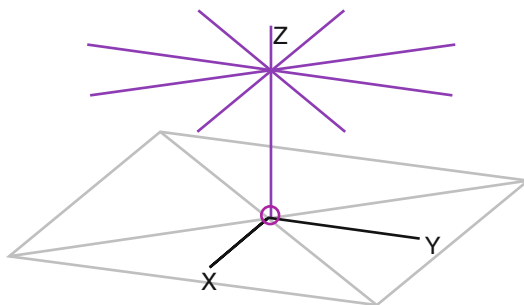
Two common methods used for addressing these performance limitations when reducing antenna size are toploading and folding. These techniques are well documented and are discussed here to provide a baseline for expected performance improvements and also to demonstrate how current design methods and approaches restrict the antenna elements to the surface of the enclosed volume or increase the overall size of the antenna.

### 6.3.1 Toploading

Toploading is one of the earliest mechanisms employed for reducing the physical size of an HF antenna without giving up too much performance. Marconi described a radial network for reducing the height of vertical HF antennas, documented in his 1904 patent [13]. This antenna design consisted of a reduced height vertical



**Fig. 6.5** NEC model of Marconi's 1904 radially toploaded antenna



element with a system of eight radial elements extending outward from the top. Marconi's design, as modeled in NEC, is depicted in Fig. 6.5. The small circle at the base of the antenna represents the feed point. The purpose of toploading is to modify the electrical current distribution on the vertical (radiating) element from being triangular (as previously depicted in Fig. 6.3) to being maximum and uniform in magnitude along the entire length. The improved current distribution provides for corresponding increases in radiation resistance and radiated power. A sampling of toploaded designs described by Best and Hanna [8] was modeled and simulated in NEC to validate the antenna metrics and algorithms implemented herein and to provide a baseline for comparing antenna performance. A comparative analysis of mesh versus radial toploading was conducted to determine the impact on performance for both structures. The term *mesh* is used here to describe a weblike wire structure with radial and cross radial components for providing multiple symmetric paths for current flow.

### 6.3.2 Simulation Results

NEC models with electrical current distribution for two monopole antennas, with and without toploading, are depicted in Fig. 6.6. These antennas were simulated using a perfect electric conductor (PEC) infinite ground plane, with current distribution represented by color per the scale on the left side of the figure. The small circle at the base of each antenna is its feed point. The change in current distribution along the vertical component of the monopole antenna (1) is readily apparent, with maximum current at the base and minimum current at the top. The monopole with toploading (2) displays maximum and uniform current along the entire vertical component; this improvement in current distribution improves antenna input impedance, reduces the antenna's  $Q$ , and provides for much lower resonant frequencies without increasing antenna height.

Two monopole antennas were modeled in NEC for further evaluation of the effects of toploading at different frequencies. The first configuration, designated monopole A, was modeled in NEC with a height of 8.48 cm and evaluated

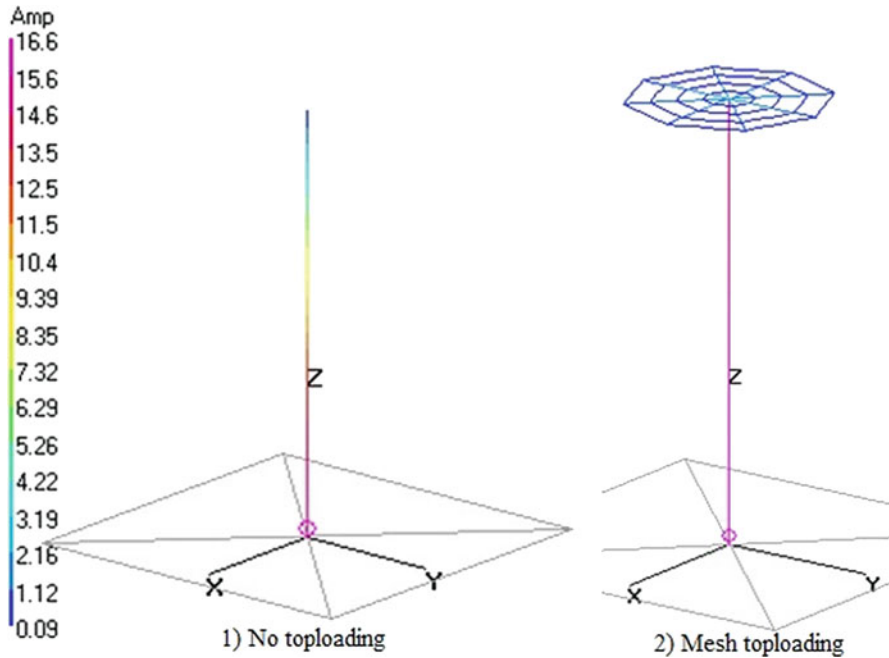


Fig. 6.6 Electrical current distribution in two monopole antennas

Table 6.2 Effects of toploading on monopole performance

Antenna	Freq (MHz)	$ka$	Height (m)	Resistance ( $\Omega$ )	Reactance ( $\Omega$ )	$Q_z$	$r'/h$
Monopole A No topload	300	0.52	0.0848	3.0	-461.4	173	0.56
Mesh topload	300	0.59	0.0848	10.7	0.8	16	1.2
Monopole B No topload	6	0.52	4.22	3.0	-463.7	176	0.56
Mesh topload	6	0.59	4.22	10.6	-0.6	16	1.2
Radial topload	6	0.63	4.22	10.6	-0.2	16	1.2

at 300 MHz with and without toploading. The second configuration, designated monopole B, was modeled with a height of 4.22 m and evaluated at 6 MHz, with and without toploading. This configuration was also evaluated with radial toploading (as depicted in Fig. 6.5) for comparison to mesh toploading (as depicted in Fig. 6.6). The NEC simulation results for these antenna configurations are listed in Table 6.2, where overall performance at 6 MHz and 300 MHz is observed to be similar and the effect of toploading was an increase in input resistance and effective radius, together with a significant decrease in input reactance and  $Q_z$ .

The toploading technique improves performance by providing a longer path (relative to wavelength) for electrical current, resulting in a more uniform current

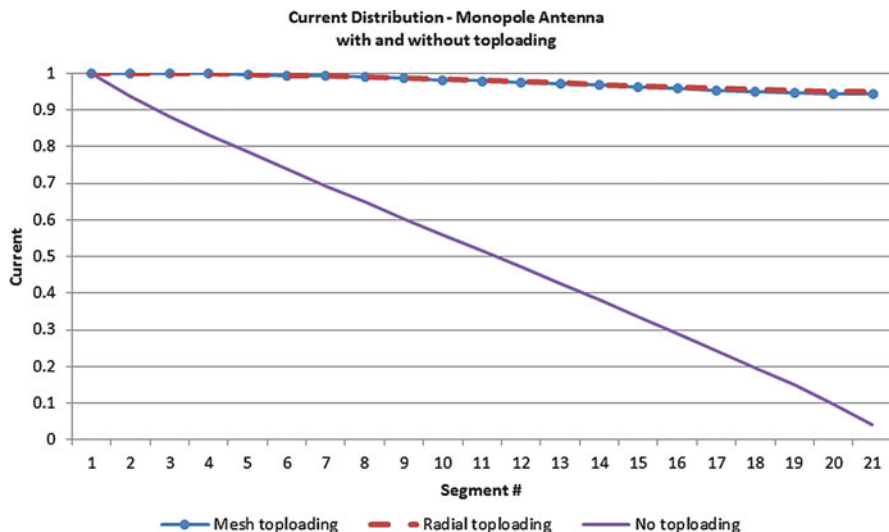


Fig. 6.7 Current distribution for monopole with and without toploading

distribution along the radiating element of the antenna (the primary element connected to the feed point). This improves the ratio of average to maximum current and its effect on radiation resistance as described earlier in Eqs. (6.15), (6.16), and (6.17). Figure 6.7 plots the current distribution for a monopole antenna modeled in NEC, with and without toploading, and also provides a comparison of radial and mesh toploading geometries.

The effect of radial and mesh toploading on electrical current distribution is very similar and consistent with the results in Table 6.2. Given that the ratio of average to maximum current ( $I_{\text{avg}}/I_{\text{max}}$ ) for a triangular distribution is about 0.5 and the ratio for uniform distribution is about 1.0, the resulting increase of uniform over triangular distribution is roughly 2:1. The radiation resistance is proportional to the square of the current ratio, so the maximum achievable improvement in radiation resistance is roughly a factor of 4. The trade-off, however, is an increase in  $ka$  resulting from the additional width added by the toploading structure. This may or may not be acceptable depending on the specific design requirements for the physical dimensions of the antenna.

### 6.3.3 Folding

One popular method for increasing the radiation resistance is commonly referred to as *folding* or *folded arms*. The fundamental properties of folding have been well documented in books and journals [8, 14–16]. The geometry of a folded antenna typically consists of the initial element (e.g., a quarter-wavelength, straight-wire

monopole), with additional elements reflecting the geometry of the initial one. The additional components are positioned at a specified gap distance and connected at the top (or at the ends for dipole geometries). The antenna feed point is connected at the base of the initial element while the bases of additional elements are short-circuited to ground. When properly connected, this structure constitutes a folded arm geometry. Additional arms may be added by short-circuiting the base of the additional elements to ground and connecting all elements to each other at the top. Balanis [15] provided a derivation of the input impedance for folded antennas, which for a simple straight-wire design is approximately equal to the square of the total number of arms multiplied by the initial input impedance. For example, the input impedance of a quarter-wave monopole antenna (single arm) is about  $36 \Omega$ , while the input impedance with two folded arms is about four times that, or  $144 \Omega$ . This property can be very useful when trying to increase input impedance of an electrically small antenna for matching purposes and improving performance. Figure 6.8 depicts folded monopole antennas with two and three arms, as modeled in NEC. The vertical elements are connected together at the top and connected to the PEC ground at the bottom. The small circle indicates the feed point.

The value of folding is realized in the corresponding increase in input resistance due to the cumulative effects of current distribution in the folded arms. Folding may result in an increase of the enclosed spherical volume; this increase is typically only realized with the addition of the first additional element. Additional folded arms may be added without further increase in volume if symmetry is maintained.

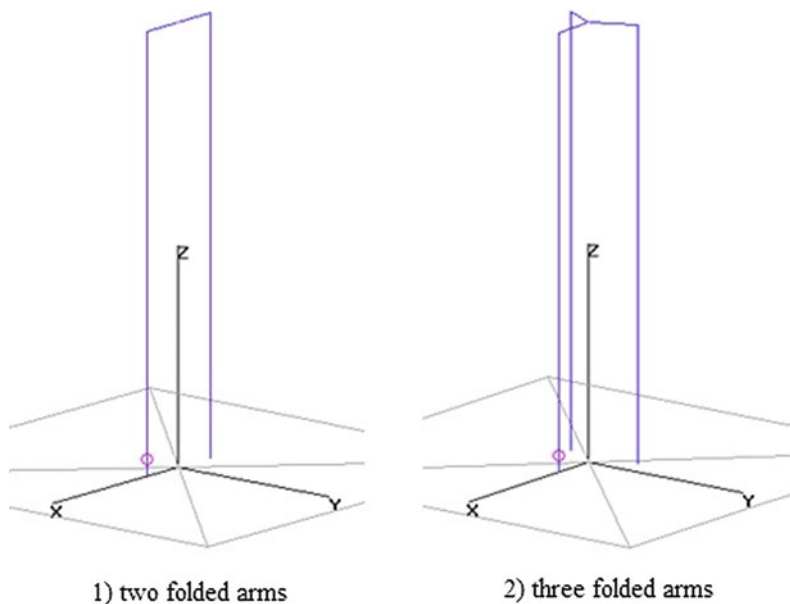


Fig. 6.8 Two-arm and three-arm folded monopole antennas

The relationship between the number of folded arms and the radiation resistance of an antenna provides a method for optimization of antenna impedance for input matching and improvement of radiation properties. This can be extremely useful for improving the performance of electrically small antennas which typically exhibit input impedances well under  $10 \Omega$ .

## 6.4 New Concept and Design Approaches

A currently prevalent theme in ESA methodologies is that *optimization* involves maximizing the placement of wire on the surface of the sphere enclosing the antenna volume [15]. A new approach, inspired by Professor Magdy Iskander, is provided here. This new and alternative design methodology utilizes the inner space of the enclosed volume to achieve self-resonances at much lower frequencies, with performance consistent with the fundamental properties related to antenna height, volume, and wire length. This methodology offers designers an alternative when the design requirements and restrictions on maximum height and volume would otherwise not support self-resonance at a lower required frequency. Several alternative designs have been simulated and analyzed, comparing performance parameters including radiation resistance,  $Q$ , bandwidth, and the minimum operating frequency. Results from these simulations are presented and trade-offs discussed. The design approach presented herein provides innovative methods to more fully utilize the entire volume of the space enclosing the antenna [17], a departure from methods typically described in current publications. The concept of *inner toploading* is further explored with two design approaches for implementing this new concept.

### 6.4.1 Inner Toploading

Inner toploading uses the inner volume of antenna geometry for positioning toploading elements. This design concept, depicted in Fig. 6.9, provides the improved current distribution associated with toploading without the corresponding increase in antenna spherical enclosed volume. In this method, the radius  $a$  of the enclosing sphere is kept constant, yet the overall  $ka$  is reduced due to the lower resonant frequencies (i.e., longer wavelengths) achieved.

The concept of inner toploading was demonstrated by modeling a helical antenna with inner toploading. The resonant frequency of this design was tuned by changing the length of the toploading radials inside the volume, similar to traditional toploading. A 25% reduction in resonant frequency, with no increase in antenna enclosed volume, is achievable using this technique. Table 6.3 provides the resonant performance characteristics including resonant frequency, input resistance,  $Q$ , and  $ka$  for helical antennas with 1, 1.5, and 2 turns, with and without inner toploading. Wire length includes the additional elements used for radial toploading when applicable.

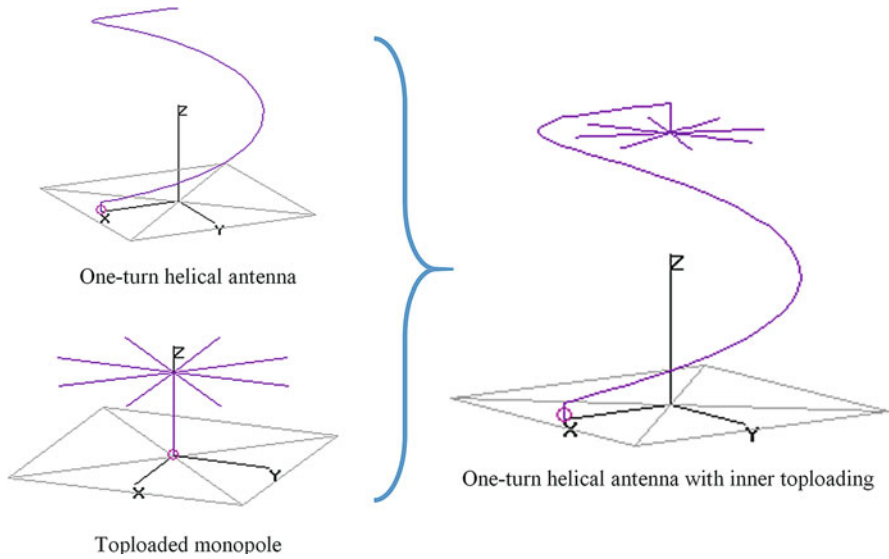


**Fig. 6.9** The concept of inner toploading applied to a one-turn helical antenna

**Table 6.3** Resonant properties of helical antennas, with and without inner toploading

Antenna geometry	Resonant frequency (MHz)	Resistance ( $\Omega$ )	$ka$	$Q_c$	Wire length (m)
1.0 turn	21.5	4.572	0.51	67	3.83
No toploading					
1.5 turns	15.8	2.674	0.38	123	5.35
No toploading					
2.0 turns	12.5	1.864	0.3	187	6.9
No toploading					
1.0 turn	16	3.433	0.38	97	6.93
Inner toploading					
1.5 turns	12.9	2.381	0.31	152	8.45
Inner toploading					
2.0 turns	10.7	1.78	0.26	214	10.0
Inner toploading					

The reduction in self-resonant frequency and the matching reduction in  $ka$  were achieved within the same occupied volume due to the improved current distribution provided by the toploading elements. The electrical current distribution for one-turn helical antennas, with and without inner toploading, were analyzed in NEC and plotted in Fig. 6.10. This design approach offers an alternative when the system design requirements and restrictions on maximum height and volume would otherwise not support self-resonance at a lower (yet required) frequency.

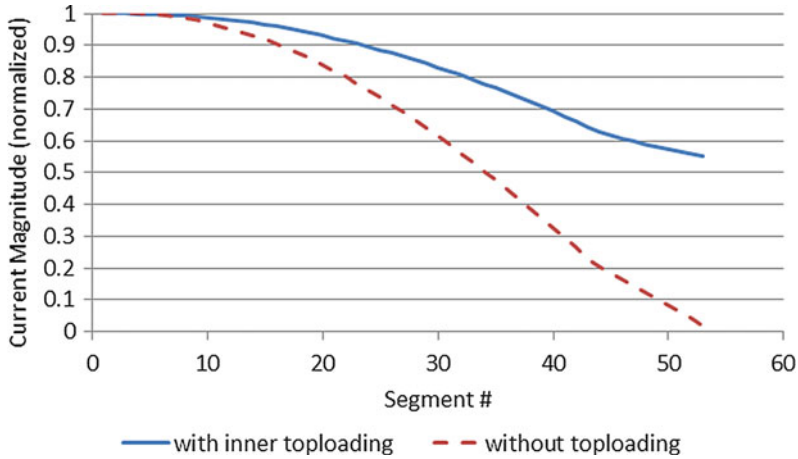


**Fig. 6.10** Current distribution along helical wire antenna, with and without inner toploting

### 6.4.2 Design Methodology

The following methodology was developed to optimize the implementation of inner toploting when traditional methods are unable to achieve design requirements for reduced size or lower resonant frequencies. There are a variety of methods for adding elements to the surface of the antenna's enclosed volume to improve performance [8]. In one example, straight-wire components of canonical antenna geometries are replaced with helical components to lower the resonant frequency within a given volume [18]. The design approach presented herein builds on those initial concepts and provides a framework for determining more efficient utilization of the entire volume enclosed by an antenna.

1. Establish the maximum height limitation for the physical antenna.
2. Establish the maximum volume limitation for the physical antenna.
3. Establish the requirement for lowest operating frequency.
4. Determine the  $ka$  for the above parameters.
5. Determine whether the expected performance for this  $ka$  is acceptable.
6. Effectively use the antenna's inner volume for placing elements in order to achieve required performance, e.g., inner toploting.

This is a departure from methods typically described in current publications which focus only on the outer surface. Several new design approaches developed using this methodology are presented.

## 6.5 Novel Designs for Electrically Small HF Antennas

Inner toploading can be applied to traditional designs such as the normal-mode helical (NMH) antenna [11]. The current distribution in a helical antenna at resonance is similar to other wire antennas, with maximum current at the feed point, zero current at the open end of the wire, and a continuous distribution along the length of the wire. Traditional toploading techniques might place a disk or radial network at the top of the helical antenna to provide for more uniform current distribution and for lowering the resonant frequency [8]. One of the drawbacks of this method is the increased volume and corresponding  $ka$  of the antenna due to the additional external components. Inner toploading can be used in this case to reduce the antenna volume and lower the resonant frequency within the original volume [17]. A two-turn helical antenna was constructed using copper wire and later modified as depicted in Fig. 6.11, using aluminum tape to implement inner toploading. A comparison of simulated and measured  $S_{11}$  for the two-turn helical antenna, with and without inner toploading, is provided in Fig. 6.12. A frequency reduction of 15% was achieved with no increase in antenna size.

**Fig. 6.11** Prototype helical antenna with inner toploading





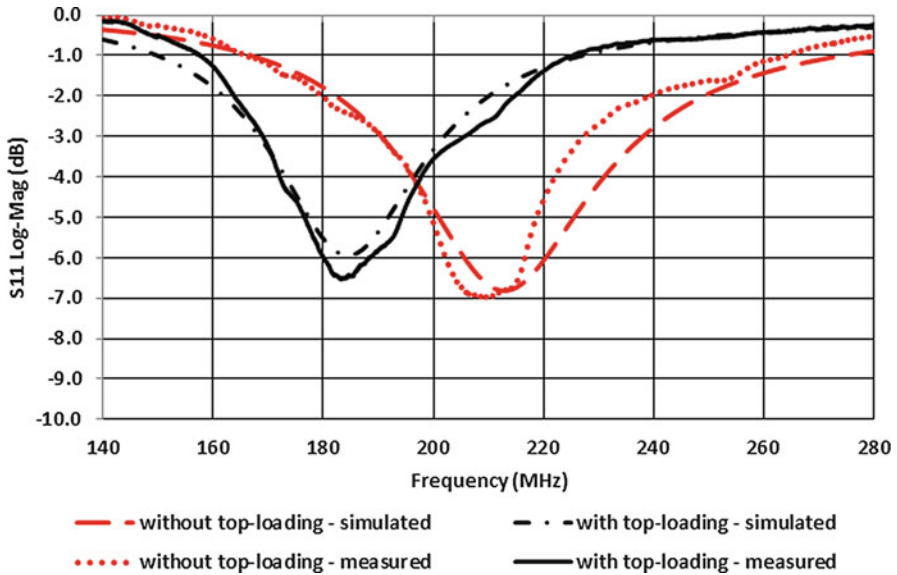


Fig. 6.12 Simulated and measured  $S_{11}$ , with and without inner toploading

### 6.5.1 Helical Meandering Line Antenna (MLA)

A new design combining helical and meandering line elements together for compact high frequency (HF) antennas was presented in Refs. [17, 19, 20]. This antenna was designed to be portable and rapidly deployable, while maintaining a comparatively small profile for mobile radar applications. The helical MLA design is low profile (less than one meter high for HF applications) and provides effective performance, improved antenna radiation resistance, and strong vertical polarization while maintaining an omnidirectional radiation pattern with low takeoff angle. The helical MLA, depicted in Fig. 6.13, also provides for multiple self-resonance frequencies allowing for selectable channels, even without the use of an external antenna tuner or matching network. Figure 6.14 displays the far-field radiation pattern for the three-arm helical MLA as modeled in FEKO [21]. The pattern is vertically polarized and omnidirectional with low takeoff angle.

Open-circuit (inner toploaded) and short-circuit (inner folded arm) antenna mode configurations were implemented using switches installed at the interfaces between antenna wire and the ground plane. These switches provided for mode selection from the available frequency channels by switching the two (nonfeed) arms between open-circuit and short-circuit modes. These switches can also be replaced with more robust capacitive and inductive tuning networks to achieve specific frequencies. Performance was primarily analyzed without the use of matching networks or other tuning mechanisms in order to determine antenna self-resonant characteristics. Two prototypes of the helical MLA designed for HF operations were constructed

**Fig. 6.13** NEC model of helical MLA with three arms

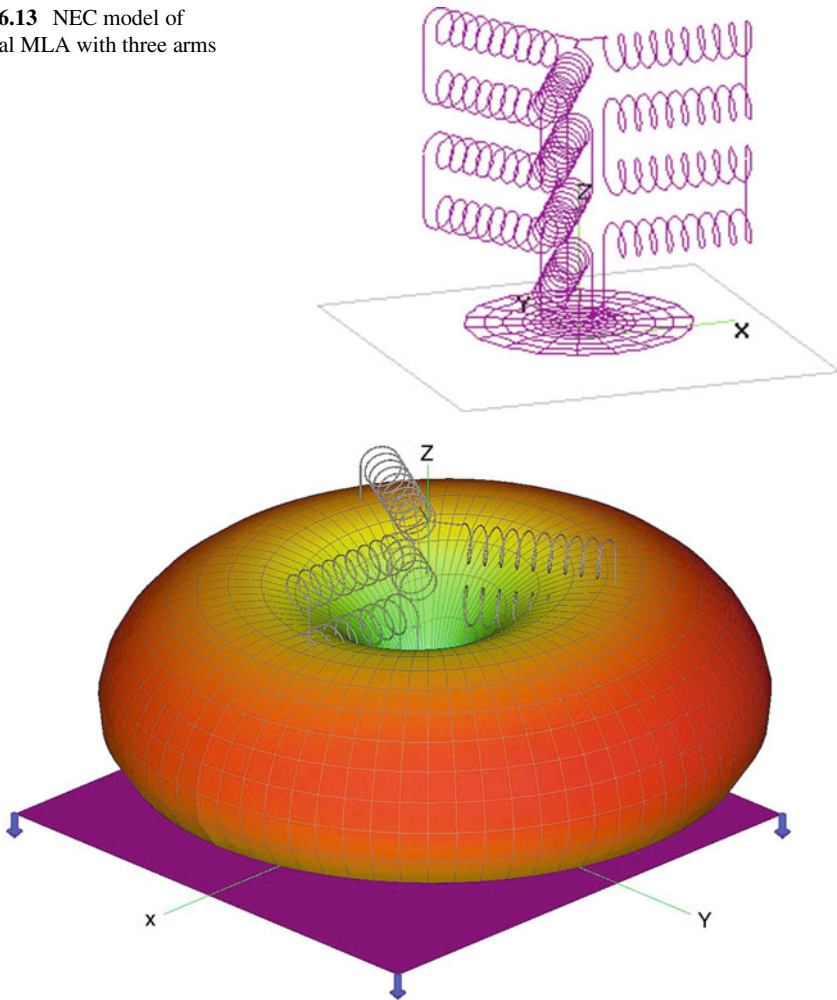


**Fig. 6.14** Far-field radiation pattern for three-arm helical MLA at resonant frequency

and experimentally verified through field testing, demonstrating functional input impedance and vertical polarization at frequencies throughout the HF band while maintaining an omnidirectional antenna pattern with low takeoff angle [20, 22].

### 6.5.2 Considerations for Field Equipment

An in-line 1:1 RF isolator was installed underneath the ground plate at the feed point to isolate the coax cable and minimize reflected energy. RF isolation is very

important, yet often overlooked, when measuring performance characteristics of electrically small antennas. Reflected energy from the antenna feed point (usually a result of a mismatch between the coax cable and antenna connector) is not captured by instruments such as a VSWR meter or a network analyzer, making the antenna performance appear better than it really is. The input resistance, measured with a properly calibrated network analyzer, can appear to be as much as ten times higher than the true value. There are numerous examples of published experimental results which, upon closer examination, are only achieved if the feed line (e.g., coax cable) is also radiating.

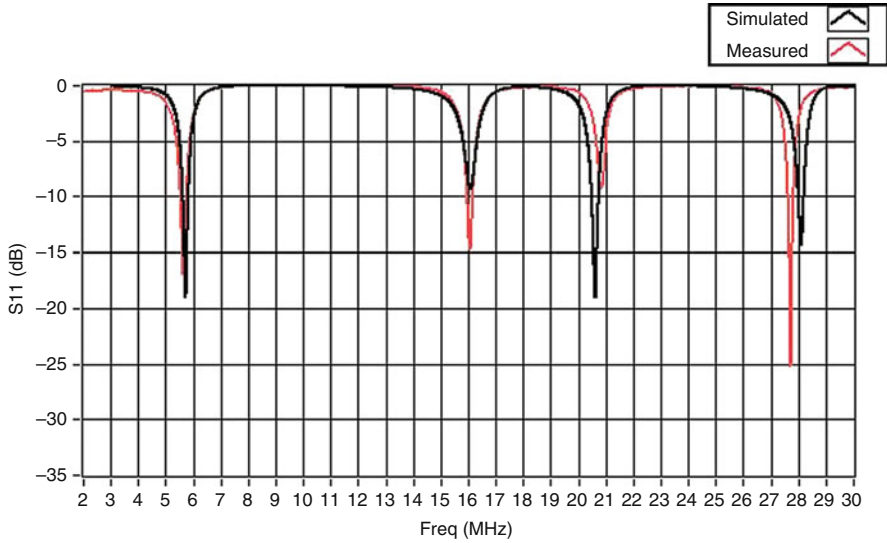
### 6.5.3 *Field Measurements*

A prototype HMLA was constructed using copper wire. Overall dimensions were height, 85 cm, and width, 110 cm. Antenna performance for the prototype HMLA was measured using vector network analyzers and RF power meters. Basic antenna measurements recorded during field testing included  $S_{11}$ , input impedance, and voltage standing wave ratio (VSWR). Gain patterns were measured at 16 MHz in the open-circuit mode by transmitting a 1 mW continuous wave (CW) signal from a quarter-wave vertical reference antenna and then measuring received power at the test antenna as it was manually rotated through  $360^\circ$  of azimuth. Phase linearity was also verified within each resonant bandwidth for open and closed configurations.

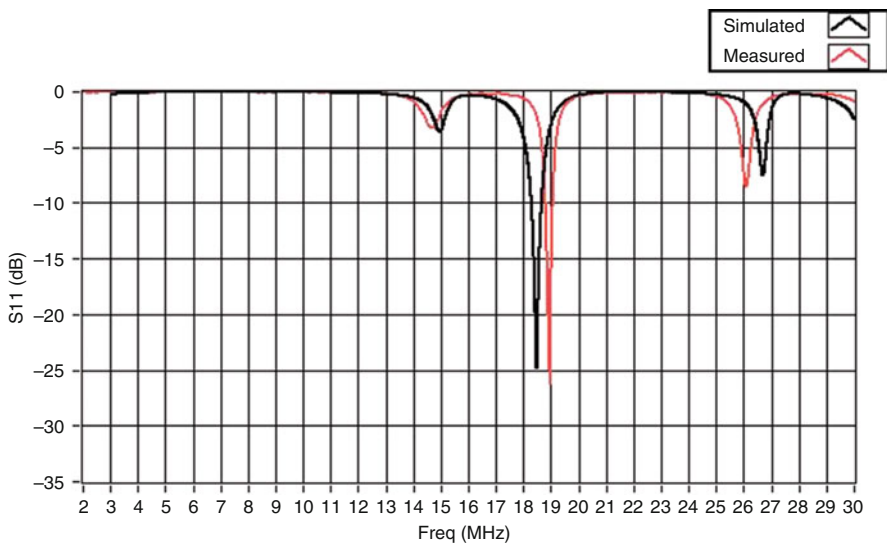
Communications testing was conducted within authorized HF amateur radio bands for voice and CW modes of operation. Test setup consisted of one helical MLA antenna prototype connected to an amateur radio transceiver via 100 ft of coax cable and RF isolation at the antenna feed point. Transmit power was maintained between 50 and 75 W due to limitations on the portable battery used to power the radio during system operation on the beach.

Figure 6.15 shows a comparison of simulated and measured  $S_{11}$  (dB) data for the open-circuit (inner toploaded) configuration of a three-arm helical MLA. Simulation parameters for relative permittivity and conductivity were selected to accurately model real losses in the physical environment. This antenna configuration was self-resonant at four frequencies in the HF band, with no matching network used. This prototype demonstrated HF operations at 5.8 MHz with a total antenna height less than one meter. Figure 6.16 depicts these measurements for the short-circuit (inner folded arm) mode. This configuration was resonant at three frequencies in the HF band, with higher input resistances than the open-circuit mode [20].

The photo in Fig. 6.17 shows a prototype helical MLA on a beach near the Makai Research Pier, Oahu, Hawaii, during field testing with a Kenwood TS-570D HF transceiver. The purpose of this test was to communicate with other amateur radio operators using voice and continuous wave (CW), transmit and receive modes, in the HF band. Over the course of these field test events at Oahu, communications were established with amateur radio stations around the world, as far away as South



**Fig. 6.15** Simulated and measured  $S_{11}$ , three-arm HMLA, open-circuit mode



**Fig. 6.16** Simulated and measured  $S_{11}$ , three-arm HMLA, short-circuit mode

Africa. It is worth noting that this antenna did not require any site preparation and could be easily moved as the tide rolled in [20].

Figure 6.18 shows the setup used during field testing of two prototype antennas for measuring the beamforming and phase properties of a two-element array. Prof. Magdy Iskander (standing) often participated in field experiments, sharing the



**Fig. 6.17** Field testing of HMLA on beach near the Makai Research Pier

excitement over the results produced during these tests. A digital, multichannel receiver developed at the Hawaii Center for Advanced Communications by Dr. Nuri Celik [23] (seated) was used to record and analyze signal characteristics. This photo provides a visual indication of the relatively low height (less than one meter) of the HF antennas [20].

## 6.6 Future Work

There are a variety of directions where future work and research in electrically small wire antennas is encouraged. These include the further exploration of wire geometries that better utilize the inner volume of the sphere enclosing the antenna while increasing the effective volume and reducing the  $Q$ . Some work has been done in exploring fractal geometries, such as space-filling curves, with promising results [20]. These types of designs may also be suitable for 2-D and 3-D antenna printing. Another direction for further research is the use of genetic algorithms and modern computation and optimization methods for exploring a larger range of antenna design parameters and producing optimized designs.



**Fig. 6.18** Measuring two-element array beam-forming properties at Waimanalo Park

## 6.7 Summary

The fundamental properties and design challenges for electrically small wire antennas have been reviewed in the context of traditional antenna design. New design methods for reducing the size of wire antennas have been presented and demonstrated using constructed prototypes. The basic concept of inner toploading has been presented and demonstrated using a two-turn helical wire antenna, with advanced concepts demonstrated using a helical meandering line antenna. These methods provide alternative options when antenna design requirements restrict the volume and height to minimal limits.

Developed antenna designs have been presented, demonstrating the concepts of inner toploading and inner folding. These antennas satisfy the general criteria for electrically small antennas ( $ka \leq 0.5$ ) while providing for lower resonant frequencies with acceptable input impedance and bandwidth. HMLA antenna structures, designed for high frequency (HF) surface wave radar applications, have been used to demonstrate the concepts of inner toploading and inner folding to achieve HF operations with antennas less than one meter high. These wire antennas exhibited vertical polarization, omnidirectional radiation patterns, and linear phase shift within their resonant bandwidths. The antenna structures were easily and rapidly transportable, required no site preparation, and left no environmental footprint

when removed, making them suitable for operations in unprepared environments. Experimental performance measurements were reproduced in simulation models with a high degree of correlation. The concepts presented provide options for reducing the enclosed volume of wire antennas and for achieving lower operating frequencies.

## References

1. H.A. Wheeler, Fundamental limitations of small antennas. Proc. IRE **35**(12), 1479–1488 (1947)
2. H.A. Wheeler, Small antennas. IEEE Trans. Antennas Propag. **23**, 463–469 (1975)
3. L.J. Chu, Physical limitations of omni-directional antennas. J. Appl. Phys. **19**, 1163–1175 (1948)
4. S.R. Best, Small and fractal antennas, in *Modern Antenna Handbook*, C.A. Balanis (Ed), (Wiley, New York, 2008), ch.10
5. R.C. Hansen, R.E. Collin, *Small Antennas* (Wiley, Hoboken, NJ, 2011)
6. R.C. Hansen, R.E. Collin, A new Chu formula for Q. IEEE Antennas Propag. Mag. **51**(5), 38–41 (2009)
7. J.S. McLean, A re-examination of the fundamental limits on the radiation Q of electrically small antennas. IEEE Trans. Antennas Propag. **44**(5), 672–676 (1996)
8. S.R. Best, D.L. Hanna, A performance comparison of fundamental small-antenna designs. IEEE Antennas Propag. Mag. **52**(1), 47–70 (2010)
9. A.D. Yaghjian, S.R. Best, Impedance, bandwidth, and Q of antennas. IEEE Trans. Antennas Propag. **53**(4), 1298–1324 (2005)
10. M.F. Iskander, *Electromagnetic Fields and Waves* (Waveland Press, Prospect Heights, IL, 2000)
11. J.D. Kraus, *Antennas* (McGraw-Hill, New York, 1988)
12. G.J. Burke, NEC (Numerical Electromagnetics Code), Lawrence Livermore Nat. Laboratory, Jan 1992. [Online]. Available: <https://ipo.llnl.gov/>
13. G. Marconi, Wireless signalling system. U.S. Patent US760463, 24 May 1904.
14. S.R. Best, The performance properties of electrically small resonant multiple-arm folded wire antennas. IEEE Antennas Propag. Mag. **47**(4), 13–27 (2005)
15. C.A. Balanis, *Antenna Theory – Analysis and Design* (Wiley, New York, 1997)
16. J.D. Kraus, The T-matched antenna. QST **24**, 24–25 (1940)
17. J.M. Baker, M.F. Iskander, A new design approach for electrically small high frequency antennas. IEEE Antennas Wirel. Propag. Lett. **14**, 402–405 (2015)
18. J.J. Adams, J.T. Bernhard, A low Q electrically small spherical antenna, in *Proceedings of IEEE Antennas and Propagation International Symposium*, San Diego, 2008
19. J.M. Baker, H.-S. Youn, N. Celik, M.F. Iskander, Low-profile multifrequency HF antenna for coastal radar applications. IEEE Antennas Wireless Propag. Lett. **9**, 1119–1122 (2010)
20. J.M. Baker, Design and optimization of electrically small antennas for high frequency applications, PhD dissertation, Department of Electrical Engineering, University of Hawaii-Manoa, Honolulu, 2014
21. FEKO, Altair, [Online]. Available: <http://www.feko.info/>
22. J.M. Baker, M.F. Iskander, H.-S. Youn, N. Celik, High performance compact antenna for radar and communication applications, in *Proceedings of IEEE Antennas and Propagation Society International Symposium*, Toronto, July 2010
23. N. Celik, W. Kim, M. Demirkol, M. Iskander, R. Emrick, Implementation and experimental verification of hybrid smart-antenna beamforming algorithm. IEEE Antennas Wireless Propag. Lett. **5**(1), 280–283 (2006)



**James M. Baker** received a Ph.D. degree in electrical engineering from the University of Hawaii at Manoa in 2014. He earned a B.G.S. degree in history from Kansas University in 1974, a B.S. degree in electrical engineering from the University of Utah in 1995 (his first classroom experience with Professor Magdy Iskander), and an M.S. degree in systems engineering from Johns Hopkins University in 2004. He is retired from the US Marine Corps where he served as Electronic Countermeasures Officer in an airborne tactical electronic warfare squadron. Dr. Baker has been a member of IEEE since 1995 and has published six articles in major journals and fourteen international symposium papers.



# Chapter 7

## Metamaterial-Based Antennas and a Metasurface-Based Terahertz Frequency Splitter

Hisamatsu Nakano, Jun Shibayama, and Junji Yamauchi

### 7.1 Introduction

The word *meta* is a prefix having a variety of meanings, including *after*, *beyond*, *with*, and *change*. Metamaterials and metasurfaces are composed of periodically arrayed elements that lead to unique electromagnetic characteristics [1, 2].

Earlier representative studies of metamaterial-based antennas are found in Refs. [2–4], where antenna miniaturization is realized on the basis of the fact that  $\beta$ , the propagation phase constant of the current flowing along the radiation element, can be designed to be zero at a specific frequency. The zero- $\beta$  current has an infinitely long guide-wavelength, and hence the antenna size can be chosen to be arbitrarily small. Note that a miniaturized zero- $\beta$  antenna operates across a very narrow frequency regime.

An inhomogeneous conducting surface excited by an antenna (such as a monopole antenna) can form a specified phase and amplitude distribution over its surface. A thin dielectric layer on which multiple conducting elements (such as patches or loops) are printed can also form a specified phase and amplitude distribution for an incident electromagnetic wave. A surface that has inhomogeneity for the purpose of realizing special requirements is sometimes called a metasurface. A frequency-selective-surface (FSS) structure [5], a reflect-array structure [6], and a corrugated-surface structure [7] are representative metasurface examples. One study shows that a surface composed of homogeneous patches above a fed patch antenna generates a high-gain beam in the broadside direction [8]. Recent study has revealed that a high-gain tilted beam can be formed using an inhomogeneous loop-based metasurface [9].

---

H. Nakano (✉) • J. Shibayama • J. Yamauchi  
Hosei University, Koganei, Tokyo 184-8584, Japan  
e-mail: [nakano@hosei.ac.jp](mailto:nakano@hosei.ac.jp)

This paper focuses on recent progress in metamaterial-based antenna and metasurface-based waveguide topics. The main discussions are in Sects. 7.2 and 7.3.

Section 7.2 defines and discusses metamaterial-based antennas [10]. A single metamaterial-based line antenna (metaline) forms a linearly polarized beam that scans from the backward direction, through the broadside direction, to the forward direction (BBF scanning), with change in operating frequency [11]. It is found that the frequency regime over which broadside or quasi-broadside BBF scanning can be performed is very narrow. In order to solve this issue, a double metamaterial-based line (double metaline) antenna [12] is investigated in Sect. 7.2.1.

Metamaterial-based antennas are discussed further in Sects. 7.2.2 and 7.2.3, where a metamaterial-based loop (metaloop) antenna [13] and a metamaterial-based spiral (metaspiral) antenna [14] are presented, respectively. These antennas are designed to radiate a left-handed circularly polarized (LHCP) wave across a specific frequency band and a right-handed circularly polarized (RHCP) wave across a different frequency band. Note that this type of dual-band counter circularly polarized radiation cannot be realized using conventional/natural loop and spiral antennas.

The circularly polarized metaspiral antenna has separate maximum gains, one at a low frequency and one at a high frequency. If equal gains are required, then the maximum gain at the low frequency must be increased. One way to do this is presented in Sect. 7.2.3, where a dielectric slab is placed above the metaspiral antenna [15, 16].

Section 7.3 presents a metasurface-based terahertz frequency splitter. For this analysis, a novel electromagnetic (EM) solver based on an implicit finite-difference time-domain (FDTD) algorithm in cylindrical coordinates is presented [17]. This algorithm is developed on the basis of a locally one-dimensional (LOD) scheme [18]. Section 7.3.1 presents the basic equations of the LOD-FDTD method in cylindrical coordinates. The Sherman-Morrison formula [19, 20] is introduced in Sect. 7.3.2 to treat a cyclic matrix, and image theory [21] is used to impose the perfect electric conductor boundary condition. The effectiveness of this electromagnetic solver is confirmed in Sect. 7.3.3, through the analysis of a metasurface-based terahertz frequency splitter [22]. The computation time is found to be reduced to approximately one-half of the computation time for the explicit FDTD method while maintaining comparable accuracy.

## 7.2 Metamaterial-Based Antennas

The propagation phase constant of a plane wave traveling within a material is specified by the permittivity  $\varepsilon$  and permeability  $\mu$ . A plane wave within a non-dissipative material of positive  $\varepsilon$  and positive  $\mu$  travels with a positive propagation phase constant ( $\beta = \omega \sqrt{\varepsilon\mu} > 0$ , with  $\omega$  denoting an angular frequency), and a plane wave within a non-dissipative material of negative  $\varepsilon$  and negative  $\mu$  travels with a negative propagation phase constant ( $\beta < 0$ ). Note that a negative phase constant within a *dissipative* material is discussed in Ref. [23].

A material characterized by a positive propagation phase constant is categorized as a natural material, and a material characterized by a negative propagation phase constant is categorized as a metamaterial. A relationship between a transmission line configuration composed of periodically arrayed small line segments and the non-dissipative metamaterial  $\epsilon$  and  $\mu$  designation is clarified in Refs. [2, 10], where  $\epsilon$  and  $\mu$  for the non-dissipative metamaterial correspond to the total shunt admittance and total series impedance of the transmission line segment, respectively.

An antenna can be categorized according to the nature of  $\beta$ , the propagation phase constant of the current on the antenna that causes an electromagnetic wave to be radiated into free space. An antenna with a positive  $\beta$  is defined as a natural antenna. In contrast, an antenna with a negative  $\beta$  or zero  $\beta$  is defined as a metamaterial-based antenna [10]. Note that a system where a natural radiation element (with  $\beta > 0$ ), such as a monopole antenna or a dipole antenna) is parasitically coupled to metamaterials ( $\beta < 0$ ) [1] or nearby reactance elements not arrayed in a periodic manner is often called a metamaterial-inspired antenna.

The propagation phase constant of the current flowing along a microstrip line is specified using distributed circuit parameters (series inductance  $L$  per unit length [H/m] and shunt capacitance  $C$  per length [F/m]). In this case, the current flows with a positive  $\beta$ . When capacitors and inductors are inserted at a fixed interval into this transmission line (microstrip line), with capacitors in series and inductors in shunt, the propagation phase constant can become negative ( $\beta < 0$ ) at frequencies below a specific frequency,  $f_T$ . Thus, the microstrip line becomes a metamaterial-based antenna. This antenna is called a composite right- and left-handed transmission line [2] and is also referred to as a metamaterial-based line antenna, or just a metaline antenna.

### 7.2.1 Single and Double Metaline Antennas

Figure 7.1 shows a natural line antenna, which acts as a leaky wave antenna. The horizontal section ranging from point  $F$  to point  $T$ , parallel to the conducting plate (ground plane), acts as a radiation element, where point  $F$  is used as the feed point and point  $T$  is terminated to the ground plane through a resistive load. The current flowing out from point  $F$  toward point  $T$  has a positive  $\beta$ . This means that, as the current travels toward point  $T$ , the phase is delayed along the line. As a result, the natural line antenna forms a tilted beam in the half space  $x > 0$ , i.e., a forward radiation beam. The radiation in the half space  $x > 0$  is linearly polarized (LP) in the  $\theta$ -direction of the spherical coordinate system; the copolarized component is the  $E_\theta$ -field in the  $x$ - $z$  (elevation) plane. Note that the natural line antenna does not form a tilted beam in the half space  $x < 0$ , i.e., a backward radiation beam.

Figure 7.2 shows a metaline antenna, where multiple strip segments constitute the antenna, each segment having length  $p_0$ . Point  $F$  is the feed point and point  $T$  is terminated to the ground plane through a Bloch impedance (resistive load), as in the natural line shown in Fig. 7.1. There is a gap of length  $\Delta g$  between neighboring

Fig. 7.1 Natural line antenna

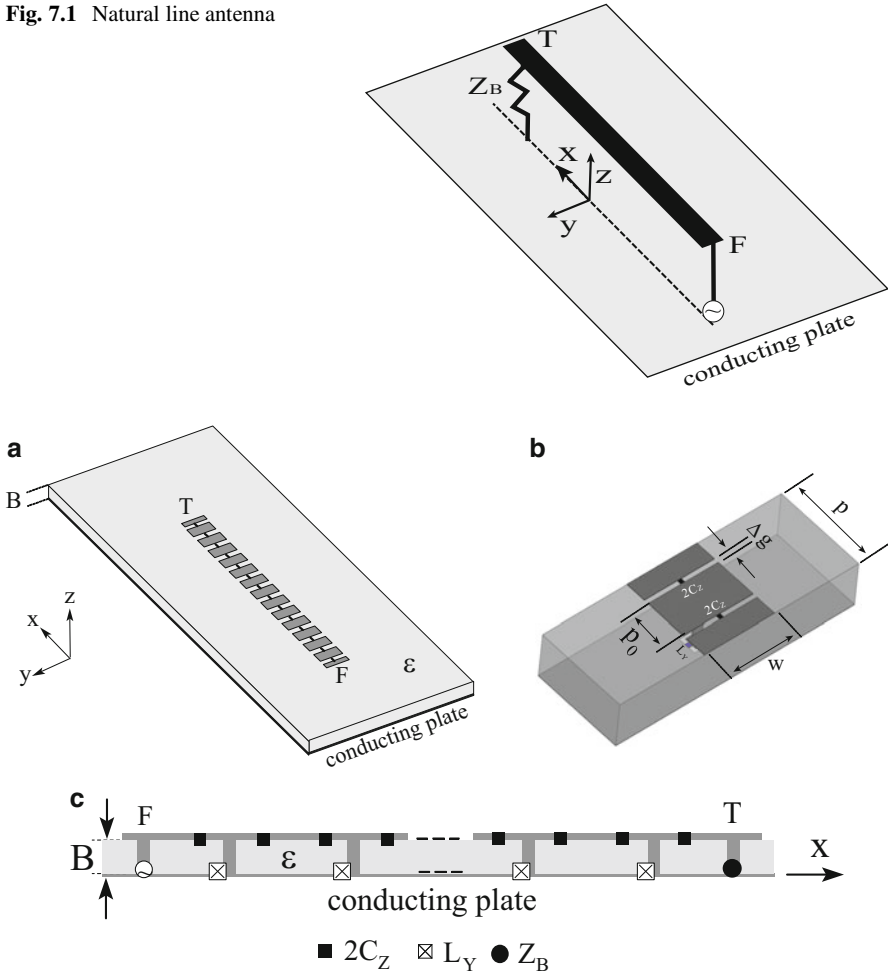


Fig. 7.2 Metaline antenna. (a) Perspective view. (b) Unit cell. (c) Side view

strip segments. The section of length  $p$  is called the unit cell. The central segment of the unit cell has a vertical probe connected to the conducting plate through a chip inductor,  $L_Y$ . Neighboring segments are connected through a chip capacitor,  $2C_Z$ .

The dispersion diagram of this metaline unit cell for a particular set of parameters [10] is shown in Fig. 7.3, where phase constant  $\beta$  is normalized to the free space phase constant  $k_0$ . The value of  $\beta$  is negative at frequencies below frequency  $f_T$  and positive at frequencies above  $f_T$ . Based on this fact,  $f_T$  is called the *transition frequency*. Radiation occurs between frequencies  $f_L$  and  $f_U$ , where these two frequencies are respectively called the lower- and upper-band edge frequencies for a fast wave. Note that a positive  $\beta$  at frequencies above  $f_T$  results from the inherent property of the microstrip line, i.e., the right-handed property.

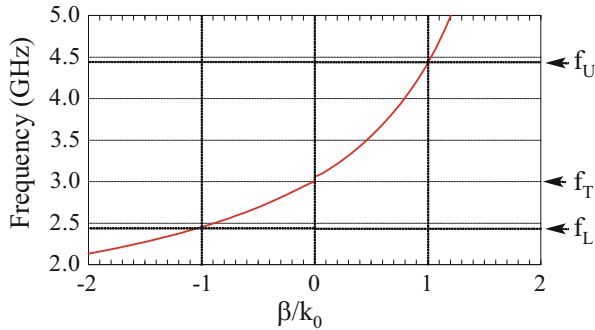


Fig. 7.3 Dispersion diagram for the metaline unit cell

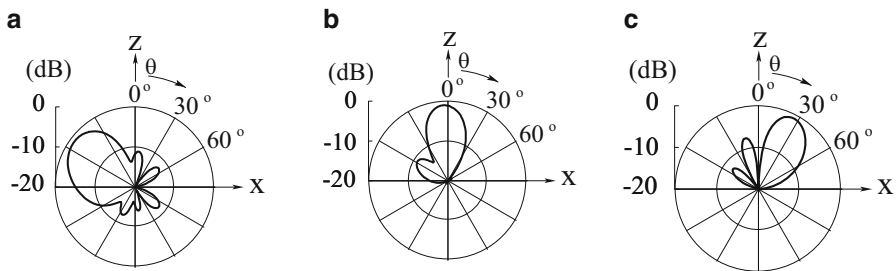
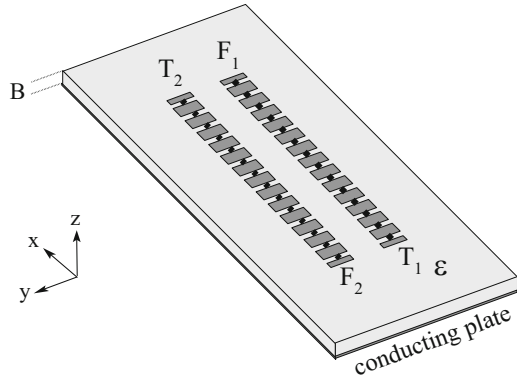


Fig. 7.4 Linearly polarized BBF scanning by a metaline antenna. (a) Backward radiation at  $f < f_T$ . (b) Broadside radiation at  $f = f_T$ . (c) Forward radiation at  $f > f_T$  (©2016IEICE)

The metaline operating at frequencies below  $f_T$  ( $f < f_T$ ) forms a radiation beam in the half space  $x < 0$ , as shown in Fig. 7.4a, because the propagation phase constant is negative ( $\beta < 0$ ). When the frequency reaches  $f_T$ , the phase constant becomes zero ( $\beta = 0$ ), and the metaline forms a broadside beam, as shown in Fig. 7.4b. When the frequency increases past  $f_T$  ( $f > f_T$ ), the radiation beam becomes tilted in the forward direction, due to a positive  $\beta$  ( $\beta > 0$ ), i.e., the metaline forms a forward beam, as shown in Fig. 7.4c. Such movement of the radiation beam with frequency is called Backward-Broadside-Forward scanning and abbreviated as BBF scanning. Note that the natural line antenna in Fig. 7.1 does not have a BBF scanning capability. Also, note that the radiation from the metaline is linearly polarized.

The frequency band where the metaline forms a broadside beam or a quasi-broadside beam is very narrow. The radiation pattern within this frequency band is not perfectly symmetric with respect to the  $z$ -axis in the  $x$ - $z$  plane, as shown in Fig. 7.4b. To increase the bandwidth and make the broadside beam symmetric, two metalines are arrayed parallel to each other, as shown in Fig. 7.5. This system (double metaline antenna) has two feed points,  $F_1$  and  $F_2$ , which are excited in balanced mode (equal amplitude and opposite phase). The radiation beams from these metalines point in directions that are symmetric with respect to the  $z$ -axis in the  $x$ - $z$  plane. This means that the resulting radiation pattern is always symmetric with respect to the  $z$ -axis in the  $x$ - $z$  plane.

**Fig. 7.5** Double metaline antenna



As the frequency increases toward  $f_T$ , the backward radiation from metaline 1 with feed point  $F_1$  (i.e., the radiation in the positive  $x$ -direction) moves toward the  $z$ -axis from the half space  $x > 0$ . Similarly, the backward radiation from metaline 2 with feed point  $F_2$  (i.e., the radiation in the negative  $x$ -direction) moves relative to feed point  $F_2$  toward the  $z$ -axis from the half space  $x < 0$ . Thus, superposition of these beams at frequencies  $f_T - \Delta f$ , which are close to  $f_T$ , forms a symmetric broadside radiation pattern with respect to the  $z$ -axis in the elevation ( $x$ - $z$ ) plane. This also happens with the superposition of the two beams in the forward radiation at frequencies  $f_T + \Delta f$ , which are close to  $f_T$ . As a result, a symmetrical broadside radiation pattern is obtained across a frequency region of  $2\Delta f$ . Generally, the bandwidth of  $2\Delta f$  is determined by the edge frequencies where the gain for the broadside beam drops by 3-dB from its maximum value. It is found that the double metaline antenna has a bandwidth of more than 30% [12].

## 7.2.2 Metaloop Antennas

Figure 7.6a shows a natural loop antenna backed by a conducting plate. The loop is made of a conducting wire or a conducting strip. The loop radiates a linearly polarized wave in the  $z$ -direction at the frequency when the peripheral length corresponds to one wavelength. The loop height above the conducting plate is chosen to be one quarter wavelength ( $\lambda/4$ ) so that electromagnetic waves reflected by the conducting plate add in-phase to electromagnetic waves radiated directly from the loop into free space. Note that the radiation is linearly polarized in the  $z$ -direction.

Figure 7.6b also illustrates a loop antenna with a single feed point, which is a modified version of the loop in Fig. 7.6a; two perturbation elements are added to diagonally opposite corners of the loop, thereby establishing a traveling wave current that radiates a circularly polarized (CP) wave. In this case, the rotational sense of the circularly polarized wave is uniquely determined by the location of the

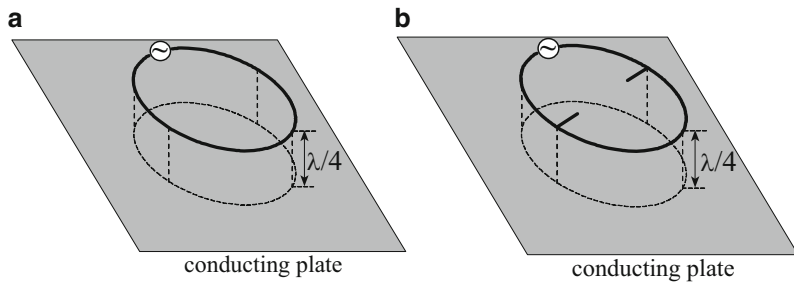


**Fig. 7.6** Natural loop antennas. (a) Linearly polarized loop. (b) Circularly polarized loop

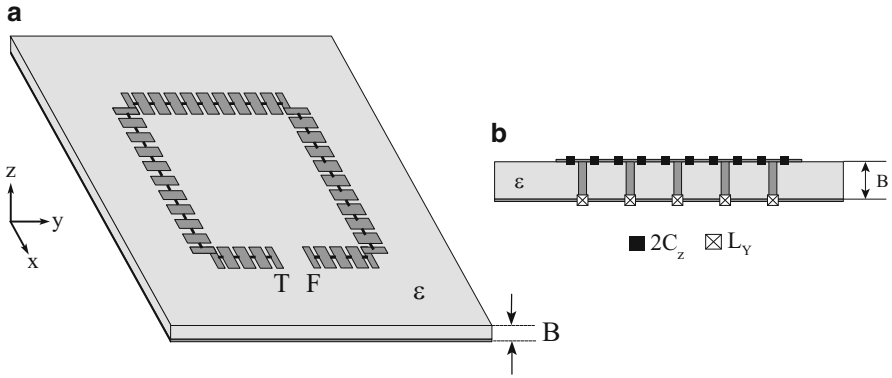
perturbation elements, i.e., either right-handed (RH) or left-handed (LH). Note that, if the circularly polarized loop is required to radiate both RHCP and LHCP waves, two feed points are needed.

The abovementioned requirement for generation of RHCP and LHCP radiation is for operation at a single frequency. Such a circularly polarized natural loop antenna cannot be used when an RHCP wave at a specific frequency,  $f_1$ , and LHCP wave at a different frequency,  $f_2$ , are required. In other words, the circularly polarized natural loop with a single feed point cannot act as a dual-band counter circularly polarized radiation element; two circularly polarized natural loops of different sizes, each having a single feed point, are required to realize dual-band counter circularly polarized radiation. Note that signal transmission from a satellite and signal reception by the same satellite are often performed using circularly polarized waves that have opposite rotational senses in separate frequency bands, in order to avoid interference between the transmitted and received signals.

Let us consider realizing dual-band counter circularly polarized radiation using the metaloop shown in Fig. 7.7. Point  $F$  is the feed point and point  $T$  is the end point. Point  $T$  is shorted to the ground plane through a resistive load. The propagation phase constant,  $\beta$ , is designed to be negative at frequencies below transition frequency  $f_T$  and positive at frequencies above  $f_T$ . This leads to the desired behavior where the metaloop radiates an LHCP wave at frequencies below  $f_T$  and an RHCP wave at frequencies above  $f_T$ .

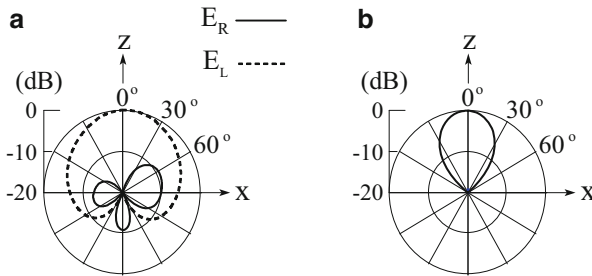
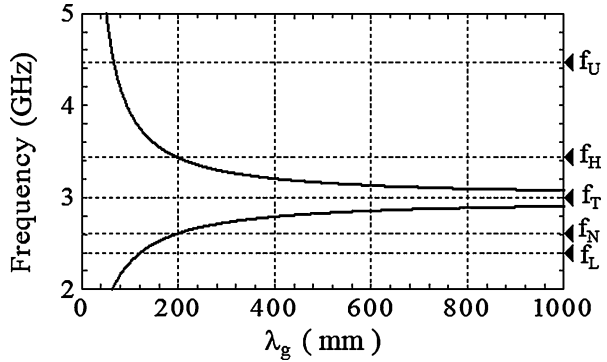
Circularly polarized broadside radiation (radiation in the  $z$ -direction) is obtained at a frequency where the physical loop length,  $S_{\text{ant}}$ , corresponds to one-guided wavelength:  $S_{\text{ant}} = 1\lambda_g$ . Figure 7.8 shows the guided wavelength,  $\lambda_g$ , for a particular set of the unit-cell parameters, as a function of frequency [10]. There are two frequencies where  $S_{\text{ant}}$  equals the guided wavelength. When  $S_{\text{ant}}$  is  $1\lambda_g$  at  $f_N$ , an LHCP wave is radiated; when  $S_{\text{ant}}$  is  $1\lambda_g$  at  $f_H$ , an RHCP wave is radiated.

Figure 7.9 shows the radiation patterns at  $f_N$  and  $f_H$ . The radiation pattern at  $f_N$  is wider than that at  $f_H$ . This is attributed to a difference in the *electrical* antenna size (i.e., physical loop length,  $S_{\text{ant}}$ , normalized to the operating wavelength). It is obvious that  $S_{\text{ant}}/\lambda_N < S_{\text{ant}}/\lambda_H$ , because  $f_N < f_H$ , where  $\lambda_N$  and  $\lambda_H$  are the free space wavelengths at  $f_N$  and  $f_H$ , respectively.



**Fig. 7.7** Circularly polarized metaloop antenna. (a) Perspective view. (b) Side view

**Fig. 7.8** Relationship between the guided wavelength and the operating frequency for a metaloop



**Fig. 7.9** Radiation pattern for the metaloop. (a) At frequency  $f_N$ . (b) At frequency  $f_H$  (©2016IEICE)

The frequency response of the gain,  $G_L$  for an LHCP wave and  $G_R$  for an RHCP wave, is shown in Fig. 7.10 [11]. The 3-dB reduction gain bandwidth for  $G_L$  is moderately wide, with a value of 13%, and that for  $G_R$  is also moderately wide, with a value of 12%. Note that the VSWR within these gain bandwidths is less than 2.0, as shown in Fig. 7.11 [11].



**Fig. 7.10** Frequency response of the gain for the metaloop (©2016IEICE)

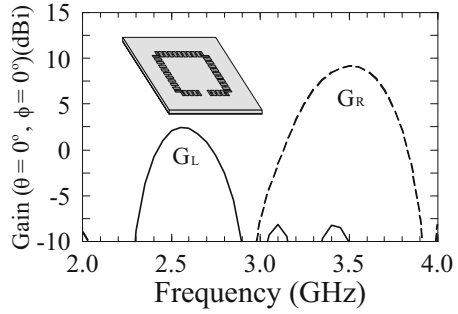
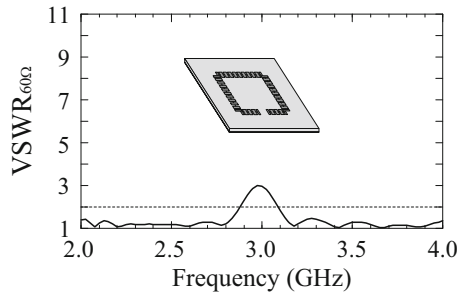


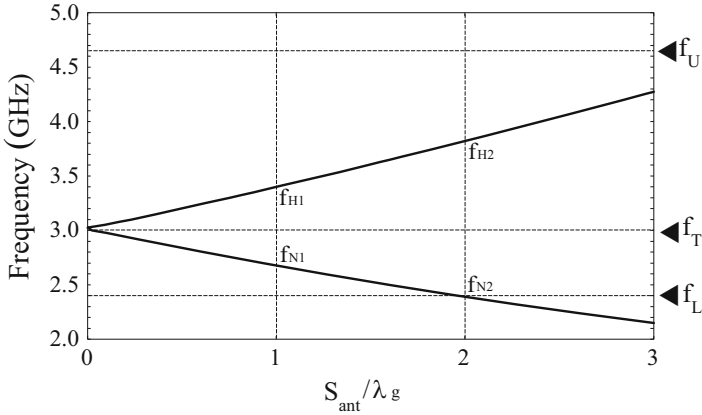
**Fig. 7.11** Metaloop VSWR relative to  $60 \Omega$  (©2016IEICE)



Some supplementary comments are necessary here. The aforementioned circularly polarized metaloop has an open structure; points  $F$  and  $T$  are slightly separated from each other. When  $F$  and  $T$  are connected to form a closed loop and this loop is excited at the connection point by a single voltage source, the loop acts as a linearly polarized radiation element. A linearly polarized broadside beam is realized at a pair of frequencies,  $f_{N1}$  and  $f_{H1}$  (see Fig. 7.12), where  $S_{ant}$  corresponds to  $1\lambda_g$ . Note that the maximum radiation at frequencies  $f_{N2}$  and  $f_{H2}$  (where  $S_{ant}$  corresponds to  $2\lambda_g$ ) appears at field points off the  $z$ -axis.

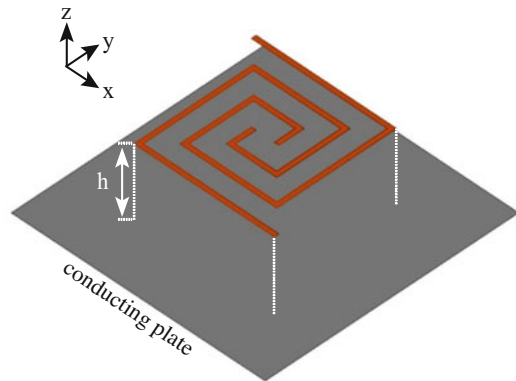
### 7.2.3 Metaspiral Antenna

Figure 7.13 shows a conventional natural two-arm circularly polarized spiral antenna backed by a conducting plate. The spacing between the spiral and the conducting plate is chosen to be one quarter wavelength at the desired operating frequency. It has been revealed that, as the spacing is decreased, the inherent wideband characteristics of the radiation pattern, axial ratio, input impedance, and gain deteriorate. To restore the inherent circularly polarized wideband antenna characteristics, some techniques have been proposed, for example, insertion of absorbing material under the spiral and replacement of the conducting plate by an electromagnetic band gap (EBG) plate [10].



**Fig. 7.12** Dispersion diagram for the unit cell of a closed metaloop

**Fig. 7.13** Natural spiral antenna above a conducting plate



The rotational sense of the circularly polarized radiation from the natural spiral antenna is uniquely determined by the relationship between the winding sense of the spiral and the location of the feed. The spiral in Fig. 7.13 radiates an RHCP wave when the inner arm ends are excited in balanced mode; it radiates an LHCP wave when the feed points are moved to the outer arm ends and excited in balanced mode. That is, radiation of a different rotational sense is obtained by changing the location of the feed points; it does not change once the feed points are fixed. In other words, the natural spiral antenna with fixed feed points does not have a counter circularly polarized capability.

To create counter circularly polarized radiation, we consider a low-profile spiral structure (in the order of  $1/100$  wavelength thickness at the lower band edge operating frequency). Each arm of this spiral is made of  $M$  metaline filaments, as shown in Fig. 7.14. The length of the last filament is denoted as  $L_M$ .

Figure 7.15 shows the relationship between the antenna peripheral length and the operating frequency, where the antenna peripheral length is defined as  $4L_M$  and the

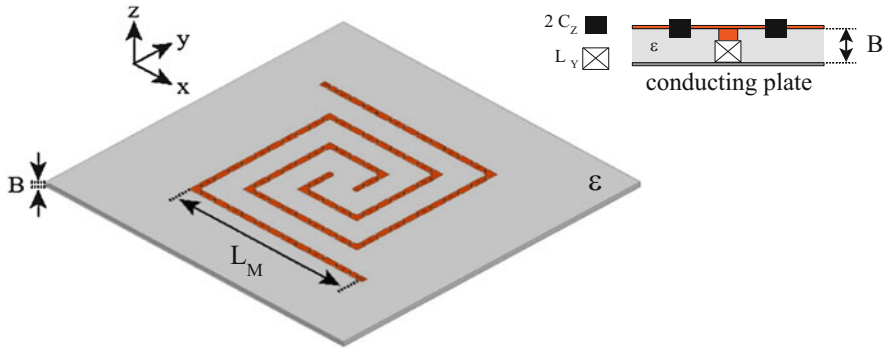


Fig. 7.14 Metasprial antenna printed on a dielectric substrate backed by a conducting plate

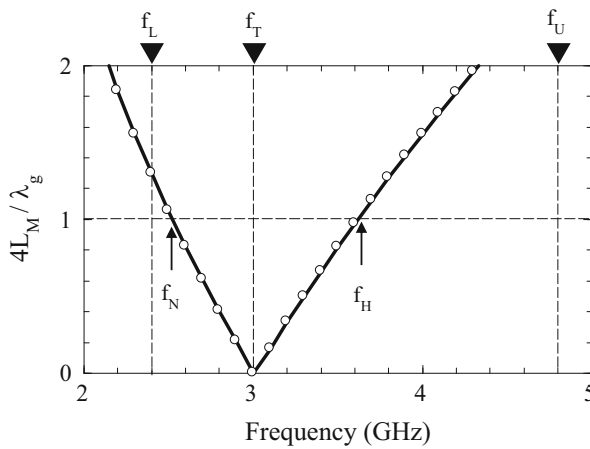


Fig. 7.15 Relationship between the normalized peripheral length and the operating frequency for the metasprial

guided wavelength of the current is denoted as  $\lambda_g$ . There are two frequencies,  $f_N$  and  $f_H$ , where the normalized antenna peripheral length is equal to 1 ( $4L_M/\lambda_g = 1$ ). These frequencies are called the nion frequency (or  $N$  frequency) and the hion frequency (or  $H$  frequency), respectively. Note that the nion frequency is lower than transition frequency  $f_T$  and the hion frequency is higher than  $f_T$ .

Circularly polarized radiation occurs at frequencies lower than the nion frequency  $f_N$  and higher than the hion frequency  $f_H$ , due to the active current region on the spiral plane for circularly polarized radiation [10]. Thus, the metasprial shown in Fig. 7.14 acts as a dual-band counter circularly polarized radiation element. Note that, as the antenna size is increased, the frequency separation between the nion and hion frequencies becomes smaller.

Dual-band counter circularly polarized radiation is confirmed clearly by Fig. 7.16 [11], which shows the frequency response of the gain,  $G_L$  for an LHCP wave and

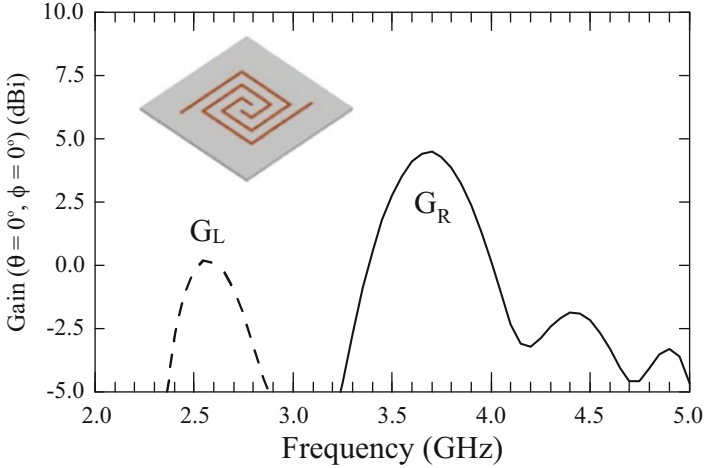


Fig. 7.16 Gain example for a metasprial ( $M = 6$ ) (©2016IEICE)

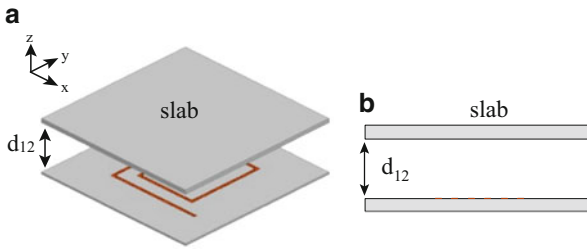
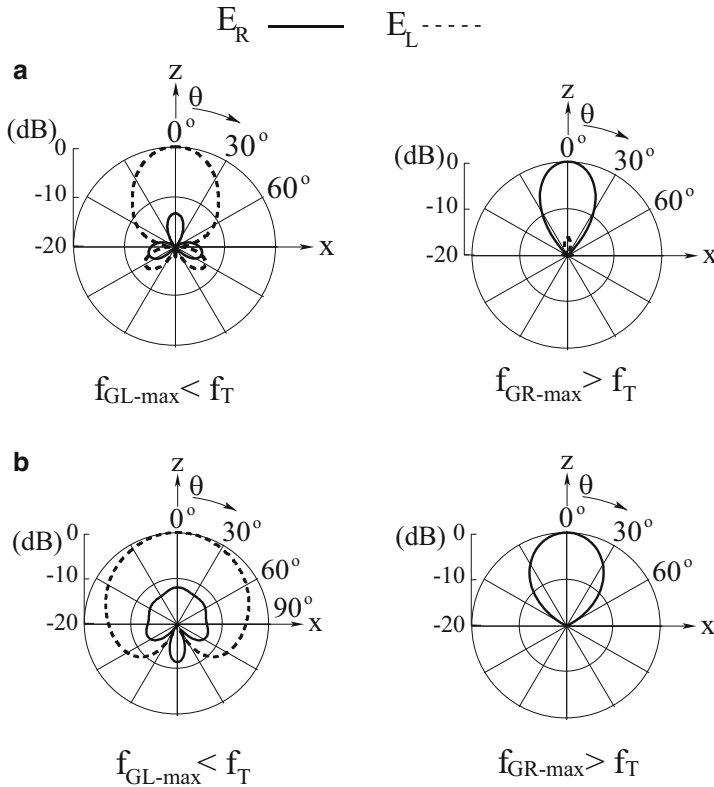


Fig. 7.17 Metasprial with a dielectric slab. (a) Perspective view. (b) Side view

$G_R$  for an RHCP wave. It is found that  $G_L$  is dominant in the low-frequency region and  $G_R$  is dominant in the high-frequency region.

In addition, Fig. 7.16 indicates that there is a difference in the maximum values of  $G_L$  and  $G_R$ , as in the metaloop antenna. If this gain difference is not desirable, then a simple technique can be applied to the metasprial, based on the Fabry-Perot principle [16]. This technique uses a dielectric slab, which is placed above the metasprial, as shown in Fig. 7.17 [15]. The spacing between the metasprial and the slab,  $d_{12}$ , is chosen to be approximately one-half of the wavelength at the frequency requiring gain enhancement (i.e.,  $G_L$ ), and the thickness of the slab,  $B_2$ , is adjusted to the point where the desired condition (maximum  $G_L =$  maximum  $G_R$ ) is satisfied. Figure 7.18 shows the radiation patterns for the metasprial in the presence and absence of the dielectric slab, respectively, and Fig. 7.19 shows the frequency response of the gain for the metasprial in the presence of the dielectric slab.

Spacing  $d_{12}$  is chosen to be one-half of the wavelength, as already described. Therefore, it is inferred that the impact of the presence of the slab on the input



**Fig. 7.18** Radiation from the metaspiral. (a) In the presence of the slab at the maximum gain frequencies. (b) In the absence of the slab at the maximum gain frequencies (©2016IEICE)

impedance will be not large. This is confirmed theoretically and experimentally. It is found that the VSWR across the 3-dB reduction gain bandwidth for  $G_L$  and  $G_R$  is less than 2.

### 7.3 Metasurface-Based Terahertz Frequency Splitter

We now move from a metamaterial-related antenna to a waveguiding structure utilizing a metasurface. It is known that a spoof surface plasmon polariton (SPP) propagates along a periodically corrugated surface of a metal at THz frequencies. Using the characteristics of the spoof SPP, a metasurface-based bi-directional splitter has been numerically investigated with the two-dimensional (2D) FDTD method. Bi- and multi-directional splitters consisting of metal gratings with finite

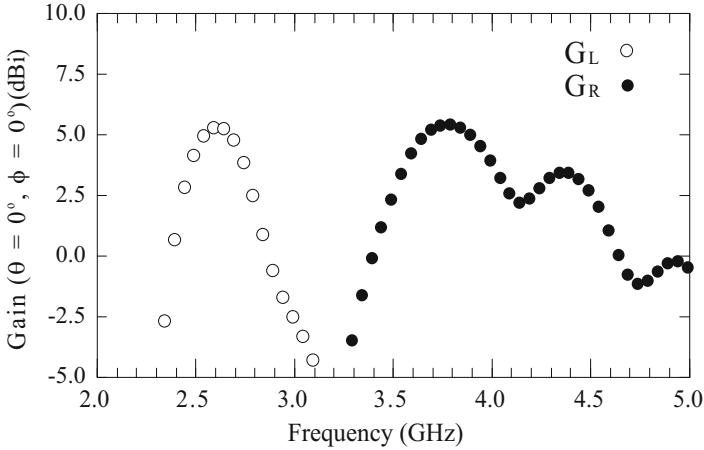


**Fig. 7.19** Reduced difference in the maximum gain peaks for the metaspiral. A square slab is used, where the side length is approximately one wavelength at the maximum  $G_L$  frequency of 2.6 GHz (©2016IEICE)

thickness have also been studied numerically and experimentally. Unfortunately, the wave coupling in these splitters is limited to the narrow grating regions. This fact inspires us to consider a splitter structure with larger coupling regions. Then, we propose a metasurface-based THz frequency splitters consisting of metal disk with a center hole and radially placed gratings [22]. For the proposed splitters, the gratings are located in fan-shaped regions, to which THz waves are widely coupled.

The FDTD method in cylindrical coordinates is favorable for the analysis of the disk-shaped splitter. However, the conventional cylindrical FDTD method suffers from the Courant-Friedrichs-Lewy (CFL) condition with respect to the time step ( $\Delta t$ ). Note that the circumferential mesh size close to the center axis becomes inevitably small in cylindrical coordinates. This gives rise to a small time step, resulting in a long computation time. To remove this restriction, we develop an implicit cylindrical FDTD method [17] based on the LOD scheme [18].

### 7.3.1 The Cylindrical LOD-FDTD Method

The cylindrical LOD-FDTD method [17] is expressed in the matrix form as

$$\left( [I] - \frac{\Delta t}{2} [A] \right) u^{n+1/2} = \left( [I] + \frac{\Delta t}{2} [A] \right) u^n \quad (7.1)$$

for the first step and

$$\left([I] - \frac{\Delta t}{2} [B]\right) u^{n+1} = \left([I] + \frac{\Delta t}{2} [B]\right) u^{n+1/2} \quad (7.2)$$

for the second step, where

$$u = [E_\rho \ E_\phi \ E_z \ H_\rho \ H_\phi \ H_z]^T, \quad (7.3)$$

$$[A] = \begin{bmatrix} 0 & 0 & 0 & 0 & 0 & \frac{c}{\varepsilon_r \rho} \frac{\partial}{\partial \phi} \\ 0 & 0 & 0 & \frac{c}{\varepsilon_r} \frac{\partial}{\partial z} & 0 & 0 \\ 0 & 0 & 0 & 0 & \frac{c}{\varepsilon_r \rho} \frac{\partial}{\partial \rho} \rho & 0 \\ 0 & \frac{c}{\mu_r} \frac{\partial}{\partial z} & 0 & 0 & 0 & 0 \\ 0 & 0 & \frac{c}{\mu_r} \frac{\partial}{\partial \rho} & 0 & 0 & 0 \\ \frac{c}{\mu_r \rho} \frac{\partial}{\partial \phi} & 0 & 0 & 0 & 0 & 0 \end{bmatrix}, \quad (7.4)$$

$$[B] = \begin{bmatrix} 0 & 0 & 0 & 0 & \frac{-c}{\varepsilon_r} \frac{\partial}{\partial z} & 0 \\ 0 & 0 & 0 & 0 & 0 & \frac{-c}{\varepsilon_r} \frac{\partial}{\partial \rho} \\ 0 & 0 & 0 & \frac{-c}{\varepsilon_r \rho} \frac{\partial}{\partial \phi} & 0 & 0 \\ 0 & 0 & \frac{-c}{\mu_r} \frac{\partial}{\partial \phi} & 0 & 0 & 0 \\ \frac{-c}{\mu_r} \frac{\partial}{\partial z} & 0 & 0 & 0 & 0 & 0 \\ 0 & \frac{-c}{\mu_r \rho} \frac{\partial}{\partial \rho} \rho & 0 & 0 & 0 & 0 \end{bmatrix}, \quad (7.5)$$

in which  $c$  is the speed of light in a vacuum,  $\varepsilon_r$  is the relative permittivity, and  $\mu_r$  is the relative permeability. As a result, we derive the following basic equations of the cylindrical LOD-FDTD method:

$$E_\rho^{n+\frac{1}{2}} = E_\rho^n + \frac{c\Delta t}{2\varepsilon_r \rho} \left( \frac{\partial H_z^{n+\frac{1}{2}}}{\partial \phi} + \frac{\partial H_z^n}{\partial \phi} \right), \quad (7.6a)$$

$$E_\phi^{n+\frac{1}{2}} = E_\phi^n + \frac{c\Delta t}{2\varepsilon_r} \left( \frac{\partial H_\rho^{n+\frac{1}{2}}}{\partial z} + \frac{\partial H_\rho^n}{\partial z} \right), \quad (7.6b)$$

$$E_z^{n+\frac{1}{2}} = E_z^n + \frac{c\Delta t}{2\varepsilon_r \rho} \left( \frac{\partial}{\partial \rho} \rho H_\phi^{n+\frac{1}{2}} + \frac{\partial}{\partial \rho} \rho H_\phi^n \right), \quad (7.6c)$$

$$H_\rho^{n+\frac{1}{2}} = H_\rho^n + \frac{c\Delta t}{2\mu_r} \left( \frac{\partial E_\phi^{n+\frac{1}{2}}}{\partial z} + \frac{\partial E_\phi^n}{\partial z} \right), \quad (7.6d)$$

$$H_\varphi^{n+\frac{1}{2}} = H_\varphi^n + \frac{c\Delta t}{2\mu_r} \left( \frac{\partial E_z^{n+\frac{1}{2}}}{\partial \rho} + \frac{\partial E_z^n}{\partial \rho} \right), \quad (7.6e)$$

$$H_z^{n+\frac{1}{2}} = H_z^n + \frac{c\Delta t}{2\mu_r\rho} \left( \frac{\partial E_\rho^{n+\frac{1}{2}}}{\partial \varphi} + \frac{\partial E_\rho^n}{\partial \varphi} \right), \quad (7.6f)$$

for the first step and

$$E_\rho^{n+1} = E_\rho^{n+\frac{1}{2}} - \frac{c\Delta t}{2\varepsilon_r} \left( \frac{\partial H_\varphi^{n+1}}{\partial z} + \frac{\partial H_\varphi^{n+\frac{1}{2}}}{\partial z} \right), \quad (7.7a)$$

$$E_\varphi^{n+1} = E_\varphi^{n+\frac{1}{2}} - \frac{c\Delta t}{2\varepsilon_r} \left( \frac{\partial H_z^{n+1}}{\partial \rho} + \frac{\partial H_z^{n+\frac{1}{2}}}{\partial \rho} \right), \quad (7.7b)$$

$$E_z^{n+1} = E_z^{n+\frac{1}{2}} - \frac{c\Delta t}{2\varepsilon_r\rho} \left( \frac{\partial H_\rho^{n+1}}{\partial \varphi} + \frac{\partial H_\rho^{n+\frac{1}{2}}}{\partial \varphi} \right), \quad (7.7c)$$

$$H_\rho^{n+1} = H_\rho^{n+\frac{1}{2}} - \frac{c\Delta t}{2\mu_r\rho} \left( \frac{\partial E_z^{n+1}}{\partial \varphi} + \frac{\partial E_z^{n+\frac{1}{2}}}{\partial \varphi} \right), \quad (7.7d)$$

$$H_\varphi^{n+1} = H_\varphi^{n+\frac{1}{2}} - \frac{c\Delta t}{2\mu_r} \left( \frac{\partial E_\rho^{n+1}}{\partial z} + \frac{\partial E_\rho^{n+\frac{1}{2}}}{\partial z} \right), \quad (7.7e)$$

$$H_z^{n+1} = H_z^{n+\frac{1}{2}} - \frac{c\Delta t}{2\mu_r\rho} \left( \frac{\partial}{\partial \rho} \rho E_\varphi^{n+1} + \frac{\partial}{\partial \rho} \rho E_\varphi^{n+\frac{1}{2}} \right), \quad (7.7f)$$

for the second step. First, Eq. (7.6d) is substituted into Eq. (7.6b), leading to a tridiagonal system of linear equations regarding the  $E_\varphi$  component. Then, the  $E_\varphi$  component is obtained using the Thomas algorithm. After obtaining the  $E_\varphi$  component, the  $H_\rho$  component is explicitly calculated with Eq. (7.6d). The other components are similarly solved for the first and second steps.

### 7.3.2 The Treatment of the Cyclic Matrix and Perfect Electric Conductor

In cylindrical coordinates, the fields are regarded as periodic in the circumferential direction. Therefore, it is necessary to connect the fields at a specific plane in the



circumferential direction using the periodic boundary condition. For the implicit FDTD method, its application gives rise to the problem with a cyclic matrix. This holds true for the  $E_\rho$  and  $E_z$  components for the first and second steps, respectively, the equations of which include the derivatives in the  $\varphi$  direction. For example, the equation regarding the  $E_\rho$  component to be solved is as follows:

$$[M] \vec{x} = \vec{b}, \tag{7.8}$$

where  $\vec{x}$  is a column vector including the unknown  $E_\rho$  component,  $\vec{b}$  is that including the known  $E_\rho$  and  $H_z$  components (resulting from substituting Eq. (7.6f) into Eq. (7.6a)), and

$$[M] = \begin{bmatrix} -c & 1 & 0 & \dots & \dots & \dots & 1 \\ 1 & -c & 1 & 0 & \dots & \dots & 0 \\ 1 & 1 & -c & 1 & 0 & \dots & 0 \\ \vdots & \ddots & \ddots & \ddots & \ddots & \dots & \vdots \\ 0 & \dots & 0 & 1 & -c & 1 & 0 \\ 0 & \dots & \dots & 0 & 1 & -c & 1 \\ 1 & \dots & \dots & \dots & 0 & 1 & -c \end{bmatrix} \tag{7.9}$$

in which

$$c = 2 + \frac{4\varepsilon_r\mu_r\rho_i^2\Delta\varphi^2}{(c\Delta t)^2}. \tag{7.10}$$

Note that  $[M]$  is a cyclic matrix with non-zero components at the upper right and lower left elements. Therefore, Eq. (7.8) cannot directly be solved using the Thomas algorithm for a tridiagonal system of linear equations. Then, we rewrite Eq. (7.8) as

$$[M] = [N] + \vec{w}_1 \vec{w}_2^T \tag{7.11}$$

in which

$$\vec{w}_1 = \vec{w}_2 = [1, 0, \dots, 0, 1]^T, \tag{7.12}$$

$$[N] = \begin{bmatrix} -c-1 & 1 & 0 & \dots & \dots & \dots & 0 \\ 1 & -c & 1 & 0 & \dots & \dots & 0 \\ 0 & 1 & -c & 1 & 0 & \dots & 0 \\ \vdots & \ddots & \ddots & \ddots & \ddots & \dots & \vdots \\ 0 & \dots & 0 & 1 & -c & 1 & 0 \\ 0 & \dots & \dots & 0 & 1 & -c & 1 \\ 0 & \dots & \dots & \dots & 0 & 1 & -c-1 \end{bmatrix}. \tag{7.13}$$

Here, we utilize the Sherman-Morrison formula [19, 20], leading to

$$[M]^{-1} = [N]^{-1} - \frac{[N]^{-1} \vec{w}_1 \vec{w}_2^T [N]^{-1}}{1 + \vec{w}_2^T [N]^{-1} \vec{w}_1}. \quad (7.14)$$

To solve  $\vec{x}$ , the following two auxiliary equations are introduced:

$$[N] \vec{x}_1 = \vec{b}, \quad (7.15)$$

$$[N] \vec{x}_2 = \vec{w}_1. \quad (7.16)$$

Once  $\vec{x}_1$  and  $\vec{x}_2$  are available, we obtain  $\vec{x}$  in Eq. (7.8) as

$$\vec{x} = \vec{x}_1 + A \vec{x}_2, \quad (7.17)$$

where

$$A = -\frac{\vec{w}_2^T \vec{x}_1}{1 + \vec{w}_2^T \vec{x}_2}. \quad (7.18)$$

Fortunately, Eqs. (7.15) and (7.16) are tridiagonal systems of linear equations, to which the Thomas algorithm is applicable. Since  $\vec{w}_1$  is constant,  $\vec{x}_2$  of Eq. (7.16) is solved once and stored throughout the analysis.

Metal is often regarded as a PEC below terahertz frequencies [24], so that the tangential components of the electric field are set to be zero on the metal surface. The PEC boundary condition can readily be implemented for the explicit FDTD method. For the implicit scheme, however, it is difficult to directly impose the condition on the unknown terms in the simultaneous equations discussed above. Therefore, we resort to the image theory for the magnetic field to take into account the PEC boundary condition [21]. That is, the two magnetic fields at the current time step, between which the electric field on the metal surface is sandwiched, are forced to be the same, leading to  $E = 0$  at the next time step on the metal surface.

### 7.3.3 Numerical Results

To examine the effectiveness of the present method, we analyze the metal disk-type terahertz surface wave splitter [22] shown in Fig. 7.20. Considering the operation at separate frequencies of 1.0 and 1.5 THz, we choose the depths of gratings to be  $h_R = 50 \mu\text{m}$  and  $h_L = 30 \mu\text{m}$  on the right and left sides, respectively. The number of grating periods is selected to be 9, in which  $w_B = 480 \mu\text{m}$ ,  $w_T = 200 \mu\text{m}$ ,  $l = 400 \mu\text{m}$ ,  $r = 80 \mu\text{m}$ ,  $p = 50 \mu\text{m}$ ,  $d = 20 \mu\text{m}$ ,  $\varphi_R = \varphi_L = 135^\circ$ , and  $\varphi_m = 45^\circ$

**Fig. 7.20** Configuration of a surface wave splitter

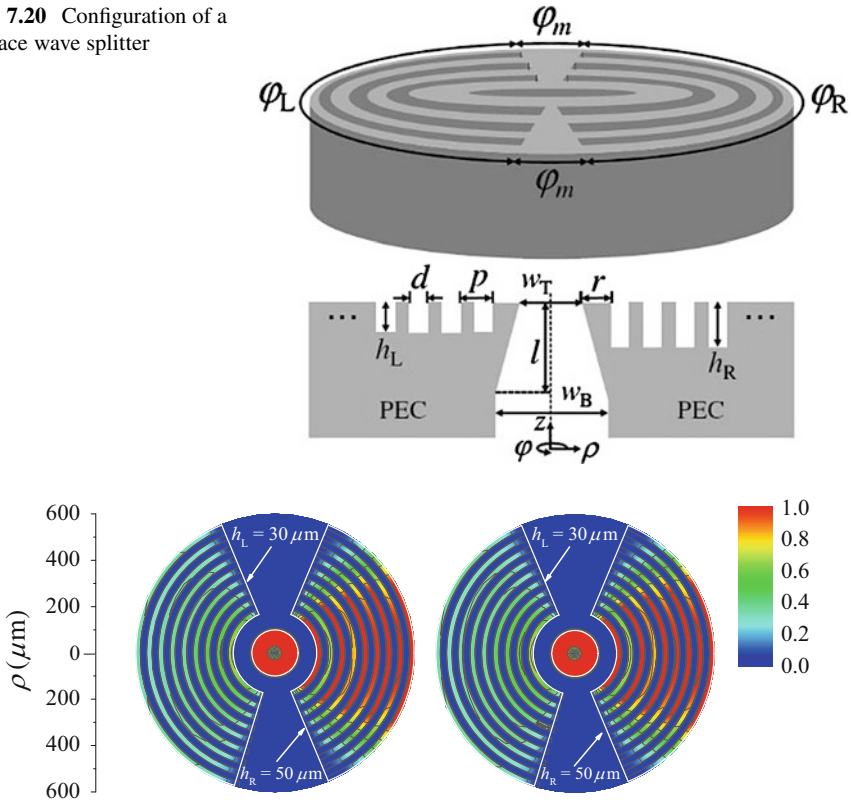


**Fig. 7.21**  $H_\phi$  field distributions at 1.0 THz. (a) FDTD method for CFLN = 1 and (b) LOD-FDTD method for CFLN = 10

are used. The mesh sizes are  $\Delta\rho = \Delta z = 2.0 \mu\text{m}$  and  $\Delta\phi = 7.5^\circ$ . We define the time step size to be CFLN ( $= \Delta t/\Delta t_{\text{CFL}}$  in which  $\Delta t_{\text{CFL}}$  is the upper limit of the FDTD method).

First, we show the field distributions on the upper surface of the splitter. Figures 7.21 and 7.22 illustrate the  $H_\phi$  field distributions at 1.0 and 1.5 THz, respectively, in which the results of the FDTD and LOD-FDTD methods are compared. The surface waves at 1.0 and 1.5 THz are seen to mainly propagate in the right and left directions, respectively. It is found, even for CFLN = 10, that the LOD results are in good agreement with the FDTD results.

Finally, we mention the CPU time for this analysis using a PC with Core i7 (3.60 GHz), in which only a single core is employed for a fair comparison. The CPU times of the FDTD and LOD-FDTD methods are shown in Fig. 7.23. For CFLN = 10, the CPU time of the LOD-FDTD method is reduced to approximately 50% of that of the FDTD method.

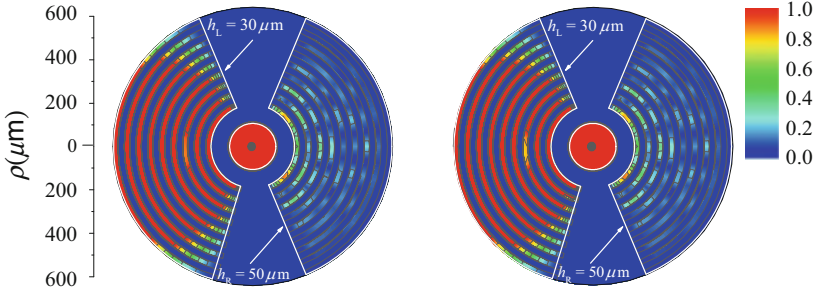
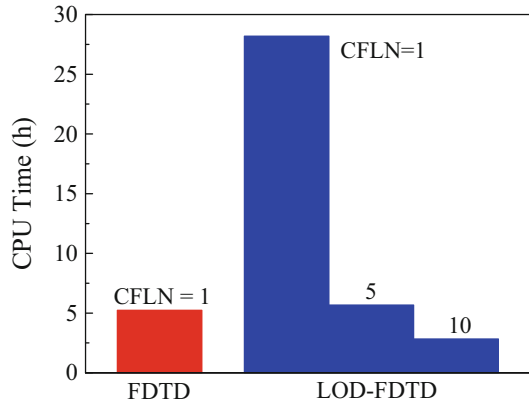


**Fig. 7.22**  $H_\varphi$  field distributions at 1.5 THz. (a) FDTD method for CFLN = 1 and (b) LOD-FDTD method for CFLN = 10

**Fig. 7.23** CPU time



### 7.4 Conclusions

Three metamaterial-based antennas, including metaline, metaloop, and metasprial antennas, have been investigated. A single metaline scans a linearly polarized beam from the backward direction, through the broadside direction, to the forward direction, with change in frequency. This means that the symmetric broadside beam with respect to the normal direction appears across a very narrow frequency range. To obtain a wideband symmetric broadside beam, a double metaline antenna has been proposed. It is found that the double metaline antenna has a symmetric broadside beam across an approximately 30% bandwidth.

The radiation from the metaloop antenna is circularly polarized unlike the radiation from the metaline antenna. The gain for an LHCP wave,  $G_L$ , reaches its maximum value at a frequency below the transition frequency  $f_T$  and that for an RHCP wave,  $G_R$ , reaches its maximum value at a frequency above  $f_T$ . The frequency bandwidths for  $G_L$  and  $G_R$  are approximately 13% and 12%, respectively. Thus, the metaloop antenna behaves as a dual-band counter circularly polarized radiation element.

The metasprial antenna also behaves as a dual-band counter circularly polarized radiation element. The radiation is in the broadside direction. As the antenna size is increased, the frequency separation between the nion and hion frequencies becomes smaller.  $G_L$  is dominant in the low-frequency region below  $f_T$ , and  $G_R$  is dominant in the high-frequency region above  $f_T$ , with different maximum gain values. It is found that placing a dielectric slab above the metasprial is effective for reducing the gain difference.

A metasurface-based terahertz frequency splitter has been investigated using the efficient implicit FDTD algorithm in cylindrical coordinates, based on a LOD scheme. The formulation is given, in which the Sherman-Morrison formula is introduced to treat a cyclic matrix and the image theory is applied to imposing the perfect electric conductor boundary condition. It is found that the computation time for the analysis is reduced to 50% of that of the explicit FDTD method, while maintaining the comparable accuracy. The splitting behavior is deeply dependent on the grating depth, realizing the frequency separation between 1.0 and 1.5 THz.

The algorithm of the LOD-FDTD method can be significantly simplified using the fundamental scheme [25], in which convenient matrix-operator-free forms are obtainable in the right-hand sides of resultant basic equations. In addition, a hybrid implicit-explicit (HIE) technique can be applied to the cylindrical FDTD method, where only the derivatives in the circumferential direction are treated implicitly. In future work, we will compare the numerical efficiency of our LOD-FDTD method to HIE-FDTD method. Tolerance issues when fabricating our splitter for operation in the terahertz range have yet to be discussed.

**Acknowledgment** We thank V. Shkawrytko for his assistance in the preparation of this manuscript.

## References

1. N. Engheta, R.W. Ziolkowski (Eds.), *Metamaterials* (Wiley, Hoboken, NJ, 2006)
2. C. Caloz, T. Itoh, *Electromagnetic Metamaterials* (Wiley, Hoboken, NJ 2006)
3. A. Sanada, M. Kimura, I. Awai, H. Kubo, C. Caloz, T. Itoh, A planar zeroth-order resonator antenna using left-handed transmission line, in *Proceedings of the European Microwave Conference*, Amsterdam, Oct 2004, pp. 1341–1344
4. A. Lai, K.M.K.H. Leong, T. Itoh, Infinite wavelength resonant antennas with monopolar radiation pattern based on periodic structures. *IEEE Trans. Antennas Propag.* **55**(3), 868–876 (2007)
5. D. Singh, A. Kumar, S. Meena, V. Agarwala, Analysis of frequency selective surfaces for radar absorbing materials. *Prog. Electromagn. Res. B* **38**, 297–314 (2012)
6. F. Yang, K. Yanghyo, Y. Ang, J. Huang, A. Elsherbeni, A single layer reflectarray antenna for C/X/Ka bands applications, in *Proceedings of International Conference on Electromagnetics in Advanced Applications (ICEAA)*, Torino, Sept 2007, pp. 1058–1061

7. K. Watanabe, Spectral-domain analysis of electromagnetic scattering by periodically corrugated surfaces with local deformation, in *Proceedings of the Asia-Pacific Microwave Conference*, Seoul, 2013, pp. 301–303
8. A. Feresidis, G. Goussetis, S. Wang, J. Vardaxoglou, Artificial magnetic conductor surfaces and their application to low-profile high gain planar antennas. *IEEE Trans. Antennas Propag.* **53**(1), 209–215 (2005)
9. H. Nakano, S. Mitsui, J. Yamauchi, Tilted-beam high gain antenna system composed of a patch antenna and periodically arrayed loops. *IEEE Trans. Antennas Propag.* **62**(6), 2917–2925 (2014)
10. H. Nakano, *Low-profile Natural and Metamaterial Antennas* (Wiley-IEEE Press, Hoboken, NJ, 2016)
11. H. Nakano, Line, loop, and spiral antennas composed of metamaterial arms. *IEICE Trans. Commun.* **J99-B**(8), 563–571 (2016)
12. H. Nakano, K. Sakata, J. Yamauchi, Wide-band broadside radiation from a double metaline system, in *Proceedings of the IEEE Antennas and Propagation Society International Symposium*, Puerto Rico, 2016
13. H. Nakano, K. Yoshida, J. Yamauchi, Radiation characteristics of a metaloop antenna. *IEEE Antennas Wirel. Propag. Lett.* **12**, 861–863 (2013)
14. H. Nakano, J. Miyake, T. Sakurada, J. Yamauchi, Dual-band counter circularly polarized radiation from a single-arm metamaterial-based spiral antenna. *IEEE Trans. Antennas Propag.* **61**(6), 2938–2947 (2013)
15. H. Nakano, T. Shimizu, J. Yamauchi, Metaspiral antenna system, in *Proceedings of the International Symposium on Antennas and Propagation*, Tasmania, Nov 2015, pp. 1–3
16. G.V. Trentini, Partially reflecting sheet arrays. *IRE Trans. Antennas Propag.* **4**, 666–671 (1956)
17. J. Shibayama, M. Itoh, J. Yamauchi, H. Nakano, Analysis of a metal disc-type terahertz surface wave splitter using the cylindrical LOD-FDTD method, in *Proceedings of the 16th International Conference Numerical Simulation Optoelectronic Devices*, Sydney, 2016, ThA3
18. J. Shibayama, M. Muraki, J. Yamauchi, H. Nakano, Efficient implicit FDTD algorithm based on locally one-dimensional scheme. *Electron. Lett.* **41**(19), 1046–1047 (2005)
19. J.W. Thomas, *Numerical Partial Differential Equations: Finite Difference Methods* (Springer, Berlin, 1995)
20. J. Shibayama, R. Ando, J. Yamauchi, H. Nakano, An LOD-FDTD method for the analysis of periodic structures at normal incidence. *IEEE Antennas Wirel. Propag. Lett.* **8**, 890–893 (2009)
21. W.C. Tay, E.L. Tan, Implementations of PMC and PEC boundary conditions for efficient fundamental ADI- and LOD-FDTD. *J. Electromagn. Waves Appl.* **24**(4), 565–573 (2010)
22. J. Shibayama, J. Yamauchi, H. Nakano, Metal disc-type splitter with radially placed gratings for terahertz surface waves. *Electron. Lett.* **51**(4), 352–353 (2015)
23. R.A. Depine, A. Lakhtakia, A new condition to identify isotropic dielectric-magnetic materials displaying negative phase velocity. *Microw. Opt. Technol. Lett.* **41**, 315–316 (2004)
24. J. Shibayama, Y. Uchizono, S. Ozaki, J. Yamauchi, H. Nakano, Treatment of metal for the FDTD analysis of terahertz devices. *Opt. Quant. Electron.* **46**(2), 345–356 (2014)
25. E.L. Tan, Fundamental schemes for efficient unconditionally stable implicit finite-difference time-domain methods. *IEEE Trans. Antennas Propag.* **56**(1), 170–177 (2008)



**Hisamatsu Nakano** received a D.Eng. degree from Hosei University, Tokyo, Japan, in 1974. Since 1973, he has been with Hosei University, where he is now a professor emeritus and a special appointment researcher at the *Electromagnetic Wave Engineering Research Institute* attached to the graduate school of the same university. He has been an IEEE Life Fellow since 2011. Professor Nakano has published over 300 articles in major refereed journals, more than 400 international symposium papers, more than 1550 national symposium papers, and 11 books/book chapters, including *Low-profile Natural and Metamaterial Antennas* (Wiley and IEEE Press). Professor Nakano received the IEEE Transactions on Antennas and Propagation H. A. Wheeler Award in 1994. He was also the recipient of the IEEE Antennas and Propagation Society Chen-To Tai Distinguished Educator Award in 2006 and the Prize for Science and Technology (from Japan's Minister of Education, Culture, Sports, Science, and Technology) in 2010. More recently, he received the 2016 Distinguished Achievement Award from the IEEE Antennas and Propagation Society.



**Jun Shibayama** was born in Kashiwa, Japan, on July 1, 1969. He received the B.E., M.E., and D.Eng. degrees from Hosei University, Tokyo, Japan, in 1993, 1995, and 2001, respectively. In 1995, he joined Opto-Technology Laboratory, Furukawa Electric Co., Ltd., Ichihara, Japan. He became an Assistant of Hosei University in 1999, where he is currently a Professor. His research interests include the numerical analysis of electromagnetic problems. Dr. Shibayama is a Member of the IEEE, OSA, ACES, and IEICE.



**Junji Yamauchi** was born in Nagoya, Japan, on August 23, 1953. He received the B.E., M.E., and D.Eng. degrees from Hosei University, Tokyo, Japan, in 1976, 1978, and 1982, respectively. From 1984 to 1988, he served as a Lecturer in the Electrical Engineering Department of Tokyo Metropolitan Technical College. Since 1988, he has been a Member of the faculty of Hosei University, where he is currently a Professor. His research interests include optical waveguides and circularly polarized antennas. He is the author of *Propagating Beam Analysis of Optical Waveguides* (Research Studies Press, 2003). Dr. Yamauchi is a Fellow of the IEEE and a Member of the Optical Society of America and the Institute of Electronics, Information and Communication Engineers of Japan.

# Chapter 8

## Electromagnetic Research and Challenges for Tactical Communication

Mahbub Hoque and Jeffrey Boksiner

### 8.1 Introduction

The success of today's tactical military operations is becoming more and more dependent on reliable communications. To this end, tactical-communications systems must operate reliably in rural, suburban, and dense urban areas which are often highly congested and contested. Diverse propagation phenomena under varying environmental conditions and the complex and dynamic nature of the spectrum environment represent many of the electromagnetic research challenges for tactical communications. This chapter discusses these challenges in detail and describes research accomplishments that improve tactical communications in degraded, contested, and congested environments.

According to military doctrine, the communications system is the principal tool to collect, monitor, transport, process, protect, and disseminate information [1]. Network connectivity is mission critical and can determine mission viability during planning and execution. Since a significant portion of the tactical communications system relies upon wireless transmissions using radio-frequency (RF) waves, the physics of electromagnetic wave generation, propagation, and reception is a critical research area for the advancement of communications capabilities.

Military communications face relevant challenges associated with a military operating environment that includes the need to operate in urban areas and other complex terrain as well as in the presence of both friendly and adversarial systems [2]. The US Army Capabilities Integration Center [3] provides a concise summary of the operational challenge in the published *Army Warfighting Challenge #7: Conduct Space and Cyber Electromagnetic Operations and Maintain Communications*. The

---

M. Hoque (✉) • J. Boksiner

United States Army Communications-Electronics Research, Development and Engineering Center (CERDEC), Aberdeen Proving Ground, MD 21001, USA

e-mail: [mahbub.hoque1.civ@mail.mil](mailto:mahbub.hoque1.civ@mail.mil); [jeffrey.boksiner.civ@mail.mil](mailto:jeffrey.boksiner.civ@mail.mil)



Warfighter Challenge description states [3] “How to assure uninterrupted access to critical communications and information links (satellite communications [SAT-COM], positioning, navigation, and timing [PNT], and intelligence, surveillance, and reconnaissance [ISR]) across a multi-domain architecture when operating in a contested, congested, and competitive operating environment.”

From the electromagnetic point of view, the crucial aspect is the impact of the electromagnetic operating environment (EME). The EME comprises the RF propagation environment and the ambient signals present in the electromagnetic spectrum (EMS). From a broader perspective, all military operations depend on assured EMS access throughout the operational environment. Operations in the air, on land, on and under the sea, in space, and in cyberspace are fundamentally dependent on the use and control of the EMS [4].

This chapter examines the research challenges and some corresponding research activities associated with military communications system operation in a contested and congested EMS. The focus is on the RF electromagnetic issues such as propagation, interference, and antenna system performance.

### 8.1.1 Metrics

The performance of a military communications system is characterized by many parameters and metrics. Some common RF and network performance measures are capacity, capacity utilization (%), packet jitter, packet latency, quality of services, packet completion rate, connectivity, communications systems range, system scalability, and robustness.

This chapter focuses on electromagnetic phenomena and hence the physical layer of the communications systems. However, the physical-layer performance does inform the design and performance of the higher layers of the protocol stack. From the physical-layer perspective, the key design consideration is the signal environment at the receiver.

### 8.1.2 The Signal Model

The performance of a communications system depends on the ability of the receiver to decode the received signal in the presence of noise and interference. A primary determinant of the capacity and range of a communications link is a generalized signal-to-interference plus noise (SINR) criterion [5]:

$$I = \frac{P^S}{N + \sum_i \rho_i (\Delta f_i) P_i^I}, \quad (8.1)$$

where  $p^S$ ,  $N$ , and  $p^I$  are the numerical values of received signal power, noise, and interference power at the receiver, respectively;  $\rho_i(\Delta f_i)$  is an adjustment factor that depends on the frequency separation  $\Delta f_i$ ; and  $i$  enumerates interfering signals. The interfering signals can be divided into the following three categories:

- **Interference from nodes in the same network.** Network channel access protocols, such as time, frequency, or code division, are responsible for controlling these signals. Physical-layer techniques such as multiple-input multiple-output (MIMO) or directional antennas can also play a significant role in reducing interference from nodes within the network and increase the overall capacity and scalability of the system. Section 8.5 discusses the application of directional antennas to military networks.
- **Interference from transmitters in other networks or systems not collocated with the receiver.** Spectrum management processes, spectrum planning, or real-time spectrum access protocols, such as listen-before-talk, are the means to control this type of interference, for networks or systems controlled or managed by the operators of the system receiving interference. Section 8.3 discusses the use of site-specific propagation models for communications or spectrum planning in complex rural and urban environments.
- **Interference from collocated emitters (co-site interference).** Various co-site mitigation measures are employed to reduce this type of interference. Section 8.4 discusses co-site interference and its mitigation through electromagnetic modeling.

The received power, either from the desired or interfering non-collocated transmitter, is given by the basic link budget [6]:

$$p^R = p^T g^R g^T \frac{\alpha}{l_{50}}, \quad (8.2)$$

where  $p^R$  is the received power,  $p^T$  is the transmitter power of the desired transmitter or the potential interferer,  $g^R$  is the antenna gain at the receiver in the direction of the transmitter,  $g^T$  is the antenna gain at the transmitter in the direction of the receiver,  $l_{50}$  is the mean power (i.e., 50%) path-loss function, and  $\alpha$  is the fading amplitude, which, in this formulation, is a random variable with a mean value of unity.

Other possible losses within the transmitter, such as line losses, can be included in  $p^T$ . Received power throughout the receiver chain is extracted from  $p^R$  by included additional losses within the receiver.

The key electromagnetic parameters in the analysis of tactical systems are the path losses, antenna gains, and frequency responses of analog RF components such as filters. For co-site interference, the key parameter is the coupling between collocated antennas. In addition to received power, channel characteristics, such as slow and fast fading, are important for receiver performance.

### 8.1.3 *Specific Considerations for Tactical Systems*

In contrast to commercial communications architectures, military systems must address certain specific considerations that include:

- **Lack of fixed infrastructure.** The expeditionary and mobile nature of military operations often precludes the ability to employ fixed infrastructure, which implies that the majority of communications paths are peer-to-peer with range requirements determined by the operation of forces and the operations theater.
- **Congested and contested EMS.** As EMS is a critical enabler for a variety of systems, military systems must coexist with a diverse and disparate set of electromagnetic signals. In addition, tactical systems often operate in an electromagnetic environment that is unregulated, under-regulated, and/or hostile.
- **Size, weight, and power (SWAP) constraints.** Military platforms, such as ground vehicles, fixed or rotary wing aircraft, and dismounted users, provide stringent limitations on SWAP and, in particular, on SWAP of antenna apertures.

## 8.2 Frequency Response Considerations

Before considering path-loss and antenna gain, it is useful to quickly consider how the frequency response of the RF components affects the system performance in terms of the receiver SINR. If, as a reasonably good first approximation, the impact of interference signals is treated as noise, then the adjustment factor  $\rho_i(\Delta f_i)$ , in the SINR Eq. (8.1), can be computed using the frequency-dependent rejection (FDR) algorithm. Representing the power loss due to receiver filtering, the FDR is given by

$$FDR(\Delta f) = 10 \log \frac{\int_0^\infty P(f) df}{\int_0^\infty P(f) H(f + \Delta f) df}, \quad (8.3)$$

where  $P(f)$  is the emission spectral density generally normalized to unit maximum power spectral density and  $H(f)$  is the receiver selectivity.

The responses of RF components including the antenna, the front-end (pre-selector) filters, and, most importantly, the intermediate frequency filters determine  $H(f)$ . In modern software radios, FDR also has to incorporate the digital filtering implemented in the receiver digital signal processing.

## 8.3 Propagation Considerations

Commercial communications networks can often overcome RF propagation issues by using dedicated fixed infrastructure and deploying advantages of fixed RF relays. For tactical and on-the-move communications, complex propagation environments

often dictate the quality of the RF communications. In particular, mobile-to-mobile mountainous rural environments and mobile-to-mobile urban environments can be extremely challenging for RF communications. Each of these environments is characterized by extensive multipath and possibility of line-of-sight obstructions.

### 8.3.1 Rural Environment

Mobile tactical communications systems typically employ omnidirectional antennas to support mobility and multi-cast communications. Omnidirectional emissions give rise to lateral reflections in mountainous environments. Figure 8.1 illustrates the mechanism for generating the lateral reflections. Appropriate propagation models are needed to properly address these phenomena for spectrum and communications planning purposes. There are several path-loss prediction models which utilize ray-tracing techniques whereby lateral reflection can be estimated accurately. However, these techniques often require lengthy calculations with the calculation time increasing dramatically for large numbers of interference computations. Thus, it is often impractical to use these approaches for spectrum planning or real-time analysis. Researchers have addressed this issue by using a concept called 3-D rural propagation model. This model can quickly estimate path-loss including contribution of lateral reflection caused by irregular terrain. In this concept, the propagation zone is initially identified a priori. Using the available terrain data, a special algorithm is used to determine the scattering point. The step-by-step analysis is as follows:

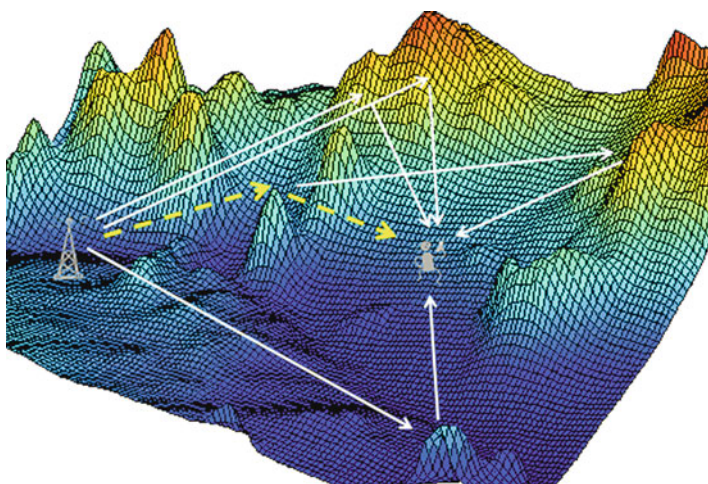


**Fig. 8.1** Physical process leading to lateral reflections

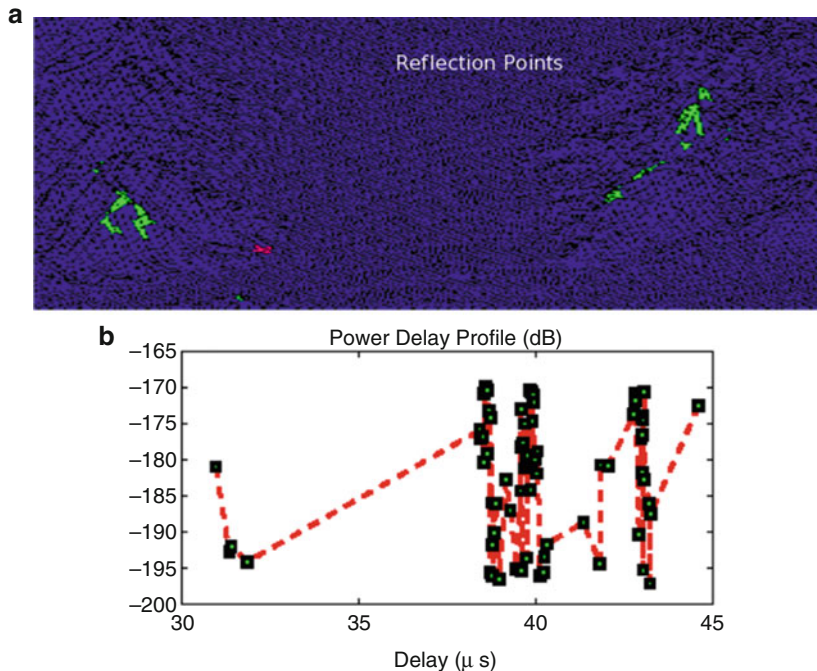
- Develop a low-complexity fast-propagation model taking into account multiple lateral reflections from terrain features.
- Develop a preprocessing visibility algorithm to determine the terrain elements that are scattering points.
- Develop analytical models and programs for efficient 3-D prediction of the path gain for rural environments. For each of the scattering points, a reflection coefficient is estimated to predict the received field.
- The aggregated path-loss is calculated using an existing point-to-point propagation model, such as terrain-integrated rough-earth model (TIREM), at each vertical plan between the scatterer and receiver considering phase lag of the receiving signal.
- Finally, the model is integrated with the current TIREM model that determines the path gain in the vertical plane.

Figure 8.1 shows the illumination regions identified by the model and delay spread of the direct and reflected signals. The total power is the sum of all signals, but the ability of the model to generate the power-delay channel provides important additional information useful for communications and spectrum planning. It has been observed that consideration of the impact of lateral reflection results in a more accurate path-loss prediction. Since the analysis is based on preprocessed data, the analysis at a certain location can be performed faster and almost in real time (Fig. 8.2).

### ***8.3.2 Ground-to-Ground Communication in the Urban Environment***

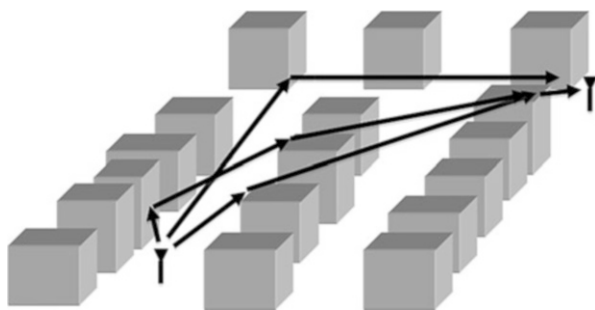
The challenge for urban propagation is similar to that of mountainous rural environments, if not more complex due to obstructions and multipaths created by buildings. There are statistical RF propagation models such as the Okumura or Hata models based on large numbers of measurements in the high-rise cities such as New York, Tokyo, and Los Angeles. However, these models cannot provide site-specific propagation predictions. Site-specific, mobile-to-mobile, urban propagation modeling is critical to a variety of applications, including spectrum management, spectrum and communications systems planning, and dynamic spectrum-access policy development (Fig. 8.3).

To achieve an efficient site-specific model, army researchers have developed a novel urban propagation model (UPM) for the UHF band (0.3–3 GHz) that uses building geometry derived from a detailed geographic information system (GIS) data file. For each path, the model computes the mean path-loss using the main propagation modes relevant to the urban environment. It specifically addresses mobile-to-mobile communications by providing a formulation valid when both the transmitter and the receiver are below the surrounding rooftops. The UPM is based



**Fig. 8.2** Intermediate and final results of the rural 3-D propagation model. (a) Illuminated regions. (b) Power-delay profile resulting from summation of direct and reflected signals

**Fig. 8.3** Schematic of urban mobile-mobile propagation



on the theory developed in Ref. [7]. In order to achieve a minimal computational time, UPM limits the choice of rays considered to those most likely to be of significant value.

For frequencies in the UHF range, the wavelength is smaller than typical building dimensions. As a result, ray-tracing methods based on the geometric theory of diffraction are an appropriate basis for this propagation model. Of primary concern is the prediction of propagation loss for the narrow band where the average path-loss would be measured by averaging out wavelength-scale (fast) fading of the received signal  $V$ .

To reduce the computation time, the analytical UPM considers the significant ray paths that travel in the vertical plane (VP) and horizontal plane (HP) in an urban environment. The VP model determines the path gain as a result of field reduction with respect to free space, multiple diffractions over passed building rows, and diffraction of the rooftop to a mobile station. The VP model is developed to address different propagation scenarios when the transmitter antenna is above, below, and near the average rooftop level for any range between the two antennas.

For the HP model, the dominant contribution to the path gain for mobile-to-mobile communications is expected to come from rays that propagate through the street canyons. The anticipated range between mobiles in HP is up to 1 km in urban settings. The overall path gain is then computed by adding the powers received via the vertical and horizontal propagation models.

The UPM extracts the required data from the Environmental Systems Research Institute (ESRI) shapefile database. The model then computes and returns the average values and flags of the key input parameters for the UPM. The geospatial data derived from shapefiles provides key features of the urban environment (e.g., roads and buildings) to predict the path gain of the VP and HP models. A list of attribute fields is associated with each feature. Such attributes are the road width, building height, the number of buildings along the path, building length, building area, and building location. The UPM retrieves the intersecting key aspects from the shapefile's products and computes the UPM primary input parameters as follows [8]:

1. Calculate the horizontal distance  $d$  between Tx and Rx locations in meter.
2. Gather the following input data required to predict the losses due to VP from the shapefile and the user:
  - Average height  $h_B$  of building roofs in meter
  - Average building separation  $b$  in meter
  - Average road width  $w$  in meter
  - Average building height variation  $h_{var}$  in meter
  - Total number  $N_t$  of buildings along the path
  - Propagation orientation in degree
  - Building height  $h_{tx}$  in meter when the transmitter is located on a building
  - Tx and Rx locations
3. Based on the foregoing site-specific information, compute and return the number of turns between the transmitter and receiver.
  - Type of route (line of sight (LOS), one-turn, or two-turn) (Fig. 8.4 illustrates the one-turn and two-turn paths)
4. Compute and return the path-loss for LOS route types between the Tx and Rx locations.
5. Compute and return the path-loss for one-turn route type between the Tx and Rx locations.

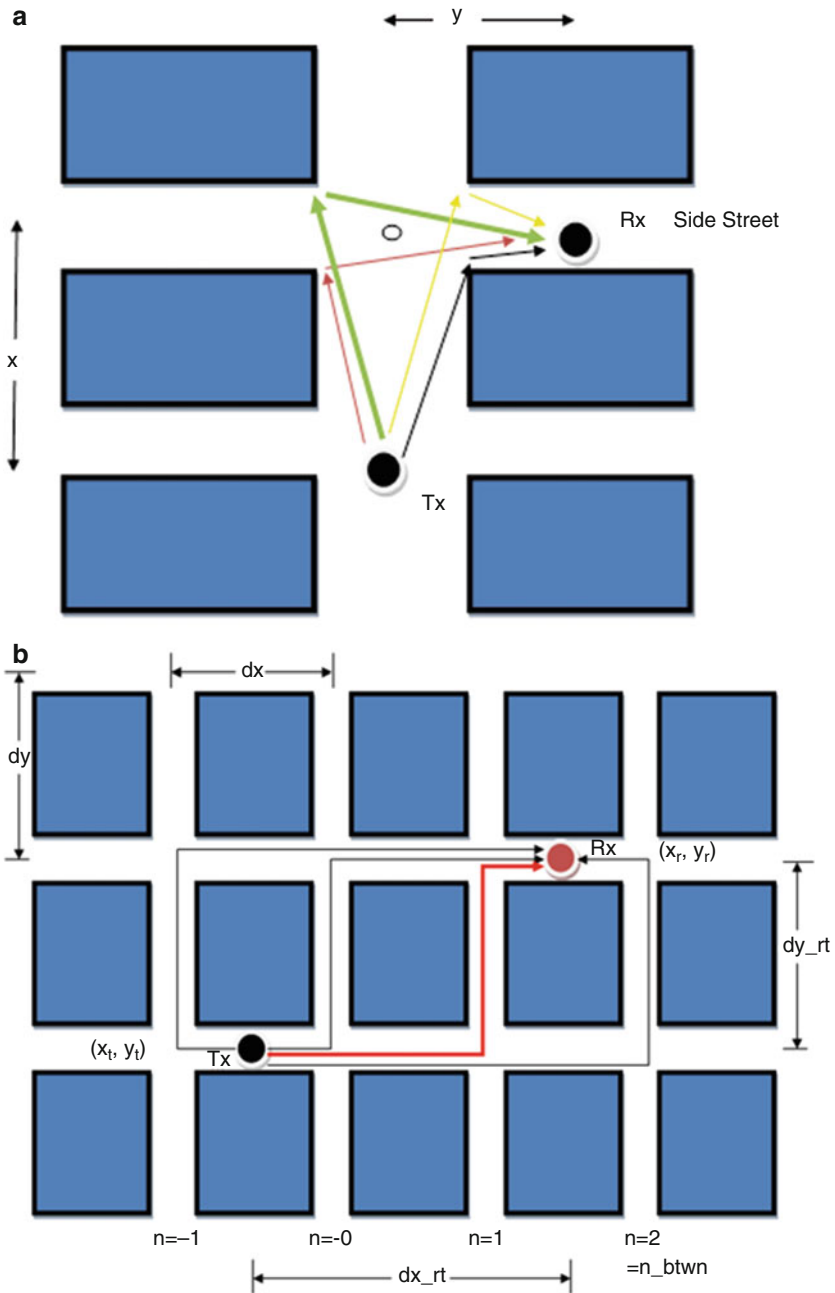


**Fig. 8.4** Schematics of one-turn and two-turn HP paths. (a) Illustration of one-turn path. (b) Illustration of two-turn path



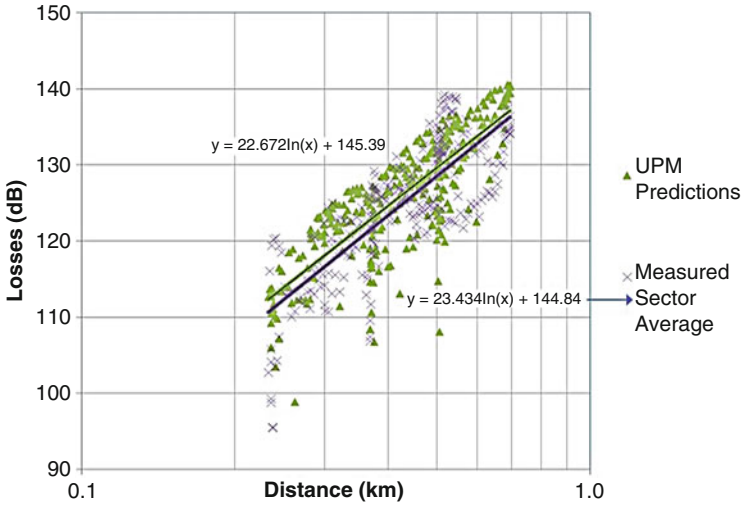


**Fig. 8.5** Physical process leading to lateral reflections

- Distance  $x$  from transmitter to intersection where turn occurs in meter
  - Distance  $y$  from receiver to intersection where turn occurs in meter
6. Compute and return the path-loss for two-turn route type between the Tx and Rx locations.
- Average horizontal block distance  $d_x$  in meter
  - Average vertical block distance  $d_y$  in meter
  - Horizontal distance  $d_{xrt}$  between antennas in meter
  - Vertical distance  $d_{yrt}$  between antennas in meter

The UPM will determine whether it is necessary to find the HP parameters based on the Tx and Rx antenna locations:

1. For all cases, the program determines the VP parameters.
2. When the distance is greater than 1 km, the HP parameters are not required and the HP route type is default to “Not Applicable” (NA).
3. When the transmitter antenna is located on a building, the HP route type is default to “Not Applicable” (NA). The info that the transmitter antenna is located on building and the building height ( $h_{tx}$ ) are determined.
4. When the distance is less than 1 km and the transmitting antenna is not on a building (e.g., the antenna could be located on a road or open area such as a parking lot), then the program determines the HP parameters.

The UPM sums the powers computed for the various paths to obtain the mean propagation loss. Figure 8.5 shows a comparison of UPM results with measured data. The results show good agreement between UPM predictions and the mean path loss [9].

## 8.4 The Issue of Co-site Interference

One issue that affects receiver performance is related to co-site signals emanating from systems located on the platforms (vehicular or airborne systems or dismounted soldier). To limit the scope of the chapter, we confine the co-site interference discussion to ground vehicles. Figure 8.6 illustrates an example of multiple communication systems/antennas on a vehicle that can cause mutual co-site interference. Although standard spectrum planning avoids in-band interference among systems, the electromagnetic coupling among antennas on the vehicle is much stronger than coupling by propagation. As a result, interference effects can occur due to out-of-band emissions or reception of spurious emissions. Also, while MIL-STD-461G establishes interface and associated verification requirements for the control of electromagnetic interference (EMI), emission parameters or coupling levels may still allow co-site interference to occur.

In addition to antennas on the rooftop, many tactical vehicles also contain multiple metal structures (e.g., weapon systems) which can negatively affect communications systems. Additionally, in some cases, there are more than 12 or 13 omnidirectional whip antennas at the top of vehicles. These can be high-power transmitters that cause out-of-band interference due to front-end nonlinearities. In addition, there is a need to ensure personnel safety and avoid potential radiation hazards due to high-power multiple transmitters. It is possible to mitigate many of these interference issues by judicious placement of antennas on the rooftop to minimize coupling between the antennas. Good antenna placement can take advantage of organic vehicular metallic obstruction such as gunner kits.

One approach to address this complex interference scenario is to take numerous measurements to characterize antenna coupling and relocate antennas to reduce coupling, often by trial and error. This approach can be time consuming and costly. Thus, there is a need to develop an analysis and mitigation technique that treats the entire platform as an integrated system and is:

- Cost-effective,
- High-resolution,



**Fig. 8.6** Images of two tactical vehicles with multiple antennas and rooftop structures

- Accurate,
- Flexible to variance,
- Not platform specific, and
- Capable of being performed remotely when needed.

These considerations have guided the tactical community to develop a sophisticated modeling and simulation approach that has become the most effective technique to address the relevant challenges mentioned previously.

### ***8.4.1 Modeling and Simulation Approach***

The coupling between multiple antennas is dependent on the shapes and sizes of the antennas, their radiation characteristics, physical locations, and the presence of the platform itself along with other surrounding structures. In addition, when antennas are installed on the platform, their emission characteristics are perturbed by the presence of other devices. Therefore, it is imperative to assess the radiation characteristics of the antennas in a complete and integrated system configuration.

Determining the radiation characteristics and coupling between collocated on-platform antennas is an important problem in applied electromagnetics. To perform this analysis in an effective and efficient manner, researchers have developed numerical electromagnetic models that implement standard electromagnetic methods to determine realistic emission characteristics of mounted antennas. These characteristics are not only dependent on the shape and sizes of the platform and their corresponding ancillary objects but also on the object's electromagnetic properties. Many tactical vehicles and their rooftop structures are not metallic but are made of composite materials. As a result, the electromagnetic model should consider the constitutive properties (e.g., relative permittivity, loss tangent, and relative permeability) of the platform and its structures. Platform windshields and windows should also be characterized with their appropriate dielectric properties since RF emissions can penetrate inside vehicles through them and get reflected back.

In the VHF spectral regime, the situation is compounded by the fact that scattering and coupling occur in the near-field zone of the emitter. As a result, near-field analysis is performed to determine the coupling and emitter characteristics. Numerical electromagnetic computational models are typically used to perform this analysis due to the complexity of the problem. One numerical electromagnetic method that has been used by the defense community is the finite-difference time-domain (FDTD) method. This method discretizes the entire volumetric space of the problem being modeled (i.e., a fully integrated antenna on-platform system) into cubes called *Yee cells*. The size of the cubes is dependent on the frequency under consideration. The FDTD method requires that the size of the cubes be at least one tenth of the wavelength of the highest frequency under consideration. Typically, the

size of the volumetric space being considered for simulation will be limited by the available memory of the computational infrastructure.

Once the volumetric problem space is created, the cubes that represent the integrated system are assigned with the correct dielectric properties. Passive and active sources are placed on cubes that model the tactical antennas under consideration.

The US Army typically considers a four-step process in modeling antenna on-platform problems. The first step involves the development of a validated electromagnetic model for each antenna that is considered to be part of the integrated system. Part of the process requires detailed modeling of the antenna's physical structure, feed design, excitations, and radome. The antenna metric typically measured and modeled is the far-field radiation pattern. This preliminary antenna model is then simulated in free space using an appropriate numerical electromagnetic method (e.g., the FDTD method, the method of moments, and the finite-element method) to obtain the radiation pattern. In parallel, the antenna is measured in free space in an anechoic chamber of the correct dimensions to obtain the measured radiation pattern. Once the two data sets are obtained, the predicted results are compared with the free space measurements of the antenna. Figure 8.7 illustrates a typical example of the validation process.

The second step involves the validation of the military platform and any rooftop obstructions (e.g., gunner protection kits, weapon system, etc.) under consideration. This step typically involves a complete survey of the vehicle to capture platform configuration details for accurate platform modeling.

The third step is to construct a complete numerical electromagnetic model that includes the antennas, platforms, and other ancillary objects with their dielectric properties. Figure 8.8 also illustrates this process.

The fourth and final step is to compute the radiation characteristics of each of the antennas for the antenna on-platform configuration. The antenna radiation pattern being computed represents the realistic 3-D antenna pattern. Figure 8.9 illustrates a few examples of such 3-D patterns of a typical integrated system.

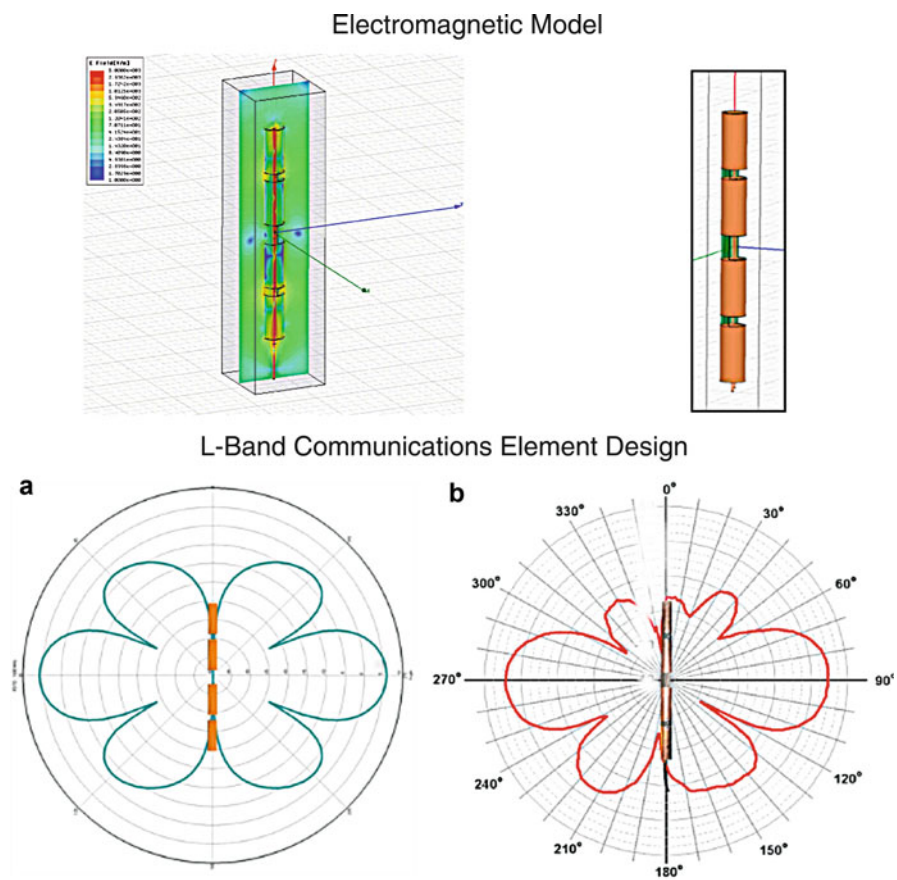
The antenna radiation-pattern metric is typically utilized for link-budget calculations to predict communications range or an interference assessment to predict the communications degradation of victim tactical communications radio receivers. Numerical modeling can also be utilized to determine the effective RF field distribution around the vehicle. This type of analysis generates an RF protection bubble that is utilized to assess military electronic protection systems. It is typically desired to obtain an undistorted RF protection bubble, and in many cases this will be unrealistic because rooftop scattering structures can distort the protection bubble. Such an effect can be easily mitigated by adjusting the heights and location of the transmitters.

Figure 8.10 illustrates an example of a typical analysis where the desired RF protection bubble is achieved after multiple adjustments of the antenna transmitter height. In Fig. 8.10a, the presence of a null on the RF field distribution around the vehicle with a six-inch riser is shown. In Fig. 8.10b, the null is mitigated by employing a 12-inch riser for the transmitter antenna. The null can also be mitigated by relocating the antenna to different positions on the platform. The utilization of

computational electromagnetic (CEM) modeling is not only cost-effective but also highly efficient for the rapid development of antenna placement solutions. Thus CEM modeling and simulation techniques play an important role in predicting performance of the integrated system.

### 8.5 Tactical Antennas

This section describes research challenges and some recent research in the field of tactical-communications antennas. The research on tactical-communications antennas focuses on three areas:



**Fig. 8.7** An example comparison of measured vs. simulated radiation pattern for a military antenna. **(a)** FDTD simulation. **(b)** Chamber measurements

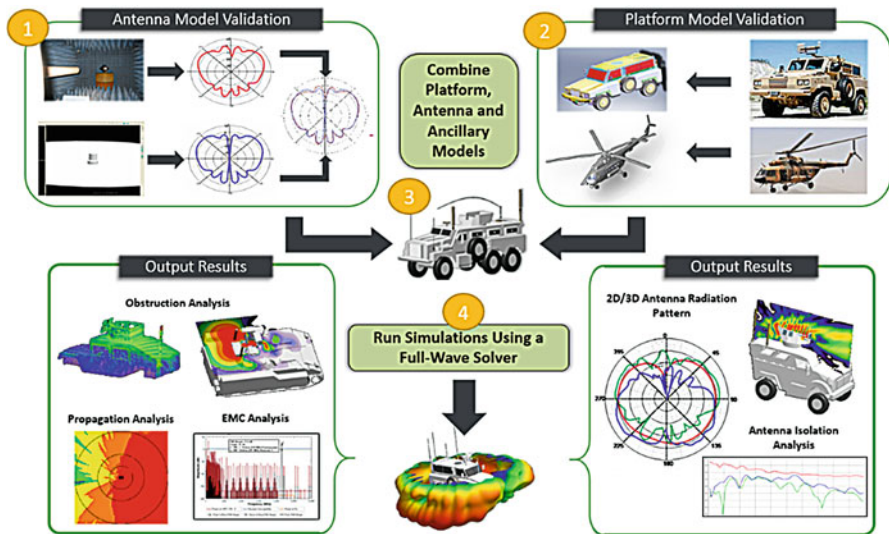


Fig. 8.8 Illustration of the process to construct an integrated numerical model

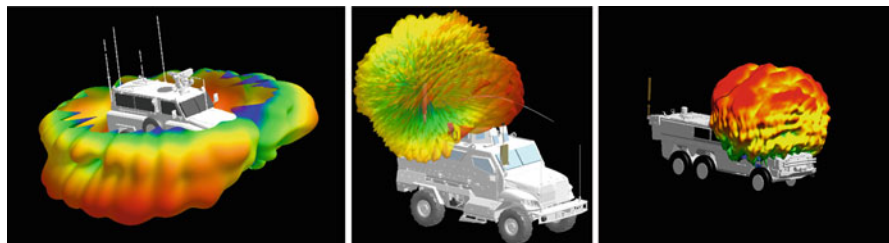
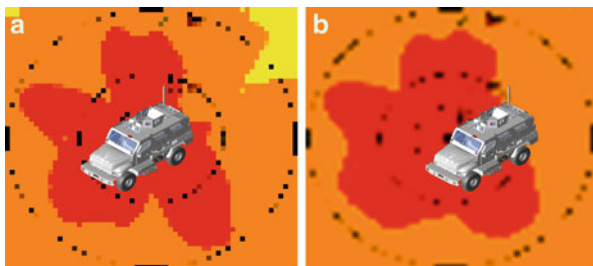


Fig. 8.9 Examples of radiation patterns of antennas integrated in a vehicle

Fig. 8.10 Examples of effect on RF field distribution due to riser obstruction. (a) 6” riser, (b) 12” riser



- Multifunctional and multiband antennas.** As described earlier in this chapter, the proliferation of RF systems on platforms has led to a corresponding proliferation of topside antennas. It is desirable to reduce the number of antennas by combining the functions of several individual antennas into a single multifunctional antenna for enhanced operations.

- **Conformal/embedded antennas.** Conformal antennas or antennas embedded into the platform's outer surface help to address the shortage of vehicle real estate for mounting of traditional antennas.
- **Directional antennas.** The dynamic nature of mobile ad-hoc networking (MANET) led to the widespread use of omnidirectional whip antennas. However, such antennas are more likely to experience interference and lead to suboptimal spectrum use. Directional antennas in conjunction with appropriate directional networking protocols enable more efficient spectrum use and mitigation of some interference effects.

### ***8.5.1 Multifunctional and Multiband Antennas***

In many cases, tactical communications systems use separate omnidirectional whip antennas which compete for space atop tactical platforms. This scenario required the researchers to reduce the number of antennas by using multiband antennas. As a result, there has been a great emphasis in developing broadband or multiband tactical antennas. However, the laws of physics place physical limitations on the size of the antenna based on the multiple frequencies of operations.

The basic concept of many multiband antennas is to utilize a stacked-antenna design, whereas there is minimum coupling between the two antenna elements by aligning the nulls of each element. A similar concept has also been used for multifunctional antennas, where communications antennas are stacked on top of the high-power broadband antennas used for creating an RF protection bubble. These concepts have been useful to address several of the challenges encountered for tactical-communications systems. However, due to increased numbers of systems with highly sensitive receivers, researchers are looking for breakthrough concepts.

One possible concept is to develop conformal, directional antennas with cognitive capabilities. The following sections briefly describe a few concepts utilized for developing such antennas.

### ***8.5.2 Conformal/Embedded Antennas***

One of the major issues in developing conformal antennas is related to the physical size of the antennas. Research has shown that using metamaterials to reduce the size of the antennas is possible; however, in many cases, the metamaterials are optimized at a single resonance frequency. As a result, developing broadband metamaterial antennas is quite challenging. In an attempt to develop low-signature antennas for tactical operations, many researchers have developed conformal antennas using metamaterials. This can help reduce the size of whip antennas that are being developed for tactical operations.

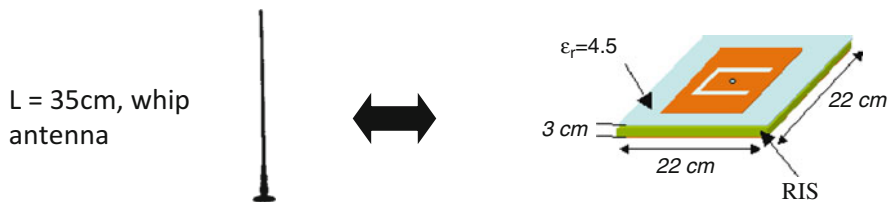


**Fig. 8.11** Prototype metamaterial antenna for replacing a whip antenna

**Fig. 8.12** Design of a six-element mesh antenna and embedded in the windshield

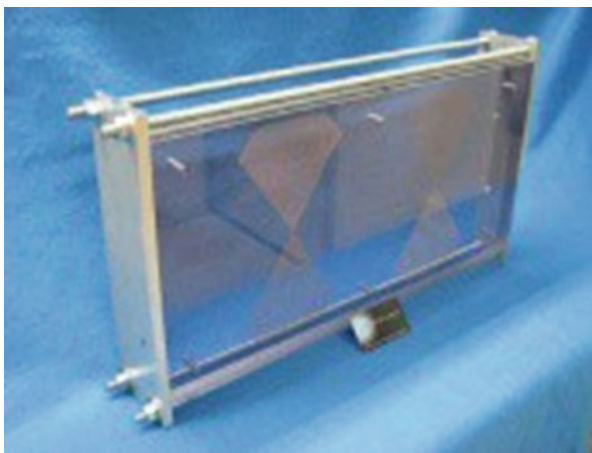


Figure 8.11 indicates that a 35-cm whip antenna can be reduced to a 3-cm height patch antenna with dielectric material of relative permittivity 4.5 as the ground plane. The performance is quite comparable. However, the pattern in the vertical plane is not the same as that of whip antenna. The metamaterial antenna also suffers from heavy weight due to a ceramic ground plane. Thus, application of these types of antenna varies on a case-by-case basis.

In a similar approach, research was conducted to develop transparent antennas for the windshields and windows of tactical vehicles. In this approach, thin-wire mesh antennas were designed to be embedded into the windshields. While the antenna performance results were promising, the transparency of the antennas can become an issue. The design for developing such an antenna is the same as for a thin-wire mesh antenna where the antenna is submerged into the windshield. A slot-antenna array has been designed for implementation into the windshield of a tactical vehicle. Simulations of both four- and six-element array configurations demonstrated good performance in both directionality and gain. Figure 8.12 shows an example antenna embedded inside the windshield.



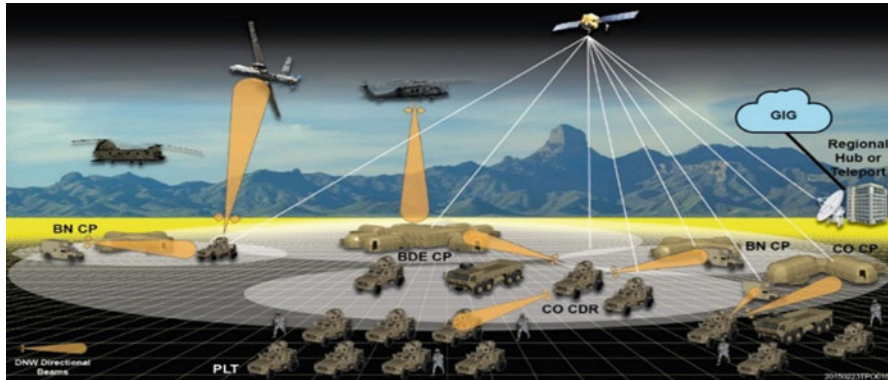


Fig. 8.13 Operational view of directional networking

### 8.5.3 Directional Antennas

As discussed previously, one critical challenge for a tactical-communications system is to provide uninterrupted communication in an RF-contested and congested environment. Additionally, tactical-communications systems often suffer from interference caused by both intended and unintended emissions. This is often compounded by the fact that in many cases tactical communications use MANET which does not rely on any fixed infrastructure. Thus, the approach to establish communications links between mobile nodes has historically been to employ omnidirectional antennas resulting in large coverage areas. The challenge with this approach is that the omnidirectional nature of the coverage area often may cause (or suffer) interference with the neighboring nodes. Research is being conducted to address these issues using sophisticated directional antennas where highly directive array antennas can switch or steer beams for establishing links as per requirements of the real-time cognitive networking management system. These directional networking antennas use novel concepts to sustain communication in the presence of intended and unintended interference.

For tactical communications utilizing a real-time network management system, the scenario is also compounded when the antennas lose situational awareness due to terrain obstructions or other forms of interference. Fortunately, directional antennas with beam-steering or beam-switching capabilities can overcome this challenge. In this scenario, one approach is to gradually broaden the antenna beam to reestablish the communications link. Also, for interference in a particular direction, the directional antennas can steer the antenna patterns to create nulls along the direction of the interference. The concept for directional networking is shown in Fig. 8.13.

The directional networking communications system has two major components, namely, the directional networking waveform and the directional networking antennas. The major advantages of a directional networking system can be summarized as follows:

- Reliability due to the point-to-point nature of the communication,
- Rerouting capabilities of the network to avoid interference,
- Spectrum efficiency,
- Ability to avoid adversary interference by beam switching or steering, and
- Ability to avoid friendly interference via spectrum management.

### 8.5.4 Conformal Directional Antennas

This section describes the development of the conformal antennas with directional capabilities which interface with a tactical-network-management system. It has been observed that a typical omnidirectional whip antenna can be replaced by a set of low-signature distributed quasi-conformal antennas. These antennas are quite efficient and can support a tactical network to function as a part of the cognitive system with beam-switching/beam-steering capabilities. Recent research on beam-switching antennas indicates that, with proper design, such antennas can be highly efficient and cost effective. In addition to that, such beam-steering/switching capability can also be used for sustaining communication in the presence of intended interference from adversaries. However, one of the major challenges for such antennas is to integrate with the directional networking management system providing cognitive capabilities.

Figure 8.14 shows the development of two types of directional antennas. Figure 8.14a shows the distributed switched-beam antennas where there are four elements installed on each side of the vehicle. Each element has eight sectors where

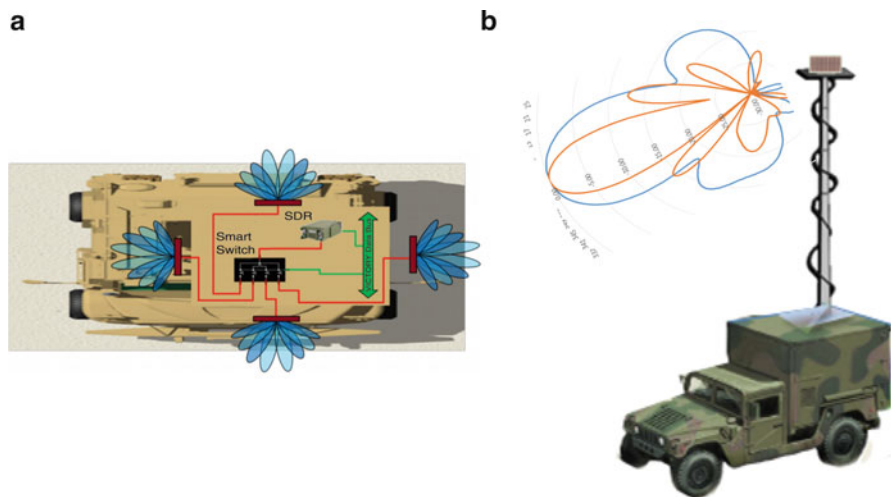


**Fig. 8.14** (a) Distributed and (b) mast-mount directional antennas using beam-switching concept. (a) Four-element array. (b) mast-mount directional antenna

beams can be switched based on cognitive networking requirements. As a result of the low-signature distributed elements, the antennas are less vulnerable to suffer interference from other antennas on the platform. At the same time, the beam-switching nature of the antennas provides a low-cost directional antenna product. The second directional antenna shown in Fig. 8.14b demonstrates similar beam-switching capabilities around 360° of the vehicle with high gain to provide large communications ranges. Again, the beam switching is synchronized according to the cognitive network requirements.

This section discussed a cost-effective beam-switching antenna which can address the challenges of sustaining communications in the tactical environment. Coupled with the cognitive networking management system, such a directional antenna with beam-steering capability will also be able to establish the link when it loses situational awareness due to intended interference or terrain obstruction.

## 8.6 Concluding Remarks

This chapter discussed a few challenges and corresponding novel approaches to combat these issues encountered during tactical communications. As discussed, sustaining communications in a tactical environment is challenged by a highly congested electromagnetic environment. This poses a few relevant challenges in comparison with typical commercial communications. This is also compounded by the dynamic network infrastructure supporting tactical networking waveforms with entirely mobile infrastructure. The chapter discussed the relevant propagation phenomena in the tactical environment and addresses a novel approach to predict almost real-time propagation loss in the rural and urban environments for tactical communication. The chapter also discussed some of the challenging scenarios, such as the presence of multiple collocated antennas on a tactical vehicle, performing omnidirectional communications using low-signature conformal antennas, perturbation of the antenna characteristics in the presence of other structures, sustaining communications in the presence of severe intended interference, and interfacing the antennas with a cognitive networking management system.

**Acknowledgments** The authors acknowledge many of the contributions by the dedicated researchers in the Department of Defense (DoD) laboratories and their academic collaborators where many of the basic ideas described in this chapter have been nurtured. Though the detailed work is not provided, some fundamental concept developed in the academia and at DoD labs demonstrates the success for providing viable solutions.

The authors thank Dr. Magdy F Iskandar, Mr. Stephen R Goodall, Mr. Daniel Duvak, Mr. George Palafox, Dr. Shunhuang Chan, Mr. Frank A Bohn, Mr. Chrysanthou Chrysanthou, Mr. Mathew Cannon, and many others for their research collaboration.

## References

1. US Department of Defense, Joint publication P 6-0. Joint communications system (2015), Available from the Defense Technical Information Center (DTIC), [www.dtic.mil/doctrine/new\\_pubs/jp60.pdf](http://www.dtic.mil/doctrine/new_pubs/jp60.pdf)
2. United States (US) Army Training and Doctrine Command (TRADOC), TRADOC Pamphlet 525-3-1. The U.S. Army operating concept: Win in a complex world (2014), Available from TRADOC [www.tradoc.army.mil/tpubs/pams/TP525-3-1.pdf](http://www.tradoc.army.mil/tpubs/pams/TP525-3-1.pdf)
3. United States (US) Army, Army Capabilities Integration Center (ARCIC), Army Warfighting Challenges (AWFCs) (2016), Available from ARCIC. [www.arcic.army.mil/Initiatives/ArmyWarfightingChallenges](http://www.arcic.army.mil/Initiatives/ArmyWarfightingChallenges). As of 12 Feb 2016
4. United States (US) Department of Defense (DoD) Chief Information Officer (CiO), The DoD electromagnetic spectrum strategy: A call to action (2013). Available from DoD. <http://archive.defense.gov/news/dodspectrumstrategy.pdf>
5. J.D. Parsons, *The Mobile Radio Propagation Channel* (Wiley, Chichester, United Kingdom, 2000)
6. H.L. Bertoni, *Radio Propagation for Modern Wireless Systems* (Prentice-Hall, Upper Saddle River, NJ, 2000)
7. C. Chrysanthou, J.K. Breakall, K.L. Labowski, S.G. Bilen, W.J. Glessner, A simplified analytical urban propagation model (UPM) for use in CJSMP, in *Proceedings of MILCOM 2007 – IEEE Military Communications Conference*, Oct 2007, pp. 1–7
8. J.S. Lu, H.L. Bertoni, C. Chrysanthou, J. Boksiner, Simplified path gain model for mobile-to-mobile communications in an urban high-rise environment, in *Proceedings of 2010 IEEE Sarnoff Symposium*, Apr 2010, pp. 1–6
9. J. Boksiner, Y. Posherstnik, M. Murphy, C. Chrysanthou, T. Marsault, J.P. Millet, Validation of an analytical Urban Propagation Model, in *Proceedings of MILCOM 2016 – IEEE Military Communications Conference*, Baltimore, 2016, pp. 717–722



**Mahbub Hoque** is presently serving as the Chief, International Programs and Global Technology Research in CERDEC (since July 2016). In this capacity, Dr. Hoque leads CERDEC international programs and research and provides strategic vision to conduct research through international collaboration. Prior to that, he served as the division chief (from May 2006 to July 2016) of the Radio Frequency Communications Division of the Space & Terrestrial Communications Directorate (S&TCD) in the US Army's Communications Electronics Research Development and Engineering Center (CERDEC), Aberdeen Proving Ground, Maryland. During the period of June 2007 to June 2016, Dr. Hoque simultaneously served as the Chief Scientist of S&TCD. From June 2012 to January 2013, Dr. Hoque also served as the acting director of S&TCD in 2012. As the chief of an international program, Dr. Hoque coordinates all international research activities and develops the future vision of CERDEC international research for Army mission. As division chief, Dr. Hoque leads his 100+ strong workforce providing engineering solutions in the areas of spectrum management and electromagnetics. The Division operates in several critical technology areas, including the research, development, and engineering of new antenna technologies; modeling and simulation to study and mitigate coupling issues between collocated antennas; metamaterial research and development; and various spectrum management initiatives, et al. During his tenure as the directorate's chief scientist, Dr. Hoque led S&TCD's basic research program. Prior to joining S&TCD in 2000, Dr. Hoque was a director at Telcordia Technologies where he received the 1996 Bellcore Presidential Award for his work analyzing the impacts of radio interference on digital subscriber line technology. He

has authored more than 70 publications and has chaired many sessions in various national and international conferences and symposiums. Dr. Hoque received his PhD in electrical engineering (1983) from University College London, UK, in electromagnetics and antennas. Dr. Hoque has been elevated to IEEE Fellow effective January 2017 for his leadership in developing innovative antennas and advanced tactical-communications technologies. He is the recipient of various awards, including the Commanders Award for Civilian Service and Department of the US Army Superior Civilian Service Award.



**Jeffrey Boksiner** is the Senior Research Scientist (Electronic Warfare Technology) at the US Army CERDEC Intelligence and Information Warfare Directorate (I2WD). In this role, he is responsible for helping to plan, implement research, and develop new concepts for military application of Cyber Electromagnetic Activity (CEMA) with a focus on electronic warfare and offensive cyber and intelligence operations technique. Dr. Boksiner formulates complex research programs, contributes to research, and develops technology road maps to maximize the effectiveness and interoperability of next-generation electronic warfare and cyber capabilities. Prior to this appointment, Jeff was the chief engineer for the RF Communications Division at the CERDEC Space and Terrestrial Communications Directorate (S&TCD). At S&TCD

he led research and development efforts focused on electronic protection of communications systems and efforts on overall spectrum efficiency and effectiveness in the electromagnetic environment. His research activities at CERDEC have included interference modeling, signal detection and sensing, RF propagation modeling, policy-based radio (PBR), dynamic spectrum access (DSA), and various physical-layer technologies. Also, he has carried out basic research on metamaterials and their application to antenna systems for tactical RF applications. Dr. Boksiner holds a PhD in physics from Rutgers University, Piscataway, NJ; and an MS and a BS in electrical engineering from Polytechnic University (now the New York University Tandon School of Engineering), Brooklyn, NY. Prior to joining CERDEC, Dr. Boksiner was with Telcordia Technologies (now part of Ericsson) specializing in spectrum management, electromagnetic compatibility (EMC) focusing on analysis of and protection against electromagnetic pulse, high-power electromagnetic radiation, lightning and high-power transients, as well as electrical and RF safety. He has also held leadership positions in various standards activities including International Telecommunication Union, International Electrotechnical Commission, Institute of Electrical and Electronics Engineers, and the National Fire Protection Association.

# Chapter 9

## Antenna Miniaturization in Mobile Communication Systems

Yue Li, Zhijun Zhang, and Magdy F. Iskander

### 9.1 Introduction

The antenna, as an important component to transmit and receive electromagnetic wave, is widely studied and used in the fields of communication, sensing, positioning, and so on [1]. The performance, e.g., bandwidth and efficiency, of an antenna is determined by its occupied volume [2–4]. For example, in free space, an antenna with a smaller occupied volume, which is defined as a minimum sphere covering the whole body of the antenna, exhibits larger quality factor, i.e., smaller impedance bandwidth. From a theoretical point of view, for an antenna with a given volume in free space, there is a bandwidth (or quality factor) limit, which can be proved either by mode expansion analysis or by numerical simulations [5–6]. Another quantity affecting the antenna performance is the electromagnetic environment, e.g., metal or lossy dielectric. An antenna with closer space from the metallic boundary performs lower radiating efficiency, due to the radiation cancellation from its mirror image [7–8]. Therefore, sophisticated structures are usually designed to prevent the mirror cancellation.

For mobile communication applications, the wireless terminals, such as cell phones, portable access points, laptops, and so on, are usually with small volumes. Antennas mounted inside such terminals must be designed in a relatively small volume with specific shapes and areas. On the other hand, from the aspect of antennas, sufficient bandwidth and radiation efficiency are required by various services with high-speed data rate, e.g., data services in the fourth- or fifth-generation (4G or 5G)

---

Y. Li • Z. Zhang (✉)

Department of Electronic Engineering, Tsinghua University, Beijing 100084, China  
e-mail: [zjzh@tsinghua.edu.cn](mailto:zjzh@tsinghua.edu.cn)

M.F. Iskander

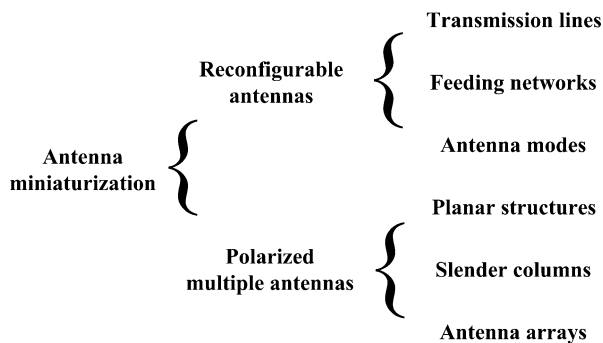
Hawaii Center of Advanced Communications, University of Hawaii at Manoa, Honolulu, HI 96822, USA

wireless communication and virtual reality (VR). Therefore, a contradiction appears between the performance and volume for antenna design. In other words, it is still a challenge to design an antenna with good bandwidth or efficiency in a small-volume mobile terminal [8].

Antenna miniaturization is an important topic for antenna or multiple-antenna design. In the field of electrical small antennas (ESA), metamaterial-inspired structures, i.e., artificial resonance with distributed inductors and capacitors, are widely studied in the minimum sphere of free space to evaluate the theoretical limit [3–4]. ESA is an effective avenue from a theoretical point of view, which can tell us where we can go or cannot go. For practical applications, for a given volume with specific electromagnetic boundaries, there are two basic rules we need to obey: First, we should take fully advantage of the volume. Second, we should properly position the antenna according to the boundaries [8]. For example, the part with maximum current density is positioned in the place with the furthest distance away from the electric boundary. The general purpose of antenna miniaturization is to increase the antenna performance without increasing the antenna volume or to reduce the antenna volume without deteriorating the antenna performance.

In this chapter, we briefly introduce several techniques for antenna miniaturization in mobile communication systems based on our recent works. To begin with, we give a classification of the proposed techniques, as illustrated in Fig. 9.1. First, as an opposite direction of conventional static antennas, dynamic antennas with temporal reconfigurable feature are introduced to achieve the antenna miniaturization. Nonlinear active components, e.g., PIN diodes, varactors, and switches, with properly designed bias circuits, are utilized to control the operating states of the reconfigurable antennas [9–11]. Besides the original operating state, additional operating states are built without increasing the antenna volume. By combining the bandwidths of different operating states, a wider bandwidth is achieved. Differently from a typical reconfigurable antenna with switchable structures, the reconfigurable mechanism is utilized in the feeding transmission lines and matching networks. What's more, the operating modes can also be switched, e.g., loop mode, slot mode, antenna inverted-F antenna (IFA) mode. And we aim to utilize such mode

**Fig. 9.1** Classification of the techniques of antenna miniaturization presented in this chapter



reconfigurable mechanism into the mobile handset antenna design. In Sect. 9.2, we give several examples to demonstrate the design strategy.

The second classification of antenna miniaturization techniques is for multiple antennas, e.g., diversity to mitigate the multipath fading or multi-input multi-output (MIMO) systems to increase the channel capacity [12–15]. In our research group, a single dual (i.e., orthogonal)-polarized antenna is utilized to take the place of two space-isolated antennas with identical polarization. In this way, the space between two single-polarized antennas is saved with similar correlation performance. The target for polarized multiple antennas is to achieve orthogonal polarizations in a small volume but with high port isolation. In Sect. 9.3, we show feasible examples of polarized multiple antennas in planar structures for bidirectional radiation patterns and in slender columns for omnidirectional radiation patterns. At the end, the idea of polarized multiple antennas is achieved in the array configurations for high-gain requirement.

## 9.2 Reconfigurable Antennas

With the rapid development of wireless communication systems, the reconfigurable antennas have drawn significant attention for their function-agile properties. There are several types of reconfigurable antennas discussed in recent papers, including radiation-pattern-reconfigurable, polarization-reconfigurable, and frequency-reconfigurable antennas for different purposes. The basic idea of reconfigurable antennas is to build other operating states based the original antenna body, without adding extra structures [16–18]. It is more important to achieve several operating states for antenna miniaturization. By introducing additional operating states or modes, the performance of the antenna can be enhanced, e.g., widening the bandwidth. Once again, the overall volume of antenna should not be enlarged. Keeping these rules in mind, in this section, we show some examples with new reconfigurable techniques, e.g., reconfigurable transmission line for multiple modes feed [19], reconfigurable matching network [20–21] for wide impedance bandwidth, and reconfigurable mode switch [22] for mobile handset applications.

### 9.2.1 Reconfigurable Transmission Lines

Transmission lines are utilized to feed the antennas. The most common feed mode is the transverse electromagnetic (TEM) mode with the merit of zero cutoff frequency and nearly frequency-invariant characteristic impedance. Here, we require a dual TEM-mode transmission line structure for reconfigurable configuration. As shown in Fig. 9.2, the coplanar waveguide (CPW) transmission line supports two orthogonal modes: the odd mode and the even mode. For the odd mode in Fig. 9.2a, the electric potential is added between the inner and outer conductors of the CPW,



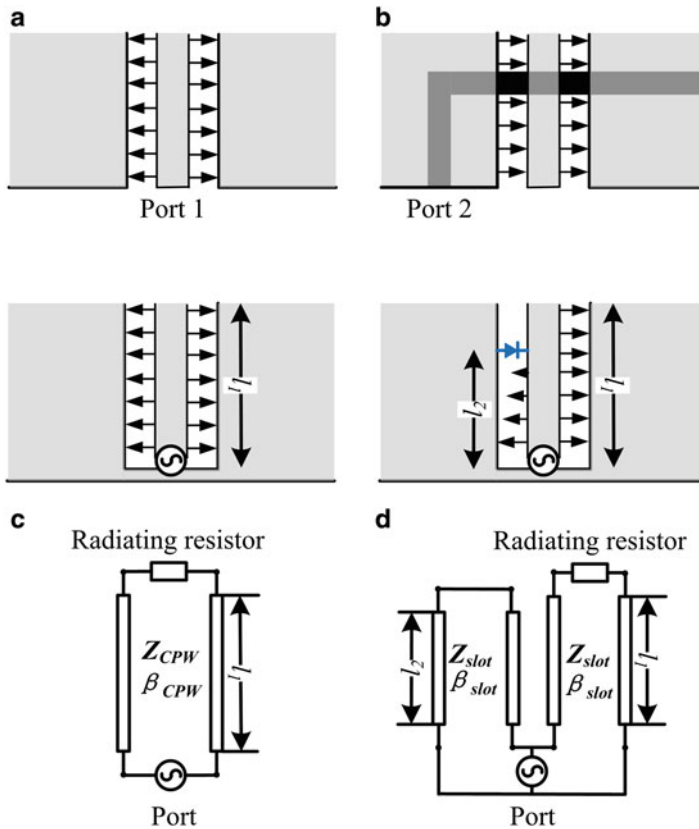


**Fig. 9.2** General diagrams of the CPW-to-slotline reconfigurable transmission lines: (a) odd mode of CPW transmission line; (b) even mode of CPW transmission line, this mode can be treated as a slot transmission line; circuit model of the CPW-to-slotline reconfigurable transmission line (c) without switch (switch is “OFF”; this mode is operating as the CPW transmission line); and (d) with switch (switch is “ON”; this mode is operating as the slot transmission line with a matching branch) © [2010] IEEE. Reprinted, with permission, from Ref. [35] © [2011] IEEE. Reprinted, with permission, from Ref. [19])

and the outer conductors on both sides of the inner conductor are usually connected by air bonding wires (over the inner conductor) to make sure of the single mode operation. The characteristic impedance is determined by the width of the inner conductor and the gap between the inner and outer conductors. This odd mode is the typical CPW operating mode. For the even mode in Fig. 9.2b, the electrical potential is added between the two outer conductors of the CPW, which is operating as a slot transmission line without considering the existence of inner conductor. A capacitive-coupled microstrip line on the back side of the substrate is usually adopted to excite the even odd. The odd and even modes of the CPW are with intrinsic orthogonality, making sure of high isolation between Port 1 and Port 2.

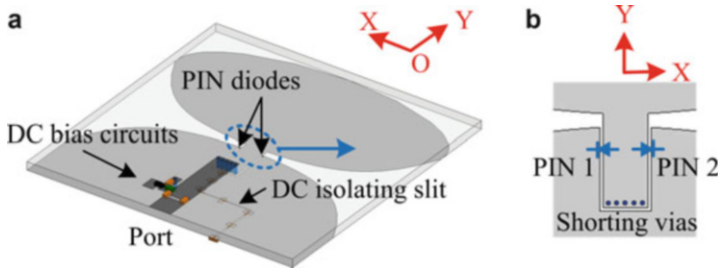


**Fig. 9.3** Example of a pattern-reconfigurable antenna using the CPW-to-slotline reconfigurable transmission lines: (a) perspective view with bias circuits of PIN diodes and (b) zoom-in view of the PIN diodes configuration in the dashed circuit of (a)

Inspired by the dual TEM-mode operation of the CPW, we have proposed a CPW-to-slotline reconfigurable transmission line by switching the odd mode (i.e., CPW mode) and even mode (i.e., slot mode), which are illustrated in Figs. 9.2a and b [19]. As shown in Fig. 9.2c and d, the proposed structure consists of a typical 50-ohm CPW with a single port and a PIN diode on the left slot of the CPW. By controlling the “ON” and “OFF” of the single PIN diode, the CPW mode and the slot mode can be switched to feed different radiating apertures. The most important issue is that the two operating states of the transmission line share the same CPW structure, without adding extra area or volume. As shown in Fig. 9.2c, when the PIN diode is “OFF,” it operates as a typical CPW transmission line. As shown in Fig. 9.2d, when the PIN diode is “ON,” the right slot of CPW is used as the transmission line to feed the radiating structure and the left slot operates as a shorting branch (i.e., a shunt inductive or capacitive element) to match the impedance of the right slot by tuning the position of the PIN diode. Therefore, it operates as a matched slot transmission line.

Figure 9.3 presents an example of the proposed CPW-to-slotline reconfigurable transmission line. The geometry of the antenna and the bias circuit of the PIN diodes is shown in Fig. 9.3a, and the zoom-in view of the PIN diodes is shown in Fig. 9.3b. Two symmetrically positioned PIN diodes are utilized to achieve four switchable feed modes. First, when PIN 1 and PIN 2 are both “OFF,” the CPW transmission line is shorted with no feed. Second, when PIN 1 is “OFF” and PIN 2 is “ON,” the left slot transmission (LS feed) is achieved to feed the left Vivaldi slot aperture for the beam steering to  $-X$  direction. Likewise, when PIN 1 is “ON” and PIN 2 is “OFF,” the right slot transmission (RS feed) is achieved to feed the right Vivaldi slot aperture for the beam steering to  $+X$  direction. As the fourth feed mode, when PIN 1 and PIN 2 are both “OFF,” the typical CPW transmission line (CPW feed) feeds the monopole structure to achieve omnidirectional radiation pattern.

The performance of the antenna in Fig. 9.3 is illustrated in Fig. 9.4, including the reflection coefficients and radiation patterns. The simulated and measured reflection coefficients of LS feed, RS feed, and CPW feed transmission line modes are shown in Figs. 9.4a and b. The overlapped  $-10$ -dB measured band for three feed modes

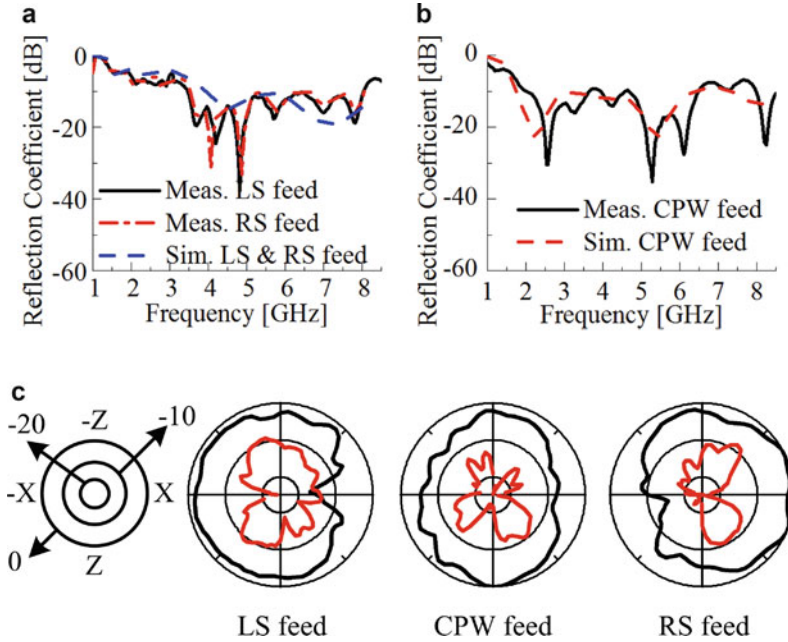


**Fig. 9.4** Antenna performance with the CPW-to-slotline reconfigurable transmission lines: (a) simulated and measured reflection coefficients of LS and RS feeds; (b) simulated and measured reflection coefficients of CPW feed; (c) measured normalized radiation patterns at 5 GHz of LS, RS, and CPW feeds, the *black curve* is co-polarization, and the *red curve* is cross-polarization (© [2011] IEEE. Reprinted, with permission, from Ref. [19])

is 3.53–6.49 GHz, which contains the operating frequency of the proposed antenna with the CPW-to-slotline reconfigurable transmission line. The radiation pattern at 5 GHz is illustrated in Fig. 9.4c. Agreeing well with the above discussion, the  $-X$  and  $+X$  directional beam steering are achieved through the LS and RS feeds, and an omnidirectional pattern appears for the CPW feed. The detailed dimensions and experiment data are provided by Li et al. [19]. From this example, by adding two PIN diodes, two extra operating states with different radiation patterns are achieved without increasing the antenna volume.

## 9.2.2 Reconfigurable Matching Networks

Input impedance is a significant concept in the development of antennas. Antennas with different structures are described by a simple but important complex number, which is named as input impedance. The reflection coefficient at the antenna feed port is determined by the values of the input impedance and the characteristic impedance of the transmission line. And the input impedance is

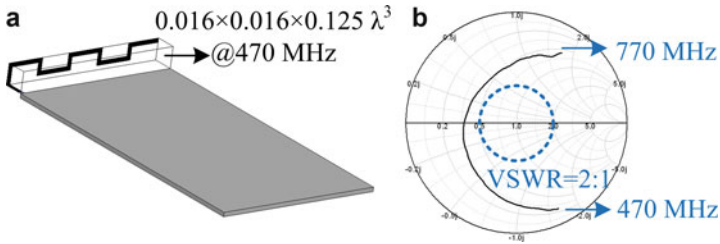


**Fig. 9.5** An example of compact and mismatched antenna in mobile terminals: (a) perspective view, the antenna is inside a rectangular electrical-small volume; (b) input impedance curve on Smith chart of the antenna in (a), operating from 470 to 770 MHz (© [2010] IEEE. Reprinted, with permission, from Ref. [20])

significantly affected by the antenna volume. An antenna with electrical small volume, i.e., a quarter of wavelength, exhibits that the input impedance is with a large imaginary part and a small real part (i.e., radiating resistance for the lossless case). Therefore, it is difficult to use a typical transmission line with a real value of the characteristic impedance to match the input impedance with small antenna volume. Therefore, the impedance matching method is widely studied and adopted for antenna miniaturization based on distributed or lumped inductive and capacitive elements.

In this section, we aim to adopt the reconfigurable mechanism into the impedance matching networks, developing the concept of reconfigurable matching networks [20–21]. In this concept, the nonlinear active components are integrated with the matching elements, e.g., inductors and capacitors, providing multiple matching states. Here, as an example to verify the idea of reconfigurable matching networks, we aim to match an antenna in a volume-limited mobile terminal, e.g., integrated services digital broadcasting-terrestrial (ISDB-T) handset. As shown in Fig. 9.5a, the antenna is mounted in the clearance of the ground plane with a relative small volume of  $0.016\lambda \times 0.016\lambda \times 0.125\lambda$  ( $\lambda$  is free-space wavelength at 470 MHz). The required band of ISDB-T is from 470 to 770 MHz. Due to the small-volume property, the antenna is impedance matched very badly. The impedance curve of the antenna in Fig. 9.5a on the Smith chart is shown in Fig. 9.5b. Briefly speaking, we aim to move the impedance curve into the matching circuit with voltage standing wave ratio (VSWR) of 2:1 for the overall band from 470 to 770 MHz. It is impossible to match over such a wide bandwidth (fractional bandwidth of 48.3%) using a simple T- or  $\pi$ -shaped matching circuits. This is the reason why we proposed the reconfigurable matching networks with multiple matching states.

The multiple matching states are described as following: first, the impedance curve is divided into four sub-bands, Band 1 to Band 4, as shown in Fig. 9.6a. Then, we match each sub-band using a simple two-elements matching circuit. As illustrated in Figs. 9.6b and c, four different matching circuits are utilized to match the curves in Band 1 to Band 4. For example, for the impedance curve in Band 1, we use a series inductor and a shunt inductor. If we carefully examine the four

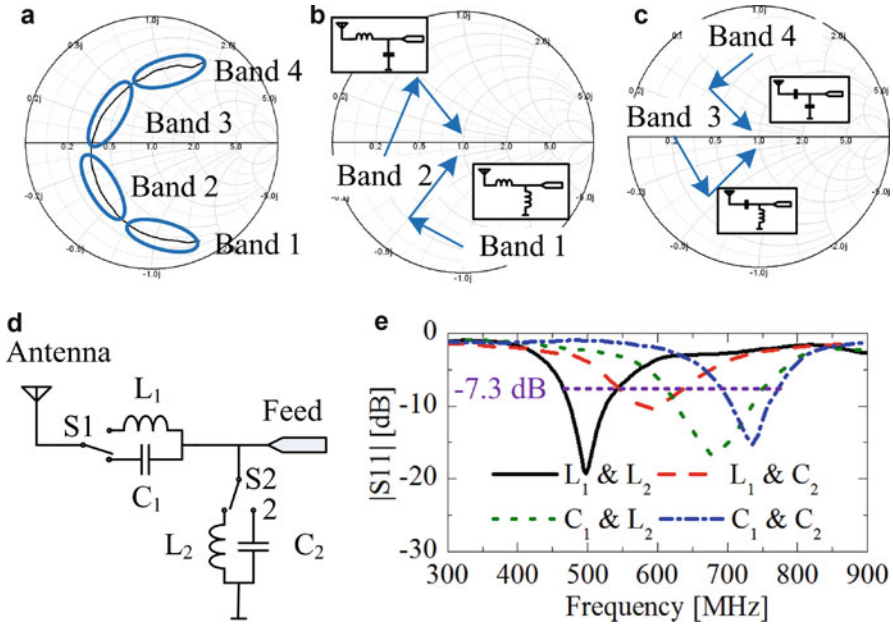


**Fig. 9.6** Reconfigurable matching networks with discrete matching states based on switches: (a) four sub-bands of the impedance curve from Fig. 9.5; (b) and (c) four matching circuits for four sub-bands in (a); (d) circuit diagram of the reconfigurable matching networks based on the circuits shown in (b) and (c); there are two switches (S1 and S2) used to control the four matching states; (e) reflection coefficients of the antenna in Fig. 9.5 with the reconfigurable matching networks in (d) © [2010] IEEE. Reprinted, with permission, from Ref. [20])

matching circuits in Figs. 9.6b and c, an interesting arrangement can be found that the series inductor has been used twice, i.e., in Band 1 and Band 2; the series capacitor has also been used twice, i.e., in Band 3 and Band 4. Likewise, the shunt inductor has been used in Band 1 and Band 3, and the shunt capacitor has been used in Band 2 and Band 4. Therefore, we can use only four components to achieve four different matching states, which are controlled by two switches, as shown in Fig. 9.6d. Next, we use gradient optimization to determine the value of  $L_1$ ,  $L_2$ ,  $C_1$ , and  $C_2$ , and the detailed procedures are provided by Li et al. [20]. Using the value of  $L_1 = 10.3$  nH,  $L_2 = 15.6$  nH,  $C_1 = 4.7$  pF, and  $C_2 = 4.6$  pF, the unmatched impedance curve in Fig. 9.6a is matched with a reflection coefficient of  $-7.3$  dB, as illustrated in Fig. 9.6e, by combining the four matching states for four sub-bands.

Besides the discrete states of reconfigurable matching networks, we also design the continuous states to achieve even wider bandwidth. Instead of using PIN diodes or switches, variable capacitors, i.e., varactors, are usually adopted into the reconfigurable matching networks. The identical antenna in Fig. 9.5 is used here for continuous states of impedance matching and compared with discrete states of

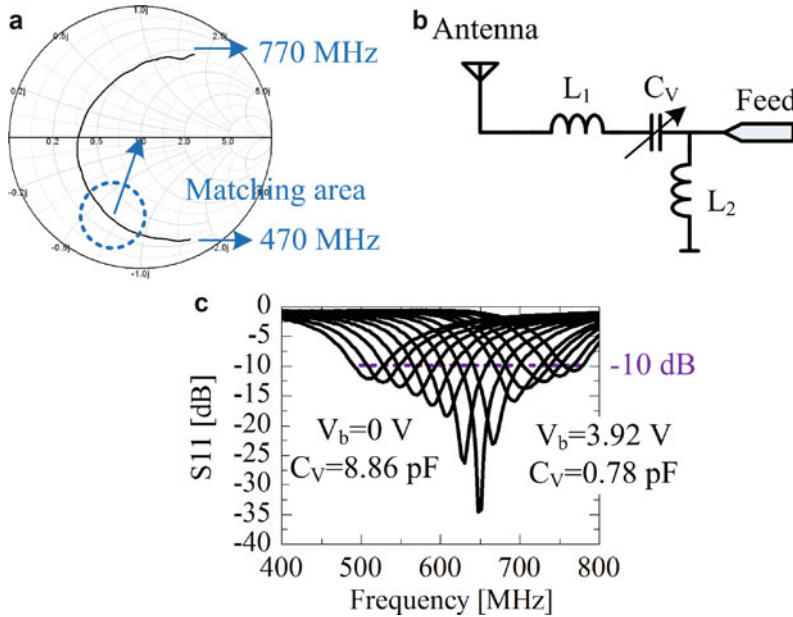


**Fig. 9.7** Reconfigurable matching networks with continuous matching states based on varactors: (a) matching strategy, the curve inside the *blue circle*, i.e. matching area, can be matched by using a shunt inductor; (b) circuit diagram of reconfigurable matching networks in (a); (c) reflection coefficients of the antenna in Fig. 9.5 with the reconfigurable matching networks in (b) (Reprinted from Ref. [21], with the permission of John Wiley & Sons, Inc.)

impedance matching in Fig. 9.6. The general idea of continuous states of impedance matching is shown in Fig. 9.7a; the impedance curve inside the matching area (expressed by blue dashed circle) can be moved to the matching points by a shunt inductor. Therefore, we aim to move the overall curve into the matching area by a series varactor. For the lower band outside the matching area, e.g., 470 MHz, another series inductor is needed. Based on the above analysis, the reconfigurable matching networks with continuous matching states is shown in Fig. 9.7b. The values of used components are  $L_1 = 15$  nH,  $L_2 = 22$  nH, and varactors is 8.86 pF with a bias voltage of 0 V and 0.78 pF with a bias voltage of 3.92 V. By tuning the bias voltage, the impedance curve in Fig. 9.7a can be matched continuously. By combining all the matching states, the overall band of 470–770 MHz can be matched with a reflection coefficient smaller than  $-10$  dB, as shown in Fig. 9.7c [21]. From the discussion of the discrete and continuous states of reconfigurable matching networks, it is theoretically possible to achieve good impedance matching for volume-limited antennas as a feasible technique for antenna miniaturization in mobile communication systems.

### 9.2.3 Reconfigurable Antenna Modes

In this section, we talk about another technique of reconfigurable antenna by switching the antenna modes. With the rapid development of mobile antennas, it is possible to achieve miniaturization in a handset terminal. Different antenna modes are utilized for the internal antenna design in the mobile handset applications, such as inverted-F antennas (IFA), loop antennas, and slot antennas. Our idea is to adopt the reconfigurable mechanism into the multiband antenna designs, supporting various wireless services. The challenge is still the small volume of the antenna inside a handset, which limits the operating bandwidth. Here, additional operating modes are constructed based on the original mode. In recent studies, the reconfigurable strategy is becoming more and more popular in the handset antenna design, especially for the smartphone applications.

To begin with, a brief review of loop antennas inside a handset is presented here. As discussed in recent literature, loop antennas have been widely adopted for mobile handset due to their merits of wide bandwidth, ease of mode control, and self-balance of the current [23–26]. The loop antenna is designed as folded inverted conformal antenna in several commercial products. As an improved technique, the tuning pad proposed in Refs. [23, 24] shows the ability to enhance the impedance matching by controlling the higher modes. In our work, we modify the loop antenna into other modes, such as IFA mode, by adding PIN diodes. A general schematic of the loop-IFA reconfigurable antenna is shown in Fig. 9.8a. A PIN diode is integrated in the loop structure with a feeding point and a shorting point. When the PIN diode is “ON,” as shown in Fig. 9.8b, the antenna operates as a typical loop mode, and the branch between the feeding and shorting points behaves as a matching bridge for impedance matching of the loop mode. When the PIN diode is “OFF,” as shown in Fig. 9.8c, the antenna operates as an IFA antenna with a parasitic branch. By tuning the distance between the feeding and shorting points, the impedance matching for both the loop mode and IFA mode is achieved. By combing the operating bands of the loop mode and IFA mode, a relatively wide bandwidth is achieved to cover the different mobile-service bands. Once again, the importance of mode reconfigurable antenna in Fig. 9.8 is to achieve additional modes without increasing the volume of the antenna.

An example of antenna design for mobile applications is given based on the idea of the loop-IFA reconfigurable mechanism, as shown in Figs. 9.9a and b. The volume of the antenna is only  $0.013\lambda \times 0.013\lambda \times 0.16\lambda$  ( $\lambda$  is free-space wavelength at 800 MHz). Figures 9.9c and d present the impedance bandwidth and radiating efficiency of the loop and IFA moods. The combined bandwidth is able to cover seven mobile-service bands, including the Global System for Mobile Communications (GSM850, 824–894 MHz; GSM900, 880–960 MHz), the Global Positioning System (GPS, 1575 MHz), the Digital Cellular System (DCS: 1710–1880 MHz), the Personal Communication System (PCS, 1850–1990 MHz), the Universal Mobile Telecommunication System (UMTS, 1920–2170 MHz), and the

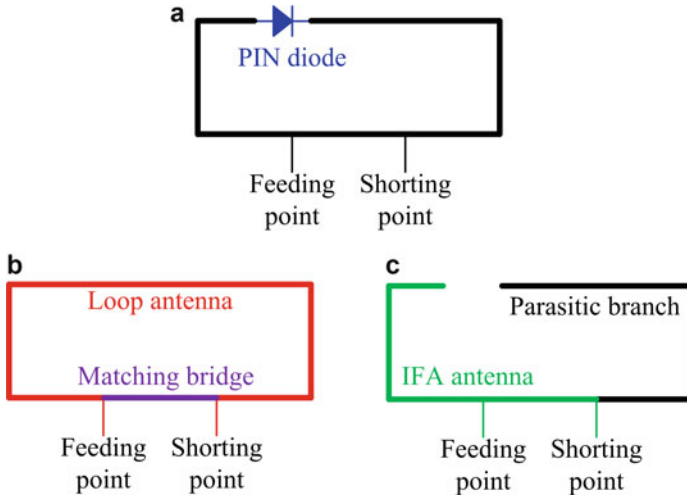


**Fig. 9.8** Reconfigurable antenna structures between loop antenna and IFA antenna. **(a)** General structure of the reconfigurable antenna controlled by a PIN diode; **(b)** PIN diode is “ON”; the reconfigurable structure operates as a loop antenna (red color) with a matching bridge (purple color); **(c)** PIN diode is “OFF”; the reconfigurable structure operates as an IFA antenna (green color) with a parasitic branch (black color)

Wireless Local Area Networks (WLAN, 2400–2484 MHz), with the efficiency higher than 47.4%. Detailed information of this antenna is provided by Li et al. [22].

### 9.3 Polarized Multiple Antennas

For mobile communication systems, another effective way to increase the data rate is using the multiple-antenna systems, as diversity or MIMO. For the application as diversity, the multipath fading is mitigated to keep a stable performance of the antennas. For MIMO systems, multiple antennas are utilized to increase the channel capacity, i.e., spectral efficiency. In this section, we utilize the polarization property of the antennas to build polarized multiple-antenna systems. Generally speaking, the polarized multiple antennas can be treated as a single antenna to support multiple orthogonal polarizations, such as the dual-polarized antennas and the tri-polarized antennas. For example, a dual-polarized antenna is used to take the place of two spatially segregated antennas with identical polarizations, saving the space between them [27–30]. For the volume-limited systems, dual-polarized antennas are good candidate to enhance the system performance, exhibiting exciting possibilities for multiple-antenna miniaturization. In this section, we achieve dual-polarized antenna using different structures, such as planar and column structures [31–34]. What’s more, the dual-polarized strategy is also adopted in the array design, i.e., dual-polarized antenna array, for high-gain requirement.



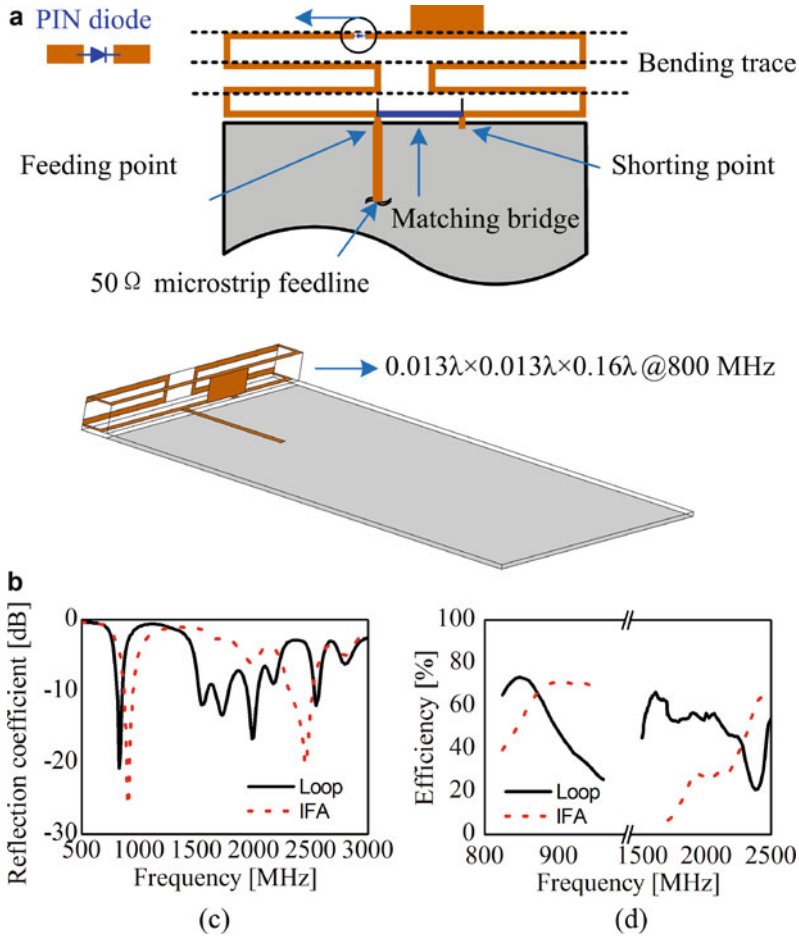


**Fig. 9.9** Antenna design based on the idea in Fig. 9.8. **(a)** Expanded view of the loop-IFA reconfigurable antenna used in mobile handset; **(b)** perspective view of the antenna in **(a)**; **(c)** reflection coefficient; and **(d)** efficiency of the loop and IFA modes of the antenna in **(a)**

### 9.3.1 Dual-Polarized Antennas in Planar Structures

Next, we introduce some interesting planar structures to achieve dual-polarized antennas. To achieve dual orthogonal polarizations sharing the same radiating aperture, we analyze the dual-polarized planar structures from the mode point of view. From symmetry, a rectangular slot or loop is a feasible candidate to support dual orthogonal and degenerate modes, as shown in Fig. 9.10. As shown in Figs. 9.10a and b, a rectangular slot has two mutually orthogonal basic modes, a vertical polarized half-wavelength mode and a horizontal polarized half-wavelength mode. These two modes operate simultaneously in the identical radiating aperture with

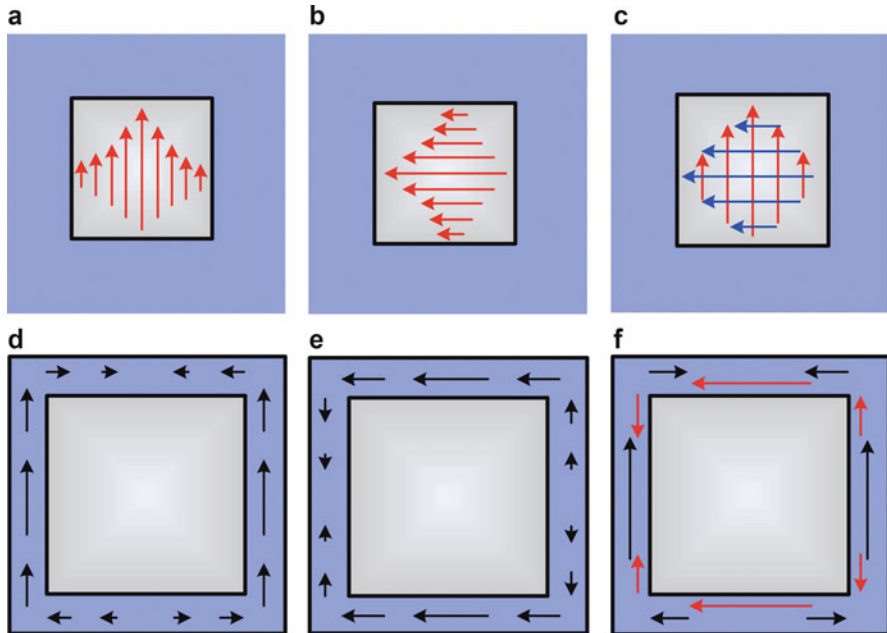


**Fig. 9.10** Orthogonal modes for dual-polarized antennas. (a) Vertical and (b) horizontal polarized half-wavelength modes inside a slot, and (c) dual-polarized modes configuration inside a slot as a dual-polarized antenna. (d) Vertical and (e) horizontal polarized one-wavelength modes along a loop and (f) dual-polarized modes along a loop as a dual-polarized antenna

high port isolation, as shown in Fig. 9.10c. Similarly, the dual orthogonal and degenerate modes are also provided by the rectangular loop structures, a vertical polarized one-wavelength mode shown in Fig. 9.10d and a horizontal polarized one-wavelength mode shown in Fig. 9.10e, operating simultaneously along the same loop with high port isolation, as shown in Fig. 9.10f.

Next, we show how to design dual-polarized planar antennas based on the distributions illustrated in Figs. 9.10c and f. Based on the orthogonal polarizations in Fig. 9.10c, a dual-mode slot antenna is proposed for 2.4-GHz Wireless Local Area Networks (WLAN) applications, as expressed in Fig. 9.11a [35]. The proposed antenna consists of a dual-mode slot aperture and a dual-mode CPW feed structure with two ports (Port 1 and Port 2). When the antenna is fed through Port 1, the CPW transmission line operates with the even mode to excite the horizontal polarization of Fig. 9.10b. When the antenna is fed through Port 2, the CPW transmission line operates with the odd mode to excite the vertical polarization of Fig. 9.10a. The measured S-parameters are illustrated in Fig. 9.11b and agree well with the simulations: the measured bandwidths of  $-10$ -dB reflection coefficient are 670 and 850 MHz for the horizontal and vertical polarizations, respectively. For the WLAN frequency band from 2.4 to 2.48 GHz, the isolation between two ports is lower than  $-32.6$  dB, which means the dual polarizations can be used as a dual-antenna system

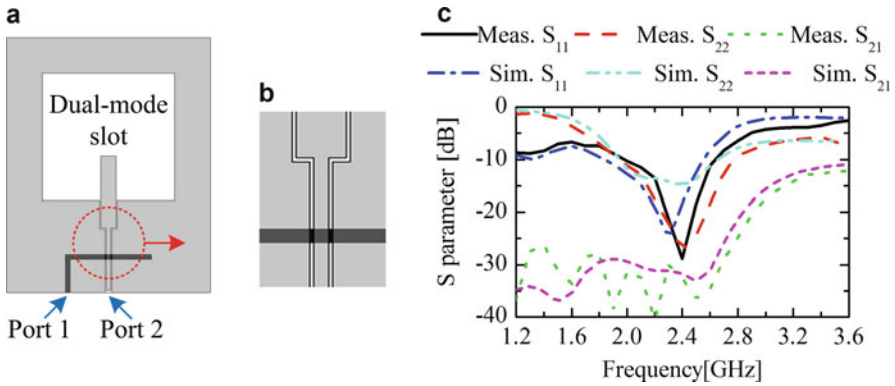


**Fig. 9.11** Polarized dual antennas using the dual-mode slot in Fig. 9.10c. (a) General structure of the dual-polarized slot antenna with Port 1 and Port 2; (b) simulated and measured S-parameters of the antenna in (a) (© [2010] IEEE. Reprinted, with permission, from Ref. [35])

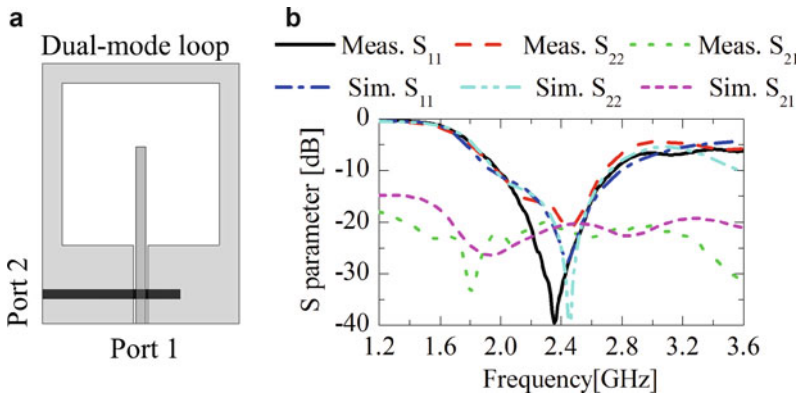


**Fig. 9.12** Polarized dual antennas using the dual-mode loop in Fig. 9.10f. (a) General structure of the dual-polarized loop antenna with Port 1 and Port 2; (b) simulated and measured S-parameters of the antenna in (a) (© [2011] IEEE. Reprinted, with permission, from Ref. [36])

to enhance the communication quality as polarization diversity antenna or MIMO antenna systems. It is worthy to mention that the overall area of the antenna is only  $100 \times 80 \text{ mm}^2$ . The detailed dimension and other performances of the dual-mode slot antenna are provided by Li et al. [35].

In order to achieve the high-isolated dual polarizations in a smaller area, the structure in Fig. 9.10f is utilized to operate as a dual-mode loop antenna, as shown in Fig. 9.12a [36]. The feed structure is similar as that of dual-mode slot antenna in Fig. 9.11a, with two feed ports, including Port 1 and Port 2 for the odd and even modes of CPW transmission line, respectively. The operating principle is also similar to that of the dual-mode slot antenna. When fed through Port 1, the antenna operates at one-wavelength mode with the vertical polarization of Fig. 9.10d. When

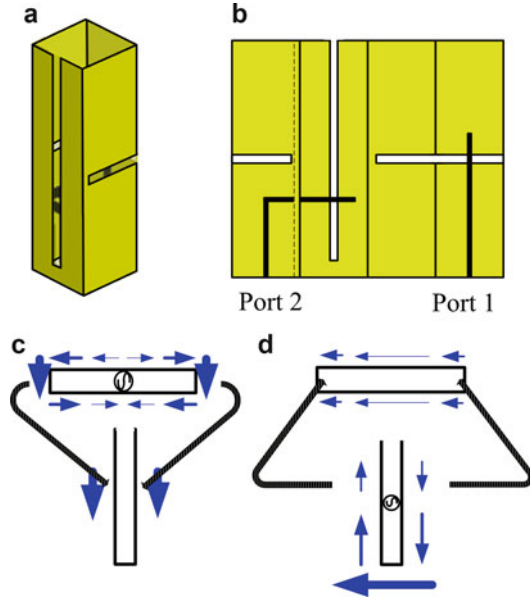
fed through Port 2, the antenna operates at another one-wavelength mode with the horizontal polarization of Fig. 9.10e. We also show the simulated and measured S-parameters in Fig. 9.12b. The measured  $-10$ -dB bandwidths of reflection coefficient are 770 and 730 MHz for the vertical and horizontal polarizations, and the isolation between two ports is lower than  $-21.3$  dB in the WLAN frequency band from 2.4 to 2.48 GHz. The overall area of the antenna is  $53 \times 40$  mm<sup>2</sup>, only 26.5% of the area of the dual-mode slot antenna in Fig. 9.11a. The isolation between two ports is  $-21.3$  dB, lower than the dual-mode slot antenna, but still acceptable for practical usage. The detailed dimension and other performances of the dual-mode loop antenna are provided by Li et al. [36].

### 9.3.2 Dual-Polarized Antennas in Slender Columns

Antennas with planar structures provide bidirectional patterns, and omnidirectional patterns can be achieved by a cylindrical or columnar structure. Here, we introduce the dual-polarized antennas in a slender columnar structure for horizontally omnidirectional coverage. Various techniques are used to achieve omnidirectional radiation patterns with vertical and horizontal polarizations. For vertical polarization, it is trivial by using a coaxial collinear structure with different types of elements, e.g., the microstrip and the dipoles [37–40]. For horizontal polarization, a magnetic dipole (small loop with a uniform current distribution) can be used. However, the impedance of small loop is difficult to match due to its small volume. Other sophisticated metastructures are employed, including the Alford-loop-structure and the left-handed loading loop [41–43]. We try to combine the omnidirectional vertical and horizontal polarizations in polarized dual-antenna systems, but the overall volume is usually large and not suitable for the volume-limited wireless communication systems.

We have proposed a dual-slot structure warped on a slender column to behave as a dual-polarized omnidirectional antenna, as shown in Figs. 9.13a and b [44]. A quarter-wavelength vertical notch, i.e., open-ended slot, is positioned in the front side of the column. The notch is excited by a conductive coupled microstrip line (fed through Port 2) to provide horizontal polarization. Due to the small cross section in the azimuthal plane, the wave from the notch can radiate to the back side, achieving a near omnidirectional pattern. By decreasing the area of the azimuthal cross section, the gain variation in the azimuthal plane is smaller but the impedance matching is deteriorated. A trade-off is carried out in the optimization of the antenna dimensions. Another half-wavelength slot is positioned on the other three sides of the column, providing vertical polarization. The horizontal slot is also excited by a conductive coupled microstrip line (fed through Port 1). The overall volume is only  $0.096\lambda \times 0.096\lambda \times 0.336\lambda$  ( $\lambda$  is free-space wavelength at 2.4 GHz). In this design, we aim to construct the dual-polarized antenna to cover the 2.4-GHz WLAN band with minimum azimuthal gain variation for omnidirectional coverage.

**Fig. 9.13** Geometry and operating principle of the polarized dual antenna in a slender column. (a) Perspective view of the polarized dual antenna in a slender column; (b) expanded view of the antenna in (a); mutual coupling between two slots in (a) and (b) when the antenna is fed through (c) Port 1 and (d) Port 2



One challenge is the port isolation in such a small volume. However, in our structure, the vertical notch and the horizontal folded slot are arranged in the special orthogonal positions. The currents along the colocated slots are spatially symmetric for intrinsic high port isolation, which can be explained from the current distribution shown in Figs. 9.13c and d. As shown in Fig. 9.13c, when the antenna is fed through Port 1, the horizontal slot operates at the one-wavelength current mode (i.e., half-wavelength slot mode). There are current nulls in the middle of the slot. The peak current at both slot ends is inphase. The currents coupled to the vertical notch edges are also inphase. Therefore, little energy can be coupled to Port 2 from Port 1. When the antenna is fed through Port 2, as shown in Fig. 9.13d, the currents along the two edges of the vertical notch are out-phase. The coupled currents to the horizontal slot are shown in Fig. 9.13d: along the upper and lower edges of the horizontal slot, the currents are inphase and weak. Therefore, little energy can be coupled to Port 1 from Port 2. Spatial distributions of the magnitude of the magnetic field inside the vertical notch and horizontal slot are shown in Figs. 9.14a and b. It is easy to see the modes: a quarter-wavelength mode for vertical notch and half-wavelength mode for horizontal slot. We can see the physical length of the notch is longer than a quarter-wavelength in free space due to impedance matching. The measured S-parameters are illustrated in Fig. 9.14b and agree well with the simulated ones. The 10-dB bandwidths of the reflection coefficient are from 2.34 to 2.72 GHz for vertical polarization when fed through Port 1 and from 2.39 to 2.49 GHz for horizontal polarization when fed through Port 2. In the 2.4-GHz WLAN band of 2.4–2.48 GHz, the isolation between

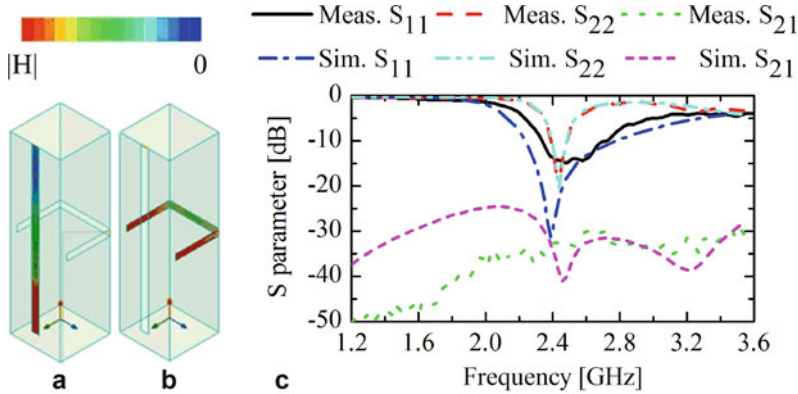


**Fig. 9.14** Magnitude of magnetic field distributions in the dual slots of the antenna in Fig. 9.13a. The antenna is fed through (a) Port 2 and (b) Port 1; (c) simulated and measured S-parameters of dual modes of the antenna as shown in (a) and (b)

Port 1 and Port 2 is lower than  $-32.5$  dB. High port isolation is achieved in such a small volume of  $0.096\lambda \times 0.096\lambda \times 0.336\lambda$ . The detailed dimension and other performances of the dual-polarized antenna wrapped on slender column can be provided by Li et al. [44].

### 9.3.3 Dual-Polarized Antenna Arrays

To increase the gain of the polarized multiple-antenna systems, i.e., compensate for the path loss, dual-polarized antenna array with large number of elements is preferred. In the existing designs, the overall antenna array needs complex feeding networks, e.g., multiple substrate layers for large number of ports. The feeding lines are distributed around the radiating apertures, making it difficult to design a larger-scaled array with more elements.

Here, a nontrivial crossover structures based on CPW transmission lines is proposed to achieve a simple feeding network, using only one layer of substrate [45]. An example of such a crossover is shown in Fig. 9.15a with four ports, operating at 2.4-GHz WLAN band. The red area is the metal on the front side and the blue area is the metal on the back side. The two sides are connected by shorting vias to form a common ground. What we required is that: the CPW transmission line between Port 1 and Port 2 on the front side is with no effect to that between Port 3 and Port 4 on the back side. The simulated S-parameters of the four-port crossover are illustrated in Fig. 9.15b. In the desired band of 2.4–2.48 GHz, the reflection coefficient (i.e.,  $S_{11}$ ) is lower than  $-23$  dB. The transmission coefficient (i.e.,  $S_{21}$ ) is higher than  $-0.1$  dB. The ports isolation (i.e.,  $S_{31}$  and  $S_{41}$ ) is lower than  $-22$  dB. The numerical results

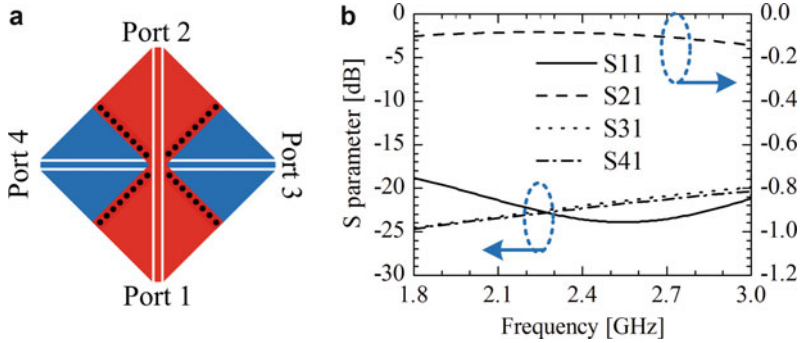
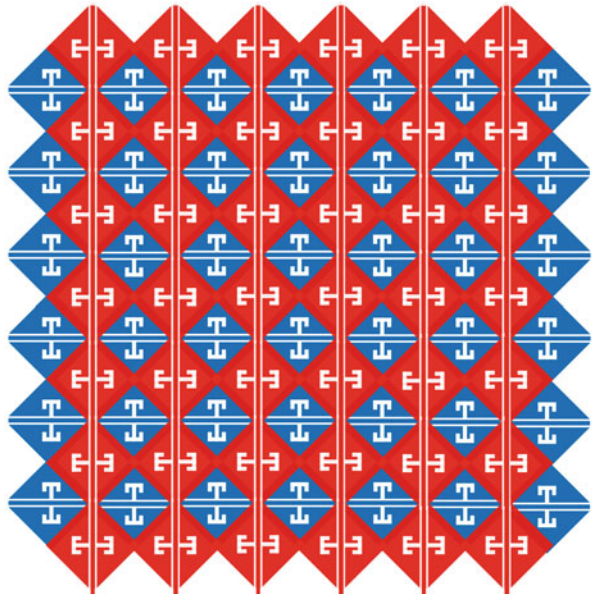


**Fig. 9.15** High-isolated CPW crossover for dual-polarized antenna array. (a) General structure of the 4-port CPW crossover, (b) simulated S-parameters of the 4-port CPW crossover in (a)

**Fig. 9.16** Example of 6×7-element dual-polarized antenna array based on the high-isolated CPW crossover in Fig. 9.15a



reveal that the CPW-based crossover in Fig. 9.15a is with good performance as two isolated channels with orthogonal topological structures, exhibiting the potential to feed spatial orthogonal elements.

In Fig. 9.16, we show an example of 6×7-element dual-polarized antenna array based on the high-isolated CPW crossover in Fig. 9.15a, consisting of two identical 6×7-element single-polarized arrays. For the red area (i.e., on the front side), we have the vertical-polarized antenna array, including six series-fed 7-element sub-arrays. For the blue area (i.e., on the back side), the horizontal-polarized antenna array is achieved by rotating the front array by 90° and positioned in the space of the front array. For the vertical polarized array, each sub-array is series-fed

by the CPW transmission line, and all the sub-arrays are fed by a 1 to 6 power divider. The sub-arrays of the horizontal polarized antenna array are fed by the same method. As shown in Fig. 9.16, the overlapping parts on the front and back sides are connected by a series of shorting vias, identical to the configuration in Fig. 9.15a. Therefore, the overall array, including the radiating apertures and the feeding network, is connected, using a single layer of substrate. For the radiating aperture, a slot with two E-shaped at both ends is fed through the CPW transmission line. To maintain the transmission characteristic of CPW, the length of half slot on each side is nearly half wavelength to achieve a shorting boundary at the CPW edges. By controlling the width of the slot, the radiating energy from a single slot can be tuned. Therefore, we can arrange a desired number of radiating slots by tuning the width of each slot. As another merit of the proposed antenna array, more elements can be added by increasing the element number of a sub-array or adding more sub-arrays, i.e., with the potential to operate as a scalable dual-polarized antenna array with desired gain. In Ref. [45], we fabricated a  $3 \times 2$ -element dual-polarized antenna array for measurement. And the results prove our idea to build a scalable dual-polarized antenna array by using the CPW-based crossover in Fig. 9.15a.

## 9.4 Conclusions

In this chapter, we have provided a brief review of our work in the field of antenna miniaturization in mobile systems. From an interesting insight of the temporal and polarized features of antennas, we have proposed various design strategies to achieve antenna miniaturization, e.g., reconfigurable antennas and polarized multiple antennas. Practical examples are presented to prove the proposed ideas from engineering point of view. For the reconfigurable techniques, the system complexity is still a challenge for practical applications. We can easily integrate one or two switches or tuning elements with the antenna, but it is difficult to use more radio-frequency switches. For the polarized multiple-antenna systems, the array design for higher gain is still needed. The directions for this topic will be large element number (i.e., massive polarized MIMO) and high operating frequency (i.e., millimeter wave). As we can imagine for the future, the reconfigurable antennas with switchable mechanism is a potential candidate for the mobile antenna design, and polarized multiple antenna will be widely adopted for small-volume-based stations, portable accessing points, and so on.

**Acknowledgments** This work was supported by the National Natural Science Foundation of China 61301001, the China Postdoctoral Science Foundation funded project 2015T80084, and the Beijing Excellent Doctoral Dissertation Instructor project 20131000307.



## References

1. C.A. Balanis, *Antenna Theory, Analysis, and Design* (Wiley, Hoboken, NJ, 1997)
2. D.B. Miron, *Small Antenna Design* (Newnes, Burlington, MA, 2006)
3. R.C. Hansen, *Electrically Small, Superdirective, and Superconducting Antennas* (Wiley, Hoboken, NJ, 2006)
4. G. Breed, Basic principles of electrically small antennas. *High Frequency Electronics*, 50–53 (2007)
5. L.J. Chu, Physical limitations of omni-directional antennas. *J. Appl. Phys.* **19**, 1163–1175 (1948)
6. R.C. Hansen, Fundamental limitations in antennas. *Proc. IEEE* **69**, 170–182 (1981)
7. C.A. Balanis, *Advanced Engineering Electromagnetics* (Wiley, New York, 1989), pp. 894–896
8. Z. Zhang, *Antenna Design for Mobile Devices* (Wiley (Asia), Singapore, 2011)
9. Y. Li, Z. Zhang, J. Zheng, Z. Feng, Compact heptaband reconfigurable loop antenna for mobile handset. *IEEE Antennas Wirel. Propag. Lett.* **10**, 1162–1165 (2011)
10. N. Behdad, K. Sarabandi, Dual-band reconfigurable antenna with a very wide tunability range. *IEEE Trans. Antennas Propag.* **54**, 409–416 (2006)
11. Y. Li, Z. Zhang, W. Chen, Z. Feng, Polarization reconfigurable slot antenna with a novel compact CPW-to-slotline transition for WLAN application. *IEEE Antennas Wirel. Propag. Lett.* **9**, 252–255 (2010)
12. J.-M. Molina-Garcia-Pardo, J.-V. Rodriguez, L. Juan-Llacer, Polarized indoor MIMO channel measurements at 2.45 GHz. *IEEE Trans. Antennas Propag.* **56**(12), 3818–3828 (2008)
13. Y. Li, Z. Zhang, J. Zheng, Z. Feng, Channel capacity study of polarization reconfigurable slot antenna for indoor MIMO system. *Microw. Opt. Technol. Lett.* **53**(6), 1209–1213 (2011)
14. D.G. Landon, C.M. Furse, Recovering handset diversity and MIMO capacity with polarization-agile antennas. *IEEE Trans. Antennas Propag.* **55**(11), 3333–3340 (2007)
15. T. Brown, Indoor MIMO measurements using polarization at the mobile. *IEEE Antennas Wirel. Prop. Lett.* **7**, 400–403 (2008)
16. D. Peroulis, K. Sarabandi, L. Katehi, Design of reconfigurable slot antennas. *IEEE Trans. Antennas Propag.* **53**, 645–654 (2005)
17. Y. Li, Z. Zhang, W. Chen, Z. Feng, M. Iskander, A quadband antenna with reconfigurable feedings. *IEEE Antennas Wirel. Propag. Lett.* **8**, 1069–1071 (2009)
18. A. Mak, C. Rowell, R. Murch, C. Mak, Reconfigurable multiband antenna designs for wireless communication devices. *IEEE Trans. Antennas Propag.* **55**, 1919–1928 (2007)
19. Y. Li, Z. Zhang, J. Zheng, Z. Feng, M.F. Iskander, Experimental analysis of a wideband pattern diversity antenna with compact reconfigurable CPW-to-slotline transition feed. *IEEE Trans. Antennas Propag.* **59**(11), 4222–4228 (2011)
20. Y. Li, Z. Zhang, W. Chen, Z. Feng, M.F. Iskander, A switchable matching circuit for compact wideband antenna designs. *IEEE Trans. Antennas Propag.* **58**(11), 3450–3457 (2010)
21. Y. Li, Z. Zhang, W. Chen, Z. Feng, M.F. Iskander, A compact DVB-H antenna with varactor-tuned matching circuit. *Microw. Opt. Technol. Lett.* **52**(8), 1786–1789 (2010)
22. Y. Li, Z. Zhang, J. Zheng, Z. Feng, M.F. Iskander, A compact hepta-band loop-inverted F reconfigurable antenna for mobile phone. *IEEE Trans. Antennas Propag.* **60**(1), 389–392 (2012)
23. Y.S. Shin, S.O. Park, A compact loop type antenna for Bluetooth, S-DMB, Wibro, WiMax, and WLAN applications. *IEEE Antennas Wirel. Propag. Lett.* **6**, 320–323 (2007)
24. Y.W. Chi, K.L. Wong, Internal compact dual-band printed loop antenna for mobile phone application. *IEEE Trans. Antennas Propag.* **55**, 1457–1462 (2007)
25. K.L. Wong, C.H. Huang, Printed loop antenna with a perpendicular feed for penta-band mobile phone application. *IEEE Trans. Antennas Propag.* **56**, 2138–2141 (2008)
26. Y.W. Chi, K.L. Wong, Compact multiband folded loop chip antenna for small-size mobile phone. *IEEE Trans. Antennas Propag.* **57**, 3797–3803 (2008)

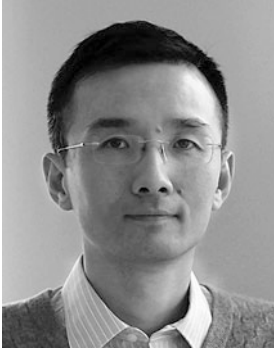
27. Y.X. Guo, K.W. Khoo, L.C. Ong, Wideband dual-polarized patch antenna with broadband baluns. *IEEE Trans. Antennas Propag.* **55**(1), 78–83 (2007)
28. C. Deng, Y. Li, Z. Zhang, Z. Feng, Wideband high-isolated dual-polarized patch antenna using two different balun feedings. *IEEE Antennas Wirel. Propag. Lett.* **13**, 1617–1619 (2014)
29. S.C. Gao, L.W. Li, M.S. Leong, T.S. Yeo, Dual-polarized slot-coupled planar antenna with wide bandwidth. *IEEE Trans. Antennas Propag.* **51**(3), 441–448 (2003)
30. C. Deng, Y. Li, Z. Zhang, Z. Feng, Hexa-band high-isolated dual-polarized loop antenna for mobile communications. *Prog. Electromagn. Res. Lett.* **52**, 121–128 (2015)
31. Y. Li, Z. Zhang, J. Zheng, Z. Feng, Design of dual-polarized monopole-slot antenna with small volume and high isolation. *IEEE Trans. Antennas Propag.* **60**(5), 2511–2514 (2012)
32. Y. Li, Z. Zhang, J. Zheng, Z. Feng, Compact azimuthal omnidirectional dual-polarized antenna using highly isolated co-located slots. *IEEE Trans. Antennas Propag.* **60**(9), 4037–4045 (2012)
33. Y. Li, Z. Zhang, J. Zheng, Z. Feng, A dual-polarized monopole-slot co-located MIMO antenna for small-volume terminals. *Electron. Lett.* **47**(23), 1259–1260 (2011)
34. H. Dyball, MIMO wraps up. *Electron. Lett.* **47**(24), 1304 (2011)
35. Y. Li, Z. Zhang, W. Chen, Z. Feng, M.F. Iskander, A dual-polarization slot antenna using a compact CPW feeding structure. *IEEE Antennas Wirel. Propag. Lett.* **9**, 191–194 (2010)
36. Y. Li, Z. Zhang, Z. Feng, M.F. Iskander, Dual-mode loop antenna with compact feed for polarization diversity. *IEEE Antennas Wirel. Propag. Lett.* **10**, 95–98 (2011)
37. T.J. Judasz, B.B. Balsley, Improved theoretical and experimental models for the coaxial colinear antenna. *IEEE Trans. Antennas Propag.* **37**(3), 289–296 (1989)
38. R. Bancroft, B. Bateman, An omnidirectional planar microstrip antenna. *IEEE Trans. Antennas Propag.* **52**(11), 3151–3153 (2004)
39. F.-R. Hsiao, K.-L. Wong, Omnidirectional planar folded dipole antenna. *IEEE Trans. Antennas Propag.* **52**(7), 1898–1902 (2004)
40. K.-L. Wong, F.-R. Hsiao, T.-W. Chiou, Omnidirectional planar dipole array antenna. *IEEE Trans. Antennas Propag.* **52**(2), 624–628 (2004)
41. C.-C. Lin, L.-C. Kuo, H.-R. Chuang, A horizontally polarized omnidirectional printed antenna for WLAN applications. *IEEE Trans. Antennas Propag.* **54**(11), 3551–3556 (2006)
42. C.-H. Ahn, S.-W. Oh, K. Chang, A dual-frequency omnidirectional antenna for polarization diversity of MIMO and wireless communication applications. *IEEE Antennas Wirel. Prop. Lett.* **8**, 966–969 (2009)
43. A.L. Borja, P.S. Hall, Q. Liu, H. Iizuka, Omnidirectional loop antenna with left-handed loading. *IEEE Antennas Wirel. Prop. Lett.* **6**, 495–498 (2007)
44. Y. Li, Z. Zhang, Z. Feng, M.F. Iskander, Design of omnidirectional dual-polarized antenna in slender and low-profile column. *IEEE Trans. Antennas Propag.* **62**(4), 2323–2326 (2014)
45. Y. Li, Z. Zhang, C. Deng, Z. Feng, M.F. Iskander, 2-D planar scalable dual-polarized series-fed slot antenna array using single substrate. *IEEE Trans. Antennas Propag.* **62**(4), 2280–2283 (2014)



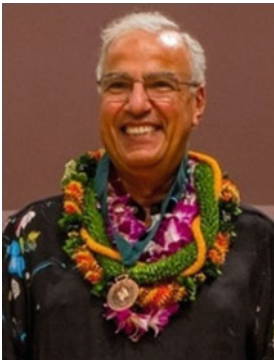
**Yue Li** received the B.S. degree in telecommunication engineering from the Zhejiang University, Zhejiang, China, in 2007, and the Ph.D. degree in electronic engineering from Tsinghua University, Beijing, China, in 2012. In June 2012, he was a postdoctoral fellow in the Department of Electronic Engineering, Tsinghua University. In December 2013, he was a research scholar in the Department of Electrical and Systems Engineering, University of Pennsylvania. He was also a visiting scholar in Institute for Infocomm Research (I<sup>2</sup>R), A\*STAR, Singapore, in 2010, and Hawaii Center of Advanced Communication (HCAC), University of Hawaii, USA, in 2012. Since January 2016, he has

been with Tsinghua University, where he is an assistant professor. He has authored and coauthored over 70 journal papers and over 30 international conference papers and holds 14 granted Chinese patents. He was the recipient of the Young Scientist Awards from URSI AP-RASC 2016, the Young

Scientist Award from EMTS 2016, Best Student Paper Award from ICMMT 2016, Best Paper Award from ISAPE 2016, the Young Scientist Award from URSI General Assembly in 2014, the Outstanding Doctoral Dissertation of Beijing Municipality in 2013, and the Principal Scholarship of Tsinghua University in 2011.



**Zhijun Zhang** received the B.S. and M.S. degrees from the University of Electronic Science and Technology of China, in 1992 and 1995, and the Ph.D. degree from Tsinghua University, Beijing, China, in 1999. In 1999, he was a postdoctoral fellow with the Department of Electrical Engineering, University of Utah, where he was appointed a research assistant professor in 2001. In May 2002, he was an assistant researcher with the University of Hawaii at Manoa, Honolulu. In November 2002, he joined Amphenol T&M Antennas, Vernon Hills, IL, as a senior staff antenna development engineer and was promoted to the position of antenna engineer manager. In 2004, he joined Nokia Inc., San Diego, CA, as a senior antenna design engineer. In 2006, he joined Apple Inc., Cupertino, CA, as a senior antenna design engineer and was promoted to the position of principal antenna engineer. Since August 2007, he has been with Tsinghua University, where he is a professor in the Department of Electronic Engineering. He is the author of *Antenna Design for Mobile Devices* (Wiley, 2011). He served as associate editor of the *IEEE Transactions on Antennas and Propagation* (2010–2014) and *IEEE Antennas and Wireless Propagation Letters* (2009–2015).



**Magdy F. Iskander** is the director of the Hawaii Center for Advanced Communications and professor of Electrical Engineering, University of Hawaii at Manoa. He is co-director of the NSF I/UCRC and a fellow of IEEE (1993). He was the 2002 president of the IEEE AP-S, Distinguished Lecturer, and a program director in the ECCS Division at NSF. Dr. Iskander joined the University of Hawaii in 2002, and prior to that, he was a professor of ECE Department and the Engineering Clinic Endowed Chair Professor at the University of Utah. He received many awards for excellence in research and teaching including the University of Hawaii Board of Regents' Medal for Excellence in Research and Medal for Teaching Excellence, IEEE MTT-S Distinguished Educator Award, IEEE AP-S Chen-To Tai Distinguished Educator Award, Northrop Grumman Excellence in Teaching Award, and others. He has published over 270 papers in journals and books and holds ten patents. He authored/edited several books including the textbook *Electromagnetic Fields and Waves*. He is the founding editor of *Computer Applications in Engineering Education* published by John Wiley & Sons 1992–present. His research has been funded by NSF, NIH, Army Research Office, US Army CERDEC, Office of Naval Research, and corporate sponsors.

# Chapter 10

## Making UWB Antennas Unidirectional: Phase Coherence with an Ultra-Wide Band Frequency Selective Surface Reflector

Yogesh Ranga, Karu P. Esselle, and Ladislau Matekovits

### 10.1 Introduction

Ultra-wide band (UWB) applications have been limited by tough restraints imposed on transmitted power by the Federal Communication Commission (FCC). An improvement of the link-budget, even just by a few dB, is of huge practical importance. Since regulatory limits are defined in terms of the effective isotropic radiated power (EIRP) at the transmitter end, one way to enhance system performance is to increase antenna gain at the receiver end. Many UWB printed monopole and slot antennas proposed in the recent past have more than 106% bandwidth (3.1–10.6 GHz) and bidirectional radiation patterns (see, e.g., Ref. [1]). It is desirable to convert this bidirectional radiation pattern to a unidirectional radiation pattern to increase gain and reduce power wastage. This cannot be achieved over a wide frequency range using a perfect electric conductor (PEC) type reflector.

Recent developments of periodic structures have helped to solve some of the crucial antenna problems. With the possibility of realising an artificial perfect magnetic conductor (PMC) and its in-phase reflection, efficient radiation from antennas placed close to an electromagnetic bandgap (EBG) ground plane [2] has been achieved. In addition, by forbidding the propagation of electromagnetics (EM) waves in certain frequency bands, these EBG structures can be used to block the propagation of waves and/or guide them in a desired direction [2–7]. In the case of narrowband applications, achieving in-phase reflection of an incident plane wave from a mushroom-like high-impedance surface [3] or a uniplanar compact photonic

---

Y. Ranga • K.P. Esselle (✉)

School of Engineering, Faculty of Science and Engineering, Macquarie University, Sydney, NSW, Australia

e-mail: [karu.esselle@mq.edu.au](mailto:karu.esselle@mq.edu.au)

L. Matekovits

Dipartimento di Elettronica e Telecomunicazioni, Politecnico di Torino, Torino, Italy

band-gap (UC-PBG) surface has been demonstrated [7]. Among periodic structures, frequency-selective surfaces (FSSs) and partially reflecting surfaces (PRSs) are good candidates to be employed in conjunction with printed planar antennas [8–10] due to their planar configuration. Such configurations have been extensively studied in the past for enhancing the performance of antennas for both narrowband and broadband operations [8–19].

FSSs are spatial EM filters that exhibit controlled reflection and transmission over a given frequency band to an incident electromagnetic wave [8–10]. Pasian et al. [8] discuss a reconfigurable printed dipole array is examined in the presence of a multilayer FSS. The FSS is positioned in the ground plane of a reflector array, aiming to achieve broadband operation by controlling the phase of the reflected wave. In some recent articles, a FSS has been used as a backing reflector to extend the frequency range of usability. Erdemli et al. [9] discuss another FSS for wideband applications; an FSS has been sandwiched between the antenna and the ground plane, providing an additional reflecting plane for the most critical higher-frequency band. In most of these cases, the FSS is limited to narrowband operation. Dual- and wide-band operations have been considered in some current publications [9], exploiting the potential offered by the association of two different patch elements over a single unit cell, namely, a square loop and a crossed dipole. This design demonstrates a  $-10$  dB transmission bandwidth of 52%.

Further extending this bandwidth to UWB regime, this chapter describes a dual-layer FSS and a four-layer FSS to cover and exceed the FCC-sanctioned 106% UWB bandwidth from 3.1 to 10.6 GHz. These FSSs have been demonstrated as reflectors for few printed UWB antennas, converting bidirectional radiation patterns to unidirectional patterns, and have the potential to be employed as a reflector for any UWB antenna. These surfaces allow a printed UWB antenna to be mounted just above a conducting surface, with negligible effect on the antenna matched bandwidth, and are good candidates for low-profile devices. When a UWB slot antenna was placed above the four-layer compact FSS, gain variation of the antenna was only 0.5 dB over its 110% impedance bandwidth.

The main focus of this chapter is on UWB antenna reflectors. A novel concept of phase coherence over the UWB bandwidth is presented in Sect. 10.2. The design of the reflector is based on the FSS concept. In particular, the desirable phase behaviour over a UWB bandwidth can be achieved by appropriately combining several of such surfaces. The first example is a dual-layer FSS as presented in Sect. 10.3, while the second illustration is a four-layer FSS described in Sect. 10.5. The optimisation of the dual-layer FSS, its oblique-incidence performance, experimental implementations and measurements results are presented in Sects. 10.3.1 and 10.3.2. This FSS has a 133% transmission bandwidth, which seems to be the best available in the scientific literature, that far overcomes its competitors, who stop at a bandwidth of 52% (explained in more detail in Sect. 10.3.3). Based on the concept of the dual-layer FSS, in Sect. 10.5 a four-layer FSS is also presented. Both FSSs were tested as a reflector with a UWB slot antenna. The dual-layer FSS needs a shorter gap between the antenna and the reflector. The four-layer FSS offers more control of gain by changing the periodicity in each layer.

## 10.2 Principle and Operation of FSS Reflectors

### 10.2.1 Reflector Design

It is known that reflectors behind antennas only work properly when the radiation reflected back by the backing plane is in phase with the radiation directly generated by the antenna itself.

When the reflector is a good conductor with a reflection phase of  $\pi$  is radians, as shown in Fig. 10.1, this requires the following condition to be satisfied:

$$2\frac{2\pi}{\lambda}d - \pi = 2\pi N, \tag{10.1}$$

where  $d$  is the distance between the antenna plane and the backing plane,  $\lambda$  is the wavelength and  $N$  is an integer greater than or equal to zero (typically zero is chosen). This means that the distance between the antenna and the backing plane must be an odd integer multiple of one quarter of the wavelength, and is given by:

$$d = (1 + 2N)\frac{\lambda}{4}. \tag{10.2}$$

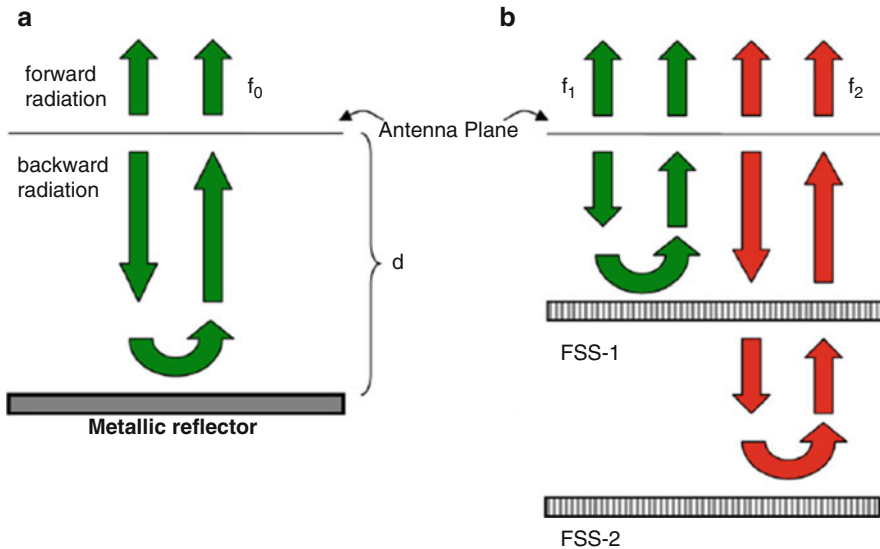
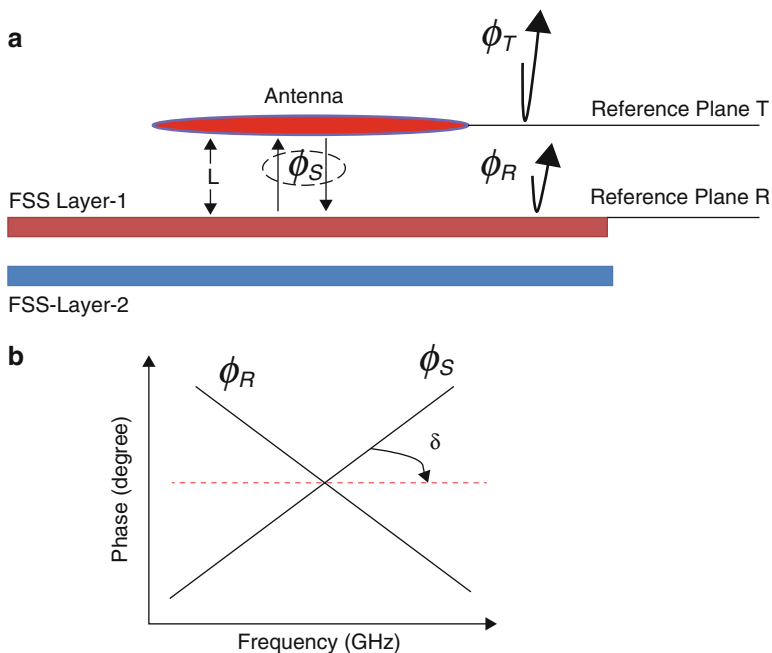


Fig. 10.1 (a) Standard metallic reflector. (b) Multiple FSS reflectors

### 10.2.2 Phase Coherence Over an Ultra-Wide Band

FSSs can be efficiently employed in a planar reflector design for broadband and ultra-broadband applications. The basic idea is to design a multilayer FSS structure where each layer provides reflectivity for a specific frequency band. Each reflective plane is placed at an appropriate distance from the antenna, generating reflections from different layers and therefore broadening the usable range of the composite reflector, as shown in Fig. 10.1. In order to function properly, the uppermost reflective plane must be transparent to frequencies to be reflected by the lower planes. For this type of application, it is natural to make the uppermost FSS to operate in the passband, when signals are reflected from the lower layers. As mentioned earlier, phase plays a critical role, which is explained next for a dual-layer structure. In order to understand the functionality of the dual-layer FSS, its layout and the components of the reflected wave at the reference plane T are illustrated in Fig. 10.2.

A typical bidirectional antenna placed above the FSS radiates towards the FSS (downwards) as well as away from the FSS (upwards). The downward wave is expected to be reflected almost completely by the FSS layers at all concerned frequencies. To generate a reflected wave with a nearly constant reflection phase



**Fig. 10.2** (a) FSS application for gain enhancement: reflection at different frequencies occurs at different layers (top). (b) Frequency response of the two phases,  $-\phi_R$  and  $\phi_R$  (bottom)

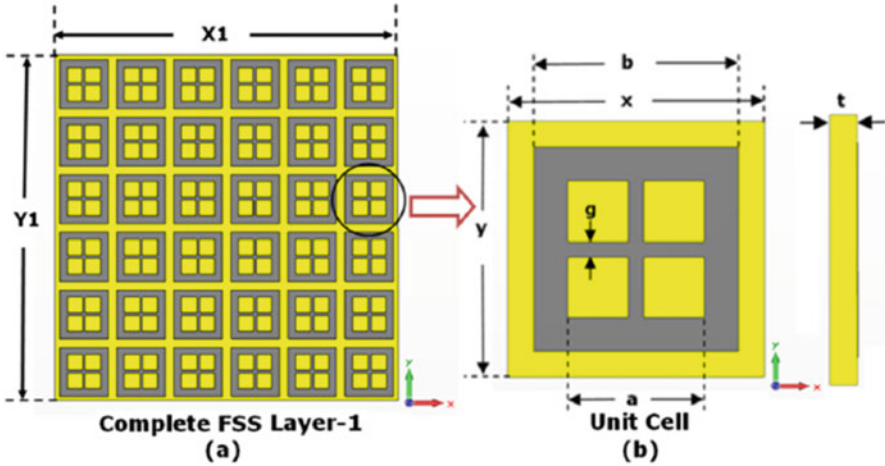


**Fig. 10.3** (a) Frequency selective surface Layer-1, which reflects higher frequencies (b) Unit cell of Layer-1

over an ultra-wide band, the two layers of the FSS must be optimised. In this example, FSS Layer-1 is composed of a set of cross dipoles and slots (Fig. 10.3a). This layer exhibits a reflection phase of  $\phi_1$  (at Reference Plane R) and is responsible for providing reflection at higher frequencies. Layer-2 of the FSS, placed below Layer-1, consists of similar cross dipoles and slots with an additional rectangular slit in the rectangular metal loop (Fig. 10.4a). FSS Layer-2 is designed to reflect lower frequencies and is characterised by a reflection phase delay of  $\phi_2$  (at the Reference Plane R). The phase delay of the combined reflected wave from the multilayer FSS is  $\phi_R$  at Plane R. At Plane T, the reflection phase is  $\phi_T = \phi_R + \phi_S$  where  $\phi_S$  is the two-way free-space propagation phase delay over the distance  $L$  given by:

$$\phi_s = 2 \times 2 \frac{\pi}{C} f \times L. \tag{10.3}$$

The objective is to achieve an approximately constant  $\phi_T$  over an ultra-wide band as shown in Fig. 10.2b (dotted line), so that the reflected wave interferes with the direct wave in the same way at all frequencies. This  $\phi_T$  should be ideally zero but in practice values in the range of  $-90$  to  $+90$  degrees are acceptable. The delay  $\phi_S$  is obviously frequency dependent, and its positive slope depends on the spacing between the antenna and the reflector ( $L$ ). Hence, ideally,  $\phi_R$  must have a negative constant slope to compensate for the positive slope of  $\phi_S$ .



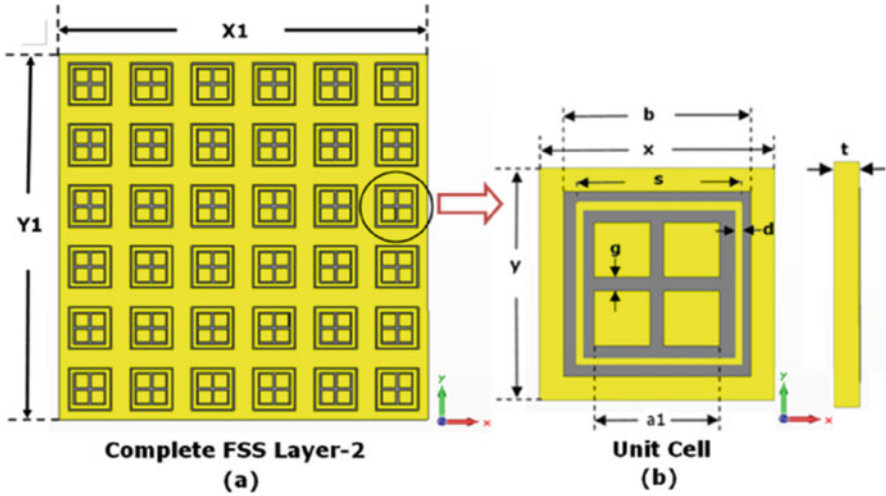


**Fig. 10.4** (a) Frequency-selective surface Layer-2, which reflects lower frequencies. (b) Unit cell of Layer-2

### 10.3 Dual-Layer FSS Design

Initially, the design of a dual-layer FSS is considered. The first layer of the FSS unit cell discussed by Ranga et al. [10] consists of a cross dipole and a slot, as shown in Fig. 10.3.

The effect of the width  $a$  of the slot window was numerically studied with the help of CST Microwave Studio using a technique based on the waveguide model. This design parameter affects the resonance frequency and primarily controls the upper part of the UWB from 8 GHz onwards, giving a stop bandwidth of around 50%. The Layer-1 unit cell resonates at frequencies between 8.9 and 13.6 GHz, as shown in Fig. 10.5, and the widest stop bandwidth is achieved for  $a = 10$  mm. The complete geometry and unit cell of Layer-1 are shown in Fig. 10.3.

The Layer-2 unit cell is shown in Fig. 10.4. This FSS is optimised to reflect the frequencies that are passed by Layer-1, as shown in Fig. 10.6. The unit cell of Ranga et al. [10] has been considered for Layer-1, with an additional slit inserted in the metal loop, as shown in Fig. 10.4. The thickness  $d$  has been optimised and set to 1 mm to get maximum possible bandwidth for the additional frequencies. These two layers are then stacked together. Figure 10.7 shows the waveguide model of the dual-layer unit cell. Note that the PMC boundary condition has been assigned to the two boundaries orthogonal to the  $x$  axis, while, the perfect electric conductor (PEC) boundary condition has been employed on the two boundaries orthogonal to the  $y$  axis.

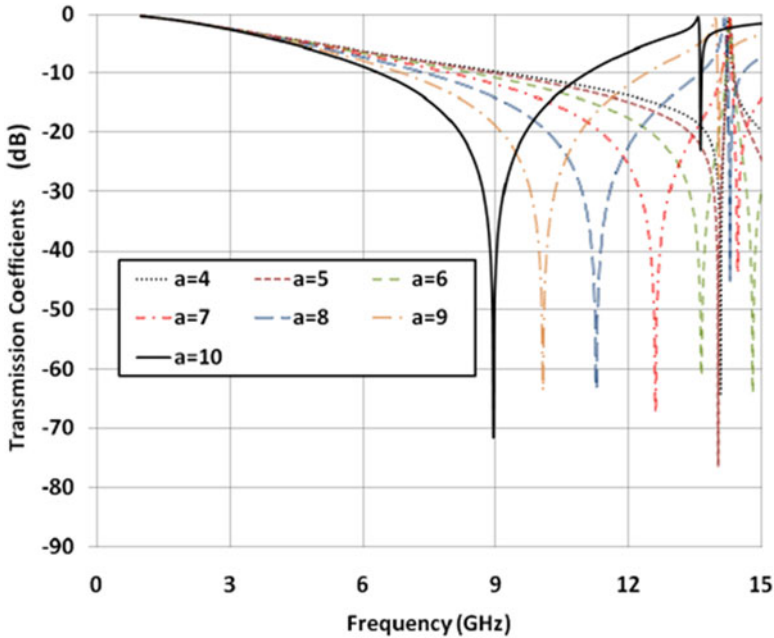


Fig. 10.5 Parametric sweep of parameter  $a$  for the unit cell shown in Fig. 10.3

The gap  $L$  between the two stacked layers plays a critical role and has been optimised. The dimensions of the dual-layer unit cell are given in Table 10.1 and Fig. 10.8.

Figure 10.9 shows the reflection magnitude of the dual-layer composite unit cell. The magnitude of the transmission coefficient is below  $-10$  dB over a 133% bandwidth (3.5–11.45 GHz). Note that, wave is incident at port 2; port 1 is the port on the back side of the unit cell. Figure 10.10 shows the predicted reflection phase of the composite FSS, which produces a coherent reflected wave at the plane of the antenna over an ultra-wide band. More significantly, the variation in phase is almost linear across the whole band (See  $S_{22}$  curve in Fig. 10.10).

### 10.3.1 Field Analysis of Dual-Layer FSS

The waveguide simulator approach has been used for analysis of the electric fields in the unit cell. Figure 10.11 shows the electric-field distribution in the unit cell at 3 GHz, 6 GHz, 8 GHz, and 10 GHz, respectively. It is clearly visible that at lower frequencies fields are reflected from the lower FSS layer. As the frequency increases, more reflection occurs from the top layer of the FSS. In particular, Fig. 10.11c

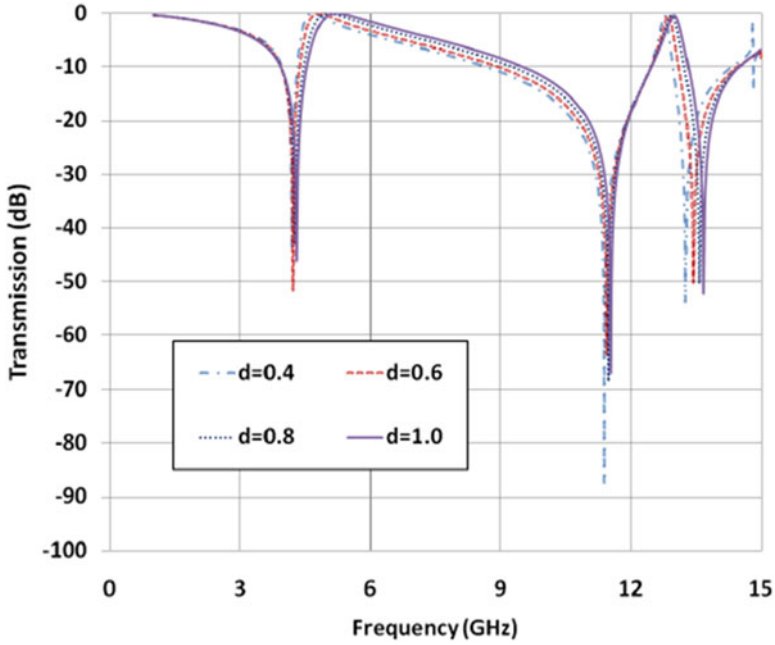


Fig. 10.6 Parametric sweep of the parameter  $d$  for the unit cell shown in Fig. 10.4 ( $a = 10$  mm)

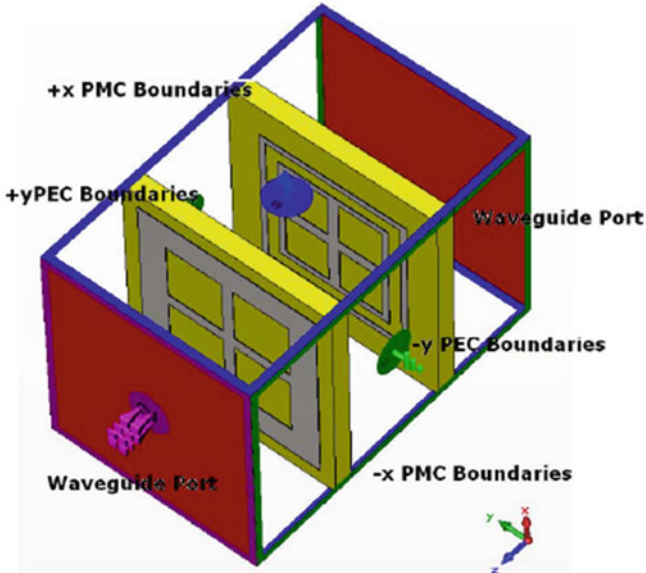
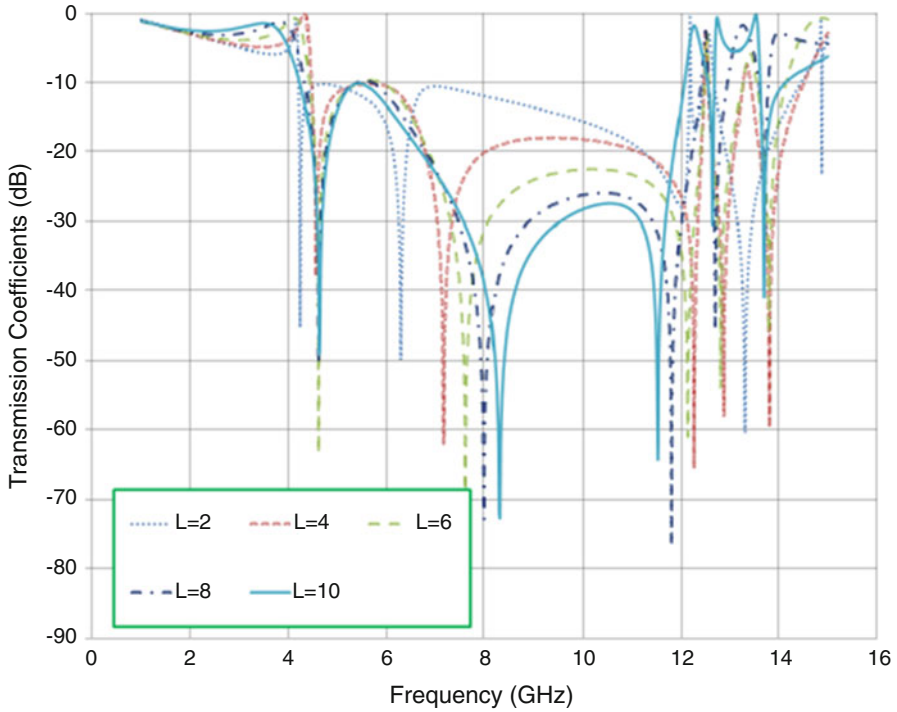


Fig. 10.7 Waveguide model for a multilayer unit cell

**Table 10.1** Dimensions of the optimised dual-layer FSS unit cell

Parameters	X	Y	a	a1	b	g	d	s	L
Values (in mm)	15	15	10	8	12	0.9	1	11	9.5



**Fig. 10.8** Parametric sweep of separation length  $L$  between layers of the dual-layer unit cell

displays significant reflection above the top layer of the FSS. It corresponds to a transmission coefficient of  $-50$  dB at 8 GHz (see Fig. 10.9).

### 10.3.2 Oblique Incidence Performance of the Dual-Layer UWB Reflector

Before proceeding to fabrication, the performance of the dual-layer FSS reflector to obliquely incident electromagnetic waves has been theoretically investigated.

When the electric field is perpendicular to the plane of incidence, the incidence is Transverse Electric (TE), and when it is parallel to the plane of incidence, the incidence is Transverse Magnetic (TM). For normal incidence, the bandwidth is around 100%, and it reduces to 70% in the case of TM incidence at an angle of  $50^\circ$ . The widest bandwidth previously described in the literature for normal incidence is

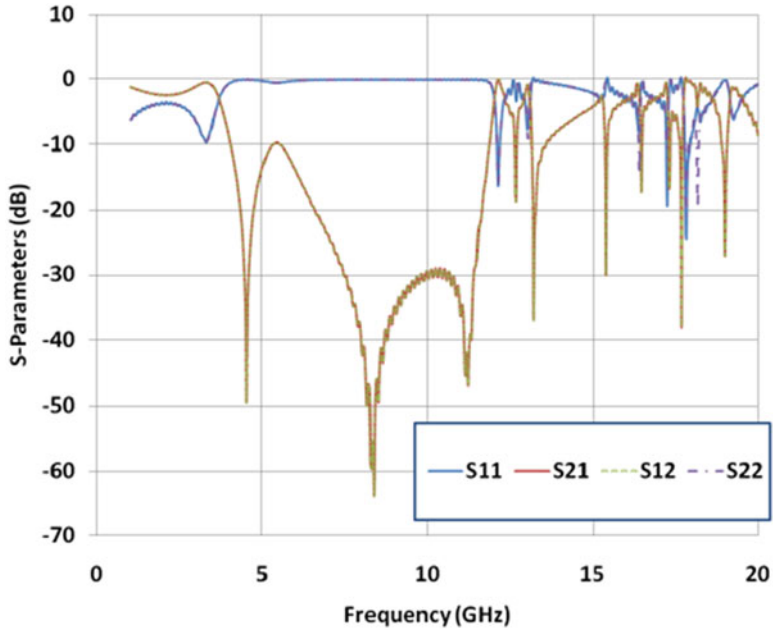


Fig. 10.9 Predicted reflection and transmission magnitudes of the composite unit cell

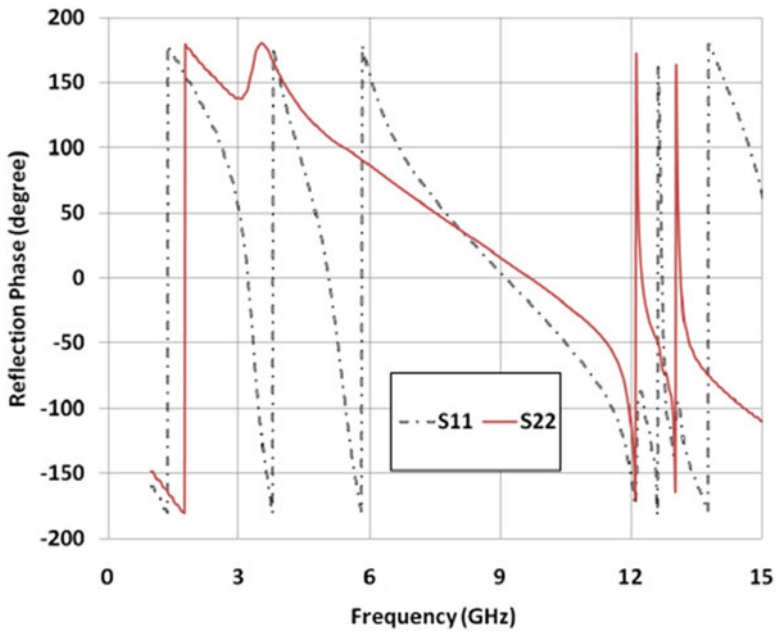
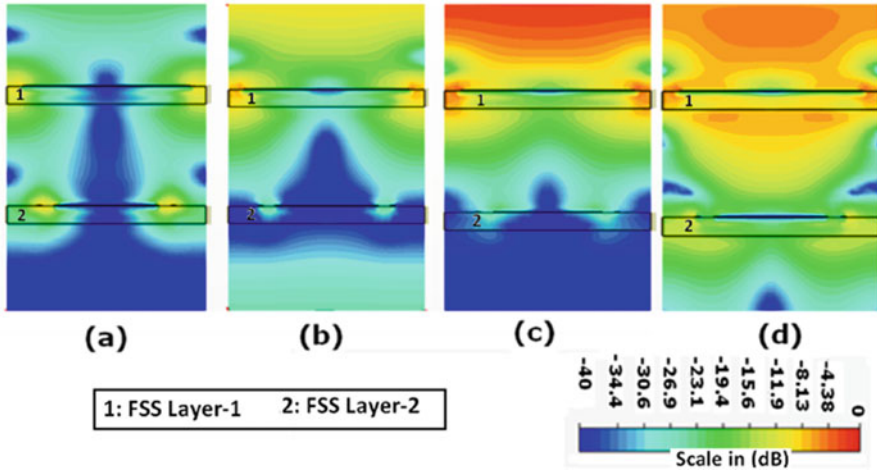


Fig. 10.10 Predicted reflection phases of the composite unit cell



**Fig. 10.11** Total electric-field distributions orthogonal to the FSS reflector at (a) 3 GHz, (b) 6 GHz, (c) 8 GHz, and (d) 12 GHz

50% [8]. To investigate oblique-incidence performance, a Floquet port analysis has been carried out for different incidence angles where  $\theta$  is defined with respect to the normal to the surface of the reflector.

Figure 10.12 shows the transmission characteristics of the FSS for TE-polarised waves up to an incidence angle of  $\theta = 50^\circ$ . It is evident from Fig. 10.12 that, apart from small peaks of around  $-7$  dB between 7 and 8 GHz, the FSS transmission is stable over a 90% bandwidth. The performance for TM incidence has been evaluated for the same range, and the results are presented in Fig. 10.13. For this case, with the increase of angle of incidence, the lower frequency limit shifts from 4 to 4.41 GHz. It is noted that this limit is stable for TE polarisation for all incidence angles considered. Also, the reflection bandwidth of the FSS reduces from 99% to 70% when the incidence changes from the normal to  $\theta = 50^\circ$ .

For further analysis of the field behaviour, several probes have been placed in the unit cell during simulation done with the CST software. These probes have been placed below the lower FSS layer, in the middle of the two layers of the FSS and above the upper FSS layer at a distance of 9.5 mm. Probes have been placed for monitoring both co- and cross-polarised components at all three locations. The critical information is conveyed by the upper probe, which is placed on the top of the FSS screen. This corresponds to the location where a planar UWB antenna would typically be placed when the FSS is used as a UWB reflector (Fig. 10.14).

The magnitudes of the electric field at the probes are shown in Fig. 10.14. As expected, the electric field is very low below the two FSS layers (see curve for lower probe in Fig. 10.14).

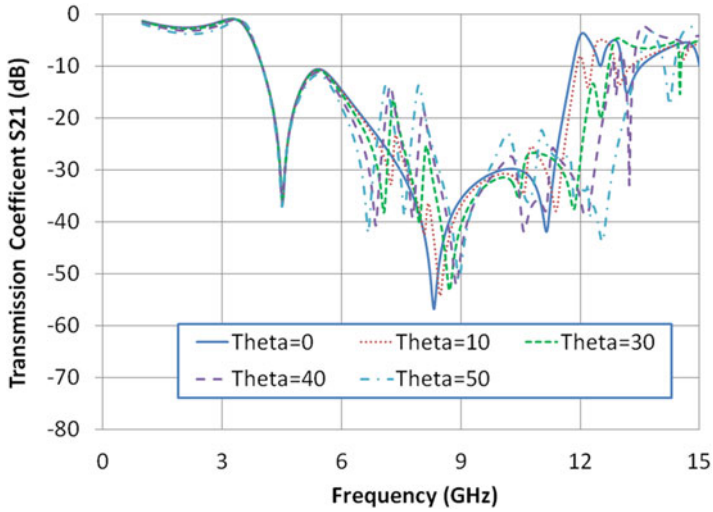


**Fig. 10.12** Predicted transmission coefficients for TE-polarised waves. Theta is the angle of incidence

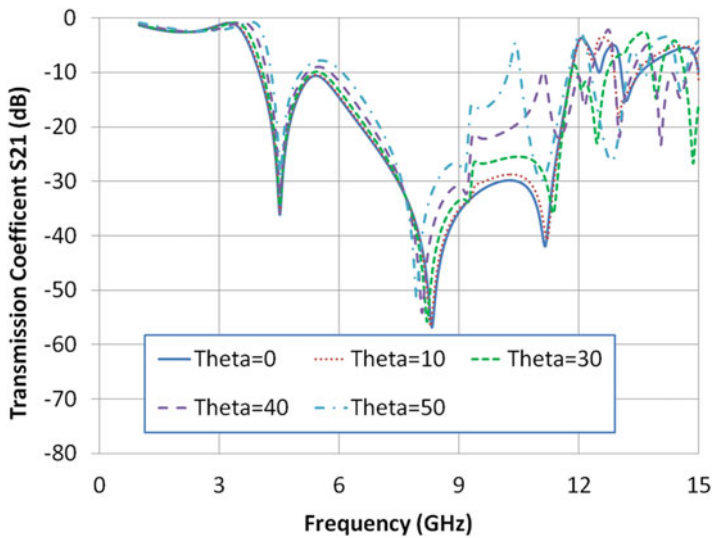


**Fig. 10.13** Predicted transmission coefficients for TM-polarised waves. Theta is the angle of incidence

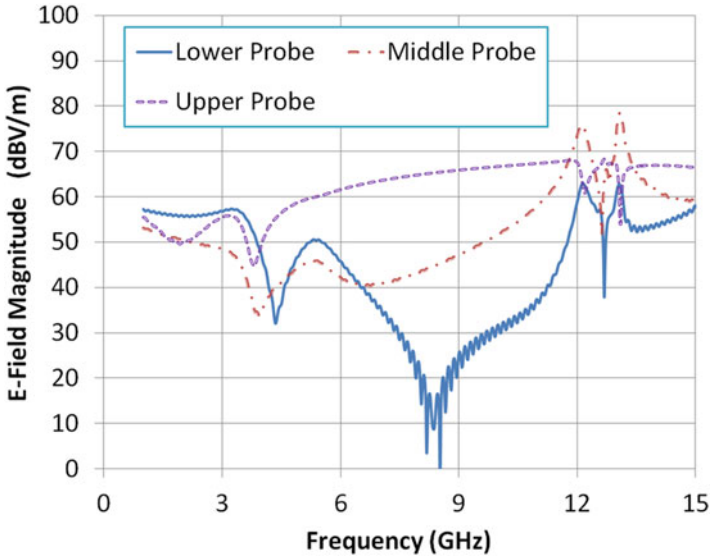
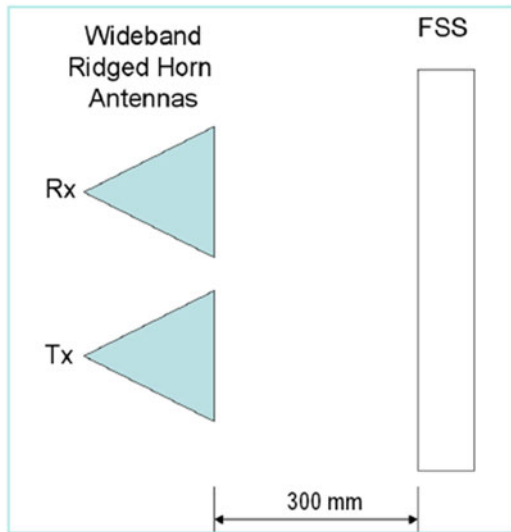


**Fig. 10.14** Magnitude of the total electric field component parallel to the incident polarisation (Co-Pol) at different levels of FSS

**Fig. 10.15** Schematic of the setup for reflection phase measurement





### 10.3.3 Measured Results for a $32 \times 22$ FSS

In order to experimentally validate the performance of the UWB reflector design, an array of  $32 \times 22$  unit cells has been fabricated and measured. Teflon spacers of fixed thickness were specially manufactured to ensure the spacing between the two layers. To measure the reflection phase and transmission magnitude of this FSS, two dual-ridge H-1498 horns from BAE Systems, with an operating bandwidth from 2 to 18 GHz, were used in the measurement setup, which is shown schematically in Fig. 10.15. A wooden frame was used to reduce reflections, as shown in the photo in Fig. 10.16.

Additional grooves for mounting provided good support for making the dual-layer structure. To determine the reflection coefficient at a distance of 9.5 mm in front of the FSS, the electrical delay for the FSS measurement was set to  $-19$  mm (i.e.  $2 \times 9.5$  mm). Phase was unwrapped from the measured data for comparison with the simulation. The FSS screen was positioned 300 mm away from the horn antennas. A comparison of predicted and measured reflection phase is shown in Fig. 10.17.

Transmission measurements were carried out with a setup similar to that used for reflection phase measurements. The difference in the placement of horns is shown in Fig. 10.18, and a photograph of the measurement setup is in Fig. 10.19. A similar setup was also used for the measurement of reflection at different angles of incidence. The FSS screens placed on the wooden board were manually rotated to appropriate angles (Fig. 10.19).

Figure 10.20 shows the measured transmission for normal incidence, and it agrees very well with predicted results. The measured  $-10$  dB transmission bandwidth of 121.8% (3.85–11.23 GHz) compares well with the predicted bandwidth of

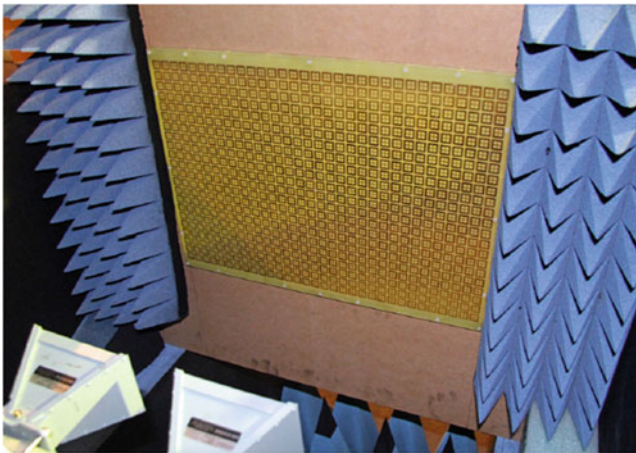


**Fig. 10.16** The measurement setup for reflection phase measurement

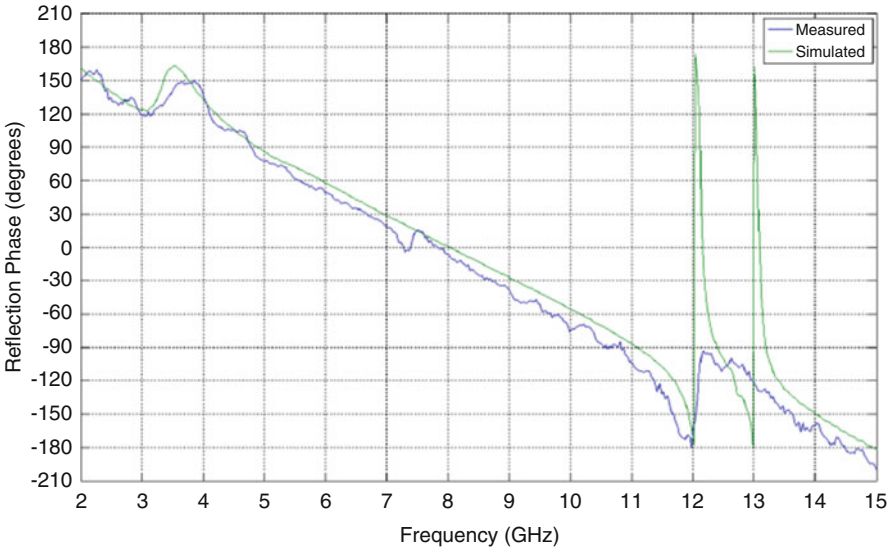


**Fig. 10.17** Comparison of measured and predicted reflection phase of the dual-layer UWB reflector

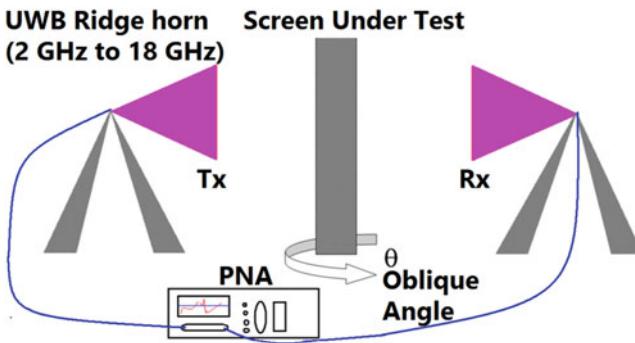


**Fig. 10.18** Schematic of the setup used for measuring transmission coefficients

133% (3.5–11.45 GHz). Transmissions of both TE and TM polarisations have been measured at three different incidence angles, namely, 15, 30, and 45 degrees, with the aforementioned setup.

As shown in Figs. 10.21a, b, and c, in the case of TE polarisation, the performance of the FSS is stable as predicted, with a bandwidth greater than 100% in each case. Figures 10.21d, e, and f show the screening performance of the screens in the case of TM incidence at 15, 30, and 45 degrees, respectively. A good match is noted in the lower band of frequencies. At higher frequencies some discrepancies are noted.

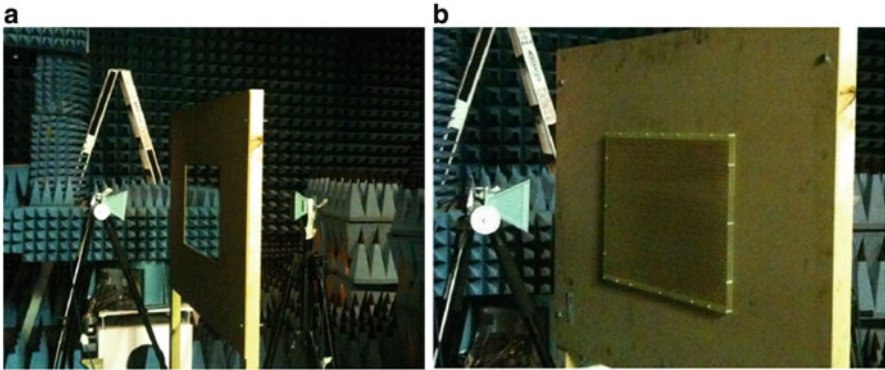


**Fig. 10.19** Setups for (a) transmission measurements and (b) reflection measurements at oblique incident angles (using a rotating board with FSS screen)

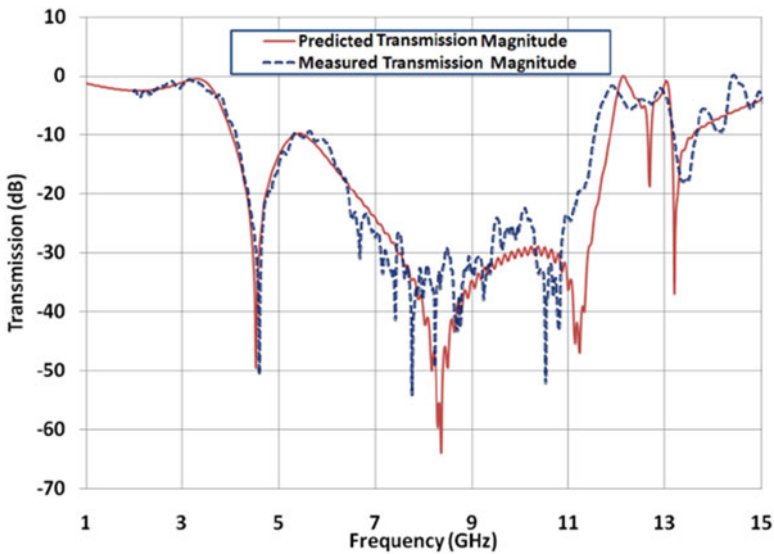


**Fig. 10.20** Theoretical and measured transmission magnitude at normal incidence for the  $32 \times 22$  array of unit cells

### 10.4 Antenna Performance Over the Dual-Layer FSS Reflector

After optimising the FSS screen, a UWB slot antenna excited by a microstrip-fed patch [11] has been mounted above the UWB reflector. Note that this UWB reflector concept is not limited to the particular slot antenna described here; designers can use any other UWB antenna available in the literature, including printed monopole-type

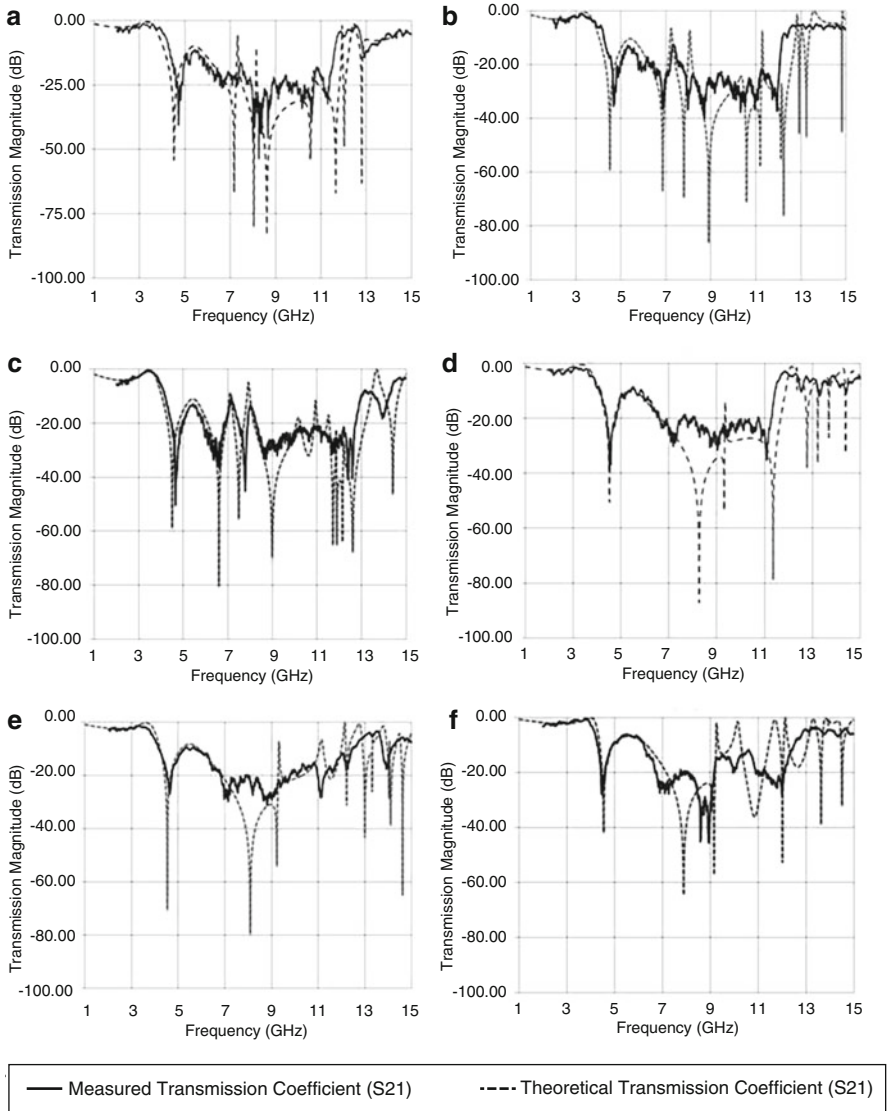
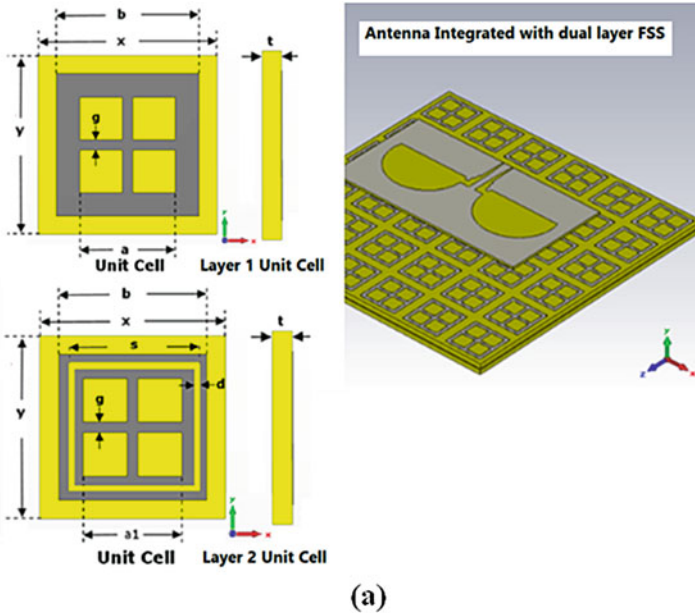
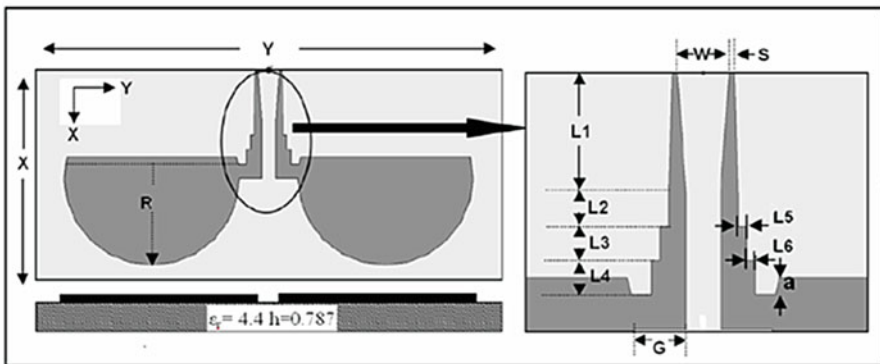


**Fig. 10.21** Predicted and measured transmission magnitudes for TE polarisation with incidence at (a) 15, (b) 30, and (c) 45 degrees and for TM polarisation with incidence at (d) 15, (e) 30, and (f) 45 degrees

antennas. The slot antenna and all the FSS reflectors have been fabricated at low cost, using FR-4 substrates with a relative permittivity of 4.4 and a thickness  $t$  of 0.8 and 1.6 mm, respectively. A graphical overview of the antenna design with the



(a)



(b)

**Fig. 10.22** (a) Slot antenna over the dual-layer FSS reflector. The unit cell geometry is shown in the inset. Unit cell of the FSS first layer; unit cell of the FSS second layer that has dual band behaviour has all dimensions same as in layer 1 except  $d = 1.0$  mm grey areas have metal coating. (b) CPW-fed semicircular slot antenna details [11]  $X = 30$ ;  $Y = 60$ ;  $L1 = 7$ ;  $L2 = L3 = L4 = 2$ ;  $L5 = L6 = 0.5$ ;  $W = 3S = 0.3$ ;  $G = 2.5$ ;  $R = 12$  and  $a = 1$  (all dimensions are in mm)

reflector is given in Fig. 10.22. The placement of the antenna over the reflector is critical.

Figure 10.23 shows the effect of the separation between the antenna and the UWB reflector screen on antenna gain. The gap between the reflector and the antenna has been varied from 0 to 16 mm. Following the parametric study, the gap

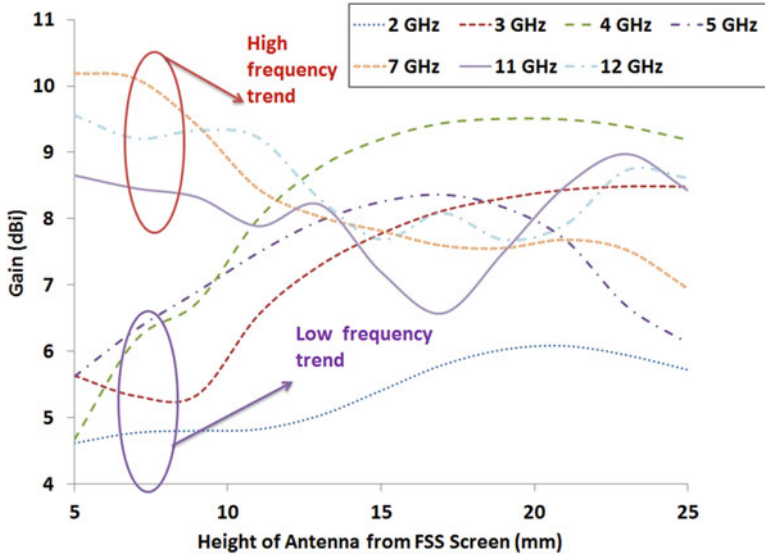


**Fig. 10.23** Investigation of the optimum spacing between the antenna and the reflector for stable gain performance

has been set to 11 mm, which yields a desirable response over the entire FCC UWB bandwidth and even beyond. With the use of a dual-layer FSS reflector, the gain increases over the entire frequency band. The performance enhancement due to the FSS-based reflector is evaluated with the UWB semicircular slot antenna shown in Figs. 10.24, 10.25, 10.26, 10.27, and 10.28.

The predicted and measured input reflection coefficients are shown in Fig. 10.24, with and without the reflector. The reflector does not significantly affect the antenna return loss. More importantly, the antenna with the reflector maintains a good impedance match (return loss  $>9$  dB) over the entire FCC UWB band from 3.1 to 10.6 GHz. To further explore the effectiveness of the FSS reflector, the UWB reflector was brought closer to the antenna and placed only 2 mm away from the antenna (the minimum possible due to connector spacing & dielectric thickness). Even with such close proximity, the slot antenna has good impedance match in the large frequency range shown in Fig. 10.25. When this UWB FSS reflector was replaced by a conducting reflector at the same location, matching at most frequencies deteriorated significantly, as shown in the same figure. Nonetheless, 11 mm spacing has been chosen to get the best impedance match and gain enhancement over a broad bandwidth.

Predicted and measured antenna radiation patterns of the antenna with and without the reflector screen are plotted in Figs. 10.26 and 10.27, respectively. Figure 10.26a shows the predicted radiation pattern of the CPW-fed single-slot antenna (SSA) at 3 GHz and Fig. 10.26b with the FSS reflector. The antenna itself has a typical bidirectional radiation pattern with two beams directed towards  $+90$  and  $-90$ -degree directions. With the addition of the FSS reflector, the pattern

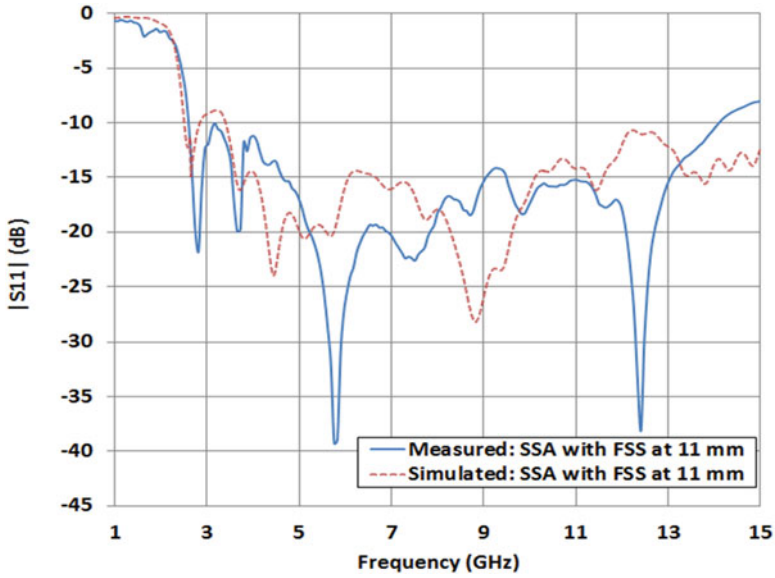


Fig. 10.24 Predicted and measured input reflection coefficients of the slot antenna with the reflector

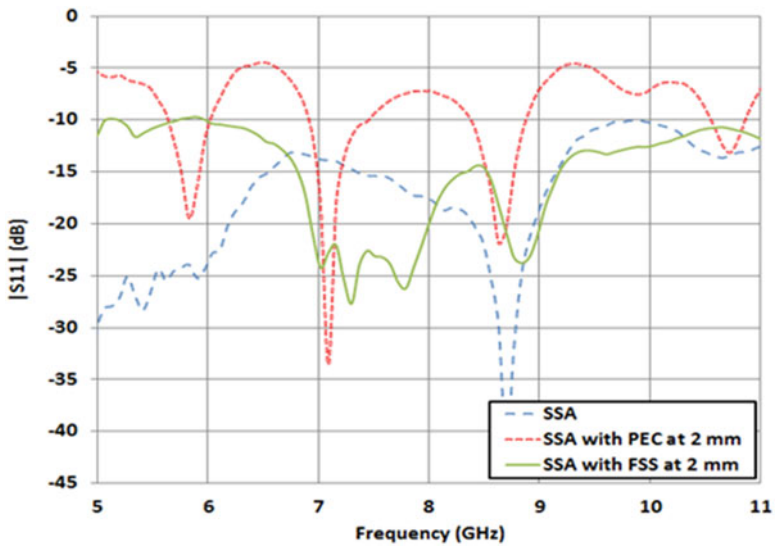


Fig. 10.25 Measured input reflection coefficient of the slot antenna with and without the dual-layer UWB FSS reflector at 2-mm spacing and with a PEC reflector at 2-mm spacing

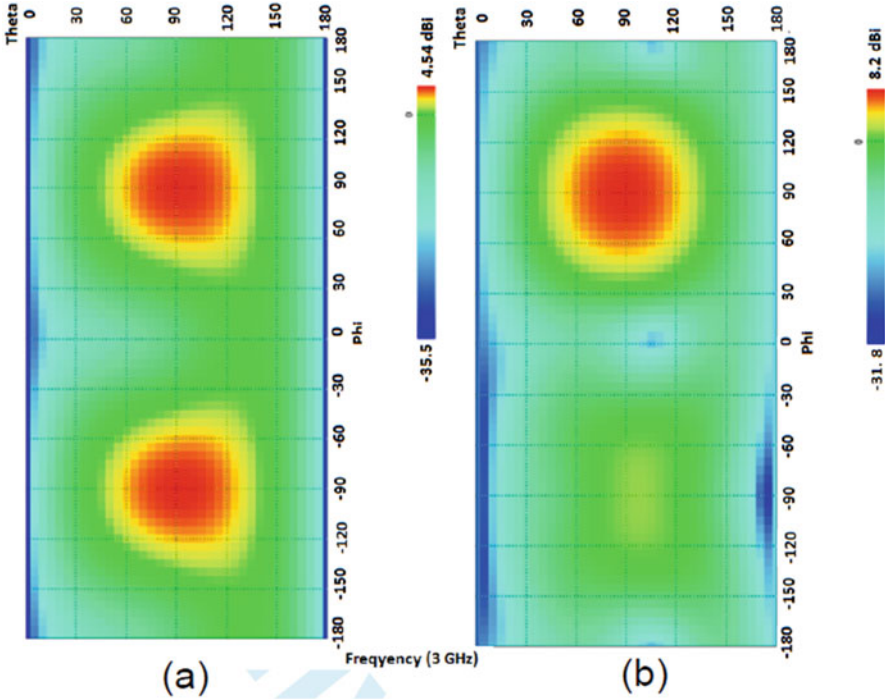
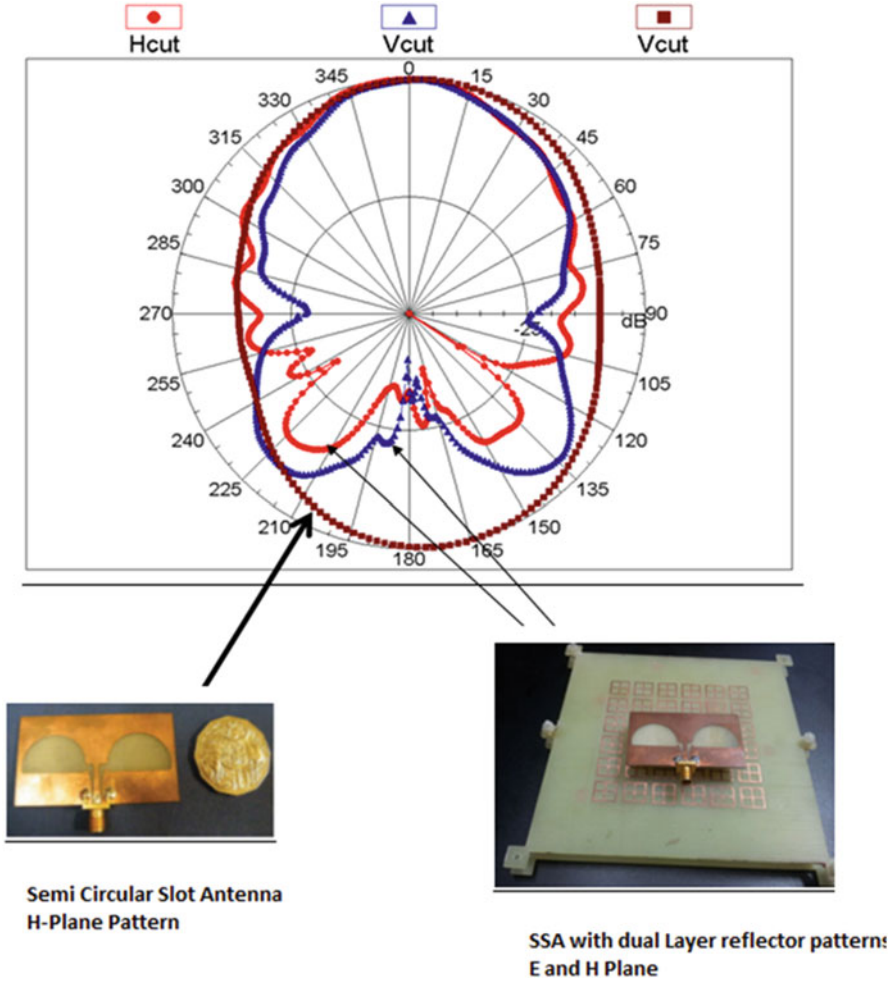


Fig. 10.26 Predicted radiation patterns of the new antenna with and without reflector at 3 GHz

becomes unidirectional. Figure 10.28 shows the measured radiation patterns of the slot antenna with and without the FSS. The polar plot clearly indicates a good symmetrical unidirectional beam at 3 GHz compared to bidirectional patterns of the solo SSA. The gain enhancement due to the presence of the reflector across the entire band is clearly observable in the plots in Fig. 10.28a. An extensive study on the predicted and measured gain and efficiency of antenna with and without FSS reflector is carried out in detail as shown in Fig. 10.28b. Results with an additional PEC backing, just below the FSS, are also included for comparison. The minimum gain enhancement is about 2.5 dB, at the lower end of the UWB, and the maximum gain enhancement is about 4 dB at 4.2 GHz. The maximum gain is 9.5 dBi at 4.2 GHz. The gain variation is  $\pm 1.5$  dB from 3 to 10 GHz. Figures 10.29a–e show the measured radiation patterns of the SSA with the reflector at 3 GHz, 5 GHz, 6 GHz, 7 GHz, and 8 GHz, respectively.

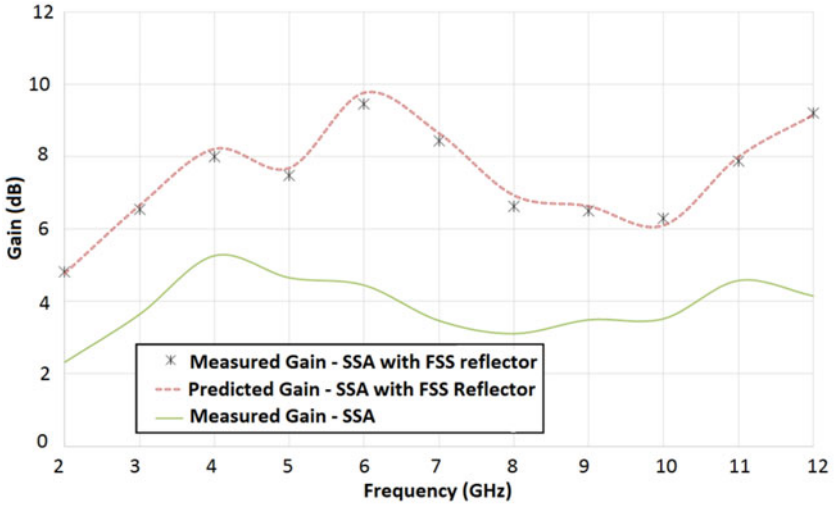
At lower frequencies a broad strongly directional beam is observed, but with the increase of the frequency, the beam starts narrowing; this can be easily noted in Figure 10.29d. This beam splitting is not due to the reflector but basically to the inherent property of this slot antenna at higher frequencies. Use of an antenna with a more stable radiation pattern in conjunction with this reflector allows getting a more directive beam at higher frequencies.



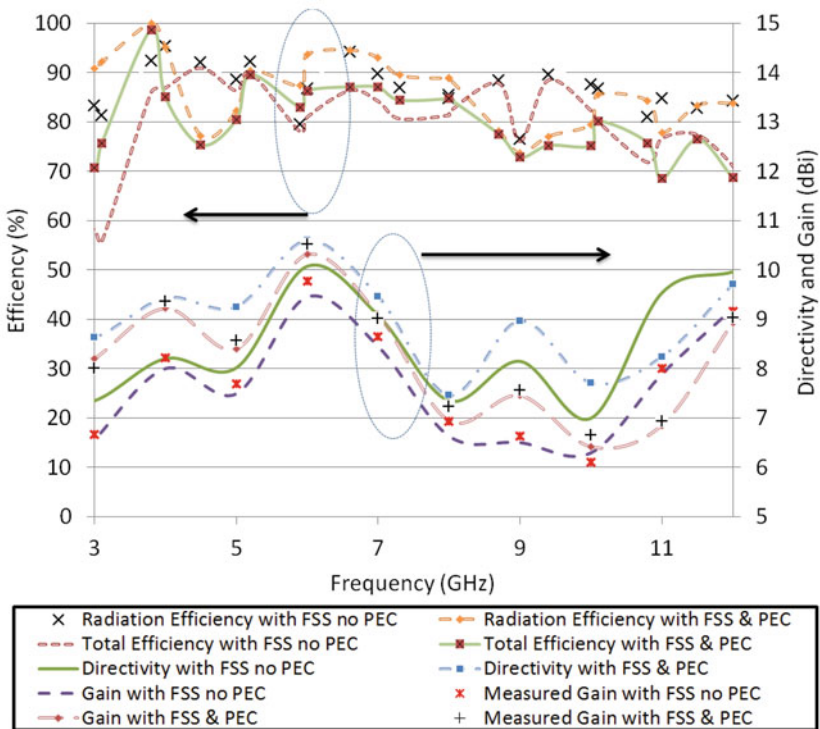


**Fig. 10.27** Measured radiation patterns of the slot antenna with and without the reflector at 3 GHz

Even without an electric conductor backing, the front-to-back ratio with the FSS reflector is better than 15 dB over the whole matched bandwidth. It peaks to 27 dB at 6.5 GHz.



(a)



(b)

**Fig. 10.28** (a) Predicted and measured gain of the antenna with and without the FSS reflector. (b) Additional performance figures including measured efficiency of the antenna with and without the FSS reflector. Results with an additional PEC backing are also included for comparison

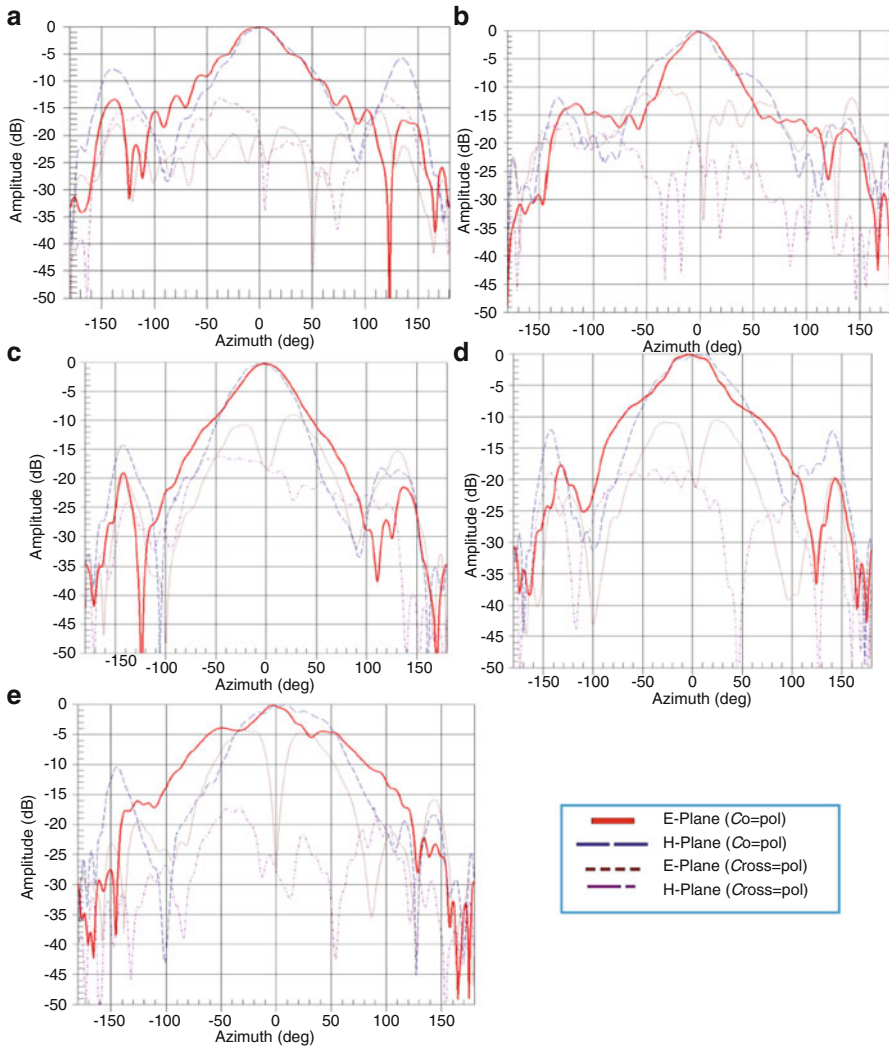


**Fig. 10.29** Measured radiation patterns of the SSA with the FSS reflector at (a) 3 GHz, (b) 5 GHz, (c) 6 GHz, (d) 7 GHz and (e) 8 GHz

### 10.5 A Constant-Gain UWB Antenna with a Four-Layer Frequency Selective Surface Reflector

The two-layer FSS described in previous sections proved to be an efficient design because the periodicity in both layers is identical. After gaining an understanding of the FSS function as a reflector, further improvements in gain flatness and

compactness were sought. To achieve the target, the FSS design methodology of previous dual-layer FSS was followed with some modifications.

The first layer of FSS acts on the higher frequency region and the bottom layer on the lower frequency region, providing in-phase reflection characteristics. This FSS is not backed by a perfect metal reflector in order to allow some back radiation at some frequencies, lower the gain in the main beam direction, and hence to provide nearly constant gain across its ultra-wide operating band.

To demonstrate the concept, another slot antenna was chosen, which was also used in previous sections. Alone this slot antenna has an ultra-wide bandwidth of 140% (2.9–18.38 GHz) [11], a predicted gain of 4.5 dBi at 3 GHz and a gain variation of around  $\pm 1.5$  dB over the impedance bandwidth. The configuration of the antenna and the four-layer FSS reflector is shown in Fig. 10.30. In the initial design process, the screens FSS-1 and FSS-2 were taken from literature [13, 14]. Two additional layers of FSS-3 and FSS-4 were added and optimised carefully to achieve ultra-wide band performance. FSS-1, FSS-3 and FSS-4 are bandpass filters, and FSS-2 acts as a band-stop for the low frequencies passed on by FSS-1. In this multilayer composite FSS design, FSS-1 and FSS-2 have the same periodicity but, in order to support lower frequencies, FSS-3 and FSS-4 unit cells are larger and hence the periodicity of layers 3 and 4 are different from layers 1 and 2.

The shape and dimensions of the antenna system are reported in Fig. 10.30. An extensive optimisation was conducted for the different layers to improve the gain flatness when combined with the UWB slot antenna. Figure 10.31 shows the hardware profile of the antenna with various FSS layers the hardware profile of antenna and each layer of the composite FSS. Note that, unlike in the two-layer UWB FSS reflector described previously, this four-layer composite FSS does not have air gaps between FSS layers. Each printed pattern is separated from the adjacent pattern by a 0.787-mm thick Roger 5880 substrate. The total thickness of the composite reflector assembly (without the antenna) is 2.36 mm.

Measured and computed results are presented here to confirm the performance of the antenna. The antenna input reflection coefficient and the gain are shown in Figs. 10.32a and b, respectively. It can be observed that the optimised FSS reflector has only a very small effect on the impedance bandwidth (145% bandwidth with FSS versus 149% without FSS). However, the gain has increased significantly with the FSS reflector. A peak gain of 9.3 dBi has been achieved with the FSS, but the most significant feature of introducing the FSS reflector is the improvement in gain flatness. The variation in the gain is only  $\pm 0.5$  dB across the whole impedance band. Figure 10.33 shows the measured radiation patterns in the ZY (H-Cut) and the ZX (V-Cut) planes, a maximum gain of 9.3 dBi and the variation of 0.5 dB have been achieved for the designed structure.

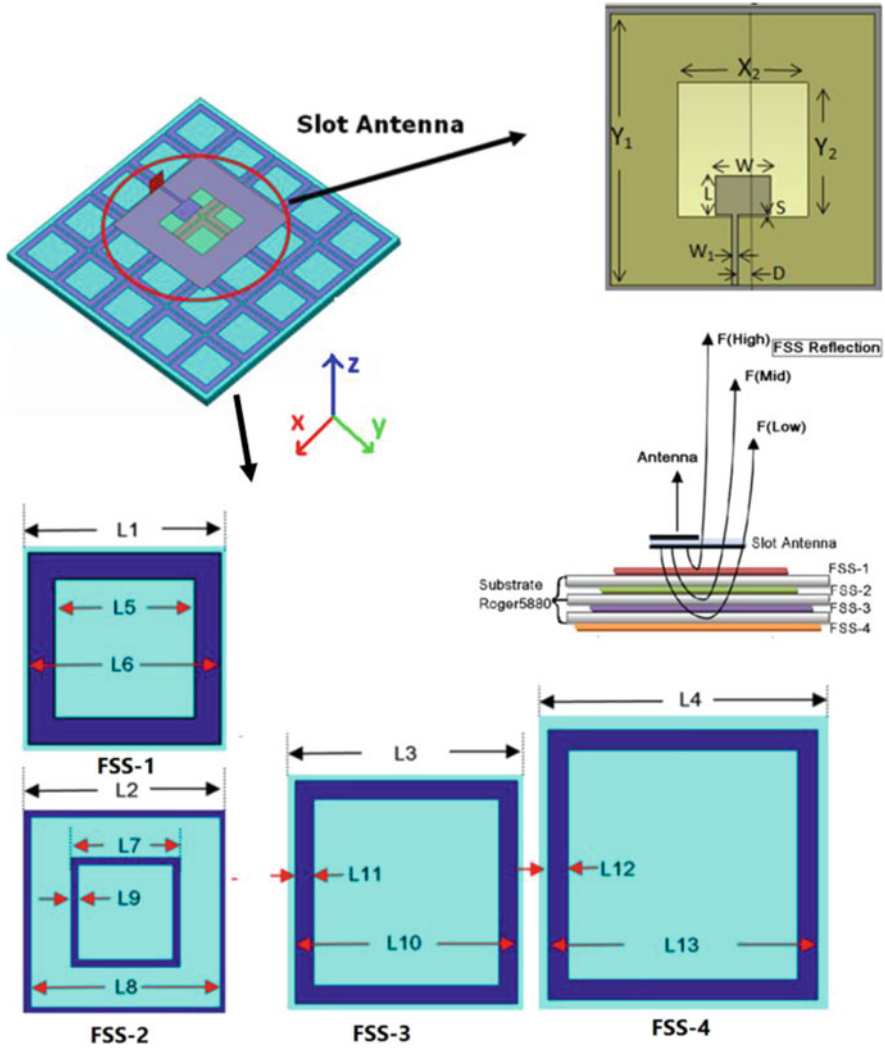


**Fig. 10.30** Four-layer frequency-selective surface reflector with a UWB slot antenna (Ref. [17], reproduced courtesy of The Electromagnetics Academy)

### 10.6 Conclusion and Future Work

Two planar FSS reflectors, covering the entire FCC UWB band and beyond, have been discussed. The first is a dual-layer low-cost planar FSS. It has a high reflection coefficient magnitude and sufficiently linear reflection phase to be used as a reflector for nearly all types of low-cost (planar and/or printed) UWB antennas. The oblique incidence performance of this dual-layer FSS has also been investigated. Through

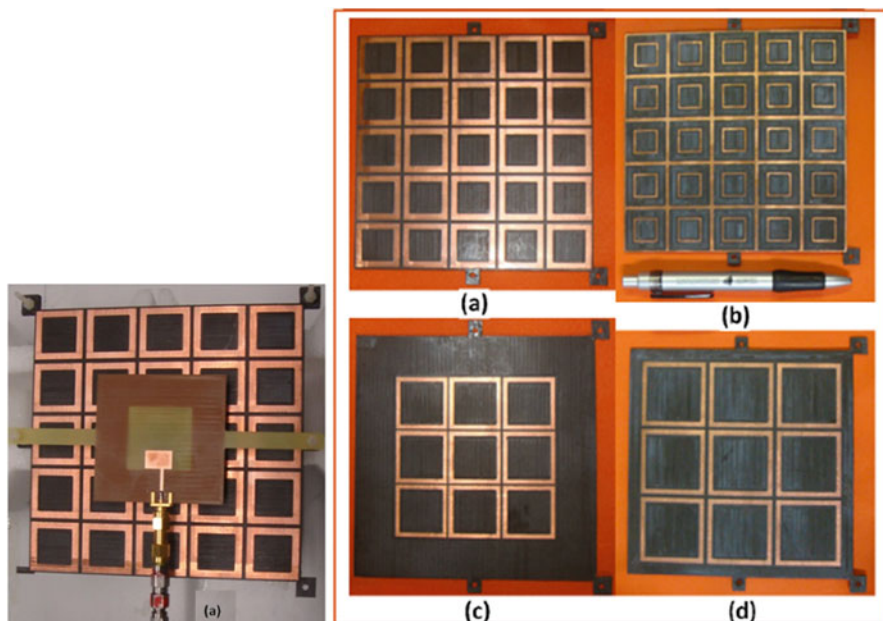
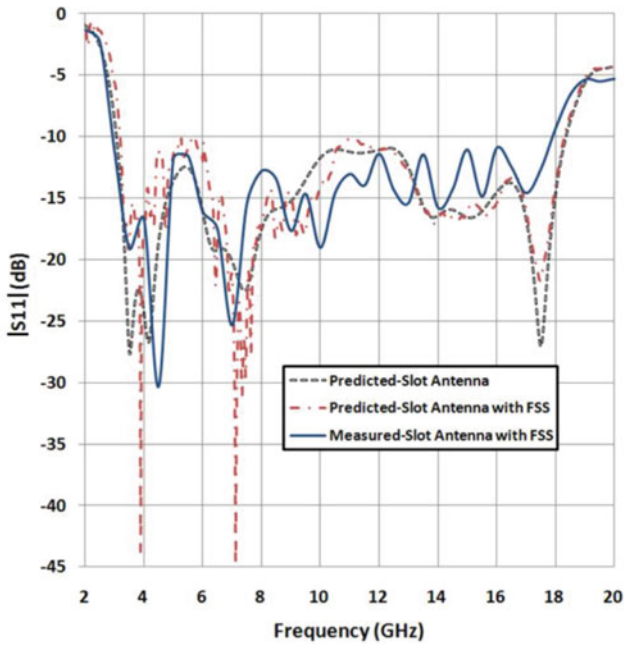


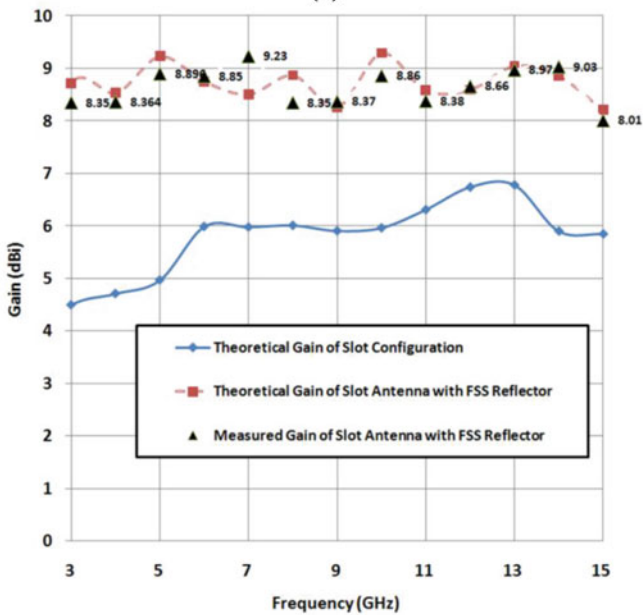
**Fig. 10.31** (a) Prototype of the UWB slot antenna with the four-layer composite FSS reflector (*left*) and patterns of each FSS layer (*right*): (a) FSS-1, (b) FSS-2, (c) FSS-3 and (d) FSS-4 (Ref. [17], reproduced courtesy of The Electromagnetics Academy)

careful design, the FSS transmission frequency response has been made stable against variations in the incidence angle and polarisation. A significant phase coherent bandwidth of 100% has been reached for reflector applications, and a stable frequency response for oblique incidence has been demonstrated. Further, phase analysis and field analysis at various locations of the FSS have been conducted by placing several probes in the FSS structure. The reflector combined with a UWB slot antenna has been experimentally demonstrated successfully. This antenna and FSS reflector combination demonstrates an impedance bandwidth of 122% and an average gain of around 7.5 dBi over the UWB frequency band. The described dual-layer FSS also proves valuable for many other applications requiring a low-cost reflector with wideband performance. The second planar UWB reflector is a four-layer FSS, but its thickness is even less than the dual-layer FSS mentioned above because it does not have air gaps between layers. Measured and computed results are presented for an UWB slot antenna placed just above this reflector. A maximum gain of 9.3 dBi and a gain variation of  $\pm 0.5$  dB (from 3 to 15 GHz) have been achieved from this four-layer FSS together with the slot antenna.

When one of these UWB FSS structures is used as the separator/shield, a printed UWB antenna can be fitted close to the conducting surfaces (such as metal enclosures, printed circuits, screens) that are commonly found in modern microwave



(a)



(b)

**Fig. 10.32** (a) Measured and predicted antenna input reflection coefficients with 4-layer FSS reflector. (b) Comparison of gain of the slot antenna with and without the 4-layer FSS reflector (Ref. [17], reproduced courtesy of The Electromagnetics Academy)

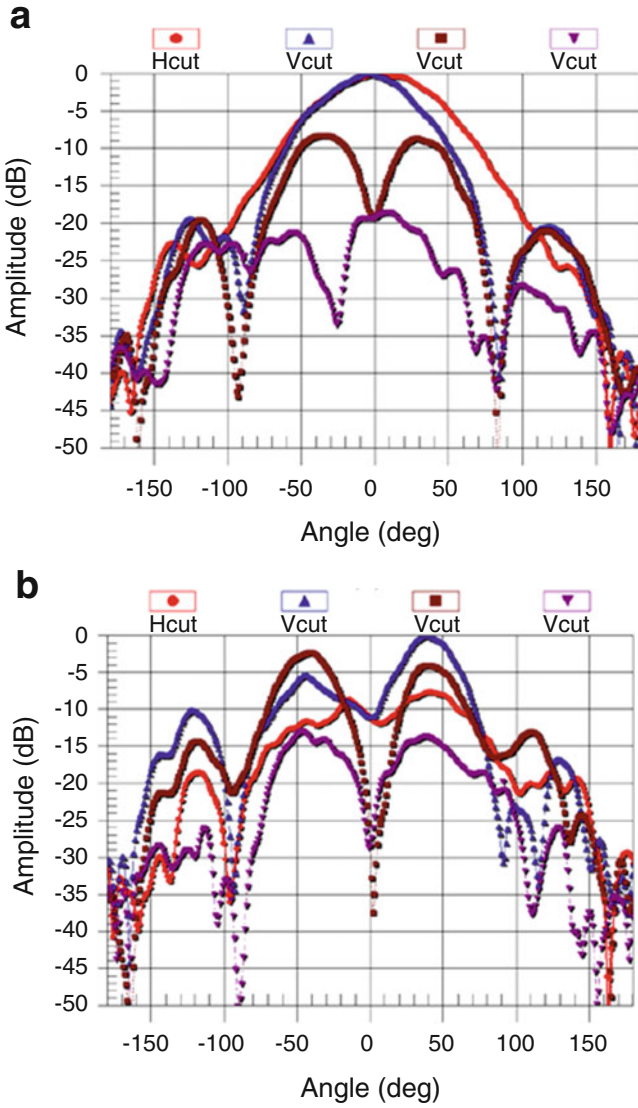


**Fig. 10.33** Measured radiation patterns at (a) 3 GHz and (b) 6 GHz (Ref. [17], reproduced courtesy of The Electromagnetics Academy)



and wireless devices. It has been verified that the use of an UWB FSS prevents deterioration of antenna impedance matching and significantly increases antenna gain.

The two FSS reflectors presented in this chapter lead to several interesting antenna configurations, which are yet to be explored. For example, a single-layer FSS with a 110% bandwidth appropriate to be used in the UWB frequency band is not yet available. It would be a good alternative to traditional reflectors that are however more space demanding. Moreover, the proposed reflectors based on the FSS concept allow some additional degrees of freedom to further control the gain and bandwidth over a certain frequency band and offer, for example, the possibility to filter WiFi and (WLAN) HIPERLAN signals.

## References

1. B. Allen, M. Dohler, E.E. Okon, W.Q. Malik, A.K. Brown, D.J. Edwards, *Ultra-wideband Antennas and Propagation for Communication, Radar and Imaging* (Wiley, Chichester, United Kingdom, 2007)
2. N. Engheta, R.W. Ziolkowski (Eds.), *Electromagnetic Metamaterials: Physics and Engineering Exploration* (Wiley-IEEE Press, Hoboken, NJ, 2006)
3. B.A. Munk, *Frequency Selective Surfaces: Theory and Design* (Wiley- Interscience, New York, 2000)
4. J.D. Shumpert, W.J. Chappell, L.B. Katehi, Parallel-plate mode reduction in conductor backed slots using electromagnetic bandgap substrates. *IEEE Trans. Microwave Theory Tech.* **47**(11), 2099–2104 (1999)
5. D. Sievenpiper, L. Zhang, R.F.J. Broas, N.G. Alexopoulos, E. Yablonovitch, High-impedance electromagnetic surfaces with a forbidden frequency band. *IEEE Trans. Microwave Theory Tech.* **47**(11), 2059–2074 (1999)
6. F. Elek, R. Abhari, G.V. Eleftheriades, A unidirectional ring-slot antenna achieved by using an electromagnetic bandgap surface. *IEEE Trans. Antennas Propag.* **53**(1), 181–190 (2005)
7. J.Y. Park, C.-C. Chang, Y. Qian, T. Itoh, An improved low-profile cavity-backed slot antenna loaded with 2-D UC-PBG reflector, in *Proceedings of the IEEE International Antennas and Propagation Symposium*, Boston, 2001 pp. 194–197
8. M. Pasion, S. Monni, A. Neto, M. Ettorre, G. Gerini, Frequency selective surfaces for extended bandwidth backing reflector functions. *IEEE Trans. Antennas Propag.* **58**(1), 43–50 (2010)
9. Y.E. Erdemli, K. Sertel, R.A. Gilbert, D.E. Wright, J.L. Volakis, Frequency-selective surfaces to enhance performance of broad-band reconfigurable arrays. *IEEE Trans. Antennas Propag.* **50**(12), 1716–1724 (2002)
10. Y. Ranga, L. Matekovits, K.P. Esselle, A.R. Weily, Multi-octave frequency selective surface reflector for ultra-wideband antennas. *IEEE Antennas Wirel. Propag. Lett.* **10**, 219–222 (2011)
11. Y. Ranga, K.P. Esselle, A. Weily, Compact ultra-wideband CPW-fed printed semicircular slot antenna. *Microw. Opt. Technol. Lett.* **52**(10), 2367–2372 (2010)
12. L. Guo, J. Liang, C.C. Chiau, X. Chen, C.G. Parini, J. Yu, Performances of ultra-wideband disc monopoles in time domain. *IET Microwaves Antennas Propag.* **1**(4), 955–959 (2007)
13. L. Moustafa, B. Jecko, Design and realization of a wide-band EBG antenna based on FSS and operating in the Ku-band. *Int. J. Antennas Propag.* **2010**, 139069 (2010)
14. L. Moustafa, B. Jecko, M. Thevenot, T. Monediere, R. Gonzalo, EBG antenna performance enhancement using conducting element FSS, in *Proceedings of the Second European Conference on Antennas and Propagation*, Nov 2007, EuCAP 2007, pp. 1–4
15. J. Romeu, Y. Rahmat-Samii, Fractal FSS: a novel dual-band frequency selective surface. *IEEE Trans. Antennas Propag.* **48**(7), 1097–1105 (2000)

16. A. Chuprin, E. Parker, J. Batchelor, Resonant frequencies of open and closed loop frequency selective surface arrays. *Electron. Lett.* **36**(19), 1601–1603 (2000)
17. Y. Ranga, L. Matekovits, A.R. Weily, K.P. Esselle, A constant gain ultra-wideband antenna with a multi-layer frequency selective surface. *Prog. Electromagn. Res. Lett.* **38**, 119–125 (2013)
18. Y. Ranga, K.P. Esselle, L. Matekovits, S.G. Hay, Increasing the gain of a semicircular slot UWB antenna using an FSS reflector, in *Proceedings of the 2012 IEEE-APS Topical Conference on Antennas and Propagation in Wireless Communications*, Cape Town, 2012, pp. 478–481
19. Y. Ranga, L. Matekovits, A.R. Weily, K.P. Esselle, A low-profile dual-layer ultra-wideband frequency selective surface reflector. *Microw. Opt. Technol. Lett.* **55**, 1223–1227



**Yogesh Ranga** (M'06–SM'15) received the Ph.D. degree in electronics engineering from Macquarie University, Sydney, N.S.W., Australia, in 2011. He joined Australian Patent Office in 2015 as Examiner of Patents. Prior to that, he worked with Macquarie University as Senior Research Associate and the Commonwealth Scientific and Industrial Research Organisation (CSIRO), Sydney, as a Postdoctoral Research Fellow and was also appointed as the Honorary Research Fellow at Macquarie University in 2011. Prior to joining CSIRO, he worked with Flomerics group (now CST Microstrips) as the Quality Assurance Engineer and SAMEER, IIT Powai as a Research Scientist. He has authored more than 60 research papers in his area of expertise. Dr. Ranga has served as the Chair of the IEEE New South Wales (NSW) MTT/AP Joint Chapter, Vice Chair of IEEE NSW GOLD

Affinity group, and a Member of the IEEE NSW Committee. He has served in technical programme committees of international conferences and as a reviewer for the IEEE Transactions on Antennas and Propagations, IEEE Transactions on Electromagnetic Compatibility, IEEE Antenna and Wireless Propagation Letters, Electronics Letters, and Journal of Electromagnetic Waves and Applications. He received the Super Science Fellowship at CSIRO, iMQRS Fellowship, and CSIRO Top Award. He also received PGRF and AcRON Researcher Awards for participating in the IEEE AP-S International Symposiums in 2009 and 2010.



**Karu P. Esselle** (M'92–SM'96–F'16) received B.Sc. degree in electronic and telecommunication engineering with First Class Honours from the University of Moratuwa, Sri Lanka, and MASC and Ph.D. degrees in electrical engineering from the University of Ottawa, Canada. He is a Professor of Electronic Engineering, Macquarie University, Sydney, Codirector of WiMed Research Centre and the Past Associate Dean – Higher Degree Research (HDR) of the Division of Information and Communication Sciences. He has also served as a member of the Dean's Advisory Council and the Division Executive from 2003 to 2008 and as the Head of the Department several times. He is also the chair of the Board of management of Australian Antenna Measurement Facility and elected Chair of both IEEE New South Wales (NSW) Section and IEEE NSW AP/MTT Chapter, in 2016 and

2017. He directs the Centre for Collaboration in Electromagnetic and Antenna Engineering and has been selected as one of the three new Distinguished Lecturers of IEEE AP Society for 2017–2020. He is the first Australian AP Distinguished Lecturer in almost two decades and second ever. When Professor Esselle was elected to the IEEE Antennas and Propagation Society Administrative Committee for a 3-year term in 2014, he became the only person residing in the Asia-Pacific Region (IEEE Region 10) to be elected to this highly competitive position over a period of at least 6 years (2010–2015). He was elevated to IEEE Fellow grade for his contributions to

resonance-based antennas. He is also a Fellow of Engineers Australia and an Associate Editor of IEEE Transactions on Antennas and Propagation and IEEE Access. Professor Esselle has authored almost 500 research publications, and his papers have been cited almost 4000 times. He is the first Australian antenna researcher ever to reach Google Scholar h-index of 30, and his current h-index is the highest among Australian antenna researchers when Google Scholar errors are corrected. Since 2002, his research team has been involved with research grants, contracts and Ph.D. scholarships worth over 15 million dollars. His research has been funded by many national and international organisations including Australian Research Council, Intel, US Air Force, Cisco Systems and Hewlett-Packard and Australian and Indian governments. Professor Esselle has been invited to serve as an international expert/research grant assessor by several nationwide research funding bodies overseas including the Netherlands, Canada, Finland, Hong Kong, Georgia and Chile. He has been invited by Vice-Chancellors of Australian and overseas universities to assess applications for promotion to professorial levels. He has also been invited to assess grant applications submitted to Australia's most prestigious schemes such as Australian Federation Fellowships and Australian Laureate Fellowships. He leads the Implantable Wireless Program of the WiMed Research Centre. In addition to the large number of invited conference speeches he has given, he has been an invited keynote speaker of IEEE workshops and conferences. Professor Esselle's other awards include 2016 and 2012 Best Published Paper Awards from IESL NSW Chapter, 2011 Outstanding Branch Counsellor Award from IEEE headquarters (USA), 2009 Vice Chancellor's Award for Excellence in Higher Degree Research Supervision and 2004 Inaugural Innovation Award for best invention disclosure. His mentees have been awarded many fellowships, awards and prizes for their research achievements. Thirty-six international experts who examined the theses of his recent Ph.D. graduates ranked them in the top 5% or 10%. Professor Esselle has provided expert assistance to more than a dozen companies including Intel, Hewlett Packard Laboratory (USA), Cisco Systems (USA), Cochlear, Optus, ResMed and Katherine-Werke (Germany). Professor Esselle is the Technical Program Committee Co-Chair of ISAP 2015, APMC 2011 and TENCON 2013 and the Publicity Chair of ICEAA 2016, IWAT 2014 and APMC 2000. Professor Esselle's research activities are posted in the web at <http://web.science.mq.edu.au/~esselle/>.



**Ladislau Matekovits** was born in Arad (Romania), on November 19, 1967. He received the first degree in Electronic Engineering from Institutul Politehnic din Bucuresti, Romania, and the Ph.D. (Dottorato di Ricerca) in Electronic Engineering from Politecnico di Torino, Italy, in 1992 and 1995, respectively. Since 1995 he has continuously been with the Electronics Department of the Politecnico di Torino where he was appointed as Assistant Professor in 2001 and Associate Professor in 2014, respectively. Beginning July 1, 2009, for 2 years, he has been a Marie Curie Fellow at Macquarie University, Sydney, NSW, Australia, where since 2014 he is Honorary Fellow. His main research activities concern numerical analysis of printed antennas and in particular development of new, numerically efficient full-wave techniques to analyse large arrays, optimization techniques and active and

passive metamaterials. He has delivered seminars on these topics all around the world: Europe, USA (AFRL/MIT-Boston), and Australia. Prof. Matekovits is a recipient of various awards, including the 1998 URSI Young Scientist Award (Thessaloniki, Greece) and the Best AP2000 Oral Paper on Antennas, ESA-EUREL Millenium Conference on Antennas & Propagation (Davos, Switzerland). Prof. Matekovits has been Assistant Chairman and Publication Chairman of the European Microwave Week 2002 (Milan, Italy) and general Chair of the 11th International Conference on Body Area Networks, 2016, (Torino, Italy). He is a member of the organising committee of the International Conference on Electromagnetics in Advanced Applications (ICEAA), and he serves as Associated Editor of the IEEE Access and IET MAP. Since 2016 he is a member of the American Romanian Academy of Arts and Sciences.

# Chapter 11

## Radar Cross Sections of Six Different Radar Reflectors Mounted on Power Boats

Hsing Yi Chen and Chien Yi Lin

### 11.1 Introduction

Radar cross section (RCS) [1–3] plays an essential role in detecting a moving target, such as aircraft [4–7], ships [8, 9], spacecraft [10, 11], missiles [12, 13], etc. Generally, the RCS of a target depends on several factors, such as its electrical size, shape, and constitutive properties; the viewing direction; the operating frequency and wave polarization; etc. The RCS is expressed in terms of an area. The larger the RCS of a target is, the more easily it is detected. Recently, there are considerable studies on RCS reduction for stealth (low visibility) design in military applications [7, 14]. Numerous numerical methods, such as physical optics (PO) [15–17], physical theory of diffraction (PTD) [18, 19], geometrical theory of diffraction (GTD) [14, 20], method of moments (MoM) [21], and finite-difference time-domain (FDTD) [22, 23], have been successfully applied to RCS prediction. Measurements of RCS for different objects have been reported in the literature [1, 5, 24].

The prediction of the RCS of a radar reflector is important in designing high-visibility power boats. Radar reflector is an important device which is mounted on power boats to avoid collisions with other power boats or ships. Most power boats are constructed with wood, fiberglass, or composite materials and so are inherently poor reflectors of radar energy. For this reason, they are often equipped with radar reflectors. Radar is the primary equipment used by all commercial vessels for collision avoidance in bad weather, poor visibility, and at night. When visibility is limited or when small vessels are navigating at night or in potentially busy shipping areas, ship captains must ensure that everything possible is done to maximize the size of the radar reflection that their vessel produces. For emergency purpose, radar reflectors are also available to assist search and rescue personnel in locating missing

---

H.Y. Chen (✉) • C.Y. Lin

Department of Communications Engineering, Yuan Ze University, Taoyuan City, Taiwan

e-mail: [ehychen@saturn.yzu.edu.tw](mailto:ehychen@saturn.yzu.edu.tw)

persons and power boats. Therefore, it is highly desirable to develop a power boat radar reflector with the largest RCS under the cost-effective principle.

In this chapter, a brief introduction of the FDTD method [25] is presented in Sect. 11.2. Formulas for computing scattered fields radiated from a RADAR reflector are described in Sect. 11.3. In Sect. 11.4, the validity of the FDTD method [25] is first checked by comparing numerical results of RCSs with those obtained using analytic solution [26] for a perfectly conducting sphere with a radius of 16.2 mm in a wide range of frequencies. After validating the accuracy of the FDTD method, the FDTD method is used to calculate the RCSs of six aluminum radar reflectors with different structures mounted on power boats at frequencies of 600-4000 MHz. Numerical results of the RCSs of the six different radar reflectors versus frequency plots are presented in this chapter. Comments on structure effects on RCS are presented in Sect. 11.5.

## 11.2 A Brief Introduction of the FDTD Method

The FDTD method [25] is a direct solution for Maxwell's time-dependent curl equations. It is based on space-time mesh sampling of the unknown electromagnetic (EM) fields within and surrounding the object of interest. Due to its accuracy and simplicity, the FDTD method has been widely applied in antenna design, electromagnetic interference (EMI), EM wave propagation and scattering problems, design of microwave circuits, photonic device design, bioelectromagnetics, and many other problems.

In the FDTD solution procedure, the coupled Maxwell's equations in differential form are solved for various points of the scatterer as well as the surroundings in a time-stepping manner until converged solutions are obtained. Following Yee's notation and using centered difference approximation on both the time and space first-order partial differentiations, six finite-difference equations for six unique field components within a unit cell are obtained. In these six finite-difference equations, electric fields are assigned to half-integer ( $n + 1/2$ ) time steps, and magnetic fields are assigned to integer ( $n$ ) time steps for the temporal discretization of fields.

To ensure numerical stability, the time step  $\delta_t$  is set to  $\delta/(2c_0)$ , where  $\delta$  and  $c_0$  are the cell size and the speed of light in free space, respectively. The center-difference approximation ensures that the spatial and temporal discretizations have second-order accuracy, where errors are proportional to the square of the cell size and time step [25]. An important issue encountered in solving the time-domain electromagnetic-field equations, by the FDTD method, is the of absorbing boundary conditions. Several absorbing boundary conditions (ABC) have been proposed in the FDTD method such as second-order Mur [27], and Liao [28], and perfectly matched layer (PML) [29]. Liao's ABC and Berenger's PML require a lot of memory. Second-order Mur absorbing boundary conditions are among the most frequently cited and are successful in many cases. In our formulation, the second-order Mur approximation of absorbing boundary conditions [27] is used for the near-field irradiation problems. In this study, the second-order Mur absorbing

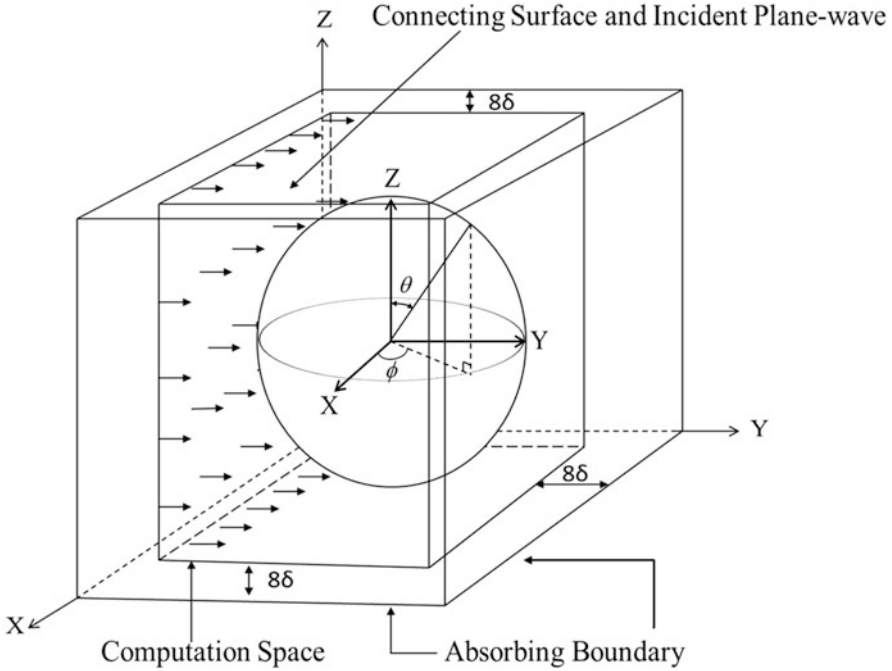


**Fig. 11.1** FDTD model of a sphere, where  $\delta = 0.1$  or  $0.8$  mm is the cell size

boundaries are employed to design a FDTD computer program because they do not require much memory and have a reasonable accuracy. The external absorbing boundaries are placed at a distance of  $8\delta$  on all sides of the scattering object as shown in Fig. 11.1, where  $\delta = 0.1$  or  $0.8$  mm is the cell size.

### 11.3 Scattered Fields from a Radar Reflector

In this section, a time dependency of the form  $\exp(j\omega t)$  is assumed, where  $\omega$  is the angular frequency. The induced electric fields in a radar reflector can be obtained by using the computation procedure described in Sect 11.2 by the FDTD method. For FDTD simulations, all materials used for the radar reflector are assumed to be non-magnetic ( $\mu_r = 1.0$ ). As the induced electric fields in the radar reflector are obtained, the equivalent free-space current density [30] in the radar reflector can be computed by

$$\vec{J}_{eq}(\vec{r}) = [\sigma + j\omega\epsilon_0 (\epsilon_r - 1)] \vec{E}(\vec{r}'), \tag{11.1}$$

where  $\vec{E}(\vec{r}')$  is the electric field in the radar reflector,  $\omega$  is the angular frequency,  $\sigma$  and  $\epsilon_r$  denote the conductivity and relative permittivity of the radar reflector,

respectively. The first term of Eq. (11.1) is the conduction current density, and the second term represents the polarization current density. Therefore, the electric field scattered from the radar reflector can be obtained from the equivalent free-space current density expressed as [31]

$$\vec{E}^s(\vec{r}) = -j\eta_0 k_0 \int_v \vec{J}_{eq}(\vec{r}') \cdot \left[ \overleftrightarrow{I} + \frac{\nabla\nabla}{k_0^2} \right] G_0(\vec{r}, \vec{r}') dv', \quad (11.2)$$

where

$$G_0(\vec{r}, \vec{r}') = \frac{\exp(-jk_0 R)}{4\pi R}, \quad (11.3)$$

$$\eta_0 = \sqrt{\frac{\mu_0}{\varepsilon_0}}, \quad (11.4)$$

$$R = |\vec{r} - \vec{r}'| = \sqrt{(x-x')^2 + (y-y')^2 + (z-z')^2}, \quad (11.5)$$

$$k_0 = \omega \sqrt{\mu_0 \varepsilon_0}. \quad (11.6)$$

In the above equations,  $\vec{E}^s$  denotes the scattered electric field,  $\overleftrightarrow{I}$  denotes the identity tensor,  $v$  denotes a volume integral,  $\varepsilon_0 = 8.854 \times 10^{-12}$  F/m is the permittivity of free space,  $\mu_0 = 4\pi \times 10^{-7}$  H/m is the permeability of free space,  $k_0$  is the wave propagation constant of free space, and  $(x, y, z)$  and  $(x', y', z')$  are field position vector and source position vector, respectively. For far-field approximation ( $k_0 R \gg 1$ ,  $r \gg r'$ ), a simpler formula for the integral Eq. (11.2) can be obtained by using the following derivations,

$$\begin{aligned} \nabla G_0(\vec{r}, \vec{r}') &= \frac{\partial}{\partial x} G_0(\vec{r}, \vec{r}') \hat{a}_x + \frac{\partial}{\partial y} G_0(\vec{r}, \vec{r}') \hat{a}_y + \frac{\partial}{\partial z} G_0(\vec{r}, \vec{r}') \hat{a}_z \\ &= \frac{-je^{-jk_0 R}}{4\pi} \frac{k_0 R}{R^2} \left( \frac{\partial R}{\partial x} \hat{a}_x + \frac{\partial R}{\partial y} \hat{a}_y + \frac{\partial R}{\partial z} \hat{a}_z \right) \\ &\approx \frac{-je^{-jk_0 R}}{4\pi} \frac{k_0 R}{R^2} \frac{(x-x')\hat{a}_x + (y-y')\hat{a}_y + (z-z')\hat{a}_z}{R} \\ &\approx \frac{-jk_0 e^{-jk_0 R}}{4\pi R} \frac{\vec{R}}{R} \\ &\approx \frac{-jk_0 e^{-jk_0 R}}{4\pi R} \hat{a}_R \\ &\approx \frac{-jk_0 e^{-jk_0 R}}{4\pi R} \hat{a}_r \end{aligned} \quad (11.7)$$

where  $\hat{a}_r$  is the unit radial vector.

$$\vec{J}_{eq}(\vec{r}') \cdot \nabla = J_x(\vec{r}') \frac{\partial}{\partial x} + J_y(\vec{r}') \frac{\partial}{\partial y} + J_z(\vec{r}') \frac{\partial}{\partial z}, \quad (11.8)$$

$$\begin{aligned} \frac{\partial}{\partial x} \nabla G_0(\vec{r}, \vec{r}') &= \frac{-jk_0 e^{-jk_0 R}}{4\pi} \frac{(-jk_0 R)}{R^2} \frac{\partial R}{\partial x} \hat{a}_r, \\ &= \frac{-k_0^2 e^{-jk_0 R}}{4\pi R} \frac{\partial R}{\partial x} \hat{a}_r, \end{aligned} \quad (11.9)$$

$$\frac{\partial}{\partial y} \nabla G_0(\vec{r}, \vec{r}') = \frac{-k_0^2 e^{-jk_0 R}}{4\pi R} \frac{\partial R}{\partial y} \hat{a}_r, \quad (11.10)$$

$$\frac{\partial}{\partial z} \nabla G_0(\vec{r}, \vec{r}') = \frac{-k_0^2 e^{-jk_0 R}}{4\pi R} \frac{\partial R}{\partial z} \hat{a}_r. \quad (11.11)$$

Then,

$$\begin{aligned} \left[ \vec{J}_{eq}(\vec{r}') \cdot \nabla \nabla \right] G_0(\vec{r}, \vec{r}') &= J_x(\vec{r}') \frac{\partial}{\partial x} \nabla G_0(\vec{r}, \vec{r}') + \\ &J_y(\vec{r}') \frac{\partial}{\partial y} \nabla G_0(\vec{r}, \vec{r}') + J_z(\vec{r}') \frac{\partial}{\partial z} \nabla G_0(\vec{r}, \vec{r}') \\ &= \frac{-k_0^2 e^{-jk_0 R}}{4\pi R} \left[ J_x(\vec{r}') \frac{\partial R}{\partial x} + J_y(\vec{r}') \frac{\partial R}{\partial y} + J_z(\vec{r}') \frac{\partial R}{\partial z} \right] \hat{a}_r \\ &= \frac{-k_0^2 e^{-jk_0 R}}{4\pi R} \left[ \vec{J}_{eq}(\vec{r}') \cdot \frac{\vec{R}}{R} \right] \hat{a}_r \\ &= \frac{-k_0^2 e^{-jk_0 R}}{4\pi R} \left[ \vec{J}_{eq}(\vec{r}') \cdot \hat{a}_r \right] \hat{a}_r \\ &= -k_0^2 G_0(\vec{r}, \vec{r}') J_r(\vec{r}') \hat{a}_r, \end{aligned} \quad (11.12)$$

and

$$\begin{aligned} \vec{J}_{eq}(\vec{r}') \cdot \left[ \vec{\nabla} + \frac{\nabla \nabla}{k_0^2} \right] G_0(\vec{r}, \vec{r}') &= \vec{J}_{eq}(\vec{r}') G_0(\vec{r}, \vec{r}') - G_0(\vec{r}, \vec{r}') \vec{J}_r(\vec{r}') \hat{a}_r \\ &= \left[ \vec{J}_{eq}(\vec{r}') - J_r(\vec{r}') \hat{a}_r \right] G_0(\vec{r}, \vec{r}') \\ &= \left[ J_\theta(\vec{r}') \hat{a}_\theta + J_\varphi(\vec{r}') \hat{a}_\varphi \right] \frac{e^{-jk_0 R}}{4\pi R}, \end{aligned} \quad (11.13)$$



where  $\hat{a}_\theta$  and  $\hat{a}_\varphi$  are unit vectors in a spherical coordinate system. Finally, Eq. (11.2) becomes

$$\vec{E}^s(\vec{r}) = -j\eta_0 k_0 \int_s \left[ J_\theta(\vec{r}') \hat{a}_\theta + J_\varphi(\vec{r}') \hat{a}_\varphi \right] \frac{e^{-jk_0 R}}{4\pi R} ds', \quad (11.14)$$

where  $s$  denotes a surface integral, and  $\theta$  and  $\phi$  are the polar and azimuthal angles defined in a spherical coordinate system. For far-field observations,  $R$  is approximately expressed as

$$\begin{aligned} R &\cong r - r' \cos \psi, \\ &\approx r - \vec{r}' \cdot \hat{a}_r, \end{aligned} \quad \text{for phase variations,} \quad (11.15)$$

$$R \cong r, \quad \text{for distance variations,} \quad (11.16)$$

where  $\psi$  is the angle between the vectors  $\vec{r}$  and  $\vec{r}'$ . The transformations between rectangular and spherical components for  $\hat{a}_r$ ,  $J_\theta(\vec{r}')$ , and  $J_\varphi(\vec{r}')$  are given by

$$\hat{a}_r = \sin \theta \cos \varphi \hat{a}_x + \sin \theta \sin \varphi \hat{a}_y + \cos \theta \hat{a}_z, \quad (11.17)$$

$$J_\theta(\vec{r}') = J_x(\vec{r}') \cos \theta \cos \varphi + J_y(\vec{r}') \cos \theta \sin \varphi - J_z(\vec{r}') \sin \theta, \quad (11.18)$$

$$J_\varphi(\vec{r}') = -J_x(\vec{r}') \sin \varphi + J_y(\vec{r}') \cos \varphi. \quad (11.19)$$

The scattered far-field components  $E_\theta$  and  $E_\varphi$  can easily be found by calculating the far-field radiated from currents distributed in the radar reflector as [31]

$$\begin{aligned} \vec{E}^s(\theta, \varphi) &= E_\theta \hat{a}_\theta + E_\varphi \hat{a}_\varphi \\ &= \frac{-j\eta_0 k_0}{4\pi r} \exp(-jk_0 r) \int_v \left\{ \hat{a}_\theta [J_x(\vec{r}') \cos \theta \cos \varphi \right. \\ &\quad \left. + J_y(\vec{r}') \cos \theta \sin \varphi - J_z(\vec{r}') \sin \theta] + \hat{a}_\varphi [-J_x(\vec{r}') \sin \varphi \right. \\ &\quad \left. + J_y(\vec{r}') \cos \varphi] \right\} \exp[jk_0(x' \sin \theta \cos \varphi + y' \sin \theta \sin \varphi \\ &\quad \left. + z' \cos \theta)] dv' \end{aligned} \quad (11.20)$$

where  $J_x(\vec{r}')$ ,  $J_y(\vec{r}')$ , and  $J_z(\vec{r}')$  are the current densities flowing in the  $x$ -,  $y$ -, and  $z$ -axis inside the radar reflector, respectively.

The total scattering power of the radar reflector is given by

$$P_{tsp} = \frac{1}{2} \int_s \frac{|\vec{E}^s|^2}{\eta_0} ds = \int_{\theta=0}^{\pi} \int_{\varphi=0}^{2\pi} \frac{|\vec{E}^s|^2}{\eta_0} R^2 \sin \theta d\theta d\varphi \quad [\text{W}], \quad (11.21)$$

where  $s$  is the Gaussian surface enclosing the radar reflector. The back-scattering power can be calculated by

$$P_{bsp} = \frac{1}{2} \int_s \frac{|\vec{E}^s|^2}{\eta_0} ds = \int_{\theta=0}^{\pi} \int_{\varphi=\pi}^{2\pi} \frac{|\vec{E}^s|^2}{\eta_0} R^2 \sin \theta d\theta d\varphi \quad [\text{W}]. \quad (11.22)$$

The total scattering cross section and the radar cross section (back-scattering cross section) are defined by

$$\sigma_{tscs} = \frac{P_{tsp}}{P_i} [\text{m}^2], \quad (11.23)$$

$$\sigma_{rcs} = \frac{P_{bsp}}{P_i} [\text{m}^2], \quad (11.24)$$

$$P_i = \frac{|\vec{E}^i|^2}{2\eta_0} [\text{W}/\text{m}^2], \quad (11.25)$$

where  $P_i$  is the incident power density and  $\vec{E}^i$  is the incident electric field.

## 11.4 Simulation Results

Before using the FDTD method to calculate the RCSs of six aluminum radar reflectors, the validity of the FDTD method was checked by comparing numerical results of the RCSs with those obtained using analytic solutions [26] for a perfectly conducting sphere with a radius of 16.2 mm in a wide range of frequencies of 37.3 MHz–7.5 GHz. In the FDTD simulation, the cell size was taken to be 0.1 mm. Comparison of normalized RCSs of the perfectly conducting sphere obtained by the FDTD method and analytic solution is shown in Fig. 11.2. It is clear that simulation and analytical results show a good agreement. From Fig. 11.2, it is shown that the normalized monostatic RCS for a perfecting sphere is a function of its radius. The term monostatic is used when the transmitter and receiver are collocated.

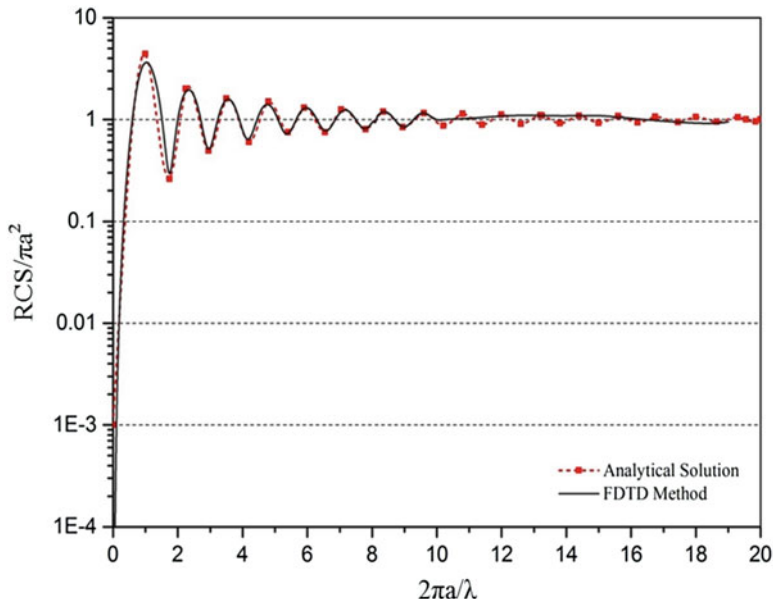


**Fig. 11.2** Comparison of normalized RCSs of a perfectly conducting sphere obtained by the FDTD method and analytical solution

The curve shown in Fig. 11.2 can be divided into the Rayleigh, the Mie (resonance), and the optical regions [26]. The Rayleigh region represents the part of the curve for small values of the radius ( $a < \lambda/2\pi$ ,  $\lambda$  is the wavelength), and the optical region represents the RCS of the sphere for large values of the radius ( $a > 5\lambda/\pi$ ). The region between Rayleigh and optical regions is the Mie or resonance region. For small values of the radius, the RCS is linear and can be calculated as  $\sigma_{\text{rcs}} = (\pi a^2) \times (7.11) \times (k_0 a)^4$  [32]. For intermediate values of the radius, the RCS is oscillatory about the value of  $\pi a^2$ , the maximum and minimum values of RCSs are found to be  $4\pi a^2$  and  $0.26\pi a^2$ , respectively [32]. For large values of the radius, the RCS approaches the value of  $\pi a^2$  that is the physical area of the cross section of the sphere, which means that the RCS is independent of frequency.

After validating the accuracy of the FDTD method, it was used to calculate the RCSs of six aluminum radar reflectors with different structures at frequencies of 600–4000 MHz. The six aluminum radar reflectors, named reflectors 1–6, are shown in Figs. 11.3, 11.4, 11.5, 11.6, 11.7, and 11.8. The six radar reflectors have the same aluminum volume of  $48,202 \text{ mm}^3$  in the exterior but their shapes and structures are different. Reflectors 1–6 are complex structured plates, crossed plates, hollow cylinder, hollow cuboid, hollow cube, and hollow sphere. In FDTD simulations, reflectors 1–6 have 4,404,220; 5,587,644; 3,193,900; 2,117,220; 20,346,417; and 12,812,904 cubic cells, respectively. The cell size in these models is 0.8 mm. The RCS was calculated from the scattered fields caused by a normal incident plane wave hitting the maximum physical cross section of the model.

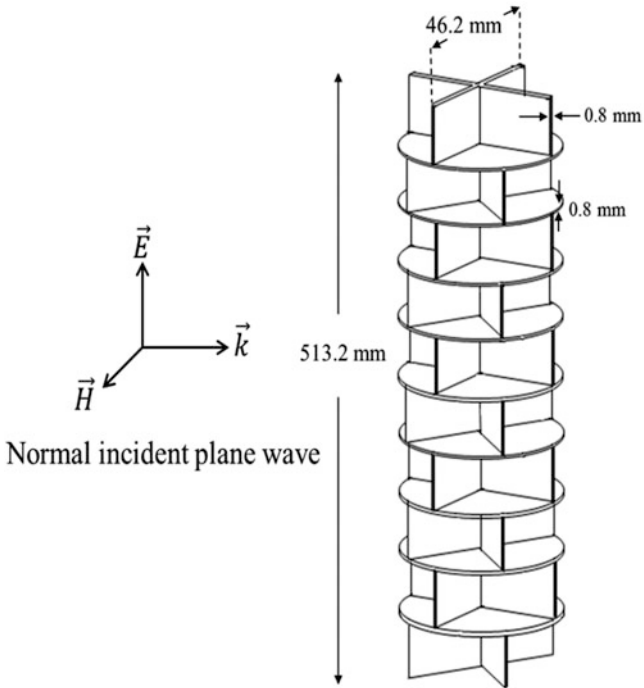


**Fig. 11.3** Reflector 1 (complex structured plates)

Figure 11.9 shows the RCSs of the six different aluminum radar reflectors calculated by the FDTD method. From Fig. 11.9, it is found that the maximum values of the RCSs of the six aluminum radar reflectors are in the range of 0.17–0.77 m<sup>2</sup>. Reflector 2 (crossed plates) has the largest RCS of 0.77 mm<sup>2</sup> at 600 MHz. Even with the same aluminum volume of 48,202 mm<sup>3</sup>, each radar reflector has a different maximum value of RCS at its individual resonant frequency. The maximum RCS of each radar reflector compared with its maximum physical cross section (PCS) is listed in Table 11.1. Obviously, the hollow sphere (reflector 6) has the smallest value of the ratio of maximum RCS to maximum PCS at 3600 MHz. The hollow cuboid (reflector 4) has the largest value of the ratio of maximum RCS to maximum PCS at 600 MHz. Basically, the RCS of a target depends on its electrical size, shape, and the operating frequency and incident wave polarization. It is very difficult to evaluate the RCS of a complex object by a simple computing equation.

## 11.5 Conclusions

The validity of the RCS simulation results of a perfectly conducting sphere was first checked by analytical data when we began this research work. After validating the accuracy of the FDTD method, the FDTD method was first proposed to calculate

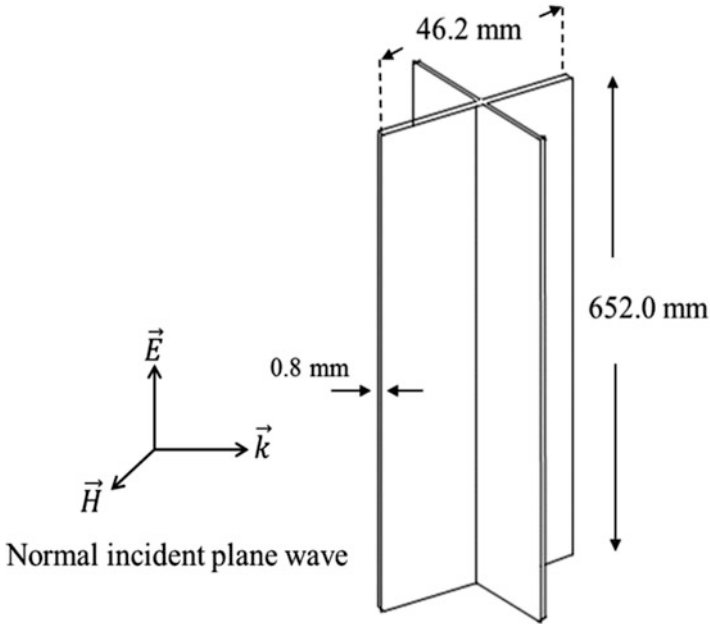


Fig. 11.4 Reflector 2 (crossed plates)

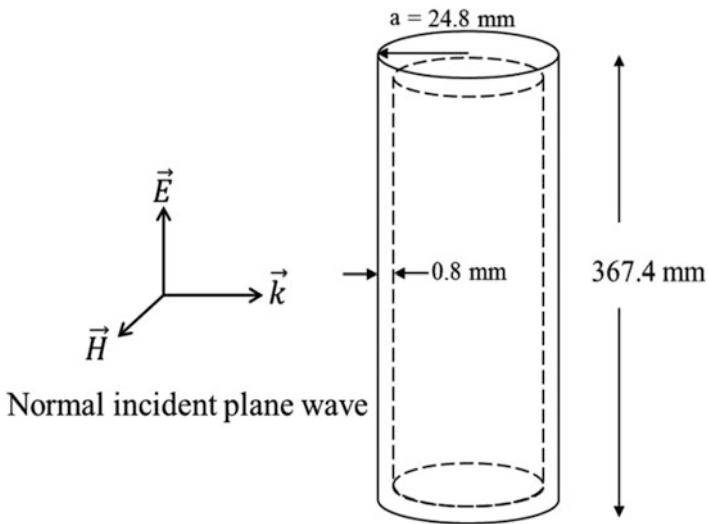


Fig. 11.5 Reflector 3 (hollow cylinder)

the RCSs of six aluminum radar reflectors with different structures at frequencies of 600–4000 MHz. It was found that the maximum values of the RCSs of the six aluminum radar reflectors are in the range of 0.17–0.77 m<sup>2</sup>. Even with the

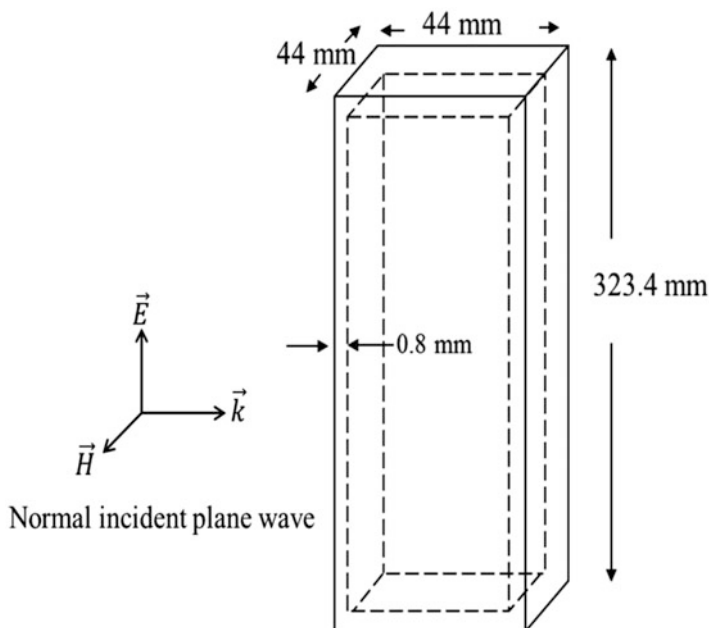


Fig. 11.6 Reflector 4 (hollow cuboid)

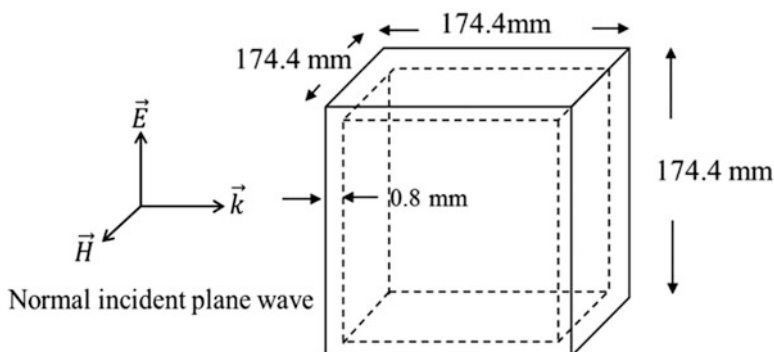


Fig. 11.7 Reflector 5 (hollow cube)

same volume, each radar reflector has a different maximum value of RCS at its individual resonant frequency. The radar reflector features, including shape, constitutive properties, and structure, will significantly affect the RCS at the same frequency. Every power boat needs a compact, lightweight, and economical radar reflector with larger RCS. In the future, these six reflectors will be fabricated and their RCSs will be measured in an anechoic chamber and compared with those obtained by the FDTD method. RCS simulation and measurement are important in radar system design. The interested reader is advised to go over the material provided in Refs. [1–3].

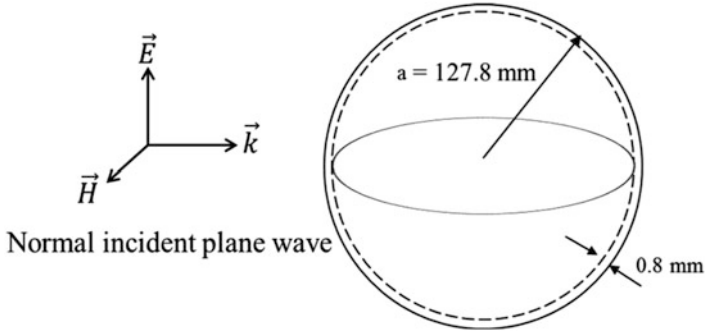


Fig. 11.8 Reflector 6 (hollow sphere)

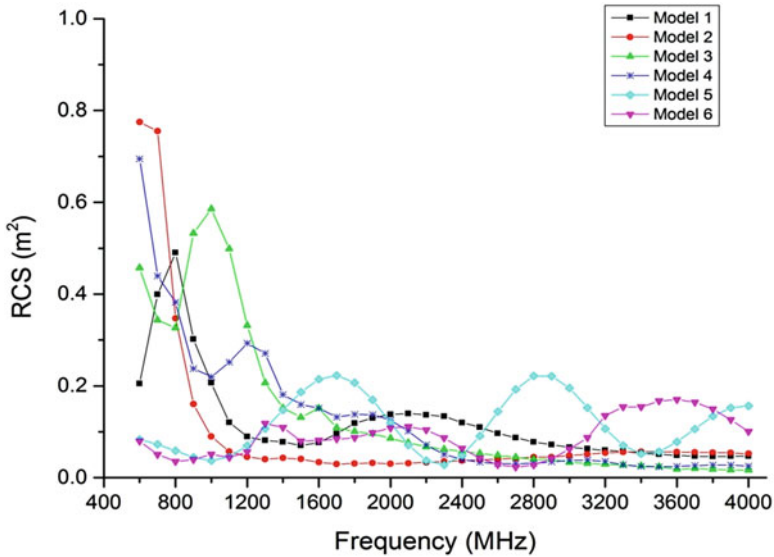


Fig. 11.9 Simulated radar cross sections (RCSs) of six different aluminum radar reflectors

Table 11.1 The maximum RCS of each radar reflector compared with its maximum PCS

	Frequency (MHz)	Maximum RCS ( $\text{m}^2$ )	Maximum PCS ( $\text{m}^2$ )	RCS/PCS
Reflector 1	800	0.49034	0.02371	20.68
Reflector 2	600	0.77487	0.03012	25.73
Reflector 3	1000	0.58574	0.01822	32.15
Reflector 4	600	0.69466	0.01422	48.85
Reflector 5	1700	0.22252	0.03028	7.35
Reflector 6	3600	0.17021	0.05129	3.32

## References

1. U.F. Knott, *Radar Cross Section Measurements* (Van Nostrand Reinhold, New York, 1993)
2. J.F. Shaeffer, M.T. Tuley, E.F. Knot, *Radar Cross Section* (Artech House, Norwood, MA, 1985)
3. A.K. Bhattacharyya, D.L. Sengupta, *Radar Cross Section Analysis & Control* (Artech House, Norwood, MA, 1991)
4. J.D. Wilson, Probability of detecting aircraft targets. *IEEE Trans. Aerosp. Electron. Syst.* **8**(6), 757–761 (1972)
5. A. Jain, I. Patel, Dynamic imaging and RCS measurements of aircraft. *IEEE Trans. Aerosp. Electron. Syst.* **31**(1), 211–226 (1995)
6. B. Persson, M. Norsell, On modeling RCS of aircraft for flight simulation. *IEEE Antennas Propag. Mag.* **56**(4), 34–43 (2014)
7. A.A. Mauro, R.J. Port, M.C. Rezende, Simulations of the radar cross section of a stealth aircraft, in *Proceedings of the IEEE MTT-S International Microwave and Optoelectronics Conference*, Brazil, 29 Oct–1 Nov 2007, pp. 409–412
8. L. Sevgi, Target reflectivity and RCS interactions in integrated maritime surveillance systems based on surface-wave high-frequency radars. *IEEE Antennas Propag. Mag.* **43**(1), 36–51 (2001)
9. Y. Zhao, M. Zhang, H. Chen, X.F. Yuan, Radar scattering from the composite ship-ocean scene: doppler spectrum analysis based on the motion of six degrees of freedom. *IEEE Trans. Antennas Propag.* **62**(8), 4341–4347 (2014)
10. R.B. Dybdal, H. King, 93-GHz radar cross section measurements of satellite elemental scatterers. *IEEE Trans. Antennas Propag.* **25**(3), 396–402 (1977)
11. X. Li, X. Meng, RCS simulation of spacecraft based on orbital dynamics, in *Proceedings of the 3rd IEEE International Symposium on Microwave, Antenna, Propagation and EMC Technologies for Wireless Communications*, Beijing, 27–29 Oct 2009, pp. 568–572
12. M.B. Perotoni, S.E. Barbin, A study on RCS of missile models using the method of moments, in *Proceedings of the IEEE MTT-S International Microwave and Optoelectronics Conference*, Brazil, 29 Oct–1 Nov 2007, pp. 492–495
13. M. Martorella, R. Soletti, F. Berizzi, E. Dalle Mese, Plume effect on radar cross section of missiles at HF band, in *Proceedings of the International Conference on Radar*, Adelaide, 3–5 Sep 2003, pp. 656–661
14. P.Y. Ufimtsev, Comment on diffraction principles and limitations of RCS reduction techniques. *Proc. IEEE* **84**(12), 1830–1851 (1996)
15. C. Bourlier, P. Pouliguen, Useful analytical formulae for near-field monostatic radar cross section under the physical optics: far-field criterion. *IEEE Trans. Antennas Propag.* **57**(1), 205–214 (2009)
16. M.H. Vogel, The physical optics approximation in the near-field region, TNO Physics and Electronics Laboratory, Rep. no. FEL 1989-100n, 1989. [https://www.researchgate.net/publication/252745178\\_The\\_physical\\_optics\\_approximation\\_in\\_the\\_near-field\\_region](https://www.researchgate.net/publication/252745178_The_physical_optics_approximation_in_the_near-field_region)
17. P. Pouliguen, P. Gadenne, J.Y. Marty, Radar reflectivity of a target illuminated by a spherical wave. Presented at the AGARD conference radar signature analysis and imaging of military targets, Ankara, 7–10 Oct 1996
18. C.L. Yu, R. Kipp, D.J. Andersh, S.W. Lee, Near-field electromagnetic modeling and analysis. Presented at the IEEE AP-S International Symposium and URSI Radio Science Meeting, Montreal, 13–18 July 1997
19. S.W. Lee, S. K. Jeng, NcPTD 1.2 a high frequency near-field RCS computation code based on physical theory of diffraction, DEMACO, Inc., Champaign, IL, 1991
20. J.B. Keller, Geometrical theory of diffraction. *J. Opt. Soc. Am.* **52**(2), 116–130 (1962)
21. A. Ishimaru, *Electromagnetic Wave Propagation. Radiation and Scattering* (Prentice–Hall, Englewood Cliffs, NJ, 1991)



22. L. Gurel, H. Bagci, J.C. Castelli, A. Cheraly, F. Tardivel, Validation through comparison: measurement and calculation of the bistatic RCS of a stealth target. *Radio Sci.* **38**(3), 10 46–10 57 (2003)
23. L. Sevgi, S. Paker, FDTD based RCS calculations and antenna simulations. *AEÜ Int. J. Electron. Commun.* **52**(2), 65–75 (1998)
24. L. Sevgi, Z. Rafiq, I. Majid, Radar cross section (RCS) measurements. *IEEE Antennas Propag. Mag.* **55**(6), 278–291 (2013)
25. K.S. Yee, Numerical solution of initial boundary value problems involving Maxwell's equations in isotropic media. *IEEE Trans. Antennas Propag.* **14**(5), 302–307 (1966)
26. C.A. Balanis, *Advanced Engineering Electromagnetics* (Wiley, New York, 1989), pp. 650–658
27. G. Mur, Absorbing boundary conditions for the finite-difference approximation of the time-domain electromagnetic-field equations. *IEEE Trans. Electromagn. Compat.* **23**, 377–382 (1981)
28. Z.P. Liao, H.L. Wong, B.P. Yang, Y.F. Yuan, A transmitting boundary for transient wave analysis. *Sci. Sin. (Ser. A)* **27**(10), 1063–1076 (1984)
29. J.P. Berenger, A perfectly matched layer for the absorption of electromagnetic waves. *J. Comput. Phys.* **114**, 185–200 (1994)
30. D.E. Livesay, K.M. Chen, Electromagnetic fields induced inside arbitrarily shaped biological bodies. *IEEE Trans. Microwave Theory Tech.* **22**(12), 1273–1280 (1974)
31. K. Karimullah, Theoretical and experimental study of the proximity effects of thin-wire antenna in presence of biological bodies, PhD dissertation, Michigan State University, Michigan, 1979
32. A.E. Fuhs, Radar cross section lectures, in *The No-See-Um Book* (American Institute of Aeronautics and Astronautics, New York, 1982)



**Hsing Yi Chen** was born in Taiwan, Republic of China, in 1954. He received the B.S. degree from the Chung Yuan Christian University, Chung-Li, Taiwan, in 1978, the M. S. degree from the National Tsing Hua University, Hsinchu, Taiwan, in 1981, and the Ph.D. degree from the University of Utah, Salt Lake City, Utah in 1989, all in electrical engineering. He joined the faculty of the Department of Electrical Engineering, Yuan Ze University, Taiwan, in September 1989. From 1995 to 1996, he was the Director of the Research and Development Center for Far-Eastern Group. He was the Chairman of Electrical Engineering from 1996 to 2002, the Chairman of Communications Engineering from 2001 to 2002, the Dean of Engineering College from 2002 to 2006, the Dean of Electrical and Communication Engineering College

from 2006 to 2012, and the Dean of Research and Development Office from 2012 to 2013. He was a Director of Board Meeting, Far Eastone Telecommunications Co., Ltd. from 2003 to 2006. Currently, he is an Independent Director of Board Meeting, Universal Microwave Technology, Inc. He is working for the Department of Communications Engineering and is also the Dean of General Affairs Office, Yuan Ze University. His current interests include electromagnetic scattering and absorption, waveguide design, radar systems, electromagnetic compatibility and interference, bioelectromagnetics, electromagnetic radiation hazard protection, wireless communications, and applications of frequency selective surface. Dr. Chen is a member of Phi Tau Phi. He was also a member of the editorial board of the *Journal of Occupational Safety and Health* from 1996 to 1997. He was elected an Outstanding Alumnus of the Tainan Second High School in 1995. He has been the recipient of numerous awards including the 1990 Distinguished Research, Service, and Teaching Award presented by the Yuan Ze University, the 1999 and 2002 YZU Outstanding Research Award, and the 2005 Y. Z. Hsu Outstanding Professor Award for Science, Technology & Humanity Category. He was awarded Chair Professor by Far Eastern Y. Z. Hsu Science and Technology Memorial Foundation in 2008. His name is listed in *Who's Who in the World* in 1998.



**Chien Yi Lin** was born in Taiwan, Republic of China, in 1993. She received the B.S. degree in communications engineering, Yuan Ze University, Taoyuan, Taiwan, in 2016. Her current interests include electromagnetic scattering and absorption, antenna design, frequency selective surface, and computational electromagnetics.

# Chapter 12

## Radio Propagation Modeling and Simulation Using Ray Tracing

Zhengqing Yun and Magdy F. Iskander

### 12.1 Introduction

When a medium is disturbed at some location, a wave can be generated and energy can be carried with the wave. A daily-life and easy-to-see example of waves is the water wave generated by, e.g., dropping a stone into the water. One important feature of wave is that it travels or propagates from the source of disturbance to other locations. It is also important to note that the source of waves and the medium do not necessarily move with the waves. In fact, the source causes local movement of the medium (creating the disturbance), and this local movement affects the neighboring parts of the medium and, as a consequence, makes them move locally. This chain effect forms the propagation of the wave. Waves can be also reflected, e.g., a water wave hits a shore or a dam and gets reflected. When the reflected wave combines with the original wave (called the incident wave), a more complicated pattern of local movement forms. This effect can be easily observed when a small stone is dropped into the water in a small tank. For acoustic waves (sound), echoes are examples of reflected waves.

Electromagnetic (EM) waves are disturbances in the electromagnetic field. Although they cannot be observed directly (water and other mechanical waves can be seen directly), EM waves have similar properties: they propagate along straight lines in a homogenous medium and can be reflected by and transmitted through interfaces between different mediums. Because they propagate and carry energy, they can be employed to transfer information from one location to another. Wireless communication systems utilize EM waves to deliver information at the speed of light (which is  $2.99792458 \times 10^8$  meters per second in vacuum). Radio waves are

---

Z. Yun (✉) • M.F. Iskander  
Hawaii Center for Advanced Communications, College of Engineering,  
University of Hawaii at Manoa, Honolulu, HI 96822, USA  
e-mail: [zyun@hawaii.edu](mailto:zyun@hawaii.edu)

EM waves with frequencies in the range of kilohertz to hundreds of GHz. In this chapter, we concentrate on EM waves with frequencies in the GHz band which are widely used for modern wireless communication. More importantly, this frequency range belongs to the high-frequency regime relative to the sizes of objects in the environment of interest. This allows the use of ray optics and ray concepts to provide practical tools that can simulate radio propagation in large and realistic environments.

In addition to reflection and transmission, radio waves (and other waves) can also be diffracted and scattered by certain objects in the propagation environment. They are more complex phenomena and can interfere with the other waves. The interference among the waves causes dramatic changes of the field (or signal) strengths at a distance around half of a wavelength (the change is called small-scale fading in wireless communications). Note that the wavelength of a 2-GHz EM wave is about 15 cm or 6 in. In practice, we average the signal strengths along a distance about tens of wavelength to get the large-scale fading. Signal strength is a function of many parameters such as the types of antennas, input power to the antennas, radiation patterns, frequencies, and others. To characterize the large-scale fading in a more generic manner, we calculate path losses (or path gains) instead of signal strengths. Path loss is the ratio of the transmitted power to the received power (path gain is the inverse of path loss). In this way, we avoid the effect of input power on the signal strengths. Path loss values are key parameters for the planning of wireless networks (determination of the locations of base stations).

Propagation modeling provides a simple set of formulas or simulation methods which predict the path loss (or gain) at designated points or areas when parameters of the transmitter (location, height, radiation pattern, frequency, etc.) are given. Propagation simulation is a term with broader meaning than propagation modeling. It uses numerical methods such as the finite-difference time-domain (FDTD) method to solve Maxwell's equations with boundary conditions. In this chapter, ray tracing is the simulation method used. The simplest propagation model is the Friis equation which calculates the path loss in free space [1]:

$$\frac{P_r}{P_t} = G_t G_r \left( \frac{\lambda}{4\pi r} \right)^2 \quad (12.1)$$

where  $P_t$  and  $P_r$  are the transmitted and received power,  $G_t$  and  $G_r$  are the gains for transmitting and receiving antenna,  $\lambda$  is the wavelength, and  $r$  is the distance of the receiver from the transmitter. Note that the ratio in (12.1) is really the path gain, not the path loss which is  $P_t/P_r$ . But in the propagation community, it is common to use the two terms interchangeably. The Friis equation is also used for calculating the path loss associated with a direct ray (line-of-sight (LoS) scenario).

When the reflection from the ground is considered, a two-ray model can be used [2]:

$$\frac{P_r}{P_t} = \left( \frac{\lambda}{4\pi} \right)^2 \left| \frac{e^{-jkr_1}}{r_1} + \Gamma(\theta) \frac{e^{-jkr_2}}{r_2} \right|^2, \quad (12.2)$$

where  $r_1$  and  $r_2$  are the path lengths for the LoS and reflected rays, respectively,  $k$  is the wave number, and  $\Gamma(\theta)$  is the reflection coefficient at the ground for incidence angle  $\theta$ . It should be noted that in (12.1) and (12.2), we factored out the term  $\frac{\lambda}{4\pi}$  which is related to the wavelength and the antenna effective area.

For propagation over terrains where LoS (direct), diffraction from mountains, and scattering from the atmosphere must be considered, many propagation models have been developed. The most widely used is the Longley–Rice model [3, 4] covering frequencies from 20 MHz to 20 GHz, distances from 1 to 2,000 km, and antenna heights from 0.5 to 3,000 m. Polarization, ground parameters (permittivity and conductivity), terrain irregularity, radio climate, and other factors are considered. The model has since been implemented in different computer programming languages, such as Fortran and C/C++, and is free for download. A detailed description of the model and its usage can be found in Hufford et al. [5].

In the calculation of diffraction due to mountain structures, a knife-edge method is commonly used. This assumes that any diffraction structure can be approximated by a half-plane sheet where the edge of the sheet is the knife edge used for diffraction calculation. The analytical derivation of the diffraction field due to a half plane can be found in Ref. [6]. Durgin in Ref. [7] discusses the physical meaning of the knife-edge diffraction formula and its applications. This method has also been used for diffraction due to multiple edges. To determine the knife edges involved in a radio link, the height profile must be obtained from contour maps or digital elevation models (DEMs). For a given pair of transmitter (Tx) and receiver (Rx) locations, the height profile is obtained by dropping a vertical plane through Tx and Rx. The height profile is the cross-section. From the height profile, the knife edges can be extracted. Many heuristic methods have been developed to calculate the diffraction field for multiple knife edges, such as the Bullington model [8, 9], and Epstein-Peterson model [10]. Other methods with modifications exist including the Deygout [11] and Giovaneli methods [12].

For propagation prediction over the earth's surface (including land and sea), the parabolic equation (PE) method [13–15] can be used which solves the wave equation in a paraxial region. It is a two-dimensional (2D) method and uses the height profile as the input. It can simulate long-range (hundreds and thousands of miles) propagation with fast computational speed. The PE method has been extended to accommodate larger regions beyond the paraxial region [16] and to attack three-dimensional (3D) problems [17].

For commercial wireless communication applications, most propagation modeling research is focused on urban environments. Analytical solutions are usually unattainable, so many simplifications and assumptions are used to derive approximate propagation models. An example of this type of theoretical models from Walfisch and Bertoni [18] assumes that buildings are parallel and uniformly spaced and have similar heights. Then the path loss can be decomposed into three parts: the LoS, the rooftop diffraction, and the rooftop-to-ground diffraction.

Most of the propagation models for urban environments are empirical models which are extracted from extensive measurements. These models can be represented by a set of formulas and are very easy to implement and use. The fast computational

speed of these models makes them the first choice for area coverage calculations or real-time applications. The drawbacks of empirical models are that they are not sensitive to local building structures, are valid only for similar urban types where the models were developed, are not suitable for complicated geometries (such as in downtown areas), and so on.

The most popular and widely used model of this kind is the Hata-Okumura model which was developed using measurements in Tokyo, Japan [2, 19–21]. The path loss ( $PL$ ) is obtained as

$$PL = 10 \log \left( \frac{P_t}{P_r} \right) = 69.55 + 26.16 \log f_{\text{MHz}} - 13.82 \log H_m - \alpha(h_m) + (44.9 - 6.55 \log H_m) \log R_{\text{km}}, \quad (12.3)$$

where  $f_{\text{MHz}}$  is the frequency in megahertz (150–1,500 MHz),  $R_{\text{km}}$  is the distance from the base station in kilometers (1–20 km),  $H_m$  and  $h_m$  are the heights of the base station and mobile unit in meters ( $30 \text{ m} \leq H_m \leq 200 \text{ m}$ ,  $1 \text{ m} \leq h_m \leq 10 \text{ m}$ ), and  $\alpha(h_m)$  is a function of the receive antenna height, the frequency, and the size of the urban area (such as small- to medium-sized city, large city; details can be found in, e.g., Ref. [21], Section 4.10.4). The Hata-Okumura model was developed in the 1980s and is commonly used for macrocell communication systems.

Extensions to the Hata-Okumura model accommodate cellular systems with smaller size (such as microcells) and higher frequency. For example, the COST Hata model [22] changes the first two terms in (12.3) to treat frequencies in the range of 1,500–2,000 MHz.

In addition to the theoretical and empirical models, another method for urban propagation modeling is the ray-optics (or geometrical-optics) method. It is based on the assumption that the frequency is high enough that the radio waves behave similar to light. On using this high-frequency approximation, Maxwell's equations and wave equations can be recast into equations expressed in terms of the optical path length, or the eikonal [6]. From these equations, a concise and beautiful equation (the eikonal equation) can be derived:

$$(\nabla S)^2 = n^2, \quad (12.4)$$

where  $S$  is the eikonal and  $n$  is the index of refraction. Note that  $(\nabla S)^2 = \left( \frac{\partial S}{\partial x} \right)^2 + \left( \frac{\partial S}{\partial y} \right)^2 + \left( \frac{\partial S}{\partial z} \right)^2$  and a wave front of the EM wave is a surface determined by  $S = \text{Const}$ .

It can be shown that the time-averaged Poynting vector points in a direction perpendicular to the wave front in free space. The ray concept is thus introduced: a ray is a thin tube (or line) aligned with the direction of the time-averaged Poynting vector; the electromagnetic energy is flowing in the tube without leaking out from the walls of the tube. In homogenous mediums, the ray is a straight line and will be reflected and/or transmitted (refracted) according to the laws of reflection and refraction.

Traditionally, ray optics does not consider diffraction. Keller extended the ray-optics method to establish the geometrical theory of diffraction (GTD) [23]. GTD has intrinsic problems for calculating diffracted fields in the region close to shadow boundaries. To overcome this difficulty, the uniform theory of diffraction (UTD) [24, 25] has been developed, and other methods such as the uniform approximation of physical optics are also introduced [26].

For urban environments, building sizes range from tens of meters to hundreds of meters. For frequencies in GHz range (wavelength in the cm range, e.g., 37.5 cm for 800 MHz), the high-frequency assumption is quite valid in urban environments. Ray optics is commonly used for radio propagation modeling and simulation by applying the *ray-tracing* algorithm which traces every ray launched from the transmitter and finds all rays reaching the receiver. Each of these received rays represents a field vector, and the total field at the receiver is the sum of all these individual fields.

Ray-tracing methods use a detailed environmental model as the input. They calculate the field at any point or area of interest. Compared with theoretical and empirical models, ray tracing is much more computationally intensive but much more general and can provide site-specific solutions. The computational burden of the ray-tracing method is from the determination of received rays involving many ray-object intersection calculations. A naïve ray-tracing algorithm is usually not practical because of its slow computational speed. Many acceleration methods have been developed and tested for application in large and complex propagation environments. Details can be found, e.g., in Refs. [27, 28] and elsewhere.

In the following sections, we present some research work of our group related to ray tracing including algorithms for accelerating ray-tracing speed, methods for extracting 3D urban structures (buildings) for establishing accurate propagation environments, and application of ray tracing for source localizations using time reversal and machine learning. A discussion of the future of radio propagation modeling and ray tracing is given at the end of this chapter.

## 12.2 Space Division Methods for Accelerating Ray Tracing

A basic step in a ray-tracing method is to determine which object the ray will hit. These objects can be building structures and ground surfaces and can be represented as collections of triangles making up the surface of the structure. In an urban environment, the number of these triangles can be huge, depending on the details to be represented.

When a ray is launched at a source point in a certain direction, the next step is to find which triangle the ray will hit. A simple method is to do intersection tests of the ray with all triangles. Since a ray can pierce many triangles, the triangle which is closest to the source point is the one sought. Thus, when a triangle is intersected by the ray, the distance from the intersection point to the ray origin is calculated and stored in order to pick the correct triangle pierced by the ray. This is the triangle with the smallest distance to the ray origin.

When a ray hits a triangle, reflected and/or transmitted rays will be generated. The new rays will be traced further in a similar way until some criterion is met. It is evident that such an algorithm is slow if the number of triangles is large and many levels of reflection and diffraction are needed. To find the rays from Tx to Rx, we need to launch a large number of rays. The total ray-tracing time for this simple method is very large, limiting its usefulness for propagation modeling and simulation in large and realistic urban environments.

Space division is one of the methods that can accelerate the ray-tracing process to make its use for realistic urban environments feasible. The basic idea for space division is:

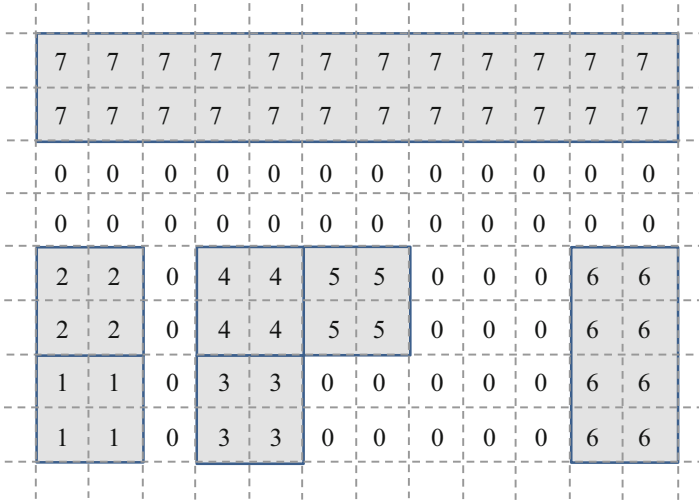
- (1) Divide the entire space into small cells (uniform or nonuniform).
- (2) Determine which objects are residing in each cell or vice versa. Store the results in a lookup table or array for later use.
- (3) Establish the spatial relationship among these cells. For example, for rectangular cells, we can determine which cell is the neighbor on the right of the current cell.
- (4) Develop algorithms for traversing these cells efficiently. This is the key part of the ray tracing which determines which cell a ray enters when it is leaving the current cell.
- (5) When a cell is hit by the ray, the objects in the cell will be retrieved using the table or array obtained in (2), and these objects will be tested for ray intersection.

It can be seen that the essence of space division methods is to reduce the number of ray/triangle intersection tests. When the reduction is significant, the speedup of the ray-tracing algorithm will be enormous. Rectangular and triangular cells are used to divide a two-dimensional (2D) space representing the 2D projection of the 3D urban environment in Refs. [29–31]; the 3D space is divided into tetrahedrons leading to a true 3D ray-tracing method in Ref. [32].

When the space is divided into uniform rectangular cells, the relationship between the cells is very simple: a cell can have at most eight neighbors, i.e., top, bottom, left, right, top right, top left, bottom right, and bottom left. This relationship is implicit and need not be explicitly built into a table or map for retrieval. Well-established algorithms exist for fast determination of the next cell. An efficient algorithm for traversing a rectangular grid is presented in Ref. [33]. The algorithm only involves simple operations such as addition and comparison of two numbers to determine the next cell for the ray to enter.

The contribution of Ref. [30] is to identify a special case for the rectangular grid method which reaches its optimal performance when all the reflection objects are aligned with the grid lines. This is possible for propagation environments with regular building structures. One example discussed in Ref. [30] is where a floor of an office building is considered. All the rooms on the floor are of similar shape and size, and a rectangular grid can be built to align with the interior walls of the rooms.





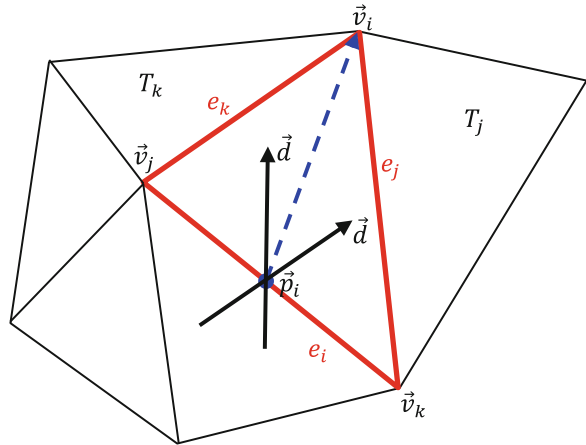
**Fig. 12.1** Rectangular grid (dotted lines) and rooms (shaded) in an office building. The interior walls are aligned with the grid. The numbers are labels for the grid cells; a room is composed of several cells with the same labels (thus there are seven rooms in total). Label “0” represents hallways

Figure 12.1 shows part of the rooms and associated rectangular cells (squares in this case). The solid lines are real walls while the dotted lines are for cell definition. In this particular case, all the walls (solid lines) are on the dotted lines; there is no object (wall) inside any cell. Based on this fact, a fast ray-tracing algorithm was developed in Ref. [30]. In the traversing method of Ref. [33], when a ray is entering the next cell (a square), it is either piercing a wall or going through a cell boundary. To determine which case is happening, we establish a table which is different than the one suggested in step (2) since there are no objects in the cells. We first assign each room with a unique identification number. Then, the cells in the same room are assigned an identical label (the room number). Therefore, the cells in the same room will have the same label, and cells in different rooms have different labels. Now, if a ray is leaving a cell which has the same label as the one it enters, the ray is passing through a cell boundary, not a real wall; otherwise the ray is transmitting through a real wall. There is no ray/wall intersection test at all. The achieved computational speed is about seven times the speed of the visibility method.

A triangular-grid method was developed for 2D scenarios composed of indoor and outdoor propagation environments [29]. The triangular-grid method was further applied to an urban environment (Munich, Germany) in Ref. [30], and the path loss results had satisfactory accuracy compared with the measurements.

The main feature of the triangular-grid method is twofold. First, the scene is triangulated using the well-known Delaunay method, more precisely, the *constrained Delaunay triangulation* (which is actually not a Delaunay triangulation). The

**Fig. 12.2** Determination of which edge a ray will hit. The ray is entering the triangle via edge  $e_i$  at point  $\vec{p}_i$ . Using the vector product of the direction of the ray with vector  $(\vec{v}_i - \vec{p}_i)$ , we can determine if the hit edge is  $e_j$  or  $e_k$



triangulation keeps all the edges of objects (such as walls) intact; thus no wall will be divided into several segments to obtain the traditional Delaunay triangulation. This property is ideal for efficient calculations since dividing a wall into several segments would increase the number of objects in the scene and reduce the computational efficiency.

After triangulation, all the reflection edges are grid lines (edges of triangles) and, again, there is no object in the cells (triangles). The edges of each triangle will be tagged as a real wall or a pure triangle boundary based on the information of the environment. The relations among the cells are also obtained during the triangulation process: each cell (a triangle) has information about its neighbors when the three vertices and edges of each cell are ordered (clockwise or counterclockwise).

The determination of which edge a ray hits is straightforward, although not as simple as in the rectangular-grid method developed in Ref. [30]. Suppose the three edges of a triangle are labeled  $e_i$ ,  $e_j$ , and  $e_k$  counterclockwise; the vertices opposite the edges are labeled  $\vec{v}_i$ ,  $\vec{v}_j$ , and  $\vec{v}_k$ , respectively, as shown in Fig. 12.2. If the ray enters this triangle with a direction  $\vec{d}$  and via edge  $e_i$  at point  $\vec{p}_i$ , to determine which triangle it enters,  $T_j$  or  $T_k$ , we only need to determine which edge,  $e_j$  or  $e_k$ , will be hit by the ray. We construct a vector  $\vec{v}_i - \vec{p}_i$ ; then the sign of the cross product  $\vec{d} \times (\vec{v}_i - \vec{p}_i)$  can be used to decide which edge to be hit: if positive,  $e_j$  is hit; if negative,  $e_k$  is hit; if zero, the ray will hit the vertex.

Similar to the rectangular-grid method, when a ray is hitting an edge of a triangle, the edge tag will be looked up to determine if this edge is a wall or a cell line. The triangular-grid method is an efficient method that is more general than the rectangular-grid method in Ref. [30]. There are many other space division-methods which can be found in Refs. [27, 28].

## 12.3 Utilization of Geospatial Resources for Propagation Modeling

With the rapid growth of the availability of geospatial resources, it is meaningful to use them for building more accurate environmental models for propagation modeling and simulation. In this section we present two such applications.

The first application is using NASA's SRTM (Shuttle Radar Topography Mission) database for extracting terrain elevation and constructing a 3D propagation environment; the second is using Google Earth for extracting 3D urban building structures.

NASA's SRTM was carried out in February 2000 on the Space Shuttle Endeavour. It collected elevation data for about 80% of the Earth's land surfaces (mission details can be found at <http://www2.jpl.nasa.gov/srtm/mission.htm>). A recent release of the elevation data in 2014 made high-resolution data (1 arc-second, or around 30 m or 98 ft) available globally (this was already available in the United States); see <http://www2.jpl.nasa.gov/srtm/> for more details and how to access the databases.

More recently, NASA released Version 3 DEM with void-filled elevation data points. These voids were caused by the geographical and weather conditions and are assigned a value of  $-32768$  in the DEM files. For example, for Oahu Island, HI, there are about 600 points without elevation in previous DEM databases (90 m resolution).

The SRTM data is stored as big endian binary integers (rounded to meter). Different programming languages have different functions or means to read such data. Figure 12.3 shows the elevation of an area in Oahu Island with different resolutions (Note: Endianness is about the way to store a number in computer memory. A big endian number has the most significant byte stored first, while a little endian number stores the least significant byte first).

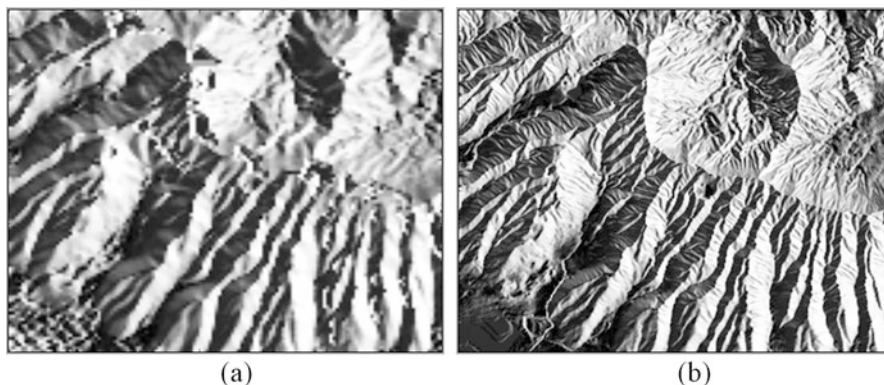


**Fig. 12.3** Elevation data of Oahu, HI, rendered in shade relief. (a) Resolution of 90 m. (b) Resolution of 30 m

The SRTM elevation data can be used for propagation modeling over terrain. A typical application is the calculation of path loss. In this case, an elevation profile is used and direct ray, diffraction rays, and reflection rays (and scattering) are considered. To extract elevation or height profile using SRTM (or other similar digital) elevation database, two methods are commonly used. One is projecting the elevation values on the grid points in the database to the line connecting the source and field points. This will create an elevation profile with unequal distances between points. In the second method, a great circle passing through the source and field points is determined; then sampling points with equal distance on the great circle are calculated; finally, for each sampling point, a bilinear interpolation is employed to find the elevation at the point using elevation values at four grid points in the database; see Ref. [34] for more details.

The SRTM elevation data can also be used for point-to-area propagation modeling. We have developed an algorithm for calculating the path gain over a large area. Figure 12.4 shows an example result, and others can be found in Ref. [35].

The algorithm is implemented for both CPU and graphics processing unit (GPU). GPUs were originally designed for rendering graphics. A GPU is very different from a CPU which mainly controls the data flow and performs heavy-duty computational tasks. A GPU is good at carrying out small but a large number of similar tasks in parallel. For example, to render a picture on the computer screen, the computer needs to assign colors of each pixel to the area on the screen corresponding to the picture. A very important feature for this rendering process is that the color of each pixel is independent from that of the rest of the pixels. This means that the

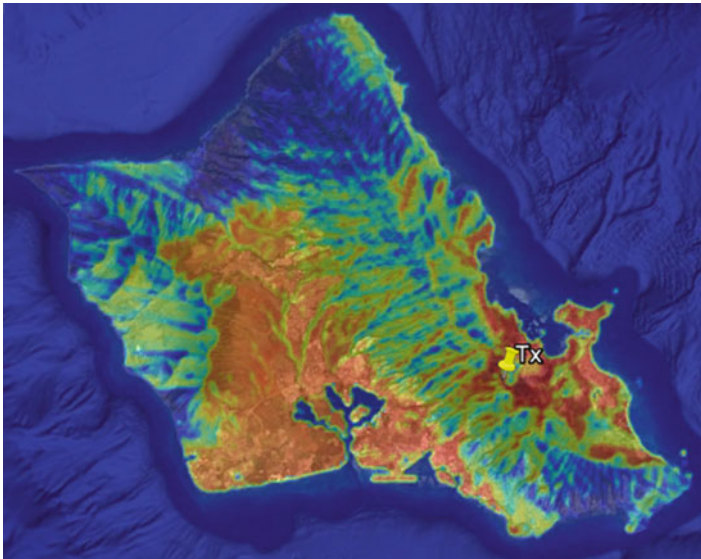


**Fig. 12.4** Path gains on the entire Oahu Island for an antenna at Tx (The image is rendered in Google Earth as an overlay)

computer can render the color of a pixel without knowing any other pixel colors. Color rendering is intrinsically a parallel process.

For path-gain calculations in an area, there is an obvious parallelism using ray tracing on knife edges: the height profiles originating from the Tx and ending at a boundary point are all independent of one another. Thus, tracing rays along one profile is completely independent of tracing rays along a different height profile, though the ray tracing algorithms are all the same. This parallelism fits the GPU very well, enabling the GPU to accelerate the computational speed.

The basic steps in the implementation are:

- (1) Load SRTM elevation data and determine Tx location based on the user's input of the region of interest. A rectangular region can be represented by two diagonal points, while a general polygon region can be represented by a sequence of points. These points can be determined easily in Google Earth by setting a path with several points. The path can be saved as a Keyhole Markup Language (KML, or .kml) file. The location of the Tx can be determined using one point in a .kml file created in Google Earth.
- (2) The region of interest will have  $m \times n$  grid points. Starting from Tx, we launch rays toward each boundary point (total of  $K = m \times n - (m - 2) \times (n - 2) = 2(m + n) - 4$  points). The  $K$  ray tubes will cover the entire region of interest.
- (3) For each ray, we trace it from Tx toward a boundary cell. When a new grid cell is traversed, the height will be calculated using the projection method and the diffracted field at the cell will be calculated using knife edge method.

These steps are the same for both CPU and GPU implementations. We use C++ as the programming language and Microsoft's Visual C++ 2013 as the compiler. For the GPU implementation, NVIDIA's CUDA is used. The program is run on a Lenovo laptop with NVIDIA's GPU Quadro K2000M.

For the path-gain calculation of the entire area in Fig. 12.4, the number of field points is about 480,000 using SRTM 3 arc-second DEM. The GPU computational speed is 3.18 times faster than the CPU version.

The second application of geospatial resources is in urban environments. For planning and simulation of wireless communication systems in urban environments, detailed building structures are needed for small cellular systems. With Google Earth, it is possible to extract 3D building structures for many cities and towns. We developed in Refs. [36, 37] two methods to extract 3D building geometries from Google Earth's 3D images.

It is assumed in Ref. [36] that the rooftop and partial ground foundation of a building are visible in Google Earth. This implies that the image is not photographed directly over the buildings. For a building with rectangular-shaped rooftop, we can identify the four corner points of the rooftop and one point on the ground. The latitudes and longitudes of these five points can be obtained from Google Earth. This way, we can determine the footprint of the building. As for the height of the building, we use an iterative method which initially assumes an estimated height. Then the outline of the building is rendered back in Google Earth, and a better



**Fig. 12.5** The constructed 3D buildings of Rosslyn City, VA, using the method of Ref. [33] and the calculated path gains using ray tracing. The transmitter is located in the center of the image (The results are rendered in Google Earth)

height estimation can be obtained by observing the discrepancy between the height of the Google Earth image and the approximated height. After several iterations, the height can be determined well.

Figure 12.5 shows the reconstructed buildings in Rosslyn City, VA, using this method and the calculated path gains along several streets. Comparisons of the path loss values with measurements and simulation results in literature can be found in Ref. [36].

The method proposed in Ref. [37] has better performance and is more general (it does not require the ground foundation of buildings to be visible in Google Earth). The algorithm is based on projective geometry [38, 39] which deals with simple relations between the Euclidean space and its perspective projection onto a 2D plane. For example, two parallel lines in Euclidean space will intersect in the projective plane at a point called the vanishing point, and a set of parallel lines in 3D space will converge to the same vanishing point on the projective plane. Figure 12.6 illustrates some relevant key concepts where two vertical lines and two sets of horizontal lines are presented in both the Euclidean space and the projective plane.

**Fig. 12.6** From 3D Euclidean space to 2D projective plane. The two parallel line segments,  $S_1$  and  $S_2$ , in 3D Euclidean space (top right) become two line segments that intersect at a vanishing point  $v$ . Also, two sets of parallel lines on the horizontal plane in Euclidean space converge to vanishing points  $p$  and  $q$  in the projective plane

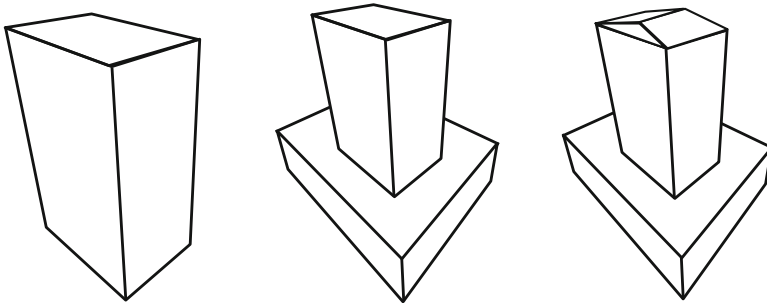
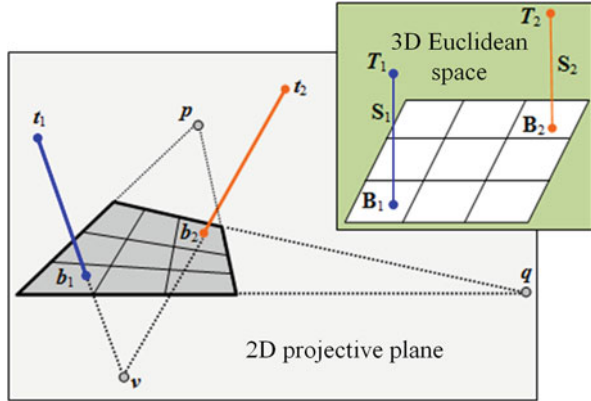


**Fig. 12.7** Typical building structures that can be reconstructed using the method proposed in Ref. [37]

In order to determine the height and footprint of a building seen in Google Earth, several calibration steps are needed, including height calibration and establishing the projective transformation by setting four points on the ground. The latitude and longitude grid lines visible in Google Earth are used for calculating the vanishing point. Figure 12.7 shows some structures that can be reconstructed using the method of Ref. [37]. In Fig. 12.8, reconstructed buildings in Rosslyn, VA, using this method and the path gains along the streets (see Fig. 12.5) are shown.

Geospatial resources provide a great opportunity for radio-propagation modeling and simulation. For example, with Google Earth’s 3D buildings visible to any user, we now can extract building structures with great accuracy. The quality of the geospatial data is rapidly improving, providing more accurate and realistic environmental models which will greatly enhance the accuracy of the results of propagation modeling and simulation. The method requires large computation resources (larger disk storage, slower computation time, etc.). In the following two sections, we take a look at these problems and propose solutions.

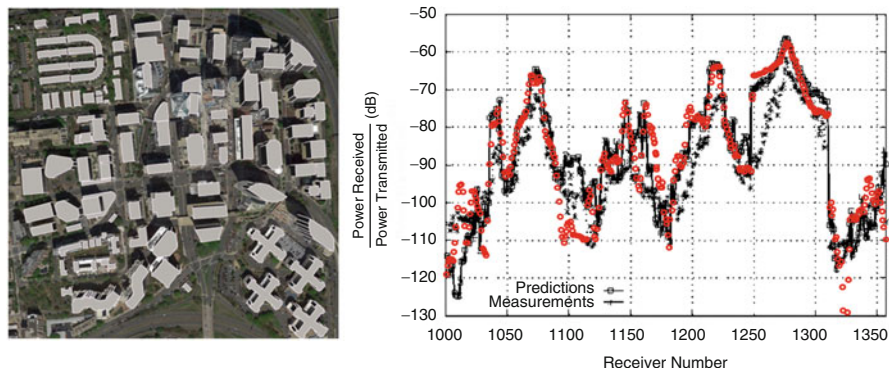


**Fig. 12.8** Reconstructed 3D buildings in Rosslyn, VA, using the method in Ref. [37] rendered in Google Earth (*left*) and the path gain results compared with the results in Ref. [2]

## 12.4 Ridge Feature Extraction and Vector Form Representation

Diffraction fields due to mountainous structures are essential in the radio propagation simulation for terrestrial wireless communications. It is common practice to calculate the diffracted field using a height profile extracted from (DEM) when the transmitter and the receiver locations are given. Diffraction points can then be identified from the height profile. The knife-edge method or UTD can be used to calculate the diffracted field.

The height profile, although it can be extracted conveniently from a DEM, has some drawbacks. First, the identification of diffraction points from height profile is not trivial if the terrain surface is rough and the DEM has high resolution. Data smoothing is often needed. Second, the height profile does not have any information about the ridge orientations and interior angles which are important parameters for the UTD method. Third, the height profile is extracted directly from a DEM which may involve large computer storage space for importing the DEM database. For example, the 3 arc-second SRTM DEM ( $\sim 90$  m resolution) has more than 14,000 files; each has a size around 2.8 MB. The total storage space required is 30–40 GB. This may be not a problem for current computers, but for higher-resolution DEM (about 10-m resolution or higher), the storage space will become an issue. The computational time is also increased due to such enhancement in resolution.

To more realistically represent the ridge structures and their diffraction effect, we proposed a method to extract the 3D ridges using DEM [40]. Suppose the DEM data are located at the center of square cells of a grid. To determine if a cell  $C$  is on a ridge, we consider its eight neighboring cells shown in Fig. 12.9. We observe that there will be eight possible ridges containing the cell  $C$  represented by eight directions: from  $C$  to  $C_i$ ,  $i = 1, 2, \dots, 8$  (three directions are shown in Fig. 12.9). If there is a ridge running upward through  $C$ , we have the height of  $C$  greater than



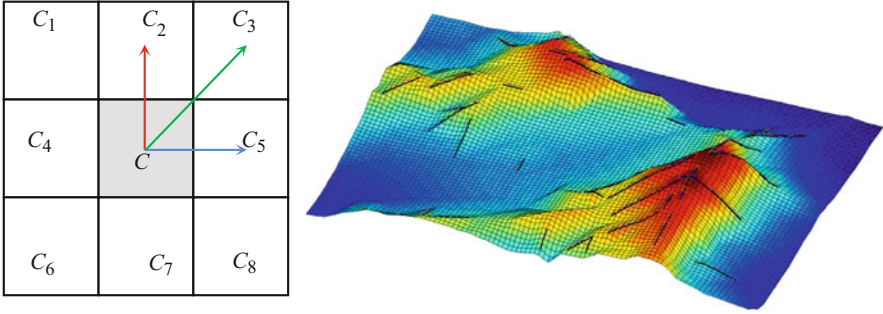


**Fig. 12.9** *Left:* A  $3 \times 3$  cell DEM data set; there are eight possible directions for a ridge to run through the center cell  $C$ . *Right:* reconstructed ridges using a DEM data and superimposed on it

that of  $C_4$  and  $C_5$ , the height of  $C_2$  greater than that of  $C_1$  and  $C_3$ , and the height of  $C_7$  greater than that of  $C_6$  and  $C_8$ . For other directions, similar criteria can be established.

Note that a cell can be on several ridges at the same time. This happens when a ridge turns or several ridges intersect. Using the proposed method, we can extract ridges from DEM data, and an example of which is shown in Fig. 12.9.

When 3D ridge structures are available, it is possible to extract the height profile more easily for knife-edge models, and more importantly, we are able to calculate the diffraction accurately using UTD because all the parameters of the wedge (ridge) are available. We examined in Refs. [40, 41] how diffracted fields from 3D ridge structures differ from those calculated using the height profile.

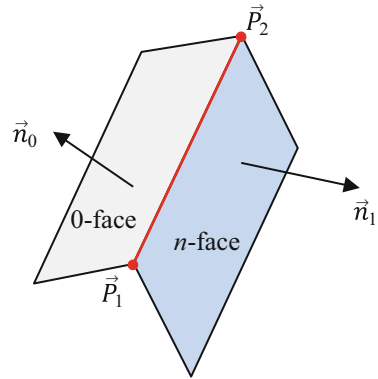
The effect of ridge orientation on the diffracted field was studied in Ref. [40]. The orientation of a ridge can be characterized by the angle between the edge of the ridge and the incident ray. This angle is commonly represented by  $\beta'_0$  [24, 25]. When  $\beta'_0 = 90^\circ$ , the ray is normally incident on the edge. This is the common assumption in the diffraction calculation using a height profile. The orientation angle  $\beta'_0$  affects the diffraction coefficient directly as shown in the formula (for the definition of the variables, see Refs. [24, 25]):

$$D^{i,r} = -\frac{e^{-j\pi/4}}{2n\sqrt{2\pi\beta}\sin\beta'_0} \left\{ \cot\left[\frac{\pi + (\varphi \mp \varphi')}{2n}\right] \cdot F[\beta Lg^+(\varphi \mp \varphi')] \right. \\ \left. + \cot\left[\frac{\pi - (\varphi \mp \varphi')}{2n}\right] \cdot F[\beta Lg^-(\varphi \mp \varphi')] \right\}, \quad (12.5)$$

where, for spherical wave incidence,

$$L = \frac{ss'\sin^2\beta'_0}{s + s'}. \quad (12.6)$$

**Fig. 12.10** Definition of a 3D ridge using a wedge which is common in the calculation of diffraction with UTD



For example, a ridge in a mountainous region with interior angle of  $177.7^\circ$ , the oblique incidence will differ about 11 dB for  $\beta'_0 = 15^\circ$  and 5–6 dB for  $\beta'_0 = 30^\circ$ . The effect of the interior angle of a ridge on the diffracted field is discussed in Ref. [41]. For the diffraction of two ridges with the same interior angle  $\alpha$ , the average path-loss difference compared with that of the height profile method is about 6 dB for  $\alpha = 40^\circ, 60^\circ$ , and  $80^\circ$ . The maximum difference can reach 10 dB.

We observe that 3D representation of ridge structures is superior to the height-profile representation for the calculation of diffracted field. Therefore, we propose to replace the conventional DEM databases with 3D ridge structures for the calculation of diffraction. Using the computer graphics language, we are replacing raster databases (DEM) with vectors. The significant savings in computer storage is evident.

A ridge or wedge can be defined (see Fig. 12.10) by a pair of 3D points ( $\vec{P}_1, \vec{P}_2$ ) and two unit vectors,  $\vec{n}_0$  and  $\vec{n}_1$ , which are the normal, respectively, to the 0 face and  $n$  face of the wedge. Note that the two faces of the ridge are not explicitly defined. This is because in reality, it is rare that a slope of a ridge appears as a regular shape and the calculation of diffraction coefficient using UTD does not require an explicit definition of the surface. All the necessary parameters needed in the diffraction coefficient calculation can be derived from  $\vec{P}_1, \vec{P}_2, \vec{n}_0$ , and  $\vec{n}_1$  when the incident ray is given. This definition is also sufficient for the extraction of the height profile.

In the long run, we will build a map (regional and ultimately worldwide) which describes the propagation environment with explicit 3D structures (ridges, buildings, etc.) in vector forms. This map can be thought as a higher layer on the current DEMs or a superstructure on the conventional maps. It provides a more accurate and physically meaningful representation of the propagation environment, and thus a more accurate and efficient propagation simulation can be developed.

## 12.5 Level of Detail: How It Matters

With the rapid improvement of the resolution of the elevation data and urban structures, an important question is: “how much detail do we need for building an environmental model which provides satisfactory accuracy for propagation modeling and, at the same time, does not demand too much computational resource (storage and speed)?”

In the previous sections, we touched on some aspects of the benefits and drawbacks of high-resolution elevation databases. In this section, we try to answer this question and propose methods that can exploit geospatial resources appropriately.

First, for accurate propagation prediction, the necessary details of the environments needed depend on the frequency of the EM wave under consideration. Higher frequency (shorter wavelength) requires higher resolution. This can be explained, e.g., using the Rayleigh roughness criterion [42]:

$$g = 4\pi \left( \frac{S_h}{\lambda} \right) \sin \varphi, \quad (12.7)$$

where  $S_h$  is the standard deviation of the height with respect to the local mean,  $\lambda$  is the free-space wavelength, and  $\varphi$  is the grazing angle between the incident wave’s propagation direction and the tangential direction of the surface. It can be seen that the roughness is directly related to the wavelength (therefore, frequency): a small wavelength leads to larger roughness. In terms of reflection from a rough surface, the specular reflection coefficient will be reduced by a factor of  $e^{-\frac{1}{2}g^2}$  which also indicates that for higher frequency, the reduction is more severe.

We explored the effect of different levels of detail of the environmental model on the accuracy and computational speed of path loss calculations in Ref. [43]. For point-to-point path loss calculation over terrains, we considered the elevation database of SRTM with two different resolutions: 30 and 90 m. Figure 12.11 shows the height profiles for a point-to-point link for the two resolutions. It can be seen that the main propagation features (such as the diffraction peaks or ridges) of both profiles are very close and we can expect the path loss values will be also similar. In this case, we can safely use the height profile with lower resolution to save computational resources (storage and speed) without losing computational accuracy.

Furthermore, we also investigated the level-of-detail effect for urban propagation environments. When microcells for wireless communications are considered and when the transmitting antennas are mounted at a height similar to or below the average building height, the street guiding of EM waves is an important mechanism for the power distribution. In this case, the detailed structural information of buildings may be ignored for frequency bands around 1 GHz. In many publications (see, e.g., references in Refs. [27, 28]) regarding the ray-tracing methods, buildings are usually simplified as extruded polygons with smooth surfaces. The path loss values obtained in this manner are of satisfactory accuracy.

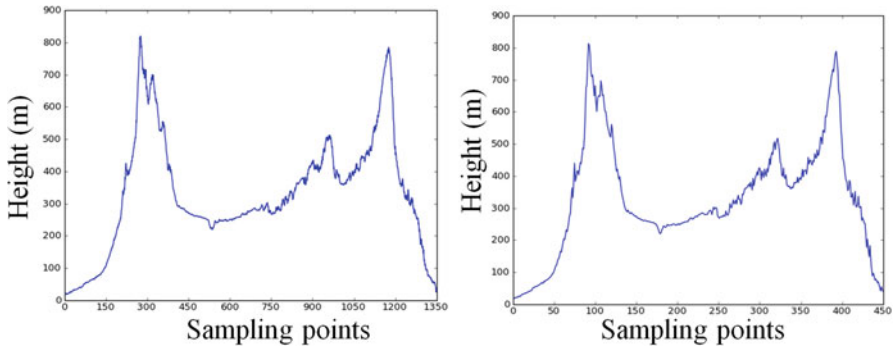


**Fig. 12.11** Height profiles for different resolutions using SRTM elevation databases. *Left*, 30 m; *right*, 90 m

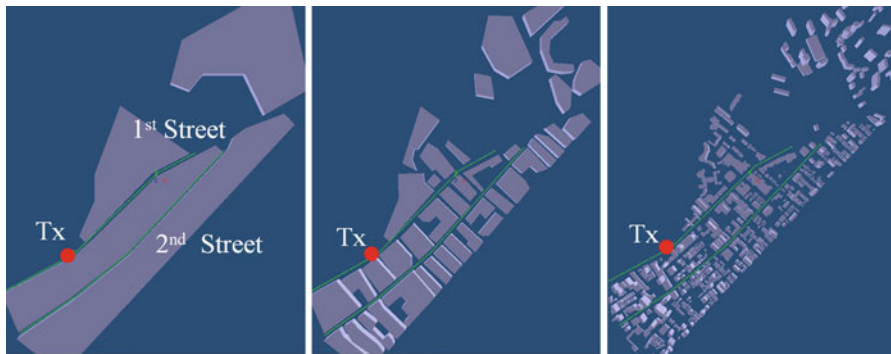


**Fig. 12.12** Urban environmental models for Waikiki area with three different levels of detail: *left*, lowest; *center*, medium; and *right*, highest. Two main streets (green lines) are preserved and path loss values are calculated along the streets

In this study, we went more aggressively to group buildings in a block or several blocks into a single extruded polygon with an average height. This means that some minor streets may be ignored if we are not interested in the path loss values there. Figure 12.12 shows three models for the Waikiki area of Honolulu, HI.

The transmitter is located on the first street (upper one). The path gains along the first and second streets are shown in Fig. 12.13. It can be seen that on the first street where most of the receiver positions are visible to the transmitter, the path gain results are similar for the three very different levels of detail. Only for some Rx locations in the northeast end do the effects of environmental details become significant. For the second street where most Rx locations are in the non-LOS region, different levels of detail of the environment have clear impact on the simulated path loss.

One benefit of using an environmental model with a lower level of detail is saving computational time. For the three cases in Fig. 12.12, the computational times of the medium and highest resolution model are 6.5 and 27 times that of the

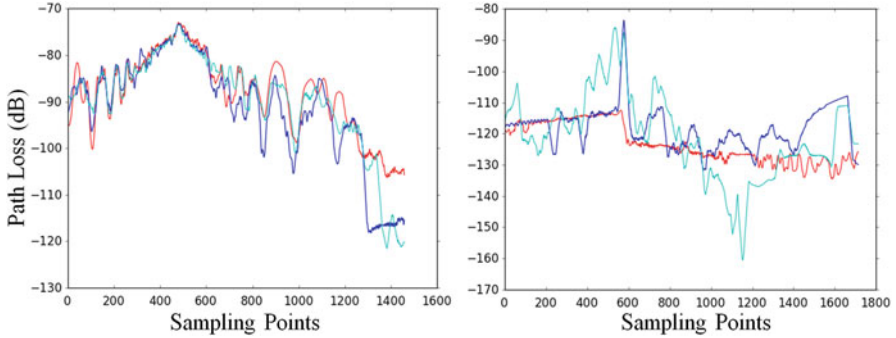


**Fig. 12.13** Path gains along the first (*left*) and the second (*right*) streets. *Red*, lowest resolution; *blue*, medium; and *cyan*, highest

lowest resolution model. Our goal is to develop an intelligent propagation simulation system that can automatically determine the level of detail needed for a user input. This requires databases with different levels of detail for propagation environments, which we plan to build.

## 12.6 Source Localization Using Time Reversal and Machine Learning

Detection of radio-frequency sources is useful in many applications, such as disaster rescue, antijamming operation, and so on. Time reversal is one method that can estimate the source locations by transmitting the time-reversed signal received by one or several receivers. This has been studied in acoustics [44] and electromagnetics [45, 46]. We investigated the time-reversal characteristics in Ref. [47] for single-transmitter-and-single-receiver systems. The indoor environment we used was an indoor office with rooms and cubicles there. Two-dimensional finite-difference time-domain (FDTD) method was employed to simulate the wave propagation. The effect of furniture and scattering objects on the focusing of energy at the transmitter is studied.

Although FDTD method can provide a full-wave solution for Maxwell's equations, which is usually more accurate than the ray tracing method, FDTD demands much larger computational resources. Using common desktop computers available in an academic unit, the FDTD method can simulate a region, e.g., a cube with tens of wavelengths each side. It is not suitable for the simulation of radio propagation in an urban environment for microcells. This is where ray tracing can play a key role for propagation modeling and simulation.

We discussed the use of time reversal of source localization using ray tracing in 3D environments [48–50]. In Fig. 12.14, a part of the 3D urban area is shown with one Tx, three Rx's, and the rays from Tx to one Rx. An inset in the figure represents

**Fig. 12.14** 3D urban environment for time reversal source localization. The source (Tx) and three receiver locations (Rx, Rx2, Rx3) are shown with rays received by Rx. The inset shows the grid points around Tx. Time-reversed signals will be calculated on the grid for identifying the source locations

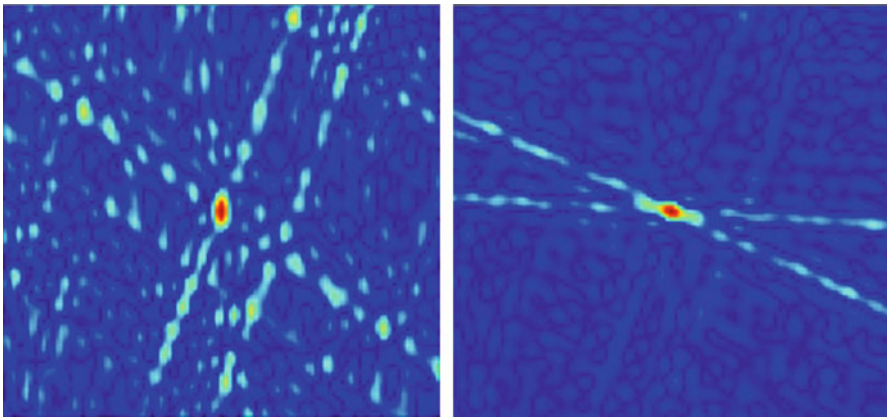
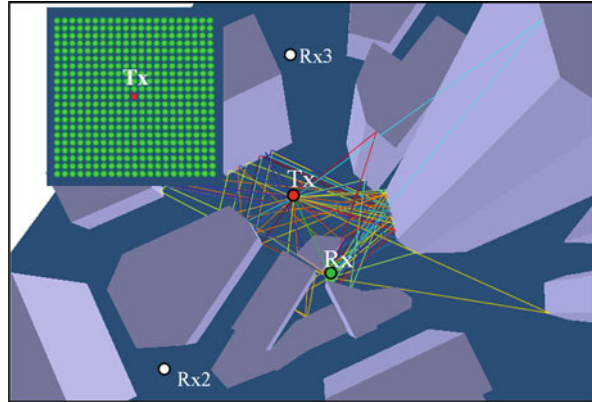


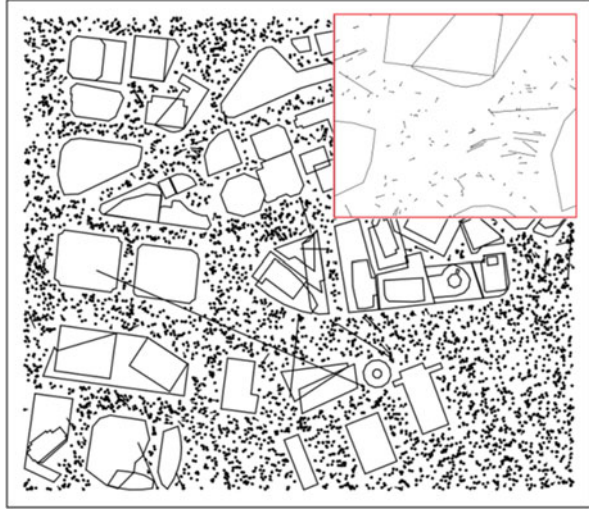
**Fig. 12.15** Time-reversed signal strength distribution in a square area centered at Tx. *Left*, single receiver (Rx) results; *right*, three-receiver (Rx, Rx1, Rx2) results

the square centered at Tx over which the time-reversed field distribution will be calculated. In Fig. 12.15, the time-reversed field distributions on the square are shown for different numbers of receivers. It can be seen that more receive antennas give a better identification of the source locations.

There is a computational-speed issue with the time-reversal method using 3D ray tracing. This is due to the fact that if the entire region (which is much bigger than the square area around Tx in Fig. 12.14) is used for the identification of the source, the number of points on which the field needs to be calculated can be large, which increases the computation time significantly or even make the simulation unpractical.

We proposed a machine-learning method in Ref. [51] to combine with the time reversal method to improve the computational speed. The basic idea is as follows. Using machine learning's classification or regression method, a set of randomly selected locations of sources are used for training. Several receiver locations are

**Fig. 12.16** Source localization using machine learning's regression method. The line segments shown represent the distance from true source locations to the respective predicted locations



designated for recording the received signal. After training, when a source with unknown location is transmitting, signals at these designated receivers are used as input to the machine-learning system. The source location can then be determined in a region (using classification) or at a point (using regression).

The predicted source location can be further improved using time reversal in a small area which is the subregion containing the source for the classification method or a region surrounding the source point for the regression method.

The prediction results using the regression method are shown in Fig. 12.16 for an urban environment. We randomly selected 30,000 points in the region of interest in which a transmitter is placed and signals on six receiver locations are recorded. The ray-tracing method developed in our group is employed for calculating received fields. The 30,000 transmitting points are divided into 2 groups: one with 25,000 points for training purposes and the one with the remaining 5,000 signals for determining the prediction accuracy.

The line segments in Fig. 12.16 represent the distance between the true and predicted locations of the source. Therefore, a short segment represents better prediction accuracy. It can be seen in the figure that most of the segments are short and look like points. In the inset with the red boundary, these segments are enlarged in a small area for clearer visualization. The average localization accuracy is around 1.75 m.

It should be noted that, using different features of the received signals, different prediction accuracy can occur. These features include time of arrival, direction of arrival, received power, and the distances to the source point. The effect of some of these features on the prediction accuracy is investigated in Ref. [48]. Ray-tracing methods provide a feasible tool for 3D radio-propagation simulation in large urban environments that most other numerical methods are not able to handle.

## 12.7 Conclusion and Discussion

In the chapter, major work for propagation modeling and simulation using ray-tracing methods in the Hawaii Center for Advanced Communications (HCAC) is summarized. We have developed several software packages in different programming languages (mainly C/C++ and Python) to implement the ray-tracing algorithms.

The future of the ray-tracing method is very promising. This is due to several developments or trends in the community of radio-propagation modelers. First, as an accurate simulation method, ray tracing is becoming a commonly used method. Second, ray tracing can provide fast calculation for path loss and many other useful parameters such as angle of arrival, time delay, and multipath statistics (delay spread, for example) for large propagation environments. Third, as higher-resolution environmental data become available, ray tracing can be used to model more realistic radio wave propagation.

But the challenges are also becoming larger. One important challenge is the real-time capability for ray-tracing simulation. Although real time has a different meaning under different contexts, our goal for real-time ray tracing is mainly related to system simulations with dynamic Tx and/or Rx locations or environments. As an example, suppose we need to simulate the received signal in a moving vehicle such as a car running on a freeway or a helicopter on a rescue mission. The real-time signal strengths (or other parameters such as angle of arrival) are needed for the calculation of bit error rates and other communications quantities. Here real time means we can have the simulation results continuously updated as a function of vehicle location without pausing the system-wise simulations. Depending on the speed of the vehicle, the signal should be updated as fast as in microseconds. This is a difficult task for 3D ray-tracing methods. We expect new algorithms with better computational speed and accuracy will be developed, and acceleration using CPUs and GPUs will help achieve the goal of real-time simulation (see some relevant references in Ref. [28]).

Another challenge is how to accurately build environmental models which have the right complexity for a particular propagation simulation task. More importantly, when the users change system parameters, how do we determine if the environmental model needs to be updated? For example, if the frequency is increased, should we use an environmental model with higher resolution? The concept of multiple levels of detail discussed in this chapter plays an important role in making such decisions.

We expect in the near future we can have geospatial databases specifically designed for propagation modeling. Intelligent algorithms will be developed to serve as the brain of a propagation modeling and simulation systems. The intelligent algorithms will be able to choose and construct the suitable environmental models, determine how to launch rays and what kind of rays (LoS, reflection, diffraction rays, etc.) to trace, and decide when to stop the ray tracing engine and output results with satisfactory accuracy in designated time period (real-time ultimately).



## References

1. H.T. Friis, A note on a simple transmission formula. *Proc. IRE Waves Electron.* **34**, 254–256 (1946)
2. H.L. Bertoni, *Radio Propagation for Modern Wireless Systems* (Prentice-Hall, Upper Saddle River, NJ, 2000)
3. P.L. Rice, A.G. Longley, K.A. Norton, A.P. Barsis, Transmission loss predictions for tropospheric communication circuits. *Natl. Bur. Stand. Tech. Note 101. I & II* (1965)
4. A.G. Longley, P.L. Rice, Prediction of tropospheric radio transmission loss over irregular terrain. ESSA Technical Report ERL 79-ITS 67, U.S. Government Printing Office, July 1968.
5. G.A. Hufford, A.G. Longley, W.A. Kissick, A guide to the use of the ITS Irregular Terrain Model in the area prediction mode. U.S. Department of Commerce, DC, USA, April (1982). [Online]. Available: [http://www.ntia.doc.gov/files/ntia/publications/ntia\\_82-100\\_20121129145031\\_555510.pdf](http://www.ntia.doc.gov/files/ntia/publications/ntia_82-100_20121129145031_555510.pdf).
6. M. Born, E. Wolf, *Principles of Optics: Electromagnetic Theory of Propagation, Interference, and Diffraction of Light*, 6th edn. (Pergamon Press, New York, 1980)
7. G.D. Durgin, The practical behavior of various edge-diffraction formulas. *IEEE Antennas Propag. Mag.* **51**(3), 24–35 (2009)
8. K. Bullington, Radio propagation at frequencies above 30 megacycles. *Proc. IRE* **35**(10), 1122–1136 (1947)
9. Propagation by diffraction, *Recommendation ITU-R P.526-12*, (Downloadable from ITU website, [www.itu.int](http://www.itu.int)), 2012
10. J. Epstein, D.W. Peterson, An experimental study of wave propagation at 850 Mc. *Proc. IRE* **41**(5), 595–611 (1953)
11. J. Deygout, Multiple knife-edge diffraction of microwaves. *IEEE Trans. Antennas Propag.* **14**(4), 480–489 (1966)
12. C.L. Giovanelli, An analysis of simplified solutions for multiple knife-edge diffraction. *IEEE Trans. Antennas Propag.* **32**(3), 297–310 (1984)
13. G.D. Dockery, Modeling electromagnetic wave propagation in the troposphere using the parabolic equation. *IEEE Trans. Antennas Propag.* **36**(10), 1464–1470 (1988)
14. A.E. Barrios, Parabolic equation modeling in horizontally inhomogeneous environments. *IEEE Trans. Antennas Propag.* **40**(7), 791–797 (1992)
15. A.E. Barrios, A terrain parabolic equation model for propagation in the troposphere. *IEEE Trans. Antennas Propag.* **42**(1), 90–98 (1994)
16. J.R. Kuttler, Differences between the narrow-angle and wide-angle propagators in the split-step Fourier solution of the parabolic wave equation. *IEEE Trans. Antennas Propag.* **47**(7), 1131–1140 (1999)
17. K.B. Thiem, A 3D parabolic equation based technique for predicting propagation path loss in an Urban Area, Master thesis, Naval Postgraduate School, Monterey, Sept 2001
18. J. Walfisch, H.L. Bertoni, A theoretical model of UHF propagation in urban environments. *IEEE Trans. Antennas Propag.* **36**(12), 1788–1796 (1988)
19. M. Hata, Empirical formula for propagation loss in land mobile radio services. *IEEE Trans. Veh. Technol.* **29**, 317–325 (1980)
20. Y. Okumura, E. Ohmori, T. Kawano, K. Fukuda, Field strength and its variability in VHF and UHF land-mobile service. *Rev. Electr. Commun. Lab.* **16**(9–10), 825–873 (1968)
21. T. Rappaport, *Wireless Communications: Principles and Practice*, 2nd edn. (Prentice-Hall, Upper Saddle River, NJ, 2002)
22. *COST Action 231 Final Report, Digital Mobile Radio Towards Future Generation Systems*, ed. By E. Damosso, L.M. Correia. (Luxembourg, 1999). [Online]. Available: [http://www.lx.it.pt/cost231/final\\_report.htm](http://www.lx.it.pt/cost231/final_report.htm)
23. J.B. Keller, Geometrical theory of diffraction. *J. Opt. Soc. Am.* **52**(2), 116–130 (1962)
24. R.G. Kouyoumjian, P.H. Pathak, A uniform geometrical theory of diffraction for an edge in a perfectly conducting surface. *Proc. IEEE* **62**(11), 1448–1461 (1974)
25. C.A. Balanis, *Advanced Engineering Electromagnetics* (Wiley, New York, 1989)

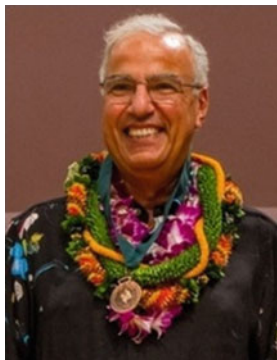
26. Y. Rahmat-Samii, R. Mittra, A spectral domain interpretation of high frequency diffraction phenomena. *IEEE Trans. Antennas Propag.* **25**(5), 676–687 (1977)
27. M.F. Iskander, Z. Yun, Propagation prediction models for wireless communication systems. *IEEE Trans. Microwave Theory Tech.* **50**(3), 662–673 (2002)
28. Z. Yun, M.F. Iskander, Ray tracing for radio propagation modeling: Principles and applications. *IEEE Access* **3**, 1089–1100 (2015)
29. Z. Zhang, Z. Yun, M.F. Iskander, Ray tracing method for propagation models in wireless communications. *Electron. Lett.* **36**(5), 464–465 (2000)
30. Z. Yun, M.F. Iskander, Z. Zhang, A fast ray tracing procedure using space division with uniform rectangular grid. *Electron. Lett.* **36**(10), 895–897 (2000)
31. Z. Yun, Z. Zhang, M.F. Iskander, A ray-tracing method based on triangular grid approach and application to propagation prediction in urban environments. *IEEE Trans. Antennas Propag.* **50**(5), 750–758 (2002)
32. Z. Zhang, Z. Yun, M.F. Iskander, 3D tetrahedron ray tracing algorithm. *Electron. Lett.* **37**(6), 334–335 (2001)
33. J.G. Cleary, G. Wyvill, Analysis of an algorithm for fast ray tracing using uniform space subdivision. *Vis. Comput.* **4**(2), 65–83 (1988)
34. Digital topographic databases for propagation studies, Rec. ITU-R P. 1058-2. Available online: [https://www.itu.int/dms\\_pubrec/itu-r/rec/p/R-REC-P.1058-2-199910-I!!MSW-E.doc](https://www.itu.int/dms_pubrec/itu-r/rec/p/R-REC-P.1058-2-199910-I!!MSW-E.doc).
35. F.A. Qazi, A. Das, Z. Yun, M.F. Iskander, Optimizing cellular coverage in Maui Island, Hawaii, in *2016 IEEE/ICES International Conference on Wireless Information and Systems (ICWITS) and Applied Computational Electromagnetics (ACES)*. (Available in IEEE Xplore Digital Library)
36. Z. Yun, M.F. Iskander, S.Y. Lim, D. He, R. Martinez, Radio wave propagation prediction based on 3D building structures extracted from 2D images. *IEEE Antennas Wirel. Propag. Lett.* **6**, 557–559 (2007)
37. Z. Yun, S.Y. Lim, M.F. Iskander, Use of geospatial resources for radio propagation prediction in urban areas. *IEEE Antennas Wirel. Propag. Lett.* **8**, 587–591 (2009)
38. R. Hartley, A. Zisserman, *Multiple View Geometry in Computer Vision*, 2nd edn. (Cambridge University Press, Cambridge, 2004)
39. F. Klen, *Geometry* (Dover Publications, Inc., New York, 1939)
40. Z. Yun, N. Omaki, M.F. Iskander, Ridge feature extraction and effect on radio propagation for wireless communications, in *IEEE APS Conference and USNC/URSI Meeting*, Chicago, 8–14 July 2012
41. Z. Yun, M.F. Iskander, Diffraction from multiple ridges: Comparing three- and two-dimensional results, in *The 8th EuCAP*, The Hague, Netherlands, April 2014. (Available in IEEE Xplore Digital Library)
42. R. Luebbers, A heuristic UTD slope diffraction coefficient for rough lossy wedges. *IEEE Trans. Antennas Propag.* **37**(2), 206–211 (1989)
43. Z. Yun, M.F. Iskander, Multiple levels of detail environment modeling for radio propagation simulation and prediction, in *Radio Science Meeting (Joint with AP-S Symposium)*, 2015. (Available in IEEE Xplore Digital Library)
44. A.T. Derode, M. Fink, Random multiple scattering of ultrasound. I. Coherent and ballistic waves. *Phys. Rev. E* **64**(3), 036605 (2001)
45. G. Montaldo, G. Lerosey, A. Derode, A. Tourin, J. de Rosny, M. Fink, Telecommunication in a disordered environment with iterative time reversal. *Waves Random Med.* **15**, 287–302 (2004)
46. G. Lerosey, J. de Rosny, A. Tourin, A. Derode, G. Montaldo, M. Fink, Time reversal of electromagnetic waves. *Phys. Rev. Lett.* **92**(19), 193904 (2004)
47. Z. Yun, M.F. Iskander, Time reversal with single antenna systems in indoor multipath environments, in *Ultra-Wideband, Short-Pulse Electromagnetics 8*, C.E. Baum, A.P. Stone, J.S. Tyo (Eds.) (Springer, New York, 2007)
48. D.A. Bibb, Z. Yun, M.F. Iskander, Source localization using time reversal in urban environments: A ray tracing approach, in *2014 IEEE International Symposium on Antennas and Propagation and the 2014 USNC/URSI National Radio Science Meeting*, Memphis, TN, 2014. (Available in IEEE Xplore Digital Library)

49. D.A. Bibb, Z. Yun, M.F. Iskander, Time reversal for source localization in urban environments considering the effect of Doppler shift, in *2015 IEEE International Symposium on Antennas and Propagation and the 2015 USNC/URSI National Radio Science Meeting*, Vancouver, Canada, 2015. (Available in IEEE Xplore Digital Library)
50. D.A. Bibb, Z. Yun, M.F. Iskander, Source localization using time reversal in urban environments using ray tracing. *IEEE Antennas Wirel. Propag. Lett.*, Under review
51. D.A. Bibb, Z. Yun, M.F. Iskander, Machine learning for source localization in urban environments, in *IEEE Military Communications Conference, MILCOM 2016-2016*, Baltimore, 1–3 November



**Zhengqing Yun** received the PhD degree in electrical engineering from Chongqing University, Chongqing, China, in 1994. He was an assistant researcher at the Hawaii Center for Advanced Communications (HCAC) from 2002 to 2005, where he became an assistant professor in 2006. He was involved in a postdoctoral work with the University of Utah and Southeast University, China, before he joined the University of Hawaii at Manoa (UH). He is currently an associate professor at the Hawaii Center for Advanced Communications (HCAC), College of Engineering, UH. Dr. Yun's current research interests include radio propagation in complex environments, such as urban, indoor, and mountainous areas. He served as the technical program co-chair of the IEEE Antenna and Propagation Society International Symposium, Honolulu, in 2007, and the technical program chair of the IEEE

International Conference on Wireless Information Technology and Systems, Honolulu, in 2010 and 2016, and Maui, HI, in 2012. He was an associate editor of the IEEE Transactions on Vehicular Technology and the IEEE Transactions on Antennas and Propagation. He is currently an associate editor of the IEEE Access.



**Magdy F. Iskander** is the director of the Hawaii Center for Advanced Communications and professor of Electrical Engineering, University of Hawaii at Manoa. He is co-director of the NSF I/UCRC and a fellow of IEEE (1993). He was the 2002 president of the IEEE AP-S, a distinguished lecturer, and a program director in the ECCS Division at NSF. Dr. Iskander joined the University of Hawaii in 2002, and prior to that he was professor of ECE Department and the Engineering Clinic Endowed Chair Professor at the University of Utah. He received many awards for excellence in research and teaching including University of Hawaii Board of Regents' Medal for Excellence in Research and Medal for Teaching Excellence, IEEE MTT-S Distinguished Educator Award, IEEE AP-S Chen-To Tai Distinguished Educator Award, Northrop Grumman Excellence in Teaching Award, and others.

He has published over 270 papers in journals and books and holds ten patents. He authored/edited several books including the textbook *Electromagnetic Fields and Waves*. He is the founding editor of *Computer Applications in Engineering Education* published by John Wiley & Sons from 1992 onwards. His research has been funded by NSF, NIH, Army Research Office, US Army CERDEC, Office of Naval Research, and corporate sponsors.

# Chapter 13

## Radio Propagation Modeling: A Unified View of the Ray-Tracing Image Method Across Emerging Indoor and Outdoor Environments

Soo Yong Lim, Zhengqing Yun, and Magdy F. Iskander

### 13.1 Introduction

Wireless mobile communications have recorded a steady growth over the last several decades within the communications industry. Unlike broadcast systems that are intended to cover a whole metropolitan area from a single transmitter, cellular radio and personal communication services (PCS) were designed to give mobile subscribers access to the communication system by utilizing radio over comparatively short links. With PCS, the final aim is to provide instant communications to people worldwide round-the-clock. In this regard, propagation prediction and modeling plays an important role in the successful design and implementation of wireless communication systems. A quick look at history shows that the ability to provide wireless communications to an entire population was first achieved following the development of cellular concept by Bell Laboratories in the 1960s and 1970s [1]. Since then, the wireless communications era has blossomed thanks to both cellular concept (geographic service divided into smaller “cells”) and the maturing of integrated circuit technology that has allowed intelligence, control functions, and signal processing to be integrated in the fixed system and in the subscriber units [2].

The characteristics of radio propagation have been widely recognized as one of the fundamental key steps in the design of cellular and PCS systems. With the current proliferation of wireless applications, the needs to gain a working knowledge

---

S.Y. Lim (✉)

Department of Electrical and Electronic Engineering, University of Nottingham  
Malaysia Campus, Semenyih, Malaysia  
e-mail: [Grace.Lim@nottingham.edu.my](mailto:Grace.Lim@nottingham.edu.my)

Z. Yun • M.F. Iskander

Hawaii Center for Advanced Communications, College of Engineering, University of Hawaii  
at Manoa, Honolulu, HI, USA  
e-mail: [zyun@hawaii.edu](mailto:zyun@hawaii.edu); [magdy@hawaii.edu](mailto:magdy@hawaii.edu)

of the properties of radio waves and how they interact with various environments have never before been so apparent. With smaller cell sizes, higher operation frequency, and more advanced antenna systems, radio propagation modeling becomes more difficult and challenging. This is because the traditional propagation models that simplify the environment by ignoring the small and fine structures are no longer valid for such complex environments.

The first objective of this chapter is to investigate radio propagation in emerging indoor and outdoor environments such as indoor stairwells, periodic building facades, and open-trench drains in urban environments. Collectively, the research findings from these works contribute especially toward a better design and implementation of small radio cells. Among the small radio cells that will benefit from these findings are picocells (cell radius  $< 100$  m) and femtocells (cell radius  $< 50$  m), the latter of which have gained substantial attention in recent years due to their profits in terms of infrastructure cost savings and improved user experience in indoor environments [3]. Aside from benefiting small radio cells, the research findings from these works are foreseen to also enhance short-path propagation. In fact, back in the year 1997, Holloway et al. [4] have observed a growing need to predict signal levels for short propagation paths in the range of 2–100 m. This prediction needs arose because for such short propagation paths, accurate behavior of reflecting waves from the surrounding objects like building facades plays a crucial role in signal prediction. Hence, the research findings from these works are also set to profit other applications like microcellular PCS deployments in malls and airports, business campuses utilizing wireless private branch exchanges (PBXs) and wireless local area network (WLAN), and vehicular communications through urban canyons to nearby relays.

The second objective of this chapter is to offer a unified view of the ray-tracing image method, which can be utilized for both indoor and outdoor environments because these two environments are governed by the same propagation mechanisms. The physics-based explanation provided from ray theory sees each propagation mechanism as separate, these being the direct rays, reflected rays, transmitted rays, diffracted rays, and hybrid rays, which are a combination of any of the aforementioned rays. The ray approach is different from solving the boundary value problems using Maxwell's equations or wave equations in that the results obtained from the latter approaches do not distinguish any propagation mechanisms, whether they are reflection, transmission, diffraction, or others.

Since ray theory approach clearly distinguishes between several propagation phenomena, it is especially useful to interpret actual field measurement results, which are always a mix of all propagation phenomena. When both ray-tracing simulation and actual field measurement are carried out to study a particular propagation environment, better propagation modeling can be achieved, which will then pave the way to improved propagation prediction. The frequency bands chosen for our investigation into various complex environments are primarily 2.4 and 5.8 GHz because these two frequency bands have wide applications predominantly among the deployment of WLAN.

### ***13.1.1 Background Information***

Radio propagation in indoor stairwell is a relatively less explored area in propagation prediction. This is in contrast to radio propagation within buildings where extensive studies have been done during the last several decades. For instance, specific propagation features within building due to their layouts, construction materials, and types have been investigated [5]. In addition, a comprehensive list of measurement and modeling efforts for characterizing radio propagation within and into buildings are available; see, for example, the references cited by Hashemi [6].

Previous work done in the propagation environment of indoor stairwell is scarce – Refs. [7] and [8] are two examples of such work. In Ref. [7], a hybrid approach that combines ray-tracing method with a periodic moment method (PMM) was developed to examine the wave propagation, penetration, and scattering by periodic structures. Each section of the stairs is modeled as a periodic wedge panel having material properties similar to those of the reinforced concrete wall. Measurements for waves propagating inside a staircase have been compared and discussed at 900 MHz and 1.8 GHz with two sets of simulation results – ray tracing with and without the PMM method. The authors found that the PMM can improve the accuracy of the simulations for wave penetrating through the stair structures.

A three-dimensional propagation model that is based on a beam tracing variant was proposed by Teh and Chuah [8], which the authors termed ray-polygon tracing [9]. In order to validate the capability of this model, the authors have carried out propagation measurements in a multifloor stairwell in the frequency range of 1.2–1.8 GHz. A location-by-location comparison between the measured and simulated results was reported over a 45 dB range of the measured path loss. The authors found that signal strength decreases by about 15 dB when the transmitter makes corner turns at intermediate staircase landings next to the concrete louver. This attenuation reflects loss of dominant signal paths that exist prior to the turns.

By comparison, there has been more work done in the modeling of scattered electromagnetics field from periodic building facades. This is because building facades, as part of urban propagation environments, affect the propagation characteristics very much in the frequency range above 300 MHz [10]. The elements of building façade such as periodic walls and windows all contribute to the total received electromagnetics power; therefore the examination of their effects has been a research interest for many years. Table 13.1 summarizes the results by various researchers worldwide in a chronological order, listing the key points in their investigations, such as the frequency bands, focus of research, simulation method, measurement approach (if any), as well as the outcome of their research works. One observation from Table 13.1 reveals that among the available simulation methods that include analytical techniques and full numerical approaches, ray-tracing and geometrical-optics (GO) models have been the most frequently used approach owing to their suitability for high-frequency radio signal prediction.

**Table 13.1** Summary of propagation research on building facades and their electrical parameters

Authors (year)	Features	Description
Honcharenko et al. (1994) [11]	Frequency	900 MHz, 1.8 GHz, and 2.4 GHz (simulation) 3 GHz (measurement)
	Focus	Typical concrete block walls
	Simulation	Theoretical calculation of reflection and transmission coefficients
	Measurement	Measurements of transmission through a concrete block wall
	Outcome	Frequency dependence of specularly and non-specularly transmitted and reflected fields examined
Al-Nuaimi et al. (1994) [12]	Frequency	11.2 GHz
	Focus	Building façade
	Simulation	Aperture analysis (Huygens-Kirchhoff method for far field region)
	Measurement	Scattering measurements from real buildings
	Outcome	Prediction models based on plane reflector developed
Landron et al. (1996) [13]	Frequency	1.9 GHz and 4.0 GHz
	Focus	Smooth and rough exterior building surfaces
	Simulation	Ray tracing
	Measurement	Microwave reflection coefficient measurements (a wideband spread-spectrum sliding correlation system)
	Outcome	A reflection model for rough surfaces proposed
Holloway et al. (1997) [4]	Frequency	900 MHz
	Focus	Composite material commonly used in construction
	Simulation	Homogenization method (a method for analyzing periodic structures) Four-ray model (direct ray, left and right wall-reflected ray, and ground-reflected ray)
	Measurement	Various walls measurements
	Outcome	A multilayer model for analyzing the reflection and transmission of EM waves from periodic composite brick walls presented
Cuias et al. (2001) [14]	Frequency	5.8 GHz
	Focus	EM parameters of 6 typical building materials
	Simulation	Ray tracing
	Measurement	A channel sounder based on swept frequency technique (vector network analyzer)
	Outcome	EM parameters at 5.8 GHz (vertical polarization) for façade, brick wall, chip wood, glass, doors, and plasterboard obtained

(continued)

**Table 13.1** (continued)

Authors (year)	Features	Description
Zhang et al. (2002) [15]	Frequency	1.8 GHz
	Focus	Building windows
	Simulation	Ray tracing and finite-difference time-domain (FDTD)
	Measurement	A millimeter-wave scale model test set
	Outcome	A ray model for metal-framed structure for urban environment developed
Pena et al. (2003) [16]	Frequency	900 MHz
	Focus	Prediction of wall losses
	Simulation	Ray-tracing
	Measurement	A noncoherent pulsed transmitter-receiver system
	Outcome	Through-wall attenuation, the permittivity and conductivity of brick and concrete walls estimated
Pongsilamane et al. (2004) [17]	Frequency	900 MHz, 1.0 GHz, 2.0 GHz, 3.0 GHz, and 4.0 GHz
	Focus	Building façade
	Simulation	Monte Carlo simulation for ray calculation
	Measurement	None
	Outcome	A statistical model for building façade developed
Dimitriou et al. (2006) [18]	Frequency	2.0 GHz
	Focus	Building façade
	Simulation	Ray tracing and uniform theory of diffraction (UTD)
	Measurement	Continuous wave (CW) measurement
	Outcome	A method for modeling the influence of scatterers from building façade proposed
Degli-Esposti et al. (2007) [19]	Frequency	1.296 GHz
	Focus	Three types of building walls: (i) Metal, relatively smooth wall (ii) Uniform brick wall (iii) Typical brick wall with windows, doors, and other elements
	Simulation	3D ray tracing
	Measurement	CW measurement
	Outcome	An existing diffuse scattering model modified and tuned
Cuias et al. (2007) [20]	Frequency	5.8 GHz
	Focus	Brick walls, chip wood panels
	Simulation	Physical optics (PO) scattering models
	Measurement	Scattering measurement (VNA)
	Outcome	A PO model for dielectric surfaces improved

(continued)



**Table 13.1** (continued)

Authors (year)	Features	Description
Kwon et al. (2008) [21]	Frequency	3.0 GHz, 5.0 GHz, and 6.5 GHz
	Focus	Smooth and rough exterior building surfaces
	Simulation	Ray-tracing
	Measurement	Reflection coefficient measurements (dielectric probe kit, network analyzer)
	Outcome	A model for an inhomogeneous building façade proposed
Lim et al. (2010) [22]	Frequency	2.4 GHz
	Focus	Periodic building façade (Moore Hall)
	Simulation	Ray tracing (image method) and uniform theory of diffraction (knife edge assumed)
	Measurement	Narrowband measurement
	Outcome	Flat surface approximation and knife-edge approximation of the building façade compared
Lim et al. (2011) [23]	Frequency	2.4 GHz and 5.8 GHz
	Focus	Simplified building façade structure
	Simulation	Ray tracing (image method) and uniform theory of diffraction (single diffraction)
	Measurement	Narrowband measurement in an anechoic chamber environment
	Outcome	Small-scale fading due to the multipath effect studied

On the other hand, propagation studies conducted on open-trench drains in urban environments concern a unique situation in several Asian countries, because the drainage systems in these countries differ notably from those in the USA and Europe, in that the former are partially open on the top, while the latter are primarily below ground and covered. The propagation characteristics in this type of open-trench drain environment have not been studied by other researchers in the past, which brought us to dive into this topic. Comprehending the complicated wave-propagation behavior inside an open-trench drain and the ground nearby serves as a useful indicator in designing reliable wireless communication systems, especially in environments where such open-trench drains are present. In addition, knowledge gained from the measurement results will aid in improving the accuracy of radio propagation prediction, which, in turn, can help in establishing dependable wireless communication networks in urban and other complex propagation environments.

## 13.2 Emerging Indoor and Outdoor Environments

An examination of the major research on radio propagation in cellular mobile telephone systems shows that theoretical studies, numerical simulations, and field measurements have always been closely intertwined. Published research findings of

these works are available mostly from the 1980s onward although the topic of indoor radio propagation channel can be dated all the way back to 1959 [6]. It has been found that any realistic propagation model should take into account a good variety of factors, and its parameters should be validated through actual field measurements rather than simplified theory. In this section, special focus is placed on our studies of three emerging indoor and outdoor environments, namely, indoor stairwell, periodic building façade, and open-trench drain.

### ***13.2.1 Indoor Stairwell***

Since there have already been many existing empirical path loss models for indoor environments, one question arises as to whether or not these models can be straightforwardly applied to any indoor stairwell environment without adjustment and modification. To answer this question, we have to comprehend the behavior of electromagnetic waves in an indoor stairwell condition, to find out what propagation mechanisms are prominent in it and whether they are different from those outside of the stairwell. Aside from that, the influence of frequency on indoor stairwell propagation is also a key factor that we studied.

In an indoor stairwell, the propagation environment resembles that of a leaky waveguide with inhomogeneous fillings (stairs) inside. This unique propagation environment is indeed different from multifloor and other indoor scenarios and deserves careful studies. In Refs. [24, 25], we have conducted a series of field measurements in four different stairwells at 2.4 and 5.8 GHz and reported their findings. In particular, in Ref. [24], we measured the received power in an indoor stairwell at 2.4 GHz for three transmit (Tx)/receive (Rx) antenna polarizations, namely, vertical/vertical (VV), horizontal/horizontal (HH), and vertical/horizontal (VH) polarizations. During the measurement, the Tx antenna was placed outside the building and faced the entry door to the stairs while the Rx antenna was moved up the stairs step by step. On each stair step, the Rx antenna was rotated around the post of an entire revolution while 100 received signals were recorded. These 100 recorded signals were subsequently averaged to filter out the small-scale fading effects, after which the mean path gain at each stair step was obtained. To model radio propagation in the stairwell, we have developed an image-based ray-tracing procedure and provided physics-based explanation for the trends and characteristics in the obtained results. In Fig. 13.1, ray-tracing results are compared with the measurement results for VV polarizations. A good agreement is observed from this comparison, with a standard deviation of less than 2 dB, which is very good for indoor propagation cases.

Based on the ray-tracing results in Fig. 13.1, we may observe that the main propagation mechanisms in the stairwell include reflections from the stairwell walls, transmission through the stairs, and their combinations. The line-of-sight (LOS) only exists in the first section, while reflections do not contribute to the higher sections of the stairs. Since the reflectivity of the stairwell walls is relatively

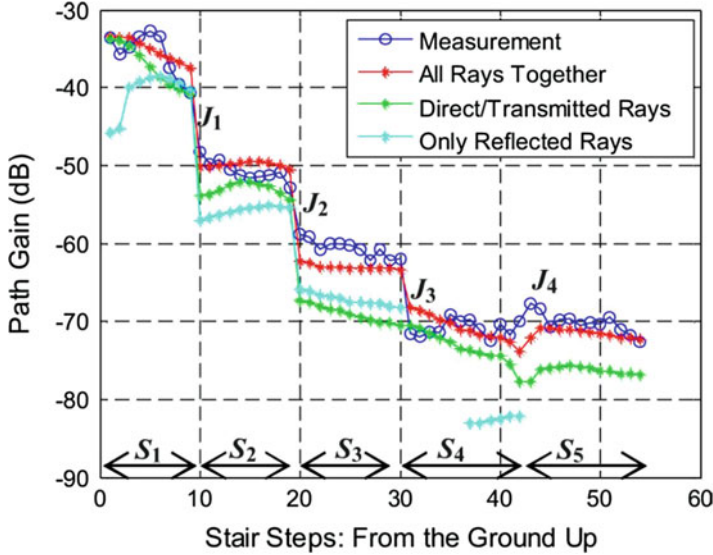


Fig. 13.1 The simulated and measured results for VV polarization [24]

small, reflected rays seem to be less important than transmission through the stairs. Transmission is thus very important and could not be ignored, even though multiple transmissions would greatly reduce their power. Hybrid rays that combine reflections and transmissions are also important, and they contribute significantly for higher stair sections.

Aside from presenting our results for VV polarization, we have also measured for HH and HV polarizations in the same stairwell at 2.4 GHz. All three measured polarizations results are shown in Fig. 13.2. Comparisons among the measured results for VV, HH, and VH polarizations show that VV polarization has the best received power in most cases: about 10-dB gain over HH and VH polarizations for the first section of the stair and about 5-dB gain for the second section. It is also found that the propagation in stairwell is significantly depolarized when the electromagnetic waves travel upward stair steps due to the multiple reflections from the walls, transmissions through the stairs, and their combined effects.

From the study of a single stairwell, we have extended our scope to examine four types of stairwells that are often encountered in the two general categories of *stairwell around a square well* and *dog-leg stairwell*. Figures 13.3 and 13.4 show the top view of a dog-leg stairwell and a stairwell around a square well, respectively.

Based on a series of field measurement campaigns conducted at all four stairwells at two frequencies, i.e., 2.4 and 5.8 GHz, we have proposed a new path-loss model based on the *accumulative distance* the receiver has traveled, in addition to the conventional separation distance between Tx and Rx antennas. The mean path

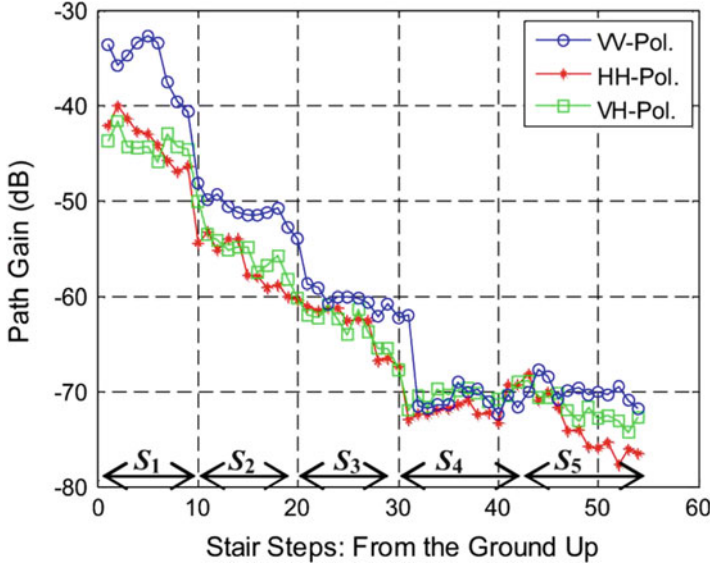


**Fig. 13.2** The measured results for VV, HH, and VH polarizations in the five sections of the stairs [24]

loss/gain can be explicitly expressed in terms of a reference path loss/gain  $P(d_0)$  and the distance to the source ( $d$ ) [25].

$$P(d) [dB] = P(d_0) [dB] + 10n \log_{10} \left( \frac{d}{d_0} \right) + X_\sigma [dB], \quad (13.1)$$

where  $P(d_0)$  is the reference path loss at a distance  $d_0$  from Tx,  $d$  is the separation distance between Tx and Rx,  $n$  is the path loss exponent, and  $X_\sigma$  represents the log-normal distribution which has zero mean and is thus solely determined by its deviation ( $\sigma$ ). In Table 13.2, we present the  $n$  values calculated for all measurement cases using separation distance and walking distance, respectively. As for Table 13.3, the  $X_\sigma$  values are presented.

It can be seen from Table 13.2 that the  $n$  values of the walking distance are about 35% (5.39/8.30) and 34% (6.42/9.74) of the values using separation distances for 2.4 GHz and 5.8 GHz, respectively. From the same table, we may also observe that the standard deviation  $\sigma_m$  of the walking distance model is smaller. This standard deviation  $\sigma_m$  is different from the standard deviation  $\sigma$  of  $X_\sigma$  in that it refers to the standard deviation between the model and the actual field measurements. As for the log-normal distribution of path loss about its mean, i.e.,  $X_\sigma$ , we calculate the standard deviation  $\sigma$  of  $X_\sigma$  for the four stairwells. The log-normal distribution describes the random shadowing effects, which occur over a large number of measurement locations that have the same transmitter-receiver separation. To meet

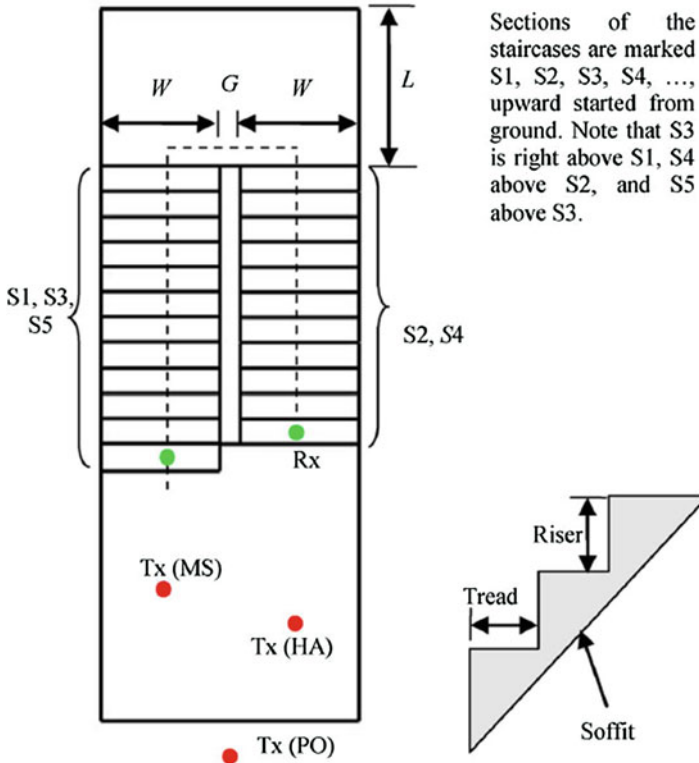


**Fig. 13.3** Top view of the dog-leg stairwell structure [25]

the criterion of a large number of measurement locations, we have combined all the measured results into two large groups for VV and HH polarizations at 2.4 and 5.8 GHz, respectively, instead of calculating the  $\sigma$  values of each individual stairwell (shown in Table 13.3).

It is found that when the conventional separation distance is used in the path loss model, the  $n$  values are significantly higher than the values for urban and other indoor propagation environments, indicating faster power drop in stairwells. When walking distance is introduced for the calculation of  $n$  values, we found that the  $n$  values drop to the similar level as other indoor scenarios. More importantly, the standard deviation ( $\sigma_m$ ) between the model and the measurement values is smaller than that when separation distance is employed. Furthermore, the standard deviation ( $\sigma$ ) of the log-normal distribution of the excess path loss is also smaller. These smaller standard deviation values indicate that the path loss model based on walking distance predicts more accurately than the one based on separation distance.

The results reported in this section are beneficial for understanding radio propagation in indoor stairwell environment, which is crucial for emergency applications (law enforcement and firefighting purposes). Besides, they can also

**Fig. 13.4** Top view of the stairwell around a square well structure [25]

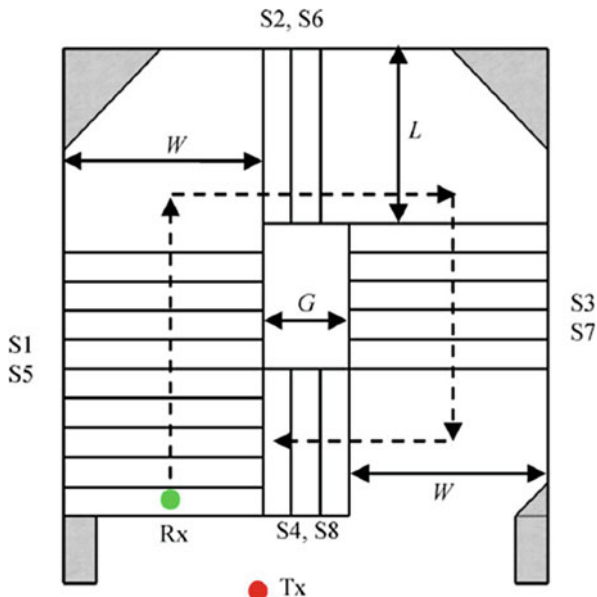


**Table 13.2** Path loss exponent: separation versus walking distance

Freq.	Stairwell/pol	<i>n</i> values		$\sigma_m$ (dB)	
		S. dist.	W. dist.	S. dist.	W. dist.
2.4 GHz	HL/VV	8.93	5.75	7.23	3.94
	HL/HH	7.48	4.83	6.39	3.71
	PO/VV	9.64	5.79	7.62	3.22
	PO/HH	8.57	4.97	5.83	2.20
	PO/VH	7.77	4.62	5.82	2.28
	HA/VV	8.76	5.73	5.16	4.21
	HA/HH	7.62	5.01	5.77	4.80
	MS/VV	8.17	6.53	5.06	3.25
	MS/HH	7.33	5.82	4.37	3.20
	PO/HH (II)	8.75	4.83	5.66	2.13
	<b>Average</b>	<b>8.30</b>	<b>5.39</b>	<b>5.89</b>	<b>3.29</b>
5.8 GHz	HL/VV	10.12	6.36	6.28	2.72
	HL/HH	7.49	4.89	6.64	3.66
	PO/VV	12.94	7.45	9.59	2.84
	PO/HH	8.74	5.06	6.63	2.08
	MS/VV	10.96	8.58	7.72	1.77
	MS/HH	8.16	6.16	5.88	4.11
		<b>Average</b>	<b>9.74</b>	<b>6.42</b>	<b>7.12</b>

**Table 13.3**  $\sigma$  values for 2.4 GHz and 5.8 GHz

Freq.	Pol.	Stairwell	$\sigma$ (dB)	
			S. dist.	W. dist.
2.4 GHz	VV	PO	11.62	5.32
		HA	1.00	7.08
		MS	6.24	12.73
		HL	9.28	2.04
	HH	PO	3.57	2.63
		HA	4.10	5.08
		MS	1.00	5.65
		HL	9.42	4.25
5.8 GHz	VV	PO	13.84	4.80
		MS	2.66	3.29
		HL	10.87	3.15
	HH	PO	2.83	3.07
		MS	12.31	2.20
		HL	1.83	1.00

help to develop effective indoor communications systems and may be useful for the design and simulation of small cell wireless communication systems such as pico- and femtocells, whose cell radii are less than 100 and 50 m, respectively.

### 13.2.2 Periodic Building Façade

In the area of wireless communications, the electromagnetic fields scattered from or transmitted through the building wall/façade often show complicated patterns that results in a difficult match using simple ray-tracing model. Yet, modeling the interaction between realistic wall/façade and electromagnetics field is crucial to accurate propagation prediction that in turn guarantees reliable wireless communications. This section attempts to examine the accuracy of ray tracing when the building façade is replaced with those of simpler geometry like that of a flat smooth surface. For this purpose an idealized building façade model has been built and placed inside an anechoic chamber for experimental verification of the effects of diffraction. The findings of this work give a clue as to how much accuracy will be compromised in a ray-tracing simulation when the complex building façade is approximated by a simpler structure.

The primary propagation mechanism in this study is the scattered field from the building façade. If the façade is treated as one of knife-edge structure, diffracted rays from the edges are to be calculated. Uniform theory of diffraction (UTD) [26] can be used to calculate the diffraction coefficient from the knife edges by treating them as perfect electric conductors. In fact, UTD is used for solving a wide variety of perfectly conducting electromagnetic problems, such as the analysis of patterns for antennas mounted on aircraft and ships [27], and to solve diffraction problems

involving metal objects [28]. In addition, heuristic UTD diffraction coefficients have been introduced to analyze structures having penetrable wedges of complex geometry.

For the purpose of collecting field measurement data in this work, one data acquisition system has been assembled to operate at 2.4 and 5.8 GHz. On the transmitting end, one horn antenna (A. H. Systems SAS-571) that operates in the range of 700 MHz to 18 GHz is employed. This horn antenna is manufactured by A. H. Systems, Inc. [29]. Its average 3 dB beamwidth (E-field) is  $48^\circ$  and the average 3 dB beamwidth (H-field) is  $30^\circ$ . This antenna is pointed to face the façade model only but not the receiver. Two sets of dipole antennas at 2.4 and 5.8 GHz have been used at the Rx locations. They are the 8 dBi high-performance omnidirectional WLAN antennas (HyperLink Technologies HGV-2409U [30]) at 2.4 GHz and the 8 dBi ISM/UNII band omnidirectional WLAN antenna (HyperLink Technologies HG5808U [31]) at 5.8 GHz. At 2.4 GHz, the vertical beamwidth is  $15^\circ$  and the horizontal beamwidth is  $360^\circ$ , while at 5.8 GHz, the vertical beamwidth is  $16^\circ$  and the horizontal beamwidth is  $360^\circ$ . The Tx and Rx antennas are oriented for vertical-vertical (VV) polarization.

An idealized building façade model that features one of the basic structural elements of typical building – periodic wall – has been built and placed inside an anechoic chamber located on the campus of the University of Hawaii at Manoa. Because we are interested in examining the knife-edge diffraction from the façade, aluminum sheets (aluminum flashing) are used to represent the diffraction structures. The frame supporting the aluminum sheets are made of wood strips, and the dimension of this frame is 8 ft long, 5 ft wide, and 3 ft tall. Frame anchors and screws are used to fasten the frame while the 17 metal sheets are put into the frame to form a periodic structure. The separation distance between the consecutive sheets is 5 in. Figure 13.5 illustrates the top view of the idealized façade placed inside an anechoic chamber with the insets showing the photos of it.

In Fig. 13.5, the locations of the transmitter and receivers are designated as Tx and Rx, respectively. The Tx horn antenna is seen to face the façade only but not the receiver, but there is a very small leakage of the energy that travels directly from the side to the Rx dipole antenna via the direct path. For the measurement at 5.8 GHz, we allow this LOS path to exist without any blockage, while at 2.4 GHz, absorbers are set up to block the Rx antenna from seeing the Tx antenna. These absorbers are put to face the Tx antenna while the measurement data is collected behind the absorbers along the Rx route.

The idealized model that has been constructed is three dimensional, but because the Tx and Rx are placed at the same height, and also because the top and the bottom edges of the sheets are close to the absorbing materials, the propagation can be treated as a two-dimensional (2D) mechanism. Since the distance between sheets is 5 in., when the test frequency is at 5.8 GHz ( $\lambda = 5.17$  cm or  $\sim 2$  in.), the spacing between the metal sheets is approximately  $2\lambda$ , and for that at 2.4 GHz ( $\lambda = 12.5$  cm or  $\sim 5$  in.), the same spacing is about  $1\lambda$ . The distance (a) between the Tx and the façade model is 2.91 m, and the measurable distance between the Tx and the Rx on the walkway is 9.5 ft, with variable distance between these Rx locations.



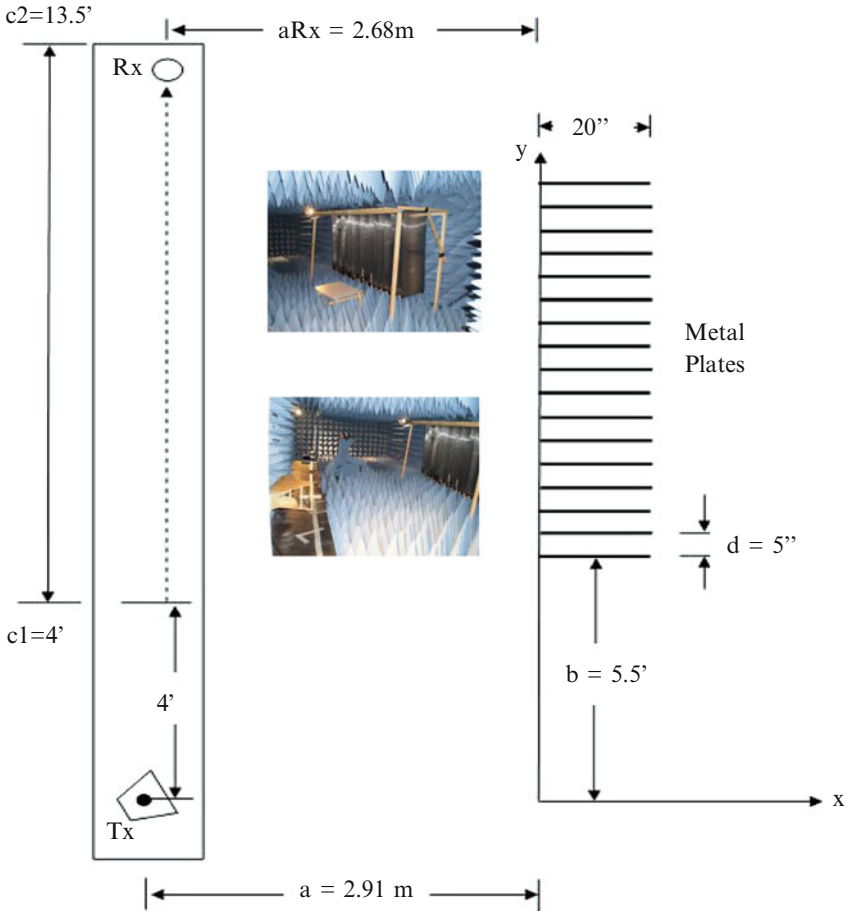


**Fig. 13.5** Top view of the idealized façade inside an anechoic chamber (not to scale). Dimensions are in meters and feet. The insets show the photos of the façade, the Tx and Rx

At 5.8 GHz, a series of measurement data has been collected along an 8.5 foot route with up to ½ in. interval between the receiver points. There is a good match between the two repeated measurements, collected at different times with a step of 1 in.

In Fig. 13.6, the measured and the simulated results at 5.8 GHz are presented. These data have been measured and simulated at ½ in. interval but later averaged over a five-point window to yield the average values at each Rx location. A close scrutiny of this figure reveals that both the measured and the simulated results follow the same trend – they generally have the rise and fall at about the same locations, with some exhibiting deep fading. This set of measurement data at 5.8 GHz is collected without putting any absorbers between the Tx and Rx antennas, so a LOS ray with a 1% of the power in the main beam is counted in the calculation of the total received power.

**Fig. 13.6** Measurement and simulation results of the idealized façade structure at 5.8 GHz

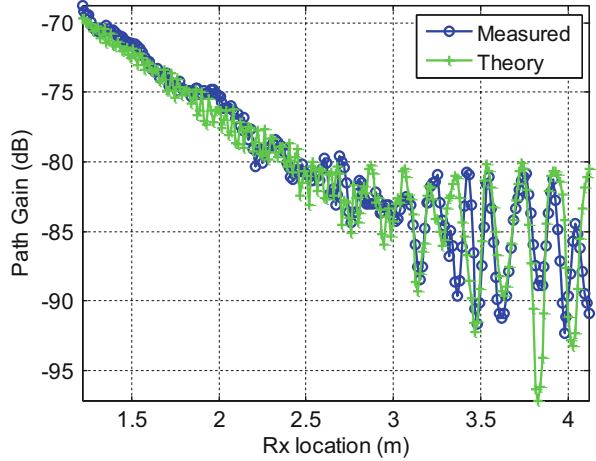
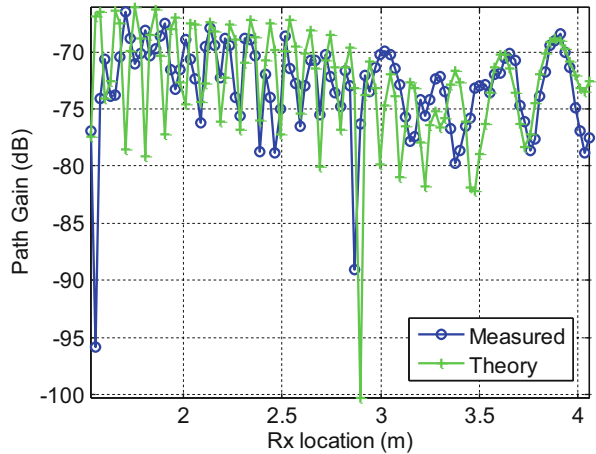
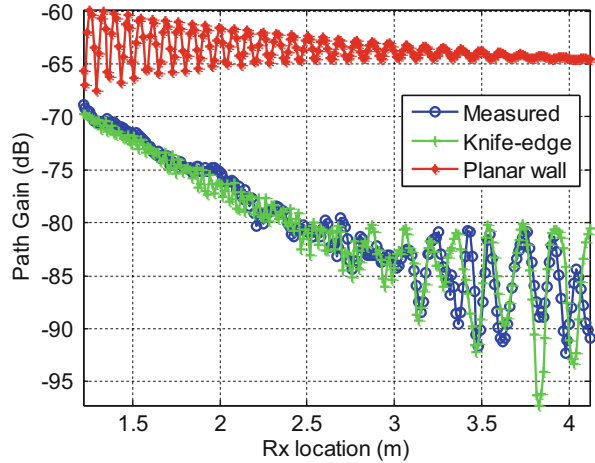


**Fig. 13.7** Measurement and simulation results of the idealized façade structure at 2.4 GHz



As for the experiment at 2.4 GHz, absorbers have been set up to block the Rx antenna from seeing the Tx antenna. Their results are presented in Fig. 13.7. We can observe that at 2.4 GHz, both the measured and the simulated fields arising from the same idealized periodic façade also share the same characteristics in that their rise and fall along the Rx route are similar. For this set of measurement data, the path gain is collected at 1 in. interval because at 2.4 GHz, the associated wavelength more than doubled the wavelength at 5.8 GHz. It should be pointed out that a LOS ray is still needed to achieve the match, although the power associated with this ray has been further reduced. The reason why this direct ray cannot be eliminated totally from the simulation is because the blockage by the absorbers is not a perfect one. Also, some rays that come forth from the Tx horn antenna might have got diffracted by the edges of the absorbers and after that make their way to reach the Rx.

**Fig. 13.8** The planar wall replacement results at 5.8 GHz



Since it is common in practical ray-tracing software to replace an inhomogeneous building façade with a flat smooth surface, next we approximate the façade of metal sheets with a flat smooth perfect electrically conducting (PEC) surface and see how much accuracy would be compromised. All other settings remain the same. Figure 13.8 presents the simulated reflection results when such replacement takes place at 5.8 GHz.

From Fig. 13.8, we can see that when the diffracting façade is approximated by a flat smooth PEC surface, the simulated path gain is significantly different. The signal variation in the beginning of the Rx route is larger compared with the one for diffracting façade, while at the end part of the measurement route, the signal variation is smaller. This trend is opposite to both the measurement and diffraction simulation results. Also, the path gain only slightly drops along the measurement route. Since the replacement of a periodic façade by a planar smooth surface will lead to very different path gain predictions, we conclude that in this particular case, it is not a good idea to use a planar surface to approximate the periodic façade.

### 13.2.3 Open-Trench Drain

As terrestrial wireless communication systems become more ubiquitous, there is a rising need to study the propagation characteristics of every habitable environment so that effective communication systems can be established. Past research showed that open-trench drains, whose presence is prevailing in many Asian cities, make up an additional channel in which radio signal can adequately travel [32]. In this section, we present field measurement results of an open-trench drain for LOS and

**Fig. 13.9** Layout of the measurement environment (not to scale). The inset shows the Tx and Rx antennas being used [33]

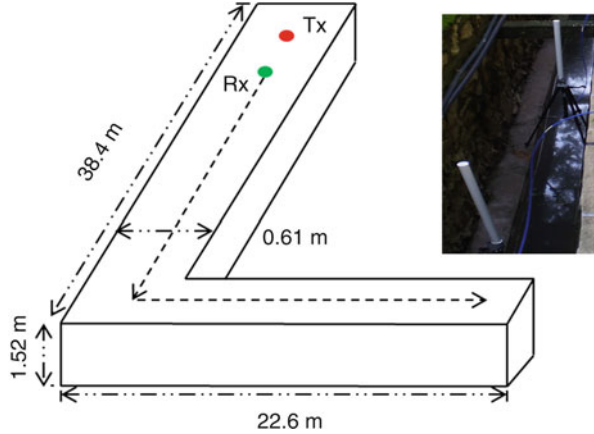


**Table 13.4** Measurement parameters

Frequency (GHz)	Distance between Tx and the first Rx (m)			Interval (m)		
	VV	HH	HV	VV	HH	HV
0.9	0.9	0.9	0.9	0.3	0.6	0.6
2.4	0.9	0.9	0.9	0.3	0.6	0.6
5.8	0.9	0.9	0.9	0.3	0.6	0.6

non-LOS (NLOS) portions at three frequencies (900 MHz, 2.4 and 5.8 GHz) for three different polarizations, namely, VV, HH, and HV polarizations. Subsequently, we have adopted K-means clustering approach to process the obtained data in deriving path loss exponent  $n$  and their associated standard deviation. Comparison is made of the  $n$  values, as well as the standard deviation values, before and after employing K-means clustering [33]. Figure 13.9 presents the geometric configuration of the measurement site of this work.

During measurements, the condition of the open-trench drain was a relatively dry one, and its surface relatively smooth and flat. For HH and HV polarization measurements, the horizontal antennas were oriented in two different ways, namely, parallel to the drain’s axis (endfire to endfire configuration) and perpendicular to the drain’s axis (broadside to broadside orientation). Table 13.4 summarizes the distance between the Tx and the first Rx location and their interval at which measurement data were recorded, while Tables 13.5 and 13.6 summarize the single  $n$  values and the sub- $n$  values computed from one entire cluster and from two clusters, respectively, before and after applying K-means clustering, together with the corresponding standard deviation  $\sigma_m$  values. The implication of the  $\sigma_m$  value is such that a smaller value will lead to a more accurate propagation model and vice-versa.

**Table 13.5** Path loss exponent and standard deviation values *before* applying K-means clustering

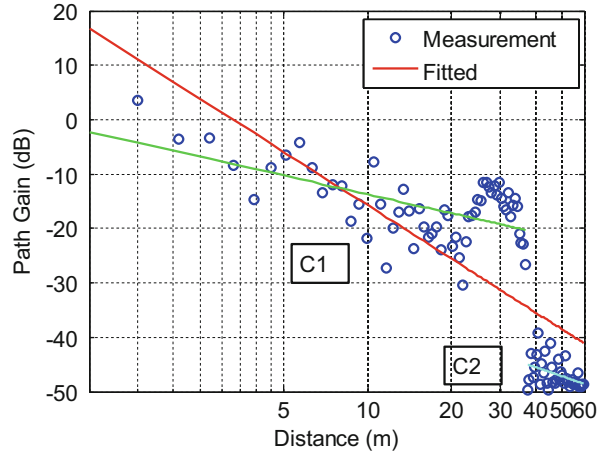
Freq.	Polarization	Path loss exponent $n$		$\sigma_m(dB)$	
		c1	c2	c1	c2
900 MHz	VV-Pol.	4.78		6.07	
	HH-Pol. (endfire)	4.06		6.04	
	HV-Pol. (endfire)	3.27		6.17	
	Average	<b>4.04</b>		<b>6.09</b>	
2.4 GHz	VV-Pol.	5.01		14.42	
	HH-Pol. (endfire)	3.09		6.61	
	HH-Pol. (broadside)	3.35		6.34	
	HV-Pol. (endfire)	3.79		9.42	
	HV-Pol. (broadside)	3.07		7.32	
	Average	<b>3.66</b>		<b>8.82</b>	
5.8 GHz	VV-Pol.	3.71		5.21	
	HH-Pol. (endfire)	3.35		9.01	
	HH-Pol. (broadside)	2.09		3.65	
	HV-Pol. (endfire)	3.26		10.25	
	HV-Pol. (broadside)	1.68		5.72	
	Average	<b>2.28</b>		<b>6.77</b>	

**Table 13.6** Path loss exponent and standard deviation values *after* applying K-means clustering

Freq.	Polarization	Path loss exponent $n$		$\sigma_m(dB)$	
		c1	c2	c1	c2
900 MHz	VV-pol.	2.95	5.25	3.64	4.44
	HH-pol. (endfire)	2.86	3.50	3.26	6.02
	HV-pol. (endfire)	3.50	1.97	3.87	6.09
	Average	<b>3.10</b>	<b>3.57</b>	<b>3.59</b>	<b>5.52</b>
2.4 GHz	VV-Pol.	1.86	5.43	4.16	4.59
	HH-Pol. (endfire)	1.78	3.76	3.44	5.41
	HH-Pol. (broadside)	1.71	5.44	3.97	4.79
	HV-Pol. (endfire)	2.07	3.15	4.12	6.38
	HV-Pol. (broadside)	1.36	3.67	4.44	3.95
	Average	<b>1.75</b>	<b>4.29</b>	<b>4.03</b>	<b>5.02</b>
5.8 GHz	VV-Pol.	2.69	3.62	3.92	4.65
	HH-Pol. (endfire)	1.62	3.50	3.65	4.22
	HH-Pol. (broadside)	1.61	1.39	2.04	3.60
	HV-Pol. (endfire)	1.15	1.75	5.07	2.29
	HV-Pol. (broadside)	0.77	1.27	2.95	4.85
	Average	<b>1.57</b>	<b>2.31</b>	<b>3.53</b>	<b>3.92</b>

From Tables 13.5 and 13.6, we may observe that after executing K-means clustering processing, a reduction in both the path loss exponent  $n$  values and the standard deviation  $\sigma_m$  values is obtained. On one hand, the reduced  $n$  values imply that signal propagation is stronger especially in the first cluster where LOS scenario

**Fig. 13.10** Path gains are grouped into two clusters by executing K-means clustering (HV endfire polarization at 5.8 GHz) [33]



exists; on the other hand, the reduced  $\sigma_m$  values indicate that the clustered exponents have better accuracy in calculating path loss. Figure 13.10 displays a sample graph of where path gains are grouped into two clusters for HV polarization (endfire) at 5.8 GHz by executing K-means clustering.

In Fig. 13.10, we can notice that the shorter lines from C1 and C2 have smaller slope compared to the major straight line, which indicates that the  $n$  values of the clustered path gain are generally smaller. This observation from Fig. 13.10 is consistent with the comparison of Tables 13.5 and 13.6, where a reduction in the  $n$  values is recorded when a single  $n$  is split into two  $n$  values for C1 and C2, respectively. It is worth pointing out that when there exists data that includes both LOS and NLOS of the structure, e.g., VV-Pol., HH-Pol., and HV-Pol. (endfire to endfire) at all three frequencies, K-means clustering is capable of dividing one chunk of data into two groups, primarily according to the LOS and NLOS scenarios. We can notice that C1 have recorded a smaller  $n$  value in comparison to C2, and this is consistent with the physical interpretation of data – C1 should have a smaller  $n$  value because LOS scenario occurs at C1 so signal propagation should be stronger in this portion of the structure. As for C2, it generally has higher  $n$  values because signal attenuates faster in this portion of the structure. Further to that, when the data consists of only LOS portion of the structure, e.g., HH-Pol. and HV-Pol. (broadside to broadside) at 2.4 and 5.8 GHz, K-means clustering shows that signal propagates stronger in the first half portion of the structure when the Rx is closer to the Tx. It is also interesting to point out from Table 13.6 that there exists a wave-guiding effect at the LOS portions of the structure particularly at 2.4 and 5.8 GHz. This is exemplified by the lower than 2 values of the  $n$  values, which are comparable to other published results for *in-building LOS* scenarios, whose  $n$  values range between 1.6 and 1.8 [5].

## 13.3 Radio Propagation Modeling

Mobile radio channels are random in nature and therefore do not lend themselves to simple analysis. Historically, modeling the radio channel has been one of the most important parts of mobile radio system design. This modeling is typically conducted in a statistical fashion based on actual field measurements carried out specifically for an intended communication system or spectrum allocation.

Accurate propagation prediction contributes to the successful implementation of wireless communication systems. For instance, for a proper coverage planning, path loss information corresponding to large-scale path loss can help with the determination and optimization of a base station (BS) placement. Other benefits from propagation predictions include the knowledge of multipath effects as well as other statistical information on local field variations, such as small-scale parameters, which help improve receiver designs and combat multipath fading.

The environments where wireless communication systems are intended to be installed have been extended from large outdoor areas to small in-house areas. In view of this, radio propagation prediction methods are expected to cover the whole range of macro-, micro-, pico-, and even femtocells including indoor scenarios and situations in special environments like tunnels, railways, indoor stairwell, periodic building facades, and open-trench drains. Without propagation predictions, key design parameters can only be obtained from actual field measurements that are both time-consuming and expensive.

### 13.3.1 Basic Propagation Mechanisms

The four basic propagation mechanisms that impact propagation in a mobile communication system include reflection, transmission, diffraction, and scattering. Based on the physics of these propagation mechanisms, path loss can be predicted for large-scale propagation models using ray optics with the assumption that the operation frequency is high or wavelength is small compared with the typical size of objects in the environments. For radio waves of 2.4 and 5.8 GHz, ray optics is valid for objects such as stairwells and building facades considered in this chapter. Figure 13.11 illustrates the four basic propagation mechanisms in a graphical form.

Reflection and transmission are the simplest propagation mechanisms. The propagation direction of the reflected (transmitted) waves is determined by the law of reflection (refraction), while the magnitude of the reflected (transmitted) waves can be determined using Fresnel equations (reflection and transmission coefficients).

Diffraction is a phenomenon that explains the transition of electromagnetic waves from the lit region to the shadow region such as that behind the corner of a building. Without diffraction the shadow regions will receive little or no signal. Diffraction effects caused by the edges can be described using relatively simple mathematics (Kirchhoff-Huygens approximation [2]). Huygens principle assumes

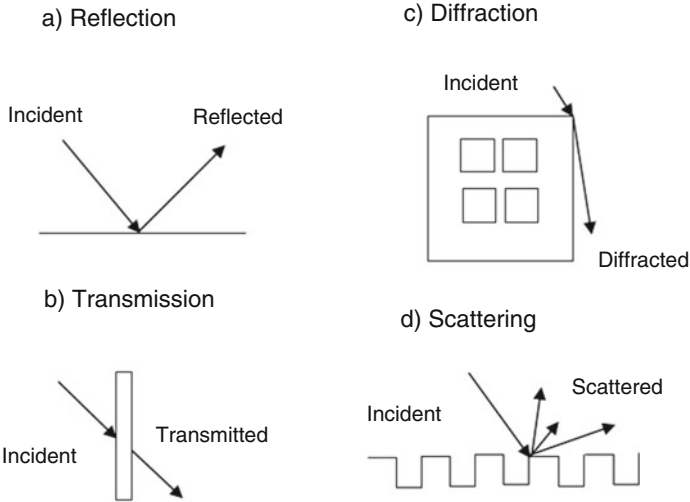


**Fig. 13.11** The four basic propagation mechanisms

that the fields reaching any mathematical surface between a source and a receiver can be thought of as producing secondary point sources on the surface that in turn generate the received fields. Diffraction can also be calculated by other methods, such as geometrical theory of diffraction (GTD) and UTD. For wedges in real environment such as those of building façades, heuristic UTD methods can be used to provide good approximate results.

As for scattering, it is a phenomenon caused by rough surfaces and finite surfaces. The scattered energy goes in all directions with a radiation pattern that depends on the roughness and size of the surface or volume.

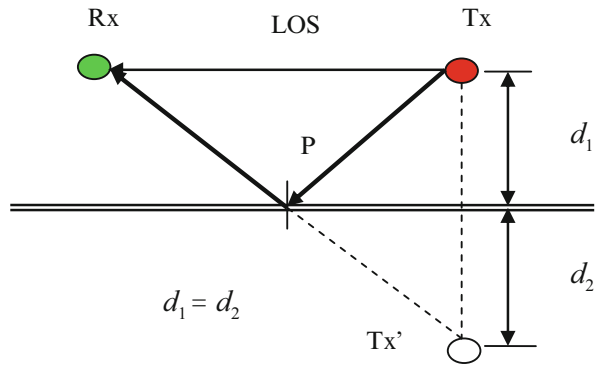
### 13.3.2 Ray-Tracing Image Method

Ray-tracing image method provides a simple and accurate way for determining the ray trajectory between a transmitter and a receiver [1]. To illustrate the basic idea of how the image method works, Fig. 13.12 shows a simple reflection surface.

For the scenario shown in Fig. 13.12, LOS is the path between the Tx and the Rx. To calculate the reflection from the surface, the image of Tx with respect to the surface is identified and is denoted as Tx'. Note that the distance from Tx to the surface and the distance from Tx' to the same surface are equal ( $d_1 = d_2$ ). Next, by connecting Tx' and Rx, the intersection point on the surface (P) is the reflection point where reflection occurs. For multiple reflections, multiple images with respect to the relevant surfaces will be determined in a similar way, and the corresponding ray paths can be obtained.



**Fig. 13.12** Illustration of the ray-tracing image method



Although the image method does suffer from inefficiency when the number of interface (e.g., walls) involved is very large and the number of reflections is high, it is suitable within the context of this chapter because in indoor stairwell propagation environment, the number of surrounding walls is limited. As the rays move up to higher floors, however, the number of reflection will increase and the image method will become slightly more complicated in terms of programming. For other propagation scenarios outside the scope of this chapter such as an entire city that requires a large number of reflections from a large number of objects like buildings, special techniques exist to increase the computation speed of the ray-tracing methods [34–36].

### 13.3.3 Methodology

At microwave frequencies, typically between 300 MHz and 300 GHz, the corresponding wavelengths can range from as long as 1 m to as short as 1 mm. At high frequencies with small wavelengths, radio wave propagation can be treated similar to light rays. With this assumption, radio waves interact with the propagation environments like terrain, buildings, and walls through reflection, diffraction, scattering, and transmission (penetration/absorption).

Theoretically, solving Maxwell's equations with the appropriate initial and boundary conditions provides the solution to a problem. But in practical cases, the solutions can only be obtained analytically for few simple problems. Consequently, for analyzing the propagation of electromagnetic waves at sufficiently high frequencies, physicists and engineers have frequently resorted to the approximate but much simpler methods of GO and its extended version such as GTD and UTD.

In principle, GO is an approximate high-frequency method for determining wave propagation for incident, reflected, and refracted (transmitted) fields [37]. Another name for GO is ray optics since it utilizes ray concepts. From the ray concepts, electromagnetic energy flows in the normal direction to a wave front and a ray is the

trajectory of the flowing energy. A ray tube or ray cone can be treated as a collection of rays in which electromagnetic energy travels without going out through the walls of the tube (cone). Plane waves, cylindrical waves, and spherical waves are examples that can be represented by such rays.

In free space, the transmitter sends out spherical waves that travel directly to the receiver. Mathematically, the electric field of direct rays (also called incident rays) can be written as follows:

$$E_i = \frac{1}{r} e^{-j\beta r} \left( \frac{\lambda}{4\pi} \right), \quad (13.2)$$

where  $r$  is the distance along the direct ray path,  $\lambda$  is the wavelength,  $\beta$  is the wave number (also denoted as  $k$  in some literature,  $\beta = \frac{2\pi}{\lambda}$ ),  $e^{-j\beta r}$  is the phase factor, and  $\frac{\lambda}{4\pi}$  is a parameter related to the antenna effect.

For reflected rays, the associated electric field can be calculated in a similar manner as Eq. (13.2) except to add an extra factor for reflection coefficient, such as

$$E_r = \frac{1}{r} e^{-j\beta r} \left( \frac{\lambda}{4\pi} \right) \Gamma_{\parallel, \perp}, \quad (13.3)$$

where  $r$  is the distance along the reflected ray path measured from the transmitter,  $\Gamma_{\parallel}$  is the Fresnel reflection coefficient for parallel polarization ( $\Gamma_{\parallel} = \frac{\eta_2 \cos \theta_i - \eta_1 \cos \theta_t}{\eta_2 \cos \theta_i + \eta_1 \cos \theta_t}$ ),  $\Gamma_{\perp}$  is the Fresnel reflection coefficient for perpendicular polarization ( $\Gamma_{\perp} = \frac{\eta_2 \cos \theta_i - \eta_1 \cos \theta_t}{\eta_2 \cos \theta_i + \eta_1 \cos \theta_t}$ ),  $\theta_i$  is the incident angle, and  $\theta_t$  is the transmission angle. As for the impedance  $\eta$ , it is equal to  $\sqrt{\frac{j\omega\mu}{\sigma + j\omega\epsilon}}$ , where  $\mu$ ,  $\epsilon$ , and  $\sigma$  are the permeability, permittivity, and conductivity, respectively.

Similar to reflected rays, the associated electric field for transmitted rays can be obtained by adding the appropriate transmission coefficient to Eq. (13.2), such as

$$E_t = \frac{1}{r} e^{-j\beta r} \left( \frac{\lambda}{4\pi} \right) T_{\parallel, \perp}, \quad (13.4)$$

where  $r$  is the distance along the transmitted ray path measured from the transmitter,  $T_{\parallel}$  is the Fresnel transmission coefficient for parallel polarization ( $T_{\parallel} = \frac{2\eta_2 \cos \theta_i}{\eta_1 \cos \theta_i + \eta_2 \cos \theta_t}$ ), and  $T_{\perp}$  is the Fresnel transmission coefficient for perpendicular polarization ( $T_{\perp} = \frac{2\eta_2 \cos \theta_i}{\eta_2 \cos \theta_i + \eta_1 \cos \theta_t}$ ).

Diffracted rays can be calculated using GTD and UTD. GTD was first proposed by Keller in 1959 [38]. Following the first publication on GTD, subsequent research work has been carried out in this area. In 1962, a numerically simple and elegant solution to wedge diffraction that serves as a canonical problem in GTD was published, again by the same author [39]. As of 1980 this paper has been cited over 215 times [40]. The beauty of GTD lies at the introduction of the then new

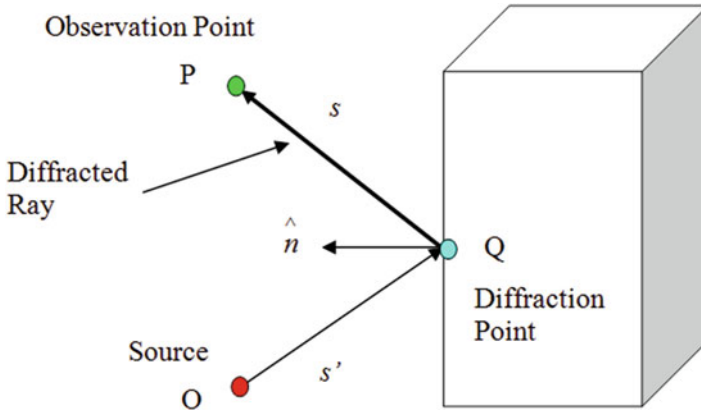


Fig. 13.13 Determination of the diffraction point

class of rays or the so-called edge-diffracted rays. Some elements such as the *law of edge diffraction*, *edge diffraction coefficients*, and the *method of canonical problems* have been integrated to determine the diffraction coefficients.

One classic paper that precedes GTD is the method of Fresnel knife edge that accounts for the intervening terrain that has one dominant diffracting ridge. First published by Schelleng, Burrows, and Ferrell in 1933, this theory is still in wide use today. The Fresnel approach applies knife-edge diffraction, which is extended using image theory to include reflections from any relatively level ground that might exist between the ridge and the transmission or reception points [41]. This knife-edge approach has the advantage of simplicity and for many geometries yields accurate results.

UTD is an extension of Keller’s GTD – it is a high-frequency method for solving electromagnetic scattering problems from electrically small discontinuities or discontinuities in more than one dimension at the same point [26]. One computer code for UTD that was originally written in FORTRAN language is provided in Ref. [37], and a MATLAB version of the code can be converted from there. Figure 13.13 shows a simple illustration of diffraction by a straight wedge.

The diffracted field  $E_d$  can be written as follows:

$$E_d = \frac{e^{-j\beta s'}}{s'} \sqrt{\frac{s'}{s(s'+s)}} e^{-j\beta s} D_{\parallel,\perp} \left( \frac{\lambda}{4\pi} \right), \tag{13.5}$$

where  $s'$  is the distance along the incident ray path from the source to the diffraction point,  $s$  is the distance along the diffracted ray path from the diffraction point to the observation point,  $\sqrt{\frac{s'}{s(s'+s)}}$  is the spreading factor, and  $D_{\parallel,\perp}$  is the diffraction coefficient for soft and hard polarizations.

The total E-field that can be received at the receiver, considering the incident, reflected, transmitted and diffracted rays, can be written as follows:

$$E_{tot} = E_i + E_r + E_t + E_d. \quad (13.6)$$

Regardless of which types of rays have been considered, the total received power in decibels (dB) can be obtained from the total electric field, e.g., in Eq. (13.6)

$$P_{tot} = 20 \log_{10} |E_{tot}|. \quad (13.7)$$

Once the total received power has been calculated from these rays, it can be compared with the measurement results. The path loss/gain can also be further obtained.

## 13.4 Conclusion

This chapter has concisely presented several emerging and not well-explored wireless communication environments, such as indoor stairwell, periodic building façade, and open-trench drain. In view of the rising importance to recognize the propagation characteristics of every habitable environment so that ubiquitous communications can be established everywhere, environments that were once overlooked and regarded as trifling and minor are now rising to the surface and demand a careful examination of each of them. When a proper understanding of the propagation characteristics of these environments is obtained, such knowledge contributes toward accurate propagation prediction, which in turn guarantees reliable wireless communication systems in those places. There are several ways to study the propagation characteristics of a specific environment, and ray-tracing image method has been one of the more popular ones due to its simplicity and straightforwardness in yielding solutions. Other available methods include empirical studies and various numerical studies. In the second half of this chapter, we have discussed the fundamental working principles of ray-tracing image method that can be utilized not only for indoor but outdoor environments as well. Along with this discussion, we have also covered the basic propagation mechanisms, together with their methodology, which will be especially useful to the newcomers to this exciting field of radio propagation modeling. As a matter of fact, the second half of this chapter has been intricately tied to the first half of the chapter in many ways. Readers would find that the principles discussed in the second half of the chapter have been applied to the various propagation scenarios presented earlier in the first half of the chapter. Such applications serve as inductive examples of how the same principles can be further extended to solve other propagation environments as they evolve.

## References

1. M.F. Iskander, Z. Yun, Propagation prediction models for wireless communication systems. *IEEE Trans. Microwave Theory Tech.* **50**(3), 662–673 (2002)
2. H.L. Bertoni, *Radio Propagation for Modern Wireless Systems* (Prentice–Hall, Upper Saddle River, NJ, 2000), pp. 2–55
3. R. Y. Kim, J.S. Kwak, K. Etemad, WiMAX femtocells: requirements, challenges, and solutions. *IEEE Commun. Mag.* **47**(9), 84–91 (2009)
4. C.L. Holloway, P.L. Perini, R.R. DeLyser, K.C. Allen, Analysis of composite walls and their effects on short-path propagation modeling. *IEEE Trans. Veh. Technol.* **46**(3), 730–738 (1997)
5. T.S. Rappaport, *Wireless Communications: Principles and Practice (Second Edition)*. (Prentice–Hall, Upper Saddle River, NJ, 2002), pp. 157–167
6. H. Hashemi, The indoor radio propagation channel. *Proc. IEEE* **81**(7), 943–968 (1993)
7. C.F. Yang, B.C. Wu, A ray-tracing/PMM hybrid approach for determining wave propagation through periodic structures. *IEEE Trans. Veh. Technol.* **50**(3), 791–795 (2001)
8. C.H. Teh, H.T. Chuah, Propagation measurement in a multi-floor stairwell for model validation. Paper presented at the 28th International Union of Radio Science General Assembly, New Delhi, Oct 2005.
9. C.H. Teh, H.T. Chuah, An improved image-based propagation model for indoor and outdoor communication channels. *J. Electromagn. Waves Appl.* **17**(1), 31–50 (2003)
10. W.M. Smith, Urban propagation modeling for wireless systems, PhD dissertation, Stanford University, United States, Feb 2004
11. W. Honcharenko, H.L. Bertoni, Transmission and reflection characteristics at concrete block walls in the UHF bands proposed for future PCS. *IEEE Trans. Antennas Propag.* **42**(2), 232–239 (1994)
12. M.O. Al-Nuaimi, M.S. Ding, Prediction models and measurements of microwave signals scattered from buildings. *IEEE Trans. Antennas Propag.* **42**(8), 1126–1137 (1994)
13. O. Landron, M.J. Feuerstein, T.S. Rappaport, A comparison of theoretical and empirical reflection coefficients for typical exterior wall surfaces in a mobile radio environment. *IEEE Trans. Antennas Propag.* **44**(3), 341–351 (1996)
14. I. Cuinas, M.G. Sanchez, Measuring, modeling, and characterizing of indoor radio channel at 5.8 GHz. *IEEE Trans. Veh. Technol.* **50**(2), 526–535 (2001)
15. Z. Zhang, R. Sorensen, Z. Yun, M.F. Iskander, A ray-tracing approach for indoor/outdoor propagation through window structures. *IEEE Trans. Antennas Propag.* **50**(5), 742–748 (2002)
16. D. Pena, R. Feick, H.D. Hristov, W. Grote, Measurement and modeling of propagation losses in brick and concrete walls for the 900-MHz band. *IEEE Trans. Antennas Propag.* **51**(1), 31–39 (2003)
17. P. Pongsilamane, H.L. Bertoni, Specular and nonspecular scattering from building facades. *IEEE Trans. Antennas Propag.* **52**(7), 1879–1889 (2004)
18. A.G. Dimitriou, G.D. Sergiadis, Architectural features and urban propagation. *IEEE Trans. Antennas Propag.* **54**(3), 774–784 (2006)
19. V. Degli-Esposti, F. Fuschini, E.M. Vitucci, G. Falciasecca, Measurement and modelling of scattering from buildings. *IEEE Trans. Antennas Propag.* **55**(1), 143–153 (2007)
20. I. Cuinas, D. Martinez, M.G. Sanchez, A.V. Alejos, Modelling and measuring reflection due to flat dielectric surfaces at 5.8 GHz. *IEEE Trans. Antennas Propag.* **55**(4), 1139–1147 (2007)
21. S. Kwon, I.-S. Koh, H.-W. Moon, J.-W. Lim, Y.J. Yoon, Model of inhomogeneous building façade for ray tracing method. *Electron. Lett.* **44**(23), 1341–1342 (2008)
22. S.Y. Lim, Z. Yun, M.F. Iskander, Modeling scattered EM field from a periodic building facade, in *Proceedings of the IEEE International Symposium on Antennas and Propagation (AP-S)*, Toronto, 11–17 July 2010
23. S.Y. Lim, Z. Yun, M.F. Iskander, Modeling scattered EM field from a façade-like structure for wireless communications, in *Proceedings of the IEEE International Symposium on Antennas and Propagation (AP-S) and URSI*, Spokane, 3–9 July 2011

24. S.Y. Lim, Z. Yun, J.M. Baker, N. Celik, H. Youn, M.F. Iskander, Propagation modeling and measurement for a multi-floor stairwell. *IEEE Antennas Wirel. Propag. Lett.* **8**, 583–586 (2009)
25. S.Y. Lim, Z. Yun, M.F. Iskander, Propagation measurement and modeling for indoor stairwells at 2.4 and 5.8 GHz. *IEEE Trans. Antennas Propag.* **62**(9), 4754–4761 (2014)
26. R.G. Kouyoumjian, P.H. Pathak, A uniform geometrical theory of diffraction for an edge in a perfectly conducting surface. *Proc. IEEE* **62**, 1448–1461 (1974)
27. W.D. Burnside, K.W. Burgener, High frequency scattering by thin lossless dielectric slab. *IEEE Trans. Antennas Propag.* **31**(1), 104–110 (1983)
28. P. Bernardi, R. Cicchetti, O. Testa, A three-dimensional UTD heuristic diffraction coefficient for complex penetrable wedges. *IEEE Trans. Antennas Propag.* **50**(2), 217–224 (2002)
29. A. H. Systems, Inc. Double ridge guide horn antenna. Available: <http://www.ahsystems.com/catalog/SAS-571.php>
30. L-Com 2.4 GHz 8dBi Omnidirectional Antenna. Available: <http://www.l-com.com/wireless-antenna-24-ghz-8-dbi-omnidirectional-antenna-n-female-connector>
31. L-Com 5.8 GHz 8 dBi Omnidirectional Wireless LAN Antenna. Available: <http://www.l-com.com/wireless-antenna-58-ghz-8-dbi-omnidirectional-wireless-lan-antenna>
32. S.Y. Lim, C.C. Pu, Measurement of a tunnel-like structure for wireless communications. *IEEE Antennas Propag. Mag.* **54**(3), 148–156 (2012)
33. S.Y. Lim, A.K. Awelemdy, Z. Yun, M.F. Iskander, Experimental study of propagation characteristics in an open-trench drain. *IEEE Antennas Wirel. Propag. Lett.* **15**, 60–63 (2016)
34. Z. Yun, Z. Zhang, M.F. Iskander, A ray-tracing method based on the triangular grid approach and application to propagation prediction in urban environments. *IEEE Trans. Antennas Propag.* **50**(5), 750–758 (2002)
35. Z. Yun, M.F. Iskander, Z. Zhang, Fast ray tracing procedure using space division with uniform rectangular grid. *Electron. Lett.* **36**(10), 895–897 (2000)
36. Z. Zhang, Z. Yun, M.F. Iskander, Ray tracing method for propagation models in wireless communications systems. *Electron. Lett.* **36**(5), 464–465 (2000)
37. C.A. Balanis, *Advanced Engineering Electromagnetics* (Wiley, Hoboken, NJ, 1989), pp. 743–850
38. J.B. Keller, The geometric optics theory of diffraction. *McGill Symp. Microwave Optics* **2**, 207–210 (1959)
39. J.B. Keller, Geometrical theory of diffraction. *J. Opt. Soc. Am.* **52**(2), 116–130 (1962)
40. J.B. Keller, This week's citation classic, Institute Mathematical Sciences, New York University, cc/no. 14, Apr 1980
41. R.J. Luebbers, Finite conductivity uniform GTD versus knife edge diffraction in prediction of propagation path loss. *IEEE Trans. Antennas Propag.* **32**(1), 70–76 (1984)



**Soo Yong Lim** (Grace) received the B.Eng. (Hons.) degree in electronics majoring in telecommunications from Multimedia University, Malaysia, in 2003 and the Ph.D. degree in electrical engineering from the University of Hawaii at Manoa, USA, in 2010. She is currently an assistant professor with the Department of Electrical and Electronic Engineering, University of Nottingham Malaysia Campus. Prior to joining the University of Nottingham in January 2014, she was with the Centre for Applied Electromagnetics, Multimedia University from 2004 to 2006 and with Sunway University from 2011 to 2013. Since January 2013, she has been appointed as an adjunct faculty with the Hawaii Center for Advanced Communications (HCAC), College of Engineering, University of Hawaii at Manoa. Her current research interest includes radio propagation modeling, channel measurements, and ray tracing. Dr. Grace Lim is a fellow

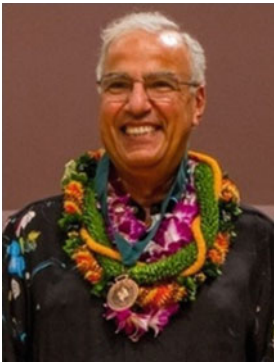
of the Higher Education Academy (HEA, UK), a senior member of the IEEE, and a registered

professional engineer both with the Boards of Engineers Malaysia (BEM) and with the Institution of Engineers Malaysia (IEM). She has served the IEEE Antennas and Propagation Society as a member of the Education Committee since 2011 and is currently an associate editor of the *Computer Applications in Engineering Education*, published by John Wiley and Sons. In 2012, she won the award for Achievement in Research for Early Career Researchers, Sunway University, and a bronze medal at the Malaysia Technology Expo, awarded by the Malaysian Association of Research Scientists.



**Zhengqing Yun** received the PhD degree in electrical engineering from Chongqing University, Chongqing, China, in 1994. He was an assistant researcher at the Hawaii Center for Advanced Communications (HCAC) from 2002 to 2005, where he became an assistant professor in 2006. He was involved in a postdoctoral work with the University of Utah and Southeast University, China, before he joined the University of Hawaii at Manoa (UH), Honolulu, HI. He is currently an associate professor at the Hawaii Center for Advanced Communications (HCAC), College of Engineering, UH. Dr. Yun's current research interests include radio propagation in complex environments, such as urban, indoor, and mountainous areas. He served as the technical program co-chair of the IEEE Antenna and Propagation Society International Symposium, Honolulu, in 2007, and the technical

program chair of the IEEE International Conference on Wireless Information Technology and Systems, Honolulu, in 2010 and 2016, and Maui, HI, in 2012. He was an associate editor of the IEEE Transactions on Vehicular Technology and the IEEE Transactions on Antennas and Propagation. He is currently an associate editor of the IEEE Access.



**Magdy F. Iskander** is the director of the Hawaii Center for Advanced Communications and professor of Electrical Engineering, University of Hawaii at Manoa. He is co-director of the NSF I/UCRC and a fellow of IEEE (1993). He was the 2002 president of the IEEE AP-S, Distinguished Lecturer, and a program director in the ECCS Division at NSF. Dr. Iskander joined the University of Hawaii in 2002, and prior to that, he was a professor of ECE Department and the Engineering Clinic Endowed Chair Professor at the University of Utah. He received many awards for excellence in research and teaching including the University of Hawaii Board of Regents' Medal for Excellence in Research and Medal for Teaching Excellence, IEEE MTT-S Distinguished Educator Award, IEEE AP-S Chen-To Tai Distinguished Educator Award, Northrop Grumman Excellence in Teaching Award, and others. He has published over 270 papers

in journals and books and holds ten patents. He authored/edited several books including the textbook *Electromagnetic Fields and Waves*. He is the founding editor of *Computer Applications in Engineering Education* published by John Wiley & Sons 1992–present. His research has been funded by NSF, NIH, Army Research Office, US Army CERDEC, Office of Naval Research, and corporate sponsors.

# Chapter 14

## Wireless Performance in Dense-Transceiver Scenarios to Enable Context-Aware Scenarios

Peio Lopez-Iturri, Leyre Azpilicueta, Erik Aguirre, and Francisco Falcone

### 14.1 Introduction

Context-aware environments are being progressively adopted, as paradigms such as Internet of things (IoT) and cyber-physical systems are successfully implemented. A context-aware environment is a scenario in which interaction between users and systems is established in order to provide added value services, in terms of quality of service, new types of actions, or enhanced time response. This type of strong user-environment interaction is provided by means of real-time monitoring, which is by great means provided by wireless communication systems, due to their inherent mobility. This type of systems has been employed since the advent of sensor systems employed in telecontrol and telemetry roles, such as in vehicle operation, evolving toward building and home automation systems or e-health systems, to name a few of multiple applications within a growing application ecosystem. In this sense, initiatives such as smart cities/smart regions or Industry 4.0 are native environments in which high interactivity between users and devices is compulsory. Integration of different systems such as intelligent transportation systems, e-health/mHealth/Smart Health, ambient-assisted living, smart grids, or eGovernment is essential in the successful deployment of context-aware environments [1–8]. In order to achieve high degrees of interactivity, Information and Communication Systems play a key role in terms of information processing capabilities as well as in providing efficient and seamless communication systems. Communication systems and networks are hence evolving toward higher levels of integration in terms of joint infrastructure, capacity, interoperability, and cooperation, leading toward heterogeneous networks (HetNets). Within this context, several considerations in relation with the use of wireless communication systems must be taken into account, such as the

---

P. Lopez-Iturri • L. Azpilicueta • E. Aguirre • F. Falcone (✉)  
EE Department, UPNA, Campus Arrosadia, 31006 Pamplona, Navarra, Spain  
e-mail: [francisco.falcone@unavarra.es](mailto:francisco.falcone@unavarra.es)



deployment of large number of transceivers (in order to enable device-to-device (D2D) or machine-to-machine (M2M) communications), different quality of service requirements, or spectrum management. One of the main restrictions is given by coverage/capacity relations, in which interference management plays a key role in order to guarantee optimal system performance.

Therefore, radio planning analysis is needed in order to estimate power levels (useful transmit link power as well as non-desired interference) in scenarios with a large number of nodes, particularly if the scenario is complex in terms of number and distribution of potential scatterers within it. Several approaches can be followed in order to estimate wireless channel behavior, from full-wave electromagnetic analysis to empirical-analytical models, which are strongly site specific.

In this chapter, interference analysis as a function of increasing node density is addressed for the case of indoor system operation, a situation that is commonplace for IoT scenarios, D2D communications, and context-aware scenarios, such as home automation, building automation, or ambient-assisted living. The methodology employs a deterministic 3D ray-launching algorithm, in which sources and all indoor elements of the scenario are included. This is described in Sect. 14.2.

## 14.2 Deterministic Simulation Methodology in Complex Wireless Scenarios

Analysis of power and interference in the complex wireless scenarios described above is based on an in-house simulation tool using a ray-launching (RL) algorithm that is based on geometrical optics (GO) and geometrical theory of diffraction (GTD) [9]. It considers reflection, refraction, and diffraction phenomena. Different applications of this algorithm can be found in the literature, including the analysis of wireless propagation in closed environments [10–14], interference analysis [15], and electromagnetic dosimetry evaluation in wireless systems [16]. The RL method considers a bundle of transmitted rays that may or may not reach the receiver. The available spatial resolution and the accuracy of the model are determined by the number of rays considered and the distance from the transmitter to the receiver. The basic idea is that a finite sample of the possible directions of the propagation from the transmitter is chosen, and a ray is launched for each such direction. If a ray hits an obstacle, then a reflected ray and a refracted ray are generated. If a ray impacts an edge, then a family of diffracted rays is generated.

The 3D RL algorithm has been designed for evaluating the wireless communication in an indoor environment. Hence, this algorithm has the following features:

- Recreation of a realistic multipath scenario.
- Three-dimensional modeling of all types of rooms with different shapes and sizes.
- Creating complex environments as large as desired, with multiple plants and multiple buildings.

- Characterization and modeling of any obstacle (windows, tables, chairs, walls, etc.) through its three-dimensional shape and relative permittivity and conductivity.
- Modeling of reflection, refraction, and diffraction.
- Calculation of the interaction between rays and obstacles taking into account the polarization wave.
- Modeling of any transceiver.
- Duration of the simulation of a ray is determined by the number of reflections and the maximum delay.
- Scenario can be analyzed by extracting parameters such as electric field strength, signal/interference, power delay, dispersion, and so on.

The use of advanced radio planning tools, such as the 3D RL algorithm, is usually divided into three phases:

1. **Phase 1:** Creating the scenario. This phase sets the scenario, consisting in rooms with obstacles and the transmitters and receivers.
2. **Phase 2:** Simulation of ray tracing in three dimensions. In this phase, the rays are launched from each transmitter, keeping the parameters in each position in space.
3. **Phase 3:** Analysis of the results. In this phase, the values are obtained from the simulation to calculate the desired parameters.

### ***14.2.1 Phase 1: Creation of a Scenario***

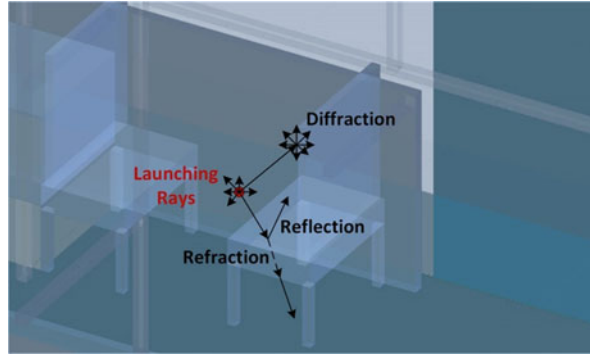
The scenario is created with the information which characterized the room and the obstacles within it, the interconnections of the different rooms, and all the information which characterizes the transmitters and receivers.

The room's characterization is given by its size. In this algorithm, the rooms are defined as different hexahedra with different dimensions along the  $x$ -axis,  $y$ -axis, and  $z$ -axis. Besides, the material which is in the room can be defined. Normally, this material is air, but it is possible to consider any material for the room.

Complex forms can be created by interconnection of several hexahedral. Moreover, dividing an environment in multiple hexahedra gives the possibility of analyzing each room with different resolution, providing more flexibility. Each room is divided into multiple hexahedra, and the parameters of the rays that arrive at each hexahedron are stored. Thus, the resolution in each axis of each room is defined as the number of hexahedra of that axis. So, each room is divided into multiple equidimensional hexahedra, and the precision of each axis can be chosen independently. Figure 14.1 represents a typical office with the rays launched from the transmitter.

Obstacles are defined as different hexahedra in the algorithm. Using this basic geometric shape, it is very easy to form other much more complex obstacles, such as tables, chairs, and shelves, and place them into the room. In a generic room, walls can be formed by windows, doors, frames, etc. Therefore, to characterize the walls

**Fig. 14.1** Typical scenario with the rays launched from the transmitter



of a room, each discontinuity on the wall must be characterized. Each obstacle in the room is defined by its central position, the width in each dimension, and the material that it is made of. Rooms are created individually and interconnected with the interconnection matrix, which defines the portion of the wall of a room that is connected with the wall portion of another room.

In the creation of the scenario, transmitters are defined in a generic way. Thus, performing a single simulation of phases 1 and 2 and the parameters of the transceiver, such as the radiated power and the directivity of the antennas, can vary in phase 3, saving a lot of calculation time. Each transceiver can be defined with the following parameters:

- Location: Room and coordinates
- Number of launching rays and directions
- Cuboid dimension
- Maximum number of reflections of the rays
- Maximum delay of the rays
- Frequency of emission  $f_c$
- Radiated power ( $P_r$ )
- Directivity  $D(\theta, \varnothing)$
- Polarization ( $X^\perp, X^\parallel$ )

A receiver is modeled taking into account that it absorbs the rays that come to it in certain directions. To define a receiver, the following parameters are characterized:

- Location: Room and coordinates
- Angular range in which the receiver absorbs the rays

In this phase of simulation, there are several options to be chosen such as the calculation of parameters inside the obstacles, which are used to analyze the radiated power inside the obstacle, for example, a human body. The different materials in the obstacles should always be taken into account. Whether or not to consider diffraction can also be chosen in this phase of the algorithm. A trade-off between

computational time and accuracy of results must be chosen to obtain best results from the simulation.

### 14.2.2 Phase 2: 3D Ray-Launching Simulation

In this phase, the rays are launched from each transmitter. These rays propagate through the space, interacting with the obstacles in their path and causing physical phenomena such as reflection, refraction, and diffraction. The parameters of these rays are stored as they enter each hexahedron until the ray has a certain number of reflections or it has exceeded the pre-propagation time set. Figure 14.2 shows the basic principle of the RL technique, in which the wave front is identified with a number of rays that propagates along the space. These rays are analyzed following a combination of optics and electromagnetic theories.

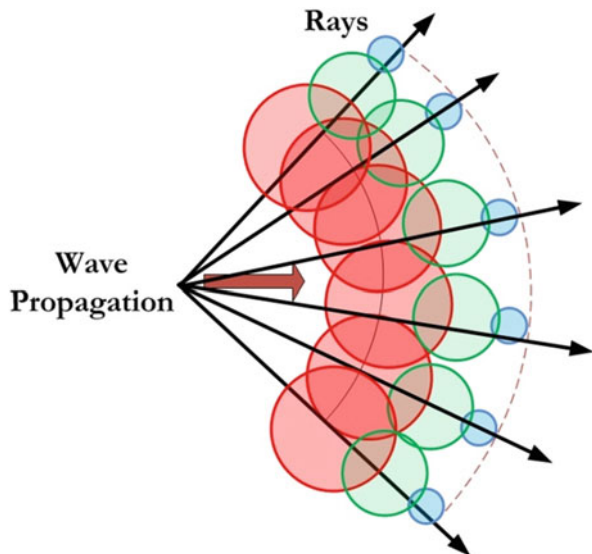
In the algorithm, the reflection phenomenon is considered until the ray reaches a predefined number. When the ray impinges with an edge, the new parameters are stored for processing later the diffraction phenomenon.

The 3D RL algorithm has three recurrent steps. The first step is to simulate all of the antennas of the same room. The second step is to simulate the room. The third step is to analyze the rays coming out of the room and build the equivalent antennas to analyze the radio wave propagation in other rooms.

The most important steps of the algorithm are the following:

- Calculating the impact point between a ray and an obstacle
- Tour, starting at the initial point to the point of impact, storing the path loss parameters

**Fig. 14.2** Wave front propagation with rays associated with single wave front points



- Calculation of the reflected ray
- Calculation of the transmitted ray
- Calculation of the diffractive rays

The calculation of the impact point has been done by decomposing the three-dimensional problem to one-dimensional problems, calculating the Cartesian components of the propagation velocity as:

$$\left. \begin{aligned} V_x &= V_p \sin(\theta_0) \cos(\phi_0) \\ V_y &= V_p \sin(\theta_0) \sin(\phi_0) \\ V_z &= V_p \cos(\theta_0) \end{aligned} \right\}. \quad (14.1)$$

In Eq. (14.1),  $V_p = c/n$  is the propagation speed,  $c$  is the speed of light, and  $n$  is the refraction index of the medium. The angles  $\theta_0$  and  $\phi_0$  are the output angles of the ray. The impact between the ray and the obstacle happens in the first instant of time that the three projections overlap with the obstacle projection. If the ray does not impact any obstacles, the algorithm calculates the point of impact with the wall in the same way.

Once the point of impact is calculated, it is necessary to follow the straight line joining the initial point  $(x_i, y_i, z_i)$  and the final impact point  $(x_f, y_f, z_f)$  saving the parameters of each ray. It is important to emphasize that a grid is defined in the space to save the parameters of each ray. Accordingly, the environment is divided into a number of cuboids of a fixed size. When a ray enters a specific hexahedron, its parameters are saved in a matrix. The information stored in each hexahedron that the ray passes in its trajectory is:

- Time taken for the ray to arrive ( $\tau$ )
- Distance traveled by the ray ( $d$ )
- Loss coefficient in each polarization ( $L^\perp, L^\parallel$ )
- Ray direction in the transmitter ( $\theta_t, \phi_t$ )
- Ray direction in the receiver ( $\theta_r, \phi_r$ )
- Transmitting antenna ( $n$ )
- Diffraction

Figure 14.3 represents the phenomena of reflection and transmission when the ray impacts an obstacle and the diffraction phenomena when the ray impacts an edge.

### 14.2.3 Phase 3: Analysis of Radio Planning Results

In the third phase of the simulation procedure, the results are analyzed using the stored parameters of each ray. The Cartesian components of the electric field  $\mathbf{E}$  radiated by an antenna with a radiated power  $P_{\text{rad}}$  in the  $(\theta, \phi)$  direction with a

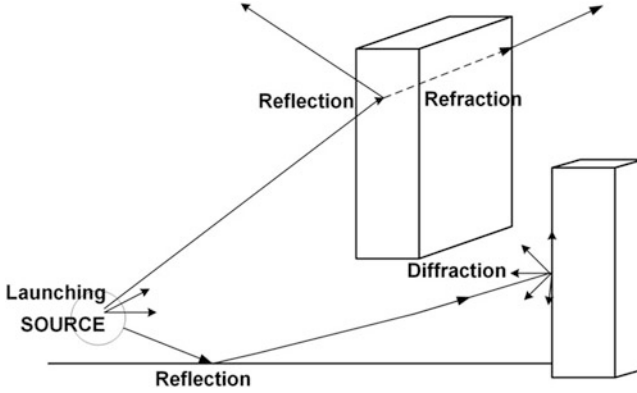


Fig. 14.3 Principle of RL method: reflection, transmission, and diffraction

directivity  $D(\theta, \phi)$  and polarization ratio ( $X^\perp, X^\parallel$ ) at distance  $d$  in the free space are calculated as:

$$E_i^\perp = \sqrt{\frac{P_{\text{rad}} D_t(\theta_t, \phi_t) \eta_0}{2\Pi}} \frac{e^{-j\beta_0 r}}{r} X^\perp L^\perp, \quad (14.2)$$

$$E_i^\parallel = \sqrt{\frac{P_{\text{rad}} D_t(\theta_t, \phi_t) \eta_0}{2\Pi}} \frac{e^{-j\beta_0 r}}{r} X^\parallel L^\parallel. \quad (14.3)$$

The parameters employed in Eqs. (14.2) and (14.3) are  $\beta_0 = 2\pi f_c \sqrt{\varepsilon_0 \mu_0}$ ,  $\varepsilon_0 = 8.854 \cdot 10^{-12}$  F/m,  $\mu_0 = 4\pi \cdot 10^{-7}$  H/m, and  $\eta_0 = 120\pi \Omega$ ;  $L^\perp$  and  $L^\parallel$  are the path-loss coefficients for the polarization ratios  $X^\perp$  and  $X^\parallel$ , respectively;  $P_{\text{rad}}$  is the radiated power; and  $D_t(\theta_t, \phi_t)$  is the transmitter directivity.

The Cartesian components of the diffracted field are calculated as [17]:

$$E_{\text{UTD}}^\perp = e_0 \frac{e^{-jks_1}}{s_1} D^\perp \sqrt{\frac{s_1}{s_2(s_1 + s_2)}} e^{-jks_2}, \quad (14.4)$$

$$E_{\text{UTD}}^\parallel = e_0 \frac{e^{-jks_1}}{s_1} D^\parallel \sqrt{\frac{s_1}{s_2(s_1 + s_2)}} e^{-jks_2}, \quad (14.5)$$

where  $D^\perp$  and  $D^\parallel$  are diffraction coefficients [17],  $s_1$  is the distance from the source to the edge, and  $s_2$  is the distance from the edge to the receiver point [18].

The received power is calculated at each point taking into account the losses of propagation through a medium ( $\varepsilon, \mu, \sigma$ ) at a distance  $d$ , with the attenuation constant  $\alpha$  (Np/m), and the phase constant  $\beta$  (rad/m). The received power is calculated with the sum of incident electric vector fields in an interval of time  $\Delta t$  inside each cuboid of the defined mesh. Based on the above theory, the main characteristic of the RL

**Table 14.1** Challenges and solutions of the RL performance analysis

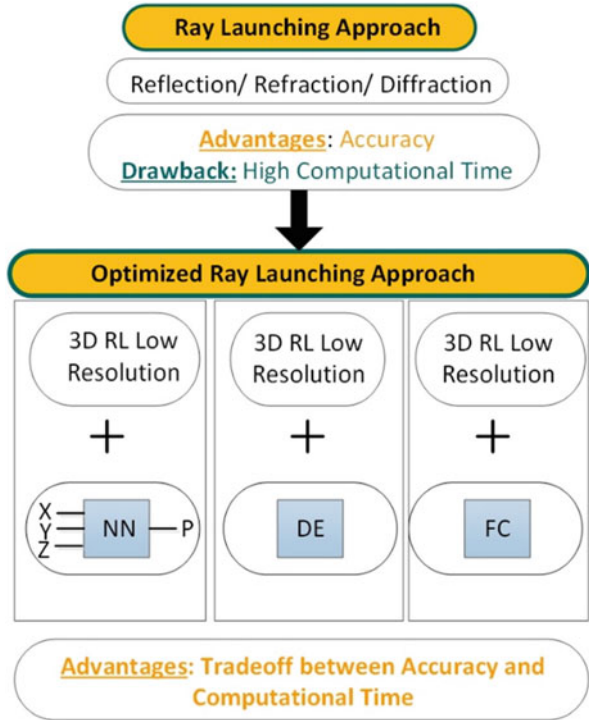
Ray-launching performance analysis		
Challenges	Solutions	Reference
To achieve a commitment between accuracy results and computational time	Convergence analysis to find the optimal input parameters of angular and spatial resolution, number of reflections, and number of diffracted rays	[9, 19]
Implementation of more electromagnetic phenomena in the algorithm	Diffraction phenomenon implementation Scattering by water surface implementation Scattering for environments with high obstacle density	[19, 20, 22]
Dosimetric analysis	Modularization to save the parameters of the electromagnetic waves within the obstacles (human beings) with the consideration of several reflections inside the obstacles	[16]
Acceleration techniques to obtain accurate results with affordable computational time	New hybrid acceleration techniques: RL-NN, RL-DE, and RL-CF	[21–23]
Mobile channel modeling	Implementation of a new module which captures the non-stationarity of the channel	[24]

technique is that it provides the impulse response of the channel  $h(t, f_c, \Delta f, d)$  for each transmitter, at a given position, carrier frequency ( $f_c$ ), and bandwidth ( $f_c \pm \Delta f$ ), where the materials have a similar function transfer response, that is to say, the same behavior in the considered frequencies. With this information, a stationary channel can be wholly characterized.

For optimum performance of the algorithm, it is important to take into account different aspects in the implementation and development of the RL methodology. The main challenges of the RL performance analysis and the authors' solutions to them are presented in Table 14.1.

It is also worth mentioning that for large scenarios the computational time of simulations can be really high depending on the accuracy needed for the results. To reduce computational time, novel hybrid techniques have also been analyzed combining the in-house RL approach with different techniques, such as neural networks (NN) [21], diffusion equation (DE) [22], or collaborative filtering (CF) [23]. These techniques achieve accurate results with considerably lower computational times. The combination of these techniques with the RL approach gives an optimized RL methodology that is more robust for complex scenarios and can be used for more applications (i.e., more complex scenarios with a large number of obstacles could be analyzed with such techniques). For better comprehension, Fig. 14.4 shows a scheme of the improvement of the RL technique, which has led to the optimal approach combining different techniques.

**Fig. 14.4** Optimization of the in-house 3D ray-launching approach

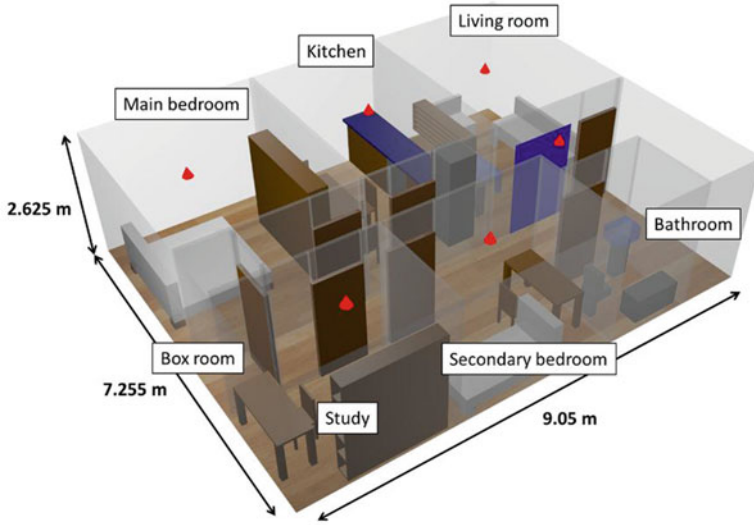


### 14.3 Deterministic Simulation Methodology in Complex Wireless Scenarios

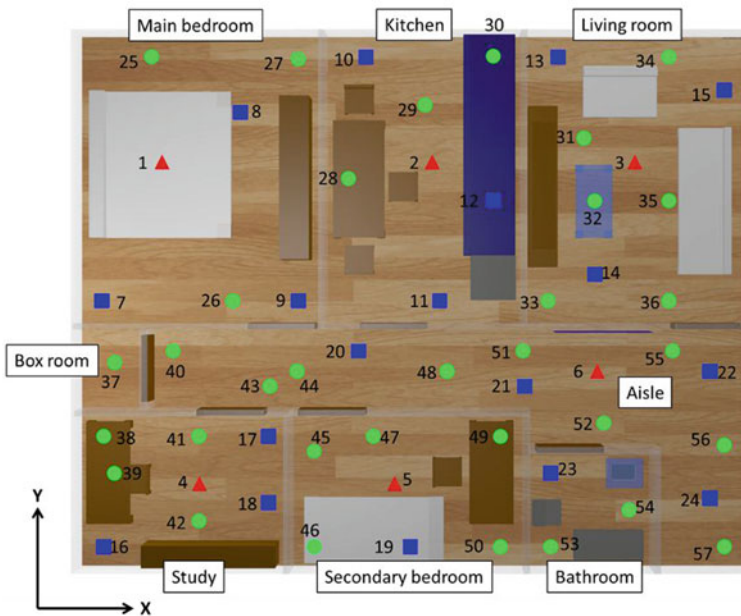
In order to gain insight in the impact of node densification, results in an indoor test scenario have been obtained. The test scenario is a recreation of a real apartment, and it consists of a typical interior section of an apartment, which is schematically depicted in Fig. 14.5. The apartment is approximately 65 m<sup>2</sup> and consists of two bedrooms, a kitchen, bathroom, study room, living room, and small box room, as shown in Fig. 14.5. The dimensions of the scenario are 9.05 × 7.255 × 2.625 m<sup>3</sup>. All of the interior details and furniture in the rooms have been considered. The constitutive parameters (relative and conductivity) of all the furniture such as chairs, tables, doors, beds, wardrobes, bath, walls, etc. have been carefully taken into account. These are shown in Table 14.3 for both frequencies of operation.

Once the scenario under analysis has been created for the 3D ray-launching simulations, transceiver node densification analysis has been conducted by progressively increasing the number of nodes per room from 1 node/room (6 nodes in total) to 4 nodes/room (24 nodes in total) to a final value of 9 nodes/room (57 nodes in total). The locations of the nodes can be seen in Fig. 14.5a for the 6-node wireless sensor network (WSN) and in Figs. 14.5c and d for the 24-node WSN and 57-node





(a)



(b)

**Fig. 14.5** Schematic view of the simulation scenario, for a 6-node WSN (a), a 24-node WSN (c), and a 57-node WSN (d). Transceiver node densification is carried out by progressively increasing the number of nodes per room from one node/room, four nodes/room, and to a final value of nine nodes/room. (b) Upper view of the WSN deployment strategy

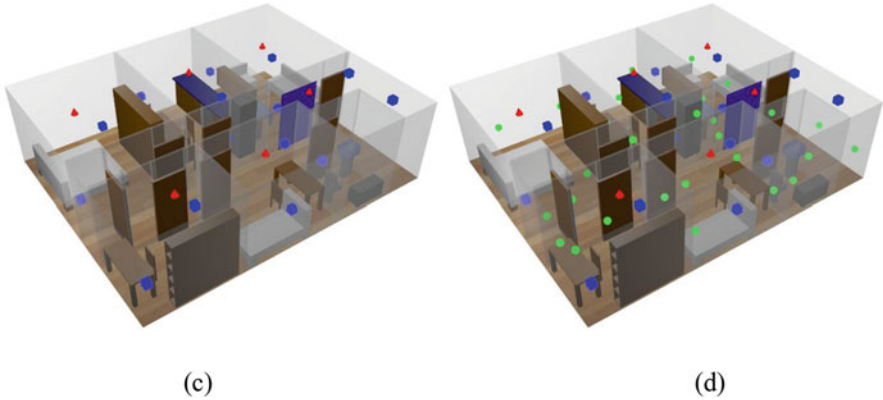


**Fig. 14.5** (continued)

WSN, respectively. The coordinates of the nodes are shown in Table 14.2, where the different node density configurations within the scenario are highlighted by different gray scales. Regarding this, it is worth noting that in Fig. 14.5b, the newly added nodes for each node density configuration are represented by different dot shapes: The first 6 nodes are represented by triangles, the nodes from 7 to 24 are represented by squares, and, finally, the nodes added last (i.e., from node 25 to node 57) are represented by circles.

As previously stated, constitutive parameters have been also considered, including their frequency dispersive behavior for both operating frequencies. The list of materials as well as their relative permittivity and conductivity values is presented in Table 14.3, the data having been obtained from Refs. [25–28].

Simulation results have been obtained using an in-house-implemented 3D ray-launching code. The simulation parameters, including ray-launching resolution, cuboid meshing dimensions, maximum number of allowed reflections, and transceiver parameters, are shown in Table 14.4.

Figure 14.6 shows bidimensional radio-frequency (RF) power distribution obtained from the 2.4-GHz simulation results. The proposed three-node density configurations are depicted, for 1.3 and 2.5 m heights. As expected, deploying more nodes within the scenario leads to a considerable increase in the overall RF power level, obtaining better coverage throughout the scenario. Similar results for 5 GHz are shown in Fig. 14.7. Although the same RF power level increase is seen with more nodes, the higher propagation losses at the higher frequency significantly lower power levels for the 5-GHz results. It is important to note that in all cases, the typical rapid variations in power levels due to multipath propagation are noticeable.

In order to gain insight in the estimation of path loss, the influence of multipath propagation, and their influence in the RF power distribution within indoor complex scenarios which have a large number of radio wave reflections, two nodes have been chosen to show their linear path vs. received power levels. Figure 14.8 shows the linear paths that have been depicted in Fig. 14.9. The results correspond to nodes

**Table 14.2** Node location within the simulation scenario

Source	Source Position (X, Y, Z) (m)	Source	Source Position (X, Y, Z) (m)
1	(1.2,5.5,2.4)	25	(1.7,1)
2	(4.8,5.5,2.4)	26	(2.1,3.7,1)
3	(7.5,5.5,2.4)	27	(3.7,1)
4	(1.7,1.2,2.4)	28	(3.7,5.3,1.1)
5	(4.3,1.2,2.4)	29	(4.7,6.3,1)
6	(7.2,7.2,4)	30	(5.7,7.1,4)
7	(0.4,3.7,1)	31	(6.9,5.9,1)
8	(2.2,6.2,1)	32	(7.5,0.8)
9	(3.3,7.1)	33	(6.4,3.7,1)
10	(3.9,7,1)	34	(8.7,1)
11	(4.9,3.7,1)	35	(8.5,1)
12	(5.7,5.1,4)	36	(8.3,7.1)
13	(6.5,7,1)	37	(0.5,2.8,1)
14	(7.4,1)	38	(0.4,1.8,1)
15	(8.8,6.5,1)	39	(0.5,1.3,1.1)
16	(0.4,0.3,1)	40	(1.3,3,1)
17	(2.6,1.8,1)	41	(1.7,1.8,1)
18	(2.6,0.9,1)	42	(1.7,0.7,1)
19	(4.5,0.3,1)	43	(2.6,2.5,1)
20	(3.8,3,1)	44	(3.2,7.2,4)
21	(6.1,2.5,1)	45	(3.2,1.6,1.1)
22	(8.5,2.7,2.4)	46	(3.2,0.3,1)
23	(6.4,1.3,1)	47	(4.1,8,1)
24	(8.5,1,2.4)	48	(5.2,7.2,4)
		49	(5.8,1.8,1.1)
		50	(5.8,0.3,1)
		51	(6.1,3,1)
		52	(7.2,2,1)
		53	(6.4,0.3,1)
		54	(7.5,0.8,1)
		55	(8.1,3,1)
		56	(8.8,1.7,1)
		57	(8.8,0.3,1)

**Table 14.3** Constitutive parameters for both frequencies of operation considered within the simulation analysis

Material	Relative permittivity ( $\epsilon_r$ )		Conductivity (S/m)	
	2.4 GHz	5 GHz	2.4 GHz	5 GHz
Brick wall	4.44	3.56	0.11	$9.46 \times 10^{-2}$
Concrete	8.1	5.5	0.02	$5.01 \times 10^{-2}$
Wood	2.88	2.05	0.21	$8.23 \times 10^{-2}$
Plasterboard	2.02	2.02	0	$1.48 \times 10^{-2}$
Glass	6.06	5.98	0.11	$2.99 \times 10^{-1}$

**Table 14.4** Simulation parameters employed in the 3D ray-launching code for the simulation scenario previously depicted

Parameter	Value
Frequency	2.4 GHz/5 GHz
Transmitted power	0 dBm
Antenna type	Monopole
Antenna gain	1.5 dBi
Horizontal plane angle resolution ( $\Delta\Phi$ )	1°
Vertical plane angle resolution ( $\Delta\theta$ )	1°
Maximum permitted reflections	6
Cuboids resolution	10 cm $\times$ 10 cm $\times$ 10 cm

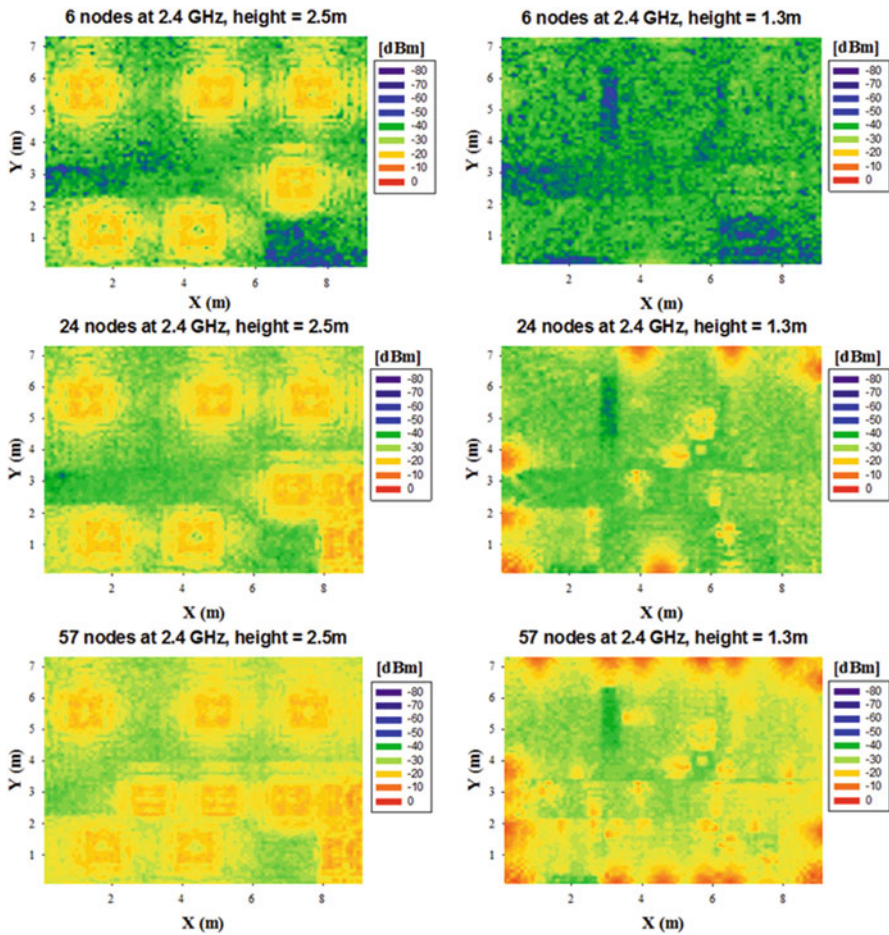


**Fig. 14.6** Bidimensional cut planes depicting received power level estimations, for different heights and transceiver density, for 2.4 GHz

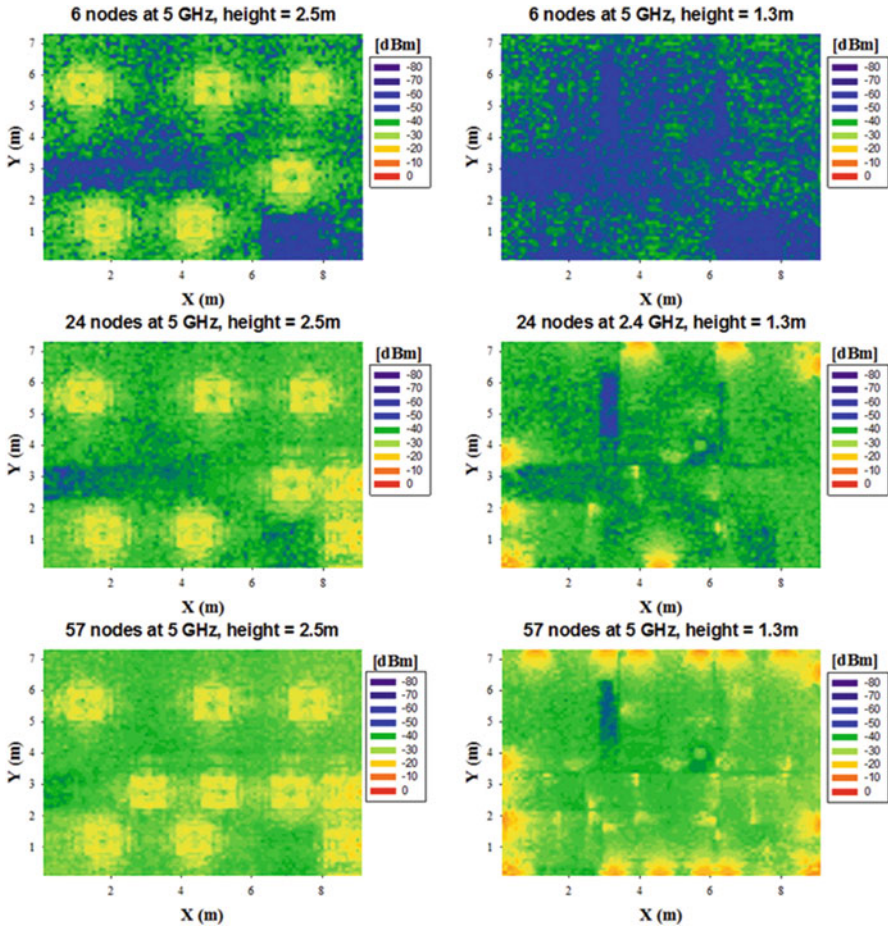


**Fig. 14.7** Bidimensional cut planes depicting received power level estimations, for different heights and transceiver density, for 5 GHz

#19 and #37. As can be seen, received power levels are different between the nodes, which in turn impacts the service delivery levels within the scenario. In linear path graphs, estimations based on different empirical models have been added to those obtained by the 3D ray-launching simulation tool for both 2.4 and 5 GHz. Although results from all the methods follow the same tendency, only the 3D ray-launching estimations give effect of multipath propagation and the influence of the losses due to walls and big obstacles, giving much more accurate power level estimations for this kind of scenarios.

The received power estimations depicted can lead to an optimized deployment of WSNs, since the results give valuable information regarding the validity of deploying wireless transceivers with a specific sensitivity level. These results can

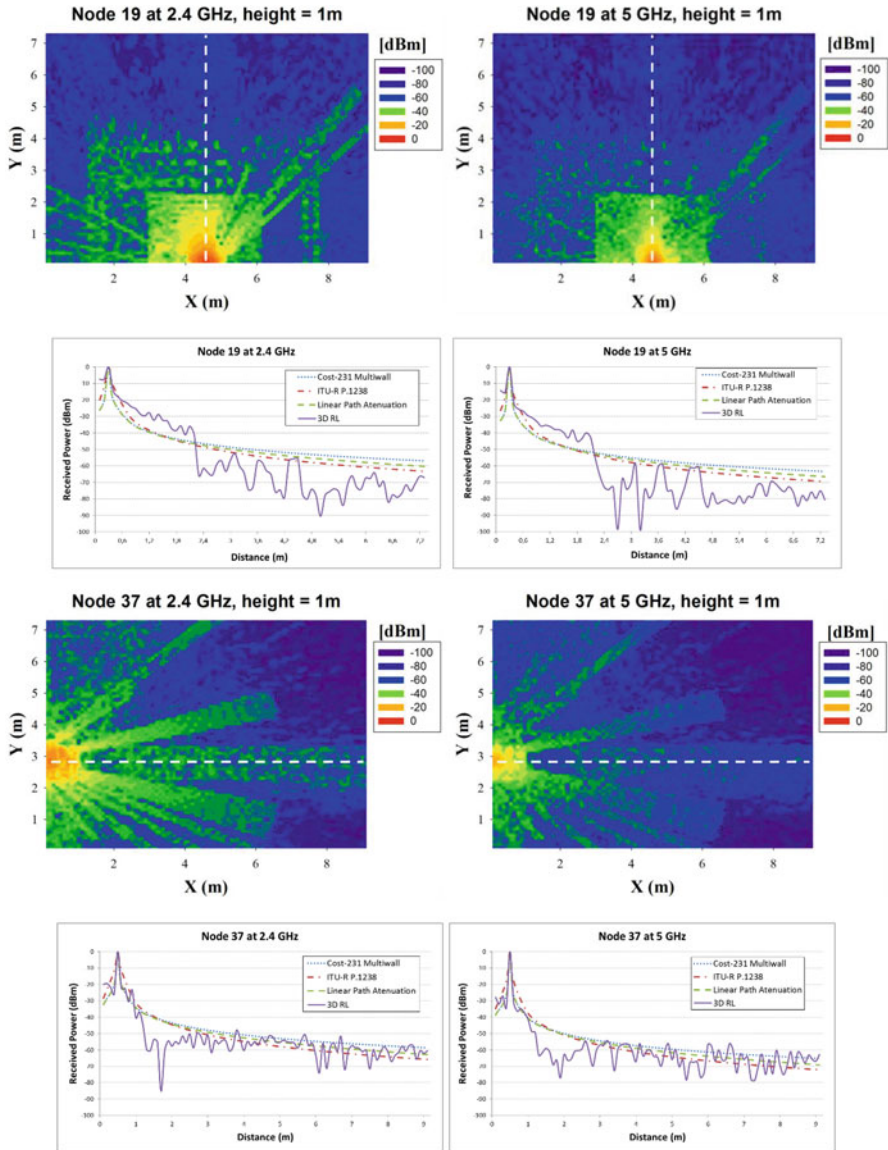


**Fig. 14.8** Path loss estimations for node #19 and node #37. Bidimensional received power level distributions as well as linear TX-RX radials (compared with empirical-based simulation methods) are depicted. Fast-fading components are observed, corresponding to strong multipath propagation within the scenario

also lead to an optimal overall performance of the WSN in terms of data rate and energy consumption, which are key issues in the deployment of dense WSNs. For that purpose, signal-to-noise ratio (SNR) values can be obtained for the whole

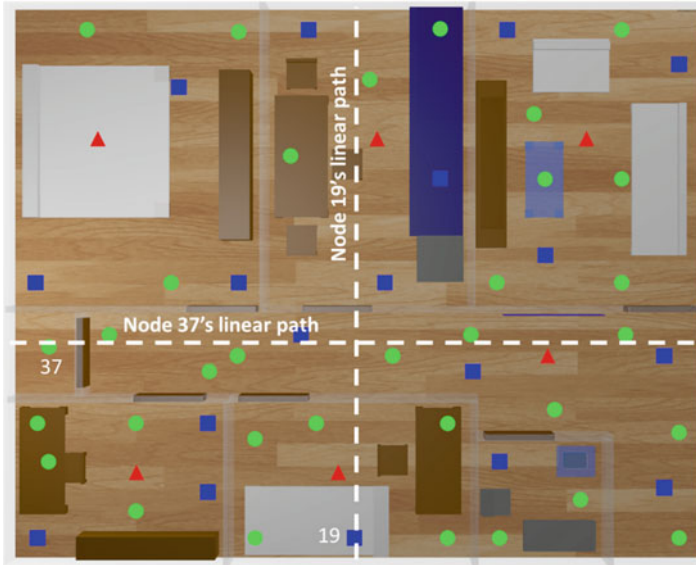


**Fig. 14.9** Layout of employed TX-RX radials in order to obtain path loss estimations for node #19 and node #37, as a subset of the complete node distribution within the scenario

volume of the scenario under analysis. As an example, Fig. 14.10 shows the SNR planes at heights 1.3 and 2.5 m when node #1 acts as transmitter and the rest of the deployed nodes are considered interference sources. As expected, the higher SNR values are obtained near the transmitter. It is important to note how the increase of deployed nodes leads to a degradation of the SNR, which in turn could lead to lower Quality of Service (QoS) of the wireless link.

As an illustrative example, the analysis of the wireless communication between node #1 (acting as transmitter) and node #6 (acting as receiver) is presented. First, the received power level at node #6 has been obtained, which at 2.4 GHz is  $-58.99$  dBm and at 5 GHz is  $-65.00$  dBm. The corresponding power delay profiles for both cases are depicted in Fig. 14.11 showing the effect of multipath propagation for this specific wireless communication link. Taking into account the results for 2.4 GHz, for this example, a ZigBee-based communication has been assumed. ZigBee nodes can communicate at 250 Kbps, operating at 2.4 GHz with a bandwidth of 3 MHz. After applying the well-known Shannon formula

$$C = BW \times \log_2(1 + S/N) \quad (14.6)$$

for the channel capacity  $C$  (in bps) in relation to the communication system bandwidth (BW) (in Hz, 3 MHz for ZigBee), the power level  $S$  of the received signal and the power level  $N$  of received noise, a minimum required SNR value of  $-12.26$  dB is obtained. The obtained threshold value is represented in Fig. 14.12

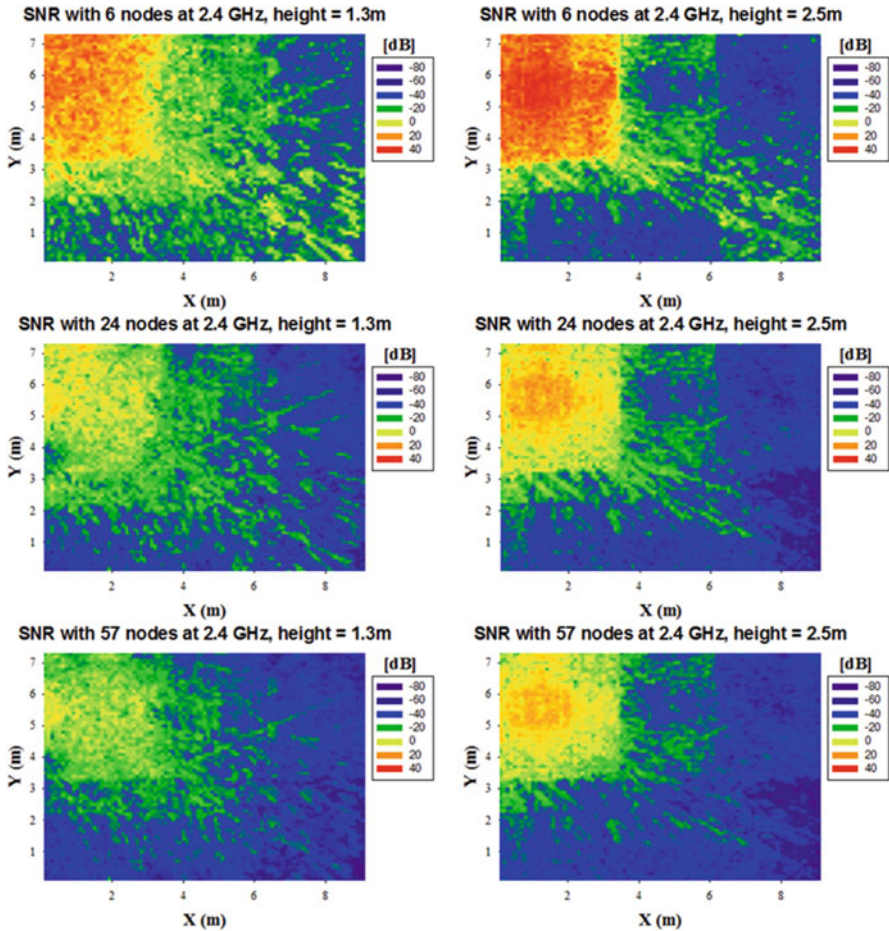


**Fig. 14.10** Bidimensional distributions of SNR as a function of node density, for  $f_{operation} = 2.4$  GHz, at cut planes at heights 1.3 and 2.5 m, respectively

by a dashed line, indicating when a ZigBee-based communication will operate correctly, i.e., when the SNR value is higher than this limit. The graph shows the obtained SNR values for each node density configuration and for three different transmitted power levels of node #1: 0 dBm, which is a common value in ZigBee communications; 10 dBm, which is the highest permitted level in Europe for narrowband communications in the ISM 2.4 GHz band (specified in Annex F.7 and Annex E of the standard IEEE 802.15.4); and 20 dBm, a higher power level used in this example to demonstrate how to reach the required SNR value for the cases with many nodes within the scenario. Figure 14.12 shows how the communication will be successful for all transmitted power levels. When the density of the WSN increases, high transmitted power levels will be required, which in turn will lead to



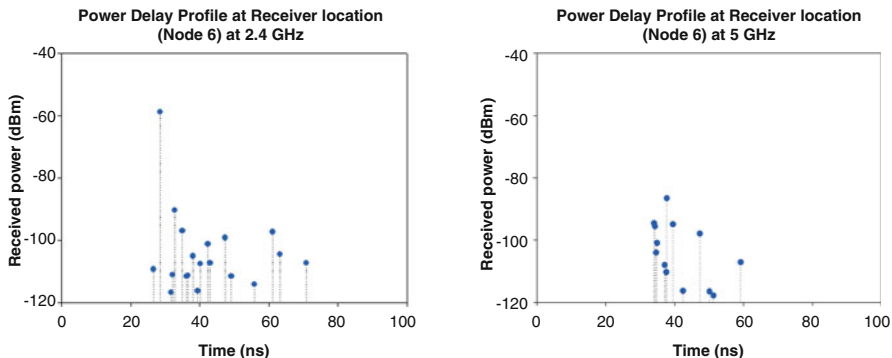


**Fig. 14.11** Power delay profile results corresponding to the receiver location of node #6, for both frequencies of operation (2.4 and 5 GHz). As can be seen, power levels as well as propagating component distributions vary with frequency, given the different interaction between transmitter sources and potential scatterers within the scenario

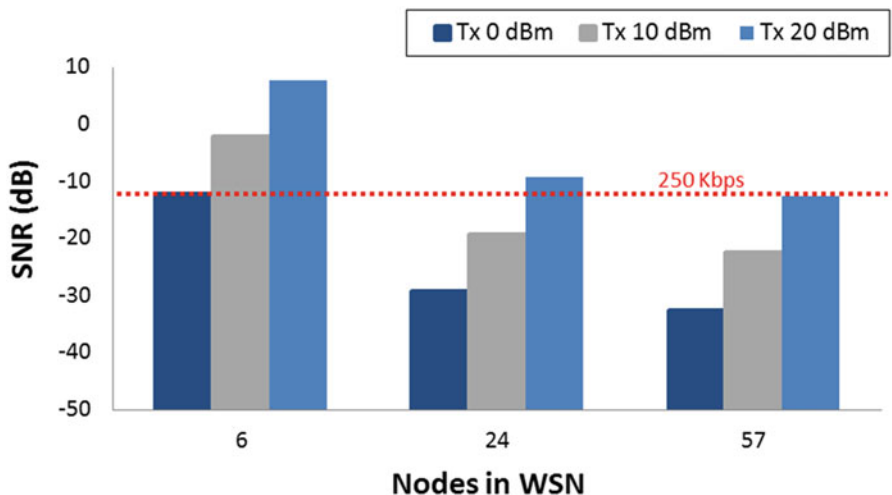


**Fig. 14.12** Minimum SNR thresholds as a function of TX power and as a function of node density within the scenario, for ZigBee nodes operating at a transmission rate of 250 Kbps

a higher current consumption of the wireless transceivers. Note that the results are for the worst case possible, i.e., when the rest of nodes of the WSN are interfering with the communication at the same time. Nevertheless, it can be clearly seen that the deployment of dense WSNs requires an in-depth radio planning analysis since in addition to the estimation of RF power distribution of the transmitters, the influence of intersystem as well as intra-system interferences is a key issue.

## 14.4 Concluding Remarks

In this chapter, the analysis of node density impact on wireless system operation has been analyzed. To that extent, three different network topologies have been considered within a conventional indoor scenario, in which node density is increased in each one of them. Received power levels for the information signal as well as potential interference generated by intra-system operation have been obtained, revealing the evolution in SNR behavior, which is strongly dependent on the number and location of the transceivers as well as on the specific characteristics of the scenario. Node density impacts on SNR values, with variations in excess of 10 dB for the proposed domestic scenario, a relevant value when considering future full-scale wireless sensor network deployments. The use of deterministic techniques can aid in radio planning phases prior to massive deployments in order to optimize HetNet and D2D operation, among others. For future research, it is worth noting the need to:

- (a) Optimize energy consumption, especially in the case of on-body wireless sensors or infrastructure monitoring nodes (such as civil structures: bridges, roads, dams, etc. in which low maintenance cost is compulsory)
- (b) Consider the impact of human users within the scenarios, in terms of radio propagation losses as well as in the density and location of wireless transceivers
- (c) New transceiver architectures implemented in order to reduce device complexity and hence reduce overall cost, with inherent restrictions in terms of processing capabilities as well as memory storage

New architectures will open new challenges in which radio channel analysis can play a key role in overall system optimization.

## References

1. J.S. Sussman, *Perspectives on Intelligent Transportation Systems (ITS)* (Springer, New York, 2005)
2. S. Ghosh, T.S. Lee, *Intelligent Transportation Systems: Smart and Green Infrastructure Design*, 2nd edn. (CRC Press, Boca Raton, FL, 2010)
3. B. Ai, X. Cheng, T. Kürner, Z.-D. Zhong, K. Guan, R.-S. He, L. Xiong, D.W. Matolak, D.G. Michelson, C. Briso-Rodriguez, Challenges toward wireless communications for high-speed railway. *IEEE Trans. Intell. Transp. Syst.* **15**(5), 2143–2158 (2014)
4. R. Sundar, S. Hebbar, V. Golla, Implementing intelligent traffic control system for congestion control, ambulance clearance, and stolen vehicle detection. *IEEE Sensors J.* **15**, 1109–1113 (2014)
5. A. Kumar, G.P. Hancke, A Zigbee-based animal health monitoring system. *IEEE Sensors J.* **15**, 610–616 (2015)
6. J. Vales-Alonso, P. Pablo Lopez-Matencio, F.J. Gonzalez-Castaño, H. Navarro-Hellin, P.J. Baños-Guirao, F.J. Perez-Martinez, R.P. Martinez-Alvarez, D. Gonzalez-Jimenez, F. Gil-Castiñeira, R. Duro-Fernandez, Ambient intelligence systems for personalized sport training. *Sensors* **10**, 2359–2385 (2010)

7. P.J. Soh, G.A.E. Vandenbosch, M. Mercuri, D.M.M.-P. Schreurs, Wearable wireless health monitoring: Current developments, challenges, and future trends. *IEEE Microw. Mag.* **16**(4), 55–70 (2015)
8. A. Pantelopoulos, N.G. Bourbakis, A survey on wearable sensor-based systems for health monitoring and prognosis. *IEEE Trans. Syst. Man Cybern. Part C Appl. Rev.* **40**(1), 1–12 (2010)
9. L. Azpilicueta, M. Rawat, K. Rawat, F. Ghannouchi, F. Falcone, Convergence analysis in deterministic 3D ray launching radio channel estimation in complex environments. *Appl. Comput. Electromagn. Soc. J.* **29**(4), 256–271 (2014)
10. L. Azpilicueta, F. Falcone, J.J. Astráin, J. Villadangos, I.J. García Zuazola, H. Landaluze, I. Angulo, A. Perallos, Measurement and modeling of a UHF-RFID system in a metallic closed vehicle. *Microw. Opt. Technol. Lett.* **54**(9), 2126–2130 (2012)
11. A. Moreno, I. Angulo, A. Perallos, H. Landaluze, I.J.G. Zuazola, L. Azpilicueta, J.J. Astráin, F. Falcone, J. Villadangos, IVAN: Intelligent van for the distribution of pharmaceutical drugs. *Sensors* **12**, 6587–6609 (2012)
12. J.A. Nazábal, P. López Iturri, L. Azpilicueta, F. Falcone, C. Fernández-Valdivielso, Performance analysis of IEEE 802.15.4 compliant wireless devices for heterogeneous indoor home automation environments. *Int. J. Antennas Propag.* **2012**, 176383 (2012)
13. I. Sesma, L. Azpilicueta, J.J. Astráin, J. Villadangos, F. Falcone, Analysis of challenges in the application of deterministic wireless channel modelling in the implementation of WLAN-based indoor location system in large complex scenarios. *Int. J. Ad Hoc Ubiquitous Comput.* **15**(1–3), 171–184 (2014)
14. S. Led, L. Azpilicueta, E. Aguirre, M. Martínez de Espronceda, L. Serrano, F. Falcone, Analysis and description of HOLTIN service provision for AECG monitoring in complex indoor environments. *Sensors* **13**(4), 4947–4960 (2013)
15. P.L. Iturri, J.A. Nazábal, L. Azpilicueta, P. Rodriguez, M. Beruete, C. Fernández-Valdivielso, F. Falcone, Impact of high power interference sources in planning and deployment of wireless sensor networks and devices in the 2.4GHz frequency band in heterogeneous environments. *Sensors* **12**(11), 15689–15708 (2012)
16. E. Aguirre, J. Arpón, L. Azpilicueta, S. de Miguel, V. Ramos, F. Falcone, Evaluation of electromagnetic dosimetry of wireless systems in complex indoor scenarios within body human interaction. *Prog. Electromagn. Res. B* **43**, 189–209 (2012)
17. R.J. Luebbers, A heuristic UTD slope diffraction coefficient for rough lossy wedges. *IEEE Trans. Antennas Propag.* **37**, 206–211 (1989)
18. H.D. Hristov, *Fresnel Zones in Wireless Links, Zone Plate Lenses and Antennas* (Artech House, Boston, 2000)
19. L. Azpilicueta, P. López-Iturri, E. Aguirre, F. Falcone, An accurate UTD extension to a ray launching algorithm for the analysis of complex indoor radio environments. *J. Electromagn. Waves Appl.* **30**(1), 43–60 (2016)
20. H. Baghdadi, E. Aguirre, P. López, L. Azpilicueta, J.J. Astrain, J. Villadangos, F. Falcone, Characterization of UHF radio channels for wireless sensor systems embedded in surfboards. *IEEE Antennas Wirel. Propag. Lett.* **14**, 1526–1529 (2015)
21. L. Azpilicueta, M. Rawat, K. Rawat, F. Ghannouchi, F. Falcone, A ray launching–neural network approach for radio wave propagation analysis in complex indoor environments. *IEEE Trans. Antennas Propag.* **62**(5), 2777–2786 (2014)
22. L. Azpilicueta, F. Falcone, R. Janaswamy, A hybrid ray launching–diffusion equation approach for propagation prediction in complex indoor environments. *IEEE Antennas Wirel. Propag. Lett.* **16**, 214–217 (2017)
23. F. Casino, L. Azpilicueta, P. López-Iturri, E. Aguirre, F. Falcone, A. Solanas, Hybrid-based optimization of wireless channel characterization for health services in medical complex environments, in *Proceedings of 6th International Conference on Information, Intelligence, Systems and Applications* (IISA 2015), Ionian University, Corfu 6–8 July 2015
24. L. Azpilicueta, C. Vargas-Rosales, F. Falcone, Deterministic propagation prediction in vehicular environments. *IEEE Veh. Technol. Mag.* **11**(3), 29–37 (2016)

25. A. Muqaibel, A. Safaai-Jazi, A. Bayram, S.M. Riad, Ultra wideband material characterization for indoor propagation. *IEEE Antennas Propag. Soc. Int. Symp.* **4**, 623–626 (2003)
26. A. Muqaibel, A. Safaai-Jazi, A. Bayram, A.M. Attiya, S.M. Riad, Ultrawideband through-the-wall propagation. *IEE Proc. Microwaves Antennas Propag.* **152**(6), 581–588 (2005)
27. Y. Pinhasi, A. Yahalom, S. Petnev, Propagation of ultra wide-band signals in lossy dispersive media, in *Proceedings of IEEE International Conference on Microwaves, Communications, Antennas and Electronic Systems, COMCAS 2008*, 2008, pp. 1–10
28. C.A. Grosvenor, R.T. Johnk, J. Baker-Jarvis, M.D. Janezic, B. Riddle, Time-domain free-field measurements of the relative permittivity of building materials. *IEEE Trans. Instrum. Meas.* **58**(7), 2275–2282 (2009)



**Peio Lopez-Iturri** received his Telecommunications Engineering Degree from the Public University of Navarre (UPNA), Pamplona, Navarre, in 2011. He has worked in the FASTER research project at UPNA. He obtained a Master in Communications in 2012, held by the UPNA, and he is currently pursuing the Ph.D. degree in telecommunication engineering while he is working as a researcher at UPNA. He has over 90 contributions in journal and conference publications. His research interests include radio propagation, modeling of radio interference sources, wireless sensor networks, electromagnetic dosimetry, wireless power transfer, and mobile radio systems.



**Leyre Azpilicueta** (M15) received her Telecommunications Engineering Degree (2009), her Master's degree in Communications (2011), and her Ph.D. degree in Telecommunication Technologies (2015), at the Public University of Navarre at Pamplona in Spain. In 2010 she worked in the R&D department of RFID Osés as radio engineer. She is assistant editor of the journal *Microwave Processing*. She is currently working as associate professor at Tecnológico de Monterrey, Campus Monterrey, Mexico. Her research interests are in radio propagation, mobile radio systems, ray tracing, and channel modeling. She has over 110 contributions in relevant journals and conference publications. She has been the recipient of the Best Ph.D. in 2016 awarded by the Colegio Oficial Ingenieros de Telecomunicación, the *IEEE Antennas and Propagation Society Doctoral Research*

*Award 2014*, and the *Young Professors and Researchers Santander Universities 2014 Mobility Award*.



**Erik Aguirre** received his M.Sc. in Telecommunications Engineering from the Public University of Navarre, Pamplona, Spain, in 2012. Then he began working at the University of Vigo, Spain, on a research project related to dispersive propagation. He obtained the Ph.D. degree in telecommunication engineering in 2014. His research interests include radio propagation in dispersive media, body-centric communications, and wireless sensor networks.



**Francisco Falcone** (M05, SM09) received his Telecommunications Engineering Degree (1999) and Ph.D. in Communications Engineering (2005), both at the Public University of Navarre (UPNA) in Spain. From 1999 to 2000 he worked as microwave commissioning engineer at Siemens-Italtel. From 2000 to 2008, he worked as radio network engineer in Telefónica Móviles. In 2009 he cofounded Tafco Metawireless, a spin-off devoted to complex EM analysis. From 2003 to 2009, he was also an assistant lecturer at UPNA, becoming associate professor in 2009. His research areas are artificial electromagnetic media, complex electromagnetic scenarios, and wireless system analysis. He has over 400 contributions in journal and conference publications. He has been recipient of the CST Best Paper Award in 2003 and 2005, Best Ph.D. in 2006 awarded by the Colegio Oficial

Ingenieros de Telecomunicación, Doctorate award 2004–2006 awarded by UPNA, Juan Lopez de Peñalver Young Researcher Award 2010 awarded by the Royal Academy of Engineering of Spain, Premio Talgo 2012 for Technological Innovation, and Engineer of the Year 2013 awarded by the Asociación Navarra Ingenieros de Telecomunicación.

# Chapter 15

## Bioelectromagnetic Dosimetry: Simulating Electromagnetic Fields in the Human Body

Cynthia M. Furse

### 15.1 Introduction

Bioelectromagnetics is the study of how electromagnetic fields interact with a biological body. The need to understand this interaction has driven the development of dosimetry simulations that started with modeling the human as a sphere and today model the entire detailed body with a resolution on the order of a millimeter or finer. Bioelectromagnetic dosimetry, the measurement or prediction of the *dose* of electromagnetic fields in the body, is used for three major purposes: designing devices that are meant to be used in or near the body, evaluating how much microwave sources interact with the body, and understanding or controlling the natural body electric.

Electromagnetic dosimetry is used extensively to design and evaluate devices that are meant to be used in or near the body including implantable medical devices such as cardiac pacemakers and defibrillators; cochlear and retinal implants; medical imaging devices such as magnetic resonance imagers (MRI), for cancers and other deep-seated pathologies in the human tissue, and microwave breast-cancer imaging; devices to heat or stimulate parts of the body for hyperthermia; cardiac ablation; pulsed-electromagnetic-field healing and pain control; and neural recording and stimulation.

Dosimetry has also been used to understand how power from numerous other electrical devices and installations interacts with the body. Such devices include power lines, hair dryers, electric blankets, and industrial devices, but by far the most extensive use of dosimetry has been in the evaluation of the power deposition in the

---

C.M. Furse (✉)

Department of Electrical and Computer Engineering, University of Utah, Salt Lake City,  
UT 84112, USA

e-mail: [cfurse@ece.utah.edu](mailto:cfurse@ece.utah.edu)

head from cellular telephones. That area alone has driven numerous advancements in dosimetry simulation methods.

Another major application of dosimetry is to understand how natural or endogenous electromagnetic fields propagate throughout the body [1] and, in many applications, how they may be used for medical diagnostics and therapeutics. The cardio-pulmonary stethoscope developed by Dr. Magdy F. Iskander and his research group falls into this category (see Chap. 18), as do electromyography (EMG) to record signals going to the muscles, electroencephalography (EEG) to record brain signals, electrocardiography (ECG or EKG) to record signals driving the heart, and neural recording and stimulation.

All of these applications of bioelectromagnetic dosimetry today rely on detailed simulations of the human body. The simulations require (1) a detailed model of the body (or part of the body) and source of the fields, (2) knowledge (generally measurements of) of the dielectric properties of the tissues and materials, and (3) a computational method that can simulate the electromagnetic equations (Maxwell's equations, wave equation, etc.) for field propagation from the source into and around the body. This chapter reviews how these three key features have evolved to the detailed human models used today and where this field is likely to move in the future.

## 15.2 Radiofrequency Exposure Guidelines

Regulatory standards have long played important roles in the development of modern industry, and bioelectromagnetics is no exception. Concerns raised over the safety of radio and television transmitters, microwave ovens, industrial radiofrequency (RF) heat sealers, military and civilian radar systems, early wireless communication systems (satellite and mobile radios), and early RF medical devices led to the need for dosimetry methods. Although the incident fields from RF devices could be measured, it was much more difficult to measure the electromagnetic fields inside the exposed human body. These had to be calculated. Internal fields depend on the external excitation (its frequency, incident power level, distance from the object, and polarization); the size, shape, and electrical properties (conductivity and permittivity) of the body; and if the object is grounded, ungrounded, alone, or near other objects. Biological effects would depend on the internal fields, so dosimetry is used to calculate the internal fields from the incident fields (which are usually external).

Initially, standards and guidelines were based on whole-body exposures. Early Soviet standards were based on central nervous system and behavioral responses to RF fields induced inside the human body. In Western countries, the standards were based on thermal load, which is a function of total absorbed power in the body, defined using the specific absorption rate (SAR). SAR at a given location is given by:

$$\text{SAR} = (1/2) (\sigma/\rho) E^2, \quad (15.1)$$

where  $\sigma$  is the electrical conductivity,  $\rho$  is the mass density, and  $E$  is the magnitude of the electric field at the location of interest.

Standards and guidelines were developed by exposing laboratory animals (mice, guinea pigs, rats, rabbits, dogs, monkeys) to electromagnetic fields and observing their responses and behavior. Dosimetry was used to determine the internal fields in the laboratory animal and to correlate those fields to behavioral changes. It was also used to determine equivalent internal fields in humans (adults and children) and how much external field would be required to produce those internal fields.

Whole-body exposure limits made sense for plane-wave exposure applications, but the rise of personal communication systems – the cellular telephone – led to questions about localized exposure, particularly of the brain and nerves. To answer the question of how much power was absorbed in the brain from a cell phone, near-field dosimetry with detailed anatomical models was needed. This required new models, new simulation methods, advances in computer memory and speed, and new methods to measure and verify the results (often with detailed measurement phantoms). These advances brought about a new age in electromagnetics and greatly expanded our understanding of how electromagnetic fields propagate inside and interact with the body.

These new measurement and simulation capabilities enabled new guidelines for RF exposure limits. The first localized power deposition guideline appeared in late 1996 when the Federal Communications Commission (FCC) adopted the ANSI/IEEE C95.1-1991 SAR guideline of 1.6 W/kg averaged over 1 g of biological tissue. The International Commission on Non-Ionizing Radiation Protection (ICNIRP) released a new guideline in 1998 relaxing SAR limits to a maximum of 2 W/kg averaged over any 10 g of tissue. The latest ANSI/IEEE guideline, C95.1-2005, closely aligns the maximum SAR with the ICNIRP guideline allowing a 2 W/kg limit. Despite the IEEE revision in 2006, the FCC continues to use the more restrictive 1.6 W/kg limit established in 1996.

### 15.3 Dosimetry Models

The first step in dosimetry is to choose a model for the body or part of the body of interest. Early dosimetry was based on theoretical formulations for plane waves impinging on planar-layered models, spheres, cylinders, and prolate spheroids, shown in Fig. 15.2. These simplified models were adjusted in size and aspect ratio to represent adults, children, and laboratory animals. They were used to determine whole-body averaged SAR. These models were valid (and remain valid today) for estimates of whole-body absorption from plane waves (far-field sources) but are not accurate for localized power absorption from near-field sources. The internal fields in the models were calculated using long-wavelength analysis, the extended-boundary-condition method (EBCM), the iterative EBCM (IEBCM), the cylindrical approximation, the method of moments (MOM), the surface-integral-equation (SIE) technique, and some attempts at empirical formulations.



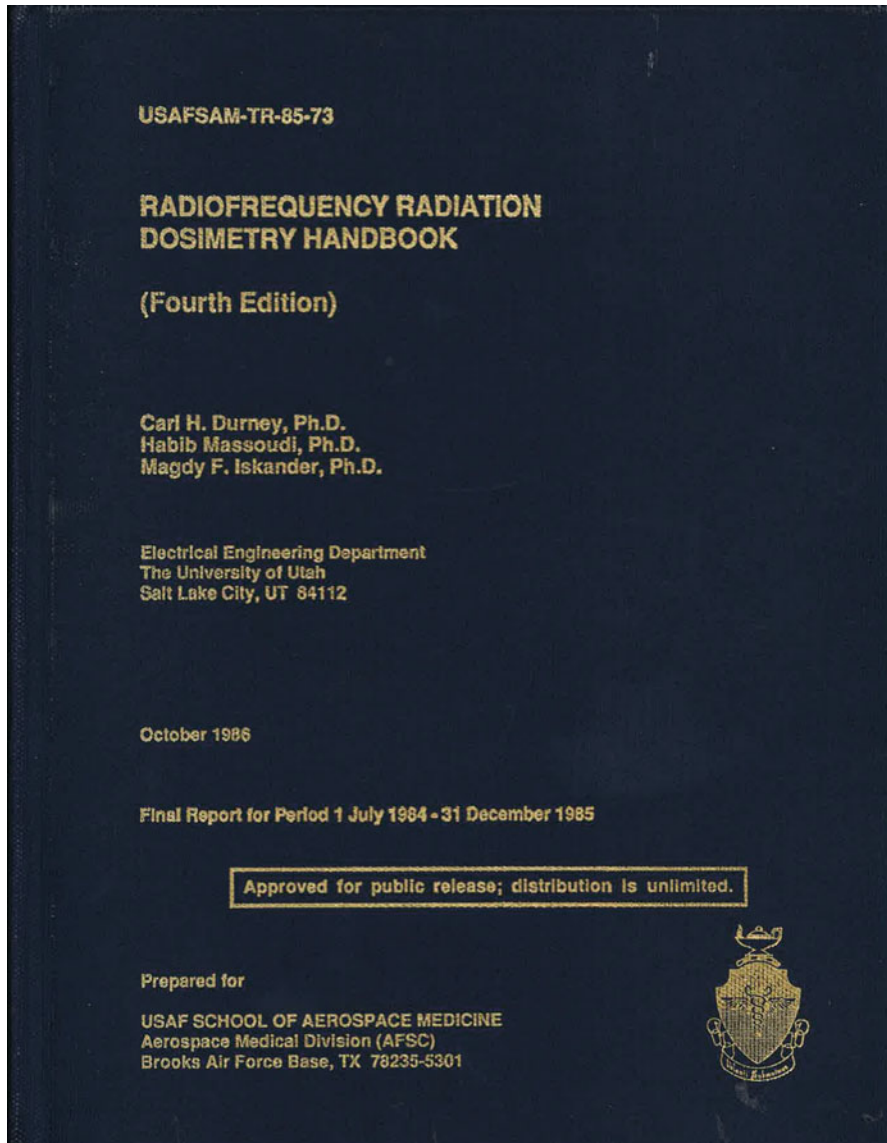


**Fig. 15.1** The *Radiofrequency Radiation Dosimetry Handbook*, 4th edition provided a compilation of data on human and animal dosimetry (1986)

These dosimetry results were collected into an extensive volume called the *Radiofrequency Radiation Dosimetry Handbook*, of which four editions were published [2]. The cover of the 4th edition is shown in Fig. 15.1. Dr. Magdy Iskander participated as one of the authors of these handbooks. Each edition included the work of the previous edition, plus new contributions.

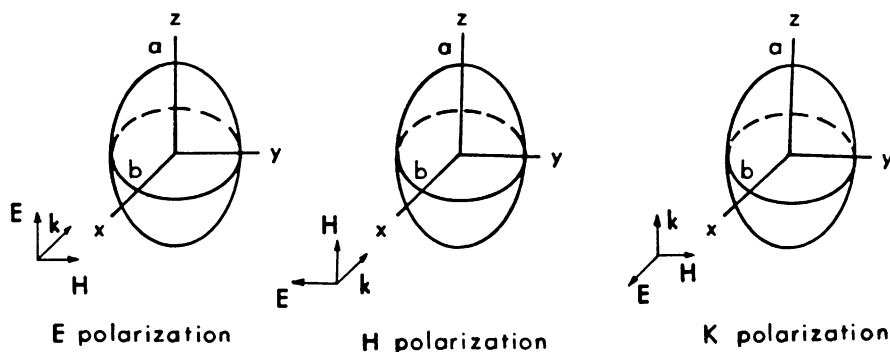
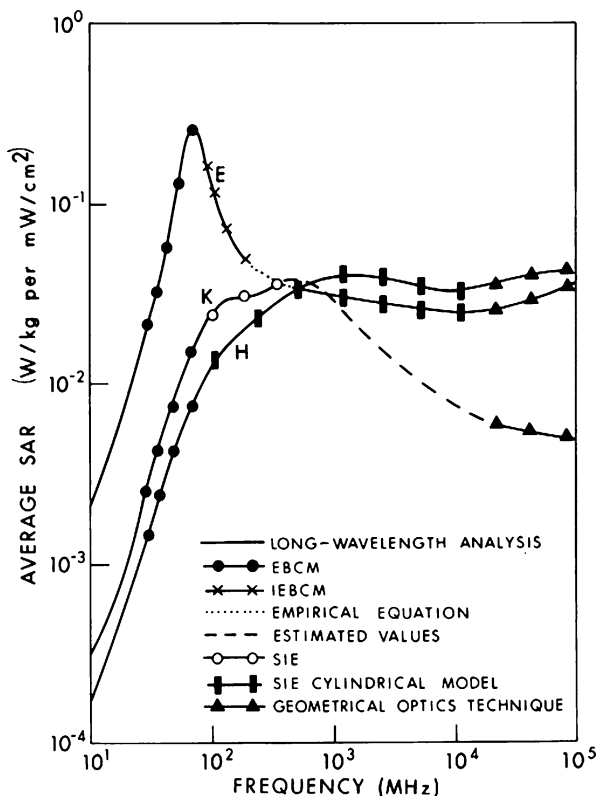


**Fig. 15.2** Prolate-spheroidal models were used to analyze the interaction of plane waves with the body for various polarization states. The same models were also used for near-field dosimetry. (From Ref. [2])

Models have progressed from the cylindrical and prolate-spheroidal models used during the 1970s and 1980s [2] (Fig. 15.2) to simple block models in the 1980s [3] (Fig. 15.4), to millimeter-resolution models based on anatomical cross sections which were the hallmarks of research in the 1990s and remain useful today (Fig. 15.5) [3–8]. In order to evaluate detailed internal fields arising from exposure to the near fields of various sources, such as the fields induced inside the brain or the eye, several voxel-based models were created from MRI scans. MRI provides a map of tissue densities, which shows the tissues visually but does not have a one-to-one correspondence to tissue type. The first models of this type were created by manually segmenting the images into individual tissue types. The Utah Anatomic Model [6] has 31 tissues at  $1.875 \times 1.875 \times 3 \text{ mm}^3$  resolution, using MRI scans of a live volunteer. The Visible Man Model from the National Institutes of Health was initially segmented at 4-mm resolution from the computer-tomographic (CT) scans of a cadaver.

The detail and precision of the dosimetry model should be chosen based on known electromagnetic principles. This led to several challenges for developing these early models. Detailed anatomical expertise was needed when segmenting the MRI models. The anatomical detail of the material between organs is not clear from MRI scans. Whether this material is air, fluid, connective tissue, etc. has a strong impact on how the fields propagate inside. Creating a clear, full-body MRI scan from a live person requires optimizing the MRI settings for good contrast between the soft tissues, minimizing pulsatile blood flow artifacts, and time gating to reduce blurring from breathing and the beating heart. The MRI scans for the first full-body anatomical model (Utah Anatomic Model [6]) took near 18 h and were done on three separate days. The volunteer was repositioned after breaks to relax, and it was critical to rematch the images from successive positions, so that the electromagnetic fields would propagate correctly in the dosimetry model. Both live and cadaver models were scanned lying down, so the organs sunk toward the back of the body, the arms slipped out of range of the MRI scans, the cadaver organs and airways

**Fig. 15.3** Average whole-body SAR for an average (prolate-spheroidal) man with plane-wave exposure at different polarization states, showing comparison between different dosimetry calculation methods (From the RF Dosimetry Handbook, 4th edition [2])

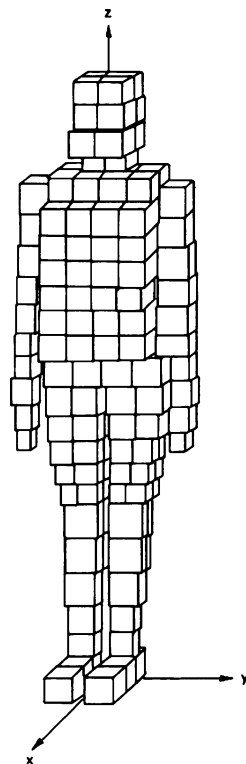


shrunk or swelled, the feet were relaxed with toes slightly pointed, and the head protruded slightly forward if a pillow was used. These anatomical features actually had significant effects on the dosimetry calculations, depending on the application, and had to be adjusted in the dosimetry model.

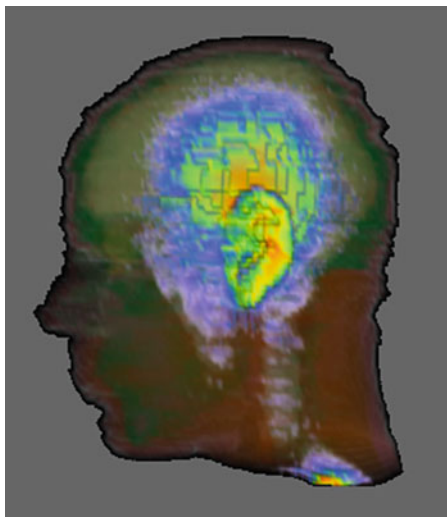
An additional problem with MR-scanned images is a shift in the apparent location of the fat and water-based tissues such as muscle by as much as 4–5 mm [9]. This causes difficulty defining the skin, which is important in dosimetry calculations, as its relative dryness somewhat insulates the body from direct contact with conductive surfaces. For the early models, the skin of uniform thickness was added to the models.

Perhaps the most important consideration is the question of uniqueness of individuals. Early studies on prolate-spheroidal models showed the strong effect height has on the full-body resonance and how much current will be induced in the body from high-voltage power lines [10], early research on block models showed how individual portions of the body such as the head had their own size-dependent resonances [11], and early studies with anatomical models showed that the size of the head (children as compared to adults) affects the 1-g averaged SAR from cellular telephones [12]. The vast majority of dosimetry calculations to date have focused

**Fig. 15.4** The block model of man used by Chatterjee et al. for plane-wave spectral analysis (From Ref. [3])



**Fig. 15.5** SAR computed in the Utah Anatomic Model from a simplified cellular-telephone model operating at 835 MHz (From Ref. [4])



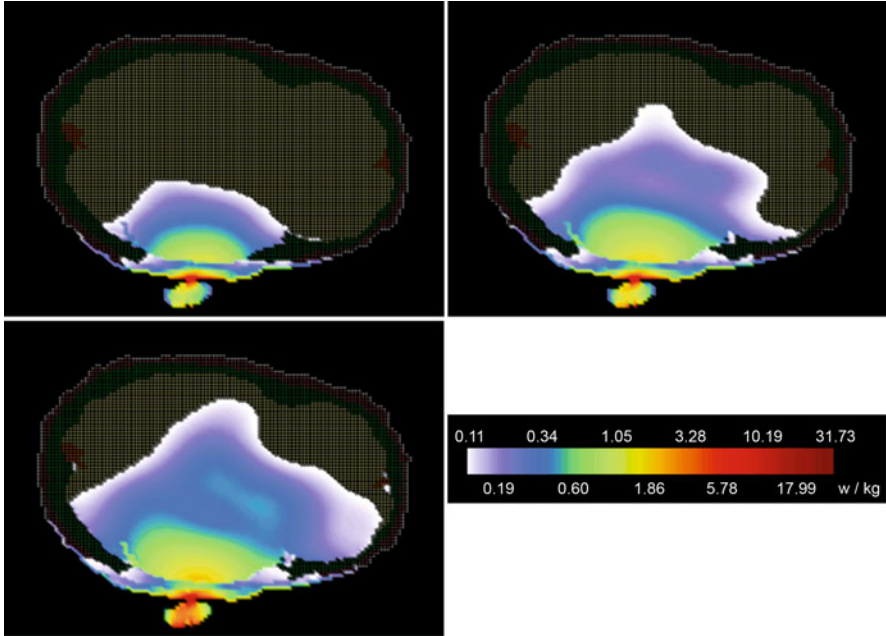


**Fig. 15.6** SAR in a cross section of the Utah Anatomic Model of (*top left*) adult, (*top right*) 10-year-old, and (*bottom left*) 5-year-old models for a simplified cellular-telephone model operating at 835 MHz (From Ref. [12])

on the average adult male. The average man is defined by (Snyder et al. [13]), and voxel models are often scaled to exactly the height (176 cm) and weight (71 kg) of the reference man. However, individual variation does matter, and numerous voxel models have been created for adult and juvenile males, females, and various types of lab animals.

One of the most interesting issues in model development has played out in the debate on whether children do or do not absorb more electromagnetic power from a cell phone than adults. This could have implications on RF absorption guidelines and other bioelectromagnetic analyses. Initially, Gandhi et al. observed that power absorbed was significantly higher in children than adults, as shown in Fig. 15.6 [12, 14], primarily due to the thinner ears of children, which brought the physical location of the phone closer to the head [15]. Since the phone is in the very near field wherein the fields decrease as the cube of the distance, even a very small difference in distance can result in a significantly higher exposure. Significant differences in SAR were observed when this effect was considered [14, 16], but minimal differences were observed in models without an ear or without considering the effect of the smaller pinnae of the ear [17, 18]. This debate, which has continued for two decades, highlights the importance of considering the electromagnetic significance of the model used for dosimetry.

## 15.4 Electrical Properties of Tissue

Whether the dosimetry model is a simple homogenous or layered model or a more complex anatomical model, the dielectric properties of the tissues in that model have a significant effect on how the electromagnetic fields propagate inside the model. The dielectric properties of tissue depend on the tissue type; e.g., wetter tissues such as muscle and cerebral spinal fluid are more conductive than dryer or oily tissues such as the bone and fat. Tissues with elongated cells, such as the femur and parts of the heart, can be anisotropic. There is also substantial spatial variation [19] in the dielectric properties within a given organ, from person to person, as a function of age [20], and more. Also, dielectric properties vary strongly with frequency. Biological tissues are so weakly magnetic that they are generally considered nonmagnetic.

There is a wide range of measured data published on tissue properties [2, 21–26]. Much of this data collection was driven by the needs of numerical dosimetry, and in many cases, new methods of measurement were devised to measure them.

As expected, dosimetry results are significantly affected by the dielectric properties of the tissues [12, 27]. The normal statistical variation of these tissues can result in detuning of antennas designed for medical implants [28] and uncertainty in absorbed power [29]. When homogeneous models are used, for quick approximation of whole-body exposures to far-field sources, it is standard to use 2/3 muscle for the tissue properties. This means the permittivity and conductivity are each multiplied by a factor of 2/3.

## 15.5 Dosimetry Calculations

Initially, the absorption of the electromagnetic field was calculated by solving various boundary value problems. Models were very simple (1D-layered models, cylinders, spheres, and prolate spheroids), and the source was a simple plane wave, because only very simple problems could be solved analytically and/or computationally then [30]. These gave way to heterogeneous modeling techniques, particularly the MOM and the finite-difference time-domain (FDTD) method, especially in the later 1980s when computers became widely available, and the demand for near-field, detailed human models was driven by safety concerns over the burgeoning cell phone industry. The simplified models and methods described in this section were state of the art in their day, and each gives us important insights into the propagation and interaction of fields with the body. Today, these methods also remain useful for validating more complex models and methods.

### ***15.5.1 1-D Planar Models***

Layered models of the body were useful at very high frequencies where the local curvature of the body could be neglected. Simple transmission-line approaches were used for both isotropic and anisotropic models, the incident field being that of a plane wave. Near-field sources were also evaluated. This model showed that layering increases the average SAR [31] and that plane-wave exposures provide maximum (worst case) whole-body-averaged SAR [9].

### ***15.5.2 Long-Wavelength Approximation (Perturbation Approach)***

When the frequency is low enough that the body is very small compared to the wavelength  $\lambda$  in free space (typically  $< \lambda/5$ ), the body will cause only a very small perturbation of the electrostatic field. SAR can then be approximated based on the first-order term of a power-series expansion with respect to the free-space wave number  $k = 2\pi/\lambda$ . This approach was used to approximate the SAR for human and animal models up to about 30 MHz, above which frequency the numerical errors make this approach incorrect [32, 33]. The long-wavelength analysis showed that the power absorption is greatest when the electrical field is aligned with the long axis of the human body [32, 33].

### ***15.5.3 Extended-Boundary-Condition Method (EBCM) and Iterative EBCM***

In the EBCM, all fields are expanded in terms of vector spherical wave functions, and an integral equation is converted into a matrix equation (see Chap. 19). This semi-analytical approach was found to be applicable for prolate-spheroidal models, but numerical errors limited its use to below 80 MHz for human models [34, 35]. The frequency range for which the EBCM could be used was expanded considerably by using multiple subregional expansion of the internal fields and solving the problem iteratively. The IEBCM approach was used to calculate the SAR in the average-man model up to 300 MHz [36]. Magdy Iskander and his first PhD student, Akhlesh Lakhtakia, developed this approach (see Chaps. 2 and 19).

### ***15.5.4 Lorenz–Mie Theory***

Homogeneous or concentrically layered spheres can also be analyzed using the Lorenz–Mie theory wherein the incident, scattered, and internal fields are expanded in terms of vector spherical wave functions. Analysis of a layered spherical model of the head indicated that the skull reduced heating of the brain [37].

### ***15.5.5 Cylindrical Approximation***

A similar approach can be taken for infinitely long circular cylindrical models. At frequencies where the free-space wavelength is much smaller than the major dimension of the prolate spheroid, the spheroid can be approximated by an infinitely long cylinder. This approximation was useful for man-sized spheroids for E-polarization (see Fig. 15.2) when the wavelength was about 2/5 the major dimension of the spheroid [31, 38]. Analysis of concentrically layered cylinders confirmed that SAR is a function of frequency [39], that clothing does not change the power absorbed at frequencies below 2 GHz [31], and (for finite-length cylinders) that direct contact with a ground plane can give an order-of-magnitude enhancement in the SAR even at frequencies below resonance [40].

### ***15.5.6 Surface-Integral-Equation Technique***

The SIE technique formulates the fields in terms of integrals of induced current densities on the surface of the body. This technique was mainly used for finite-length cylinders capped on each end with a hemisphere, which gave results very similar to those for prolate spheroids. This analysis confirmed that the greatest power absorption occurs when the electric field is aligned with the cylindrical axis and when the frequency is near the first resonance (80 MHz for an ungrounded man). It also predicted hot spots in the neck [41].

### ***15.5.7 Method of Moments***

The MOM involves a volume integral over the body. It has been used to calculate the internal and/or scattered fields from block models, such as the one shown in Fig. 15.4. MOM analysis showed that the resonant frequency for an adult man shifts from 77 MHz (ungrounded) to 47 MHz when standing on a ground plane. It predicted an order-of-magnitude SAR enhancement at frequencies below 30 MHz [42]. Measurements confirmed these results. Problems were noted, however, when



the calculated value of SAR increased with the number of cells used [43]. We now know this to be caused by much higher fields near the surface of the body, which are progressively better (and higher) calculated with more cells. Internal-field calculations were unreliable, particularly for coarse-celled models [44], and the use of a pulse-basis expansion can create nonphysical charge discontinuities at tissue boundaries [45].

### ***15.5.8 Finite-Difference Time-Domain Method***

The FDTD method was originally developed by Yee [46] and further developed by Holland [47], Taflove [48], Taflove and Brodwin [49], Umashankar and Taflove [50], and many others. The FDTD method has become the most widely used method for bioelectromagnetic dosimetry [51], because of its ease of detailed, heterogeneous modeling (including anisotropy [52], frequency dependence [53], statistical variation [29], etc.) and the ease of use when simulating a wide variety of near- and far-field exposure conditions from 60 Hz through THz and even optical spectral regimes and the ability to integrate it with multiphysics analysis such as temperature rise [54]. Perhaps the most critical reason for the shift from using method of moments to FDTD was its computational efficiency. Simulations of interstitial antennas to heat brain tumors were limited to a very coarse model of the tumor with method of moments [55], but much greater resolution could be achieved with FDTD [56]. In addition to localized or full-body SAR, the FDTD method provides current density, field distributions, absorbed power, and radiated power (including radiation pattern and polarization state [57]).

In the FDTD method, the time-domain differential Maxwell's equations are converted to finite differences and stepped iteratively through time and space [58]. The model space comprising the body and its close proximity is divided into a lattice of discrete unit cells, which is ideal for the anatomical voxel models described in the previous section. It is worth noting that for very detailed modeling (such as the cell phone and its antenna in the very near field of the ear), the precise location of the source and tissues matters. In that case, the metallic components must be carefully modeled, considering their exact location in the FDTD mesh of unit cells (tangential electric fields should be set to zero along the sides of metal wires and plates), and tissues must also be precisely located (averaging properties of adjacent tissues or not averaging, depending on their location) [59]. The voxel dimensions are most often practically constrained by the smallest item of interest, such as details of the source or precise areas where the current or SAR is to be calculated. The FDTD voxel should typically be smaller than 1/10 of the smallest wavelength in the model, although coarser resolutions have been successfully used [53]. Bioelectromagnetic simulations, particularly in nonresonant regimes, can be more forgiving than other types of simulations, because the field is absorbed before it can propagate very far.

The stability constraint of the FDTD method is that the time resolution of the stepped electromagnetic fields must be sufficiently small such that the field can

propagate across the diagonal of the cell in a single time step. This constraint has some important nuances in bioelectromagnetic simulations. First, biological effects are often associated with heating, so it is only natural that dosimetry will often be used to compute temperature rise. The complication is that electromagnetic effects occur much more quickly than temperature effects, and the dielectric properties of tissues can change with temperature. Hybrid thermal-electromagnetic models may do this calculation and may often be done in stages, adapting the model as its temperature rises [60].

A second interesting nuance is seen in low-frequency analysis, where the high resolution of the voxel model necessitates a very small value for time resolution. This means an impractically large number of time steps would be needed in order to complete a full cycle of a low-frequency wave in order to complete analysis. Fortunately, the nonresonant simulation converges much more quickly than in the slow cycle of the low-frequency wave, and we can use a small fraction of the wave for analysis [61]. This is done using the two equations two unknowns (2E2U) method, where a sine wave can be identified from two samples and solved for two unknowns (magnitude and phase), if the frequency is known [62].

A final interesting nuance of the stability limit of the FDTD grid is what happens if the source frequencies exceed this limit, such as in many pulsed simulations? Then, numerical dispersion in the FDTD method effectively acts like a low-pass filter and does not allow the high-frequency components to propagate, thus preventing frequency aliasing [63].

## 15.6 Further Research in Dosimetry

Today, numerical electromagnetic codes are available commercially and widely used for design and evaluation of electromagnetic devices. The key to obtaining quality results with these codes is proper modeling of the source, the biological model of interest, and the surrounding region. Understanding the theoretical basis of the fields, along with how they should propagate and couple with the body, is very important to choosing the right model. Each simulation requires careful thought, care, and validation. Researchers continue to seek additional insight into the characteristics of electromagnetic fields and use this insight in their modeling.

Much of the prior development of numerical electromagnetic methods has been driven by the need for improved detail and accuracy in a reasonable amount of computer-simulation time. The FDTD method has risen as a clear leader in this respect and is likely to continue to be the mainstay method for some time to come. Other methods have certain modeling advantages too and may be combined in hybrid approaches. This is particularly true for multiphysics simulations, where electromagnetic power deposition can be combined with strength of materials, thermal, and other effects for a full understanding of device performance. The trend toward simulating and understanding integrated-system effects is likely to continue. Automatic optimization routines are now standard, although they are deeply

dependent on the cost functions describing optimal behavior. These algorithms and methods for defining optimal behavior can still be improved.

In addition to hybrid codes that integrate multiphysics and electromagnetics, we can expect to see even more integration between theory, design, build, and test. In the future, codes could allow you to start with theoretical or known approaches to predict basic electromagnetic behavior, refine and enhance that understanding with numerical dosimetric simulations, and optimize it based on multiple constraints and parameters. The design code could then integrate with a 3D printer, etcher, etc. and produce a prototype of the design. When connected to a network analyzer, oscilloscope, or other test equipment, the test data could be directly integrated with the simulation data to identify parameters that could be modified for even better designs. It might even be possible to have a shared library of simulated and experimental data to draw from, already integrated with the design software. Users could contribute their designs and measurements automatically, and they could be used to continually improve the dosimetric models and simulations.

Areas of research in dosimetry that are particularly groundbreaking are those that allow us to evaluate effects that we are unable to with traditional methods. For example, traditional approaches use average tissue properties and average models to determine coupling to the body. Individual variation can be considered by running many individual simulations, but this is time consuming and expensive. Methods that can incorporate uncertainty, variation, and change in numerical simulations are just beginning to emerge [29] and much remains to be done in this area.

Another area of interest is what can be learned from the large amount of data obtained from each and every numerical simulation. Generally, we are looking for only one or a few parameters – radiation pattern and  $S_{11}$ , for instance. Yet there is a host of other information, in some cases hidden, within the data sets that are generated by numerical simulations. 2D and 3D visualization such as Fig. 15.6 can help immensely, but just scanning in detail through these images can be challenging. Methods to improve extraction of knowledge and understanding from data sets will continue to improve.

Finally, the application areas of numerical methods will continue to expand. Understanding the electrical body is one of these areas. The brain and nervous system are complex, nonlinear, distributed electrical circuits. Understanding and potentially healing or controlling the function of our internal electrical system is one of the frontiers of bioelectromagnetic simulations, a challenge worthy of the next generation of bioelectromagnetic researchers.

**Acknowledgment** The author thanks Andy Chrysler for the assistance in the preparation of portions of this manuscript.

## References

1. R.A. Hart, O.P. Gandhi, Comparison of cardiac-induced endogenous fields and power frequency induced exogenous fields in an anatomical model of the human body. *Phys. Med. Biol.* **43**, 3083–3099 (1998)
2. C.H. Durney, H. Massoudi, M.F. Iskander, Radiofrequency radiation dosimetry handbook. DTIC Document, 1986
3. I. Chatterjee, O.P. Gandhi, An inhomogeneous thermal block model of man for the electromagnetic environment. *IEEE Trans. Biomed. Eng.* **30**, 707–715 (1983)
4. V. Pandit, R. McDermott, G. Lazzi, C.M. Furse, O.P. Gandhi, Electrical energy absorption in the human head from a cellular telephone, in *Proceedings of IEEE Visualization'96*, 1996, pp. 371–374
5. P. Dimbylow, The development of realistic voxel phantoms for electromagnetic field dosimetry, in *Proc. Int. Workshop on Voxel Phantom Development*, 1996, pp. 1–7
6. O.P. Gandhi, C.M. Furse, Millimeter-resolution MRI-based models of the human body for electromagnetic dosimetry from ELF to microwave frequencies, in *Proc. Int. Workshop on Voxel Phantom Development*, 1995, pp. 24–31
7. O.P. Gandhi, G. Y-G, J.-Y. Chen, H.I. Bassen, Specific absorption rates and induced current distributions in an anatomically based human model for plane-wave exposures. *Health Phys.* **63**, 281–290 (1992)
8. P. Olley, P. Excell, Classification of a high-resolution voxel image of a human head, in *Proceedings of International Workshop at the National Radiological Protection Board*, Chilton, United Kingdom, 1995, pp. 16–23
9. I. Chatterjee, M.J. Hagmann, O.P. Gandhi, Electromagnetic absorption in a multilayered slab model of tissue under nearfield exposure conditions. *Bioelectromagnetics* **1**, 379–388 (1980)
10. D.W. Deno, Currents induced in the human body by high voltage transmission line electric field – Measurement and calculation of distribution and dose. *IEEE Trans. Power App. Syst.* **96**, 1517–1527 (1977)
11. M.J. Hagmann, O.P. Gandhi, J.A. D'andrea, I. Chatterjee, Head resonance: Numerical solutions and experimental results. *IEEE Trans. Microwave Theory Tech.* **27**, 809–813 (1979)
12. O.P. Gandhi, G. Lazzi, C.M. Furse, Electromagnetic absorption in the human head and neck for mobile telephones at 835 and 1900 MHz. *IEEE Trans. Microwave Theory Tech.* **44**, 1884–1897 (1996)
13. W. Snyder, M. Cook, E. Nasset, L. Karhausen, G.P. Howells, I. Tipton, Report of the Task Group on Reference Man. *Annals of ICRP*, 1979
14. O.P. Gandhi, G. Kang, Inaccuracies of a plastic “pinna” SAM for SAR testing of cellular telephones against IEEE and ICNIRP safety guidelines. *IEEE Trans. Microwave Theory Tech.* **52**, 2004–2012 (2004)
15. O.P. Gandhi, Yes the children are more exposed to radiofrequency energy from mobile telephones than adults. *IEEE Access* **3**, 985–988 (2015)
16. O.P. Gandhi, L.L. Morgan, A.A. de Salles, Y.-Y. Han, R.B. Herberman, D.L. Davis, Exposure limits: The underestimation of absorbed cell phone radiation, especially in children. *Electromagn. Biol. Med.* **31**, 34–51 (2012)
17. K.R. Foster, C.-K. Chou, Are children more exposed to radio frequency energy from mobile phones than adults? *IEEE Access* **2**, 1497–1509 (2014)
18. V. Hombach, K. Meier, M. Burkhardt, E. Kuhn, N. Kuster, The dependence of EM energy absorption upon human head modeling at 900 MHz. *IEEE Trans. Microwave Theory Tech.* **44**, 1865–1873 (1996)
19. C. Gabriel, A. Peyman, Dielectric measurement: Error analysis and assessment of uncertainty. *Phys. Med. Biol.* **51**, 6033–6046 (2006)
20. C. Gabriel, Dielectric properties of biological tissue: Variation with age. *Bioelectromagnetics* **26**, S12–S18 (2005)

21. K.R. Foster, H.P. Schwan, Dielectric properties of tissues, in *Handbook of Biological Effects of Electromagnetic Fields*, 2nd edn, vol. 2, C. Polk, E. Postow (Eds.) (CRC Press, Boca Raton, FL, 1995), pp. 25–102
22. C. Gabriel, Compilation of the dielectric properties of body tissues at RF and microwave frequencies, Final report AL/OE-TR-1996-0037, Brooks AFB, San Antonio, 1996
23. C. Gabriel, S. Gabriel, E. Corthout, The dielectric properties of biological tissues: I. Literature survey. *Phys. Med. Biol.* **41**, 2231–2249 (1996)
24. L. Geddes, L. Baker, The specific resistance of biological material – A compendium of data for the biomedical engineer and physiologist. *Med. Biol. Eng. Comput.* **5**, 271–293 (1967)
25. S. Rush, J. Abildskov, R. McFee, Resistivity of body tissues at low frequencies. *Circ. Res.* **12**, 40–50 (1963)
26. M. Stuchly, S. Stuchly, Dielectric properties of biological substances – Tabulated. *J. Microw. Power* **15**, 19–25 (1980)
27. A. Peyman, C. Gabriel, E. Grant, G. Vermeeren, L. Martens, Variation of the dielectric properties of tissues with age: The effect on the values of SAR in children when exposed to walkie-talkie devices. *Phys. Med. Biol.* **54**, 227–242 (2008)
28. J. Johnson, C.M. Furse, Statistical analysis of detuning effects for implantable microstrip antennas, in *North American Radio Science Conference URSI-CNC/USNC*, Ottawa, 2007
29. S.M. Smith, C.M. Furse, Stochastic FDTD for analysis of statistical variation in electromagnetic fields. *IEEE Trans. Antennas Propag.* **60**, 3343–3350 (2012)
30. C.H. Durney, Electromagnetic dosimetry for models of humans and animals: A review of theoretical and numerical techniques. *Proc. IEEE* **68**, 33–40 (1980)
31. P.W. Barber, O.P. Gandhi, M.J. Hagmann, I. Chatterjee, Electromagnetic absorption in a multilayered model of man. *IEEE Trans. Biomed. Eng.* **26**, 400–405 (1979)
32. C.C. Johnson, C.H. Durney, H. Massoudi, Long-wavelength electromagnetic power absorption in prolate spheroidal models of man and animals. *IEEE Trans. Microwave Theory Tech.* **23**, 739–747 (1975)
33. H. Massoudi, C.H. Durney, C.C. Johnson, Long-wavelength electromagnetic power absorption in ellipsoidal model of man and animals. *IEEE Trans. Microwave Theory Tech.* **25**, 47–52 (1977)
34. P.W. Barber, Electromagnetic power deposition in prolate spheroid models of man and animals at resonance. *IEEE Trans. Biomed. Eng.* **24**, 513–521 (1977)
35. P.C. Waterman, Symmetry, unitarity, and geometry in electromagnetic scattering. *Phys. Rev. D* **3**, 825–839 (1971)
36. M.F. Iskander, A. Lakhtakia, C.H. Durney, A new procedure for improving the solution stability and extending the frequency range of the EBCM. *IEEE Trans. Antennas Propag.* **31**, 317–324 (1983)
37. S. Rukspollmuang, K.-M. Chen, Heating of spherical versus realistic models of human and infrahuman heads by electromagnetic waves. *Radio Sci.* **14**, 51–62 (1979)
38. H. Massoudi, C.H. Durney, C.C. Johnson, A geometrical optics and an exact solution for internal fields in and energy absorption by a cylindrical model of man irradiated by an electromagnetic plane wave. *Radio Sci.* **14**, 35–42 (1979)
39. R. Ruppim, Electromagnetic power deposition in a dielectric cylinder in the presence of a reflecting surface. *IEEE Trans. Microwave Theory Tech.* **27**, 910–914 (1979)
40. M.F. Iskander, C.H. Durney, H. Massoudi, C.C. Johnson, Approximate calculation of SAR for planewave irradiation of man model near a ground plane, in *Proceedings of 1978 Symposium on Electromagnetic Fields in Biological Systems* (International Microwave Power Institute, Edmonton, Alberta, 1978), pp. 304–323
41. T.-K. Wu, Electromagnetic fields and power deposition in body-of-revolution models of man. *IEEE Trans. Microwave Theory Tech.* **27**, 279–283 (1979)
42. M.J. Hagmann, O.P. Gandhi, Numerical calculation of electromagnetic energy deposition in models of man with grounding and reflector effects. *Radio Sci.* **14**, 23–29 (1979)

43. J.F. DeFord, O.P. Gandhi, M.J. Hagmann, Moment-method solutions and SAR calculations for inhomogeneous models of man with large number of cells. *IEEE Trans. Microwave Theory Tech.* **31**, 848–851 (1983)
44. H. Massoudi, C.H. Durney, M.F. Iskander, Limitations of the cubical block model of man in calculating SAR distributions. *IEEE Trans. Microwave Theory Tech.* **32**, 746–752 (1984)
45. C.-T. Tsai, H. Massoudi, C.H. Durney, M.F. Iskander, A procedure for calculating fields inside arbitrarily shaped, inhomogeneous dielectric bodies using linear basis functions with the moment method. *IEEE Trans. Microwave Theory Tech.* **34**, 1131–1139 (1986)
46. K. Yee, Numerical solution of initial boundary value problems involving Maxwell's equations in isotropic media. *IEEE Trans. Antennas Propag.* **14**, 302–307 (1966)
47. R. Holland, THREDE: A free-field EMP coupling and scattering code. *IEEE Trans. Nucl. Sci.* **24**, 2416–2421 (1977)
48. A. Taflove, Application of the finite-difference time-domain method to sinusoidal steady-state electromagnetic-penetration problems. *IEEE Trans. Electromagn. Compat.* **22**, 191–202 (1980)
49. A. Taflove, M.E. Brodwin, Numerical solution of steady-state electromagnetic scattering problems using the time-dependent Maxwell's equations. *IEEE Trans. Microwave Theory Tech.* **23**, 623–630 (1975)
50. K. Umashankar, A. Taflove, A novel method to analyze electromagnetic scattering of complex objects. *IEEE Trans. Electromagn. Compat.* **24**, 397–405 (1982)
51. J.C. Lin, O.P. Gandhi, Computational methods for predicting field intensity, in *Handbook of Biological Effects of Electromagnetic Fields*, 2nd edn, vol. 2, C. Polk, E. Postow (Eds.) (CRC Press, Boca Raton, FL, 1995), pp. 337–402
52. J. Schneider, S. Hudson, A finite-difference time-domain method applied to anisotropic material. *IEEE Trans. Antennas Propag.* **41**, 994–999 (1993)
53. C.M. Furse, J.-Y. Chen, O.P. Gandhi, The use of the frequency-dependent finite-difference time-domain method for induced current and SAR calculations for a heterogeneous model of the human body. *IEEE Trans. Electromagn. Compat.* **36**, 128–133 (1994)
54. P.C. Cherry, M.F. Iskander, Calculations of heating patterns of an array of microwave interstitial antennas. *IEEE Trans. Biomed. Eng.* **40**, 771–779 (1993)
55. C.M. Furse, M.F. Iskander, Three-dimensional electromagnetic power deposition in tumors using interstitial antenna arrays. *IEEE Trans. Biomed. Eng.* **36**, 977–986 (1989)
56. P.C. Cherry, M.F. Iskander, FDTD analysis of power deposition patterns of an array of interstitial antennas for use in microwave hyperthermia. *IEEE Trans. Microwave Theory Tech.* **40**, 1692–1700 (1992)
57. M.F. Iskander, Z. Yun, R. Quintero-Illera, Polarization and human body effects on the microwave absorption in a human head exposed to radiation from handheld devices. *IEEE Trans. Microwave Theory Tech.* **48**, 1979–1987 (2000)
58. A. Taflove, S.C. Hagness, *Computational Electrodynamics* (Artech House, Boston, 2005)
59. C.M. Furse, C. Waterman, L. Griffiths, To-average or not-to-average in FDTD modeling of dielectric interfaces. *Appl. Comput. Electromagn. Soc. J.* **21**, 173–176 (2006)
60. S.C. DeMarco, G. Lazzi, W. Liu, J.D. Weiland, M.S. Humayun, Computed SAR and thermal elevation in a 0.25-mm 2-D model of the human eye and head in response to an implanted retinal stimulator-Part I: Models and methods. *IEEE Trans. Antennas Propag.* **51**, 2274–2285 (2003)
61. C.M. Furse, O.P. Gandhi, Calculation of electric fields and currents induced in a millimeter-resolution human model at 60 Hz using the FDTD method. *Bioelectromagnetics* **19**, 293–299 (1998)
62. C.M. Furse, Faster than Fourier: Ultra-efficient time-to-frequency-domain conversions for FDTD simulations. *IEEE Antennas Propag. Mag.* **42**(6), 24–34 (2000)
63. C.M. Furse, Use of the FDTD method for broad band calculations of electromagnetic scattering and absorption from large, heterogeneous scatterers, PhD dissertation, University of Utah, 1994



**Cynthia M. Furse** is the Associate Vice President for Research at the University of Utah and Professor in the Electrical and Computer Engineering Department. Dr. Furse is a Fellow of the IEEE and the National Academy of Inventors. Dr. Furse's research focuses on sensors and antennas for biology and remote sensing, including sensors for location of faults on aging aircraft wiring and telemetry systems in the human body. She is a founder of LiveWire Innovation, a spin-off company commercializing sensors for locating electrical faults on live wires. Dr. Furse has taught electromagnetics, wireless communication, circuits, computational electromagnetics, microwave engineering, business for engineers, and antenna design and is currently a leader in the flipped classroom teaching method. She works to interest young students, including women and minorities, in engineering and routinely volunteers in Utah's K-12 schools.

She has received numerous research and teaching awards including the 2009 IEEE Harriett B. Rigas Medal for Excellence in Teaching.

# Chapter 16

## Crossed Viewpoints on Microwave-Based Imaging for Medical Diagnosis: From Genesis to Earliest Clinical Outcomes

Jean-Charles Bolomey

### 16.1 Foreword

This chapter deals with medical applications of microwaves and, more particularly, their use for diagnosis imaging. In this festschrift book dedicated to Prof. Magdy F. Iskander, the choice of this topic is far from being arbitrary and could be easily justified. Firstly, as far as I remember, it was undoubtedly a review paper, co-authored by him and Prof. Carl H. Durney, that attracted my attention in the late 1970s on the medical diagnostic capabilities offered by microwaves [1]. At that time, I was involved in the development of rapid near-field antenna measurement systems with modulated probe arrays, and I immediately realized how to take advantage of such a technology for medical imaging applications. Secondly, very fortunately, a few years later in the mid-1980s, Magdy spent a sabbatical leave in my laboratory, just at the moment when a prototype microwave camera was starting to be engaged for noninvasive temperature control during hyperthermia sessions. Beside this targeted application and, again, under Magdy's influence, the camera was also used in very early investigations at Institut Curie (Paris) on its possible use for not only detecting lung edemas (as previously demonstrated by Magdy and his group) but also localizing lung water content changes. On-phantom experiments confirmed that the microwave camera could offer such a localization capability that has not been clinically exploited, in the same way that, as explained later in this chapter, microwave imaging techniques are continuing to encounter major persistent difficulties in gaining their clinical acceptance.

Since the late 1970s [1], Magdy had already identified the deepest difficulties and prophetically warns us:

---

J.-C. Bolomey (✉)  
University Paris-Sud XI, Orsay, France  
e-mail: [jch.bolomey@gmail.com](mailto:jch.bolomey@gmail.com)



Among many factors contributing to slow development in this area of research is the complexity and lack of understanding of the nature of the interaction between electromagnetic waves and the human body. For example, attempts to estimate the sensitivity and the accuracy of a given procedure have frequently been frustrated by the complexity of the body structure and limitations on computer storage and expenses when numerical calculations were performed. This forced workers in this area either to base their conclusions on simple and idealized models with questionable adequacy and accuracy, or to conduct pilot experiments and ignore the ever necessary basic understanding. The situation is further complicated by the variability of the human body from person to person . . . .

Time has proven him absolutely right, and he has continued his well-targeted investigations on sensing thorax vital signs and developed a microwave cardiopulmonary stethoscope (see Chap. 18 and Ref. 2).

May this modest contribution, aiming to clarify the genesis of microwave diagnosis imaging and to explain its difficulties to gain clinical acceptance, testify to Magdy my friendship and express my sincere admiration for the so enthusiastic way he has been conducting his career.

## 16.2 Introduction

This chapter is dedicated to the possible use of microwave imaging for medical diagnostic purposes. The small number of related publications in medical journals demonstrates, if necessary, the low clinical acceptance of currently developed microwave imaging systems, despite a significant research effort deployed throughout the past 30 years. Testimony to this effort is the current COST European program dedicated to microwave imaging for medical applications (MiMed) [3] that brings together more than 200 academic and industry contributors from 30 participating and associated countries.

In the early 1980s, microwaves were already supposed to “offer promises as imaging modality” [4], but they are still today claimed to offer promises for a continuously increasing number of diagnostic scenarios. Hence, one key question is what exactly are microwaves promising for, and by when? In addition, one wonders if the current situation results from insufficient technological development of microwave imaging systems or if microwaves must be considered unable to do the job. Providing answers to such fundamental interrogations constitutes the main motivation of this chapter.

The status of microwave imaging for medical applications and its opportunities and challenges is regularly and abundantly reported in review papers (e.g., [5, 6]). Such reviews provide the instantaneous and not yet stabilized state of the art of this new recognition-seeking imaging modality. They are usually emphasizing the half-filled part of the glass. In this chapter, on the contrary, one is not so much concerned with its half-empty part than by looking how to fill it. Focusing exclusively on microwave-based diagnostic imaging did not prove sufficient for properly addressing the aforementioned questions. Rather, it appeared necessary

to enlarge the scope of investigation to take into account and fully understand the consequences of the duality of the medical imaging and microwave worlds.

On the one hand, looking back at the successful development of existing medical imaging modalities allows understanding of some of the specific reasons why microwave techniques have yet to gain clinical acceptance, despite their supposed comparative advantages and beyond their expected limitations. The comparison of their evolutionary timeline with those of microwave techniques reveals the trivial result that the latter has already gone through a much longer development. More constructively, it also offers some explanations for the delay and may suggest better strategies to fulfill clinical requirements.

On the other hand, considering other, more successful, applications of microwaves allows retrieval of the radar imaging and dielectric sensing roots of medical imaging, as well as identification of possible technological improvement opportunities and resources not yet fully exploited for medical diagnostic purposes. But overall, what this double-perspective analysis confirms is that a close interaction between imaging system developers and end users is necessary. The problem with microwave techniques is that they have not yet gained a sufficient relevance threshold to arouse interest of the clinical community and, hence, that they are unable to exploit its strong driving capability.

To begin the story of microwave-based medical imaging, two distinct periods can be conveniently considered. The first one consisted of preliminary investigations on samples or isolated organs to find the most promising imaging concepts compatible with the available microwave technology. These early stages of the story are usually ignored or forgotten, and yet, most of the current research is still prolonging this stage. For that reason, the chaining of the concepts considered for microwave diagnostic imaging during this period is explained, and major steps are identified at both hardware and software levels. This first period extended roughly from the end of the 1970s to the mid-1990s.

The second period started with the development of the first generation of operational imaging systems dedicated to early preclinical assessment. This period, which is still running, has been rich in advances at different levels, mostly due to a growing involvement of electromagnetic science and engineering communities which took advantage of drastically increasing computing power for system design and optimization, realistic numerical modeling for feasibility assessment, and new image reconstruction algorithms. Successive generations of equipment were developed for selected key applications and are still under evaluation in clinical centers. The global process aiming to introduce microwave-based imaging equipment in the clinical practice is analyzed. In light of the available information, some persistent difficulties are identified and the available resources to possibly overcome them are suggested.

This chapter is organized in four main sections. Section 16.3 deals with medical imaging in general. For the sake of comparison with microwave techniques, the timelines of X-ray, ultrasound, magnetic resonance imaging (MRI), and positron-emission tomography (PET) are briefly considered to emphasize the crucial role played by the clinical pull in the development of these modalities. In Sect. 16.4,

medical diagnosis imaging is considered as part of the widely diversified landscape of current applications of microwaves. It is shown how microwave-based diagnosis should be able to take advantage of advanced technologies developed for other microwave applications. Section 16.5 is a detailed presentation of ideas, concepts, and experiments that emerged at the genesis of microwave-based imaging techniques for medical applications. Section 16.6 is dedicated to the second period, which is still going on, with particular attention to the budget of *from computer model to patient bed* process currently engaged. A few examples are used to illustrate different targeted applications, objectives, technologies, and strategies. Finally, after some suggestions and recommendations, concluding remarks are given in Sect. 16.7.

## 16.3 On Medical Imaging, in General

### 16.3.1 X-Rays, at Birth of Medical Imaging

Medical imaging started in the late nineteenth century, when W.C. Röntgen inadvertently discovered X-ray, while he was conducting experiments on electrical discharges in gases. For this discovery, he received the first Nobel Prize in Physics in 1901. In December 1895, the radiography of Mrs. Röntgen's hand (Fig. 16.1a) showing distinctly the bone structure and her wedding ring undoubtedly constitutes the founding event of medical imaging [7]. The unbelievable possibility to see, noninvasively, inside the human body immediately impacted medical practices. Physicians put it to direct use, despite the fact that physicists were still unable to explain the nature of these newly discovered rays and, consequently, did not suspect their possible danger for patients and operators.

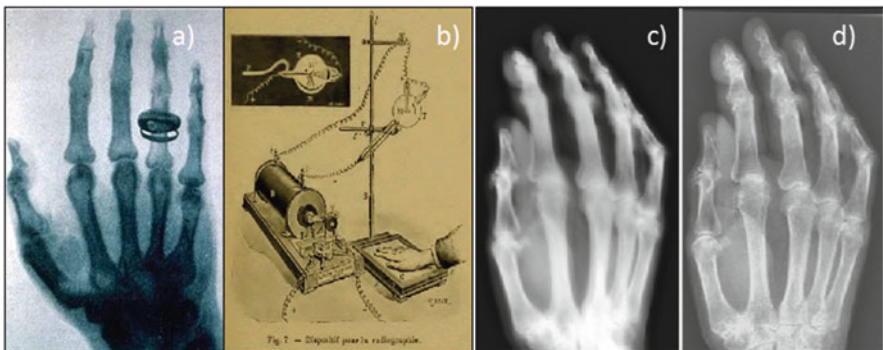


**Fig. 16.1** Hand X-ray radiography: (a) Mrs. Röntgen's hand (1895) [7], (b) typical X-ray arrangement for hand imaging (ca 1900) [8], (c) hand radiographies obtained from X-ray machine reassembled with original components (1896) and (d) with today's machine [9]

Remarkable is the fact that for obtaining radiographs with such explicit details, quite simple equipment was required (Fig. 16.1b): namely, a vacuum tube, its induction coil power supply, and a recording plate or a fluorescent screen. Even with such simple arrangements, the image quality was excellent. Figures 16.1c and d represent the same hand radiography obtained, respectively, with a more than century-old machine, rebuilt by assembling original components (1896), and a modern machine [9]. The quality of these two images looks surprisingly very similar, but the big difference is that the first one required an exposure time of 91 min, while the second one only needed 21 ms with an irradiation dose 1,500 times smaller! For the general public, the practice of X-ray imaging was rapidly popularized as the photography of the invisible [8]. The practitioners themselves empirically, but very efficiently, developed the X-ray technology. Equipment was ruggedized for transport in ambulances on battlefields during World War I for visualizing bullets and shrapnel in injured soldiers. Later, X-ray imaging machines were continuously improved, taking advantage of advances in solid-state detectors, electronics, digital technology, etc.

More particularly, the combination of mathematical algorithms, such as the Radon transform (1920) or the algebraic reconstruction technique (ART), with the calculation capability offered by newly appearing computers paved the way to computed tomography (CT) imaging. CT constituted an additional breakthrough revolutionary step in the evolution of medical imaging. G. Hounsfield obtained the first tomographic image of a human brain in 1971 with a scanner of Electric and Musical Industries (EMI), installed at Atkinson Morley Hospital in Wimbledon, London, a specialist neuroscience hospital. A. Cormack and G. Hounsfield received the 1979 Nobel Prize in Physiology and Medicine for the development of CT. Additional turning points in the CT history can be found in Ref. [10].

To conclude with what can be considered as a model success story, it is worth noting that the rapid and continuous development of X-ray imaging primarily resulted from the interest of clinicians, who served as powerful technology drivers for different applications. Today, X-ray imaging, radiography and CT scan con-foundedly, occupy approximately not far of 50% of the worldwide medical imaging market [11].

### ***16.3.2 Evolution Timeline of Medical-Imaging Modalities***

The quick development of X-rays is perhaps unique. For other imaging modalities, the evolution scheme may be more complex, and clinical acceptance requires a longer duration. However, a careful look at the history of several imaging modalities (ultrasound [12, 13], MRI [14], or PET [15]) shows that, even if the duration may be different, they follow almost the same evolution scheme. It is beyond the scope of this chapter to exhaustively consider all these modalities. For its relative similarity with microwaves, the case of ultrasound imaging is used to exemplify the timeline model shown in Fig. 16.2.

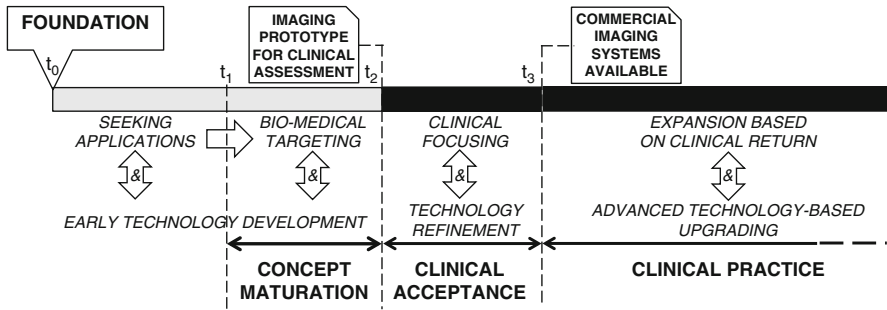


**Fig. 16.2** Typical evolutionary timeline of a medical imaging modality

At the start of the imaging process (time  $t_0$ ), there is usually what can be considered a foundational discovery, which may or may not be related to any clinical need. This discovery may be the result of a pure coincidence, as it happened for X-rays, but more often stems from a continuous effort of physical research conducted at a fundamental level, frequently awarded one or several Nobel Prizes later.

Following the foundation discovery, some ideas of practical exploitation emerge, thanks to appropriate source and sensor developments. Then, the evolutionary timeline involves three rather distinct but continuously connected periods. First, there is the concept maturation period: at time  $t_1$ , the moment arrives when, among all possible applications of the discovery, some biomedical applications are targeted. This targeting is achieved by means of preliminary investigations and feasibility assessment on living tissues, samples, organs, or animals. Successful proofs of concept based on numerical models and/or phantom experiments may result in early prototypes, which can be used for validating a diagnosis scenario on volunteers.

Second, the clinical acceptance period starts at time  $t_2$  to get preclinical returns for this particular scenario, after possible minor iterative modifications of the early prototype. In any case, this period requires the launching of long-term, large-scale, and multicenter trials involving sufficiently representative patient samples. As such, all the financial and administrative difficulties inherent to any certification and assessment campaign of a medical instrument are encountered during this necessarily long acceptance period.

Third, commercial machines are introduced in clinics at time  $t_3$ . Indeed, depending on the results obtained in the second phase, the new imaging modality may be considered as sufficiently validated for routine use. Its performance will be then continuously improved, thanks to clinical returns and by incorporation of available technological advances.

### 16.3.3 *Examples*

The case of ultrasound imaging, which shows some similarity with microwaves, constitutes a good example of the previous evolution scheme. A very detailed chronology of ultrasound technology development is available in Refs. [12, 13]. One can consider that the foundational event is the discovery of the piezoelectric effect (and its reversal) by Pierre and Jacques Curie in 1880. This effect was used in transducers to generate and detect ultrasonic waves in air and water. Its early applications were not at all medically oriented but rather motivated by underwater iceberg detection, especially after the sinking of the sealiner Titanic in 1912. In addition, sonar (sound navigation and ranging) was invented by R.A. Fessenden for detecting submarines during World War I and later extensively developed during World War II, thanks to P. Langevin's work on hydrophones.

As suggested by S. Sokolov in 1928, another application of ultrasound technology was flaw detection in metal structures. Later, in early 1940s, time-of-flight supersonic "reflectoscopes" were developed and patented for nondestructive testing and evaluation (NDT/NDE) purposes. They were later used for preliminary medical assessments.

The ultrasound maturation period, as previously defined in Sect. 16.3.2, did not start until the late 1930s, with the first attempts to use ultrasound in medical diagnosis. In 1946, brain imaging investigations were undertaken at 1.2 MHz by K.T. Dussig [12], but they failed due to difficulties related to the skull envelope, revealing the difficulties of coping with bone tissues. A few years later, an extensive study of medical applications demonstrated the detection and localization of foreign objects in the human body.

Finally, it was only in the mid-1950s that the clinical acceptance period really started, with ultrasound examination for obstetrics and gynecology. Due to ultrasound millimeter-ranging wavelengths, ultrasound images, like X-rays, enabled reasonably clear and direct vision of anatomical structures and organs. In addition, differently to X-rays, ultrasound appeared to be a safe way to perform observation inside the human body.

From 1963, commercial imaging systems providing two-dimensional images became available on the market for clinical use. The clinical use was stimulated by a strong technology push resulting from an acute competition between small companies. A prompt and continuous integration of innovative technologies resulted in improved spatial resolution and faster imaging process using mechanical (1969) or electronic (1972) beam scanning [13]. Accordingly, new functionalities such as real-time or Doppler imaging for visualizing blood circulation and cardiac activated enlarged the range of clinical applications.

Globally, the ultrasound medical imaging maturation and the clinical acceptance periods extended roughly 15 (1940–1955) years and less than 10 (1955–1963) years, respectively; about ten years (1963–1973) were then required to develop more

sophisticated ultrasound systems, such as those used today in the clinical practice. These now represent about 25% of the medical imaging market [11].

The same general development scheme can be discerned for two other major *advanced* imaging modalities, namely, MRI [14] and PET [15]. These occupy about 25% of the medical imaging market [11]. Even if the foundational discovery and duration of their concept maturation period differ from those of ultrasound imaging, the duration of the clinical acceptance period corresponding to the time elapsed from early prototypes to clinical practice did not exceed a dozen years.

### **16.3.4 Discussion**

To summarize, some important, even commonsense, observations on the development of existing medical imaging modalities can be made. First, attracting the interest of the medical community requires the demonstration of a minimum image quality and clinical effectiveness. Second, as soon as new technology entered clinical practice, the developments of X-rays, ultrasound, and MRI modalities were rapidly supported by strong clinical motivation. The clinical practice during the first 10 years improved the performance of imaging systems and diversified their use. Such a clinical pull has been all the more effective that it was well prepared by early investigations conducted during the maturation period. Third, the imaging systems have been rapidly improved thanks to both a closed interaction loop between engineers and clinicians and a strong competition between many medical imaging companies. This resulted in short-term integration of technological advances, as and when they became available. Particularly, computers have offered a decisive breakthrough opportunity enabling the development of tomographic modalities.

## **16.4 On Microwave Applications, in General**

### **16.4.1 Panorama of Microwave Applications**

In 1887, H. Hertz conclusively proved the existence of electromagnetic waves, with experiments conducted at submeter wavelengths, corresponding to the lower-frequency part of the microwave spectrum spanning 300 MHz to 300 GHz or, equivalently, 1 m to 1 mm wavelength [16]. But, Hertz did not envision any practical applications of electromagnetic waves and died seven years later.

Except for additional experiments conducted by Hertz and some contemporary physicists at higher frequencies to confirm the light nature of electromagnetic waves (up to 60 GHz, by J.C. Bose [17]!), the microwave frequency spectrum was rapidly abandoned by Marconi and other engineers for developing long-distance signaling applications [18]. Indeed, much larger wavelengths were required to carry enough

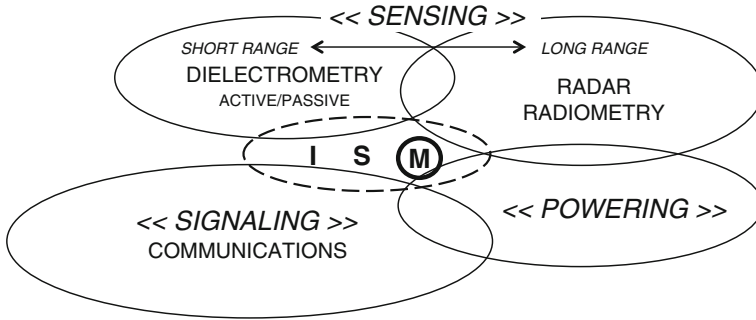


**Fig. 16.3** Simplified panorama of microwave applications: industrial scientific medical (ISM) applications at the crossroad of signaling, powering, and sensing technologies

energy in order to overcome the limitation of the signaling distance by the Earth's curvature.

The spark-gap transmitters used in early experiments were used for alternators at the beginning of the twentieth century. Then, boosted by the invention of electronic tubes, the signaling frequency was continuously increased, a trend that continues to this day. Microwaves came back on the stage a few decades later for echolocation. Today, their applications have been widely diversified as illustrated by Fig. 16.3. Microwaves are used for three main categories of sometimes overlapping applications: (i) signaling, (ii) powering, and (iii) sensing, according to the manner their at-a-distance action capability is exploited.

#### 16.4.1.1 Signaling

By the way, signaling was the term used for early telegraphy. It was then extended to wireless transmission and, in this chapter, means communications in the current usage of the word. Signaling is undoubtedly the predominant microwave application. During the post-World War II period, microwave technology, which was initially developed for radar applications, has been progressively used for long-distance signaling, such as line-of-sight point-to-point terrestrial and space communications.

More recently, microwaves have found use in supporting wireless communication networks with nomadic devices, accommodating either large or short distances, in complex multipath and variable environments. The current development of 5G networks all along a wide part of the microwave spectrum, from a few GHz to about 70 GHz, constitutes a good example of the key role played today by microwaves. It also illustrates the continuous frequency growth of electronic technology transmission systems observed since the beginning of the twentieth century. The development of current wireless networks, still unimaginable a few



decades ago, has required huge advances in microwave technology, particularly in terms of miniaturization, as well as innovative signal processing techniques, including multiple-input multiple-output (MIMO) communications [19]. This application catalogue would not be complete without mentioning communication-based geographical location, whose first Global Positioning System (GPS) was operated in 1995 [20].

Signaling technology is increasingly used for communication-based sensing. Wearable and implanted sensors can wirelessly communicate within smart sensing and control grids dedicated to general public applications and especially to e-health monitoring purposes [21].

### 16.4.1.2 Powering

Started in 1900 with N. Tesla's attempts to build a worldwide wireless power broadcast system [22], wireless power is another application of electromagnetic waves. This power can be used either for feeding passive electrical or electronic circuits or to be locally dissipated at a selected place in the propagation medium. A very interesting review of the history of power transmission by radio waves is given in Ref. [23]. More particularly, it explains how this application had to wait a decade after World War II before recovering significant interest. For instance, the current interest in wireless-powered flying objects (already prophesized by N. Tesla!) was initiated in the beginning of the 1960s with early microwave-powered helicopters. Similarly, the solar power satellite (SPS) concept introduced in the late 1960s to transmit the solar energy captured by solar panels onboard a geostationary satellite toward the Earth by means of a microwave beam remains a relevant topic in the context of clean energy production. Today, wireless power transmission (WPT) and power harvesting technologies constitute a growing field of interest due to their application for autonomous wireless devices and connected objects, such as those involved in the Internet of Things (IoT) or radio-frequency identification (RFID) tags, more particularly for sensing applications (e.g., Refs. [24, 25]).

Another aspect of microwave powering concerns industrial, scientific, and medical (ISM) applications where some in-depth thermal effect is required for material processing (drying, polymerization, sterilization, etc.) [26] or therapeutic treatment (hyperthermia, surgical ablation, etc.) [27, 28]. Material processing requires high power, whereas medical applications limit power levels for safety. There are standard regulations, as in the case of wireless communications. The exploitation of thermal effects induced by microwaves is used for a while for ISM applications but represents a rather limited field of activity when compared to signaling, except for the domestic microwave oven market.

A very brief summary of how microwave hyperthermia was introduced into clinical practice is instructive. According to an exhaustive review dedicated to medical applications of microwave energy [29], it appears that, at the end of the nineteenth century, heating living tissues was already recognized as beneficial for

health and for treating some diseases. Marked improvement observed in the health of patients suffering from arthritic, rheumatic, and gouty conditions stimulated the practice of diathermy treatments with high-frequency currents. With more or less happiness, overenthusiasm, lack of precautions, and lively debates on clinical results, diathermy entered the clinical practice that, in return, helped to improve the equipment efficiency.

After World War II, centimeter waves were used for focused heating in deep tissues while avoiding excessive skin heating. Furthermore, applicators consisting in reflectors fed by monopole antennas were considered to offer more flexibility than previous inductive or capacitive contact applicators. In 1947, the Federal Communications Commission (FCC) allocated frequency bands dedicated to ISM applications. The first commercially available hyperthermia equipment operating at 2.45 GHz was fabricated by Raytheon and called *Microtherm*. It was introduced for oncology applications, while clinical research tried to identify the best applications and optimize related protocols. From the mid-1970s, encouraging clinical results attracted the attention of the oncology community in using hyperthermia, either alone or, still better, in combination with radio- and chemotherapies.

However, the interest for hyperthermia reached a plateau in the late 1980s. One technical reason was the difficulty of controlling temperature elevation during hyperthermia sessions. Another was that hyperthermia was often considered as a last-chance modality and used only in desperate clinical situations which delivered disappointing results. Today, hyperthermia has had a renewal of interest, mainly due to a better patient selection and significant improvement of treatment planning, even though noninvasive thermometry remains an open challenge. Compared to early expectations, microwave hyperthermia is sparingly used, mostly as a supplement to other conventional modalities.

In an extension of the galvanic cautery practiced since the eighteenth century, the powering capabilities of microwaves have been recently exploited for surgical ablation [30]. Since the mid-1990s, microwave ablation has developed rapidly and found a niche in surgical practice.

### **16.4.2 Sensing Applications**

Microwave sensing has two rather different aspects, depending on the sensing purpose and the operating distance. Radar (radio detection and ranging) systems are usually dedicated to long-range detection and localization of discrete targets. Dielectric sensing systems include a variety of sensors to determine some constitutive parameter of targets located at short distance, or even in contact with them. These sensing applications are called *dielectrometry*, due to the fact that they are intimately, quantitatively, or qualitatively related to the direct or indirect measurement of the dielectric properties of the targets.

### 16.4.2.1 Radar

The first significant application of microwaves, which led to microwave imaging, was echolocation in a broad sense. In 1904, C. Hülsmeier, using the spark-gap/coherer technology previously used by the pioneers of wireless transmissions, successfully developed his *telemobiloskop* [31], the earliest boat echolocator system, to compete with or complement lighthouses and steam pipes under foggy weather conditions. But it was too early, and nobody (navy, insurance companies, etc.) was interested, despite its 3 km detection range. Later, power electronic tubes were progressively introduced for radar-like systems. World War II offered a unique opportunity for the microwave technology to be actively developed by many conflicting countries.

In typical radar applications, the sensing task consists of detecting and localizing distant targets, typically boats and aeroplanes, located in a “free-space” environment. After World War II, radar technology was significantly advanced, but its applications are far too many to be included here. However, two very significant advances deserve special attention because of their relevance to imaging.

These advances are: (i) phased arrays for electronic scanning, beam forming, or focusing and (ii) synthetic aperture radar (SAR) processing techniques for radar imaging with high spatial resolution. Beyond their impact on typical radar applications, these imaging-oriented techniques explain the rapid development, in the late 1960s, of air- and spaceborne active (radar) or passive (radiometer) microwave systems for Earth and atmosphere remote sensing (e.g., Ref. [32]). In such applications, radar augmented traditional visible and infrared observations. Microwaves allow all-weather observation from satellites because microwaves can penetrate through clouds. Furthermore, due to the specific scattering and emission properties of natural media at microwave frequencies, radar and radiometers can provide a broad variety of relevant geophysical parameters such as soil moisture content, ice extent and concentration, vegetation, rain and snow falls, temperature profile of atmosphere, etc.

Microwave sensing and penetration capabilities have also been progressively exploited in more complex echolocation scenarios. Anti-collision radars for cars constitute a current relevant example involving complex multipath environments. Microwaves are also used for shorter-distance sensing in still more complex environments. Since the late 1980s, ground-penetrating radar (GPR) (e.g., Ref. [33]) are being used for military applications, e.g., for detecting and locating unexploded ammunitions, buried landmines, and tunnels. Civilian companies use GPR for mapping pipes and utility lines under city streets. With through-the-wall (TTW) radar (e.g., Ref. [34]), microwaves are used to penetrate construction materials and image building interiors to detect and possibly identify human activities and/or moving objects. Still more recently, mm-wave scanners are used to scan passengers for security checks at airports or railway stations. Such scenarios dealing with hidden targets embedded in inhomogeneous media require a multicomponent approach involving much more than electromagnetics expertise. The data processing schemes must account for complicated propagation regimes.

In most of the previous applications, radar data are displayed as constellations of spots for distinct targets or terrain maps, rather than as images *stricto sensu*. But, in the early 1970s, the first attempts to produce images, in the optical sense of the word, were inspired by optical and acoustical holography techniques. These used only amplitude measurements, phase measurements being complicated at microwave frequencies. E.N. Leith bridged radar data processing with holography, particularly for multifrequency and multi-angle analysis [35]. A review paper by N. Farhat and G. Tricoles [36] provides a complete review of the state of the art of microwave holography in the late 1970s, indicating a number of possible short-range imaging applications including radar target mockup imaging, antenna metrology and radome diagnostics, detection of weapons hidden in opaque media, or noninvasive evaluation and detection of defaults in materials. As shown later in Sect. 16.5, microwave-based medical diagnosis imaging finds part of its roots in the know-how gained with radar and holography techniques.

#### 16.4.2.2 Dielectrometry

Microwaves have also been exploited for quantitative measurement of relevant quantities of materials or biological tissues. In the microwave spectrum, dielectric properties may show specific sensitivity to several parameters of practical relevance. Many investigations have been dedicated to the dielectric characterization of materials. Different setups have been used, based on S-parameter measurement with samples introduced in a transmission line, a waveguide, or a cavity. Noninvasive measurements have also been conducted with open-ended lines or waveguides. The rapid development of vector network analyzer (VNA) instrumentation in the 1960s has greatly supported such measurement techniques and contributed to increasing their accuracy thanks to efficient computer-controlled calibration.

Accordingly, the dielectric properties of many materials of practical relevance have been measured and are available. Mathematical models have been developed to model their variation with frequency and/or some other relevant parameter. For instance, due to the well-known dependence of the relative permittivity on the water content, microwaves can be used for moisture measurements, a key issue in many industrial processes. Moreover, as already mentioned, microwaves can penetrate most opaque materials, except conductors. Microwave sensors are particularly useful for noninvasive measurements of such parameters for ISM applications (e.g., Refs. [37, 38]).

Their development started in the 1970s, when sensors of any kind became necessary on production lines for controlling and steering manufacturing processes. Microwave sensors were developed for various applications consisting either in a quantified measurement of the thickness or the moisture of a layered product or for qualitative visualization of faults such as knots in sawed timber or fatigue cracks in materials, gas analysis, etc. The advantages of microwave sensors include: no need for mechanical contact, safety (nonionizing radiation), rapidity, and noninvasiveness. On the contrary, recognized drawbacks are a possible lack of

specificity resulting from a sensitivity to more than one parameter, the need for separate calibration for different materials, the near-impossibility to have general-purpose sensors, and low spatial resolution at frequencies in the GHz range. It may be worth noting that these are almost the same pros and cons for microwave-based medical sensors and imaging systems.

### 16.4.2.3 Sensing for Medical Applications

In the late 1970s, the first microwave-based diagnostic sensors for medical applications were directly inspired by simple contact reflection/transmission arrangements similar to those previously used for industrial applications. As such they exhibit the same kind of advantages and limitations, with additional specific aspects resulting from the living nature of the *materials* to be tested and more, particularly related sensitivity and specificity issues. For medical diagnosis, sensitivity refers to the detection capability of small features, whether normal or pathological, while specificity deals with the ability to discriminate between these two situations. From this viewpoint, microwave sensing is directly, but not uniquely, dependent on the dielectric properties of living tissues. Indeed, the organs under investigation are *seen* according to properties that directly govern the tissue attenuation and wave velocity (or equivalently, the wavelength).

In the microwave spectrum, relative permittivity is strongly impacted by the resonance of the water molecule. Hence, living tissues are usually categorized as high-water content (HWC) (muscle, blood, brain) and low-water content (LWC) (bone, fat) tissues. Because of the large relative permittivity of water, HWC and LWC tissues exhibit a large dielectric contrast, significantly larger, for instance, than density contrasts for X-ray imaging. Early attempts for dielectric characterization of living tissues date back to the 1950s [39]. Correlation between dielectric permittivity and various physiological parameters as well as possible pathologies were investigated, particularly on lung and brain tissues. More generally, the dielectric data for living tissues are pretty well documented in the frequency range used for diagnostic purposes that roughly extends from 1 to 30 GHz (e.g., Refs. [40, 41]). Many tables are currently available that give measured and/or modeled relative permittivity of living tissues, in vitro or in vivo and under some pathological conditions. Their change with frequency and biological/physiological factors may be more or less accurately depicted by means of mathematical/physical models. However, due to inaccurate measurement or inconvenient preparation of the samples under investigation, the robustness of these results may have been criticized and sometimes led to unrealistic modeling during proof-of-concept investigations.

Practically, in the 1970s, microwave sensors consisted in at-a-distance or contact reflecting or transmitting sensor arrangements for detecting the movement of organs [42] or changes of tissue composition such as for lung [43] and brain [44] edema. These two examples of test cases that exploit the sensitivity of the relative permittivity to water content have inspired later investigations for imaging purposes. So far, none of these applications were really oriented toward medical imaging applications (despite the title of Ref. [44]).

### **16.4.3 Discussion**

The simplified panorama of microwave applications suggests some straightforward conclusions. Firstly, ISM applications only represent a very minor part of the global microwave activity, especially when compared to communications or radar applications. For ISM applications, microwaves have to compete with other well-respected modalities, in contrast to communications radar applications where they are an absolute monopoly. Nevertheless, despite this competitive situation, and thanks to their specific propagation regimes and sensing capabilities, microwaves have already successfully found some sensing niches for complementing or replacing more conventional optical, infrared, X-ray, or acoustical sensing modalities nonexclusively.

Microwave-based diagnostic ISM imaging suffers the same competitive handicap with respect to existing medical imaging modalities, aggravated by a last-comer effect in the clinical practice. But, as with other ISM applications, medical imaging is located at the crossroad between signaling, sensing, and powering technologies. As such, it should be able to fully profit from these technologies. It is shown in the following that this is not yet the case. For instance, current developments in wireless technologies and related applications are still far from impacting microwave-based imaging for medical diagnosis.

As a general trend, microwaves are appreciated for their penetration in opaque media, as long as their spatial resolution capability is maintained compatible with the considered application. This is a key issue for diagnostic imaging, and it remains despite demonstrating that contrasts are sufficient medical diagnostic modalities.

## **16.5 Concept Maturation for Microwave-Based Diagnosis**

### **16.5.1 Prologue**

This section aims to relate why and how microwave-based imaging technology has been oriented toward medical applications since the beginning of the 1980s. As already explained in Sect. 16.4.1, it is thanks to the early radar engineering viewpoint, initially dedicated to wireless signaling and echolocation, that microwaves found their way to imagery a few decades after Hertz's experiments. In that sense, one may observe some indisputable similarity between radar and microwave imaging, on the one hand, and sonar and ultrasound imaging, on the other hand. Both ultrasound and microwave cases started with echolocation before finding industrial NDT/NDE applications and, finally, medical imaging perspectives.

A schematic timeline of microwave-based medical imaging is given on Fig. 16.4. It provides the different development steps in terms of reconstruction algorithms, imaging system geometry, and applications. At a glance, the concept maturation

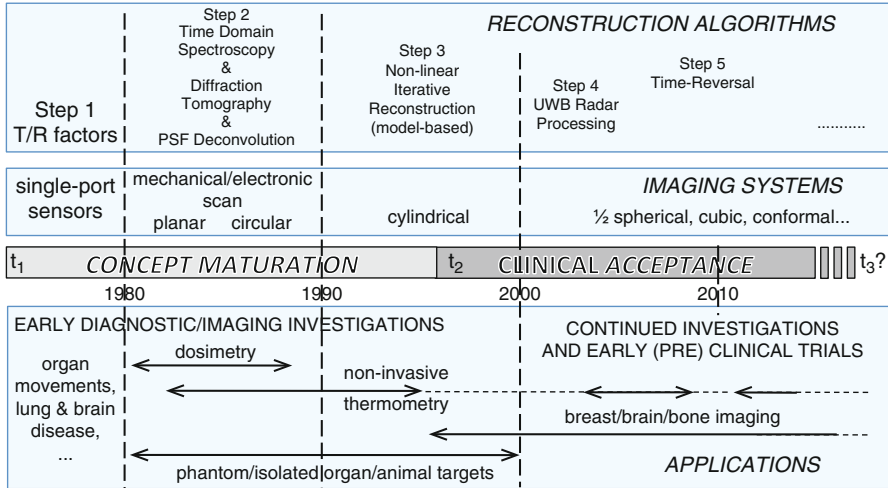


Fig. 16.4 Evolution of microwave imaging systems for medical diagnosis

started from the late 1970s ( $t_1$ ) with early medically oriented investigations, and imaging *stricto sensu* did not show up until the 1980s [28]. This first period extended until the mid-1990s ( $t_2$ ) with the development of the first few operational prototypes. Then a second period for gaining clinical acceptance was initiated. Today, early (pre) clinical trials are in progress, and the clinical practice period ( $t_3$ ) is still waiting for the results of these trials. That globally means that, without achieving the transfer to clinics and lasting over more than 30 years, the timing of microwave imaging is already comparatively significantly longer than for ultrasound and even any other previous imaging modality.

### 16.5.1.1 Reconstruction Algorithms

As compared to X-rays, microwaves suffer much more complex propagation mechanisms inside living tissues with large relative permittivity. While X-ray sources produce a well-collimated thin beam that propagates along a linear path, whatever the tissues encountered, microwave beams can no longer be so tightly collimated, and their spatial extent strongly depends on the tissue distribution. In X-ray systems, detectors are only sensitive to the response of tissues located on a known linear beam trajectory. As a result, the tissue structure can be easily deduced from single projection imaging (radiography) thanks to its shadowing effect, or tomographic density map can be simply obtained by solving a system of linear equations [1]. On the contrary, with microwave systems, a receiving antenna is located in a multipath environment: indeed, it collects the contributions stemming from a broad and poorly known region in the target. In these circumstances, single

projection imaging becomes useless, and the tomographic reconstruction becomes a much harder nonlinear problem [1].

To face such multipath configurations, time-domain spectroscopy (TDS) has been suggested for isolating the most direct ray between the transmitting and the receiving antennas [45]. A second simplified approach to take into account diffraction effects has consisted in neglecting multiple scattering inside tissues. Based on this simplified assumption, the image reconstruction remains linear. So-called point spread function (PSF) deconvolution or diffraction tomography (DT) algorithms [46], inspired by ultrasound imaging, enable images of noninteracting “hot spots.” Reconstructed images are *qualitative*, because they only provide a picture of hot spot distributions, possibly including artifacts stemming from neglected interactions from multiple scattering.

On the contrary, the *quantitative* reconstruction of the relative-permittivity distribution inside the target requires solving a complicated, computationally very demanding, nonlinear, and ill-conditioned inverse scattering problem [47]. Solving such a problem is based on an iterative reconstruction of a model representing the imaging scenario and providing the best possible match with the acquired data, using all a priori available propagation and scattering phenomenology information.

Next, radar-based image reconstruction was considered. Like DT, radar processing aims to retrieve the contribution of the different points or areas in the target, considered as isolated in a homogeneous medium and free from mutual interactions. As such, it provides only qualitative images. Later, inspired by ultrasound, time-reversal algorithms have been introduced to help radar imaging account for inhomogeneous propagation media. As shown in Sect. 16.6.1.1, the practical implementation of all these reconstruction algorithms has benefitted from many different processing options [6].

### 16.5.1.2 Imaging Systems

The choice of the operating frequency band is a key point for imaging systems. It must account for the required penetration depth and spatial resolution. As a general trend, spatial resolution is improved with frequency, but, at the same time, attenuation is also increased, resulting in decreasing penetration depth. For living tissues, the penetration/spatial resolution compromise is obtained at frequencies of the order of a few GHz [48] but may significantly differ according to the image reconstruction method and the anatomical configuration. For instance, in the case of breast imaging, quantitative and qualitative images are achieved from operating frequencies lower and higher than 3 GHz, when using inverse scattering or radar data processing, respectively.

In the continuation of the first simple reflection/transmission arrangements providing only spatially averaged information, multifrequency and/or multi-view data acquisition schemes were required to obtain the desired spatial resolution, thanks to tomographic imaging procedures. After using the mechanical scan of a



single probe antenna, the investigation time has been drastically reduced by using probe arrays, either totally fixed or partly translated/rotated.

Hence, different array geometries have been considered, depending on the imaging scenario, the shape, and the dimensions of the area of interest. Almost all simple coordinate systems have been used, including simple plane, circular, cylindrical, hemispherical, and conformal coordinate systems.

### 16.5.1.3 Applications

Microwave imaging was initially motivated by dosimetry applications but was rapidly re-oriented toward medical applications. Figure 16.4 schematically shows how experiments on phantom, isolated organs of animals have resulted in targeting supposedly clinically relevant applications. It is shown, in the following, that these suppositions were most often severely underestimated the difficulty of the task. What was indeed missing was a comprehensive and quantitative understanding of the sensitivity of tissues to pathological factors. This lack of knowledge, largely resulting from inaccurate measurements of dielectric properties, has constituted a serious drawback for realistically assessing sensitivity/specificity issues. It may also have resulted in questionable proofs of concept, when exclusively based on numerical modeling. Breast, brain, bone, and lung imaging constitute some examples of topics that are currently investigated (see Sect. 16.6.2).

## 16.5.2 From Dosimetry to Imaging

It is precisely at the end of the 1970s that, for the first time, microwaves were solicited for medical imaging. Surprisingly, the initial motivation of these early investigations was dosimetry, a slightly different topic. Dosimetry aims to quantify the effects resulting from exposure to microwaves and, ultimately, seeks for the dose-response curve. During their investigations on dosimetry at the Walter Reed Army Institute (WRAI, Silver Spring, MD, USA), L.E. Larsen and J.H. Jacobi rapidly understood that microwave imaging was relevant to their dosimetry project. They were convinced that microwaves constituted, as they wrote, “the best hope for non-invasive dosimetry analysis of bio-systems exposed to microwave radiation” [49]. On the one hand, dosimetry considers microwaves as an *effector*, which may induce some modification of the functionalities of living tissues and organs. But, alternatively, microwaves may be seen as a *sensor* of functionalities and accordingly be used for diagnostic imaging.

This explains that the impact of the images produced by Larsen and Jacobi has largely overpassed the framework of their initial dosimetry project and can be now considered as the founding triggering event of the research devoted to current microwave-based medical imaging.

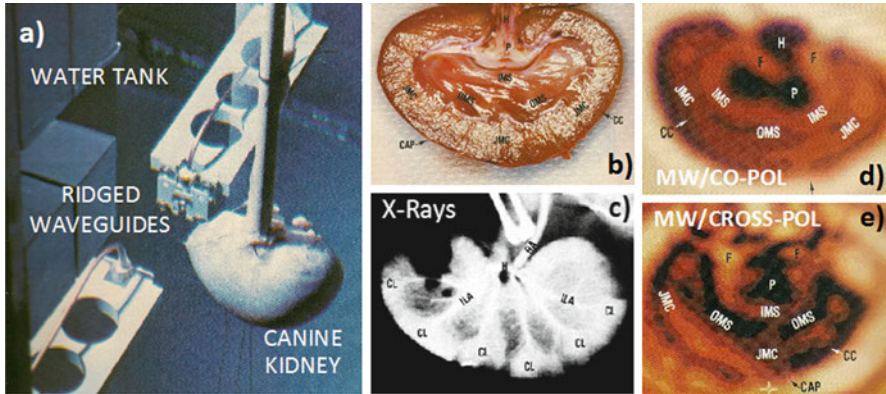


**Fig. 16.5** Early experiment at WRAI: raster scan arrangement for canine kidney imaging (a), canine kidney anatomical cut (b) and X-ray image (c), microwave images in co- (d) and cross-polar (e) at 3.9 GHz in water (from Ref. [50], © 1986 IEEE)

For its innovative aspects, the WRAI program deserves some attention. Many of its main features are still currently exploited. The basic idea was to visualize absorption in living organs, a relevant parameter for dosimetry assessments. Canine kidney was selected as a favorable test case for its soft (no bone) constitution and high water content. The experimental protocol consisted in a simple raster scan arrangement, where the transmitting and the receiving antennas were simultaneously translated on two parallel planes on each side of the organ under investigation (OUT) immersed in a water tank [49, 50].

Figure 16.5a shows the ridged waveguide antennas and the kidney, whose anatomical cross section and X-ray radiography are given in Figs. 16.5b and c, respectively. The kidney was supported by a tube allowing its perfusion to be measured on a grid of  $64 \times 64$  points spaced by 1.4 mm. After proper interpolation, the resulting 2D plot of the transmission coefficient between the two antennas formed an image revealing the internal structure of the kidney, as shown in Figs. 16.5d and e with typical examples of co-polar and cross-polar images obtained at 3.9 GHz.

The publication of these photos produced a strong effect, not only due to their unexpected mm-sized spatial resolution at such a frequency but also for their biological significance, as carefully argued by Larsen, a medical doctor. Such a good spatial resolution was the result of immersing the kidney in water whose relative permittivity is close to 80 at the operating frequency. As a result, the wavelength at 3.9 GHz is decreased from about 77 mm in air to 8.5 mm in water. The antenna dimensions are reduced by the same ratio (Sinclair's similitude theorem). Globally, using such an immersion technique, similarly used in optics with immersion microscopes, provides three major favorable effects as compared to the case where the organ would have been located in air: (i) the improvement of the spatial resolution, approximately estimated at one-half wavelength, (ii) less

reflection at the organ boundary and, hence, more microwave power is penetrating in the organ, and (iii) strong attenuation of parasitic multipath propagation outside the organ thanks to the few dB's/cm absorption loss of water. Further reduction of parasitic multipath may be obtained thanks to time-domain spectroscopy (TDS), by sweeping the frequency of the microwave interrogation signal [45]. TDS provides a possibility to select the *most direct path* contribution and, to some extent, to consider the wave propagating between both transmitting and receiving antennas as a linear ray. This was supposed to pave the way for adapting the X-ray tomographic reconstruction algorithms to microwaves.

However, a major drawback of these experiments was their long durations, approximately 4.5 h, with resulting difficulties in maintaining the organ properly perfused. There was also a possible drift of the instrumentation. Accordingly, reducing the time required for collecting the data was considered as a priority for a thorough investigation of this new imaging protocol, either on isolated organs or, a fortiori, on the human body. More particularly, due to their simple transmission aspect, these early experiments on isolated organs did not take into account for the complex tissue surroundings and the resulting shadowing effect.

It is worth noting that the computer power available in the early 1980s did not allow for modeling complex anatomical structures and that, consequently, the only possible approach for dealing with them was experimental. Naturally the idea arrived that, for observing an organ embedded in a complex environment, microwave tomography could be the good solution, as it was for other imaging modalities. The next section describes the different tomographic options, which were successively considered.

It is important to point out that, from the beginning of its research program on microwave dosimetry and related imaging issues, the WRAI supported basic research in the field of dielectric characterization of living tissues, more particularly in the difficult context of isolated perfused organs, to determine the effect of different parameters such as temperature and blood flow rate. The objective was to see up to what extent it was possible to use the relative permittivity as a calibrated marker of such parameters.

### ***16.5.3 From Projection to Tomography***

In their original simple transmission experiment between two aligned antennas, L.E. Larsen and J.H. Jacobi obtained the equivalent of microwave projection radiography, built pixel by pixel, thanks to a mechanical raster scan. Tomography requires more complicated data acquisition schemes. The first solution could have been to use the same plane-to-plane transmission arrangement but to dissociate the movement of transmitting and receiving antennas: for instance, the receiving antenna could have been scanned over its probing surface for each successive position of the

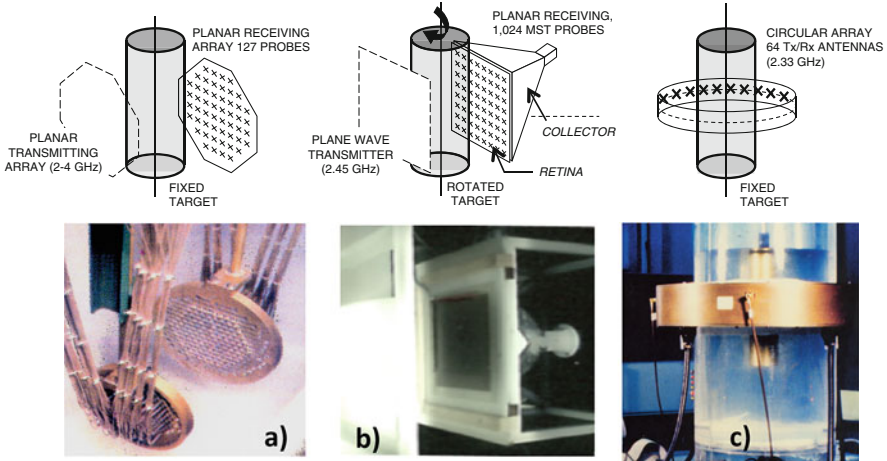


**Fig. 16.6** Early 1980–1990 microwave water-immersed probe array systems for medical imaging. (a) Planar transmit/receive arrays of cavity-backed slot antennas (151Tx/127Rx): sampling distance, 14 mm; frequency range, 2–4 GHz; PSF at 3 GHz; Trans. 7/6 mm; axial, 16 mm (from Ref. [51], © 1986 IEEE). (b) Planar receive array of MST probes, printed diode-loaded dipoles ( $32 \times 32$ ): sampling distance, 7 mm; frequency, 2.45 GHz; PSF; Trans. 7/7 mm; axial, 25 mm [52]. (c) Circular transmit/receive array of water-filled horn antennas (64 Tx/Rx): diameter, 25 cm; frequency, 2.33 GHz [53]

transmitting antenna. It is clear that such a solution was unacceptable as it would take too long. This naturally led to considering using transmit and receive arrays whose two arbitrary antennas can be individually addressed for rapidly measuring their transmission coefficient, as required by tomographic multi-view imaging. In passing, the possibility of focusing both the transmitting and/or receiving arrays on the same point is equivalent to confocal microscopy in optics. The objective is to obtain a narrow field depth in the OUT and, accordingly, to be able to analyze it slice by slice.

Figure 16.6a shows the water-immersed arrays developed at the WRAI [51]. Each antenna was connected to the source or the receiver via a set of electromechanical switches. The total measurement time was on the order of minutes per frequency, compared to the 4.5-h duration with the first mechanical raster scan system. The bandwidth was 2 to 4 GHz. At mid-frequency, the PSF that represents the response to a point source and, hence, defines the spatial resolution extends about 7 and 16 mm in transverse and axial directions, respectively, for a confocal imaging mode. At the same time, the capability of DT-based reconstruction was starting to be investigated on simple-shaped objects [46].

Surprisingly, all these efforts, well documented in Ref. [49], did not result in any published result of organ imaging, still leaving open the question of if the limited clinical application was due to technical problems, unsatisfactory results, or lack of financial support.

### 16.5.4 Perfused Organ and In Vivo Preliminary Investigations

Stimulated by the first images produced by the WRAI, another probe array system was developed at Supelec (France), with the primary objective to drastically reduce the acquisition time while maintaining a high spatial sampling rate, at acceptable cost and complexity. The modulated scattering technique (MST), recently implemented on rapid near-field antenna measurements setups, was used [52].

Figure 16.6b shows an MST-based setup consisting of the combination of an array of diode-loaded dipoles (the retina) placed in front of a receiving horn antenna (the collector). A fast field record on the retina is obtained by successively modulating the probes, via on-off switching of their loading diodes, without any need for a microwave multiplexer. A 32-element linear receiving array of dipoles for water-immersion operation at 2.45 GHz was first designed (Fig. 16.7a). It was used for sensitivity assessment and preliminary investigations towards true tomography imaging of isolated organs, namely, pork and horse kidneys [54, 55].

Indeed, a fast measurement on a line, combined with translation and rotation of the OUT, enables a full tomographic multi-view analysis. For eight views, the global duration of the data acquisition was still comparable with that of the single-view raster scan at WRAI, but with the major difference that tomographic reconstructions were possible.

As an example, DT algorithms were employed to produce the cross-sectional images shown on Fig. 16.7b. These reconstructed images do not show the same qual-

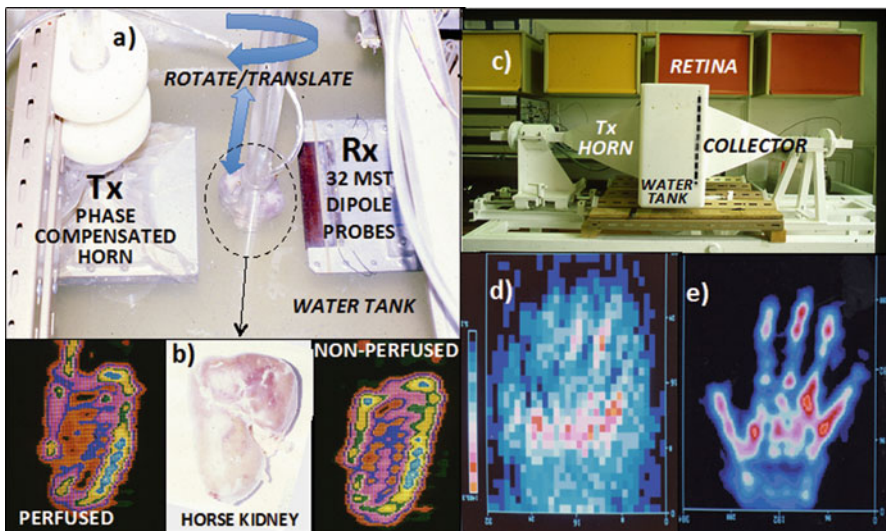


**Fig. 16.7** Diffraction tomography and MST-based imaging at 2.45 GHz: (a) linear MST sensor array [50], (b) isolated horse kidney tomographic images (eight views, DT reconstruction algorithm) [52], (c) 2D MST-based planar microwave camera [49], human hand: (d) before, (e) after one view of DT reconstruction

ity as previous WRAI images, probably mainly due to the imperfectly controlled movement of the kidney during its rotation. But the images are clearly sensitive to the perfusion of the liquid inside the tissues and its temperature.

To speed up the measurement and minimize OUT movements, a 2D planar camera was developed. The receiving probe array was designed according to the MST technology previously developed for fast antenna near-field measurements, duly modified for water-immersion operation at 2.45 GHz [52]. The array of  $32 \times 32 = 1024$  diode-loaded printed dipoles was placed in front of a phase-corrected horn antenna (Fig. 16.7c). This camera obtained the first microwave images of human hands (Fig. 16.7d), within minutes in the 1980s and in real-time 20 years later, supported by increase of computer power [56].

The comparison of the scattered field distribution measured over the retina of the camera with the hand footprint obtained by Röntgen (Fig. 16.1a), with a very simple X-ray system, illustrates very well the difficulties faced by microwave imaging. Bone structures produce scattering effects so that the hand shape and structure are almost impossible to recognize from the rough data recorded with the camera. However, despite working at fixed frequency, when focusing the image in the plane where the hand is placed, it becomes much easier to recognize the hand by its contour as well as the bone location, even if they are much less distinctly visible than with X-rays.

These results show the limitations of DT algorithms. Based on a linearized formulation of the inverse scattering problem to be solved, they only provide qualitative images representing the equivalent currents induced in tissues and not their dielectric permittivity. It became clear from these experiments that we needed (i) systems capable of multi-view measurement without any movement of the OUT and (ii) reconstruction algorithms fully taking into account the scattering effects in their full complexity.

### ***16.5.5 The Microwave Scanner: Toward Quantitative Tomography***

After his stay at Supelec, Professor L. Jofre was determined to develop, at UPC Barcelona, a *true* microwave scanner with an architecture similar to those of other medical tomographic machines. The major objective was to avoid any movement of the target while obtaining multi-view data. A solution was then provided by a circular array of antennas operated either in a transmitting or receiving mode [53]. The prototype of the first ever-constructed microwave scanner is shown on Fig. 16.6c. It consisted of a circular array of 64 water-immersed horn antennas. As for fan-beam X-ray scanners, when a given antenna was transmitting, the receiving antennas were located in the opposite part of the array.

The system was carefully designed to avoid cross-channel interference resulting from the limited isolation of microwave switches. A double modulation scheme was

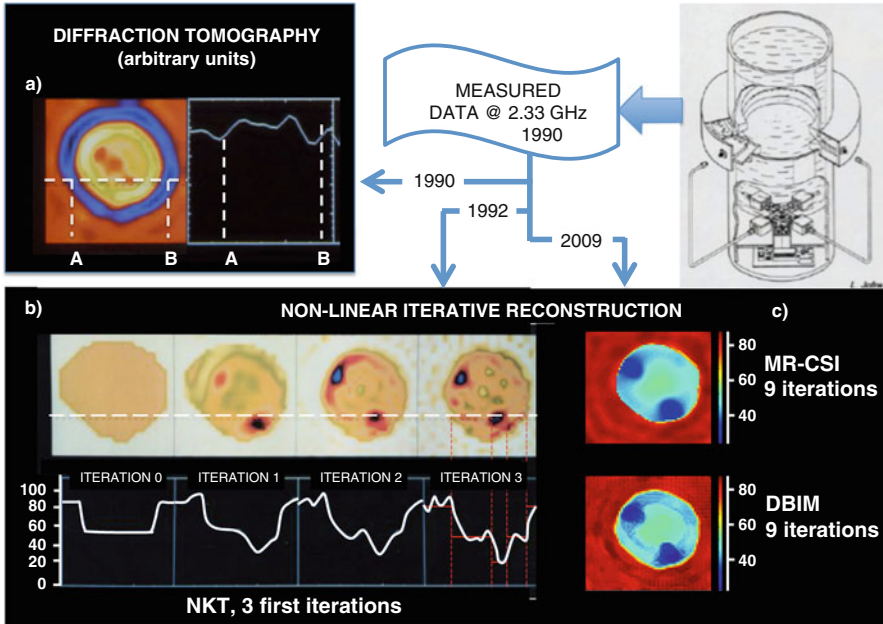


**Fig. 16.8** Human forearm tomographic images at 2.45 GHz: the same data measured with the scanner shown on Fig. 16.6c are successively used for different reconstruction algorithms. (a) Linear diffraction tomography (1990) [56]; nonlinear reconstruction (b) Newton-Kantorovich (NKT), 1992 [58]; (c) multiplier regularization/contrast source inversion (MR-CSI) and distorted born iterative method (DBIM), 2009 [60]

used for that purpose, consisting of modulating the transmitted and receiving signals at two different frequencies before performing a synchronous detection at the beat frequency. Such a demodulation scheme enabled isolation of the signal stemming from the selected antenna set from other parasitic signals.

DT algorithms, first used for reconstructing cross-sectional images, provided disappointing results. For instance, Fig. 16.8a shows a human forearm cross section, where only the external contour is properly reconstructed [57]. The internal structures, and more particularly the bones, despite their high dielectric contrast with muscle, are not clearly visible.

During the two following years, new nonlinear iterative reconstruction algorithms were independently developed by Supelec [58] and the University of Illinois at Urbana-Champaign [59], trying to obtain quantitative images. Both of these algorithms show only minor differences. The image is built, pixel by pixel, until the scattered field calculated from a numerical model converges toward the measured scattered field. Then, the same original measured data set was then processed with the new algorithms with the result shown on Fig. 16.8b. After a few iterations, the image clearly reveals the bones at their correct locations. If one considers a cut of

the image, it appears that the reconstructed permittivity (here, the real part) agrees with the expected values, namely, about 80, 50, and 30, for water, muscle, and bone, respectively.

The nonlinear iterative reconstruction was continuously improved in terms of sensitivity to model error or to increased convergence rates by means of various regularization techniques. It may be interesting to note that, almost 20 years later, the most advanced versions are providing image quality comparable to that obtained in 1992 (Fig. 16.8c) [60]. This demonstrated a posteriori both the quality of the measured data and the difficulty of recent reconstruction algorithms to significantly improve image quality.

### 16.5.6 Seeking Applications of Clinical Relevance

At the beginning of the 1990s, beyond isolated organ imaging, the identification of possible clinical application was mainly guided by trying to exploit the known specific features of interactions between microwaves and living tissues. Such specificity resulted from the recognized sensitivity of their dielectric properties in the microwave frequency range with respect to water content or temperature. However, moving toward in situ organ and tissue imaging paved the way for many complications whose impact on image quality was clearly underestimated.

The microwave camera and the scanner stimulated very early investigations on scenarios of possible clinical relevance. Temperature and blood flow rate phenomena as well as inflammatory processes were particularly considered. Diagnosis of non-intentional irradiation of workers manipulating radioactive sources or of rejection process after kidney transplants was investigated at Institut Curie and Hopital Kremlin Bicêtre in Paris, respectively. Other trials were conducted for diseases known to directly impact changes in the relative permittivity of tissues with water content and temperature, respectively, such as lung edema (on phantom), blood flow rate (human arms, in vivo) monitoring, or organ defrost.

Beyond these pioneering investigations, the first application being considered for clinical relevance at the moment is related to hyperthermia treatments. Indeed, in the beginning of the 1980s, hyperthermia had a renewal of interest for oncology. This clinical interest stimulated a significant sponsorship and financing by national entities, especially in Europe, the USA, and Japan. At that time, the major *technical* problem with hyperthermia was how to efficiently control the temperature inside tumor tissues while maintaining acceptable temperature in surrounding healthy tissues. The most frequent practice consisted of introducing thermocouples or optical fiber thermometers in tumors via catheters. This practice suffered from being invasive, providing temperature only at a limited number of points, and possibly sensitive to interference with microwave radiation.

Several modalities were then in competition for noninvasive thermometry: X-ray CT, MRI, and ultrasound imaging. Active/passive microwave imaging, and electrical impedance tomography (EIT) appeared as challengers [61]. In this



competition, active microwave imaging was objectively a priori attractive for its temperature sensitivity and nonionizing aspect (as compared to X-ray CT) and its expected cost (as compared to MRI). The possibility for simultaneously heating and imaging (today designated as theranostic) with microwaves was also considered as a possible advantage over other modalities.

The method soon encountered very practical implementation issues and the lack of appropriate image reconstruction algorithms. After very promising experiments on phantoms and organs, the temperature sensitivity was confirmed [62], but moving to clinical environments proved unsuccessful. Within the framework of the European program COMAC-BME Hyperthermia, the camera was transported to the Akademik Ziekenhuis, in Amsterdam (NL), to be coupled with a heating system consisting in water-filled waveguide applicators operated at 27 MHz. Unstable artifacts were engendered by a water bolus between the camera and the patient. Furthermore, DT algorithms were far from bringing a sufficient image reconstruction quality.

Afterward, it is clear that the major reasons of such a disappointment may be explained by (i) the lack of sufficient computing power for either processing measured data or assessing feasibility on realistic numerical models, (ii) the reduced number of research groups working on that subject, and (iii), more pragmatically, the decrease of financial support. Nevertheless, it is really worth noting that, despite all these difficulties, all the concepts and techniques considered in this finishing maturation period have been either continued or reconsidered in the coming second step of development: immersion technique, confocal imaging and UWB radar systems, circular scanner, and nonlinear iterative image reconstruction algorithms are some examples.

## 16.6 Current Trends Toward Clinical Acceptance

### 16.6.1 *Ongoing Research and Achievements*

The clinical acceptance period may be considered as starting in the mid-1990s, after a continuing effort maintained by pioneering research groups practicing inverse scattering image reconstruction, in different applications: breast imaging [63] or whole-body animal thermal and functional imaging [64, 65]. Recent review papers provide a thorough review of the state of the art (e.g., Refs. [5, 6]). They clearly show that most of the work done on microwave imaging for medical applications was based on numerical modeling, with a more or less close contact to clinical reality.

In 2000, the trigger of a new evolution step of microwave imaging came from the rebirth of radar techniques, abandoned for many years after Larsen's era, and now focused on breast cancer screening (e.g., Refs. [66, 67]). The arguments for such an infatuation for this application resulted from both its undisputable socio-economical

relevance and, at the same time, from supposed specific advantages of microwaves over existing modalities, especially X-ray mammography. The geometry, the dimensions, and the protuberant aspect of breast anatomy, as well as the supposed dielectric contrast between healthy and tumor tissues, were initially considered as very promising conditions. Breast imaging has stimulated a rapidly growing interest from the electromagnetics community and resulted in the engagement of an increasing number of researchers, as testified by the number of publications dealing with this topic (e.g., Refs. [5, 6]).

More marginally, other applications such as bone or lung imaging were also beginning to be investigated. All this research activity took advantage of the drastic increase of computing resources, which were cruelly lacking during the previous concept maturation period. As shown below, these resources were essential in the design and the optimization of the array of sensors or for improving reconstruction algorithms and assessing their efficiency on realistic, MRI-based, numerical models (e.g., Ref. [68]).

### 16.6.1.1 Reconstruction Algorithms

As already explained in Sect. 16.5.1.1, image reconstruction algorithms can be divided into inverse scattering and radar, including holography, categories. In the considered period, they have constituted a very active field of investigations, remembering, to some extent, what happened with the flourishing development of numerical techniques in the beginning of the 1960s, when computers were started being used by the electromagnetic community. Similarly, many imaging algorithm variants and options (see an exhaustive review in Ref. [6]) have been imported from other fields of applied physics, numerical analysis, or signal processing.

Unfortunately, they most often produce only minor incremental improvement, and their efficiency remained quite dependent on the target configuration and experimental arrangement for the test case. Consequently, it is not easy to definitely identify which are the most efficient algorithms, especially because, instead of being assessed with experimental data, their performance has been investigated with only simulated data.

Inverse scattering algorithms aim to iteratively retrieve the dielectric constant in the target by minimizing the difference between the measured scattered field and the scattered field calculated by a numerical model supposed to replicate the experimental imaging scenario. Due to convergence issues and trapping risks in local minima inherent to the ill-posedness of any inverse problem, such an approach is highly sensitive to the model error resulting from the inability of the numerical model to reproduce accurately the experimental scenario. The model error depends on the complexity in modeling the antenna array arrangement and its interaction with the patient. Usually, these interactions are neglected, due to limited computing resources. They may also significantly vary from one system to another. For instance, low-profile short monopole antenna arrays immersed in a large tank

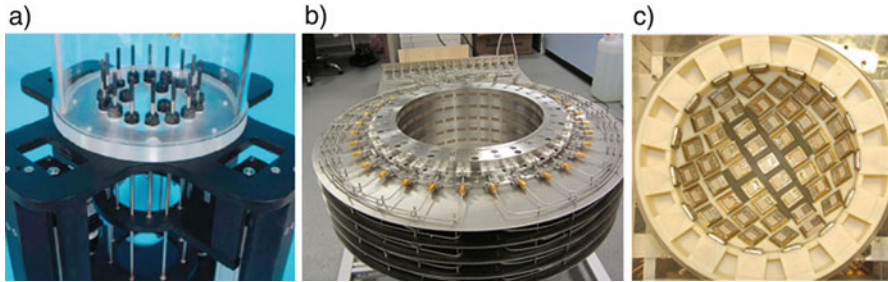


**Fig. 16.9** Examples of antenna array configurations for medical imaging. Breast imaging: (a) circular array of 16 monopole antennas, diameter 15 cm, vertical/rotation mechanical scan (Courtesy Prof. P. Meaney, [70]), and (c) one-half-spherical array of 60 slot cavity-backed antennas, diameter 17 cm, Mechanical rotation (© 1986 Micrima, [71]). Brain imaging: (b) cylindrical array of five rings of 32 ceramic-loaded waveguide antennas, diameter 28.5 cm, height 28 cm (Courtesy Dr. S Semenov, [69])

filled with a lossy liquid (Fig. 16.9a) require less computing resources than more invasive printed-circuit or waveguide antennas (Figs. 16.9b and c).

In the case of radar-based reconstruction, the first problem is that the simplified scattering model neglects multiple scattering. The propagation medium is implicitly supposed homogeneous and its wave velocity known. In fact, it is not the case, and this may introduce localization errors: an inaccurate wave velocity may result in tumors calculated to be impossibly outside the breast. Practically, the wave velocity is an adjustable parameter to be optimized, afterward, based on various metrics for quantifying image quality. Another problem is the skin surface echo that is usually much higher than the smaller ones stemming from the abnormalities to be observed. Its elimination by time windowing or using software usually results in a degradation of the image quality.

Neither method produces reliable images. For instance, the algorithm is dependent on systems and patients. Furthermore, quite variable image quality may be observed, from one algorithm to another, even when considering the same scattered field data set, or from one anatomical configuration to another, even when using the same algorithm.

Such image variability can be easily understood and tolerated within reasonable limits for qualitative radar imaging. For quantitative imaging, the reliability can be significantly improved, thanks to a priori information introduced when starting the iterative reconstruction process, as interestingly demonstrated by trials conducted on volunteers [72], and not on models. A priori information may consist of external shape, possibly obtained from laser or molding, and/or regional/averaged dielectric permittivity imported from other imaging modalities such as microwave monostatic radar, MRI, or X-ray CT (e.g., Ref. [73]). The need for some a priori information may represent a significant disadvantage when compared to other

imaging modalities. On the contrary to standard processing of complex-valued data, log-transform-based algorithms enable repeatable and accurate images, as demonstrated by clinical practice (see Sect. 16.6.2).

The difference of the images obtained by the inverse scattering and radar approaches is amplified by the fact that, until now, they are using different frequency bands, below and above 3 GHz, respectively. However, it is not useless to note that such a practice results currently from the computational cost required by full system modeling at high frequencies.

The reconstruction time issue is posed quite differently for inverse scattering and radar reconstruction. In the first case, the nonlinear reconstruction requires long calculation times for considering a full 3D modeling of a realistic experimental imaging scenario. Simplifying the model impacts the convergence of the iterative process and the reliability of the reconstructed image. As compared to inverse scattering algorithms, radar-based reconstruction, such as delay-and-sum (DAS), can be achieved in much shorter times. Then, it is for inverse scattering reconstruction that the largest image quality improvement may be expected from an increase of the computing power. Reconstruction time aspects are more extensively addressed in Chap. 17 of this festschrift book.

### 16.6.1.2 Microwave Systems

Technology offers many possible options in terms of sensor arrangements and interrogation modalities. Several geometries (linear/planar, circular/cylindrical, one-half spherical, cubic, conformal) of switched sensor arrays were considered for mono-, bi-, or multi-static data acquisition. Figure 16.9 shows some examples of array configurations that are currently used in (pre)clinical trials. They are operated at frequencies extending roughly from 1 to 8 GHz, in either CW or narrow to ultrawide bands (UWB) interrogation modes. Depending on the interrogation mode, the data are acquired in the frequency domain or directly in the time domain.

For frequency domain interrogation, which is used most often, commercial VNA were a convenient of-the-shelf solution that progressively evolved from dual signal/reference channels to multiport (16 or 32) systems. Except for very few exceptions [74, 75], the idea of using dedicated modular transceivers was not exploited nor a fortiori that of using integrated antenna-transceiver chips. One of the major reasons is probably that the design and fabrication of such receivers were uncommon in antenna laboratories.

Sensitivity and dynamic range constitute crucial issues for medical diagnostic imaging. Indeed, the signals stemming from the relevant details to be detected are not only weak, but, above all, they are embedded in much stronger signals due to surrounding regions. The example of skin has already been reported. When possible, differential imaging constitutes an efficient way to reduce the dynamic range requirements. Differential imaging can be used when it is possible to follow up continuously the evolution of a physiological parameter or the diffusion of contrast

agents. But of course, differential imaging cannot be considered for tumor detection on a long-term basis without an acceptable image reliability.

The number of sensors and their positioning have been considered either from a pure practical viewpoint (how to arrange antennas covering a certain frequency band in the available space) or based on more theoretical sensitivity-based considerations, such as singular value decomposition (SVD) for system optimization [76, 77]. Such sensitivity analysis is very valuable, even if usually conducted on simplified systems neglecting possible mutual coupling between the array sensors and between the array and the patient. Nevertheless, they have clearly demonstrated the overall difficulty in improving the quality of reconstructed images. It is now clearly understood that improving spatial resolution requires more than just increasing the number of sensors. Indeed, for taking advantage of a larger number of sensors, the available dynamic range must be correlatively increased. In other words, spatial resolution is governed, in an unavoidable way, by the available signal-to-noise ratio (SNR).

### 16.6.1.3 Antennas

Commercial electromagnetic codes were abundantly used for designing a large variety of antenna types: open waveguides, slot cavity backed, mono-/di-poles, patch, Vivaldi-like, etc. As compared to antenna design for communication purposes, the case of imaging applications raised the additional difficulty of defining relevant optimization criteria. Indeed, the antenna, whether in contact on the patient or contactless and immersed in a coupling medium, is used in a near-field region and inhomogeneous environments. Due to the dependence of the antenna behavior on the patient configuration, the antenna can no longer be usefully characterized by its far-field pattern or gain, as it is too often done. At least the map of near-field distribution in the presence of a representative phantom is required to have an idea of the wave penetration in tissues. Independent of penetration in human body requirements, other antenna-related issues must be addressed such as the minimization of multipath contributions, thanks to a proper control of leakage, shielding, and mutual coupling. Dual-polarized antennas were rarely considered.

Ultimately, only the global imaging production process for canonical configurations allows estimation of the antenna performance, and various metrics were then introduced for quantifying the image quality. Due to the strong variability of patients, it was not possible to thoroughly address specificity/sensitivity issues. Globally, an objective and quantitative comparison between the respective merits of various antennas remains to be done.

### 16.6.1.4 Summary

A very significant amount of knowledge has been gained, even if not necessarily efficiently aggregated, from the mid-1990s, due mainly to the increase of both

research groups involved in the topic and to the computer power that allowed expertise to be gained from simulation. The two reasons were strongly correlated: the increased modeling capabilities offered by computers constituted an attractive and cheap entry point for electromagnetic laboratories. Nevertheless, to a large extent, this effort looks more like a dispersed leak forward rather than deliberate efforts in reducing the distance between computer-based modeling and clinical practice. There is an evident contrast between the observable clinical stagnation and the repeated promises resulting from investigations conducted on numerical models.

The treatment of any problem begins from the recognition of the problem. In the case of microwave imaging, the major problem is undoubtedly the lack of clinical results for stimulating and driving in a sound way new researches and advances. In the case of disappointing results, the engineering viewpoint has been, quite naturally, to imagine how to solve the problem by increasing the complexity of the imaging process. But, too often, this was done without clearly understanding if such an increased complexity was effectively converging toward a clinically acceptable solution. Feasibility studies on contrast agents constitute an example of this trend. The use of magnetic nanoparticles (MNP) as contrast agents clearly results in increased complexity at both equipment and clinical practice levels. Consequently, investment and functioning costs are also necessarily increased, without a fully clear estimation of MNP's possible toxicity and sensitivity/specificity diagnostic added value. In addition, worth observing is that the need for contrast agents constitutes, per se, a demonstration of the microwave inability to do the job in question and does not particularly advocate in favor of microwaves vs. with other imaging modalities.

If one may consider increasing complexity as justified to improve imaging performance and reach the targeted objective, one should not exclude the possibility of readjusting the target and finding modified or different applications accommodating the current performance. Examples of such application-driven adjustments are given in the next section.

### ***16.6.2 Examples of Clinical Outcomes***

The engagement of the clinical community is a key driver for the successful development of medical imaging modalities. Unfortunately, until very recently, the clinical trials of microwave imaging were more the fruit of a microwave push rather than that of a real clinical pull. This can be explained by the difficulties encountered by microwaves to reach the minimum attractiveness threshold required for raising the interest of the clinical community. However, the situation could now be rapidly changing, as demonstrated by the few following examples. Two applications, namely, breast imaging and brain diagnosis, have been selected for their exemplary value in illustrating different technical options, diagnostic schemes, and development strategies for gaining clinical acceptance.

These applications correspond to rather different contrast situations: tumor versus normal tissues for breast imaging and blood versus brain tissue for brain



**Fig. 16.10** Three examples of advanced microwave systems used for clinical assessment of breast imaging. (a) Monostatic radar with adaptive antenna positioning conforming to breast geometry (Courtesy University of Calgary) [81], (b) tomographic system equipped with circular arrays mechanically translated (Courtesy Microwave Imaging Syst. Tech. Inc.) [70], (c) multi-static radar system MARIA<sup>TM</sup>, electronic scan, and mechanical rotation (Copyright © Micrima Ltd. 2016) [71]

diagnosis. They have been interestingly developed by using both inverse scattering and radar diagnosis approaches. But, for the sake of comparison, nonimaging-based classification algorithms have been also considered. The clinical targets have been adjusted in accordance with the operational capabilities offered by these different, and sometimes competing, diagnostic approaches. More generally, with these two examples, one retrieves typical development problems that microwaves are facing. Other applications such as lung water content monitoring [78], bone imaging [79], or noninvasive thermometry [80] could have been also considered for their clinical relevance. However, it seems that they have not yet reached the same development level.

### 16.6.2.1 Breast Imaging

#### Three Different Microwave Systems

Figure 16.10 shows three different microwave systems for breast imaging. The patient is lying on a bed, with her breast pending in the imaging chamber. Despite their apparent similarity, their operating modes are quite different.

The first system (Fig. 16.10a) is a UWB monostatic radar arrangement [81], where the transmitting and the receiving antennas are closely located and simultaneously mechanically scanned around the breast surface. The second system (Fig. 16.10b) is a multi-static arrangement for inverse scattering imaging, with a circular array of 16 monopole antennas (Fig. 16.9a), which can be translated vertically to explore a cylinder around the breast [70]. The third system (Fig. 16.10c) is a multi-static UWB radar (MARIA<sup>TM</sup> [71]), utilizing a one-half spherical array of 60 antennas (Fig. 16.9c).

The first and the third UWB radar-based systems are operating, roughly, from 1.5 up to 8 GHz. The second one, dedicated to inverse scattering reconstruction and, hence, for reasons already explained in Sect. 16.5.1.1, is operating in a lower

frequency band, namely, 500 MHz up to 3 GHz in a CW mode; but multifrequency image reconstruction is possible as well. Chronologically, imaging systems based on inverse scattering were engaged in clinical assessment from the mid-1990s, while radar systems came a few years later.

For all the three selected examples, several prototype generations have been successively built in academic laboratories, sometimes in close relationship with start-up companies. Their clinical destinations have been strongly influenced by their current image reconstruction effectiveness for screening, diagnosis, and treatment monitoring applications.

### Treatment Monitoring

Breast imaging via inverse scattering effectively started at the Dartmouth College (Hanover, NH, USA) [82]. While the Dartmouth system has been utilized extensively in screening and diagnostic settings (over 400 patient exams) [83, 84], work has been extended for use in the neoadjuvant chemotherapy monitoring setting [70]. In the former two, the system was able to statistically significantly distinguish tumors from normal tissue and benign abnormalities down to lesion sizes of 1 cm. Thanks to an efficient inverse algorithm [85], diagnostically relevant images are reconstructed under 10 min utilizing conventional, single processor computers. Projections are that the associated 2D algorithm will be able to recover corresponding images under 5 s. More importantly, their log transform-based algorithm enabled them to generate repeatable and accurate images without the use of a priori information, an unrivaled advantage over most other existing algorithms. Both the slow speed and a priori information pitfalls plague most other inverse algorithm approaches. This repeatability is crucial in a treatment monitoring setting to enable reliable image comparisons in a longitudinal study. This approach synergistically combines good image resolution with repeatability for accurately monitoring tumor progression.

This equipment constitutes a noticeable exception in the world of microwave-based diagnosis imaging for its early clinical engagement and has provided relevant matter for several publications in medical journals [70, 83, 84]. Several hundreds of patients have taken advantage of such a new treatment monitoring technique that proved its clinical relevance as compared to contrast agent-enhanced MRI, X-ray CT, and ultrasound. In addition, this microwave system is more compact and cheaper than MRI machines.

The Dartmouth approach is currently undergoing a substantial upgrade through funding from NIH/NCI in conjunction with a team from GE's Global Research Center. The ultimate goal will be to build two new breast imaging systems and deploy them for a multicenter clinical trial beginning in 2018. The most significant departure from the earlier systems is the utilization of commercially available software-defined radio (SDR) technology to fabricate a 16-channel low-cost and compact system. These advances will allow even higher-frequency operation that



will subsequently also improve image resolution. This is a strong step toward one of the original promises of microwave imaging in terms of projected low costs.

### Screening and Diagnosis

Microwaves have been considered as a possible alternative to X-ray mammography since 1991 [86]. But the early 2000s before the UWB radar technology could be effectively used for that purpose. The equipment shown on Fig. 16.10c is dedicated to breast cancer screening and diagnostic. It is based on research originally conducted at the University of Bristol, where a series of radar scanner prototypes (with increasing number of antennas: 16, 31, and then 60) were successively constructed with funding of the company Micrima Ltd., now in charge of the construction of new scanners.

While the first clinical evaluations conducted around 2010 highlighted a number of practical problems [87], papers published six years later report better results with the current prototype that is equipped with the largest number of antennas and enables faster data acquisition (120 s/breast) [88–90]. Such short examination times and absence of breast compression are more particularly appreciated by patients.

The still relatively small number of subjects (roughly 350 symptomatic patients and 200 volunteers) analyzed does not permit extensive statistical comparisons. However, some trends demonstrate that the microwave system compares well with digital mammography, even more favorably for dense breasts, i.e., for young women. Furthermore, combining mammography and microwave results is shown to increase the overall sensitivity. Promising early results have been published demonstrating that lesion tissue type can be determined from the UWB scattering data, enabling automatic separation of cancer from benign findings [91] using frequency feature discrimination

Furthermore, a compound imaging strategy has been developed as a new skin echo removal technique assisted in acquiring more data, by rotating the array of sensors and aggregating the scans corresponding to different rotation angles [92].

With a multicenter UK-based trial now concluded, Micrima's MARIA™ system will next be deployed in British and European breast imaging centers where it will be used to assess symptomatic and high-risk screening patients, as well as patients receiving therapeutic interventions such as chemotherapy.

### Coming Back to Basic Investigations

After early test case investigations on volunteers by the University of Calgary, Canada [81], with a first monostatic system, the need to have better knowledge of the average permittivity of the volunteer's breast tissue became obvious. To that end, a system with a simplified plane-to-plane (like X-ray mammography) antenna array arrangement has been designed (Fig. 16.11a) for in situ dielectric characterization of breast tissues of volunteers [93]. This simplified system demonstrates great

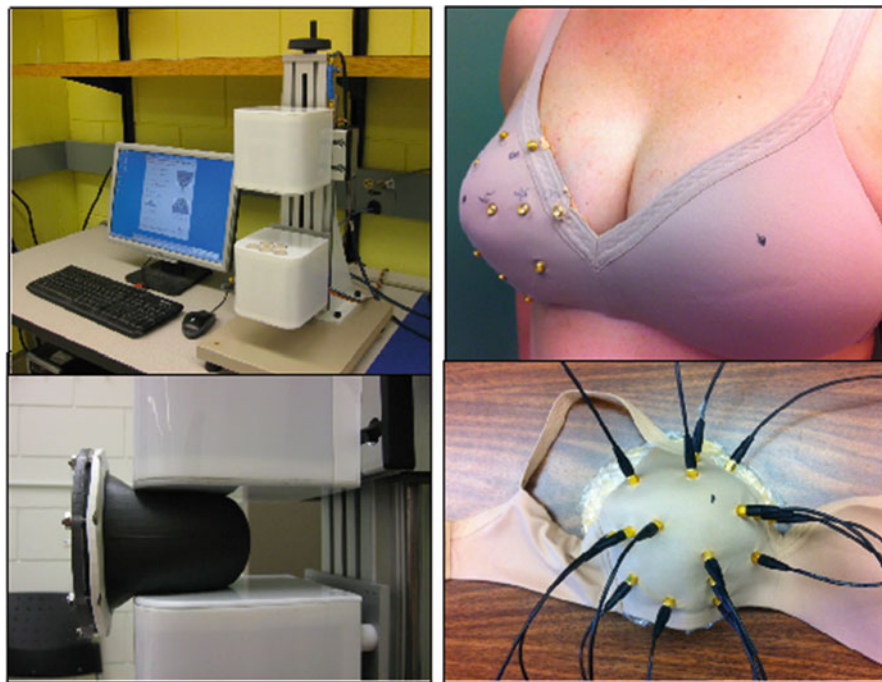


**Fig. 16.11** Examples of advanced microwave systems for basic assessment of breast imaging. (*Left*) Parallel plate array setup for measuring the dielectric properties of the breast on volunteers, five antipodal Vivaldi antennas for each array, frequency band, 1.5–10 GHz (Courtesy University of Calgary) [92]. (*Right*) Bra-shaped sensor array for individual self-tracking, 16 monopole antennas, frequency band, 2–4 GHz (Courtesy McGill University) [96]

sensitivity to breast tissue properties and ability to map basic tissue distribution [94]. Thanks to the short scan time (15 s) and simplicity (no complex mechanics, no matching medium), this system enables larger-scale study in a clinical environment with minimal operating cost. This led to a fruitful reorientation of the research group activity toward more basic investigations such as the variability of these properties from volunteer to volunteer, stability over time as well as their time dependence (menstrual cycles, for instance) for a given volunteer [95]. Such a return to basic investigations on breast tissue dielectric properties constitutes a good example of constructive rebound and should prove very useful for the future of microwave-based breast imaging.

### Breast Health Monitoring

The innovative project that resulted in a flexible bra-integrated array of antennas (Fig. 16.11a) started at McGill University, Montreal, Canada, as in many other

antenna laboratories, with an imaging prototype consisting in a UWB time-domain radar equipped with a hemispherical array of 16 printed monopole antennas, operated in a 2–4 GHz frequency band. Both DAS and classification algorithms were employed for the processing of the collected data. This work primarily focused on the short- and long-term reliability and stability (up to 8 months) of the measurements and on feasibility of low-cost, homemade transmit/receive units. Initial testing was convincingly conducted with volunteers [97].

Concurrently with the noted work, the McGill group investigated a flexible probe array with, again, emphasis on the stability and the reliability of the measurements in order to assess the feasibility of differential imaging over short to long periods for breast health monitoring [96]. If validated, the envisioned goal of such innovative approach is an antenna-equipped bra for anomaly detection, based on frequent tracking, which would allow for triggering alarms in case of significant and unexpected changes [98]. This procedure would not necessarily require an image reconstruction, but instead a classification-based algorithm.

If one considers the rough data being transmitted wirelessly to a remote center in charge of their analysis, this scheme, if validated through clinical trials, would perfectly fit the current e-health trend of implanted or wearable sensors, connected objects, and wireless health-monitoring devices.

### 16.6.2.2 Brain Diagnosis

#### Two Different Microwave Systems

Diagnosis of brain edema has been one of the earliest domains of investigation for microwave sensing techniques, due to favorable dielectric contrast between brain tissue and water [44]. Similarly, two rather distinct approaches are currently considered for early diagnosis of brain stroke and traumatic injury. Basically, they differ by the algorithms over which the diagnosis is based: classification, or image reconstruction. The difference between the two sorts of algorithms severely impacts the array complexity, via the number of data to be collected for processing requirements. Accordingly, both approaches are competing in terms of cost and diagnostic performance trade-off. As such, each should find its own best place to fit various clinical needs ranging widely from patient triage to treatment follow-up.

#### Classification-Based System

The objective of the classification algorithm is to suggest which class a patient belongs to, among two arbitrary classes that manifest themselves in differences of the dielectric properties in the brain (bleeding stroke/non-bleeding stroke, brain injury/non-brain injury, for instance) and, possibly, to provide a global indication of location (right or left brain hemisphere, for instance). Figure 16.12 shows the third-generation transportable system using a classification algorithm constructed



**Fig. 16.12** Advanced microwave systems for brain stroke diagnostics based on classification technique (Courtesy Chalmers University, Medfield Diagnostics [99])

by the company *Medfield Diagnostics* (founded in 2005 [99]), resulting from the research conducted at Chalmers University since the 1990s.

The array consists in eight slot antennas operating in the 400 MHz–2 GHz frequency band. The antennas are manually adjusted on the patient head. All the system is easily transportable in ambulances for reducing the time required to diagnose a bleeding or non-bleeding occurrence, a key issue in the medical decision to start a pre-hospital thrombolytic treatment. Preclinical evaluation started in 2008 and is currently continued in five hospitals around the world. Until now, such trials have been conducted on around 600 patients and 100 volunteers [100, 101].

### Inverse Scattering-Based System

The inverse scattering algorithm is providing an image and, hence, an accurate location in addition to discrimination capability between ischemic and hemorrhagic strokes [102, 103]. Figure 16.9b shows the imaging chamber of the system constructed by the company *EMTensor* (founded in 2012, [69]). The operation frequency is between 0.9 and 1.1 GHz. The array consists of five rings of 32 ceramic-loaded waveguide antennas, i.e., a total of 160 antennas, to be compared to the eight antennas of the system using classification algorithms. This system is the result of continuous efforts conducted, since the mid-1990s, in inverse scattering-based microwave imaging for medical applications, including full 3D imaging on animals and functional imaging [64, 65]. Image reconstruction is achieved via an iterative nonlinear algorithm that requires solving the corresponding direct scattering problem several times. Coupling high-order finite elements and parallel preconditioners makes it possible to reduce the overall computational cost and simulation time while maintaining accuracy [103]. After initial assessment for brain stroke [104], two systems will be manufactured for starting clinical trials in 2017.

### ***16.6.3 Suggestions and Recommendations***

Previous examples should be sufficient to demonstrate that microwave-based diagnostic techniques are finally, even if very recently, entering a critical step for gaining their clinical acceptance. Indeed, the advanced prototypes that left academic laboratories and are currently engaged in trials seem to have reached a sufficient attractiveness level for raising clinical interest. Even if success is not yet guaranteed, at least the results should serve as precious guidelines either (i) to improve/modify the prototypes with maintained clinical objectives or (ii) to readjust/change objectives within the capability of the available prototypes.

Of course, the first option will be preferred if clinical needs are really pulling the technology and if it is economically viable. But, in such a case, the question is to determine what can be done and what is the improvement margin, either for the microwave technology and/or computer power levels, for better data acquisition and processing, respectively. Four suggestions/recommendations are provided for that purpose.

#### **16.6.3.1 Exploiting Available Microwave Technology for “Better” Data**

When looking around to different microwave applications, it is evident that the best of microwave technology has not been yet exploited for medical imaging applications. The time has clearly arrived to move from switched antenna arrays and expensive commercial network analyzers to integrated on-chip transceivers. All the technology developed for wireless communications operating in the same frequency bands may be considered for that purpose. Reduced losses, decreased mutual coupling, increased sensitivity, and dynamic range may be expected to increase the data quality. Furthermore, miniaturization should also enable increasing the number of sensors to be deployed on a given surface and hence obtaining more data.

For both radar and inverse scattering imaging reconstruction algorithms, increasing data number and quality should definitely impact the image quality in terms of spatial and contrast resolutions and improve the sensitivity. It is worth noting that besides pure fabrication aspects, modulation and processing schemes could be also reconsidered, as it has been done in the domain of communications and radar. For instance, a multi-static imaging system is nothing but a MIMO system and, hence, should profit of the know-how gained in MIMO technology [19].

Finally, it could be also recommended having a look around to consider the technology developed for microwave-based industrial sensing applications, such as process tomography, that may exhibit some exploitable similarity with medical imaging systems and could suggest technically relevant solutions [105, 106].

### 16.6.3.2 Anticipating Increased Computer Power for Better Processing

There is no doubt that expected advances in computer technology will result in a dramatic increase of the computing power, despite an unavoidable midterm failure of Moore's law. New computer generations (quantum computers) will certainly appear providing unbelievable computer power. For radar systems, this power will be perfectly used for real-time processing of data. In case of inverse scattering, the power increase will make possible modeling more and more realistically full 3D imaging scenarios. More particularly, accurately accounting for patient-system interactions should allow reducing model errors and improving both the convergence rate and the accuracy of iterative reconstructions. In addition, the possibility to solve large systems will enable considering higher operating frequencies, until a point where the data stemming from same multi-static imaging system will be possibly processed either by radar or inverse scattering algorithms, with subsequent improvement of spatial resolution and image reliability by combining results derived from these two approaches.

### 16.6.3.3 Returning to Basic MW/Bioinvestigations

In the past, the dielectric characterization of living tissues proved to be problematic. Several times, the validity of measurements was contested for reasons related to the measurement methodology and probe structure or resulting from excision and sample preparation in case of *in vitro* measurements. *In vitro* dielectric characterization is assuming homogeneous and isotropic tissue samples, which is not necessarily valid. *In vivo* measurements are still more complicated and can only be conducted either invasively or by use of MRI imaging, with evident limitations in both cases. MRI systems, for instance, are operating at frequencies lower than those effectively used by microwave imagers.

And yet, dielectric characterization is mandatory for identifying the most relevant situations to exploit specific microwave-tissue interactions. The imaging sensitivity and specificity are very directly dependent on dielectric contrast. Accurate dielectric data are indispensable for relevant numerical-based feasibility studies and for translating/calibrating microwave images in terms of physiological parameters. Dielectric characterization is also useful to correlate the evolution of tissues with their related dielectric properties, enabling following up the evolution of tissues under pathological conditions, such as a growing tumor for instance. High-resolution scanning microscopy (a few micrometers at 2 GHz [107]) could be interestingly considered for such small-scale investigations, filling the gap between usual dielectric probing at macroscopic level and microfluidic cell-size characterization [108].

#### 16.6.3.4 Increasing Interactions with Medical Community

L.E. Larsen, the founder of microwave imaging for medical applications, was a medical doctor by profession. One can easily imagine that, if more medical doctors had been engaged in the microwave imaging story, the present situation could be quite different. An increased involvement of medical community is necessary, not only for the assessment and validation purposes but also to drive the evolution of microwave imaging equipment according to its needs, as it did and is still continuing to do with other modalities. The medical community is the judge of the relevance of microwave techniques as compared to other diagnostic modalities whose better knowledge would be highly beneficial to microwave researchers and engineers for guiding their R&D efforts.

### 16.7 Concluding Remarks

Coming back to the initial question: after such a long period of uncertainty, or even disappointments, are there still some chances for microwave-based imaging to take off? Which segment of the medical imaging market could be occupied by microwaves [11]? We are just at a point where significant trial results conducted over the past few years are beginning to be returned. It should then become easier to compare the relative merits of the different microwave-based diagnostic approaches and strategies and if their future is to be used alone, combined together, and/or in complementarity with other modalities. But it will be necessary to be wary of hasty judgments. As it has happened in the past, a so-called *promising* modality can durably stagnate, remain marginally used, or even fall into oblivion after gaining a peak of attractiveness, despite encouraging early trials and commercial developments.

In any case, the clinical validation process will still require time-consuming and expensive multicenter and multimodality assessment campaigns. The challenges are evident in terms of demonstrated clinical relevance and added value with respect to already existing imaging modalities. Economic issues are also crucial: how will clinical trials be funded, and who will invest in the necessary technology developments? What microwave-based imaging has the most need now seems to be money for taking the best profit of the existing technology resources.

To conclude, some of the difficulties anticipated by Prof. Magdy Iskander and remembered in the foreword have been overcome. Thanks to the experience gained these past decades and at the light of the results to come soon from current trials, we should be able to finally decide if, as L.E. Larsen promised more than 30 years ago, microwaves have a significant future in medical diagnosis imaging.

**Acknowledgments** Special thanks are given to Prof. Luis Jofre (UPC Barcelona), Prof. Paul Meaney (Dartmouth College), Prof. Mikael Persson (Chalmers University), Prof. Milica Popovich (McGill University), Prof. Maria Stuchly (University of Victoria), Dr. Serguei Semenov (EMTen-

sor), Dr. Jeremie Bourqui (University of Calgary), and Dr. Peter Bannister (Micrima Ltd.) for sharing their valuable experience and results, and Prof. Akhlesh Lakhtakia (Penn State University) and Prof. Cynthia M. Furse (University of Utah) for their patient and stimulating assistance during the preparation of this chapter and for all their efforts as editors of Magdy's festschrift book.

## References

1. M.F. Iskander, C.H. Durney, Electromagnetic techniques for medical diagnosis: a review. *Proc. IEEE* **68**, 126–132 (1980)
2. N. Celik, G.C. Huang, M.F. Iskander, B.W. Berg, Microwave stethoscope and benchmarking of a vital signs sensor using computer-controlled phantoms and human studies. *IEEE Trans. Biomed. Eng.* **61**, 2341–2349 (2014)
3. MiMed COST Action, <http://cost-action-td1301.org>
4. L.E. Larsen, J.H. Jacobi, Microwaves offer promise as imaging modality. *Diagn. Imaging Clin. Med.* **11**, 44–47 (1982)
5. N. Nikolova, Microwave biomedical imaging, in *Wiley Encyclopedia of Electrical and Electronics Engineering* (Wiley, New York), pp. 1–22
6. R. Chandra, H. Zhou, I. Balasingham, R.M. Narayanan, On the opportunities and challenges in microwave medical sensing and imaging. *IEEE Trans. Biomed. Eng.* **62**, 1667–1681 (2015)
7. A. Assmus, Early history of X rays. *Beam Line*, 10–24 (1995), (published online) <http://www.slac.stanford.edu/pubs/beamline/25/2/25-2-assmus.pdf>
8. L. Aubert, La photographie de l'Invisible, les Rayons X, in *Petite Encyclopédie Populaire Illustrée*, Schleicher Frères (Ed.) (Paris, 1898)
9. L. Grossman, 115-year-old medical X-ray machine come back to life. *Wired Com, Science*, 16 Mar (2011), Online <https://www.wired.com/2011/03/old-x-rays/>
10. R. Ciernak, *X-Ray Computed Tomography in Biomedical Engineering* (Springer, London, 2011)
11. For medical imaging market informations, see for instance: <http://www.siemens.com/innovation/en/home/pictures-of-the-future/health-and-well-being/medical-imaging-facts-and-forecasts.html> and <https://www.transparencymarketresearch.com/pressrelease/medical-imaging-equipment-market.htm>
12. J. Woo, A short history of the development of ultrasound in obstetrics and gynecology. Parts I, (<http://www.ob-ultrasound.net/history1.html>), II (<http://www.ob-ultrasound.net/history2.html>) and III (<http://www.ob-ultrasound.net/history3.html>)
13. T.L. Szabo, *Diagnostic Ultrasound Diagnostic Imaging* (Elsevier, Cambridge, MA, 2004)
14. T. Geva, Magnetic resonance imaging: historical perspective. *J. Cardiovasc. Magn. Reson.* **8**, 573–580 (2006)
15. R. Nut, The history of positron emission tomography. *Mol. Imaging Biol.* **4**, 11–26 (2002)
16. M. Thumm, German contributions to physics and applications of electromagnetic waves, in *History of Wireless* (Chap. 11) (Wiley, Hoboken, NJ, 2006), pp. 327–348
17. T.P. Sarkar, D.L. Sengupta, An appreciation of J.C. Bose's pioneering work in millimeter and microwaves, in *History of Wireless* (Chap. 9) (Wiley, Hoboken, 2006), pp. 291–310
18. J.S. Belrose, The development of wireless telegraphy and telephony, and pioneering attempts to achieve transatlantic wireless communications, in *History of Wireless* (Chap. 12) Wiley, Hoboken, 2006), pp. 349–420
19. D.W. Bliss, K.W. Forsythe, A. Chan, MIMO wireless communication. *Lincoln Lab. J.* **15**, 97–126 (2005)
20. See for instance: GPS History, Dates and Timelines, <http://www.radio-electronics.com/info/satellite/gps/history-dates.php>



21. Y.L. Zheng, X.R. Ding, C.C. Yan Poon, B.P. Lai Lo, H. Zhang, X.L. Zhou, G.Z. Yang, N. Zhao, Y.T. Zhang, Nonobtrusive sensing and wearable devices for health informatics. *IEEE Trans. Biomed. Eng.* **61**, 1538–1554 (2014)
22. W.B. Carlson, *Tesla, Inventor of the Electric Age* (Princeton University Press, Princeton/Woodstock, 2013)
23. W.C. Brown, The history of power transmission by radio waves. *IEEE Trans. Microwave Theory Tech.* **32**, 1230–1242 (1984)
24. L. Roselli, F. Alimenti, G. Orecchini, C. Mariotti, P. Mezzanotte, M. Virili.: WPT, RFID and energy harvesting: Concurrent technologies for the future networked society, *2013 Asia-Pacific Microwave Conference Proceedings*, pp. 462–464
25. A. Rida, L. Yang, M. Tentzeris, *RFID-Enabled Sensor Design and Applications* (Artech House, Boston, 2010)
26. R. Meredith, *Engineers' Handbook of Industrial Microwave Heating*. IEE Power Series, vol. 25 (The Institution of Electrical Engineers, London, 1998)
27. J.M. Osepchuk, A history of microwave heating applications. *IEEE Trans. Microwave Theory Tech.* **32**, 1200–1224 (1984)
28. M. Stuchly, Applications of microwaves in medicine. IEEE Antennas and Propagation Society, Distinguished Lecturer Presentation at 2006 IEEE AP-S Conference, 2006. Available at [https://www.ieee.li/pdf/viewgraphs/applications\\_microwaves\\_medicine.pdf](https://www.ieee.li/pdf/viewgraphs/applications_microwaves_medicine.pdf)
29. A.W. Guy, History of biological effects and medical applications of microwave energy. *IEEE Trans. Microwave Theory Tech.* **32**, 1182–1200 (1984)
30. C.J. Simon, D.E. Dupuy, W.W. Mayo-Smith, Microwave ablation: principles and applications. *RadioGraphics*. **25**, S69–S83 (2005), [http://pubs.rsna.org/doi/full/10.1148/rg.25si055501#\\_i11](http://pubs.rsna.org/doi/full/10.1148/rg.25si055501#_i11)
31. A.O. Bauer, Christian Hülsmeier and about the early days of radar invention, a survey, Available at <https://aobauer.home.xs4all.nl/Huelspart1def.pdf>, see also J. Ender, 98 years of the radar principle: the inventor Christian Hülsmeier, *Proc. EUSAR*, 2002
32. F.T. Ulaby, R.L. Moore, A.K. Fung, *Microwave Remote Sensing: Active and Passive Sensing. Vol. II, Surface Scattering and Emission Theory* (Artech House, Norwood, MA, 1986)
33. A.P. Annan, GPR-history, trends and future developments. *Subsurf. Sens. Technol. Appl.* **3**, 253–270 (2002)
34. M.G. Amin (Ed.), *Through-the-Wall Radar Imaging* (CRC Press, Boca Raton, FL, 2010)
35. E.M. Leith, Quasi-holographic techniques in the microwave region. *Proc. IEEE* **50**, 1305–1318 (1971)
36. G. Tricoles, N. Farhat, Microwave holography: applications and techniques. *Proc. IEEE* **65**, 108–121 (1977)
37. E. Nyförs, P. Vainikainen, *Industrial Microwave Sensors* (Artech House, Boston, 1989)
38. R. Zoughi, *Microwave Non-destructive Testing and Evaluation Principles* (Springer, Dordrecht, The Netherlands, 2000)
39. C.C. Johnson, A.W. Guy, Nonionizing electromagnetic wave effects in biological materials and systems. *Proc. IEEE* **60**, 692–718 (1972)
40. C. Gabriel, S. Gabriel, E. Corhout, The dielectric properties of biological tissues: I. Literature survey. *Phys. Med. Biol.* **41**, 2231–2249 (1996)
41. S. Gabriel, R.W. Lau, C. Gabriel, The dielectric properties of biological tissues: II. Measurements in the frequency range 10 Hz to 20 GHz. *Phys. Med. Biol.* **41**, 2231–2249 (1996)
42. J.C. Lin, Noninvasive microwave measurement of respiration. *Proc. IEEE* **63**, 1530 (1975)
43. P.C. Pedersen, C.C. Johnson, C.H. Durney, D.G. Bragg, Microwave reflection and transmission measurements for pulmonary diagnosis and monitoring. *IEEE Trans. Biomed. Eng.* **25**, 40–48 (1984)
44. J.C. Lin, M.J. Clarke, Microwave imaging of cerebral edema. *Proc. IEEE* **70**, 523 (1982)
45. J.H. Jacobi, L.E. Larsen, Linear FM pulse compression radar techniques applied to biological imaging, in *Medical Applications of Microwave Imaging* (IEEE Press, New York, 1986), pp. 138–147

46. M. Slaney, M. Azimi, A.C. Kak, L.E. Larsen, Microwave imaging with first order diffraction tomography, in *Medical Applications of Microwave Imaging* (IEEE Press, New York, 1986), pp. 184–212
47. M. Pastorino, *Microwave Imaging* (Wiley, Oxford, 2010)
48. J.C. Lin, Frequency optimization for microwave imaging of biological tissues. *Proc. IEEE* **73**, 374–375 (1985)
49. L.E. Larsen, J.H. Jacobi, Introduction (3–11) and methods for active microwave imagery for dosimetric applications, in *Medical Applications of Microwave Imaging*. (IEEE Press, New York, 1986), pp. 118–137
50. L.E. Larsen, J.H. Jacobi, Microwave scattering parameter imaging of an isolated canine kidney. *Med. Phys.* **6**, 394–403 (1979)
51. S.J. Foti, R.P. Flam, J.F. Aubin, L.E. Larsen, J.H. Jacobi, A water-immersed microwave phased array system for interrogation of biological targets, in *Medical Applications of Microwave Imaging* (IEEE Press, New York, 1986), pp. 148–166
52. J.C. Bolomey, F.E. Gardiol, *Engineering Applications of the Modulated Scatterer Technique* (Artech House, Boston, 2001), pp. 226–229
53. L. Jofre, M.S. Hawley, A. Broquetas, E. de los Reyes, M. Ferrando, A.R. Elias-Fusté, Medical imaging with a microwave scanner. *IEEE Trans. Biomed. Eng.* **37**, 303–312 (1990)
54. J.C. Bolomey, A. Izadnagahdar, L. Jofre, C. Pichot, G. Peronnet, M. Soleimani, Microwave diffraction tomography for biomedical applications. *IEEE Trans. Microwave Theory Tech.* **30**, 1998–2000 (1982)
55. C. Pichot, L. Jofre, G. Peronnet, J.C. Bolomey, Active microwave imaging of inhomogeneous bodies. *IEEE Trans. Antennas Propag.* **33**, 416–425 (1985)
56. A. Joisel, J. C. Bolomey, Rapid microwave imaging of living tissues. *Proc. SPIE* **3977**, 320–330 (2000)
57. A. Broquetas, J. Romeu, J.M. Rius, A.R. Elias-Fusté, A. Cardama, L. Jofre, Cylindrical geometry: A further step in active microwave tomography. *IEEE Trans. Microwave Theory Tech.* **39**, 836–844 (1991)
58. N. Joachimowicz, C. Pichot, J.P. Hugonin, Inverse scattering: an iterative numerical method for electromagnetic imaging. *IEEE Trans. Antennas Propag.* **39**, 1742–1752 (1991)
59. W.C. Chew, Y.M. Wang, Reconstruction of two-dimensional permittivity distribution using the distorted Born iterative method. *IEEE Trans. Med. Imaging* **9**, 218–225 (1990)
60. C. Gilmore, P. Mojabi, J. Lo Vetri, Comparison of an enhanced DBIM method and the multiplicative-regularized contrast source inversion method. *IEEE Trans. Antennas Propag.* **57**, 2341–2351 (2009)
61. J.C. Bolomey, M.S. Hawley, Noninvasive control of hyperthermia, in *Clinical Thermology, Methods of Hyperthermia Control*, M. Gautherie (Ed.) (Springer, Berlin/Heidelberg, 1990), pp. 35–111
62. J.C. Bolomey, L. Jofre, G. Peronnet, On the possible use of microwave-active imaging for remote thermal sensing. *IEEE Trans. Microwave Theory Tech.* **30**, 1998–2000 (1982)
63. P.M. Meaney, M.W. Fanning, D. Li, S.P. Poplack, K.D. Paulsen, A clinical prototype for active microwave imaging of the breast. *IEEE Trans. Microwave Theory Tech.* **48**, 1841–1853 (2000)
64. S. Semenov, Microwave tomography: review of the progress toward clinical applications. *Phil. Trans. R. Soc. A* **367**, 3021–3042 (2009)
65. S. Semenov, J. Kellam, Y. Sizov, A. Nazarov, T. Williams, B. Nair, A. Pavlovsky, V. Posukh, M. Quinn, Microwave tomography of extremities: 1. Dedicated 2D system and physiological signatures. *Phys. Med. Biol.* **56**, 2005–2017 (2011)
66. E.C. Fear, S.C. Hagness, P.M. Meaney, M. Okoniewski, M.A. Stuchly, Near-field imaging for breast tumor detection. *IEEE Microw. Mag.* **3**(1), 48–56 (2002)
67. N.K. Nikolova, Microwave imaging for breast cancer. *IEEE Microw. Mag.* **12**(7), 78–94 (2011)

68. E. Zastrow, S.K. Davis, M. Lazebnik, F. Kelcz, B.D. Van Veen, S.C. Hagness, Development of anatomically realistic breast phantoms with accurate dielectric properties for modeling microwave interactions with the human breast. *IEEE Trans. Biomed. Eng.* **55**, 2792–2800 (2008)
69. EMTensor GmbH (Vienna, Austria), <http://emtensor.com>
70. P. Meaney, P.A. Kaufman, L.S. Muffly, M. Click, S.P. Poplack, W.A. Wells, G.N. Schwartz, R.M. di Florio-Alexander, T.D. Tosteson, Z. Li, S.D. Geimer, M.W. Fanning, T. Zhou, N.R. Epstein, K.D. Paulsen, Microwave imaging for neoadjuvant chemotherapy monitoring: initial clinical experience. *Breast Cancer Res.* **15**, R35 (2013)
71. Micrima Ltd (Bristol, United Kingdom), <http://www.micrima.com>
72. C. Gilmore, E. Zakaria, S. Pistorius, J. Lo Vetri, Microwave imaging of human forearms pilot study and image enhancement. *Int. J. Biomed. Imaging* **2013**, 673027 (2013)
73. A. Baran, D. Kurrant, E. Fear, J. Lo Vetri, Monitoring breast cancer treatment progress with microwave tomography and radar-based tissue-regions estimation, in *Proceeding of the 9th EuCAP*, Lisbon, 2015, pp. 1–2
74. V. Zhurbenko, T. Rubaek, V. Krozer, P. Meincke, Design and realization of a microwave three-dimensional imaging system with application to breast-cancer detection. *IET Microwaves Antennas Propag.* **4**, 2200–2211 (2010)
75. A. Bevilacqua, CMOS UWB transceivers for short-range microwave medical imaging, Chap. 12, in *Wireless Transceivers Circuits, System Perspectives and Design Aspects*, W. Rhee (Ed.) (CRC Press, Boca Raton, FL, 2008)
76. Q. Fang, P.M. Meaney, K.D. Paulsen, Singular value analysis of the Jacobian matrix in microwave image reconstruction. *IEEE Trans. Antennas Propag.* **54**, 2371–2380 (2006)
77. O.M. Bucci, L. Crocco, R. Spadaccini, G. Belizzi, On the design of phased arrays for medical applications. *Proc. IEEE* **104**, 633–648 (2016)
78. S.A. Rezaeieh, A.M. Abbosh, Review of systems for the detection and monitoring of accumulated fluids in the human torso, in *ISAP Conference* (IEEE Press, New York, 2015)
79. P. Meaney, D. Goodwin, A.H. Golnabi, M. Pallone, S.D. Geimer, G. Burke, K.D. Paulsen, Microwave tomographic imaging of the calcaneus: a first-in-human case study of two subjects. *IEEE Trans. Biomed. Eng.* **59**, 3304–3313 (2012)
80. P.M. Meaney, M.W. Fanning, K.D. Paulsen, S.A. Pendergrass, Q. Fang, K.L. Moodie, Microwave thermal imaging: initial in vivo experience with a single heating zone. *Int. J. Hyperther.* **19**, 617–641 (2003)
81. E.C. Fear, J. Bourqui, C. Curtis, D. Mew, B. Docktor, C. Romano, Microwave breast imaging with a monostatic radar-based system: a study of application to patients. *IEEE Trans. Microwave Theory Tech.* **61**, 2119–2128 (2013)
82. P.M. Meaney, M.W. Fanning, D. Li, S.P. Poplack, K.D. Paulsen, A clinical prototype for active microwave imaging of the breast. *IEEE Trans. Microw. Theory Tech.* **48**, 1841–1853 (2000)
83. S.P. Poplack, K.D. Paulsen, A. Hartov, P.M. Meaney, B. Pogue, T. Tosteson, M. Grove, S. Soho, W. Wells, Electromagnetic breast imaging: pilot results in women with abnormal mammography. *Radiology* **243**, 350–359 (2007)
84. P.M. Meaney, M.W. Fanning, T. Raynolds, C.J. Fox, Q. Fang, C.A. Kogel, S.P. Poplack, K.D. Paulsen, Initial clinical experience with microwave breast imaging in women with normal mammography. *Acad. Radiol.* **14**, 207–218 (2007)
85. T.M. Grzegorzczuk, P.M. Meaney, P.A. Kaufman, R.M. di Florio-Alexander, K.D. Paulsen, Fast 3-D tomographic microwave imaging for breast cancer detection. *IEEE Trans. Med. Imaging* **31**, 1584–1592 (2012)
86. A.W. Preece, M.P. Robinson, J.L. Green, M. Horrocks, Dielectric imaging – an alternative to x-ray mammography? 6th Scientific Meeting of the British Oncological Association (BOA), 64 (Supplement XV (P34)): 25, 1991
87. M. Klemm, I. Craddock, J.A. Leendertz, A. Preece, D.R. Gibbins, M. Shere, R. Benjamin, Clinical trials of a UWB imaging radar for breast cancer, in *Proceedings of the 4th EuCAP*, Barcelona, 2010, pp. 1–4

88. A.W. Preece, I. Craddock, M. Shere, L. Jones, H.L. Winton, MARIA M4: clinical evaluation of a prototype ultrawideband radar scanner for breast cancer detection. *J. Med. Imaging* **3**(3), 033502 (2016)
89. M. Shere, L. Jones, I. Lyburn, R. Geach, H. Massey, L. Hobson, S. Taylor, P. Bannister, N. Ridley, Radio-wave radar-based breast imaging system: an initial multi-site clinical evaluation, in *Proceedings of the Symposium Mammographicum*, Liverpool, 2016
90. N. Ridley, M. Shere, I. Lyburn, P. Bannister, Cancer detection in dense tissue using radiofrequency imaging – a clinical evaluation, in *Proceeding of the European Congress on Radiology*, Vienna, 2017
91. N. Ridley, A. Iriarte, L. Tsui, C. Bore, M. Shere, I. Lyburn, P. Bannister, Automatic labelling of lesions using radiofrequency feature discrimination, in *Proceedings of the European Congress on Radiology*, Vienna, 2017
92. D. Byrne, M. Sarafianou, I.J. Craddock, Compound radar approach for breast imaging. *IEEE Trans. Biomed. Eng.* **64**, 40–51 (2017)
93. J. Bourqui, E.C. Fear, System for bulk dielectric permittivity estimation of breast tissues at microwave frequencies. *IEEE Trans. Microwave Theory Tech.* **64**, 3001–3009 (2016)
94. J. Bourqui, E. C. Fear, Average breast permittivity measurements: preliminary results from current patient study, in *Proceedings of the 10th EuCAP*, Davos, 2016, pp. 1–4
95. J. Bourqui, S. Zarnke, J.R. Budzis, D.C. Garrett, D.J.Y. Mew, E. Fear, Bulk permittivity variations in the human breast over the menstrual cycle, in *Proceedings of the 11th EUCAP*, Paris, 2017, pp. 1–4
96. H. Bahtamiabarghouei, E. Porter, A. Santorelli, B. Gosselin, M. Popovic, Flexible 16 antenna array for microwave breast cancer detection. *IEEE Trans. Biomed. Eng.* **62**, 2516–2525 (2015)
97. E. Porter, M. Coates, M. Popovic, An early clinical study of time-domain microwave radar for breast health monitoring. *IEEE Trans. Biomed. Eng.* **63**, 530–539 (2016)
98. E. Porter, Microwave time-domain radar for monitoring breast health: development and testing of an early prototype, PhD thesis, McGill University, Montreal, 2015, Sec. 5.4., pp. 110–127
99. Medfield Diagnostics (Göteborg, Sweden) <http://www.medfielddiagnostics.com/en/products/>
100. M. Persson, A. Fhager, H.D. Trefna, Y. YU, T. McKelvet, G. Pegenius, J.E. Karlsson, M. Elam, Microwave-based stroke diagnosis making global prehospital thrombolytic treatment possible. *IEEE Trans. Biomed. Eng.* **61**, 2806–2817 (2014)
101. J. Ljungqvist, S. Candefjord, M. Persson, L. Jönsson, T. Skoglund, M. Elam, Clinical evaluation of a microwave-based device for detection of traumatic intracranial hemorrhage. *J. Neurotrauma* (2017). doi:10.1089/neu.2016.4869
102. S. Semenov, B. Seiser, E. Stoegmann, E. Auff, Electromagnetic tomography for brain imaging: from virtual to human brain. in *First IEEE Conference on Antenna Measurements & Applications (CAMA)* 2014
103. M. Bonazzoli, V. Dolean, F. Rapetti, P.H. Tournier, Parallel preconditioners for high order discretization arising from full system modeling for brain imaging. *Int. J. Numer. Modell. Electron. Networks Devices Fields* **00**, 1–10 (2016). <https://hal.archives-ouvertes.fr/hal-01328197/file/paperEMF.pdf>
104. S. Semenov, R. Planas, M. Hopfer, A. Hamidipour, A. Vasilenko, E. Stoegmann, E. Auff, Electromagnetic tomography for brain imaging: Initial assessment for stroke detection. in *BIOCAS Conference*, Atlanta, 2014
105. D.M. Scott, R.A. Williams, *Frontiers in Industrial Process Tomography* (Engineering Foundation, New York, 1995)
106. Wu, Zhipeng, Microwave Tomography as a New Modality for Biomedical and Biopharmaceutical Imaging, ed. by M. Takhashi. in *International Conference on Medicine and Biopharmaceutical, Proceeding* (World Scientific, Singapore, 2015), pp. 687–692

107. M. Tabib-Azar, J.L. Katz, S.R. LeClair, Evanescent microwaves: a novel super-resolution non-contact nondestructive imaging technique for biological applications. *IEEE Trans. Instrum. Meas.* **48**, 1111–1116 (1999)
108. M. Nikolic-Jaric, S.F. Romanuik, G.A. Ferrier, G.E. Bridges, M. Butler, K. Sunley, D.J. Thomson, M.R. Freeman, Microwave frequency sensor for detection of biological cells in microfluidic channels. *Biomicrofluidics* **3**, 034103 (2009)



**Jean-Charles Bolomey** graduated with a radio engineering degree from Supelec in 1963 and obtained his Ph.D. at Paris-Sud University where he became a professor in 1976. Since 1981, his research contributions have been devoted to innovative near-field techniques in a broad sense, including antenna measurement, EMC testing as well as industrial, scientific, and medical (ISM) applications, and more particularly microwave-based imaging techniques. He has pioneered the modulated probe array technology, demonstrating its unrivaled accuracy/cost-effectiveness for fast near-field scanning. He has coauthored with Prof. F. Gardiol a reference book on principles and applications of the modulated scatterer technique (MST) and is holder of numerous patents covering various MST-based probe array arrangements for microwave sensing and imaging systems; he founded the

Microwave Vision Company SATIMO in 1986. He has actively contributed to several cooperative European programs ranging from microwave hyperthermia to industrial process tomography. His recent research was related to rapid specific absorption rate measurements. Diagnostic and imaging applications of very-near-field techniques constitute his current domain of investigation. He is currently contributing as a member of several Scientific and Technical Advisory Boards for European institutions and start-up companies. Professor Bolomey is fellow of the IEEE and was distinguished lecturer of the IEEE Antenna and Propagation Society from 2010 to 2013. He is Edmond S. Gillespie Fellow of the Antenna Measurement Technique Association (AMTA) from whom he received the Distinguished Achievement Award in 2001. He received several awards including the 2004 Medal of the French URSI Chapter and recently the 2015 Joseph F. Keithley Award from the IEEE Instrumentation and Measurement Society and the 2017 Antenna Award of the European Association for Antennas and Propagation (EurAAP).

# Chapter 17

## Real-Time Quantitative Reconstruction Methods in Microwave Imaging

Denys S. Shumakov, Daniel Tajik, Alexander S. Beaverstone,  
and Natalia K. Nikolova

### 17.1 Introduction

Microwave imaging is at the center of attention for many researchers around the world. It has a wide breadth of applications in areas such as through-the-wall imaging [1], concealed weapon detection [2, 3], nondestructive testing and evaluation [4, 5], and biomedical imaging [6]. Another promising application, early-stage breast cancer detection, is ongoing [7]. Microwaves are nonionizing and they can be emitted and received with relatively cheap and compact components. However, when it comes to microwave tissue imaging, fundamental problems such as penetration depth, coupling power into the tissue, resolution limits, tissue heterogeneity, etc., impose a significant challenge to the progress in this area [8].

Microwave imaging aims at reconstructing the dielectric properties of objects as functions of position. Qualitative approaches produce the location and shape of objects which exhibit electrical contrast with respect to the background medium. The quantitative approaches, on the other hand, yield an estimate of the target's electrical properties at each spatial point. Qualitative methods are widely used for detection of abnormalities even though there is no quantitative feedback. These methods often employ a linearized model of scattering allowing for quick inversion. Thus, an image is reconstructed practically in real time. However, the results may not be satisfactory if the linearized forward model is an inadequate representation of the actual scattering processes. Qualitative methods include holographic [9–12], sensitivity-based [13, 14], confocal [15–17], and time-reversal [18, 19] methods.

Quantitative techniques that are widely used in microwave imaging are Born iterative methods [20–22], stochastic optimization methods [23–25], and

---

D.S. Shumakov • D. Tajik • A.S. Beaverstone • N.K. Nikolova (✉)  
Department of Electrical and Computer Engineering, McMaster University,  
Hamilton, ON, Canada  
e-mail: [nikolova@ieee.org](mailto:nikolova@ieee.org)

deterministic iterative procedures [26–28]. These methods update the forward model in an iterative manner to match the measured data. The quantitative reconstruction usually involves solving the nonlinear scattering problem which takes into account multiple scattering effects and is valid for scatterers of any electrical size and dielectric contrast. The inverse-scattering problem is intrinsically ill-posed and is tackled by time-consuming iteration loops aided by appropriate regularization strategies. The convergence of the quantitative methods depends critically on the fidelity of the forward model.

Recently, two methods have been proposed offering the benefits of the quantitative reconstruction in real time while not being nonlinear and/or iterative. These methods are quantitative microwave holography (QMH) [29] and scattered-power mapping (SPM) [30]. Both of them are direct inversion techniques with the resolvent kernel extracted from measurements. Note that the QMH and SPM methods presented here have undergone substantial modifications compared to the methods they are derived from. Being conceptually different, the previous developments of QMH and SPM exploited  $k$ -space and real-space inversion schemes, respectively. Here, the convolution-based inversion theory is employed to place both methods in a common framework. Thus, the performance of QMH and SPM can be compared analytically and experimentally within this framework.

Calibration measurements are used to obtain the resolvent kernel in the integral equation of scattering, thus providing a high-fidelity forward model in both QMH and SPM. The key aspect that enables their quantitative outcome is the use of the calibration object, or CO. It is an electrically small scatterer with known relative permittivity, embedded in the background medium. The calibration object response constitutes a point-spread function (PSF) which in turn provides the respective resolvent kernel of the data equation.

The focus of this chapter is the comparison of the reconstruction fidelity of images obtained with analytical, simulated, and measured resolvent kernels. This study is carried out with examples in near-field microwave imaging, which is known to be sensitive to modeling errors. We commence with a discussion of the different strategies for the estimation of resolvent kernel in the forward model of scattering. Then, the reconstruction theory is derived for planar raster-scanning acquisition in the frequency domain. The QMH and SPM methodologies are presented in the common framework of reconstruction through deconvolution. Their limitations are discussed. Finally, examples of reconstruction with QMH and SPM are shown. The image fidelity is discussed in relation to the type of resolvent kernel that has been used by the reconstruction algorithms. Comparison between the two algorithms provides insight into their advantages and shortcomings.

## 17.2 Forward Model of Scattering

Let the object under test (OUT) have a relative permittivity contrast  $\Delta\varepsilon_{\text{OUT}}(\mathbf{r}) = \varepsilon_{\text{OUT}}(\mathbf{r}) - \varepsilon_{\text{RO}}(\mathbf{r})$ , where  $\varepsilon_{\text{OUT}}$  is the relative complex permittivity of the OUT and  $\varepsilon_{\text{RO}}$  is that of the reference object (RO) which represents the scatterer-free

environment. It is assumed here that  $\Delta\varepsilon_{\text{OUT}}$  is frequency independent in the bandwidth of interest; however, the dispersive contrast can be incorporated into the resolvent kernel of data equation as  $\Delta\varepsilon_{\text{OUT}}(\mathbf{r}, f) = \Delta\varepsilon_{\text{OUT}}(\mathbf{r})\varphi(f)$ , where  $\varphi(f)$  is a known frequency dependence [31].

Since the frequency-sweep measurements are performed one frequency at a time,  $f^{(m)}$  denotes one of the frequencies in a discrete set of  $N_f$  frequencies, where  $m = 1, \dots, N_f$ . A network of  $N_r$  ( $i = 1, \dots, N_r$ ) receivers and  $N_t$  ( $j = 1, \dots, N_t$ ) transmitters is employed. We start with the data equation written in terms of the scattering parameters as [32, 33]:

$$S_{\text{OBJ},n}^{(m)}(\mathbf{r}) = S_{\text{RO},n}^{(m)}(\mathbf{r}) + \kappa_n^{(m)} \int_{V'} \Delta\varepsilon_{\text{OBJ}}(\mathbf{r}') \left[ \mathbf{E}_{\text{RO},i}(\mathbf{r}'; \mathbf{r}) \cdot \mathbf{E}_{\text{OBJ},j}(\mathbf{r}'; \mathbf{r}) \right]^{(m)} d\mathbf{r}', \quad n = 1, \dots, N_r N_t, \quad (17.1)$$

where  $n$  is the response measured in the  $n$ th experiment at position  $\mathbf{r}$ ,  $m$  is the frequency index,  $V'$  is the volume of the OUT,  $\mathbf{r}'$  is the position inside  $V'$ , and  $\kappa_n^{(m)}$  is a known complex constant dependent on the type of response. The  $n$ th experiment involves a unique pair of receiving ( $i$ th) and transmitting ( $j$ th) antennas. The abbreviation OBJ stands for the CO or the OUT. Henceforth, we denote the number of responses as  $N_D$ , which is  $N_D = N_r N_t$ .

It is important to clarify the physical meaning of the field quantities comprising the kernel in the square brackets of the integral equation in (17.1).  $\mathbf{E}_{\text{RO},i}(\mathbf{r}'; \mathbf{r})$  is the field in the RO (the incident field) that is generated by the  $i$ th (receiving) antenna provided it operated as a transmitter.  $\mathbf{E}_{\text{OBJ},j}(\mathbf{r}'; \mathbf{r})$  is the total internal field due to the  $j$ th transmitting antenna. Note that the ordered pair  $(\mathbf{r}'; \mathbf{r})$  indicates that the internal field distribution is a function of  $\mathbf{r}' \in V'$ , whereas the position of the respective transmitting antenna is at  $\mathbf{r}$ . It is consistent with the existing convention  $(\mathbf{r}_o; \mathbf{r}_s)$ , in which the first position vector is that of the observation point, while the second position vector is that of the source point.

Under the Born approximation, (17.1) becomes linear with respect to the unknown permittivity contrast and the  $n$ th response at the  $m$ th frequency:

$$S_{\text{OBJ},n}^{(m)}(\mathbf{r}) = S_{\text{RO},n}^{(m)}(\mathbf{r}) + \kappa_n^{(m)} \int_{V'} \Delta\varepsilon_{\text{OBJ}}(\mathbf{r}') \left[ \mathbf{E}_{\text{RO},i}(\mathbf{r}'; \mathbf{r}) \cdot \mathbf{E}_{\text{RO},j}(\mathbf{r}'; \mathbf{r}) \right]^{(m)} d\mathbf{r}'. \quad (17.2)$$

The field dot product distribution in the square brackets in (17.2) is referred to as the linearized resolvent kernel, and its acquisition is part of the system calibration. We next examine different strategies of estimating the resolvent kernel.



### 17.2.1 *Acquiring the Resolvent Kernel Analytically*

In far-zone microwave imaging, the incident fields can be approximated analytically, which is computationally inexpensive and does not require any specific hardware or simulation software. The far field of an antenna in an open space can be approximated using: (a) the plane wave approximation or  $\sim \exp(-i\mathbf{k}_b \cdot \mathbf{r})$ , (b) locally plane wave approximation or  $\sim \exp(-ik_b r)$ , (c) the spherical wave (also known as isotropic wave) approximation or  $\sim \frac{\exp(-ik_b r)}{r}$ , and (d) the cylindrical wave approximation or  $\sim H_0^{(2)}(k_b \rho)$ . Here,  $k_b$  represents the background wave number,  $\mathbf{k}_b$  is the wave vector,  $r$  is the distance from the antenna to the observation point, and  $\mathbf{r}$  is the position vector of the observation point relative to the antenna. Note that the cylindrical wave approximation is used in the 2D case of microwave tomography with  $\rho$  being the distance from the antenna to the observation point.

The locally plane wave approximation is extensively used in millimeter wave reflection holography [5, 12]. This approximation is sufficiently accurate when the following conditions are met: (i) the target is in the far zone of the transmitting and receiving antennas, (ii) the distance between the target and the scanned aperture is larger than the biggest dimension of the scanned aperture, and (iii) this distance is at least an order of magnitude larger than the wavelength. However, in near-field imaging some or all of these conditions may not hold, which deteriorates the fidelity of the forward model used in the reconstruction.

The linearized model of scattering (17.2) can be improved by taking the radiation pattern of the antenna into account [34]. This is beneficial when high-gain antennas are used because their radiated power is significantly smaller off boresight. Besides, the phaseless radiation pattern of antennas is always known. It should be noted that in microwave imaging, it is customary to use wide-beam antennas so that the target is interrogated from wider viewing angles, thereby improving the spatial resolution.

Most importantly, the analytical approximations of the resolvent kernel yield only a qualitative outcome. This is because they lack the proper scaling that depends on: (i) the power and phase of the actual excitation and (ii) the volume and contrast of an actual small scatterer. Also note that analytically obtained resolvent kernels are not valid in near-field imaging applications.

### 17.2.2 *Acquiring the Resolvent Kernel in Simulations*

In this case, the field dot product distribution is estimated by simulating the measurements in the background medium for all  $N_D$  responses at all  $N_f$  frequencies. Two simulations have to be done at each response – one for the excitation with a transmitter and one for the excitation with a receiver set to operate in a transmitting

mode. Keeping in mind that the complexity of an imaging setup is fairly high, the computational time may exceed even a week.

The major advantage of using simulations is in obtaining both vectorial distributions,  $\mathbf{E}_{\text{RO},i}^{(m)}(\mathbf{r}'; \mathbf{r})$  and  $\mathbf{E}_{\text{RO},j}^{(m)}(\mathbf{r}'; \mathbf{r})$  in (17.2). Note that one represents Green's function whereas the other approximates the total internal field. Knowing these quantities enables quantitative imaging via nonlinear iterative reconstruction which involves updating the two field distributions separately. Also, simulations are advantageous due to the absence of stochastic noise.

On the other hand, numerical errors such as mesh convergence errors or imperfect absorbing boundary conditions are present. They can be reduced, however, by performing a mesh convergence study and using a refined mesh in the subsequent simulations. Unfortunately, this refinement may also lead to a prohibitive computational burden.

The main disadvantage of the simulated resolvent kernels is that they are often incapable of properly modeling the actual setup due to modeling errors [35, 36]. Unlike numerical errors, modeling errors are much more difficult to eliminate. They arise from the inability to account for errors within the fabrication tolerances of the antennas and the imaging setup, uncertainties in the constitutive parameters of the materials used in the measurement enclosure, deformations caused by temperature or humidity, aging of the materials, etc. Moreover, the complexities in the cables, connectors, screws, supporting plates, and so on are often ignored. Finally, the electromagnetic interference and positioning errors in the acquisition setup as well as the measurement errors are difficult to predict. All these factors corrupt the forward model fidelity, thereby making the quantitative results obtained with a simulated resolvent kernel not reliable, especially in near-field imaging.

### 17.2.3 *Acquiring the Resolvent Kernel in Measurements*

The experimental acquisition of the resolvent kernel  $\mathbf{E}_{\text{RO},i}^{(m)}(\mathbf{r}'; \mathbf{r}) \cdot \mathbf{E}_{\text{RO},j}^{(m)}(\mathbf{r}'; \mathbf{r})$  offers the best fidelity [29, 36]. An electrically small scatterer of known permittivity contrast is placed in the RO and is measured. This scatterer can be a cube or a sphere with a maximum dimension equal to or smaller than  $\lambda/4$ , where  $\lambda$  is the shortest wavelength in the calibration object. As a whole, the small scatterer's volume and relative permittivity must satisfy the limits of Born's approximation [37]. We emphasize that since the CO response represents the resolvent kernel of each particular imaging system, the rule of thumb is that if the CO cannot be imaged, the OUT cannot be reconstructed either. Thus, this calibration measurement also provides information about the system sensitivity.

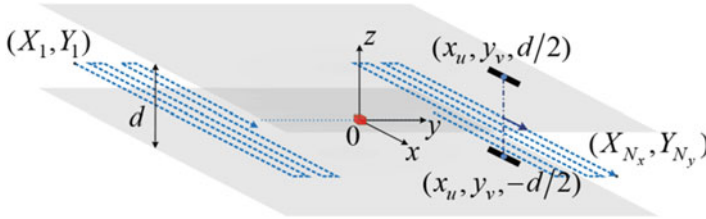


**Fig. 17.1** Schematic configuration of the planar scanning setup for the calibration object measurements: two aligned antennas (shown with *thick black lines*) separated by a distance  $d$  are moving together along the scanning route (shown with *blue dash lines*) in a raster fashion. A small scatterer (*red cube*) is placed at the origin. The sampling position is  $\mathbf{r}_{uv} = (x_u, y_v | z)$ . The sampling involves  $N_x$  samples along  $x$  and  $N_y$  samples along  $y$

The small scatterer is positioned at the center of the inspected domain ( $\mathbf{r}'_0 = 0$ ), and the sensors scan over the whole acquisition surface (Fig. 17.1). For a single voxel-size scatterer of known relative permittivity contrast  $\delta\epsilon_{\text{CO}}$  embedded in the reference object, the resolvent kernel at  $\mathbf{r}'_0 = 0$  can be obtained from (17.2) as

$$[\mathbf{E}_{\text{RO},i} \cdot \mathbf{E}_{\text{RO},j}]_{(\mathbf{r}'=0;\mathbf{r})}^{(m)} \approx \frac{\Delta S_{\text{CO},n}^{(m)}(\mathbf{r})}{\kappa_n^{(m)} \delta\epsilon_{\text{CO}} \Omega_v}, \quad (17.3)$$

where  $\Omega_v$  is the volume of the scatterer and  $\Delta S_{\text{CO},n}^{(m)}(\mathbf{r}) = S_{\text{CO},n}^{(m)}(\mathbf{r}) - S_{\text{RO},n}^{(m)}(\mathbf{r})$  are the scattered calibration object responses. These responses form the PSF of the imaging system.

In a uniform RO, measuring the PSF with a small scatterer at the center of an imaged domain is sufficient since the CO responses at all other lateral locations  $\mathbf{r}'_p \in V'$ ,  $p = 1, \dots, N_v$  can be obtained from it by coordinate translation. Let the CO responses acquired on a planar surface with the small scatterer at the center,  $\mathbf{r}'_0 = (x'_0, y'_0 | z')$ , be denoted as  $\Delta S_{\text{CO},0,n}^{(m)}(\mathbf{r}_{uv})$ ,  $u = 1, \dots, N_x$ ,  $v = 1, \dots, N_y$ . Let the CO responses due to a point scatterer at  $\mathbf{r}'_p = (x'_p, y'_p | z')$  be denoted as  $\Delta S_{\text{CO},p,n}^{(m)}(\mathbf{r}_{uv})$ . Then,

$$\Delta S_{\text{CO},p,n}^{(m)}(\mathbf{r}_{uv}) = \Delta S_{\text{CO},0,n}^{(m)}(\mathbf{r}_{uv} - \Delta\mathbf{r}), \quad (17.4)$$

where  $\Delta\mathbf{r} = \mathbf{r}'_p - \mathbf{r}'_0 = (x'_p - x'_0, y'_p - y'_0 | 0)$ .

Obtaining the CO responses from the PSFs at various range locations of the small scatterer is not as straightforward since the planar system scans only laterally and translations along range do not apply. The simplest and most reliable approach is to acquire the PSFs at several range locations of the small scatterer inside the volume of interest. By interpolating the acquired PSFs with respect to  $z$ , images at other range locations can be obtained.

In conclusion, if the inspected volume is uniform, one measurement of the system PSF with a small scatterer at the center suffices in estimating the resolvent kernel of the data equation for all responses. Even though such measurement has to be repeated for several range locations, it still proves to be faster than simulations.

As a final remark, we note that the acquisition of the measured resolvent kernel is impossible when the imaged domain is inaccessible for a small scatterer to be embedded in it. In addition, both simulated and measured resolvent kernels cannot be estimated in the case of a completely unknown imaged scene since it cannot be emulated before the imaging system is deployed on site. In such cases, we have to resort to analytical approximations.

### 17.3 Direct Inversion

The reconstruction theory presented here is derived for planar raster-scanning acquisition in the frequency domain; however it can easily be modified to accommodate time-domain measurements and/or the acquisition surfaces of other shapes. It should be emphasized that we incorporate the  $\exp(i\omega t)$  time dependence.

We begin with rewriting (17.1) for the case of the calibration measurement:

$$S_{\text{CO},n}^{(m)}(\mathbf{r}) = S_{\text{RO},n}^{(m)}(\mathbf{r}) + \kappa_n^{(m)} \int_{V'} \delta \varepsilon_{\text{CO}} \left[ \mathbf{E}_{\text{RO},i}(\mathbf{r}'; \mathbf{r}) \cdot \mathbf{E}_{\text{CO},p,j}(\mathbf{r}'; \mathbf{r}) \right]^{(m)} d\mathbf{r}', \quad n = 1, \dots, N_D. \quad (17.5)$$

The field distribution  $\mathbf{E}_{\text{CO},p,j}^{(m)}(\mathbf{r}'_p; \mathbf{r})$  inside the small scatterer in the CO is in principle unknown. We utilize the localized quasi-linear (LQL) approximation based on the assumption that the total internal field in an electrically small scatterer is linearly proportional to the incident field via an electrical reflectivity tensor  $\overline{\overline{\lambda}}$  [38]:

$$\mathbf{E}_{\text{CO},p,j}^{(m)}(\mathbf{r}'_p; \mathbf{r}) \approx \overline{\overline{\lambda}}_{\text{CO}}^{(m)}(\mathbf{r}'_p) \cdot \mathbf{E}_{\text{RO},j}^{(m)}(\mathbf{r}'_p; \mathbf{r}). \quad (17.6)$$

Thus, (17.5) can be rewritten as:

$$\Delta S_{\text{CO},p,n}^{(m)}(\mathbf{r}) \approx \kappa_n^{(m)} \delta \varepsilon_{\text{CO}} \Omega_v \left[ \mathbf{E}_{\text{RO},i}(\mathbf{r}'_p; \mathbf{r}) \cdot \left( \overline{\overline{\lambda}}_{\text{CO}}^{(m)}(\mathbf{r}'_p) \cdot \mathbf{E}_{\text{RO},j}(\mathbf{r}'_p; \mathbf{r}) \right) \right]^{(m)}, \quad (17.7)$$

where the CO scattered response is:

$$\Delta S_{\text{CO},p,n}^{(m)}(\mathbf{r}) = S_{\text{CO},p,n}^{(m)}(\mathbf{r}) - S_{\text{RO},n}^{(m)}(\mathbf{r}). \quad (17.8)$$

A subtraction analogous to (17.8) is used to obtain the OUT scattered response:

$$\Delta S_{\text{OUT},n}^{(m)}(\mathbf{r}) = S_{\text{OUT},n}^{(m)}(\mathbf{r}) - S_{\text{RO},n}^{(m)}(\mathbf{r}). \quad (17.9)$$

Assuming that  $\mathbf{E}_{\text{CO},p,j}^{(m)}$  and  $\mathbf{E}_{\text{RO},j}^{(m)}$  are collinear,  $\overline{\overline{\lambda}}_{\text{CO}}^{(m)}$  becomes a reflectivity tensor defined by a scalar:

$$\overline{\overline{\lambda}}_{\text{CO}}^{(m)} = \lambda_{\text{CO}}^{(m)} \overline{\mathbf{I}}. \quad (17.10)$$

With (17.10), the resolvent kernel in (17.7) is obtained as

$$\left[ \mathbf{E}_{\text{RO},i}(\mathbf{r}'_p; \mathbf{r}) \cdot \mathbf{E}_{\text{RO},j}(\mathbf{r}'_p; \mathbf{r}) \right]^{(m)} \approx \frac{\Delta S_{\text{CO},p,n}^{(m)}(\mathbf{r})}{\kappa_n^{(m)} \delta \varepsilon_{\text{CO}} \Omega_v \lambda_{\text{CO}}^{(m)}}. \quad (17.11)$$

Equation (17.11) represents the resolvent kernel of the forward model under the LQL approximation.

The forward model of scattering for an OUT is derived from (17.1) as

$$\Delta S_{\text{OUT},n}^{(m)}(\mathbf{r}) = \kappa_n^{(m)} \int_{V'} \Delta \varepsilon_{\text{OUT}}(\mathbf{r}') \left[ \mathbf{E}_{\text{RO},i}(\mathbf{r}'_p; \mathbf{r}) \cdot \mathbf{E}_{\text{OUT},j}(\mathbf{r}'_p; \mathbf{r}) \right]^{(m)} d\mathbf{r}'. \quad (17.12)$$

If we neglect the mutual coupling and the multiple scattering effects, we can apply the LQL approximation (17.10) to obtain

$$\Delta S_{\text{OUT},n}^{(m)}(\mathbf{r}) \approx \kappa_n^{(m)} \int_{V'} \Delta \varepsilon_{\text{OUT}}(\mathbf{r}') \lambda_{\text{OUT}}^{(m)}(\mathbf{r}') \left[ \mathbf{E}_{\text{RO},i}(\mathbf{r}'_p; \mathbf{r}) \cdot \mathbf{E}_{\text{RO},j}(\mathbf{r}'_p; \mathbf{r}) \right]^{(m)} d\mathbf{r}'. \quad (17.13)$$

Substituting (17.11) into (17.13) gives

$$\Delta S_{\text{OUT},n}^{(m)}(\mathbf{r}) \approx \int_{V'} \Delta \varepsilon_{\text{OUT}}(\mathbf{r}') \lambda_{\text{OUT}}^{(m)}(\mathbf{r}') \left[ \frac{\Delta S_{\text{CO},p,n}^{(m)}(\mathbf{r})}{\delta \varepsilon_{\text{CO}} \Omega_v \lambda_{\text{CO}}^{(m)}} \right] d\mathbf{r}'. \quad (17.14)$$

Since all the quantities in the square brackets of (17.14) are known, such forward model inherently incorporates the specifics of the imaging setup. As shown in [30], the ratio  $\lambda_{\text{OUT}}^{(m)}(\mathbf{r}') / \lambda_{\text{CO}}^{(m)}$  reaches unity as the calibration object permittivity contrast  $\delta \varepsilon_{\text{CO}}$  approaches the OUT permittivity contrast  $\Delta \varepsilon_{\text{OUT}}$ . Henceforth, we assume that

$$\lambda_{\text{OUT}}^{(m)}(\mathbf{r}') / \lambda_{\text{CO}}^{(m)} \approx 1. \quad (17.15)$$

### 17.3.1 Quantitative Microwave Holography

Since we operate with frequency domain data acquired on planar surfaces, the scattered responses (17.8) and (17.9) at each frequency are functions of  $x$  and  $y$ . As per (17.4), for an imaging system which is translationally invariant in the lateral directions, the PSFs at all locations of the small scatterer in a plane  $z' = z_0$  can be obtained from the one at the plane's center as (see 17.4):

$$\Delta S_{\text{CO},p,n}^{(m)}(x, y|z_0) = \Delta S_{\text{CO},0,n}^{(m)}(x - (x'_p - x'_0), y - (y'_p - y'_0)|z_0). \quad (17.16)$$

Substituting (17.16) into (17.14), we notice that the integral is a 2D convolution of two functions:

$$\Delta S_{\text{OUT},n}^{(m)}(x, y) = \frac{1}{\Omega_v} \int_z \left[ \tau(x', y'|z') \otimes \Delta S_{\text{CO},0,n}^{(m)}(x', y'|z') \right] dz', \quad (17.17)$$

where  $\tau(\mathbf{r}') = \Delta \varepsilon_{\text{OUT}}(\mathbf{r}') / \delta \varepsilon_{\text{CO}}$  is the unknown contrast function, whereas the operator  $\otimes$  represents a 2D convolution over  $x'$  and  $y'$  at each  $z'$  plane. Thus, having estimated the system PSF and having measured the OUT, the 3D image can be reconstructed slice by slice by deconvolution. Linear deconvolution methods offer the fastest and the simplest choice when computing the unknown  $\tau$  in (17.17). These algorithms employ some form of the linear reconstruction filter in a single step. The classical inverse filter, the pseudo-inverse filter, Wiener's filter, and the constrained least-squares filters belong to this group of methods [39, 40].

In this paper, we show the most straightforward method of deconvolution, which is performed in Fourier space. Equation (17.17) can be represented as:

$$\Delta \tilde{S}_{\text{OUT},n}^{(m)}(k_x, k_y) = \frac{\Delta \Omega}{\Omega_v} \sum_{j=1}^{N_z} \tilde{\tau}(k_x, k_y|z'_j) \cdot \Delta \tilde{S}_{\text{CO},0,n}^{(m)}(k_x, k_y|z'_j), \quad (17.18)$$

where the *tilda* denotes the 2D Fourier transform of a function of  $(x, y)$ , whereas  $\Delta \Omega = \Delta x \Delta y \Delta z$  is the voxel's volume with  $\Delta x$ ,  $\Delta y$ ,  $\Delta z$  being the sampling steps along  $x$ ,  $y$ , and  $z$ , respectively.  $N_z$  is the number of imaged range locations.

Microwave imaging systems usually operate with frequency-swept data. We denote the data vector as  $\mathbf{b}(\boldsymbol{\kappa})$ . At each point in Fourier space  $\boldsymbol{\kappa} = (k_x, k_y)$ ,  $\mathbf{b}$  is a vectorized arrangement of all  $N_D$  responses at all  $N_f$  frequencies:

$$\mathbf{b}(\boldsymbol{\kappa}) = [\mathbf{b}_1^T(\boldsymbol{\kappa}) \cdots \mathbf{b}_{N_D}^T(\boldsymbol{\kappa})]^T, \quad (17.19)$$

where:

$$\mathbf{b}_n(\boldsymbol{\kappa}) = \left[ \Delta \tilde{S}_{\text{OUT},n}^{(1)}(\boldsymbol{\kappa}) \cdots \Delta \tilde{S}_{\text{OUT},n}^{(N_f)}(\boldsymbol{\kappa}) \right]^T, \quad n = 1, \dots, N_D. \quad (17.20)$$

Thus, the size of  $\mathbf{b}(\boldsymbol{\kappa})$  is  $N_D N_f$ . Similarly, the system matrix  $\mathbf{A}(\boldsymbol{\kappa})$  is constructed from the PSFs as:

$$\mathbf{A}(\boldsymbol{\kappa}) = \begin{bmatrix} \mathbf{A}_1(\boldsymbol{\kappa}) \\ \vdots \\ \mathbf{A}_{N_D}(\boldsymbol{\kappa}) \end{bmatrix}_{(N_D N_f) \times N_z}, \quad (17.21)$$

where

$$\mathbf{A}_n(\boldsymbol{\kappa}) = \begin{bmatrix} \Delta \tilde{\mathcal{S}}_{\text{CO},n@}(0,0,z'_1)(\boldsymbol{\kappa}, z'_1, f_1) \cdots \Delta \tilde{\mathcal{S}}_{\text{CO},n@}(0,0,z'_{N_z})(\boldsymbol{\kappa}, z'_{N_z}, f_1) \\ \Delta \tilde{\mathcal{S}}_{\text{CO},n@}(0,0,z'_1)(\boldsymbol{\kappa}, z'_1, f_2) \cdots \Delta \tilde{\mathcal{S}}_{\text{CO},n@}(0,0,z'_{N_z})(\boldsymbol{\kappa}, z'_{N_z}, f_2) \\ \vdots \quad \ddots \quad \vdots \\ \Delta \tilde{\mathcal{S}}_{\text{CO},n@}(0,0,z'_1)(\boldsymbol{\kappa}, z'_1, f_{N_f}) \cdots \Delta \tilde{\mathcal{S}}_{\text{CO},n@}(0,0,z'_{N_z})(\boldsymbol{\kappa}, z'_{N_z}, f_{N_f}) \end{bmatrix}_{N_f \times N_z} \quad (17.22)$$

Therefore, we can formulate (17.18) as the linear system of equations:

$$\mathbf{A}(\boldsymbol{\kappa}) \cdot \mathbf{x}(\boldsymbol{\kappa}) = \mathbf{b}(\boldsymbol{\kappa}), \quad (17.23)$$

where the solution vector contains the values of the unknown contrast at the point  $\boldsymbol{\kappa}$  in Fourier space for all  $N_z$  range positions:

$$\mathbf{x}(\boldsymbol{\kappa}) = \frac{\Delta \Omega}{\Omega_v} \left[ \tilde{\tau}(\boldsymbol{\kappa}, z'_1) \cdots \tilde{\tau}(\boldsymbol{\kappa}, z'_{N_z}) \right]^T. \quad (17.24)$$

Since the size of  $\mathbf{A}_n(\boldsymbol{\kappa})$  is  $N_f \times N_z$  with  $N_f$  typically exceeding  $N_z$  by an order of magnitude, the system of equations for each  $\boldsymbol{\kappa} = (k_x, k_y)$  in (17.23) is overdetermined and may not be of a full column rank. Thus, the solution can be obtained by the Moore-Penrose inverse [41]. The problem of nonuniqueness necessitates imposing the constraints to ensure the physicality of the obtained solution. Employing the time dependence as  $\exp(i\omega t)$ , typical physical constraints on the relative permittivity distribution of the OUT would require that

$$\text{Re} \{ \varepsilon_{\text{OUT}}(\mathbf{r}') \} \geq 1 \quad \text{Im} \{ \varepsilon_{\text{OUT}}(\mathbf{r}') \} \leq 0, \quad \mathbf{r}' \in V'. \quad (17.25)$$

Once we have  $\tilde{\tau}(\boldsymbol{\kappa}, z')$  for  $\forall \boldsymbol{\kappa}$  and for  $\forall z'$ , the frequency-combined 3D ratio contrast is recovered via 2D inverse Fourier transform slice by slice:

$$\tau(x', y' | z'_l) = F_{2D}^{-1} \{ \tilde{\tau}(\boldsymbol{\kappa}, z'_l) \}, \quad z'_l = z'_1, \dots, z'_{N_z}. \quad (17.26)$$

Finally, the relative complex permittivity of the OUT is found from

$$\varepsilon_{\text{OUT}}(x', y' | z'_l) = \varepsilon_{\text{RO}}(x', y' | z'_l) + \delta\varepsilon_{\text{CO}} \cdot \tau(x', y' | z'_l). \quad (17.27)$$

Note that some normalization strategy should be used each time the frequency-swept measured data are processed. By doing so, the signals with larger magnitudes at low frequencies will have the same impact on the final result as the high-frequency signals with lesser magnitudes. Also, the normalization accounts for the reflection and transmission  $S$ -parameters of different strength. The following normalization can be used at each frequency:

$$\Delta\bar{S}_{\text{OBJ},n}^{(m)}(\mathbf{r}) = \Delta S_{\text{OBJ},n}^{(m)}(\mathbf{r}) / \max\left(\left|\Delta S_{\text{CO},n}^{(m)}(\mathbf{r})\right|\right). \quad (17.28)$$

### 17.3.2 Scattered-Power Mapping

The SPM formulation proposed here is derived in a similar way to QMH. However, there are important differences in the two approaches. First of all, the concept of *power maps* is introduced, hence the name SPM. We define the OUT or CO power map as:

$$M_{\text{OBJ}}^{(m)}(\mathbf{r}'_p) = \sum_{n=1}^{N_D} \Delta S_{\text{OBJ},n}^{(m)} \cdot \Delta S_{\text{CO},p,n}^{(m)*}, \quad p = 1, \dots, N_v. \quad (17.29)$$

An immediate advantage of the power maps is that a qualitative image can be obtained via (17.29). These images are obtained practically instantaneously. Also, (17.29) provides a good initial guess for the OUT contrast, which is estimated quantitatively by direct inversion as explained next. More insights into the concept of power maps can be found in Ref. [30].

In the case of wideband data, it is convenient to combine the power maps for all sampled frequencies. The recommended normalization for the SPM is [42]:

$$M_{\text{OBJ}}(\mathbf{r}'_p) = \frac{1}{N_f} \sum_{m=1}^{N_f} \frac{|M_{\text{OBJ}}^{(m)}(\mathbf{r}'_p)|}{\eta^{(m)}} \cdot e^{i\angle M_{\text{OBJ}}^{(m)}(\mathbf{r}'_p)}, \quad (17.30)$$

where  $\eta^{(m)}$  is the maximum magnitude value of the CO power maps at the  $m$ th frequency:

$$\eta^{(m)} = \max\left(\left|M_{\text{CO},q}^{(m)}(\mathbf{r}'_p)\right|\right). \quad (17.31)$$



Note that the coordinate translation described for the CO scattered responses also holds for the CO power maps. Following similar discretization methodology as that for the QMH, we formulate a square linear system of equations at each point in Fourier space  $\boldsymbol{\kappa} = (k_x, k_y)$  as:

$$\begin{bmatrix} \mathbf{M}_1(\boldsymbol{\kappa}) \\ \vdots \\ \mathbf{M}_{N_D}(\boldsymbol{\kappa}) \end{bmatrix}_{N_D \times N_z} \cdot \mathbf{x}(\boldsymbol{\kappa}) = \begin{bmatrix} \mathbf{m}_1(\boldsymbol{\kappa}) \\ \vdots \\ \mathbf{m}_{N_D}(\boldsymbol{\kappa}) \end{bmatrix}_{N_D}, \quad (17.32)$$

where the following notations are introduced:

$$\mathbf{x}(\boldsymbol{\kappa}) = \frac{\Delta\Omega}{\Omega_v} \left[ \tilde{\tau}(\boldsymbol{\kappa}, z'_1) \cdots \tilde{\tau}(\boldsymbol{\kappa}, z'_{N_z}) \right]^T, \quad (17.33)$$

$$\mathbf{m}_n(\boldsymbol{\kappa}) = \left[ \tilde{M}_{\text{OUT},n}(\boldsymbol{\kappa}, z_1) \cdots \tilde{M}_{\text{OUT},n}(\boldsymbol{\kappa}, z_{N_z}) \right]^T, \quad (17.34)$$

$$\mathbf{M}_n(\boldsymbol{\kappa}) = \begin{bmatrix} \tilde{M}_{\text{CO},n@}(0,0,z'_1)(\boldsymbol{\kappa}, z'_1) & \cdots & \tilde{M}_{\text{CO},n@}(0,0,z'_{N_z})(\boldsymbol{\kappa}, z'_1) \\ \tilde{M}_{\text{CO},n@}(0,0,z'_1)(\boldsymbol{\kappa}, z'_2) & \cdots & \tilde{M}_{\text{CO},n@}(0,0,z'_{N_z})(\boldsymbol{\kappa}, z'_2) \\ \vdots & \ddots & \vdots \\ \tilde{M}_{\text{CO},n@}(0,0,z'_1)(\boldsymbol{\kappa}, z'_{N_z}) & \cdots & \tilde{M}_{\text{CO},n@}(0,0,z'_{N_z})(\boldsymbol{\kappa}, z'_{N_z}) \end{bmatrix}_{N_z \times N_z} \quad (17.35)$$

Note that unlike the system of equations in QMH, the system of equations (17.32) is not overdetermined. The system matrix is square of size  $N_z \times N_z$ , due to the advantage of having multifrequency power maps as per (17.30).

It can be shown using (17.23) and (17.34) that  $\mathbf{A}_n^\dagger \mathbf{A}_n \mathbf{x} = \mathbf{A}_n^\dagger \mathbf{b}_n$  is equivalent to the system  $\mathbf{M}_n \mathbf{x} = \mathbf{m}_n$ . Here,  $\mathbf{A}_n^\dagger$  is the Hermitian of  $\mathbf{A}_n$ . Since the data  $\mathbf{b}_n$  may not be entirely in the range of the forward operator represented by  $\mathbf{A}_n$ , the direct solution of  $\mathbf{A}_n \mathbf{x} = \mathbf{b}_n$  may not exist. On the other hand, under the same conditions,  $\mathbf{A}_n^\dagger \mathbf{A}_n \mathbf{x} = \mathbf{A}_n^\dagger \mathbf{b}_n$  may have a solution, and it would minimize the least-square error of  $\mathbf{A}_n \mathbf{x} = \mathbf{b}_n$  [19, 43]. This argument also speaks in favor of obtaining the PSFs experimentally, which ensures that the system matrix  $\mathbf{M}_n$  provides the physically correct functional space encompassing all possible responses acquired with the particular imaging setup.

As a final remark, we note that in general, the SPM method is more versatile than the QMH since its inversion procedure is not limited to that in the Fourier space [30]. The power maps of the SPM are a coherent summation of the products of responses related to each point in space. Therefore, the data acquired at any random set of observation points can still be processed by the SPM.

### 17.3.3 Limitations of QMH and SPM

The reconstruction methods described above cannot account for the multiple scattering and the mutual coupling effects present in the OUT, which is typical for all linear inversion methods. That is why the applications of QMH and SPM are limited to the weak scattering problem. On the other hand, these methods can serve as a module providing an initial guess within the nonlinear iterative procedure such as the Born iterative method or the distorted Born iterative method.

The limitations stemming from the assumption in (17.15) are derived in Ref. [30]. It has been shown that the quantitative reconstruction accuracy of QMH and SPM improves when the following holds:

$$\varepsilon_{\text{CO}} \approx \varepsilon_{\text{OUT}}(\mathbf{r}'). \quad (17.36)$$

This condition serves as a guideline when choosing the properties of the CO for the system calibration. Note, however, that the fidelity of the qualitative reconstruction with (17.29) is not dependent on the choice of the relative permittivity of the electrically small scatterer in the CO.

The size  $\Omega_v$  of the small scatterer in the CO should be large enough to be detected by the imaging system and small enough to ensure approximately uniform field distribution within its volume. Therefore, the lateral size of a scatterer equal or somewhat smaller than  $\lambda/4$  is necessary, where  $\lambda$  is the shortest wavelength in the CO across the frequency sweep. As for the vertical dimension, it should be approximately the same as the thickness of the measured spatial step along range. However, in some challenging scenarios, particularly in biomedical imaging, the CO response can be significantly corrupted by attenuation and noise. In such cases, it is recommended to increase its contrast  $\delta\varepsilon_{\text{CO}}$ .

## 17.4 Validation Examples

### 17.4.1 Experimental Setup

The experimental setup used for acquiring the measured resolvent kernel is shown in Fig. 17.2a. It consists of the two open-ended WR42 waveguides aligned along their boresight, which move together in a planar raster fashion. The distance between them is approximately 74 mm. The antennas operate in air. The data acquisition involves transmission and reflection measurements.

The OUT is suspended between the antennas. It consists of letter-shaped objects placed in a block of polystyrene with a thickness of 66 mm. The objects shaped as letters *C* and *A* are fabricated from Eccostock HiK material [44]. As measured

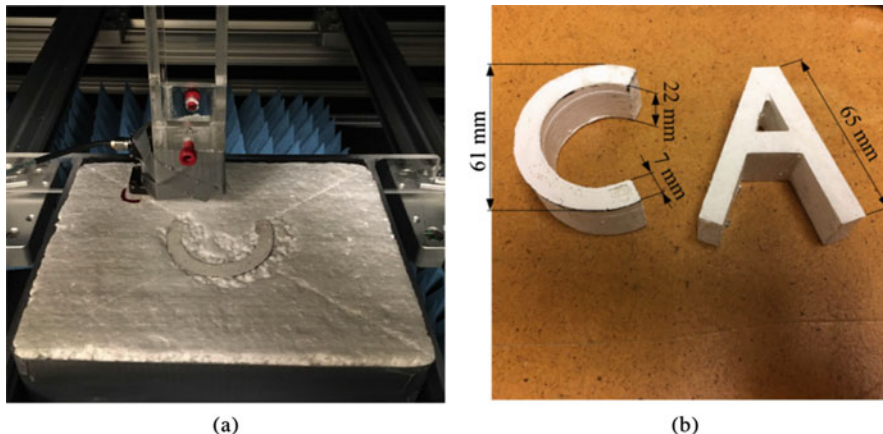


**Fig. 17.2** Photograph of (a) the imaged setup for the letters experiment and (b) the letters *C* and *A* with their respective dimensions

by a dielectric probe [45], its averaged relative permittivity value in the frequency range from 18 to 25 GHz is  $\epsilon_r \approx 4.8 - i2.2$ . The width of the letters is 7 mm whereas the thickness is 22 mm (Fig. 17.2b). The maximum lateral dimension of the letter *A* is 65 mm. It is placed at the center of the bottom plane. The maximum lateral dimension of the letter *C* is 61 mm, and it is placed at the center of the top plane (see Fig. 17.2a).

The imaged area is 10 cm by 10 cm. The scanning step is 2 mm in both lateral directions. The frequency sweep is from 18 to 25 GHz with 71 frequency samples. The vector network analyzer output power is 0 dBm.

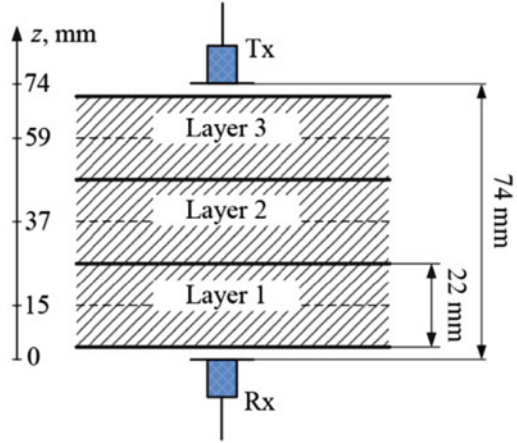
Note that the calculated range resolution for the given frequency range is about 21 mm. Since the thickness of the fabricated *C* and *A* letters equals 22 mm, we should be able to distinguish them reasonably well in the range direction.

#### 17.4.2 *Reconstruction with Analytically Acquired Resolvent Kernel*

We start with reconstructing the proposed OUT by employing the resolvent kernel approximated analytically. For that, the spherical wave approximation is used. More specifically, from (17.2) in case of reflection data, we have:

$$\left[ \mathbf{E}_{\text{RO},i}(\mathbf{r}'; \mathbf{r}) \cdot \mathbf{E}_{\text{RO},j}(\mathbf{r}'; \mathbf{r}) \right]^{(m)} \sim \frac{e^{-i2k_{\text{RO}}^{(m)}r}}{r^2}, \quad (17.37)$$

**Fig. 17.3** Sketch of the imaged setup. Transmitter Tx and receiver Rx are aligned along their boresight. The OUT consists of three layers being 22 mm thick. The distance from the antenna flanges to the OUT is 4 mm



where  $r = \|\mathbf{r}' - \mathbf{r}\|$ ,  $\mathbf{r}' = (0, 0, z')$ , and  $\mathbf{r} = (x, y, z)$ . The respective range distances for transmitting antenna are  $\Delta z_{1,\text{Tx}} = z'_1 - z_{\text{Tx}} = -59$  mm,  $\Delta z_{2,\text{Tx}} = z'_2 - z_{\text{Tx}} = -37$  mm, and  $\Delta z_{3,\text{Tx}} = z'_3 - z_{\text{Tx}} = -15$  mm, whereas those for receiving antenna are  $\Delta z_{1,\text{Rx}} = z'_1 - z_{\text{Rx}} = 15$  mm,  $\Delta z_{2,\text{Rx}} = z'_2 - z_{\text{Rx}} = 37$  mm, and  $\Delta z_{3,\text{Rx}} = z'_3 - z_{\text{Rx}} = 59$  mm (see Fig. 17.3).

In case of the transmission data, we have:

$$\left[ \mathbf{E}_{\text{RO},i}(\mathbf{r}'; \mathbf{r}) \cdot \mathbf{E}_{\text{RO},j}(\mathbf{r}'; \mathbf{r}) \right]^{(m)} \sim \frac{e^{-ik_{\text{RO}}^{(m)} r_{\text{Tx}}}}{r_{\text{Tx}}} \cdot \frac{e^{-ik_{\text{RO}}^{(m)} r_{\text{Rx}}}}{r_{\text{Rx}}}, \quad (17.38)$$

where  $r_{\text{Tx}} = \|\mathbf{r}' - \mathbf{r}_{\text{Tx}}\|$ ,  $r_{\text{Rx}} = \|\mathbf{r}' - \mathbf{r}_{\text{Rx}}\|$  and  $\mathbf{r}_{\text{Tx}} = (x, y, z_{\text{Tx}})$ , and  $\mathbf{r}_{\text{Rx}} = (x, y, z_{\text{Rx}})$ . Analogously, the respective range distances are  $\Delta z_{1,\text{Tx}} = -59$  mm,  $\Delta z_{2,\text{Tx}} = -37$  mm, and  $\Delta z_{3,\text{Tx}} = -15$  mm, while  $\Delta z_{1,\text{Rx}} = 15$  mm,  $\Delta z_{2,\text{Rx}} = 37$  mm, and  $\Delta z_{3,\text{Rx}} = 59$  mm (see Fig. 17.3). The wavenumber  $k_{\text{RO}}^{(m)}$  is calculated at each sampled frequency from 18 to 25 GHz (with 100 MHz step) in polystyrene. To do this, the relative permittivity of polystyrene is measured with a dielectric probe. The averaged relative permittivity value of polystyrene across the given frequency sweep is  $\varepsilon_r \approx 1.05 - i0.03$ . Finally, the respective reference object measurements are obtained with the polystyrene layer being 66 mm thick.

The QMH and SPM reconstructed results with analytically acquired kernel are shown in Figs. 17.4 and 17.5. The images are qualitative. With the reflection data processed in Figs. 17.4a and b, we observe the spurious solution shaped as a C letter in the middle layer. Figures 17.5a and b demonstrate qualitative images obtained by processing the transmission data with QMH and SPM, respectively. It is seen that the fidelity of the reconstruction is rather poor in both cases. Additionally, the images obtained with transmission data only lack range resolution, which is an expected result [46].

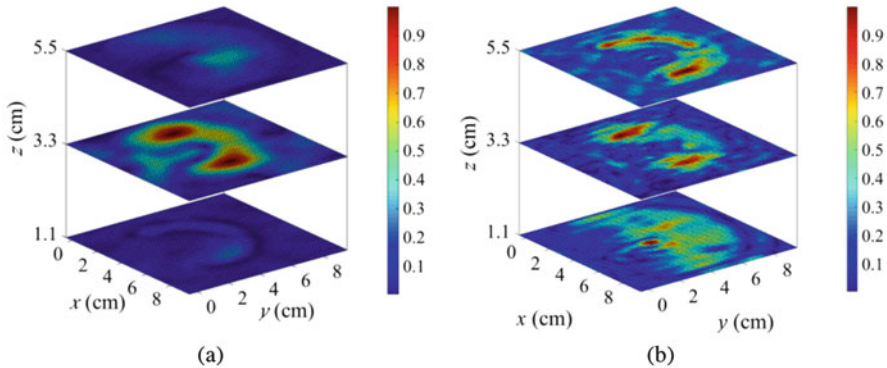


**Fig. 17.4** Qualitative multifrequency images obtained with analytically acquired (spherical wave approximation) kernel by (a) QMH and (b) SPM. Only the reflection data are processed. The results are normalized to 1

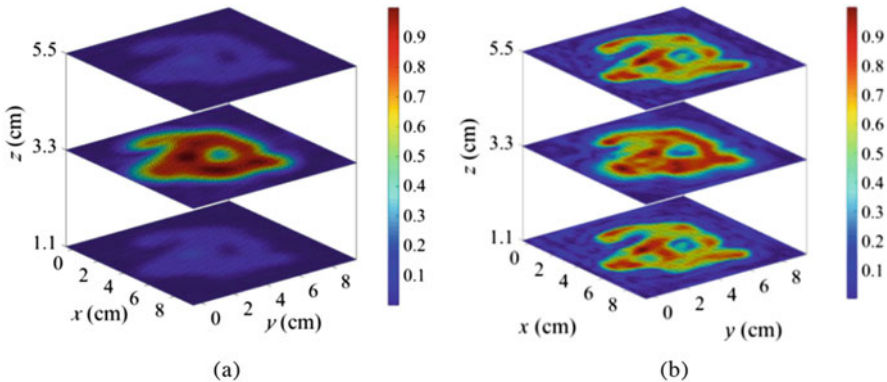


**Fig. 17.5** Qualitative multifrequency images obtained with analytically acquired (spherical wave approximation) kernel by (a) QMH and (b) SPM. Only the transmission data are processed. The results are normalized to 1

Both QMH and SPM fail to provide a reasonable quantitative outcome in case of an analytical resolvent kernel. An example of such quantitative images obtained with the SPM is shown in Fig. 17.6.

Finally, we attempt the reconstruction with another far-field analytical approximation, the locally plane wave approximation. In case of the reflection data, the kernel is proportional to

$$\left[ \mathbf{E}_{\text{RO},i}(\mathbf{r}'; \mathbf{r}) \cdot \mathbf{E}_{\text{RO},j}(\mathbf{r}'; \mathbf{r}) \right]^{(m)} \sim e^{-i2k_{\text{RO}}^{(m)}r}, \quad (17.39)$$

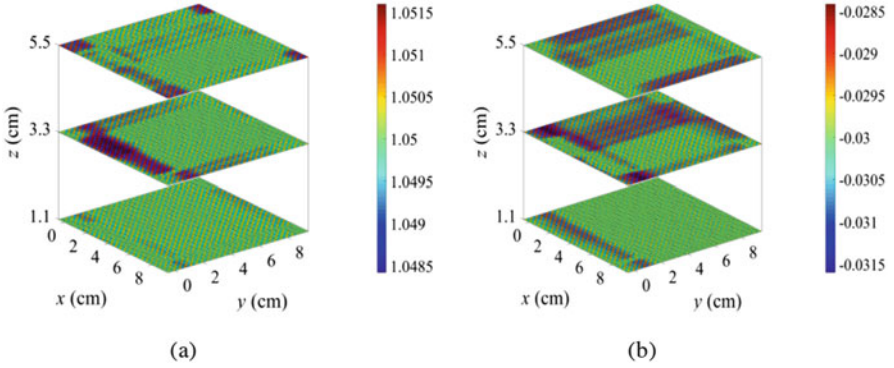


**Fig. 17.6** Quantitative multifrequency images obtained with analytically acquired (spherical wave approximation) kernel by SPM: (a) real and (b) imaginary parts of the relative permittivity. Only the reflection data are processed

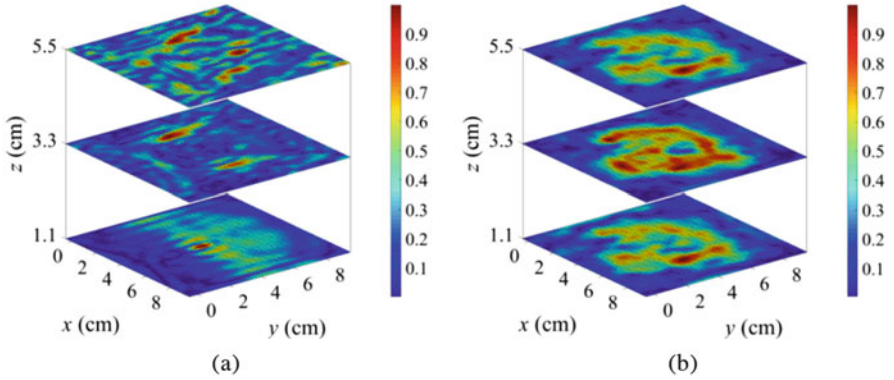


**Fig. 17.7** Qualitative multifrequency images obtained with analytically acquired (locally plane wave approximation) kernel by SPM in case of (a) reflection and (b) transmission data. The results are normalized to 1

where  $r = \|\mathbf{r}' - \mathbf{r}\|$ ,  $\mathbf{r}' = (0, 0, z')$ , and  $\mathbf{r} = (x, y, z)$ . In case of the transmission data, the resolvent kernel becomes

$$\left[ \mathbf{E}_{\text{RO},i}(\mathbf{r}'; \mathbf{r}) \cdot \mathbf{E}_{\text{RO},j}(\mathbf{r}'; \mathbf{r}) \right]^{(m)} \sim e^{-ik_{\text{RO}}^{(m)} r_{\text{Tx}}} \cdot e^{-ik_{\text{RO}}^{(m)} r_{\text{Rx}}}, \quad (17.40)$$

where  $r_{\text{Tx}} = \|\mathbf{r}' - \mathbf{r}_{\text{Tx}}\|$ ,  $r_{\text{Rx}} = \|\mathbf{r}' - \mathbf{r}_{\text{Rx}}\|$  and  $\mathbf{r}_{\text{Tx}} = (x, y, z_{\text{Tx}})$ , and  $\mathbf{r}_{\text{Rx}} = (x, y, z_{\text{Rx}})$ . In (17.39) and (17.40), the respective range distances are the same as in (17.37) and (17.38). However, this approximation does not provide meaningful results neither with QMH nor with SPM. An example of such reconstruction in the case of SPM is shown in Fig. 17.7.

### 17.4.3 Reconstruction with Simulated Resolvent Kernel

For this case, a simulation setup emulating the scenario shown in Fig. 17.2a in the absence of the OUT is implemented in FEKO [47] in a much simplified form as shown in Fig. 17.8. The modeled radiating structure here is an open-ended WR42 waveguide transition. The waveguide excitation is accomplished by using the pins as wire ports (see Fig. 17.8). The voltage source with a magnitude of 1 V and a port impedance of 50 Ohms is used. The polystyrene structure is modeled as part of the planar multilayer (free space – polystyrene – free space) substrate, which does not require meshing during the simulation thus drastically improving the running time. The layer of polystyrene is 66 mm thick, and its relative permittivity is modeled as  $\epsilon_r = 1.05 - i0.03$ . The distance from the antenna flanges to the polystyrene layer is 4 mm.

In the simulation, the field distribution generated by each antenna is acquired at  $z'_1 = 15$  mm,  $z'_2 = 37$  mm, and  $z'_3 = 59$  mm (Fig. 17.3). The kernel is obtained by taking the dot product of  $\mathbf{E}_{\text{RO},i}^{(m)}(\mathbf{r}'; \mathbf{r})$  and  $\mathbf{E}_{\text{RO},j}^{(m)}(\mathbf{r}'; \mathbf{r})$  (see Eq. (17.2)), acquired at each sampled point inside the imaged area of 10 cm by 10 cm. The spatial sampling is kept the same as in the measurement, which is 2 mm. The linearly spaced frequency samples are from 18 to 25 GHz, with 100 MHz step (71 frequency samples in total). Each near-field request (out of 6) takes about 6 h to be completed by FEKO on a computer with following parameters: Intel(R) Xeon(R) 12-core CPU X5670 @ 2.93 GHz with 32.0 GB RAM.

Note that due to modeling errors, the simulated field values are limited in their accuracy when compared with experimental measurements. Not only are the simulated waveguides made with ideal materials and simplified geometry, but the simulated power leaving the guides is only an approximation of the actual power leaving the experimental (physical) waveguides during a real-world measurement. Thus, we expect to see the credible qualitative (not quantitative) images in this case.

The qualitative 3D-reconstructed images obtained with QMH utilizing the simulated kernel are shown in Fig. 17.9. QMH may require a filtering step depending

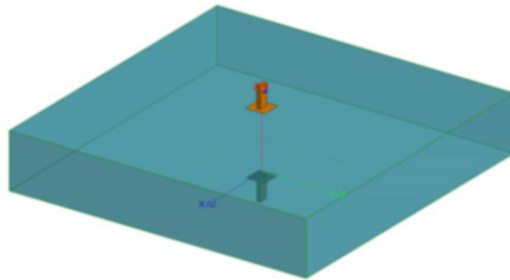


**Fig. 17.8** The simulation setup in FEKO emulating the planar scan with two open-ended WR42 waveguides aligned along each other's boresight. The polystyrene is shown with a blue box. The near-fields' values are requested at the middle of each of the three layers along  $z$

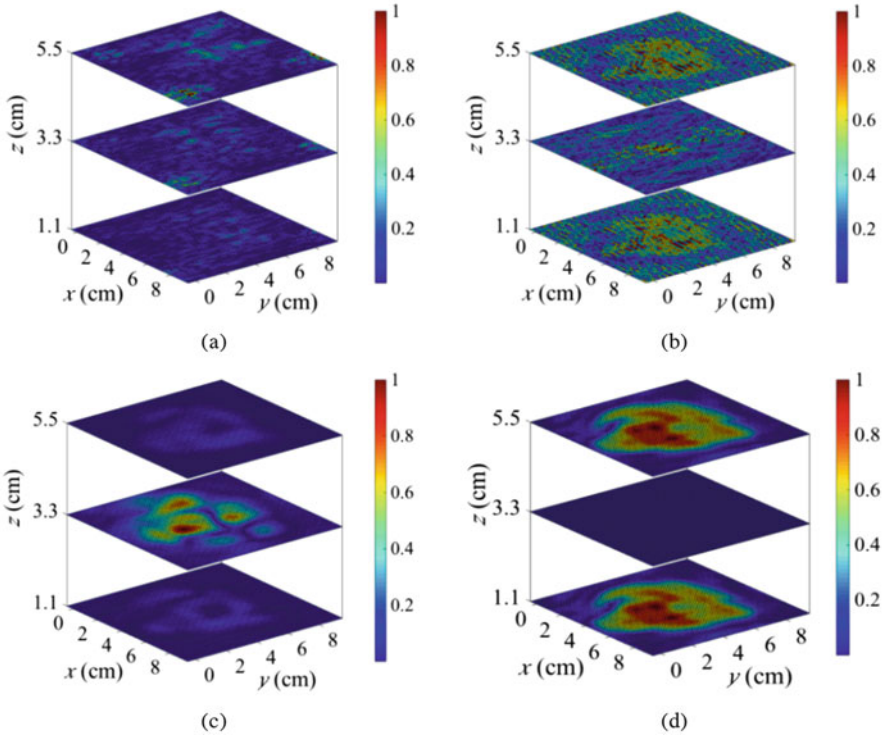


**Fig. 17.9** Qualitative multifrequency images obtained with simulated kernel by QMH: (a) the reflection data and (b) transmission data; (c) the reflection data and (d) transmission data processed using low-pass Gaussian filter. The results are normalized to 1

on the number of  $x$  and  $y$  samples captured during data acquisition. This is due to the inherent ill-posedness of the matrices being solved. In the Fourier space, each spectral position  $\kappa = (k_x, k_y)$  has an associated system of equations that needs to be solved. The spectral position represents a spatial frequency that is determined through the Fourier transform by the sampling step and the number of samples measured in the real domain, following the Nyquist criterion. The highest value of the spatial frequency is therefore equal to  $1/2\Delta x$ , where  $\Delta x$  is the size of the sampling step. However, the highest spatial frequency that is physically detectable is limited by the wavelength of the radiation. Unfortunately, due to noise and other factors, the solutions to the systems of equations at the highest spectral positions are inaccurate, drastically impacting the output of the reconstruction algorithm in real space. In order to suppress the high spatial frequency noise, a low-pass Gaussian filter can be applied. The effect of such filtering can be observed in Fig. 17.9: the images become somewhat improved.

The qualitative reconstruction with SPM is shown in Fig. 17.10. Note that no filtering has been used in this case. The reflection data in Fig. 17.10a provides a



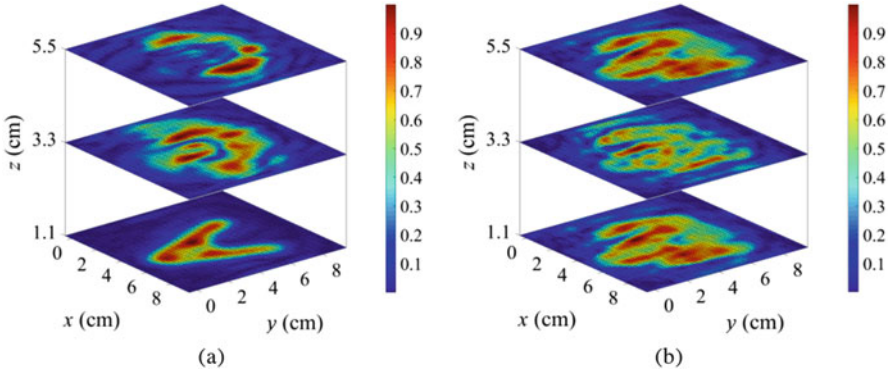


**Fig. 17.10** Qualitative multifrequency images obtained with SPM utilizing the simulated kernel in case of (a) reflection and (b) transmission data. The results are normalized to 1

relatively good fidelity of reconstruction, with the letters *C* and *A* being reconstructed in their respective locations (top and bottom) along with some artifacts in the top layer. The transmission data in Fig. 17.10b are not able to separate the reconstructed letters along the range, which is expected [46].

As for the quantitative reconstruction, both methods fail to produce a meaningful outcome. The resulting images look similar to the ones shown in Fig. 17.6.

#### 17.4.4 Reconstruction with Experimentally Acquired Resolvent Kernel

Finally, we attempt the reconstruction with the PSF (see Eq. (17.3)) obtained from measurements. The calibration object is composed of the same polystyrene block with a dielectric cylinder of 5 mm diameter and 20 mm height, embedded at the center of the imaged plane. The cylinder is made of a dielectric with  $\epsilon_r \approx 12$ . The height of the scatterer is chosen to be approximately the same as that of the inspected objects.

Since we aim at 3D reconstruction, the respective calibration object measurements are performed at the center of each of the three  $z$  planes (see Fig. 17.3). The whole set of OUT, reference object, and three calibration object measurements are obtained in about 10 h employing a mechanical scanning hardware. It should be emphasized that this scan time can be significantly reduced by exploiting electronically switched sensor arrays.

The QMH and SPM multifrequency qualitative images in the case of reflection data are shown in Fig. 17.11, whereas the transmission data are shown in Fig. 17.12. Note that a low-pass Gaussian filter has been used in QMH. Another option can be to use the de-noising algorithm proposed in Ref. [48].

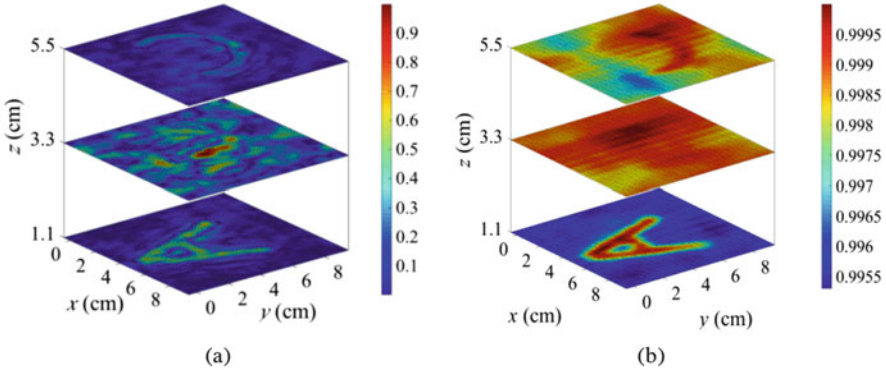


**Fig. 17.11** Qualitative multifrequency images obtained by using the measured kernel with reflection data: (a) the QMH and (b) the SPM outcome. The results are normalized to 1

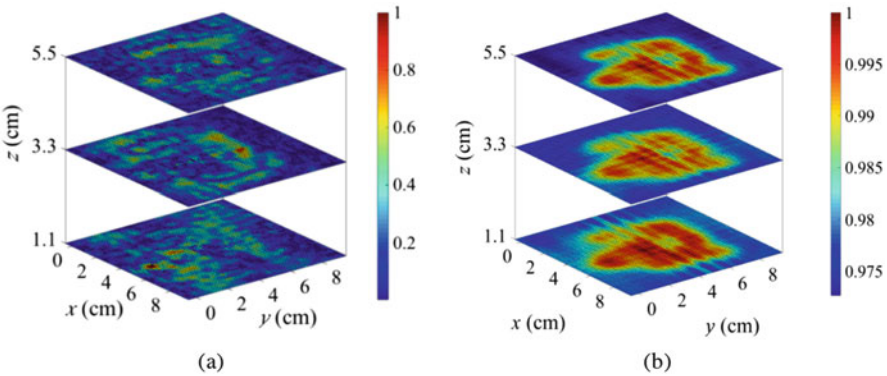


**Fig. 17.12** Qualitative multifrequency images obtained by using the measured kernel with transmission data: (a) the QMH and (b) the SPM outcome. The results are normalized to 1

The quantitative images obtained with QMH are shown in Fig. 17.13, whereas those obtained with SPM are shown in Fig. 17.14. The overall quantitative output is satisfactory. However, we observe some nonphysical values both in the real and imaginary parts of the reconstructed relative permittivity. There are a few possible causes of such artifacts: (i) the ill-posed nature of the inversion problem, (ii) the small scatterer in the calibration object is large enough to violate the assumed uniform field distribution within its volume, (iii) the discrete Fourier transforms lead to edge artifacts appearing in the form of  $2D$  *sinc* functions due to the inability of capturing high spatial frequency transitions [49], and (iv) stochastic noise and measurement uncertainties present in the acquired data.

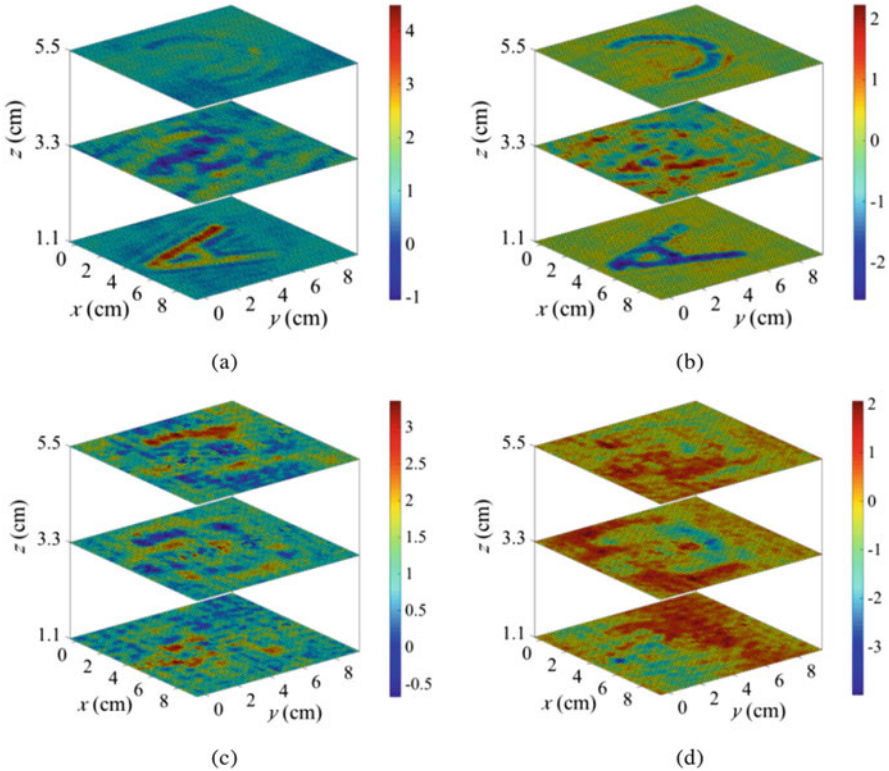


**Fig. 17.13** Quantitative multifrequency images obtained by QMH using the measured kernel: (a) real and (b) imaginary parts of the relative permittivity with reflection data; (c) real and (d) imaginary parts of the relative permittivity with transmission data. Low-pass Gaussian filter has been used

## 17.5 Conclusion

Two reconstruction methods, QMH and SPM, have been discussed in terms of a common convolution-based direct inversion theory. The performance of both methods is compared both analytically and experimentally in near-field imaging. For that, the analytical, simulated, and experimental resolvent kernels are investigated. It has been shown that the qualitative images obtained with SPM do not require filtering when processing the simulated kernel, while those obtained with QMH need to be filtered in order to produce meaningful results. This is attributed to the fact that the SPM qualitative maps are obtained through a simple coherent summation of power maps with no inversion procedure required.

In all examples, the quantitative images are obtained in the most straightforward way, which is by linear deconvolution through a classical inverse filter with no

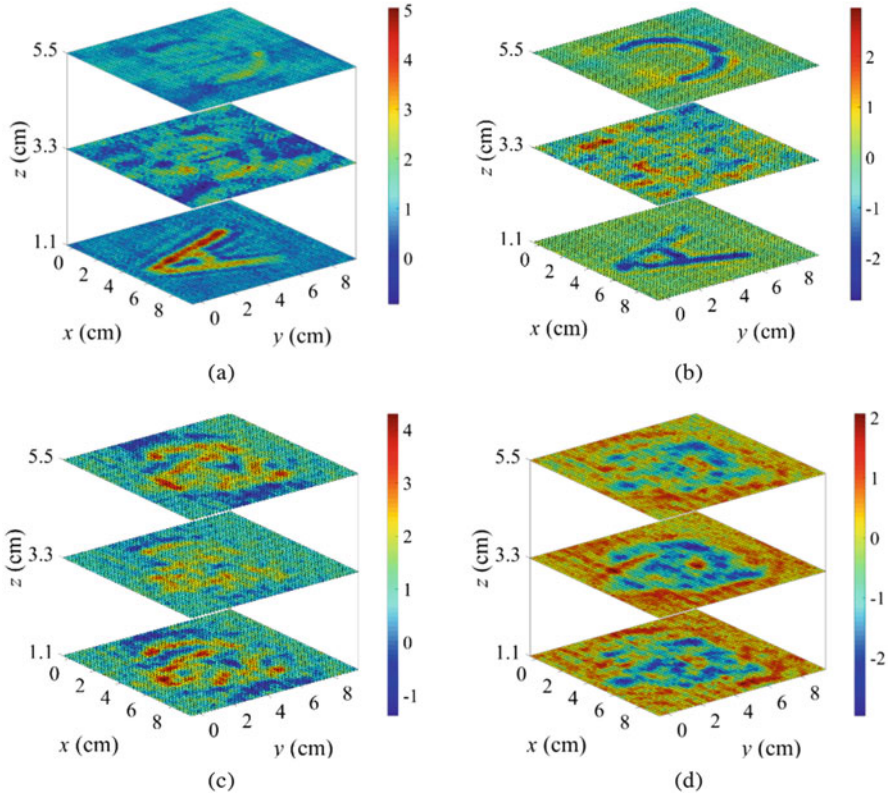


**Fig. 17.14** Quantitative multifrequency images obtained by SPM using the measured kernel: (a) real and (b) imaginary parts of the relative permittivity with reflection data; (c) real and (d) imaginary parts of the relative permittivity with transmission data

physics constraints and no regularization. Both methods provide quantitative images practically in real time; however, nonphysical artifacts are present.

The obtained reconstruction results suggest that the quantitative outcome is possible only with a resolvent kernel obtained through the calibration measurements. Such measurements can be performed on an electrically small scatterer embedded in the background medium. Not only does the calibration measurement provide the proper scaling of the resolvent kernel in the forward model, but it is also significantly less time-consuming than simulations (especially, if an electronically switched scanning hardware is used).

The proposed SPM and QMH inversion procedures are performed in Fourier space. In general, however, SPM is more versatile than QMH since its linear inversion can also be formulated in real space. For example, in Refs. [30, 50], and, where the data is acquired with planar scanning, the permittivity contrast is

reconstructed directly as a function of  $x$ ,  $y$ , and  $z$ . In applications where the data are acquired on a random shape with any spatial sampling, the same approach can be used with very few modifications since the construction of the linear system of equations in real space is independent of the geometry. Also, the fact that, in its first processing step, the SPM produces a qualitative OUT image practically instantaneously is an important advantage. This feature makes the SPM method preferable in qualitative imaging. Examples of such applications include on-body concealed weapon detection, scanning of luggage, and the detection of defects (e.g., cracks and pits) in metallic and composite structures. While qualitative holography has a relatively long history in these applications, the SPM is a very recent development, which is yet to realize its potential in both qualitative and quantitative imaging.

Both, the QMH and the SPM reconstruction methods, are limited by the linearizing approximations of the forward model of scattering. Consequently, they are incapable of accounting for mutual coupling and multiple scattering. Such effects dominate the scattering in complex heterogeneous objects such as living tissue, luggage items, structural components in civil engineering, etc. Often, from a qualitative point of view, the QMH and the SPM images are valuable even with strongly heterogeneous scattering objects that feature high contrast. Yet, these results lack quantitative accuracy. That is why future work aims at incorporating the QMH and the SPM methods inside nonlinear reconstruction schemes such as the Born iterative or the distorted Born iterative algorithms. The distinguishing feature of these algorithms is that they employ the Born series to successively improve the accuracy of the contrast estimate and that of the total field. Since they utilize linear reconstruction modules inside the iterative loop, they can greatly benefit from the quantitative real-time performance of either QMH or SPM.

## References

1. M.G. Amin (Ed.), *Through-the-Wall Radar Imaging* (CRC Press, Boca Raton, FL, 2011)
2. J. Nanzer, *Microwave and Millimeter-wave Remote Sensing for Security Applications* (Artech House, Norwood, MA, 2012)
3. D.J. Daniels, *EM Detection of Concealed Targets* (Wiley-IEEE Press, Hoboken, NJ, 2009)
4. R. Zoughi, *Microwave Non-destructive Testing and Evaluation* (Kluwer, Dordrecht, The Netherlands, 2000)
5. D.M. Sheen, D.L. McMakin, T.E. Hall, Near-field three-dimensional radar imaging techniques and applications. *Appl. Opt.* **49**(19), E83–E93 (2010)
6. N.K. Nikolova, Microwave biomedical imaging, in *Wiley Encyclopedia of Electrical and Electronics Engineering* (published online 25 Apr 2014)
7. A. Rosen, M.A. Stuchly, A.V. Vorst, Applications of RF/microwaves in medicine. *IEEE Trans. Microw. Theory Tech.* **50**(3), 963–974 (2002)
8. A.V. Vorst, A. Rosen, Y. Kotsuka, *RF/Microwave Interaction with Biological Tissues* (Wiley, Hoboken, NJ, 2006)

9. M. Ravan, R.K. Amineh, N.K. Nikolova, Two-dimensional near-field microwave holography. *Inverse Prob.* **26**(5), 055011 (2010)
10. R.K. Amineh, A. Khalatpour, H. Xu, Y. Baskharoun, N.K. Nikolova, Three-dimensional near-field microwave holography for tissue imaging. *Int. J. Biomed. Imaging*, **2012**, 291494 (2012)
11. M. Elsdon, D. Smith, M. Leach, S.J. Foti, Experimental investigation of breast tumor imaging using indirect microwave holography. *Microw. Opt. Technol. Lett.* **48**, 480–482 (2006)
12. D.M. Sheen, D.L. McMakin, T.E. Hall, Three-dimensional millimeter-wave imaging for concealed weapon detection. *IEEE Trans. Microw. Theory Tech.* **49**(9), 1581–1592 (2001)
13. L. Liu, A. Trehan, N.K. Nikolova, Near-field detection at microwave frequencies based on self-adjoint response sensitivity analysis. *Inverse Prob.* **26**, 105001 (2010)
14. Y. Zhang, S. Tu, R. K. Amineh, N. K. Nikolova, Resolution and robustness to noise of the sensitivity-based method for microwave imaging with data acquired on cylindrical surfaces. *Inverse Prob.* **28**(11), 115006 (2012)
15. E.C. Fear, X. Li, S.C. Hagness, M.A. Stuchly, Confocal microwave imaging for breast cancer detection: localization of tumors in three dimensions. *IEEE Trans. Biomed. Eng.* **49**(8), 812–822 (2002)
16. H.B. Lim, N.T.T. Nhung, E.P. Li, N.D. Thang, Confocal microwave imaging for breast cancer detection: delay-multiply-and-sum image reconstruction algorithm. *IEEE Trans. Biomed. Eng.* **55**(6), 1697–1704 (2008)
17. P.M. Meaney, M.W. Fanning, D. Li, S.P. Poplack, K.D. Paulsen, A clinical prototype for active microwave imaging of the breast. *IEEE Trans. Microw. Theory Tech.* **48**(11), 1841–1853 (2000)
18. P. Kosmas, C.M. Rappaport, Time reversal with the FDTD method for microwave breast cancer detection. *IEEE Trans. Microw. Theory Tech.* **53**(7), 2317–2323 (2005)
19. A.J. Devaney, *Mathematical Foundations of Imaging, Tomography and Wave Field Inversion* (Cambridge University Press, Cambridge, 2012)
20. W.C. Chew, Y.M. Wang, Reconstruction of two-dimensional permittivity distribution using the distorted Born iterative method. *IEEE Trans. Med. Imag.* **9**(2), 218–225 (1990)
21. T.J. Cui, W.C. Chew, A.A. Aydiner, S. Chen, Inverse scattering of two-dimensional dielectric objects buried in lossy earth using the distorted Born iterative method. *IEEE Trans. Geosci. Remote Sens.* **39**(2), 339–346 (2001)
22. A.G. Tijhuis, K. Belkebir, A.C.S. Litman, B.P. de Hon, Multiple-frequency distorted-wave Born approach to 2D inverse profiling. *Inverse Prob.* **17**(6), 1635–1644 (2001)
23. M. Pastorino, Stochastic optimization methods applied to microwave imaging: a review. *IEEE Trans. Antennas Propag.* **55**(3), 538–548 (2007)
24. P. Rocca, M. Benedetti, M. Donelli, D. Franceschini, A. Massa, Evolutionary optimization as applied to inverse scattering problems. *Inverse Prob.* **25**, 1–41 (2009)
25. M. Donelli, G. Franceschini, A. Martini, A. Massa, An integrated multiscale strategy based on a particle swarm algorithm for inverse scattering problems. *IEEE Trans. Geosci. Remote Sens.* **44**(2), 298–312 (2006)
26. H. Harada, D.J.N. Wall, T. Takenaka, M. Tanaka, Conjugate gradient method applied to inverse scattering problem. *IEEE Trans. Antennas Propag.* **43**(8), 784–792 (1995)
27. C. Estatico, M. Pastorino, A. Randazzo, An inexact-Newton method for short-range microwave imaging within the second-order Born approximation. *IEEE Trans. Geosci. Remote Sens.* **43**, 2593–2605 (2005)
28. A. Abubakar, P.M. van den Berg, J.J. Mallorqui, Imaging of biomedical data using a multiplicative regularized contrast source inversion method. *IEEE Trans. Microw. Theory Tech.* **50**(7), 1761–1771 (2002)
29. D. Tajik, J. Thompson, A.S. Beaverstone, N.K. Nikolova, Real-time quantitative reconstruction based on microwave holography, in *IEEE AP-S/URSI International Symposium on Antennas and Propagation*, Fajardo, Puerto Rico, June 2016

30. S. Tu, J.J. McCombe, D.S. Shumakov, N.K. Nikolova, Fast quantitative microwave imaging with resolvent kernel extracted from measurements. *Inverse Prob.* **31**(4), 045007 (2015)
31. R.K. Amineh, M. Ravan, A. Khalatpour, N.K. Nikolova, Three-dimensional near-field microwave holography using reflected and transmitted signals. *IEEE Trans. Antennas Propag.* **59**(12), 4777–4789 (2011)
32. N.K. Nikolova, D.S. Shumakov, A.S. Beaverstone, Obtaining system-specific Green's functions through measurements: theory and applications in microwave imaging, in *IEEE AP-S/URSI International Symposium on Antennas and Propagation*, Fajardo, Puerto Rico, June 2016
33. A.S. Beaverstone, D.S. Shumakov, N.K. Nikolova, Frequency-domain integral equations of scattering for complex scalar responses. *IEEE Trans. Microw. Theory Tech.* **65**(4), 1120–1132
34. R.K. Amineh, J. McCombe, N.K. Nikolova, Microwave holographic imaging using the antenna phaseless radiation pattern. *IEEE Antennas Wirel. Propag. Lett.* **11**, 1529–1532 (2012)
35. M. Ostadrahimi, P. Mojabi, C. Gilmore, A. Zakaria, S. Noghianian, S. Pistorius, J. LoVetri, Analysis of incident field modeling and incident/scattered field calibration techniques in microwave tomography. *IEEE Antennas Wirel. Propag. Lett.* **10**, 900–903 (2011)
36. R.K. Amineh, J.J. McCombe, A. Khalatpour, N.K. Nikolova, Microwave holography using point-spread functions measured with calibration objects. *IEEE Trans. Instrum. Meas.* **64**(2), 403–417 (2015)
37. T.M. Habashy, R.W. Groom, B.R. Spies, Beyond the Born and Rytov approximations: a nonlinear approach to electromagnetic scattering. *J. Geophys. Res. Solid Earth* **98**(B2), 1759–1775 (1993)
38. M.S. Zhdanov, E. Tartaras, Three-dimensional inversion of multitransmitter electromagnetic data based on the localized quasi-linear approximation. *Geophys. J. Int.* **148**, 506–519 (2002)
39. D.S.C. Biggs, *Accelerated iterative blind deconvolution*, PhD thesis, University of Auckland, New Zealand, 1998
40. T.G. Savelyev, A.G. Yarovoy, Fast imaging by 3-D deconvolution in short-range UWB radar for concealed weapon detection, in *Proceedings of the 9th European Radar Conference (2012 EuMA)*, 31 Oct–2 Nov 2012
41. G. Strang, *Linear Algebra and Its Applications*, 4th edn. (Brooks Cole, Belmont, CA, 2005)
42. D.S. Shumakov, *Comparison of Multi-frequency PSF Normalization Strategies*, CEM-R-76 (McMaster University, 2016)
43. M. Pastorino, *Microwave Imaging* (Wiley, Hoboken, NJ, 2010)
44. Emerson and Cuming Microwave Products, a unit of Laird Technologies
45. Agilent 85070E Dielectric Probe Kit, Keysight Technologies, USA ([www.keysight.com](http://www.keysight.com))
46. R.K. Amineh, M. Ravan, J. McCombe, N. K. Nikolova, Three-dimensional microwave holographic imaging employing forward-scattered waves only. *Int. J. Antennas Propag.* **2013**, 897287 (2013)
47. FEKO Suite 7.0.1 for Altair. EM Software & Systems – S. A. (Pty) Ltd., USA ([www.feko.info](http://www.feko.info))
48. D.S. Shumakov, A.S. Beaverstone, N.K. Nikolova, De-noising algorithm for enhancing microwave imaging. *IET J. Eng.* doi: [10.1049/joe.2016.0207](https://doi.org/10.1049/joe.2016.0207) (2017)
49. I.N. Bankman, Enhancement: frequency domain techniques, in *Handbook of Medical Imaging* (Academic Press, San Diego, 2000), p. 16
50. D.S. Shumakov, A.S. Beaverstone, N.K. Nikolova, Optimal illumination schemes for near-field microwave imaging. *Prog. Electromagn. Res.* **157**, 93–110 (2016)



**Denys S. Shumakov** received the bachelor's degree in radio engineering in 2008 and the master's degree in radio engineering in 2010 from National Technical University of Ukraine "KPI," Kyiv, Ukraine. He is currently pursuing the Ph.D. degree in electrical engineering at McMaster University, Hamilton, Canada. From 2009 to 2013, he was a medical engineer with Materialise NV. He is the author of 9 articles and 11 conference proceedings. His research interests include microwave imaging, inverse scattering, medical imaging, and antenna design. Mr. Shumakov is a student member of the IEEE Antennas and Propagation Society and Microwave Theory and Techniques Society. He is a reviewer for the IEEE Transactions on Microwave Theory and Techniques. Mr. Shumakov was a recipient of the McMaster International Excellence Award in 2014 and 2015, as well as the High Field MRI Winter School Scholarship from the Centre for Functional and Metabolic Mapping at the University of Western Ontario in 2015.



**Daniel Tajik** received the B.Eng. degree (electrical and biomedical) from McMaster University, Hamilton, Ontario, Canada, in 2015. He is currently pursuing the M.A.Sc. degree at McMaster University, where he is working on microwave imaging algorithms for use in medical diagnostics. His research interests include microwave imaging and image processing, applications in optimization algorithms for electromagnetic-based problems, and high-frequency antenna design. Mr. Tajik has authored several conference papers, and in 2016, he was awarded the Ontario Graduate Fellowship.



**Alexander S. Beaverstone** received the B.Eng. (2011) and M.A.Sc. (2015) degrees in electrical engineering from McMaster University, Hamilton, Ontario, Canada. He is currently pursuing a Ph.D. in microwave imaging in the same institution. His research interests include high-frequency circuit and antenna design, mathematical physics, and computational electromagnetics.





**Natalia K. Nikolova** received the Dipl. Eng. (Radioelectronics) degree from the Technical University of Varna, Bulgaria, in 1989, and the Ph.D. (Electrical Engineering) degree from the University of Electro-Communications, Tokyo, Japan, in 1997. From 1998 to 1999, she held a Postdoctoral Fellowship of the Natural Sciences and Engineering Research Council of Canada (NSERC), during which time she was initially with the Microwave and Electromagnetics Laboratory, Daltech, Dalhousie University, Halifax, Canada, and later with the Simulation Optimization Systems Research Laboratory, McMaster University, Hamilton, Canada. In July 1999, she joined the Department of Electrical and Computer Engineering, McMaster University, where she is currently a professor. Her research interests include microwave imaging and inverse scattering, theoretical and computational electromagnetism, as well as computer-aided design of high-frequency structures and antennas. Prof. Nikolova held a University Faculty

Award of NSERC from 2000 to 2005. Since 2008, she is a Tier 2 Canada Research Chair in High-frequency Electromagnetics. She is a Fellow of the Institute of the Electrical and Electronic Engineers (IEEE). In 2011, she was appointed an IEEE Distinguished Microwave Lecturer for a 3-year term and has given numerous invited lectures around the world. Prof. Nikolova is a Fellow of the Canadian Academy of Engineering.

# Chapter 18

## Electromagnetics in Medical Applications: The Cardiopulmonary Stethoscope Journey

Ruthsenne R.G. Perron, Magdy F. Iskander, Todd B. Seto, Gui Chao Huang,  
and Darcy A. Bibb

### 18.1 Introduction

Dr. Magdy F. Iskander's research in the medical field started in the early 1970s with his work on the measurement of dielectric properties of biological substances [1]. Since then, his group has published numerous journal articles and books in the application of electromagnetics in hyperthermia, radio-frequency radiation, numerical calculations of specific absorption rate (SAR), and antenna designs for medical applications [2–16]. His work on measuring lung water content has spanned throughout his career, from his time in Utah and now in Hawaii with the cardiopulmonary stethoscope (CPS). This chapter highlights the development of the cardiopulmonary-stethoscope system, a noninvasive, portable, low-cost device, capable of continuous monitoring of vital signs such as heart rate and respiratory rate and, most importantly, detecting changes in lung fluid content.

#### 18.1.1 Importance of Measuring Pulmonary Edema

Pulmonary edema occurs when fluid within the blood vessels extravasates into the alveoli, or air sacs, of the lung due to a variety of conditions, including increased intravascular pressure, decreased oncotic pressure, or direct vascular damage [17]. A potentially life-threatening condition, pulmonary edema can present as shortness of

---

R.R. G. Perron (✉) • M.F. Iskander • G.C. Huang • D.A. Bibb  
Hawaii Center for Advanced Communications, University of Hawaii at Manoa, Honolulu,  
HI, USA  
e-mail: [ruthsenn@hawaii.edu](mailto:ruthsenn@hawaii.edu)

T.B. Seto  
The Queen's Medical Center, Honolulu, HI, USA

breath and/or decreased blood oxygen and is a final common pathway for a number of acute and chronic conditions, including heart failure [18], acute respiratory distress syndrome (ARDS), and kidney failure.

The ability to detect early signs of pulmonary edema and follow its course over time is important for the diagnosis and management of its associated conditions. For example, heart failure, a condition that affects nearly 7 million people in the USA, is the most common cause of hospitalizations among the elderly at a cost that exceeds US \$17 billion, with the primary signs and symptom being fluid retention, pulmonary edema, and shortness of breath [19, 20]. Despite efforts to improve the quality of outpatient and inpatient heart failure care [21], the morbidity and mortality of heart failure remain high [22], and only 50% of heart failure patients that develop pulmonary edema survive after 1 year [23]. It is widely believed that the early detection and continuous monitoring of volume status, and specifically pulmonary edema, are key to provide timely fluid assessment and improve treatment for patients with chronic diseases such as heart failure. However, available modalities are either invasive and/or not suitable for continuous monitoring. The cardiopulmonary-stethoscope system aims to address this need.

### ***18.1.2 Existing Methodologies for Measuring Lung Water Content***

Currently, there is no single clinical test that is accurate, sensitive, reproducible, noninvasive, practical, and inexpensive [24]. Current methods to assess pulmonary edema include pulmonary artery catheter-based measurements, imaging modalities, indicator dilution techniques, impedance cardiography (ICG), and changes in total body weight. Aside from measuring total body weight, many of these current methods are only available in clinical settings, require trained personnel, and may not be suitable for continuous outpatient monitoring of pulmonary edema.

Imaging modalities such as chest radiographs and computerized tomography (CT) scans are commonly used by clinicians to assess for pulmonary edema, but coexisting lung conditions can obscure evidence of pulmonary edema or lead to false positives [25], with a reported sensitivity of 30% [26]. The current *gold standard* to assess for fluid status is the pulmonary artery catheter, which is an invasive method that directly and indirectly measures intracardiac blood pressures and is occasionally used to assess and manage patients with pulmonary edema [27]. An increasingly common method, impedance cardiography, is a noninvasive technology that measures total electrical conductivity of the thorax to estimate cardiovascular hemodynamic parameters, as well as measures of thoracic fluid content. Extensively studied, with evidence of good correlation with other clinically accepted methods, impedance cardiography has yet to achieve broad clinical acceptance amid concerns about accuracy and suggestions that it may not improve patient outcome or decrease heart failure readmissions [28]. Although following total body weight as a method to

assess and follow volume status is inexpensive, noninvasive, and readily available, concerns about its ability to detect early changes, lack of reproducibility, and patient compliance have limited its impact in the management of patients with heart failure and other conditions with changes in volume status [29]. Clearly, a new method to measure pulmonary edema that is continuous, noninvasive, sensitive, and suitable in outpatient settings is overdue.

## 18.2 Diagnosis of Pulmonary Edema Using Noninvasive Microwave Technique

The beginning of the cardiopulmonary stethoscope journey started in the 1970s. Dr. Iskander and colleagues published their work on a noninvasive microwave technique for measuring water content in the lungs in 1979 [4]. Their theoretical predictions were experimentally validated on phantom agar model, animal, and isolated lung experiments. Results and discussion of the initial publications are included in this section.

### 18.2.1 Electromagnetic Coupler

To implement the microwave technique, a  $50\Omega$  surface strip transmission line (coplanar waveguide) was first designed and developed [5–8]. It was designed to couple microwave energy at the point of contact to the tissue with minimal leakage of radiation around the body. This new electromagnetic coupler was ideal for clinical purposes as it was flat, lightweight, and small as shown in Fig. 18.1. Optimal frequency was between 740 MHz and 1.5 GHz.

### 18.2.2 Animal Testing

The feasibility of using microwave technology for measuring lung water content was evaluated in animal (dog) experiments. Pulmonary edema was induced by injecting blood from donor dogs into the femoral vein of the experimental dog, and changes in the transmitted 915-MHz microwave signal were measured in vivo. A continuous recording of the phase of the microwave transmission coefficient as shown in Fig. 18.2 shows results from a typical lung water measurement experiment on dogs [4]. The figure shows correlated trends between phase of the microwave signal (*top plot*) and pulmonary arterial pressure (*bottom plot*) with blood transfusion and subsequent bleeding.

**Fig. 18.1** Diagram of the electromagnetic coupler [4]

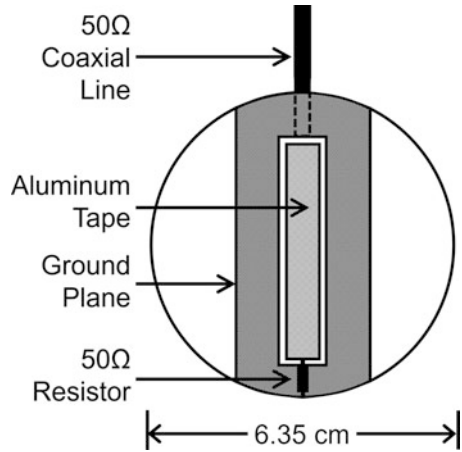
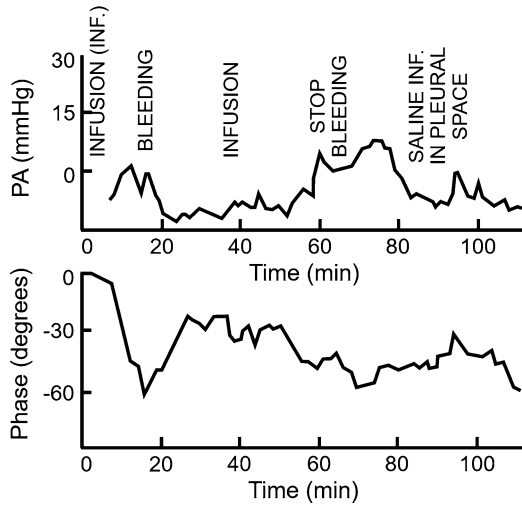


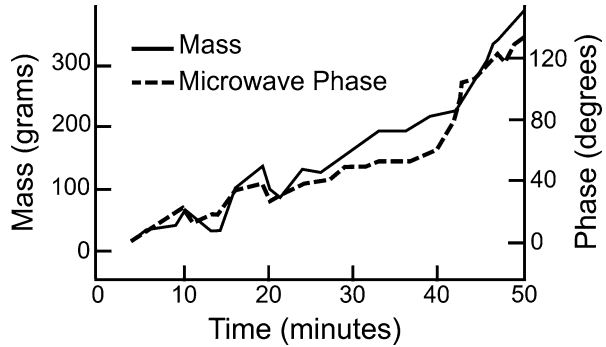
**Fig. 18.2** Results from canine experiment: Changed in phase vs. pulmonary arterial pressure [4]



### 18.2.3 Isolated Lung Experiments

In addition to animal experiments, efforts were also made to evaluate the accuracy of the method, particularly in detecting early stages of interstitial edema. Several experiments on isolated lungs were conducted through a lobe of an isolated dog's lung and were compared with the lung mass as the edema developed [4]. These results clearly show the immediate and direct change in the phase of the microwave transmitted signal as the mass of the isolated lung was changed as shown in Fig. 18.3.

**Fig. 18.3** Results from isolated lung experiment: Changed in phase vs. mass of the lung [4]



These results have shown that changes in the phase of the microwave transmitted signal are in good agreement with changes in the pulmonary edema as indicated by changes in the mean pulmonary artery (PA) pressure in the animal experiment and changes in the mass of the isolated lung.

## 18.3 Cardiopulmonary-Stethoscope System

With promising results from the animal and isolated lung experiments, efforts were focused on further development of the existing technology to a complete system suitable for human clinical trials. This section discusses these improvements which included sensor design, advance digital signal processing techniques for signal classification and extraction, wireless/mobile-based system [30], and simulations on dynamic human 3D models [31]. These improvements led to the development of the CPS system which includes sensor, microcontroller unit (MCU), and mobile device with CPS mobile app for real-time and remote patient monitoring. From a single CPS measurement, parameters such as heart rate, respiratory rate, and changes in lung water content can be extracted. Schematic of the CPS system that was used for the human clinical trials is illustrated in Fig. 18.4.

### 18.3.1 Wearable Sensor

With advancements of wearable technology [32] such as the smart shirt [33] and textile-based Bluetooth antenna [34], Ref. [35] aimed to develop a sensor that was textile based for applications such as dehydration detection for soldiers or first responders in the field.

Three types of conductive textile materials including woven copper fabric, knitted silver-plated fabric, and two-ply steel thread were investigated to evaluate the effect of the textile material's conductivity to detect changes in lung fluid content.

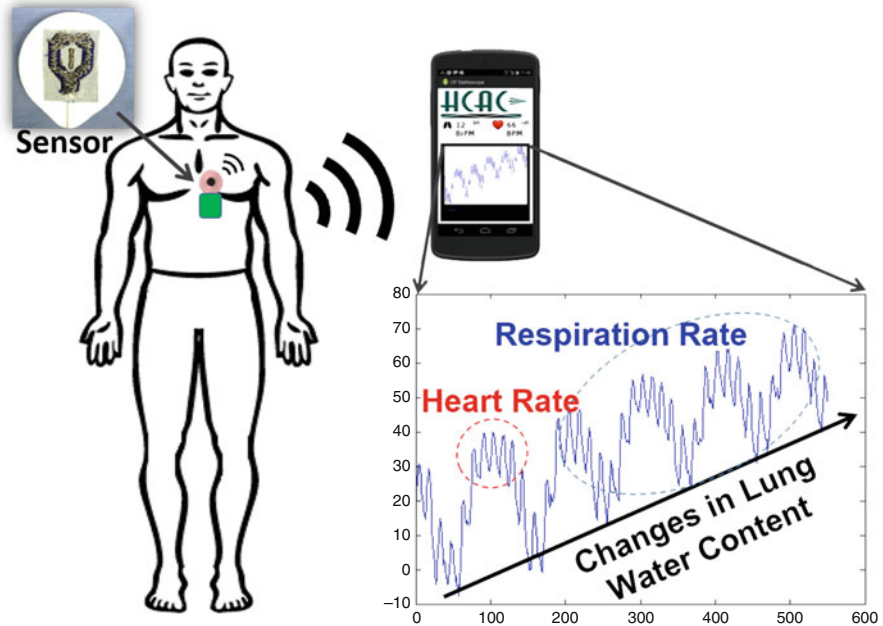


**Fig. 18.4** Schematic of the CPS system which includes sensor, microcontroller unit, and mobile device with CPS mobile app for real-time and remote patient monitoring. Parameters such as heart rate, respiratory rate, and changes in lung water content can be extracted from a single CPS measurement

Two sewing techniques, applique and embroidery, were also investigated for the fabrication of a robust and structurally stable textile electromagnetic coupler and feeding arrangement. Parameters such as coupling efficiency, ease of fabrication, and durability and stability of the feeding structure to minimize susceptibility to motion artifacts were the criteria to determine the best suitable sensor.

### 18.3.1.1 Conductive Material

Woven copper fabric, knitted silver-plated fabric, and two-ply steel thread were used to construct the coplanar waveguide (CPW) structure of the electromagnetic couplers. These conductive textile materials were chosen for their low resistivity and conformability to the human body. Summary of the surface resistivity and thickness of the conductive materials are included in below.

1. Woven copper fabric or pure copper polyester taffeta (PCPTF) fabric [36] is coated with pure copper. It is lightweight and flexible. It is 0.08 mm thick, weighs 80 g/m<sup>2</sup>, and has a surface resistivity of less than 0.05 Ω/m<sup>2</sup>.

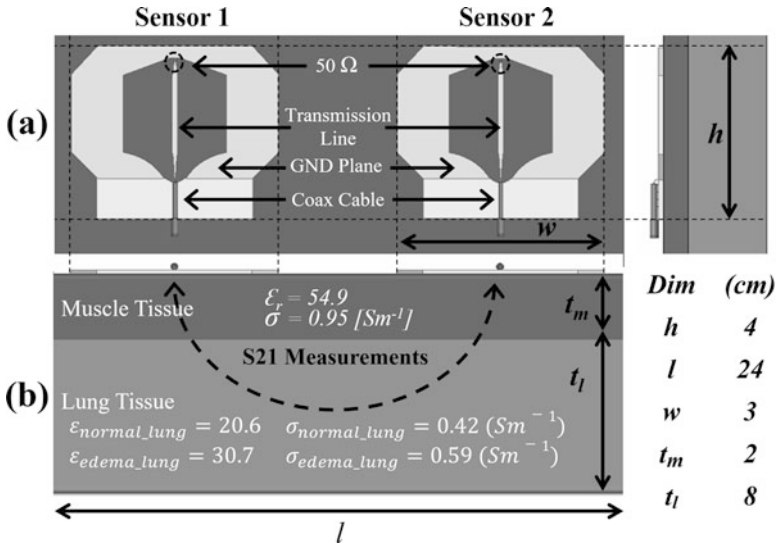


**Fig. 18.5** Simulation setup: (a) Two couplers constructed with the conductive textiles placed side by side on multilayer phantom model. (b) Dimension and electrical properties of the muscle and lung tissues for normal and edema lung state at 915 MHz [35]

- Knitted silver-plated fabric [36] is a medical grade fabric with 76% nylon and 24% elastic fiber and has a 99% pure silver coating. It is 0.4 mm thick, weighs 145.8 g/m<sup>2</sup>, and has a surface resistivity of less than 0.5 Ω/m<sup>2</sup>. It is also lightweight, flexible, and stretchable. The knitted silver-plated fabric was used in [34] to construct a textile patch antenna for wireless personal area networks (WPAN).
- Steel thread (two-ply) [37] is thin, flexible, and sturdy and has a low surface resistance, 51.2 Ω•m. There are many conductive threads, but some are not suitable for embroidery because they are too thick/thin, have low conductivity, or suffer from fraying of the metal fibers.

### 18.3.1.2 Electromagnetic Textile Coupler Simulation

Simulation studies were first conducted to characterize and examine the effect of the textile material's conductivity to detect changes in lung fluid content from normal to edematous state [35]. Changes in lung water content were modeled by adjusting the fractional lung tissue volume from 20% (normal lung) to 40% (edematous lung). As shown in Fig. 18.5, two coaxial-fed electromagnetic couplers placed side by side on a simplified multilayer phantom model of the lung and muscle tissue were simulated at 915 MHz. In addition to the conductive textiles, perfect electric conductor material was also simulated to serve as a baseline.



**Table 18.1** Summary of the coupling efficiency of the conductive textiles [35]

Conductive material	Lung state	$S_{11}$ Magnitude (dB)	$S_{22}$ Magnitude (dB)	$S_{21}$ Magnitude (dB)
PEC (Benchmark)	Normal	-21.4	-21.5	-54.2
	Edema	-21	-20.9	-57.1
			$\Delta S_{21}$	<b>2.9</b>
Copper	Normal	-21.5	-21.3	-54.2
	Edema	-20.9	-21.1	-57.1
			$\Delta S_{21}$	<b>2.9</b>
Silver	Normal	-21.8	-21.9	-55.3
	Edema	-21.4	-21.5	-58.4
			$\Delta S_{21}$	<b>3.1</b>
Steel	Normal	-21.4	-21.5	-54
	Edema	-21	-21	-56.9
			$\Delta S_{21}$	<b>2.9</b>

Obtained simulation results showed that all the conductive textile materials were well coupled to the muscle tissue with  $S_{11}$  and  $S_{22}$  magnitudes less than -20 dB. Measured  $S_{21}$  magnitude ranged between -54 dB to -55 dB for normal lung and -56 dB to -58 dB for edema lung for the various textiles as well as the perfect-electric-conductor (PEC) case. Between the three textiles, the steel thread textile material had the least amount of transmission losses which was 0.2 dB better than copper and 1.1 dB better than silver as shown in Table 18.1. The measured phase change of the transmission coefficient from the normal lung to lung with edema for all textiles and PEC case ranged between 18 and 20 deg. These simulation results have shown that all three conductive textiles were well matched to the phantom muscle tissue, have minimal difference in transmission losses, and are sensitive to changes in lung water content.

It may be worth noting that even 1% change in lung water content, which resulted in 1.6 degree change in the phase of the transmission coefficient, is easily detectable in these simulations. This agrees with results found in earlier animal studies [4] where 1% change in lung water content corresponds to 1 degree phase change of the transmission coefficient. Sensitivity to 1% change in lung water content is far more significant compared to a chest X-ray (sensitive after 30% lung water increase [38]) and extra-vascular lung water (EVLW) measurements which can detect 10–20% lung water changes [39]. Furthermore, a study [40] with critically ill patients has shown that there is about 65% mortality rate in patients with EVLW levels greater than 15 ml/kg compared to 33% in patients with less than 10 mL/kg. Essentially, the 5 ml/kg difference increases mortality rate from 33% to 65% for a critically ill patient. At this point, however, clinical significance of sensitivity to 1% change in lung water content has not been investigated which may or may not be needed as fluctuation could be as much as 1–3%. On the other hand, availability of a device like the CPS that is capable of continuous monitoring and sensitive to small changes is

critically important for effective intervention and remediation, as it may detect early and progressive stages of diseases such as heart failure.

### 18.3.1.3 Fabrication Techniques

Two sewing techniques, applique and embroidery, were examined for the fabrication of the coupler prototype.

*Applique* The woven copper and knitted silver-plated textiles were fabricated using a sewing technique called applique, where the conductive textile is attached to a supporting nonconductive fabric structure (cotton and felt). Method of attachment can include fabric glue, sewing, or the usage of adhesive sheets. However, the attachment procedure must not affect the electrical properties of the conductive textile. Similar to the results in Ref. [35], fabric glues are stiff and brittle, and the glue should not seep through the fabric; otherwise it would change the surface resistivity of the conductive textile. Consequently, the conductive textile coupler was sewn to the stabilizer fabrics.

*Embroidery* The second fabrication technique was embroidery of the conductive two-ply steel thread. Using an embroidery machine, pattern of the CPW geometry was sewn onto the support fabrics, with 20 mm long, 1 mm separation, and 0-degree angle stitches. The stitch parameters can be further adjusted to determine the appropriate thread density, which affects the coupling efficiency and rigidity of the structure. S-parameter results from side-by-side measurement in a human experiment and using three different types of textile electromagnetic couplers, and schematic diagram of the material layers including the conductive textile material, supporting fabrics and the coaxial feed are shown in Fig. 18.6. Preliminary results of the  $S_{11}$  magnitude when the sensors were placed on a human skin were below -10 dB.

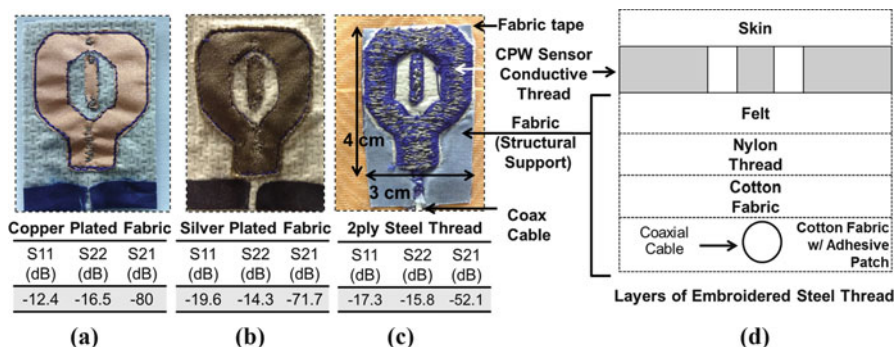


**Fig. 18.6** S-parameter results from side-by-side measurement in a human experiment and using three different types of textile electromagnetic couplers: (a) copper fabric, (b) silver fabric, and (c) embroidered steel thread, (d) schematic diagram of the fabricated coupler layers [35]

#### 18.3.1.4 Feed Options

Several feeding structures such as microstrip, stripline, and direct coaxial feed described in Ref. [41] were considered. The microstrip and stripline fed ports were beneficial due to their planar structure; however, the transition to the SMA connector was difficult to stabilize and was prone to breaking. Consequently, all of the couplers were fed using coaxial cables. The cable was sewn to the back of the coupler and conductive thread was used to connect the center conductor of the cable to the center transmission line of the electromagnetic coupler. Since the center conductor of the cable is thin and is prone to breaking, a fabric patch with adhesive was ironed and sewn on the back of the coupler to minimize the twisting of the cable.

#### 18.3.1.5 Preliminary Experimental Results and Observations

Initial observations indicated that fabrication of the electromagnetic coupler using the applique technique was not ideal. The conductive fabrics had to be sewn precisely; otherwise, uneven tension on the fabric will result in wrinkling or folding, making it difficult to maintain proper structure or shape of the coupler. Fraying around the edges of the coupler also occurred causing the conductive fabric to unravel and eventually separate from the supporting fabrics. On the contrary, the embroidered pattern of the coupler was accurate, and shape was maintained and secured on the supporting fabrics.

The fabricated electromagnetic couplers were placed on a human torso, and all of the conductive textiles were found to be well matched ( $< -10$  dB) to the human skin. However, when using these different textile materials in typical human measurements, these textiles have different physical characteristics, e.g., folding and wrinkling that makes it difficult in some material to maintain stable contact with the human skin. It is these physical implementation issues that make textiles such as those shown in Figs. 18.6a and b difficult from practical point of view. On the contrary, the embroidered coupler in Fig. 18.6c was stable on the skin ( $S_{21} = -52.1$  dB) which was also in better agreement with the simulation results. Therefore, the embroidered steel thread was chosen for the initial human vital sign clinical validation studies, which will be discussed in Sect. 18.4.2.

### 18.3.2 Signal Classification and Extraction

Digital signal processing (DSP) algorithms were developed to extract useful information from the single microwave signal [42, 43]. These algorithms were based on the characteristics of the heart and respiratory signals. The single microwave signal consists of subsurface signals (changes in lung water content) and superficial signals (heart rate and respiratory rate). Changes in lung water content are slow changing, strong, and have a linear trend. The respiratory waveform is low-frequency, sinusoidal cycle, while the heart waveform contains high-frequency cycles with distinguishable peaks. For adults at rest, normal rates range from 12

to 20 breaths/min or 0.2–0.33 Hz for respiratory rates and 60–100 beats/min or  $\sim 1.6$  Hz for heart rates [44]. Several digital signal processing algorithms such as multiple signal classification [45], wavelet transform, and wavelet decomposition were initially considered to extract or separate the heart and respiration rate and changes in lung water content. Although these algorithms were more than sufficient to extract the vital signs, key consideration was computational efficiency and simplicity for real-time viewing and processing of the data. Consequently, the best suitable sets of algorithms were combinations of windowed linear regression or averaging, short-term Fourier transform (STFT), band-pass, and the threshold-based peak detection method [46].

Regress function was first applied to the signal. The residual signals were then subtracted from the original signal which provided a piecewise linear plot which can be used to estimate the changes in lung water content. With the remaining signal, a windowed STFT was applied, and the resulting averaged spectrum contained two major peaks which corresponded to the respiratory and heart waveform. A low-pass (LP) filter was used to separate the respiratory waveform from the heart waveform. Lastly, the residual signal was band-pass filtered with a 3 dB passband of 1–1.6 Hz. A threshold-based peak detection method was used to calculate the heart rate. A block diagram of the DSP algorithms used to extract the vital signs and changes in lung water content is illustrated in Fig. 18.7. These algorithms were integrated in the wireless-based and mobile app CPS system for real-time extraction and viewing of the RAW waveforms and calculated vital signs, which will be discussed in the proceeding section.

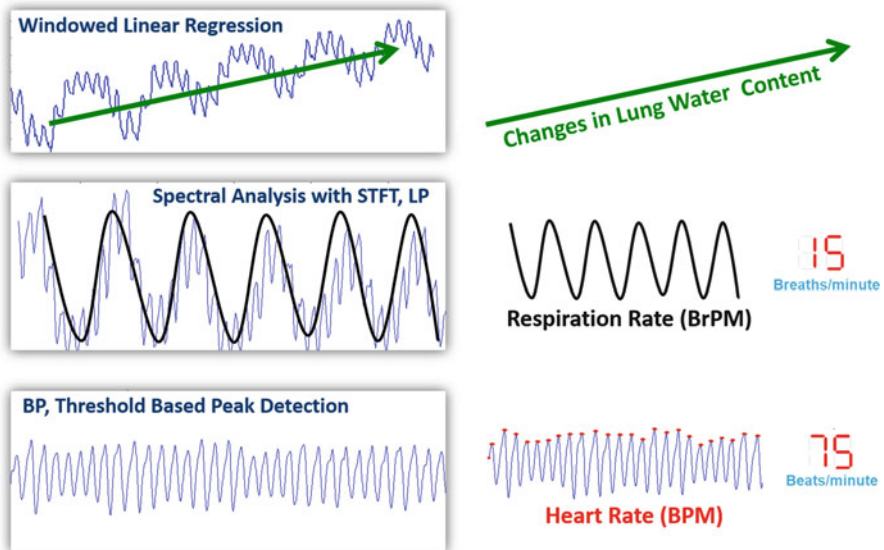


**Fig. 18.7** DSP algorithm used to extract vital signals as well as changes in the lung fluid from the single microwave signal [30]

### ***18.3.3 Wireless/Mobile Integration***

With the objective of using the CPS system as a bedside and home care monitoring device, efforts were made to eliminate the bulky and expensive network analyzer. The new CPS system consisted of an RF module, microcontroller unit, Bluetooth, and mobile app. Using an MCU, C code was developed to convert the analog I and Q signals to digital data at a sampling rate of 80 Hz. Every four samples were averaged to minimize conversion error which resulted with an effective sampling rate of 20 Hz. From the digital in-phase and quadrature-phase signals, the raw phase and magnitude of the transmission coefficient were obtained. Signal processing techniques that were previously discussed in the preceding section were used to extract the heart and respiration rate as well as the changes in the lung water content from the single microwave signal. A mobile app was also developed for real-time and remote viewing of the extracted signals. Block diagram of the wireless assimilation system and screenshot of the mobile app are shown in Figs. 18.8a and b, respectively. Setup of CPS system on a study participant is included in Fig. 18.8c. Detailed description of the system is included in Ref. [47].

### ***18.3.4 Dynamic 3D Human Thorax***

To further investigate propagation characteristics of the CPS during the human clinical trials to help identify parameters that will affect its sensitivity to changes in lung water content and vital signs, a dynamic 3D human thorax was developed [48].

A 3D human voxel model was first evaluated to determine if it demonstrated the complexity of the human thorax as well as provided sufficient structural flexibility and adaptability to emulate physiological events such as a heartbeat, chest wall movement during expiration and inhalation of the respiratory cycle, and changes in lung fluid content. Furthermore, various sensor placements on the thorax were also simulated to emulate how it affects the sensitivity to changes in lung water content. With a complex, accurate, and dynamic model, efforts to minimize computational cost are also discussed in this section. The section concludes with description of experimental validation using a phantom cross section of the thorax.

#### **18.3.4.1 Human Voxel Models**

After comparing various human 3D models, the human voxel model in high-frequency structure simulator (HFSS) best fit the objectives. The use of tetrahedral elements in finite-element model (FEM) allows for curved surfaces, such as the human body, to be more accurately represented using adaptive meshing techniques [49]. Moreover, some SAR simulation studies using HFSS [50] have shown faster convergence when compared with CST microwave studio simulation software which is based on the finite-difference time-domain (FDTD) method. The Federal

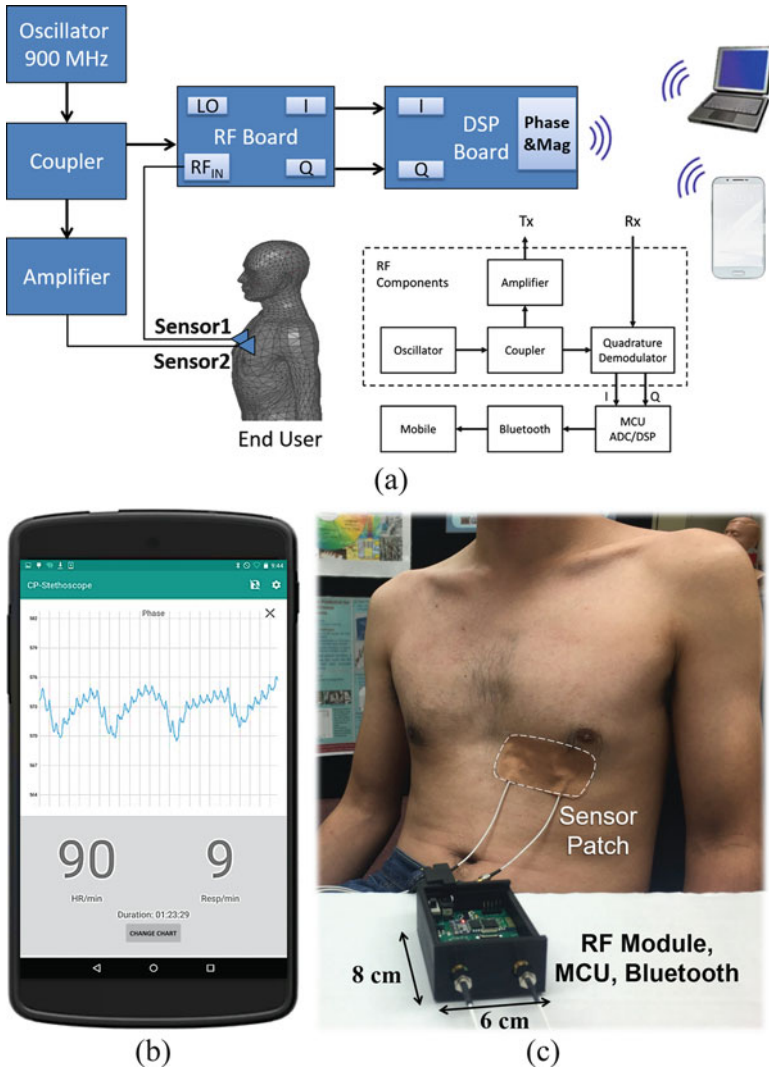


**Fig. 18.8** (a) Block diagram of the new CPS wireless system used to acquire and display data in real time during the human clinical trials. (b) Screenshot of the developed mobile app that displays the raw phase of the transmitted signal as well as the calculated heart and respiration rate and changes in lung water content in real time. (c) Setup of CPS system on a study participant [30, 31, 47]

Communications Commission (FCC) has also approved the use of FEM for numerical modeling techniques to determine safety compliance [51]. The HFSS human model has a millimeter level of accuracy with over 300 geometries such as the bones, organs, and muscles. The entire human model consisted of half a million tetrahedra. Figure 18.9 shows a transverse cross section of HFSS' thoracic mesh model to illustrate the level of accuracy of the human 3D voxel model.

**Fig. 18.9** Transverse cross section of HFSS' thoracic mesh model

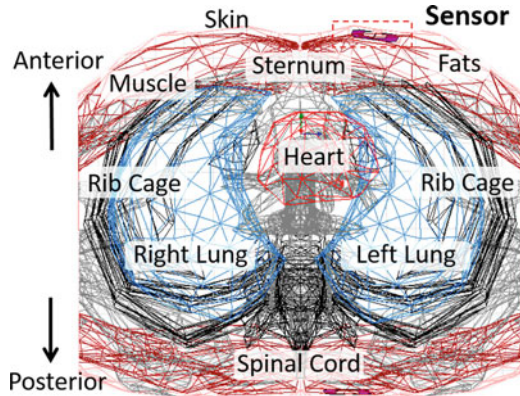
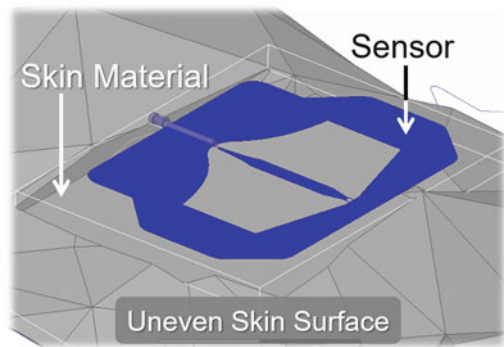


**Fig. 18.10** Thin skin material was added between the electromagnetic sensor and the phantom model to ensure sufficient contact with the uneven phantom surface



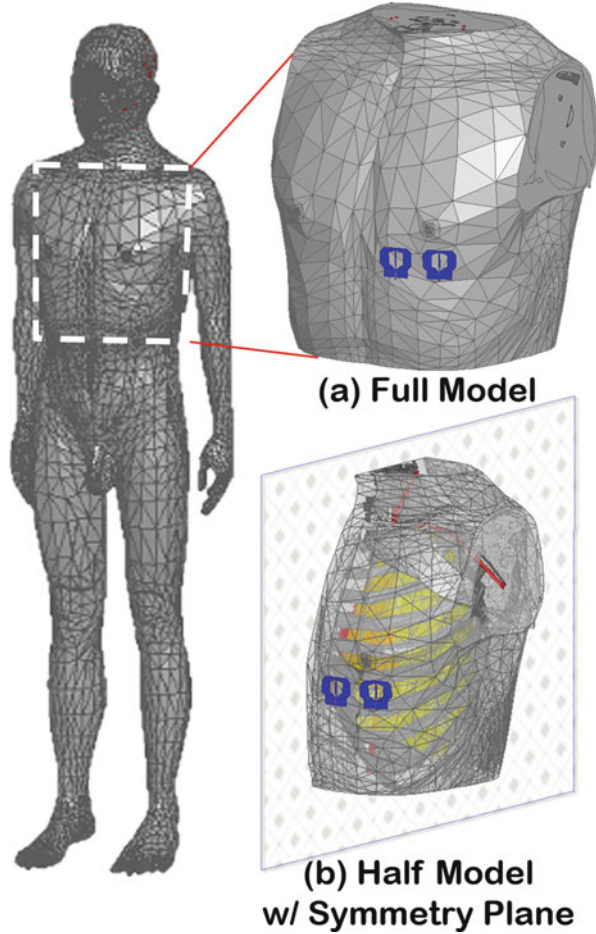
#### 18.3.4.2 Sensor Coupling

Since the electromagnetic sensor was designed to couple to human skin, the sensor has to be in direct contact with surface of the 3D model. However, the uneven surface and curvatures of the 3D model resulted in air gaps between the sensor and the model, which caused an impedance mismatch. To overcome the mismatch, a thin layer of skin material was placed between the sensor and the skin which is illustrated in Fig. 18.10. Resulting magnitude of the reflection coefficient ( $S_{11}$ ) was  $-14.5$  dB.

#### 18.3.4.3 Computational Cost

Since the heart and lungs are in the thoracic region of the human model, geometries beyond the thoracic region were omitted to minimize computational cost. Similar to the previous simulations, fluid accumulation in the lungs was modeled by adjusting the fractional lung tissue volume from 15% (normal lung) to 45% (edematous lung) at 915 MHz.

**Fig. 18.11** Simulation setup of the changes in lung water content using (a) Full thoracic model and (b) Half model with a vertical symmetry plane boundary [48]



To further minimize computational cost, a symmetrical boundary in the sagittal plane, which separates the left and the right side of the thorax, was also included [48]. Simulation setup of the computational cost evaluation with the full thorax and half model is included in Figs. 18.11a and b, respectively. Simulation parameters are included in Table 18.2.

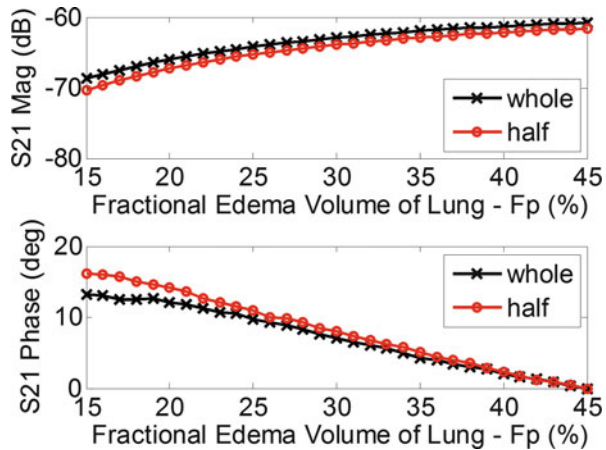
The accuracy of the half model is in good agreement with the full model and reduced total simulation time by nearly half as shown in Fig. 18.12 and Table 18.2, respectively. Therefore, the half model with the symmetry plane was used for the emulation of vital sign simulations, which will be discussed in the proceeding section.



**Table 18.2** Simulation parameters [48]

<b>Frequency:</b>	915 MHz	<b>Simulation profile</b> (Half model-1 variation) Total # of adaptive passes: 4 Mesh (volume, adaptive): 307302 tetrahedra Simulation time Real time: 11m:25s CPU time: 47m:56s HFSS ComEngine memory: 287M Field recovery memory: 12.7G System information Processor: Intel Core i7-4930K, 64 bit RAM: 64 GB
<b>Excitation:</b>	2 Wave ports	
<b>Boundary:</b>	Radiation	
<b>Simulation basis order:</b>	Mixed	
<b>Convergence criterion:</b>	0.02	
<b>Min. consecutive passes:</b>	1	
<b>Number of variations:</b>	31	
<b>Total simulation time:</b>	Full model: 16 h:53 min:34 s Half model: 9 h:21 min:23 s	

**Fig. 18.12** Results indicated a good agreement between the whole and half model with symmetry plane boundary to further minimize computational cost [48]



**18.3.4.4 Emulation of Vital Signs**

To properly characterize the performance of the sensors during clinical trials, the 3D model was dynamically simulated to reflect, as much as possible, vital sign changes during a typical clinical trial. Specifically, parts of the model were scaled or moved to emulate a heartbeat and the breathing cycle.

The cardiac cycle consists of systole and diastole [52], and where systole represents the contraction of the heart to pump blood to the body and diastole is the relaxation of the ventricles to allow blood to fill in. To mimic the contraction and relaxation of the heart, the size of the heart was equally scaled up and down in an alternating manner. There are eight simulated heartbeats in one respiratory cycle. With three respiratory cycles in a minute, the resulting heart rate would be 24 beats per minute (BPM). This rate was only a fraction of a normal adult heart rate which ranges from 60 to 100 (BPM) in a typical healthy person. However, each additional data point would significantly increase processing time. Consequently, to minimize processing time, initial heartbeat simulations were set to 24 BPM.

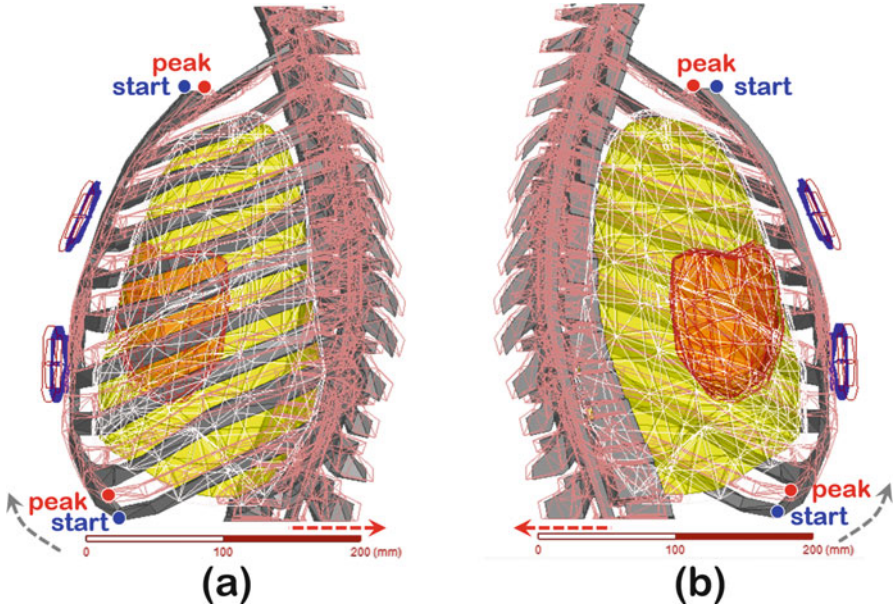


**Fig. 18.13** Setup of the HFSS simulation model illustrating the positions of the ribcage and the lungs during inhalation cycle. The *red* outline is the position of the ribcage at the peak of inhalation. The *dots* labeled start and peak also represent the initial and final position of the ribcage and sternum. (a) *Left side view*. (b) *Right side view* [48]

For the respiratory cycle, the two main moving components in this model included the ribcage and the lungs. The ribcage consisted of ribs, sternum, and costal cartilage. During inhalation, the lungs expand and the ribs rotate upwards and outwards. This motion is similar to the rotation of a bucket handle which increases the transverse (left to right) diameter of the thorax [53]. The second movement is the sternum and the costal cartilage moving upward which also increases the thorax diameter between front and back [53]. This motion is similar to that of a water pump handle. After a complete cycle of inhalation and exhalation, the conductivity and permittivity of the lung were also adjusted from normal to edema in three stages (20%, 30%, and 40% edema) to mimic changes in lung water. The setup of the simulation in HFSS is illustrated in Fig. 18.13.

#### 18.3.4.5 Results and Discussion

Figure 18.14 contains the results of the three respiratory cycles with the first cycle at 20% edema (normal lung) to the last cycle at 40% edema (edematous lung). Using the algorithm to extract vital signs from Refs. [40] and [43], the linear trend from the changes in fluid content and the respiration cycles and heartbeats were extracted

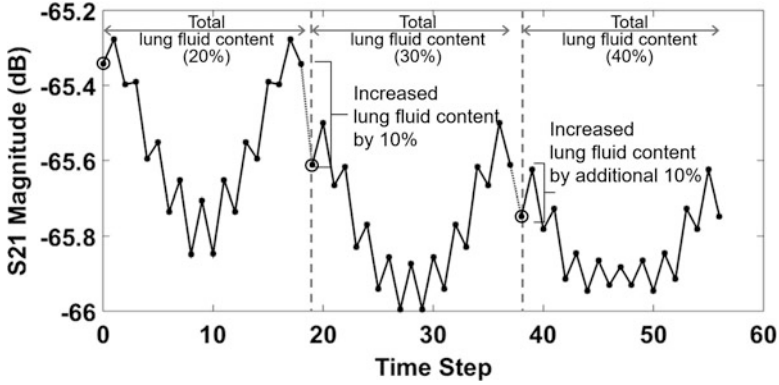


**Fig. 18.14**  $S_{21}$  magnitude simulation results from the three respiratory cycles with eight heartbeats per cycle. The three respiratory cycles each represent lung water content from normal lung (20% edema) to full edema lung (40%) [48]

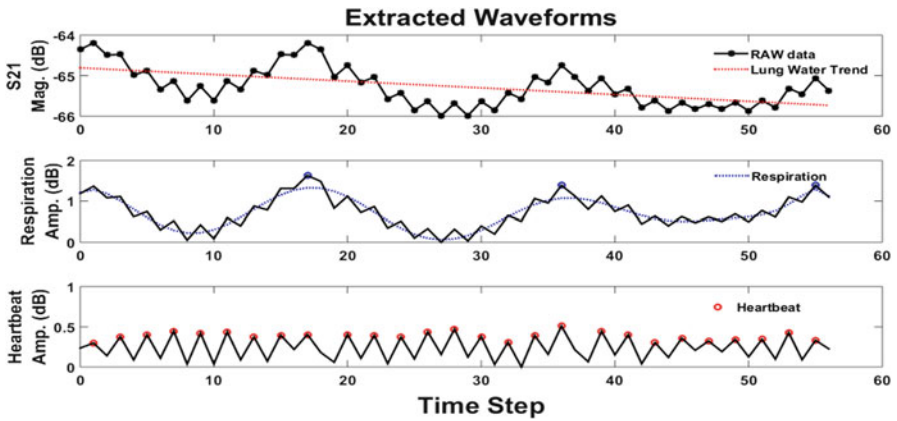


**Fig. 18.15** Extracted values from the  $S_{21}$  magnitude: (a) linear trend of the changes in fluid content, (b) respiration cycles, and (c) heartbeats

from the  $S_{21}$  magnitude, which is illustrated in Fig. 18.15. The waveform generated from the heartbeat as well as the respiration cycle were similar to the ones that were extracted from the human clinical trials.

**18.3.4.6 Effect of Sensor Placement: 3D Model**

To investigate how the sensor placement affects the sensitivity of the electromagnetic sensors to detect changes in lung fluid content, a full thoracic model was needed. Unlike the previous half thoracic model, these simulations were conducted with the full thoracic model to account for a full representation of the electromagnetic scattering and propagation effects in inhomogeneous 3D model of

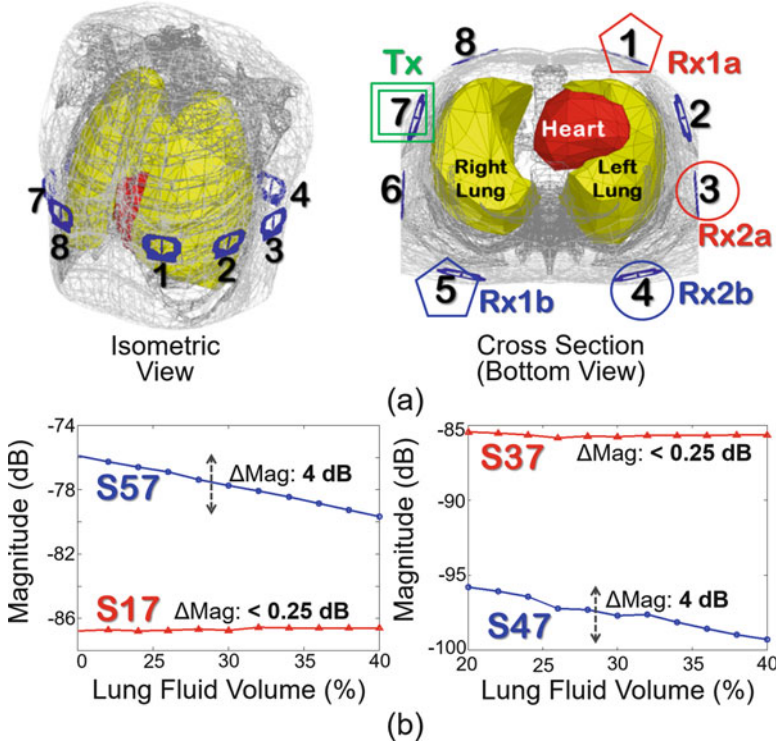


**Fig. 18.16** Simulations on a 3D CAD model of a human thorax have shown that sensor placement affects the sensitivity of the CPS system to detect changes in lung fluid content. Setup of the eight sensors around the thorax and sample results from this study are included in (a) and (b), respectively [54]

a thorax. Changes in the lung fluid content in both the left and right lungs were modeled similar to the previous simulations from normal (20%) to edematous (40%) lung at rate of 2% increase for a total of 11 lung states. A total of eight sensors were added to the human 3D model as illustrated in Fig. 18.16a.

Paths between various transmitter and receiver sensor pairs were evaluated. Transmitters (Tx) 3 and 7 were selected as examples to illustrate how their placement around the thorax relative to the other receivers (Rx) affect the sensitivity to detect changes in lung fluid content. Results of sensor pairs (S37, S47, S17, and S57) from these simulations are illustrated in Fig. 18.16b.

As seen in Fig. 18.16a, with sensor 7 as the transmitter and sensors 3 and 4 as the receivers, a  $-4 \text{ dB}$  change in  $S_{47}$  was observed with a 20% to 40% change in the lung fluid content compared to a minimal change of less than  $0.25 \text{ dB}$  for  $S_{37}$ . Similarly, in Fig. 18.16b,  $S_{57}$  changed by  $-4 \text{ dB}$  compared to less than  $0.25 \text{ dB}$  for  $S_{17}$ . From these results, sensor placement is important, and trade-off needs to be considered between sensitivity to changes in vital signs and accurate and early determination of lung water content.

Therefore, it can be concluded that the human torso model in HFSS is sufficiently accurate to mimic the complexity of the human organs as well as model dynamic physiological events such vital signs, respiration cycle, and, more importantly, changes in lung fluid content. Clearly, the model in its present form represents a first step toward more accurate representation of the physiological changes in a typical clinical trial, a task that our team is presently pursuing.

## 18.4 Human Clinical Trials

Human clinical trial for the CPS was conducted in three phases. First phase was the safety evaluation of the system followed by the evaluation of vital signs and changes in lung water content.

### 18.4.1 Safety Compliance

To conduct human clinical trials, all research protocol must be submitted and approved by an Institutional Review Board (IRB). Part of the protocol needed to clearly identify and address the risks and safety of the study participants. Since the system is microwave-based technology, safety measurements were conducted by following the guidelines set forth by the Federal Communications Commission (FCC) for safety compliance. In 1997, the FCC adopted the guidelines set by ANSI and IEEE and developed a document called OET Bulletin 65 [51] to provide assistance in determining whether proposed or existing transmitting facilities, operations, or devices comply with limits for human exposure to radio-frequency (RF) fields.

Safety standards for human exposure to RF energy are evaluated by the specific absorption rate (SAR), which quantifies the rate at which energy is absorbed per unit mass in an exposed object. Exposure to very high RF intensities may result in tissue damage due to thermal effects or heating of the tissue. SAR is the time derivative of the incremental energy  $dW$  absorbed by or dissipated in an incremental mass  $dm$  contained in a volume  $dV$  of a given mass density  $\rho$ :

$$\text{SAR} = \frac{d}{dt} \left( \frac{dW}{dm} \right) = \frac{d}{dt} \left( \frac{dW}{\rho dV} \right). \quad (18.1)$$

SAR should be considered an “absorbed dose rate” and is related to the electric field  $E$  at a point by:

$$\text{SAR} = \frac{\sigma |E|^2}{2\rho}, \quad (18.2)$$

where  $\sigma$  is the conductivity. FCC SAR limits are included in Table 18.3.

**Table 18.3** FCC limits for SAR [51]

	SAR [W/kg] Controlled/occupational	SAR [W/kg] Uncontrolled/general population (localized)
Whole body	0.4	0.08
1 g. Av (partial body)	8	1.6
10 g. Av (Hands, wrists, feet, and ankles)	20	4

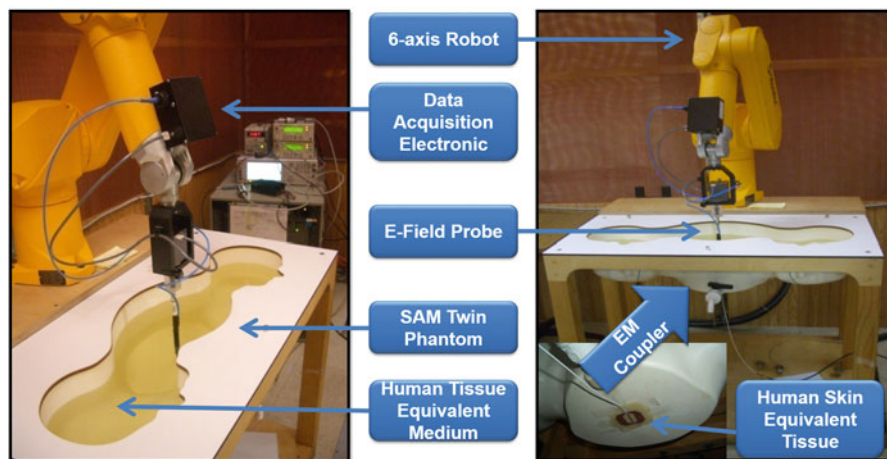


**Fig. 18.17** Setup of the SAR measurements conducted in Kyocera Wireless Labs (San Diego, CA) with the DASY4 system and the specific anthropomorphic mannequin (SAM) twin phantom that holds the human phantom tissue. The electromagnetic coupler was placed on the flat thoracic section of the phantom [54]

SAR experiments reported in Ref. [53] were conducted at Kyocera Wireless Labs in San Diego, CA, using the DASY4 system (Schmid & Partner Engineering AG – SPEAG, Zurich, Switzerland) [55], an automated near-field scanning system that measures SAR levels on biological tissues. Setup of the SAR experiments is shown in Fig. 18.17 which includes the DASY4 components and the specific anthropomorphic mannequin (SAM 12) phantom model that holds about 25 l of tissue equivalent liquid. The electromagnetic sensors were placed on the thoracic region of the phantom. The shell is in compliance to the specifications in IEEE 1528–2003 [56], CENELEC 50361 [57], and IEC 62209 [58]. The shell thickness is  $2 \pm 0.2$  mm and is 1000 mm long and 500 mm wide. Reference markings on the phantom shell allow the complete setup of all predefined phantom positions and measurement grids with respect to the robot. System parameters of the SAR experiments at 915 MHz are included in Fig. 18.18.

The plastic sensor (without the skin tissue in between the sensor and the plastic container) was first used to determine the highest input power that would result in acceptable SAR levels (less than the FCC guidelines). Table 18.4 includes the four

**Device #\_M915 Flat with 15dBm 0mm Air Space, 10-13-09**

Communication System: LPD 900, Frequency: 915 MHz, Duty Cycle: 1:1  
 Medium: M915, Medium parameters used:  $f = 915 \text{ MHz}$ ;  $\sigma = 1.03 \text{ mho/m}$ ;  $\epsilon_r = 54.6$ ;  $\rho = 1000 \text{ kg/m}^3$

Phantom: SAM 12, Phantom section: Flat Section

**DASY4 Configuration:**

Probe: ET3DV6 - SN1664, ConvF(6.11, 6.11, 6.11), Calibrated: 6/22/2009

Sensor-Surface: 4mm (Mechanical Surface Detection),

Electronics: DAE4 Sn603, Calibrated: 9/15/2009

Measurement SW: DASY4, V4.7 Build 71

Postprocessing SW: SEMCAD, V1.8 Build 184

**Temperature:**

Room T = 21.8 +/- 1 deg C, Liquid T = 22.0 +/- 1 deg C

Fig. 18.18 System parameters of the SAR experiments

Table 18.4 Measured SARs with various input power

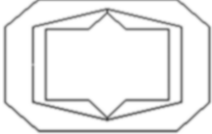
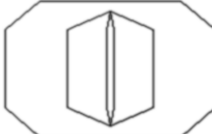
Input power		Measured SAR (W/kg) [1 g Av] *Limit is 1.6 (W/kg)
(dBm)	(mW)	
10	10	0.12
15	32	0.42
17	50	0.99
20	100	2.1

input power settings that were tested and the measured SARs. Although these input power settings were significantly higher than what is required for the system (1–10 mW), this part of the study was designed to determine the worst-case scenario.

According to the measured SAR results, the maximum input power would be 50 mW with an SAR of about 1 W/kg. However, 32 mW input power (SAR = 0.42 W/kg) was chosen for the remaining SAR measurements to account for any variability in the design and size of the sensors. Results from the SAR measurements for both the plastic and human sensor with input power at 32 mW are included in Table 18.5.

Measured magnitude of the reflection coefficient ( $S_{11}$ ) for any of the sensors are well below  $-10 \text{ dB}$ , which means that all sensors were properly matched and that the signal was coupled to the liquid phantom. Furthermore, the measured SAR 1 g average for both the plastic and human sensor were similar at about  $0.4 \text{ mW/g}$  (only 1/4th of the FCC limit), which indicates that the additional phantom skin placed between the human sensor and the plastic container did not absorb or impede the signal. To put the SAR values in perspective, Fig. 18.19 shows the measured results of the electromagnetic sensor have significantly lower SARs compared to commercially available common mobile cell phone models. Results and documentation from the SAR measurements significantly played a role in the approval of the IRB protocols.

**Table 18.5** SAR measurement results (input power: 32 mW, Freq: 915 MHz) [54]

Sensor (Scale: a = 100%, b = 75%)	Sensor #	Sensor design	Mag S <sub>11</sub> (dB)	SAR 1-g Average (mW/g)	
				Limit	Measured
	1	1(a)	-22.84	1.6	0.416
	2	1(b)	-13.15	1.6	0.415
	3	2(a)	-27.46	1.6	0.435
	4	2(b)	-31.52	1.6	0.319

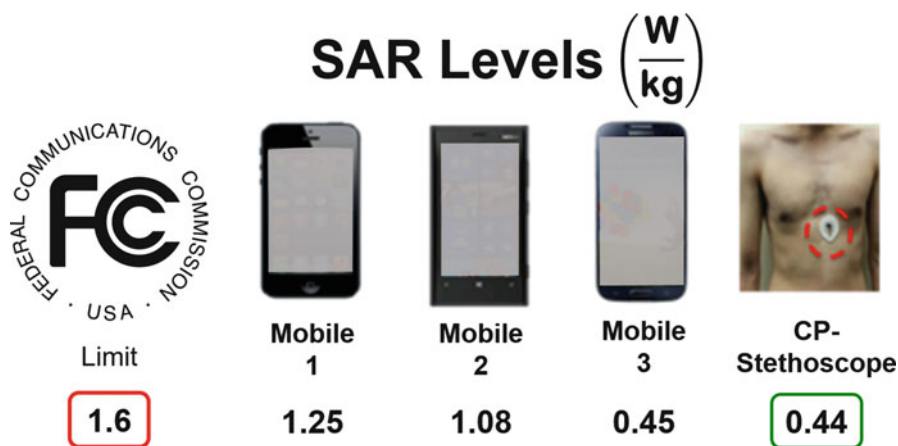


**Fig. 18.19** Commercially available mobile devices have higher SARs compared to the electromagnetic sensor

### 18.4.2 Human Vital Sign Validation

Human vital sign evaluation experiments were conducted in collaboration with the Telehealth Research Institute, at John A. Burns School of Medicine (JABSOM) to validate the feasibility of extracting vital signs such as heart rate and respiratory rate from healthy participants. Healthy participants were the initial target population for these experiments for the convenience of patient availability and to establish a baseline for normal heart and respiration rate. Some of the exclusion criteria included currently under care of a physician, drug allergies, cardiac-related medical history, and medications. Each participant was also required to complete a medical



history questionnaire, which was used by a physician to screen and approve the participants. All participants signed an informed consent form prior to participating in the clinical trials. This study was approved by the IRB at the University of Hawaii at Manoa. The accuracy of the CPS system to measure heart and respiratory rate was evaluated while patients were at rest and while running on the treadmill. Setup and experimental results from Refs. [35] and [43] are discussed in the proceeding sections.

#### 18.4.2.1 Vital Sign Evaluation: At Rest

Data from three adult males with an average age of 26.33 years were analyzed. Each male represented a small, medium, and large body built as indicated by their height, weight, and chest circumference as shown in Table 18.6. In addition to the evaluation of the vital signs, the purpose in the variation of the sizes was to evaluate if the patient size was a limiting factor to accurately detect and calculate vital signs. Participants were asked to sit on a chair for the installation of the three EKG electrodes from the Propaq LT, Welch Allyn [59] and the two electromagnetic sensors on the chest. Placement of the EKG electrodes and the electromagnetic sensors are illustrated in Fig. 18.20. Textile-based electromagnetic sensors were attached to a network analyzer and placed side by side (2–3 cm apart) near the bottom left of the sternum. Tape was used to stabilize the contact of the sensors to the skin.

While sitting on a chair for 2–3 min, participants were asked to perform a series of normal breathing followed by breath holds. The breath holds were included to establish a raw data baseline for the heartbeat to compare with the extracted heartbeat. Simultaneous heart and respiration rate measurements were recorded from the Propaq LT and the CPS for all the experiments.

Measured  $S_{11}$  and  $S_{22}$  magnitudes ranged from  $-15$  to  $-17$  dB, while the  $S_{21}$  magnitude ranged from  $-53$  to  $-57$  dB, which indicated well-matched sensors on the skin with sufficient transmitted signal strength on all study participants. The figures below include the raw  $S_{21}$  phase waveforms, extracted heartbeat and respiration waveforms, calculated heart, and respiration rate from both CPS and Propaq LT for the three study participants.

As seen in Fig. 18.21, the  $S_{21}$  phase waveform clearly indicates the expiration and inhalation pattern during the breathing cycle with amplitudes ranging from 10 to 20 deg. peak-to-peak for all three participants. The heartbeat waveform with

**Table 18.6** Demographic of study participants

Patient #	Age (yrs.)	Weight (lbs.)	Height (ft. in.)	Chest circumference (cm)
1	27	130	5'7"	83.36
2	25	175	5'4"	93.98
3	27	190	6'	109.22

**Fig. 18.20** Photo of the embroidered couplers held by a tape on the chest [35]

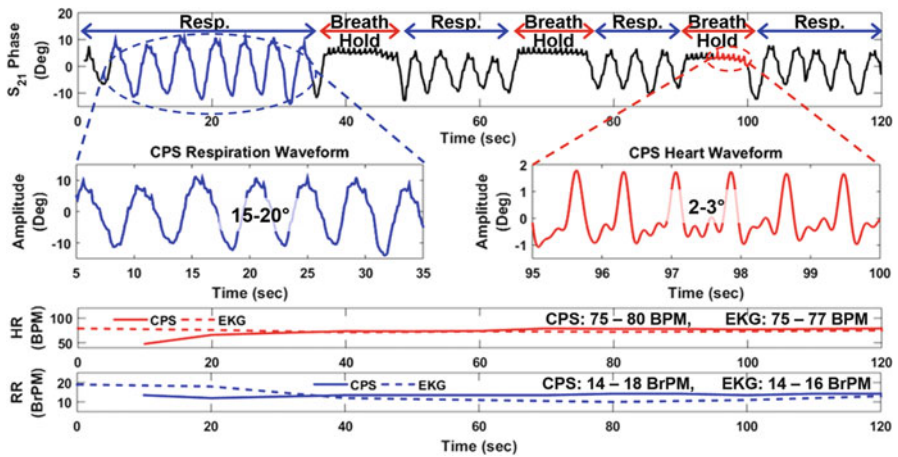
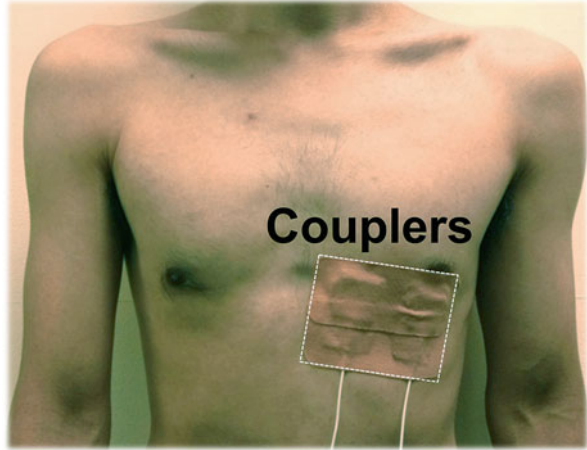


**Fig. 18.21** Sample results from a participant while in a sitting position. Results include extracted heartbeat and respiration waveform from the CPS. Comparison of the calculated heart and respiration rate from the CPS and EKG is also included [35]

amplitudes ranging from 1 to 3 deg. is easily identifiable when the study participants held their breath. The small male participant's respiration and heartbeat waveform amplitude were slightly greater than the medium and large male participants by 5–10 deg. and 1–2 deg., respectively. However, regardless of the differences in the amplitude, the CPS system was able to extract and calculate the heart and respiration rate with considerable accuracy when compared to the measured rates from the benchmark device, Propaq LT. A difference between the two systems was also observed between the extracted and measured heart rate for the medium male participant with a difference of 15–20 BPM. Source of this discrepancy will be further investigated in future human clinical studies. Summary of the results

**Table 18.7** Summary of heart and respiration rate results while patients were seated [35]

Patient type	Heartbeat amplitude (deg)	Respiration amplitude (deg)	Heart rate (BPM)		Respiration rate (BrPM)	
			CPS	Propaq LT	CPS	Propaq LT
Small	2	15–20	75–80	75–78	14–18	14–16
		mean	77.5	76.5	16	15
Medium	1	5–10	60–75	80–90	10–21	10–18
		mean	67.5	85	15.5	14
Large	1	10–15	60–78	75–80	15–22	10–17
		mean	69	77.5	18.5	13.5

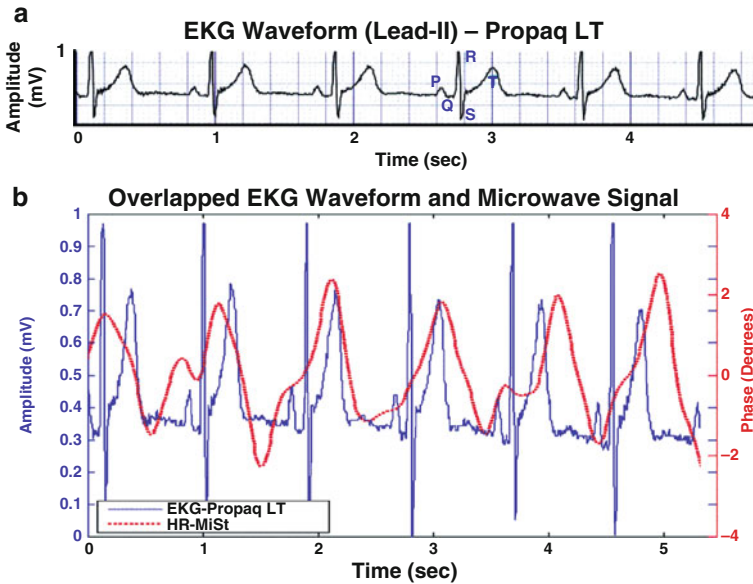


**Fig. 18.22** (a) Printout of the EKG waveform from Propaq LT. (b) Comparison of the recorded EKG waveform (digitized) and the measured  $S_{11}$  phase of the microwave signal [43]

from the human clinical studies are included in Table 18.7. Statistical analysis was performed using Pearson correlation coefficient method to compare the measured values between the CPS system and the Propaq LT. Overall, good agreement was observed between the two devices for both heart rate ( $r = 0.7$ ) and respiration rate ( $r = -0.64$ ).

A similar study to validate feasibility of detecting heart and respiratory rates was also conducted in Ref. [43] with normal healthy participants. In this study, the heart and respiration rates were extracted from the measured phase of the reflection coefficient ( $S_{11}$ ) from a single sensor. Measurements were also compared with the EKG from the Propaq LT. Results were in good agreement with the EKG measurements. Results from one of the participants are included in Fig. 18.22.

Based on these results, it can be concluded that the proposed microwave system with a single sensor or an array of sensors has sufficient sensitivity to extract vital signs accurately regardless on the size of the participants.

#### 18.4.2.2 Vital Sign Evaluation: Stress Test

To further evaluate the accuracy of the CPS to monitor human vital signs, a stress test based on a modified Bruce protocol [60] was conducted to vary the heart and respiration rate of the study participants. Data from four male participants with an average age of 25.75 years were analyzed. Demographic summary of the study participants for the stress test is included in Table 18.8.

The copper-based electromagnetic sensors were used for these experiments since it provided better coupling than the current textile-based sensor. From additional preliminary tests, it was also determined that the strength of the heartbeat signal was stronger when the electromagnetic sensors were placed side by side to the left of the sternum. Furthermore, preliminary test with the modified Bruce protocol at 3 mph has indicated a limitation of the Propaq LT to accurately measure respiration rate during exercise. Respiration rate such as 53 breaths/min (BrPM) was observed while patients were running on the treadmill which is significantly greater than the normal breathing rate (12–20 BrPM) for the participants. Therefore, a respiratory belt unit (Vernier Software and Technology, Portland, OR, USA) [61] was used as the benchmark device for the respiratory rate measurements. The air-filled respiratory belt consisted of an air pressure sensor to determine the end of the inspiration and expiration of the respiration cycle. Accuracy of the measured heart rate from the Propaq LT at 3 mph was revalidated by counting the pulse of the patients on the radial artery, located on the inside of the wrist near the thumb, while the participants were running with their hand rested on the handle bar of the treadmill. Measured heart and respiration rate was recorded simultaneously from all three devices throughout the experiments for all of the participants.

The breathing exercises from the previous experiments were added at the beginning of the tests while the patients were standing on the treadmill, followed by the modified Bruce protocol which included four 3 min stages or levels of exercise. The stages included a warm-up period of walking, exercise (jog and run), and cooldown. The test was concluded with a 1 min normal breathing cycle while the

**Table 18.8** Demographic of study participants for the stress test experiments

Patient	Age (yrs.)	Weight (lbs.)	Height (ft, in.)	Chest circumference (in.)
1	26	157	5'10	35
2	28	155	5'10	36
3	26	135	5'7	36
4	23	155	5'9	34
Average	25.75	150.5	5'8	35.25

**Table 18.9** Stress test procedure with the modified Bruce protocol [31]

Stage	Time [mm:ss]	Duration [mm:ss]	Tasks	Speed [mph]	Incline (%)
1: At rest (acquire data)	00:00	01:00	Breathe	0	0
	01:00	00:10	Breath hold	0	0
	01:10	00:30	Breathe	0	0
	01:40	00:10	Breath hold	0	0
	01:50	00:30	Breathe	0	0
2: Warm-up	02:20	03:00	Walk	1.7	0
Acquire data	05:20	01:00	Rest	0	0
3: Warm-up	06:20	03:00	Walk	1.7	10
Acquire data	09:20	01:00	Rest	0	10
4: Exercise	10:20	03:00	Jog	2.5	12
Acquire data	13:20	01:00	Rest	0	12
5: Exercise	14:20	03:00	Run	3.0	15
Acquire data	17:20	01:00	Rest	0	15
6: Exercise	18:20	03:00	Jog	2.5	12
Acquire data	21:20	01:00	Rest	0	12
7: Cooldown	22:20	03:00	Walk	1.7	10
Acquire data	25:20	01:00	Rest	0	10
8: Cooldown	26:20	03:00	Walk	1.7	0
Acquire data	29:20	01:00	Rest	0	0
Test complete	30:20	00:00	End		

patient was standing on the treadmill. Protocol summary for this study is included in Table 18.9. Setup and results of the stress test are included in Figs. 18.23a, b, respectively. Measured heart and respiration rate from the CPS system increased and decreased with the changed in the speed and incline of the treadmill. These results were in agreement with the values from the EKG and respiration belt.

### 18.4.3 Lung Fluid Validation

In 2014, the CPS project was awarded a 2-year NIH grant (R21HL124457), to further validate reliability and accuracy of the CPS system through human clinical trials. The objective was to clinically validate the sensitivity of the CPS system to monitor heart rate and respiratory rate and assess changes in lung water content with hospitalized patients. The human clinical trials were conducted in collaboration with a medical team lead by Dr. Todd Seto at The Queen's Medical Center (QMC), Honolulu, HI. Institutional review boards from QMC and the University of Hawaii approved the study protocol.

Patient populations that were eligible for this study included two adult patient populations: patients with a pulmonary artery catheter and patients undergoing

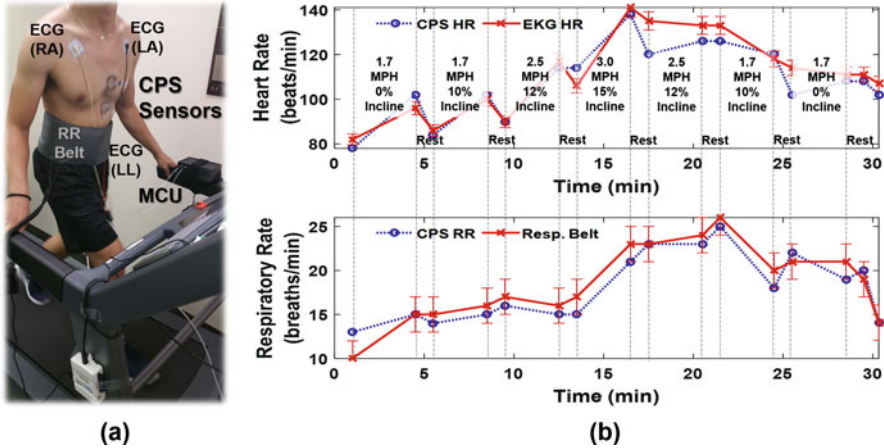


**Fig. 18.23** (a) Photo of a study participant running on a treadmill with the electromagnetic sensors and the benchmark devices; EKG leads for the heart rate and respiration belt for the respiration rate. (b) Sample results of heart and respiration rate from one of the study participants during the stress test [31]

**Table 18.10** Patient demographic summary

Patient type	Number of patients	Number of male	Number of female
HF	12	10	2
HD	13	11	2
Total	25	21	4

hemodialysis. Exclusion criteria included patients with an intra-aortic balloon pump, automatic implantable cardioverter defibrillator or pacemaker, patients with an open chest, those who had a scheduled procedure during the study period, patients who were unstable to the point where setting up or obtaining data from the CPS would interfere with patient care, and pregnant women. All patients or their surrogate provided written informed consent. Summary of patient demographic is included in Table 18.10.

Of the 25 enrolled patients, 7 heart failure and 11 hemodialysis patients completed the study. Incomplete studies ( $n = 7$ ) were due to unexpected deterioration in the subject’s clinical status and/or unplanned procedures that interfered with data collection. For all patients, heart and respiration rate were monitored simultaneously every 5 min and compared with standard clinical devices. Pearson correlation and correlation by mixed model approach were used to assess the strength of association, and concordance correlation and intraclass correlation coefficient (ICC) were used to measure agreement between values from EKG and CPS. All showed good correlation values over 0.9 for both heart and respiration rate measurements (see Table 18.11).

**Table 18.11** Agreement between Heart Rate (HR) and Respiratory Rate (RR) values from EKG and CPS among Hemodialysis (HD) and Heart Failure (HF) Patients

Patient type	Statistical methods				
	Variable	Pearson	Concordance	Mixed	ICC
HF	HR	0.98	0.98	0.98	0.99
	RR	0.98	0.97	0.97	0.99
HD	HR	0.97	0.97	0.97	1.00
	RR	0.93	0.93	0.93	0.99
Combined	HR	0.98	0.98	0.98	1.00
	RR	0.95	0.95	0.96	0.99

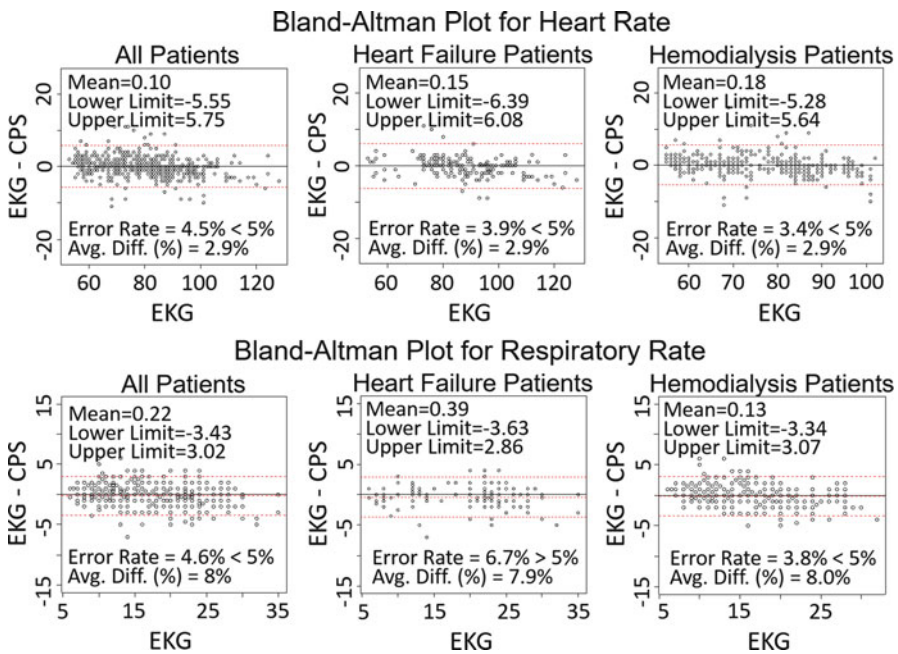
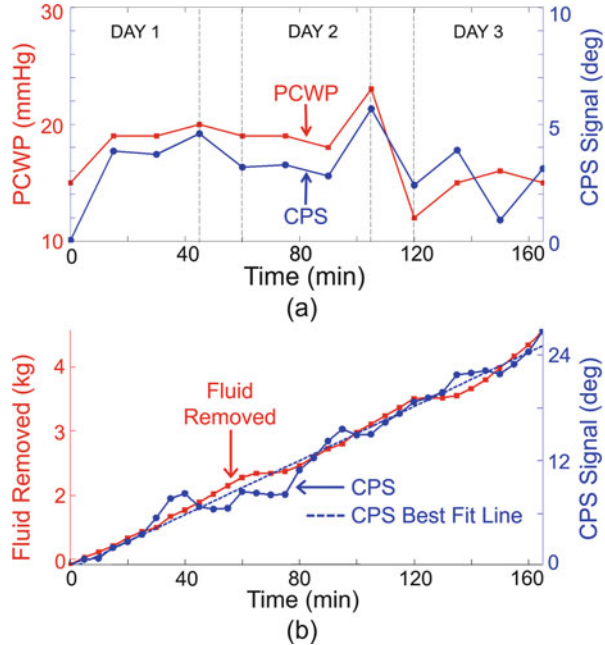


**Fig. 18.24** Bland-Altman plot for heart rate and respiratory rate for heart failure and hemodialysis patients

Bland-Altman statistical representation/plots for heart rate and respiratory rate for heart failure and hemodialysis patients are shown in Fig. 18.24. Once again results are clearly in good agreements with EKG data and available methods for monitoring respirations.

For the assessment of changes in lung water content, the changes in the baseline of the CPS signal were compared with pressure measurements from a pulmonary artery catheter (PAC) for HF patients and fluid removed during hemodialysis treatment. Several clinical trials were conducted over a 1-h monitoring period, and limited data (3–4 wedge pressure measurements) were made during this period.

**Fig. 18.25** (a) Clinical results of wedge pressure measurements compared with changes in the CPS signal trend of a heart failure patient. Measurements were taken in three 1-h periods over 3 days. (b) Results comparing fluid removed and trend of CPS signal from a hemodialysis patient



For these patients, no statistically significant changes in both the wedge and CPS measurements were observed. Additional IRB approval was obtained to allow for extended monitoring for patients with pulmonary artery catheters for several days. The results in Fig. 18.25a represent data from one of these experiments, which were conducted over three 1-h periods on three consecutive days. As noted, the wedge pressure measurements correlated well with the baseline trend in the detected CPS signal. Overall, statistical correlation analysis between the measured lung water trend from the CPS and PCWP was between 0.52 and 0.97.

For the hemodialysis patients, the baseline of the CPS signal was compared with the total fluid extracted during hemodialysis treatment. These measurements were taken over a longer time period (2–4 h), and hence more data points were collected which facilitated a more reliable comparison and validation of the CPS measurements. Table 18.12 lists a summary of the obtained results with correlation factors ranging from 0.82 to 1.0. Sample results of the lung water trend compared with the fluid removed during a hemodialysis treatment are included in Fig. 18.25b. Overall, clinical results from both the heart failure and hemodialysis patients have shown that the CPS system is indeed capable of measuring heart and respiration rate and, more importantly, detecting changes in lung water content.



**Table 18.12** Pearson correlation analysis of CPS measurements validation in clinical trials on hemodialysis patients

Experiment #	Pearson correlation (fluid removed vs. CPS trend)
1	0.99
2	0.93
3	0.85
4	0.98
5	0.99
6	1.00
7	0.96
8	0.98
9	0.82
10	0.90
11	0.97
12	0.82
13	0.88

## 18.5 Conclusion

Presented in this chapter is the development of the cardiopulmonary-stethoscope system, a noninvasive technique for monitoring vital signs and measurement of lung water content and is also suitable for continuous measurements. Measurement of lung water is the corner stone in the management of many chronic cardio and pulmonary diseases such as heart failure and acute lung injuries. Currently, there is no method that can measure lung water continuously and noninvasively.

The latest developments in the cardiopulmonary-stethoscope system include a mobile-based system that is suitable for real-time and remote monitoring, a prototype of a wearable sensor, and advanced dynamic 3D modeling on anatomically realistic model.

The CPS has been clinically validated in animal and isolated lung experiments as well as human clinical trials on healthy, heart failure, and hemodialysis patients. Overall, statistical correlation between the CPS with existing clinical methods/techniques (EKG, PAC, fluid removed) has shown good agreement. With these developments, the CPS is one step closer to addressing the “holy grail” in the medical community, which is a noninvasive and continuous measurement of changes in lung water content. Future considerations for the CPS system include potential commercialization for clinical and outpatient use for fluid management. Future research will also include investigating potential applications for other cardiopulmonary-related diseases.

**Acknowledgments** This work was in collaboration with University of Hawaii John A. Burns School of Medicine and The Queen’s Medical Center. This project was supported by the National Natural Science Foundation (ECCS1340364) and National Institutes of Health (R21HL124457).

## References

1. M.F. Iskander, S.S. Stuchly, A time-domain technique for measurement of the Dielectric properties of biological substances. *IEEE Trans. Instrum. Meas.* **21**(4), 425–429 (1972)
2. C.H. Durney, C.C. Johnson, P.W. Barber, H. Massoudi, M.F. Iskander, S.J. Allen, J.C. Mitchell, Descriptive summary: radiofrequency radiation dosimetry handbook-second edition. *Radio Sci.* **14**(6S), 5–7 (1979)
3. C.H. Durney, M.F. Iskander, H. Massoudi, C.C. Johnson, An empirical formula for broad-band SAR calculations of Prolate Spheroidal models of humans and animals. *IEEE Transactions on Microwave Theory and Techniques* **27**(8), 758–763 (1979)
4. M.F. Iskander, C.H. Durney, D.J. Shoff, D.G. Bragg, Diagnosis of pulmonary edema by a surgically noninvasive microwave technique. *Radio Sci.* **14**(6S), 265–269 (1979)
5. M.F. Iskander, C.H. Durney, An electromagnetic energy coupler for medical applications. *Proc. IEEE* **67**(10), 1463–1465 (1979)
6. D.J. Shoff, Noninvasive microwave methods for measuring tissue volume in normal dogs after whole blood infusion, M.S. thesis, Department of Electrical Engineering, University of Utah, March 1978
7. M.F. Iskander, C.H. Durney, Electromagnetic energy coupler/receiver apparatus and method. U.S. Patent 4,240,445, 23 Dec 1980
8. M.F. Iskander, C.H. Durney, Electromagnetic techniques for medical diagnosis: a review. *Proc. IEEE* **68**(1), 126–132 (1980)
9. M.F. Iskander, R. Maini, C.H. Durney, D.G. Bragg, A microwave method for measuring changes in lung water content: numerical simulation. *IEEE Trans. Biomed. Eng.* **28**(12), 797–804 (1981)
10. M.F. Iskander, C.H. Durney, D.G. Bragg, B.H. Ovard, A microwave method for estimating absolute value of average lung water. *Radio Sci.* **17**(5S), 111S–118S (1982)
11. M.F. Iskander, C.H. Durney, Microwave methods of measuring changes in lung water. *Journal of Microwave Power* **18**(3), 265–275 (1983)
12. M.F. Iskander, Apparatus and method for measuring lung water content. U.S. Patent 4,488,559, 18 Dec 1984
13. M.F. Iskander, C.H. Durney, T. Grange, C.S. Smith, Radiometric technique for measuring changes in lung water (short papers). *IEEE Transactions on Microwave Theory and Techniques* **32**(5), 554–556 (1984)
14. V. Sathiseelan, M.F. Iskander, G.C.W. Howard, N.M. Bleehen, Theoretical analysis and clinical demonstration of the effect of power pattern control using the annular phased-array hyperthermia system. *IEEE Transactions on Microwave Theory and Techniques* **34**(5), 514–519 (1986)
15. C. Durney M. Iskander, Antennas for medical applications, in *Antenna Handbook Theory, Applications, and Design*, 1st edn., Y.T. Lo, S.W. Lee (Eds.) (Springer, New York, 1988), pp. 1729–1788
16. M.F. Iskander, A.M. Tumei, Design optimization of interstitial antennas. *IEEE Trans. Biomed. Eng.* **36**(2), 238–246 (1989)
17. M. C. Staff, Pulmonary edema definition, Mayo Clinic, Jul 2014. [Online]. Available: <http://www.mayoclinic.org/diseases-conditions/pulmonary-edema/basics/definition/con-20,022,485>. Accessed 10 Jan 10 2017
18. J. Powell, D. Graham, S. O'Reilly, G. Punton, Acute pulmonary oedema. *Nurs. Stand.* **30**(23), 51–60 (2016)
19. M.S. Nieminen, V.-P. Harjola, Definition and epidemiology of acute heart failure syndromes. *Am. J. Cardiol.* **96**(6), 5–10 (2005)

20. Centers for Medicare and Medicaid Services, Medicare & Medicaid statistical supplement. [Online]. Available: <https://www.cms.gov/Research-Statistics-Data-and-Systems/Statistics-Trends-and-Reports/MedicareMedicaidStatSupp/2007.html>. Accessed Jan 2017
21. U. S. Government Publishing Office, An act Entitled The Patient Protection and Affordable Care Act. Public Law 111–148, 2010. [Online]. Available: <https://www.gpo.gov/fdsys/pkg/PLAW-111publ148/pdf/PLAW-111publ148.pdf>. Accessed 10 Jan 2017
22. O. Chioncel et al., The Romanian Acute Heart Failure Syndromes (RO-AHFS) registry. *Am. Heart J.* **162**(1), 142.e1–153.e1 (2011)
23. F. Peacock, Heart failure and acute pulmonary edema in the emergency department, in *The Textbook of Emergency Cardiovascular Care and CPR*, J. Field (Ed.) (Lippincott Williams & Wilkins, Philadelphia, 2009), pp. 96–113
24. N.R. Lange, D.P. Schuster, The measurement of lung water. *Crit. Care.* **3**(2), R19–R24 (1999)
25. B.K. Gehlbach, E. Geppert, The pulmonary manifestations of left heart failure. *Chest* **125**(2), 669–682 (Feb. 2004)
26. P.D. Snashall, S.J. Keyes, B.M. Morgan, R.J. McAnulty, P.F. Mitchell-Heggs, J.M. McIvor, K.A. Howlett, The radiographic detection of acute pulmonary oedema. A comparison of radiographic appearances, densitometry and lung water in dogs. *Br. J. Radiol.* **54**(640), 277–288 (1981)
27. S.G. Sakka, C.C. Ruhl, U.J. Pfeiffer, R. Beale, A. McLuckie, K. Reinhart, A. Meier-Hellmann, Assessment of cardiac preload and extravascular lung water by single transpulmonary thermomodulation. *Intensive Care Med.* **26**(2), 180–187 (2000)
28. D.J. van Veldhuisen, F. Braunschweig, V. Conraads, I. Ford, M.R. Cowie, G. Jondeau, J. Kautzner, R.M. Aguilera, M. Lunati, C.M. Yu, B. Gerritse, M. Borggrefe, for the DOT-HF Investigators, Intrathoracic impedance monitoring, audible patient alerts, and outcome in patients with heart failure. *Circulation* **124**(16), 1719–1726 (2011)
29. D.K. Moser, L.V. Doering, M.L. Chung, Vulnerabilities of patients recovering from an exacerbation of chronic heart failure. *Am. Heart J.* **150**(5), 984.e7–984.e13 (2005)
30. M.F. Iskander, N. Celik, R. Gagarin, G.C. Huang, D.A. Bibb, Microwave stethoscope for measuring cardio-pulmonary vital signs and lung water content. U.S. Patent 9,526,438, Dec 2016
31. R.R.G. Perron, Noninvasive electromagnetic sensors for continuous monitoring of human vital signs and assessment of lung fluid content, PhD dissertation, Department of Electrical Engineering, College of Engineering, University of Hawaii at Manoa, 2016
32. A. Pantelopoulos, N.G. Bourbakis, A survey on wearable sensor-based systems for health monitoring and prognosis. *IEEE Trans. Syst. Man Cybern. Part C Appl. Rev.* **40**(1), 1–12 (2010)
33. C. Gopalsamy, S. Park, R. Rajamanickam, S. Jayaraman, The Wearable Motherboard? The first generation of adaptive and responsive textile structures (ARTS) for medical applications. *Virtual Reality* **4**(3), 152–168 (1999)
34. I. Locher, M. Klemm, T. Kirstein, G. Trster, Design and characterization of purely textile patch antennas. *IEEE Trans. Adv. Packag.* **29**(4), 777–788 (2006)
35. R.R.G. Perron, G.C. Huang, M.F. Iskander, Textile electromagnetic coupler for monitoring vital signs and changes in lung water content. *IEEE Antennas Wirel. Propag. Lett.* **14**, 151–154 (2015)
36. Less EMF, Shielding and conductive fabrics. [Online]. Available: <http://www.lessemf.com/fabric1.html#321>. Accessed 12 Jan 2017
37. A. Industries, Stainless thin conductive thread. [Online]. Available: [https://www.adafruit.com/products/640?gclid=CjwKEAjlw1q24BRDMjdK7g8mD6BASJABB18n3dRwyZRf4rhar3RDzNICd7xXwsDT10VB5tZikSiTtBoC8Drw\\_wcB](https://www.adafruit.com/products/640?gclid=CjwKEAjlw1q24BRDMjdK7g8mD6BASJABB18n3dRwyZRf4rhar3RDzNICd7xXwsDT10VB5tZikSiTtBoC8Drw_wcB). Accessed 12 Jan 2017
38. D. Halperin, T.W. Feeley, F.G. Mihm, C. Chiles, D.F. Guthaner, N.E. Blank, Evaluation of the portable chest roentgenogram for quantitating Extravascular lung water in critically ill adults. *Chest* **88**(5), 649–652 (1985)

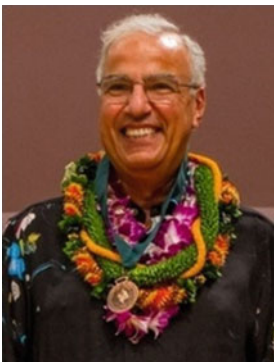
39. E. Fernandez-Mondejar, R. Rivera-Fernandez, M. Garccia-Delgado, A. Touma, J. Machado, J. Chavero, Small increases in extravascular lung water are accurately detected by transpulmonary thermodilution. *J. Trauma: Injury Infection Crit. Care* **59**(6), 1420–1424 (2005)
40. S.G. Sakka, M. Klein, K. Reinhart, A. Meier-Hellmann, Prognostic value of extravascular lung water in critically ill patients. *Chest* **122**(6), 2080–2086 (2002)
41. G.C. Huang, R. Gagarin, N. Celik, H.S. Youn M.F. Iskander, Wideband EM coupler/appliator design and characterization for the clinical benchmarking tests of microwave stethoscope (MiSt), in *Proceedings of the 2012 IEEE International Symposium on Antennas and Propagation*, Chicago, 2012, pp. 1–2. doi: [10.1109/APS.2012.6349099](https://doi.org/10.1109/APS.2012.6349099)
42. N. Celik, R. Gagarin, H.s. Youn, M.F. Iskander, A noninvasive microwave sensor and signal processing technique for continuous monitoring of vital signs. *IEEE Antennas Wirel. Propag. Lett.* **10**, 286–289 (2011)
43. N. Celik, R. Gagarin, G.C. Huang, M.F. Iskander, B.W. Berg, Microwave stethoscope: development and benchmarking of a vital signs sensor using computer-controlled phantoms and human studies. *IEEE Trans. Biomed. Eng.* **61**(8), 2341–2349 (2014)
44. E. Charbek, Normal vital signs: normal vital signs, in *Medscape*, 2015. [Online]. Available: <http://emedicine.medscape.com/article/2172054-overview>. Accessed 13 Jan 2017
45. R. Schmidt, Multiple emitter location and signal parameter estimation. *IEEE Trans. Antennas Propag.* **34**(3), 276–280 (1986)
46. K.H. Jarman, D.S. Daly, K.K. Anderson, K.L. Wahl, A new approach to automated peak detection. *Chemom. Intell. Lab. Syst.* **69**(1–2), 61–76 (2003)
47. D. Bibb, R.R.G. Perron, G.C. Huang, M.F. Iskander, Development of a wireless monitoring system for microwave-based comprehensive vital sign measurement. *IEEE Antennas Wirel. Propag. Lett.* **15**, 1249–1252 (2016)
48. R.R.G. Perron, M.F. Iskander, Dynamic 3D model of human thorax for the assessment of changes in lung fluid content and vital signs, in *2016 IEEE/ACES International Conference on Wireless Information Technology and Systems (ICWITS) and Applied Computational Electromagnetics (ACES)*, 2016, pp. 1–2
49. J.F. Lee, Z. Cendes, D.K. Sun, Adaptive mesh refinement, h-version, for solving multiport microwave devices in three dimensions. *IEEE Trans. Magn.* **36**(4), 1596–1599 (2000)
50. M. Kozlov, R. Turner, A comparison of Ansoft HFSS and CST microwave studio simulation software for multi-channel coil design and SAR estimation at 7 T MRI. *PIERS Online* **6**(4), 395–399 (2010)
51. D. Means, K. Chan, Evaluating compliance with FCC guidelines for human exposure to radiofrequency electromagnetic fields, in *Federal Communications Commission*, 2001. [Online]. Available: <https://transition.fcc.gov/bureaus/oet/info/documents/bulletins/oet65/oet65c.pdf>. Accessed 13 Jan 2017
52. M.J. Mirro, E.W. Rogers, A.E. Weyman, H. Feigenbaum, Angular displacement of the papillary muscles during the cardiac cycle. *Circulation* **60**(2), 327–333 (1979)
53. J.E. Cotes, D.J. Chinn, M.R. Miller, *Lung function: Physiology, Measurement and Application in Medicine* (John Wiley & Sons, New York, 2009)
54. R. Gagarin, H.s. Youn, N. Celik, M. Iskander, Noninvasive microwave technique for hemodynamic assessments, in *IEEE Antennas and Propagation Society International Symposium*, Toronto, July 2010
55. Schmid & Partner Engineering AG, DAK » SPEAG, Schmid & partner engineering AG, 2010. [Online]. Available: <https://www.speag.com/products/>. Accessed 13 Jan 2017
56. IEEE recommended practice for determining the peak spatial-average Specific Absorption Rate (SAR) in the human head from wireless communications devices: measurement techniques, in *IEEE Std 1528–2013* (Revision of IEEE Std 1528–2003), pp. 1–246, 6 Sept 2013
57. European Committee for Electrotechnical Standardization, CENELEC – EN 50361 Basic standard for the measurement of specific absorption rate related to human exposure to electromagnetic fields from mobile phones (300 MHz–3 GHz), Brussels, Belgium, 2001
58. IEC, IEC 62209 evaluation of the human exposure to radio frequency fields from handheld and body-mounted wireless communication devices in the frequency range of 30 MHz to 6 GHz: human models instrumentation and procedures, Geneva, Switzerland, 2009

59. Welch Allyn, Propaq® LT monitor, 2015. [Online]. Available: <https://www.welchallyn.com/en/products/categories/patient-monitoring/continuous-monitoring-systems/propaq-lt-monitor.html>. Accessed 13 Jan 2017
60. G.F. Fletcher, G.J. Balady, E.A. Amsterdam, B. Chaitman, R. Eckel, J. Fleg, V.F. Froelicher, A.S. Leon, I.L. Pina, R. Rodney, D.A. Simons-Morton, M.A. Williams, T. Bazzarre, Exercise standards for testing and training: a statement for healthcare professionals from the American heart association. *Circulation* **104**(14), 1694–1740 (2001)
61. Vernier Software and Technology, Respiration monitor belt > vernier software & technology, 2017. [Online]. Available: <http://www.vernier.com/products/sensors/rmb/#section4>. Accessed 13 Jan 2017



**Ruthsenne R.G. Perron** received the MS and PhD degrees in Electrical Engineering from the University of Hawaii at Manoa, in 2011 and 2016, respectively. She joined the Hawaii Center for Advanced Communications in 2007 and has been a part of the development of the CP-Stethoscope, a medical device for early detection of heart failure. The CP-Stethoscope project has been featured in the IEEE Spectrum magazine and has earned national recognition at the National Science Foundation I-CORP program. The CP-Stethoscope project is funded by the National Science Foundation and National Institutes of Health. Her research interests include biomedical devices and telemedicine. Her work on the CP-Stethoscope project has been published in several IEEE journal publications. Dr. Perron is active in outreach STEM

activities such as the Hawaii State Science and Engineering Fair. She has served as president for the Society of Women Engineers, UH Manoa Student Section and served as the technical program chair in the Society Women Engineers Western Region Conference. She was the recipient of the Bretzloff Award in Engineering and was selected as the Scholar of the Year by the Achievement Rewards for College Scientists (ARCS) in 2015. She was also selected as a mentee for the NIH – National Research Mentoring Network (NRMN) Program in 2016.



**Magdy F. Iskander** is the Director of the Hawaii Center for Advanced Communications and Professor of Electrical Engineering, University of Hawaii at Manoa. He is Codirector of the NSF I/UCRC and a Fellow of IEEE (1993). He was the 2002 President of the IEEE AP-S, Distinguished Lecturer, and a Program Director in the ECCS Division at NSF. Dr. Iskander joined the University of Hawaii in 2002, and prior to that he was Professor of ECE Department and the Engineering Clinic Endowed Chair Professor at the University of Utah. He received many awards for excellence in research and teaching including University of Hawaii Board of Regents' Medal for Excellence in Research and Medal for Teaching Excellence, IEEE MTT-S Distinguished Educator Award, IEEE AP-S Chen-To Tai Distinguished Educator Award, Northrop Grumman Excellence in Teaching Award, and

others. He has published over 270 papers in journals and books and holds ten patents. He authored/edited several books including the textbook *Electromagnetic Fields and Waves*. He is the founding editor of *Computer Applications in Engineering Education* published by John Wiley & Sons 1992 onwards. His research has been funded by NSF, NIH, Army Research Office, US Army CERDEC, Office of Naval Research, and corporate sponsors.



**Todd B. Seto** focuses on noninvasive cardiology and outcomes research. He is a graduate of the University of Hawaii, John A. Burns School of Medicine and completed his training in Internal Medicine and Cardiovascular Disease at Beth Israel Hospital and Harvard Medical School in Boston. He also completed a Fellowship in General Medicine at Harvard Medical School, which included training in health services and outcomes research. Dr. Seto is currently the Medical Director of the Non-Invasive Cardiology Laboratory at The Queen's Medical Center and is an Associate Professor of Medicine at the University of Hawaii's John A. Burns School of Medicine (JABSOM). He is also Medical Director of the Center for Outcomes Research and Evaluation

(CORE), a multidisciplinary group that is involved in data analysis, process and outcomes assessment, and quality improvement initiatives at The Queen's Medical Center. Dr. Seto has received continuous research funding from the National Institutes of Health since 2004 and maintains an active research program evaluating innovative ways to improve the quality of cardiovascular care and decrease racial and ethnic disparities in health outcomes. Dr. Seto is a Co-PI in the NIH-funded human clinical trials to assess and validate the accuracy of the CP-Stethoscope in measuring the changes in lung water content and other vital signs with hemodialysis and heart failure patients. These studies were conducted in collaboration with The Queen's Medical Center in Honolulu, HI.



**Gui Chao Huang** received his BS degree in Electrical Engineering from the University of Hawaii at Manoa, in 2012. He is currently a PhD candidate in the Department of Electrical Engineering at the University of Hawaii at Manoa. He joined the Hawaii Center for Advanced Communications as a student research assistant in 2011. His research interests include antenna design, specifically, broadband antenna and phased array. His research in antenna design has been funded by the US Army CERDEC. He has also designed and developed several prototypes of the CP-Stethoscope system. His work has been published in IEEE Antenna and Wireless Propagation Letters. He is a member of Eta Kappa Nu (HKN), the National Honor Society

for Electrical and Computer Engineers. He was awarded the Kresser ARCS Award in Engineering in 2015.



**Darcy A. Bibb** received the BS and MS degrees in Electrical Engineering from the University of Hawaii at Manoa in 2013 and 2016, respectively. From 2013 to 2016, he was a Graduate Research Assistant with the Hawaii Center for Advanced Communications at the University of Hawaii at Manoa. He is currently an electrical engineer at Raytheon Space and Airborne Systems in El Segundo, CA. His research interests and areas of work include radio source localization techniques using ray tracing, time reversal signal processing, and machine learning; microwave, digital, and mixed-signal circuits; and embedded systems. His contributions include design and development for

the wireless integration of the CP-Stethoscope system which is currently being used for the human clinical studies. His work has been presented at several IEEE conferences including the AP-S Symposium on Antennas and Propagation and the Conference on Antenna Measurements & Applications, and published in the IEEE Antennas and Wireless Propagation Letters journal. He is also a member of Eta Kappa Nu, the IEEE electrical and computer engineering honor society.

# Chapter 19

## The Ewald–Oseen Extinction Theorem and the Extended Boundary Condition Method

Akhlesh Lakhtakia

### Prolog

“Akhil, try not to make waves,” said Prof. Magdy F. Iskander as he escorted me out of the Merrill Engineering Building one fine day in July 1983. I had defended my PhD thesis in March that year and was leaving the University of Utah for a postdoctoral position at the Pennsylvania State University.

Produced under the supervision of Prof. Iskander, both my MS and PhD theses addressed the scattering and absorption of monochromatic electromagnetic waves in the microwave regime by prolate-spheroidal models of humans and other animals. My graduate supervisor would discuss electromagnetic theory and experiments animatedly with one and all. He would sing and dance while teaching electromagnetism courses. Why would then he advise me not to make waves?

“Just work hard and your career will proceed smoothly,” he continued. I have tried to follow Prof. Iskander’s advice throughout the ensuing years.

All of a sudden, I realized last year that 33 years had elapsed since that fateful day. Then came the realization that my graduate supervisor had followed his own advice very well for four decades and was renowned in the applied-electromagnetics research community. Here was a career that must be applauded. Now was the time to wish that this career would extend further, not that Prof. Iskander is in need of any motivation to continue research for the next two decades and more. He continues to stride forth in the research world, enthusiastically and with a delight that spills out of his lips whenever he speaks.

---

A. Lakhtakia (✉)

NanoMM – Nanoengineered Metamaterials Group, Department of Engineering Science and Mechanics, Pennsylvania State University, University Park, PA 16802, USA

e-mail: [akhlesh@psu.edu](mailto:akhlesh@psu.edu)

## 19.1 Introduction

During all of my MS research [1] and the first phase of my PhD research [2], I used the extended boundary condition method (EBCM) [3–5] to determine the frequency-domain scattering and absorption characteristics of prolate spheroids made of a homogeneous, dissipative, dielectric material. Sometimes called the *null-field method* [6–9], the EBCM is better known as the *T-matrix method* [10]. The latter appellation is mildly inappropriate, as I have discussed in Sect. 19.4.

The EBCM is widely used to calculate scattering and absorption of monochromatic electromagnetic waves by periodically corrugated surfaces, infinitely long cylinders, and three-dimensional objects [10–18]. It is also used equally widely to investigate scattering of acoustic and elastodynamic waves [9, 10, 19, 20]. Typically, the scatterer is made of a linear homogeneous medium.

The term *extended boundary condition* was introduced in 1965 by Waterman [3] when formulating a matrix method for scattering by a perfectly conducting three-dimensional object. He argued that [3] “[t]he induced surface currents on the [object] must produce a field that, through interference, precisely cancels the incident wave throughout the interior volume. Employing this statement as a *boundary condition* leads to an ‘extended’ integral equation, defined to be one in which the unknown (surface current) appears in an integral over the surface, whereas the equation itself is required to hold throughout the volume bounded by that surface.” Although the field inside a perfectly conducting scatterer would indeed be zero, exactly the same concept underlies the EBCM for scattering by, say, a dielectric scatterer, as shown by Waterman in 1969 [4]. Although Waterman used the Huygens principle [21, Sect. 9.8], identical equations were later derived by Barber and Yeh [5] using the surface equivalence principle [22, Sect. 3–5].

Since the incident electromagnetic field is annulled throughout the interior of the scatterer by the electromagnetic field produced by (i) the electric surface current density induced on the surface of a perfectly conducting scatterer and (ii) the electric as well as magnetic surface current densities induced on the surface of a dielectric scatterer, the *null-field method* is an appropriate name for the EBCM.

This nulling or extinction concept is embodied in the Ewald–Oseen extinction theorem, which has two progenitors: Paul Peter Ewald [23] and Carl Wilhelm Oseen [24]. Considerable controversy [25] has emerged on the meaning of this theorem which was derived formally using the equations of macroscopic electromagnetics. If the electromagnetic field produced by the surface current densities annuls the incident electromagnetic field everywhere in the interior of the scatterer, what role do the molecules of the scatterer play in that annulment? Since all matter is molecular, surely every molecule in the scatterer must get excited and radiate an electromagnetic field that would participate in that annulment. Happily, both the macroscopic and the molecular approaches produce the same equations [25] for the boundary-value problem to determine the scattered electromagnetic field.

The Ewald–Oseen extinction theorem was initially formulated for scattering by a dielectric object in free space. About 75 years later, it was extended to encompass the homogeneous external medium being isotropic chiral [26] and biisotropic [27].



With the recent formulation [28] of the Huygens principle for a very general, but not the most general, linear bianisotropic medium [29, 30], it has now become possible to similarly enlarge the scope of the Ewald–Oseen extinction theorem. Formally at least, it is therefore possible to extend the scope of the EBCM.

The plan of this chapter is as follows. Mathematical statements of the Ewald–Oseen extinction theorem are formulated for a very (but not the most) general homogeneous medium in Sect. 19.2. During the formulation, four dyadic Green functions are set up and their characteristics are elucidated. Mathematical statements of the Huygens principle are presented [28] and the surface equivalence principle is postulated to derive the Ewald–Oseen extinction theorem. Section 19.3 is dedicated to the conceptual framework of the EBCM and its salient features. The chapter concludes with some remarks in Sect. 19.4.

An  $\exp(-i\omega t)$  time-dependence is assumed with  $\omega$  being the angular frequency,  $t$  the time, and  $i = \sqrt{-1}$ . Single-underlined letters denoted vectors, with  $\underline{0}$  denoting the null vector, and the caret  $\hat{\phantom{x}}$  identifying unit vectors. Dyadics [21, Chap. 1] are underlined twice, with  $\underline{\underline{I}}$  denoting the identity dyadic and  $\underline{\underline{0}}$  the null dyadic. Matrices and column vectors are enclosed within square brackets. The permittivity and permeability of free space are denoted by  $\epsilon_0$  and  $\mu_0$ , respectively.

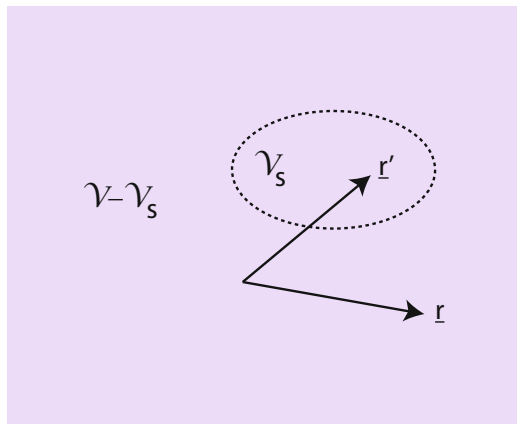
## 19.2 The Ewald–Oseen Extinction Theorem

### 19.2.1 Constitutive Relations

Let all space  $\mathcal{V}$  shown in Fig. 19.1 be occupied by a linear, homogeneous, bianisotropic medium with the frequency-domain constitutive relations

$$\left. \begin{aligned} \underline{D}(\underline{r}) &= \underline{\underline{\epsilon}} \cdot \underline{E}(\underline{r}) + \left[ \underline{\underline{\xi}} + (\underline{K} - \underline{\Gamma}) \times \underline{\underline{I}} \right] \cdot \underline{H}(\underline{r}) \\ \underline{B}(\underline{r}) &= \underline{\underline{\mu}} \cdot \underline{H}(\underline{r}) - \left[ \underline{\underline{\xi}} - (\underline{K} + \underline{\Gamma}) \times \underline{\underline{I}} \right] \cdot \underline{E}(\underline{r}) \end{aligned} \right\}, \tag{19.1}$$

**Fig. 19.1** Schematic showing the unbounded region  $\mathcal{V}$  as well as the bounded region  $\mathcal{V}_s \subset \mathcal{V}$  relevant to Eqs. (19.4). The source electric and magnetic current density phasors are confined to the region  $\mathcal{V}_s$



where the arbitrary vectors  $\underline{K}$  and  $\underline{\Gamma}$  as well as the symmetric dyadics  $\underline{\underline{\varepsilon}} = \underline{\underline{\varepsilon}}^T$ ,  $\underline{\underline{\mu}} = \underline{\underline{\mu}}^T$ , and  $\underline{\underline{\xi}} = \underline{\underline{\xi}}^T$  are implicit functions of the angular frequency  $\omega$ , and the superscript  $T$  denotes the transpose.

When  $\underline{\Gamma} = \underline{0}$ , Eqs.(19.1) describe the most general linear, homogeneous, bianisotropic medium that is Lorentz reciprocal [31, 32]. Then, the scope of these constitutive relations includes and extends beyond the following kinds of mediums [28]: orthorhombic dielectric-magnetic mediums and their simplifications, certain biaxial bianisotropic mediums [33] and their simplifications, uniaxial chiro-omega mediums [34], pseudo-chiral (or  $\Omega$ ) mediums [35], and the linearized quantum-electrodynamic vacuum [36]. When  $\underline{\Gamma} \neq \underline{0}$ , the scope of Eqs.(19.1) extends even further to encompass mediums inspired by gravitationally affected vacuum [37, 38].

### 19.2.2 Dyadic Green Functions

The electromagnetic field phasors satisfy the frequency-domain Maxwell curl postulates

$$\left. \begin{aligned} \nabla \times \underline{H}(\underline{r}) + i\omega \underline{D}(\underline{r}) &= \underline{J}_e(\underline{r}) \\ \nabla \times \underline{E}(\underline{r}) - i\omega \underline{B}(\underline{r}) &= -\underline{J}_m(\underline{r}) \end{aligned} \right\}, \quad \underline{r} \in \mathcal{V}, \quad (19.2)$$

where  $\underline{J}_e$  is the source electric current density phasor and  $\underline{J}_m$  is the source magnetic current density phasor. Substitution of Eqs.(19.1) in Eqs.(19.2) yields

$$\left. \begin{aligned} \nabla \times \underline{H}(\underline{r}) + i\omega \underline{\underline{\varepsilon}} \cdot \underline{E}(\underline{r}) + i\omega \left[ \underline{\underline{\xi}} + (\underline{K} - \underline{\Gamma}) \times \underline{I} \right] \cdot \underline{H}(\underline{r}) &= \underline{J}_e(\underline{r}) \\ \nabla \times \underline{E}(\underline{r}) - i\omega \underline{\underline{\mu}} \cdot \underline{H}(\underline{r}) + i\omega \left[ \underline{\underline{\xi}} - (\underline{K} + \underline{\Gamma}) \times \underline{I} \right] \cdot \underline{E}(\underline{r}) &= -\underline{J}_m(\underline{r}) \end{aligned} \right\}, \quad \underline{r} \in \mathcal{V}. \quad (19.3)$$

The linearity of the constitutive relations (19.1) allows the prescription of Green functions [39] for the chosen medium. With both  $\underline{J}_e$  and  $\underline{J}_m$  confined to the bounded region  $\mathcal{V}'_s \subset \mathcal{V}$ , as shown in Fig. 19.1, four Green functions for this medium can be formally defined through the equations

$$\left. \begin{aligned} \underline{E}(\underline{r}) &= \int \int \int_{\mathcal{V}'_s} \left[ \underline{\underline{G}}^{ee}(\underline{r}, \underline{r}') \cdot \underline{J}_e(\underline{r}') + \underline{\underline{G}}^{em}(\underline{r}, \underline{r}') \cdot \underline{J}_m(\underline{r}') \right] d^3 \underline{r}' \\ \underline{H}(\underline{r}) &= \int \int \int_{\mathcal{V}'_s} \left[ \underline{\underline{G}}^{me}(\underline{r}, \underline{r}') \cdot \underline{J}_e(\underline{r}') + \underline{\underline{G}}^{mm}(\underline{r}, \underline{r}') \cdot \underline{J}_m(\underline{r}') \right] d^3 \underline{r}' \end{aligned} \right\}, \quad \underline{r} \in \mathcal{V}. \quad (19.4)$$

Denoted by  $\underline{\underline{G}}^{ee}(\underline{r}, \underline{r}')$ ,  $\underline{\underline{G}}^{em}(\underline{r}, \underline{r}')$ ,  $\underline{\underline{G}}^{me}(\underline{r}, \underline{r}')$ , and  $\underline{\underline{G}}^{mm}(\underline{r}, \underline{r}')$ , all four Green functions are dyadics as each relates two vectors. One of those vectors is a source located at  $\underline{r}'$ , and the other is a field at  $\underline{r}$  radiated by that source. Accordingly, one can think of a Green function as a transfer function in a linear system [40].

The dyadic Green functions  $\underline{\underline{G}}^{me}(\underline{r}, \underline{r}')$  and  $\underline{\underline{G}}^{em}(\underline{r}, \underline{r}')$  can be obtained from the other two as follows:

$$\left. \begin{aligned} \underline{\underline{G}}^{me}(\underline{r}, \underline{r}') &= \frac{1}{i\omega} \underline{\underline{\mu}}^{-1} \cdot \left\{ \nabla \times \underline{\underline{I}} + i\omega \left[ \underline{\underline{\xi}} - (\underline{\underline{K}} + \underline{\underline{\Gamma}}) \times \underline{\underline{I}} \right] \right\} \cdot \underline{\underline{G}}^{ee}(\underline{r}, \underline{r}') \\ \underline{\underline{G}}^{em}(\underline{r}, \underline{r}') &= -\frac{1}{i\omega} \underline{\underline{\varepsilon}}^{-1} \cdot \left\{ \nabla \times \underline{\underline{I}} + i\omega \left[ \underline{\underline{\xi}} + (\underline{\underline{K}} - \underline{\underline{\Gamma}}) \times \underline{\underline{I}} \right] \right\} \cdot \underline{\underline{G}}^{mm}(\underline{r}, \underline{r}') \end{aligned} \right\}. \quad (19.5)$$

The remaining two dyadic Green functions are solutions of the differential equations

$$\left( \left\{ \nabla \times \underline{\underline{I}} + i\omega \left[ \underline{\underline{\xi}} + (\underline{\underline{K}} - \underline{\underline{\Gamma}}) \times \underline{\underline{I}} \right] \right\} \cdot \underline{\underline{\mu}}^{-1} \cdot \left\{ \nabla \times \underline{\underline{I}} + i\omega \left[ \underline{\underline{\xi}} - (\underline{\underline{K}} + \underline{\underline{\Gamma}}) \times \underline{\underline{I}} \right] \right\} - \omega^2 \underline{\underline{\varepsilon}} \right) \cdot \underline{\underline{G}}^{ee}(\underline{r}, \underline{r}') = i\omega \underline{\underline{I}} \delta(\underline{r} - \underline{r}') \quad (19.6)$$

and

$$\left( \left\{ \nabla \times \underline{\underline{I}} + i\omega \left[ \underline{\underline{\xi}} - (\underline{\underline{K}} + \underline{\underline{\Gamma}}) \times \underline{\underline{I}} \right] \right\} \cdot \underline{\underline{\varepsilon}}^{-1} \cdot \left\{ \nabla \times \underline{\underline{I}} + i\omega \left[ \underline{\underline{\xi}} + (\underline{\underline{K}} - \underline{\underline{\Gamma}}) \times \underline{\underline{I}} \right] \right\} - \omega^2 \underline{\underline{\mu}} \right) \cdot \underline{\underline{G}}^{mm}(\underline{r}, \underline{r}') = i\omega \underline{\underline{I}} \delta(\underline{r} - \underline{r}'), \quad (19.7)$$

where  $\delta(\cdot)$  is the Dirac delta function. Although these dyadic Green functions are known in closed form for only a few special cases [41–43], their spectral forms can be obtained in general by using the spatial Fourier transform [28, 31, 44].

### 19.2.3 Transformation of Fields, Sources, and Dyadic Green Functions

The anti-symmetric term  $\underline{\underline{\Gamma}} \times \underline{\underline{I}}$  in Eqs. (19.1) can be eliminated by using the transformation [43, 45, 46]

$$\left. \begin{aligned} \underline{E}(\underline{r}) &= \underline{e}(\underline{r}) \exp(i\omega \underline{\underline{\Gamma}} \cdot \underline{r}), & \underline{H}(\underline{r}) &= \underline{h}(\underline{r}) \exp(i\omega \underline{\underline{\Gamma}} \cdot \underline{r}) \\ \underline{J}_e(\underline{r}) &= \underline{j}_e(\underline{r}) \exp(i\omega \underline{\underline{\Gamma}} \cdot \underline{r}), & \underline{J}_m(\underline{r}) &= \underline{j}_m(\underline{r}) \exp(i\omega \underline{\underline{\Gamma}} \cdot \underline{r}) \end{aligned} \right\}. \quad (19.8)$$

Accordingly, Eqs. (19.3) transform to

$$\left. \begin{aligned} \nabla \times \underline{h}(\underline{r}) + i\omega \underline{\underline{\varepsilon}} \cdot \underline{e}(\underline{r}) + i\omega \left( \underline{\underline{\xi}} + \underline{\underline{K}} \times \underline{\underline{I}} \right) \cdot \underline{h}(\underline{r}) &= \underline{j}_e(\underline{r}) \\ \nabla \times \underline{e}(\underline{r}) - i\omega \underline{\underline{\mu}} \cdot \underline{h}(\underline{r}) - i\omega \left( -\underline{\underline{\xi}} + \underline{\underline{K}} \times \underline{\underline{I}} \right) \cdot \underline{e}(\underline{r}) &= -\underline{j}_m(\underline{r}) \end{aligned} \right\}, \quad \underline{r} \in \mathcal{V}, \quad (19.9)$$

and Eqs. (19.4) to

$$\left. \begin{aligned} \underline{\underline{e}}(\underline{r}) &= \int \int \int_{\mathcal{V}'_s} \left[ \underline{\underline{g}}^{ee}(\underline{r}, \underline{r}') \cdot \underline{j}_e(\underline{r}') + \underline{\underline{g}}^{em}(\underline{r}, \underline{r}') \cdot \underline{j}_m(\underline{r}') \right] d^3 \underline{r}' \\ \underline{\underline{h}}(\underline{r}) &= \int \int \int_{\mathcal{V}'_s} \left[ \underline{\underline{g}}^{me}(\underline{r}, \underline{r}') \cdot \underline{j}_e(\underline{r}') + \underline{\underline{g}}^{mm}(\underline{r}, \underline{r}') \cdot \underline{j}_m(\underline{r}') \right] d^3 \underline{r}' \end{aligned} \right\}, \underline{r} \in \mathcal{V}'. \quad (19.10)$$

The dyadic Green functions for the transformed field phasors and source current density phasors are related to the ones in Eqs. (19.4) by

$$\left. \begin{aligned} \underline{\underline{g}}^{ee}(\underline{r}, \underline{r}') &= \underline{\underline{G}}^{ee}(\underline{r}, \underline{r}') \exp[-i\omega \underline{\underline{\Gamma}} \cdot (\underline{r} - \underline{r}')] \\ \underline{\underline{g}}^{em}(\underline{r}, \underline{r}') &= \underline{\underline{G}}^{em}(\underline{r}, \underline{r}') \exp[-i\omega \underline{\underline{\Gamma}} \cdot (\underline{r} - \underline{r}')] \\ \underline{\underline{g}}^{me}(\underline{r}, \underline{r}') &= \underline{\underline{G}}^{me}(\underline{r}, \underline{r}') \exp[-i\omega \underline{\underline{\Gamma}} \cdot (\underline{r} - \underline{r}')] \\ \underline{\underline{g}}^{mm}(\underline{r}, \underline{r}') &= \underline{\underline{G}}^{mm}(\underline{r}, \underline{r}') \exp[-i\omega \underline{\underline{\Gamma}} \cdot (\underline{r} - \underline{r}')] \end{aligned} \right\}. \quad (19.11)$$

Substitution of Eqs. (19.10) in Eqs. (19.9) allows us to relate  $\underline{\underline{g}}^{me}(\underline{r}, \underline{r}')$  to solely  $\underline{\underline{g}}^{ee}(\underline{r}, \underline{r}')$  as

$$\underline{\underline{g}}^{me}(\underline{r}, \underline{r}') = \frac{1}{i\omega} \underline{\underline{\mu}}^{-1} \cdot \left[ \nabla \times \underline{\underline{I}} - i\omega \left( -\underline{\underline{\xi}} + \underline{\underline{K}} \times \underline{\underline{I}} \right) \right] \cdot \underline{\underline{g}}^{ee}(\underline{r}, \underline{r}'), \quad (19.12)$$

and  $\underline{\underline{g}}^{em}(\underline{r}, \underline{r}')$  to solely  $\underline{\underline{g}}^{mm}(\underline{r}, \underline{r}')$  as

$$\underline{\underline{g}}^{em}(\underline{r}, \underline{r}') = -\frac{1}{i\omega} \underline{\underline{\varepsilon}}^{-1} \cdot \left[ \nabla \times \underline{\underline{I}} + i\omega \left( \underline{\underline{\xi}} + \underline{\underline{K}} \times \underline{\underline{I}} \right) \right] \cdot \underline{\underline{g}}^{mm}(\underline{r}, \underline{r}'). \quad (19.13)$$

The same substitution also gives

$$\nabla \times \underline{\underline{g}}^{me}(\underline{r}, \underline{r}') = -i\omega \underline{\underline{\varepsilon}} \cdot \underline{\underline{g}}^{ee}(\underline{r}, \underline{r}') - i\omega \left( \underline{\underline{\xi}} + \underline{\underline{K}} \times \underline{\underline{I}} \right) \cdot \underline{\underline{g}}^{me}(\underline{r}, \underline{r}') + \underline{\underline{I}} \delta(\underline{r} - \underline{r}'). \quad (19.14)$$

Substitution of  $\underline{\underline{g}}^{me}(\underline{r}, \underline{r}')$  from Eq. (19.12) in Eq. (19.14) yields the differential equation

$$\left\{ \left[ \nabla \times \underline{\underline{I}} + i\omega \left( \underline{\underline{\xi}} + \underline{\underline{K}} \times \underline{\underline{I}} \right) \right] \cdot \underline{\underline{\mu}}^{-1} \right. \\ \left. \cdot \left[ \nabla \times \underline{\underline{I}} - i\omega \left( -\underline{\underline{\xi}} + \underline{\underline{K}} \times \underline{\underline{I}} \right) \right] - \omega^2 \underline{\underline{\varepsilon}} \right\} \cdot \underline{\underline{g}}^{ee}(\underline{r}, \underline{r}') = i\omega \underline{\underline{I}} \delta(\underline{r} - \underline{r}') \quad (19.15)$$

for  $\underline{\underline{g}}^{ee}(\underline{r}, \underline{r}')$ . Finally, the substitution of  $\underline{\underline{g}}^{em}(\underline{r}, \underline{r}')$  from Eq. (19.13) in

$$\nabla \times \underline{\underline{g}}^{em}(\underline{r}, \underline{r}') = i\omega \underline{\underline{\mu}} \cdot \underline{\underline{g}}^{mm}(\underline{r}, \underline{r}') + i\omega \left( -\underline{\underline{\xi}} + \underline{\underline{K}} \times \underline{\underline{I}} \right) \cdot \underline{\underline{g}}^{em}(\underline{r}, \underline{r}') - \underline{\underline{I}} \delta(\underline{r} - \underline{r}') \quad (19.16)$$

delivers the differential equation

$$\left\{ \left[ \nabla \times \underline{\underline{L}} - i\omega \left( -\underline{\underline{\xi}} + \underline{\underline{K}} \times \underline{\underline{L}} \right) \right] \cdot \underline{\underline{\xi}}^{-1} \right. \\ \left. \cdot \left[ \nabla \times \underline{\underline{L}} + i\omega \left( \underline{\underline{\xi}} + \underline{\underline{K}} \times \underline{\underline{L}} \right) \right] - \omega^2 \underline{\underline{\mu}} \right\} \cdot \underline{\underline{g}}^{mm}(\underline{\underline{r}}, \underline{\underline{r}}') = i\omega \underline{\underline{I}} \delta(\underline{\underline{r}} - \underline{\underline{r}}') \quad (19.17)$$

for  $\underline{\underline{g}}^{mm}(\underline{\underline{r}}, \underline{\underline{r}}')$ . Even though  $\underline{\underline{L}}$  is absent from Eqs. (19.15) and (19.17), closed-form expressions of  $\underline{\underline{g}}^{ee}(\underline{\underline{r}}, \underline{\underline{r}}')$  and  $\underline{\underline{g}}^{mm}(\underline{\underline{r}}, \underline{\underline{r}}')$  have been obtained only for a few special cases [41–43].

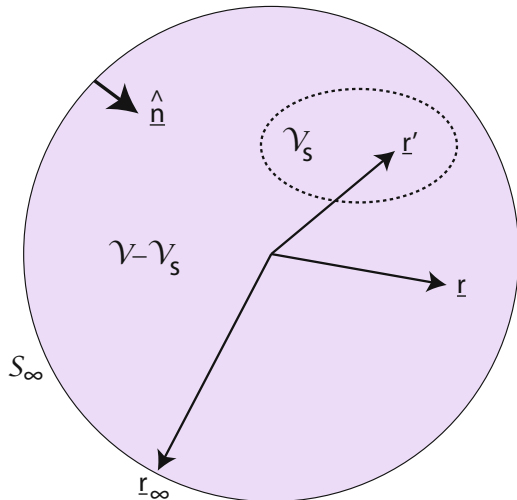
### 19.2.4 Symmetries of the Dyadic Green Functions

In order to determine the symmetries of the dyadic Green functions defined in Sects. 19.2.2 and 19.2.3, let us now consider  $\mathcal{V}$  to be the sphere bounded by the surface  $S_\infty$  of radius  $r_\infty$ , as shown in Fig. 19.2. The region  $\mathcal{V}$  is still occupied by the medium characterized by Eqs. (19.1), and the source-containing region  $\mathcal{V}'_s$  remains inside  $\mathcal{V}$ .

If  $\underline{\underline{a}}$  is a vector and  $\underline{\underline{A}}$  is a dyadic, then  $\nabla \cdot (\underline{\underline{a}} \times \underline{\underline{A}}) = (\nabla \times \underline{\underline{a}}) \cdot \underline{\underline{A}} - \underline{\underline{a}} \cdot (\nabla \times \underline{\underline{A}})$  [21, p. 52]. Using this identity, we get [28]

$$\nabla \cdot \left[ \underline{\underline{e}}(\underline{\underline{r}}) \times \underline{\underline{g}}^{me}(\underline{\underline{r}}, \underline{\underline{r}}') + \underline{\underline{h}}(\underline{\underline{r}}) \times \underline{\underline{g}}^{ee}(\underline{\underline{r}}, \underline{\underline{r}}') \right] \\ = [\nabla \times \underline{\underline{e}}(\underline{\underline{r}})] \cdot \underline{\underline{g}}^{me}(\underline{\underline{r}}, \underline{\underline{r}}') - \underline{\underline{e}}(\underline{\underline{r}}) \cdot [\nabla \times \underline{\underline{g}}^{me}(\underline{\underline{r}}, \underline{\underline{r}}')] \\ + [\nabla \times \underline{\underline{h}}(\underline{\underline{r}})] \cdot \underline{\underline{g}}^{ee}(\underline{\underline{r}}, \underline{\underline{r}}') - \underline{\underline{h}}(\underline{\underline{r}}) \cdot [\nabla \times \underline{\underline{g}}^{ee}(\underline{\underline{r}}, \underline{\underline{r}}')]. \quad (19.18)$$

**Fig. 19.2** Schematic showing the region  $\mathcal{V}$  bounded by the surface  $S_\infty$  and containing the region  $\mathcal{V}'_s$



On the right side of Eq.(19.18), we substitute  $\nabla \times \underline{h}(\underline{r})$  from Eq.(19.9)<sub>1</sub>,  $\underline{h}(\underline{r})$  from Eq.(19.9)<sub>2</sub>,  $\nabla \times \underline{\underline{g}}^{me}(\underline{r}, \underline{r}')$  from Eq.(19.14), and  $\underline{\underline{g}}^{me}(\underline{r}, \underline{r}')$  from Eq.(19.12). After some manipulations to exploit the symmetries of  $\underline{\underline{\varepsilon}}$ ,  $\underline{\underline{\mu}}$ , and  $\underline{\underline{\xi}}$ , Eq.(19.18) simplifies to

$$\begin{aligned} & \nabla \cdot \left[ \underline{e}(\underline{r}) \times \underline{\underline{g}}^{me}(\underline{r}, \underline{r}') + \underline{h}(\underline{r}) \times \underline{\underline{g}}^{ee}(\underline{r}, \underline{r}') \right] \\ &= -\underline{e}(\underline{r})\delta(\underline{r} - \underline{r}') + \underline{j}_e(\underline{r}) \cdot \underline{\underline{g}}^{ee}(\underline{r}, \underline{r}') - \underline{j}_m(\underline{r}) \cdot \underline{\underline{g}}^{me}(\underline{r}, \underline{r}'), \quad \underline{r} \in \mathcal{V}. \end{aligned} \quad (19.19)$$

Analogous to Eq.(19.18) is the identity [28]

$$\begin{aligned} & \nabla \cdot \left[ \underline{h}(\underline{r}) \times \underline{\underline{g}}^{em}(\underline{r}, \underline{r}') + \underline{e}(\underline{r}) \times \underline{\underline{g}}^{mm}(\underline{r}, \underline{r}') \right] \\ &= [\nabla \times \underline{h}(\underline{r})] \cdot \underline{\underline{g}}^{em}(\underline{r}, \underline{r}') - \underline{h}(\underline{r}) \cdot [\nabla \times \underline{\underline{g}}^{em}(\underline{r}, \underline{r}')] \\ &+ [\nabla \times \underline{e}(\underline{r})] \cdot \underline{\underline{g}}^{mm}(\underline{r}, \underline{r}') - \underline{e}(\underline{r}) \cdot [\nabla \times \underline{\underline{g}}^{mm}(\underline{r}, \underline{r}')] , \end{aligned} \quad (19.20)$$

which can be simplified to deliver

$$\begin{aligned} & -\nabla \cdot \left[ \underline{h}(\underline{r}) \times \underline{\underline{g}}^{em}(\underline{r}, \underline{r}') + \underline{e}(\underline{r}) \times \underline{\underline{g}}^{mm}(\underline{r}, \underline{r}') \right] \\ &= -\underline{h}(\underline{r})\delta(\underline{r} - \underline{r}') - \underline{j}_e(\underline{r}) \cdot \underline{\underline{g}}^{em}(\underline{r}, \underline{r}') + \underline{j}_m(\underline{r}) \cdot \underline{\underline{g}}^{mm}(\underline{r}, \underline{r}'), \quad \underline{r} \in \mathcal{V}. \end{aligned} \quad (19.21)$$

Integration of both sides of Eqs.(19.19) and (19.21) with respect to  $\underline{r}$  over  $\mathcal{V}$ , followed by the use of the divergence theorem, yields

$$\begin{aligned} & -\int \int_{\mathcal{S}_\infty} \hat{\underline{n}}(\underline{r}) \cdot \left[ \underline{e}(\underline{r}) \times \underline{\underline{g}}^{me}(\underline{r}, \underline{r}') + \underline{h}(\underline{r}) \times \underline{\underline{g}}^{ee}(\underline{r}, \underline{r}') \right] d^2\underline{r} \\ &= -\underline{e}(\underline{r}') + \int \int \int_{\mathcal{V}'_s} \left[ \underline{j}_e(\underline{r}) \cdot \underline{\underline{g}}^{ee}(\underline{r}, \underline{r}') - \underline{j}_m(\underline{r}) \cdot \underline{\underline{g}}^{me}(\underline{r}, \underline{r}') \right] d^3\underline{r} \end{aligned} \quad (19.22)$$

and

$$\begin{aligned} & \int \int_{\mathcal{S}_\infty} \hat{\underline{n}}(\underline{r}) \cdot \left[ \underline{h}(\underline{r}) \times \underline{\underline{g}}^{em}(\underline{r}, \underline{r}') + \underline{e}(\underline{r}) \times \underline{\underline{g}}^{mm}(\underline{r}, \underline{r}') \right] d^2\underline{r} \\ &= -\underline{h}(\underline{r}') + \int \int \int_{\mathcal{V}'_s} \left[ -\underline{j}_e(\underline{r}) \cdot \underline{\underline{g}}^{em}(\underline{r}, \underline{r}') + \underline{j}_m(\underline{r}) \cdot \underline{\underline{g}}^{mm}(\underline{r}, \underline{r}') \right] d^3\underline{r}, \end{aligned} \quad (19.23)$$

respectively. Here,  $\underline{r}' \in \mathcal{V}$  and  $\hat{\underline{n}}(\underline{r})$  is the unit normal to  $\mathcal{S}_\infty$  at  $\underline{r} \in \mathcal{S}_\infty$ , as shown in Fig.19.2. As  $r_\infty \rightarrow \infty$ , the surface integrals on the left sides of Eqs.(19.22) and (19.23) go to zero under the assumption that the Sommerfeld

radiation conditions [47, Sect. 5.2.2] hold. This assumption ensures that the fields are not affected by sources that are infinitely far away.

Interchanging  $\underline{r}$  and  $\underline{r}'$  thereafter, we get

$$\left. \begin{aligned} \underline{e}(\underline{r}) &= \int \int \int \left[ \underline{j}_e(\underline{r}') \cdot \underline{\underline{g}}^{ee}(\underline{r}', \underline{r}) - \underline{j}_m(\underline{r}') \cdot \underline{\underline{g}}^{me}(\underline{r}', \underline{r}) \right] d^3 \underline{r}' \\ \underline{h}(\underline{r}) &= \int \int \int_{\mathcal{V}'_s} \left[ -\underline{j}_e(\underline{r}') \cdot \underline{\underline{g}}^{em}(\underline{r}', \underline{r}) + \underline{j}_m(\underline{r}') \cdot \underline{\underline{g}}^{mm}(\underline{r}', \underline{r}) \right] d^3 \underline{r}' \end{aligned} \right\}, \quad \underline{r} \in \mathcal{V}. \quad (19.24)$$

Finally, employment of Eqs. (19.8) and (19.11) in Eqs. (19.24) leads to

$$\left. \begin{aligned} \underline{E}(\underline{r}) &= \int \int \int_{\mathcal{V}'_s} \left[ \underline{J}_e(\underline{r}') \cdot \underline{\underline{G}}^{ee}(\underline{r}', \underline{r}) - \underline{J}_m(\underline{r}') \cdot \underline{\underline{G}}^{me}(\underline{r}', \underline{r}) \right] \\ &\quad \times \exp[2i\omega \underline{\Gamma} \cdot (\underline{r} - \underline{r}')] d^3 \underline{r}' \\ \underline{H}(\underline{r}) &= \int \int \int_{\mathcal{V}'_s} \left[ -\underline{J}_e(\underline{r}') \cdot \underline{\underline{G}}^{em}(\underline{r}', \underline{r}) + \underline{J}_m(\underline{r}') \cdot \underline{\underline{G}}^{mm}(\underline{r}', \underline{r}) \right] \\ &\quad \times \exp[2i\omega \underline{\Gamma} \cdot (\underline{r} - \underline{r}')] d^3 \underline{r}' \end{aligned} \right\}, \quad \underline{r} \in \mathcal{V}. \quad (19.25)$$

A comparison of Eqs. (19.10) and (19.24) delivers the symmetries

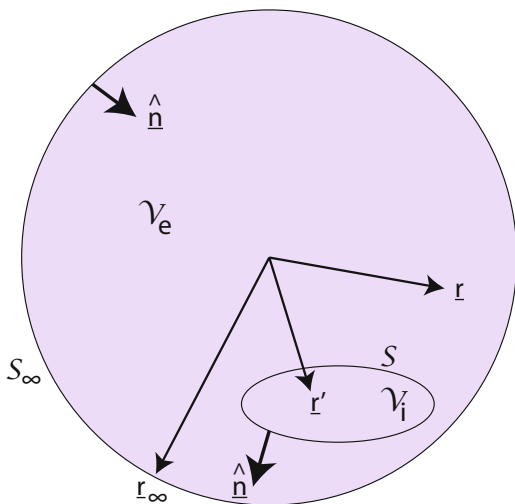
$$\left. \begin{aligned} \underline{\underline{g}}^{ee}(\underline{r}, \underline{r}') &= \left\{ \underline{\underline{g}}^{ee}(\underline{r}', \underline{r}) \right\}^T \\ \underline{\underline{g}}^{mm}(\underline{r}, \underline{r}') &= \left\{ \underline{\underline{g}}^{mm}(\underline{r}', \underline{r}) \right\}^T \\ \underline{\underline{g}}^{em}(\underline{r}, \underline{r}') &= - \left\{ \underline{\underline{g}}^{me}(\underline{r}', \underline{r}) \right\}^T \end{aligned} \right\} \quad (19.26)$$

and a comparison of Eqs. (19.4) and (19.25) yields the symmetries

$$\left. \begin{aligned} \underline{\underline{G}}^{ee}(\underline{r}, \underline{r}') &= \left\{ \underline{\underline{G}}^{ee}(\underline{r}', \underline{r}) \right\}^T \exp[2i\omega \underline{\Gamma} \cdot (\underline{r} - \underline{r}')] \\ \underline{\underline{G}}^{mm}(\underline{r}, \underline{r}') &= \left\{ \underline{\underline{G}}^{mm}(\underline{r}', \underline{r}) \right\}^T \exp[2i\omega \underline{\Gamma} \cdot (\underline{r} - \underline{r}')] \\ \underline{\underline{G}}^{em}(\underline{r}, \underline{r}') &= - \left\{ \underline{\underline{G}}^{me}(\underline{r}', \underline{r}) \right\}^T \exp[2i\omega \underline{\Gamma} \cdot (\underline{r} - \underline{r}')] \end{aligned} \right\}. \quad (19.27)$$

The symmetries of the dyadic Green functions in Eqs. (19.26) and (19.27) are consistent with Eqs. (19.11). The presence of  $\exp[2i\omega \underline{\Gamma} \cdot (\underline{r} - \underline{r}')] on the right sides of Eqs. (19.27) is indicative of the Lorentz nonreciprocity inherent in the term  $\underline{\Gamma} \times \underline{I}$  contained in Eqs. (19.1). This is to be expected, since the interchange of  $\underline{r}$  and  $\underline{r}'$  cannot be inconsequential in a medium that is Lorentz nonreciprocal.$

**Fig. 19.3** Schematic showing all space  $\mathcal{V}$  divided into two mutually disjoint regions: (i)  $\mathcal{V}_e$  bounded by the surfaces  $S_\infty$  and  $S$  and (ii)  $\mathcal{V}_i$  enclosed by the surface  $S$ . The unit vector  $\hat{\underline{n}}$  always points into  $\mathcal{V}_e$



### 19.2.5 Huygens Principle

In order to apply the Huygens principle following Faryad and Lakhtakia [28], let us again consider all space  $\mathcal{V}$  to be occupied by the medium characterized by Eqs. (19.1), as shown in Fig. 19.3. Furthermore, all space is partitioned into two mutually disjoint regions  $\mathcal{V}_e$  and  $\mathcal{V}_i$  separated by the closed surface  $S$ . The region  $\mathcal{V}_e$  is bounded by the surfaces  $S_\infty$  and  $S$ . As in Sect. 19.2.4,  $S_\infty$  is the surface of a sphere of radius  $r_\infty$  that is made to recede to infinity, while the region  $\mathcal{V}_i$  is the interior of  $S$  which is sufficiently smooth so that a unit normal  $\hat{\underline{n}}$  can be prescribed at any point on  $S$ .

The equivalents of Eqs. (19.19) and (19.21) are

$$\nabla \cdot \left[ \underline{e}(\underline{r}) \times \underline{\underline{g}}^{me}(\underline{r}, \underline{r}') + \underline{h}(\underline{r}) \times \underline{\underline{g}}^{ee}(\underline{r}, \underline{r}') \right] = -\underline{e}(\underline{r})\delta(\underline{r} - \underline{r}'), \quad \underline{r} \in \mathcal{V}_e, \quad (19.28)$$

and

$$-\nabla \cdot \left[ \underline{h}(\underline{r}) \times \underline{\underline{g}}^{em}(\underline{r}, \underline{r}') + \underline{e}(\underline{r}) \times \underline{\underline{g}}^{mm}(\underline{r}, \underline{r}') \right] = -\underline{h}(\underline{r})\delta(\underline{r} - \underline{r}'), \quad \underline{r} \in \mathcal{V}_e, \quad (19.29)$$

respectively, because  $\mathcal{V}_e$  is source free. Furthermore,

$$\int \int \int_{\mathcal{V}_e} f(\underline{r})\delta(\underline{r} - \underline{r}') d^3 \underline{r} = f(\underline{r}'), \quad \underline{r}' \in \mathcal{V}_e, \quad (19.30)$$

for any function  $f(\underline{r})$ . Hence, when  $\underline{r}' \in \mathcal{V}_e$  in Eqs. (19.28) and (19.29), the integration of both sides of each of the two equations with respect to  $\underline{r}$  over  $\mathcal{V}_e$ , followed by the use of the divergence theorem, yields



$$-\int_{S \cup S_\infty} \hat{\underline{n}}(\underline{r}) \cdot \left[ \underline{e}(\underline{r}) \times \underline{\underline{g}}^{me}(\underline{r}, \underline{r}') + \underline{h}(\underline{r}) \times \underline{\underline{g}}^{ee}(\underline{r}, \underline{r}') \right] d^2 \underline{r} = -\underline{e}(\underline{r}') \quad (19.31)$$

and

$$\int_{S \cup S_\infty} \hat{\underline{n}}(\underline{r}) \cdot \left[ \underline{h}(\underline{r}) \times \underline{\underline{g}}^{em}(\underline{r}, \underline{r}') + \underline{e}(\underline{r}) \times \underline{\underline{g}}^{mm}(\underline{r}, \underline{r}') \right] d^2 \underline{r} = -\underline{h}(\underline{r}'), \quad (19.32)$$

where  $\hat{\underline{n}}(\underline{r})$  is the unit normal to  $S \cup S_\infty$  at  $\underline{r} \in S \cup S_\infty$ , as shown in Fig. 19.3. The unit vector  $\hat{\underline{n}}(\underline{r})$  always points into  $\mathcal{V}'_e$ .

On assuming that the Sommerfeld radiation conditions [47, Sect. 5.2.2] hold as  $r_\infty \rightarrow \infty$ , the integrals on  $S_\infty$  in Eqs. (19.31) and (19.32) vanish. Thereafter, interchanging  $\underline{r}$  and  $\underline{r}'$ , we get

$$\left. \begin{aligned} \underline{e}(\underline{r}) &= \int_S \int_S \hat{\underline{n}}(\underline{r}') \cdot \left[ \underline{e}_+(\underline{r}') \times \underline{\underline{g}}^{me}(\underline{r}', \underline{r}) + \underline{h}_+(\underline{r}') \times \underline{\underline{g}}^{ee}(\underline{r}', \underline{r}) \right] d^2 \underline{r}' \\ \underline{h}(\underline{r}) &= - \int_S \int_S \hat{\underline{n}}(\underline{r}') \cdot \left[ \underline{h}_+(\underline{r}') \times \underline{\underline{g}}^{em}(\underline{r}', \underline{r}) + \underline{e}_+(\underline{r}') \times \underline{\underline{g}}^{mm}(\underline{r}', \underline{r}) \right] d^2 \underline{r}' \end{aligned} \right\}, \quad \underline{r} \in \mathcal{V}'_e, \quad (19.33)$$

where the subscript  $+$  indicates evaluation on the exterior side of  $S$  (i.e.,  $f_+(\underline{r})$  is the limiting value of  $f(\underline{r}_e)$  as  $\underline{r}_e \in \mathcal{V}'_e$  approaches  $\underline{r} \in S$ ). Finally, inversion of the transformations in Eqs. (19.8) and (19.11) yields

$$\begin{aligned} \underline{E}(\underline{r}) &= \int_S \int_S \left\{ [\hat{\underline{n}}(\underline{r}') \times \underline{E}_+(\underline{r}')] \cdot \underline{\underline{G}}^{me}(\underline{r}', \underline{r}) + [\hat{\underline{n}}(\underline{r}') \times \underline{H}_+(\underline{r}')] \cdot \underline{\underline{G}}^{ee}(\underline{r}', \underline{r}) \right\} \\ &\quad \times \exp[2i\omega \underline{\Gamma} \cdot (\underline{r} - \underline{r}')] d^2 \underline{r}', \quad \underline{r} \in \mathcal{V}'_e, \end{aligned} \quad (19.34)$$

as the mathematical statement of the Huygens principle for the electric field phasor [28] and

$$\begin{aligned} \underline{H}(\underline{r}) &= - \int_S \int_S \left\{ [\hat{\underline{n}}(\underline{r}') \times \underline{H}_+(\underline{r}')] \cdot \underline{\underline{G}}^{em}(\underline{r}', \underline{r}) + [\hat{\underline{n}}(\underline{r}') \times \underline{E}_+(\underline{r}')] \cdot \underline{\underline{G}}^{mm}(\underline{r}', \underline{r}) \right\} \\ &\quad \times \exp[2i\omega \underline{\Gamma} \cdot (\underline{r} - \underline{r}')] d^2 \underline{r}', \quad \underline{r} \in \mathcal{V}'_e, \end{aligned} \quad (19.35)$$

as the mathematical statement of the Huygens principle for the magnetic field phasor [28]. Equations (19.34) and (19.35) can be written alternatively as

$$\begin{aligned} \underline{E}(\underline{r}) &= \int_S \int_S \left\{ -\underline{\underline{G}}^{em}(\underline{r}, \underline{r}') \cdot [\hat{\underline{n}}(\underline{r}') \times \underline{E}_+(\underline{r}')] \right. \\ &\quad \left. + \underline{\underline{G}}^{ee}(\underline{r}, \underline{r}') \cdot [\hat{\underline{n}}(\underline{r}') \times \underline{H}_+(\underline{r}')] \right\} d^2 \underline{r}', \quad \underline{r} \in \mathcal{V}'_e, \end{aligned} \quad (19.36)$$

and

$$\underline{H}(\underline{r}) = - \int \int_S \left\{ -\underline{\underline{G}}^{me}(\underline{r}, \underline{r}') \cdot [\hat{\underline{n}}(\underline{r}') \times \underline{H}_+(\underline{r}')] \right. \\ \left. + \underline{\underline{G}}^{mm}(\underline{r}, \underline{r}') \cdot [\hat{\underline{n}}(\underline{r}') \times \underline{E}_+(\underline{r}')] \right\} d^2 \underline{r}', \quad \underline{r} \in \mathcal{V}_e, \quad (19.37)$$

respectively, after using Eqs. (19.27).

According to Eqs. (19.34) and (19.36), the electric field phasor at any location  $\underline{r} \in \mathcal{V}_e$  can be determined if the tangential components of the electric and magnetic field phasors on the exterior side of the surface  $S$  are known. The same knowledge also guarantees the determination of the magnetic field phasor at any location  $\underline{r} \in \mathcal{V}_e$ , according to Eqs. (19.35) and (19.37).

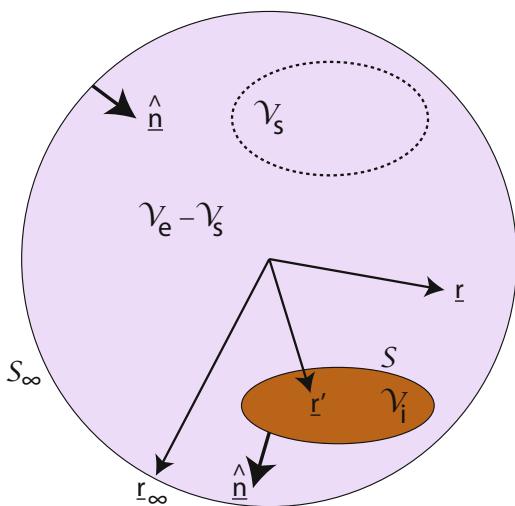
### 19.2.6 Ewald–Oseen Extinction Theorem

Finally, let us derive the Ewald–Oseen extinction theorem. All space  $\mathcal{V}$  is divided into two mutually disjoint regions:

- (i)  $\mathcal{V}_e$  bounded by the surfaces  $S_\infty$  as well as  $S$  and
- (ii)  $\mathcal{V}_i$  enclosed by the surface  $S$ ,

as shown in Fig. 19.4. The source current density phasors are confined to the bounded region  $\mathcal{V}_s \subset \mathcal{V}_e$ . The region  $\mathcal{V}_e$  is occupied by the medium characterized by Eqs. (19.1). The identity of the medium occupying  $\mathcal{V}_i$  is irrelevant to the Ewald–Oseen extinction theorem.

**Fig. 19.4** Schematic showing all space  $\mathcal{V}$  divided into (i)  $\mathcal{V}_e$  bounded by the surfaces  $S_\infty$  as well as  $S$  and (ii)  $\mathcal{V}_i$  enclosed by the surface  $S$ . The source current density phasors are confined to the region  $\mathcal{V}_s \subset \mathcal{V}_e$



Equations (19.19) and (19.21) apply for  $\underline{r} \in \mathcal{V}'_e$ . Integrating both sides of these equations with respect to  $\underline{r}$  over  $\mathcal{V}'_e$ , and assuming the Sommerfeld radiation conditions [47, Sect. 5.2.2] to hold as  $r_\infty \rightarrow \infty$ , we get

$$\begin{aligned} & - \int \int_S \hat{\underline{n}}(\underline{r}) \cdot \left[ \underline{e}_+(\underline{r}) \times \underline{\underline{g}}^{me}(\underline{r}, \underline{r}') + \underline{h}_+(\underline{r}) \times \underline{\underline{g}}^{ee}(\underline{r}, \underline{r}') \right] d^2 \underline{r} \\ & = - \int \int \int_{\mathcal{V}'_e} \underline{e}(\underline{r}) \delta(\underline{r} - \underline{r}') d^3 \underline{r} \\ & \quad + \int \int \int_{\mathcal{V}'_s} \left[ \underline{j}_e(\underline{r}) \cdot \underline{\underline{g}}^{ee}(\underline{r}, \underline{r}') - \underline{j}_m(\underline{r}) \cdot \underline{\underline{g}}^{me}(\underline{r}, \underline{r}') \right] d^3 \underline{r} \end{aligned} \quad (19.38)$$

and

$$\begin{aligned} & \int \int_S \hat{\underline{n}}(\underline{r}) \cdot \left[ \underline{h}_+(\underline{r}) \times \underline{\underline{g}}^{em}(\underline{r}, \underline{r}') + \underline{e}_+(\underline{r}) \times \underline{\underline{g}}^{mm}(\underline{r}, \underline{r}') \right] \\ & = - \int \int \int_{\mathcal{V}'_e} \underline{h}(\underline{r}) \delta(\underline{r} - \underline{r}') d^3 \underline{r} \\ & \quad + \int \int \int_{\mathcal{V}'_s} \left[ -\underline{j}_e(\underline{r}) \cdot \underline{\underline{g}}^{em}(\underline{r}, \underline{r}') + \underline{j}_m(\underline{r}) \cdot \underline{\underline{g}}^{mm}(\underline{r}, \underline{r}') \right] d^3 \underline{r}. \end{aligned} \quad (19.39)$$

By virtue of Eqs. (19.24), we define the electric and magnetic field phasors

$$\left. \begin{aligned} \underline{e}_s(\underline{r}') &= \int \int \int_{\mathcal{V}'_s} \left[ \underline{j}_e(\underline{r}) \cdot \underline{\underline{g}}^{ee}(\underline{r}, \underline{r}') - \underline{j}_m(\underline{r}) \cdot \underline{\underline{g}}^{me}(\underline{r}, \underline{r}') \right] d^2 \underline{r} \\ \underline{h}_s(\underline{r}') &= \int \int \int_{\mathcal{V}'_s} \left[ -\underline{j}_e(\underline{r}) \cdot \underline{\underline{g}}^{em}(\underline{r}, \underline{r}') + \underline{j}_m(\underline{r}) \cdot \underline{\underline{g}}^{mm}(\underline{r}, \underline{r}') \right] d^2 \underline{r} \end{aligned} \right\}, \underline{r}' \in \mathcal{V}, \quad (19.40)$$

as the ones that exist everywhere when  $\mathcal{V}'_i$  is also occupied by the same medium as the one in  $\mathcal{V}'_e$ . Furthermore,

$$\int \int \int_{\mathcal{V}'_e} f(\underline{r}) \delta(\underline{r} - \underline{r}') d^3 \underline{r} = \begin{cases} f(\underline{r}') \\ 0 \end{cases}, \quad \begin{cases} \underline{r}' \in \mathcal{V}'_e \\ \underline{r}' \in \mathcal{V}'_i \end{cases}, \quad (19.41)$$

for any function  $f(\underline{r})$ .

Therefore, Eqs. (19.38) and (19.39) can be simplified to

$$\begin{aligned} \left. \begin{aligned} \underline{e}(\underline{r}') \\ \underline{0} \end{aligned} \right\} &= \underline{e}_s(\underline{r}') + \int \int_S \left\{ [\hat{\underline{n}}(\underline{r}) \times \underline{e}_+(\underline{r})] \cdot \underline{\underline{g}}^{me}(\underline{r}, \underline{r}') \right. \\ &\quad \left. + [\hat{\underline{n}}(\underline{r}) \times \underline{h}_+(\underline{r})] \cdot \underline{\underline{g}}^{ee}(\underline{r}, \underline{r}') \right\} d^2\underline{r}, \quad \left\{ \begin{aligned} \underline{r}' \in \mathcal{V}'_e \\ \underline{r}' \in \mathcal{V}'_i \end{aligned} \right\}, \quad (19.42) \end{aligned}$$

and

$$\begin{aligned} \left. \begin{aligned} \underline{h}(\underline{r}') \\ \underline{0} \end{aligned} \right\} &= \underline{h}_s(\underline{r}') - \int \int_S \left\{ [\hat{\underline{n}}(\underline{r}) \times \underline{h}_+(\underline{r})] \cdot \underline{\underline{g}}^{em}(\underline{r}, \underline{r}') \right. \\ &\quad \left. + [\hat{\underline{n}}(\underline{r}) \times \underline{e}_+(\underline{r})] \cdot \underline{\underline{g}}^{mm}(\underline{r}, \underline{r}') \right\} d^2\underline{r}, \quad \left\{ \begin{aligned} \underline{r}' \in \mathcal{V}'_e \\ \underline{r}' \in \mathcal{V}'_i \end{aligned} \right\}, \quad (19.43) \end{aligned}$$

respectively. The interchange of  $\underline{r}$  and  $\underline{r}'$  followed by the inversion of the transformations in Eqs. (19.8) and (19.11) yields

$$\begin{aligned} \left. \begin{aligned} \underline{E}(\underline{r}) \\ \underline{0} \end{aligned} \right\} &= \underline{E}_s(\underline{r}) + \int \int_S \left\{ [\hat{\underline{n}}(\underline{r}') \times \underline{E}_+(\underline{r}')] \cdot \underline{\underline{G}}^{me}(\underline{r}', \underline{r}) \right. \\ &\quad \left. + [\hat{\underline{n}}(\underline{r}') \times \underline{H}_+(\underline{r}')] \cdot \underline{\underline{G}}^{ee}(\underline{r}', \underline{r}) \right\} \exp[2i\omega\underline{\Gamma} \cdot (\underline{r} - \underline{r}')] d^2\underline{r}', \quad \left\{ \begin{aligned} \underline{r} \in \mathcal{V}'_e \\ \underline{r} \in \mathcal{V}'_i \end{aligned} \right\}, \quad (19.44) \end{aligned}$$

and

$$\begin{aligned} \left. \begin{aligned} \underline{H}(\underline{r}) \\ \underline{0} \end{aligned} \right\} &= \underline{H}_s(\underline{r}) - \int \int_S \left\{ [\hat{\underline{n}}(\underline{r}') \times \underline{H}_+(\underline{r}')] \cdot \underline{\underline{G}}^{em}(\underline{r}', \underline{r}) \right. \\ &\quad \left. + [\hat{\underline{n}}(\underline{r}') \times \underline{E}_+(\underline{r}')] \cdot \underline{\underline{G}}^{mm}(\underline{r}', \underline{r}) \right\} \exp[2i\omega\underline{\Gamma} \cdot (\underline{r} - \underline{r}')] d^2\underline{r}', \quad \left\{ \begin{aligned} \underline{r} \in \mathcal{V}'_e \\ \underline{r} \in \mathcal{V}'_i \end{aligned} \right\}. \quad (19.45) \end{aligned}$$

Let us note that  $\hat{\underline{n}} \times \underline{E}_+$  and  $\hat{\underline{n}} \times \underline{H}_+$  in the two foregoing equations are tangential components of the electric and magnetic field phasors, respectively, on the exterior side of  $\mathcal{S}$ . A comparison of the integrals in Eqs. (19.25) with those in Eqs. (19.44) and (19.45) suggests the postulation of *equivalent* surface current density phasors

$$\left. \begin{aligned} \underline{J}_e^{\text{surf}}(\underline{r}) &= \hat{\underline{n}}(\underline{r}) \times \underline{H}_+(\underline{r}) \\ \underline{J}_m^{\text{surf}}(\underline{r}) &= -\hat{\underline{n}}(\underline{r}) \times \underline{E}_+(\underline{r}) \end{aligned} \right\}, \quad \underline{r} \in \mathcal{S}. \quad (19.46)$$

Equations (19.46) constitute the surface equivalence principle [22, Sects. 3–5] which leads to

$$\left. \begin{aligned} \underline{E}(\underline{r}) \\ \underline{0} \end{aligned} \right\} &= \underline{E}_s(\underline{r}) + \int \int_S \left[ -\underline{J}_m^{\text{surf}}(\underline{r}') \cdot \underline{\underline{G}}^{me}(\underline{r}', \underline{r}) + \underline{J}_e^{\text{surf}}(\underline{r}') \cdot \underline{\underline{G}}^{ee}(\underline{r}', \underline{r}) \right] \\ &\times \exp[2i\omega \underline{\Gamma} \cdot (\underline{r} - \underline{r}')] d^2 \underline{r}', \quad \begin{cases} \underline{r} \in \mathcal{V}_e \\ \underline{r} \in \mathcal{V}_i \end{cases}, \end{aligned} \quad (19.47)$$

and

$$\left. \begin{aligned} \underline{H}(\underline{r}) \\ \underline{0} \end{aligned} \right\} &= \underline{H}_s(\underline{r}) + \int \int_S \left[ -\underline{J}_e^{\text{surf}}(\underline{r}') \cdot \underline{\underline{G}}^{em}(\underline{r}', \underline{r}) + \underline{J}_m^{\text{surf}}(\underline{r}') \cdot \underline{\underline{G}}^{mm}(\underline{r}', \underline{r}) \right] \\ &\times \exp[2i\omega \underline{\Gamma} \cdot (\underline{r} - \underline{r}')] d^2 \underline{r}', \quad \begin{cases} \underline{r} \in \mathcal{V}_e \\ \underline{r} \in \mathcal{V}_i \end{cases}. \end{aligned} \quad (19.48)$$

Finally, the use of Eqs. (19.27) leads to

$$\left. \begin{aligned} \underline{E}(\underline{r}) \\ \underline{0} \end{aligned} \right\} &= \underline{E}_s(\underline{r}) + \int \int_S \left[ \underline{\underline{G}}^{em}(\underline{r}, \underline{r}') \cdot \underline{J}_m^{\text{surf}}(\underline{r}') + \underline{\underline{G}}^{ee}(\underline{r}, \underline{r}') \cdot \underline{J}_e^{\text{surf}}(\underline{r}') \right] d^2 \underline{r}', \\ &\begin{cases} \underline{r} \in \mathcal{V}_e \\ \underline{r} \in \mathcal{V}_i \end{cases}, \end{aligned} \quad (19.49)$$

and

$$\left. \begin{aligned} \underline{H}(\underline{r}) \\ \underline{0} \end{aligned} \right\} &= \underline{H}_s(\underline{r}) + \int \int_S \left[ \underline{\underline{G}}^{me}(\underline{r}, \underline{r}') \cdot \underline{J}_e^{\text{surf}}(\underline{r}') + \underline{\underline{G}}^{mm}(\underline{r}, \underline{r}') \cdot \underline{J}_m^{\text{surf}}(\underline{r}') \right] d^2 \underline{r}', \\ &\begin{cases} \underline{r} \in \mathcal{V}_e \\ \underline{r} \in \mathcal{V}_i \end{cases}. \end{aligned} \quad (19.50)$$

Equations (19.47)<sub>2</sub> and (19.49)<sub>2</sub> indicate the cancellation throughout  $\mathcal{V}_i$  of the electric field phasor due to the sources contained in  $\mathcal{V}_s$  by the electric field phasor radiated jointly by the two equivalent surface current density phasors on the exterior side of  $S$ . In the same vein, Eqs. (19.48)<sub>2</sub> and (19.50)<sub>2</sub> indicate the cancellation throughout  $\mathcal{V}_i$  of the magnetic field phasor due to the sources contained in  $\mathcal{V}_s$  by the magnetic field phasor radiated jointly by the two equivalent surface current density phasors on the exterior side of  $S$ . These four expressions thus constitute the Ewald–Oseen extinction theorem. Originally derived for free space [23, 24] (and therefore easily extended to homogeneous dielectric-magnetic mediums) and later for homogeneous biisotropic mediums [26, 27], this theorem has been extended here for homogeneous bianisotropic mediums described by Eqs. (19.1).

The cancellations in Eqs. (19.47)<sub>2</sub>, (19.48)<sub>2</sub>, (19.49)<sub>2</sub>, and (19.50)<sub>2</sub> take place regardless of the nature of the medium occupying  $\mathcal{V}_i$ . Whether that medium is homogeneous or nonhomogeneous is irrelevant. Whether that medium is isotropic or anisotropic or bianisotropic is equally irrelevant. That medium can even be free space, i.e., devoid of any molecules. All that are needed are the two surface current density phasors on the exterior side of  $S$ . These can be, after deeper analysis, attributed to the constitution of the medium occupying  $\mathcal{V}_i$ , but that issue is irrelevant to the formulation of the Ewald–Oseen extinction theorem.

### 19.2.7 Application for Scattering Problems

By definition, the incident field in a scattering problem is the field that exists everywhere when the region occupied by the scatterer is filled with the same medium as the one occupying the region outside the scatterer. Therefore, if the region  $\mathcal{V}_i$  is filled with a medium different from the one in  $\mathcal{V}_e$ , then

$$\left. \begin{aligned} \underline{E}_{\text{inc}}(\underline{r}) &= \underline{E}_s(\underline{r}) \\ \underline{H}_{\text{inc}}(\underline{r}) &= \underline{H}_s(\underline{r}) \end{aligned} \right\}, \quad \underline{r} \in \mathcal{V}, \quad (19.51)$$

are the *incident* electric and magnetic field phasors.

Furthermore, the scattered field in  $\mathcal{V}_e$  must be the difference of the actual field and the incident field. Hence, the *scattered* field phasors are given by

$$\left. \begin{aligned} \underline{E}_{\text{sca}}(\underline{r}) &= \underline{E}(\underline{r}) - \underline{E}_{\text{inc}}(\underline{r}) \\ \underline{H}_{\text{sca}}(\underline{r}) &= \underline{H}(\underline{r}) - \underline{H}_{\text{inc}}(\underline{r}) \end{aligned} \right\}, \quad \underline{r} \in \mathcal{V}_e. \quad (19.52)$$

Next, the continuity of tangential components of the electric and magnetic field phasors across  $S$  yields

$$\left. \begin{aligned} \hat{n}(\underline{r}) \times \underline{E}_+(\underline{r}) &= \hat{n}(\underline{r}) \times \underline{E}_-(\underline{r}) \\ \hat{n}(\underline{r}) \times \underline{H}_+(\underline{r}) &= \hat{n}(\underline{r}) \times \underline{H}_-(\underline{r}) \end{aligned} \right\}, \quad \underline{r} \in S, \quad (19.53)$$

where  $\hat{n} \times \underline{E}_-$  and  $\hat{n} \times \underline{H}_-$  are the tangential components of the electric and magnetic field phasors, respectively, on the interior side of  $S$  (i.e.,  $f_-(\underline{r})$  is the limiting value of  $f_-(\underline{r}_i)$  as  $\underline{r}_i \in \mathcal{V}_i$  approaches  $\underline{r} \in S$ ).

But the field phasors on the interior side of  $S$  must be the internal field phasors induced in  $\mathcal{V}_i$  and evaluated on  $S$ . Hence,

$$\left. \begin{aligned} \hat{n}(\underline{r}) \times \underline{E}_+(\underline{r}) &= \hat{n}(\underline{r}) \times \underline{E}_{\text{int}}(\underline{r}) \\ \hat{n}(\underline{r}) \times \underline{H}_+(\underline{r}) &= \hat{n}(\underline{r}) \times \underline{H}_{\text{int}}(\underline{r}) \end{aligned} \right\}, \quad \underline{r} \in S, \quad (19.54)$$

where  $\underline{E}_{\text{int}}$  and  $\underline{H}_{\text{int}}$  are the *internal* electric and magnetic field phasors, respectively.

The foregoing considerations allow the transformation of Eqs. (19.44) and (19.45) to

$$\left. \begin{array}{l} \underline{E}_{\text{sca}}(\underline{r}) \\ -\underline{E}_{\text{inc}}(\underline{r}) \end{array} \right\} = \int \int_{\mathcal{S}} \left\{ -\underline{\underline{G}}^{em}(\underline{r}, \underline{r}') \cdot [\hat{\underline{n}}(\underline{r}') \times \underline{E}_{\text{int}}(\underline{r}')] \right. \\ \left. + \underline{\underline{G}}^{ee}(\underline{r}, \underline{r}') \cdot [\hat{\underline{n}}(\underline{r}') \times \underline{H}_{\text{int}}(\underline{r}')] \right\} d^2 \underline{r}', \quad \left\{ \begin{array}{l} \underline{r} \in \mathcal{V}'_e \\ \underline{r} \in \mathcal{V}'_i \end{array} \right., \quad (19.55)$$

and

$$\left. \begin{array}{l} \underline{H}_{\text{sca}}(\underline{r}) \\ -\underline{H}_{\text{inc}}(\underline{r}) \end{array} \right\} = - \int \int_{\mathcal{S}} \left\{ -\underline{\underline{G}}^{me}(\underline{r}, \underline{r}') \cdot [\hat{\underline{n}}(\underline{r}') \times \underline{H}_{\text{int}}(\underline{r}')] \right. \\ \left. + \underline{\underline{G}}^{mm}(\underline{r}, \underline{r}') \cdot [\hat{\underline{n}}(\underline{r}') \times \underline{E}_{\text{int}}(\underline{r}')] \right\} d^2 \underline{r}', \quad \left\{ \begin{array}{l} \underline{r} \in \mathcal{V}'_e \\ \underline{r} \in \mathcal{V}'_i \end{array} \right., \quad (19.56)$$

respectively. Equations (19.55)<sub>2</sub> and (19.56)<sub>2</sub> are a pair of coupled integral equations that must be solved for all  $\underline{r} \in \mathcal{V}'_i$  in order to determine  $\hat{\underline{n}}(\underline{r}') \times \underline{E}_{\text{int}}(\underline{r}')$  and  $\hat{\underline{n}}(\underline{r}') \times \underline{H}_{\text{int}}(\underline{r}')$  at all  $\underline{r}' \in \mathcal{S}$ . Once these quantities have been determined, they can be used on the right sides of Eqs. (19.55)<sub>1</sub> and (19.56)<sub>1</sub> to calculate  $\underline{E}_{\text{sca}}(\underline{r})$  and  $\underline{H}_{\text{sca}}(\underline{r})$  at any point  $\underline{r} \in \mathcal{V}'_e$ .

If the medium occupying  $\mathcal{V}'_i$  is homogeneous, then knowledge of  $\hat{\underline{n}}(\underline{r}') \times \underline{E}_{\text{int}}(\underline{r}')$  and  $\hat{\underline{n}}(\underline{r}') \times \underline{H}_{\text{int}}(\underline{r}')$  at all  $\underline{r}' \in \mathcal{S}$  should be sufficient to determine  $\underline{E}_{\text{int}}(\underline{r})$  and  $\underline{H}_{\text{int}}(\underline{r})$  at any  $\underline{r} \in \mathcal{V}'_i$ , provided that mathematical statements of the Huygens principle have been formulated [28] for that medium. Of course, these mathematical statements would employ the dyadic Green functions for the medium occupying  $\mathcal{V}'_i$ , not  $\mathcal{V}'_e$ .

If globally applicable series representations of electromagnetic field phasors are available for the homogeneous medium occupying  $\mathcal{V}'_i$ , then the expansion coefficients for the series for  $\underline{E}_{\text{int}}(\underline{r})$  and  $\underline{H}_{\text{int}}(\underline{r})$  can be determined for all  $\underline{r} \in \mathcal{V}'_i$  after the solution of Eqs. (19.55)<sub>2</sub> and (19.56)<sub>2</sub>. That is the route taken in the EBCM [4, 26, 27, 43, 48], as discussed in Sect. 19.3.

Suppose, however, that no field can exist in  $\mathcal{V}'_i$ —because that region is occupied by an impenetrable medium—exemplified by the so-called perfect electric conductor. Then, Eqs. (19.49) and (19.50) can be recast as

$$\left. \begin{array}{l} \underline{E}_{\text{sca}}(\underline{r}) \\ -\underline{E}_{\text{inc}}(\underline{r}) \end{array} \right\} = \int \int_{\mathcal{S}} \left[ \underline{\underline{G}}^{em}(\underline{r}, \underline{r}') \cdot \underline{J}_m^{\text{surf}}(\underline{r}') + \underline{\underline{G}}^{ee}(\underline{r}, \underline{r}') \cdot \underline{J}_e^{\text{surf}}(\underline{r}') \right] d^2 \underline{r}', \\ \left\{ \begin{array}{l} \underline{r} \in \mathcal{V}'_e \\ \underline{r} \in \mathcal{V}'_i \end{array} \right., \quad (19.57)$$

and

$$\left. \begin{aligned} \underline{H}_{\text{sca}}(\underline{r}) \\ -\underline{H}_{\text{inc}}(\underline{r}) \end{aligned} \right\} = \int \int_{\mathcal{S}} \left[ \underline{\underline{G}}^{me}(\underline{r}, \underline{r}') \cdot \underline{J}_e^{\text{surf}}(\underline{r}') + \underline{\underline{G}}^{mm}(\underline{r}, \underline{r}') \cdot \underline{J}_m^{\text{surf}}(\underline{r}') \right] d^2 \underline{r}',$$

$$\left. \begin{aligned} \underline{r} \in \mathcal{V}'_e \\ \underline{r} \in \mathcal{V}'_i \end{aligned} \right\}, \quad (19.58)$$

respectively. Equations (19.57)<sub>2</sub> and (19.58)<sub>2</sub> are a pair of coupled integral equations to be solved for the determination of  $\underline{J}_e^{\text{surf}}(\underline{r}')$  and  $\underline{J}_m^{\text{surf}}(\underline{r}')$  at all  $\underline{r}' \in \mathcal{S}$ . Once these quantities have been determined, they can be used on the right sides of Eqs. (19.57)<sub>1</sub> and (19.58)<sub>1</sub> to calculate  $\underline{E}_{\text{sca}}(\underline{r})$  and  $\underline{H}_{\text{sca}}(\underline{r})$  at any point  $\underline{r} \in \mathcal{V}'_e$ .

The implementation of the EBCM exploits either Eqs. (19.55) and (19.56) for a scatterer in which the internal fields are not null valued or Eqs. (19.57) and (19.58) for a scatterer in which the internal fields are null valued.

### 19.3 Extended Boundary Condition Method

The conceptual framework of the EBCM for a penetrable scatterer is premised on the knowledge of two types of entities. Entities of the first type are the bilinear expansions [49, Chap. 13] of the dyadic Green functions  $\underline{\underline{G}}^{ee}(\underline{r}, \underline{r}')$  and  $\underline{\underline{G}}^{mm}(\underline{r}, \underline{r}')$  for the medium occupying  $\mathcal{V}'_e$ . These bilinear expansions involve sets of eigenfunctions that are mutually orthogonal on some closed surface. Knowledge of these bilinear expansions allows the formulation of bilinear expansions of  $\underline{\underline{G}}^{me}(\underline{r}, \underline{r}')$  and  $\underline{\underline{G}}^{em}(\underline{r}, \underline{r}')$  for the same medium, in light of relations such as Eqs. (19.5). Furthermore, the same bilinear expansions provide series representations of the incident and the scattered electric and magnetic field phasors in terms of the aforementioned eigenfunctions, as may be surmised from the structure of Eqs. (19.4).

Entities of the second type are the bilinear expansions of the dyadic Green functions for the medium occupying  $\mathcal{V}'_i$ , because those expansions provide series representations of the internal electric and magnetic field phasors.

#### 19.3.1 Bilinear Expansions of the Dyadic Green Functions for the Medium Occupying $\mathcal{V}'_e$

Let the vector wavefunctions  $\underline{\Phi}_v^{(j)}(\underline{r})$  be the eigensolutions of the differential equation

$$\left\{ \left[ \nabla \times \underline{I} + i\omega \left( \underline{\underline{\xi}} + \underline{K} \times \underline{I} \right) \right] \cdot \underline{\underline{\mu}}^{-1} \right. \\ \left. \cdot \left[ \nabla \times \underline{I} - i\omega \left( -\underline{\underline{\xi}} + \underline{K} \times \underline{I} \right) \right] - \omega^2 \underline{\underline{\xi}} \right\} \cdot \underline{\Phi}_v^{(j)}(\underline{r}) = \underline{0}, \quad (19.59)$$



where the subscripted index  $\nu \in \{1, 2, 3, \dots\}$  and the superscripted index  $j \in \{1, 3\}$ . Whereas  $\underline{\Phi}_\nu^{(1)}(\underline{r})$  are regular at the origin,  $\underline{\Phi}_\nu^{(3)}(\underline{r})$  are regular at infinity. Similarly to  $\underline{\Phi}_\nu^{(j)}(\underline{r})$ , let the vector wavefunctions  $\underline{\Psi}_\nu^{(j)}(\underline{r})$  be the eigensolutions of the differential equation

$$\left\{ \left[ \nabla \times \underline{I} - i\omega \left( -\underline{\underline{\xi}} + \underline{K} \times \underline{I} \right) \right] \cdot \underline{\underline{\xi}}^{-1} \right. \\ \left. \cdot \left[ \nabla \times \underline{I} + i\omega \left( \underline{\underline{\xi}} + \underline{K} \times \underline{I} \right) \right] - \omega^2 \underline{\underline{\mu}} \right\} \cdot \underline{\Psi}_\nu^{(j)}(\underline{r}) = \underline{0}. \quad (19.60)$$

These two sets of vector wavefunctions can then be used to formulate the following two additional sets of wavefunctions:

$$\left. \begin{aligned} \underline{\Theta}_\nu^{(j)}(\underline{r}) &= \frac{1}{i\omega \underline{\underline{\mu}}} \cdot \left[ \nabla \times \underline{I} - i\omega \left( -\underline{\underline{\xi}} + \underline{K} \times \underline{I} \right) \right] \cdot \underline{\Phi}_\nu^{(j)}(\underline{r}) \\ \underline{\Xi}_\nu^{(j)}(\underline{r}) &= -\frac{1}{i\omega \underline{\underline{\xi}}} \cdot \left[ \nabla \times \underline{I} + i\omega \left( \underline{\underline{\xi}} + \underline{K} \times \underline{I} \right) \right] \cdot \underline{\Psi}_\nu^{(j)}(\underline{r}) \end{aligned} \right\}. \quad (19.61)$$

The bilinear expansions of the four dyadic Green functions must then be

$$\underline{\underline{G}}^{ee}(\underline{r}, \underline{r}') = \exp[i\omega \underline{\Gamma} \cdot (\underline{r} - \underline{r}')] \\ \times \begin{cases} \sum_{\nu=1}^{\infty} [\alpha_\nu \underline{\Phi}_\nu^{(3)}(\underline{r}) \underline{\Phi}_\nu^{(1)}(\underline{r}') + \beta_\nu \underline{\Xi}_\nu^{(3)}(\underline{r}) \underline{\Xi}_\nu^{(1)}(\underline{r}')] , & r > r' , \\ \sum_{\nu=1}^{\infty} [\alpha_\nu \underline{\Phi}_\nu^{(1)}(\underline{r}) \underline{\Phi}_\nu^{(3)}(\underline{r}') + \beta_\nu \underline{\Xi}_\nu^{(1)}(\underline{r}) \underline{\Xi}_\nu^{(3)}(\underline{r}')] , & r' > r , \end{cases} \quad (19.62)$$

$$\underline{\underline{G}}^{mm}(\underline{r}, \underline{r}') = -\exp[i\omega \underline{\Gamma} \cdot (\underline{r} - \underline{r}')] \\ \times \begin{cases} \sum_{\nu=1}^{\infty} [\alpha_\nu \underline{\Theta}_\nu^{(3)}(\underline{r}) \underline{\Theta}_\nu^{(1)}(\underline{r}') + \beta_\nu \underline{\Psi}_\nu^{(3)}(\underline{r}) \underline{\Psi}_\nu^{(1)}(\underline{r}')] , & r > r' , \\ \sum_{\nu=1}^{\infty} [\alpha_\nu \underline{\Theta}_\nu^{(1)}(\underline{r}) \underline{\Theta}_\nu^{(3)}(\underline{r}') + \beta_\nu \underline{\Psi}_\nu^{(1)}(\underline{r}) \underline{\Psi}_\nu^{(3)}(\underline{r}')] , & r' > r , \end{cases} \quad (19.63)$$

$$\underline{\underline{G}}^{me}(\underline{r}, \underline{r}') = \exp[i\omega \underline{\Gamma} \cdot (\underline{r} - \underline{r}')] \\ \times \begin{cases} \sum_{\nu=1}^{\infty} [\alpha_\nu \underline{\Theta}_\nu^{(3)}(\underline{r}) \underline{\Phi}_\nu^{(1)}(\underline{r}') + \beta_\nu \underline{\Psi}_\nu^{(3)}(\underline{r}) \underline{\Xi}_\nu^{(1)}(\underline{r}')] , & r > r' , \\ \sum_{\nu=1}^{\infty} [\alpha_\nu \underline{\Theta}_\nu^{(1)}(\underline{r}) \underline{\Phi}_\nu^{(3)}(\underline{r}') + \beta_\nu \underline{\Psi}_\nu^{(1)}(\underline{r}) \underline{\Xi}_\nu^{(3)}(\underline{r}')] , & r' > r , \end{cases} \quad (19.64)$$

and

$$\underline{\underline{G}}^{em}(\underline{r}, \underline{r}') = -\exp[i\omega \underline{\Gamma} \cdot (\underline{r} - \underline{r}')] \times \begin{cases} \sum_{v=1}^{\infty} [\alpha_v \underline{\Phi}_v^{(3)}(\underline{r}) \underline{\Theta}_v^{(1)}(\underline{r}') + \beta_v \underline{\Xi}_v^{(3)}(\underline{r}) \underline{\Psi}_v^{(1)}(\underline{r}')] , & r > r' , \\ \sum_{v=1}^{\infty} [\alpha_v \underline{\Phi}_v^{(1)}(\underline{r}) \underline{\Theta}_v^{(3)}(\underline{r}') + \beta_v \underline{\Xi}_v^{(1)}(\underline{r}) \underline{\Psi}_v^{(3)}(\underline{r}')] , & r' > r , \end{cases} \quad (19.65)$$

with the coefficients  $\alpha_v$  and  $\beta_v$  to be determined using a standard technique [49, Chap. 13]. These bilinear expansions satisfy Eqs. (19.5), (19.6), and (19.7) when  $\underline{r} \neq \underline{r}'$ , and they also conform to the symmetry constraints provided in Eqs. (19.27).

### 19.3.2 Incident and Scattered Field Phasors

Figure 19.5 presents a schematic of the scattering problem as envisioned for the application of the EBCM. The scattering region  $\mathcal{V}_i$  is bounded by the surface  $\mathcal{S}$ , whereas the medium described by Eqs. (19.1) occupies the region  $\mathcal{V}_e$ . The surface  $\mathcal{S}_e$  circumscribes  $\mathcal{V}_i$ , whereas the surface  $\mathcal{S}_i$  is inscribed in  $\mathcal{V}_i$ , these two surfaces being concentric and of the same shape. The origin of the coordinate system lies inside  $\mathcal{V}_i$ .

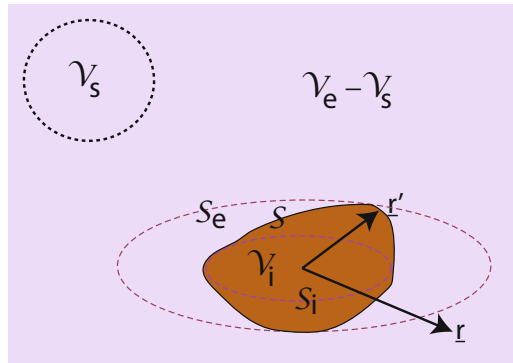


**Fig. 19.5** Schematic of the scattering problem. All space  $\mathcal{V}$  is divided into two mutually disjoint regions  $\mathcal{V}_e$  and  $\mathcal{V}_i$  that are separated by the surface  $\mathcal{S}$ . The sources of the incident field phasors are confined to the region  $\mathcal{V}_s \subset \mathcal{V}_e$ . The origin of the coordinate system lies inside the scatterer  $\mathcal{V}_i$ . The surface  $\mathcal{S}_e$  circumscribes  $\mathcal{V}_i$ , whereas the surface  $\mathcal{S}_i$  is inscribed in  $\mathcal{V}_i$ , the two surfaces being concentric and of the same shape

The vector wavefunctions  $\underline{\Phi}_\nu^{(j)}(\underline{r})$  and  $\underline{\Xi}_\nu^{(j)}(\underline{r})$ ,  $\nu \in \{1, 2, 3, \dots\}$ , are assumed to be mutually orthogonal on  $S_e$  (and, therefore, on  $S_i$ ). Likewise, the vector wavefunctions  $\underline{\Theta}_\nu^{(j)}(\underline{r})$  and  $\underline{\Psi}_\nu^{(j)}(\underline{r})$ ,  $\nu \in \{1, 2, 3, \dots\}$ , are assumed to be mutually orthogonal on  $S_e$  and  $S_i$ .

The sources of the incident field phasors are confined to the region  $\mathcal{V}'_s \subset \mathcal{V}_e$ . The source-containing region  $\mathcal{V}'_s$  is assumed to lie outside  $S_e$  and sufficiently far away from  $\mathcal{V}'_i$  as to remain unaffected by the scattering phenomenon. Then, the incident field phasors must be of finite magnitudes on and inside  $S_e$  as well as in the exterior neighborhood of that surface. Accordingly, the incident field phasors may be expanded as

$$\left. \begin{aligned} \underline{E}_{\text{inc}}(\underline{r}) &= \exp(i\omega \underline{\Gamma} \cdot \underline{r}) \sum_{\nu=1}^{\infty} [a_\nu \alpha_\nu \underline{\Phi}_\nu^{(1)}(\underline{r}) + b_\nu \beta_\nu \underline{\Xi}_\nu^{(1)}(\underline{r})] \\ \underline{H}_{\text{inc}}(\underline{r}) &= \exp(i\omega \underline{\Gamma} \cdot \underline{r}) \sum_{\nu=1}^{\infty} [a_\nu \alpha_\nu \underline{\Theta}_\nu^{(1)}(\underline{r}) + b_\nu \beta_\nu \underline{\Psi}_\nu^{(1)}(\underline{r})] \end{aligned} \right\}, \quad \underline{r} \in \mathcal{V} - \mathcal{V}'_s, \tag{19.66}$$

where the expansion coefficients  $a_\nu$  and  $b_\nu$ ,  $\nu \in \{1, 2, 3, \dots\}$ , are presumed to be known.

The scattered field phasors do not have to be of finite magnitude at the origin but must be regular at infinity. Therefore,

$$\left. \begin{aligned} \underline{E}_{\text{sca}}(\underline{r}) &= \exp(i\omega \underline{\Gamma} \cdot \underline{r}) \sum_{\nu=1}^{\infty} [c_\nu \alpha_\nu \underline{\Phi}_\nu^{(3)}(\underline{r}) + d_\nu \beta_\nu \underline{\Xi}_\nu^{(3)}(\underline{r})] \\ \underline{H}_{\text{sca}}(\underline{r}) &= \exp(i\omega \underline{\Gamma} \cdot \underline{r}) \sum_{\nu=1}^{\infty} [c_\nu \alpha_\nu \underline{\Theta}_\nu^{(3)}(\underline{r}) + d_\nu \beta_\nu \underline{\Psi}_\nu^{(3)}(\underline{r})] \end{aligned} \right\}, \quad \underline{r} \in \mathcal{V}_e, \tag{19.67}$$

where the expansion coefficients  $c_\nu$  and  $d_\nu$ ,  $\nu \in \{1, 2, 3, \dots\}$ , have to be determined.

### 19.3.3 Algebraic Equations

Let us now enforce Eq. (19.55)<sub>2</sub> with  $\underline{r}$  lying in the interior of  $S_i$ . As  $\underline{r}' \in S$ , it is clear that  $r' > r$ . On substituting Eqs. (19.62)<sub>2</sub>, (19.65)<sub>2</sub>, and (19.66)<sub>1</sub> in Eq. (19.55)<sub>2</sub> and then enforcing the orthogonality properties of  $\underline{\Phi}_\nu^{(1)}(\underline{r})$  and  $\underline{\Xi}_\nu^{(1)}(\underline{r})$ ,  $\nu \in \{1, 2, 3, \dots\}$ , on  $S_i$ , we get

$$\begin{aligned} -a_\nu &= \int \int_S \exp(-i\omega \underline{\Gamma} \cdot \underline{r}') \{ \underline{\Theta}_\nu^{(3)}(\underline{r}') \cdot [\hat{n}(\underline{r}') \times \underline{E}_{\text{int}}(\underline{r}')] \\ &\quad + \underline{\Phi}_\nu^{(3)}(\underline{r}') \cdot [\hat{n}(\underline{r}') \times \underline{H}_{\text{int}}(\underline{r}')] \} d^2 r', \quad \nu \in \{1, 2, 3, \dots\}, \end{aligned} \tag{19.68}$$

and

$$\begin{aligned}
 -b_\nu &= \int \int_S \exp(-i\omega \underline{\Gamma} \cdot \underline{r}') \{ \underline{\Psi}_\nu^{(3)}(\underline{r}') \cdot [\hat{\underline{n}}(\underline{r}') \times \underline{E}_{int}(\underline{r}')] \\
 &\quad + \underline{\Xi}_\nu^{(3)}(\underline{r}') \cdot [\hat{\underline{n}}(\underline{r}') \times \underline{H}_{int}(\underline{r}')] \} d^2 \underline{r}', \quad \nu \in \{1, 2, 3, \dots\}. \quad (19.69)
 \end{aligned}$$

Substitution of Eqs. (19.63)<sub>2</sub>, (19.64)<sub>2</sub>, and (19.66)<sub>2</sub> in Eq. (19.56)<sub>2</sub> followed by the exploitation of the orthogonality properties of  $\underline{\Theta}_\nu^{(1)}(\underline{r})$  and  $\underline{\Psi}_\nu^{(1)}(\underline{r})$ ,  $\nu \in \{1, 2, 3, \dots\}$ , on  $S_i$  also yields Eqs. (19.68) and (19.69).

Next, let us use Eq. (19.55)<sub>1</sub>. As  $\underline{r}' \in S$ , it is best to choose  $\underline{r}$  lying in the exterior of  $S_e$  so that  $r > r'$ . On substituting Eqs. (19.62)<sub>1</sub>, (19.65)<sub>1</sub>, and (19.67)<sub>1</sub> in Eq. (19.55)<sub>1</sub> and then enforcing the orthogonality properties of  $\underline{\Phi}_\nu^{(3)}(\underline{r})$  and  $\underline{\Xi}_\nu^{(3)}(\underline{r})$ ,  $\nu \in \{1, 2, 3, \dots\}$ , on  $S_e$ , we get

$$\begin{aligned}
 c_\nu &= \int \int_S \exp(-i\omega \underline{\Gamma} \cdot \underline{r}') \{ \underline{\Theta}_\nu^{(1)}(\underline{r}') \cdot [\hat{\underline{n}}(\underline{r}') \times \underline{E}_{int}(\underline{r}')] \\
 &\quad + \underline{\Phi}_\nu^{(1)}(\underline{r}') \cdot [\hat{\underline{n}}(\underline{r}') \times \underline{H}_{int}(\underline{r}')] \} d^2 \underline{r}', \quad \nu \in \{1, 2, 3, \dots\}, \quad (19.70)
 \end{aligned}$$

and

$$\begin{aligned}
 d_\nu &= \int \int_S \exp(-i\omega \underline{\Gamma} \cdot \underline{r}') \{ \underline{\Psi}_\nu^{(1)}(\underline{r}') \cdot [\hat{\underline{n}}(\underline{r}') \times \underline{E}_{int}(\underline{r}')] \\
 &\quad + \underline{\Xi}_\nu^{(1)}(\underline{r}') \cdot [\hat{\underline{n}}(\underline{r}') \times \underline{H}_{int}(\underline{r}')] \} d^2 \underline{r}', \quad \nu \in \{1, 2, 3, \dots\}. \quad (19.71)
 \end{aligned}$$

Equations (19.70) and (19.71) also emerge on the substitution of Eqs. (19.63)<sub>1</sub>, (19.64)<sub>1</sub>, and (19.67)<sub>2</sub> in Eq. (19.56)<sub>1</sub> followed by the exploitation of the orthogonality properties of  $\underline{\Theta}_\nu^{(3)}(\underline{r})$  and  $\underline{\Psi}_\nu^{(3)}(\underline{r})$ ,  $\nu \in \{1, 2, 3, \dots\}$ , on  $S_e$ .

### 19.3.4 *T Matrix*

Let the scattering region  $\mathcal{V}_i$  in Fig. 19.5 be occupied by a linear, homogeneous, bianisotropic medium with the frequency-domain constitutive relations

$$\left. \begin{aligned}
 \underline{D}(\underline{r}) &= \underline{\tilde{\epsilon}} \cdot \underline{E}(\underline{r}) + \left[ \underline{\tilde{\zeta}} + (\underline{\tilde{K}} - \underline{\tilde{L}}) \times \underline{I} \right] \cdot \underline{H}(\underline{r}) \\
 \underline{B}(\underline{r}) &= \underline{\tilde{\mu}} \cdot \underline{H}(\underline{r}) - \left[ \underline{\tilde{\zeta}} - (\underline{\tilde{K}} + \underline{\tilde{L}}) \times \underline{I} \right] \cdot \underline{E}(\underline{r})
 \end{aligned} \right\}, \quad \underline{r} \in \mathcal{V}_i, \quad (19.72)$$

wherein  $\underline{\tilde{\epsilon}}$ ,  $\underline{\tilde{\mu}}$ , and  $\underline{\tilde{\zeta}}$  are symmetric.

Accordingly, the internal field phasors may be expanded as

$$\left. \begin{aligned} \underline{E}_{int}(\underline{r}) &= \exp(i\omega \tilde{\Gamma} \cdot \underline{r}) \sum_{\nu=1}^{\infty} \left[ e_{\nu} \tilde{\underline{\Phi}}_{\nu}^{(1)}(\underline{r}) + f_{\nu} \tilde{\underline{\Xi}}_{\nu}^{(1)}(\underline{r}) \right] \\ \underline{H}_{int}(\underline{r}) &= \exp(i\omega \tilde{\Gamma} \cdot \underline{r}) \sum_{\nu=1}^{\infty} \left[ e_{\nu} \tilde{\underline{\Theta}}_{\nu}^{(1)}(\underline{r}) + f_{\nu} \tilde{\underline{\Psi}}_{\nu}^{(1)}(\underline{r}) \right] \end{aligned} \right\}, \quad \underline{r} \in \mathcal{V}_i, \quad (19.73)$$

where the expansion coefficients  $e_{\nu}$  and  $f_{\nu}$ ,  $\nu \in \{1, 2, 3, \dots\}$ , are unknown. The vector wavefunctions  $\tilde{\underline{\Phi}}^{(j)}(\underline{r})$ , etc., are the same as  $\underline{\Phi}^{(j)}(\underline{r})$ , etc., except that the constitutive quantities appearing in Eqs. (19.72) are used in place of those appearing in Eqs. (19.1).

Substitution of Eqs. (19.73) in Eqs. (19.68) and (19.69) leads to

$$\left. \begin{aligned} a_{\nu} &= \sum_{\nu'=1}^{\infty} I_{1\nu\nu'}^{(1)} e_{\nu'} + I_{2\nu\nu'}^{(1)} f_{\nu'} \\ b_{\nu} &= \sum_{\nu'=1}^{\infty} I_{3\nu\nu'}^{(1)} e_{\nu'} + I_{4\nu\nu'}^{(1)} f_{\nu'} \end{aligned} \right\}, \quad \nu \in \{1, 2, 3, \dots\}, \quad (19.74)$$

and in Eqs. (19.70) and (19.71) to

$$\left. \begin{aligned} c_{\nu} &= - \sum_{\nu'=1}^{\infty} I_{1\nu\nu'}^{(3)} e_{\nu'} + I_{2\nu\nu'}^{(3)} f_{\nu'} \\ d_{\nu} &= - \sum_{\nu'=1}^{\infty} I_{3\nu\nu'}^{(3)} e_{\nu'} + I_{4\nu\nu'}^{(3)} f_{\nu'} \end{aligned} \right\}, \quad \nu \in \{1, 2, 3, \dots\}, \quad (19.75)$$

where the surface integrals

$$\begin{aligned} I_{1\nu\nu'}^{(j)} &= - \int \int_S \exp[i\omega (\tilde{\Gamma} - \Gamma) \cdot \underline{r}] \left\{ \underline{\Theta}_{\nu}^{(j)}(\underline{r}) \cdot \left[ \hat{\underline{n}}(\underline{r}) \times \tilde{\underline{\Phi}}_{\nu'}^{(1)}(\underline{r}) \right] \right. \\ &\quad \left. + \underline{\Phi}_{\nu}^{(j)}(\underline{r}) \cdot \left[ \hat{\underline{n}}(\underline{r}) \times \tilde{\underline{\Theta}}_{\nu'}^{(1)}(\underline{r}) \right] \right\} d^2 \underline{r}, \quad j \in \{1, 3\}, \end{aligned} \quad (19.76)$$

$$\begin{aligned} I_{2\nu\nu'}^{(j)} &= - \int \int_S \exp[i\omega (\tilde{\Gamma} - \Gamma) \cdot \underline{r}] \left\{ \underline{\Theta}_{\nu}^{(j)}(\underline{r}) \cdot \left[ \hat{\underline{n}}(\underline{r}) \times \tilde{\underline{\Xi}}_{\nu'}^{(1)}(\underline{r}) \right] \right. \\ &\quad \left. + \underline{\Phi}_{\nu}^{(j)}(\underline{r}) \cdot \left[ \hat{\underline{n}}(\underline{r}) \times \tilde{\underline{\Psi}}_{\nu'}^{(1)}(\underline{r}) \right] \right\} d^2 \underline{r}, \quad j \in \{1, 3\}, \end{aligned} \quad (19.77)$$

$$\begin{aligned} I_{3\nu\nu'}^{(j)} &= - \int \int_S \exp[i\omega (\tilde{\Gamma} - \Gamma) \cdot \underline{r}] \left\{ \underline{\Psi}_{\nu}^{(j)}(\underline{r}) \cdot \left[ \hat{\underline{n}}(\underline{r}) \times \tilde{\underline{\Phi}}_{\nu'}^{(1)}(\underline{r}) \right] \right. \\ &\quad \left. + \underline{\Xi}_{\nu}^{(j)}(\underline{r}) \cdot \left[ \hat{\underline{n}}(\underline{r}) \times \tilde{\underline{\Theta}}_{\nu'}^{(1)}(\underline{r}) \right] \right\} d^2 \underline{r}, \quad j \in \{1, 3\}, \end{aligned} \quad (19.78)$$

and

$$I_{4\nu\nu'}^{(j)} = - \int \int_S \exp [i\omega (\tilde{\Gamma} - \Gamma) \cdot \underline{r}] \left\{ \underline{\Psi}_{\nu}^{(\ell)}(\underline{r}) \cdot \left[ \hat{\underline{n}}(\underline{r}) \times \underline{\tilde{\Xi}}_{\nu'}^{(1)}(\underline{r}) \right] \right. \\ \left. + \underline{\Xi}_{\nu}^{(\ell)}(\underline{r}) \cdot \left[ \hat{\underline{n}}(\underline{r}) \times \underline{\tilde{\Psi}}_{\nu'}^{(1)}(\underline{r}) \right] \right\} d^2 \underline{r}, \quad j \in \{1, 3\}, \quad (19.79)$$

have to be evaluated with  $\ell = j + 2(\bmod 4) \in \{3, 1\}$ .

After restricting  $\nu$  and  $\nu'$  to a maximum value denoted by  $N$ , Eqs. (19.74) can be down in matrix form as

$$\begin{bmatrix} a_{\nu} \\ - \\ b_{\nu} \end{bmatrix} = \begin{bmatrix} I_{1\nu\nu'}^{(1)} & | & I_{2\nu\nu'}^{(1)} \\ - & - & - \\ I_{3\nu\nu'}^{(1)} & | & I_{4\nu\nu'}^{(1)} \end{bmatrix} \begin{bmatrix} e_{\nu'} \\ - \\ f_{\nu'} \end{bmatrix} \equiv [Y^{(1)}] \begin{bmatrix} e_{\nu'} \\ - \\ f_{\nu'} \end{bmatrix} \quad (19.80)$$

and Eqs. (19.75) as

$$\begin{bmatrix} c_{\nu} \\ - \\ d_{\nu} \end{bmatrix} = - \begin{bmatrix} I_{1\nu\nu'}^{(3)} & | & I_{2\nu\nu'}^{(3)} \\ - & - & - \\ I_{3\nu\nu'}^{(3)} & | & I_{4\nu\nu'}^{(3)} \end{bmatrix} \begin{bmatrix} e_{\nu'} \\ - \\ f_{\nu'} \end{bmatrix} \equiv -[Y^{(3)}] \begin{bmatrix} e_{\nu'} \\ - \\ f_{\nu'} \end{bmatrix}, \quad (19.81)$$

where  $[Y^{(1)}]$  and  $[Y^{(3)}]$  are  $2N \times 2N$  matrices. Equations (19.80) and (19.81) yield a matrix relationship between the incident-field coefficients and the scattered-field coefficients that can be expressed as

$$\begin{bmatrix} c_{\nu} \\ - \\ d_{\nu} \end{bmatrix} = [T] \begin{bmatrix} a_{\nu'} \\ - \\ b_{\nu'} \end{bmatrix}, \quad (19.82)$$

where the T matrix is defined as

$$[T] = -[Y^{(3)}][Y^{(1)}]^{-1}. \quad (19.83)$$

### 19.3.5 Impenetrable Scatterer

Suppose that the region  $\mathcal{V}_i$  is occupied by an impenetrable scatterer. Then, Eqs. (19.57) and (19.58) must be used in lieu of Eqs. (19.55) and (19.56).

The surface current density phasors may be represented as

$$\left. \begin{aligned} \underline{J}_e^{\text{surf}}(\underline{r}) &= \exp(i\omega \Gamma \cdot \underline{r}) \hat{\underline{n}}(\underline{r}) \times \sum_{\nu=1}^{\infty} [e_{\nu} \underline{\Theta}_{\nu}^{(1)}(\underline{r}) + f_{\nu} \underline{\Psi}_{\nu}^{(1)}(\underline{r})] \\ \underline{J}_m^{\text{surf}}(\underline{r}) &= \underline{0} \end{aligned} \right\}, \quad \underline{r} \in S, \quad (19.84)$$

for a perfect electrically conducting scatterer and as

$$\left. \begin{aligned} \underline{J}_e^{\text{surf}}(\underline{r}) &= \underline{0} \\ \underline{J}_m^{\text{surf}}(\underline{r}) &= -\exp(i\omega \underline{\Gamma} \cdot \underline{r}) \hat{\underline{n}}(\underline{r}) \times \sum_{v=1}^{\infty} [e_v \underline{\Phi}_v^{(1)}(\underline{r}) + f_v \underline{\Xi}_v^{(1)}(\underline{r})] \end{aligned} \right\}, \quad \underline{r} \in \mathcal{S}, \quad (19.85)$$

for a perfect magnetically conducting scatterer. In either case, the derivation of the T matrix proceeds thereafter in exactly the same way as in Sects. 19.3.3 and 19.3.4.

### 19.3.6 Convergence

A significant issue is the convergence of the internal and the scattered field phasors with increasing  $N$ . Convergence slows down with increased constitutive differences between the mediums occupying  $\mathcal{V}_e$  and  $\mathcal{V}_i$ , which is to be expected.

Convergence also slows down (and even vanishes) with increasing deviation of  $\mathcal{S}$  from  $\mathcal{S}_i$ , especially with enhancement in the electrical size of the scatterer. The reason is rooted in the application of the orthogonality properties of the functions  $\underline{\Phi}_v^{(1)}(\underline{r})$ , etc. Whereas the boundary conditions (19.54) are enforced on  $\mathcal{S}$ , the cancellation of the incident field in accordance with the Ewald–Oseen extinction theorem is enforced via Eqs. (19.68) and (19.69) only on and inside  $\mathcal{S}_i$ .

When  $\mathcal{S}_i$  deviates significantly from  $\mathcal{S}$ , EBCM users have to implicitly rely on analytic continuation of the internal field phasors for the enforcement of the Ewald–Oseen extinction theorem throughout  $\mathcal{V}_i$  [3]. The reliance on analytic continuation becomes overly optimistic with increased electrical size of the scatterer, as has been cataloged by Iskander et al. [50].

While analytic continuation for a field phasor expressed as an infinitely long series is guaranteed in a source-free region, that of a terminated series is not [10]. Lewin [51] remarked in 1970 that when  $\mathcal{S}_i$  and  $\mathcal{S}$  are significantly different from each other, analytic continuation “is like the supergain antenna problem. To get an appreciable amount of supergain, an extraordinarily precise distribution has to be maintained. A minute change and the effect is lost.” No wonder, Lefschetz [52] had stated in 1963 that “no one has ever viewed analytical continuation as a practical procedure.”

The poor-convergence problem may be overcome to some extent when absorption is absent in the mediums occupying  $\mathcal{V}_e$  and  $\mathcal{V}_i$  and the external medium is Lorentz reciprocal. Additionally, when the external medium is free space, the constraints

$$\left. \begin{aligned} [T]^T &= [T] \\ [T][T]^* &= -\text{Re}\{[T]\} \end{aligned} \right\} \quad (19.86)$$

emerge, with the asterisk denoting the complex conjugate [53]. These symmetry and unitarity constraints on  $[T]$  can be exploited to improve convergence by repeated orthogonalization of  $[Y^{(1)}]$  [54–56].

### 19.3.7 Iterative EBCM

Another way to alleviate the poor-convergence problem was devised during my PhD research [50, 57–59] and used subsequently [60–63]. In the Iterative EBCM (IEBCM), Eqs. (19.68) and (19.69) are not used to enforce the Ewald–Oseen extinction theorem. Instead, the conceptual framework of IEBCM involves both an iterative procedure to enforce the Ewald–Oseen extinction theorem and multiple subregional expansions of the internal field phasors.

Implementation of the IEBCM begins with

- (i) the initial estimates  $\hat{\mathbf{n}}(\underline{r}) \times \underline{E}_+^{(0)}(\underline{r})$  and  $\hat{\mathbf{n}}(\underline{r}) \times \underline{H}_+^{(0)}(\underline{r})$  of  $\hat{\mathbf{n}}(\underline{r}) \times \underline{E}_+(\underline{r})$  and  $\hat{\mathbf{n}}(\underline{r}) \times \underline{H}_+(\underline{r})$ , respectively, for all  $\underline{r} \in \mathcal{S}$ , and
- (ii) the initial estimates  $\underline{E}_{int}^{(0)}(\underline{r})$  and  $\underline{H}_{int}^{(0)}(\underline{r})$  of  $\underline{E}_{int}(\underline{r})$  and  $\underline{H}_{int}(\underline{r})$ , respectively, for all  $\underline{r} \in \mathcal{V}_i$ .

These initial estimates are obtained either from the known solution at a lower frequency or from the known solution for a scatterer of a somewhat different shape or constitution at the same frequency.

The  $\ell$ -th iteration,  $\ell \in \{1, 2, 3, \dots\}$  comprises the following two steps:

- Step I: simultaneous solution of the two sets of integral equations

$$\begin{aligned}
 -a_\nu & - \int \int_{\mathcal{S}} \exp(-i\omega \underline{\Gamma} \cdot \underline{r}') \left\{ \underline{\Theta}_\nu^{(3)}(\underline{r}') \cdot \left[ \hat{\mathbf{n}}(\underline{r}') \times \underline{E}_+^{(\ell-1)}(\underline{r}') \right] \right. \\
 & \left. + \underline{\Phi}_\nu^{(3)}(\underline{r}') \cdot \left[ \hat{\mathbf{n}}(\underline{r}') \times \underline{H}_+^{(\ell-1)}(\underline{r}') \right] \right\} d^2 \underline{r}' \\
 & = \int \int_{\mathcal{S}} \exp(-i\omega \underline{\Gamma} \cdot \underline{r}') \left\{ \underline{\Theta}_\nu^{(3)}(\underline{r}') \cdot \left[ \hat{\mathbf{n}}(\underline{r}') \times \Delta \underline{E}_{int}^{(\ell)}(\underline{r}') \right] \right. \\
 & \left. + \underline{\Phi}_\nu^{(3)}(\underline{r}') \cdot \left[ \hat{\mathbf{n}}(\underline{r}') \times \Delta \underline{H}_{int}^{(\ell)}(\underline{r}') \right] \right\} d^2 \underline{r}', \quad \nu \in [1, N], \quad (19.87)
 \end{aligned}$$

$$\begin{aligned}
 -b_\nu & - \int \int_{\mathcal{S}} \exp(-i\omega \underline{\Gamma} \cdot \underline{r}') \left\{ \underline{\Psi}_\nu^{(3)}(\underline{r}') \cdot \left[ \hat{\mathbf{n}}(\underline{r}') \times \underline{E}_+^{(\ell-1)}(\underline{r}') \right] \right. \\
 & \left. + \underline{\Xi}_\nu^{(3)}(\underline{r}') \cdot \left[ \hat{\mathbf{n}}(\underline{r}') \times \underline{H}_+^{(\ell-1)}(\underline{r}') \right] \right\} d^2 \underline{r}' \\
 & = \int \int_{\mathcal{S}} \exp(-i\omega \underline{\Gamma} \cdot \underline{r}') \left\{ \underline{\Psi}_\nu^{(3)}(\underline{r}') \cdot \left[ \hat{\mathbf{n}}(\underline{r}') \times \Delta \underline{E}_{int}^{(\ell)}(\underline{r}') \right] \right. \\
 & \left. + \underline{\Xi}_\nu^{(3)}(\underline{r}') \cdot \left[ \hat{\mathbf{n}}(\underline{r}') \times \Delta \underline{H}_{int}^{(\ell)}(\underline{r}') \right] \right\} d^2 \underline{r}', \quad \nu \in [1, N], \quad (19.88)
 \end{aligned}$$



and several algebraic equations to determine  $\Delta \underline{E}_{int}^{(\ell)}(\underline{r})$  and  $\Delta \underline{H}_{int}^{(\ell)}(\underline{r})$  for all  $\underline{r} \in \mathcal{V}_i$ , followed by

- Step II: determination of the  $\ell$ -th estimates

$$\left. \begin{aligned} \underline{E}_{int}^{(\ell)}(\underline{r}) &= \underline{E}_{int}^{(\ell-1)}(\underline{r}) + \Delta \underline{E}_{int}^{(\ell)}(\underline{r}) \\ \underline{H}_{int}^{(\ell)}(\underline{r}) &= \underline{H}_{int}^{(\ell-1)}(\underline{r}) + \Delta \underline{H}_{int}^{(\ell)}(\underline{r}) \end{aligned} \right\}, \quad \underline{r} \in \mathcal{V}_i, \quad (19.89)$$

of the internal field phasors, followed by the determination of the  $\ell$ -th estimates

$$\left. \begin{aligned} \hat{\underline{n}}(\underline{r}) \times \underline{E}_+^{(\ell)}(\underline{r}) &= \hat{\underline{n}}(\underline{r}) \times \underline{E}_{int}^{(\ell)}(\underline{r}) \\ \hat{\underline{n}}(\underline{r}) \times \underline{H}_+^{(\ell)}(\underline{r}) &= \hat{\underline{n}}(\underline{r}) \times \underline{H}_{int}^{(\ell)}(\underline{r}) \end{aligned} \right\}, \quad \underline{r} \in \mathcal{S}, \quad (19.90)$$

of the tangential components of the electric and magnetic field phasors on the exterior side of  $\mathcal{S}$ , in order to start the  $(\ell + 1)$ -th iteration.

This iterative procedure is repeated until it is deemed to have either converged or become unstable.

The scattering region  $\mathcal{V}_i$  is partitioned into  $M$  subregions  $\mathcal{V}_i^{(m)}$ , the intersection of the closed surface  $\mathcal{S}$  and the subregion  $\mathcal{V}_i^{(m)}$  being the open surface  $\mathcal{S}^{(m)}$ , as shown in Fig. 19.6. In the  $m$ -th subregion,  $\Delta \underline{E}_{int}^{(\ell)}(\underline{r})$  and  $\Delta \underline{H}_{int}^{(\ell)}(\underline{r})$  are expanded as the truncated series

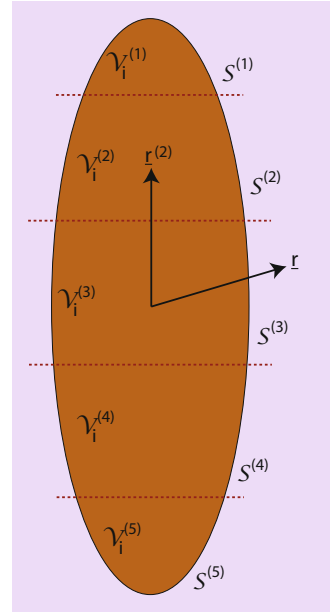
$$\left. \begin{aligned} \Delta \underline{E}_{int}^{(\ell)}(\underline{r}) &\equiv \Delta \underline{E}_{int}^{(\ell,m)}(\underline{r}) = \exp[i\omega \tilde{\underline{r}} \cdot (\underline{r} - \underline{r}^{(m)})] \\ &\quad \times \sum_{\nu=1}^{N^{(m)}} \left[ e_{\nu}^{(\ell,m)} \tilde{\underline{\Phi}}_{\nu}^{(1)}(\underline{r} - \underline{r}^{(m)}) + f_{\nu}^{(\ell,m)} \tilde{\underline{\Xi}}_{\nu}^{(1)}(\underline{r} - \underline{r}^{(m)}) \right] \\ \Delta \underline{H}_{int}^{(\ell)}(\underline{r}) &\equiv \Delta \underline{H}_{int}^{(\ell,m)}(\underline{r}) = \exp[i\omega \tilde{\underline{r}} \cdot (\underline{r} - \underline{r}^{(m)})] \\ &\quad \times \sum_{\nu=1}^{N^{(m)}} \left[ e_{\nu}^{(\ell,m)} \tilde{\underline{\Theta}}_{\nu}^{(1)}(\underline{r} - \underline{r}^{(m)}) + f_{\nu}^{(\ell,m)} \tilde{\underline{\Psi}}_{\nu}^{(1)}(\underline{r} - \underline{r}^{(m)}) \right] \end{aligned} \right\}, \quad (19.91)$$

$$\underline{r} \in \mathcal{V}_i^{(m)},$$

where  $\underline{r}^{(m)}$  serves as the origin of a local coordinate system designated for the  $m$ -th subregion.

Thus, the total number of the unknown expansion coefficients  $e_{\nu}^{(\ell,m)}$  and  $f_{\nu}^{(\ell,m)}$  entering the right sides of Eqs.(19.87) and (19.88) is  $N^{\Sigma} = 2[N^{(1)} + N^{(2)} + \dots + N^{(M)}]$ . As  $N^{\Sigma} > 2N$ , additional  $N^{\Sigma} - 2N$  algebraic equations are generated by matching

**Fig. 19.6** Schematic for implementing the IEBCM. The scattering region  $\mathcal{V}_i$  is partitioned into several subregions denoted by  $\mathcal{V}_i^{(m)}$ ,  $m \in [1, M]$ . The intersection of the closed surface  $S$  and the subregion  $\mathcal{V}_i^{(m)}$  is the open surface  $S^{(m)}$ . The origin of a local coordinate system designated for the  $m$ -th subregion is denoted by  $\underline{r}^{(m)}$



$$\left. \begin{aligned} \Delta \underline{E}_{int}^{(1,m)}(\underline{r}) + \Delta \underline{E}_{int}^{(2,m)}(\underline{r}) + \cdots + \Delta \underline{E}_{int}^{(\ell,m)}(\underline{r}) \\ = \Delta \underline{E}_{int}^{(1,m+1)}(\underline{r}) + \Delta \underline{E}_{int}^{(2,m+1)}(\underline{r}) + \cdots + \Delta \underline{E}_{int}^{(\ell,m+1)}(\underline{r}) \\ \Delta \underline{H}_{int}^{(1,m)}(\underline{r}) + \Delta \underline{H}_{int}^{(2,m)}(\underline{r}) + \cdots + \Delta \underline{H}_{int}^{(\ell,m)}(\underline{r}) \\ = \Delta \underline{H}_{int}^{(1,m+1)}(\underline{r}) + \Delta \underline{H}_{int}^{(2,m+1)}(\underline{r}) + \cdots + \Delta \underline{H}_{int}^{(\ell,m+1)}(\underline{r}) \end{aligned} \right\} \quad (19.92)$$

at several points on and in the proximity of the boundary of the mutually adjacent subregions  $\mathcal{V}_i^{(m)}$  and  $\mathcal{V}_i^{(m+1)}$ ,  $m \in [1, M-1]$ . Equations (19.87), (19.88), and (19.92) are solved simultaneously in Step I.

The computational scheme outlined above can be modified for different types of scatterers [50, 58, 60]. Its use extended the maximum frequency for the computation of microwave-dosimetry data for prolate spheroidal models of the average man from about 30 MHz [64–67] to about 300 MHz [50, 58, 59]. The reason for this sixfold extension is clearly the enforcement of the Ewald–Oseen extinction theorem in a much larger portion of  $\mathcal{V}_i$  than is possible with the EBCM.

## 19.4 Closing Remarks

The foregoing developments confirm that the EBCM requires:

- A. formulation of the Ewald–Oseen extinction theorem for the medium occupying the external region  $\mathcal{V}_e$ ,

- B. bilinear expansions of the dyadic Green functions for the same medium, and
- C. bilinear expansions of the dyadic Green functions for the medium occupying the scattering region  $\mathcal{V}_i$ .

Requirement A does not automatically fulfill requirement B. This is evident from the fact that although the Ewald–Oseen extinction theorem has been formulated here for the set of all mediums described by Eqs. (19.1), the needed bilinear expansions are available for only a small subset comprising (i) reciprocal biisotropic mediums [26] as well as their simplifications and (ii) orthorhombic dielectric-magnetic mediums with gyrotropic-like magnetoelectric properties [43].

Three additional characteristics of the EBCM must be noted. First, after truncation, the series on the right sides of Eqs. (19.67) are valid for the calculation of the scattered field phasors strictly in the region exterior to  $S_e$ .

Second, one can choose to calculate only  $\hat{n}(\underline{r}) \times \underline{E}_-(\underline{r})$  and  $\hat{n}(\underline{r}) \times \underline{H}_-(\underline{r})$  for a multitude of points  $\underline{r} \in S$ , instead of  $\underline{E}_{int}$  and  $\underline{H}_{int}$ , thereby making the EBCM in effect a point-matching technique [51, 68]. This characteristic is embodied in the IEBCM. The internal field phasors can be found from  $\hat{n}(\underline{r}) \times \underline{E}_-(\underline{r})$  and  $\hat{n}(\underline{r}) \times \underline{H}_-(\underline{r})$  for  $\underline{r} \in S$ , using the Huygens principle for the medium occupying  $\mathcal{V}_i$ .

Third, determination of  $[T]$  is possible without using the EBCM. One can assume that the incident electric field phasor is a single term in the series on the right side of Eqs. (19.66)<sub>1</sub>; solve the scattering problem using, e.g., the method of moments [69] or the finite-difference time-domain method [70]; match the scattered field phasors on  $S_e$  to the series on the right sides of Eqs. (19.67) in order to determine  $c_\nu$  and  $d_\nu$ ; and thereby fill up successive columns of  $[T]$ . This is the reason why the appellation *T-matrix method* is not totally appropriate for the EBCM.

What lies in the future for the EBCM? During the early 1990s, it seemed to me that further progress would be difficult to make, except to speed up computations. Computational research indeed picked up at the beginning of this century and continues unabated [11–18]. But, extension of the scope of the EBCM beyond biisotropic materials [26, 27] appeared in the mid-1990s to be elusive. Except for possible extension to a very specific bianisotropic medium earlier this decade [43], that prognosis has held true.

Nevertheless, first the formulation of the Huygens principle [28] and now that of the Ewald–Oseen extinction theorem in a considerably more general medium renew hope. Fulfillment of that hope will occur only when the needed bilinear expansions of the dyadic Green functions have been devised.

## Epilog

Like any thing of beauty, I find the Ewald–Oseen extinction theorem to be a joy forever. I was fortunate enough to learn it as a graduate student and to have extended its scope in later publications [26, 27, 43] and now in this chapter.

The EBCM would not have emerged in the absence of the Ewald–Oseen extinction theorem. Again, I was fortunate that Prof. Iskander asked me to use the EBCM for microwave-dosimetry calculations for my graduate research [65–67]. I continued to use the EBCM thereafter, not only in electromagnetics but also in acoustics and elastodynamics [10]. More than three decades later, I can unhesitatingly state that the gift from my graduate supervisor turned out to be a cornucopia.

Last but not the least, this chapter is a fuller reply than the one I gave to a question asked by Prof. Carl H. Durney during my PhD defense. He asked me to explain the most salient feature of the *extended boundary condition method*. My short answer has not changed in 34 years: Whereas the boundary conditions are enforced on the actual boundary of the scatterer, the explicit satisfaction of the Ewald–Oseen extinction theorem extends over a region that is usually smaller than the scatterer.

**Acknowledgements** I am grateful to the Charles Godfrey Binder Endowment at Penn State for ongoing support of my research activities. I thank Drs. Cynthia M. Furse (University of Utah), Tom G. Mackay (University of Edinburgh), and Muhammad Faryad (Lahore University of Management Sciences) for going through the pre-final version of this chapter.

## References

1. A. Lakhtakia, Radio-frequency absorption of near-field energy by prolate spheroidal models of humans and animals, MS thesis, University of Utah, Salt Lake City (1981)
2. A. Lakhtakia, Near-field scattering and absorption by lossy dielectrics at resonance frequencies, PhD thesis, University of Utah, Salt Lake City (1983)
3. P.C. Waterman, Matrix formulation of electromagnetic scattering. *Proc. IEEE* **53**, 805–812 (1965)
4. P.C. Waterman, Scattering by dielectric obstacles. *Alta Frequenza (Speciale)* **38**, 348–352 (1969)
5. P.W. Barber, C. Yeh, Scattering of electromagnetic waves by arbitrarily shaped dielectric bodies. *Appl. Opt.* **14**, 2864–2872 (1975)
6. R.H.T. Bates, D.J.N. Wall, Null-field approach to scalar diffraction: I. General method. *Philos. Trans. R. Soc. Lond. A* **287**, 45–78 (1977)
7. R.H.T. Bates, D.J.N. Wall, Null-field approach to scalar diffraction: II. Approximate methods. *Philos. Trans. R. Soc. Lond. A* **287**, 79–95 (1977)
8. R.H.T. Bates, D.J.N. Wall, Null-field approach to scalar diffraction: III. Inverse methods. *Philos. Trans. R. Soc. Lond. A* **287**, 97–114 (1977)
9. B. Stupfel, A. Lavie, J.N. Decarpigny, Combined integral equation formulation and null-field method for the exterior acoustic problem. *J. Acoust. Soc. Am.* **83**, 937–941 (1988)
10. V.V. Varadan, A. Lakhtakia, V.K. Varadan, Comments on recent criticism of the T-matrix method. *J. Acoust. Soc. Am.* **84**, 2280–2284 (1988)
11. M.I. Mishchenko, G. Videen, V.A. Babenko, N.G. Khlebtsov, T. Wriedt, T-matrix theory of electromagnetic scattering by particles and its applications: a comprehensive reference database. *J. Quant. Spectrosc. Radiat. Transf.* **88**, 357–406 (2004)
12. M.I. Mishchenko, G. Videen, V.A. Babenko, N.G. Khlebtsov, T. Wriedt, Comprehensive T-matrix reference database: a 2004–2006 update. *J. Quant. Spectrosc. Radiat. Transf.* **106**, 304–324 (2007)
13. M.I. Mishchenko, G. Videen, N.G. Khlebtsov, T. Wriedt, N.T. Zakharova, Comprehensive T-matrix reference database: a 2006–2007 update. *J. Quant. Spectrosc. Radiat. Transf.* **109**, 1447–1460 (2008)

14. M.I. Mishchenko, N.T. Zakharova, G. Videen, N.G. Khlebtsov, T. Wriedt, Comprehensive T-matrix reference database: a 2007–2009 update. *J. Quant. Spectrosc. Radiat. Transf.* **111**, 650–658 (2010)
15. N.T. Zakharova, G. Videen, N.G. Khlebtsov, Comprehensive T-matrix reference database: a 2009–2011 update. *J. Quant. Spectrosc. Radiat. Transf.* **113**, 1844–1852 (2012)
16. M.I. Mishchenko, G. Videen, N.G. Khlebtsov, T. Wriedt, Comprehensive T-matrix reference database: a 2012–2013 update. *J. Quant. Spectrosc. Radiat. Transf.* **123**, 145–152 (2013)
17. M.I. Mishchenko, N.T. Zakharova, N.G. Khlebtsov, T. Wriedt, G. Videen, Comprehensive T-matrix reference database: a 2013–2014 update. *J. Quant. Spectrosc. Radiat. Transf.* **146**, 349–354 (2014)
18. M.I. Mishchenko, N.T. Zakharova, N.G. Khlebtsov, G. Videen, T. Wriedt, Comprehensive thematic T-matrix reference database: a 2014–2015 update. *J. Quant. Spectrosc. Radiat. Transf.* **178**, 276–283 (2016)
19. V.K. Varadan, V.V. Varadan (eds.), *Acoustic, Electromagnetic, and Elastic Wave Scattering—Focus on the T-matrix Method* (Pergamon Press, New York, 1980)
20. L.W. Schmerr Jr., *Fundamentals of Ultrasonic Nondestructive Evaluation—A Modeling Approach*, 2nd edn. (Springer, Cham, Switzerland, 2016)
21. H.C. Chen, *Theory of Electromagnetic Waves: A Coordinate-Free Approach* (McGraw-Hill, New York, 1983)
22. R.F. Harrington, *Time-Harmonic Electromagnetic Fields* (McGraw-Hill, New York, 1961)
23. P.P. Ewald, Zur Begründung der Kristalloptik. *Annalen der Physik* (4th Series) **49**, 117–143 (1916)
24. C.W. Oseen, Über die Wechselwirkung zwischen zwei elektrischen Dipolen und über die Drehung der Polarisationssebene in Kristallen und Flüssigkeiten. *Annalen der Physik* (4th Series) **48**, 1–56 (1915)
25. H. Fearn, D.F.V. James, P.W. Milonni, Microscopic approach to reflection, transmission, and the Ewald–Oseen extinction theorem. *Am. J. Phys.* **64**, 986–995 (1996)
26. A. Lakhtakia, The extended boundary condition method for scattering by a chiral scatterer in a chiral medium. *Optik* **86**, 155–161 (1991)
27. A. Lakhtakia, On the Huygens’s principles and the Ewald–Oseen extinction theorems for, and the scattering of, Beltrami fields. *Optik* **91**, 35–40 (1992)
28. M. Faryad, A. Lakhtakia, On the Huygens principle for bianisotropic mediums with symmetric permittivity and permeability dyadics. *Phys. Lett. A* **381**, 742–746 (2017); errata: **381**, 2136 (2017)
29. E.J. Post, *Formal Structure of Electromagnetics* (Dover Press, New York, 1997)
30. T.G. Mackay, A. Lakhtakia, *Electromagnetic Anisotropy and Bianisotropy: A Field Guide* (World Scientific, Singapore, 2010)
31. J.A. Kong, Theorems of bianisotropic media. *Proc. IEEE* **60**, 1036–1046 (1972)
32. C.M. Krowne, Electromagnetic theorems for complex anisotropic media. *IEEE Trans. Antennas Propag.* **32**, 1224–1230 (1984)
33. W.S. Weiglhofer, A. Lakhtakia, On electromagnetic waves in biaxial bianisotropic media. *Electromagnetics* **19**, 351–362 (1999)
34. I.V. Lindell, S.A. Tretyakov, A.J. Viitanen, Plane-wave propagation in a uniaxial chiro-omega medium. *Microw. Opt. Technol. Lett.* **6**, 517–520 (1993)
35. M.M.I. Saadoun, N. Engheta, A reciprocal phase shifter using novel pseudo-chiral or  $\Omega$  medium. *Microw. Opt. Technol. Lett.* **5**, 184–188 (1992)
36. S.L. Adler, Photon splitting and photon dispersion in a strong magnetic field. *Ann. Phys. (N. Y.)* **67**, 599–647 (1971)
37. J. Plebanski, Electromagnetic waves in gravitational fields. *Phys. Rev.* **118**, 1396–1408 (1960)
38. A. Lakhtakia, T.G. Mackay, Dyadic Green function for an electromagnetic medium inspired by general relativity. *Chin. Phys. Lett.* **23**, 832–833 (2006); errata: **29**, 019902 (2012)
39. I. Stakgold, *Green’s Functions and Boundary Value Problems*, 2nd edn. (Wiley, New York, 1998)
40. F.M. Callier, C.A. Desoer, *Linear System Theory* (Springer, New York, 1990)

41. W.S. Weiglhofer, Analytic methods and free-space dyadic Green's functions. *Radio Sci.* **28**, 847–857 (1993)
42. F. Olyslager, I.V. Lindell, Electromagnetics and exotic media: a quest for the holy grail. *IEEE Antennas Propag. Mag.* **44**(2), 48–58 (2002)
43. A. Lakhtakia, T.G. Mackay, Vector spherical wavefunctions for orthorhombic dielectric-magnetic material with gyrotropic-like magnetoelectric properties. *J. Opt. (India)* **41**, 201–213 (2012)
44. N.R. Ogg, A Huygen's principle for anisotropic media. *J. Phys. A: Gen. Phys.* **4**, 382–388 (1971)
45. A. Lakhtakia, W.S. Weiglhofer, On electromagnetic fields in a linear medium with gyrotropic-like magnetoelectric properties. *Microw. Opt. Technol. Lett.* **15**, 168–170 (1997)
46. T.G. Mackay, A. Lakhtakia, The Huygens principle for a uniaxial dielectric-magnetic medium with gyrotropic-like magnetoelectric properties. *Electromagnetics* **29**, 143–150 (2009)
47. E.J. Rothwell, M.J. Cloud, *Electromagnetics* (CRC Press, Boca Raton, FL, 2001)
48. A. Lakhtakia, V.K. Varadan, V.V. Varadan, Scattering and absorption characteristics of lossy dielectric, chiral, nonspherical objects. *Appl. Opt.* **24**, 4146–4154 (1985)
49. P.M. Morse, H. Feshbach, *Methods of Theoretical Physics* (McGraw-Hill, New York, 1953)
50. M.F. Iskander, A. Lakhtakia, C.H. Durney, A new procedure for improving the solution stability and extending the frequency range of the EBCM. *IEEE Trans. Antennas Propag.* **31**, 317–324 (1983); see also: **32**, 209–210 (1984)
51. L. Lewin, On the restricted validity of point-matching techniques. *IEEE Trans. Microw. Theory Tech.* **18**, 1041–1047 (1970)
52. S. Lefschetz, *Differential Equations: Geometric Theory* (Wiley, New York, 1963)
53. P.C. Waterman, Symmetry, unitarity, and geometry in electromagnetic scattering. *Phys. Rev. D* **3**, 825–839 (1971)
54. P.C. Waterman, New formulation of acoustic scattering. *J. Acoust. Soc. Am.* **45**, 1417–1429 (1969)
55. M.F. Werby, L.H. Green, An extended unitary approach for acoustical scattering from elastic shells immersed in a fluid. *J. Acoust. Soc. Am.* **74**, 625–630 (1983)
56. A. Lakhtakia, V.K. Varadan, V.V. Varadan, Scattering by highly aspherical targets: EBCM coupled with reinforced orthogonalizations. *Appl. Opt.* **23**, 3502–3504 (1984)
57. M.F. Iskander, A. Lakhtakia, C.H. Durney, A new iterative procedure to solve for scattering and absorption by dielectric objects. *Proc. IEEE* **71**, 1361–1362 (1982)
58. A. Lakhtakia, M.F. Iskander, C.H. Durney, An iterative extended boundary condition method for solving the absorption characteristics of lossy dielectric objects of large aspect ratios. *IEEE Trans. Microw. Theory Tech.* **31**, 640–647 (1983)
59. A. Lakhtakia, M.F. Iskander, Theoretical and experimental evaluation of power absorption in elongated biological objects at and beyond resonance. *IEEE Trans. Electromagn. Compat.* **25**, 448–453 (1983)
60. M.F. Iskander, A. Lakhtakia, Extension of iterative EBCM to calculate scattering by low-loss or lossless elongated dielectric objects. *Appl. Opt.* **23**, 948–953 (1984)
61. A. Lakhtakia, N. Sitaram, V.K. Varadan, V.V. Varadan, Post-resonance scattering by lossy dielectric biological targets: point dipole sources. *Innov. Technol. Biol. Med.* **5**, 417–424 (1984)
62. A. Lakhtakia, V.K. Varadan, V.V. Varadan, Scattering by lossy dielectric slender objects with nonvanishing magnetic susceptibility. *J. Appl. Phys.* **56**, 3057–3060 (1984)
63. A. Lakhtakia, V.K. Varadan, V.V. Varadan, Iterative extended boundary condition method for scattering by objects of high aspect ratios. *J. Acoust. Soc. Am.* **76**, 906–912 (1984)
64. M.F. Iskander, P.W. Barber, C.H. Durney, H. Massoudi, Irradiation of prolate spheroidal models of humans in the near field of a short electric dipole. *IEEE Trans. Microw. Theory Tech.* **28**, 801–807 (1980)
65. A. Lakhtakia, M.F. Iskander, C.H. Durney, H. Massoudi, Irradiation of prolate spheroidal models of humans and animals in the near field of a small loop antenna. *Radio Sci.* **17**, 77S–84S (1982)

66. A. Lakhtakia, M.F. Iskander, C.H. Durney, H. Massoudi, Near-field absorption characteristics of prolate spheroidal models exposed to a small loop antenna of arbitrary orientation. *IEEE Trans. Microw. Theory Tech.* **29**, 588–594 (1981)
67. A. Lakhtakia, M.F. Iskander, C.H. Durney, H. Massoudi, Absorption characteristics of prolate spheroidal models exposed to the near fields of electrically small apertures. *IEEE Trans. Biomed. Eng.* **29**, 569–576 (1982)
68. R.H.T. Bates, Rayleigh hypothesis, the extended-boundary condition and point matching. *Electron. Lett.* **5**, 654–655 (1969)
69. W.C. Gibson, *The Method of Moments in Electromagnetics*, 2nd edn. (CRC Press, Boca Raton, FL, 2015)
70. A. Taflove, S.C. Hagness, *Computational Electrodynamics: The Finite-Difference Time-Domain Method*, 3rd edn. (Artech House, Norwood, MA, 2005)



**Akhlesh Lakhtakia** received the BTech (1979) and DSc (2006) degrees from the Banaras Hindu University and the MS (1981) and PhD (1983) degrees from the University of Utah. In 1983 he joined the Department of Engineering Science and Mechanics at Penn State as a post-doctoral research scholar, where he is now the Charles Godfrey Binder Professor. His research interests include surface multiplasmonics, bioreplication, forensic science, solar energy, sculptured thin films, and mimunes. He has been elected a fellow of Optical Society of America (1992), SPIE – The International Society for Optical Engineering (1996), Institute of Physics (UK) (1996), American Association for the Advancement of Science (2010), American Physical Society (2012), Institute of Electrical and Electronics Engineers (2016), Royal Society of Chemistry (2016), and Royal Society of Arts (2017). He has been designated a Distinguished Alumnus of both

of his alma maters at the highest level. Awards at Penn State include: Outstanding Research Award (1996), Outstanding Advising Award (2005), Premier Research Award (2008), and Outstanding Teaching Award (2016), and the Faculty Scholar Medal (2005). He received the 2010 Technical Achievement Award from SPIE and the 2016 Walston Chubb Award for Innovation from Sigma Xi.

# Chapter 20

## Propagator Methods in Electromagnetics

Jongchul Shin and Robert D. Nevels

### 20.1 Introduction

Propagators are a subclass of Green functions that, when integrated against the present-time electromagnetic field, produce the field at a future time. In principle, in a homogeneous region, the field at any future time can be calculated analytically if the present-time field is known throughout space. However, in an inhomogeneous region, the procedure for finding the later-time field requires discretizing time and space so that boundary conditions can be applied at locations in space where the field encounters changes in the regional material properties. A propagator method is both analytical, in which it is a Green function that must be derived, and numerical, in which it must be solved in a space-time grid, and it is recursive, in which the current time field integrated against the propagator becomes a new current time field. This process continues in small time increments from the initial time to some predetermined final time, creating what can be imagined as a set of nested integrals, each over all of space and each containing the same propagator but each multiplying the field produced by its predecessor. This nested set of integrals was described as the path integral by Richard Feynman, who is credited as its inventor.

Today, propagators are widely used in quantum mechanics [1], quantum electrodynamics [2], quantum chromodynamics [3], plasmonics [4], and in the study of phonon volume waves [5], acoustic surface waves [6], ocean waves [7], geophysical waves [8], polymer physics [9], and almost every scientific discipline involving wave motion [10, 11], but are only now being studied in electromagnetic field analysis. This delay is attributed to the complex mathematical problems associated

---

J. Shin • R.D. Nevels (✉)

Department of Electrical and Computer Engineering, Texas A&M University,  
College Station, TX, USA

e-mail: [nevels@ece.tamu.edu](mailto:nevels@ece.tamu.edu); [kolman79@tamu.edu](mailto:kolman79@tamu.edu)



with the vector nature of the electromagnetic field and subsequently the numerous tasks related to the development of a competitive numerical code.

In this chapter, we review some of the successful analytical/numerical methods that have been created leading up to the complete closed-form propagator solution for the electromagnetic field. These include the scalar path integral method, the stationary-phase Monte Carlo method, the Fourier transform path integral method, the path integral time-domain method, and the most recent propagator method. The distinguishing feature of a propagator is that it is a unitary operator that acts directly upon the field, moving its successive increments in time through a numerical space. If the space is homogeneous and the initial field is an analytical function, it is possible to perform the entire operation analytically, propagating the initial field any given distance over a corresponding causal time period with a single integration. The propagator method can therefore be described as an evolution operator rather than a numerical technique for solving a differential equation, such as the finite-difference time-domain (FDTD) method [12], or an integral equation solution method, such as the method of moments [13] or the finite element method [14]. Although propagator methods incorporate a Green function, they do not require operations on potentials or a solution for equivalent currents before arriving at the fields. Yet any problem that can be solved by other methods can potentially be solved with propagator techniques.

A primary advantage of a time-domain propagator numerical method is that the resulting fields are coincident in time and space, so all components of the electromagnetic field are found at each point in the numerical grid. This is different from, for example, the FDTD method, where the field components are not spatially coincident and the electric and magnetic fields are not coincident in time. Propagator method coincidence offers the possibility of precise calculation of inductances, capacitances, and equivalent current far fields, as well as seamless merging with other equations in physics such as the bio-heat equation for biological applications and with Schrödinger equation for applications in quantum mechanics.

## 20.2 The Fourier Transform Path Integral (FTPI) Method

One of the major obstacles to developing a propagator method for electromagnetics is that the propagator must be a solution to a hyperbolic equation with at least one first-order derivative. The Helmholtz equation is elliptic, and the wave equation of electromagnetics is hyperbolic, but its time and space derivatives are both second order. Schrödinger equation of quantum mechanics appears to be parabolic but, because of the imaginary coefficient in the total energy term which affects the energy eigenvalues, it is classified as a hyperbolic equation. This explains in part, but not entirely, why quantum mechanics were the first field in which a propagator method was developed. When Feynman originally came up with the path integral method for quantum mechanics [1], he developed his equation based on the action principle, independent of Schrödinger equation. The path integral is therefore considered

to be one of the three independent solutions to quantum processes, joined by Schrödinger probability method and Heisenberg's matrix method. However, later work showed that propagators were much easier to derive starting with Schrödinger equation.

Several successful propagator methods have been developed for calculating the quantum probability amplitude starting with Schrödinger equation. Helmholtz equation can be cast in a Schrödinger equation form that leads to a solution for the electromagnetic field propagator. With Schrödinger equation, a probability amplitude is propagated in time. However, as will be seen below, when the electromagnetic field Helmholtz equation is placed in the form of a Schrödinger equation, the field is propagated in space. This approach therefore yields a pure frequency-domain solution for the field. A suppressed time convention  $\exp(j\omega t)$  is used throughout this chapter.

### 20.2.1 FTPI Analysis

The Green function propagator  $K(x, \tau; x', \tau')$  is obtained by hypothesizing the one-dimensional equation [15]

$$\left\{ -\frac{1}{k^2} \frac{\partial^2}{\partial x^2} + V(x) + \frac{j}{k} \frac{\partial}{\partial \tau} \right\} K(x, \tau; x', \tau') = \frac{j}{k} \delta(x - x') \delta(\tau - \tau'), \quad (20.1)$$

where  $\tau'$  and  $\tau$  are, respectively, the starting and ending "times" for a wave propagating from the source point  $x'$  to the observation point  $x$ . The advantage of starting with Eq. (20.1) is that it is a parabolic equation, the mathematical form that has a propagator solution. Also, the temporal Fourier transform of Eq. (20.1) according to

$$\mathcal{F} \{ \psi(\tau) \} = \int_{-\infty}^{\infty} \psi(\tau) e^{-j\tau k} d\tau \quad (20.2)$$

gives the Helmholtz Green function equation

$$\left[ \frac{\partial^2}{\partial x^2} + k^2 n^2(x) \right] G(x, x') = -\delta(x - x') \quad (20.3)$$

with its corresponding Green function defined by

$$G(x, x') = -\frac{j}{k} \int_0^{\infty} K(x, \tau; x', 0) e^{-jk\tau} d\tau. \quad (20.4)$$

For reasons explained below, the lower integration limit in Eq. (20.4) is zero. The procedure now is to first obtain the propagator  $K$  and then, with Eq. (20.4), the Helmholtz Green function. It is emphasized here that Eq. (20.1) is only a Schrödinger-“type” equation because the definitions of some variables in Eq. (20.1) are different from those used in quantum mechanics. In Eq. (20.1),  $\tau$  is a parameter having the dimensions of length, and  $V(x)$  is a dimensionless function related to the square of the index of refraction  $n(x)$  by

$$n^2(x) = 1 - V(x). \quad (20.5)$$

Equation (20.1) can be expressed as

$$\left( H + \frac{j}{k} \frac{\partial}{\partial \tau} \right) K(x, \tau; x', 0) = \frac{j}{k} \delta(x - x') \delta(\tau - \tau') \quad (20.6)$$

by defining the operators  $H = T + V$  where  $T = -\left(\frac{1}{k^2}\right) \frac{\partial^2}{\partial x^2}$ . It can be shown by substitution that the solution to Eq. (20.6) is

$$K(x, \tau; x', 0) = e^{jk\tau H} \delta(x - x') U(\tau). \quad (20.7)$$

In Eq. (20.7),  $\tau'$  has been set to zero and  $U(\tau)$  represents a unit step function that is dropped, but implicitly understood in the remainder of this section. It reappears in the final Green function expression as a lower limit on the  $\tau$  integration to values greater than zero. By subtracting and adding  $\tau_\alpha$ , a number between 0 and  $\tau$ , in the exponent in Eq. (20.7) and appealing to the identity

$$\delta(x - x') = \int_{-\infty}^{\infty} \delta(x - x_\alpha) \delta(x_\alpha - x') dx_\alpha, \quad (20.8)$$

where  $x_\alpha$  is a number between  $x$  and  $x'$  but otherwise not related to  $\tau_\alpha$ , we get

$$\begin{aligned} K(x, \tau; x', 0) &= \int_{-\infty}^{\infty} e^{jkH(\tau - \tau_\alpha)} \delta(x - x_\alpha) e^{jkH_\alpha \tau_\alpha} \delta(x_\alpha - x') dx_\alpha \\ &\doteq \int_{-\infty}^{\infty} K(x, \tau; x_\alpha, \tau_\alpha) K(x_\alpha, \tau_\alpha; x', 0) dx_\alpha. \end{aligned} \quad (20.9)$$

$H$  is converted to  $H_\alpha$  in the integrand of Eq. (20.9), by applying the property of delta functions

$$f(x)\delta(x - x_0) = f(x_0)\delta(x - x_0) \quad (20.10)$$

and by defining  $H_\alpha \doteq T_\alpha + V_\alpha = -\left(\frac{1}{k^2}\right) \frac{\partial^2}{\partial x_\alpha^2} + V(x_\alpha)$ . Operators in an exponential do not behave the same way as variables, so the series expansion of  $e^{-a(T+V)}$  is not equal to the product of the series expansions of the two exponentials  $e^{-aT}e^{-aV}$ . However, we can take advantage of Trotter's product formula [16]

$$e^{-a(T+V)} = \lim_{N \rightarrow \infty} \left[ e^{-\frac{aT}{N}} e^{-\frac{aV}{N}} \right]^N. \quad (20.11)$$

In practice, Eq. (20.11) can be applied in Eq. (20.9) with  $N$  limited to some large but finite value such that  $\frac{\tau}{(N+1)} \doteq \varepsilon$  is a small number compared to  $\tau$ . Equation (20.8) applied successively  $N$  times in Eq. (20.9) gives the ordered product propagator expression

$$K(x, \tau; x', 0) = \lim_{N \rightarrow \infty} \int_{-\infty}^{\infty} dx_1 \cdots \int_{-\infty}^{\infty} dx_N \prod_{i=1}^{N+1} e^{jk_\varepsilon H_i} \delta(x_i - x_{i-1}), \quad (20.12)$$

where the source point  $x'$  is  $x_0$  on the right-hand side of Eq. (20.12) and the observation point  $x$  is  $x_{N+1}$ . The property

$$f(x)\delta(x - x_0) = \left[ \frac{f(x) + f(x_0)}{2} \right] \delta(x - x_0) \quad (20.13)$$

applied to only the function  $V_i$  in Eq. (20.12) gives

$$e^{jk_\varepsilon H_i} \delta(x_i - x_{i-1}) = e^{jk_\varepsilon (V_i + V_{i-1})/2} e^{jk_\varepsilon T_i} \delta(x_i - x_{i-1}). \quad (20.14)$$

An ‘‘averaged’’  $V(x)$  is not necessary, but it improves the accuracy of numerical calculations. The delta function can now be expanded in the eigenfunctions (exponentials) and eigenvalues ( $k_{x_i}$ ) of the operator  $T_i$ , giving

$$\begin{aligned} e^{jk_\varepsilon T_i} \delta(x_i - x_{i-1}) &= e^{jk_\varepsilon T_i} \frac{1}{2\pi} \int_{-\infty}^{\infty} e^{-jk_{x_i}(x_i - x_{i-1})} dk_{x_i} \\ &= \frac{1}{2\pi} \int_{-\infty}^{\infty} e^{\frac{j\varepsilon k_{x_i}^2}{k}} e^{-jk_{x_i}(x_i - x_{i-1})} dk_{x_i}. \end{aligned} \quad (20.15)$$

Finally, Eqs. (20.14) and (20.15) are substituted into Eq. (20.12), giving the discrete one-dimensional path integral form

$$\begin{aligned} K(x, \tau; x', 0) &= \lim_{N \rightarrow \infty} \left( \frac{1}{2\pi} \right)^{N+1} \int_{-\infty}^{\infty} \prod_{i=1}^N dx_i \int_{-\infty}^{\infty} \prod_{i=1}^{N+1} dk_{x_i} \\ &\quad \cdot e^{-jk \sum_{i=1}^{N+1} \left[ k_{x_i}(x_i - x_{i-1})/k - \varepsilon k_{x_i}^2/k^2 - \varepsilon(V_i + V_{i-1})/2 \right]}. \end{aligned} \quad (20.16)$$

The second integral on the right-hand side in Eq. (20.16) can be easily evaluated resulting in

$$K(x, \tau; x', 0) = \lim_{N \rightarrow \infty} \frac{1}{A^{N+1}} \int_{-\infty}^{\infty} \prod_{i=1}^N dx_i e^{-jk\varepsilon \sum_{i=1}^{N+1} \left[ \frac{1}{4} \left( \frac{x_i - x_{i-1}}{\varepsilon} \right)^2 - \left( \frac{v_i + v_{i-1}}{2} \right) \right]}, \quad (20.17)$$

where  $A = (4\pi\varepsilon/jk)^{\frac{1}{2}}$ .

The discrete and compact forms of the path integral Green function for Helmholtz equation can be found by substituting Eq. (20.17) for  $K(x, \tau; x', 0)$  into Eq. (20.4). The result is

$$G(x, x') = -\frac{j}{k} \int_0^{\infty} \Phi(x, \tau; x', 0) d\tau, \quad (20.18)$$

where

$$\Phi(x, \tau; x', 0) = \frac{1}{A^{N+1}} \int_{-\infty}^{\infty} \prod_{i=1}^N dx_i e^{-jk\varepsilon \sum_{i=1}^{N+1} \left[ \frac{1}{4} \left( \frac{x_i - x_{i-1}}{\varepsilon} \right)^2 + \left( \frac{n^2(x_i) + n^2(x_{i-1})}{2} \right) \right]}. \quad (20.19)$$

By extension of the methods above, a two-dimensional expression can be shown to have the discrete form

$$\Phi(\mathbf{r}, \tau; \mathbf{r}', 0) = \lim_{N \rightarrow \infty} \left( \frac{1}{2\pi} \right)^{2N+2} \int_{-\infty}^{\infty} \prod_{i=1}^N ds_i \int_{-\infty}^{\infty} \prod_{i=1}^{N+1} d\kappa_i e^{-jk\varepsilon \sum_{i=1}^{N+1} \left[ \frac{\mathbf{k}_i \cdot (\mathbf{r}_i - \mathbf{r}_{i-1})}{\varepsilon} - \frac{k_i^2}{k^2} + \left( \frac{n^2(\mathbf{r}_i) + n^2(\mathbf{r}_{i-1})}{2} \right) \right]}, \quad (20.20)$$

where  $ds_i = dx_i dy_i$ ,  $d\kappa_i = dk_{x_i} dk_{y_i}$ ,  $\mathbf{k}_i = k_{x_i} \hat{\mathbf{x}} + k_{y_i} \hat{\mathbf{y}}$  and  $\mathbf{r}_i = x_i \hat{\mathbf{x}} + y_i \hat{\mathbf{y}}$ .

### 20.2.2 Numerical Method for FTPI

The path integral expression Eq. (20.19) can be rearranged according to the definition of the Fourier transform in Eq. (20.2) and the inverse Fourier transform given by

$$\mathcal{F}^{-1} \{ \psi(v) \} = \frac{1}{2\pi} \int_{-\infty}^{\infty} \psi(v) e^{i\mu v} dv, \quad (20.21)$$

so that it is in the form of the following nested sequence:

$$\begin{aligned} \Phi(x, \tau; x', 0) = \lim_{N \rightarrow \infty} e^{-jk\epsilon[n^2(x)+n^2(x')]/2} \mathcal{F}^{-1} \left\{ e^{jk\epsilon k_{x1}^2/k} \mathcal{F} \left\{ e^{-jk\epsilon n^2(x_1)} \mathcal{F}^{-1} \left\{ e^{jk\epsilon k_{x2}^2/k} \right. \right. \right. \\ \left. \left. \left. \dots \mathcal{F} \left\{ e^{-jk\epsilon n^2(x_N)} \mathcal{F}^{-1} \left\{ e^{-j(k_{x,N+1}x' - \epsilon k_{x,N+1}^2/k)} \right\} \right\} \dots \right\} \right\}. \end{aligned} \quad (20.22)$$

This contribution greatly enhances this method because, from a mathematical standpoint, the Fourier transform is a unitary operation and therefore unconditionally stable, and, from a numerical standpoint, the fast Fourier transform (FFT) is a remarkably fast integration procedure.

In Eq. (20.22), there are  $N + 1$  nested inverse Fourier transforms in the spectral ( $k_{xi}$ ) domain and  $N$  Fourier transforms in the spatial ( $x_i$ ) domain. The complete path integration in Eq. (20.21) is carried out by evaluating  $\Phi(x, \tau; x', 0)$  at  $M$  discrete points  $\tau_m$  sufficient for accurate numerical integration on the truncated infinite  $\tau$  interval. Each successive value of  $\tau_m$  corresponds to a value of  $N$  increased by 2, while  $\epsilon$  remains a predetermined constant. In this way, each calculation of  $\Phi(x, \tau_m; x', 0)$  is used in two ways. It is summed to an array whose end result is the integral in Eq. (20.22), and it is the input data for calculating  $\Phi(x, \tau_{m+1}; x', 0)$ . The total number of FFTs necessary to find the electromagnetic field at  $L$  sample points on a spatial grid is therefore  $2N + 1$ .

It can be shown that, by setting the index of refraction  $n(x) = 1$ , Eq. (20.18) reduces to the free-space Green function,

$$G_f(x, x') = -\frac{j}{k} \int_0^{\infty} \left\{ \left( \frac{jk}{4\pi} \right)^{\frac{1}{2}} e^{-jk\tau \left[ \frac{(x-x')^2}{2\tau} + 1 \right]} / \tau^{\frac{1}{2}} \right\} d\tau = -\frac{j}{2k} e^{-jk|x-x'|}. \quad (20.23)$$

The integral expression in Eq. (20.23) displays two characteristics that present major numerical difficulties for the FTPI numerical method when the scattering region is not homogeneous: a singularity at  $\tau = 0$  and a highly oscillatory integrand as  $\tau \rightarrow 0$ . Fortunately, both of these complications can be resolved by subtracting the free-space function  $\Phi_f(x, \tau; x', 0)$  and adding the free-space Green function in the general path integral expression, i.e.,

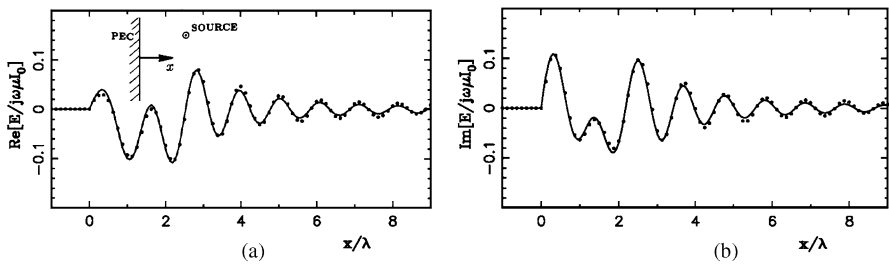
$$G(x, x') = -\frac{j}{k} \int_0^{\infty} \left[ \Phi(x, \tau; x', 0) - \Phi_f(x, \tau; x', 0) \right] d\tau + G_f(x, x'). \quad (20.24)$$

This step increases the accuracy of the calculation of  $G(x, x')$  because  $\Phi(x, \tau; x', 0)$  for any finite index of refraction approaches the free-space  $\Phi_f(x, \tau; x', 0)$  when  $\tau \rightarrow 0$ .

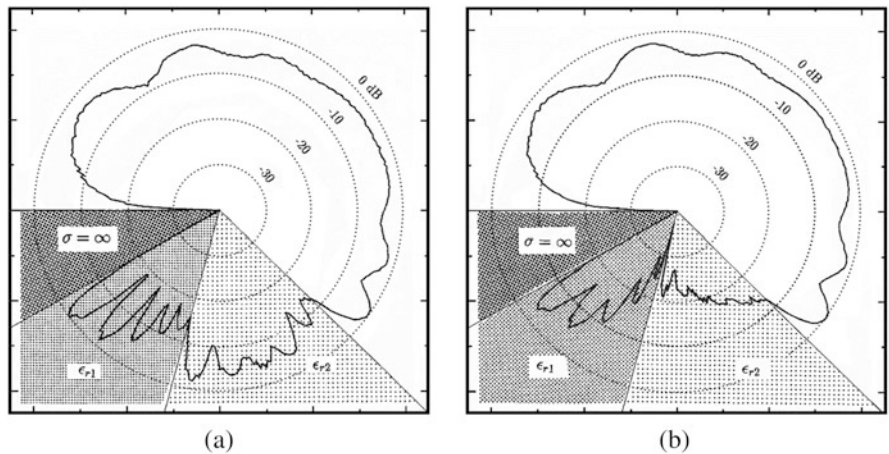
### 20.2.3 FTPI Results

Figure 20.1 shows the real and imaginary parts of the total electric field calculated with the FTPI method as compared to the exact solution when a line source in a two-dimensional ( $xy$ ) region is located in air 2.6 wavelengths ( $\lambda$ ) from the boundary of a planar perfect electric conductor (PEC). The observation position extends along the  $x$ -axis from  $x = -1\lambda$  inside the conductor  $x = 9\lambda$ . The lack of aliasing error commonly associated with FFT routines is attributed to an imposed limit ( $2\lambda$ ) on the thickness of the PEC region. These results were computed in a  $10\lambda \times 0.5\lambda$  region containing  $100 \times 50$  FFT sample points.

Figures 20.2a and b show the effect of considering the loss in the calculation of the electric field scattered from three coincident triangular segments representing a spilling ocean breaker wave as computed by the FTPI method [17]. The ocean itself



**Fig. 20.1** Total (a) real and (b) imaginary electric field along  $x$ -axis due to a two-dimensional line source located at  $x = 1.5\lambda$  and  $y = 1.2\lambda$  radiating in the presence of a planar PEC boundary with FTPI method (dots) and analytical solution (solid line) (Adapted from Ref. [15] © IET)



**Fig. 20.2** The FTPI scattered electric field for a wedge representing a breaking wave where  $\sigma = \infty$ ,  $\epsilon_{r,1} = 2.5$  with (a)  $\epsilon_{r,2} = 1.5$  and (b)  $\epsilon_{r,2} = 1.5 - j0.1$ . The source point is located at  $0, 0, 2.0\lambda$  above the apex of the wedges (Adapted from Ref. [17] © IEEE)

is a perfect conductor, the region containing  $\epsilon_{r1} = 2.5$  depicts air pocket conditions beneath the wave, and the segment  $\epsilon_{r2} = 1.5 - j0.1$  is the spilling portion of the wave. A comparison of the results in Fig. 20.2a and those in b clearly shows that the field is attenuated in the lossy wedge section but remains virtually the same in the exterior free-space region. For these two cases, the field patterns inside the air pocket have the same number of lobes, while in Fig. 20.2b, the field pattern has a smaller magnitude due to attenuation in the lossy wedge. In both examples, as expected, the largest lobes are in the backscatter direction. All of the FTPI results presented in Figs. 20.1 and 20.2 have been computed without a numerical filter. A numerical filter added to the FFT will mitigate the effects of aliasing and extend the range of accuracy of the FTPI method closer to the numerical boundary.

### 20.2.4 Conclusions Concerning the FTPI Method

In this section, a derivation of the Fourier transform path integral method and an FTPI numerical technique have been presented. The data for each of the numerical examples presented here were obtained with source codes that only require specification of the scattering region permeability  $\mu$  and permittivity  $\epsilon$  as a function of position and the positions of the source and observation points. This is because the FTPI method is a direct evaluation of the electromagnetic field propagator (Green function) integrated over the field distribution. The FTPI method can calculate the electromagnetic fields in a region that contains intersecting or isolated dielectric bodies that are homogeneous, inhomogeneous, or perfect conductors. It does not suffer from various requirements inherent in many current numerical techniques, including knowledge of the field potentials, selection of a basis set, matrix inversion, or ray tracing.

On the negative side, the FFTs are subject to aliasing [18] which is an effect caused by sampling over a discrete band, a function which is not bandwidth limited. This limitation can be minimized by incorporating a numerical filter, which can be thought of as a type of frequency-domain absorbing boundary condition, into the FTPI computer program. Alternatively one could simply use the field near the scatterer, which is inside the aliasing region, to generate equivalent currents that will, by Fourier transformation, produce the correct far field.

Another difficulty is that the path integral propagator is singular and highly oscillatory near  $\tau \rightarrow 0$ . It can be shown analytically that the singularity and the rapidly oscillating integrand near  $\tau \rightarrow 0$  do not contribute to the path integral. FFTs in the FTPI method tend to filter out these rapid oscillations of the path integral integrand. Nevertheless, some small error is accrued in the numerical integration over the highly oscillatory region. Naturally, an alternative integration path off the real axis near  $\tau \rightarrow 0$  would completely avoid these rapid oscillations, but computation time would increase significantly. Also, the method presented here is restricted to scalar field applications, and it is computationally time intensive. In conclusion, the FTPI method is useful for solving two-dimensional scattering



problems in electromagnetics and in quantum field theory where the scalar field is all that is required. Because electromagnetics is a vector field theory, FTPI is not a general full-wave solution method for the electromagnetic field.

## 20.3 The Stationary-Phase Monte Carlo (SPMC) Method

For mathematical analysis of electromagnetic wave propagation, the Helmholtz equation is often approximated by a scalar hyperbolic equation with one first-order derivative term, referred to as the paraxial wave equation [19]. The path integral is one of the few methods that can solve the parabolic equation for the electromagnetic fields in inhomogeneous media, whether in the atmosphere or in layered wave-guiding structures. However, the hallmark of the path integral method, a large set of nested integrals, can be time consuming to evaluate. It is therefore natural to resort to the Monte Carlo method, the traditional “go to” numerical technique for evaluating nested integrals. An additional difficulty encountered when calculating the path integral in an inhomogeneous medium is that the propagator integrand is strongly oscillatory over most of its range. However, advantage may be taken of the stationary-phase nature of the propagator integrand under transversely inhomogeneous conditions [19]. The stationary-phase Monte Carlo (SPMC) method [20] has shown promise in a number of special cases, but has both accuracy and stability issues. The method presented below avoids these problems through the introduction of a numerical filter and by taking advantage of the Markov property [21] of the propagator. As with FTPI, SPMC again yields a frequency-domain solution.

### 20.3.1 SPMC Analysis

We consider an electromagnetic wave propagating in the positive  $z$ -direction in a transversely inhomogeneous medium with a refractive index  $n^2(x, y)$ . The FTPI method begins with a parabolic equation that, through Fourier transformation, becomes a Helmholtz Green function equation. However, the SPMC method begins with a Helmholtz equation

$$[\nabla^2 + k^2(x, y)]E(x, y, z) = 0 \quad (20.25)$$

for the frequency-domain scalar electric field  $E(x, y, z)$  that is then reduced to a parabolic equation

$$\frac{j}{k} \frac{\partial U}{\partial z} + \frac{1}{2k^2} \nabla_{xy}^2 U + \frac{1}{2} [n^2(x, y) - 1] U = 0 \quad (20.26)$$

by employing the waveguide condition  $E(x, y, z) = U(x, y, x) \exp\{ikz\}$  and by assuming that the index of refraction  $n(x, y, z)$  is slowly varying along the  $z$ -axis [10, 20]. In Eq. (20.26),  $k$  is the free-space wave number.

The solution to Eq. (20.26) can be expressed in terms of the Markov property as

$$U(x, y, z) = \int_{-\infty}^{+\infty} \int_{-\infty}^{+\infty} dx_0 dy_0 U(x_0, y_0, z_0) K(x, y, z; x_0, y_0, z_0). \quad (20.27)$$

In Eq. (20.27),  $U(x_0, y_0, z_0)$  is the initial field at the source point  $(x_0, y_0, z_0)$ , and  $U(x, y, z)$  is the final field that has propagated a distance of  $z - z_0$  along the waveguide to an observation point  $(x, y, z)$ . The term  $K(x, y, z; x_0, y_0, z_0)$  is a path integral propagator, which represents a sum over all possible paths between the source and observation points.

In the following presentation, for convenience, we consider an index of refraction which is a function of  $x$  only. Generalization to two and three dimensions is straightforward. The discrete form of the propagator  $K(x, z; x_0, z_0)$ , obtained following the FTPI method, is

$$K(x, z; x_0, z_0) = \lim_{N \rightarrow \infty} \left( \frac{k}{j2\pi\varepsilon} \right)^{(N+1)/2} \int_{-\infty}^{+\infty} \cdots \int_{-\infty}^{+\infty} \prod_{i=1}^N dx_i \exp\{j\alpha f(\mathbf{x})\}, \quad (20.28)$$

where  $N$  is the number of intermediate steps, each of length  $\varepsilon = (z - z_0)/(N + 1)$ ,  $\alpha = k/(2\varepsilon)$ , and the phase function  $f(\mathbf{x})$  is given by

$$f(\mathbf{x}) = \sum_{i=1}^{N+1} (x_i - x_{i-1})^2 + \frac{\varepsilon^2}{2} \sum_{i=0}^{N+1} (n^2(x_i) - 1). \quad (20.29)$$

In Eqs. (20.28) and (20.29), we have used vector  $\mathbf{x}$  to denote an ordered sequence of the intermediate coordinates  $x_1, x_2, \dots, x_N$ .

Since the exponent in Eq. (20.28) is purely imaginary, the severe phase oscillations of the integrand make it very difficult to perform numerical integration by using an ordinary Monte Carlo technique. The SPMC method has been developed to evaluate nested integrals of this type by the introduction of a filter. The filter, designed to sample the integrand more densely in regions where the phase interference is constructive, is

$$\Lambda(\mathbf{x}) = \int_{-\infty}^{+\infty} dx' P(\mathbf{x}') e^{i\alpha[f(\mathbf{x}-\mathbf{x}')-f(\mathbf{x})]}, \quad (20.30)$$

where  $P(\mathbf{x})$  is an arbitrary normalized probability distribution. Unfortunately, the probability distribution filters are difficult to implement in more than one dimension, and stability problems persist. However, a versatile and accurate Monte Carlo evaluation of the multidimensional path integral can be accomplished based on the following line of reasoning: First, it is apparent that, while the first term in the

phase function in Eq. (20.29) corresponds to the free-space contribution, the second term in Eq. (20.29) is due to the inhomogeneity of the electromagnetic system. Secondly, the free-space path integral can be evaluated exactly and therefore, by choosing an appropriate distribution function, the free-space part of the difference term  $f(\mathbf{x} - \mathbf{x}') - f(\mathbf{x})$  can also be exactly calculated. Thus, approximation is only required when evaluating terms that include index of refraction.

An appropriate distribution function is [22]

$$P(\mathbf{x}) = \sqrt{\frac{N+1}{\pi^N \delta^{2N}}} \exp \left\{ -\frac{1}{\delta^2} \sum_{i=1}^{N+1} (x_i - x_{i-1})^2 \right\} \tag{20.31}$$

with  $x_0 = x_{N+1} = 0$ . When Eq. (20.31) is substituted into Eq. (20.30), the free-space part of the difference between  $f(x - x')$  and  $f(x)$  can be obtained exactly, and the phase function difference associated with the inhomogeneity of the medium can be found by the first gradient approximation. The resulting analytical expression for the filter is

$$\Lambda(x) = \sqrt{\frac{1}{(1 - j\alpha\delta^2)^N}} \exp \left\{ \frac{\alpha^2\delta^2}{1 - j\alpha\delta^2} (x^2 + x_0^2) \right\} \Lambda_S(\mathbf{x}) \Lambda_G(\mathbf{x}), \tag{20.32}$$

where  $\Lambda_S(x)$  is the free-space filter given by

$$\Lambda_S(x) = \exp \left\{ -\frac{(\alpha\delta)^2}{1 + (\alpha\delta)^2} \sum_{i=1}^{N+1} (x_i - x_{i-1})^2 \right\} \tag{20.33}$$

and  $\Lambda_G(x)$ , the filter due to the inhomogeneity, is

$$\begin{aligned} \Lambda_G(x) = \exp \left\{ -\frac{j\alpha^3\delta^4}{1 + \alpha^2\delta^4} \sum_{i=1}^{N+1} (x_i - x_{i-1})^2 - \frac{\alpha^2\delta^2}{1 - j\alpha\delta^2} \sum_{i=1}^N q_i x_i \right\} \\ \cdot \exp \left\{ \sum_{m=1}^{N-1} \frac{(\sum_{n=1}^m \frac{np_n}{2})^2}{m(m+1)b} + \frac{b}{N(N+1)} \left( \frac{j\alpha Nx}{1/\delta^2 - j\alpha} - \sum_{m=1}^N \frac{mp_m}{2b} \right)^2 \right\}. \end{aligned} \tag{20.34}$$

In Eq. (20.34), we have used the following quantities for convenience:

$$\left. \begin{aligned} b &= \frac{1}{\delta^2} - j\alpha \\ q_i &= \frac{\partial}{\partial x_i} \left\{ \frac{\epsilon^2}{2} \sum_{j=1}^{N+1} g_j [n^2(x_j) - 1] \right\} \\ p_i &= j\alpha q_i - \frac{j b \alpha x_0}{1/\delta^2 - j\alpha} \delta_{1i} \end{aligned} \right\}. \tag{20.35}$$

The filter in Eq. (20.32) thus enables us to find the solution to the propagator in Eq. (20.28) by the Monte Carlo technique. If one chooses to use  $\Lambda_S(x)$  as the actual sampling function, then the final expression for the propagator in the Monte Carlo calculation is

$$K(x, z; x_0, z_0) = \lim_{N \rightarrow \infty} g(x, x_0) \left\langle \Lambda_G(x) e^{j\alpha f(x)} \right\rangle_{\Lambda_S(x)}, \quad (20.36)$$

where the coefficient

$$g(x, x_0) = \sqrt{\frac{\alpha \left( \frac{1}{j\alpha\delta^2 + 1} \right)^N}{j\pi(N+1)}} \cdot \exp \left\{ -\frac{\alpha^2\delta^2}{1 + \alpha^2\delta^4} \frac{(x - x_0)^2}{N+1} + \frac{\alpha^2\delta^2}{1 - j\alpha\delta^2} (x^2 + x_0^2) \right\}. \quad (20.37)$$

Equations (20.34) and (20.36) give the complete expression for the propagator of a general electromagnetic system with smoothly varying indices of refraction. It can be seen from Eq. (20.37) that the coefficient  $g(x, x_0)$  of our Monte Carlo formulation for the propagator does not have a strong dependence on the choice of parameters since  $\alpha$  is in general very large, and hence the coefficient in front of the complex exponential is almost a constant regardless of the choice of  $\delta$ .

### 20.3.2 Results for the SPMC Method

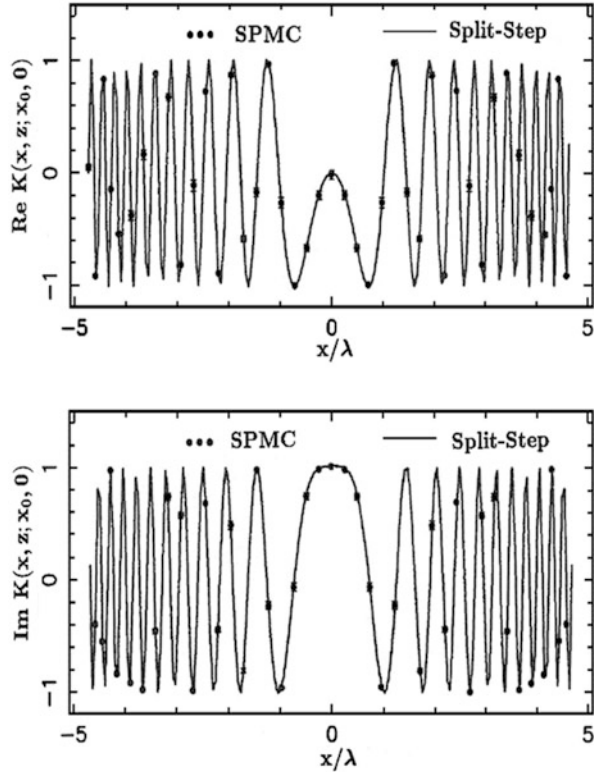
Microwave and optical integrated circuits are often constructed in transversely inhomogeneous wave-guiding structures referred to as graded-index waveguides [19]. A graded-index waveguide is typically approximated by a Gaussian-type refractive index profile. As an example, consider a two-dimensional waveguide with a transverse ( $x$ -) direction refractive index

$$n^2(x) = 1 + \Delta \exp \left\{ -\frac{x^2}{2\rho_x^2} \right\}, \quad (20.38)$$

where  $\Delta$  is the amplitude and  $\rho_x$  is the width of the waveguide. As the magnitude of  $x$  increases from 0 to  $\infty$ ,  $n^2(x)$  decreases smoothly from  $1 + \Delta$  to 1 (the index of refraction for air). Sample results shown in Figs. 20.3 and 20.4 are for a refractive index with  $\Delta = 0.75$  and  $\rho_x = \sqrt{5/2}\lambda$ , where  $\lambda$  is the free-space wavelength of the electromagnetic field. The SPMC parameters are chosen to be  $\delta = 1.90\lambda$ ,  $l = 0.002\lambda$ ,  $M = 100,000$ , and  $N = 40$  for  $z - z_0 = 1.0\lambda$ . The split-step path integral method [19] is used to validate our numerical results. The split-step method is based on the phase-space path integral formulation and has been developed for solving general one- and two-dimensional electromagnetic propagation configurations.

The transverse ( $x$ -) direction field pattern at a distance  $z = 1\lambda$  in the longitudinal direction from the origin is plotted in Fig. 20.3. This figure clearly shows that the field is concentrated at the center of the guide where the refractive index is at a

**Fig. 20.3** Real and imaginary parts of the field at  $z = 1\lambda$  as a function of the transverse direction  $x$  with  $\Delta = 0.75$  and  $\rho_x = \sqrt{5/2}\lambda$  (Adapted from Ref. [22] © IEEE)

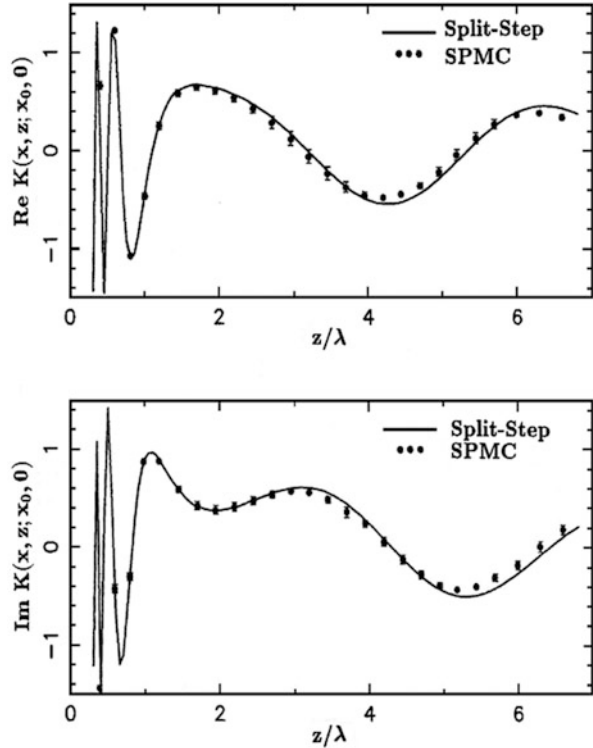


maximum. Figure 20.4 illustrates the evolution of the field along the direction of propagation of an observation point,  $x_f = 0.5\lambda$ , outside the core region. This result shows that the field essentially bounces in and out of the core region similar to the case in a homogeneous waveguide with PEC walls. This nonuniform dielectric generalization achieved by the SPMC method is not easily accomplished with classical techniques. In both figures, the SPMC and split-step method [19] results are virtually identical. The SPMC method also demonstrated remarkable stability with respect to changes in the numerical algorithm parameters.

### 20.3.3 Conclusions Concerning the SPMC Method

We have reviewed the stationary-phase Monte Carlo propagator method for calculating the electromagnetic field in a transversely inhomogeneous medium. In this method, the electric field is expressed in terms of a convolution of the initial field and a path integral propagator developed directly from the Helmholtz equation. The series of nested propagator integrals are evaluated by applying a mathematical filter designed to overcome the difficulties associated with multidimensional Monte Carlo integration over an integrand consisting of a pure-phase term. Although

**Fig. 20.4** Real and imaginary parts of the field at  $x = 0.5\lambda$  as a function of the propagation distance  $z$  with  $\Delta = 0.75$  and  $\rho_x = \sqrt{5/2}\lambda$  (Adapted from Ref. [22] © IEEE)



sample results presented here are computed for the graded-index waveguides, by only specifying the electric permittivity distribution in space, virtually any paraxial propagation configuration with a transversely inhomogeneous medium can be analyzed without changing the filter expression. However, the SPMC method, as well as the FTPI method, can only solve electromagnetics problems in one and two dimensions, due to the vector nature of the electromagnetic field. The FTPI method can solve for the total (i.e., incident plus scattered) electromagnetic field. The SPMC method is better suited for in a transversely inhomogeneous region, where the index of refraction is a smoothly varying function of position, but it is only valid for one-way propagation, i.e., it does not provide the backscattered field. Both methods can be used to find the scalar field of quantum electrodynamics in one, two, or three dimensions.

## 20.4 Path Integral Time-Domain (PITD) Method

The FTPI and the SPMC methods are frequency-domain techniques that are solutions to Helmholtz equation. However, in order to apply path integral methods, the Helmholtz equation must be converted to a hyperbolic equation. A hyper-

bolic equation, similar to the Schrödinger equation, for the electromagnetic field is obtained for the FTPI method by hypothesizing a first-order artificial time derivative, and for the SPMC method, approximations are made in the Helmholtz equation by taking advantage of a slowly varying permittivity in an inhomogeneous medium. Although adequate for two-dimensional or two-and-a-half-dimensional (i.e., rotationally symmetric) wave propagation, these methods are computationally time consuming, are restricted to the frequency domain, and are not sufficient for full-wave three-dimensional electromagnetic scattering analysis. The path integral time-domain (PITD) method described below is a full-wave time-domain technique that avoids these constraints [23].

### 20.4.1 PITD Analysis

In a source-free homogeneous region, the time-domain Maxwell curl equations in terms of the electric and magnetic field intensities,  $\mathbf{E}$  and  $\mathbf{H}$ , are

$$\frac{\partial \mathbf{E}}{\partial t} = \frac{1}{\varepsilon} \nabla \times \mathbf{H}, \quad (20.39)$$

$$\frac{\partial \mathbf{H}}{\partial t} = -\frac{1}{\mu} \nabla \times \mathbf{E}. \quad (20.40)$$

Equations (20.39) and (20.40) can be cast in the general matrix form

$$\frac{\partial \mathbf{F}}{\partial t} = \bar{\mathbf{S}} \mathbf{F} \quad (20.41)$$

with the field vector  $\mathbf{F}$  defined by

$$\mathbf{F} = [E_x \ E_y \ E_z \ H_x \ H_y \ H_z]^T \quad (20.42)$$

and the  $6 \times 6$  matrix operator expressed symbolically by

$$\bar{\mathbf{S}} = \begin{bmatrix} \bar{\mathbf{0}} & \frac{1}{\varepsilon} \nabla \times \\ -\frac{1}{\mu} \nabla \times & \bar{\mathbf{0}} \end{bmatrix}, \quad (20.43)$$

where  $\bar{\mathbf{0}}$  is a  $3 \times 3$  null matrix. The solution to Eq. (20.41) can be placed in path integral form by first finding a propagator matrix  $\bar{\mathbf{K}}(\mathbf{r}, \mathbf{r}'; t, t')$  that satisfies the matrix equation

$$\frac{\partial \bar{\mathbf{K}}}{\partial t} - \bar{\mathbf{S}} \bar{\mathbf{K}} = 0 \quad (20.44)$$

subject to the initial condition

$$\lim_{t \rightarrow t'} \bar{\mathbf{K}} = \bar{\mathbf{I}} \delta(\mathbf{r} - \mathbf{r}') \quad (20.45)$$

and the Sommerfeld condition

$$\bar{\mathbf{K}} \rightarrow 0, \quad \text{as } |\mathbf{r}| \rightarrow \infty. \quad (20.46)$$

Here  $\bar{\mathbf{I}}$  is the identity matrix,  $t'$  and  $t$ , respectively, are the initial and final times,  $\delta(\mathbf{r} - \mathbf{r}')$  is the Dirac delta function, and  $\mathbf{r}'$  and  $\mathbf{r}$  are the initial and final spatial positions with  $\mathbf{r} = x\hat{\mathbf{x}} + y\hat{\mathbf{y}} + z\hat{\mathbf{z}}$ .

Condition (20.45) is the feature that distinguishes a propagator Green function from all other Green functions. Other Green functions would have a delta function on the right-hand side of Eq. (20.44). However, such Green functions are not unitary, whereas a propagator is assured of being unitary through condition (20.45). Unitarity is the property that allows a propagator to act on a field to produce the field at a later time without loss of energy.

By substitution, it can be shown that a solution to Eq. (20.44) is

$$\bar{\mathbf{K}} = e^{\bar{\mathbf{S}}t} \bar{\mathbf{K}}_0 \quad (20.47)$$

The coefficient  $\bar{\mathbf{K}}_0$  can be found by enforcing Eq. (20.45), which gives

$$\bar{\mathbf{K}} = e^{\bar{\mathbf{S}}(t-t')} \delta(\mathbf{r} - \mathbf{r}'). \quad (20.48)$$

An inverse Fourier transform representation of the delta function in Eq. (20.48)

$$\delta(\mathbf{r} - \mathbf{r}') = \frac{1}{(2\pi)^3} \int_{-\infty}^{\infty} e^{j\mathbf{k} \cdot (\mathbf{r} - \mathbf{r}')} d\mathbf{k} \quad (20.49)$$

gives the complete propagator expression

$$\bar{\mathbf{K}} = \frac{1}{(2\pi)^3} \int_{-\infty}^{\infty} e^{\bar{\mathbf{S}}\tau} e^{j\mathbf{k} \cdot (\mathbf{r} - \mathbf{r}')} d\mathbf{k}. \quad (20.50)$$

Here  $\tau = t - t'$  is the time increment between the initial and final times. The differential  $d\mathbf{k} = dk_x dk_y dk_z$  and  $\mathbf{k} = k_x \hat{\mathbf{x}} + k_y \hat{\mathbf{y}} + k_z \hat{\mathbf{z}}$  are in terms of the spatial frequency components  $k_x$ ,  $k_y$  and  $k_z$ .

The matrix exponential  $e^{\bar{\mathbf{S}}\tau}$  is then expanded as the power series

$$e^{\bar{\mathbf{S}}\tau} = \bar{\mathbf{I}} + \bar{\mathbf{S}}\tau + \bar{\mathbf{S}}^2 \tau^2 / 2! + \bar{\mathbf{S}}^3 \tau^3 / 3! + \dots, \quad (20.51)$$



each term of which is allowed to operate on the Fourier basis function  $e^{j\mathbf{k}\cdot\mathbf{r}}$ . This operation creates a new matrix  $\overline{\mathbf{S}}(\mathbf{r}, \mathbf{k})$  in which the differential operators are replaced according to  $\partial/\partial x \rightarrow jk_x$ ,  $\partial/\partial y \rightarrow jk_y$ , and  $\partial/\partial z \rightarrow jk_z$ . The series is summed, producing a matrix exponential  $e^{\overline{\mathbf{S}}(\mathbf{r}, \mathbf{k}) \tau}$ .

Next the eigenvalue method [24] is used to reduce the matrix exponential  $e^{\overline{\mathbf{S}}(\mathbf{r}, \mathbf{k}) \tau}$  to a standard  $6 \times 6$  matrix  $\overline{\mathbf{A}}(\mathbf{r}, \mathbf{k})$ . The eigenvalue method consists of first finding the eigenvalues and the corresponding eigenvectors of  $\overline{\mathbf{S}}(\mathbf{r}, \mathbf{k})$ . The eigenvectors comprise the modal matrix  $\overline{\mathbf{M}}$ , and the eigenvalues  $\lambda_i$  are incorporated in  $e^{\lambda_i \tau}$  which form the diagonal matrix  $\overline{\mathbf{P}}(\lambda)$ . The matrix  $\overline{\mathbf{A}}$  can then be found by taking the matrix product,

$$\overline{\mathbf{A}} = \overline{\mathbf{M}}\overline{\mathbf{P}}(\lambda)\overline{\mathbf{M}}^{-1}. \tag{20.52}$$

The result is remarkably simple  $\overline{\mathbf{A}}$  matrix components, for example,

$$A_{11} = A_{44} = [k_x^2 + (k_y^2 + k_z^2) \cos(kv\tau)]/k^2, \tag{20.53}$$

where  $k^2 = k_x^2 + k_y^2 + k_z^2$  and  $v = 1/\sqrt{\mu\varepsilon}$  are the phase velocity, which is a function of position in a medium that is inhomogeneous.

The initial field  $\mathbf{F}_0$  in a region can be propagated by one-time increment  $\tau$  by evaluating

$$\mathbf{F}(\mathbf{r}, t) = \int_{-\infty}^{\infty} \overline{\mathbf{K}}(\mathbf{r}, \mathbf{r}'; \tau) \mathbf{F}_0(\mathbf{r}', t') d\mathbf{r}', \tag{20.54}$$

where  $d\mathbf{r}' = dx' dy' dz'$ . A general propagator equation, with  $e^{\overline{\mathbf{S}}\tau}$  replaced by  $\overline{\mathbf{A}}$ , is obtained by substituting Eq. (20.50) into Eq. (20.54) above and interchanging the order of integration, yielding

$$\mathbf{F}(\mathbf{r}, t) = \frac{1}{(2\pi)^3} \int_{-\infty}^{\infty} \overline{\mathbf{A}}(\mathbf{r}, \mathbf{k}) \left[ \int_{-\infty}^{\infty} \mathbf{F}_0(\mathbf{r}', t') e^{-j\mathbf{k}\cdot\mathbf{r}'} d\mathbf{r}' \right] e^{j\mathbf{k}\cdot\mathbf{r}} d\mathbf{k}. \tag{20.55}$$

Equation (20.55) reveals that propagation of the field in an inhomogeneous region can be performed by a spatial Fourier transform of the initial field  $\mathbf{F}_0$ , multiplication of the result by the matrix  $\overline{\mathbf{A}}$ , and followed by spatial frequency domain inverse Fourier transformation. Because this is an operation that evolves the wave in both space and time,  $\overline{\mathbf{A}}$  is referred to as an *evolution operator* or as a *transition matrix*. Equation (20.55) is all that is needed to propagate the field through a single time period  $\tau$ . The resulting time-stepped field  $\mathbf{F}$  then becomes the new initial field  $\mathbf{F}_0$  ready to be propagated by another time increment. The complete expression for a field that has evolved through  $N$  successive time iterations

starting at  $t' = t_0$  and ending at time  $t$  is known as a path integral. However, this form to the path integral is exact because it does not depend on the Trotter product formula, i.e., the time increment can be of any extent and is independent of the number of nested iterations. The path integral for time evolution of the electromagnetic field, found by successive applications of Eq. (20.55), can be expressed as a nested sequence of forward,  $\mathcal{F}$ , and inverse,  $\mathcal{F}^{-1}$ , Fourier transforms, written symbolically as

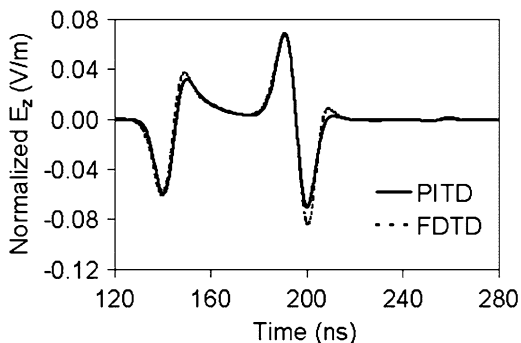
$$F(\mathbf{r}, t) = \frac{1}{(2\pi)^{3N}} \mathcal{F}^{-1} \left\{ \bar{\mathbf{A}} \mathcal{F} \left\{ \mathcal{F}^{-1} \left\{ \bar{\mathbf{A}} \dots \mathcal{F} \left\{ \mathcal{F}^{-1} \left\{ \bar{\mathbf{A}} \mathcal{F} \{F_0(\mathbf{r}_0, t_0)\} \right\} \dots \right\} \right\} \right\} \right\}. \tag{20.56}$$

One observation concerning the FTPI method is brought out in Eq. (20.56) where, after multiplication by the evolution operator, there is a Fourier transform followed immediately by an inverse Fourier transform, the combination of which seems unproductive. The reason for retaining this Fourier combination is that boundary conditions must be implemented on conductors and dielectrics in the numerical region at the interval between these Fourier operations.

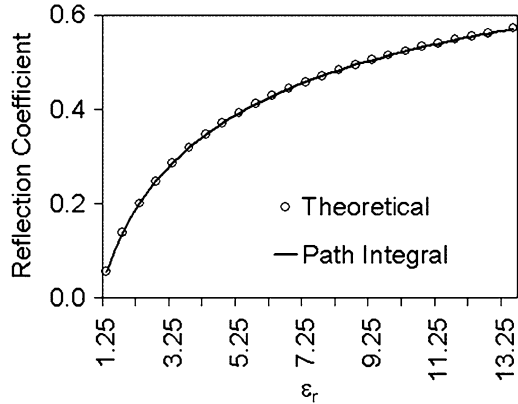
### 20.4.2 Numerical Results for the PITD Method

Figure 20.5 shows the history of the  $E_z$  component of the total electric field collected at  $x = 31.5$  m and  $y = 29.0$  m in front of a rectangular dielectric cylinder. The cylinder has a relative permittivity  $\epsilon_r = 1.75$  and is positioned between  $34 \text{ m} \leq x \leq 40 \text{ m}$  and  $34 \text{ m} \leq y \leq 40 \text{ m}$  in a numerical space of  $63.75 \text{ m}^2$  centered at the origin. Comparison is made with the same field component calculated with the FDTD method under the same conditions. The incident field is a transverse electric (TM) plane wave traveling in the x-direction and containing a Gaussian profile in time  $\exp[-(n - 4\beta)^2/\beta^2]$  where  $n$  is the time step. The numerical space grid size is  $\Delta x = \Delta y = 0.25 \text{ m}$ , and the time step is  $\Delta t = \Delta x/c$  and  $\Delta t = \Delta x/(2c)$

**Fig. 20.5** The time history of the  $E_z$  component of the total electric field due to a plane wave Gaussian pulse incident on a rectangular dielectric cylinder (Adapted from Ref. [23]© IEEE)



**Fig. 20.6** Reflection coefficient as a function of dielectric constant for the one-dimensional case of a plane wave incident on a dielectric half-space (Adapted from Ref. [23] © IEEE)



for PITD and FDTD methods, respectively. The difference between the results obtained by these two methods can be attributed to dispersion in the high-frequency FDTD components and a lack of accuracy in numerical FFTs at the dielectric-air discontinuity.

The reflection coefficient for a plane wave propagating in air and reflected from a dielectric half-space with progressively larger relative permittivity is pictured in Fig. 20.6. Comparison is made between the PITD method and exact calculation. There is virtually no difference between the two calculations. This shows that the PITD method can handle cases where a variety of material objects can be modeled in a numerical space without significant error being created due to the differences in material properties.

### 20.4.3 Conclusions Concerning the PITD Method

The numerical implementation of Eq. (20.56) has several positive assets. It is a full-wave time-domain solution for the electromagnetic field, it is relatively simple to implement, and both the electric and magnetic field components are computed at each time step. Also, because an analytical Fourier transform is a unitary transformation, the numerical FFT is at least conditionally stable and is unconditionally stable with a small added loss. As with the FTPI and SPMC methods, numerical filters can reduce aliasing associated with FFTs. The negative aspects of the PITD method primarily stem from problems with three-dimensional implementation including difficulties in handling discontinuities between dielectric regions and corners of the numerical region with the three-dimensional fast Fourier transform and in the development of an effective filter to reduce aliasing.

One possibility for future research is to apply the FTPI method to *one-way* time-domain propagation cases where the medium has a slowly varying index of

refraction, such as the atmosphere and dielectric waveguides. Such conditions may allow the removal of the Fourier transform pair, leaving a product of  $\bar{\mathbf{A}}$  matrices that perform the task of evolving the field through a series of time steps, similar to the ABCD matrices [25] in circuit analysis.

## 20.5 The Propagator Method (PM)

Unlike the FTPI and SPMC methods, both of which rely upon the Trotter product approximation to form the propagator, both the PITD method and the propagator method (PM) contain un-approximated expressions for the propagator. In fact, the PM can be developed in the same manner as the PITD method up through Eq. (20.55). However, an important step was taken when it was discovered that all spatial frequency ( $\mathbf{k}$ -) domain integrals over the terms in the  $\bar{\mathbf{A}}$  matrix in Eq. (20.55) produce analytical expressions [26, 27]. In this section, we present the exact closed-form propagator for Maxwell's equations. The general propagator matrix can then be used to obtain the electromagnetic field in each of the three spatial dimensions. Analytical and numerical examples are presented for a propagating plane wave.

### 20.5.1 PM Analysis

The order of integration in the PITD propagator equation

$$\mathbf{F}(\mathbf{r}, t) = \frac{1}{(2\pi)^3} \int_{-\infty}^{\infty} \bar{\mathbf{A}}(\mathbf{r}, \mathbf{k}) \left[ \int_{-\infty}^{\infty} \mathbf{F}_0(\mathbf{r}', t') e^{-j\mathbf{k}\cdot\mathbf{r}'} d\mathbf{r}' \right] e^{j\mathbf{k}\cdot\mathbf{r}} d\mathbf{k} \quad (20.57)$$

is changed thereby forming the coupled field propagator equation

$$\mathbf{F}(\mathbf{r}, t) = \int_{V'} \bar{\mathbf{K}}(\mathbf{r}, t|\mathbf{r}', t_0) \cdot \mathbf{F}_0(\mathbf{r}', t_0) d\mathbf{r}', \quad (20.58)$$

where

$$\bar{\mathbf{K}}(\mathbf{r}, t|\mathbf{r}', t') = \int_{-\infty}^{\infty} \bar{\mathbf{A}}(t, \mathbf{k}) e^{j\mathbf{k}\cdot(\mathbf{r}-\mathbf{r}')} d\mathbf{k}; \quad \mathbf{F} = [E_x \ E_y \ E_z \ H_x \ H_y \ H_z]^T. \quad (20.59)$$

The analytical expression for the propagator found by evaluating Eq. (20.59) is a single expression that travels forward in time when  $t > 0$  and backward in time when  $t < 0$ . This emphasizes the difference between the classical definitions of a

propagator and a Green function. A propagator is the solution to the homogeneous differential equation

$$\frac{\partial \bar{\mathbf{K}}}{\partial t} - \bar{\mathbf{S}} \cdot \bar{\mathbf{K}} = 0 \quad (20.60)$$

subject to

$$\bar{\mathbf{K}}(\mathbf{r}, t' | \mathbf{r}', t') = \bar{\mathbf{I}} \delta(\mathbf{r} - \mathbf{r}'), \quad \text{at time } t = t', \quad (20.61)$$

and the Sommerfeld condition  $\bar{\mathbf{K}} \rightarrow 0$ , as  $|\mathbf{r}| \rightarrow \infty$ . However, from a mathematical standpoint, a Green function is a solution to the nonhomogeneous differential equation

$$\frac{\partial \bar{\mathbf{G}}}{\partial t} - \bar{\mathbf{S}} \cdot \bar{\mathbf{G}} = \bar{\mathbf{I}} \delta(\mathbf{r} - \mathbf{r}') \delta(t - t'), \quad t > 0. \quad (20.62)$$

The relationship between the propagator and the Green function is

$$\bar{\mathbf{G}}(\mathbf{r}, t | \mathbf{r}', t') = U(t - t') \bar{\mathbf{K}}(\mathbf{r}, t | \mathbf{r}', t'), \quad (20.63)$$

where the unit step function

$$U(t - t') = \begin{cases} 0, & t < t' \\ 1, & t > t' \end{cases} \quad (20.64)$$

enforces causality in the sense that the wave traveling forward in time is determined by the  $t > 0$  part of the propagator. According to Eq. (20.63), a Green function  $\bar{\mathbf{G}}$  is called for in our calculations. It is, however, common practice in physics to refer to Eq. (20.58) as a propagator equation and to retain the symbol  $\bar{\mathbf{K}}$  when using only the  $t > 0$  portion of the propagator. Here we will use the mathematical terminology in Eq. (20.63).

The  $6 \times 6$  tensor Green function propagator  $\bar{\mathbf{G}}$  is expressed in terms of four related  $3 \times 3$  sub matrices as

$$\bar{\mathbf{G}} = \begin{bmatrix} \bar{\mathbf{G}}_{11} & \bar{\mathbf{G}}_{12} \\ \bar{\mathbf{G}}_{21} & \bar{\mathbf{G}}_{22} \end{bmatrix}. \quad (20.65)$$

The submatrices have been shown to have the exact closed-form expressions [22, 23],

$$\bar{\mathbf{G}}_{11} = \bar{\mathbf{G}}_{22} = \frac{\delta'(c\tau - R)}{4\pi R} \bar{\mathbf{I}} - \nabla \nabla \frac{[U(c\tau - R) - U(-R)]}{4\pi R}, \quad (20.66)$$

$$\bar{\mathbf{G}}_{12} = -\eta^2 \bar{\mathbf{G}}_{21} = \eta \nabla \times \frac{\delta(c\tau - R)}{4\pi R} \bar{\mathbf{I}}, \quad (20.67)$$

where  $\bar{\mathbf{I}}$  is a  $3 \times 3$  identity matrix. A key observation is that the  $\nabla \nabla$  term in Eq. (20.66) is not needed outside the source region [28]. Therefore, if the initial field is given in a volume region, only Eq. (20.67) and the first term on the right-hand side in Eq. (20.66) are required in order to propagate the field one time step. The final and most compact form of the propagator equation is now

$$\mathbf{F}(\mathbf{r}, t) = \int_{V'} \bar{\mathbf{G}}(\mathbf{r}, t | \mathbf{r}', t_0) \cdot \mathbf{F}_0(\mathbf{r}', t_0) d\mathbf{r}' \quad (20.68)$$

with the closed-form expressions in Eqs. (20.66) and (20.67). At the initial time  $t_0$  the initial field  $\mathbf{F}_0$  can be a plane wave, an antenna current, a waveguide mode, a plasmonic surface wave, an aperture source, or any given field throughout a volume.

## 20.5.2 Analytical Example of the Propagator Method

For many initial field distributions, Eq. (20.68) can be solved analytically because it is a solution to Maxwell's equations in a homogeneous region. In the following, an example where Eq. (20.68) can be evaluated analytically is presented. Assume an initial time-domain plane wave field with unity amplitude given by

$$E_{xo} = \cos(\omega t - kz) = \cos(\omega t - kr \cos \theta) \quad (20.69)$$

with  $H_{yo} = E_{xo}/\eta$ . Because in one-dimensional, there are only two terms  $E_{xo}$  and  $H_{yo}$  in the  $\mathbf{F}_0$  vector; only the first and fifth terms in the first row of the  $6 \times 6$  Green function matrix are required in the update expression for the  $E_x$  component of the electric field [26]

$$E_x(\mathbf{r}, t) = \int_{vol} \left( G_{11}(\mathbf{r}, t | \mathbf{r}', t') + G_{15}(\mathbf{r}, t | \mathbf{r}', t')/\eta \right) E_{xo}(\mathbf{r}', t') d\mathbf{r}'. \quad (20.70)$$

With the Green function components inserted into Eq. (20.70), the resulting equation in spherical  $(r, \theta, \phi)$  coordinates, with  $c\tau \doteq r_o$ ,  $\tau = t - t_o$ , and  $a \doteq \omega t$ , becomes

$$E_x(\mathbf{r}_o, t) = \int_v \left\{ \frac{\delta'(r_o - r')}{4\pi r'} + \left[ \frac{\delta(r_o - r')}{4\pi r'^2} + \frac{\delta'(r_o - r')}{4\pi r'} \right] \cos \theta' \right\} \cos(a - kr' \cos \theta') dv' \quad (20.71)$$

The result of this integration is

$$\begin{aligned}
 E_x(\mathbf{r}_o, t) &= \cos a \cos(kr_o) + \sin a \left[ \frac{\sin(kr_o)}{(kr_o)^2} - \frac{\cos(kr_o)}{kr_o} \right] \\
 &\quad - \sin a \left[ \frac{\sin(kr_o)}{(kr_o)^2} - \frac{\cos(kr_o)}{kr_o} \right] + \sin a \sin(kr_o) \cdot \\
 &= \cos(\omega t - kr_o \cos 0^\circ) = \cos(\omega t - kz_o)
 \end{aligned} \tag{20.72}$$

The first and second terms after the first equality sign in Eq. (20.72) are, respectively, from the first and second delta function terms in Eq. (20.71). The third and fourth terms on the right-hand side for Eq. (20.72) are from the third delta function term in Eq. (20.71). This result shows that the Green function propagator has advanced the electromagnetic plane wave from its initial position  $r' = 0$  at time  $t_0$  to the surface of a sphere along the  $z$ -axis at the point  $z_0$  at a later time  $t$ .

The key to creating an effective propagator numerical method capable of handling propagation and scattering in inhomogeneous regions lies both in the numerical evaluation of the volume integral in Eq. (20.68) and in enforcing stability conditions on that numerical expression. The dyadic Green function, containing the vector and generalized function operations embodied in Eqs. (20.66) and (20.67), presents a high level of difficulty. Over the last several years, many complications inherent in evaluating Eq. (20.68) have been overcome, yielding a relatively simple set of working numerical equations in one, two, and three dimensions. In one dimension, the propagator becomes a  $2 \times 2$  matrix of delta functions, readily reducing Eq. (20.68) to

$$\begin{aligned}
 &\begin{bmatrix} E_x(z, t) \\ H_y(z, t) \end{bmatrix} \\
 &= \frac{1}{2} \begin{bmatrix} [E_{xo}(z + \Delta z) + E_{xo}(z - \Delta z)] & -\eta [H_{yo}(z + \Delta z) - H_{yo}(z - \Delta z)] \\ -[E_{xo}(z + \Delta z) - E_{xo}(z - \Delta z)] / \eta & [H_{yo}(z + \Delta z) + H_{yo}(z - \Delta z)] \end{bmatrix},
 \end{aligned} \tag{20.73}$$

which is the exact D'Alembert analytical solution for a coupled set of first-order differential equations. Although in the one-dimensional case the numerical expression is also an exact analytical expression, exact numerical expressions for two- and three-dimensional propagator equations are not possible. This is because the two- and three-dimensional cases require integration over a circle and the surface of a sphere, respectively, integrations which when performed numerically, with field values on a set of numerical grid points, cannot provide an exact analytical solution.

The PM has also been extended to include electromagnetic waves in lossy media, whether homogeneous or inhomogeneous [29]. One example, that of three coupled microstrip transmission lines having different conductor widths, is shown in Fig. 20.7a. For time-domain simulation, the microstrip lines are terminated by resistive loads  $Z_{S1} = Z_{S2} = Z_{S3} = 50\Omega$  and  $Z_{L1} = Z_{L2} = Z_{L3} = 100\Omega$ . Each fundamental mode of an applied input signal is represented by a set of three voltage sources. In

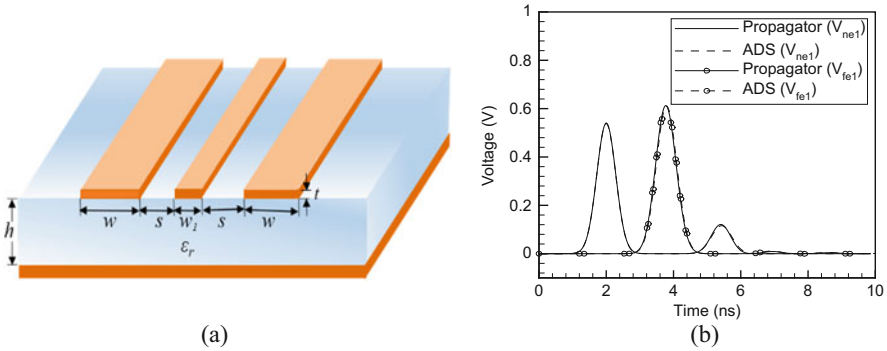


**Fig. 20.7** (a) Geometry of three coupled microstrip lines. (b) Voltage responses  $V_{ne2}$  at the input and  $V_{fe2}$  at the termination point of line 2 (Adapted from Ref. [29] © IEEE)

Fig. 20.7b, the transient response of the fundamental mode near the source end of the lines ( $V_{ne2}$ ) and at the termination end ( $V_{fe2}$ ) found by the propagator method are compared with those obtained using a circuit simulator software. In each case, the degree of accuracy is within 1%, but computation time has been reduced by an order of magnitude with the propagator method.

In two dimensions, a typical electric field numerical field expression is

$$E_z(i, j) = \frac{1}{4} [E_z(i + 1, j) + E_z(i - 1, j) + E_z(i, j + 1) + E_z(i, j - 1)] + \frac{\eta}{2\sqrt{2}} [H_y(i + 1, j) - H_y(i - 1, j)] - \frac{\eta}{2\sqrt{2}} [H_x(i, j + 1) - H_x(i, j - 1)] \tag{20.74}$$

where  $i$  and  $j$  refer to the respective  $x$ - and  $y$ -axis grid point positions.

Figure 20.8a shows a Gaussian pulse plane wave incident on a rectangular dielectric cylinder set in the upper right corner of the numerical space. In a sequence of time steps shown in Fig. 20.8b, the diffracted and scattered fields are as expected. Figure 20.8c is an overhead view of just the scattered electric field (total minus incident) with a comparison between the PM and the FDTD method at two different instances in time. The box is offset in the numerical space in order to clearly display the circular wave pattern leaving the corner of the box, demonstrating the accuracy of the normal and tangential boundary conditions on the front and lateral sides of the box, and to compare the effectiveness of the two absorbing boundary conditions shown at the top of the two figures. The results are virtually indistinguishable both visually and numerically, indicating that our boundary conditions are accurate in higher dimensions.

The three-dimensional propagator numerical method including the dispersion relation and stability condition has recently been developed. Several papers are being prepared and will be published shortly. A three-dimensional example of the electric field scattered by a square box due to an incident plane wave is shown in Figs. 20.9a, b, and c. This figure shows views of the scattered electric field in three orthogonal planes.



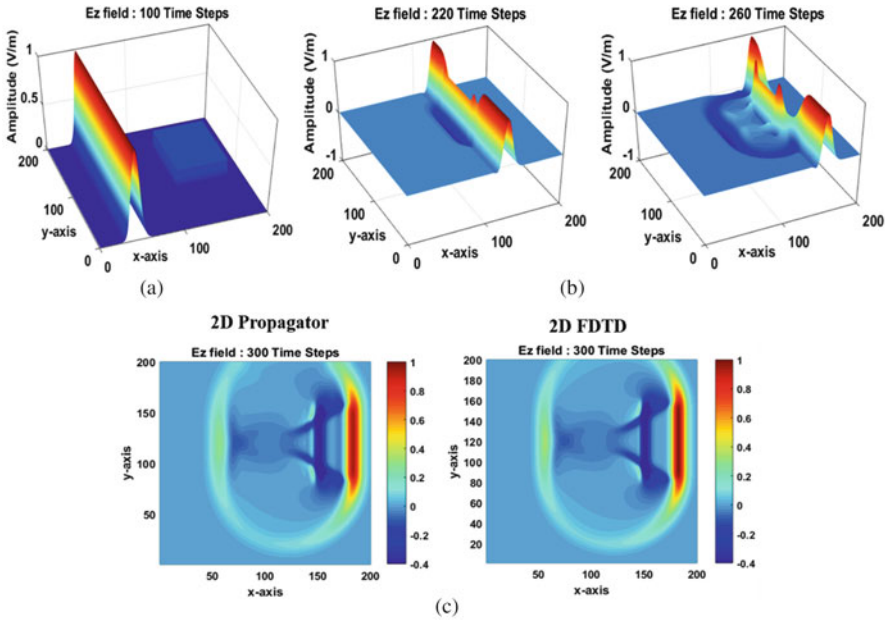


**Fig. 20.8** (a) Electric field of a Gaussian pulse plane wave in air propagating toward a two-dimensional dielectric cylinder box ( $\epsilon_r = 4$ ) in *upper right-hand corner*. (b) The field amplitude in a sequence of time steps. (c) Overhead view and comparison with the FDTD method

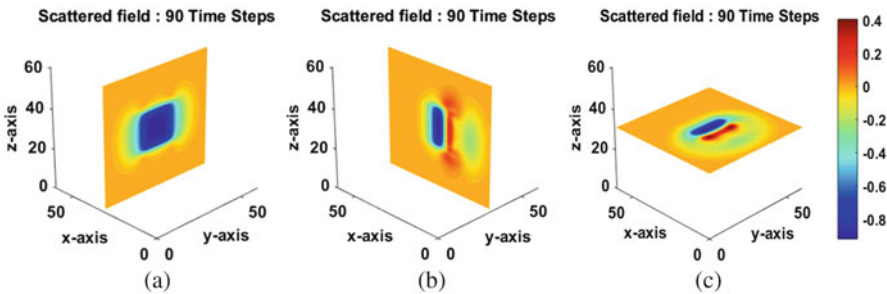


**Fig. 20.9** The  $x$ -,  $y$ -, and  $z$ -components of the three-dimensional electric field scattered from a square dielectric box shown, respectively, in the (a)  $y$ - $z$ , (b)  $x$ - $z$ , and (c)  $x$ - $y$  planes through the center of the box

### 20.5.3 Conclusions Concerning the PM

A primary advantage of a propagator method is that all six components of the electromagnetic field are coincident in time and space at all points in the numerical grid. This is different from integral equation methods and differential equation methods, such as the FDTD method, where the field components are not spatially

coincident and the electric and magnetic fields are not coincident in time. Propagator method coincidence offers the possibility of precise calculation of inductances and capacitances, equivalent current far fields, and seamless merging with the bio-heat equation for biological applications and with Schrödinger equation of quantum mechanics. Some success was had by converting earlier scalar and Fourier transform forms of the PM into numerical methods, including the FTPI, SPMC and PITD methods; however, the recent exact closed-form propagator, the development over the past 2 years of dielectric and PEC boundary conditions along with an effective first-order absorbing boundary condition [30], and the introduction of *numerical* and *physical* time concepts [30] have resulted in accurate one-, two-, and three-dimensional numerical electromagnetic scattering codes.

However, many issues remain:

- (1) The most natural numerical cell for PM is a sphere centered at a grid point that is to be updated and with a radius intersecting the six nearest neighbor grid points in a three-dimensional numerical space. The cells in a PM numerical lattice therefore overlap each other, and several cells may occupy the same space on a boundary between two different mediums. An effective conformal boundary condition is needed to clearly and accurately compute the field on an irregular boundary.
- (2) The null absorbing boundary condition we have described has an accuracy greater than 98% even when the wave enters the boundary at angles exceeding  $45^\circ$ . However, for practical applications, much higher accuracy is required. Methods for achieving higher-accuracy absorbing conditions are needed.
- (3) Complex valued numerical wave numbers can arise due to sharp signal discontinuities. The effect that complex wave numbers have on propagator method stability needs to be determined and is accompanied with the expectation of obtaining a lower bound on grid sampling density.
- (4) The capability of analyzing wave propagation in dispersive materials is a bottom-line necessity for any time-domain numerical method. This should be one of the key priorities in the development of the propagator method.

## References

1. R.P. Feynman, A.R. Hibbs, *Quantum Mechanics and Path Integrals* (McGraw-Hill, New York, 1965)
2. J. Schwinger, *Quantum Electrodynamics* (Dover, New York, 1958)
3. R. Oehme, W. Zimmermann, Quark and gluon propagators in quantum chromodynamics. *Phys. Rev. D* **21**, 471–484 (1980)
4. A. Arbouet, A. Mlayah, C. Girard, G.C. des Francs, Electron energy losses and cathodoluminescence from complex plasmonic nanostructures: Spectra, maps and radiation patterns from a generalized field propagator. *New J. Phys.* **16**, 113012 (2014)
5. P.W. Anderson, K.A. Muttalib, T.V. Ramakrishnan, Theory of the universal degradation of  $T_c$  in high-temperature superconductors. *Phys. Rev. B* **28**, 117–120 (1983)

6. X. Du, R.P. Fletcher, P.J. Fowler, Pure P-wave propagators versus pseudo-acoustic propagators for RTM in VTI media, in *72nd EAGE Conference and Exhibition Incorporating SPE EUROPEC*, Barcelona, June 2010
7. M. Badiey, I. Jaya, A.H.-D. Ching, Propagator matrix for plane wave reflection from inhomogeneous anisotropic poroelastic seafloor. *J. Comput. Acoust.* **2**, 11–27 (1994)
8. F. Gilbert, G.E. Backus, Propagator matrices in elastic wave and vibration problems. *Geophysics* **31**, 326–332 (1966)
9. H. Kleinert, *Path Integrals in Quantum Mechanics, Statistics, Polymer Physics, and Financial Markets* (World Scientific, Singapore, 1990)
10. L.S. Schulman, *Techniques and Applications of Path Integration* (Wiley, New York, 1981)
11. J.B. Keller, D.W. McLaughlin, The Feynman integral. *Am. Math. Mon.* **82**, 451–465 (1975)
12. A. Taflov, S. Hagness, *Computational Electrodynamics, The Finite-Difference Time-Domain Method*, 3rd edn. (Artech House, Boston, 2005)
13. R.F. Harrington, *Field Computation by Moment Methods* (Macmillan Co., New York, 1968)
14. J.M. Jin, *The Finite Element Method in Electromagnetics*, 3rd edn. (Wiley, Hoboken, NJ, 2014)
15. R.D. Nevels, C. Huang, Z. Wu, The Fourier transform path integral method, a numerical technique for scalar scattering in inhomogeneous regions. *IEE Proc. H* **140**, 488–492 (1993)
16. T. Kato, Trotter's product formula for some nonlinear semigroups, in *Nonlinear Evolution Equations*, M.G. Crandall (Ed.) (Academic Press, New York, 1977)
17. C. Huang, Z. Wu, R.D. Nevels, Edge diffraction in the vicinity of the tip of a composite wedge. *IEEE Trans. Geosci. Remote Sens.* **31**, 1044–1050 (1993)
18. E.O. Brigham, *The Fast Fourier Transform* (Prentice-Hall, Englewood Cliffs, NJ, 1974)
19. M.D. Feit, J.A. Fleck Jr., Light propagation in graded-index optical fibers. *Appl. Opt.* **17**, 3990–3998 (1978)
20. J.D. Doll, T.L. Beck, D.L. Freeman, Quantum Monte Carlo dynamics: The stationary phase Monte Carlo path integral calculation of finite temperature time correlation functions. *J. Chem. Phys.* **89**, 5753–5763 (1988)
21. Y.A. Rozanov, *Markov Random Fields* (Springer, New York, 1982)
22. C. Huang, Z. Wu, R.D. Nevels, Stationary phase Monte Carlo path integral analysis of electromagnetic wave propagation in graded-index waveguides. *IEEE Trans. Microw. Theory Tech.* **42**, 1709–1714 (1994)
23. R.D. Nevels, J.A. Miller, R.M. Miller, A path integral time domain method for electromagnetic scattering. *IEEE Trans. Antennas Propag.* **48**, 565–573 (2000)
24. P.M. Derusso, R.J. Roy, C.M. Close, *State Variables for Engineers* (Wiley, New York, 1965)
25. R.E. Collin, *Foundations for Microwave Engineering*, 2nd edn. (Wiley, New York, 2001)
26. R.D. Nevels, J. Jeong, Time domain Green's function and propagator for Maxwell's equations. *IEEE Trans. Antennas Propag.* **52**, 3012–3018 (2004)
27. R.D. Nevels, J. Jeong, Corrections to 'the complete free space Green's function and propagator for Maxwell's equations'. *IEEE Trans. Antennas Propag.* **56**, 1212–1213 (2008)
28. I.A. Maksoudi, H. Elkamchouchi, Complete time domain free space dyadic Green's function for Maxwell's equations, in *Proceedings of 26th National radio Science Conference*, Egypt, Mar 2009
29. J. Jeong, I.-P. Hong, R.D. Nevels, The time domain propagator method for lossless multiconductor quasi-TEM lines. *IEEE Trans. Adv. Packag.* **32**, 619–626 (2009)
30. J. Shin, R. Nevels, Recent progress in the development of a propagator method for electromagnetic fields, in *IEEE AP-S/URSI International Symposium on Antennas and Propagation*, Fajardo, Puerto Rico, June 2016



**Jongchul Shin** received the B.S. and M.S. degrees in electrical engineering from Hongik University, Seoul, Korea, in 2006 and 2012, respectively. He is currently working toward Ph.D. degree in electrical engineering at Texas A&M University, College Station, TX, USA. From 2006 to 2010, he was with GM Korea, Incheon, Korea, as an electrical engineer. His research interests are mathematical and numerical methods in electromagnetics and scattering problems.



**Robert D. Nevels** received a BSEE at the University of Kentucky, MSEE at Georgia Institute of Technology, and Ph.D. EE at the University of Mississippi. He is an IEEE Life Fellow and a Professor in Electrical Engineering at Texas A&M University in College Station, Texas. His interests include analytical and numerical methods in electromagnetics, antennas, scattering, and plasmonics. In 1992 he was a Visiting Professor in the Physics Department, Institute for Light Sources, Fudan University, Shanghai, China and, in 2015, a distinguished lecturer at the University of Electronic Science and Technology Summer School, Chengdu, China. Dr. Nevels has coauthored book chapters on “Wavelets,” “Gauges in Electromagnetics,” and “Nano-Antennas.” He has authored two monographs on gauge theory and its application to numerical methods in electromagnetics. He served as an editor of

the Wiley book series on *Microwave and Optical Components* in 1992 and again in 2003 and as an Associate Editor of the periodicals *IEEE Antennas and Propagation (AP-S) Transactions* and *Microwave and Optical Technology Letters*. Dr. Nevels was General Chairman of the 2002 IEEE AP-S/URSI Symposium and IEEE AP-S Society President-Elect in 2009 and President in 2010. He also served on the IEEE AP-S Administrative Committee from 1997 to 2000 and again from 2011 to 2015.

# Chapter 21

## Wave Propagation and Field Manipulation in Non-Hermitian Metamaterials

Silvio Savoia, Giuseppe Castaldi, and Vincenzo Galdi

### 21.1 Introduction and Background

In quantum mechanics, operators are conventionally assumed to be Hermitian, i.e., to coincide with their adjoint (Hermitian conjugate) operator. This assumption implies that the energy eigenspectra are inherently real-valued and the eigenfunctions form an orthonormal, complete set [1]. In a series of seminal papers [2–4], Bender and coworkers proposed a non-Hermitian extension of quantum mechanics in which such conventional assumption is replaced by a weaker condition based on the so-called *parity-time* ( $\mathcal{PT}$ ) symmetry. In essence, these studies focused on families of quantum potentials obeying the symmetry condition  $V(x) = V^*(-x)$ , which involves the combined parity (i.e., spatial reflection,  $\mathcal{P}$ ) and time-reversal (i.e., complex-conjugation,  $\mathcal{T}$ ) operator. Interestingly, they proved that, though non-Hermitian,  $\mathcal{PT}$ -symmetric systems can still exhibit entirely real-valued eigenspectra provided that their eigenstates are likewise  $\mathcal{PT}$ -symmetric. However, in view of the antilinear character of the  $\mathcal{PT}$  operator, this last condition typically holds only within a certain non-Hermiticity threshold, beyond which a  $\mathcal{PT}$ -symmetric system may undergo an abrupt phase transition to a complex eigenspectrum, typically referred to as spontaneous symmetry breaking [2–4].

Although certain aspects of the  $\mathcal{PT}$ -symmetric quantum-mechanics extension are still controversial (see, e.g., Refs. [5–7]), the general concepts are rather pervasive and have resonated in several research communities, triggering a surge of interest in the study of more general non-Hermitian systems. In particular, thanks to

---

S. Savoia (✉)

GreenWaves srl, I-20064 Gorgonzola (MI), Italy  
e-mail: [silvio.savoia85@gmail.com](mailto:silvio.savoia85@gmail.com)

G. Castaldi • V. Galdi

Waves Group, Department of Engineering, University of Sannio, I-82100 Benevento, Italy  
e-mail: [castaldi@unisannio.it](mailto:castaldi@unisannio.it); [vgaldi@unisannio.it](mailto:vgaldi@unisannio.it)

the well-known formal analogies between quantum mechanics and (paraxial) optics, non-Hermitian concepts can be translated to electromagnetic structures by means of spatial modulation of loss and gain, which is becoming technologically viable in artificial materials and metamaterials. In fact, in metamaterial engineering, the introduction of material constituents featuring gain is a well-established strategy to overcome the inevitable presence of losses. Nonetheless, the above ideas have inspired novel, unconventional ways of mixing material constituents featuring loss and gain, so as to attain a wealth of anomalous light-matter interactions that extend well beyond the mere loss-compensation effects. The reader is referred to Ref. [8] for a recent review of theoretical foundations, implications, and applications of  $\mathcal{PT}$  symmetry in optics. More recently, potential applications have also been proposed in connection with acoustic [9] and magnetic [10] structures.

From the theoretical viewpoint, the interest in non-Hermitian optical structures is motivated by the possibility to conceive technologically feasible testbeds for the (otherwise impossible) experimental study of controversial quantum-physics effects [11], as well as to gain a deeper understanding of phenomena and properties that are typical of non-Hermitian systems, such as spontaneous symmetry breaking [12] and exceptional points [13–16], unidirectional invisibility [17, 18], Bloch oscillations [19], and coherent perfect absorption [20–22]. From the application viewpoint, a variety of light-matter interaction effects (e.g., unidirectional invisibility, coherent perfect absorption, lasing, negative refraction and focusing, cloaking) have been demonstrated and observed, which may set the stage for the development of novel optical components and devices (see Refs. [23–50] and references therein).

In a series of ongoing investigations [28, 34, 41, 46, 50], we have been concerned with the study of field-manipulation and wave-guiding properties of non-Hermitian metamaterials. In this chapter, we compactly review some representative results. In particular, in Sect. 21.2, we present a *complex-coordinate* extension of the transformation-optics framework, which may naturally handle media featuring loss and gain. More specifically, after some generalities on the approach (Sect. 21.2.1), we illustrate the field-manipulation capabilities in conjunction with the well-established complex source point (CSP) formalism (Sect. 21.2.2), as well as possible applications to the manipulations of leaky waves (Sect. 21.2.3). Subsequently, in Sect. 21.3, we illustrate certain interesting wave-guiding phenomena that can occur in  $\mathcal{PT}$ -symmetric bilayers. Finally, in Sect. 21.4, we provide some brief concluding remarks and hints for future research.

## 21.2 Complex-Coordinate Transformation Optics

### 21.2.1 Generalities

The conventional transformation-optics framework [51, 52] exploits the form invariance of Maxwell's and Helmholtz equations [53] with respect to real-valued coordinate transformations to systematically design transformation media with

desired field-manipulation capabilities. Thanks to its powerfulness and versatility, this approach has been one of the major catalysts for the formidable advances in metamaterial science and engineering (see, e.g., Ref. [54]). It is worth pointing out that, before its recent popularization, the approach had been utilized as a computational tool to rigorously solve diffraction problems involving multicoated gratings [55, 56].

In Refs. [28] and [46], we proposed a complex-coordinate extension of the transformation-optics framework that allows to handle complex-valued constitutive parameters (typical of non-Hermitian metamaterials) while retaining an insightful geometrical interpretation in terms of the complexification of geometrical objects.

As in conventional (real-valued) transformation optics [52], we start by considering an auxiliary space with Cartesian coordinates  $\mathbf{r}' \equiv (x', y', z')$  filled by a lossless medium characterized by (real-valued) relative permittivity and permeability distributions  $\varepsilon'(\mathbf{r}')$  and  $\mu'(\mathbf{r}')$ , respectively. In such space, we consider some time-harmonic electric ( $\mathbf{J}'$ ) and magnetic ( $\mathbf{M}'$ ) sources (with suppressed  $\exp(-i\omega t)$  time dependence) radiating an electromagnetic field distribution  $\mathbf{E}', \mathbf{H}'$ . We then consider the field/source-manipulation effects induced by a coordinate transformation

$$\mathbf{r}' = \mathbf{F}(\mathbf{r}), \quad (21.1)$$

with  $\mathbf{F}$  denoting a vector function of the spatial coordinates. By exploiting the form-invariance properties of Maxwell's equations, such effects can be equivalently interpreted in terms of a new set of electromagnetic fields

$$\{\mathbf{E}, \mathbf{H}\}(\mathbf{r}) = \underline{\underline{\underline{\Lambda}}}^T(\mathbf{r}) \cdot \{\mathbf{E}', \mathbf{H}'\}[\mathbf{F}(\mathbf{r})], \quad (21.2)$$

generated by a new set of sources

$$\{\mathbf{J}, \mathbf{M}\}(\mathbf{r}) = \det[\underline{\underline{\underline{\Lambda}}}(\mathbf{r})] \underline{\underline{\underline{\Lambda}}}^{-1}(\mathbf{r}) \cdot \{\mathbf{J}', \mathbf{M}'\}[\mathbf{F}(\mathbf{r})], \quad (21.3)$$

radiating in a new physical space  $\mathbf{r} \equiv (x, y, z)$ , which is flat as the auxiliary space, but filled up by an inhomogeneous, anisotropic transformation medium characterized by relative permittivity and permeability tensors [52]

$$\begin{aligned} \underline{\underline{\underline{\varepsilon}}}(\mathbf{r}) &= \varepsilon'[\mathbf{F}(\mathbf{r})] \det[\underline{\underline{\underline{\Lambda}}}(\mathbf{r})] \underline{\underline{\underline{\Lambda}}}^{-1}(\mathbf{r}) \cdot \underline{\underline{\underline{\Lambda}}}^{-T}(\mathbf{r}), \\ \underline{\underline{\underline{\mu}}}(\mathbf{r}) &= \mu'[\mathbf{F}(\mathbf{r})] \det[\underline{\underline{\underline{\Lambda}}}(\mathbf{r})] \underline{\underline{\underline{\Lambda}}}^{-1}(\mathbf{r}) \cdot \underline{\underline{\underline{\Lambda}}}^{-T}(\mathbf{r}). \end{aligned} \quad (21.4)$$





as the complex-coordinate-stretching-based absorbing boundary conditions [60]. With specific reference to transformation optics, complex-coordinate extensions are not entirely new and have been proposed in order to enable field-amplitude control [61] and to generate single-negative transformation media [62]. Also worth of mention are some very recent applications to reflectionless media [63].

In what follows, we illustrate two representative examples.

### 21.2.2 Complex Source Point-Based Beam Manipulation

Referring to the schematic in Fig. 21.1, we consider a two-dimensional (2-D) scenario, geometrically invariant along the  $z$ -direction, and a transverse magnetic polarization (with  $z$ -directed magnetic field). We are specifically interested in slab-type configurations, generated from an auxiliary space  $(x', y', z')$  (Fig. 21.1a), to which we apply a general class of coordinate transformations

$$x' = u(x), \quad y' = v(x)y + w(x), \quad z' = \alpha z, \quad (21.8)$$

within the region  $|x| < d$ . This class of transformations formally resembles the one considered in Ref. [64]. However, the functions  $u$ ,  $v$ , and  $w$  and the constant parameter  $\alpha$  are now generally complex valued. By particularizing to this scenario the general transformation-optics machinery in (21.2), (21.3), and (21.4), we obtain a transformation slab occupying the region  $|x| < d$  in the actual physical space  $(x, y, z)$  (Fig. 21.1b), filled up with a (generally anisotropic and inhomogeneous) medium characterized by relative permittivity and permeability tensors

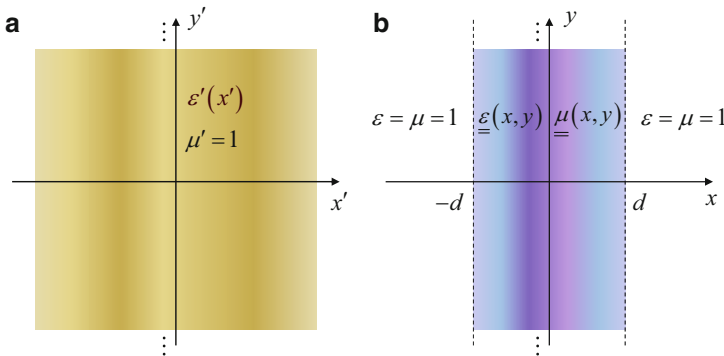


**Fig. 21.1** (a) Auxiliary space, filled up with a nonmagnetic medium with generic relative permittivity distribution  $\varepsilon'(x')$ . (b) Physical space containing the transformation slab, with constitutive tensors given by (21.9). Different color shadings are used to indicate regions that are generally inhomogeneous

$$\frac{\underline{\underline{\varepsilon}}(x, y)}{\varepsilon'(x')} = \underline{\underline{\mu}}(x, y) = \begin{bmatrix} \frac{\alpha v}{\dot{u}} & -\frac{\alpha(\dot{v}y + \dot{w})}{\dot{u}} & 0 \\ -\frac{\alpha(\dot{v}y + \dot{w})}{\dot{u}} & \frac{\alpha[\dot{u}^2 + (\dot{v}y + \dot{w})^2]}{\dot{u}v} & 0 \\ 0 & 0 & \frac{\dot{u}v}{\alpha} \end{bmatrix}, \quad (21.9)$$

where the overdot indicates differentiation with respect to the argument and, for notational compactness, the explicit  $x$ -dependence is omitted. It is worth stressing that the transformation-optics-based analytical field mapping in (21.2) is strictly valid only for continuous coordinate transformations. Under the assumption of a vacuum exterior region  $|x| > d$  (see Fig. 21.1b), the mapping in (21.8) is continuous provided that [46]

$$v(-d) = v(d) = \alpha = 1. \quad (21.10)$$

The above conditions dictate that the transformations reduce to the identity at the interfaces  $x = \pm d$ , apart from a (possibly complex-valued) shift along the  $x$ - and  $y$ -directions, which, in turn, implies the preservation of the reflection/transmission properties of the auxiliary space, apart from (possibly complex-valued) phase factors. Furthermore, it can be shown that the condition

$$v(x) = \frac{1}{\alpha \dot{u}(x)} \quad (21.11)$$

ensures an effectively nonmagnetic (i.e.,  $\mu_z = 1$ ) character of the resulting transformation medium [46].

The above theoretical framework can be insightfully applied and interpreted in conjunction with the CSP formalism, a powerful tool originally introduced by Deschamps [57] and Felsen [58] to analytically model the propagation of Gaussian-beam-like wave objects. To simply illustrate this concept, we consider a unit-amplitude ( $V/m^2$ ),  $z$ -directed magnetic line source radiating in vacuum,

$$M_z(x, y) = \delta(x - \tilde{x}_s) \delta(y - \tilde{y}_s), \quad (21.12)$$

where  $\delta$  denotes a Dirac delta and

$$\tilde{x}_s = x_s + ib_s \cos \theta_s, \quad \tilde{y}_s = y_s + ib_s \sin \theta_s \quad (21.13)$$

represents a complex-valued position, with  $x_s$ ,  $y_s$ ,  $b_s$ , and  $\theta_s$  assumed as real-valued and  $b_s > 0$ . Here and henceforth, the tilde  $\sim$  identifies complex-valued spatial quantities. Via analytic continuation of a 2-D Green's function and proper choice of the branch cut in the arising complex-valued distance, the corresponding radiated field can be shown to be paraxially equivalent to a Gaussian beam with waist located at  $(x_s, y_s)$ , propagation axis forming an angle  $\theta_s$  with the  $x$ -axis, and Rayleigh parameter (diffraction length)  $b_s$  [57, 58].

Accordingly, for a vacuum auxiliary space ( $\varepsilon' = 1$  in Fig. 21.1a) and under the reflectionless conditions in (21.10), the transformation-induced field manipulation on a CSP admits a simple geometrical interpretation. Assuming a CSP beam with waist located at one side of the slab (say  $x_s \leq -d$ ), the radiated field at the other side of the slab ( $x \geq d$ ) can be interpreted as generated by an image CSP ( $\tilde{x}_i, \tilde{y}_i$ ) which can be directly related to the source and transformation via

$$\tilde{x}_i \equiv \tilde{x}_s + u(-d) - u(d) + 2d, \quad \tilde{y}_i \equiv \tilde{y}_s + w(-d) - w(d). \quad (21.14)$$

It can be observed that the field manipulation implied by (21.14) depends solely on the boundary values of the mapping functions and not on their actual behavior within the slab region, which potentially leaves useful degrees of freedom in the design. Moreover, we note that while real-valued transformations only allow for the manipulation of the beam waist position, complex-coordinate transformations give, in principle, full control of the CSP beam parameters, including the propagation direction and Rayleigh parameter. Below, we show some representative examples.

We start considering a transformation slab that exactly reproduces at the output interface  $x = d$  the illuminating field generated by a CSP beam impinging at the input interface  $x = -d$ , thereby behaving as an electromagnetic nullity. To this aim, we particularize the general transformations in (21.8) to the form

$$u(x) = i\chi \left(1 - \frac{|x|}{d}\right), \quad v(x) = 1, \quad w(x) = 0, \quad (21.15)$$

where  $\chi$  denotes a real, positive constant. This maps the auxiliary space onto a piece-wise homogeneous, anisotropic,  $\mathcal{PT}$ -symmetric bilayer with constitutive parameters [46]

$$\varepsilon_{xx}(x) = \text{sgn}(x) \frac{id}{\chi}, \quad \varepsilon_{yy}(x) = \mu_{zz}(x) = -\text{sgn}(x) \frac{i\chi}{d}, \quad (21.16)$$

with  $\text{sgn}$  denoting the signum function. Such transformation medium was also considered in Ref. [28] within a different context, and a possible multilayered implementation was explored. Similar uniaxial media, simultaneously featuring gain and loss along different directions, have also been recently studied in Ref. [65].

Figure 21.2 shows the response of such a nullity metamaterial transformation slab of width  $d = 0.5\lambda_0$  (with  $\lambda_0$  denoting the free-space wavelength), transverse aperture of  $30\lambda_0$ , and  $\chi = 0.3\lambda_0$ , due to a CSP beam impinging from the left side along the positive  $x$ -direction ( $x_s = -\lambda_0, y_s = 0, \theta_s = 0$ ) with Rayleigh parameter  $b_s = 0.1\lambda_0$ . Results are obtained via full-wave numerical simulations carried out by means of the finite-element-based commercial software COMSOL Multiphysics [66]; implementation details and simulation parameters can be found in Ref. [46]. More in detail, Fig. 21.2a shows the magnetic-field (real-part) map, from which it is apparent that the impinging wavefront at the input slab interface  $x = -d$  is reproduced at its output  $x = d$ . This is quantitatively more evident in Figs. 21.2b

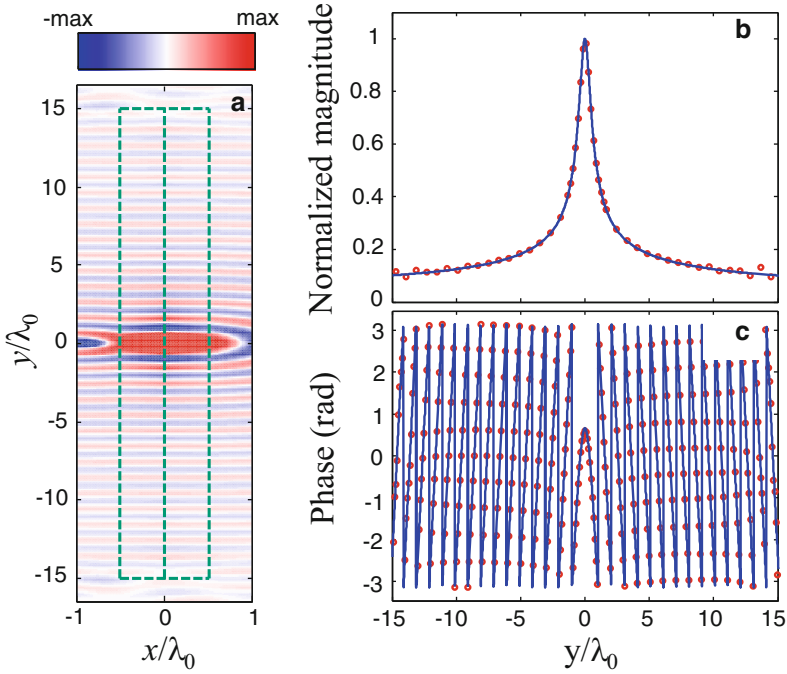


**Fig. 21.2** (a) Finite-element-computed magnetic-field ( $H_z$ ) real-part map pertaining to the  $\mathcal{PT}$ -symmetric transformation bilayer in (21.16), with  $d = 0.5\lambda_0$ ,  $\chi = 0.3\lambda_0$ , and finite aperture of  $30\lambda_0$ , excited by a CSP with  $x_s = -\lambda_0$ ,  $y_s = 0$ ,  $b_s = 0.1\lambda_0$ , and  $\theta_s = 0$ . The corresponding material parameters are  $\varepsilon_{xx} = \mp i5/3$  and  $\varepsilon_{yy} = \mu_{zz} = \pm i3/5$  for  $-d < x < 0$  and  $0 < x < d$ , respectively. (b) Magnitude and (c) phase distributions (red dots) computed at the interface  $x = d + \lambda_0/100$ , compared with the theoretical predictions (blue-solid curves) in terms of an image CSP with  $x_i = x_s + 2d$ ,  $y_i = y_s$ ,  $b_i = b_s$ ,  $\theta_i = \theta_s$ . Results are normalized with respect to the theoretical solution evaluated at  $x = d + \lambda_0/100$  and  $y = 0$ . The dashed contour delimits the bilayer region (Reproduced from Ref. [46] with permission from Institute of Physics Publishing)

and c, which compare the magnitude and phase distributions, respectively, at the slab output with the theoretical predictions for an infinite slab. A very good agreement can be observed, with the small oscillations toward the end of the slab aperture attributable to truncation effects.

As a further example, we now consider a different kind of transformation, which enables full control of the CSP beam parameters. In particular, we focus on a simple class of linear transformations

$$u(x) = u_0x, \quad v(x) = 1, \quad w(x) = w_0x, \quad \alpha = 1, \quad (21.17)$$

with  $u_0$  and  $w_0$  denoting complex-valued parameters represented in polar form as

$$u_0 = |u_0| \exp(i\phi), \quad w_0 = |w_0| \exp(i\psi). \quad (21.18)$$

Such transformation satisfies the matching conditions in (21.10) and affects both the real (via  $u_0$ ) and the imaginary (via  $w_0$ ) parts of the CSP, yielding a homogeneous and generally anisotropic transformation medium (21.9) with  $\mu_{zz} = u_0$  and

$$\underline{\underline{\varepsilon}} = \begin{bmatrix} \frac{1}{u_0} & -\frac{w_0}{u_0} & 0 \\ -\frac{w_0}{u_0} & u_0 \left(1 + \frac{w_0^2}{u_0^2}\right) & 0 \\ 0 & 0 & u_0 \end{bmatrix}. \quad (21.19)$$

In Ref. [46], we analytically derived some conditions on the transformation in (21.17) under which the anisotropy reduces to a simple uniaxial form (with tilted optical axis).

As a representative example, Fig. 21.3 illustrates the response of such a transformation slab designed so as to convert a conventional line source ( $x_s = -\lambda_0, y_s = 0, b_s = 0$ ) into an image CSP representative of a beam propagating along the negative  $y$ -direction ( $\theta_i = -\pi/2$ ), with waist located at  $x_i = -1.118\lambda_0, y_i = 0$ , and  $b_i = 0.5\lambda_0$ . Parameters are chosen in such a way that the transformation medium reduces to a homogeneous, uniaxially anisotropic material with a  $45^\circ$ -tilted optical axis and components exhibiting both gain and loss along different directions (see Ref. [46] for details). The field map in Fig. 21.3a illustrates the conversion of the isotropic radiation produced by the real line source into a directional beam. Also in this case, an excellent agreement with the theoretical prediction is obtained, as shown in Figs. 21.3b and c (magnitude and phase distributions, respectively).

Finally, we consider a scenario where an impinging CSP beam is shifted and steered. More specifically, we assume an obliquely incident ( $\theta_s = -\pi/6$ ) CSP beam with waist located at  $x_s = -3\lambda_0, y_s = 0$ , and  $b_s = \lambda_0$ , and we design the transformation slab so as to generate an image CSP beam with waist located at  $x_i = x_s, y_i = 0.25\lambda_0$ , and same Rayleigh parameter, but tilted of an angle  $\theta_i = 0.379\pi$  (about  $40^\circ$ ). The resulting transformation medium assumes a uniaxially anisotropic form (with a tilted optical axis of  $\sim 25^\circ$  and components exhibiting both gain and loss). Results are shown in Fig. 21.4; once again, a very good agreement between numerical simulations and theoretical predictions is observed.

### 21.2.3 Leaky-Wave Manipulation

We move on to illustrating the application of our proposed complex-coordinate transformation-optics framework in conjunction with the leaky-wave concept, which typically arises in the study of open (e.g., dielectric) waveguides and is associated with complex-valued roots of the dispersion equations [67]. For illustration, we start considering a lossless slab of thickness  $2d$ , embedded in the auxiliary space, viz.,

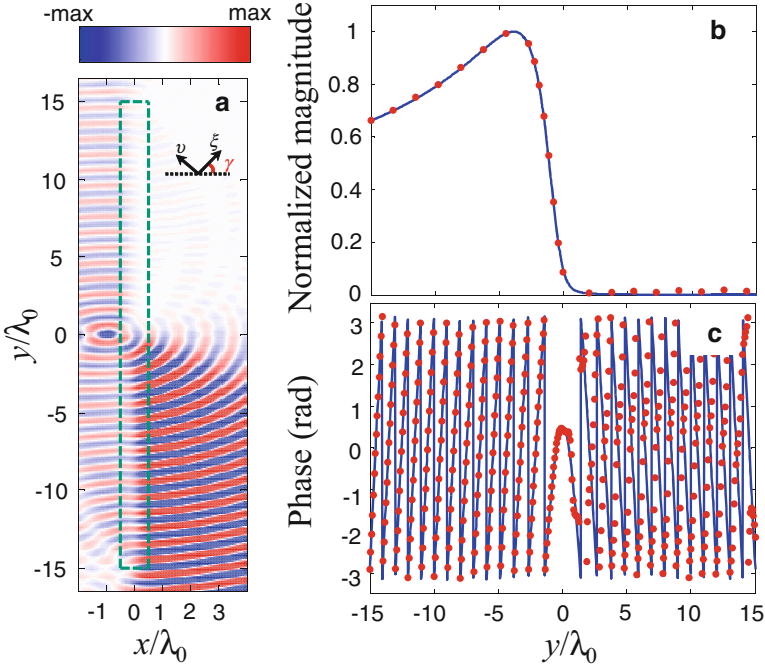


**Fig. 21.3** (a) Finite-element-computed magnetic-field ( $H_z$ ) real-part map pertaining to the transformation slab in (21.17), with  $u_0 = 1.118$  ( $\phi = 0$ ),  $|w_0| = 0.5$ ,  $\psi = \pi/2$ ,  $d = 0.5\lambda_0$ , and finite aperture of  $30\lambda_0$ , excited by a real (i.e.,  $b_s = 0$ ) line source located at  $x_s = -\lambda_0$ ,  $y_s = 0$ . (b) Magnitude and (c) phase distributions (red dots) computed at the interface  $x = d + \lambda_0/100$ , compared with the theoretical predictions (blue-solid curves) in terms of an image CSP with  $x_i = -1.118\lambda_0$ ,  $y_i = 0$ ,  $b_i = 0.5\lambda_0$ ,  $\theta_i = -\pi/2$  (cf. (21.14)). Results are normalized with respect to the theoretical solution evaluated at  $x = d + \lambda_0/100$  and  $y = -3.875\lambda_0$ . The dashed contour delimits the slab region. Also shown in panel (a) is the principal reference system ( $\xi, \nu$ ), rotated by an angle  $\gamma = \pi/4$ , in which the transformation medium assumes a uniaxial form, with relevant components  $\varepsilon_{\xi\xi} = 0.894 - i0.447$ ,  $\varepsilon_{\nu\nu} = 0.894 + i0.447$ ,  $\mu_{zz} = 1.118$  (Reproduced from Ref. [46] with permission from Institute of Physics Publishing)

$$\varepsilon'(x') = \begin{cases} \varepsilon_b, & |x'| < d, \\ 1, & |x'| > d, \end{cases} \quad (21.20)$$

with  $\varepsilon_b \neq 1$ , in Fig. 21.1a. The guided and radiated modes supported by such a structure can be obtained by finding the generally complex-valued solutions of the dispersion equation [67]

$$\cot(2k'_{xb}d) = \frac{i\varepsilon_b k'_x}{2k'_{xb}} + \frac{ik'_{xb}}{2\varepsilon_b k'_x}, \quad (21.21)$$

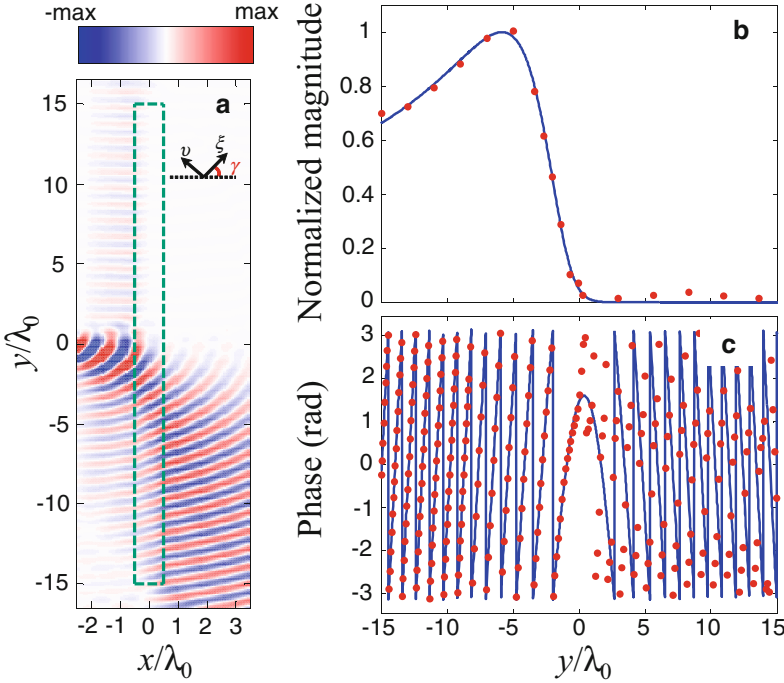


**Fig. 21.4** (a) Finite-element-computed magnetic-field ( $H_z$ ) real-part map pertaining to the transformation slab in (21.17), with  $|u_0| = 1.085$ ,  $\phi = -0.150\pi$ ,  $|w_0| = 0.5$ ,  $\psi = \pi/3$ ,  $d = 0.5\lambda_0$ , and finite aperture of  $30\lambda_0$ , excited by a CSP with  $x_s = -3\lambda_0$ ,  $y_s = 0$ ,  $b_s = \lambda_0$ , and  $\theta_s = -\pi/6$ . (b) Magnitude and (c) phase distributions (red dots) computed at the interface  $x = d + \lambda_0/100$ , compared with the theoretical predictions (blue-solid curves) in terms of an image CSP with  $x_i = x_s$ ,  $y_i = 0.25\lambda_0$ ,  $b_i = b_s$ ,  $\theta_i = -0.379\pi$  (cf. (21.14)). Results are normalized with respect to the theoretical solution evaluated at  $x = d + \lambda_0/100$  and  $y = -5.866\lambda_0$ . The dashed contour delimits the slab region. Also shown in panel (a) is the principal reference system  $(\xi, \nu)$ , rotated by an angle  $\gamma = 0.137\pi$ , in which the transformation medium assumes a uniaxial form, with relevant components  $\varepsilon_{\xi\xi} = 0.829 - i0.628$ ,  $\varepsilon_{\nu\nu} = 0.766 + i0.581$ ,  $\mu_{zz} = 0.970 + i0.495$  (Reproduced from Ref. [46] with permission from Institute of Physics Publishing)

where  $k'_y$  and  $k'_x = \sqrt{k_0^2 - k_y'^2}$  denote the  $y'$ - and  $x'$ -domain wavenumbers, respectively, and  $k'_{xb} = \sqrt{k_0^2 \varepsilon_b - k_y'^2}$ . Here and henceforth,  $k_0 = 2\pi/\lambda_0$  denotes the vacuum wavenumber. In what follows, due to symmetry considerations, we restrict our attention to the propagation along the positive  $y'$ -direction, i.e.,  $\text{Re}(k'_y) > 0$ . It is well-known that real-valued solutions,

$$\text{Im}(k'_y) = 0, \quad k'_y > k_0, \quad \text{Im}(k'_x) \geq 0, \quad (21.22)$$

correspond to guided modes propagating without attenuation along the  $y'$ -direction, and decaying exponentially along the  $x'$ -direction [67]. However, also of interest are

a class of complex-valued solutions (leaky-wave modes) characterized by [67]

$$\operatorname{Re}(k'_y) < k_0, \quad \operatorname{Im}(k'_x) \leq 0, \quad (21.23)$$

which, though improper (exponentially growing along the  $x'$ -direction), can still be exploited to represent the near-field distribution so as to effectively capture the radiation properties of the slab. Basically, in the presence of a suitably excited dominant leaky wave with complex propagation constant  $k'_{ys} = \pm(\beta + i\eta)$ , the field radiated by the slab can be approximated as generated by an equivalent aperture field distribution [68]

$$H_z^{(eq)}(y') \sim \exp(i\beta |y'|) \exp(-\eta |y'|), \quad (21.24)$$

which yields the (far region) radiation pattern [68]

$$|H_z^{(eq)}(\theta')|^2 \sim \cos^2 \theta' \left\{ \frac{\beta^2 + \eta^2}{[k_0^2 \sin^2 \theta' - (\beta^2 - \eta^2)]^2 + (2\beta\eta)^2} \right\}, \quad (21.25)$$

with  $\theta'$  denoting the radiation angle measured from the  $x'$ -axis.

This represents another interesting example of a complex-valued quantity (the leaky-wave propagation constant) which admits a simple and insightful interpretation that is physically tied with the main radiation characteristics (direction and beamwidth). Our complex-coordinate transformation-optics approach can be exploited to tailor this quantity so that, starting from a given leaky-wave solution supported by the dielectric slab in the auxiliary domain, a metamaterial transformation slab is designed which supports (among others) a leaky wave with desired propagation constant.

To illustrate this concept, we consider a simple complex-coordinate scaling

$$u(x) = u_0 x, \quad v(x) = v_0, \quad w(x) = 0, \quad \alpha = u_0 v_0, \quad (21.26)$$

with  $u_0$  and  $v_0$  denoting complex-valued constant parameters. It is worth stressing that, unlike the previous examples in Sect. 21.2.2, the matching conditions in (21.10) do not hold (apart from the trivial case  $u_0 = v_0 = 1$ ), whereas the non-magnetic condition in (21.11) is now satisfied. The dispersion equation in the transformed domain can be written as

$$\cot(2k_{xb}u_0d) = \frac{i\varepsilon_b u_0 k_x}{2k_{xb}} + \frac{ik_{xb}}{2\varepsilon_b u_0 k_x}, \quad (21.27)$$

with  $k_y$  and  $k_x = \sqrt{k_0^2 - k_y^2}$  denoting the  $y$ - and  $x$ -domain wavenumbers, respectively, and  $k_{xb} = \sqrt{k_0^2 \varepsilon_b - k_y^2 / v_0^2}$ . We assume that a leaky wave with propagation constant  $k'_{ys}$  is supported by the slab in the auxiliary domain and a leaky wave with



modified propagation constant  $k_{ys}$  is desired in the transformed domain. In Ref. [46], we analytically derived the conditions on the transformation parameters that enable for the desired mapping:

$$v_0 = \begin{cases} \pm \frac{k_{ys}}{\sqrt{\varepsilon_b (k_0^2 - \varepsilon_b k'_{xs} k_{xs})}}, \\ \pm \frac{k_{ys} \sqrt{k'_{xs}}}{\sqrt{\varepsilon_b k_0^2 (k'_{xs} - k_{xs}) + k_{xs} k_{ys}^2}}, \end{cases} \quad (21.28)$$

$$u_0 = \sqrt{\frac{k_0^2 \varepsilon_b - k_{ys}^2}{k_0^2 \varepsilon_b - \frac{k_{ys}^2}{v_0^2}}}, \quad (21.29)$$

where  $k_{xs} = \sqrt{k_0^2 - k_{ys}^2}$  and  $k'_{xs} = \sqrt{k_0^2 - k_{ys}^2}$ , and any of the signs in (21.28) can be chosen. It is worth highlighting that the above transformation is not restricted to the leaky-wave solution  $k'_{ys}$  of specific interest, but it rather affects the entire eigenspectrum of the slab in the auxiliary domain. Therefore, care should be exerted to ensure that the transformed leaky wave is actually the dominant mode.

Figure 21.5 illustrates a representative application example. We choose a slab in the auxiliary domain with  $d = 0.125\lambda_0$  and  $\varepsilon_b = 0.05$ , supporting a leaky-wave mode with propagation constant  $k'_{ys} = \pm (0.257 + i0.120)k_0$ . From the field map shown in Fig. 21.5a, assuming a line source excitation at  $x = y = 0$ , a radiated field is clearly observed, together with an exponential decay (along  $y$ ) of the field inside and nearby the slab, as predicted by the leaky-wave-based modeling in (21.24). For a more quantitative assessment, Fig. 21.5b compares the finite-element-computed far-field radiation pattern with the leaky-wave-based theoretical prediction in (21.25); the good agreement indicates the dominant character of the leaky-wave mode. With the aim of attaining a leaky wave with a modified propagation constant  $k_{ys} = (0.707 + i0.05)k_0$ , so as to steer the beam direction to  $\theta = \pi/4$  and achieve a significantly smaller beamwidth (i.e., higher directivity), we apply the coordinate transformations in (21.26) (with (21.28) and (21.29)), obtaining  $u_0 = 1.170 + i0.0212$  and  $v_0 = 2.582 - i0.756$ . This yields a non-magnetic, uniaxial transformation medium exhibiting loss and gain along different directions. Figures 21.5c, d show the transformed slab field map and radiation pattern, respectively, excited by the same line source. As it can be observed, the desired radiation characteristics are obtained, in fairly good agreement with the theoretical predictions.

The above results provide a compact overview of the field-manipulation capabilities (and physical interpretation) enabled by non-Hermitian metamaterials designed via complex-coordinate transformation optics. The reader is referred to Ref. [28] for further examples involving other types of CSP manipulations as well as the

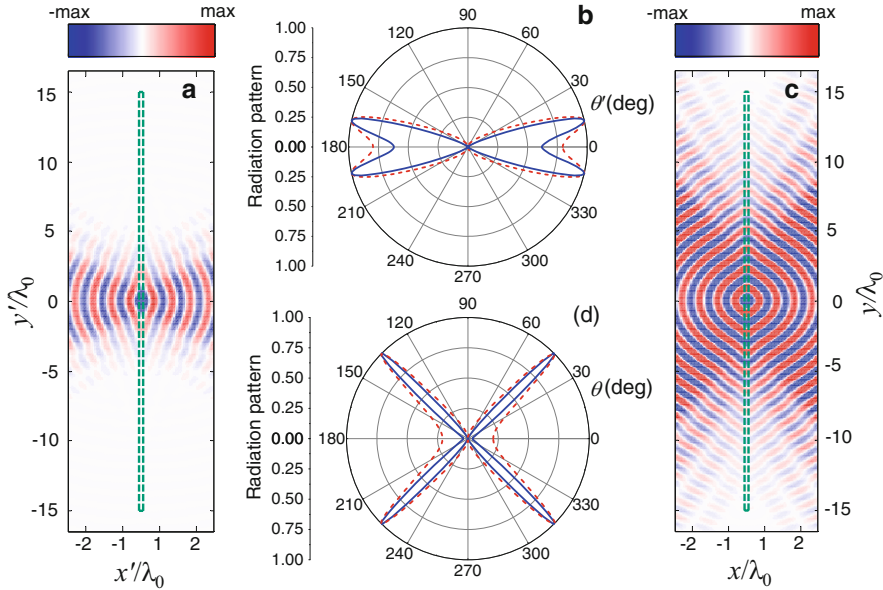


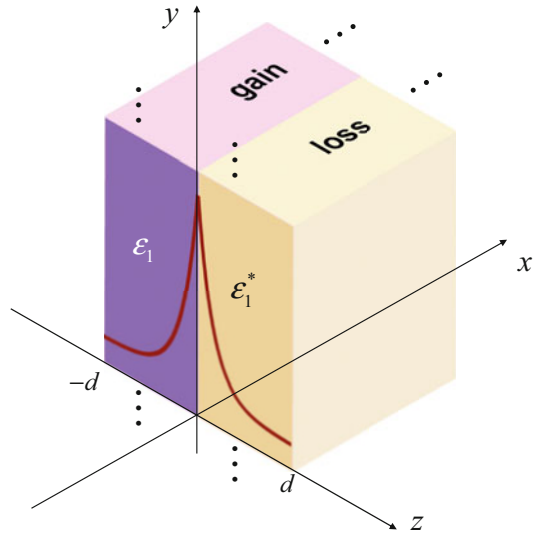
**Fig. 21.5** (a) Finite-element-computed magnetic-field ( $H_z$ ) real-part map pertaining to a slab in the auxiliary domain with  $\varepsilon_b = 0.05$ ,  $d = 0.125\lambda_0$ , and finite aperture of  $30\lambda_0$ , excited by a magnetic line source located at  $x' = y' = 0$ . (b) Corresponding radiation pattern (*red-dashed curve*) compared with theoretical leaky-wave prediction (*blue-solid curve*) in (21.25), with  $k'_{ys} = \pm(0.257 + i0.120)k_0$ . (c), (d) Same as panels (a) and (b), respectively, but pertaining to a homogeneous, uniaxial transformation slab (cf. (21.26)), with  $u_0 = 1.170 + i0.0212$  and  $v_0 = 2.582 - i0.756$  with  $\varepsilon_{xx} = 0.305 - i0.195$ ,  $\varepsilon_{yy} = 0.068 + i0.003$ ,  $\mu_{zz} = 1$ , which supports a leaky wave with  $k_{ys} = \pm(0.707 + i0.05)k_0$  (Reproduced from Ref. [46] with permission from Institute of Physics Publishing)

exploitation of discontinuous coordinate transformations for the engineering of anisotropic transmission resonances (unidirectional invisibility).

### 21.3 Wave-Guiding in $\mathcal{PT}$ -Symmetric Epsilon-Near-Zero Bilayers

The concept of gain guiding is well-established in linear [69] and nonlinear [70] optics. Recently, the more general non-Hermitian-optics framework has revamped the interest in this topic and has inspired additional perspectives in wave confinement and guiding. For instance, it was shown in Ref. [23] that a  $\mathcal{PT}$ -symmetric gain-loss half-space or bilayer is capable to sustain surface waves propagating unattenuated along the gain-loss interface and transversely confined with exponential decay controlled by the gain/loss level. Interestingly, the governing dispersion equation formally resembles that of surface plasmon polaritons (SPPs) [71]. In a

**Fig. 21.6** A  $\mathcal{PT}$ -symmetric bilayer consisting of two slabs of identical thickness  $d$  and relative permittivity distribution as in (21.31), which can support transversely magnetic polarized modes exponentially bound and the gain-loss interface  $z = 0$ , and propagating without attenuation along the  $x$ -direction (Reproduced from Ref. [41] with permission from American Physical Society)



recent study [41], we have explored the possibility for these structures to operate in the epsilon-near-zero (ENZ) regime [72] (i.e., vanishingly small real part of the permittivities), in view of its well-known capabilities to dramatically enhance the effects of relatively low levels of loss and/or gain [73–75]. Indeed, we showed that, in this regime, the gain/loss level necessary to sustain the wave confinement and guiding effects can be significantly reduced. In what follows, we summarize the main outcomes of this investigation.

As schematized in Fig. 21.6, our configuration features two slabs of identical thickness  $d$ , paired along the  $z$ -direction and of infinite extent along the  $x$ - and  $y$ -directions. The slabs are characterized by complex-conjugate relative permittivities  $\epsilon_1$  and  $\epsilon_1^*$ , respectively, thereby fulfilling the necessary condition for  $\mathcal{PT}$ -symmetry,

$$\epsilon(-z) = \epsilon^*(z). \quad (21.30)$$

The relative permittivities are assumed as follows:

$$\epsilon_1 = \epsilon' - i\epsilon'', \quad \epsilon' > 0, \quad \epsilon'' > 0, \quad (21.31)$$

so that, with the assumed time-harmonic convention, the left and right halves ( $-d < z < 0$  and  $0 < z < d$ , respectively) are characterized by gain and loss, respectively. As anticipated, we are especially interested in the ENZ regime,

$$\epsilon' \ll \epsilon'' \ll 1, \quad (21.32)$$

in order to limit the amount of gain required.

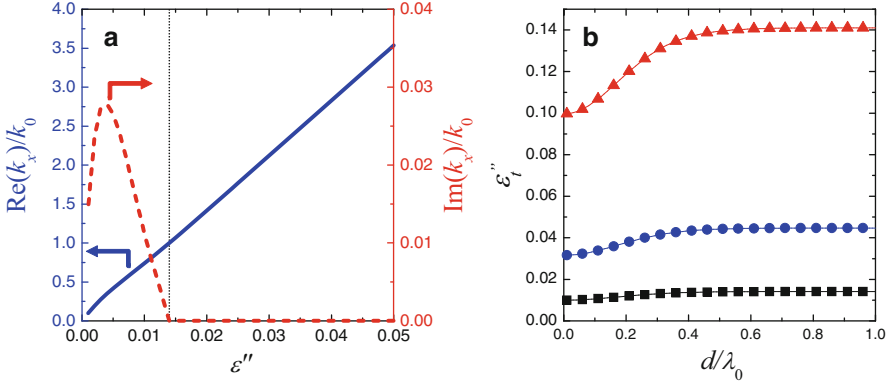


**Fig. 21.7** Geometry as in Fig. 21.6, for  $\varepsilon' = 10^{-4}$  and  $d = 0.5\lambda_0$ . (a) Real (blue solid; left axis) and imaginary part (red dashed; right axis) of the numerically computed (from (21.34)) propagation constant, as a function of the gain/loss level  $\varepsilon''$ , illustrating the transition from leaky to bound modes occurring at the threshold  $\varepsilon''_l = 0.014$  (black dotted vertical line). (b) Gain/loss level threshold (cf. (21.36)) as a function of  $d/\lambda_0$ , for  $\varepsilon' = 10^{-4}$  (squares),  $\varepsilon' = 10^{-3}$  (circles),  $\varepsilon' = 10^{-2}$  (triangles) (Reproduced from Ref. [41] with permission from American Physical Society)

It can be shown (see Ref. [41] for details) that, in the half-space limit ( $d \rightarrow \infty$ ), the structure supports a surface wave propagating at the gain/loss interface with propagation constant governed by the dispersion relation

$$k_x^{(SW)} = k_0 \sqrt{\frac{\varepsilon_1 \varepsilon_1^*}{\varepsilon_1 + \varepsilon_1^*}} = k_0 \sqrt{\frac{(\varepsilon')^2 + (\varepsilon'')^2}{2\varepsilon'}}. \quad (21.33)$$

This formally resembles the Uller-Zenneck-wave [76, 77] and SPP-wave [71] cases, though with some substantial differences. First, in our case, both media exhibit the same positive value of permittivity (real part). Second, the  $\mathcal{PT}$ -symmetry condition inherently yields unattenuated propagation along the gain/loss interface, sustained by a transverse component of the power flux (from the gain to loss region). Overall, such wave-guiding mechanism looks quite attractive in a perspective of *wave-guiding on demand*. For instance, one could envision the deploying of gain-medium channels in a lossy background and their selective enabling (and possibly reconfiguring) via optical pumping or other gain-inducing mechanisms.

For the more realistic bilayer configuration in Fig. 21.5, the dispersion equation is more complicated. Nevertheless, in the assumed ENZ limit, it can be approximated by the simpler form (see Ref. [41] for details)

$$ik_{z0}\{|\tau_1|^2 \text{Re}[\varepsilon_1^2(k_{z1}^*)^2] - |\varepsilon_1|^2 |k_{z1}^2|\} - |k_{z1}|^2 \text{Re}(\varepsilon_1 k_{z1}^* \tau_1^*) = 0, \quad (21.34)$$

where  $k_{z0} = \sqrt{k_0^2 - k_x^2}$ ,  $k_{z1} = \sqrt{\varepsilon_1 k_0^2 - k_x^2}$ , and  $\tau_1 = \tan(k_{z1}d)$ . Focusing, without loss of generality, on the case  $\text{Re}(k_x) > 0$  (i.e., propagation along the positive

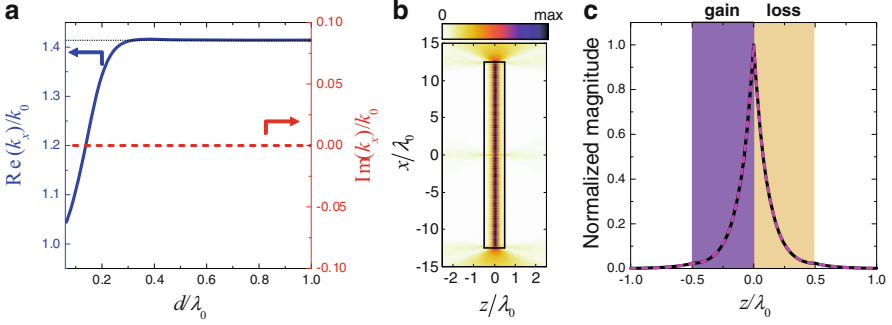


**Fig. 21.8** (a) As in Fig. 21.7a, but as a function of  $d/\lambda_0$  (dispersion relationship), for  $\varepsilon' = 10^{-4}$  and  $\varepsilon'' = 0.02$  (super-threshold case). Also shown (*black-dotted horizontal line*), as a reference, is the asymptotic limit (21.34). (b) Numerically computed field magnitude ( $|H_y|$ ) map for a bilayer with  $d = 0.5\lambda_0$  and finite-size (along  $x$ ) width of  $25\lambda_0$  (delimited by a *black solid rectangle*), excited by a magnetic line source located at  $x = z = 0$ . Values are sampled so as to avoid the singularity at the source and are normalized with respect to the maximum. (c) Transverse cut (*magenta-dashed*) at  $x = 4.17\lambda_0$ , compared with analytical bound-mode prediction (*black-solid*) with  $k_x = 1.414k_0$  (Reproduced from Ref. [41] with permission from American Physical Society)

$x$ -direction), we are especially interested in bound modes, i.e., solutions of (21.34) characterized by

$$\text{Re}(k_x) > k_0, \quad \text{Im}(k_{z0}) \geq 0. \quad (21.35)$$

It can be shown (see Ref. [41] for details) that, in order for the structure to sustain such modes, the gain/loss level  $\varepsilon''$  must exceed a threshold value

$$\varepsilon_t'' = \sqrt{\frac{\varepsilon'(2 - \varepsilon')[\varepsilon'k_0d(\tau_0^2 - 1) + 2\tau_0]}{k_0d(\varepsilon' - 2)(\tau_0^2 - 1) + 2\tau_0}}, \quad (21.36)$$

with  $\tau_0 = \tan(k_{z0}d)$ . Conversely, for sub-threshold loss/gain levels, the structure is not capable of sustaining the wave-guiding mechanism, and the modes tend to radiate in the surrounding space. This phenomenon can be effectively modeled in terms of leaky waves characterized by complex-valued propagation constants

$$\text{Re}(k_x) < k_0, \quad \text{Im}(k_x) > 0, \quad \text{Im}(k_{z0}) \leq 0. \quad (21.37)$$

The transition from the bound to the leaky regime is clearly exemplified (for  $\varepsilon' = 10^{-4}$  and  $d = 0.5\lambda_0$ ) in Fig. 21.7a. Figure 21.7b instead illustrates the behavior of the threshold loss/gain level in (21.36), as a function of the bilayer electrical thickness, for representative values of the relative-permittivity real-part  $\varepsilon'$  in the ENZ regime. As it can be observed, the threshold exhibits a weak dependence on the bilayer electrical thickness, and, for sufficiently thick bilayers ( $k_0d \gg 1$ , i.e.,

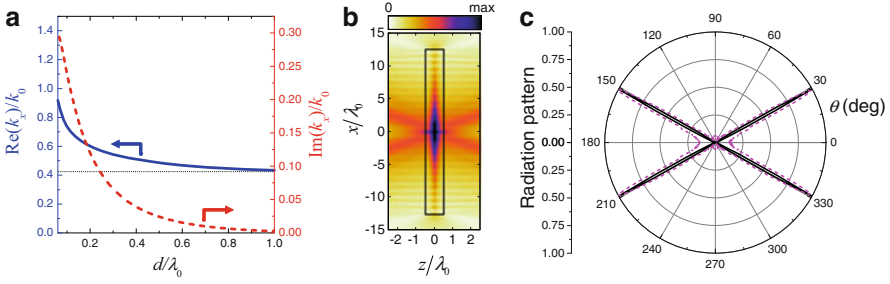


**Fig. 21.9** (a), (b) As in Figs. 21.4a, b, respectively, but for  $\varepsilon'' = 0.006$  (sub-threshold case). (c) Numerically computed radiation pattern (with the angle  $\theta$  measured with respect to the  $z$ -axis) compared with leaky-mode-based theoretical prediction for  $k_x = (0.486 + i0.02)k_0$  (Reproduced from [41] with permission from American Physical Society)

$\tau_0 \approx 1$ ), it approaches the asymptotic value

$$\varepsilon''_{\infty} = \sqrt{\varepsilon'(2 - \varepsilon')}, \quad (21.38)$$

which is consistent with enforcing  $|k_x| > k_0$  in the half-space dispersion relationship (21.34). Moreover, as it can be expected, the threshold increases with increasing values of  $\varepsilon'$ , but maintains moderately small values within the ENZ regime of interest.

We illustrate some representative examples for  $\varepsilon' = 10^{-4}$  and two feasible gain/loss levels. More specifically, in Fig. 21.8, we consider a super-threshold gain/loss level ( $\varepsilon'' = 0.02$ ) for which a bound mode is predicted by the numerically computed dispersion relationship (Fig. 21.8a). To verify the actual excitability of this mode, we study a finite-size (along  $x$ ) bilayer excited by a magnetic line source located at the gain/loss interface at  $x = 0$ , by means of finite-element-based full-wave numerical simulations [66] (see Ref. [41] for implementation details and parameters). A bound-mode structure is clearly visible in the near-field map shown in Fig. 21.8b, with a standing-wave pattern attributable to the structure truncation along the  $x$ -direction. Figure 21.8c shows a transverse ( $z$ ) cut, from which the exponential localization at the gain/loss can be observed, in excellent agreement with the theoretical prediction (see Ref. [41] for more details).

As a second example, Fig. 21.9 illustrates the response pertaining to a sub-threshold gain/loss level ( $\varepsilon'' = 0.006$ , for the same  $\varepsilon'$ ). In this case, a complex-valued propagation constant (see (21.37)) is expected and is clearly observed in Fig. 21.9a. This is representative of a leaky wave, i.e., a physical resonant radiative state supported by the bilayer, whose character is clearly visible in the near-field map in Fig. 21.9b. Finally, for a more quantitative assessment, Fig. 21.9c shows the numerically computed (far-field) radiation pattern, in good agreement with the theoretical leaky-wave-based prediction (see Ref. [41] for more details).

The reader is referred to Ref. [41] for a possible rod-based metamaterial implementation of  $\mathcal{PT}$ -symmetric ENZ metamaterials, which relies on a realistic

(semiconductor) gain material. Such implementation is inspired by some recently proposed all-dielectric implementations of near-zero-refractive-index metamaterials based on periodic arrays of high-permittivity cylindrical rods exhibiting Dirac-cone dispersion at the center of the Brillouin zone [78, 79]. Also closely related to the topic in this section is the study in Ref. [34] of  $\mathcal{PT}$ -symmetry-induced tunneling phenomena in ENZ bilayers.

## 21.4 Concluding Remarks and Perspectives

We have attempted a compact overview of some recent results on non-Hermitian metamaterials, with emphasis placed on the manipulation of CSP beam-like wave object inspired by complex-coordinate transformation-optics framework, as well as wave-guiding phenomena in  $\mathcal{PT}$ -symmetric ENZ bilayers.

In principle, the uniaxial metamaterials of interest for the complex-coordinate transformation optics may be engineered via periodic stacking of thin subwavelength layers of basic material constituents with opposite-signed permittivities (and/or permeabilities) and suitable levels of loss and gain. We stress that the parameter configurations chosen in the examples above serve only as simple illustrations of the phenomena (with moderately sized computational domains), but may give rise to unrealistic constitutive parameters. Nevertheless, lower values of gain/loss for the constituent media may be traded off for larger values of the slab thickness (see Ref. [28] for more details and examples in this respect). Moreover, in more recent studies on non-Hermiticity-induced wave-guiding [50], we have paid closer attention to the practical feasibility, by also taking into account realistic material dispersion models.

It is hoped that these results may provide useful insight into the electromagnetic wave interactions with non-Hermitian scenarios and may indicate new avenues in the design of active optical devices and radiating systems, with the use of gain not limited to attain mere loss compensation. Within this framework, current and future research is aimed at exploring more complex manipulations, including 3-D scenarios as well as cylindrical and spherical configurations. Also of great interest is the exploration of non-Hermitian metasurfaces. Finally, the optimization of the parameter configurations, in order to address their practical implementation with feasible material constituents, remains a crucial aspect to investigate.

## References

1. R. Shankar, *Principles of Quantum Mechanics* (Springer, New York, 2012)
2. C.M. Bender, S. Boettcher, Real spectra in non-Hermitian Hamiltonians having  $\mathcal{PT}$  symmetry. *Phys. Rev. Lett.* **80**(24), 5243–5246 (1998)

3. C.M. Bender, D.C. Brody, H.F. Jones, Complex extension of quantum mechanics. *Phys. Rev. Lett.* **89**(27), 270401 (2002)
4. C.M. Bender, Making sense of non-Hermitian Hamiltonians. *Rep. Prog. Phys.* **70**(6), 947–1018 (2007)
5. Y.C. Lee, M.H. Hsieh, S.T. Flammia, R.K. Lee, Local  $\mathcal{PT}$  symmetry violates the no-signaling principle. *Phys. Rev. Lett.* **112**(13), 130404 (2014)
6. S.L. Chen, G.Y. Chen, Y.N. Chen, Increase of entanglement by local  $\mathcal{PT}$ -symmetric operations. *Phys. Rev. A* **90**(5), 054301 (2014)
7. D.C. Brody, Consistency of  $\mathcal{PT}$ -symmetric quantum mechanics. *J. Phys. A: Math. Theor.* **49**(10), 10LT03 (2016)
8. A.A. Zyablovsky, A.P. Vinogradov, A.A. Pukhov, A.V. Dorofeenko, A.A. Lisyansky,  $\mathcal{PT}$ -symmetry in optics. *Physics-Uspekhi* **57**(11), 1063–1082 (2014)
9. X. Zhu, H. Ramezani, C. Shi, J. Zhu, X. Zhang,  $\mathcal{PT}$ -symmetric acoustics. *Phys. Rev. X* **4**(3), 031042 (2014)
10. J.M. Lee, T. Kottos, B. Shapiro, Macroscopic magnetic structures with balanced gain and loss. *Phys. Rev. B* **91**(9), 094416 (2015)
11. S. Longhi, G. Della Valle, Photonic realization of  $\mathcal{PT}$ -symmetric quantum field theories. *Phys. Rev. A* **85**(1), 012112 (2012)
12. C.E. Rüter, K.G. Makris, R. El-Ganainy, D.N. Christodoulides, M. Segev, D. Kip, Observation of parity–time symmetry in optics. *Nat. Phys.* **6**(3), 192–195 (2010)
13. S. Longhi, G. Della Valle, Optical lattices with exceptional points in the continuum. *Phys. Rev. A* **89**(5), 052132 (2014)
14. B. Zhen, C.W. Hsu, Y. Igarashi, L. Lu, I. Kaminer, A. Pick, S.L. Chua, J.D. Joannopoulos, M. Soljačić, Spawning rings of exceptional points out of Dirac cones. *Nature* **525**(7569), 354–358 (2015)
15. C. Hahn, Y. Choi, J.W. Yoon, S.H. Song, C.H. Oh, P. Berini, Observation of exceptional points in reconfigurable non-Hermitian vector-field holographic lattices. *Nat. Commun.* **7**, 12201 (2016)
16. A. Cerjan, A. Raman, S. Fan, Exceptional contours and band structure design in parity-time symmetric photonic crystals. *Phys. Rev. Lett.* **116**(20), 203902 (2016)
17. Z. Lin, H. Ramezani, T. Eichelkraut, T. Kottos, H. Cao, D.N. Christodoulides, Unidirectional invisibility induced by  $\mathcal{PT}$ -symmetric periodic structures. *Phys. Rev. Lett.* **106**(21), 213901 (2011)
18. A. Regensburger, C. Bersch, M.A. Miri, G. Onishchukov, D.N. Christodoulides, U. Peschel, Parity-time synthetic photonic lattices. *Nature* **488**(7410), 167–171 (2012)
19. Y.L. Xu, W.S. Fegadolli, L. Gan, Z.Y. Li, A. Scherer, Y.F. Chen, M.H. Lu, X.P. Liu, Experimental realization of Bloch oscillations in a parity-time synthetic silicon photonic lattice. *Nat. Commun.* **7**, 11319 (2016)
20. S. Longhi,  $\mathcal{PT}$ -symmetric laser absorber. *Phys. Rev. A* **82**(3), 031801 (2010)
21. Y.D. Chong, L. Ge, A.D. Stone,  $\mathcal{PT}$ -symmetry breaking and laser-absorber modes in optical scattering systems. *Phys. Rev. Lett.* **106**(9), 093902 (2011)
22. Y. Sun, W. Tan, H.q. Li, J. Li, H. Chen, Experimental demonstration of a coherent perfect absorber with  $\mathcal{PT}$  phase transition. *Phys. Rev. Lett.* **112**(14), 143903 (2014)
23. J. Čtyroký, V. Kuzmiak, S. Eyderman, Waveguide structures with antisymmetric gain/loss profile. *Opt. Express* **18**(21), 21585–21593 (2010)
24. H. Benisty, A. Degiron, A. Lupu, A. De Lustrac, S. Chénais, S. Forget, M. Besbes, G. Barbillion, A. Bruyant, S. Blaize, G. Lérondel, Implementation of  $\mathcal{PT}$  symmetric devices using plasmonics: principle and applications. *Opt. Express* **19**(19), 18004–18019 (2011)
25. J. Schindler, A. Li, M.C. Zheng, F.M. Ellis, T. Kottos, Experimental study of active LRC circuits with  $\mathcal{PT}$  symmetries. *Phys. Rev. A* **84**(4), 040101 (2011)
26. N. Lazarides, G.P. Tsironis, Gain-driven discrete breathers in  $\mathcal{PT}$ -symmetric nonlinear metamaterials. *Phys. Rev. Lett.* **110**(5), 053901 (2013)
27. X. Zhu, L. Feng, P. Zhang, X. Yin, X. Zhang, One-way invisible cloak using parity-time symmetric transformation optics. *Opt. Lett.* **38**(15), 2821–2824 (2013)



28. G. Castaldi, S. Savoia, V. Galdi, A. Alù, N. Engheta,  $\mathcal{PT}$  metamaterials via complex-coordinate transformation optics. *Phys. Rev. Lett.* **110**(17), 173901 (2013)
29. M. Kulishov, B. Kress, R. Slavík, Resonant cavities based on parity-time-symmetric diffractive gratings. *Opt. Express* **21**(8), 9473–9483 (2013)
30. M. Kang, F. Liu, J. Li, Effective spontaneous  $\mathcal{PT}$ -symmetry breaking in hybridized metamaterials. *Phys. Rev. A* **87**(5), 053824 (2013)
31. K.G. Makris, L. Ge, H.E. Türeci, Anomalous transient amplification of waves in non-normal photonic media. *Phys. Rev. X* **4**(4), 041044 (2014)
32. H. Alaeian, J.A. Dionne, Non-Hermitian nanophotonic and plasmonic waveguides. *Phys. Rev. B* **89**(7), 075136 (2014)
33. H. Alaeian, J.A. Dionne, Parity-time-symmetric plasmonic metamaterials. *Phys. Rev. A* **89**(3), 033829 (2014)
34. S. Savoia, G. Castaldi, V. Galdi, A. Alù, N. Engheta, Tunneling of obliquely incident waves through  $\mathcal{PT}$ -symmetric epsilon-near-zero bilayers. *Phys. Rev. B* **89**(8), 085105 (2014)
35. B. Peng, Ş.K. Özdemir, F. Lei, F. Monifi, M. Gianfreda, G.L. Long, S. Fan, F. Nori, C.M. Bender, L. Yang, Parity-time-symmetric whispering-gallery microcavities. *Nat. Phys.* **10**(5), 394–398 (2014)
36. B. Peng, S.K. Özdemir, S. Rotter, H. Yilmaz, M. Liertzer, F. Monifi, C.M. Bender, F. Nori, L. Yang, Loss-induced suppression and revival of lasing. *Science* **346**(6207), 328–332 (2014)
37. R. Fleury, D.L. Sounas, A. Alù, Negative refraction and planar focusing based on parity-time symmetric metasurfaces. *Phys. Rev. Lett.* **113**(2), 023903 (2014)
38. M.G. Silveirinha, Spontaneous parity-time-symmetry breaking in moving media. *Phys. Rev. A* **90**(1), 013842 (2014)
39. D.L. Sounas, R. Fleury, A. Alù, Unidirectional cloaking based on metasurfaces with balanced loss and gain. *Phys. Rev. Appl.* **4**(1), 014005 (2015)
40. M. Principe, G. Castaldi, M. Consales, A. Cusano, V. Galdi, Supersymmetry-inspired non-hermitian optical couplers. *Sci. Rep.* **5**, 8568 (2015)
41. S. Savoia, G. Castaldi, V. Galdi, A. Alù, N. Engheta,  $\mathcal{PT}$ -symmetry-induced wave confinement and guiding in  $\epsilon$ -near-zero metamaterials. *Phys. Rev. B* **91**(11), 115114 (2015)
42. H. Alaeian, J.A. Dionne, Controlling electric, magnetic, and chiral dipolar emission with  $\mathcal{PT}$ -symmetric potentials. *Phys. Rev. B* **91**(24), 245108 (2015)
43. H. Benisty, A. Lupu, A. Degiron, Transverse periodic  $\mathcal{PT}$  symmetry for modal demultiplexing in optical waveguides. *Phys. Rev. A* **91**(5), 053825 (2015)
44. S. Longhi, D. Gatti, G. Della Valle, Robust light transport in non-Hermitian photonic lattices. *Sci. Rep.* **5**, 13376 (2015)
45. C. Poli, M. Bellec, U. Kuhl, F. Mortessagne, H. Schomerus, Selective enhancement of topologically induced interface states in a dielectric resonator chain. *Nat. Commun.* **6**, 6710 (2015)
46. S. Savoia, G. Castaldi, V. Galdi, Complex-coordinate non-Hermitian transformation optics. *J. Opt.* **18**(4), 044027 (2016)
47. Y. Ra’di, D.L. Sounas, A. Alù, S.A. Tretyakov, Parity-time-symmetric teleportation. *Phys. Rev. B* **93**, 235427 (2016)
48. P.Y. Chen, J. Jung,  $\mathcal{PT}$  symmetry and singularity-enhanced sensing based on photoexcited graphene metasurfaces. *Phys. Rev. Appl.* **5**(6), 064018 (2016)
49. E. Hurwitz, G. Gbur, Localized  $\mathcal{PT}$ -symmetric directionally invisible scatterers. *Phys. Rev. A* **93**(4), 041803 (2016)
50. S. Savoia, G. Castaldi, V. Galdi, Non-Hermiticity-induced wave confinement and guiding in loss-gain-loss three-layer systems. *Phys. Rev. A* **94**(4), 043838 (2016)
51. U. Leonhardt, Optical conformal mapping. *Science* **312**(5781), 1777–1780 (2006)
52. J.B. Pendry, D. Schurig, D.R. Smith, Controlling electromagnetic fields. *Science* **312**(5781), 1780–1782 (2006)
53. E.J. Post, *Formal Structure of Electromagnetics: General Covariance and Electromagnetics* (Dover Publications, New York, 1997)

54. D.H. Werner, D.H. Kwon (Eds.), *Transformation Electromagnetics and Metamaterials: Fundamental Principles and Applications* (Springer, Dordrecht, The Netherlands, 2013)
55. J. Chandezon, Les equations de Maxwell sous forme covariante. Application a l'étude de la propagation dans les guides periodiques et à la diffraction par les reseaux, PhD thesis, Clermont-Ferrand University, Aubiere, France (1979)
56. J. Chandezon, M.T. Dupuis, G. Cornet, D. Maystre, Multicoated gratings: a differential formalism applicable in the entire optical region. *J. Opt. Soc. Am.* **72**(7), 839–846 (1982)
57. G.A. Deschamps, Gaussian beam as a bundle of complex rays. *Electron. Lett.* **7**(23), 684–685 (1971)
58. L.B. Felsen, Complex source point solution of the field equations and their relation to the propagation and scattering of gaussian beams. *Symp. Math.* **18**(23), 39–56 (1976)
59. S.J. Chapman, J.M.H. Lawry, J.R. Ockendon, R.H. Tew, On the theory of complex rays. *SIAM Rev.* **41**(3), 417–509 (1999)
60. W.C. Chew, J.M. Jin, E. Michielssen, Complex coordinate stretching as a generalized absorbing boundary condition. *Microw. Opt. Technol. Lett.* **15**(6), 363–369 (1997)
61. B.I. Popa, S.A. Cummer, Complex coordinates in transformation optics. *Phys. Rev. A* **84**(6), 063837 (2011)
62. G. Castaldi, I. Gallina, V. Galdi, A. Alù, N. Engheta, Transformation-optics generalization of tunnelling effects in bi-layers made of paired pseudo-epsilon-negative/mu-negative media. *J. Opt.* **13**(2), 024011 (2011)
63. S.A.R. Horsley, C.G. King, T.G. Philbin, Wave propagation in complex coordinates. *J. Opt.* **18**(4), 044016 (2016)
64. I. Gallina, G. Castaldi, V. Galdi, A. Alù, N. Engheta, General class of metamaterial transformation slabs. *Phys. Rev. B* **81**(12), 125124 (2010)
65. T.G. Mackay, A. Lakhtakia, Dynamically controllable anisotropic metamaterials with simultaneous attenuation and amplification. *Phys. Rev. A* **92**(5), 053847 (2015)
66. COMSOL Group, COMSOL Multiphysics: Version 5.0. COMSOL, Stockholm (2015)
67. R.E. Collin, *Field Theory of Guided Waves* (Wiley-IEEE Press, Piscataway, 1991)
68. D.R. Jackson, A. Oliner, A leaky-wave analysis of the high-gain printed antenna configuration. *IEEE Trans. Antennas Propag.* **36**(7), 905–910 (1988)
69. A.E. Siegman, Propagating modes in gain-guided optical fibers. *J. Opt. Soc. Am. A* **20**(8), 1617–1628 (2003)
70. D.A. Zelyulin, Y.V. Kartashov, V.V. Konotop, Solitons in a medium with linear dissipation and localized gain. *Opt. Lett.* **36**(7), 1200–1202 (2011)
71. S.A. Maier, *Plasmonics: Fundamentals and Applications* (Springer US, Boston, 2007)
72. N. Engheta, Pursuing near-zero response. *Science* **340**(6130), 286–287 (2013)
73. Y. Jin, S. Xiao, N.A. Mortensen, S. He, Arbitrarily thin metamaterial structure for perfect absorption and giant magnification. *Opt. Express* **19**(12), 11,114–11,119 (2011)
74. L. Sun, S. Feng, X. Yang, Loss enhanced transmission and collimation in anisotropic epsilon-near-zero metamaterials. *Appl. Phys. Lett.* **101**(24), 241101 (2012)
75. S. Feng, K. Halterman, Coherent perfect absorption in epsilon-near-zero metamaterials. *Phys. Rev. B* **86**(16), 165103 (2012)
76. K. Uller, Beiträge zur Theorie der Elektromagnetischen Strahlung, PhD thesis, Universität Rostock, Germany (1903)
77. J. Zenneck, Über die Fortpflanzung ebener elektromagnetischer Wellen längs einer ebenen Leiterfläche und ihre Beziehung zur drahtlosen Telegraphie. *Annalen der Physik* **328**(10), 846–866 (1907)
78. X. Huang, Y. Lai, Z.H. Hang, H. Zheng, C. Chan, Dirac cones induced by accidental degeneracy in photonic crystals and zero-refractive-index materials. *Nat. Mater.* **10**(8), 582–586 (2011)
79. P. Moitra, Y. Yang, Z. Anderson, I.I. Kravchenko, D.P. Briggs, J. Valentine, Realization of an all-dielectric zero-index optical metamaterial. *Nat. Photonics* **7**(10), 791–795 (2013)



**Silvio Savoia** was born in Benevento, Italy, in 1985. He received a master's degree in telecommunication engineering and a PhD degree in information engineering in 2010 and 2016, respectively, both from the University of Sannio, Benevento, Italy. He has held visiting student positions at the TNO Defence, Security and Safety (The Hague, NL, 2010), the University of Texas at Austin (2014), and the University of Pennsylvania (2015). In 2014, he was awarded an IEEE APS Doctoral Research Award. In October 2016, he joined GreenWaves srl, Gorgonzola (MI), Italy, where he is currently working as an antenna engineer. His main research and professional interests include antenna theory and design and artificial materials.



**Giuseppe Castaldi** was born in Benevento, Italy, in 1968. He received the Laurea degree (summa cum laude) in electrical engineering from the "Federico II" University of Naples, Italy, in 1993, and the PhD degree in applied electromagnetics from the University of Salerno, Italy, in 1999. In 2001, he was a postdoctoral research fellow at the TNO Physics and Electronics Laboratory, The Hague, the Netherlands. In 2004, he was appointed assistant professor of electromagnetics and joined the Department of Engineering, University of Sannio, Benevento, Italy, where he is currently working as an associate professor. He has coauthored over a hundred scientific papers in international journals and books. His research interests include metamaterials, non-Hermitian optics, transformation electromagnetics, aperiodically ordered structures, electromagnetic chaos, antenna array diagnostics, and phase retrieval.



**Vincenzo Galdi** is an associate professor of electromagnetics at the University of Sannio, Benevento, Italy, where he has also served as an associate chair for undergraduate studies in telecommunication engineering (2005–2010). He has held several visiting positions at abroad research institutions, including the European Space Research and Technology Centre (Noordwijk, NL), Boston University, Massachusetts Institute of Technology, and California Institute of Technology. He has coedited two books and coauthored over 120 papers in peer-reviewed international journals, 4 book chapters, and 140 conference papers (50 invited). He is currently serving as a track editor of the IEEE Transactions on Antennas and Propagation, an associate editor of the *International Journal of Antennas and Propagation* and of *Heliyon*, and a regular reviewer for several journals, conferences, and funding agencies. His research interests encompass wave interactions with complex structures and media, multiphysics metamaterials, electromagnetic chaos, inverse scattering, and gravitational interferometry. Dr. Galdi is a fellow of the IEEE and a member of the LIGO Scientific Collaboration, the Optical Society of America, and Sigma Xi. He is also the recipient of an Outstanding Associate Editor Award (IEEE Transactions on Antennas and Propagation, 2014) and a Young Scientist Award (URSI, 2001).

# Chapter 22

## Unidirectional, Defect-Immune, and Topologically Protected Electromagnetic Surface Waves

George W. Hanson, Seyyed Ali Hassani Gangaraj,  
and Andrei M. Nemilentsau

### 22.1 Berry Phase Concepts

We begin by introducing the main idea of Berry phase, potential, and curvature and summarize some related concepts.

#### 22.1.1 Motivation: Backscattering-Immune One-Way SPP Wave Propagation

Surface-plasmon-polariton (SPP) waves are well-known and long-studied waves that can be guided at the interface between two materials (nominally, for an SPP wave to exist in an isotropic environment, one material has relative permittivity  $\varepsilon = \varepsilon_1 < 0$ , and the other has  $\varepsilon = \varepsilon_2 > 0$ , such as an air-plasma (metal) interface). For a wave traveling as  $e^{\pm ikz}$  ( $z$  parallel to the interface), the SPP wave dispersion relation is [1]

$$k = \frac{\omega}{c} \sqrt{\frac{\varepsilon_1 \varepsilon_2}{\varepsilon_1 + \varepsilon_2}}, \quad (22.1)$$

---

G.W. Hanson (✉) • S.A.H. Gangaraj  
Department of Electrical Engineering, University of Wisconsin-Milwaukee, Milwaukee,  
WI 53211, USA  
e-mail: [george@uwm.edu](mailto:george@uwm.edu); [ali.gangaraj@gmail.com](mailto:ali.gangaraj@gmail.com)

A.M. Nemilentsau  
Department of Electrical and Computer Engineering, University of Minnesota, Minneapolis,  
MN 55455, USA  
e-mail: [andrei.nemilentsau@gmail.com](mailto:andrei.nemilentsau@gmail.com)

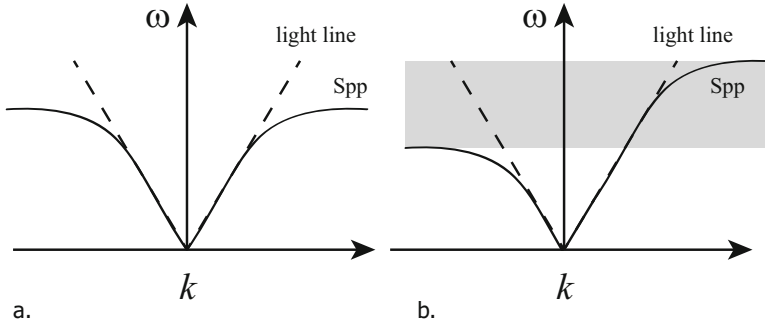


**Fig. 22.1** (a) Dispersion of reciprocal SPP wave. (b) Nonreciprocal SPP wave; shaded region depicts frequency range of unidirectional propagation

where  $\varepsilon_\alpha = \varepsilon_\alpha(\omega)$ . For example, for a simple lossless plasma  $\varepsilon(\omega) = 1 - \omega_p^2/\omega^2$  with  $\omega_p$  being the plasma frequency. Plotting the dispersion equation (Fig. 22.1a), we see that propagation is reciprocal,  $\omega(-k) = \omega(k)$ , so that forward-propagating ( $k$ ) and backward-traveling ( $-k$ ) waves exist at the same frequency. A source near the surface will excite SPP waves traveling in both directions ( $\pm z$ ), and upon encountering a discontinuity, an SPP wave traveling in, say, the  $+z$  direction will undergo both reflection and transmission, again resulting in both forward- and backward-traveling waves.

Waves can be excited in a single direction using a directive source (e.g., planar Yagi-Uda antenna or by a circularly polarized source that couples to the SPP wave's spin polarization), but upon encountering a discontinuity, partial reflection of the wave will occur since the material itself allows propagation in both directions.

However, if the medium only supports modes that can travel in one direction, say, via nonreciprocity as depicted in Fig. 22.1b (e.g., via a magnetic-field biased plasma having a tensor permittivity with non-zero off-diagonal elements [2–4]), then upon encountering a discontinuity, an SPP wave cannot be reflected (backscattered). This is a rather remarkable occurrence and has important applications in waveguiding (e.g., defect-immune waveguides). In general, there will be a range of energies where only propagation in one direction is possible (e.g., in Fig. 22.1b in the indicated frequency band, only forward-propagating modes can exist and there are no states with  $-k$ ).

However, the idea of one-way (backscattering-immune) surface-wave propagation is more general than indicated above. In particular, one does not necessarily need a nonreciprocal material. A broad class of materials exist known as photonic topological insulators (PTIs) which have this characteristic, generally supporting Hall/chiral edge states. This class of materials includes biased nonreciprocal magneto-plasmas (more generally, materials with broken time-reversal symmetry, photonic analogs of quantum Hall materials), but it also includes time-reversal-invariant materials with broken inversion symmetry (photonic analogs

of topological insulators). In the latter case, photon states are separated in two “spin” subspaces (usually through geometry such as via a hexagonal lattice), and “spin-orbit” coupling is introduced through inversion symmetry breaking. Furthermore, as described in [5], before the Berry phase was understood as the general concept it is now, in various fields this extra phase had been found. In electromagnetics, the most notable discoveries were by Pancharatnam in 1956 [6], who studied polarization evolution of light, and Budden and Smith [7, 8], who considered propagation through the ionosphere, modeled as an inhomogeneous medium whose parameters varied gradually with height.

On the electronic side, topological insulators (TIs) and quantum Hall edge state materials (which utilize many of the same concepts described here) came first, and, noting the analogy between electronic and optical systems, the first work on PTIs was described in Refs. [9, 10]. The first experimental demonstration of an optical TI was shown by Rechtsman et al. [11] and in various material systems [12–14], and Ref. [15], among others. Understanding the broad field of PTIs necessitates understanding the Berry phase, potential, curvature, and the concept of Chern invariants.

### 22.1.2 Origin of the Berry Phase

We consider a system described by a Hamiltonian dependent on parameters that vary in time,  $H = H(\mathbf{R})$ , such that  $\mathbf{R} = \mathbf{R}(t) = (R_1(t), R_2(t), R_3(t), \dots)$ . We will consider a path in parameter space  $C$  along which  $\mathbf{R}$  changes. For example,  $\mathbf{R}$  could describe the position of a particle  $(x(t), y(t), z(t))$ , and  $C$  could be a path in physical space. However, here we are primarily interested in the case when  $\mathbf{R}(t)$  lives in momentum (reciprocal) space.

The evolution of the system is assumed to be adiabatic, such that the parameters  $\mathbf{R}(t)$  of the Hamiltonian change slowly along path  $C$  in parameter space. The adiabatic theorem states that if a system is initially in the  $n$ th eigenstate of the initial Hamiltonian  $H(\mathbf{R}(0))$  and the system is moved slowly enough as  $\mathbf{R}(t)$  changes, it will arrive at the  $n$ th eigenstate of the final Hamiltonian  $H(\mathbf{R}(T))$ . Development of the adiabatic solution below will show how the Berry phase comes about.

We will assume that the time-dependent state evolves through an evolution equation

$$i\hbar \partial_t |\Psi(t)\rangle = H(\mathbf{R}(t)) |\Psi(t)\rangle, \quad (22.2)$$

which is typically taken to be the Schrödinger equation, where  $|\Psi(t)\rangle$  is a scalar, but it could also represent the Dirac equation where  $|\Psi(t)\rangle$  is a spinor and classical Maxwell’s equations ( $\hbar = 1$ ), where  $|\Psi(t)\rangle$  is the 6-vector of electromagnetic fields  $(\mathbf{E}, \mathbf{H})$ .

Because of the slow variation of the Hamiltonian parameters, we can assume that at every time the instantaneous eigenstates of the Hamiltonian satisfy

$$H(\mathbf{R}) |n(\mathbf{R})\rangle = E_n |n(\mathbf{R})\rangle. \tag{22.3}$$

However, (22.3) does not uniquely determine the function  $|n(\mathbf{R})\rangle$ , since we could include an arbitrary phase factor (gauge choice) that depends on  $\mathbf{R}(t)$ .

To motivate the following derivation, note that if the Hamiltonian is independent of time, then a system that starts out in the  $n$ th eigenstate  $|n\rangle$  remains in the  $n$ th eigenstate but may simply pick up a phase factor,

$$|\Psi_n(t)\rangle = |n\rangle e^{-\frac{i}{\hbar} E_n t}. \tag{22.4}$$

So, to represent the evolution of the system with slowly varying Hamiltonian, we use a superposition of these instantaneous eigenvectors, adjusting the phase factor to account for the time variation,

$$|\Psi(t)\rangle = \sum_n a_n(t) e^{-\frac{i}{\hbar} \int_0^t E_n(\mathbf{R}(t')) dt'} |n(\mathbf{R}(t))\rangle = \sum_n a_n(t) e^{i\alpha_n} |n(\mathbf{R}(t))\rangle, \tag{22.5}$$

where  $\alpha_n(t) = -\frac{1}{\hbar} \int_0^t E_n(\mathbf{R}(t')) dt'$  is called the dynamical phase. If we substitute this general form of solution in the evolution equation (22.2), we obtain

$$\left. \begin{aligned} i\hbar \sum_n (\partial_t a_n + i a_n \partial_t \alpha_n) e^{i\alpha_n} |n\rangle + i\hbar \sum_n a_n e^{i\alpha_n} |\partial_t n\rangle &= H |\Psi\rangle \\ i\hbar \sum_n (\partial_t a_n) e^{i\alpha_n} |n\rangle + \sum_n E_n a_n e^{i\alpha_n} |n\rangle + i\hbar \sum_n a_n e^{i\alpha_n} |\partial_t n\rangle &= H |\Psi\rangle, \end{aligned} \right\} \tag{22.6}$$

and taking the inner product of both sides by  $\langle m|$ , it yields

$$\partial_t a_m = - \sum_n a_n e^{i(\alpha_n - \alpha_m)} \langle m | \partial_t n \rangle. \tag{22.7}$$

In the adiabatic limit, where excitation of other instantaneous eigenvectors is negligible (see Appendix 1), the choice of initial state  $|\Psi(t)\rangle = |n(\mathbf{R}(t=0))\rangle$  will imply that  $|a_n(t)| = 1$ ,  $a_m(t) = 0$  for  $m \neq n$ . We then have

$$\partial_t a_n = -a_n \langle n | \partial_t n \rangle \rightarrow a_n = e^{i\gamma_n}; \quad \partial_t \gamma_n = i \langle n | \partial_t n \rangle. \tag{22.8}$$

Therefore, the adiabatic evolution of the state vector becomes

$$|\Psi(t)\rangle = e^{i\gamma_n} e^{i\alpha_n} |n(\mathbf{R}(t))\rangle. \tag{22.9}$$

We have

$$\begin{aligned}
 \gamma_n &= i \int_0^t \langle n(\mathbf{R}(t')) | \frac{\partial}{\partial t} | n(\mathbf{R}(t')) \rangle dt' \\
 &= i \int_0^t \langle n(\mathbf{R}(t')) | \frac{\partial}{\partial \mathbf{R}} | n(\mathbf{R}(t')) \rangle \cdot \frac{\partial \mathbf{R}}{\partial t'} dt' \\
 &= \int_{R_i}^{R_f} d\mathbf{R} \cdot i \langle n(\mathbf{R}) | \nabla_{\mathbf{R}} | n(\mathbf{R}) \rangle = \int_{R_i}^{R_f} d\mathbf{R} \cdot \mathbf{A}_n(\mathbf{R}) \quad (22.10)
 \end{aligned}$$

(setting  $\nabla_{\mathbf{R}} = \partial/\partial \mathbf{R}$ ), where  $R_i$  and  $R_f$  are the initial and final values of  $\mathbf{R}(t)$  in parameter space and where

$$\mathbf{A}_n(\mathbf{R}) = i \langle n(\mathbf{R}) | \nabla_{\mathbf{R}} | n(\mathbf{R}) \rangle = -\text{Im} \langle n(\mathbf{R}) | \nabla_{\mathbf{R}} | n(\mathbf{R}) \rangle \quad (22.11)$$

is called the *Berry vector potential* (also called *the Berry connection* since it connects the state at  $\mathbf{R}$  and the state at  $\mathbf{R} + d\mathbf{R}$ ) and  $\gamma_n$  is called the *Berry phase*. One can also obtain this result by assuming the existence of this extra phase [17],  $|\Psi(t)\rangle = e^{i\gamma_n} e^{i\alpha_n} |n(\mathbf{R}(t))\rangle$ , and inserting into the Schrödinger equation. Taking the inner product with  $\langle n(\mathbf{R}(t)) |$  and using  $\langle n(\mathbf{R}(t)) | H(\mathbf{R}) | n(\mathbf{R}(t)) \rangle = E_n$  lead to the desired result.

Equation (22.10) shows that, in addition to the dynamical phase, the state will acquire an additional phase  $\gamma_n$  during the adiabatic evolution (note that  $\gamma_n$  is real-valued;  $e^{i\gamma_n(t)}$  is a phase, not a decay term;  $\langle n(\mathbf{R}) | \nabla_{\mathbf{R}} | n(\mathbf{R}) \rangle$  is imaginary since  $\langle n(\mathbf{R}) | n(\mathbf{R}) \rangle = 1$ , and so taking a derivative on both sides yields  $\langle n(\mathbf{R}) | \nabla_{\mathbf{R}} | n(\mathbf{R}) \rangle = -\langle n(\mathbf{R}) | \nabla_{\mathbf{R}} | n(\mathbf{R}) \rangle^*$ ). The existence of this phase has been known since the early days of quantum mechanics, but it was thought to be nonobservable since a gauge transformation could remove it. It was Berry who, in 1984, showed that for cyclic variation ( $\mathbf{R}_f = \mathbf{R}_i$ ), the phase is not removable under a gauge transformation [17] (discussed below) and was also observable. This net phase change depends only on the path  $C$  in parameter space that is traversed by  $\mathbf{R}(t)$  but not on the rate at which it is traversed (assuming the adiabatic hypothesis still holds). It is therefore called a *geometrical phase*, in distinction to the dynamical phase which depends on the elapsed time. This geometric phase has been generalized for nonadiabatic evolution [18].

### 22.1.2.1 Geometric Phase

Geometric phases have a long history and arise in many branches of physics [19]. They are well-illustrated by considering parallel transport of a vector along a curved surface. To consider an intuitive example, as widely discussed (see, e.g., Ref. [20]) and depicted in Fig. 22.2, consider at  $t = 0$  a pendulum at the north pole of a sphere,



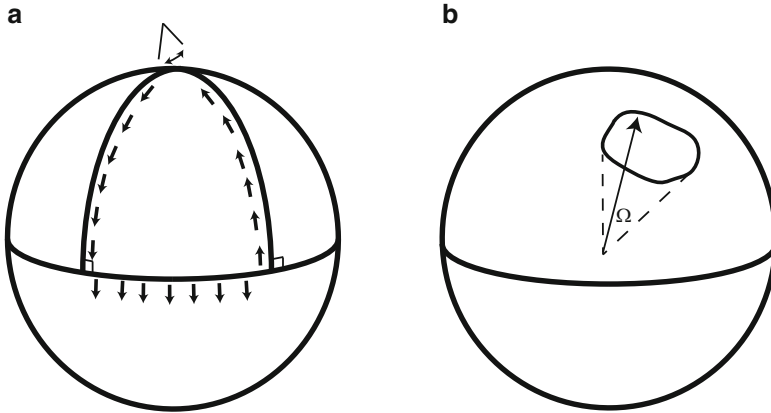


**Fig. 22.2** (a) Parallel transport around a sphere. (b) Parallel transport about a closed contour on a sphere and solid angle subtended

swinging along a longitude line. If the pendulum is moved along the longitude line to the equator, across the equator some distance, and at  $t = T$  arriving back at the north pole via a different longitude line (and assuming the movement is sufficiently slow, in keeping with the adiabatic assumption), the angle of the pendulum swing with some fixed reference is obviously different from its initial angle (this difference is called the defect angle, which is a mechanical analog of phase). The defect angle is given by the solid angle  $\Omega$  subtended by the path of movement. For example,  $\Omega_{\text{sphere}} = 4\pi$  for a sphere, and so if the longitude lines are 180 degrees apart, the subtended angle is  $\Omega_{\text{sphere}}/4 = \pi$ . For the electronic case, moving along a contour in parameter space, the Berry phase is equal to  $s\Omega$ , where  $s$  is the particle spin. Parallel transport along a non-curved surface does not lead to a defect angle, and so we see that a non-zero Berry phase has its origins in the curvature of parameter space. In optics, an optical fiber wound into a helix has been used to demonstrate Berry phase [21], among other results (see, e.g., Ref. [22]). In these cases the momentum is  $\mathbf{p} = \hat{x}p_x + \hat{y}p_y + \hat{z}p_z = \hbar\mathbf{k}$ , where  $\mathbf{k}$  is the propagation vector of the optical wave,  $|\mathbf{k}| = k = 2\pi/\lambda$ . Therefore,  $|\mathbf{p}|^2 = p_x^2 + p_y^2 + p_z^2 = (\hbar k)^2$ , which is a sphere, and so rotation of momentum is equivalent to movement on the surface of a sphere.

When  $\mathbf{R}$  is a real-space parameter, consider an electron in the ground state of an atom. As the atom is slowly moved through a static magnetic field, the electron stays in the ground state (adiabatic) but picks up a Berry phase, which is the Aharonov-Bohm phase. As detailed in the electromagnetic examples in Sect. 22.3, we will be more interested in the case when the parameter space  $\mathbf{R}$  is momentum space,  $\mathbf{R} = \mathbf{k}$ . In this case, we can simply consider moving through  $\mathbf{k}$ -space without necessitating the time variable and simply consider  $\gamma_n(\mathbf{k})$ , which will depend on the path taken in  $\mathbf{k}$ -space.

### 22.1.2.2 Gauge

The Berry potential  $A_n(\mathbf{R})$  is a gauge-dependent quantity. If we make a gauge transformation  $|n(\mathbf{R})\rangle \rightarrow e^{i\xi(\mathbf{R})} |n(\mathbf{R})\rangle$  with  $\xi(\mathbf{R})$  an arbitrary smooth function (this is equivalent to an electromagnetic gauge transformation, see [Appendix 2](#)), the Berry potential transforms to  $A_n(\mathbf{R}) \rightarrow A_n(\mathbf{R}) - \nabla_{\mathbf{R}}\xi(\mathbf{R})$ . Consequently, the additional phase  $\gamma_n$  will be changed by  $\xi(\mathbf{R}_i) - \xi(\mathbf{R}_f)$  after the gauge transformation, where  $\mathbf{R}_i$  and  $\mathbf{R}_f$  are the initial and final points of the path  $C$ . For an arbitrary path, one can choose a suitable  $\xi(\mathbf{R})$  such that accumulation of that extra phase term vanishes, and we are left only with the dynamical phase. However, by considering a closed path (cyclic evolution of the system)  $C$  where  $\mathbf{R}_f = \mathbf{R}_i$  and noting that the eigenfunctions should be single-valued,  $|n(\mathbf{R}_i)\rangle = |n(\mathbf{R}_f)\rangle$ , then  $e^{i\xi(\mathbf{R}_i)} |n(\mathbf{R}_i)\rangle = e^{i\xi(\mathbf{R}_f)} |n(\mathbf{R}_f)\rangle = e^{i\xi(\mathbf{R}_f)} |n(\mathbf{R}_i)\rangle$ , and so  $e^{i\xi(\mathbf{R}_i)} = e^{i\xi(\mathbf{R}_f)}$ . That is, single-valuedness of the eigenbasis means that  $e^{i\xi(\mathbf{R})}$  (but not necessarily  $\xi(\mathbf{R})$ ) must be single-valued, and therefore we must have

$$\xi(\mathbf{R}_i) - \xi(\mathbf{R}_f) = 2\pi m, \quad (22.12)$$

where  $m$  is an integer. This shows that  $\gamma_n$  can be only change by an integer multiple of  $2\pi$  under a gauge transformation using a smooth gauge function; this phase cannot be removed. Note that this holds for  $\text{Dim}(R) > 1$ , so that we have a path integral in (22.10). For a one-parameter space  $R$ , (22.10) becomes a simple integral over a vanishing path; for  $R_f = R_i = R$   $\int_R^R i \langle n(R) | \frac{\partial}{\partial R} | n(R) \rangle dR = 0$ . However, when applied to periodic solids (for which the Berry phase is also called the *Zac phase*, electrons crossing the Brillouin zone (BZ) can indeed pick up a Berry phase, which persists in 1D because of the periodicity of the Brillouin zone; after assuming period  $a$ , when  $k$  sweeps across the BZ due to, say, an applied field, a phase can be acquired since  $\int_{-\pi/a}^{\pi/a} (\cdot) dk = \oint_{-\pi/a}^{\pi/a} (\cdot) dk$ .

As described in the following, we will only be interested in paths  $C$  that are closed in parameter space, and so we write

$$\gamma_n = \gamma_n(\mathbf{R}) = \oint_C d\mathbf{R} \cdot \mathbf{A}_n(\mathbf{R}). \quad (22.13)$$

In the space of gauge functions  $\xi$  where  $e^{i\xi(\mathbf{R})}$  is single-valued, (22.13) is gauge-dependent (one could say it is gauge-invariant up to factors of  $2\pi$ ). If we restrain the class of gauge functions  $\xi$  to be themselves single-valued, then (22.13) is gauge-independent (this is easily seen since  $\oint_C d\mathbf{R} \cdot \nabla_{\mathbf{R}}\xi(\mathbf{R}) = 0$  for  $\xi$  a smooth, single-valued function).

For a two-dimensionally periodic material (such as graphene as an electronic example or a hexagonal array of infinite cylinders as an electromagnetic example),  $C$  is typically the boundary of the first Brillouin zone, and  $\mathbf{S}$  is its surface in  $\mathbf{k}$ -space. In this case, the *cyclic* variation forming the closed path  $C$  in  $\mathbf{k}$ -space is the perimeter of the first Brillouin zone.

## 22.2 Electromagnetic Description: Berry Quantities for Photons

Although the concept of Berry phase is general for any cyclic variation through some parameter space  $\mathbf{R}$ , a primary application is to crystalline solid-state systems (e.g., electrons in a crystal lattice). However, here we are primarily interested in the photonic analogous of those systems and photonic topological insulators for both photonic crystals and for continuum media.

For simplicity in observing the correspondence between Maxwell's equations and the evolution equation (22.2), we first assume lossless and dispersionless materials characterized by dimensionless real-valued parameter  $\bar{\epsilon}$ ,  $\bar{\mu}$ ,  $\bar{\xi}$ ,  $\bar{\zeta}$ , representing permittivity, permeability, and magnetoelectric coupling tensors. Although any real material must have frequency dispersion, this simple model allows a straightforward conversion of various Berry quantities from the electronic to the electromagnetic case. The inclusion of both frequency and spatial dispersion will be discussed later.

In this case, Maxwell's equations are

$$\left. \begin{aligned} \nabla \times \mathbf{E} &= -\mu_0 \bar{\mu} \cdot \frac{\partial \mathbf{H}}{\partial t} - \frac{\bar{\zeta}}{c} \cdot \frac{\partial \mathbf{E}}{\partial t} - \mathbf{J}_m \\ \nabla \times \mathbf{H} &= \epsilon_0 \bar{\epsilon} \cdot \frac{\partial \mathbf{E}}{\partial t} + \frac{\bar{\xi}}{c} \cdot \frac{\partial \mathbf{H}}{\partial t} + \mathbf{J}_e \end{aligned} \right\}. \quad (22.14)$$

By defining the matrices

$$\begin{aligned} M &= \begin{pmatrix} \epsilon_0 \bar{\epsilon} & \frac{1}{c} \bar{\xi} \\ \frac{1}{c} \bar{\zeta} & \mu_0 \bar{\mu} \end{pmatrix}, \quad N = \begin{pmatrix} 0 & i \nabla \times \mathbf{I}_{3 \times 3} \\ -i \nabla \times \mathbf{I}_{3 \times 3} & 0 \end{pmatrix}, \\ f &= \begin{pmatrix} \mathbf{E} \\ \mathbf{H} \end{pmatrix}, \quad g = \begin{pmatrix} \mathbf{D} \\ \mathbf{B} \end{pmatrix} = Mf, \quad J = \begin{pmatrix} \mathbf{J}_e \\ \mathbf{J}_m \end{pmatrix} \end{aligned} \quad (22.15)$$

where  $M$  is Hermitian and real-valued, we can write Maxwell's equations in a compact form [23],

$$N \cdot f = i \left[ \frac{\partial g}{\partial t} + J \right] = i \left[ M \frac{\partial f}{\partial t} + \frac{\partial M}{\partial t} f + J \right]. \quad (22.16)$$

Note that the units of the sub-blocks of  $M$  differ (as do the dimensions of the 6-vectors  $f$  and  $g$ ) and that  $\epsilon$ ,  $\xi$ ,  $\zeta$ , and  $\mu$  are dimensionless. In the absence of an external excitation ( $J = 0$ ) and assumption of nondispersive (instantaneous) materials, Maxwell's equations become

$$i \frac{\partial f}{\partial t} = H_{cl} \cdot f, \quad (22.17)$$

where  $H_{cl} = M^{-1} \cdot N$ , which has the same form as the evolution equation (22.2) (e.g., the Schrödinger equation) with  $\hbar = 1$ , where the operator  $H_{cl}$  plays the role of a classical Hamiltonian. Because of this similarity between Maxwell's equations and the evolution equation (22.2), it is straightforward to extend the Berry potential concept to the electromagnetic field (photons); rather than, say, electrons acquiring a Berry phase while transversing a path in parameter space, photons will do the same (the polarization of the photon plays the role of particle spin). In this case, we define  $f_n$  as a six-component eigenmode satisfying

$$H_{cl} \cdot f_n = E_n f_n, \quad (22.18)$$

where  $E_n = \omega_n$  (in the following, we assume  $e^{-i\omega t}$  time dependence). Under a suitable inner product (discussed below),  $H_{cl}$  is Hermitian, and assuming the normalization condition  $\langle f_n | f_m \rangle = \delta_{nm}$ , the Berry vector potential has the same form as (22.11), i.e.,

$$\mathbf{A}_n = i \langle f_n | \nabla_{\mathbf{R}} f_n \rangle. \quad (22.19)$$

### 22.2.1 Berry Quantities for Photonic Crystals

If we assume a photonic crystal (periodic structure),  $f_n$  has the Bloch form  $f_n(\mathbf{r}) = u_n(\mathbf{r}) e^{i\mathbf{k}\mathbf{r}}$ , where  $u_n(\mathbf{r})$  is the periodic Bloch function and  $\mathbf{k}$  is the Bloch wavevector. In this case,  $\nabla_{\mathbf{R}} = \nabla_{\mathbf{k}}$  operates over parameter space  $\mathbf{k} = (k_x, k_y, k_z)$  and

$$\mathbf{A}_n = i \langle u_n | \nabla_{\mathbf{k}} u_n \rangle, \quad (22.20)$$

where the inner product is

$$\langle u_n | u_m \rangle = \frac{1}{2} \int_{\text{BZ}} u_n^*(\mathbf{r}) M(\mathbf{r}) u_m(\mathbf{r}) d\mathbf{r}. \quad (22.21)$$

This is the dispersionless special case of the result presented in Ref. [10] (see (41) in that reference), generalized to account for magnetoelectric coupling parameters in  $M$ .

The extension to dispersive media (i.e., real materials) would seem difficult since the simple product  $g = Mf$  in (22.15) becomes a convolution in time. However, it is shown by Haldane and Ragu [10] (omitting magnetoelectric parameters, although this can also be included) that the only necessary modification to allow for dispersive materials  $M = M(\omega)$  is to replace  $M$  in (22.21) with  $\partial(\omega M(\omega)) / \partial\omega$ , so that

$$\langle u_n | u_m \rangle = \frac{1}{2} \int_{\text{BZ}} u_n^*(\mathbf{r}) \frac{\partial(\omega M(\omega))}{\partial\omega} u_m(\mathbf{r}) d\mathbf{r}. \quad (22.22)$$

### 22.2.2 *Berry Quantities for Continuum Media*

Although the electronic case and, by analogy, the photonic case were developed for periodic systems (for which the relations provided in Sects. 22.1.2 and 22.2.3 hold), it turns out that continuum material models can also lead to nontrivial Berry phase effects. The simplest example is of a biased plasma (magneto-plasma) with relative permittivity tensor

$$\bar{\epsilon} = \begin{pmatrix} \epsilon_{11} & \epsilon_{12} & 0 \\ \epsilon_{21} & \epsilon_{22} & 0 \\ 0 & 0 & \epsilon_{33} \end{pmatrix}, \quad (22.23)$$

where typically  $\epsilon_{21} = \epsilon_{12}^*$  and  $\epsilon_{11} = \epsilon_{22} = \epsilon_{33}$  (in the absence of a bias field  $\epsilon_{12} = 0$ , the material is reciprocal, and  $\bar{\epsilon}$  reduces to a scalar). An example involving this type of material is provided below. At the interface between the magneto-plasma and an ordinary (unbiased) plasma, a topologically protected edge mode can exist [2–4]. In addition, more complicated materials combining hyperbolic and chiral response have been shown to be topologically nontrivial [24].

To account for material dispersion, following the result in Ref. [10] for lossless dispersive local periodic media, in Ref. [4] continuum models of dispersive lossless and possibly wavevector-dependent (nonlocal) materials, the Berry potential is again given by (22.11), with the inner product

$$\langle f_n | f_m \rangle = \frac{1}{2} f_n^* \frac{\partial (\omega M(\omega))}{\partial \omega} f_m. \quad (22.24)$$

The most general result is more complicated [4], but for a wide range of material classes, the simpler result shown here holds.

### 22.2.3 *Berry Curvature, Flux, and Tensor, and Chern Number*

Equation (22.13) is an analogy to the equation for magnetic flux  $\Phi_{\text{mag}}$ , in terms of the real-space magnetic field and magnetic vector potential  $\mathbf{A}_{\text{mag}}$  in electromagnetics,

$$\Phi_{\text{mag}} = \oint_C d\mathbf{l} \cdot \mathbf{A}_{\text{mag}}(\mathbf{r}), \quad (22.25)$$

where  $\oint_C d\mathbf{l} \cdot \mathbf{A}_{\text{mag}}(\mathbf{r})$  is also related to the Aharonov-Bohm phase in quantum mechanics. For the magnetic flux density in electromagnetics, we have

$$\mathbf{B}(\mathbf{r}) = \nabla_{\mathbf{r}} \times \mathbf{A}_{\text{mag}}(\mathbf{r}). \quad (22.26)$$

By analogy to electromagnetics, when  $2 \leq \dim(\mathbf{R}) \leq 3$ , a vector wave can be obtained from the Berry vector potential  $\mathbf{A}_n(\mathbf{R})$  as

$$\mathbf{F}_n(\mathbf{R}) = \nabla_{\mathbf{R}} \times \mathbf{A}_n(\mathbf{R}). \quad (22.27)$$

This field is called the *Berry curvature* and is obviously gauge-independent. It is a geometrical property of the parameter space and can be viewed as an effective magnetic field in parameter space; just as the motion of a moving charge is perpendicular to the magnetic field ( $\mathbf{F}_B = \mathbf{v} \times \mathbf{B}$ ), i.e., the curvature of the magnetic vector potential, the Berry curvature will induce transverse particle motion (an electronic or optical Hall effect). To continue the analogy, first note that the magnetic flux can also be written as

$$\Phi_{\text{mag}} = \int_S d\mathbf{S} \cdot \mathbf{B}(\mathbf{r}), \quad (22.28)$$

where (22.25) and (22.28) are equal via Stokes' theorem, i.e.,

$$\oint_C d\mathbf{l} \cdot \mathbf{A}_{\text{mag}}(\mathbf{r}) = \int_S d\mathbf{S} \cdot \nabla_{\mathbf{r}} \times \mathbf{A}_{\text{mag}}(\mathbf{r}) = \int_S d\mathbf{S} \cdot \mathbf{B}(\mathbf{r}). \quad (22.29)$$

For Stokes' theorem to hold, the fields must be nonsingular on and within the contour  $C$ . Given that magnetic monopoles, which would serve as singularities of the field, do not seem to exist, Stokes' theorem is valid to apply in this case. One can similarly use Stokes' theorem to connect the Berry phase and the Berry curvature,

$$\gamma_n = \oint_C d\mathbf{R} \cdot \mathbf{A}_n(\mathbf{R}) = \int_S d\mathbf{S} \cdot \mathbf{F}_n(\mathbf{R}), \quad (22.30)$$

where  $C$  and  $S$  are a contour and surface in parameter space and where the right side could be called the *Berry flux*. However, it must be kept in mind that the relation (22.30) is not always valid, since for the parameter-space fields  $\mathbf{A}_n(\mathbf{R})$ ,  $\mathbf{F}_n(\mathbf{R})$  singularities can occur, such that Stokes' theorem does not generally hold. Nevertheless, a gauge-independent Berry phase  $\gamma_n$  can be computed from the Berry flux integral,

$$\gamma_n = \int_S d\mathbf{S} \cdot \mathbf{F}_n(\mathbf{R}), \quad (22.31)$$

Stokes' theorem holding modulo  $2\pi$ .

#### 22.2.4 Chern Number, Bulk-Edge Correspondence, and Topologically Protected Edge States

Gauss's law relates the total flux over a closed surface  $S$  to the total charge within the surface,

$$\oint_S \varepsilon_0 \mathbf{E}(\mathbf{r}) \cdot d\mathbf{S} = Q^T = mq, \quad (22.32)$$

where, assuming identical charged particles,  $m$  is the number of particles and  $q$  the charge of each particle (though often approximated as a continuum,  $Q^T$  is quantized). To keep things simple, we'll assume a monopole charge of strength  $mq$  located at the origin. The electric field is given by Coulomb's law,

$$\mathbf{E} = \left( \frac{mq}{4\pi\epsilon_0} \right) \frac{\mathbf{r}}{r^3}. \quad (22.33)$$

Similarly,

$$\oint_S \mathbf{B}(\mathbf{r}, t) \cdot d\mathbf{S} = 0 \quad (22.34)$$

indicates that there are no magnetic monopoles. However, in parameter space, the flux integral over a closed manifold of the Berry curvature is quantized in units of  $2\pi$ , indicating the number of Berry monopoles (degeneracies) within the surface,

$$\oint_S d\mathbf{S} \cdot \mathbf{F}_n(\mathbf{R}) = 2\pi m_n = 2\pi C_n, \quad (22.35)$$

where  $m_n = C_n$  is an integer for the  $n$ th band known as the *Chern number*. The Chern number can be seen to be the flux associated with a Berry monopole of strength  $2\pi C_n$ , leading to the Berry curvature

$$\mathbf{F}_n = \left( \frac{C_n}{2} \right) \frac{\mathbf{k}}{k^3}. \quad (22.36)$$

The Berry monopole plays the role of source/sink of Berry curvature  $\mathbf{F}$ , just the electric charge monopole  $mq$  serves as a source/sink of electric field  $\mathbf{E} \propto \mathbf{r}/r^3$ . The Chern number can also be written in terms of the gauge form. For two dimensions, e.g.,  $\mathbf{R} = \mathbf{k} = (k_x, k_y)$ ,

$$C_n = \frac{1}{2\pi} \int_S dk_x dk_y \left( \frac{\partial}{\partial k_x} A_n^y - \frac{\partial}{\partial k_y} A_n^x \right). \quad (22.37)$$

Importantly, the Chern number is topologically invariant, meaning it is unaffected by smooth deformations in the surface that preserve topology (e.g., for a real-space surface, a teacup deforming into a torus). Moreover, the sum  $\sum_n C_n$  over all energies or bands  $n$  is zero. This is an extremely important point in understanding the most significant aspect of topological insulators (TIs), which is backscattering-protected edge propagation.

In periodic media (e.g., for electrons, in a crystalline solid, and for photons, electromagnetic waves in a photonic crystal), the Berry phase  $\gamma_n$  is a geometric (in parameter space) attribute of the  $n$ th band. The Brillouin zone is equivalent to a torus, forming the closed surface over which the Berry curvature of any nondegenerate band is integrated to compute the Chern number  $C_n$  for that band.

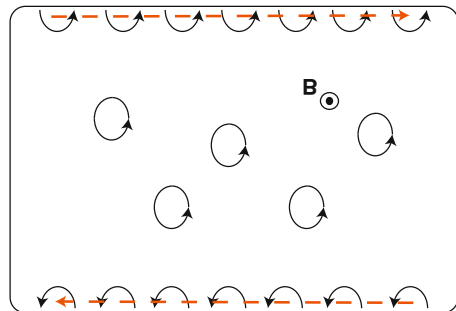
A continuum material presents a difficulty in that, rather than having a Brillouin zone that is, effectively, a closed surface (equivalent to a torus), providing the surface over which the Chern number can be computed, the momentum space of an infinite homogeneous material continuum model does not form a closed surface. However, 2D momentum space can be mapped to the Riemann sphere [4], forming the necessary surface.

### 22.2.4.1 Bulk-Edge Correspondence

An aspect of Berry curvature that is of immense interest in both electronic and photonic applications is the presence of one-way edge modes that are topologically protected from backscattering. The idea of Hall conductivity in an insulator gives some intuition about the one-way nature of these modes. Consider a finite-sized rectangle of thin material, immersed in a perpendicular magnetic field as depicted in Fig. 22.3. Bound electrons will circulate in response to the applied field, and those near the edge will have their orbits terminated by the edge[25]. The net effect is to have a unidirectional movement of electrons at the edge (orange arrows). The presence of a Hall conductivity (whether due to a magnetic field in the ordinary manner or due to non-zero Berry curvature associated with broken time-reversal or I symmetry) will elicit a similar response, although the response is quantized as described above. Thus, the bulk properties of the insulating material will result in a conducting edge state. This happens in both the electronic case and the photonic case to be described below.

Furthermore, consider that the Chern number and all Berry properties are related to an infinite bulk material, which generates bandstructure. However, in any practical application, the material is finite and has an interface with another medium. Let us consider a planar interface between medium 1 and medium 2. Far from the interface, in each region, particles (electrons, photons) will be governed by the respective Hamiltonians  $H_{1,2}$ . Let us assume that both materials share a common bandgap and that  $C_{\text{gap},1} = \sum_{n < n_g} C_n^{(1)}$ ; the Chern number sum over bands below the gap for material 1 and  $C_{\text{gap},2} = \sum_{n < n_g} C_n^{(2)}$ , the corresponding sum for material

**Fig. 22.3** Depiction of electron orbits in an insulator in the presence of a magnetic field and interrupted orbits at the edge





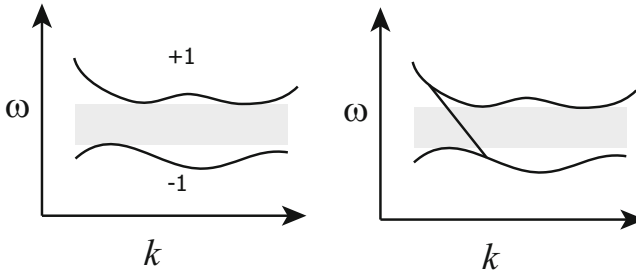


**Fig. 22.4** Bulk-edge correspondence. Materials with common bandgap and different Chern numbers share an interface where a unidirectional edge state closes the gap

2, differs,  $C_{\text{gap},\Delta} = C_2 - C_1 \neq 0$ . For some parameter value, the shared bandgap between the two mediums can close and then reopen. At the closing point, there is a degeneracy, and as the gap reopens, it can be crossed by a surface mode, as depicted in Fig. 22.4. The edge modes are circularly polarized (spin-polarized) and in periodic media are localized to a few lattice constants from the material boundary.

The existence of the surface/edge state is necessitated by the bulk material characteristics and so is independent of interface details. Therefore, the interface can possess discontinuities, defects, etc., which will not affect the surface wave. It can also be seen that the fact that the surface/edge states connect different energy levels indicates that they will have a group velocity that has definite sign (i.e., one-directional propagation). Therefore, in summary, the surface states are unidirectional and topologically protected from backscattering.

### 22.2.5 Some Electromagnetic Material Classes That Possess Nontrivial Chern Numbers

Although the field of topological photonic insulators is still being developed, there are several classes of materials and structures which possess topological protection and nontrivial Chern numbers. The approaches to design PTIs can be roughly divided into two categories. The first one relies on breaking of time-reversal symmetry by applying a static magnetic field to a gyromagnetic material [26] or time-harmonic modulation of coupled resonators [27, 28]. Another approach involves time-reversal-invariant metamaterials, where photon states are separated in two “spin” subspaces (usually through geometry such as via a hexagonal lattice), and “spin-orbit” coupling is introduced through symmetry breaking exploring such nontrivial characteristics of metamaterials as chirality, bianisotropy, and hyperbolicity [24, 29]. From an electromagnetic standpoint, the most important aspect of a PTI (of the Hall type) is that having nontrivial gap Chern number indicates the presence of surface/edge states that are topologically protected from backscattering.

In classical electromagnetics, the fields  $\mathbf{E}$ ,  $\mathbf{D}$ , and  $\mathbf{P}$  are even under time reversal (do not change with time reversal), whereas  $\mathbf{A}_{\text{mag}}$ ,  $\mathbf{B}$ ,  $\mathbf{H}$ ,  $\mathbf{J}$ , and  $\mathbf{S}$  (Poynting vector) are odd under time reversal (negated under time reversal). For systems with time-reversal symmetry,

$$\mathbf{F}(-\mathbf{k}) = -\mathbf{F}(\mathbf{k}). \quad (22.38)$$

Furthermore, the fields  $\mathbf{B}$  and  $\mathbf{H}$  are even under space inversion, whereas  $\mathbf{E}$ ,  $\mathbf{D}$ ,  $\mathbf{J}$ ,  $\mathbf{P}$ ,  $\mathbf{A}_{\text{mag}}$ , and  $\mathbf{S}$  are odd under spatial inversion. For systems with parity/inversion ( $I$ ) symmetry,

$$\mathbf{F}(-\mathbf{k}) = \mathbf{F}(\mathbf{k}), \quad (22.39)$$

so that if both symmetries are present,

$$\mathbf{F}(\mathbf{k}) = \mathbf{0}. \quad (22.40)$$

Systems having both spatial-inversion and time-reversal symmetry will exhibit trivial topology in momentum space, so that no one-way edge mode will exist (all bands have  $C_n = 0$ ).

Regarding periodic materials, Dirac (linear) degeneracies will occur for hexagonal lattices, and other lattice types may exhibit other degeneracies (e.g., quadratic degeneracies consisting of double Dirac degeneracies for a cubic lattice [30, 31]), but, regardless of degeneracy type, e.g., a simple lattice of material cylinders in a host medium, if the cylinders are made of simple isotropic materials have scalar material properties  $\varepsilon$  and  $\mu$ , the system will be both space-inversion and time-reversal symmetric, and all bands will have trivial Chern number.

In the periodic case, the degeneracies can be broken in several ways. One way that has been widely studied is to use rods with materials that themselves break time-reversal symmetry [31] or to embed, say, a hexagonal array of nonreciprocal rods into another array of simple rods [32] so that both arrays share a common bandgap. The resulting nonreciprocal structure will generally have bands of nontrivial Chern number, leading to a non-zero gap Chern number. A detailed example is provided below. Large Chern numbers can be achieved by increasing spatial symmetry to result in point degeneracies of higher order (e.g., several colocated Dirac points) and then to, say, introduce time-reversal symmetry breaking [33].

Another method to create a nontrivial Chern number is to use simple materials (simple dielectrics and metals) but to break inversion symmetry by deforming the lattice. For example, in Ref.[34], simple dielectric rods are used in a hexagonal pattern, resulting in a Dirac degeneracy. Slightly deforming the lattice can result in inversion-symmetry breaking and unidirectional edge modes (analogous to electronic topological insulators). Various other schemes have also been proposed [14, 29].

## 22.3 Photonic Examples

### 22.3.1 Periodic Photonic System Example

One way to create a PTI is via a hexagonal array of infinite cylinders. Consider a simple dielectric material of relative permittivity  $\varepsilon$  with a periodic array of air holes (cylinders of radius  $r_1 = \alpha_1 a$ , with  $a$  the lattice constant) in the form of a triangular lattice, as shown in Fig. 22.5a. The periodicity is chosen to create a bandgap in the allowed modes of the system [32]. A single defect, such as making one hole of a different radius, or filling the hole with some material, can establish a resonator having frequency in the bandgap. Making a periodic array of defects can create bandstructure within the original bandgap, in this case, creating four modes in the bandgap. Here the array of defects is created using cylinders of radius  $r_2 = \alpha_2 a$  of magneto-optic material,

$$\varepsilon_{\text{rod}} = \begin{bmatrix} \varepsilon_r & -i\varepsilon_i & 0 \\ i\varepsilon_i & \varepsilon_r & 0 \\ 0 & 0 & \varepsilon_r \end{bmatrix} \quad (22.41)$$

and arranging them in a hexagonal lattice with lattice constant  $a' = \alpha_3 a$ , as shown in Fig. 22.5b. Due to the hexagonal symmetry, for the unbiased defect array ( $\varepsilon_i = 0$ ), there are degeneracies in the modes at the  $\Gamma$  and  $K$  points. Time-reversal symmetry can be broken by applying a bias parallel to the cylinders ( $\varepsilon_i \neq 0$ ), lifting the degeneracy (see Fig. 22.9 discussed later).

To determine the bandstructure, we could solve the eigenvalue equation  $H_{cl} f_{nk}(\mathbf{r}) = E_{nk} f_{nk}(\mathbf{r})$ , where  $H_{cl}$  is the  $6 \times 6$  electromagnetic Hamiltonian

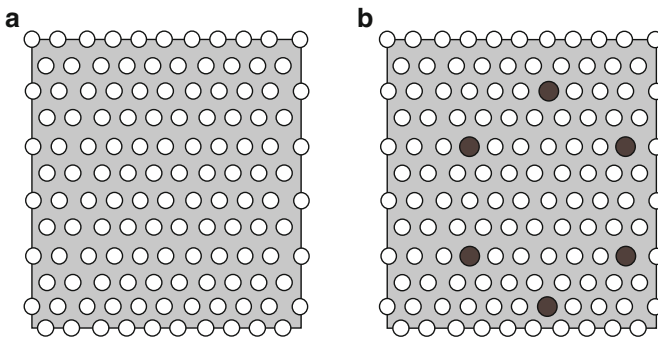


**Fig. 22.5** (a) Top view of photonic crystal made from air holes (cylinders) in a host insulating medium. Lattice constant is  $a$ , cylinders have radius  $r_1 = \alpha_1 a$ , and the host medium is characterized by  $\varepsilon$  (equivalently, one could have dielectric cylinders in a host material), (b) defected structure, here, magneto-optic cylinders forming a hexagonal array of “defects” in the air-hole medium. Magneto-optic cylinders have radius  $r_2 = \alpha_2 a$  and lattice constant  $a' = \alpha_3 a$

and  $f_{n\mathbf{k}}$  is the 6-vector of fields, both defined previously. In general, this is a quite complicated electromagnetic problem, which, however, can be solved using commercial simulators. We can simplify the problem from the  $6 \times 6$  matrix formulation by noting that from Maxwell's equations for a material characterized by this magneto-optic permittivity, transverse-electric (TE) modes have a single magnetic field component  $H_z$  parallel to the infinite cylinders and an in-plane electric field. The magnetic field satisfies the eigenvalue equation [35, 36]

$$H_{\text{cl}}(\mathbf{z}H_z) = \left(\frac{\omega}{c}\right)^2 (\mathbf{z}H_z), \quad (22.42)$$

where the operator  $H = H_{\text{cl}} = (\nabla \times \bar{\mathbf{I}}) \cdot \varepsilon^{-1} \cdot (\nabla \times \bar{\mathbf{I}})$  is Hermitian for lossless media, under the usual inner product  $\langle \mathbf{f}, \mathbf{g} \rangle = \int \mathbf{f}^* \cdot \mathbf{g} d\mathbf{r}$ . Thus, we can solve a scalar equation for  $H_z$ . Furthermore, an approximate solution can be obtained that gives considerable insight into the problem; the tight-binding method of condensed matter physics can be used to obtain an effective four-band Hamiltonian in the electromagnetic case [37] (and, as a special case we recover the graphene result).

The individual resonators support two  $p$ -type (dipole-like) modes at the same frequency  $\omega_0$ . Considering that the honeycomb lattice has two inequivalent sites  $A$  and  $B$ , each having two different states  $p_{x,y}$ , then considering the Bloch theorem, the wavefunction  $f_{n\mathbf{k}}(\mathbf{r}) = H_z(\mathbf{r})$  is expanded as

$$f_{n\mathbf{k}}(\mathbf{r}) = \frac{1}{\sqrt{N}} \sum_{\mathbf{R}} e^{i\mathbf{k}\cdot\mathbf{R}} \sum_{\beta=A,B} \sum_{\alpha=x,y} c_{\alpha}^{\beta} \phi_{p_{\alpha}}(\mathbf{r} - \mathbf{d}_{\beta} - \mathbf{R}), \quad (22.43)$$

where  $\mathbf{R}$  is the lattice vector and  $\phi$  the mode function. Plugging into the energy eigenvalue equation  $Hf_{n\mathbf{k}}(\mathbf{r}) = E_{n\mathbf{k}}f_{n\mathbf{k}}(\mathbf{r})$ , multiplying through by  $\int d\mathbf{r} \phi_{p_{\alpha}}(\mathbf{r} - \mathbf{d}_{\gamma})$ , and exploiting the assumed orthogonality of the modes lead to the Hermitian (effective, four-band) Hamiltonian matrix

$$H = \begin{bmatrix} \omega_0 & g_{xy}^{AA}(\mathbf{k}) & g_{xx}^{AB}(\mathbf{k}) & g_{xy}^{AB}(\mathbf{k}) \\ & \omega_0 & g_{yx}^{AB}(\mathbf{k}) & g_{yy}^{AB}(\mathbf{k}) \\ & & \omega_0 & g_{xy}^{BB}(\mathbf{k}) \\ & & & \omega_0 \end{bmatrix}, \quad (22.44)$$

where

$$g_{\gamma\delta}^{\alpha\beta}(\mathbf{k}) = \sum_{\mathbf{R}} e^{i\mathbf{k}\cdot\mathbf{R}} H_{\gamma\delta}^{\alpha\beta}(\mathbf{R}), \quad (22.45)$$

with  $H_{\gamma\delta}^{\alpha\beta}(\boldsymbol{\tau})$  being overlap/hopping integrals having the form

$$H_{\gamma\delta}^{\alpha\beta}(\mathbf{R}) = \int d\mathbf{r} \phi_{p\alpha}(\mathbf{r} - \mathbf{d}_\gamma) H \phi_{p\beta}(\mathbf{r} - \mathbf{d}_\delta - \mathbf{R}). \quad (22.46)$$

We assume that  $H_{\gamma\gamma}^{\alpha\alpha}$  is dominated by the self-energy,

$$\begin{aligned} H_{\gamma\gamma}^{\alpha\alpha} &= \int d\mathbf{r} \phi_{p\alpha}(\mathbf{r} - \mathbf{d}_\gamma) H \phi_{p\alpha}(\mathbf{r} - \mathbf{d}_\gamma - \mathbf{R}) \\ &\simeq \int d\mathbf{r} \phi_{p\alpha}(\mathbf{r} - \mathbf{d}_\gamma) H_\gamma \phi_{p\alpha}(\mathbf{r} - \mathbf{d}_\gamma - \mathbf{R}) \\ &= \omega_0 \int d\mathbf{r} \phi_{p\alpha}(\mathbf{r} - \mathbf{d}_\gamma) \phi_{p\alpha}(\mathbf{r} - \mathbf{d}_\gamma - \mathbf{R}) = \omega_0 \begin{cases} 1, \mathbf{R} = \mathbf{0} \\ 0, \mathbf{R} \neq \mathbf{0} \end{cases} \end{aligned} \quad (22.47)$$

where  $H_\gamma$  is the Hamiltonian of an isolated resonator, which leads to the diagonal components.

To evaluate the off-diagonal components, we consider only nearest neighbors. However, let us first digress and consider graphene, which is arranged in a hexagonal lattice and has two carbon atoms per unit cell.

### 22.3.1.1 Graphene Interlude: The Hexagonal Lattice

The direct and reciprocal lattices for a hexagonal lattice are shown in Figs. 22.6, 22.7, and 22.8.

The direct-space vectors are

$$\mathbf{a}_1 = \frac{a}{2}(\sqrt{3}, 1), \quad \mathbf{a}_2 = \frac{a}{2}(\sqrt{3}, -1), \quad (22.48)$$

**Fig. 22.6** Direct space for a hexagonal lattice, two atoms (A and B) per unit cell. Nearest neighbor vectors are  $\mathbf{R}_{1,2,3}$

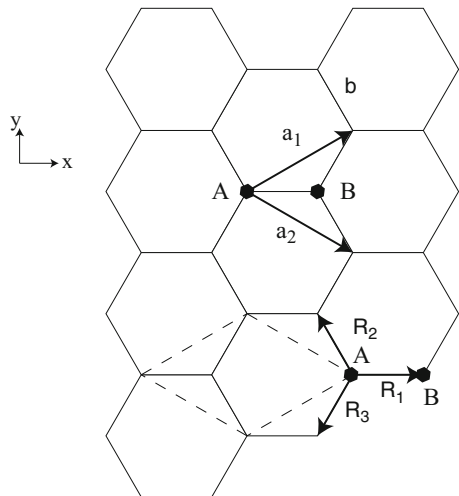


**Fig. 22.7** Reciprocal space for a hexagonal lattice.  $\Gamma$ ,  $K$ , and  $M$  are the high-symmetry points

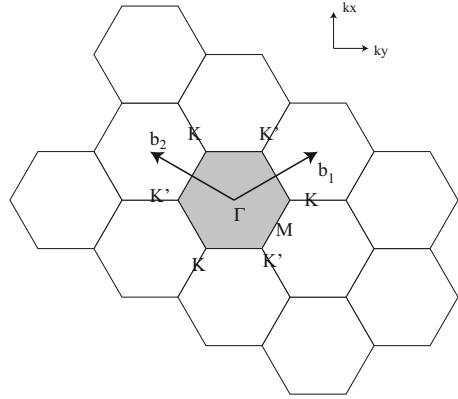
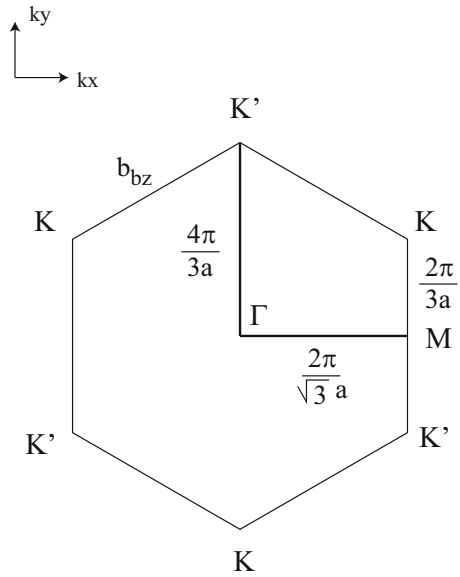


**Fig. 22.8** Close-up, reciprocal space for a hexagonal lattice



where  $a = |\mathbf{a}_1| = |\mathbf{a}_2| = \sqrt{3}b$  is the lattice constant. For graphene,  $b = 0.142 \text{ nm}$  is the interatomic distance between carbon atoms. The nearest neighbor vectors are (see Fig. 22.6)

$$\begin{aligned} \mathbf{R}_1 &= \left( \frac{a}{\sqrt{3}}, 0 \right), \quad \mathbf{R}_2 = -\mathbf{a}_2 + \mathbf{R}_1 = \left( -\frac{a}{2\sqrt{3}}, \frac{a}{2} \right), \\ \mathbf{R}_3 &= -\mathbf{a}_1 + \mathbf{R}_1 = \left( -\frac{a}{2\sqrt{3}}, -\frac{a}{2} \right), \end{aligned} \tag{22.49}$$

with  $|\mathbf{R}_1| = |\mathbf{R}_2| = |\mathbf{R}_3| = b = a/\sqrt{3}$ . The reciprocal lattice vectors are (see Fig. 22.7)

$$\mathbf{b}_1 = \frac{2\pi}{a} \left( \frac{1}{\sqrt{3}}, 1 \right), \quad \mathbf{b}_2 = \frac{2\pi}{a} \left( \frac{1}{\sqrt{3}}, -1 \right), \quad (22.50)$$

where  $|\mathbf{b}_1| = |\mathbf{b}_2| = 4\pi/\sqrt{3}a$  (the side length of the reciprocal lattice hexagon is  $b_{bz} = |\mathbf{b}_1|/\sqrt{3} = 4\pi/3a$ ).

The high-symmetry points in the Brillouin zone are

$$\Gamma = (0, 0), \quad \mathbf{K} = \left( \frac{2\pi}{\sqrt{3}a}, \frac{2\pi}{3a} \right), \quad \mathbf{M} = \left( \frac{2\pi}{\sqrt{3}a}, 0 \right), \quad (22.51)$$

and  $|\Gamma - \mathbf{M}| = 2\pi/\sqrt{3}a$ ,  $|\Gamma - \mathbf{K}| = 4\pi/3a$ , and  $|\mathbf{M} - \mathbf{K}| = 2\pi/3a$ .

For  $\pi$ -bonding in graphene (the usual low-energy case), each carbon atom contributes one  $2p_z$ -orbital, so we have half as many unknowns compared to the two-orbital photonic case described above. Then,

$$f_{n\mathbf{k}}(\mathbf{r}) = \frac{1}{\sqrt{N}} \sum_{\mathbf{R}} e^{i\mathbf{k}\cdot\mathbf{R}} \sum_{\beta=A,B} c^\beta \phi_p(\mathbf{r} - \mathbf{d}_\beta - \mathbf{R}). \quad (22.52)$$

Since there is only one symmetric orbital, confining the summation to the three nearest neighbors  $\boldsymbol{\tau}$ , we have

$$g^{\alpha\beta}(\mathbf{k}) = \sum_{\boldsymbol{\tau}} e^{i\mathbf{k}\cdot\boldsymbol{\tau}} H^{\alpha\beta}(\boldsymbol{\tau}) \simeq H^{\alpha\beta} \sum_{\boldsymbol{\tau}} e^{i\mathbf{k}\cdot\boldsymbol{\tau}}. \quad (22.53)$$

For atom  $A$ , the three nearest neighbors are the three nearby  $B$  atoms, located at  $\boldsymbol{\tau}_{1,2,3} = \mathbf{R}_{1,2,3}$ , so that

$$\begin{aligned} h(\mathbf{k}) &= \sum_{\boldsymbol{\tau}} e^{i\mathbf{k}\cdot\mathbf{fi}} = e^{ik_x \frac{a}{\sqrt{3}}} + e^{i(-k_x \frac{a}{2\sqrt{3}} + k_y \frac{a}{2})} + e^{-i(k_x \frac{a}{2\sqrt{3}} + k_y \frac{a}{2})} \\ &= e^{ik_x \frac{a}{\sqrt{3}}} + 2 \cos\left(k_y \frac{a}{2}\right) e^{-ik_x \frac{a}{2\sqrt{3}}}. \end{aligned} \quad (22.54)$$

The Hamiltonian matrix is then

$$\begin{bmatrix} \omega_0 & \gamma h(\mathbf{k}) \\ \gamma h^*(\mathbf{k}) & \omega_0 \end{bmatrix} \begin{bmatrix} c_{\mathbf{k}}^A \\ c_{\mathbf{k}}^B \end{bmatrix} = E_{n\mathbf{k}} \begin{bmatrix} c_{\mathbf{k}}^A \\ c_{\mathbf{k}}^B \end{bmatrix}, \quad (22.55)$$

where  $\gamma = H^{\alpha\beta}$  is the overlap integral (with typical values of several eV). Then, the energy dispersion is  $(\omega_0 - E_{n\mathbf{k}})^2 - |\gamma h(\mathbf{k})|^2 = 0$ , so that, since  $\omega_0 = 0$ , we have the celebrated graphene result

$$E_{n\mathbf{k}} = \pm \gamma \sqrt{1 + 4 \cos \left( k_x \frac{\sqrt{3}a}{2} \right) \cos \left( k_y \frac{a}{2} \right) + 4 \cos^2 \left( k_y \frac{a}{2} \right)}. \quad (22.56)$$

There is no bandgap because the two atoms are identical. The above is the simplest formulation; we obtain several corrections to this result if we do not drop the  $\mathbf{R} \neq 0$  terms in the diagonal components and also from the fact that the  $A$  and  $B$  orbitals have some overlap.

For the electromagnetic cylinder case considered in Ref. [32], since there are two orbitals per mode  $\phi_{p_{x,y}}$ , evaluation of the  $g_{\gamma\delta}^{\alpha\beta}(\mathbf{k})$  functions is more difficult because we cannot factorize  $\sum_{\tau} e^{i\mathbf{k}\cdot\tau} H^{\alpha\beta}(\tau) \simeq H^{\alpha\beta} \sum_{\tau} e^{i\mathbf{k}\cdot\tau}$  as above for the graphene case, due to the complexity of the orbitals. However, this is a common occurrence in condensed matter physics, and the following two-center interaction integrals are widely used,

$$\begin{aligned} H_{\gamma\delta}^{\alpha\neq\beta}(\mathbf{R}) &= \int d\mathbf{r} \phi_{p\alpha}(\mathbf{r} - \mathbf{d}_{\gamma}) H \phi_{p\beta}(\mathbf{r} - \mathbf{d}_{\delta} - \mathbf{R}) \\ &= \begin{cases} l_{\alpha}^2 V_{\sigma} + (1 - l_{\beta}^2) V_{\pi} & \text{for } \alpha = \beta = x, y \\ l_{\alpha} l_{\beta} (V_{\sigma} - V_{\pi}) & \text{for } \alpha \neq \beta, \end{cases} \end{aligned} \quad (22.57)$$

where  $l_{x,y}$  are the direction cosines  $l_{\alpha} = \boldsymbol{\alpha} \cdot \mathbf{R} / |\mathbf{R}|$ . For  $\mathbf{R} = \mathbf{R}_1$ ,  $l_x = 1$ ,  $l_y = 0$ , for  $\mathbf{R} = \mathbf{R}_2$ ,  $l_x = -1/2$  and  $l_y = \sqrt{3}/2$ , and for  $\mathbf{R} = \mathbf{R}_3$ ,  $l_x = -1/2$  and  $l_y = -\sqrt{3}/2$ . Therefore,

$$\sum_{\mathbf{R}} e^{i\mathbf{k}\cdot\mathbf{R}} H_{ABxx}(\mathbf{R}) = \sum_{\mathbf{R}} e^{i\mathbf{k}\cdot\mathbf{R}} \int d\mathbf{r} \phi_{px}(\mathbf{r} - \mathbf{d}_A) H \phi_{px}(\mathbf{r} - \mathbf{d}_B - \mathbf{R}) \quad (22.58)$$

$$= e^{ik_x \frac{a}{\sqrt{3}}} V_{\sigma} + \cos \left( k_y \frac{a}{2} \right) e^{-ik_x \frac{a}{2\sqrt{3}}} \left( \frac{1}{2} V_{\sigma} + \frac{3}{2} V_{\pi} \right). \quad (22.59)$$

For the next element,

$$\sum_{\mathbf{R}} e^{i\mathbf{k}\cdot\mathbf{R}} H_{ABxy}(\mathbf{R}) = \sum_{\mathbf{R}} e^{i\mathbf{k}\cdot\mathbf{R}} \int d\mathbf{r} \phi_{px}(\mathbf{r} - \mathbf{d}_A) H \phi_{py}(\mathbf{r} - \mathbf{d}_B - \mathbf{R}) \quad (22.60)$$

$$= -2i \sin \left( k_y \frac{a}{2} \right) e^{-ik_x \frac{a}{2\sqrt{3}}} \frac{\sqrt{3}}{4} (V_{\sigma} - V_{\pi}). \quad (22.61)$$

The other elements are evaluated in a similar fashion.

For numerical values, we assume [32]  $\varepsilon = 16$ ,  $r_1 = 0.35a$ ,  $r_2 = 0.5a$ , and  $a' = 6a$ . Making the substitution  $a \rightarrow 6a$  since in the derivation  $a = a'$  is the hexagonal lattice constant, but it is convenient to express the matrix entries in terms of the original (undeformed) lattice constant  $a$ ; the final matrix is [32]



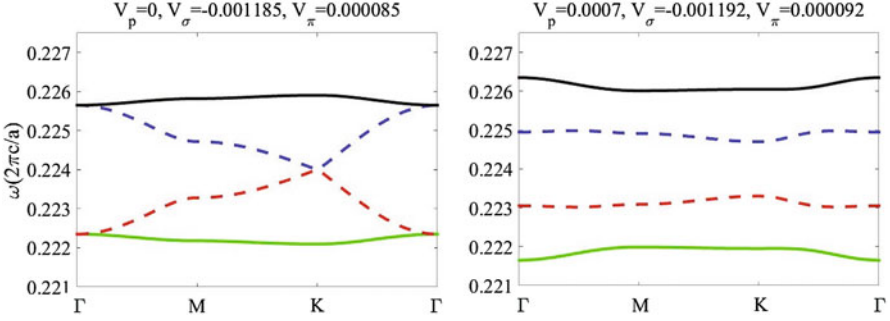


**Fig. 22.9** Bandstructure for the lattice depicted in Fig. 22.5b. *Left side* shows the reciprocal case,  $V_p = 0$ , where there are modal degeneracies that close the bandgap, and  $C_n = 0$ , and the *right side* shows the nonreciprocal case,  $V_p \neq 0$ , for which the degeneracies are lifted and two bands have  $C_n = \pm 1$

$$H = \begin{bmatrix} \omega_0 & H_{12} & H_{13} & H_{14} \\ & \omega_0 & H_{23} & H_{24} \\ & & \omega_0 & H_{34} \\ & & & \omega_0 \end{bmatrix}, \quad (22.62)$$

where  $H_{12} = -iV_p = H_{34}$ ,  $H_{13} = \left(\frac{3}{2}V_\pi + \frac{1}{2}V_\sigma\right) \cos(3k_y a) e^{-i\sqrt{3}k_x a} + V_\alpha e^{i2\sqrt{3}k_x a}$ ,  $H_{14} = -i\frac{\sqrt{3}}{2}(V_\sigma - V_\pi) \sin(3k_y a) e^{-i\sqrt{3}k_x a} = H_{23}$ , and  $H_{24} = \left(\frac{3}{2}V_\sigma + \frac{1}{2}V_\pi\right) \cos(3k_y a) e^{-i\sqrt{3}k_x a} + V_\pi e^{i2\sqrt{3}k_x a}$  (note that [32] uses a coordinate system where  $x$  and  $y$  are interchanged from those used here). The bond integrals  $V_{\sigma,\pi}$  are evaluated by matching the resulting bandstructure to numerical results from a commercial simulator. This results in the absence of applied magnetization (time-reversal-invariant case) [32]  $V_\sigma = -0.001185$ ,  $V_\pi = 0.000085$ , and  $V_p = 0$ , the overlap between  $x$  and  $y$  orbitals for the same atom. In the presence of magnetization (time-reversal symmetry is broken, assuming  $\varepsilon_i = 1$ ),  $V_\sigma = -0.001192$ ,  $V_\pi = 0.000092$ , and  $V_p = 0.0007$ , where all terms have units of radian frequency  $2\pi c/a$ .

From the projected Hamiltonian matrix  $H_{n,m}$ , one can solve the eigenvalue problem  $Hf_n = \omega_n f_n$ . Results are shown in Fig. 22.9, showing (a) the case for no magnetic bias ( $V_p = 0$ ) and (b) with bias applied, breaking time-reversal symmetry and lifting the degeneracies. Note that the high-symmetry points in Fig. 22.9 are with respect to the  $a'$  lattice,

$$\Gamma = (0, 0), \quad \mathbf{K} = \left(\frac{2\pi}{\sqrt{3}a'}, \frac{2\pi}{3a'}\right), \quad \mathbf{M} = \left(\frac{2\pi}{\sqrt{3}a'}, 0\right). \quad (22.63)$$

Bands 1 and 4 have Chern number  $C_{1,4} = \mp 1$  and the middle two bands have  $C_{2,3} = 0$ . For the reciprocal case,  $V_p = 0$ ,  $C_n = 0$  for all bands.

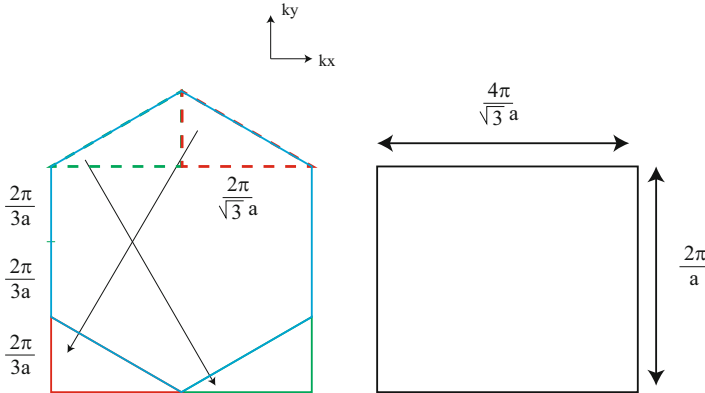


**Fig. 22.10** *Left*, original hexagonal Brillouin zone (*blue*) and *right*, equivalent rectangular Brillouin zone

For the numerical integration, it is convenient to use the fact that any two points in adjacent Brillouin zones (or any points connected by multiples of a basis vector) are equivalent. Figure 22.10 shows that the upper two right triangles (red and green) that form the top of the hexagon (blue) can be mapped to the bottom of the hexagon, so that the integration reduces to being over the simple rectangle shown at the right of the figure.

The Berry curvature for each band in the nonreciprocal case is plotted as a function of  $k_x - k_y$  in Fig. 22.11. The two bands  $C_{2,3} = 0$  have odd Berry curvature (so that they integrate to zero), and the two bands with  $C_{1,4} = \pm 1$  have even, sinusoidal Berry curvature (so that they integrate to an integer). In the reciprocal case ( $V_p = 0$ ), the Berry curvature is identically zero, by (22.40), and which is also easy to confirm numerically.

### 22.3.2 Continuum Photonic Example

This example is related to Ref. [2] (see also Ref. [3]), with Berry quantities and Chern number analysis directly taken from the seminal work [4].

As an example of a nonreciprocal continuous medium, we consider a magnetized plasma in the Voigt configuration (propagation perpendicular to the bias magnetic field  $\mathbf{B}$ ), as depicted in Fig. 22.12. For a single-component plasma biased with a static magnetic field  $\mathbf{B} = zB_z$ , the permeability is  $\mu = \mu_0$ , and the relative permittivity has the form of a Hermitian antisymmetric tensor

$$\bar{\epsilon} = \begin{pmatrix} \epsilon_{11} & \epsilon_{12} & 0 \\ \epsilon_{21} & \epsilon_{22} & 0 \\ 0 & 0 & \epsilon_{33} \end{pmatrix}, \quad (22.64)$$

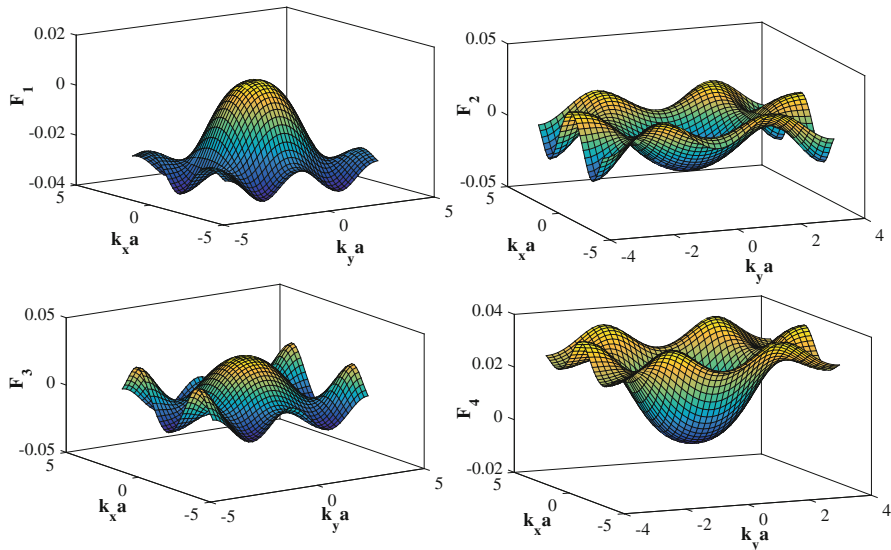
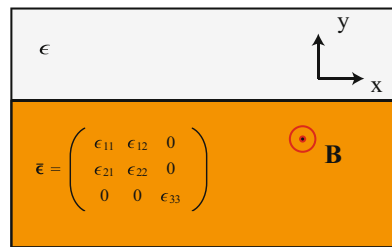


Fig. 22.11 Berry curvature for the four bands of Fig. 22.9;  $C_{1,4} = \mp 1$  and  $C_{2,3} = 0$

Fig. 22.12 Interface between a magnetic-field biased plasma (bottom) and a simple material (top)



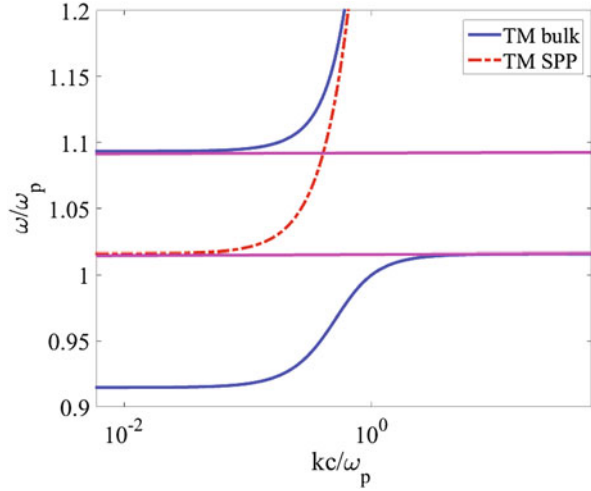
where

$$\begin{aligned} \epsilon_{11} = \epsilon_{22} &= 1 - \frac{\omega_p^2}{\omega^2 - \omega_c^2}, \quad \epsilon_{33} = 1 - \frac{\omega_p^2}{\omega^2}, \\ \epsilon_{12} = -\epsilon_{21} &= i \frac{-\omega_c \omega_p^2}{\omega (\omega^2 - \omega_c^2)} \end{aligned} \tag{22.65}$$

the cyclotron frequency is  $\omega_c = (q_e/m_e) B_z$  and the plasma frequency  $\omega_p$  satisfies  $\omega_p^2 = N_e q_e^2 / \epsilon_0 m_e$ . In the above,  $N_e$  is the free electron density, and  $q_e$  and  $m_e$  are the electron charge and mass, respectively.

For propagation in the  $x - y$  plane,  $\mathbf{k} = (k_x, k_y, 0)$ , the plane wave supported by this medium can be decoupled into TE ( $E_z \neq 0, H_z = 0$ ) and transverse-magnetic (TM) ( $E_z = 0, H_z \neq 0$ ) waves. Since there is no magnetoelectric coupling  $\xi = \bar{\zeta} = 0$ , the dispersion of these modes is

**Fig. 22.13** Band diagram for a biased plasma having (22.65) with  $\omega_p/2\pi = 9.7$  THz and  $\omega_c/2\pi = 1.73$  THz ( $\omega_p/\omega_c = 5.6$ ); blue, TM mode; red, TE mode; and black, SPP wave dispersion



$$k^2 = \frac{\epsilon_{11}^2 + \epsilon_{12}^2}{\epsilon_{11}} \left(\frac{\omega_n}{c}\right)^2, \quad \text{TM mode} \tag{22.66}$$

$$k^2 = \epsilon_{33} \left(\frac{\omega_n}{c}\right)^2, \quad \text{TE mode} \tag{22.67}$$

such that  $\omega_n$  is the eigenfrequency of each mode. Despite the nonreciprocal nature of the medium itself, in the Voigt configuration, the bulk dispersion behavior is reciprocal (an interface will break this reciprocity). The dispersion curves for these materials are shown in Fig. 22.13.

The associated electromagnetic waves envelopes can be obtained by finding the solution  $f = [\mathbf{E}, \mathbf{H}]^T$ , of (22.18),  $N \cdot f = \omega M \cdot f$ , which is

$$\begin{pmatrix} 0 & -\mathbf{k} \times \mathbf{I}_{3 \times 3} \\ \mathbf{k} \times \mathbf{I}_{3 \times 3} & 0 \end{pmatrix} \cdot \begin{pmatrix} \mathbf{E} \\ \mathbf{H} \end{pmatrix} = \begin{pmatrix} \omega \epsilon_0 \bar{\epsilon} & 0 \\ 0 & \omega \mu_0 \mathbf{I}_{3 \times 3} \end{pmatrix} \cdot \begin{pmatrix} \mathbf{E} \\ \mathbf{H} \end{pmatrix}, \tag{22.68}$$

where  $\mathbf{I}_{3 \times 3}$  is the  $3 \times 3$  identity matrix, so that

$$\begin{pmatrix} -\mathbf{I}_{3 \times 3} & -\frac{\bar{\epsilon}^{-1}}{\omega \epsilon_0} \cdot \mathbf{k} \times \mathbf{I}_{3 \times 3} \\ \frac{1}{\omega \mu_0} \cdot \mathbf{k} \times \mathbf{I}_{3 \times 3} & -\mathbf{I}_{3 \times 3} \end{pmatrix} \cdot \begin{pmatrix} \mathbf{E} \\ \mathbf{H} \end{pmatrix} = 0. \tag{22.69}$$

With  $\mathbf{H} = \hat{\mathbf{z}} \rightarrow \mathbf{E} = \bar{\epsilon}^{-1} \cdot \frac{\hat{\mathbf{z}} \times \mathbf{k}}{\omega \epsilon_0}$  (TM),  $\mathbf{E} = \hat{\mathbf{z}} \rightarrow \mathbf{H} = \frac{\mathbf{k}}{\omega \mu_0} \times \hat{\mathbf{z}}$  (TE), we have the  $6 \times 1$  vectors

$$f_{nk}^{\text{TM}} = \begin{pmatrix} \bar{\epsilon}^{-1} \cdot \hat{\mathbf{z}} \times \frac{\mathbf{k}}{\epsilon_0 \omega_{nk}} \\ \hat{\mathbf{z}} \end{pmatrix},$$

$$f_{nk}^{\text{TE}} = \left( \frac{\hat{\mathbf{z}}}{\mu_0 \omega_{nk}} \times \hat{\mathbf{z}} \right). \quad (22.70)$$

Because the envelopes of the electromagnetic waves in the above equations are not normalized, the Berry potential is computed using

$$\mathbf{A}_{nk} = \frac{\text{Re}\{if_{nk}^* \cdot \frac{\partial}{\partial \omega}(\omega M(\omega)) \partial_k f_{n,k}\}}{f_{nk}^* \cdot \frac{\partial}{\partial \omega}(\omega M(\omega)) f_{n,k}}. \quad (22.71)$$

Considering the Riemann sphere mapping of the  $k_x - k_y$  plane as detailed in [4], it is possible to write the Chern number associated with  $n$ th eigenmode branch as

$$C_n = \frac{1}{2\pi} \int \mathbf{A}_{n,k=\infty} \cdot d\mathbf{l} - \frac{1}{2\pi} \int \mathbf{A}_{n,k=0^+} \cdot d\mathbf{l}, \quad (22.72)$$

where the two line integrals are over infinite and infinitesimal radii (north and south poles of the Riemann sphere), respectively. Details of the Chern number calculation are available in Ref. [38], where the need to a nonlocal model is discussed. For the low-frequency band, we obtain  $C_n = -2$  (there is an additional low-frequency band very near  $\omega = 0$ , which has Chern number 1), and for the high-frequency TM band, the Chern number is  $C_n = 1$ .

The dispersion relation for the surface mode is [2]

$$\frac{\sqrt{k_x^2 - k_0^2 \varepsilon_s}}{\varepsilon_s} + \frac{\sqrt{k_x^2 - k_0^2 \varepsilon_{\text{eff}}}}{\varepsilon_{\text{eff}}} = \frac{k_0 \varepsilon_{12} i k_x}{\varepsilon_{11} \varepsilon_{\text{eff}}}, \quad (22.73)$$

where  $\varepsilon_s$  is the relative permittivity of the top material and

$$\varepsilon_{\text{eff}} = \frac{\varepsilon_{11}^2 + \varepsilon_{12}^2}{\varepsilon_{11}}, \quad (22.74)$$

where  $\varepsilon_{\alpha\beta}$  are the magnetoplasma relative-permittivity components.

### 22.3.2.1 Full-Wave Simulation of One-Way Propagation

We first consider a 2D structure. A 2D dipole (i.e., a line source) is at the interface between a simple plasma (upper region) having  $\varepsilon = -5$  (this specific value relatively is unimportant; we simply need a negative-permittivity material such as a metal) and a magnetoplasma (lower region) having permittivity (22.65). Figure 22.14 shows the electric field profile for three cases, unbiased, biased but operating outside the bandgap, and biased operating within the bandgap. It can be seen that in the unbiased (reciprocal) case, energy flows in both directions; in the biased (nonreciprocal) case operating outside the gap, we have one-way propagation, but energy can leak into the lower region; and in the biased case

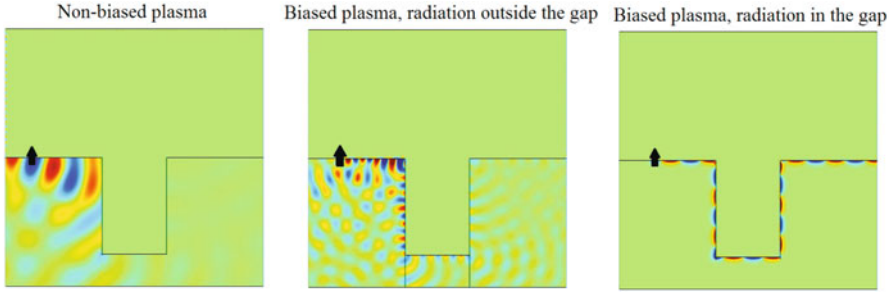


**Fig. 22.14** Electric field due to a 2D vertical dipole and  $\omega_p/2\pi = 9.7$  THz for three cases: *left*, unbiased (reciprocal) case that respects time-reversal symmetry,  $\omega_c = 0$ , at 10 THz ( $\lambda = 30 \mu\text{m}$ ); *center*, biased with  $\omega_c/2\pi = 1.73$  THz at 12 THz, outside of the bandgap ( $\omega/\omega_c = 6.93$ ); and *right*, biased with  $\omega_c/2\pi = 1.73$  THz inside the bandgap at 10 THz, ( $\omega/\omega_c = 5.78$ )

operating within the bandgap, energy just flows in one direction, is well-contained at the interface, and goes around discontinuities.

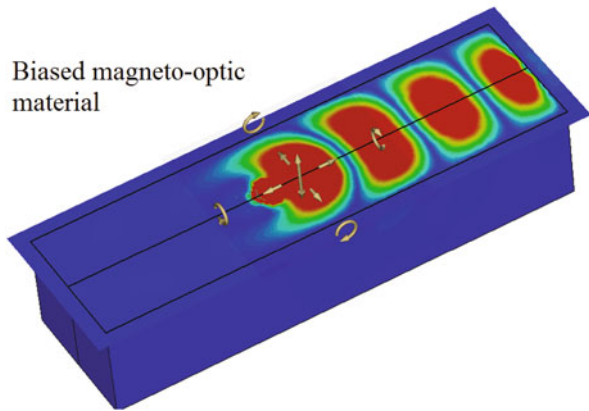
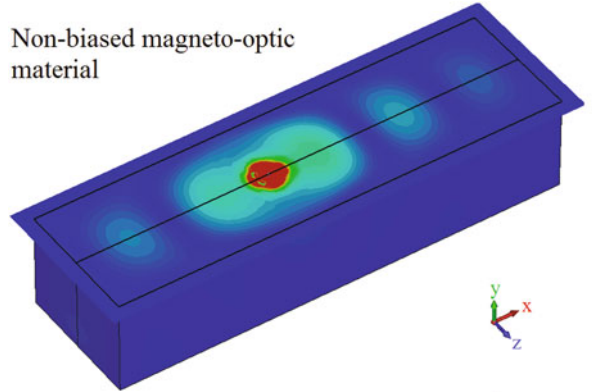
Figure 22.15 shows a 3D simulation for a  $420 \times 120 \times 90 \mu\text{m}$  rectangular block of magnetoplasma with an  $\varepsilon = -5$  plasma on the top surface and vacuum on all other sides and (top) shows the electric field profile in the reciprocal case,  $\omega_c = 0$ , at 10 THz. Figure 22.15 (bottom) shows the nonreciprocal case at 10 THz (in the bandgap). It can be seen that in the reciprocal case, energy flows in both directions, whereas in the nonreciprocal case, energy just flows to the right.

Figure 22.16 shows the nonreciprocal case when an obstacle (a half sphere) is hollowed out of each material at the interface, forming a spherical vacuum obstacle having radius  $30 \mu\text{m}$  ( $1\lambda$ ) in the SPP wave path. It can be seen that the wave goes past the obstacle without backscattering.

Finally, Figs. 22.17 and 22.18 show the power density for the case of an interface with a step discontinuity in height. The step height is  $30 \mu\text{m}$  ( $1\lambda$ ). For Fig. 22.17, as in Figs. 22.15 and 22.16, the top interface is with the  $\varepsilon = -5$  simple plasma; all other interfaces are between the magnetoplasma and vacuum. A vertical dipole source is located on the left side as indicated. Figure 22.17 (top) shows the side view of the power density in the reciprocal case, and Fig. 22.17 (bottom) shows the nonreciprocal case. It can be seen that in the reciprocal case, energy flows in both directions as well as interacting with and reflecting from the step, whereas in the nonreciprocal case, energy just flows to the right and does not scatter off of the step discontinuity. In Fig. 22.18, we surround all sides of the magnetoplasma with  $\varepsilon = -5$  plasma. In this case energy circulates around the entire structure.

One aspect of PTI waveguides is that energy cannot be backscattered, but it can scatter to the sides [39]. An alternative waveguide that eliminates side scattering and provides good confinement of the SPP wave is a ridge waveguide, as depicted in Fig. 22.19a. Ridge waveguides have been shown to provide efficient channeling of SPP waves in reciprocal photonic integrated circuits [40–43].

**Fig. 22.15** Electric field at 10 THz for a 3D vertical dipole at a magnetoplasma-plasma interface (*top* interface is between the magnetoplasma and the  $\epsilon = -5$  simple plasma; all other interfaces are between the magnetoplasma and vacuum). *Top*: unbiased ( $\omega_c = 0$ , reciprocal) case. *Bottom*: nonreciprocal case when  $\omega_c/2\pi = 1.73$  THz inside the bandgap ( $\omega/\omega_c = 5.78$ )



**Fig. 22.16** Electric field near a magnetoplasma-plasma interface, as in Fig. 22.15, in the nonreciprocal case when a large ( $1\lambda$ ) spherical vacuum obstacle is placed in the SPP wave path

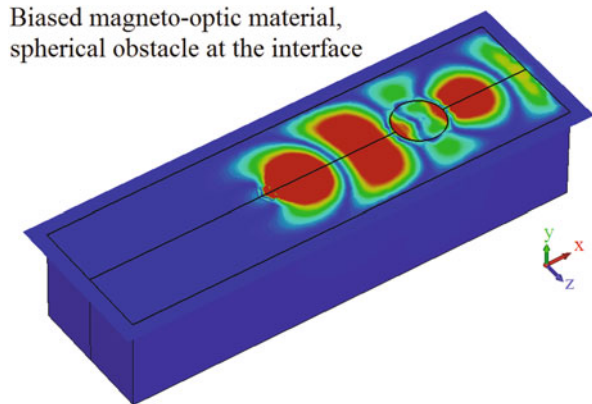
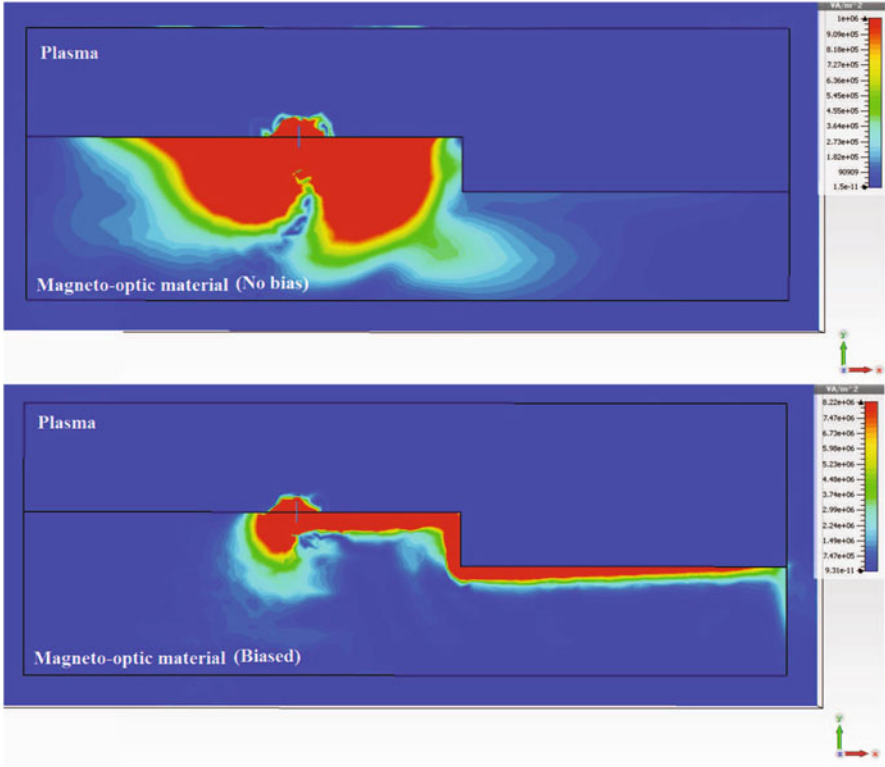
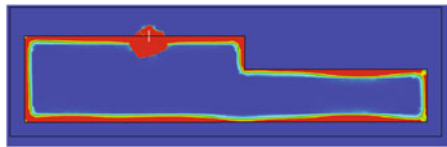


Figure 22.19 shows a perspective view of the silver ridge waveguide with height  $30\ \mu\text{m}$  and opening angle 20 degrees mounted on  $\text{SiO}_2$  substrate and covered by magnetoplasma material. Figure 22.19b shows the electric field distribution on the ridge for the non-biased ( $\omega_c = 0$ ) case. Figure 22.19c shows the biased



**Fig. 22.17** Side view of power density due to a vertical point dipole source at the interface between a magnetoplasma and a simple plasma. (top) Power density in the reciprocal case. (bottom) Nonreciprocal case



**Fig. 22.18** Side view of power density due to a vertical point dipole source at the interface between a magnetoplasma and a simple plasma, nonreciprocal case

( $\omega_c/2\pi = 1.73$  THz) case. The direction of SPP wave propagation can be reversed by reversing the direction of magnetic bias (i.e., from right to left by changing bias direction from  $z$  to  $-z$ ). Figure 22.19d shows the biased case with defects on the ridge (the defects are regions removed from the silver material, i.e., “holes”). As expected, the defect does not scatter energy, and the SPP wave propagates around the defect. The dipole source is indicated by a black arrow, lossy silver is considered, and in all cases the excitation frequency  $\omega/2\pi = 10$  THz,  $\omega_p/2\pi = 9.7$  THz.



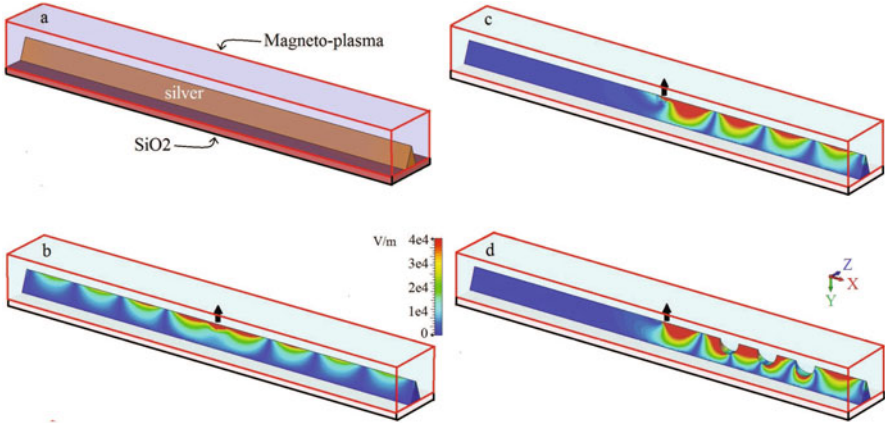


**Fig. 22.19** (a) Silver ridge waveguide with height  $30\ \mu\text{m}$  and opening angle  $20$  degree mounted on  $\text{SiO}_2$  substrate and covered by magneto-plasma material. (b) Electric field distribution on the ridge for non-biased ( $\omega_c = 0$ ) case and (c) for biased ( $\omega_c/2\pi = 1.73$  THz) case. (d) shows the biased case with defects on the ridge. The dipole source is indicated by a black arrow, lossy silver is considered, and in all cases the excitation frequency  $\omega/2\pi = 10$  THz.  $\omega_p/2\pi = 9.7$  THz

Finally, we can mention that duality can be used to model magnetic plasmas/ferrites rather than electric-type plasma [44]. For the material matrix (22.15), duality implies [45]  $(\mathbf{E}, \mathbf{H}, \mathbf{M}) \rightarrow (\mathbf{H}, -\mathbf{E}, \det(\mathbf{M}) \cdot \mathbf{M}^{-1})$ . Applying this transformation, we see the eigenmodes transform  $\text{TE} \rightleftharpoons \text{TM}$ , and for a ferrite, duality leads to  $\epsilon \rightleftharpoons \mu$ . Therefore, as the biased ferrite has a simple TM mode and nontrivial TE mode, by duality, a gyroelectric medium has a simple TE mode with dispersion  $k^2 = \delta (\omega_n/c)^2$  and nontrivial TM mode with dispersion  $k^2 = \epsilon_{\text{eff}} \mu_r (\omega_n/c)^2$ , where  $\epsilon_{\text{eff}} = (\kappa^2 - \chi^2)/\kappa$ . By duality, the TM-SPP wave dispersion equation for the interface with an electric opaque medium with negative permittivity  $\epsilon_s$  is  $\alpha_s/\epsilon_s + \alpha_p/\epsilon_{\text{eff}} = \chi k_{\text{spp}}/(\kappa \epsilon_{\text{eff}})$ , where  $\alpha_s = k_0 \sqrt{(k_{\text{spp}}/k_0)^2 - \epsilon_s}$  and  $\alpha_p = k_0 \sqrt{(k_{\text{spp}}/k_0)^2 - \epsilon_{\text{eff}}}$ . For a ferrite, we take [46]

$$\kappa = 1 - \frac{\omega_0 \omega_m}{\omega^2 - \omega_0^2}, \quad \chi = \frac{\omega \omega_m}{(\omega^2 - \omega_0^2)}, \quad \delta = 1, \tag{22.75}$$

where  $\omega_0 = \mu_0 \Gamma H_0$  is the Larmor frequency,  $\omega_m = \mu_0 \Gamma M_s$ , and  $\Gamma, H_0$  and  $M_s$  are the gyromagnetic ratio, biasing magnetic field, and saturation magnetization, respectively.

Figure 22.20 shows bulk TE and TM mode dispersion and frequency gap for a biased ferrite with  $\omega_0/2\pi = 1.73$  GHz and  $\omega_m/2\pi = 9.7$  GHz, as well as the TE-SPP mode dispersion. A one-way TE-SPP wave is formed at the interface of the biased ferrite and an opaque medium.

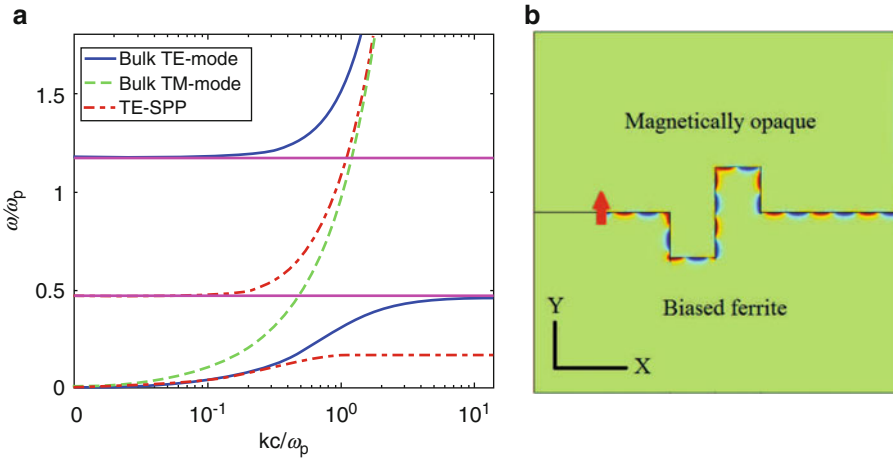


**Fig. 22.20** Bulk TE and TM mode dispersion for a biased ferrite with  $\omega_0/2\pi = 1.73$  GHz,  $\omega_m/2\pi = 9.7$  GHz, and  $f = 10$  GHz and the TE-SPP mode dispersion

## 22.4 Conclusions

The basic concepts of Berry phase, Berry potential, and Berry curvature have been presented and applied to electromagnetic problems for both discrete and continuum materials. It was shown that one-way, scattering-immune surface plasmon propagation can be achieved at the interface between a PTI material and a simple medium. Several examples were provided to illustrate the application of this theory, and results were verified using full-wave simulations.

The described phenomenon has potential to lead to new waveguides and transmission lines that are immune to defects and various imperfections. The Berry potential and related quantities provide a framework within which it is possible to classify electromagnetic materials that led to unidirectional, scattering-immune surface-wave propagation. This includes materials that break time-reversal symmetry (e.g., nonreciprocal media) but also materials that respect time-reversal symmetry but break other symmetries. Thus, the Berry framework provides a unification of diverse materials, both natural and meta, regarding their ability to guide scattering-immune surface waves. Given the huge number of degrees of freedom provided by the various material constitutive parameters, it is anticipated that many novel materials and material configurations can be engineered to provide defect-robust waveguides and various other micro-, millimeter-, and optical-wave devices.

## Appendix 1

To prove the statement that the excitation probability of states  $n \neq m$  is small, the time derivative of the energy state equation is  $\partial_t H |n\rangle + H |\partial_t n\rangle = \partial_t E_n |n\rangle + E_n |\partial_t n\rangle$ , where we can set  $\partial_t E_n = 0$  due to slow variation. The inner product with  $\langle m|$  yields  $\langle m|\partial_t n\rangle = \langle m|\partial_t H|n\rangle / (E_m - E_n)$  ( $n \neq m$ ) so we have from (22.7)  $\partial_t a_m = -\sum_n a_n e^{i(\alpha_n - \alpha_m)} \langle m|\partial_t H|n\rangle / (E_m - E_n)$  ( $n \neq m$ ). Choose the initial state to be one of the instantaneous eigenstates  $|\Psi(t=0)\rangle = |n(\mathbf{R}(0))\rangle$ , so  $a_n(t=0) = 1$  and  $a_m(t=0) = 0$  for  $n \neq m$ . Then, for  $n \neq m$ , we have  $\partial_t a_m \approx -e^{i(\alpha_n - \alpha_m)} \langle m|\partial_t H|n\rangle / (E_m - E_n)$ . Since the time dependencies of  $\langle m|\partial_t H|n\rangle$  and  $E_n - E_m$  are slow, the most important time dependence will be in the exponential, which can be approximated by  $e^{i(\alpha_n - \alpha_m)} = e^{i(E_m - E_n)t/\hbar}$ . Neglecting the other slow time dependencies then yields

$$\begin{aligned} \partial_t a_m &\approx -e^{i(\alpha_n - \alpha_m)} \langle m|\partial_t H|n\rangle / (E_m - E_n) \\ a_m(t) &= -\int_0^t e^{i(E_m - E_n)t/\hbar} \frac{\langle m|\partial_t H|n\rangle}{(E_m - E_n)} \cdot dt = \frac{i}{\hbar} \frac{\langle m|\partial_t H|n\rangle}{\omega_{mn}^2} \{e^{i\omega_{mn}t/\hbar} - 1\}, \end{aligned}$$

$\omega_{mn} = (E_m - E_n)/\hbar$ , ( $n \neq m$ ). Due to adiabatic approximation we have adopted,  $\langle m|\partial_t H|n\rangle$  is small compared to the transition frequency  $\omega_{mn} = (E_m - E_n)/\hbar$ . Therefore, the magnitude of the excitation probability to other states  $|a_m(t)|^2$  is small for  $n \neq m$ . For further reading, see Ref. [16].

## Appendix 2

In electromagnetics, the gauge transformation is

$$\Phi'(\mathbf{r}, t) = \Phi(\mathbf{r}, t) - \frac{\partial \chi(\mathbf{r}, t)}{\partial t}, \quad \mathbf{A}'(\mathbf{r}, t) = \mathbf{A}(\mathbf{r}, t) + \nabla \chi(\mathbf{r}, t), \quad (22.76)$$

which leaves the fields

$$\mathbf{E}(\mathbf{r}, t) = -\nabla \Phi(\mathbf{r}, t) - \frac{\partial \mathbf{A}(\mathbf{r}, t)}{\partial t}, \quad \mathbf{B}(\mathbf{r}, t) = \nabla \times \mathbf{A}(\mathbf{r}, t) \quad (22.77)$$

unchanged. Then,

$$i\hbar \frac{d}{dt} |\psi\rangle = \hat{H} |\psi\rangle \quad (22.78)$$

with the Hamiltonian

$$\widehat{H}(\mathbf{r}, t) = \frac{1}{2m} [\widehat{\mathbf{p}} + e\mathbf{A}(\mathbf{r}, t)]^2 - e\Phi(\mathbf{r}, t) + V(r),$$

becomes

$$i\hbar \frac{d}{dt} |\psi'\rangle = \widehat{H}' |\psi'\rangle, \quad (22.79)$$

where  $|\psi'\rangle = e^{-ie\chi(\mathbf{r}, t)/\hbar} |\psi\rangle$  and

$$\widehat{H}' = \frac{1}{2m} [\widehat{\mathbf{p}} + e\mathbf{A}'(\mathbf{r}, t)]^2 - e\Phi'(\mathbf{r}, t) + V(r). \quad (22.80)$$

Therefore, the Schrödinger equation is invariant under a gauge transformation, and the electromagnetic change of gauge is equivalent to a phase change in the wavefunction,  $|\psi'\rangle = e^{-ie\chi(\mathbf{r}, t)/\hbar} |\psi\rangle$ .

## References

1. J.M. Pitarke, V.M. Silkin, E.V. Chulkov, P.M. Echenique, Theory of surface plasmons and surface-plasmon polaritons. *Rep. Prog. Phys.* **70**, 1–87 (2007)
2. A.R. Davoyan, N. Engheta, Theory of wave propagation in magnetized near-zero-epsilon metamaterials: evidence for one-way photonic states and magnetically switched transparency and opacity. *Phys. Rev. Lett.* **111**, 257401 (2013)
3. B. Yang, M. Lawrence, W. Gao, Q. Guo, S. Zhang, One-way helical electromagnetic wave propagation supported by magnetized plasma. *Sci. Rep.* **6**, 21461 (2016)
4. M.G. Silveirinha, Chern invariants for continuous media. *Phys. Rev. B* **92**, 125153 (2015)
5. M. Berry, Anticipations of the geometric phase. *Phys. Today* **43**(12), 34–40 (1990)
6. S. Pancharatnam, Generalized theory of interference, and its applications. Part I. Coherent pencils. *Proc. Ind. Acad. Sci. A* **44**, 247–262 (1956)
7. M.S. Smith, Phase memory in W.K.B. and phase integral solutions of ionospheric propagation problems. *Proc. R. Soc. Lond. A* **346**, 59–79 (1975)
8. K.G. Budden, M.S. Smith, Phase memory and additional memory in W.K.B. solutions for wave propagation in stratified media. *Proc. R. Soc. Lond. A* **350**, 27–46 (1976)
9. F.D.M. Haldane, S. Raghu, Possible realization of directional optical waveguides in photonic crystals with broken time-reversal symmetry. *Phys. Rev. Lett.* **100**, 013904 (2008)
10. S. Raghu, F.D.M. Haldane, Analogs of quantum-Hall-effect edge states in photonic crystals. *Phys. Rev. A* **78**, 033834 (2008)
11. M.C. Rechtsman, J.M. Zeuner, Y. Plotnik, Y. Lumer, D. Podolsky, F. Dreisow, S. Nolte, M. Segev, A. Szameit, Photonic Floquet topological insulators. *Nature* **496**, 196–200 (2013)
12. M.C. Rechtsman, Y. Plotnik, J.M. Zeuner, D. Song, Z. Chen, A. Szameit, M. Segev, Topological creation and destruction of edge states in photonic graphene. *Phys. Rev. Lett.* **111**, 103901 (2013)

13. Y. Poo, R.-X. Wu,, Z. Lin, Y. Yang, C.T. Chan, Experimental realization of self-guiding unidirectional electromagnetic edge states. *Phys. Rev. Lett.* **106**, 093903 (2011)
14. W.-J. Chen, S.-J. Jiang, X.-D. Chen, B. Zhu, L. Zhou, J.-W. Dong, C.-T. Chan, Experimental realization of photonic topological insulator in a uniaxial metacrystal waveguide. *Nat. Commun.* **5**, 5782 (2014)
15. S.A. Skirlo, L. Lu, Y. Igarashi, Q. Yan, J.D. Joannopoulos, M. Soljačić, Experimental observation of large Chern numbers in photonic crystals. *Phys. Rev. Lett.* **115**, 253901 (2015)
16. L.E. Ballentine, *Quantum Mechanics: A Modern Development* (Prentice–Hall, Upper Saddle River, NJ, 1990)
17. M.V. Berry, Quantal phase factors accompanying adiabatic changes. *Proc. R. Soc. Lond. A* **392**, 45–57 (1984)
18. Y. Aharonov, J. Anandan, Phase change during a cyclic quantum evolution. *Phys. Rev. Lett.* **58**, 1593–1596 (1987)
19. J. Anandan, J. Christian, K. Wanelik, Resource Letter GPP-1: geometric phases in physics. *Am. J. Phys.* **65**, 180–185 (1997)
20. D.J. Griffiths, *Introduction to Quantum Mechanics* (Prentice–Hall, Upper Saddle River, NJ, 1995)
21. A. Tomita, R.Y. Chiao, Observation of Berry’s topological phase by use of an optical fiber. *Phys. Rev. Lett.* **57**, 937–940 (1986); erratum: **57**, 2471 (1986)
22. Q. Xu, L. Chen, M.G. Wood, P. Sun, R.M. Reano, Electrically tunable optical polarization rotation on a silicon chip using Berry’s phase. *Nat. Commun.* **5**, 5337 (2014)
23. M.G. Silveirinha, S.I. Maslovski, Exchange of momentum between moving matter induced by the zero-point fluctuations of the electromagnetic field. *Phys. Rev. A* **86**, 042118 (2012)
24. W. Gao, M. Lawrence, B. Yang, F. Liu, F. Fang, Béri, B., J. Li, S. Zhang, Topological photonic phase in chiral hyperbolic metamaterials. *Phys. Rev. Lett.* **114**, 037402 (2015)
25. G. Tkachov, *Topological Insulators: The Physics of Spin Helicity in Quantum Transport* (CRC Press, Boca Raton, FL, 2015)
26. Z. Wang, Y. Chong, J.D. Joannopoulos, M. Soljačić, Observation of unidirectional backscattering-immune topological electromagnetic states. *Nature* **461**, 772–775 (2009)
27. K. Fang, Z. Yu, S. Fan, Realizing effective magnetic field for photons by controlling the phase of dynamic modulation. *Nat. Photon* **6**, 782–787 (2012)
28. M. Hafezi, S. Mittal, J. Fan, A. Migdall, J.M. Taylor, Imaging topological edge states in silicon photonics. *Nat. Photon* **7**, 1001–1005 (2013)
29. A.B. Khanikaev, S. Hossein Mousavi, W.-K. Tse, M. Kargarian, A.H. MacDonald, G. Shvets, Photonic topological insulators. *Nat. Mater.* **12**, 233–239 (2013)
30. Y.D. Chong, X.-G. Wen, M. Soljačić, Effective theory of quadratic degeneracies. *Phys. Rev. B* **77**, 235125 (2008)
31. Z. Wang, Y.D. Chong, J.D. Joannopoulos, M. Soljačić, Reflection-free one-way edge modes in a gyromagnetic photonic crystal. *Phys. Rev. Lett.* **100**, 013905 (2008)
32. K. Fang, Z. Yu, S. Fan, Microscopic theory of photonic one-way edge mode. *Phys. Rev. B* **84**, 075477 (2011)
33. S.A. Skirlo, L. Lu, M. Soljačić, Multimode one-way waveguides of large Chern numbers. *Phys. Rev. Lett.* **113**, 113904 (2014)
34. L.-H. Wu, X. Hu, Scheme for achieving a topological photonic crystal by using dielectric material. *Phys. Rev. Lett.* **114**, 223901 (2015)
35. S. Fan, M.F. Yanik, Z. Wang, S. Sandhu, M.L. Povinelli, Advances in theory of photonic crystals. *J. Lightwave Tech.* **24**, 4493–4501 (2006)
36. J.D. Joannopoulos, S.G. Johnson, J.N. Winn, R.D. Meade, *Photonic Crystals* (Princeton University Press, Princeton, NJ, 2008)
37. E. Lidorikis, M.M. Sigalas, E.N. Economou, C.M. Soukoulis, Tight-binding parametrization for photonic band gap materials. *Phys. Rev. Lett.* **81**, 1405–1408 (1998)
38. G.W. Hanson, S.A.H. Gangaraj, A.M. Nemilentsau, Notes on photonic topological insulators and scattering-protected edge states – a brief introduction (2016). arXiv:1602.02425

39. S.A.H. Gangaraj, A.M. Nemilentsau, G.W. Hanson, The effects of three-dimensional defects on one-way surface plasmon propagation for photonic topological insulators comprised of continuum media. *Sci. Rep.* **6**, 30055 (2016)
40. H. Raether, *Surface Plasmons* (Springer, New York, 1988)
41. S.A. Maier, H.A. Atwater, Plasmonics: localization and guiding of electromagnetic energy in metal/dielectric structures. *J. Appl. Phys.* **98**, 011101 (2005)
42. J. Mu, L. Chen, X. Li, W.-P. Huang, L.C. Kimerling, J. Michel, Hybrid nano ridge plasmonic polaritons waveguides. *Appl. Phys. Lett.* **103**, 131107 (2013)
43. S.A. Hassani Gangaraj, A.M. Nemilentsau, G.W. Hanson, S. Hughes, Transient and steady-state entanglement mediated by three-dimensional plasmonic waveguides. *Opt. Express* **23**, 22330–22346 (2015)
44. S.A.H. Gangaraj, G.W. Hanson, Topologically protected unidirectional surface states in biased ferrites: duality and application to directional couplers. *IEEE Antennas Wirel. Propag. Lett.* **16**, 449–452 (2017)
45. J.A. Kong, Theorems of bianisotropic media. *IEEE Proc.* **60**, 1036–1046 (1972)
46. D.M. Pozar, *Microwave Engineering*, 2nd edn. (Wiley, Toronto, 1998)



**George W. Hanson** was born in Glen Ridge, NJ (USA), in 1963. He received the B.S.E.E. degree from Lehigh University, Bethlehem, PA, the M.S.E.E. degree from Southern Methodist University, Dallas, TX, and the Ph.D. degree from Michigan State University, East Lansing, in 1986, 1988, and 1991, respectively. From 1986 to 1988 he was a development engineer with General Dynamics in Fort Worth, TX, where he worked on radar simulators. From 1988 to 1991 he was a research and teaching assistant in the Department of Electrical Engineering at Michigan State University. He is currently Professor of Electrical Engineering and Computer Science at the University of Wisconsin in Milwaukee. His research interests include nano-

electromagnetics, plasmonics, quantum optics, and mathematical methods in electromagnetics. Dr. Hanson is a member of URSI Commission B, Sigma Xi, and Eta Kappa Nu, and was an Associate Editor for the *IEEE Transactions on Antennas and Propagation* from 2002–2007. In 2006 he received the S.A. Schelkunoff Best Paper Award from the IEEE Antennas and Propagation Society. Dr. Hanson is coauthor of the book *Operator Theory for Electromagnetics: An Introduction*, Springer, New York, 2002, and author of *Fundamentals of Nanoelectronics*, Prentice-Hall, New Jersey, 2007.



**Seyyed Ali Hassani Gangaraj** was born in Iran, in 1988. He received the B.Sc. and M.Sc. degrees from the Iran University of Science and Technology (IUST), Tehran, Iran, all in electrical engineering in 2010 and 2012, respectively. He is currently pursuing the Ph.D. degree in electrical engineering, applied electromagnetics at the University of Wisconsin-Milwaukee (UWM), Milwaukee, WI, USA. He was a research assistant with the Microwave Engineering Laboratory, IUST, and currently is a research and teaching assistant with UWM. His major research areas are plasmonics, metamaterials, quantum plasmonics and photonic topological insulators. He is a student member of IEEE and technical reviewer for *IEEE Transactions on Antennas and Propagation* and *Optics Express*.



**Andrei M. Nemilentsau** was born in Belarus in 1982. He received the M.Sc. degree in physics and the Ph.D. degree in theoretical physics from Belarussian State University, Minsk, Belarus in 2004 and 2009, respectively. He was a research associate in the Institute for Nuclear Problems of Belarussian State University from 2009 to 2011, post-doctoral associate in the Physics Department of Lehigh University from 2011 to 2014, and Visiting Professor in the Department of Electrical Engineering at University of Wisconsin-Milwaukee from 2014 to 2016. He is currently a researcher in the Department of Electrical and Computer Engineering at the University of Minnesota. His research interests include nanoelectromagnetics, optical properties of and excitons in 2D materials, plasmonics, metamaterials and metasurfaces, plasmonics and near-field radiative heat transfer.

# Chapter 23

## Single-Band and Multiband Angular Filtering Using Two-Dimensional Photonic Crystals and One-Layer Gratings

Andriy E. Serebryannikov and Ekmel Ozbay

### 23.1 Introduction

Filtering as a process is commonly known for electrical engineers and physicists. In wide sense, it means an electrical or electronic circuit or an optical structure transmits or not electrical signals or electromagnetic waves in some ranges of variation of a selected physical parameter, but not to others. Frequency-domain filters are best known and most widely used. Their common function is to transmit or reflect in a designer-defined frequency range. The main types include bandpass, low-pass, bandstop, and high-pass filters, which function depending on which parts of the frequency spectrum should be transmitted or reflected. Sharp boundaries between pass and stop bands, total transmission in pass bands, and total reflection in stop bands are the general criteria that determine the quality of performance of any filter.

Similarly, filtering can be realized in other domains, i.e., at variations of another physical parameter while frequency is fixed. In spatial filtering, directions of incidence are assumed to be variable, whereas angular filtering represents its simplified version, in which incidence angle is varied in plane only. The spatial (angular) filters are demanded for different applications that include but are not restricted to the analysis and modification of spatial (angular) spectrum, radar data processing, aerial imaging, distinguishing the incoming waves depending on source location, detection of extrasolar planets, and biomedical applications. The known theoretical and experimental performances of spatial and angular filters include

---

A.E. Serebryannikov (✉)

Faculty of Physics, Adam Mickiewicz University, Umultowska 85, 61-614 Poznan, Poland  
e-mail: [andser@amu.edu.pl](mailto:andser@amu.edu.pl)

E. Ozbay

Nanotechnology Research Center – NANOTAM, Bilkent University, 06800 Ankara, Turkey  
e-mail: [ozbay@bilkent.edu.tr](mailto:ozbay@bilkent.edu.tr)



interference patterns [1], anisotropic media [2], grating-based resonant systems [3, 4], multilayer stacks combined with a prism [5], metallic grids backed by a ground plane [6], axisymmetric photonic microstructures [7], and various photonic crystals (PhCs) [8–12] including their microwave [13] and sonic [14] analogs that represent two-dimensional arrays of the rods. To time, both transmission-mode and reflection-mode angular filters have been proposed. The coexistence of spatial (angular) and frequency-domain filtering is an important theoretical and practical extension [4, 11]. Another aspect is related to angle-tolerant frequency-domain filtering [15, 16]. While the principal possibility of rather strong sensitivity of transmission and reflection to incidence angle variations is quite evident, the main problem is how to fulfill the general requirements regarding sharpness of the band boundaries and constant efficiency within a band, e.g., see Refs. [8, 11, 15, 16]. Indeed, any structure or medium with dispersion properties different from the host medium (usually air) is sensitive to variations in incident angle, so transmission and/or reflection is modulated. It is more difficult to entirely suppress transmission or reflection in a wide range of the angle variation. And even more difficult is to keep the constant efficiency within a band.

In this chapter, we demonstrate how all the main types of angular filtering can be achieved in transmission mode in wide bands with the aid of the structures based on two-dimensional PhCs. Transmission mode utilizes specific dispersion properties of Floquet–Bloch modes and, hence, behavior of equifrequency dispersion contours (EFCs) in the entire wavevector space. Moreover, for finite-thickness slabs of PhC, obtainable dispersion can yield unusual Fabry–Perot transmission, which is particularly appropriate for wideband angular filtering. From this perspective, PhCs represent simple and very suitable platform for angular filtering, because of suggesting a rich variety of dispersion types usable for angular filtering. Similarly to our earlier studies [8, 11, 17], the structures considered here are assumed to be made of conventional isotropic, passive dielectric materials and, thus, are easily realizable. For the sake of completeness, we also consider reflection-mode angular filtering in reflector-backed single-layer gratings, which is inspired by reflection mode of PhC gratings.

The chapter is organized as follows:

1. In Sect. 23.2, angular selectivity achievable in a classical Fabry–Perot etalon is considered.
2. Section 23.3 presents an overview of advanced Fabry–Perot regimes in slabs of PhC that are applicable to angular filtering.
3. In Sect. 23.4, the basic types of wideband angular filtering achievable in transmission mode with the aid of PhCs are considered.
4. Section 23.5 is dedicated to reflection-mode wideband angular filtering in single-layer gratings.
5. Section 23.6 briefly explains connection of angular filtering to other well-known phenomena and operation regimes.
6. Finally, concluding remarks are given in Sect. 23.7.

All the electromagnetic waves considered are assumed to be plane and monochromatic;  $\varepsilon_r$  and  $\mu_r$  stand for relative permittivity and relative permeability, respectively.

## 23.2 Fabry–Perot Etalon and Angular Filtering

First, we consider the basic features of transmission in case of Fabry–Perot etalon that is probably the simplest example of a transmission-mode angular filter. The structure considered here represents a homogeneous dielectric slab with non-corrugated interfaces; see Fig. 23.1, inset. A well-known formula allows one to express transmittance,  $T$ , via characteristics of the slab and its interfaces [18]:

$$T = (1 - \hat{R})^2 / [(1 - \hat{R})^2 + 4\hat{R}\sin^2(nkD\cos\theta')], \quad (23.1)$$

where  $k = k_0 = \omega/c$  is free-space wave number,  $\theta'$  is angle of refraction at the air-dielectric interface,  $D$  is the slab thickness, and  $n$  is index of refraction of the slab material. Reflectance of an air-dielectric interface,  $\hat{R}$ , is given by

$$\hat{R} = [(\cos\theta - n\cos\theta') / (\cos\theta + n\cos\theta')]^2, \quad (23.2)$$

where  $n\cos\theta' = \sqrt{n^2 - \sin^2\theta}$  and  $\theta$  is angle of incidence. Transmittance is maximal when  $\sin(nkD\cos\theta') = 0$ . It is assumed that the slab is made of a conventional non-dispersive, isotropic, lossless dielectric with  $\varepsilon_r > 1$  and  $\mu_r = 1$ , i.e.,  $n = \sqrt{\varepsilon_r}$ .

Figure 23.1 presents three examples of behavior of  $T$  in  $(kD, \theta)$ -plane. Calculations are carried out by using Eq. (23.1). The basic effects caused by variations in  $\theta$ ,  $kD$ , and  $\varepsilon_r$  are clearly seen. They include enhancement of the effect of  $\theta$  on location of the maxima and minima of  $T$  at larger values of  $\theta$  and  $kD$ , disappearance of overlapping of the neighboring Fabry–Perot resonances and weakening sensitivity to variations in  $\theta$  at increasing  $\varepsilon_r$ , and upshift of the resonance frequencies at increasing  $\theta$  that leads to the *positive slope* of the mountains of  $T = 1$  [i.e.,  $d\theta/d(kD) > 0$  at the mountain top] and valleys of  $\min T$  between them. It is worth noting that avoiding resonance overlapping and, thus, good separation of the neighboring mountains of  $T = 1$  invoke high-permittivity dielectric materials, which are available not for all parts of the electromagnetic spectrum and may show high losses.

Let us consider the features observed in Fig. 23.1 from the angular filtering perspective. The fundamental difference between the frequency-domain and angle-domain behavior of  $T$ , which may, in principle, be realized in Fabry–Perot etalon, is that there is an infinite number of the maxima of  $T = 1$  in the frequency domain at fixed  $\theta$ , whereas the number of the maxima in the angle domain at fixed  $kD$  can vary from zero [e.g., at  $kD = 16.8$  and  $\varepsilon_r = 60$  in Fig. 23.1c] to several ones [e.g., eight maxima at  $kD = 58.7$  and  $\varepsilon_r = 2.1$  in Fig. 23.1a], when  $0 < \theta < 80^\circ$ . For low-pass

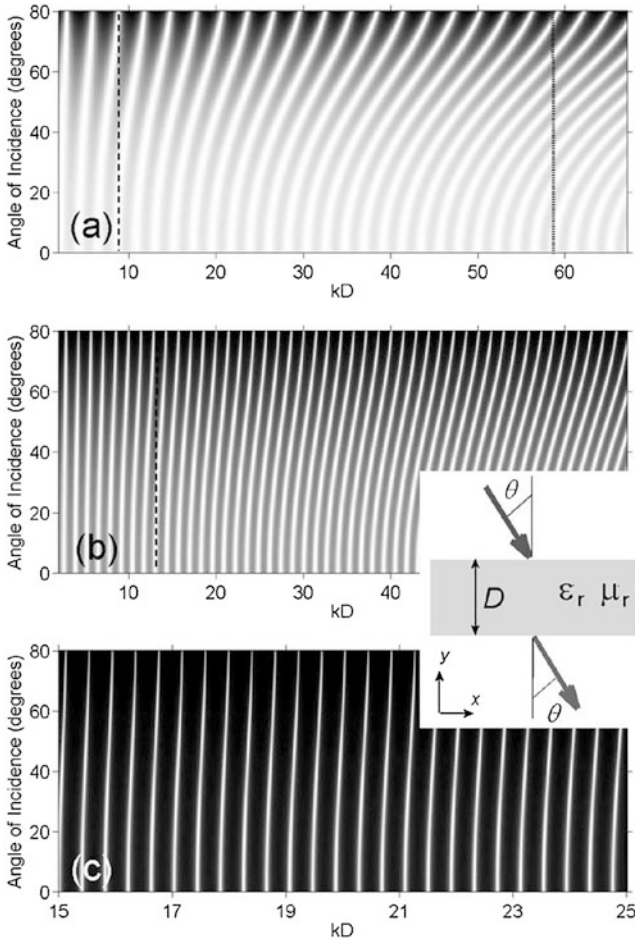


**Fig. 23.1** Transmittance in  $(kD, \theta)$ -plane for Fabry–Perot etalon at (a)  $\varepsilon_r = 2.1$ , (b)  $\varepsilon_r = 5.8$ , (c)  $\varepsilon_r = 60$ ; black and white colors correspond to  $T = 0$  and  $T = 1$ , respectively; different ranges of  $kD$ -variation are used in (a, b) and (c) to show details important for angular filtering; (a, b) only one maximum of  $T$  occurs in  $\theta$ -domain at  $kD$ -values on the left side from dashed line; (a) dotted line – example of several (here – eight) maxima of  $T$  at  $kD = \text{const}$ ; inset – general geometry

angular filtering, which is the simplest regime, it is difficult to obtain a single pass band that is well separated from the bands corresponding to the neighboring maxima of  $T$  and simultaneously has a sharp boundary between high- $T$  and low- $T$  regimes at given  $\theta = \theta_c$ , while using low-permittivity dielectric materials, see Fig. 23.1a. These materials typically do not enable a single band in the angle domain, at least in the range of high sensitivity to variations in  $\theta$ , where the slope may be appropriately small.

The use of high-permittivity materials allows one to obtain a single band and good separation, but the band boundaries remain blurred, because of a large slope of the mountains of  $T = 1$ . Indeed, low-pass filtering can be possible for high-permittivity dielectric materials owing to good separation of the neighboring mountains, provided that the slope is sufficiently small for obtaining sharp boundaries but not so small that there might be additional bands at the same  $kD$ -value. As shown in Fig. 23.1, a larger number of non-overlapping mountains can be obtained at a fixed  $kD$  while increasing  $\varepsilon_r$ . However, the realizable slope and distance between the mountains are not appropriate to fulfill the requirements of sharpness and single maximum simultaneously. When we separate the mountains with the aid of increasing  $\varepsilon_r$ , we simultaneously increase the slope. Thus, in case of Fabry–Perot etalon, the basic requirements to an angular filter can contradict with each other. For bandpass and high-pass filtering, the problem of blurred boundaries remains. Some aspects of angular selectivity in Fabry–Perot etalon have been studied in Ref. [19]. For further evidence, Fig. 23.2 presents the examples of dependencies of  $T$  on  $\theta$

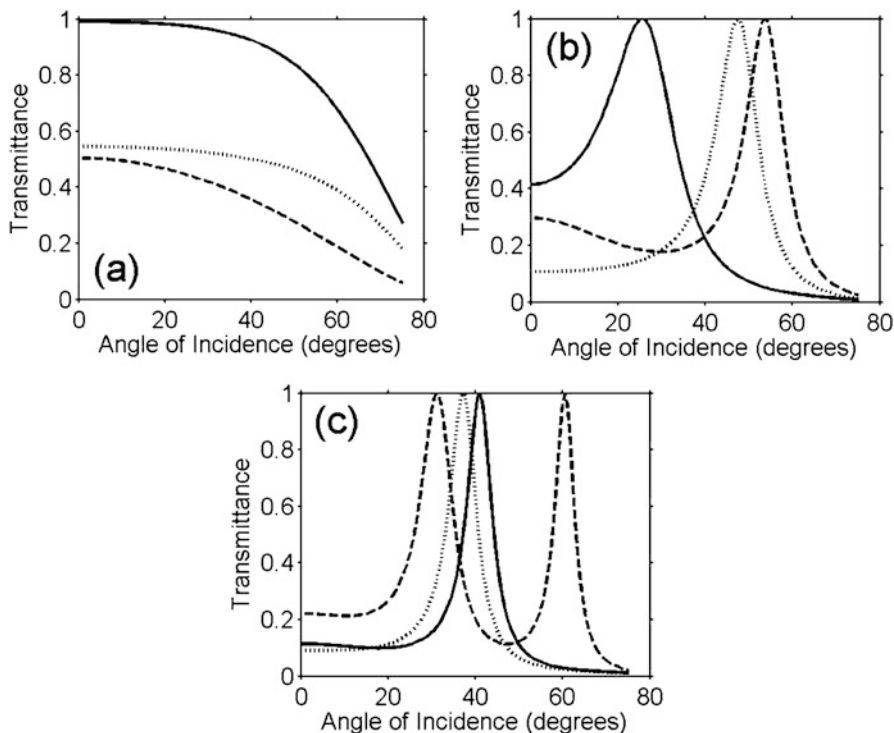


**Fig. 23.2** Transmittance vs  $\theta$  at fixed  $kD$  for Fabry–Perot etalon with (a)  $kD = 2$  and  $\varepsilon_r = 2.1$  (solid line),  $\varepsilon_r = 5.8$  (dashed line),  $\varepsilon_r = 11.9$  (dotted line); (b)  $kD = 27$  and  $\varepsilon_r = 16.3$  (dashed line),  $\varepsilon_r = 35.4$  (solid line),  $\varepsilon_r = 43$  (dotted line); (c)  $kD = 51$  and  $\varepsilon_r = 16.3$  (dashed line),  $\varepsilon_r = 35.4$  (solid line),  $\varepsilon_r = 43$  (dotted line)

at  $kD = \text{const}$ . The problem of the blurred boundaries is clearly seen. Fabry–Perot etalon based on a low-permittivity dielectric material does not yield efficient angular filtering, see Fig. 23.2a.

If requirements to band separation and sharpness of the band boundaries are not very strict, a bell-type bandpass filter can be obtained with the aid of Fabry–Perot etalon even at  $\varepsilon_r = 16.3$ , as shown in Fig. 23.2b. Typically, obtaining well-pronounced angle-domain bands requires materials that have high values of  $\varepsilon_r$ . Clearly, there is no tolerance regarding choice of operation frequency in this case, because small variations in frequency can lead to unwanted deviations from the mountain top. That is why more complex approaches and structures may be required in order to obtain efficient angular filtering.

### 23.3 Advanced Fabry–Perot Regimes Using Photonic Crystals

As has been shown above, Fabry–Perot transmission regimes promise realization of different types of angular selectivity. In fact, the ability of homogeneous dielectric slabs to show strong selectivity in  $\theta$ -domain, which is suitable for angular filtering, is connected with formation of the stop bands at large values of  $\varepsilon_r$  that occurs owing to the *impedance mismatch*. On the other hand, stop bands with sharp boundaries can be obtained with the aid of the *dispersion*-related mechanism in photonic crystals (PhCs). In this case, high-permittivity dielectric materials are not required. A rich variety of Fabry–Perot transmission regimes can be realized in finite-thickness structures based on PhCs with infinitely long rods, i.e., slabs of two-dimensional PhCs [19, 20]. It can also be achieved in PhC slabs that represent 3D structures, in which height of the rods or holes is comparable with lattice constant [21]. They may appear owing to Floquet–Bloch modes in the entirely periodic structures [19, 20], defect modes arising due to structural defects [12], and pure supercell modes, e.g., in non-uniform PhCs with parameters that are gradually varying from one unit cell to another [22]. All these structures and modes have potential in angular filtering. Moreover, in contrast with the Fabry–Perot etalon, many regimes can be realized by using PhCs made of conventional dielectric materials. Although transmission behavior of the classical Fabry–Perot etalon cannot be fully replicated in PhCs, they allow to obtain other features (e.g., sharp boundaries of the transmission bands due to the band gaps), which are highly demanded in angular filters. In fact, richness of the achievable transmission regimes is determined by richness of dispersion types in PhCs.

In the context of comparison of homogeneous dielectric slabs and finite-thickness PhCs, one should not forget that the effective boundaries of rod-type PhCs are ambiguous. This might complicate comparison of transmission in these two types of the structures. It is known that taking into account termination and matching

with the host medium is important for transmission properties of the resulting finite-thickness PhCs. In Ref. [19], multiple narrow pass bands are demonstrated for the slabs of PhCs made of conventional dielectric materials, with the aid of which, the same performance of the angular filter cannot be obtained in a homogeneous layer. It has been shown that this narrowband regime may correspond to different types of dispersion of the Floquet–Bloch modes and can be especially efficient at their band edges. Thus, narrowband angular filtering can be obtained relatively easily. This is a reason why it is worth focusing on *wideband* angular filtering.

Let us consider an example that demonstrates Fabry–Perot transmission regimes in the slabs of a square-lattice PhC ( $a$  is lattice constant) composed of the Si rods with relative permittivity  $\epsilon_r^{\text{PhC}} = 11.9$  and diameter  $d$ , see Fig. 23.3. Here and further, it is assumed that the slab is illuminated by  $s$ -polarized wave (electric field vector is parallel to the rod axes), at the angle  $\theta \geq 0$ , while the slab interfaces are along  $\Gamma$ -X direction. Two maps are presented in Figs. 23.3a and b that illustrate behavior of transmittance related to the second, third, and fourth lowest Floquet–Bloch modes (regions of  $T > 0$  indicated by the numbers 2, 3, and 4, respectively). The features observed here are very general and can be obtained for various sets of PhC parameters [8, 11].

From the Fabry–Perot transmission perspective, there are three scenarios, which are distinguished in terms of sensitivity to the variations in  $ka$  and  $\theta$ . Only one of them is realized in Fabry–Perot etalon. In this scenario, the mountains of  $T = 1$  show the positive slope, i.e.,  $d\theta/d(ka) > 0$  at the mountain top. On the contrary, the scenario with the negative slope,  $d\theta/d(ka) < 0$ , has not been observed in Fig. 23.1. In fact, this difference indicates *positive* phase velocity in the first scenario and *negative* phase velocity (NPV) in the second one, so  $\mathbf{S} \cdot \mathbf{k}^{\text{PhC}} > 0$  and  $\mathbf{S} \cdot \mathbf{k}^{\text{PhC}} < 0$ , respectively ( $\mathbf{S}$  is the time-averaged Poynting vector, and  $\mathbf{k}^{\text{PhC}}$  is the wavevector of the Floquet–Bloch mode). Finally, in the third scenario, denoted by  $v$ , there are nearly vertical mountains of  $T = 1$ , i.e.,  $|d\theta/d(ka)|$  tends to infinity. The regions of  $T > 0$  in  $(ka, \theta)$ -plane in Figs. 23.3a, b have sharp boundaries. Even though the neighboring mountains are not well separated from each other, the achievable Fabry–Perot transmission regimes show significant advantages compared to those in Fabry–Perot etalon. This is possible because different scenarios of transmission are realized due to Floquet–Bloch modes having different dispersion properties.

Comparing Figs. 23.3a and b, one can see that the regions of  $T > 0$  in the  $(ka, \theta)$ -plane have the same location, and the only significant difference is the density of the mountains of  $T = 1$ . This feature is exactly the same as that we would observe in two Fabry–Perot etalons that are made of the same dielectric material but have different thicknesses. Hence, the Fabry–Perot resonance nature of the mountains in Figs. 23.3a and b is evident. Thus, dependencies of  $T$  on  $ka$  obtained at  $\theta = \text{const}$  while  $N$  is increased would show the same densening of the minima as that obtained for Fabry–Perot etalon while  $D$  is increased. Four examples of  $T$  vs  $\theta$  are presented in Fig. 23.3c that demonstrate the principal possibility of obtaining sharp boundaries of the bands of  $T > 0$  in the  $(ka, \theta)$ -plane. In particular, the

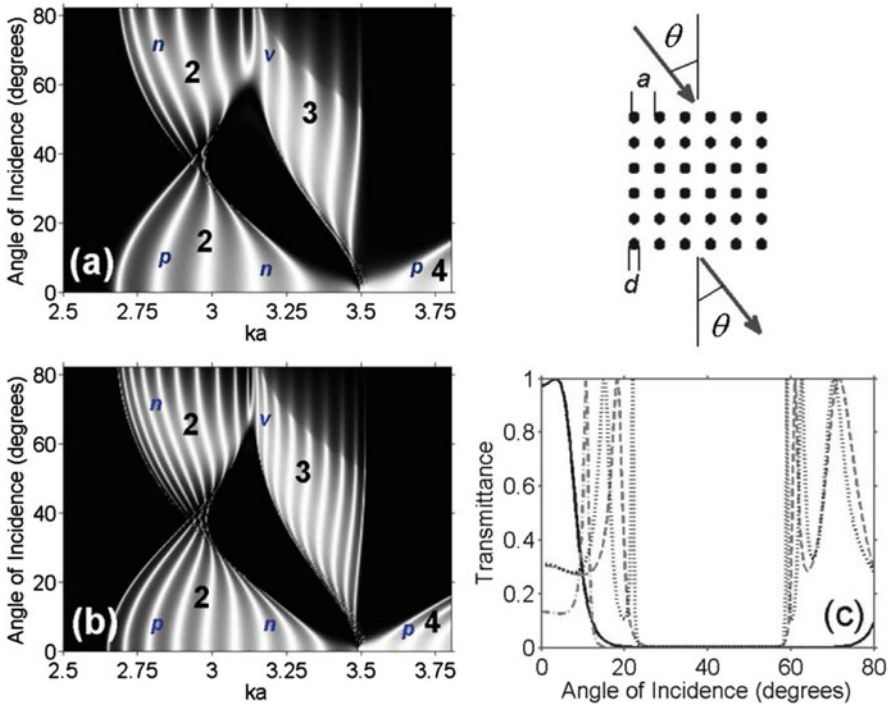


**Fig. 23.3** Transmittance for slabs of PhC with  $\epsilon_r^{\text{PhC}} = 11.9$ ,  $d/a = 0.45$  (a, b) in  $(ka, \theta)$ -plane at (a)  $N = 6$  and (b)  $N = 10$ ; and (c) as a function of  $\theta$  at  $ka = 3.269$  (solid line) and  $ka = 2.751$  (dashed line),  $N = 6$ , and at  $ka = 2.675$  (dash-dotted line) and  $ka = 2.751$  (dotted line),  $N = 10$ ; in (a, b), black and white colors correspond to  $T = 0$  and  $T = 1$ , respectively, numbers 2, 3, 4 indicate the regions in which transmission appears due to the corresponding Floquet–Bloch mode,  $p$ ,  $n$ , and  $v$  indicate the regions with positive and negative slope of mountains and vertical mountains, respectively; inset shows general geometry

possibility of low-pass (solid line), imperfect narrow bandpass (dash-dotted line), and bandstop (dashed and dotted lines) filtering is demonstrated here. The case of low-pass filtering is realized for the fourth lowest Floquet–Bloch mode, while three other cases are realized for the second lowest Floquet–Bloch mode, at the lower-frequency edge of the region of  $T > 0$  in  $(ka, \theta)$ -plane. Clearly, fulfillment of possible requirements regarding  $T$ -values at the pass bands (e.g.,  $T = \text{const}$ ) may need other sets of parameters than in Fig. 23.3c, including ones not corresponding to the near-edge regimes. The strategy of utilizing the above discussed transmission features, which can be obtained with the aid of PhC-based structures, for different types of angular filters is considered in the next sections.

## 23.4 Wideband Angular Filtering in Transmission Mode

### 23.4.1 Basic Principles from Dispersion in $k$ -Space

The distribution of the Floquet–Bloch modes in the *entire* wavevector space ( $\mathbf{k}$ -space) determines the type(s) of angular filtering, which can be realized for a chosen set of structural parameters and frequency [11]. It is known that electromagnetic waves follow in PhC Bloch’s theorem as electrons in a crystal, so the distribution of the modes in  $\mathbf{k}$ -space or its two-dimensional analog, i.e., the  $(k_x, k_y)$ -plane, can be reconstructed from the distribution of the modes in the first Brillouin Zone (BZ). To do this, one should use a *repeated zone scheme* by following the symmetry of the PhC lattice similarly to the electronic case. Strictly speaking, this approach allows one to clarify whether *coupling* is, in principle, possible or impossible for a certain range of  $\theta$  variation. An extensive analysis of anomalous refraction scenarios achievable in PhCs, which takes into account the mode distribution in the entire  $\mathbf{k}$ -space, has first been carried out in Ref. [23]. For the purposes of angular filtering, the earlier studies of PhCs are important, because they give an idea about possible types of behavior of EFCs for PhC in  $\mathbf{k}$ -space.

To obtain *wideband* angular filtering, the following requirements have to be fulfilled:

- coupling of the incident electromagnetic wave to a Floquet–Bloch wave is realized only for the desired ranges of  $\theta$ -variation and forbidden otherwise;
- switching between angular pass and stop bands (the ranges of  $T > 0$  and  $T = 0$ ) must be sharp, in the ideal case – stepwise;
- constant transmission efficiency must be preserved within the entire range of  $T > 0$  (in the ideal case –  $T = 1$ ).

Let us briefly explain the meaning of these requirements in terms of properties of Floquet–Bloch modes in  $\mathbf{k}$ -space. The first requirement means that EFCs of PhC must exist only within a part of the entire range of  $0 < k_x < k_0$  and not exist within the remaining part, in order to enable transmission for the former and block it for the latter. The second requirement is expected to be fulfilled when EFCs tend to quickly disappear while approaching the boundary of the region of existence of a Floquet–Bloch mode in  $\mathbf{k}$ -space; thickness of the slab of PhC is large enough to obtain strong energy confinement and, thus, avoid blurring of the band boundaries, and there are no surface waves or edge modes related to the finite thickness of the structure. The third requirement means, in fact, that  $k_y = \text{const}$  must be obtained for EFCs in the  $k_x$ -ranges where coupling is required. It cannot be obtained in the case of circular EFCs, which correspond to the isotropic media and some of Floquet–Bloch waves in PhCs. Instead, flat EFCs are required. Generally speaking, the first requirement represents the necessary condition of dispersion-driven angular filtering in transmission mode, whereas the second and third ones determine quality of performance of an angular filter.



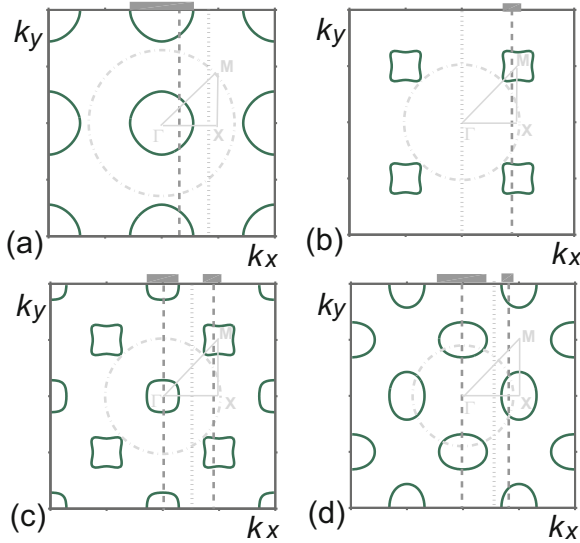


**Fig. 23.4** Examples of combination of EFCs for the regular infinite PhC (solid lines) and air host (dash-dotted lines – circles) in  $(k_x, k_y)$ -plane at fixed frequency (repeated zone diagram);  $k_x$  and  $k_y$  vary from  $-\pi/a$  to  $\pi/a$ ; triangles show boundaries of the first BZ; vertical dashed and dotted lines – construction lines corresponding to the cases when coupling is and is not possible, respectively; rectangles at plot top schematically show location of  $k_x$  ranges, in which coupling is possible; (a) one nearly monotonous band solution yielding a nearly circular EFC around  $\Gamma$ -point, (b) one nonmonotonous band solution yielding nearly square EFC around M-point, (c) two nonmonotonous band solutions yielding nearly square EFCs around  $\Gamma$ -point and M-point, (d) one nonmonotonous band solution yielding oval-shaped EFC around X-point

Figure 23.4 presents the schematics that illustrate the coupling scenarios for some of typical shapes of EFCs for two-dimensional PhCs in  $(k_x, k_y)$ -plane at a fixed frequency. In the band regimes with monotonous (isotropic-type) dispersion, which corresponds to circular EFCs, one Floquet–Bloch wave may be coupled to the incident and outgoing waves, leading to one transmission band in  $\theta$ -domain. However, if there are two band solutions, two Floquet–Bloch modes may be coupled simultaneously, resulting in two transmission bands. One band with a nonmonotonous (anisotropic) dispersion can yield either one or two transmission bands in  $\theta$ -domain. More details regarding connection between behavior of EFC in  $\mathbf{k}$ -space and achievable angular filtering regimes can be found in Ref. [11].

The richness of dispersion types in PhCs allows us to expect that the different types of angular filtering can be obtained even at the neighboring frequency ranges. Here, it is assumed that more than two Floquet–Bloch modes may not coexist at a fixed frequency. However, in the general case, the number of the simultaneous modes can be arbitrary.

The principal difference of the EFC-based coupling analysis carried out in  $\mathbf{k}$ -space for frequency and angular filtering is that only one pair of EFCs (one EFC for

air and one for PhC) is needed in the latter case, whereas such multiple pairs are required in the former case. Thus, the coupling analysis in case of angular filtering is quite simple. Its main component, i.e., conservation of the tangential wavevector (in our case  $-k_x$ ) at the slab interfaces, is common in both frequency-domain and angle-domain analysis. EFCs in air and PhC must coexist to realize coupling at given  $k = k_0 = \omega/c$  and  $k_x$  and, thus, at given  $\theta$  ( $\sin\theta = k_x/k_0$ ).

In Fig. 23.4a, the coupling scenario is schematically shown, in which a Floquet–Bloch mode has isotropic-type dispersion, so the EFC is nearly circular. However, it is narrower than in air, i.e.,  $\max|k_x^{\text{PhC},\Gamma}| < k_0$  (superscript  $\Gamma$  indicates EFC location around  $\Gamma$ -point), that corresponds to the index of refraction  $0 < |n| < 1$ . Thus, coupling is allowed by the dispersion only at  $\theta < \theta_c$ ,  $\theta_c = \arcsin(\max|k_x^{\text{PhC},\Gamma}|/k_0)$ . This results in the appearance of low-pass angular filtering at a fixed frequency. However, in Fig. 23.4a,  $k_y \neq \text{const}$  at  $k_x < \max|k_x^{\text{PhC},\Gamma}|$  and, hence,  $T = \text{const}$  is not expected to be realizable within the entire pass band. To obtain  $T = \text{const}$ , one should have square-shaped EFCs instead of the circular ones in  $\mathbf{k}$ -space. Such EFCs can be obtained in two-dimensional PhCs [31, 32].

In Fig. 23.4b, an example is presented, which corresponds to high-pass and bandpass filtering. If  $\min|k_x^{\text{PhC},\text{M}}| < k_0 < \max|k_x^{\text{PhC},\text{M}}|$  (superscript M indicates EFC location around M-point), a coupling scenario is possible that is required for the case of high-pass filtering (shown). If  $\max|k_x^{\text{PhC},\text{M}}| < k_0 < \max|k_x^{\text{PhC},\Gamma}| + 2\pi/a$ , bandpass filtering is formally allowed (not shown). The PhC's EFC shape in Fig. 23.4b enables  $k_y \approx \text{const}$  in a wide but not complete range of  $\theta$ -variation. Thus, it is possible to obtain  $T \approx \text{const}$ , according to the third requirement.

Next, the scenario in Fig. 23.4c can be appropriate for dual bandpass and bandstop angular filtering. The second (i.e., higher- $\theta$ ) band is formally either bounded or not bounded at large  $\theta$ , depending on whether  $\max|k_x^{\text{PhC},\text{M}}| < k_0 < \max|k_x^{\text{PhC},\Gamma}| + 2\pi/a$  (not shown) or  $\min|k_x^{\text{PhC},\text{M}}| < k_0 < \max|k_x^{\text{PhC},\text{M}}|$  (shown). In the former case, it is bounded, whereas in the latter case, it is not. Clearly,  $\max|k_x^{\text{PhC},\Gamma}| < \min|k_x^{\text{PhC},\text{M}}|$  is the necessary condition for these two types of filtering. The EFC shape in this example is suitable for obtaining  $T \approx \text{const}$ . For bandstop filtering, condition  $k_y = \text{const}$  is not necessary, so the requirements to the shape of PhC's EFC can be mitigated. At the same time, EFC location remains very important. An example is presented in Fig. 23.4d. The stop band may appear at  $\theta$ -values corresponding to  $\max|k_x^{\text{PhC},\Gamma}| < k_x < \min|k_x^{\text{PhC},\text{X}}|$  (superscript X indicates EFC location around X-point).

It is important that the different Floquet–Bloch modes show different types of dispersion in the same PhC [11]. This means that the different types of angular filtering may be realized in different frequency bands in *one* device that indicates new perspective routes to multiband/multifrequency operation. In fact, the abovementioned can be observed in Fig. 23.3. In this case, several types of filtering can be obtained in one structure, while only three Floquet–Bloch modes contribute to the transmission in the  $ka$ -range, for which  $f_{\max}/f_{\min} \approx 1.4$ .

### 23.4.2 Low-Pass Filtering

Low-pass filtering is considered to be the simplest type of angular filtering. In contrast to the other types of filtering, it can be obtained even if using a slab of a natural or artificial material with the index of refraction  $0 < n < 1$ . The examples include plasmas in the vicinity of plasma frequency [24], epsilon-near-zero metamaterials [25, 26], artificial ultralow-index materials [27], and natural materials showing transition from metal to dielectric state [28].

The maximal angle, at which transmission is possible, is given by

$$\theta = \theta_c = \arcsin(n). \quad (23.3)$$

In fact, low-pass filtering is based in this case on the well-known total internal reflection phenomenon, which occurs when electromagnetic wave is incident from an optically more dense medium on the interface of an optically less dense medium, e.g., see Refs. [27, 29]. However, the problem appears when  $T = \text{const}$  and, in particular, when  $T \approx 1$  is required within a wide range of  $\theta$ -variation together with sharp switching between  $T \approx 1$  and  $T = 0$ . Circular EFCs do not allow to obtain this regime. Clearly, the same is true for the mountains of  $T$  in case of Fabry–Perot etalon, which can be realized with the aid of the impedance mismatch mechanism at least if  $\varepsilon_r$  of the slab is rather high, see Fig. 23.1c.

While location of EFCs around  $\Gamma$ -point remains the necessary condition for the dispersion-based mechanism of low-pass filtering, the EFC shape is a subject of optimization. Moreover, strength of coupling is important, but it cannot be predicted based only on the dispersion results.

Figure 23.5 presents two examples of behavior of  $T$  in  $(ka, \theta)$ -plane and dependence of  $T$  on  $\theta$  at the selected parameter sets. Figure 23.5a corresponds to the case of nearly circular EFCs, which are expanded while  $ka$  is increased. This regime is appropriate when a narrow  $\theta$ -domain passband is required. The width of the passband can be varied nearly from  $2^\circ$  to  $7.5^\circ$  ( $n \approx 0.13$ ) by varying  $ka$  from 3.51 to 3.56. In this case, dependence of  $T$  on  $\theta$  shows only one maximum. Thus, transmission through a slab of ultralow-index material can be mimicked in this case.

Figure 23.5b corresponds to the case when EFCs for the second lowest Floquet–Bloch mode are located around  $\Gamma$ -point but have nearly square shape. Moreover, this mode has here such properties that high transmittance is possible within a very large region in  $(ka, \theta)$ -plane. After the wide ranges of  $T = 1$  in  $\theta$ -domain, this is the second important feature that enables efficient angular filtering with the aid of PhCs. It is not unique but needs careful parameter adjustment to be realized. In particular, large values of  $d/a$  and  $\varepsilon_r^{\text{PhC}}$  can be required. Note that it is important not only and mainly even not for low-pass angular filtering. In Sect. 23.4.4, its importance for dual bandpass filtering is demonstrated. In Fig. 23.5b, one has some freedom in choice of  $\theta_c$ , depending on  $ka$ . However, it might be difficult to obtain a wider

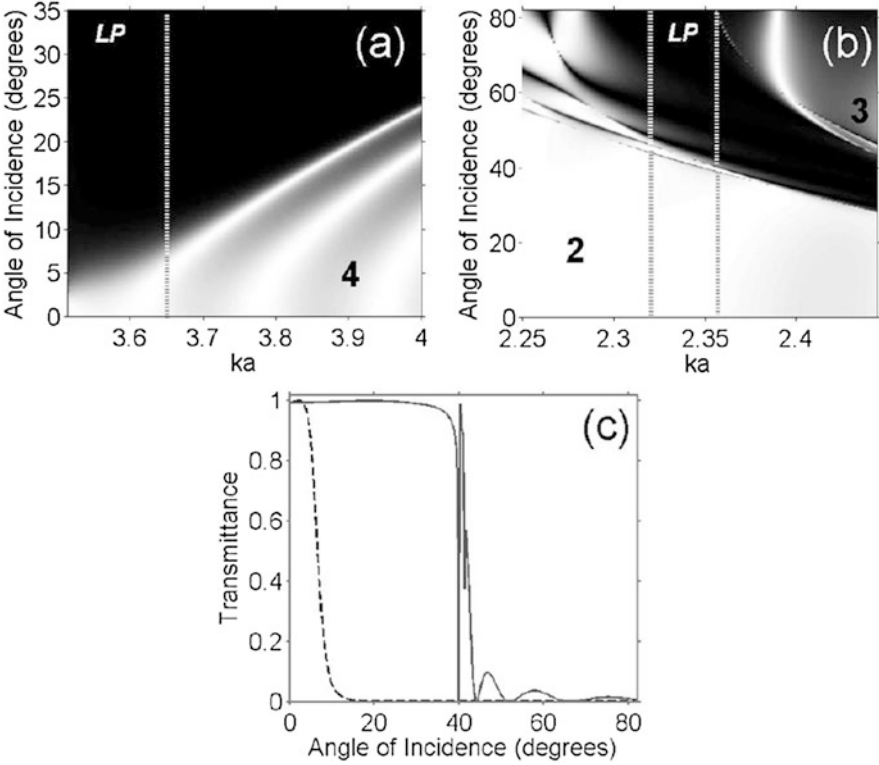


**Fig. 23.5** Transmittance for slab of PhC **(a, b)** in  $(ka, \theta)$ -plane at **(a)**  $d/a = 0.4$  and **(b)**  $d/a = 0.57$ , and **(c)** as a function of  $\theta$  at  $ka = 2.349, d/a = 0.57$  (solid line) and  $ka = 3.621, d/a = 0.4$  (dashed line);  $N = 6, \epsilon_r^{\text{PhC}} = 11.9$ ; LP indicates the possibility of obtaining low-pass filtering **(a)** on the left to dashed line and **(b)** between dashed lines; in **(a, b)**, black and white colors correspond to  $T = 0$  and  $T = 1$ , respectively; numbers 2, 3, and 4 indicate the regions, in which transmission appears due to the corresponding Floquet-Bloch modes

$ka$ -range suitable for low-pass filtering, since square-shaped EFCs located around  $\Gamma$ -point often coexist with EFCs for other Floquet-Bloch modes (or with EFCs arising due to the same mode), which contribute to transmission in unwanted ranges of  $\theta$ -variation. In this case, low-pass filtering cannot be realized.

In Fig. 23.5c,  $T$  vs  $\theta$  is shown in two selected cases from Figs. 23.5a and b. For the first of them (shown by solid line), we obtain  $\theta_c \approx 39^\circ$  and  $|n| = 0.63$  at  $ka = 2.34$ . For the second one (shown by dashed line),  $\theta_c < 10^\circ$ , so it is mimicking a material with  $0 < n < 0.17$ . Some unwanted features may appear in the  $\theta$ -dependencies of  $T$  due to the edge modes (near  $\theta = 40^\circ$ ). In spite of this,  $T \approx 1$  in a wide  $\theta$ -range, as desired.

### 23.4.3 Bandpass and High-Pass Filtering

Indefinite media [2] and hyperbolic metamaterials [30] formally fulfill the minimal requirements to a high-pass filter regarding EFC location. However, they typically do not allow one obtaining  $T = \text{const}$  in a wide  $\theta$ -range, because  $k_y = \text{const}$  cannot be achieved in a wide range of  $k_x$  variation. It is even more difficult to obtain bandpass filtering with a sharp upper boundary of the band at large values of  $\theta$ . Similarly to the case of low-pass filtering, we need square-shaped EFCs that should now be located only around M-point in  $\mathbf{k}$ -space. For  $\epsilon_r^{\text{PhC}} = 11.9$ , they can be obtained at smaller values of  $d/a$  than in Figs. 23.3 and 23.5.

Figure 23.6 presents the examples of behavior of  $T$  in  $(ka, \theta)$ -plane and dependence of  $T$  on  $\theta$  in the selected cases. In Fig. 23.6a, one can see that bandpass filtering can be obtained in a large region of the  $(ka, \theta)$ -plane, where Fabry–Perot transmission with the alternating mountains and valleys of  $T$  is observed. Several mountains can be used simultaneously, i.e., efficient bandpass filtering can be obtained at several frequencies which are quite close to each other. Since the mountains are not sharp so there is some flexibility for fine adjustment of the  $ka$ -value, some problems may appear at the band edges, e.g., due to dependence of the mountain locations on  $ka$  at the lower boundary of the transmission region. It is noteworthy that this boundary is fully determined by the properties of the third lowest Floquet–Bloch mode. On the contrary, the upper (here – blurred) boundary appears due to the effect of diffraction order  $m = -1$ . Thus, it can be approximated at given  $\theta$  by the equation

$$k_u a = 2\pi / (1 + \sin\theta), \quad (23.4)$$

which is obtained from the condition of propagation of this order [33]. In turn, for given  $ka$ ,  $\sin\theta_u = 2\pi / (ka) - 1$ .

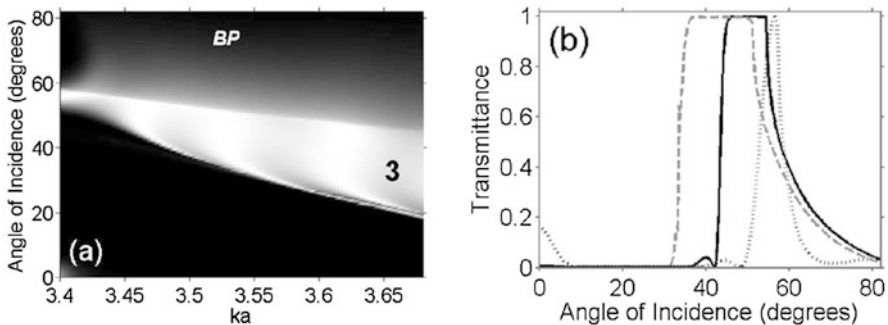


**Fig. 23.6** Zero-order transmittance for slab of PhC (a) in  $(ka, \theta)$ -plane and (b) as a function of  $\theta$  at  $ka = 3.463$  (solid line),  $ka = 3.53$  (dashed line), and  $ka = 3.412$  (dotted line);  $N = 6$ ,  $d/a = 0.36$ ,  $\epsilon_r^{\text{PhC}} = 11.9$ ; in (a), BP indicates the possibility of obtaining bandpass filtering in the entire  $ka$ -range considered; black and white colors correspond to  $T = 0$  and  $T = 1$ , respectively; number 3 indicates that transmission appears due to the third lowest Floquet–Bloch mode

In fact, bandpass filtering is realized here owing to the common effect of dispersion and diffraction. Zero-order transmission above the upper boundary in Fig. 23.6a becomes weaker due to the order  $m = -1$ . It is worth noting that the transmission regimes realized due to the order  $m = -1$  usually do not show high efficiency, so that they are of limited interest for angular filtering and, thus, are not considered here. In Fig. 23.6b, one can see the pass bands obtained at  $ka = \text{const}$ . In spite of the expected difficulties at the edges, these pass bands do not strongly suffer from them. Moreover, choosing a suitable value of  $ka$ , one may vary width and location of the band. The condition of  $T \approx 1$  is fulfilled in a wide  $\theta$ -range, as required. For instance,  $\Delta\theta \approx 15^\circ$  for the range of  $T \approx 1$  at  $ka = 3.53$  and  $\Delta\theta \approx 20^\circ$  for that at  $ka = 3.624$ .

In the considered range of parameter variation, we have  $\min|k^{\text{PhC.M}}| < k_0 < \max|k^{\text{PhC.M}}|$ , so the contribution of the propagating order  $m = -1$  is *necessary* to obtain bandpass filtering. Would this condition be satisfied while no one higher order is propagating, one should obtain rather high-pass filtering, for which coupling efficiency and transmission can be reduced at the grazing angles. The approach to obtaining the upper boundary that is realized here has been suggested in Ref. [8]. Usually, the second Floquet–Bloch mode in such a scenario, if involved, is parasitic and might not affect the principal possibility of the single bandpass filtering regime only if it is uncoupled (e.g., because of specific modal properties) to the incident wave and/or its  $k_x$ -range is entirely embedded into that of the operation mode. It is worth noting that the dispersion features required for bandpass and high-pass filtering are very general for PhCs. Many examples can be found in the literature [11, 31, 32].

### 23.4.4 Bandstop and Dual Bandpass Filtering

Next, we consider two types of angular filtering, which are closely related to each other: bandstop and dual bandpass filtering. Indeed, if we have two separated pass bands, there should be a stop band between them. The difference, however, is that for operation in bandpass regime, the condition of  $T = 1$  is required, whereas for bandstop operation the requirements to transmittance in the neighboring pass bands can be mitigated. Following the line of reasoning from Sect. 23.4.1, it is not difficult to predict which EFCs are required: the square-shaped EFC located at  $\Gamma$ -point that is responsible for the low- $\theta$  pass band and the square-shaped EFC located at M-point that is responsible for the high- $\theta$  pass band. Then, the gap between the EFCs must exist that enables a stop band.

Dual bandpass filtering can be obtained when  $\min|k^{\text{PhC.M}}| < k_0 < \max|k^{\text{PhC.M}}|$  and  $\max|k^{\text{PhC.}\Gamma}| < \min|k^{\text{PhC.M}}|$ . The first of these conditions can be modified by taking into account that the boundary of the second band in the  $\theta$ -domain can be created due to the effect of a higher diffraction order.

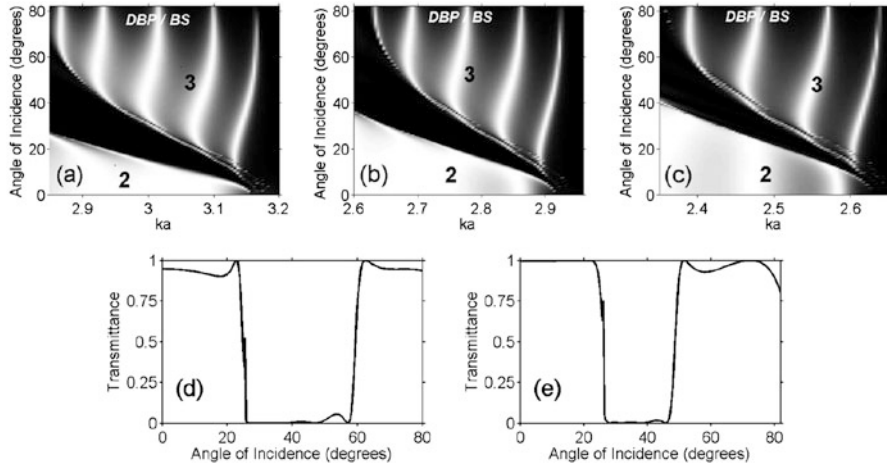


**Fig. 23.7** Transmittance for slab of PhC in  $(ka, \theta)$ -plane at (a)  $d/a = 0.45$ , (b)  $0.5$ , and (c)  $0.57$  and as a function of  $\theta$  at (d)  $d/a = 0.45$ ,  $ka = 2.869$  and (e)  $d/a = 0.5$ ,  $ka = 2.689$ ;  $N = 6$ ,  $\epsilon_r^{\text{PhC}} = 11.9$ . In (a–c), DBP and BS indicate the possibility of obtaining dual bandpass and bandstop filtering at selected values of  $ka$  and in most part of the considered  $ka$ -range, respectively, *black* and *white colors* correspond to  $T = 0$  and  $T = 1$ , respectively; numbers 2 and 3 indicate the regions, in which transmission appears due to the corresponding Floquet–Bloch mode

Figure 23.7 presents a few examples.  $T$  in the  $(ka, \theta)$ -plane is shown in Figs. 23.7a–c. The difference between the three considered structures is only in the value of  $d/a$ . One can see that the basic features are very general, i.e., they occur in a wide range of  $d/a$ -variation that provides big freedom for filter design. Transmission is obtained here due to the simultaneous contribution of the second lowest (at smaller  $\theta$ ) and the third lowest Floquet–Bloch mode (at larger  $\theta$ ). Accordingly, a stop band region size depends on how well the regions of existence of these modes in  $(ka, \theta)$ -plane are separated from each other. Both types of the above discussed unusual Fabry–Perot transmission, i.e., nearly vertical mountains and wide ranges of  $T \approx 1$  are presented here. For the second lowest mode,  $T$  is weakly sensitive to variations of  $ka$  and  $\theta$  in a large region of the  $(ka, \theta)$ -plane. Moreover,  $T \approx 1$  can be preserved at least for a larger part of this region, while the case of  $d/a = 0.5$  is preferable. The mountains of  $T \approx 1$  can be obtained for the third lowest mode that are either totally vertical or show a very large slope. The coexistence of these two types of the unusual behavior is very important for dual bandpass filtering. Indeed, if both modes would create the alternating mountains and valleys of  $T$  in  $(ka, \theta)$ -plane, an additional problem should be solved, i.e., how to match location of the mountains for two Floquet–Bloch modes. In the general case, this would be a quite challenging task. It could be even more complicated if angular filtering is required at two or more different and not close values of  $ka$ , so that the matching should simultaneously be achieved at all of these values. This cannot be done without careful parameter adjustment. Nevertheless, the principal possibility of such a matching, at least for one  $ka$ -value, has been demonstrated for the parameter set, which is similar to those used in Fig. 23.7 [8].

An alternative and more universal way of matching would need the transmission properties of the third lowest Floquet–Bloch mode that are similar to the second one. However, to time, such parameter sets are not known, and the principal possibility of realization of this case remains a subject of discussions. It is noteworthy that for the third lowest mode, most of the mountains of  $T$  show a large positive slope rather than are exactly vertical. The most appropriate of them are located closer to the left edge of the region of  $T > 0$  that corresponds to this mode. Together with the possibility of matching regimes of  $T \approx 1$  that are connected with different Floquet–Bloch modes, sharp (non-blurred) boundaries of the transmission bands, which are realizable due to localization of the Floquet–Bloch modes in  $\mathbf{k}$ -space, represent the fundamental property enabling high performance of dual bandpass angular filters. Thus, although deviation of the mountains from the vertical position can lead to imperfectness of the transmission response in the  $\theta$ -domain, it does not significantly affect the advantages of the used approach, which are connected with the specific properties of the Floquet–Bloch modes. Clearly, several regimes of dual bandpass filtering can coexist in one structure due to the same mode, but correspond to different values of  $ka$ .

Comparing Figs. 23.7a–c and 23.6a, one can see the difference in behavior of  $T$  at large values of  $\theta$ . Indeed, larger values of  $d/a$  than in Fig. 23.6 are required to obtain  $T \approx 1$  in wide ranges of variation in  $ka$  and  $\theta$ . However, this leads to the downshift of the  $ka$ -range, in which the second and third lowest Floquet–Bloch modes coexist, while larger values of  $ka$  are required for propagation of the order  $m = -1$ . Hence, an additional parameter adjustment is required in order to simultaneously obtain two Floquet–Bloch modes and the propagating order  $m = -1$ . It is noticeable that variations in  $d/a$  may lead to strong modification of some of Floquet–Bloch modes, whereas the other ones are not so strongly affected.

Two examples of behavior of  $T$  as a function of  $\theta$  are presented in Figs. 23.7d and e. In spite of some imperfectnesses that manifest themselves in a slight deviation from the regime of  $T = 1$  and possible effects of edge modes, the pass and stop bands are quite well pronounced. Different combinations of the widths of the  $\theta$ -domain pass bands arising due to different Floquet–Bloch modes can be realized. However, the left edge of the region of  $T > 0$  in  $(ka, \theta)$ -plane, which is connected with the third lowest mode, remains preferable for operation because an almost vertical mountain of  $T = 1$  can be obtained in this case.

## 23.5 Wideband Angular Filtering in Reflection Mode

In fact, any transmission-mode angular filter can be considered at  $\theta \neq 0$  as a three-port system, in which the input and output are associated with the incident and transmitted wave, respectively, while one of the ports (reflection) is blocked in the ideal case. In the general case, the output should not necessarily be connected with a transmitted wave. For reflection-mode operation, the output must be associated with one of the higher diffraction orders in reflection, into which the



incident-wave energy is entirely converted. Thus, similarity to the above considered transmission-mode filtering is only partial. Indeed, the angle at which transmitted wave propagates in the exit half-space is always given by  $\phi_{\text{out}} = \theta$ , while higher diffraction orders remain evanescent. In reflection mode, there is no other chance to achieve angular filtering than by means of extreme redistribution of the incident-wave energy in favor of a propagating higher order ( $|m| > 0$ ). In the ideal case, zero-order reflectance  $r_0 = 1$  at  $0 < \theta < \theta_c$ , where  $\theta_c$  is the angle at which switching between the two orders takes place. In turn, higher-order reflectance  $r_m = 1$  at  $\theta_c < \theta < \theta_u$ ,  $\theta_u < \pi/2$ ,  $|m| > 0$ . In this case, the grating theory gives [33]

$$\phi_{\text{out}} = \arcsin[\sin\theta + 2\pi m/(kL)], \quad (23.5)$$

where  $L$  is grating period. In Ref. [34], it has been shown that efficient bandpass filtering with a sharp switching between the orders  $m = 0$  and  $m = -1$  can be obtained in reflection mode in rod-type PhC gratings created by introducing corrugations on a non-corrugated slab of PhC, like that in Fig. 23.3, inset, and relevant single-layer rod gratings backed with a metallic reflector. For reflector performance, it does not matter how (nearly) perfect reflections are achieved.

The main advantage of the single-layer gratings is that they suggest compact performances, which can be several times thinner than the PhC-based transmission-mode filters. In this case, the ability of keeping  $r_{-1} \approx 1$  in a wide range of  $\theta$ -variation may be connected rather with the specific phase and impedance conditions. However, a disadvantage of reflection mode is that the vicinity of  $\theta = |\phi_{\text{out}}|$  should be excluded from the operation  $\theta$ -range to avoid unwanted backward reflections. Let us assume that the incident-wave energy is perfectly converted into the order  $m = -1$ , i.e.,  $r_{-1} = 1$ . Then, according to Eq. (23.5),

$$\sin\phi_{\text{out}} = \sin\theta - 2\pi/(kL). \quad (23.6)$$

Hence, the angle between two beams is  $\delta = 2\theta$  at  $0 < \theta < \theta_c$  and  $\delta = |\theta + \phi_{\text{out}}|$  at  $\theta_c < \theta < \pi/2$  (note that  $\phi_{\text{out}} < 0$  in this case). One can see that  $\delta$  is a linear function of  $\theta$  in the first case and a nonlinear function of  $\theta$  in the second case. To compare, we have always considered  $\delta = 2\theta$  for transmission mode in Sects. 23.2, 23.3, and 23.4.

Similarly to Ref. [34], nearly perfect switching between the orders  $m = 0$  and  $m = -1$  can be obtained in single-layer gratings in Fig. 23.8. Geometry of the problem is shown in Figs. 23.8a and b. In contrast with Ref. [34], the rods are assumed now to be square-shaped and located on a low-permittivity substrate. Figure 23.8c shows how  $\phi_{\text{out}}$  is changed depending on whether the order  $m = 0$  is only one propagating order or the order  $m = -1$  also may propagate and, moreover, all energy is transferred into this order.

Figure 23.9 presents an example of reflection-mode angular filtering, which is realized with the aid of the structure that comprises the components having relative

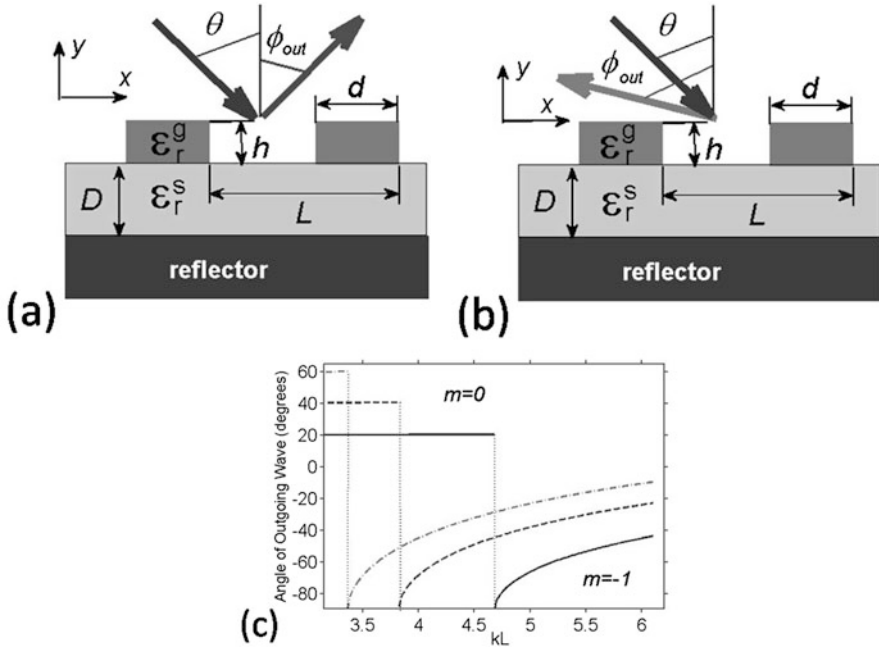


**Fig. 23.8** Schematics of reflector-backed single-layer grating with (a) zero-order and (b) first-order outgoing beam; two periods over  $x$  are shown; (c)  $\phi_{out}$  vs  $kL$  at  $\theta = 20^\circ$  (solid line),  $\theta = 40^\circ$  (dashed line), and  $\theta = 60^\circ$  (dash-dotted line) in case of ideal switching between orders  $m = 0$  and  $m = -1$

permittivity  $\epsilon_r^g = 5.8$  and  $\epsilon_r^s = 2.1$ , and is backed by a metallic reflector. The rods of square cross section have been used in order to obtain a more feasible performance. In Fig. 23.9b, one can see that there is a very large region of  $r_{-1} \approx 1$  in  $(kL, \theta)$ -plane. Hence, a bandpass filter can be realized. In turn, in Fig. 23.9a, low-pass angular filtering with  $r_0 \approx 1$  is observed. The pass bandwidth is determined in both cases by the condition of propagation of the order  $m = -1$ . In case of zero-order operation, one may introduce the equivalent index of refraction as  $n_{eq} = 2\pi/(kL) - 1$ , for given  $kL$  and, thus, for given  $\theta_c$ . It is important that similar behavior of  $r_0$  and  $r_{-1}$  in  $(kL, \theta)$ -plane can be obtained for a very large class of the structures that include various PhC gratings and single-layer gratings.

Figure 23.9c presents dependencies of  $r_{-1}$  on  $\theta$  at the selected values of  $kL$ . One can see that the lower- $\theta$  boundary is sharp, while  $r_{-1} \approx 1$  is kept in a wide  $\theta$ -range that extends over  $40^\circ$ . The total thickness of the substrate and grating is  $(h + D)/\lambda \approx 0.2$  ( $\lambda$  is free-space wavelength) at  $kL = 4.626$ . In addition to the subwavelength thickness, freedom in choice of  $kL$  and, thus, operation frequency is a big advantage compared to the structures that may show a desired angular behavior only in a narrow  $kL$ -range and/or a bell-shaped pass band in  $\theta$ -domain.

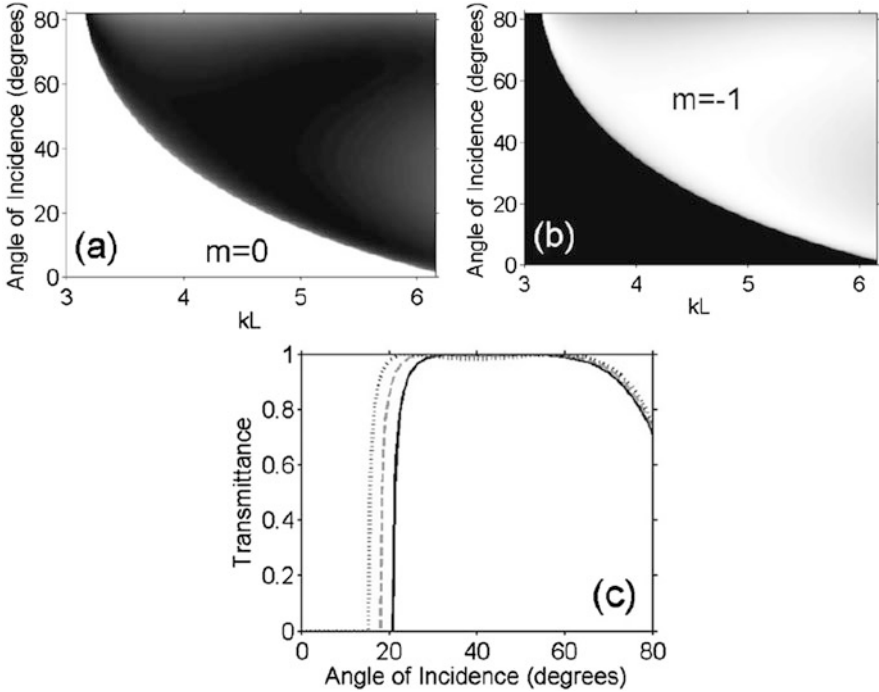


**Fig. 23.9** (a) Zero-order and first-order reflectance (b) in the  $(kL, \theta)$ -plane and (c) as a function of  $\theta$  at  $kL = 4.626$  (solid line),  $kL = 4.796$  (dashed line) and  $kL = 4.965$  (dotted line), for the structure shown in Fig. 23.8a, b at  $h/L = 1.57 \times 10^{-1}$ ,  $d/L = 1.96 \times 10^{-1}$  and  $D/L = 1.08 \times 10^{-1}$ ;  $\epsilon_r^x = 2.1$ ,  $\epsilon_r^z = 5.8$ ; in (a), black and white colors correspond to  $r_0 = 0$  and  $r_0 = 1$ , respectively; in (b), black and white colors correspond to  $r_{-1} = 0$  and  $r_{-1} = 1$ , respectively

## 23.6 Connection to Other Phenomena and Operation Regimes

One of the reasons of strong interest to PhCs at the beginning of 2000s has been connected with their ability to obtain NPV, as well as *negative refraction* with or without NPV [32, 35]. For the purposes of angular filtering, shape and location of EFCs in  $\mathbf{k}$ -space rather than sign of phase velocity and sign of refraction are important. Nevertheless, since the latter have often been obtained for Floquet–Bloch modes with square-shaped EFCs, efficient angular filtering can be realized in the same structures as and simultaneously with these phenomena.

On the other hand, angular filtering realized with the aid of square-shaped EFCs is connected with *collimation* inside the PhC [36]. However, angular filtering is associated rather with the selected-angle collimation, since desired angular selectivity could not be obtained in the all-angle collimation regime. In fact, this corresponds to the requirement regarding PhC's EFC that must coexist with EFC for air only in  $k_x$  ranges, where coupling is required for a particular type of angular filtering.

In this chapter, plane-wave approximation has been utilized. In case of narrow Gaussian beams, angular spectrum is wide so that some spectral components are suppressed while passing through a filter. Generally, wide spectrum leads to the blurring of the boundaries of pass and stop bands in  $\theta$ -domain, e.g., see Ref. [17]. For wide pass bands and relatively narrow angular spectra, effects of blurring can be mitigated. Adjusting the widths of the pass and stop bands, one can obtain strong modulation and even splitting of the incident beam, if it has a wide angular spectrum.

Radiation from a source embedded into a slab of PhC is one more aspect of angular filtering. Indeed, what may happen when a source, i.e., a dipole or a line source is placed inside the slab? If coupling to the outgoing waves is possible only within a limited range of  $k_x$  values, in line with the necessary condition of angular filtering, radiation from such a slab is allowed only in the directions corresponding to the  $\theta$ -domain pass bands. In particular, off-axis radiation can be obtained, while the total number of the radiated (on- and off-axis) beams (waves) is determined by location of EFCs in  $\mathbf{k}$ -space; compare to Ref. [13].

From this perspective, *multifunctionality* realizable in transmission mode should be understood not only in sense of coexistence of different types of angular filtering in different frequency ranges but also as possible coexistence of angular filtering with other operation regimes in one structure. Due to large regions of nearly perfect transmission in  $(ka, \theta)$ -plane, the studied structures and mechanism of angular filtering therein are particularly appropriate for *spatial-frequency* filtering.

The above mentioned partially remains true regarding reflection mode. In this case, total conversion of the incident-wave energy into the reflected order  $m = -1$  is needed, whatever the used structure is. Clearly, redistribution of the incident-wave energy in favor of one of the higher orders is nothing else than *blazing*, a diffraction grating regime that has been well known for a long time [37–39]. The difference from the conventional blazed gratings is that we require  $r_{-1} = 1$  in a wide range of  $\theta$ -variation. In turn, the known performances of the blazed gratings are expected to be usable at least as narrowband angular filters. However, the  $\theta$ -domain behavior has usually been not considered in the studies of the blazed gratings. Therefore, estimation of the ability of the earlier proposed diffraction gratings to function as efficient angular filters can be complicated without additional studies. It is worth noting that also for reflection mode, nearly perfect efficiency can be kept in a large region in  $(kL, \theta)$ -plane, so that strong selectivity with respect to  $\theta$  is expected to occur also for relatively narrow incident beams, although the boundaries of the bands can be stronger blurred in this case. When a nonsymmetric PhC grating is used in reflection mode, different regimes of diffraction inspired asymmetric transmission may appear in the neighboring frequency ranges [31, 40].

## 23.7 Concluding Remarks

To summarize, the main types of filtering, i.e., low-pass, bandpass, high-pass, and bandstop ones, can be realized in transmission mode in the incidence angle domain with the aid of the relatively simple structures which represent slabs of rod-type

PhCs. Either rod-type PhCs or single-layer rod gratings backed with a reflector can be used for reflection-mode operation. The utilized transmission mechanism combines the effects of dispersion of Floquet–Bloch modes and unusual Fabry–Perot resonances that cannot be obtained in Fabry–Perot etalon. At the same time, matching and mismatching to the host medium, which is the basis of angular filtering by using Fabry–Perot etalon, remains an important part of the resulting filtering mechanism in case of rod-type PhCs. In contrast with Fabry–Perot etalon, PhCs for angular filtering can be made of conventional dielectric materials and, nevertheless, enable better performance of some types of angular filters. Moreover, not all of the main types can be obtained without structuring like that in PhCs, at least if passive isotropic materials are utilized. On the other hand, structuring allows one avoiding the use of anisotropic materials.

What is probably most important is that the slabs of PhC can preserve the same (nearly unity) transmittance in a wide range of variation of the incidence angle, while frequency is fixed. This feature cannot be obtained by using homogeneous slabs of isotropic or anisotropic materials. In fact, (nearly) square shapes of EFCs in the wavevector space are needed to obtain the constant transmittance, whereas localization of Floquet–Bloch modes in this space together with some other properties may enable sharp boundaries of the pass and stop bands in transmission. Multiband (multifrequency) angular filtering, in which all the bands belong to the same type of filtering, can be obtained when several mountains of  $T = 1$  of the same mode are used simultaneously. It is evident that the considered approach is very promising also for spatial-frequency filtering, so its potential should be studied deeper.

All the basic transmission and dispersion features responsible for the observed effects are very general and obtainable in PhCs for a very wide range of parameter variation. Moreover, since no diffractions are needed in transmission mode, one may expect that one-dimensional PhCs can be used at least in cases when requirements to the particular design are not very strict. Thus, various multilayer structures, which were earlier designed to operate as frequency filters, may show strong angular selectivity. However, the problem of constant transmission is not expected to be fully solvable in these structures. In reflection mode, one-dimensional periodic structures are sufficient for obtaining bandpass filtering within a wide range of the incidence angle. A deeper understanding of the physics underlying sharp switching and wide-range preserving of (nearly) unitary reflectance with the aid of a dispersion-free mechanism is desirable, since it can indicate a route to new transmission mode angular filters realizable in thinner structures than the slabs of PhCs, which have been considered here. Estimation of the potential of metasurfaces in transmission-mode angular filtering is a subject of future studies. In particular, metasurfaces controlled with the aid of magnetostatic field are very promising areas of research [41]. To date, it is not clear whether all the main types of angular filtering can be obtained in compact structures that are based on metasurfaces, whereas the potential of PhCs is well investigated. For reflection mode, single-layer gratings suggest compact filter performances, although possible use of metasurfaces might improve them, e.g., by allowing the use of narrower incident beams.

**Acknowledgements** This work was supported by the projects DPT-HAMIT, ESF-EPIGRAT, and NATO-SET-181 as well as by TUBITAK under Project Nos. 107A004, 109A015, 109E301, and 110T306. The contribution of A.E.S. is partially supported by National Science Center of Poland (project MetaSel DEC-2015/17/B/ST3/00118) and by TUBITAK in the framework of the Visiting Researcher Programme. E.O. acknowledges partial support from the Turkish Academy of Sciences. The authors thank Dr. A.O. Cakmak, Dr. E. Colak, Prof. Ph. Lalanne, Dr. A. Petrov, and Dr. P.V. Usik for their contributions to joint studies and fruitful discussions.

## References

1. L. Dettwiller, P. Chavel, Optical spatial frequency filtering using interferences. *J. Opt. Soc. Am. A* **1**, 18–27 (1984)
2. D. Schurig, D.R. Smith, Spatial filtering using media with indefinite permittivity and permeability tensors. *Appl. Phys. Lett.* **82**, 2215–2217 (2003)
3. A. Sentenac, A.-L. Fehrembach, Angular tolerant resonant grating filters under oblique incidence. *J. Opt. Soc. Am. A* **22**, 475–480 (2005)
4. R. Rabaday, I. Avrutsky, Experimental characterization of simultaneous spatial and spectral filtering by an optical resonant filter. *Opt. Lett.* **29**, 605–607 (2004)
5. I. Moreno, J.J. Araiza, M. Avedano-Alejo, Thin film spatial filters. *Opt. Lett.* **30**, 914–916 (2005)
6. O.F. Siddiqui, G. Eleftheriades, Resonant modes in continuous metallic grids over ground and related spatial-filtering applications. *J. Appl. Phys.* **99**, 083102 (2006)
7. V. Purlys, L. Maigyte, D. Gailevicius, M. Peckus, M. Malinauskas, R. Gadonas, K. Staliunas, Spatial filtering by axisymmetric photonic microstructures. *Opt. Lett.* **39**, 929–932 (2014)
8. A.E. Serebryannikov, A.Y. Petrov, E. Ozbay, Toward photonic-crystal based spatial filters with wide-angle ranges of total transmission. *Appl. Phys. Lett.* **94**, 181101 (2009)
9. L. Maigyte, K. Staliunas, Spatial filtering with photonic crystals. *Appl. Phys. Rev.* **2**, 011102 (2015)
10. V. Purlys, L. Maigyte, D. Gailevicius, M. Peckus, M. Malinauskas, K. Staliunas, Spatial filtering by chirped photonic crystals. *Phys. Rev. A* **87**, 033805 (2013)
11. A.E. Serebryannikov, E. Colak, A. Petrov, P.V. Usik, E. Ozbay, Multifrequency spatial filtering: a general property of two-dimensional photonic crystals. *Photon. Nanostruct. Fundam. Appl.* **18**, 1–9 (2016)
12. J.H. Wu, L.K. Ang, A.Q. Liu, H.G. Teo, C. Lu, Tunable high-Q photonic-bandgap Fabry–Perot resonator. *J. Opt. Soc. Am. B* **22**, 1770–1777 (2005)
13. Y.J. Lee, J. Yeo, R. Mittra, W.S. Park, Application of electromagnetic bandgap (EBG) superstrates with controllable defects for a class of patch antennas as spatial angular filters. *IEEE Trans. Antennas Propag.* **53**, 224–235 (2005)
14. R. Pico, I. Perez-Arjona, V.J. Sanchez-Morcillo, K. Staliunas, Evidences of spatial (angular) filtering of sound beams by sonic crystals. *Appl. Acoust.* **74**, 945–948 (2013)
15. E.H. Cho, H.-S. Kim, B.-H. Cheong, O. Prudnikov, W. Xianyua, J.-S. Sohn, D.-J. Ma, H.-J. Choi, N.-C. Park, Y.-P. Park, Two-dimensional photonic crystal color filter development. *Opt. Express* **17**, 8621–8629 (2009)
16. B.-H. Cheong, O.N. Prudnikov, E. Cho, H.-S. Kim, J. Yu, J.-S. Cho, H.-J. Choi, S.T. Shin, High angular tolerant color filter using subwavelength grating. *Appl. Phys. Lett.* **94**, 213104 (2009)
17. E. Colak, A.O. Cakmak, A.E. Serebryannikov, E. Ozbay, Spatial filtering using dielectric photonic crystals at beam-type illumination. *J. Appl. Phys.* **108**, 113106 (2010)
18. M. Born, E. Wolf, *Principles of Optics*, 4th edn. (Pergamon Press, Oxford, 1970)
19. A.E. Serebryannikov, E. Ozbay, P.V. Usik, Defect-mode-like transmission and localization of light in photonic crystals without defects. *Phys. Rev. B* **82**, 165131 (2010)
20. K. Sakoda, *Optical Properties of Photonic Crystals* (Springer, Berlin, 2001)

21. J. Li, T.P. White, L. O'Faolain, A. Gomez-Iglesias, T.F. Krauss, Systematic design of flat band slow light in photonic crystal waveguides. *Opt. Express* **16**, 6227–6232 (2008)
22. A.E. Serebryannikov, A.O. Cakmak, E. Colak, H. Caglayan, H. Kurt, E. Ozbay, Multiple slow waves and relevant transverse transmission and confinement in chirped photonic crystals. *Opt. Express* **22**, 21806–21819 (2014)
23. S. Foteinopoulou, C.M. Soukoulis, Electromagnetic wave propagation in two-dimensional photonic crystals: a study of anomalous refractive effects. *Phys. Rev. B* **72**, 165112 (2005)
24. K. Wiesemann, A short introduction to plasma physics. CERN Yellow Report CERN-2013-007, pp. 85–122 (2013). doi:10.5170/CERN-2013-007.85
25. L.V. Alekseyev, E.E. Narimanov, T. Tumkur, H. Li, Yu.A. Barnakov, M.A. Noginov, Uniaxial epsilon-near-zero metamaterial for angular filtering and polarization control. *Appl. Phys. Lett.* **97**, 131107 (2010)
26. A. Alu, M.G. Silveirinha, A. Salandrino, N. Engheta, Epsilon-near-zero metamaterials and electromagnetic sources: tailoring the radiation phase pattern. *Phys. Rev. B* **75**, 155410 (2007)
27. B.T. Schwartz, R. Piestun, Total external reflection from metamaterials with ultralow refractive index. *J. Opt. Soc. Am. B* **20**, 2448–2453 (2003)
28. N. Kinsley, C. DeVault, J. Kim, M. Ferrera, V.M. Shalae, A. Boltasseva, Epsilon-near-zero Al-doped ZnO for ultrafast switching at telecom wavelengths. *Optica* **2**, 616–622 (2015)
29. D.A. Woods, C.D. Bain, Total internal reflection spectroscopy for studying soft matter. *Soft Matter* **10**, 1071–1096 (2014)
30. C. Rizza, A. Ciattoni, E. Spinazzi, L. Colombo, Terahertz active spatial filtering through optically tunable hyperbolic metamaterials. *Opt. Lett.* **37**, 3345–3347 (2012)
31. A.E. Serebryannikov, One-way diffraction effects in photonic crystal gratings made of isotropic materials. *Phys. Rev. B* **80**, 155117 (2009)
32. C. Luo, S.G. Johnson, J.D. Joannopoulos, J.B. Pendry, All-angle negative refraction without negative effective index. *Phys. Rev. B* **65**, 201104(R) (2002)
33. R. Petit (Ed.), *Electromagnetic Theory of Gratings* (Springer, Berlin, 1980)
34. A.E. Serebryannikov, P. Lalanne, A.Yu. Petrov, E. Ozbay, Wide-angle reflection-mode spatial filtering and splitting with photonic crystal gratings and single-layer rod gratings. *Opt. Lett.* **39**, 6193–6196 (2014)
35. D.R. Smith, N. Kroll, Negative refractive index in left-handed materials. *Phys. Rev. Lett.* **85**, 2933–2936 (2000)
36. H. Kosaka, T. Kawashima, A. Tomita, M. Notomi, T. Tamamura, T. Sato, S. Kawakami, Self-collimating phenomena in photonic crystals. *Appl. Phys. Lett.* **74**, 1212–1214 (1999)
37. M.C. Hutley, *Diffraction Gratings* (Academic Press, London, 1982)
38. Ph. Lalanne, S. Astilean, P. Chavel, E. Cambri, H. Launois, Design and fabrication of blazed binary diffractive elements with sampling periods smaller than the structural cutoff. *J. Opt. Soc. Am. A* **16**, 1143–1156 (1999)
39. C. Sauvan, Ph. Lalanne, L.M.-S. Lee, Broadband blazing with artificial dielectrics. *Opt. Lett.* **29**, 1593–1595 (2004)
40. E. Colak, A.E. Serebryannikov, P.V. Usik, E. Ozbay, Diffraction inspired unidirectional and bidirectional beam splitting in defect-containing photonic structures without interface corrugations. *J. Appl. Phys.* **119**, 193108 (2016)
41. A.E. Serebryannikov, A. Lakhtakia, E. Ozbay, Single and cascaded, magnetically controllable metasurfaces as terahertz filters. *J. Opt. Soc. Am. B* **33**, 834–841 (2016)



**Andriy E. Serebryannikov** received Diploma in Physics and Technology (1990) and Ph.D. degree in Radio Physics (1996) from Kharkiv Polytechnic University and Kharkiv National University (both Kharkiv, Ukraine), respectively. In 2014, he joined Adam Mickiewicz University in Poznan, Poland. He has published 90 journal articles and more than 50 conference papers.

His current research interests include theory and applications of metasurfaces, metamaterials, photonic crystals, surface plasmons, polarization manipulation, and magnonics.



**Ekmel Ozbay** received M.S. and Ph. D. degrees from Stanford University in electrical engineering, in 1989 and 1992. He worked as a postdoctoral research associate in Stanford University and as a scientist in Iowa State University. He joined Bilkent University (Ankara, Turkey) in 1995, where he is currently a full professor in the Department of Electrical and Electronics Engineering.

His research in Bilkent involves nanophotonics, nanometamaterials, nanoelectronics, nanoplasmonics, nanodevices, photonic crystals, GaN/AlGa<sub>N</sub> MOCVD growth, fabrication and characterization of GaN-based devices, and high-speed optoelectronics. He is the 1997 recipient of the Adolph Lomb Medal of Optical Society of America and 2005 European Union Descartes Science award. He worked as an editor for *Scientific Reports*, *Optics Letters*, *Photonics and Nanostructures Fundamental Applications*, and *IEEE Journal of Quantum Electronics*. He has published 390+ articles in SCI journals. His papers have received 11000+ SCI citations with an SCI h-index of 51. He has given 135+ invited talks in international conferences.



# Chapter 24

## Toward the Construction of Parts of the Universe on Tabletops

Tom G. Mackay and Akhlesh Lakhtakia

### 24.1 Introduction

The gravitational field of our puny planet affects the satellites of global positioning systems so much that a clock aboard a satellite advances faster than a clock on the ground by about  $45 \mu\text{s}$  per day, leading to navigational error accumulating at about 13.5 km per day if left uncorrected [1]. Spacetime is curved, gravitational forces from massive objects such as large planets, stars, and black holes affecting photon trajectories even more [2–4].

Experiments on curved spacetime scenarios in space may be impractical by direct methods for a few centuries, if not millennia. Therefore, convenient tabletop analogs of such spacetimes can play a vital role in the study of astrophysical phenomena [5], as is illustrated by the recent observation of Hawking radiation from an analog black hole laser [6], for example.

As a basis for spacetime analogs, the noncovariant equivalence between the electromagnetic properties of vacuum curved spacetime and a certain fictitious medium in flat spacetime may be exploited. This equivalence was established by Igor Tamm in the early twentieth century, and the fictitious medium became known as the Tamm medium. In general, the Tamm medium is bianisotropic,

---

T.G. Mackay (✉)

School of Mathematics and Maxwell Institute for Mathematical Sciences, University of Edinburgh, Edinburgh EH9 3FD, UK

e-mail: [T.Mackay@ed.ac.uk](mailto:T.Mackay@ed.ac.uk)

A. Lakhtakia

NanoMM – Nanoengineered Metamaterials Group, Department of Engineering Science and Mechanics, Pennsylvania State University, University Park, PA 16802, USA

e-mail: [akhlesh@psu.edu](mailto:akhlesh@psu.edu)

Lorentz nonreciprocal, and spatiotemporally nonhomogeneous [7–9]. Under all circumstances, it conforms to the Post constraint [10, 11], and it is nondissipative [12].

The concept of the Tamm medium facilitates the electromagnetic analysis of curved spacetime scenarios, so that a wealth of well-established theoretical techniques from classical electromagnetics may be implemented to shed light upon various astrophysical electromagnetic phenomena. In recent years, the Tamm medium approach has been harnessed to establish that the propagation of electromagnetic plane waves with negative phase velocity [13, 14] is feasible under certain circumstances in the Kerr spacetime [15], Kerr–Newman spacetime [16], de Sitter spacetime [17], and Schwarzschild–de Sitter spacetime [18]. Also, ray-tracing studies for cosmic spinning strings [19, 20] and for Alcubierre spacetime [21, 22] have been facilitated by the Tamm medium approach. And this approach has illuminated aspects of photon propagation in the spacetime of two colliding gravitational waves [23, 24]. However, there are limitations inherent to the noncovariant Tamm medium approach. That is, not all features of vacuous curved spacetime can be projected faithfully onto the flat spacetime of the Tamm medium – certain features may be subject to cartographic distortion [25]. Cartographic distortions can be understood by unrolling the commonplace cylindrical projection (called the Mercator projection) of our planet on a flat surface and comparing it with a map drawn on a sphere.

Via the Tamm medium, opportunities are presented for realizing tabletop analogs whose electromagnetic properties imitate those of certain curved spacetimes. The typically complicated constitutive properties needed to construct such analogs may be attained by building upon recent advances pertaining to electromagnetic metamaterials [26]. Notably, metamaterial analogs have recently been proposed for black holes [27], de Sitter spacetime [28, 29] including Schwarzschild–(anti-)de Sitter spacetime [30], strings [31] including cosmic strings [32], and wormholes [33].

While a metamaterial analog of a curved spacetime may be quite readily conceptualized, its fabrication can present severe challenges in practice. Indeed, practical conceptualizations of metamaterial analogs of curved spacetimes are scarce in the research literature. An exception is the metamaterial analog of a two-dimensional black hole described by Lu et al. [34]. In this case, the analog is a homogenized composite material (HCM) constructed using relatively simple component materials.

Hyperbolic dielectric metamaterials have been exploited to formulate certain reduced versions of the Tamm medium, in which the magnetic and magnetoelectric aspects of the Tamm medium are not accommodated [35]. However, this simplification limits the scope of the equivalent Tamm medium. For example, no black hole-like spacetime with a finite-size horizon relevant to the holographic studies can be realized by this approach [36].

In this chapter, an overview is provided of the Tamm medium approach to conceptualizing tabletop analogs of curved spacetime. The conceptualization of

these analogs as HCMs is described for two particular spacetimes: the spacetimes of Schwarzschild–(anti-)de Sitter [4] and of the collision of two linearly polarized gravitational plane waves [23, 37]. Herein, three vector quantities are denoted by boldface, and 3×3 dyadic quantities by double underlining. The identity 3×3 dyadic is denoted by  $\underline{\underline{I}}$ , and the null 3×3 dyadic by  $\underline{\underline{0}}$ . Roman indexes take the values 1, 2, and 3, while Greek indexes take the values 0, 1, 2, and 3. The scalars  $\varepsilon_0$  and  $\mu_0$  represent the permittivity and permeability of gravity-free vacuum, respectively, and  $c_0 = 1/\sqrt{\varepsilon_0\mu_0}$  is the speed of light in free space that is not affected by a gravitational field. The Cartesian spatial coordinates are  $x$ ,  $y$ , and  $z$ , while  $t$  represents time. Unit vectors in the  $x$ ,  $y$ , and  $z$  directions are denoted by  $\mathbf{e}_1$ ,  $\mathbf{e}_2$ , and  $\mathbf{e}_3$ , respectively. The position vector is denoted by  $\mathbf{r} = x\mathbf{e}_1 + y\mathbf{e}_2 + z\mathbf{e}_3$ . A table of symbols is provided as the appendix to this chapter.

## 24.2 The Tamm Medium

Let us consider an empty (i.e., material-free) spacetime that is affected by a gravitational field. The corresponding spacetime vector  $\mathcal{X}$  contains four spacetime coordinates  $x^0$ ,  $x^1$ ,  $x^2$ , and  $x^3$ . Typically,  $x^0$  is identified with the normalized time coordinate  $c_0t$  and the remaining three components of the spacetime vector with the space coordinates  $x$ ,  $y$ , and  $z$ , but any other convention can be adopted. The effects of the gravitational field are encapsulated by the metric tensor  $\mathcal{G}$  with components  $g_{\alpha\beta}$  which can vary with  $\mathcal{X}$ . The length  $ds$  of an infinitesimally small line element in spacetime is given by

$$ds = + \sqrt{\sum_{\alpha=0}^3 \sum_{\beta=0}^3 g_{\alpha\beta} dx^\alpha dx^\beta}. \tag{24.1}$$

Henceforth, the Einstein summation convention is adopted, which is to say that whenever an expression contains one index as a superscript and the same index as a subscript then summation is implied over all values the index can take. Accordingly, Eq. (24.1) is expressed as

$$ds = + \sqrt{g_{\alpha\beta} dx^\alpha dx^\beta}. \tag{24.2}$$

We choose the convention wherein  $\mathcal{G}$  possesses one positive-valued eigenvalue (associated with  $x^0$ ) and three negative-valued eigenvalues (associated with  $x^1$ ,  $x^2$ , and  $x^3$ ); i.e.,  $\mathcal{G}$  is endowed with the signature  $(+, -, -, -)$ . Thus, for spacetime not affected by a gravitational field,  $\mathcal{G}$  has the matrix representation  $\text{diag}(c_0^2, -1, -1, -1)$ . [3].

In the absence of free charges or currents, the electromagnetic fields obey the covariant Maxwell equations [8]

$$\left. \begin{aligned} f_{\alpha\beta;\nu} + f_{\beta\nu;\alpha} + f_{\nu\alpha;\beta} &= 0 \\ h^{\alpha\beta}{}_{;\beta} &= 0 \end{aligned} \right\}, \quad (24.3)$$

in Gaussian units. Herein  $f_{\alpha\beta}$  and  $h^{\alpha\beta}$ , respectively, are components of the covariant and the contravariant electromagnetic field tensors, whereas the subscript  ${}_{;\nu}$  denotes the covariant derivative with respect to the  $\nu$ th spacetime coordinate.

### 24.2.1 Noncovariant Electrodynamics for Vacuum

Following the approach of Tamm [8], it is convenient to express Eq. (24.3) in noncovariant form as

$$\left. \begin{aligned} f_{\alpha\beta,\nu} + f_{\beta\nu,\alpha} + f_{\nu\alpha,\beta} &= 0 \\ [(-g)^{1/2} h^{\alpha\beta}]_{,\beta} &= 0 \end{aligned} \right\}, \quad (24.4)$$

with the scalar  $g = \det[\mathcal{G}]$  and the subscript  ${}_{,\nu}$  denoting ordinary differentiation with respect to the  $\nu$ th spacetime coordinate. Parenthetically, the generalization of the Maxwell equations from the noncovariant formulation (24.4) to the covariant formulation (24.3) is not entirely free from ambiguity [2, 38], but the standard generalization (24.3) is commonly adopted in the absence of experimental evidence to eliminate this ambiguity.

The components  $E_\ell$ ,  $B_\ell$ ,  $D_\ell$ , and  $H_\ell$  of the electromagnetic field vectors are given by

$$\left. \begin{aligned} E_\ell &= f_{\ell 0} \\ B_\ell &= (1/2)\varepsilon_{\ell mn} f_{mn} \\ D_\ell &= (-g)^{1/2} h^{\ell 0} \\ H_\ell &= (1/2)\varepsilon_{\ell mn} (-g)^{1/2} h^{mn} \end{aligned} \right\}, \quad (24.5)$$

where  $\varepsilon_{\ell mn} = \mathbf{e}_\ell \cdot (\mathbf{e}_m \times \mathbf{e}_n)$  is the three-dimensional Levi-Civita symbol. Thus, the noncovariant Maxwell equations (24.4) may be re-expressed in the more usual form

$$\left. \begin{aligned} B_{\ell,\ell} &= 0 \\ B_{\ell,0} &= -\varepsilon_{\ell mn} E_{m,n} \\ D_{\ell,\ell} &= 0 \\ D_{\ell,0} &= \varepsilon_{\ell mn} H_{m,n} \end{aligned} \right\}. \quad (24.6)$$

The components of the electromagnetic field tensors are related via the constitutive relations

$$\left. \begin{aligned} h^{\alpha\beta} &= g^{\alpha\mu} g^{\beta\nu} f_{\mu\nu} \\ f_{\alpha\beta} &= g_{\alpha\mu} g_{\beta\nu} h^{\mu\nu} \end{aligned} \right\}, \tag{24.7}$$

in the case of vacuum. Equivalently, these constitutive relations may be expressed in terms of the components of the electromagnetic field vectors as

$$\left. \begin{aligned} D_\ell &= \gamma_{\ell m} E_m + \varepsilon_{\ell mn} \Gamma_m H_n \\ B_\ell &= \gamma_{\ell m} H_m - \varepsilon_{\ell mn} \Gamma_m E_n \end{aligned} \right\}, \tag{24.8}$$

with

$$\left. \begin{aligned} \gamma_{\ell m} &= -(-g)^{1/2} \frac{g^{\ell m}}{g_{00}} \\ \Gamma_m &= \frac{g_{0m}}{g_{00}} \end{aligned} \right\}. \tag{24.9}$$

Let us emphasize the following distinction between Eqs. (24.3) and (24.7) on the one hand and Eqs. (24.6) and (24.8) on the other. Equations (24.3) and (24.7) employ curved spacetime. The same curved spacetime is employed in Eqs. (24.6) and (24.8), but these have the appearance of the familiar electromagnetic equations in flat spacetime applied to an instantaneously reacting, spatiotemporally nonhomogeneous, bianisotropic medium – namely, the Tamm medium. A host of techniques, widely employed to tackle electromagnetic problems in the absence of gravitational fields, may therefore be usefully employed in solving Eqs. (24.6) and (24.8).

Lastly in this subsection, it is convenient to recast Eqs. (24.6) and (24.8) using standard three vectors and 3×3 dyadics as

$$\left. \begin{aligned} \nabla \cdot \mathbf{B}(c_0t, \mathbf{r}) &= 0 \\ \nabla \times \mathbf{E}(c_0t, \mathbf{r}) + \frac{\partial}{\partial t} \mathbf{B}(c_0t, \mathbf{r}) &= \mathbf{0} \\ \nabla \cdot \mathbf{D}(c_0t, \mathbf{r}) &= 0 \\ \nabla \times \mathbf{H}(c_0t, \mathbf{r}) - \frac{\partial}{\partial t} \mathbf{D}(c_0t, \mathbf{r}) &= \mathbf{0} \end{aligned} \right\} \tag{24.10}$$

and

$$\left. \begin{aligned} \mathbf{D}(c_0t, \mathbf{r}) &= \varepsilon_0 \underline{\underline{\gamma}}(c_0t, \mathbf{r}) \cdot \mathbf{E}(c_0t, \mathbf{r}) - \frac{1}{c_0} \underline{\underline{\Gamma}}(c_0t, \mathbf{r}) \times \mathbf{H}(c_0t, \mathbf{r}) \\ \mathbf{B}(c_0t, \mathbf{r}) &= \mu_0 \underline{\underline{\gamma}}(c_0t, \mathbf{r}) \cdot \mathbf{H}(c_0t, \mathbf{r}) + \frac{1}{c_0} \underline{\underline{\Gamma}}(c_0t, \mathbf{r}) \times \mathbf{E}(c_0t, \mathbf{r}) \end{aligned} \right\}. \tag{24.11}$$

Herein, SI units are adopted, with  $\underline{\gamma}(c_0t, \mathbf{r})$  being the dyadic equivalent of  $\gamma_{\ell m}$  and  $\underline{\Gamma}(c_0t, \mathbf{r})$  being the vector equivalent of  $\Gamma_m$ . Let us now proceed to the Tamm mediums for two particular curved spacetime scenarios.

### 24.2.2 Schwarzschild–(anti-)de Sitter Spacetime

Static Schwarzschild–(anti-)de Sitter spacetime is conventionally characterized in terms of spherical coordinates by [39–41]

$$d\tilde{s}^2 = (1 - \tilde{F}) d\tilde{t}^2 - \frac{1}{1 - \tilde{F}} d\tilde{r}^2 - \tilde{r}^2(d\tilde{\theta}^2 + \sin^2 \tilde{\theta} d\tilde{\phi}^2). \tag{24.12}$$

Herein the function

$$\tilde{F} = \frac{2GM}{c_0^2 \tilde{r}} + \frac{\Lambda \tilde{r}^2}{3c_0^2}, \tag{24.13}$$

where  $M \geq 0$  is the mass of the corresponding Schwarzschild black hole,  $G$  is the gravitational constant, and  $\Lambda$  is the cosmological constant. Several spacetimes of interest are encompassed within Schwarzschild–(anti-)de Sitter spacetime: Let us note that  $\Lambda > 0$  for Schwarzschild–de Sitter spacetime,  $\Lambda < 0$  for Schwarzschild–anti-de Sitter spacetime [42], and  $\Lambda = 0$  for Schwarzschild spacetime. Furthermore,  $M = 0$  and  $\Lambda > 0$  for de Sitter spacetime, whereas  $M = 0$  and  $\Lambda < 0$  for anti-de Sitter spacetime. Equation (24.12) gives rise to the metric tensor  $\tilde{\mathcal{G}}$  written in matrix form as

$$[\tilde{\mathcal{G}}] = \begin{pmatrix} \frac{1}{\gamma} & 0 & 0 & 0 \\ 0 & -1 - \frac{\gamma \tilde{F} \tilde{x}^2}{\tilde{r}^2} & -\frac{\gamma \tilde{F} \tilde{x} \tilde{y}}{\tilde{r}^2} & -\frac{\gamma \tilde{F} \tilde{x} \tilde{z}}{\tilde{r}^2} \\ 0 & -\frac{\gamma \tilde{F} \tilde{x} \tilde{y}}{\tilde{r}^2} & -1 - \frac{\gamma \tilde{F} \tilde{y}^2}{\tilde{r}^2} & -\frac{\gamma \tilde{F} \tilde{y} \tilde{z}}{\tilde{r}^2} \\ 0 & -\frac{\gamma \tilde{F} \tilde{x} \tilde{z}}{\tilde{r}^2} & -\frac{\gamma \tilde{F} \tilde{y} \tilde{z}}{\tilde{r}^2} & -1 - \frac{\gamma \tilde{F} \tilde{z}^2}{\tilde{r}^2} \end{pmatrix}, \tag{24.14}$$

expressed in Cartesian coordinates  $\tilde{x} = \tilde{r} \sin \tilde{\theta} \cos \tilde{\phi}$ ,  $\tilde{y} = \tilde{r} \sin \tilde{\theta} \sin \tilde{\phi}$ , and  $\tilde{z} = \tilde{r} \cos \tilde{\theta}$ , with the scalar

$$\gamma = (1 - \tilde{F})^{-1}. \tag{24.15}$$

In considering the Tamm medium and its possible realization as an HCM, it is preferable to deal with a diagonal metric. This is achieved by implementing the spatial coordinate transformation

$$(t \ x \ y \ z)^T = \mathcal{N} \cdot (\tilde{t} \ \tilde{x} \ \tilde{y} \ \tilde{z})^T, \quad (24.16)$$

given by the change-of-basis matrix

$$\mathcal{N} = \begin{pmatrix} 1 & 0 & 0 & 0 \\ 0 & \frac{\tilde{x}}{\tilde{r}} & -\frac{\tilde{z}}{\sqrt{\tilde{x}^2 + \tilde{z}^2}} & -\frac{\tilde{x}\tilde{y}}{\tilde{r}\sqrt{\tilde{x}^2 + \tilde{z}^2}} \\ 0 & \frac{\tilde{y}}{\tilde{r}} & 0 & \frac{\sqrt{\tilde{x}^2 + \tilde{z}^2}}{\tilde{r}} \\ 0 & \frac{\tilde{z}}{\tilde{r}} & \frac{\tilde{x}}{\sqrt{\tilde{x}^2 + \tilde{z}^2}} & -\frac{\tilde{y}\tilde{z}}{\tilde{r}\sqrt{\tilde{x}^2 + \tilde{z}^2}} \end{pmatrix}. \quad (24.17)$$

Notice that  $\tilde{r} = \sqrt{\tilde{x}^2 + \tilde{y}^2 + \tilde{z}^2} \equiv \sqrt{x^2 + y^2 + z^2} = r$ , because  $\mathcal{N}$  is an orthogonal matrix. Expressed in terms of the coordinate system introduced via Eq. (24.16), the metric has the diagonal representation

$$\mathcal{G} \equiv \mathcal{N}^T \cdot \tilde{\mathcal{G}} \cdot \mathcal{N} = \text{diag}(\gamma^{-1}, -\gamma, -1, -1). \quad (24.18)$$

The Tamm medium that represents the metric tensor  $\mathcal{G}$  in Eq. (24.18) is characterized by the constitutive relations (24.11) with

$$\left. \begin{aligned} \underline{\underline{\gamma}}(c_0 t, \mathbf{r}) &= \text{diag}(1, \gamma, \gamma) \\ \underline{\underline{\Gamma}}(c_0 t, \mathbf{r}) &= \mathbf{0} \end{aligned} \right\}; \quad (24.19)$$

that is, the Tamm medium is a uniaxial dielectric-magnetic medium with identical relative permittivity and relative permeability dyadics [12].

The spatial nonhomogeneity of the Tamm medium is endowed via the scalar  $\gamma$  per Eq. (24.15). This spatial dependency of  $\gamma$  is an important aspect when contemplating the realization of the Tamm medium as an HCM. In Fig. 24.1, graphs of  $\gamma$  against  $r$  are presented for Schwarzschild spacetime, de Sitter spacetime, and anti-de Sitter spacetime using the illustrative values  $M \in \{0, 1.4\}$  and  $\Lambda \in \{0, \pm 1.4\}$ . The normalization  $\{c_0 = 1, G = 1\}$  is implemented. In the case of Schwarzschild spacetime,  $\gamma$  exhibits a singularity at  $r = 2GM/c_0^2$  as  $r$  varies, that singularity representing an event horizon. In the case of de Sitter spacetime,  $\gamma$  exhibits a singularity at  $r = c_0 \sqrt{3/\Lambda}$  as  $r$  varies, that singularity representing a cosmological horizon. There is no corresponding horizon for anti-de Sitter spacetime. We observe that  $\gamma > 0$  outside the event horizon for Schwarzschild spacetime, inside the cosmological horizon for de Sitter spacetime, and everywhere for anti-de Sitter spacetime.

**Fig. 24.1** The constitutive parameter  $\gamma$  of Eq. (24.15) graphed against  $r$  for Schwarzschild (*solid*) spacetime with  $M = 1.4$  (and  $\Lambda = 0$ ) and de Sitter (*dashed*) and anti-de Sitter (*broken dashed*) spacetimes with  $\Lambda = \pm 1.4$ , respectively (and  $M = 0$ ), with the normalization  $\{c_0 = 1, G = 1\}$

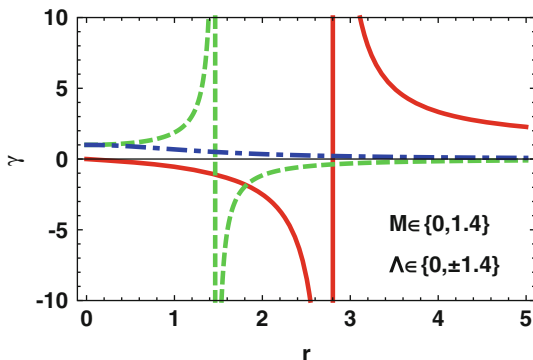
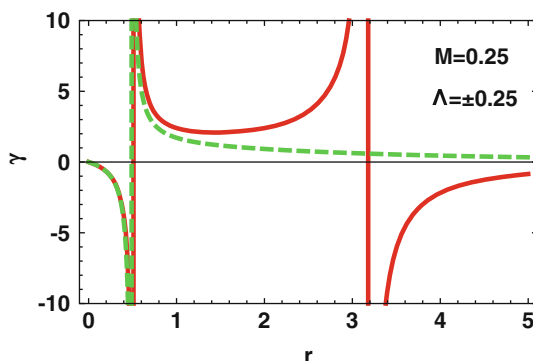


**Fig. 24.2** The constitutive parameter  $\gamma$  graphed of Eq. (24.15) against  $r$  for Schwarzschild–de Sitter (*solid*) and Schwarzschild–anti-de Sitter (*dashed*) spacetimes, when  $M = 0.25$  and  $\Lambda = \pm 0.25$ , with the normalization  $\{c_0 = 1, G = 1\}$



As illustrated in Fig. 24.2, the picture is rather more complicated in the case of Schwarzschild–(anti-)de Sitter spacetime. Therein  $\gamma$  is graphed against  $r$  for Schwarzschild–de Sitter spacetime and Schwarzschild–anti-de Sitter spacetime for the illustrative values  $M = 0.25$  and  $\Lambda = \pm 0.25$ , with the normalization  $c_0 = G = 1$ . In the case of Schwarzschild–de Sitter spacetime,  $\gamma$  exhibits two singularities as  $r$  varies, whereas  $\gamma$  exhibits only one singularity as  $r$  varies in the case of Schwarzschild–anti-de Sitter spacetime. Also,  $\gamma > 0$  for the range of  $r$  values between the two singularities for Schwarzschild–de Sitter spacetime and for  $r$  values outside the singularity for Schwarzschild–anti-de Sitter spacetime.

The issue of whether  $\gamma > 0$  and  $\gamma < 0$  is important when one considers the phenomenon of electromagnetic plane wave propagation with negative phase velocity. It transpires that negative phase velocity is possible when  $\gamma < 0$  but not when  $\gamma > 0$  [43, 44]. The homogenization procedure outlined in Sect. 24.3 in which the Tamm medium is conceptualized as an HCM is appropriate only for  $\gamma > 0$ .



### 24.2.3 Collision of Two Linearly Polarized Gravitational Plane Waves

Next we turn to the collision of two oppositely directed gravitational plane waves. This is describable as an exact solution of the Einstein field equations [37, 42, 45–47]. In the aftermath of the collision, focusing effects result in either a nonsingular Killing-Cauchy horizon or a spacetime singularity. Before the emergence of the nonsingular Killing-Cauchy horizon or the spacetime singularity, spacetime may be partitioned into the following four regions: Region I wherein the two plane waves interact, Regions II and III each of which correspond to a single plane wave prior to interacting, and Region IV which represents the initial state of flat spacetime prior to the passage of the two plane waves [37].

Let us consider Region I for two linearly polarized gravitational plane waves, propagating in opposite directions along the  $z$  axis. This region of spacetime has the bounds

$$\left. \begin{aligned} -t \leq z \leq t \\ 0 \leq t \leq \frac{\pi}{2} \end{aligned} \right\}. \quad (24.20)$$

The plane waves collide at  $t = 0$ , leading to the creation of either a nonsingular Killing-Cauchy horizon or a spacetime singularity at  $t = \pi/2$ . Accordingly [45–47],

$$ds^2 = F_{\pm}^2(t) (dt^2 - dz^2) + \frac{F_{-}(t)}{F_{+}(t)} dx^2 + \cos^2(z) F_{\pm}^2(t) dy^2, \quad (24.21)$$

with the scalar function

$$F_{\pm}(t) = 1 \pm \sigma \sin(t). \quad (24.22)$$

The scalar  $\sigma = \pm 1$ . The case of a nonsingular Killing-Cauchy horizon solution at  $t = \pi/2$  corresponds to  $\sigma = +1$ , while the case of a spacetime singularity solution at  $t = \pi/2$  corresponds to  $\sigma = -1$ . We take  $\sigma = +1$  henceforth, on the understanding that the HCM conceptualization of the Tamm medium for  $\sigma = -1$  proceeds in the same way as for  $\sigma = +1$  but the constitutive parameter regimes for  $\sigma = -1$  would be more demanding to implement in practice than those for  $\sigma = +1$ .

The Tamm medium that emerges from Eq. (24.21) is characterized by the constitutive relations (24.11) with [23]

$$\left. \begin{aligned} \underline{\underline{\gamma}}(c_0t, \mathbf{r}) &= \text{diag}(\gamma^x, \gamma^y, \gamma^z) \\ \underline{\underline{\Gamma}}(c_0t, \mathbf{r}) &= \mathbf{0} \end{aligned} \right\}; \quad (24.23)$$

that is, the Tamm medium is an orthorhombic dielectric-magnetic medium [12], with identical relative permittivity and relative permeability dyadics, whose constitutive parameters

$$\left. \begin{aligned} \gamma^x &= \cos(z) \sqrt{\frac{F_+^3(t)}{F_-(t)}} \\ \gamma^y &= \frac{1}{\cos(z)} \sqrt{\frac{F_-(t)}{F_+^3(t)}} \\ \gamma^z &= \cos(z) \sqrt{\frac{F_-(t)}{F_+^3(t)}} \end{aligned} \right\} \quad (24.24)$$

are functions of  $z$  and  $t$ .

When contemplating the realization of the Tamm medium as an HCM, the spatiotemporal dependency of  $\gamma^{x,y,z}$  is an important aspect. These constitutive parameters are graphed against  $z \in (-t, t)$  for  $t = 25\pi/180$  (dashed curves),  $50\pi/180$  (solid curves), and  $75\pi/180$  (broken dashed curves) in Fig. 24.3. The region in the vicinity of the nonsingular Killing-Cauchy horizon solution at  $t = \pi/2$  is omitted from Fig. 24.3 (and later also from Fig. 24.4), as the values of the constitutive parameters are too extreme for this region. Figure 24.3 shows that

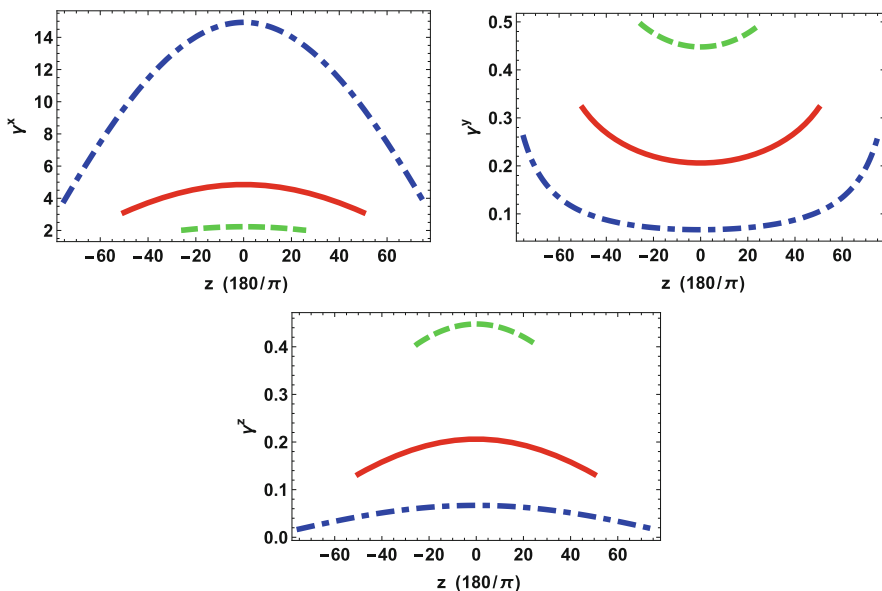


**Fig. 24.3** The constitutive parameters  $\gamma^x$ ,  $\gamma^y$ , and  $\gamma^z$  of Eq. (24.24) graphed against  $z \in (-t, t)$  for  $t = 25\pi/180$  (dashed curves),  $50\pi/180$  (solid curves), and  $75\pi/180$  (broken dashed curves)

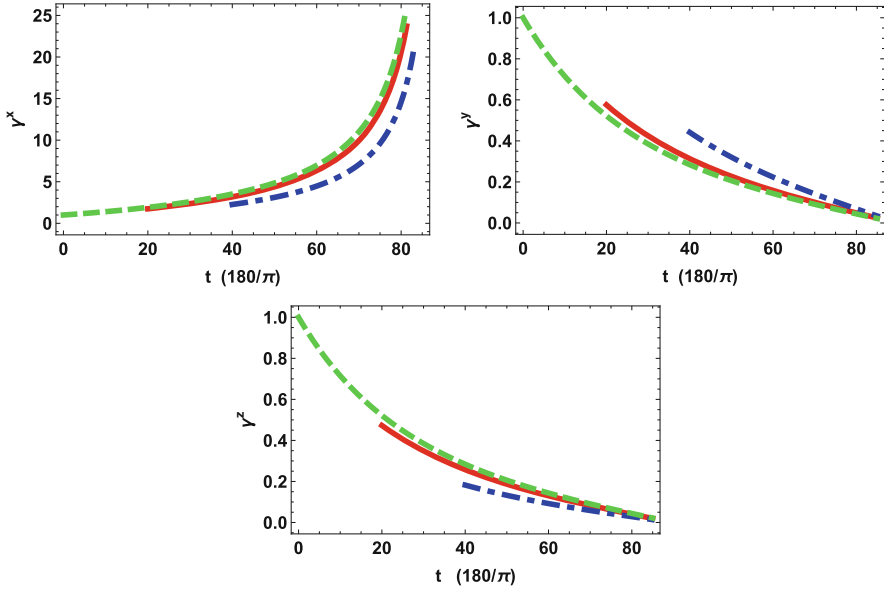


**Fig. 24.4** The constitutive parameters  $\gamma^x$ ,  $\gamma^y$ , and  $\gamma^z$  of Eq.(24.24) graphed against  $t \in (z, 85\pi/180)$  for  $z = 0$  (dashed curves),  $25\pi/180$  (solid curves), and  $50\pi/180$  (broken dashed curves)

$\gamma^x > 1$ ,  $\gamma^y < 1$ ,  $\gamma^z < 1$  for  $t > 0$ , and the constitutive parameters increasingly deviate from unity as  $t$  increases from zero. In the plane  $z = 0$ ,  $\gamma^y = \gamma^z$ , and accordingly the Tamm medium is a uniaxial dielectric-magnetic medium.

A different aspect of the spatiotemporal dependency of  $\gamma^{x,y,z}$  is illustrated in Fig. 24.4, wherein the constitutive parameters are graphed against  $t \in (z, 85\pi/180)$  for  $z = 0$  (dashed curves),  $25\pi/180$  (solid curves), and  $50\pi/180$  (broken dashed curves). For all values of  $z$  considered,  $\gamma^x$  becomes unbounded, whereas both  $\gamma^y$  and  $\gamma^z$  become null valued, in the limit  $t \rightarrow (\pi/2)$ .

### 24.2.4 Piecewise Uniform Approximation

Consider the process of solving Eqs. (24.6) and (24.8) for a particular region  $\mathcal{R}$  characterized by spacetime vector  $\mathcal{X}$ , subject to certain boundary conditions. This may be achieved by partitioning  $\mathcal{R}$  into subregions  ${}^{(p)}\mathcal{R}$ , ( $p = 1, 2, 3, \dots$ ). The positive integer  $p$  is chosen to be sufficiently large that within each subregion the nonuniform metric tensor  $\mathcal{G}$  can be replaced by the uniform metric tensor  ${}^{(p)}\mathcal{G}$  [48]. Accordingly, the nonhomogeneous vector  $\mathbf{\Gamma}(c_0t, \mathbf{r})$  and nonhomogeneous dyadic  $\underline{\underline{\gamma}}(c_0t, \mathbf{r})$  which specify the Tamm medium can be replaced by the uniform vector

${}^{(p)}\Gamma$  and dyadic  ${}^{(p)}\underline{\underline{\gamma}}$  in each subregion  ${}^{(p)}\mathcal{R}$ . Once Eqs. (24.6) and (24.8) have been solved for each subregion, the subregional solutions could be stitched together to form the solution for  $\mathcal{R}$ . Such a piecewise uniform approximation is commonly encountered in solving differential equations with nonhomogeneous coefficients [49]. In Sect. 24.3, the conceptualization of Tamm mediums as HCMs is considered for local subregions of spacetime – each individual subregion is characterized by a uniform metric, but when combined these represent global spacetime characterized by a nonuniform metric.

## 24.3 Homogenized Composite Mediums

The Tamm mediums presented in Sects. 24.2.2 and 24.2.3 may be conceptualized as HCMs, made from relatively simple particulate component materials. The conceptualization is based on the Bruggeman homogenization formalism, which is implemented in its inverse sense to provide estimates of constitutive parameters, particle-shape parameters, and volume fractions for the component materials. There are several possible component material formulations which could give rise to the Tamm mediums under consideration. In the following subsections, we focus on particularly simple ones for the purposes of illustration.

### 24.3.1 Bruggeman Homogenization Formalism

Suppose that a composite material comprising  $n$  different component materials, labeled  $1, 2, \dots, n$ , is to be homogenized. Each component material is an isotropic dielectric-magnetic material. The relative permittivities of the  $n$  component materials are denoted as  $\varepsilon_1, \varepsilon_2, \dots, \varepsilon_n$ ; and the relative permeabilities of the  $n$  component materials are  $\mu_1, \mu_2, \dots, \mu_n$ . These  $n$  component materials are randomly distributed, with respective volume fractions  $f_1 \in (0, 1), f_2 \in (0, 1), \dots, f_n \in (0, 1)$  such that  $f_n = 1 - f_1 - f_2 - \dots - f_{n-1}$ . Each component material is distributed in the form of ellipsoidal particles which – in keeping with the fundamental principle of homogenization – are small compared to all electromagnetic wavelengths under consideration. The ellipsoids for each component material are assumed to be identically oriented. Furthermore, the rotational axes of these ellipsoids for all component materials are taken to be aligned with the eigenvectors of  $\underline{\underline{\gamma}}$ . Thus, the surface of each ellipsoid of component material  $\ell$ , relative to its center, is  $\underline{\underline{\gamma}}$  prescribed by the vector

$$\mathbf{r}_s = \rho_\ell \underline{\underline{U}}_\ell \cdot \hat{\mathbf{r}}, \quad (24.25)$$

where the positive definite shape dyadic is

$$\underline{\underline{U}}_\ell = \text{diag} (U_\ell^x, U_\ell^y, U_\ell^z), \quad (\ell = 1, 2, \dots, n), \quad (24.26)$$

the radial unit vector is  $\hat{\mathbf{r}} = (\sin \theta \cos \phi, \sin \theta \sin \phi, \cos \theta)$  in terms of spherical angular coordinates  $\theta$  and  $\phi$ , and  $\rho_\ell$  is a linear measure of size.

As a consequence of the ellipsoidal shape of the particles, the HCM is generally an orthorhombic dielectric-magnetic material, whose relative permittivity dyadic  $\underline{\underline{\varepsilon}}_{Br} = \text{diag} (\varepsilon_{Br}^x, \varepsilon_{Br}^y, \varepsilon_{Br}^z)$  and relative permeability dyadic  $\underline{\underline{\mu}}_{Br} = \text{diag} (\mu_{Br}^x, \mu_{Br}^y, \mu_{Br}^z)$  may be estimated using the Bruggeman formalism as follows.

The formalism utilizes the polarizability density dyadics

$$\left. \begin{aligned} \underline{\underline{a}}_\ell^\varepsilon &= \left( \varepsilon_\ell \underline{\underline{I}} - \underline{\underline{\varepsilon}}_{Br} \right) \cdot \left[ \underline{\underline{I}} + \underline{\underline{D}}_\ell^\varepsilon \cdot \left( \varepsilon_\ell \underline{\underline{I}} - \underline{\underline{\varepsilon}}_{Br} \right) \right]^{-1} \\ \underline{\underline{a}}_\ell^\mu &= \left( \mu_\ell \underline{\underline{I}} - \underline{\underline{\mu}}_{Br} \right) \cdot \left[ \underline{\underline{I}} + \underline{\underline{D}}_\ell^\mu \cdot \left( \mu_\ell \underline{\underline{I}} - \underline{\underline{\mu}}_{Br} \right) \right]^{-1} \end{aligned} \right\}, \quad (\ell = 1, 2, \dots, n). \quad (24.27)$$

The depolarization dyadics  $\underline{\underline{D}}_\ell^{\varepsilon, \mu}$  herein are given by the double integrals [50, 51]

$$\left. \begin{aligned} \underline{\underline{D}}_\ell^\varepsilon &= \frac{1}{4\pi} \int_\phi^{2\pi} d\phi \int_\theta^\pi d\theta \sin \theta \frac{\left( \underline{\underline{U}}_\ell^{-1} \cdot \hat{\mathbf{r}} \right) \left( \underline{\underline{U}}_\ell^{-1} \cdot \hat{\mathbf{r}} \right)}{\left( \underline{\underline{U}}_\ell^{-1} \cdot \hat{\mathbf{r}} \right) \cdot \underline{\underline{\varepsilon}}_{Br} \cdot \left( \underline{\underline{U}}_\ell^{-1} \cdot \hat{\mathbf{r}} \right)} \\ \underline{\underline{D}}_\ell^\mu &= \frac{1}{4\pi} \int_\phi^{2\pi} d\phi \int_\theta^\pi d\theta \sin \theta \frac{\left( \underline{\underline{U}}_\ell^{-1} \cdot \hat{\mathbf{r}} \right) \left( \underline{\underline{U}}_\ell^{-1} \cdot \hat{\mathbf{r}} \right)}{\left( \underline{\underline{U}}_\ell^{-1} \cdot \hat{\mathbf{r}} \right) \cdot \underline{\underline{\mu}}_{Br} \cdot \left( \underline{\underline{U}}_\ell^{-1} \cdot \hat{\mathbf{r}} \right)} \end{aligned} \right\}, \quad (\ell = 1, 2, \dots, n), \quad (24.28)$$

which are expressible in terms of incomplete elliptic integrals [52]. The constitutive parameters of the HCM are related to those of the component materials, as well as the shape parameters and volume fractions of the component materials, by the dyadic equations [12, 53]

$$\left. \begin{aligned} \underline{\underline{A}}^\varepsilon &= \underline{\underline{0}} \\ \underline{\underline{A}}^\mu &= \underline{\underline{0}} \end{aligned} \right\}, \quad (24.29)$$

with

$$\left. \begin{aligned} \underline{\underline{A}}^\varepsilon &= \sum_{\ell=1}^n f_\ell \underline{\underline{a}}_\ell^\varepsilon \\ \underline{\underline{A}}^\mu &= \sum_{\ell=1}^n f_\ell \underline{\underline{a}}_\ell^\mu \end{aligned} \right\}. \quad (24.30)$$

### 24.3.2 Inverse Bruggeman Formalism

Usually, homogenization formalisms are implemented in the forward sense, to estimate the constitutive parameters of an HCM based on knowledge of the constitutive parameters, particle-shape parameters, and volume fractions of the component materials. But, our ambition here is to estimate  $\varepsilon_\ell$ ,  $\mu_\ell$ ,  $U_\ell^x$ ,  $U_\ell^y$ ,  $U_\ell^z$ , and  $f_\ell$  for all  $\ell \in \{1, 2, \dots, n\}$  such that the corresponding HCM coincides with the Tamm medium under consideration. Therefore, we implement the Bruggeman formalism in its inverse sense. Formal expressions of the inverse Bruggeman formalism have been established [54]. However, these formal expressions may be ill-defined [55]. Experience has shown it to be more efficacious to adopt direct numerical methods in implementing the inverse formalism [56]. Parenthetically, certain constitutive parameter regimes are not appropriate for the inverse Bruggeman homogenization formalism [57], but these regimes are quite distinct from those considered in the remainder of this chapter.

Let us now choose the Tamm medium for Schwarzschild–(anti-)de Sitter space-time, as specified in Sect. 24.2.2, on the understanding that the implementation of the inverse Bruggeman formalism for other spacetimes proceeds in a similar vein. Since the constitutive dyadic  $\underline{\underline{\gamma}}$  in Eq. (24.19)<sub>1</sub> is of the uniaxial type, the particles of all component materials are taken to have spheroidal shapes. And we consider the case of four different component materials (i.e.,  $n = 4$ ). Thus, we take  $U_\ell^x = 1$  and  $U_\ell^y = U_\ell^z \equiv U$ , say, for  $\ell \in \{1, 2, 3, 4\}$ , with  $U_\ell > 1$  representing prolate spheroids,  $U_\ell < 1$  representing oblate spheroids, and  $U_\ell = 1$  representing the degenerate spherical case. To further simplify matters, component materials 1 and 2 are assumed to be isotropic dielectric materials, i.e.,  $\mu_1 = \mu_2 = 1$ , and component materials 3 and 4 are assumed to be isotropic magnetic materials, i.e.,  $\varepsilon_3 = \varepsilon_4 = 1$ . Accordingly,  $\varepsilon_{Br}^y = \varepsilon_{Br}^z \equiv \varepsilon_{Br}$  and  $\mu_{Br}^y = \mu_{Br}^z \equiv \mu_{Br}$ , say. Hence, the diagonal dyadics  $\underline{\underline{A}}^m$  introduced in Eq. (24.30) have the form  $\text{diag}(A_x^m, A^m, A^m)$ ,  $m \in \{\varepsilon, \mu\}$ , and the dyadic equations (24.29) represent only four independent scalar equations, which are coupled through the constitutive parameters of the HCM.

A variety of scenarios may be envisioned that could give rise to the sought-after Tamm medium by implementing the inverse Bruggeman formalism. For example:

- (i) Assume that the relative permittivities  $\varepsilon_1$  and  $\varepsilon_2$  as well as the relative permeabilities  $\mu_3$  and  $\mu_4$  are given and that  $U_1 = U_2 = U_3 = U_4 = U$ , and then determine the common shape parameter  $U$  and the volume fractions  $f_1, f_2$ , and  $f_3$ .
- (ii) Assume that the relative permittivities  $\varepsilon_1$  and  $\varepsilon_2$  as well as the relative permeabilities  $\mu_3$  and  $\mu_4$  are given. Assume further that the volume fractions  $f_1, f_2$ , and  $f_3$  are given, and then determine the shape parameters  $U_1, U_2, U_3$ , and  $U_4$ .
- (iii) Assume that the shape parameters  $U_1, U_2, U_3$ , and  $U_4$  as well as the volume fractions  $f_1, f_2$ , and  $f_3$  are given, and then determine the relative permittivities  $\varepsilon_1$  and  $\varepsilon_2$  as well as the relative permeabilities  $\mu_3$  and  $\mu_4$ .

In each of the scenarios (i)–(iii), four scalar parameters need to be determined. As a representative example, let us focus on the numerical implementation of scenario (i), the numerical implementations for scenarios (ii) and (iii) following in a similar vein.

The volume fractions  $f_1$ ,  $f_2$ , and  $f_3$  and the common shape factor  $U$  may be extracted from Eq. (24.29) via a modified Newton–Raphson technique [58, 59], as follows. The solutions at step  $k + 1$ , i.e.,  $\{U^{(k+1)}, f_1^{(k+1)}, f_2^{(k+1)}, f_3^{(k+1)}\}$ , are computed from those at step  $k$ , i.e.,  $\{U^{(k)}, f_1^{(k)}, f_2^{(k)}, f_3^{(k)}\}$ , by means of the recursive scheme

$$\left. \begin{aligned} U^{(k+1)} &= U^{(k)} - \frac{A_x^\varepsilon(U^{(k)}, f_1^{(k)}, f_2^{(k)}, f_3^{(k)})}{\frac{\partial}{\partial U} A_x^\varepsilon(U^{(k)}, f_1^{(k)}, f_2^{(k)}, f_3^{(k)})} \\ f_1^{(k+1)} &= f_2^{(k)} - \frac{A_x^\varepsilon(U^{(k+1)}, f_1^{(k)}, f_2^{(k)}, f_3^{(k)})}{\frac{\partial}{\partial f_1} A_x^\varepsilon(U^{(k+1)}, f_1^{(k)}, f_2^{(k)}, f_3^{(k)})} \\ f_2^{(k+1)} &= f_2^{(k)} - \frac{A_x^\mu(U^{(k+1)}, f_1^{(k+1)}, f_2^{(k)}, f_3^{(k)})}{\frac{\partial}{\partial f_2} A_x^\mu(U^{(k+1)}, f_1^{(k+1)}, f_2^{(k)}, f_3^{(k)})} \\ f_3^{(k+1)} &= f_3^{(k)} - \frac{A_x^\mu(U^{(k+1)}, f_1^{(k+1)}, f_2^{(k+1)}, f_3^{(k)})}{\frac{\partial}{\partial f_3} A_x^\mu(U^{(k+1)}, f_1^{(k+1)}, f_2^{(k+1)}, f_3^{(k)})} \end{aligned} \right\} \quad (24.31)$$

with the components of the dyadics  $\underline{A}^\varepsilon$  and  $\underline{A}^\mu$  written as functions of the unknown parameters  $U, f_1, f_2$ , and  $f_3$ .

The initial estimate  $\{U^{(0)}, f_1^{(0)}, f_2^{(0)}, f_3^{(0)}\}$  for the modified Newton–Raphson scheme (24.31) was guessed to be sufficiently close to the true solution in order for the scheme to converge to the true solution. The forward Bruggeman formalism can be used to find this guess as follows. Let  $\{\check{\varepsilon}_{Br}^x, \check{\varepsilon}_{Br}, \check{\mu}_{Br}^x, \check{\mu}_{Br}\}$  represent the relative permittivity and relative permeability parameters of the HCM, as estimated by the forward Bruggeman formalism for physically reasonable ranges of the parameters  $U$  and  $f_{1,2,3}$ , that is,  $U \in (U^+, U^-)$  and  $f_\ell \in (f_\ell^+, f_\ell^-)$  for  $\ell \in \{1, 2, 3\}$ . Then:

- (1) Set  $f_1 = (f_1^- + f_1^+)/2, f_2 = (f_2^- + f_2^+)/2$ , and  $f_3 = (f_3^- + f_3^+)/2$ . Then find the value of  $U \in (U^-, U^+)$ , namely,  $U^\dagger$ , for which the scalar

$$\Delta = \left[ (\check{\varepsilon}_{Br}^x - 1)^2 + \left( \frac{\check{\varepsilon}_{Br} - \gamma}{\gamma} \right)^2 + (\check{\mu}_{Br}^x - 1)^2 + \left( \frac{\check{\mu}_{Br} - \gamma}{\gamma} \right)^2 \right]^{1/2} \quad (24.32)$$

has its smallest value.

- (2) Set  $U = U^\dagger, f_2 = (f_2^- + f_2^+)/2$ , and  $f_3 = (f_3^- + f_3^+)/2$ . Then find the value of  $f_1 \in (f_1^-, f_1^+)$ , namely,  $f_1^\dagger$ , for which  $\Delta$  has its smallest value.
- (3) Set  $U = U^\dagger, f_1 = f_1^\dagger$ , and  $f_3 = (f_3^- + f_3^+)/2$ . Then find the value of  $f_2 \in (f_2^-, f_2^+)$ , namely,  $f_2^\dagger$ , for which  $\Delta$  has its smallest value.

- (4) Set  $U = U^\dagger$ ,  $f_1 = f_1^\dagger$ , and  $f_2 = f_2^\dagger$ . Then find the value of  $f_3 \in (f_3^-, f_3^+)$ , namely,  $f_3^\dagger$ , for which  $\Delta$  has its smallest value.

The steps (1)–(4) may be repeated, with  $f_1^\dagger, f_2^\dagger$ , and  $f_3^\dagger$  as the set values of  $f_{1,2,3}$  in step (i),  $f_2^\dagger$  and  $f_3^\dagger$  as the set values of  $f_{2,3}$  in step (ii), and  $f_3^\dagger$  as the set value of  $f_3$  in step (iii), until  $\Delta$  attains a suitably small value.

The experience of numerical investigations suggests that the values of  $U^\dagger, f_1^\dagger, f_2^\dagger$ , and  $f_3^\dagger$  represent suitable initial estimates for the modified Newton–Raphson scheme (24.31) when  $\Delta < 0.01$ . Furthermore, the described technique of iteratively scanning the space of possible forward Bruggeman solutions can itself provide an efficient means of determining inverse Bruggeman solutions, in some cases requiring less computational effort than the modified Newton–Raphson scheme and in a manner that may be less sensitive to the initial estimate  $\{U^{(0)}, f_1^{(0)}, f_2^{(0)}, f_3^{(0)}\}$ .

## 24.4 Representative Numerical Examples

In this section representative numerical illustrations are provided of component materials which may be homogenized to realize the Tamm medium specified by the constitutive relations (24.11), based on the inverse Bruggeman formalism outlined in Sect. 24.3.2. More extensive numerical results are reported elsewhere [24, 30].

### 24.4.1 Schwarzschild–(anti-)de Sitter Spacetime

Let us proceed with the numerical implementation of scenario (i) presented in Sect. 24.3.2 for Schwarzschild–(anti-)de Sitter spacetime, wherein the relative permittivities and permeabilities of the component materials are given and the common shape parameter  $U$  and the volume fractions  $f_\ell$ ,  $\ell \in \{1, 2, 3\}$  are the sought-after quantities. For the purposes of illustration, we focus on two ranges of values of the Tamm constitutive parameter  $\gamma$ , namely,  $0.8 < \gamma < 0.9$  and  $1 < \gamma < 2.9$ . The particular regions of Schwarzschild–de Sitter spacetime and Schwarzschild–anti-de Sitter spacetime that these values of  $\gamma$  correspond to depend upon the magnitudes of  $M$  and  $\Lambda$ , as may be inferred from Fig. 24.2. For  $0.8 < \gamma < 0.9$ , we set  $\varepsilon_1 = 3$ ,  $\varepsilon_2 = 0.1$ ,  $\mu_3 = 2$ , and  $\mu_4 = 0.2$ ; and for  $1 < \gamma < 2.9$ , we set  $\varepsilon_1 = 9$ ,  $\varepsilon_2 = 0.3$ ,  $\mu_3 = 8$ , and  $\mu_4 = 0.4$ .

In Fig. 24.5, the common shape parameter  $U$  and the volume fractions  $f_\ell$ ,  $\ell \in \{1, 2, 3\}$ , as estimated using the inverse Bruggeman formalism, are plotted against  $\gamma$ . The common shape parameter is highly sensitive to changes in  $\gamma$ : we see that  $U$  increases dramatically as  $\gamma$  increases, for both  $0.8 < \gamma < 0.9$  and  $1 < \gamma < 2.9$  ranges. Indeed, if  $\gamma$  is either much less or much greater than unity, then the spheroidal particles of the component materials need to be highly flattened or highly elongated, respectively. In contrast, the volume fractions  $f_\ell$ ,  $\ell \in \{1, 2, 3\}$  are found to be much less sensitive to changes in  $\gamma$ .



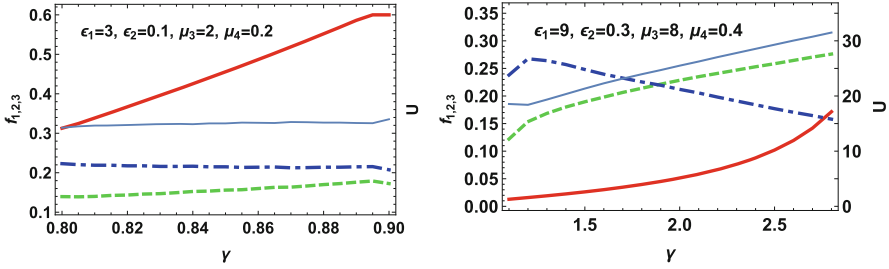


**Fig. 24.5** The common shape parameter  $U$  (*thick solid*) and volume fractions  $f_1$  (*dashed*),  $f_2$  (*broken dashed*), and  $f_3$  (*thin solid*) plotted versus  $\gamma$  for  $0.8 < \gamma < 0.9$  (*left*) and  $1 < \gamma < 2.9$  (*right*), as discussed in Sect. 24.4.1

Results from the numerical implementation of scenarios (ii) and (iii) in Sect. 24.3.2 can be found elsewhere [30].

### 24.4.2 Collision of Gravitational Plane Waves

Next let us turn to the collision of two linearly polarized gravitational plane waves. As described in Sect. 24.2.3, the corresponding Tamm medium is an orthorhombic dielectric-magnetic medium whose relative permittivity and relative permeability dyadics are specified by  $\underline{\underline{\gamma}}$  in Eq. (24.23)<sub>1</sub>. Here we consider the homogenization of two component materials (i.e.,  $n = 2$ ), for example. Both component materials are isotropic dielectric-magnetic materials characterized by  $\epsilon_1 = \mu_1 = \gamma_1$  and  $\epsilon_2 = \mu_2 = \gamma_2$ , say. While materials with such characteristics are not generally found in nature, these component materials could themselves be conceptualized as HCMs, arising from the homogenization of isotropic dielectric and isotropic magnetic materials [30]. In consonance of the orthorhombic nature of  $\underline{\underline{\gamma}}$  in Eq. (24.23)<sub>1</sub>, the component particles are assumed to be ellipsoidal. Furthermore, to simplify matters the ellipsoidal particles of component materials 1 and 2 are all assumed to have the same shape (and orientation); i.e.,  $U_1^x = U_2^x = U^x$ ,  $U_1^y = U_2^y = U^y$ , and  $U_1^z = U_2^z = U^z$ , say. Without loss of generality,  $U^x = 1$  is fixed.

Suppose that  $\underline{\underline{\gamma}}$  is known as a function of  $z$  and  $t$ . The inverse Bruggeman formalism is applied, for any specified  $z$  and  $t$ , to estimate the required values of  $\gamma_1$ ,  $f_1$ , and  $U^y$ , in terms of  $\gamma_2$  and  $U^z$ . The implementation of the inverse Bruggeman formalism is analogous to the implementation described in Sect. 24.3.2 for the case of Schwarzschild-(anti-)de Sitter spacetime.

Let the shape parameter  $U^z = 0.004$ , while  $\gamma_2 = 0.3$  for  $t = 25\pi/180$ ,  $\gamma_2 = 0.1$  for  $t = 50\pi/180$ , and  $\gamma_2 = 0.015$  for  $t = 65\pi/180$ . The corresponding estimates of  $\gamma_1$ ,  $f_1$ , and  $U^y$  are plotted against  $z$  for  $t \in \{25\pi/180, 50\pi/180, 65\pi/180\}$  in Fig. 24.6. As  $z$  increases, the values of the shape parameter  $U^y$  increase sharply for each value of  $t$  considered. Also, the values of  $U^y$  converge on 0.004, i.e., the

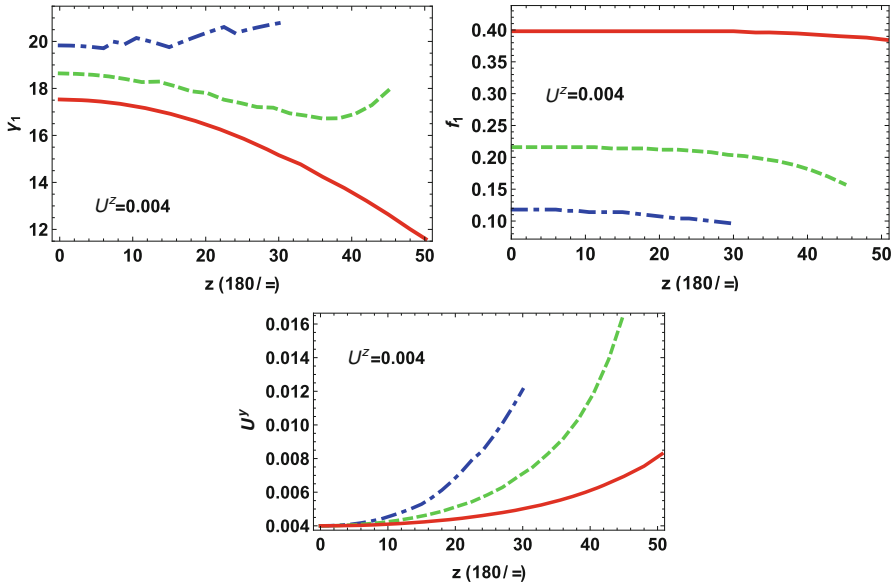


**Fig. 24.6** The parameters  $\gamma_1, f_1$ , and  $U^y$  plotted versus  $z$  for  $t = 25\pi/180$  (*broken dashed curves*),  $50\pi/180$  (*dashed curves*), and  $65\pi/180$  (*solid curves*), as discussed in Sect. 24.4.2

value of  $U^z$ , in the limit  $z \rightarrow 0$ , for each value of  $t$  considered. In other words, the Tamm medium is a uniaxial dielectric–magnetic medium in the  $z = 0$  plane. The sensitivity of  $\gamma_1$  to changes in  $z$  depends upon the value of  $t$ . Specifically,  $\gamma_1$  is more sensitive to changes in  $z$  when  $t$  is larger. In contrast, the volume fraction  $f_1$  is relatively insensitive to changes in  $z$ .

Further numerical results, in which the estimates of  $\gamma_1, f_1$ , and  $U^y$  are provided as functions of  $t$ , are available elsewhere [24].

### 24.5 Closing Remarks

With the aid of the Tamm medium, a wealth of conventional techniques that are well established for materials in flat spacetime may be harnessed to study the electromagnetic properties of vacuous curved spacetime. Furthermore, the conceptualization of Tamm mediums as HCMs opens the door to convenient tabletop analogs that mimic the electromagnetic properties of complicated curved spacetime scenarios. It is particularly notable that the HCM conceptualizations, as typified by those described in Sect. 24.3, generally involve simple arrangements of component particles of simple shapes, made from relatively simple materials. This is in contrast to the often highly elaborate metamaterial constructions that have been proposed for negative refraction and cloaking applications [26], for example.

The inverse Bruggeman formalism provides a suitable means by which the constitutive parameters, particle-shape parameters, and volume fractions of the component materials needed for the HCM realizations may be estimated. The HCM conceptualization for a given Tamm medium is not unique. For example, the Tamm medium for Schwarzschild–(anti-)de Sitter spacetime presented in Sect. 24.2.2 could be conceptualized as an HCM based on two or three component materials, as opposed to the four component materials described in Sect. 24.3.2. Also, the estimates of the constitutive parameters, particle-shape parameters, and volume fractions of the component materials presented in Sect. 24.4, as delivered by the inverse Bruggeman formalism, are not generally unique for any given Tamm medium.

The method of conceptualizing a Tamm medium as an HCM is appropriate to spacetimes for which the constitutive dyadic  $\underline{\underline{\gamma}}$ , introduced in Eq. (24.11), is positive definite. In this case the component materials can be isotropic dielectric and isotropic magnetic materials, specified by positive-valued relative permittivity and permeability scalars, distributed randomly as oriented ellipsoidal particles, for example. In order for the HCM to represent the Tamm medium in the vicinity of a spacetime singularity, component materials are needed that possess rather extreme values of relative permittivity and permeability. Such extreme values are becoming more readily attainable: recent progress with metamaterials has delivered extremely high relative permittivities and permeabilities [60] and relative permittivities and relative permeabilities very close to zero [61]. Also, since the HCM conceptualization process is essentially wavelength independent (beyond the fundamental requirement that the component particles are much smaller than the wavelengths involved), higher- and/or lower-frequency regimes could be utilized in order to access the required values of the constitutive parameters. Furthermore, the Tamm medium may be highly anisotropic for spacetime regions of high curvature. These high degrees of anisotropy may be achieved through the homogenization of highly elongated or very flattened particles [62].

The HCM conceptualization of a Tamm medium for which the constitutive dyadic  $\underline{\underline{\gamma}}$  is indefinite represents a severe challenge. In principle, component materials  $\underline{\underline{\gamma}}$  with indefinite constitutive dyadics could be used – reports of indefinite dielectric [63] and indefinite magnetic [64, 65] metamaterials are available in the literature. In practice, however, there are likely to be major practical difficulties in harnessing such metamaterials as component materials for the required HCMs. First, not only would the HCM's relative permittivity dyadic and relative permeability dyadic both be required to be indefinite, but these two constitutive dyadics would be required to be identical. Second, the HCM would be required to be nondissipative, but relatively high degrees of dissipation are associated with many metamaterials.

Parenthetically, there is also a theoretical problem in the case of indefinite  $\underline{\underline{\gamma}}$ . Conventional homogenization techniques based on depolarization dyadics, as typified by the Bruggeman formalism, cannot accommodate nondissipative HCMs characterized by indefinite constitutive dyadics because the depolarization dyadics would be undefined [50]. The incorporation of a small amount of dissipation would

overcome this mathematical problem [66] but that step would compromise the extent to which the HCM would represent the Tamm medium. In a similar vein, the HCM conceptualization of a Tamm medium with  $\underline{\underline{\gamma}}$  negative definite also represents a very tall order; that is, achieving identical relative permittivity and relative permeability dyadics, while simultaneously eliminating dissipation, seems beyond the reach of what is presently considered as practical.

In principle, bianisotropic Tamm mediums (i.e., those specified by  $\mathbf{\Gamma} \neq \mathbf{0}$  in Eq. (24.11)) may be conceptualized as HCMs. This would require rather more complicated component materials than those outlined here for the case of  $\mathbf{\Gamma} = \mathbf{0}$ . In particular, at least one of the component materials would need to be magnetoelectric [67, 68]. Also, bianisotropic Tamm mediums representing cosmic spinning strings [32], Alcubierre spacetime [22], and rotating black holes [15, 16], for example, are Lorentz nonreciprocal mediums [67]. In order to realize such Tamm mediums as HCMs, at least one of the component materials would need to be Lorentz nonreciprocal. Future studies are required for progress in this area.

### Appendix: Table of Prominent Symbols

Symbol	Meaning
$\underline{\underline{0}}$	$0 \mathbf{e}_1 \mathbf{e}_1 + 0 \mathbf{e}_2 \mathbf{e}_2 + 0 \mathbf{e}_3 \mathbf{e}_3$
$\epsilon_0$	Permittivity of free space not affected by any gravitational field
$\epsilon_\ell$	Relative permittivity (scalar) of component material $\ell$
$\underline{\underline{\epsilon}}_{Br}$	Relative permittivity dyadic of the HCM in the Bruggeman formalism
$\Lambda$	Cosmological constant
$\mu_0$	Permittivity of free space not affected by any gravitational field
$\mu_\ell$	Relative permeability (scalar) of component material $\ell$
$\underline{\underline{\mu}}_{Br}$	Relative permeability dyadic of the HCM in the Bruggeman formalism
$\underline{\underline{a}}_\ell^{\epsilon,\mu}$	Polarizability density dyadics for component material $\ell$
<b>B, D, E, H</b>	Electromagnetic field vectors (in flat spacetime)
$B_\ell, D_\ell, E_\ell, H_\ell$	Components of <b>B, D, E, H</b>
$c_0$	$1/\sqrt{\epsilon_0 \mu_0}$
$\underline{\underline{D}}_\ell^{\epsilon,\mu}$	Depolarization dyadics for component material $\ell$
$\mathbf{e}_1, \mathbf{e}_2, \mathbf{e}_3$	Unit vectors in the $x, y,$ and $z$ directions in Cartesian space
$f_\ell$	Volume fraction of component material $\ell$
$f_{\alpha\beta}$	Components of covariant electromagnetic field tensor
$g$	$\det [\mathcal{G}]$
$G$	Gravitational constant
$\mathcal{G}$	Metric tensor with components $g_{\alpha\beta}$

(continued)

(continued)

Symbol	Meaning
$h^{\alpha\beta}$	Components of contravariant electromagnetic field tensor
$\underline{\underline{I}}$	$\mathbf{e}_1 \mathbf{e}_1 + \mathbf{e}_2 \mathbf{e}_2 + \mathbf{e}_3 \mathbf{e}_3$
$M$	Mass of Schwarzschild black hole
$\mathbf{r}$	$x \mathbf{e}_1 + y \mathbf{e}_2 + z \mathbf{e}_3$
$\mathcal{R}$	Spacetime region of interest
$t$	Time
$\underline{\underline{U}}_\ell$	Shape dyadic for particles of component material $\ell$
$x, y, z$	Coordinates in Cartesian space
$\mathcal{X}$	Spacetime vector with components $x^\alpha$

## References

1. N. Ashby, Relativity and the global positioning system. *Phys. Today* **55**(5), 41–47 (2002)
2. S. Weinberg, *Gravitation and Cosmology* (John Wiley & Sons, New York, 1972)
3. B.F. Schutz, *A First Course in General Relativity* (Cambridge University Press, Cambridge, 1985)
4. R. d’Inverno, *Introducing Einstein’s Relativity* (Clarendon Press, Oxford, 1992)
5. M. Novello, M. Visser, G. Volovik (eds.), *Artificial Black Holes* (World Scientific, Singapore, 2002)
6. J. Steinhauer, Observation of self-amplifying Hawking radiation in an analogue black-hole laser. *Nat. Phys.* **10**, 864–869 (2014)
7. G.V. Skrotskii, The influence of gravitation on the propagation of light. *Sov. Phys. Dokl.* **2**, 226–229 (1957)
8. J. Plébinski, Electromagnetic waves in gravitational fields. *Phys. Rev.* **118**, 1396–1408 (1960)
9. W. Schleich, M.O. Scully, General relativity and modern optics, in *New Trends in Atomic Physics*, ed. by G. Grynberg, R. Stora (Elsevier, Amsterdam, 1984), pp. 995–1124
10. E.J. Post, *Formal Structure of Electromagnetics* (Dover Press, New York, 1997)
11. A. Lakhtakia, On the genesis of Post constraint in modern electromagnetism. *Optik* **115**, 151–158 (2004)
12. T.G. Mackay, A. Lakhtakia, *Electromagnetic Anisotropy and Bianisotropy: A Field Guide* (World Scientific, Singapore, 2010)
13. A. Lakhtakia, T.G. Mackay, Towards gravitationally assisted negative refraction of light by vacuum. *J. Phys. A Math. Gen.* **37**, L505–L510 (2004); errata: **37**, 12093 (2004)
14. A. Lakhtakia, T.G. Mackay, S. Setiawan, Global and local perspectives of gravitationally assisted negative-phase-velocity propagation of electromagnetic waves in vacuum. *Phys. Lett. A* **336**, 89–96 (2005)
15. T.G. Mackay, A. Lakhtakia, S. Setiawan, Electromagnetic negative-phase-velocity propagation in the ergosphere of a rotating black hole. *New J. Phys.* **7**, 171 (2005)
16. B.M. Ross, T.G. Mackay, A. Lakhtakia, On negative-phase-velocity propagation in the ergosphere of a charged rotating black hole. *Optik* **121**, 401–407 (2010)
17. T.G. Mackay, S. Setiawan, A. Lakhtakia, Negative phase velocity of electromagnetic waves and the cosmological constant. *Eur. Phys. J. C* **41**(Suppl. 1), 1–4 (2005). doi:10.1140/epjcd/s2005-01-001-9

18. T.G. Mackay, A. Lakhtakia, S. Setiawan, Electromagnetic waves with negative phase velocity in Schwarzschild–de Sitter spacetime. *Europhys. Lett.* **71**, 925–931 (2005)
19. M.B. Hindmarsh, T.W.B. Kibble, Cosmic strings. *Rep. Prog. Phys.* **58**, 477–562 (1995)
20. T.H. Anderson, T.G. Mackay, A. Lakhtakia, Ray trajectories for a spinning cosmic string and a manifestation of self-cloaking. *Phys. Lett. A* **374**, 4637–4641 (2010)
21. M. Alcubierre, The warp drive: hyper-fast travel within general relativity. *Class. Quantum Gravity* **11**, L73–L77 (1994)
22. T.H. Anderson, T.G. Mackay, A. Lakhtakia, Ray trajectories for Alcubierre spacetime. *J. Opt. (Bristol)* **13**, 055107 (2011)
23. D. Bini, A. Geralico, M. Haney, Refraction index analysis of light propagation in a colliding gravitational wave spacetime. *Gen. Relativ. Gravit.* **46**, 1644 (2014)
24. T.G. Mackay, A. Lakhtakia, Towards a piecewise–homogeneous metamaterial model of the collision of two linearly polarized gravitational plane waves. *IEEE Trans. Antennas Propag.* **62**, 6149–6154 (2014)
25. M. Fathi, R.T. Thompson, Cartographic distortions make dielectric spacetime analog models imperfect mimickers. *Phys. Rev. D* **93**, 124026 (2016)
26. T.J. Cui, D.R. Smith, R. Liu (eds.), *Metamaterials: Theory, Design, and Applications* (Springer, New York, 2010)
27. I.I. Smolyaninov, Surface plasmon toy model of a rotating black hole. *New J. Phys.* **5**, 147 (2003)
28. M. Li, R.-X. Miao, Y. Pang, Casimir energy, holographic dark energy and electromagnetic metamaterial mimicking de Sitter. *Phys. Lett. B* **689**, 55–59 (2010)
29. M. Li, R.-X. Miao, Y. Pang, More studies on metamaterials mimicking de Sitter space. *Opt. Express* **18**, 9026–9033 (2010)
30. T.G. Mackay, A. Lakhtakia, Towards a realization of Schwarzschild–(anti-)de Sitter spacetime as a particulate metamaterial. *Phys. Rev. B* **83**, 195424 (2011)
31. R.-X. Miao, R. Zheng, M. Li, Metamaterials mimicking dynamic spacetime, D-brane and noncommutativity in string theory. *Phys. Lett. B* **696**, 550–555 (2011)
32. T.G. Mackay, A. Lakhtakia, Towards a metamaterial simulation of a spinning cosmic string. *Phys. Lett. A* **374**, 2305–2308 (2010)
33. A. Greenleaf, Y. Kurylev, M. Lassas, G. Uhlmann, Cloaking devices, electromagnetic wormholes, and transformation optics. *SIAM Rev.* **51**, 3–33 (2009)
34. W. Lu, J. Jin, Z. Lin, H. Chen, A simple design of an artificial electromagnetic black hole. *J. Appl. Phys.* **108**, 064517 (2010)
35. I.I. Smolyaninov, E. Hwang, E. Narimanov, Hyperbolic metamaterial interfaces: Hawking radiation from Rindler horizons and spacetime signature transitions. *Phys. Rev. B* **85**, 235122 (2012)
36. D.V. Khveshchenko, Analogue holographic correspondence in optical metamaterials. *Eur. Phys. Lett.* **109**, 61001 (2015)
37. J.B. Griffiths, *Colliding Plane Waves in General Relativity* (Clarendon Press, Oxford, 1991)
38. A.P. Lightman, W.H. Press, R.H. Price, S.A. Teukolsky, *Problem Book in Relativity and Gravitation* (Princeton University Press, Princeton, NJ, 1975)
39. G.W. Gibbons, S.W. Hawking, Cosmological event horizons, thermodynamics, and particle creation. *Phys. Rev. D* **15**, 2738–2751 (1977)
40. J. Podolsky, The structure of the extreme Schwarzschild–de Sitter space-time. *Gen. Relativ. Gravit.* **31**, 1703–1725 (1999)
41. V. Cardoso, J.P.S. Lemos, Quasi-normal modes of Schwarzschild anti-de Sitter black holes: electromagnetic and gravitational perturbations. *Phys. Rev. D* **64**, 084017 (2001)
42. H. Stephani, D. Kramer, M. MacCallum, C. Hoenselaers, E. Herlt, *Exact Solutions of Einstein's Field Equations* (Cambridge University Press, Cambridge, 2003)
43. T.G. Mackay, S. Setiawan, A. Lakhtakia, Negative phase velocity of electromagnetic waves and the cosmological constant. *Eur. Phys. J. C* **41**(Suppl. 1), 1–4 (2005). doi:10.1140/epjcd/s2005-01-001-9

44. T.G. Mackay, A. Lakhtakia, S. Setiawan, Electromagnetic waves with negative phase velocity in Schwarzschild–de Sitter spacetime. *Europhys. Lett.* **71**, 925–931 (2005)
45. V. Ferrari, J. Ibañez, A new exact solution for colliding gravitational plane waves. *Gen. Relativ. Gravit.* **19**, 383–404 (1987)
46. V. Ferrari, J. Ibañez, On the collision of gravitational plane waves: a class of soliton solutions. *Gen. Relativ. Gravit.* **19**, 405–425 (1987)
47. V. Ferrari, J. Ibañez, Type-D solutions describing the collision of plane-fronted gravitational waves. *Proc. R. Soc. Lond. A* **417**, 417–431 (1988)
48. T.G. Mackay, A. Lakhtakia, S. Setiawan, Gravitation and electromagnetic wave propagation with negative phase velocity. *New J. Phys.* **7**, 75 (2005)
49. J.D. Hoffman, *Numerical Methods for Engineers and Scientists* (McGraw–Hill, New York, 1992)
50. B. Michel, A Fourier space approach to the pointwise singularity of an anisotropic dielectric medium. *Int. J. Appl. Electromagn. Mech.* **8**, 219–227 (1997)
51. B. Michel, W.S. Weiglhofer, Pointwise singularity of dyadic Green function in a general bianisotropic medium. *Archiv Electr. Übertrag.* **51**, 219–223 by (1997); errata: **52**, 310 (1998)
52. W.S. Weiglhofer, Electromagnetic depolarization dyadics and elliptic integrals. *J. Phys. A Math. Gen.* **31**, 7191–7196 (1998)
53. W.S. Weiglhofer, A. Lakhtakia, B. Michel, Maxwell Garnett and Bruggeman formalisms for a particulate composite with bianisotropic host medium. *Microw. Opt. Technol. Lett.* **15**, 263–266 (1997); errata: **22**, 221 (1999)
54. W.S. Weiglhofer, On the inverse homogenization problem of linear composite materials. *Microw. Opt. Technol. Lett.* **28**, 421–423 (2001)
55. E. Cherkaev, Inverse homogenization for evaluation of effective properties of a mixture. *Inverse Prob.* **17**, 1203–1218 (2001)
56. T.G. Mackay, A. Lakhtakia, Determination of constitutive and morphological parameters of columnar thin films by inverse homogenization. *J. Nanophotonics* **4**, 041535 (2010)
57. S.S. Jamaian, T.G. Mackay, On limitations of the Bruggeman formalism for inverse homogenization. *J. Nanophotonics* **4**, 043510 (2010)
58. P.A. Stark, *Introduction to Numerical Methods* (Macmillan, New York, 1970)
59. R.D. Kampa, A. Lakhtakia, Bruggeman model for chiral particulate composites. *J. Phys. D Appl. Phys.* **25**, 1390–1394 (1992)
60. J. Shin, J.-T. Shen, S. Fan, Three-dimensional metamaterials with an ultrahigh effective refractive index over a broad bandwidth. *Phys. Rev. Lett.* **102**, 093903 (2009)
61. M. Navarro-Cia, M. Beruete, I. Campillo, M. Sorolla, Enhanced lens by  $\epsilon$  and  $\mu$  near-zero metamaterial boosted by extraordinary optical transmission. *Phys. Rev. B* **83**, 115112 (2011)
62. T.G. Mackay, Towards metamaterials with giant dielectric anisotropy via homogenization: an analytical study. *Photonics Nanostruct. Fundam. Appl.* **13**, 8–19 (2015)
63. H. Lee, Z. Liu, Y. Xiong, C. Sun, X. Zhang, Development of optical hyperlens for imaging below the diffraction limit. *Opt. Express* **15**, 15886 (2007)
64. A.B. Kozyrev, C. Qin, I.V. Shadrivov, Y.S. Kivshar, I.L. Chuang, D.W. Van der Weide, Wave scattering and splitting by magnetic metamaterials. *Opt. Express* **15**, 11714 (2007)
65. J. Sun, L. Kang, R. Wang, L. Liu, L. Sun, J. Zhou, Low loss negative refraction metamaterial using a close arrangement of split-ring resonator arrays. *New J. Phys.* **12**, 083020 (2010)
66. T.G. Mackay, A. Lakhtakia, R.A. Depine, Uniaxial dielectric media with hyperbolic dispersion relations. *Microw. Opt. Technol. Lett.* **48**, 363–367 (2006)
67. T.G. Mackay, A. Lakhtakia, Electromagnetic fields in linear bianisotropic mediums. *Prog. Opt.* **51**, 121–209 (2008)
68. T.G. Mackay, A. Lakhtakia, *Modern Analytical Electromagnetic Homogenization* (Institute of Physics, Bristol, United Kingdom, 2015)



**Tom G. Mackay** is a reader in the School of Mathematics at the University of Edinburgh, and also an adjunct professor in the Department of Engineering Science and Mechanics at Pennsylvania State University. He graduated from the Universities of Edinburgh, Glasgow, Strathclyde. His current research interests include homogenization, complex materials, metamaterials, and sculptured thin films. His research has been supported by awards from the Carnegie Trust for The Universities of Scotland, Engineering and Physical Sciences Research Council, Nuffield Foundation, Royal Academy of Engineering/Leverhulme Trust, and Royal Society of Edinburgh/Scottish Executive. He is a fellow of

the Institute of Physics (UK) and of SPIE – The International Society for Optical Engineering.



**Akhlesh Lakhtakia** received the BTech (1979) and DSc (2006) degrees from the Banaras Hindu University and the MS (1981) and PhD (1983) degrees from the University of Utah. In 1983 he joined the Department of Engineering Science and Mechanics at Penn State as a post-doctoral research scholar, where he is now the Charles Godfrey Binder Professor. His research interests include surface multiplasmonics, bioreplication, forensic science, solar energy, sculptured thin films, and mimemes. He has been elected a fellow of Optical Society of America (1992), SPIE – The International Society for Optical Engineering (1996), Institute of Physics (UK) (1996), American Association for the Advancement of Science (2010), American Physical Society (2012), Institute of Electrical and Electronics Engineers (2016), Royal Society of Chemistry (2016), and Royal Society of Arts (2017). He has been designated a Distinguished Alumnus of both

of his alma maters at the highest level. Awards at Penn State include: Outstanding Research Award (1996), Outstanding Advising Award (2005), Premier Research Award (2008), and Outstanding Teaching Award (2016), and the Faculty Scholar Medal (2005). He received the 2010 Technical Achievement Award from SPIE and the 2016 Walston Chubb Award for Innovation from Sigma Xi.



# Chapter 25

## Electromagnetics Education: Past, Present, and Future Directions

Cynthia M. Furse and Elene Tiffany Iskander

### 25.1 Introduction

Dr. Magdy F. Iskander has been a creative force in electromagnetics education research and innovation throughout his distinguished career, for which he received the Chen-To Tai Distinguished Teaching Award from the *IEEE Antennas and Propagation Society* (APS) in 2012. His textbook [1] was among the first introductory electromagnetics books to incorporate extensive descriptions of the behavior of fields, beyond the mathematical calculations. Dr. Iskander was a pioneer in the use of computer simulations to understand and teach how electromagnetic fields propagate and interact with their environments. In the 1980s, when analytical electromagnetics was still the workhorse of choice to comprehend electromagnetic fields, Dr. Iskander utilized first the method of moments [2] and then the finite-difference time-domain (FDTD) [3] method in his research. He was one of the first educators to bring the power of numerical simulations to electromagnetics education.

He began with a graduate-level course on numerical electromagnetics [4]. He established the NSF/IEEE Center for Computer Applications in Electromagnetic Education (CAEME) at the University of Utah in the early 1990 [5]. The Center created multimedia interactive simulations of electromagnetic field experiments (such as Faraday's and Ampère's experiments), electromagnetic fields in one-dimensional (1D) and two-dimensional (2D) space, physics concepts, and even a "Calculus Castle" for demonstrating physical principles of calculus and dis-

---

C.M. Furse (✉)

Department of Electrical and Computer Engineering, University of Utah, Salt Lake City, UT 84112, USA

e-mail: [cfurse@ece.utah.edu](mailto:cfurse@ece.utah.edu)

E.T. Iskander

State of Iowa Social Security Services, Des Moines, Iowa, USA

tributed them broadly via CDs. In 1992, Dr. Iskander founded the Wiley *Computer Applications in Engineering Education (CAEE)* online journal to share peer-reviewed timely information on the innovative uses of computers, Internet, and software tools in engineering education. Besides new courses and software tools, the *CAEE* journal covers areas that support the integration of technology-based modules in the engineering curriculum and promotes discussion of the assessment and dissemination issues associated with these new implementation methods [6]. He has been a big proponent of expanding the reach of electromagnetics education through globalization and the sharing of resources among educators globally [7, 8], and he has continually been supportive of inclusion and diversity, beside serving as a strong mentor for all.

Engineering education has changed from Dr. Iskander's early teaching days to today. Perhaps the largest shift has been caused by the invention of tiny high-frequency transistors that changed electromagnetic devices from large, expensive components (e.g., military radios and radar) to the small, inexpensive consumer products of today (cell phones, handheld GPS, personal locator devices, and many more). This major shift in technology reinvigorated electromagnetic programs sagging during the 1980s, breathing new life and excitement into the field. What was originally an individual discipline – electromagnetics – became broadly multidisciplinary, integrating with communications, circuit and IC design, imaging, and more. The changing technological landscape changed *what* we teach, and it is poised to change it again, which we discuss in Sect. 25.2.

Dr. Iskander has an innate sense of how to help students learn and understand the complex concepts in electromagnetics. His early work in using visualization to teach is known today to make use of the largest part of our brain, the visual cortex, thereby allowing students to actually process and understand more conceptual information. Bringing real-world applications into the learning process is known to improve motivation for learning, and active participation in interactive learning modules is known to improve learning [9]. Although a powerful, invigorating lecturer, Dr. Iskander realized early on that education is not about the teacher, instead, it is about the student, the learner. Dr. Iskander was an early pioneer in a wave of new research on how students learn. We now know a great deal about learner-centered teaching approaches, *why* and *how* they work, and how to implement them in the classroom. These ideas on *how* we teach are covered in Sect. 25.3, along with a vision for trends in engineering education in the foreseeable future. These trends are based on solid research in engineering education, which is referenced throughout.

Finally, Dr. Iskander has raised his voice in support of the globalization of engineering education. The Internet, video chat software such as Skype, and cell phones have brought us closer together. YouTube, the Khan Academy, Coursera, and others provide an explosion of instant information of all kinds available 24/7, with translations into a myriad of languages, and instant chat questions and answers around the globe. No longer are we teaching only small classes of a few students. Now our audience includes millions of prospective engineers and scientists, working professionals, and social scientists, not to mention the general public. The variety of background, skills, needs, desires, and motivations of students

even in small classes are huge. Students hail from every part of the globe, from a variety of socioeconomic status, first-generation college students, and families of professionals. Dr. Iskander has embraced globalization of education and the diversity that encompasses. Section 25.4 is a review of the diversity of *whom* we teach. Part of this chapter is unique because it describes the research work of Dr. Magdy Iskander's daughter, Dr. Elene Tiffany Iskander, on the challenges of bringing more women into the engineering profession.

So this chapter, on the past, present, and future of electromagnetics education, is focused on *what* we teach (i.e., the changing electromagnetics curriculum), *how* we teach (i.e., new advances in pedagogy), and *whom* we teach (the opportunities and challenges of diversity). Let us begin . . .

## 25.2 Electromagnetics Curriculum: *What We Teach*

### 25.2.1 *Curriculum*

Students first learn the basics of electromagnetic fields in introductory physics during the first year of college (or while in high school), often in the same course where they learn circuits and basic electrical engineering concepts as well as introductory optics. In most universities, Introduction to Electromagnetics is taught in the third year, after students have learned basic mathematics, physics, chemistry, programming, analog and digital circuits, and more. In the 1980s, interest in electromagnetics was waning, overshadowed by rapid advancements in VLSI. Many universities that required two semesters of electromagnetics dropped their requirements to one semester, only to find increased demand once again when the development of the cell phone and other commercial applications reinvigorated electromagnetics education. Today most universities require only one semester of electromagnetics, although some require two. A wide variety of more advanced courses are available nowadays including antennas, numerical analysis, RF/microwave circuits, bioelectromagnetics, radar, electromagnetic compatibility, electromagnetic theory, signal integrity/high-speed digital, and wireless communication [10, 11].

Electromagnetics can be particularly challenging and demanding for students, because it is highly theoretical and mathematical. Students need to understand what the electromagnetic fields are really *doing*, rather than just the mathematical machinery to calculate them. Putting their learning in the context of things they already understand (e.g., circuits) or applications they are interested in greatly increases motivation, and increased motivation makes it easier to learn.

Basic electromagnetics courses typically take one of three approaches. The traditional approach (“fields first”) is to teach vector analysis, followed by static fields, and some basic time-varying fields. Transmission lines and detailed analysis of plane waves and other concepts are taught later. Another approach (“transmis-

sion lines first”) is to start with transmission line theory as a distributed circuit model, building on circuit theory students are familiar with and giving students an understanding of time-varying fields. Vectors are introduced along with static fields, then combined with the time-varying fields to explain plane wave and optical behavior. Still another approach starts with general time-varying fields and Maxwell’s equations, and then static fields are presented as a special case [10, 11]. Whichever way electromagnetics is taught, students often get entangled in learning the mathematics involved and need to be encouraged to think more deeply about the interaction of the fields and their environment and what the math actually means. Some texts emphasize these concepts [12, 13].

### **25.2.2 Laboratories**

Laboratories in electromagnetics courses have typically lagged behind laboratories in other areas of electrical engineering education because of the expense of the equipment. But, as the costs of this equipment fell in the 1990s, more universities were able to incorporate electromagnetics labs into their curriculum. Still, electromagnetics labs are often limited to smaller, upper-division courses. Simulations, virtual labs, and videos of lab experiments provide alternatives to help students gain the insight they might have obtained from hands-on labs. In some cases, these virtual labs can actually help the students understand the topics better than a hands-on lab might have, as they are able to “see” and “measure” inside and around structures in ways that are impossible in actual electromagnetics labs.

Numerous interesting hands-on labs are available [14], but the consistent availability of equipment (each university typically has different equipment) still makes it somewhat difficult to replicate labs between schools. In this environment, it would be ideal for the faculty to videotape their experiments in ways that they could be shared with others, so students could see and use the measurements for analysis even without having the equipment available. In the future, as electromagnetics equipment becomes even less expensive and more available, electromagnetics labs are likely to be as pervasive as circuit labs, allowing students more flexibility to both design and measure electromagnetics components.

### **25.2.3 The Future: What We Teach**

Engineering is becoming progressively more global, and engineering education is very much following this trend as well with curriculum materials shared widely between professors. Keeping pace with wireless communication, the Internet of Things, tracking, and locating people and objects, medical applications, and the myriad of other exciting applications is critical in preparing engineers for today’s workforce. But it is not just the applications that are changing. The workplace and

its tools are continually changing too. Working engineers now rarely calculate fields by hand. They use computer simulations. They rarely design simple antennas or circuits. They use a circuit library. Educators puzzle over the right mix of basic mathematics and theory on one hand and the more advanced tools on the other, to use in their classes. Perhaps the right way to design our classes today and tomorrow is to consider what we are actually trying to teach (i.e., the learning objectives), choose how to measure/assess that the students have learned what we are trying to teach them, and only then decide how to teach what we want the students to learn. Focusing on understanding how the fields interact with the environment is evermore important as we prepare students for the fast pace of technological change.

The global work environment demands students have skills working and thinking together, communicating and sharing their ideas, and embracing the diversity of thought in multidisciplinary teams working with a wide variety of people. Engineering students need opportunities to experience this excitement and its challenges through internships, undergraduate research experiences, and mentoring. In the following section, we will discuss ways to help teach electromagnetics to today's students.

## **25.3 In the Classroom? *How We Teach***

Teaching in higher education is unique, in that most faculty are not actually taught how to teach. While elementary and secondary education faculty spend 4 years learning about their students, how they learn, and ways to teach them better, most higher education faculty receive little if any formal training in pedagogy – the science of how to teach. And there is science in the form of engineering education research that evaluates, compares, and innovates new and often better ways to help students understand complex topics. The techniques described here are a few of the recent innovations that have helped improve electromagnetics education.

### **25.3.1 *Visualization: Making the Invisible Visible***

Electromagnetics, by its very nature, deals with an invisible subject. Making these invisible fields visible can make them much easier to understand and more exciting. Dr. Iskander's CAEME software was groundbreaking when it was released in the 1990s [5]. Most of this software used numerical methods to compute the fields and show them in 2D or three-dimensional (3D) formats. Using color to represent the strength of the field as shown in Fig. 25.1 and vectors to represent its direction now seems very normal, but it was a brave new idea at that time. Color computer monitors were still new in the mid-1980s, and color pen plotters were a fascinating new addition. Textbooks were still printed in black and white. The availability of inexpensive color displays (1980s), laptops and computer projection for the

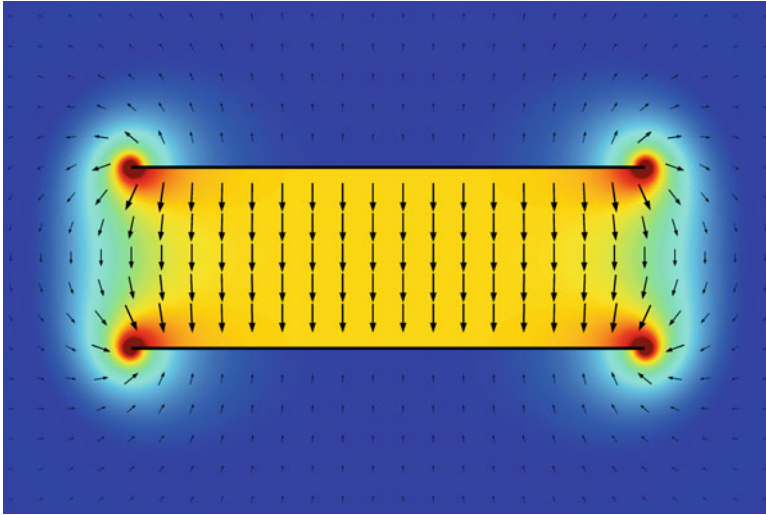


**Fig. 25.1** This image of the electric fields in a capacitor was created by Dr. James Nagel using the finite difference method as described in Ref. [15]. The two plates are modeled as Dirichlet boundaries at  $+1.0$  V and  $-1.0$  V

classroom (mid-1990s), inexpensive color printing (early 1990s), affordable full-color textbooks (2010s), YouTube [16] and video capture has brought color into the teaching of electromagnetics. The Internet has placed those resources at our fingertips.

Searching online for visualizations of Faraday's law, for instance, provides over 467,000 entries on Google, including numerous images, and over 30,000 videos on YouTube. These include lectures with a simple lab demonstration [17], numerical simulations [18] (software to run the simulations interactively is also available [19]), a lab demonstration with a realistic generator [20], a recreation of Faraday's original experiments [21], and a documentary on Michael Faraday [16].

Videos and visualizations can be used in many ways in teaching. For example, they provide quick and easy resources for inquiry-based learning, where students experience the process of discovery by exploring the physical world in much the same way the early discoverers of science did [22, 23]. Numerical simulations and their associated visualizations (which may be interactive) can help us understand how fields interact with the real world. Visualizations or videos of real-world applications can also be highly motivational for students.

Today, most faculty use visualizations and videos liberally in their teaching. Color textbooks, both in print and online, are the norm. As computers become more and more powerful, and shrink in size so that we can hold them in our hands, visualizations are becoming more interactive, personal, and available. Students now readily search the web for examples, lectures, videos, etc. to help them learn. No longer is the professor/textbook the only source of information. We rely more

and more on numerical simulations and visualizations to provide quick, accurate answers and to help us design and understand electromagnetic devices.

The availability of high-powered computer simulations and our reliance on engineering design software should help guide our teaching as well. In addition to teaching students how to calculate electromagnetic fields (analytically or numerically), we need to focus on helping students really understand how the fields interact with the real world and gain an intuitive understanding that can lead to improved design. And we need to teach how to use this intuition to evaluate the accuracy of the simulations on which we rely. The ability to evaluate and understand results is a higher level of learning than just being able to calculate them [24]. Some books are now emphasizing intuitive understanding of the fields [12, 13]. If we want to teach students at a deeper level, we also need to be able to assess that level of learning. Most exams test a student's ability to calculate something, but do not test higher-level learning. If we want to teach at this level, we also need to craft exams that test at that level. Teaching and assessing higher-level learning is an area of teaching and learning science that is in its infancy and is ripe for creativity.

### ***25.3.2 Active Learning: Focus on the Students***

Active learning engages students in active thinking, problem solving, and discussion rather than passive listening and note-taking. It puts the focus on the student (student-centered learning) rather than on the teacher. Adding active learning can increase student engagement, knowledge and understanding, retention of information, confidence, and satisfaction with the class [25, 26]. Often, activities focus on problems – homework problems, group work for larger problems, and real-world problems. This problem-based learning not only actively involves the students but also engages them in the context of their learning [9]. Active learning (also called engaged learning) is becoming the norm, either added to the traditional lecture, or displacing the in-class lecture entirely (as we will see in the next section on flipping the class).

Several active learning strategies work well in engineering classrooms [26, 27], as we now describe.

#### **25.3.2.1 Think-Pair-Share (or Just Pair-Share) [28]**

Think-Pair-Share is a super easy method of engaging students in class. This works for any kind of class (regular lecture, flipped, online, etc.). Here are the parts:

**THINK:** a student thinks about a question on her/his own.

**PAIR:** the student turns to one or two neighboring students and shares her/his ideas about this question.

**SHARE:** the student shares her/his ideas with the class.

Here is an example of how this method can be used when teaching electromagnetics: Students often struggle getting started on and setting up a problem. For instance, when asked to find the electric field from a charge distribution, should they use Coulomb's law or Gauss's law? And how should they set up the integrals to solve it? After you have taught them about the methods and when they can be used (Try using the Gauss's law song to remind them about the importance of symmetry for this law [29]), they need to do it for themselves. Then do this in class:

Hand out (or put on the board) several examples of charge distributions (perhaps several homework problems they are supposed to do).

**THINK:** Ask them to look at them for a minute or two and decide which problems should be done with each method. Thinking individually gives reflective students time to think before a more extroverted student shouts out the answer.

**PAIR:** Ask them to turn to their neighbors (usually this is two or three people sitting next to each other), compare notes quickly (2–3 min), and come up with their own “rules” for when to use each method and why.

**SHARE:** Ask for suggestions of rules. There is often an amazing array of correct answers at this point, and students are more confident expressing them and also asking questions. After a brief discussion, Ask them to solve one of the problems (thus returning to the “THINK” stage and repeating the process again).

### 25.3.2.2 Muddiest Point

**PAIR-SHARE** is essentially the same method as think-pair-share without individual thinking time. A particularly effective **PAIR-SHARE** combo is, instead of asking, “Are there any questions?” (to which the answer is inevitably no), to ask “**PAIR:** Turn to your partner and find the most confusing thing (the ‘muddiest point’) about today’s topic.” And then they **SHARE** with the class. This inevitably generates good questions and discussion.

### 25.3.2.3 Formative Assessment

Asking students to assess what they know (or don't know) is a type of formative assessment. Assessment is figuring out what you do or don't know. Formative assessment is done during the learning process and often helps change or form what a student does (such as reviewing a topic they don't understand). Muddiest points, quizzes, homework, and self-assessments are all forms of formative assessment. Summative assessment, on the other hand, assesses what a student knows at the end of a learning activity. A final exam is a summative assessment.



#### 25.3.2.4 Classroom Response Systems

Clickers, Top Hat, Kahoot, and other classroom response systems (CRS) allow the teacher to pose a question and each student to think about and answer that question. Most CRS are used for multiple-choice answers, but some (e.g., Kahoot) allow text answers.

### 25.3.3 *The Future: How We Teach*

Active learning is effective and engaging. Most faculty members now use a variety of approaches throughout the class, and active-learning methods are proliferating as faculty members see their peers enjoying using these methods. Already, the class where the professor lectures with no participation from the students has become generally unpopular. Technology for active learning (such as Kahoot) is becoming widely available free or low cost. Other methods require no special technology. Methods to engage students in online classes are being explored. The challenge most faculty face when implementing active learning is the class time it requires. This challenge is addressed next.

### 25.3.4 *Flipping the Classroom: Making TIME for Learning*

The ready availability of Internet access to information and to full course materials, inexpensive equipment to create your own multimedia presentations, and the proliferation of personal information devices (the Internet in the palm of your hand) are transforming education. One of the most promising transformative trends in science, engineering, technology, and mathematics (STEM) education is the development of hybrid courses that combine individualized online learning activities with group learning activities in the classroom [30, 31].

In the “flipped classroom” (also called the “inverted classroom”), the lectures and homework are “flipped.” Instead of lectures in class and homework out of class, students watch video lectures prior to class. The in-class face-to-face (F2F) time is then used for active and engaged problem solving, usually working with peers, guided by the professor. This effectively expands the amount of contact time (online lecture + in person) the professor spends with the students and makes time for active learning in the classroom.

“Flipping” the lectures and homework has been shown to be much more effective than the traditional “sage on the stage” lecture format for students and faculty alike. Most (but not all) students prefer the flipped format [30, 32]. Examples of electromagnetics courses include Introduction to Electromagnetics [33–37] and Numerical Electromagnetics [38], both initially flipped by Dr. Furse in 2007–2009. In many cases, the faculty uses online materials created, at least in part, by others.

This “co-flipping” can make efficient use of faculty time, but requires careful management to be sure the materials used match the teaching style of the faculty who use them [39].

Many university teaching and learning centers provide workshops, training, and support for active learning and flipped teaching. A free, online program has been developed at the University of Utah [40]. This program covers the basics of pedagogy and the flipped class in particular, active learning strategies, and how to create and use instructional videos.

## 25.4 Our Changing Students: *Whom We Teach*

Magdy Iskander has been a leader in efforts to decrease the gender disparity in engineering and other STEM fields. Though the importance of this work has not gone unnoticed, Dr. Iskander’s commitment to act has demonstrated true dedication to empowering women and minorities to find fulfilling and successful careers in engineering fields and has been extensive and notable.

### 25.4.1 *Where Are the Females? ACT Interest Surveys*

A typical electrical engineering classroom in the USA is about 13.6% women [41]. The gender gap between men and women in STEM fields has been noted for over 100 years [42]. One typical explanation is the difference in career-related interests, with females often expressing more interest in social and artistic activities and males in science and technology [43, 44]. But is this difference innate, or is it a function of our society? The fact that there is significant variation in this gender gap around the world points to society as a probable factor.

One way to see the effect of society is to compare how interests may have changed over time. The 1969 moon landing, for instance, has been touted as a boon for STEM education for the decades to follow [45]. To examine how students’ interests have changed over time, we looked at 30 years of self-reported data from surveys of high school students taken with the ACT college entrance examinations. These are shown in Figs. 25.2, 25.3 and 25.4 for all engineering disciplines together, electrical engineering, and computer/information systems, respectively. Distinct peaks of interest, which vary with discipline and gender, are seen.

Interest in engineering overall peaked between 1981 and 1983 and has been declining steadily ever since. Female students did not respond as strongly to that peak (so the *difference* in interest between male and female was greatest in 1981). Interest in electrical engineering shows an even stronger gender disparity, and the even more distinctive peak in 1983 is strongly seen for men but not women. What was going on around 1983 that would create this bubble of interest? Several societal factors are likely to be at play here. One possible factor is the rise of gaming

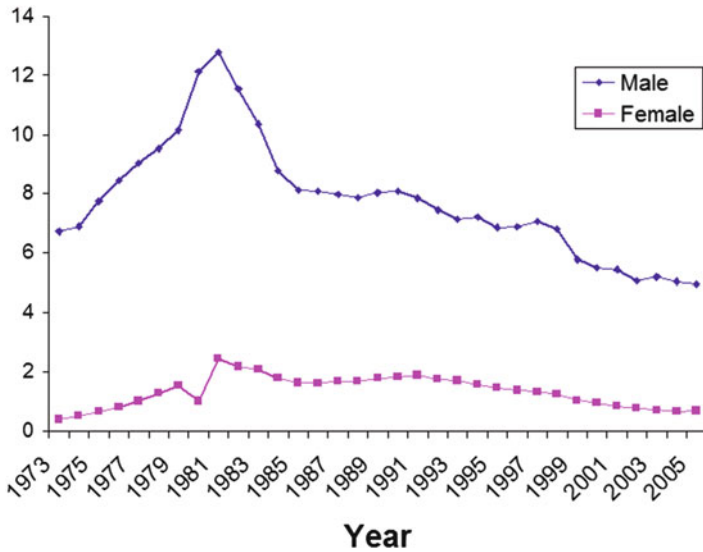


**Fig. 25.2** Percentage of high school students in the USA taking the ACT who indicated that they were interested in engineering. Note the peak between 1981 and 1983 and a steady decline since that period

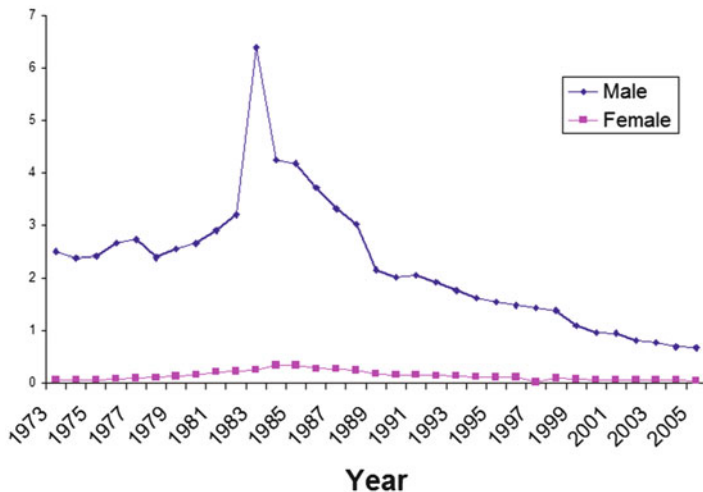


**Fig. 25.3** Percentage of high school students in the USA taking the ACT who indicated they were interested in electrical engineering

computers, early online gaming, and handheld games in the 1980s, only to crash in 1983. These games were more appealing to males than females [46]. Another, similar peak is seen for computer and information systems, followed by a male-only peak in 2000 (located around the rise of online gaming and mobile games).

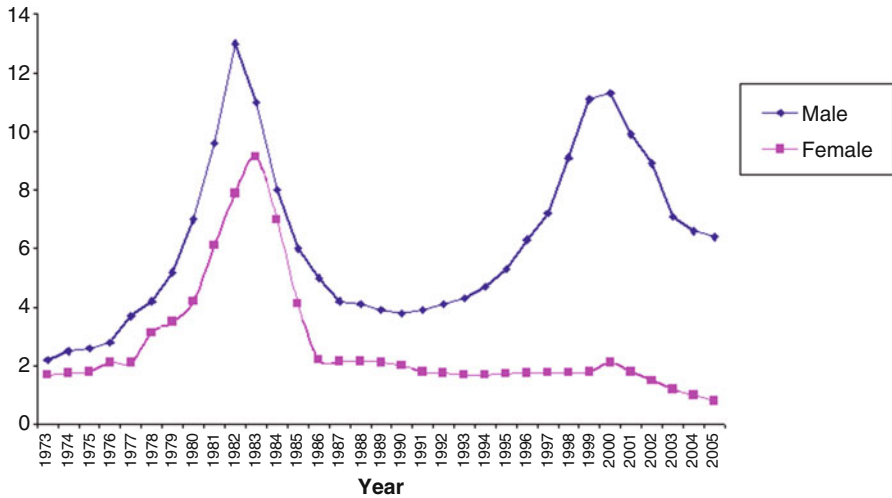


**Fig. 25.4** Percentage of high school students in the USA taking the ACT who indicated that they were interested in computer and information systems

The 1980s was a bleak time for female interest in most engineering fields, while male interest during that decade hit an all-time high. But interest is not everything. Further study of the ACT data showed that females who did express interest in engineering were more likely to have higher ACT math scores than their male counterparts [47]. This may be because males exhibit higher self-efficacy than females on average [48–51] and may therefore overestimate their readiness for a STEM degree.

### 25.4.2 Gender Disparity in Career Guidance Counseling

Most school districts in the USA have career guidance counselors to help high school students select and move toward a career. Guidance counselors are knowledgeable professionals trained for the dissemination of career information. They should, in theory, guide students toward careers matching their skills and interests. But they are also regular people within our society, with potentially the same biases that might be prevalent among the general population. Could this potentially also impact the gender disparity in engineering?

We first surveyed over 100 counselors within the state of Utah. Responses suggest that counselors were only moderately aware of the educational requirements for engineering programs within the state (skills required) and that they were somewhat biased against recommending engineering for female students. Counselors were more likely to consider a male student's abilities (grades) and interest level. While this was also true for female students, conflicting gender stereotypes and a female's

potential familial obligations made counselors less likely to advise engineering for female students. Utah counselors seemed to view engineering as a nontraditional path for females seeking more flexibility and a path with prestige and financial gain for males. Family, gender roles, and social personalities were all reasons why counselors said they would *discourage* a female from going into engineering [52].

To further evaluate counselor attitudes toward gender and engineering, we created vignettes of “John” and “Jane” students and received 185 responses from counselors around the country [52]. The vignettes represented students well-prepared for engineering but with different personalities – one a nonconformist who expresses interest in prestige and recognition and the other socially engaged and wanting to help people. The specific vignette sent to each counselor was randomly assigned a name that was either “John” or “Jane.” Counselors were then asked if and why engineering was or was not an appropriate field for this student. Nonconformist/prestige males (John) were encouraged into engineering about 30% of the time and females (Jane) about 15%. Socially engaged/helping people males (John) were encouraged about 10% of the time, but females (Jane) not at all. When asked why they would make their recommendations, counselors saw the desire to help people as a significant reason a female (but not a male) student would not like engineering, which is particularly ironic, because the main reason women engineers report choosing engineering is to change the world and help people [53].

It is easy to point fingers at biased counselors as the gatekeepers of career information, but it is important to realize that the counselors are just a microcosm of our larger society. The counselors we surveyed gave very well-meaning advice, intended to help students reach happy careers and lives. While additional training on implicit and explicit bias and the engineering field in general may help, this study corroborates the ACT interest study that there is a strong societal impact on student career choice, and all of that occurs well before the student crosses the threshold of a STEM classroom.

### ***25.4.3 The Future: Whom We Teach***

So what can we do? Many colleges and departments have instituted K-12 outreach programs to reach out to interest the community and try to get more students. The National Science Foundation and others have funded numerous of these projects, and many faculty members include them in their broader impact plans for these grants. What works, and what doesn't? What is practical, and what can one faculty member do?

Clearly, there is a problem of scale. Reaching every K-12 student even once a year is impossible for most university programs. Even reaching every high school student is impractical (and most students have selected the general area of career interest by middle school [54]). Most university programs focus on students who are readying themselves for engineering (“college-ready”), in part to recruit them to their university. Other programs focus on students who are marginally prepared, but

whom, with some additional resources, can succeed. These programs often focus their investment on underrepresented (minority and female) students.

#### **25.4.4 Outreach: Inreach – The Benefits**

Outreach is one of the ways many universities reach out to the community to help prepare and recruit future engineers. We may think of outreach as a service the university and professional community provides to recruit more of their own, but a very surprising effect occurs when university students get involved in outreach activities. By reaching out to the community, college students involved in these programs gain confidence as well as motivation and are more likely to graduate from their chosen program. So, by reaching OUT to the community, we are actually reaching IN to our students as well.

In 2008, the University of Utah launched a significant high school outreach effort funded by the National Science Foundation [55, 56]. Each year 45–50 undergraduate engineering students formed engineering ambassador teams in their respective (seven) departments, working with faculty to create active and hands-on projects with a real-world connection and took them out to mathematics, physics, chemistry, and Math, Engineering, Science Achievement (MESA) classes and clubs. They also helped with on-campus tours, summer camps, and demonstrations, visiting with over 2000 college-prep high school students each year. The student ambassadors were diverse in discipline, age, year in school, gender, ethnicity, GPA, and life experience. The college also put effective student success (retention) programs in place. Although it was difficult to quantify the effect of individual programs, the number of engineering students increased 59% from 2007 to 2012, while the enrollment of the university increased by only 9% during the same period, as shown in Fig. 25.5. The proportion of women engineering students increased from 12% to 15%, a total increase of 121% in the number of women students.

Although it was anticipated that the high school student recruitment into engineering would increase as a result of this program, what was less anticipated was the impact of the experience on the undergraduate students on the outreach teams. Engagement, broadly defined, has been seen to increase academic success, retention, and graduation [57–59]. Engagement takes many forms – e.g., academic/“educationally purposeful” [60], social [58], peer-advising [61, 62], living-learning communities [63, 64], and career socialization [65]. On interviewing the ambassadors, four themes emerged [56]. Ambassadors valued connections to faculty, connecting concepts to the real world, connecting with peers, and seeing themselves as engineers. The program was a form of both social and educationally purposeful engagement. The outreach projects they created were often nontrivial engineering that challenged them academically. The program provided a stipend, which was important to enable participation by first-generation and other students who need to work [66]. Members in many teams became very “close” to each other and clearly enjoyed the social aspects of the program [56]. In the end, the

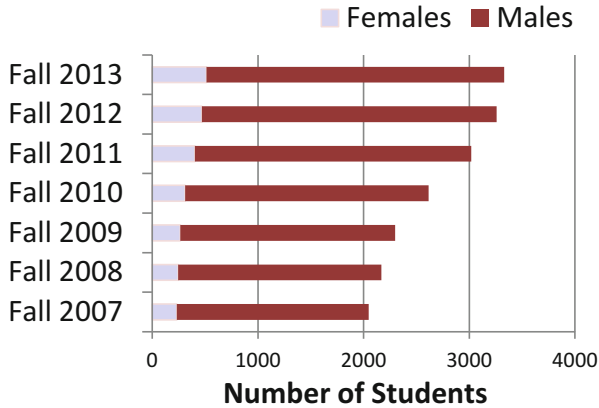


**Fig. 25.5** Enrollment of engineering students at the University of Utah increased 59% from 2007 to 2009. The proportion of women students increased from 12% to 15%, which was a 121% increase in the number of women students

value of outreach for the ambassadors was actually an INreach with substantial tangible personal benefits, gaining self-confidence and increased persistence toward graduation [56, 66, 67].

The benefits of K-12 outreach extend to graduate students as well [68]. The National Science Foundation's (NSF) Graduate Teaching Fellows in K-12 Education (GK-12) program provides graduate students the opportunity to teach in K-12 classrooms. This has been found to improve not only their teaching (which would be expected) but also their research or perspectives on science (perhaps less expected) [69]. Students' oral communication skills also improve significantly [70]. Professional communication is very important for professional success, but many people, including many graduate students, are more afraid of giving a talk than they are of snakes. Outreach is one way to help overcome this fear. Even students who are mortally afraid of presenting their research to their dissertation committees, who have English-as-second-language (ESL) barriers, or who have difficulty organizing their thoughts, will gradually gain skill and confidence that translates from the K-12 classroom to professional settings. Outreach provides enough opportunities for practice, in settings (particularly with younger children) that are successful and nonthreatening. Answering and asking questions with a smile becomes easier.

Public engagement with science goes beyond K-12 outreach to an even broader audience. This movement is gaining momentum, fueled by the need to gain public support of the scientific endeavor and its impact on funding, policy, and general scientific acceptance [71]. Several programs are springing up to help scientists (often graduate students and faculty) distil and share their message. The Alan Alda Center, for instance, uses theatrical improvisation to help scientists gain comfort and skill interacting with the general public. The idea is not so much to "dumb down" the message, but to bring it into terms that are relevant and important to the audience. This program emphasizes teaching and connecting with your audience. The NSF

STEM Ambassadors Program at the University of Utah helps (mainly) graduate students distill their message and share it with groups likely to share their interest. This program emphasizes engagement and partnership with the public and provides peer-based and professional support for training and feedback on the presentations. For example, a biologist studying avian genetics is now teaming with a pigeon fanciers' society.

Another method of reaching large numbers of K-12 students is through their teachers. Dr. Iskander initiated the creation of a Research Experiences for Teachers (RET) program that supports the participation of Hawaii middle school teachers (grades 6–8) in mentored cross-disciplinary research experiences supported by the University of Hawaii College of Engineering and the Hawaii Center for Advanced Communications. From its beginnings in Oahu middle school, this program has expanded each year and now includes 25 schools on four islands. A partnership with NSF and additional industry support called Act111 intend to continue the rollout of this program to even more Hawaii middle schools and continue to provide infrastructure and support to the teachers of Hawaii.

### ***25.4.5 The Future***

The importance and advantage of involving students in public outreach will create continued growth of these types of programs. Many centers, colleges, departments, professional societies, museums, federal agencies, and others provide various forms of teacher training engineering and science disciplines, from online support and curriculum materials to full-degree programs. With such an overwhelming array of information and resources available, students and faculty interested in getting involved in teacher education and outreach efforts are wise to contact the outreach coordinators at their university and team with them, leveraging existing efforts rather than starting from scratch.

## **25.5 The Future: Teaching Today's Learners**

Electromagnetics education has changed hugely in the past two decades. The dramatic innovations in wireless communication and other consumer applications have fueled strong interest in electromagnetics. These applications should be incorporated liberally throughout electromagnetics courses, particularly the early or junior courses that tempt students into this field. From courses that were almost exclusively mathematical to courses that now include numerical simulations and visualizations of many kinds, the ways we teach this content have also changed dramatically. Active learning in the hybrid or flipped class is now very common,



and it allows teachers to effectively spend more time with their students. The availability of relatively inexpensive equipment has increased the number of hands-on design labs, although electromagnetics labs still lag behind labs in other areas of the engineering curriculum. As equipment becomes more and more available, significant advancements are likely in this area. Engineering careers today are broad, global, and collaborative. Students need skills in communication and public outreach and must be comfortable working in diverse, multidisciplinary teams. Labs provide numerous opportunities for experiential learning that can help students gain a deeper understanding of how electromagnetic fields interact with their environment and how we can control them to design functional devices.

Teaching electromagnetics today is an exciting and magical opportunity to envision new ways to help students gain deeper understanding and the ability to work together on creative designs. Creative teachers will continue to push the envelope and research and develop new teaching strategies using the ever-greater collection of tools available. But tools don't make the teacher. It is his/her connection to the students. It is the care and mentoring, the shared excitement, and the curiosity and creativity. It is these characteristics that Dr. Iskander shared with the electromagnetics community, and that spirit of excitement and innovation moves us forward (Fig. 25.6).



**Fig. 25.6** Now-Dr. Cynthia M. Furse (as an MS student) with Dr. Magdy Iskander, making electric field measurements in an anechoic chamber at the University of Utah, 1987

## References

1. M.F. Iskander, *Electromagnetic Fields and Waves* (Prentice–Hall, Upper Saddle River, NJ, 1992)
2. C.M. Furse, M.F. Iskander, Three-dimensional electromagnetic power deposition in tumors using interstitial antenna arrays. *IEEE Trans. Biomed. Eng.* **36**, 977–986 (1989)
3. P.C. Cherry, M.F. Iskander, FDTD analysis of power deposition patterns of an array of interstitial antennas for use in microwave hyperthermia. *IEEE Trans. Microwave Theory Tech.* **40**, 1692–1700 (1992)
4. M.F. Iskander, M.D. Morrison, W.C. Datwyler, M.S. Hamilton, A new course on computational methods in electromagnetics. *IEEE Trans. Educ.* **31**, 101–115 (1988)
5. M.F. Iskander, The CAEME numerical modeling codes, in *1993 IEEE International Symposium on Electromagnetic Compatibility*, 1993, pp. 270–274
6. M.F. Iskander, *Computer Applications in Engineering Education* online journal. (Wiley, 2016), [http://onlinelibrary.wiley.com/journal/10.1002/\(ISSN\)1099-0542](http://onlinelibrary.wiley.com/journal/10.1002/(ISSN)1099-0542). Accessed 10 Nov 2016
7. M.F. Iskander, Technology-based global revitalization of electromagnetic education, in *2015 IEEE International Symposium on Antennas and Propagation & USNC/URSI National Radio Science Meeting*, 2015, pp. 1019–1020
8. M.F. Iskander, S. El-Ghazaly, P.F. Wahid Globalization: setting a new agenda for engineering education, in *IEEE International Symposium on Antennas and Propagation*, 2012
9. K.A. Smith, S.D. Sheppard, D.W. Johnson, R.T. Johnson, Pedagogies of engagement: classroom-based practices. *J. Eng. Educ.* **94**, 87–101 (2005)
10. M. Ando, A. Sihvola, L. Shafai, C.M. Furse, *Commission B (Fields and Waves) International Survey About EM Education* (URSI General Assembly, New Delhi, 2005)
11. S. Rengarajan, L. Shafai, C. Furse, D. Kelley, *Electromagnetics Education in North America* (URSI General Assembly, New Delhi, 2005)
12. D. Fleisch, *A Student's Guide to Maxwell's Equations* (Cambridge University Press, Cambridge, 2008)
13. C.M. Furse, D.A. Christensen, C.H. Durney, *Basic Introduction to Bioelectromagnetics* (CRC press, Boca Raton, FL, 2009)
14. C.M. Furse, R.J. Woodward, M.A. Jensen, Laboratory project in wireless FSK receiver design. *IEEE Trans. Educ.* **47**, 18–25 (2004)
15. J.R. Nagel, Numerical solutions to poisson equations using the finite-difference method [education column]. *IEEE Antennas Propag. Mag.* **56**, 209–224 (2014)
16. YouTube, An excerpt on Sir Michael Faraday from PBS Einstein's big idea (2005), <https://www.youtube.com/watch?v=WQ5o30LcEUI>. Accessed 17 Nov 2016
17. YouTube, Electromagnetic induction and Faraday's law (2013), <https://www.youtube.com/watch?v=vwIdZjdd8fo>. Accessed 17 Nov 2016
18. YouTube, Phet simulation: Faraday's lab on the bar magnet (2016), <https://www.youtube.com/watch?v=kUTHOTRZVLM>. Accessed 17 Nov 2016
19. Phet Interactive Simulations, University of Colorado, Boulder (2013). <https://phet.colorado.edu/en/simulation/legacy/faraday>. Accessed 17 Nov 2013
20. YouTube, Faraday's law – the generator (2016), [https://www.youtube.com/watch?v=-6cC\\_kyhR18](https://www.youtube.com/watch?v=-6cC_kyhR18). Accessed 17 Nov 2016
21. S.W. Bragg, Early experiments of Michael Faraday (1791–1861) – ca. 1933 (1933), <https://www.youtube.com/watch?v=OxTOjb-xK0>. Accessed 17 Nov 2016
22. D.C. Edelson, D.N. Gordin, R.D. Pea, Addressing the challenges of inquiry-based learning through technology and curriculum design. *J. Learn. Sci.* **8**, 391–450 (1999)
23. P. Kirschner, J. Sweller, R.E. Clark, Why unguided learning does not work: an analysis of the failure of discovery learning, problem-based learning, experiential learning and inquiry-based learning. *Educ. Psychol.* **41**, 75–86 (2006)
24. L.W. Anderson, D.R. Krathwohl, B.S. Bloom, *A Taxonomy for Learning, Teaching, and Assessing: A Revision of Bloom's Taxonomy of Educational Objectives* (Allyn & Bacon, Boston, 2001)

25. M. Prince, Does active learning work? A review of the research. *J. Eng. Educ.* **93**, 223–231 (2004)
26. M. Silberman, *Active Learning: 101 Strategies to Teach Any Subject* (Prentice–Hall, Des Moines, IA, 1996)
27. C.M. Furse, 13 crazy, notorious things to do in an EM class. *IEEE Antennas Propag. Mag.* **47**(3), 133–134 (2005)
28. R.M. Felder, D.R. Woods, J.E. Stice, A. Rugarcia, The future of engineering education II. Teaching methods that work. *Chem. Eng. Educ.* **34**, 26–39 (2000)
29. W.F. Smith, M. McKenzie, The Gauss' law song (2001), <https://ww3.haverford.edu/physics/songs/gauss.htm>
30. J. Bergmann, A. Sams, *Flip Your Classroom: Reach Every Student in Every Class Every Day* (International Society for Technology in Education, Eugene, 2012)
31. C.M. Furse, Lecture-free engineering education. *IEEE Antennas Propag. Mag.* **53**(5), 176–179 (2011)
32. R. Toto, H. Nguyen, Flipping the work design in an industrial engineering course, in *39th IEEE Frontiers in Education Conference*, 2009
33. F.T. Arslan, Improved flipped classroom teaching for electromagnetic engineering course, in *Proceedings of the 2015 ASEE Gulf, Southwest Annual Conference*, The University of Texas at San Antonio, 2015
34. M.B. Cohen, A. Zajic, Revitalizing electromagnetics education with the flipped classroom, in *2015 USNC-URSI Radio Science Meeting*, 2015
35. C.M. Furse ECE 3300 Introduction to electromagnetics (2016), <https://utah.instructure.com/courses/224865>. Accessed 5 Dec 2016
36. S.R.H. Hoole, S. Sivasuthan, V.U. Karthik, P.R.P. Hoole, Flip-teaching engineering optimization, electromagnetic product design, and nondestructive evaluation in a semester's course. *Comput. Appl. Eng. Educ.* **23**, 374–382 (2015)
37. M. Stickel, Teaching electromagnetism with the inverted classroom approach: student perceptions and lessons learned, in *Proceedings of the 2014 ASEE Annual Conference & Exposition*, Indianapolis, 2014
38. C.M. Furse, ECE 5340/6340 Numerical electromagnetics (2016), <http://www.eng.utah.edu/~cfurse/ece6340/>. Accessed 5 Dec 2016
39. C.M. Furse, D.H. Ziegenfuss, Co-flipped teaching: experiences sharing the flipped class, in *2015 IEEE International Symposium on Antennas and Propagation & USNC/URSI National Radio Science Meeting*, IEEE, 2015, pp. 1027–1028
40. C.M. Furse, D.H. Ziegenfuss, Teaching flipped (2016), <http://www.teach-flip.utah.edu>. Accessed 5 Dec 2016
41. B. Yoder, *Engineering by the Numbers* (American Society for Engineering Education, Washington, DC, 2014)
42. E.L. Thorndike, *Individuality* (Houghton Mifflin, Boston, 1911)
43. N.E. Betz, L.F. Fitzgerald, *The Career Psychology of Women* (Academic Press, Orlando, 1987)
44. R. Su, J. Rounds, P.I. Armstrong, Men and things, women and people: a meta-analysis of sex differences in interests. *Psychol. Bull.* **135**, 859 (2009)
45. R. Jastrow, H.E. Newell, The space program and the national interest. *Foreign Affairs* **50**, 532–544 (1972)
46. B.S. Greenberg, J. Sherry, K. Lachlan, K. Lucas, A. Holmstrom, Orientations to video games among gender and age groups. *Simul. Gaming* **41**, 238–259 (2010)
47. E.T. Iskander, P.A. Gore, C. Furse, A. Bergerson, Gender differences in expressed interests in engineering-related fields ACT 30-year data analysis identified trends and suggested avenues to reverse trends. *J. Career Assess.* **21**, 599–613 (2013)
48. L.B. Adamson, M.A. Foster, M.L. Roark, D.B. Reed, Doing a science project: gender differences during childhood. *J. Res. Sci. Teach.* **35**, 845–857 (1998)
49. H. Chen, M.-F. Chen, T.-S. Chang, Y.-S. Lee, H.-P. Chen, Gender reality on multi-domains of school-age children in Taiwan: a developmental approach. *Personal. Individ. Differ.* **48**, 475–480 (2010)

50. P. Mantzicopoulos, H. Patrick, A. Samarapungavan, Young children's motivational beliefs about learning science. *Early Child. Res. Q.* **23**, 378–394 (2008)
51. F. Preckel, T. Goetz, R. Pekrun, M. Kleine, Gender differences in gifted and average-ability students comparing girls' and boys' achievement, self-concept, interest, and motivation in mathematics. *Gift. Child Q.* **52**, 146–159 (2008)
52. E.T. Iskander, Gender disparity in engineering fields: an analysis of historic data and school counselors' knowledge, values and attitudes, PhD dissertation, University of Utah, 2013
53. C. Adelman, *Women and Men of the Engineering Path: A Model for Analyses of Undergraduate Careers* (U.S. Department of Education: National Institute for Science Education, Washington, DC, 1998)
54. S. Catsambis, The path to math: gender and racial-ethnic differences in mathematics participation from middle school to high school. *Sociol. Educ.* **67**, 199–215 (1994)
55. Bergerson AA, Furse CM, Work in progress-outreach and retention in the University of Utah Engineering programs, in *2009 39th IEEE Frontiers in Education Conference*, 2009
56. A.A. Bergerson, B.K. Hotchkins, C.M. Furse, Outreach and identity development: new perspectives on college student persistence. *J. Coll. Stud. Retent. Res. Theory Pract.* **16**, 165–185 (2014)
57. A.W. Astin, Student involvement: a developmental theory for higher education. *J. Coll. Stud. Pers.* **25**, 297–308 (1984)
58. J.P. Bean, Nine themes of college student retention, in *College Student Retention: Formula for Student Success* (Praeger Publishers, Westport, CT, 2005), pp. 215–243
59. V. Tinto, Toward a theory of doctoral persistence, in *Leaving College Rethinking the Causes and Cures of Student Attrition* (University of Chicago Press, Chicago, 1993), pp. 230–256
60. G.D. Kuh, T.M. Cruce, R. Shoup, J. Kinzie, R.M. Gonyea, Unmasking the effects of student engagement on first-year college grades and persistence. *J. High. Educ.* **79**, 540–563 (2008)
61. J.M. Dennis, E. Calvillo, A. Gonzalez, The role of psychosocial variables in understanding the achievement and retention of transfer students at an ethnically diverse urban university. *J. Coll. Stud. Dev.* **49**, 535–550 (2008)
62. J.M. Ostrove, S.M. Long, Social class and belonging: implications for college adjustment. *Rev. High. Educ.* **30**, 363–389 (2007)
63. M. Soldner, H. Rowan-Kenyon, K.K. Inkelas, J. Garvey, C. Robbins, Supporting students' intentions to persist in STEM disciplines: the role of living-learning programs among other social-cognitive factors. *J. High. Educ.* **83**, 311–336 (2012)
64. K. Szelényi, N. Denson, K.K. Inkelas, Women in STEM majors and professional outcome expectations: the role of living-learning programs and other college environments. *Res. High. Educ.* **54**, 851–873 (2013)
65. J. Van Maanen, E.H. Schein, *Toward a Theory of Organizational Socialization* (Massachusetts Institute of Technology, Cambridge, MA, 1977)
66. A.A. Bergerson, K.K. Petersen, CARES: mentoring through university outreach. *J. High. Educ. Outreach Engag.* **13**, 45–66 (2009)
67. D.W. James, S. Jurich, S. Estes, *Raising Minority Academic Achievement: A Compendium of Education Programs and Practices* (American Youth Policy Forum, Washington, DC, 2001)
68. B.M. Moskal et al., K-12 outreach: identifying the broader impacts of four outreach projects. *J. Eng. Educ.* **96**, 173–189 (2007)
69. N.M. Trautmann, M.E. Krasny, Integrating teaching and research: a new model for graduate education? *Bioscience* **56**, 159–165 (2006)
70. E. Cejka, M. Pickering, K. Conroy, L. Moretti, M. Portsmore, What do college engineering students learn in K-12 classrooms?: understanding the development of citizenship & communication skills, in *Proceedings of the 2005 American Society for Engineering Education Annual Conference & Exposition*, 2005
71. J. Stilgoe, S.J. Lock, J. Wilsdon, Why should we promote public engagement with science? *Public Underst. Sci.* **23**, 4–15 (2014)



**Cynthia M. Furse** is the Associate Vice President for Research at the University of Utah and Professor in the Electrical and Computer Engineering Department. Dr. Furse is a Fellow of the IEEE and the National Academy of Inventors. Dr. Furse's research focuses on sensors and antennas for biology and remote sensing, including sensors for location of faults on aging aircraft wiring and telemetry systems in the human body. She is a founder of LiveWire Innovation, a spin-off company commercializing sensors for locating electrical faults on live wires. Dr. Furse has taught electromagnetics, wireless communication, circuits, computational electromagnetics, microwave engineering, business for engineers, and antenna design and is currently a leader in the flipped classroom teaching method. She works to interest young students, including women and minorities, in engineering and routinely volunteers in Utah's K-12 schools. She has received

numerous research and teaching awards including the 2009 IEEE Harriett B. Rigas Medal for Excellence in Teaching.



**Elene Tiffany Iskander** is a Licensed Counseling Psychologist working for the State of Iowa Social Security Services. She is a Disability Determination Medical/Psychological Consultant. Prior to her work with the state, she was a Staff Psychologist at the Iowa State University Counseling Center where she coordinated the Outreach and Graduate Student Practicum programs. She graduated from the University of Southern California with degrees in Psychology, Sociology and a Minor in Advertising. She received her Master's Degree from Pepperdine University in Clinical Psychology with an emphasis on Marriage and Family Therapy and her PhD in Counseling Psychology from the University of Utah where her primary area of research was the gender disparity in STEM fields. She studied under a National Science

Foundation grant investigating this phenomenon in a number of fields, including Engineering.

# Chapter 26

## Curriculum Vitae

Magdy F. Iskander

### 26.1 Education

- B.Sc. (1st), Department of Electrical Engineering, University of Alexandria, Alexandria, Egypt, 1969, Distinction and First Class Honor
- M.Sc., University of Manitoba, Winnipeg, Manitoba, Canada, September 1972
- Ph.D., University of Manitoba, Winnipeg, Manitoba, Canada, December 1975

### 26.2 Appointments

- Director, Hawaii Center for Advanced Communications (HCAC), University of Hawaii at Manoa, 2002–present
- Professor of Electrical Engineering, University of Hawaii at Manoa, January 2002–present
- Codirector NSF I/U CRC Center for Circuits and Telecommunication Technologies “Connection One,” Hawaii Site, 2004–present
- Engineering Clinic Endowed Chair Professor, University of Utah, December 2000–2001
- Professor of Electrical and Computer Engineering, University of Utah, 1985–2001
- Program Director, Electrical and Communications and Cyber Systems Division, National Science Foundation, January 1998–October 1999

---

M.F. Iskander (✉)

Hawaii Center for Advanced Communications, University of Hawaii at Manoa,  
Honolulu, HI 96822, USA

e-mail: [magdy@hawaii.edu](mailto:magdy@hawaii.edu)

- Director, Engineering Clinic, College of Engineering, University of Utah, 1986–2001
- Director, European Conceptual Learning of Science Consortium-USA component (CoLoS USA), 1995–1997
- Director, NSF/IEEE Center for Computer Applications in Electromagnetic Education (CAEME), 1989–1994
- Director, State of Utah Center of Excellence, Center of Multimedia Technologies, 1994–1997
- Associate Professor, University of Utah, Department of Electrical Engineering, 1983–1985
- Assistant Professor, University of Utah, Department of Electrical Engineering, 1979–1982
- Research Assistant Professor, University of Utah, Department of Electrical Engineering, January 1978–July 1979
- Research Associate, University of Utah, Department of Electrical Engineering and Department of Bioengineering, March 1977–January 1978
- Research Associate, University of Manitoba, Canada, January 1977–March 1977
- Postdoctoral Fellow, University of Manitoba, Canada, 1976
- Instructor, University of Alexandria, Department of Electrical Engineering, 1969–1971

### **26.3 Awards and Scholarships**

- 2013 University of Hawaii Board of Regents Medal, Excellence in Research
- 2013 IEEE Microwave Theory and Techniques Society Distinguished Educator Award
- 2013 Hi Chang Chai College of Engineering, Teaching Excellence Award
- 2012 IEEE Antennas and Propagation Society Chen-To Tai Distinguished Educator Award
- 2010 University of Hawaii Board of Regents Medal Teaching Excellence
- 2011 Hi Chang Chai College of Engineering, Teaching Excellence Award
- 2010 Northrop Grumman Teaching Excellence Award
- 2002 Distinguished Kuhina Award, Hawaii Visitors and Conventions Bureau
- 2000 University of Utah Distinguished Teaching Award
- 1993 Fellow, The Institute of Electrical and Electronics Engineers. Citation: “For contributions to computational techniques in bioelectromagnetics, near-field dosimetry analysis, and to engineering education”
- 1994–1997 Distinguished Lecturer, IEEE Antennas and Propagation Society
- 1999 Award for Technical Achievements and Innovation in Engineering Education, Brazilian Microwave and Optoelectronics Society
- 1992 Richard R. Stoddard Award for “innovation in electromagnetics education through the establishment of a unique NSF/IEEE National Center for Computer Applications in Electromagnetic Education (CAEME),” given by the IEEE Electromagnetic Compatibility Society

- 1991 George Westinghouse Award for innovation in and distinguished contributions to engineering education. A national award sponsored by the American Society for Engineering Education (ASEE)
- 1985 Curtis W. McGraw Research Award for outstanding early achievement. National award is sponsored by the Engineering Research Council of the American Society for Engineering Education (ASEE)
- 1993 Publishing Excellence Award in the category of Science/Technology/Medicine from the American Association of Publishers, Founding Editor, Computer Application in Engineering Education
- 1984 Technical Achievement Award, Utah Section of IEEE
- 1983 College of Engineering Outstanding Teaching Award, University of Utah
- 1983 Outstanding Paper Award, International Microwave Power Institute, for the most significant technical contribution to the *Journal of Microwave Power*
- 1983 Engineer of the Year Award, by the Utah Section of IEEE
- 1983 College of Engineering, University of Utah, Patent Award for creative, innovative, and practical invention
- 1981 University of Utah President David P. Gardner Faculty Fellow Award
- 1976 National Research Council of Canada, Postdoctoral Fellowship
- 1973–1975 National Research Council of Canada, Postgraduate Scholarship
- 1972–1973 University of Manitoba, Graduate Fellowship
- 1965–1969 University of Alexandria, Undergraduate Scholarship

## 26.4 Elected Offices/Organization

- President, IEEE Antennas and Propagation Society (10,000 members), 2002
- Vice President, IEEE Antennas and Propagation Society, 2001
- Elected Member, IEEE Antennas and Propagation Society Administrative Committee, 1997–2000
- General Chair, IEEE International Conference on Wireless Information Technology and Computational Electromagnetics Conference, Honolulu, HI, March 13–17, 2016
- General Chair, IEEE International Conference on Wireless Information Technology and Systems, Maui, Hawaii, November 11–16, 2012
- Organizer, NSF-sponsored US/Ireland Research and Technology Collaboration Workshop, Dublin, Ireland, November 1–2, 2012
- Organizer, National Science Foundation Electrical, Communications, and Cyber Systems' Division Grantees Conference, Honolulu, HI, November 30–December 3, 2010.
- General Chair, IEEE International Conference on Wireless Information Technology and Systems, Honolulu, HI, August 28–September 3, 2010
- General Chair, IEEE International Symposium on Antennas and Propagation, Honolulu, HI, June 10–15, 2007
- General Chair, Joint IEEE and ACES Conference on Wireless Communications and Applied Computational Electromagnetics, Honolulu, HI, April 12–17, 2005



- Organizer of a workshop on “Wireless Communications Technology,” Cairo, Egypt, January 14–15, 2004
- General Chair, IEEE Conference on Wireless Communications Technology, Honolulu, HI, October 13–17, 2003
- Chair, NSF 1st Wireless Technology Grantees Workshop, National Academy of Sciences, Washington, DC, February 20–21, 2001
- General Chair, IEEE Antennas and Propagation International Symposium and URSI Meeting, Salt Lake City, Utah, July 16–21, 2000
- Chairman, Technical Program Committee, International Conference on Engineering and Computer Education, Rio de Janeiro, Brazil, August 11–14, 1999
- Organized a workshop on “Wireless Information Technology and Networks,” Airlie House, Virginia, July 23–24, 1998
- General Chairman, 26th International Conference, “Frontiers in Education,” sponsored by IEEE Computer Society and IEEE Education Society, Salt Lake City, Utah, November 6–9, 1996
- Organizer of four 4-day symposia on “Microwave Processing of Materials,” held in conjunction with the 1990, 1992, 1994, and 1996 Spring Meetings of the Materials Research Society, San Francisco, California
- General Chairman, International Conference on “Simulation and Multimedia in Engineering Education,” La Jolla, California, January 14–17, 1996
- Program Chairman, International Conference on Simulation in Engineering Education, Las Vegas, Nevada, January 15–19, 1995
- Member of the National Research Council Committee on “Microwave Processing of Materials,” 1992–1994

## 26.5 Publications

### 26.5.1 *Editorship*

#### 26.5.1.1 **Founder and Editor in Chief**

*Computer Applications in Engineering Education*, peer-reviewed journal published by John Wiley & Sons, Inc., 1993–present. Received the 1993 Award in Publishing Excellence in the category of Science/Technology/Medicine from the American Association of Publishers

#### 26.5.1.2 **Guest Editor, Special Issues of Journals**

1. M. F. Iskander, M. Ando, M. A. Jensen, and R. G. Vaughan, Guest Co-editors, *IEEE Transactions on Antennas and Propagation*, Special Issue on Wireless Communications, Vol. 54, No. 11, 2006.

2. M. Ando and M. F. Iskander, Guest Co-editors, *IEICE Transactions on Electronics*, Special issue on Wave Technologies for Wireless and Optical Communications, Vol. E87C, No. 4, September 2004.
3. M. F. Iskander and J. W. Mink, Guest co-editors, *IEEE Transactions on Antennas and Propagation*, Special issue on Wireless Communications, Vol. 50, May 2002.
4. M. F. Iskander, Guest editor, Special issue of the *ACES Journal* (Applied Computational Electromagnetics Society) on electromagnetic education, Vol. 8, No. 1, 1993.
5. M. F. Iskander, Guest editor, Special issue of the *Journal of Microwave Power* on Electromagnetic Techniques for Medical Diagnosis and Imaging, September 1983.
6. M. F. Iskander and C. H. Durney, Guest co-editors, Special issue of the *Journal of Microwave Power* on Electromagnetic Techniques in Energy Applications, March 1983.

### **26.5.1.3 Editor of Conference Proceedings**

1. Proceedings of the 1996 International Conference on Simulation and Multimedia in Engineering Education.
2. Proceedings of the 1996 Frontiers in Education Conference (FIE'96), three volumes and a CD-ROM electronic version.
3. Proceedings of the 1995 International Conference on Simulation in Engineering Education.

### **26.5.2 Books**

1. M. F. Iskander, *Electromagnetic Fields and Waves*, 2nd edition, Waveland Press, 2012, ISBN 1-57766-783-2.
2. M. F. Iskander, *Electromagnetic Fields and Waves*, Waveland Press, 2000, ISBN 1-57766-115-X.
3. M. F. Iskander, *Electromagnetic Fields and Waves*, Solution manual, Waveland Press, 2000, ISBN 1-57766-118-4.
4. M. F. Iskander, *Electromagnetic Fields and Waves*, Prentice-Hall, February 1992, ISBN 0-13-249442-6.
5. M. F. Iskander, *Electromagnetic Fields and Waves*, International Edition, Prentice-Hall, 1993, ISBN 0-13-249780-8.
6. M. F. Iskander, editor, *Computer Applications in Electromagnetics Education: CAEME Software Book*, Vol. II, 1995.
7. M. F. Iskander, editor, *Computer Applications in Electromagnetics Education: Software Book*, Vol. I, 1991.

8. M. F. Iskander and C. C. Guest, *Simulation and Multimedia in Engineering Education*, Guest co-editors, Society for Computer Simulation Series, Vol. 28, No. 1, 1996, ISBN 1-56555-084-6.
9. M. F. Iskander, J. Kiggans, and J.-C. Bolomey, co-editors, *Microwave Processing of Materials V*, MRS Publication, Vol. 430, 1996, ISBN 155899-333-9.
10. M. F. Iskander and C. E. Knadler, Co-editors, *Simulation in Engineering Education*, Society for Computer Simulation Series, Vol. 27, 1995, ISBN 1-56555-038-2.
11. M. F. Iskander, R. J. Lauf, and W. H. Sutton, co-editors, *Microwave Processing of Materials IV*, MRS Publication, Vol. 347, 1994, ISBN 1-55899-2472.
12. D. F. Stein, R. H. Edgar, M. F. Iskander, D. Lynn Johnson, S. M. Johnson, C. G. Lob, J. M. Shaw, W. H. Sutton, and P. K. Tien, *Microwave Processing of Materials*, National Academy Press, Publication NMAB-473, 1994, ISBN 0-309-05027-8.
13. R. Beatty, W. Sutton, and M. F. Iskander, co-editors, *Microwave Processing of Materials III*, MRS Publication, Vol. 269, 1992, ISBN 1-55899-164-6.
14. W. Snyder, W. Sutton, M. F. Iskander, and L. Johnson, co-editors, *Microwave Processing of Materials II*, MRS Publication, Vol. 189, 1991, ISBN 1-55899-078-X.
15. C. H. Durney, H. Massoudi, and M. F. Iskander, co-authors, *Radiofrequency Radiation Dosimetry Handbook*, Fourth Edition, October 1986.
16. C. H. Durney, H. Massoudi, and M. F. Iskander, co-authors, *Radio Frequency Radiation Dosimetry Handbook*, Second Edition, Departments of Electrical Engineering and Bioengineering, University of Utah, Salt Lake City, Utah, June 1978.

### 26.5.3 Book Chapters

1. M. F. Iskander, W. Kim, J. Bell, N. Celik, and Z. Yun, "Antenna Arrays Technologies for Advanced Wireless Systems", *Modern Antenna Handbook*, C. Balanis, Editor, Wiley, July 2008.
2. Z. Yun and M. F. Iskander, "Time reversal with single antenna systems in indoor multipath environments," *Ultra-wideband, Short-Pulse Electromagnetics*, C. Baum, A. P. Stone, and J. S. Tyo, Editors, Springer, pp. 171–178, 2007.
3. M. F. Iskander, W. Boulton, and J. Winters, "Asian Telecommunications Update; Part 2: Focus on China" International Technology Research Institute publication, including CD-ROM, November 2003.
4. M. F. Iskander, "Asian Telecommunication Study—Overview and Summary of Findings," in *Asian Telecommunications Update*, International Technology Research Institute, M. F. Iskander, Study Chair, 2000–2001.

5. M. F. Iskander, "Asian Telecommunication Study—Microwave Technologies and Propagation Models for Wireless Communication Systems," in *Asian Telecommunications Update*, International Technology Research Institute, M. F. Iskander, Study Chair, 2000–2001.
6. M. F. Iskander and Z. Yun, "Electromagnetic Interactions of Handheld Wireless Communication Antennas with the Human Body," in *The Handbook of Antennas in Wireless Communications*, L. Godara, Editor, CRC Press, pp. 25.1–25.21, August 2001.
7. M. F. Iskander, "Channel Characterization and Propagation Models for Wireless Communication Systems," WTEC Study on Wireless Technologies and Information Networks, January 2000.
8. M. Subirats, M. F. Iskander, M. J. White, and J. Kiggans, "FDTD Simulation of Microwave Sintering in Large (500/4000 Liter) Multimode Cavities," in *Microwave Processing of Materials V*, M. F. Iskander, J. O. Kiggans, Jr., and J.-C. Bolomey, Editors, MRS Publication Vol. 430, pp. 29–36, 1996.
9. S. Bringhamurst, M. F. Iskander, and M. J. White, "FDTD Simulations and Analysis of Thin Sample Dielectric Properties Measurements Using Coaxial Probes," in *Microwave Processing of Materials V*, M. F. Iskander, J. O. Kiggans, Jr., and J.-C. Bolomey, Editors, MRS Publication Vol. 430, pp. 237–243, 1996.
10. M. J. White, M. F. Iskander, and H. D. Kimrey, "Development of a Multi-Grid FDTD Code for Three-Dimensional Simulation of Large Microwave Sintering Experiments," in *Microwave Processing of Materials V*, M. F. Iskander, J. O. Kiggans, Jr., and J.-C. Bolomey, Editors, MRS Publication Vol. 430, pp. 325–331, 1996.
11. S. Bringhamurst, M. J. White, and M. F. Iskander, "Numerical Simulation and Experimental Validation of RF Drying," in *Microwave Processing of Materials V*, M. F. Iskander, J. O. Kiggans, Jr., and J. C. Bolomey, Editors, MRS Publication Vol. 430, pp. 339–344, 1996.
12. M. J. White, M. F. Iskander, and S. Bringhamurst, "FDTD Simulation of Induction Heating of Conducting Ceramic Ware," in *Microwave Processing of Materials V*, M. F. Iskander, J. O. Kiggans, Jr., and J.-C. Bolomey, Editors, MRS Publication Vol. 430, pp. 377–382, 1996.
13. M. J. White, S. F. Dillon, M. F. Iskander, and H. D. Kimrey, "Finite-Difference Time-Domain Simulation of Microwave Sintering in a Variable-Frequency Multimode Cavity," in *Microwave Processing of Materials V*, M. F. Iskander, J. O. Kiggans, Jr., and J.-C. Bolomey, Editors, MRS Publication Vol. 430, pp. 487–492, 1996.
14. D. F. Stein, R. H. Edgar, M. F. Iskander, D. L. Johnson, S. M. Johnson, C. G. Lob, J. M. Shaw, W. H. Sutton, P. K. Tien, and T. E. Munns, "Microwave Processing—An Emerging Industrial Technology?," in *Microwave Processing of Materials IV*, M. F. Iskander, R. J. Lauf, and W. H. Sutton, Editors, MRS Publication Vol. 347, pp. 3–7, 1994.
15. S. Bringhamurst, M. F. Iskander, and P. Gartside, "FDTD Simulation of an Open-Ended Metallized Ceramic Probe for Broadband High-Temperature

- Dielectric Properties Measurements,” in *Microwave Processing of Materials IV*, M. F. Iskander, R. J. Lauf, and W. H. Sutton, Editors, MRS Publication Vol. 347, pp. 221–228, 1994.
16. M. J. White, P. J. Gartside, and M. F. Iskander, “Numerical Modeling and Simulation of Electromagnetic Drying Processes,” in *Microwave Processing of Materials IV*, M. F. Iskander, R. J. Lauf, and W. H. Sutton, Editors, MRS Publication Vol. 347, pp. 297–304, 1994.
  17. Z. Huang, M. F. Iskander, J. Tucker, and H. D. Kimrey, “FDTD Modeling of Realistic Microwave Sintering Experiments,” in *Microwave Processing of Materials IV*, M. F. Iskander, R. J. Lauf, and W. H. Sutton, Editors, MRS Publication Vol. 347, pp. 331–345, 1994.
  18. J. Tucker, M. F. Iskander, and Z. Huang, “Calculation of Heating Patterns in Microwave Sintering Using a 3D Finite-Difference Code,” in *Microwave Processing of Materials IV*, M. F. Iskander, R. J. Lauf, and W. H. Sutton, Editors, MRS Publication Vol. 347, pp. 353–362, 1994.
  19. M. F. Iskander, O. Andrade, H. Kimrey, and R. Smith, “Computational Techniques in Modeling and Quantifying Microwave Interactions with Materials,” in *Microwave Theory and Applications in Materials Processing*, a publication of the American Ceramic Society, D. E. Clark, Editor, pp. 141–158, October 1991.
  20. M. F. Iskander, O. Andrade, A. Virkar, H. Kimrey, and R. Smith, “Microwave Processing of Ceramics at the University of Utah—Description of Activities and Summary of Progress,” in *Microwave Theory and Applications in Materials Processing*, a publication of the American Ceramic Society, D. E. Clark, Editor, pp. 35–48, October 1991.
  21. M. F. Iskander, “Potential Electromagnetic Techniques for Medical Applications,” in *Biological Effects and Medical Applications of Electro-magnetic Energy*, O. P. Gandhi, Editor, Prentice-Hall, Inc., 1990.
  22. M. F. Iskander, “Computer Modeling and Numerical Techniques for Quantifying Microwave Interactions with Materials,” in *Microwave Processing of Materials*, W. Snyder, W. Sutton, and M. F. Iskander, Editors, MRS Publication Vol. 189, pp. 149–171, 1988.
  23. C. H. Durney and M. F. Iskander, “Antennas for Medical Applications,” chapter in *Handbook on Antenna Theory and Design*, S. W. Lee and Y. T. Lo, Editors, Van Nostrand Reinhold Company, Chapter 23, pp. 24.1 to 24.60, 1988.
  24. M. F. Iskander, “Medical and Biological Applications of Electromagnetic Techniques—A Relevant Experience to the Microwave Processing of Materials Research,” *Microwave Processing of Materials*, W. H. Sutton, Editor, MRS Publication, Vol. 124, pp. 69–119, 1988.
  25. M. F. Iskander, “Biological Effects of Electromagnetic Radiation: Recent Advances in Theoretical Dosimetry,” *Review of 1984–1986 Radio Science Research*, edited by S. A. Bowhill, International Union of Radio Science, Brussels, Belgium, 1987.

26. M. F. Iskander, "Bioeffects of Electromagnetic Waves," in *Recent Advances of Radio Science 1980–83*, S.A. Bowhill, Editor, International Union of Radio Science, Brussels, Belgium, 1984.
27. M. F. Iskander, "Physical Aspects and Methods of Hyperthermia Production by RF Currents and Microwaves," in *Physical Aspects of Hyperthermia*, Gilbert H. Nussbaum, Editor, Medical Physics Publishing, Madison Wisconsin pp. 151–191, 1982.
28. M. F. Iskander, "Electromagnetic Power Deposition in Biological Models: Numerical Calculations and Phantom Experiments," published in *Physical Aspects of Hyperthermia*, G. H. Nussbaum, Editor, Medical Physics Publishing, Madison Wisconsin, pp. 462–481, 1982.
29. M. F. Iskander and C. H. Durney, "Medical Diagnosis and Imaging Using Electromagnetic Techniques," published in *Theoretical Methods for Determining the Interaction of Electromagnetic Waves with Structures*, J. R. Skwirzynski, Editor, Sijthoff and Noordhoff International Publishers, pp. 835–854, 1981.
30. M. F. Iskander, "Near-Field Irradiation of Biological Models," published in *Theoretical Methods for Determining the Interaction of Electromagnetic Waves with Structures*, J. R. Skwirzynski, Editor, Sijthoff and Noordhoff International Publishers, pp. 883–896, 1981.

#### **26.5.3.1 Electromagnetics 4 Interactive Multimedia**

*Electromagnetics*, 1997.

*Calculus Castle*, CD-ROM, 1996.

*Physics Museum*, CD-ROM, 1997.

Interactive genetics CD-ROM, in collaboration with the Eccles Institute of Human Genetics, 1997.

*Computer Applications in Electromagnetic Education*, software book Vol. II, with CDROM, 1995.

#### **26.5.4 Journal Articles**

1. M. F. Iskander, Z. Yun, F. A. Qazi, A. Das, and G. Sasaki, "Advanced Directional Networking: A Physical Layer Based Implementation," *IEEE Transactions on Antennas and Propagation*, submitted 2017.
2. F. A. Qazi, Z. Yun, M. F. Iskander, "Rural Area Cellular Coverage Optimization Using Geospatial Assets, Genetic Algorithm and Directional Networking," *IEEE Transactions on Antennas and Propagation*, submitted 2017.
3. M. F. Iskander, T. B. Seto, R. G. Perron, F. Qazi, E. Lim, "Clinical Results for Cardio-Pulmonary Stethoscope For monitoring Vital Signs and Lung Water Content Measurements," *Journal of Cardiac Failure*, submitted 2017.

4. D. Green, Z. Yun, M. F. Iskander, and J. F. Harvey, "Propagation Modeling for Realistic Modern Urban Environments: A Comparison with Empirical Models," *IEEE Antennas and Wireless Propagation Letters*, submitted, 2017.
5. D. Bibb, Z. Yun, and M. F. Iskander, "Approximate Source Localization Using Multi-Class Classification," *IEEE Antennas and Wireless Propagation Letters*, submitted, 2017.
6. G. C. Huang, M. F. Iskander, Z. Zhang, and M. Hoque, "Circularly Polarized Antenna Array Designs for Directional Networks," *IEEE Antennas and Wireless Propagation Letters*, submitted, 2017.
7. L. Chang, Z. Zhang, Y. Li, and M. F. Iskander, "Single-Layer Magnetic Current Antenna Array with High Realized Aperture Usage Rate Based on Microstrip Line Structure," *IEEE Transactions on Antennas and Propagation*, Vol. AP-65, No. 2, pp. 584–592, 2017.
8. D. Bibb, R. R. G. Perron, G. C. Huang, and M. F. Iskander, "Development of a Wireless Monitoring System for Microwave-Based Comprehensive Vital Sign Measurement," *IEEE Antennas and Wireless Propagation Letters*, Vol. 15, pp. 1249–1252, 2016.
9. J. Rayno, M. F. Iskander, and M. Kobayashi, "Hybrid Genetic Programming with Accelerating Genetic Algorithm Optimizer for 3D Metamaterial Design," *IEEE Antennas and Wireless Propagation Letters*, Vol. 15, pp. 1743–1746, 2016.
10. S. Y. Lim, A. K. Awelemdy, Z. Yun, and M. F. Iskander, "Experimental Study of Propagation Characteristics in an Open-Trench Drain," *IEEE Antennas and Wireless Propagation Letters*, Vol. 15, pp. 60–63, 2016.
11. G. C. Huang, M. F. Iskander, M. Hoque, S. R. Goodall, and T. Bocskor, "Antenna Array Design and System for Directional Networking," *IEEE Antennas and Wireless Propagation Letters*, Vol. 15, pp. 1141–1144, 2015.
12. Z. Yun and M. F. Iskander, "Ray Tracing for Radio Propagation Modeling: Principles and Applications," *IEEE Access*, pp. 1089–1100, 2015.
13. H. Wang, Z. Zhang, Y. Li, and M. F. Iskander, "A Switched Beam Antenna with Shaped Radiation Pattern and Interleaving Array Architecture," *IEEE Transactions on Antenna and Propagation*, Vol. AP-63, No. 7, pp. 2914–2291, 2015.
14. J. Baker and M. F. Iskander, "A New Design Approach for Electrically Small High-Frequency Antennas," *IEEE Antennas and Wireless Propagation Letters*, Vol. 14, pp. 402–405, 2015.
15. R. R. G. Perron, G. C. Huang, and M. F. Iskander, "Textile Electromagnetic Coupler for Monitoring Vital Signs and Changes in Lung Water Content," *IEEE Antennas and Wireless Propagation Letters*, Vol. 14, pp. 151–154, 2015.
16. J. Rayno, M. F. Iskander, and N. Celik, "Synthesis of Broadband True-3D Metamaterial Artificial Magnetic Conductor Ground Planes Using Genetic Programming," *IEEE Transactions on Antenna and Propagation*, Vol. AP-62, No. 11, pp. 5732–5744, Nov. 2014.

17. S. Y. Lim, Z. Yun, and M. F. Iskander, "Propagation Measurement and Modeling for Indoor Stairwells at 2.4 and 5.8 GHz," *IEEE Transactions on Antenna and Propagation*, Vol. AP-62, No. 9, pp. 4754–4761, 2014.
18. Y. Li, Z. Zhang, Z. Feng, and M. F. Iskander, "Design of Omnidirectional Dual-Polarized Antenna in and Low-Profile Column," *IEEE Transactions on Antenna and Propagation*, Vol. AP-62, No. 4, pp. 2323–2326, 2014.
19. Y. Li, Z. Zhang, Z. Feng, and M. F. Iskander, "Design of Penta-Band Omnidirectional Slot Antenna with Slender Columnar Structure," *IEEE Transactions on Antenna and Propagation*, Vol. AP-62, No. 2, pp. 594–601, 2014.
20. Y. Li, Z. Zhang, C. Deng, Z. Feng, and M. F. Iskander, "2-D Design Scalable Dual Polarized Series-Fed Slot Antenna Array Using Single Substrate," *IEEE Transactions on Antenna and Propagation*, Vol. AP-62, No. 4, pp. 2280–2283, 2014.
21. Y. Li, Z. Zhang, and M. F. Iskander, "Design of Dual Polarized Antenna in Slender and Low Profile Column," *IEEE Transactions on Antenna and Propagation*, Vol. AP-62, No. 4, pp. 2323–2326, 2014.
22. N. Celik, R. Gagarin, G. C. Huang, M. F. Iskander, and B. Berg, "Microwave Stethoscope: Development and Benchmarking of a Vital Signs Sensor Using Computer Controlled Phantoms and Human Studies," *IEEE Transactions on Biomedical Engineering*, Vol. BME-61, No. 8, Pages: 2341–2349, 2014.
23. Y. Li, M. F. Iskander, Z. Zhang, and Z. Feng, "A New Low Cost Leaky Wave Coplanar Waveguide Continuous Transverse Stub Antenna Array using Metamaterial-based Phase Shifters for Beam Steering," *IEEE Transactions on Antenna and Propagation*, Vol. AP-61, No. 7, pp. 3511–3518, 2013.
24. J. Rayno, N. Celik, and M. F. Iskander, "Dual Polarization Cylindrical Long-Slot Array (CLSA) Antenna Integrated with Compact Broadband Baluns and Slot Impedance Transformer," *IEEE Antennas and Wireless Propagation Letters*, Vol. 12, pp. 1384–1387, 2013.
25. K. Wei, Z. Zhang, Z. Feng, and M. F. Iskander, "A Wideband MNG-TL Dipole Antenna With Stable Radiation Patterns," *IEEE Transactions on Antenna and Propagation*, Vol. AP-61, No. 5, pp. 2418–2424, 2013.
26. W. Liu, Z. Zhang, Z. Feng, and M. F. Iskander, "A Compact Microstrip Crossover and its Application in 4x4 Butler Matrix Design," *IEEE Microwave and Wireless Components Letters*, Vol. 22, No. 5, pp. 254–256, 2012.
27. Y. Li, Z. Zhang, J. Zheng, Z. Feng, and M. F. Iskander, "A Compact Hepta-band Loop-Inverted F Reconfigurable Antenna for Mobile Phone," *IEEE Transactions on Antennas and Propagation*, Vol. AP-60, No. 1, pp. 389–392, 2012.
28. K. Wei, Z. Zhang, Z. Feng, and M. F. Iskander, "Periodic Leaky-wave Antenna Array with Horizontally Polarized Omnidirectional Pattern," *IEEE Transactions on Antennas and Propagation*, Vol. AP-60, No. 7, pp. 3165–3173, 2012.
29. K. Wei, Z. Zhang, Z. Feng, and M. F. Iskander, "A MNG-TL Loop Antenna Array with Horizontally Polarized Omnidirectional Patterns," *IEEE Transactions on Antennas and Propagation*, Vol. AP-60, No. 6, pp. 2702–2710, June 2012.



30. H. S. Youn, Y.L. Lee, N. Celik, and M. F. Iskander, "Design of a Cylindrical Long-Slot Array Antenna Integrated with Hybrid EBG/Ferrite Ground Plane," *IEEE Antennas and Wireless Propagation Letters*, Vol. 11, pp. 180–183, 2012.
31. N. Omaki, Z. Yun, N. Celik, H. S. Youn, and M. F. Iskander, "Effective HF Radar Installation in Challenging Terrain Environments for Homeland Security Applications," *IEEE Antennas and Wireless Propagation Letters*, Vol. 10, pp. 1143–1146, September 2011.
32. J. H. Deng, N. Celik, Z. Yun, and M. F. Iskander, "Low Complexity Hybrid Smart Antenna with Directional Elements over Frequency Selective Fading Channel," *Institute of Electronics, Information and Communication Engineers (IEICE) Transactions on Communications*, Vol. E94-B, No. 12, pp. 3610–3613, Dec. 2011.
33. J. S. Kobashigawa, H. S. Youn, M. F. Iskander, and Z. Yun, "Classification of Buried Targets Using Ground Penetrating Radar: Comparison Between Genetic Programming and Neural Networks," *IEEE Antennas and Wireless Propagation Letters*, Vol. 10, PP. 971–974, August 2011.
34. M. F. Iskander, J. Baker, J. K. Nakatsu, S. Y. Lim, and N. Celik, "Multimedia Modules and Virtual Organization Website for Collaborative Research Experience for Teachers in STEM," *Journal of Universal Computer Science*, Vol. 17, No. 9, pp. 1347–1364, 2011.
35. D. N. Elsheakh, H.A. Elsadek, E.A. Abdalla, H.M. Elhennaway, and M. F. Iskander, "Ultra-wideband Microstrip Monopole Antenna by Using Electromagnetic Band Gap Structures," *Progress in Electromagnetic Research Letters*, Vol. 23, pp. 109–118, 2011.
36. M. F. Iskander, Z. Yun, N. Celik, H. S. Youn, N. Omaki, and J. M. Baker, "HF and Passive Radar Designs for Homeland Security Applications," *Marine Technology Society Journal*, Vol. 45, No. 3, pp. 111–119, June 2011.
37. D. Nashaat, H. A. Elsadek, E. A. Abdallah, M. F. Iskander and H. Elhenawy, "UltraWide Bandwidth 2x2 Microstrip Patch Array Antenna Using Electromagnetic Band-gap Structure (EBG)," *IEEE Transactions on Antennas and Propagation*, Vol. AP-59, No. 5, pp. 1528–1534, May 2011.
38. Y. Li, Z. Zhang, J. Zheng, Z. Feng, and M. F. Iskander, "Experimental Analysis of a Wideband Pattern Diversity Antenna with Compact Reconfigurable CPW-to-Slotline Transition Feed," *IEEE Transactions on Antennas and Propagation*, Vol. AP-59, No. 11, pp. 4222–4228, 2011.
39. Z. Zhang, X. Gao, W. Chen, Z. Feng, and M. F. Iskander, "Study of Conformal Switchable Antenna System on Cylindrical Surface for Isotropic Coverage," *IEEE Transactions on Antennas and Propagation*, Vol. AP-59, No. 3, pp. 776–783, 2011.
40. Y. Li, Z. Zhang, Z. Feng, and M. F. Iskander, "Dual-Mode Loop antenna with Compact Feed for Polarization Diversity," *IEEE Antennas and Wireless Propagation Letters*, Vol. 10, pp. 95–98, 2011.

41. N. Celik, R. Gagarin, H. S. Youn, and M. F. Iskander, "A Non-Invasive Microwave Sensor and Signal Processing Technique for Continuous Monitoring of Vital Signs," *IEEE Antennas and Wireless Propagation Letters*, Vol. 10, pp. 286–289, 2011.
42. J. Baker, H. S. Youn, N. Celik, and M. F. Iskander, "Low-Profile Multi-frequency HF Antenna Design for Coastal Radar Applications," *IEEE Antennas and Wireless Propagation Letters*, Vol. 9, pp. 1119–1122, 2010.
43. Y. Li, Z. Zhang, W. Chen, Z. Feng, and M. F. Iskander, "A Compact DVB-H Antenna with Varactor-tuned Matching Circuit," *Microwave and Optical Technology Letters*, Vol. 52, No. 8, pp. 1786–1789, 2010.
44. D. N. Elsheakh, H. A. Elsadek, E. A. Abdallah, M. F. Iskander, and H. Elhenawi, "Reconfigurable Single and Multiband Inset Feed Microstrip Patch Antenna for Wireless Communication Devices," *Progress In Electromagnetics Research C*, Vol. 12, No. xx, pp. 191–201, 2010.
45. D. N. Elsheakh, H. A. Elsadek, E. A. Abdallah, M. F. Iskander, and H. Elhenawy, "Low Mutual Coupling Microstrip Patch Array Antenna by Using Novel Shapes of Defect Ground Structure," *Microwave and Optical Technology Letters*, Vol. 52, No. 5, pp. 1208–1215, 2010.
46. D. N. Elsheakh, H. A. Elsadek, E. A. Abdallah, M. Iskander, and H. Elhenawy, "Ultra-Wideband Coplanar Boat Microstrip Patch with Modified Ground Plane by using Electromagnetic Band-Gap Structure for Wireless Communications," *Microwave and Optical Technology Letters*, Vol. 52, No. 5, pp. 1159–1164, May 2010.
47. D. N. Elsheakh, H. A. Elsadek, E. A. Abdallah, M. F. Iskander, and H. Elhenawy, "Investigated New Embedded Shapes of Electromagnetic Bandgap Structures and Via Effect for Improved Microstrip Patch Antenna Performance," *Progress In Electromagnetics Research B*, Vol. 20, pp. 91–107, 2010.
48. D. N. Elsheakh, M. F. Iskander, E. A. Abdallah, H. A. Elsadek, and H. Elhenawy, "Microstrip Array Antenna with New 2D Electromagnetic Band Gap Structure Shapes to Reduce Harmonics and Mutual Coupling," *Progress In Electromagnetics Research C*, Vol. 12, pp. 203–213, 2010.
49. K. Wei, Z. Zhang, W. Chen, Z. Feng, and M. F. Iskander, "A Tri-band Shunt-fed Omnidirectional Planar Dipole Array," *IEEE Antennas and Wireless Propagation Letters*, Vol. 9, pp. 850–853, 2010.
50. D. N. Elsheakh, M. F. Iskander, H. A. Elsadek, E. A. Abdallah, and H. Elhenawy, "Enhancement of Ultra-Wideband Microstrip Monopole Antenna by Using Unequal Arms V- Shaped Slot printed on Metamaterial Surface," *Microwave and Optical Technology Letters*, Vol. 52, No. 10, pp. 2203–2209, 2010.
51. Y. Li, Z. Zhang, W. Chen, Z. Feng, and M. F. Iskander, "A Switchable Matching Circuit for Compact Wideband Antenna Designs," *IEEE Transactions on Antennas and Propagation*, Vol. AP-58, No. 11, pp. 3450–3457, 2010.
52. Y. Li, Z. Zhang, W. Chen, Z. Feng, and M. F. Iskander, "A Dual-Polarization Slot Antenna Using a Compact CPW Feeding Structure," *IEEE Antennas and Wireless Propagation Letters*, Vol. 9, pp. 191–194, 2010.

53. F. Liu, Z. Zhang, W. Chen, Z. Feng, and M. F. Iskander, "An Endfire Beam-switchable Antenna Array Used in Vehicular Environment," *IEEE Antennas and Wireless Propagation Letters*, Vol. 9, pp. 195–198, 2010.
54. X. Gao, H. Zhong, Z. Zhang, Z. Feng, and M. F. Iskander, "Low-Profile Planar Tri-Polarization Antenna for WLAN Communications," *IEEE Antennas and Wireless Propagation Letters*, Vol. 9, pp. 83–86, 2010.
55. Y. Li, Z. Zhang, W. Chen, Z. Feng, and M. F. Iskander, "A Quadband Antenna with reconfigurable Feedings," *IEEE Antennas and Wireless Propagation Letters*, Vol. 8, pp. 1069–1071, 2009.
56. J. M. Bell, and M. F. Iskander, "Experimental Analysis of an Ultra-wideband Hybrid EBG/Ferrite Ground Plane," *IEEE Transactions on Instrumentation and Measurements*, Vol. IM-58, pp. 2899–2905, 2009.
57. D. N. Elsheakh, H. A. Elsadek, E. A. Abdallah, M. F. Iskander, and H. Elhenawy, "Ultrawide Bandwidth Umbrella-Shaped Microstrip Monopole Antenna Using Spiral Artificial Magnetic Conductor (SAMC)," *IEEE Antennas and Wireless Propagation Letters*, Vol. 8, pp. 1255–1258, 2009.
58. D. N. Elsheakh, H. A. Elsadek, E. A. Abdallah, M. F. Iskander, and H. Elhenawy, "Enhancement of Microstrip Monopole Antenna Bandwidth by Using EBG Structures," *IEEE Antennas and Wireless Propagation Letters*, Vol. 8, pp. 959–962, 2009.
59. Z. Yun, S. Y. Lim, and M. F. Iskander, "Use of Geospatial Resources for Radio Propagation Prediction in Urban Areas," *IEEE Antennas and Wireless Propagation Letters*, Vol. 8, pp. 587–591, 2009.
60. Z. Yun, S. Y. Lim, J. M. Baker, N. Celik, H. S. Youn, and M. F. Iskander, "Propagation Modeling and Measurement for a Multifloor Stairwell," *IEEE Antennas and Wireless Propagation Letters*, Vol. 8, pp. 583–586, 2009.
61. D. N. Elsheakh, H. A. Elsadek, and M. F. Iskander, "Ultra-Wideband and Miniturization of Microstrip Monopole Patch Antenna (MMPA) with Modified Ground Plane for Wireless Applications," *Progress in Electromagnetics Research*, Vol. 10, pp. 171–184, 2009.
62. H. Zhong, Z. Zhang, W. Chen, Z. Feng, and M. F. Iskander, "A Tri-polarization Antenna Fed by Proximity Coupling and Probe," *IEEE Antennas and Wireless Propagation Letters*, Vol. 8, pp. 465–467, 2009.
63. N. Celik, M. F. Iskander, and Z. Zhang, "Experimental Verification of the Hybrid Smart Antenna Algorithm with Modulated Waveforms," *IEEE Antennas and Wireless Propagation Letters*, Vol. 8, pp. 236–239, 2009.
64. S. Lim and M. F. Iskander, "Design of a Dual-Band, Compact Yagi Antenna Over an EBG Ground Plane," *IEEE Antennas and Wireless Propagation Letters*, Vol. 8, pp. 88–91, 2009.
65. N. Celik, M. F. Iskander, R. Emrick, S. Franson, and J. Holmes, "Implementation and Experimental Verification of a Smart Antenna System Operating at 60 GHz Band," *IEEE Transactions on Antennas and Propagation*, Vol. AP-56, No. 9, pp. 2790–2800, 2008.

66. J. M. Bell, and M. F. Iskander, "Effective Propagation Properties of an Enhanced Hybrid EBG/ferrite Ground Plane," *IEEE Antennas and Wireless Propagation Letters*, Vol. 7, pp. 74–77, 2008.
67. Z. Yun, S. Lim, and M. F. Iskander, "An Integrated Method of Ray tracing and Genetic Algorithm for Optimizing Coverage in Indoor Wireless Networks," *IEEE Antennas and Wireless Propagation Letters*, Vol. 7, pp. 145–147, 2008.
68. J. M. Bell, and M. F. Iskander, "Equivalent Circuit Model of an Ultra-wideband Hybrid EBG/Ferrite Structure," *IEEE Antennas and Wireless Propagation Letters*, Vol. 7, pp. 573–576, 2008.
69. Z. Zhang, J.-C. Langer, K. Li, and M. F. Iskander, "Design of Ultrawideband Mobile Phone Stubby Antenna (824 MHz-6 GHz)," *IEEE Transactions on Antennas and Propagation*, Vol. AP-56, No. 7, pp. 2107–2111, July 2008.
70. Z. Zhang, W. Chen, Z. Feng, and M. F. Iskander, "Integrated Dual-band Antenna System Design Incorporating Cell Phone Bezel," *IEEE Antennas and Wireless Propagation Letters*, Vol. 7, pp. 585–587, 2008.
71. N. Celik, and M. F. Iskander, "Genetic-Algorithm-Based Antenna Array Design for a 60 GHz Hybrid Smart Antenna System," *IEEE Antennas and Wireless Propagation Letters*, Vol. 7, pp. 795–798, 2008.
72. Z. Yun, M. F. Iskander, and J. S. Kobashigawa, "On the Sensitivity and Resolution of Using Magneto-Telluric Gradient Method for Detecting Buried Objects," *Electronics Letters*, Vol. 44, pp. 110–111, Jan. 2008.
73. W. Kim, M. Iskander, and C. Krowne, "Modified Green's Function and Spectral Domain Approach for Analyzing Anisotropic and Multi-Dielectric Layers Coplanar Waveguide Ferroelectric Phase Shifters," *IEEE Transactions on Microwave Theory and Techniques*, Vol. AP-55, No. 2, part 2, pp. 402–409, Feb. 2007.
74. Z. Yun, M. F. Iskander, S. Y. Lim, D. He, and R. Martinez, "Radio Wave Propagation Prediction Based on 3D Building Structures Extracted from 2D Images," *IEEE Antennas and Wireless Propagation Letters*, Vol. 6, pp. 557–559, 2007.
75. J. M. Bell, M. F. Iskander, and J. J. Lee, "Ultra-wideband Hybrid EBG/Ferrite Ground Plane for Low Profile Array Antennas," *IEEE Transactions on Antennas and Propagation*, Vol. AP-55, No. 1, pp. 4–12, January 2007.
76. W.G. Hui, J. M. Bell, M. F. Iskander, and J. J. Lee, "Low Cost Microstrip Based Ferrite Phase Shifter Utilizing Circular Polarization," *IEEE Antennas and Wireless Propagation Letters*, Vol. 6, pp. 86–89, 2007.
77. C. Takahashi, Z. Yun, M. F. Iskander, "Propagation Prediction and Site Planning Software for Wireless Communication Systems," *IEEE Antennas and Propagation Magazine*, Vol. 49, No. 2, pp. 52–60, April, 2007.
78. W. Kim, M. F. Iskander, and W.D. Palmer, "Integrated Phased Array Antenna Design Using Ferroelectric Materials and Continuous Transverse Stub Technology," *IEEE Transactions on Antennas and Propagation*, Vol. AP-54, No. 11, part 1, pp. 3095–3105, 2006.

79. N. Celik, W. Kim, M. F. Demirkol, M. F. Iskander, and R. Emrick, "Implementation and Experimental Verification of Hybrid Smart-antenna Beamforming Algorithm," *IEEE Antennas and Wireless Propagation Letters*, Vol. 5, pp. 280–283, 2006.
80. Z. Zhang, M. F. Iskander, J. C. Langer, and J. Mathews, "Dual-band WLAN Antenna Using Internal Matching Technique," *IEEE Transactions on Antennas and Propagation*, Vol. AP-53, pp. 1813–1818, 2005.
81. W. Kim and M. F. Iskander, "A New Coplanar Waveguide Continuous Transverse Stub (CPW-CTS) Antenna for Wireless Communications," *IEEE Antennas and Wireless Propagation Letters*, Vol. 4, pp. 172–174, 2005.
82. M. Rezk, W. Kim, Z. Yun, and M. F. Iskander, "Performance Comparison of a Novel Hybrid Smart Antenna System Versus the Fully Adaptive and Switched Beam Antenna Arrays," *IEEE Antennas and Wireless Propagation Letters*, Vol. 4, pp. 285–288, 2005.
83. L. Yu, R. Atyia, M. F. Iskander, and R.W. Grow, "New Multimedia Modules in CAEME CD-ROM Series: Wave Motion and Mechanics," *Computer Applications in Engineering Education*, Vol. 13, No. 1, pp. 72–83, 2005.
84. J. M. Bell and M. F. Iskander, "A Low-Profile Archimedean Spiral Antenna Using an EBG Ground Plane," *IEEE Antennas and Wireless Propagation Letters*, Vol. 3, pp. 223–226, 2004.
85. W. Kim and M. F. Iskander, "High Performance Low Cost Phase Shifters Design Based on the Ferroelectric Materials Technology," *Electronics Letters*, Vol. 40, No. 21, pp. 1345–1346, Oct. 2004.
86. R. Isom, M. F. Iskander, Z. Yun, and Z. Zhang, "Design and Development of Single and Multiband Coaxial Continuous Transverse Stub (CTS) Antenna Arrays," *IEEE Transactions on Antennas and Propagation*, Vol. AP-52, No. 8, pp. 2180–2183, Aug. 2004.
87. M. F. Iskander and Z. Yun,<sup>1</sup> "Advances in Propagation Modeling of Wireless Communications Environments and Systems," *Institute of Electronics, Information and Communication Engineers (IEICE) Transactions on Electronics*, Vol. E87-C, No. 9, pp. 1441–1448, Sept. 2004.
88. Z. Yun, M. F. Iskander, and Z. Zhang, "Complex-wall Effect on Propagation Characteristics and MIMO Capacities For an Indoor Wireless Communication Environment," *IEEE Transactions on Antennas and Propagation*, Vol. AP-52, No. 4, pp. 914–922, April 2004.
89. R. K. Sorensen, M. F. Iskander, and J. J. Lee, "Low-cost Nonplanar Microstrip- line Ferrite Phase Shifter Utilizing Circular Polarization," *IEEE Microwave and Wireless Components Letters*, Vol. 14, No. 1, pp. 25–27, January 2004.
90. Z. Zhang, M. F. Iskander, Z. Yun, and A. Host-Madsen, "Hybrid Smart Antenna System Using Directional Elements – Performance Analysis in Flat Rayleigh Fading," *IEEE Transactions on Antennas and Propagation*, Vol. AP-51, No. 10, pp. 2926–2935, Oct. 2003.

---

<sup>1</sup>Invited paper.

91. M. F. Iskander and Z. Yun,<sup>2</sup> “Propagation Prediction Models for Wireless Communication Systems,” *IEEE Transactions on Microwave Theory and Techniques*, Vol. MTT-50, No. 3, pp. 662–673, March 2002.
92. M. F. Iskander,<sup>3</sup> “Technology-Based Electromagnetic Education,” *IEEE Transactions on Microwave Theory and Techniques*, Vol. MTT-50, No. 3, pp. 1015–1020, March 2002.
93. Z. Yun, Z. Zhang, and M. F. Iskander, “A Ray-Tracing Method Based on the Triangular Grid Approach and Application to Propagation Prediction in Urban Environments,” *IEEE Transactions on Antennas and Propagation*, Vol. AP-50, No. 5, pp. 750–758, 2002.
94. Z. Zhang, R. Sorensen, Z. Yun, M. F. Iskander, and J. F. Harvey, “A Ray-Tracing Approach for Indoor/Outdoor Propagation Through Window Structures,” *IEEE Transactions on Antennas and Propagation*, Vol. AP-50, No. 5, pp. 742–749, 2002.
95. M. F. Iskander, Z. Zhang, Z. Yun, R. Isom, M. Hawkins, R. Emrick, B. Bosco, J. Synowczynski, and B. Gersten, “New Phase Shifters and Phased Antenna Array Designs Based on Ferroelectric Materials and CTS Technologies,” *IEEE Transactions on Microwave Theory and Techniques*, Vol. MTT-49, No. 12, pp. 2547–2553, 2001.
96. M. F. Iskander, Z. Zhang, Z. Yun, and R. Isom, “Coaxial Continuous Transverse Stub (CTS) Array,” *IEEE Microwave and Wireless Components Letters*, Vol. 11, pp. 489–491, 2001.
97. M. F. Iskander, Z. Yun, Z. Zhang, R. Jensen, and S. Redd, “Design of a Low-Cost 2D Beam-Steering Antenna Using Ferroelectric Material and the CTS Technology,” *IEEE Transactions on Microwave Theory and Techniques*, MTT-49, No. 5, pp. 1000–1003, May 2001.
98. Z. Zhang, Z. Yun, and M. F. Iskander, “3D Tetrahedron Ray Tracing Algorithm,” *Electronics Letters*, Vol. 37, No. 6, pp. 334–335, March 2001.
99. M. J. White, M. F. Iskander, and Z. Yun, “A New 3D FDTD Multi-Grid Technique with Dielectric Traverse Capabilities,” *IEEE Transactions on Microwave Theory and Techniques*, Vol. MTT-49, No. 3, pp. 422–430 March 2001.
100. Z. Yun, M. F. Iskander, and Z. Zhang, “A Fast Ray Tracing Procedure Using Space Division with Uniform Rectangular Grid,” *Electronics Letters*, Vol. 36, No. 10, pp. 895–897, May 2000.
101. Z. Zhang, Z. Yun, and M. F. Iskander, “A New Ray Tracing Method for Propagation Models in Wireless Communications,” *Electronics Letters*, Vol. 36, No. 5, pp. 464–465, March 2000.
102. Z. Yun and M. F. Iskander, “Analysis and Design of Large Antenna Arrays Using Multi-Grid FDTD and Floquet Boundary Condition,” *Electromagnetics*, Vol. 20, pp. 445–452, 2000.

---

<sup>2</sup>Invited for the 50th Anniversary Special Issue.

<sup>3</sup>Invited for the 50th Anniversary Special Issue.

103. M. F. Iskander, R. Quintero-Illera, and Z. Yun, "Polarization and Human Body Effects on the Microwave Absorption in a Human Head Exposed to Radiation From Hand-Held Devices," *IEEE Transactions on Microwave Theory and Techniques*, Vol. MTT-48, No. 11, pp. 1979–1987, 2000.
104. S. Sanz, M. F. Iskander, and L. Yu, "Development of an Interactive Multimedia Application in Electromagnetics: Antenna Theory and Design," *Computer Applications in Engineering Education*, Vol. 8, No. 1, pp. 11–17, 1999.
105. J. Fabrega, S. Sanz, and M. F. Iskander, "New LabVIEW-Based Software Packages and Multimedia Modules for Electromagnetics Education," *Computer Applications in Engineering Education*, Vol. 6, No. 4, pp. 1347–1364, 1998.
106. N. Padros, J. Ortigosa, J. Baker, M. F. Iskander, and B. Thornberg, "Comparative Study of High Performance GPS Receiving Antenna Designs," *IEEE Transactions on Antennas and Propagation*, Vol. AP-45, No. 4, pp. 698–706, 1997.
107. S. Bringham, M. F. Iskander, and M. J White, "Thin-Sample Measurements and Error Analysis of High-Temperature Coaxial Dielectric Probes," *IEEE Transactions on Microwave Theory and Techniques*, Vol. MTT-45, No. 12, pp. 2073–2083, 1997.
108. O. de los Santos Vidal and M. F. Iskander, "Multimedia Modules for Electromagnetics Education," *Computer Applications in Engineering Education*, Vol. 5, No. 4, pp. 257–267, 1997.
109. M. J. White, M. F. Iskander, and Z. Huang, "Development of a Multi-Grid FDTD Code for Three-Dimensional Applications," *IEEE Transactions on Antennas and Propagation*, Vol. AP-45, No. 10, pp. 1512–1517, 1997.
110. M. Subirats, M. F. Iskander, and M. J White, "FDTD Simulation of Microwave Sintering in Large (500/4000 liter) Multimode Cavities," *Journal of Microwave Power and Electromagnetic Energy*, Vol. 32, No. 3, pp. 161–170, 1997.
111. S. Bringham and M. F. Iskander, "Open-Ended Metalized Ceramic Coaxial Probe for High Temperature Dielectric Properties Measurements," *IEEE Transactions on Microwave Theory and Techniques*, Vol. MTT-44, pp. 926–935, 1996.
112. M. F. Iskander, J. C. Catten, R. M. Jameson, A. Rodriguez-Balcells, and A. K. Jones, "Interactive Multimedia CD-ROMs for Education," *Computer Applications in Engineering Education*, Vol. 4, No. 1, pp. 51–60, 1996.
113. P. C. Cherry and M. F. Iskander, "FDTD Analysis of High-Frequency Electronic Packages and Interconnections Effects," *IEEE Transactions on Microwave Theory and Techniques*, Vol. MTT-43, No. 10, pp. 2445–2451, 1995.
114. M. F. Iskander, J. C. Catten, R. Jameson, A. Jones, and A. Balcells, "Development of Multimedia Modules for Education," *Computer Applications in Engineering Education*, Vol. 3, No. 2, pp. 97–110, 1995.
115. M. F. Iskander and E. Jensen, "TLLine: Software for Sinusoidal Steady-State Analysis of Transmission Lines," *Computer Applications in Engineering Education*, Vol. 2, No. 3, pp. 185–194, 1994.

116. M. F. Iskander, R. L. Smith, O. Andrade, H. Kimrey, and L. Walsh, "FDTD Simulation of Microwave Sintering in Multimode Cavities," *IEEE Transactions on Microwave Theory and Techniques*, Vol. MTT-42, pp. 793–800, 1994.
117. M. F. Iskander,<sup>4</sup> "Computer Modeling and Numerical Simulation of Microwave Heating Systems," *MRS Bulletin*, Vol. XVIII, No. 11, pp. 30–36, 1993.
118. M. F. Iskander,<sup>5</sup> "Modeling the Microwave Process—Challenges and New Directions," *Ceramic Transactions on Microwaves: Theory and Application in Materials Processing II*, D. Clark, W. Tinga, and J. Laia, Jr., Eds., Vol. 36, pp. 167–187, 1993.
119. J. Newman, L. Walsh, R. Evans, T. Tholen, O. Andrade, M. Iskander, K. Bunch, and H. Kimrey, "Experimental Validation of Numerical Simulations of the Microwave Sintering Process," *Ceramic Transactions on Microwaves: Theory and Application in Materials Processing II*, D. Clark, W. Tinga, and J. Laia, Jr., Eds., Vol. 36, pp. 229–237, 1993.
120. V. Janas, C. Malarkey, M. Iskander, O. Andrade, and S. Bringham, "Dielectric Property Measurement of Ceramic Bodies," *Ceramic Transactions on Microwaves: Theory and Application in Materials Processing II*, D. Clark, W. Tinga, and J. Laia, Jr., Eds., Vol. 36, pp. 493–502, 1993.
121. M. F. Iskander, "Computer-Based Electromagnetic Education," *ACES Journal*, Vol. 8, No. 1, pp. 77–107, 1993.
122. M. F. Iskander, T. Reed, and J. Breen III, "Interactive Video Lessons for Electromagnetic Education," *Computer Applications in Engineering Education*, Vol. 1, No. 2, pp. 147–158, 1993.
123. S. Bringham, M. Iskander, and O. Andrade, "New Metallized Ceramic Coaxial Probe for High-Temperature Broadband Dielectric Properties Measurements," *Ceramic Transactions on Microwaves: Theory and Application in Materials Processing II*, D. Clark, W. Tinga, and J. Laia, Jr., Eds., Vol. 36, pp. 503–510, 1993.
124. M. F. Iskander, "Computer-Based Electromagnetic Education" (invited), *IEEE Transactions on Microwave Theory and Techniques*, Vol. MTT-41, No. 6/7, pp. 920–931, 1993.
125. P. C. Cherry and M. F. Iskander, "Calculations of Heating Patterns of an Array of Microwave Interstitial Antennas," *IEEE Transactions on Biomedical Engineering*, Vol. BME-40, No. 8, pp. 771–779, 1993.
126. M. F. Iskander, "NSF/IEEE CAEME Center: An Exciting Opportunity to Align Electromagnetic Education with the Nineties," *Computer Applications in Engineering Education*, Vol. 1, No. 1, pp. 33–44, September 1992.
127. P. C. Cherry and M. F. Iskander, "FDTD Analysis of an Array of Interstitial Antennas for Use in Microwave Hyperthermia," *IEEE Transactions on Microwave Theory and Techniques*, Vol. MTT-40, pp. 1692–1700, August 1992.

---

<sup>4</sup>Invited paper.

<sup>5</sup>Invited paper.



128. S. Bringham, O. M. Andrade, and M. F. Iskander, "High-Temperature Dielectric Properties Measurements of Ceramics," in *Microwave Processing of Materials III*, Vol. MRS 269, pp. 561–568, 1992.
129. B. Chapman, M. F. Iskander, R. L. Smith, and O. M. Andrade, "Simulation of Sintering Experiments in Single-Mode Cavities," in *Microwave Processing of Materials III*, Vol. MRS 269, pp. 53–59, 1992.
130. J. Tucker, R. L. Smith, M. F. Iskander, and O. M. Andrade, "Dynamic Model for Calculating Heating Patterns During Microwave Sintering," in *Microwave Processing of Materials III*, Vol. MRS 269, pp. 61–67, 1992.
131. O. M. Andrade, M. F. Iskander, and S. Bringham, "High Temperature Broadband Dielectric Properties Measurement Techniques," in *Microwave Processing of Materials III*, Vol. MRS 269, pp. 527–539, 1992.
132. R. L. Smith, M. F. Iskander, O. M. Andrade, and H. Kimrey, "Finite-Difference Time-Domain Simulation of Microwave Sintering in Multimode Cavities," in *Microwave Processing of Materials III*, Vol. MRS 269, pp. 47–52, 1992.
133. T. S. Lind and M. F. Iskander, "On the Coupling Characteristics of Coplanar Waveguides and Microstrip Lines to Multi-Layer Dielectric Media," *IEEE Transactions on Electromagnetic Compatibility*, Vol. EMC-34, pp. 117–123, May 1992.
134. M. F. Iskander, "Interstitial Antennas for Microwave Hyperthermia," *CRC Critical Reviews in Biomedical Engineering*, 1992.
135. J. Butler, D. Rytting, M. F. Iskander, and R. Pollard, "16-Term Error Model and Calibration Procedure for On-Wafer Network Analysis Measurements," *IEEE Transactions on Microwave Theory and Techniques*, Vol. MTT-39, pp. 2211–2217, December 1991.
136. M. F. Iskander, "Computational Techniques in Bioelectromagnetics," *Computer Physics Communications*, Vol. 68, pp. 224–254, 1991.
137. M. F. Iskander, H. Y. Chen, and J. E. Penner, "Resonance Optical Absorption by Fractal Agglomerates of Smoke Aerosols," *Atmospheric Environment*, Vol. 25, pp. 2563–2569, 1991.
138. M. F. Iskander, "Computational Techniques in Modeling and Quantifying Microwave Interactions with Materials," *Ceramic Transactions*, Vol. 21, pp. 141–158, 1991.
139. M. F. Iskander, O. Andrade, A. Virkar, H. Kimrey, R. Smith, S. Lamoreaux, C. Cheng, C. Tanner, R. Knowlton, and K. Mehta, "Microwave Processing of Ceramics at the University of Utah—Description of Activities and Summary of Progress," *Ceramic Transactions*, Vol. 21, pp. 35–48, 1991.
140. H. Y. Chen, M. F. Iskander, and J. E. Penner, "An Empirical Formula for Optical Absorption by Fractal Aerosol Agglomerates," *Applied Optics*, Vol. 30, pp. 1547–1551, 1991.
141. M. F. Iskander, A. M. Tumeah, and C. M. Furse, "Evaluation and Optimization of the Electromagnetic Characteristics of Interstitial Antennas for Hyperthermia," *International Journal of Radiation Oncology, Biology, and Medicine*, Vol. 18, pp. 895–902, 1990.

142. H. Y. Chen, M. F. Iskander, and J. E. Penner, "Light Scattering and Absorption by Fractal Agglomerates and Coagulations of Smoke Aerosols," *Journal of Modern Optics*, Vol. 37, pp. 171–182, February 1990.
143. M. F. Iskander and T. S. Lind, "Electromagnetic Coupling of Coplanar Waveguides and Microstrip Lines to Highly Lossy Dielectric Medium," *IEEE Transactions on Microwave Theory and Techniques*, Vol. MTT-37, pp. 1910–1917, December 1989.
144. K. Joo and M. F. Iskander, "A New Procedure of Point Matching Method for Calculating the Absorption and Scattering of Lossy Dielectric Object," *IEEE Transactions on Antennas and Propagation*, Vol. AP-38, pp. 1483–1490, 1989.
145. M. Tumei and M. F. Iskander, "Performance Comparison of Available Interstitial Antennas for Microwave Hyperthermia," *IEEE Transactions on Microwave Theory and Techniques*, Vol. MTT-37, pp. 1126–1133, 1989.
146. M. Furse and M. F. Iskander, "Three-Dimensional Electromagnetic Power Deposition in Tumors Using Interstitial Antenna Arrays," *IEEE Transactions on Biomedical Engineering*, Vol. BME-36, pp. 977–986, 1989.
147. M. F. Iskander, H. Y. Chen, and J. E. Penner, "Optical Scattering and Absorption by Branched Chains of Aerosols," *Applied Optics*, Vol. 28, pp. 3083–3091, August 1989.
148. M. F. Iskander, H. Y. Chen, and T. V. Doung, "A New Sectioning Procedure for Calculating Scattering and Absorption by Elongated Dielectric Objects," *IEEE Transactions on Electromagnetic Compatibility*, Vol. EMC-31, pp. 157–163, May 1989.
149. M. F. Iskander and A. Tumei, "Optimization of Interstitial Antennas for Hyperthermia Applications," *IEEE Transactions on Biomedical Engineering*, Vol. BME-36, pp. 238–246, February 1989.
150. M. F. Iskander, H. Y. Chen, and J. E. Penner, "Scattering and Absorption of Very Long Aerosol Particles," *Aerosol Science and Technology*, Vol. 10, No. 1, pp. 172–180, 1989.
151. M. F. Iskander, M. Morrison, and M. Hamilton, "A New Course on Computer Methods in Electromagnetics," *IEEE Transactions on Education*, Vol. ED-31, pp. 101–115, 1988.
152. M. F. Iskander, "A New Undergraduate Course on Computational Methods in Engineering Electromagnetics," *Computers in Education Journal*, June 1988.
153. M. F. Iskander, S. C. Olson, and J. F. McCalmont, "Near-Field Absorption Characteristics of Spheroidal Models in the Resonance Frequency Range," *IEEE Transactions on Microwave Theory and Techniques*, Vol. MTT-35, pp. 776–780, 1987.
154. M. F. Iskander, S. C. Olson, R. E. Benner, and D. Yoshida, "Optical Scattering by Metallic and Carbon Aerosols of High Aspect Ratio," *Applied Optics*, Vol. 25, pp. 2514–2520, 1986.
155. S. C. Olson and M. F. Iskander, "A New *In Situ* Procedure for Measuring the Dielectric Properties of Low-Permittivity Materials," *IEEE Transactions on Instrumentation and Measurement*, Vol. IM-35, pp. 2–6, 1986.

156. V. Sathiaselvan, M. F. Iskander, G. C. W. Howard, and N. M. Bleehen, "Theoretical Analysis and Clinical Demonstration of the Effect of Power Pattern Control using the Annular Phased-Array Hyperthermia System," *IEEE Transactions on Microwave Theory and Techniques*, Vol. MTT-34, pp. 514–519, 1986.
157. C. T. Tsai, H. Massoudi, C. H. Durney, and M. F. Iskander, "A Linear Approximation Method for Solving Internal Field Distribution of Arbitrarily Shaped Inhomogeneous Dielectric Bodies," *IEEE Transactions on Microwave Theory and Techniques*, Vol. MTT-34, pp. 1131–1139, 1986.
158. M. F. Iskander and A. Lakhtakia, "Extension of the Iterative EBCM Method to Calculate Scattering by Low-Loss or Lossless Elongated Dielectric Objects," *Applied Optics*, Vol. 23, pp. 948–953, 1984.
159. M. F. Iskander and O. Khoshdel-Milani, "Numerical Calculations of the Temperature Distribution in Cross Sections of the Human Body," *International Journal of Radiation Oncology, Biology, Physics*, Vol. 10, pp. 1907–1912, 1984.
160. M. F. Iskander, S. L. Rattlingourd, and J. Oomrigar, "A New Electromagnetic Propagation Tool for Well Logging," *Society of Petroleum Engineers*, publication No. SPE 13189, 1984.
161. M. F. Iskander, C. H. Durney, T. Grange, and C. S. Smith, "Radiometer Technique for Measuring Changes in Lung Water," *IEEE Transactions on Microwave Theory and Techniques*, Vol. MTT-32, pp. 554–556, 1984.
162. H. Massoudi, C. H. Durney, and M. F. Iskander, "Limitations of the Cubical Block Model of Man in Calculating SAR Distribution," *IEEE Transactions on Microwave Theory and Techniques*, Vol. MTT-32, pp. 746–752, 1984.
163. A. Lakhtakia, M. F. Iskander, and C. H. Durney, "An Iterative Extended Boundary Condition Method for Solving the Absorption Characteristics of Lossy Dielectric Objects of Large Aspect Ratios," *IEEE Transactions on Microwave Theory and Techniques*, Vol. MTT-31, pp. 640–647, 1983.
164. A. Lakhtakia and M. F. Iskander, "Theoretical and Experimental Evaluation of Power Absorption in Elongated Biological Objects At and Beyond Resonance," *IEEE Transactions on Electromagnetic Compatibility*, Vol. EMC-25, pp. 448–453, 1983.
165. A. Lakhtakia and M. F. Iskander, "Scattering and Absorption of Lossy Dielectric Objects Irradiated by the Near Fields of Aperture Source," *IEEE Transactions on Antennas and Propagation*, Vol. AP-31, pp. 111–120, January 1983.
166. M. F. Iskander, A. Lakhtakia, and C. H. Durney, "A New Procedure for Improving the Solution Stability and Extending the Frequency Range of the EBCM," *IEEE Transactions on Antennas and Propagation*, Vol. AP-31, pp. 317–329, March 1983.
167. M. F. Iskander and C. H. Durney, "Microwave Methods of Measuring Changes in Lung Water," *Journal of Microwave Power*, Vol. 18, pp. 265–275, 1983.

168. M. F. Iskander and J. B. DuBow, "Time- and Frequency-Domain Techniques for Measuring the Dielectric Properties of Rocks—A Review," *Journal of Microwave Power*, Vol. 18, pp. 55–74, March 1983.
169. A. Lakhtakia, M. F. Iskander, C. H. Durney, and H. Massoudi, "Irradiation of Prolate Spheroidal Models of Humans and Animals in the Near Field of a Small-Loop Antenna," *Radio Science*, Vol. 17, No. 5S, pp. 77–84, 1982.
170. M. F. Iskander, A. Lakhtakia, and C. H. Durney, "A New Iterative Procedure to Solve for Scattering and Absorption by Dielectric Objects," *Proceedings of the IEEE*, Vol. 70, pp. 1361–1363, 1982.
171. M. F. Iskander, P. F. Turner, J. B. DuBow, and J. Kao, "Two-Dimensional Technique to Calculate the EM Power Deposition Pattern in the Human Body," *Journal of Microwave Power*, Vol. 17, pp. 175–185, 1982.
172. M. F. Iskander, C. H. Durney, D. G. Bragg, and B. H. Ovard, "A Microwave Method for Estimating Absolute Value of Average Lung Water Content," *Radio Science*, Vol. 17, pp. 111S–117S, 1982.
173. H. Massoudi, C. H. Durney, and M. F. Iskander, "Postresonance Electromagnetic Absorption by Man and Animals," *Bioelectromagnetics*, Vol. 3, No. 3, pp. 333–339, 1982.
174. A. Lakhtakia, M. F. Iskander, C. H. Durney, and H. Massoudi, "Absorption Characteristics of Prolate Spheroidal Models Exposed to the Near Fields of Electrically Small Apertures," *IEEE Transactions on Biomedical Engineering*, Vol. BME-29, pp. 269–278, August 1982.
175. R. Maini, M. F. Iskander, and C. H. Durney, "On the Sensitivity and Resolution of Microwave Imaging Using ART," *Proceedings of the IEEE*, Vol. 69, pp. 1517–1519, 1981.
176. H. Massoudi, C. H. Durney, and M. F. Iskander, "Comparison of the Absorption Characteristics of Block and Prolate Spheroidal Models of Man Exposed to Near-Fields of Short Electric Dipoles," *Proceedings of the IEEE*, Vol. 69, pp. 1086–1087, 1981.
177. M. F. Iskander, A. L. Tyler, and D. F. Elkins, "A Time-Domain Technique for Measurement of the Dielectric Properties of Oil Shale During Processing," *Proceedings of the IEEE*, Vol. 69, pp. 760–762, June 1981.
178. M. F. Iskander, R. Maini, and C. H. Durney, "A Microwave Method for Measuring Changes in Lung Water Content: Numerical Simulation," *IEEE Transactions on Biomedical Engineering*, Vol. BME-28, pp. 797–804, 1981.
179. M. F. Iskander, H. Massoudi, C. H. Durney, and S. J. Allen, "Measurements of the RF Power Absorption in Human and Animal Phantoms Exposed to Near-Field Radiation," *IEEE Transactions on Biomedical Engineering*, Vol. BME-28, pp. 258–264, March 1981.
180. M. F. Iskander and C. H. Durney, "Electromagnetic Techniques for Medical Diagnostics: A Review," *Proceedings of the IEEE*, Vol. 68, pp. 126–132, January 1980.

181. M. F. Iskander, P. W. Barber, C. H. Durney, and H. Massoudi, "Irradiation of Prolate Spheroidal Models of Humans in the Near Field of a Short Electric Dipole," *IEEE Transactions on Microwave Theory and Techniques*, Vol. MTT-28, pp. 801–807, 1980.
182. H. Massoudi, C. H. Durney, and M. F. Iskander, "Long-Wavelength Analysis of Near-Field Irradiation of Prolate Spheroidal Models of Man and Animals," *Electronics Letters*, Vol. 16, No. 3, pp. 99–100, January 31, 1980.
183. D.G. Bragg, C. H. Durney, and M. F. Iskander, "Transmission Microwave Monitoring of Lung water," *Investigative Radiology*, Vol. 15, No. 5, p. 428, 1980
184. M. F. Iskander, C. H. Durney, D. J. Shoff, and D. G. Bragg, "Diagnosis of Pulmonary Edema by a Surgically Noninvasive Microwave Technique," *Radio Science*, Vol. 14, No. 6S, pp. 265–269, December 1979.
185. H. Massoudi, C. H. Durney, and M. F. Iskander, "Electromagnetic Absorption in Multilayered Cylindrical Models of Man," *IEEE Transactions on Microwave Theory and Techniques*, Vol. MTT-27, pp. 825–830, 1979.
186. H. Durney, C. C. Johnson, P. W. Barber, H. Massoudi, M. F. Iskander, S. J. Allen, and J. D. Mitchell, "Descriptive Summary: Radio Frequency Radiation Dosimetry Handbook—Second Edition," *Radio Science*, Vol. 14, No. 6S, pp. 5–7, December 1979.
187. M. F. Iskander and C. H. Durney, "Electromagnetic Energy Coupler for Medical Applications," *Proceedings of the IEEE*, Vol. 67, pp. 1463–1465, 1979.
188. C. H. Durney, M. F. Iskander, H. Massoudi, and C. C. Johnson, "An Empirical Formula for Broadband SAR Calculation of Prolate Spheroidal Models of Humans and Animals," *IEEE Transactions on Microwave Theory and Techniques*, Vol. MTT-27, pp. 758–763, 1979.
189. M. F. Iskander and S. S. Stuchly, "Fringing Field Effect in Lumped Capacitance Method for Permittivity Measurements," *IEEE Transactions on Instrumentation and Measurements*, Vol. IM-27, pp. 107–109, 1978.
190. M. F. Iskander and M. A. K. Hamid, "Near-Field Broadside Coupling Between Two H-Plane Sectoral Horns," *Radio and Electronic Engineering*, Vol. 48, No. 12, pp. 623–630, 1978.
191. M. F. Iskander and M. A. K. Hamid, "Iterative Solution of Waveguide Discontinuity Problems," *IEEE Transactions on Microwave Theory and Techniques*, Vol. MTT-25, pp. 763–768, 1977.
192. M. F. Iskander and M. A. K. Hamid, "Simplified Solutions of a Cross-Junction and Specially Truncated Bands in Parallel Plate Waveguides," *Radio and Electronic Engineer*, Vol. 47, No. 7, pp. 269–273, 1977.
193. M. F. Iskander and M. A. K. Hamid, "A New Strip-Transmission Line for Moisture Content Measurements," *Journal of Microwave Power*, Vol. 12, No. 1, pp. 16–18, 1977.
194. M. F. Iskander and M. A. K. Hamid, "Scattering Coefficients at a Waveguide-Horn Junction," *Proceedings of the IEEE*, Vol. 123, pp. 123–127, 1976.

195. M. F. Iskander and M. A. K. Hamid, "Numerical Solution for the Near-Field Transmission Between Two H-Plane Sectoral Electromagnetic Horns," *IEEE Transactions on Antennas and Propagation*, Vol. AP-24, pp. 87–89, 1976.
196. M. F. Iskander and M. A. K. Hamid, "Scattering by a Regular Polygonal Conducting Cylinder," *Archiv für Elektronik und Übertragungstechnik*, Vol. 30, pp. 403–408, 1976.
197. M. F. Iskander and M. A. K. Hamid, "Analysis of Triangle Waveguide of Arbitrary Dimensions," *Archiv für Elektronik und Übertragungstechnik*, Vol. 28, pp. 455–461, 1974.
198. M. F. Iskander and M. A. K. Hamid, "Eigenvalues for a Trapezoidal Waveguide," *Radio and Electronic Engineer*, Vol. 44, pp. 593–596, 1974.
199. S. S. Stuchly, M. A. Rzepecka, and M. F. Iskander, "Permittivity Measurements at Microwave Frequencies Using Lumped Elements," *IEEE Transactions on Instrumentation and Measurements*, Vol. IM-23, pp. 56–62, 1974.
200. M. F. Iskander and S. S. Stuchly, "A Time-Domain Technique for the Measurement of the Dielectric Properties of Biological Substances," *IEEE Transactions on Instrumentation and Measurements*, Vol. IM-21, pp. 425–429, 1972.

### 26.5.5 Patents

1. M. F. Iskander, Z. Yun, R. Perron, T. B. Seto, and J. Yu, "Machine Learning Based Cardiopulmonary Disease Assessment Using CP Stethoscope Measurements," provisional patent application, 62/431,763 on December 8, 2016.
2. M. F. Iskander and R. G. Perron, "Lung Water Measurement System and Calibration method," US Patent Application No. 15/042109, filed February 11, 2016.
3. M. F. Iskander, N. Celik, R. Gagarin, G. C. Huang, and D. A. Bibb, "Microwave Stethoscope for Measuring Cardio-Pulmonary Vital Signs and Lung Water Content," US Patent Number 9,526, 438, 2016.
4. M. F. Iskander, H. Youn, C. Amazeen, and B. Burns, "[Systems for Transverse Electromagnetic Mode In-Situ Soil testing](#)," US Patent Number 8461851, 2013.
5. M. F. Iskander, R. Sorensen, J. J. Lee, and H. K. Kim, "Ferrite Phase Shifter and Phase Array Radar System," US Patent Number 7,417,587, August 2008.
6. M. F. Iskander, W. Kim, and J. Bell, "Multiband Coplanar Waveguide CTS Antenna," US Patent Number 7,079,082 issued on July 18, 2006.
7. C. Araya, M. F. Iskander, and J. Brennan, "Slotted Waveguide Antenna Array for Microwave Assisted Gas Kiln," US Patent Number 6,583,394, 2003.
8. Z. Zhang, M. F. Iskander, and Z. Yun, "Coaxial Continuous Transverse Stub Element Device Antenna Array and Filter," US Patent No. 6,201,509, March 2001.
9. M. F. Iskander, "Apparatus and Method for Measuring the Permittivity of a Substance," US Patent No. 4,510,437, 1985.

10. M. F. Iskander, "Apparatus and Method for Measuring Lung Water Content," US Patent No. 4,488,559, December 1984.
11. M. F. Iskander, "Apparatus and Method for Time-Domain Tracking of High-Speed Chemical Reactions," US Patent No. 4,396,062, 1983.
12. M. F. Iskander and C. H. Durney, "Electromagnetic Energy Coupler/ Receiver Apparatus and Method," US Patent No. 4,240,445, 1980.

### **26.5.6 Conference Publications**

1. M. F. Iskander, Z. Yun, F. A. Qazi, G. Sasaki, and A. Das, "Physical Layer Based Approach for Advanced Directional Networking," IEEE Military Communications Conference, MILCOM 2016, Baltimore, Maryland, November 1–3, 2016.
2. G. C. Huang, M. F. Iskander, and M. Hoque, "Advanced Antenna Array Designs for Directional Networks," IEEE Military Communications Conference, MILCOM 2016, Baltimore, Maryland, November 1–3, 2016.
3. D. A. Bibb, Z. Yun, and M. F. Iskander, "Machine Learning for Source Localization in Urban Environments," IEEE Military Communications Conference, MILCOM 2016, Baltimore, Maryland, November 1–3, 2016.
4. G. C. Huang, M. F. Iskander, and M. Hoque, "A Wideband Circularly Polarized Stacked Patch Antenna Array and Feed System," IEEE/ACES International Conference on Wireless Information Technology and Systems (ICWITS) and Applied Computational Electromagnetics (ACES), Honolulu, Hawaii, March 13–17, 2016.
5. F. A. Qazi, A. Das, Z. Yun, and M. F. Iskander, "Optimizing Cellular Coverage in Maui Island, Hawaii," IEEE/ACES International Conference on Wireless Information Technology and Systems (ICWITS) and Applied Computational Electromagnetics (ACES), Honolulu, Hawaii, March 13–17, 2016.
6. A. Das, F. A. Qazi, Z. Yun, and M. Iskander, "Performance analysis of realistic multipath modeling using a multiple detail-level approach in cognitive communication systems," IEEE/ACES International Conference on Wireless Information Technology and Systems (ICWITS) and Applied Computational Electromagnetics (ACES), Honolulu, Hawaii, March 13–17, 2016.
7. L. H. Manh, J. Rayno, M. F. Iskander, and M. H. Kobayashi, "Hybrid genetic programming with modified conjugate direction search for 3D metamaterial design," IEEE/ACES International Conference on Wireless Information Technology and Systems (ICWITS) and Applied Computational Electromagnetics (ACES), Honolulu, Hawaii, March 13–17, 2016.
8. J. Rayno and M. F. Iskander, "Novel 3D loops and coils utilizing Fourier series for low frequency AMC ground planes," IEEE/ACES International Conference on Wireless Information Technology and Systems (ICWITS) and Applied Computational Electromagnetics (ACES), Honolulu, Hawaii, March 13–17, 2016.

9. D. Green, Z. Yun, and M. F. Iskander, "Propagation characteristics in urban environments," IEEE/ACES International Conference on Wireless Information Technology and Systems (ICWITS) and Applied Computational Electromagnetics (ACES), Honolulu, HI, March 13–17, 2016.
10. L. Tamaye, R. R. G. Perron, D. Bibb, J. Tanabe, F. Suela, G. C. Huang, and M. F. Iskander, "CP-Stethoscope: Phantom model experiments," IEEE/ACES International Conference on Wireless Information Technology and Systems (ICWITS) and Applied Computational Electromagnetics (ACES), Honolulu, Hawaii, March 13–17, 2016.
11. R. R. G. Perron and M. F. Iskander, "3D modeling for realistic assessment of vital signs and lung water content," Radio Science Meeting (Joint with AP-S Symposium), 2015 USNC-URSI, Vancouver, B.C. Canada, July 19–24, 2015.
12. G. C. Huang, M. F. Iskander, M. Hoque, S. R. Goodal, and T. Bocskor, "Implementation of high performance and broadband crossover junction in butler matrix design," 2015 IEEE International Symposium on Antennas and Propagation & USNC/URSI National Radio Science Meeting, pp. 1052–1053, Vancouver, B.C. Canada, July 19–24, 2015.
13. Z. Yun and M. F. Iskander, "Multiple levels of detail environment modeling for radio propagation simulation and prediction," Radio Science Meeting (Joint with AP-S Symposium), USNC-URSI, p. 258, Vancouver, B.C. Canada, July 19–24, 2015.
14. M. F. Iskander, "Technology-based global revitalization of electromagnetic education," IEEE International Symposium on Antennas and Propagation & USNC/URSI National Radio Science Meeting, pp. 1019–1020, Vancouver, B.C. Canada, July 19–24, 2015.
15. J. Rayno and M. F. Iskander, "Hybrid genetic programming with accelerating optimizer for 3D metamaterial design," IEEE International Symposium on Antennas and Propagation & USNC/URSI National Radio Science Meeting, pp. 1334–1335, Vancouver, B.C. Canada, July 19–24, 2015.
16. D. A. Bibb, Z. Yun, and M. F. Iskander, "Time reversal for source localization in urban environments considering the effects of Doppler shift," Radio Science Meeting (Joint with AP-S Symposium), USNC-URSI, pp. 268–268, Vancouver, B.C. Canada, July 19–24, 2015.
17. J. M. Baker and M. F. Iskander, "Electrically small fractal antennas," IEEE Antennas and Propagation Society International Symposium (APS/URSI), pp. 1242–1243, Vancouver, B.C. Canada, July 19–24, 2015.
18. M. F. Iskander, "Technology-based global revitalization of electromagnetic education," IEEE Antennas and Propagation Society International Symposium (APS/URSI), pp. 1019–1020, Vancouver, B.C. Canada, July 19–24, 2015.
19. S. Y. Lim, Z. Yun, and M. F. Iskander, "A ray tracing method for propagation in a mock city with partially open drains," IEEE Antennas and Propagation Society International Symposium (APS/URSI), pp. 1802–1803, Vancouver, B.C. Canada, July 19–24, 2015.



20. M. F. Iskander, "Computational Electromagnetics: Vision for Seizing Opportunities in Growing Technologies," The 31st International Review of Progress in Applied Computational Electromagnetics (ACES 2015), Williamsburg, Virginia, March 22–26, 2015.
21. M. F. Iskander, "Advanced Communications Systems in Directional Networking and Biomedical Applications," National Science Foundation Second US-Ireland Workshop on Telecommunications and Connected Health Technologies, Belfast, Northern Ireland, and Dublin, Ireland, September 29–October 2, 2014.
22. G. C. Huang, M. F. Iskander, M. Hoque, S. R. Goodall, and T. Bocskor, S. Chen, "Antenna array design and system for directional networking," IEEE Conference on Antenna Measurements & Applications (CAMA), Antibes Juan-les-Pins, France, November 16–19, 2014.
23. D. A. Bibb, G. C. Huang, R. Perron, and M. F. Iskander, "Development of a wireless antenna and monitoring system for microwave based vital sign and lung water measurement," IEEE Conference on Antenna Measurements & Applications (CAMA), Antibes Juan-les-Pins, France, November 16–19, 2014.
24. Y. Li, Z. Zhang, Z. Feng, and M. F. Iskander, "A beam steerable CPW-CTS antenna array using reconfigurable metamaterial-based phase shifters for cognitive radio applications," General Assembly and Scientific Symposium (URSI GASS), Beijing, China, August 18–23, 2014.
25. F. Rabbi, R. Gagarin, G. C. Huang, and M. F. Iskander, "Stroke volume estimation from the new noninvasive cardiopulmonary stethoscope," IEEE Antennas and Propagation Society International Symposium (APS/URSI), pp. 967–968, Memphis, Tennessee, July 6–11, 2014.
26. D. A. Bibb, Z. Yun, and M. F. Iskander, "Source localization using time reversal in urban environments: A ray tracing approach," IEEE Antennas and Propagation Society International Symposium (APS/URSI), pp. 945–946, Memphis, Tennessee, July 6–11, 2014.
27. G. C. Huang, R. Gagarin, and M. F. Iskander, "Antenna array design for directional networking," IEEE Antennas and Propagation Society International Symposium (APS/URSI), pp. 937–938, Memphis, Tennessee, July 6–11, 2014.
28. J. Baker and M. F. Iskander, "New design methodology for electrically small HF antenna," IEEE Antennas and Propagation Society International Symposium (APS/URSI), pp. 579–580, Memphis, Tennessee, July 6–11, 2014.
29. D. A. Bibb, J. Dang, Z. Yun, and M. F. Iskander, "Computational accuracy and speed of some knife-edge diffraction models," IEEE Antennas and Propagation Society International Symposium (APS/URSI), pp. 705–706, Memphis, Tennessee, July 6–11, 2014.
30. M. F. Iskander, "Multimedia and technology based electromagnetic education," IEEE Antennas and Propagation Society International Symposium (APS/URSI), pp. 531–532, Memphis, Tennessee, July 6–11, 2014.

31. J. Rayno, N. Celik, and M. F. Iskander, "Synthesis of Broadband 3D AMC Ground Planes Using Genetic Programming," *IEEE Antennas and Propagation Society International Symposium (APS/URSI)*, pp. 35–36, Memphis, Tennessee, July 6–11, 2014.
32. R. Gagarin, G. C. Huang, A. Rabbi, and M. F. Iskander, "Textile Sensor for Monitoring Vital Signs," *IEEE Antennas and Propagation International Symposium (APS/URSI)*, pp. 965–966, Memphis, Tennessee, July 6–11, 2014.
33. S. Y. Lim, Z. Yun, and M. F. Iskander, "Channel Modeling of a Partially Open Drain at 2.4 GHz," *IEEE Antennas and Propagation International Symposium (APS/URSI)*, pp. 233–233, Memphis, Tennessee, July 6–11, 2014.
34. Z. Yun and M. F. Iskander, "Diffraction from Multiple Ridges: Comparing Three- and Two-Dimensional Results," *The 8th European Conference on Antennas and Propagation (EuCAP 2014)*, pp. 1587–1588, April 6–11, 2014.
35. N. Celik, H. Xu, T. Wilkey, Z. Yun, and M. F. Iskander, "Cognitive Radio System with Advanced Environment Awareness Engine using Integrated Propagation Models and Multiple Antennas," *IEEE Antennas and Propagation Society International Symposium (APS/URSI)*, pp. 2016–2017, Orlando, Florida, July 7–13, 2013.
36. J. T. Rayno, G. C. Huang, J. Pascual, J. Griffith, M. F. Iskander, "Dual-polarization Cylindrical Long Slot Array (CLSA) Antenna Integrated with Compact Broadband Baluns and Slot Impedance Transformers," *IEEE Antennas and Propagation Society International Symposium (APS/URSI)*, pp. 9–10, Orlando, Florida, July 7–13, 2013.
37. C. Huang, J. Pascual, J. Griffith, N. Celik, and M. Iskander, "A L-band Spherical Section Long Slot Antenna Array with Metamaterial Ground Plane for Satellite Communications," *2013 IEEE Antennas and Propagation Society International Symposium (APS/URSI)*, pp. 1814–1815 Orlando, Florida, July 7–13, 2013.
38. R. Gagarin, G. C. Huang, N. Celik, and M. F. Iskander, "Determination of Pulmonary Edema using Microwave Sensor Array: Simulation Studies with Anatomically Realistic Human CAD-Models," *2013 IEEE Antennas and Propagation Society International Symposium (APS/URSI)*, pp. 2189–2190, Orlando, Florida, July 7–13, 2013.
39. J. T. Rayno, J. S. K. Nakatsu, G. C. Huang, N. Celik, and M. F. Iskander, "3D Metamaterial Broadband Ground Plane Designed Using Genetic Programming for the Long Slot Array Antenna," *2013 IEEE Antennas and Propagation Society International Symposium (APS/URSI)*, pp. 400–401, Orlando, Florida, July 7–13, 2013.
40. S. Y. Lim, A. K. Awelemdy, K. P. Seng, Z. Yun, and M. F. Iskander, "Modeling Radio Wave Propagation in Drains," *IEEE Antennas and Propagation Society International Symposium (APS/URSI)*, pp. 1938–1939, Orlando, Florida, July 7–13, 2013.

41. Y. Li, M. F. Iskander, Z. Zhang, and Z. Feng, "A Phased CPW-CTS Array with Reconfigurable NRI Phase Shifter for Beam Steering Application," International Wireless Symposium (IWS), Beijing, China, April 14–18, 2013.
42. Y. Li, M. F. Iskander, Z. Zhang, and Z. Feng, "CPW-CTS Array with Reconfigurable NRI Phase Shifter for Beam Steering Application," International Wireless Symposium (IWS), April 14–18, Beijing, China, 2013.
43. M. F. Iskander, "Phased Antenna Array Technologies and Propagation Models for Advanced Wireless Communication Systems," Invited lecture, Action IC0803: RF/Microwave Communication Subsystems for Emerging Wireless Technologies (RFCSET), 8th Management Committee/Working Group Meeting and Workshop Program, Belfast, United Kingdom, May 17–18, 2012.
44. M. F. Iskander and S. El Ghazaly, organized a Special Session entitled "Globalization of Engineering Education and Research: Opportunities and Challenges," International Microwave Symposium (IMS 2012), Montreal, Canada, June 17–22, 2012.
45. M. F. Iskander and S. El Ghazaly, "Sixty Years of Microwave Innovation, Transformation, and Call for Globalization," International Microwave Symposium (IMS 2012), Montreal, Canada, June 17–22, 2012.
46. M. F. Iskander, S. M. El Ghazaly, and P. Wahid, "Globalization: Setting a New Agenda for Engineering Education," IEEE Antennas and Propagation International Symposium, Chicago, Illinois, July 10–16, 2012.
47. R. R. Gagarin, N. Celik, G. C. Huang, and M. F. Iskander, "Microwave Stethoscope, a New Noninvasive Multiple Vital Signs Sensor: Human Clinical Trials," IEEE Antennas and Propagation International Symposium, Chicago, Illinois, July 10–16, 2012.
48. C. Huang, R. Gagarin, N. Celik, H. S. Youn, and M. F. Iskander, "Wideband EM Coupler/Applicator Design and Characterization for the Clinical Benchmarking Tests of Microwave Stethoscope (MiSt)," IEEE Antennas and Propagation International Symposium, Chicago, Illinois, July 10–16, 2012.
49. N. Omaki, Z. Yun, and M. F. Iskander, "Accuracy of Parabolic Wave Equation Method in Short Propagation Range," IEEE Antennas and Propagation International Symposium, Chicago, Illinois, July 10–16, 2012.
50. H. S. Youn, L. Lee, N. Celik, and M. Iskander, "Dual-Polarization Cylindrical Long-Slot Array Antenna Integrated with Hybrid Ground Plane," IEEE Antennas and Propagation International Symposium, Chicago, Illinois, July 10–16, 2012.
51. Y. L. Lee, H. S. Youn, and M. Iskander, "Long Slot Array (LSA) Antenna Integrated with Compact Broadband Coupled Microstrip Impedance Transformer," IEEE Antennas and Propagation International Symposium, Chicago, Illinois, July 10–16, 2012.
52. Z. Yun, N. Omaki, and M. F. Iskander, "Ridge Feature Extraction and Effect on Radio Propagation for Wireless Communications," IEEE Antennas and Propagation International Symposium, Chicago, Illinois, July 10–16, 2012.

53. J. S. K. Nakatsu, H. S. Youn, and M. F. Iskander, "Feasibility Study for Non-Metallic IED Detection Using Forward-Looking Ground Penetrating Radar Integrated with Target Feature Classification," IEEE Antennas and Propagation International Symposium, Chicago, Illinois, July 10–16, 2012.
54. N. Celik, R. Gagarin, G. C. Huang, M. F. Iskander, and B. Berg, "Microwave Stethoscope (MiSt) as a Low-Cost Signs Sensor," 2012 IEEE International Conference on Wireless Information Technology and Systems, Maui, Hawaii, November 11–16, 2012.
55. N. Omaki, Z. Yun, and M. F. Iskander, "Split-Step Parabolic Equation Method: A Comparative Study," 2012 IEEE International Conference on Wireless Information Technology and Systems, Maui, Hawaii, November 11–16, 2012.
56. H. S. Youn, J. Pascual, Y. L. Lee, J. Griffith, G. C. Huang, J. T. Rayno, and M. F. Iskander, "Development of Ultra Wide Bandwidth (UWB) Cylindrical Long Slot Array (CLSA) Antenna Integrated with Novel Microstrip Feeders," 2012 IEEE International Conference on Wireless Information Technology and Systems, Maui, Hawaii, November 11–16, 2012.
57. Y. Li and M. F. Iskander, "A New CTS Antenna Design with High Gain and Low Cost Beam Steering Capability," 2012 IEEE International Conference on Wireless Information Technology and Systems, Maui, Hawaii, November 11–16, 2012.
58. Z. Yun, M. F. Iskander, and N. Omaki, "Role of propagation modeling and Antenna mutual coupling on estimation of MIMO capacity," 2012 IEEE International Conference on Wireless Information Technology and Systems, Maui, Hawaii, November 11–16, 2012.
59. J. Baker and M. Iskander, "Design and Optimization of a Folded Helical Meandering Line Antenna with Genetic Algorithms," 2012 IEEE International Conference on Wireless Information Technology and Systems, Maui, Hawaii, November 11–16, 2012.
60. M. F. Iskander, "Research opportunities in the Telecommunications and Wireless Technologies Areas," National Science Foundation US-Ireland Workshop on Telecommunications, Dublin, Ireland, Nov. 1–2, 2011.
61. M. F. Iskander, "Antennas, propagation modeling and DSP Technologies for Wireless Systems," National Science Foundation US-Ireland Workshop on Telecommunications, Dublin, Ireland, Nov. 1–2, 2011.
62. S Y Lim, Z. Yun, and M. F. Iskander, "Modeling Scattered EM Field from a Façade-Like Structure for Wireless Communications," 2011 IEEE Antennas and Propagation International Symposium and URSI Meeting, Spokane, Washington, July 3–9, 2011.
63. M. F. Iskander, "Professor Robert E Collin Pioneering Innovation in EM Education: The CAEME Experience," 2011 IEEE Antennas and Propagation International Symposium and URSI Meeting, Spokane, Washington, July 3–9, 2011.

64. J. Kobashigawa, Z. Zhang, N. Celik, M. F. Iskander, and J. Graham, "High Isolation Diplexer Design for Autonomous Vehicle," 2011 IEEE Antennas and Propagation International Symposium and URSI Meeting, Spokane, Washington, July 3–9, 2011.
65. N. Celik, H. S. Youn, N. Omaki, Y. L. Lee, R. Gagarin, M. F. Iskander, "Experimental Evaluation of Passive Radar Approach for Homeland Security Applications," 2011 IEEE Antennas and Propagation International Symposium and URSI Meeting, Spokane, Washington, July 3–9, 2011.
66. H. S. Youn, N. Celik, M. F. Iskander, J. Baker, J. Graham, and S. Murphy, "Miniaturized Conical Spiral Antenna with Tapered Resistive Loading and Corrugated Arms," 2011 IEEE Antennas and Propagation International Symposium and URSI Meeting, Spokane, Washington, July 3–9, 2011.
67. N. Omaki, Z. Yun, N. Celik, H. S. Youn, and M. F. Iskander, "Terrain Impact on HF Radar Deployment for Homeland Security Applications," 2011 IEEE Antennas and Propagation International Symposium and URSI meeting, Spokane, Washington, July 3–9, 2011.
68. N. Celik, Y. L. Lee, H. S. Youn, and M. F. Iskander, "An Ultrawideband Cylindrical Long-Slot Antenna with Hybrid EBG/Ferrite Ground Plane," 2011 IEEE Antennas and Propagation International Symposium and URSI Meeting, Spokane, Washington, July 3–9, 2011.
69. R. Gagarin, N. Celik, H. S. Youn, and M. F. Iskander, "Microwave Stethoscope: A New Method for Measuring Human Vital Signs," 2011 IEEE Antennas and Propagation International Symposium and URSI Meeting, Spokane, Washington, July 3–9, 2011.
70. J. H. Deng, N. Celik, Z. Yun, and M. F. Iskander, "Low Complexity Hybrid Smart Antenna with Directional Elements over Frequency-Selective Fading Channel," 13th International Conference on Advanced Communication Technology (ICACT2011), Phoenix Park Gangwon-Do, Korea (South), 13–16 February, 2011.
71. Z. Yun, S. Y. Lim, and M. F. Iskander, "Modeling Three-Dimensional Terrain in Urban Propagation Environment Using Geospatial Data in Cyberspace," 2010 IEEE International Symposium on Antennas and Propagation and the 2010 USNC/URSI National Radio Science Meeting, Toronto, Canada, July 11–17, 2010.
72. S. Y. Lim, Z. Yun, and M. F. Iskander, "Modeling Scattered EM Field from a Periodic Building Façade," 2010 IEEE International Symposium on Antennas and Propagation and the 2010 USNC/URSI National Radio Science Meeting, Toronto, Canada, July 11–17, 2010.
73. R. Gagarin, H. S. Youn, N. Celik, and M. F. Iskander, "Noninvasive Microwave Technique for Hemodynamic Assessments," 2010 IEEE International Symposium on Antennas and Propagation and the 2010 USNC/URSI National Radio Science Meeting, Toronto, Canada, July 11–17, 2010.
74. J. Kobashigawa, H. S. Youn, Z. Yun, and M. F. Iskander, "Comparison Between Genetic Programming and Neural Network in Classification of

- Buried Unexploded Ordnance (UXO) Targets,” 2010 IEEE International Symposium on Antennas and Propagation and the 2010 USNC/URSI National Radio Science Meeting, Toronto, Canada, July 11–17, 2010.
75. Y. L. Lee, H. S. Youn, C. Tanaka, W. Kim, M. F. Iskander, “Design, Development and Experimental Verification of Voltage Tunable Ferroelectric Coplanar Waveguide Phase Shifters,” 2010 IEEE International Symposium on Antennas and Propagation and the 2010 USNC/URSI National Radio Science Meeting, Toronto, Canada, July 11–17, 2010.
  76. N. Celik and M. F. Iskander, “Design, Optimization, and Verification of an Antenna Array for the 60 GHz Hybrid Smart Antenna System,” 2010 IEEE International Symposium on Antennas and Propagation and the 2010 USNC/URSI National Radio Science Meeting, Toronto, Canada, July 11–17, 2010.
  77. N. Celik, J. M. Baker, H. S. Youn, and M. F. Iskander, “An Internet Based Interactive Telemedicine System for Remote Healthcare,” 2010 IEEE International Symposium on Antennas and Propagation and the 2010 USNC/URSI National Radio Science Meeting, Toronto, Canada, July 11–17, 2010.
  78. J. M. Baker, M. F. Iskander, H. S. Youn, N. and Celik, “High-Performance Compact HF Antenna for Radar and Communication Applications,” IEEE International Symposium on Antennas and Propagation and the USNC/URSI National Radio Science Meeting, Toronto, Canada, July 11–17, 2010.
  79. J. M. Baker, M. F. Iskander, J. Kobashigawa, and S.Y. Lim, “Application of Wireless Technology in K-12 STEM Outreach Programs in Middle Schools,” 2010 IEEE International Symposium on Antennas and Propagation and the 2010 USNC/URSI National Radio Science Meeting, Toronto, Canada, July 11–17, 2010.
  80. Z. Yun, S. Y. Lim, and M. F. Iskander, “Radio propagation modeling in complex environments for wireless communications,” 2nd International IEEE Conference on Microwaves, Communications, Antennas and Electronic Systems (IEEE COMCAS’09), Tel Aviv, Israel, November 9–11, 2009.
  81. M. F. Iskander, W. Kim, J. Bell, N. Celik, Z. Yun, and H. Youn, “Antenna arrays technologies for advanced wireless systems,” 2nd International IEEE Conference on Microwaves, Communications, Antennas and Electronic Systems (IEEE COMCAS’09), Tel Aviv, Israel, November 9–11, 2009.
  82. X. Gao, Z. Zhang, W. Chen, Z. Feng, M. F. Iskander, and A.-P. Zhao, “A Novel Wrist Wear Dual-Band Diversity Antenna,” IEEE Antennas and Propagation International Symposium, Charleston, South Carolina, June 1–5, 2009.
  83. Y. Li, Z. Zhang, W. Chen, Z. Feng, M. F. Iskander, and A.-P. Zhao, “Feeding Reconfigurable PIFA for GSM/PCS/DCS Applications,” IEEE Antennas and Propagation International Symposium, Charleston, South Carolina, June 1–5, 2009.
  84. Z. Yun, M. F. Iskander, and S. Y. Lim, “The Effect of 3D Building Reconstruction Errors on Propagation Prediction Using Geospatial Data in Cyberspace,” IEEE Antennas and Propagation International Symposium, Charleston, South Carolina, June 1–5, 2009.

85. D. Nashaat, H.A. Elsadek, E. Abdallah, H. Elhenawy, and M. F. Iskander, "Enhancement of Ultra-Wide Bandwidth of Microstrip Monopole Antenna by Using Metamaterial Structures," IEEE Antennas and Propagation International Symposium, Charleston, South Carolina, June 1–5, 2009.
86. H. S. Youn, M. F. Iskander, and M. Evans, "In-situ Measurement of Electromagnetic Properties of Material Using Multi-conductor TEM transmission Line," IEEE Antennas and Propagation International Symposium, Charleston, South Carolina, June 1–5, 2009.
87. J. Kobashigawa, H. S. Youn, M. F. Iskander, and Z. Yun, "Comparative Study of Genetic Programming vs. Neural Networks for the Classification of Buried Objects," IEEE Antennas and Propagation International Symposium, Charleston, South Carolina, June 1–5, 2009.
88. S. Y. Lim, Z. Yun, J. M. Baker, N. Celik, H. S. Youn, and M. F. Iskander, "Radio Propagation in Stairwell: Measurement and Simulation Results," IEEE Antennas and Propagation International Symposium, Charleston, South Carolina, June 1–5, 2009.
89. D. Nashaat, H. A. Elsadek, E. Abdallah, H. Elhenawy, and M. F. Iskander, "Electromagnetic Analyses and An Equivalent Circuit Model of Microstrip Patch Antenna With Rectangular Defected Ground Plane," IEEE Antennas and Propagation International Symposium, Charleston, South Carolina, June 1–5, 2009.
90. N. Celik, M. F. Iskander, R. Emrick, and Z. Zhang, "Experimental Evaluation of the Hybrid Smart Antenna System with Directional Array Elements," IEEE Antennas and Propagation International Symposium, Charleston, South Carolina, June 1–5, 2009.
91. D. Nashaat, H. A. Elsadek, E. Abdallah, H. Elhenawy, and M. F. Iskander, "Multiband and Miniaturized Inset Feed Microstrip Patch Antenna Using Multiple Spiral-shaped Defect Ground Structure (DGS)," IEEE Antennas and Propagation International Symposium, Charleston, South Carolina, June 1–5, 2009.
92. M. Baker, M. F. Iskander, Z. Yun, M. Evans, J. Johnson, and D. Elsheakh, "High Performance Compact Antenna for HF Radar," IEEE Antennas and Propagation International Symposium, Charleston, South Carolina, June 1–5, 2009.
93. N. Celik, M. F. Iskander, and Z. Yun, "Design and Implementation of Advanced Wireless Communications Systems Utilizing the Hybrid Smart-Antenna Algorithm," XXIX General Assembly of the International Union of Radio Science (URSI), Chicago, Illinois, August 7–16, 2008.
94. M. F. Iskander, N. Celik, J. M. Bell, Z. Yun, "Antenna Array Designs With Advanced Beam Steering Capabilities," XXIX General Assembly of the International Union of Radio Science (URSI), Chicago, Illinois, August 7–16, 2008.
95. J. Kim, S. Lim, M. F. Iskander, J. M. Bell, "A Low Profile, Multi-band Yagi Antenna With High Gain Characteristics Over an EBG Ground Plane," XXIX General Assembly of the International Union of Radio Science (URSI), Chicago, Illinois, August 7–16, 2008.

96. J. M. Bell, M. F. Iskander, "Equivalent Circuit Model and Experimental Analysis of an Ultrawideband Hybrid EBG/Ferrite Ground Plane," XXIX General Assembly of the International Union of Radio Science (URSI), Chicago, Illinois, August 7–16, 2008.
97. Z. Zhang, W. Chen, Z. Feng, Y. Chen, and M. F. Iskander, "A Hybrid Slot and Inverted L Antenna," IEEE Antennas and Propagation International Symposium, July 5–11, San Diego, California, 2008.
98. J. M. Bell, and M. F. Iskander, "Experimental Analysis of An Ultrawideband Hybrid EBG/ferrite Ground Plane," IEEE Antennas and Propagation International Symposium, San Diego, California, July 5–11, 2008.
99. Z. Yun, S. Y. Lim, and M. F. Iskander, "Propagation Prediction In Urban Areas Using Geospatial Data Available On The Internet," IEEE Antennas and Propagation International Symposium, San Diego, California, July 5–11, 2008.
100. H. Zhong, W. Chen, Z. Zhang, Z. Feng, and M. F. Iskander, "A Conformal Tri-polarization Antenna," IEEE Antennas and Propagation International Symposium, San Diego, California, July 5–11, 2008.
101. N. Celik and M. F. Iskander, "Implementation and Experimental Verification of A Millimeter Wave Smart Antenna System," IEEE Antennas and Propagation International Symposium, San Diego, California, July 5–11, 2008.
102. W. Chen, Z. Zhang, Z. Feng, Y. Chen, K. Jiang, S. Fan, and M. F. Iskander, "Measurement of Polarized Nano-material (PNM) for Microwave Applications," 2008 IEEE MTT-S International Symposium, Atlanta, Georgia, June 15–20, 2008.
103. Z. Yun, S. Y. Lim, and M. F. Iskander, "Three Dimensional Propagation Prediction Using Online Geospatial Data," URSI National Radio Science Meeting, Boulder, Colorado, January 3–5, 2008.
104. Z. Yun, and M. F. Iskander, "Effect of Antenna Mutual Coupling on Degree of Freedom of MIMO Systems," IEEE 2007 International Symposium on Microwave, Antenna, Propagation, and EMC Technologies for Wireless Communications, Hangzhou, China, August 16–17, 2007.
105. M. F. Iskander, Z. Yun, N. Celik, J. Bell, and W. Kim, "Antenna Arrays and Propagation Models for Advance Wireless Communications," International Conference on Electromagnetics in Advanced Applications (ICEAA'07), Torino, Italy, September 17–21, 2007.
106. M. F. Iskander, Z. Yun, N. Celik, J. Bell, and W. Kim, "Antenna Arrays and Propagation Models for Advanced Wireless Systems," International Conference on Electromagnetics in Advanced Applications (ICEAA'07), Torino, Italy, September 17–21, 2007.
107. M. F. Iskander, "Low Cost Phased Array Antennas Using Analog and Digital Phase Shifters Technologies," ONE Highlight Special Session, IEEE Antennas and Propagation International Symposium, June 9–15, Honolulu, Hawaii, 2007.



108. J. M. Bell, M. F. Iskander, and J. J. Lee, "Ultrawideband Hybrid EBG/Ferrite Ground Plane for Low-Profile Array Antennas," IEEE Antennas and Propagation International Symposium, June 9–15, Honolulu, Hawaii, 2007.
109. Z. Yun, and M. F. Iskander, "Detection of Buried Metal Structures Using Ground Penetrating Radar Techniques: a Numerical Study," IEEE Antennas and Propagation International Symposium, Honolulu, Hawaii, June 9–15, 2007.
110. N. Celik, Z. Yun, and M. F. Iskander, "Employing Realistic Propagation Models in Wireless Systems Simulations," IEEE Antennas and Propagation International Symposium, Honolulu, Hawaii, June 9–15, 2007.
111. M. F. Iskander, Z. Yun, H. S. Youn, N. Celik, and W. Kim, "On the feasibility of Using GPR Technology for the UXO Detection and Discrimination in The Volcanic Soil of Hawaii," IEEE Antennas and Propagation International Symposium, Honolulu, Hawaii, June 9–15, 2007.
112. W. C. Kim, and M. F. Iskander, "A Technique for Modeling Multi-Dielectric Layers Coplanar Waveguide Ferroelectric Phase Shifters," IEEE Antennas and Propagation International Symposium, Honolulu, Hawaii, June 9–15, 2007.
113. Z. Yun and M. F. Iskander, "Time Reversal with Single Antenna Systems in Indoor Multipath Environments: Spatial Focusing and Time Compression," IEEE International Symposium on Antennas and Propagation, Albuquerque, New Mexico, July 9–14, 2006.
114. N. Celik, W. Kim, M. F. Demirkol, M. F. Iskander, R. Emrick, "Implementation and Experimental Verification of Hybrid Beamforming Algorithm," IEEE International Symposium on Antennas and Propagation, Albuquerque, New Mexico, July 9–14, 2006.
115. J. M. Bell, M. F. Iskander, and J. J. Lee, "Ultra-Wideband and Low Profile Hybrid EBG/Ferrite Ground Plane for Airborne Foliage Penetration Radar," IEEE International Symposium on Antennas and Propagation, Albuquerque, New Mexico, July 9–14, 2006.
116. W. C. Kim and M. Iskander, "Integrated Phased Antenna Array Design Using Ferroelectric Materials and the Coplanar Waveguide Continuous Transverse Stub Technologies," IEEE International Symposium on Antennas and Propagation, Albuquerque, New Mexico, July 9–14, 2006.
117. W.G. Hui, J. M. Bell, M. F. Iskander, and J. J. Lee, "Low cost Microstrip Based Ferrite Phase Shifter Utilizing Circular Polarization," IEEE International Symposium on Antennas and Propagation, Albuquerque, New Mexico, July 9–14, 2006.
118. M. F. Iskander, Z. Yun, C. Takahashi, M. Rezk, N. Celik, and M.F. Demirkol, "Advanced Propagation Models and their applications in CDMA, MIMO, and UWB Wireless Communications Systems," Mediterranean Microwave Symposium, Athens, Greece, September 2005.
119. M. F. Iskander, W. Kim, M. Rezk, and Z. Yun, "Antenna Design and a Hybrid Smart Antenna Technique for Advanced Wireless Communication Systems," Proceedings of Joint 9th International Conference on Electromagnetics in

- Advanced Applications and EESC '05 European Electromagnetic Structures Conference, Torino, Italy, September 12–16, 2005.
120. Z. Yun and M. F. Iskander, "Efficient Calculation of Field Distribution with High-Resolution Using Ray-Tracing Method," IEEE AP-S/URSI Conference, Washington, DC, July 3–8, 2005.
  121. C. Takahashi, N. Celik, M. Rezk, M.F. Demirkol, Z. Yun, and M.F. Iskander, "Integration of Propagation Modeling in Simulation of CDMA Communication Systems," IEEE AP-S/URSI Conference, Washington, DC, July 3–8, 2005.
  122. Z. Yun, and M. F. Iskander, "UWB pulse propagation through complex walls in indoor wireless communications environments," International Conference on Wireless Networks, Communications, and Mobile Computing, Maui, Hawaii, June 13–16, 2005.
  123. M. Rezk, W. Kim, Z. Yun, and M. F. Iskander, "Performance comparison of a novel hybrid smart antenna system versus the fully adaptive and switched beam antenna arrays," International Conference on Wireless Networks, Communications, and Mobile Computing, Maui, Hawaii, June 13–16, 2005.
  124. R. Gowrishankar, M. F. Demirkol, and Z. Yun, "Adaptive Modulation for MIMO Systems and Throughput Evaluation with Realistic Channel Model," International Conference on Wireless Networks, Communications, and Mobile Computing, Maui, Hawaii, June 13–16, 2005.
  125. Z. Yun, and M. F. Iskander, "Characterization of Angle of Arrival Based on Ray-Tracing for an Indoor Wireless Communications Environment," 2005 IEEE/ACES International Conference on Wireless Communications and Applied Computational Electromagnetics, Honolulu, Hawaii, April 3–7, 2005.
  126. C. Takahashi, Z. Yun, and M. F. Iskander, "Propagation Prediction Software for Wireless Communication System Optimization," 2005 IEEE/ACES International Conference on Wireless Communications and Applied Computational Electromagnetics, Honolulu, Hawaii, April 3–7, 2005.
  127. M. Rezk, W. Kim, Z. Yun, and M. F. Iskander, "Narrow Beam Adaptive Array for Advanced Wireless Applications," 2005 IEEE/ACES International Conference on Wireless Communications and Applied Computational Electromagnetics, Honolulu, Hawaii, April 3–7, 2005.
  128. Z. Yun and M. F. Iskander, "Progress in Modeling Challenging Propagation Environments," IEEE AP-S/URSI Conference, Monterey, California, June 20–26, 2004.
  129. Z. Yun and M. F. Iskander, "MIMO Capacity for Realistic Wireless Communications Environments," IEEE AP-S/URSI Conference, Monterey, California, June 20–26, 2004.
  130. Z. Yun, M. F. Iskander, "New Ray-tracing Techniques and Propagation Modeling for Challenging Communication Environments," ACES Conference, Syracuse, New York, April 19–23, 2004.

131. M. F. Iskander, "Antenna Technologies and Propagation Models for Advanced Wireless Communication Systems," IEEE Topical Conference on Wireless Communication Technology, Honolulu, Hawaii, October 15–17, 2003.
132. Z. Yun, M. F. Iskander, and Z. Zhang, "MIMO Capacity Calculation and Fading Estimation for Indoor/outdoor Wireless Communication Environments," IEEE Topical Conference on Wireless Communications Technology, Honolulu, Hawaii, October 15–17, 2003.
133. M. F. Iskander, R. Isom, T. A. Heffner, Z. Yun, and W. Milroy, "Design of Multiband Antenna Array using CTS and Photonic Band Gap Technologies," IEEE Topical Conference on Wireless Communications Technology, Honolulu, Hawaii, October 15–17, 2003.
134. R. K. Sorenson, M. F. Iskander, and J. J. Lee, "Low Cost Nonplanar Microstrip–line Ferrite Phase Shifter utilizing Circular Polarization," IEEE Topical Conference on Wireless Communications Technology, Honolulu, Hawaii, October 15–17, 2003.
135. R. Isom, M. F. Iskander, Z. Yun, and Z. Zhang, "Design and Development of Multiband Antenna Arrays for Multi-Service Wireless Communication Networks," 2003 IEEE 58th Vehicular Technology Conference, Orlando, Florida, October 6–9, 2003.
136. Z. Yun, M. F. Iskander, and Z. Zhang, "Complex-wall Effect on Fading and MIMO capacities for Wireless Communication Environments," 2003 IEEE 58th Vehicular Technology Conference, Orlando, Florida, October 6–9, 2003.
137. Z. Yun, M. F. Iskander, Z. Zhang, and R. K. Sorensen, "Outdoor/Indoor Propagation Prediction for Complex Wall and Window Structures Using Ray-Tracing Models," 2003 IEEE 58th Vehicular Technology Conference, Orlando, Florida, October 6–9, 2003.
138. Z. Zhang, M. F. Iskander, and Z. Yun, "Hybrid Smart Antenna System using Directional Elements," IEEE International Microwave Symposium, Philadelphia, Pennsylvania, June 8–13, 2003.
139. M. F. Iskander,<sup>6</sup> "Technology-Based Electromagnetic Education: Multimedia Assets and Interactive Modules for Modern EM Education," International Conference on Electromagnetics in Advanced Applications (ICEAA 01), Torino, Italy, September 10–14, 2001.
140. M. F. Iskander, Z. Yun, Z. Zhang, and R. Isom,<sup>7</sup> "Antenna Technology and Propagation Models for Next Generation Wireless Communications Systems," International Conference on Electromagnetics in Advanced Applications (ICEAA 01), Torino, Italy, September 10–14, 2001.
141. Z. Yun, Z. Zhang, and M. F. Iskander,<sup>8</sup> "Advanced and Computationally Efficient Ray-Tracing Method for Propagation Prediction in Urban Environment,"

---

<sup>6</sup>Plenary presentation.

<sup>7</sup>Plenary presentation.

<sup>8</sup>Plenary presentation.

- International Conference on Electromagnetics in Advanced Applications (ICEAA 01), Torino, Italy, September 10–14, 2001.
142. M. F. Iskander, “Asian Telecommunication Study—Overview and Summary of Findings,” International Technology Research Institute Workshop, Washington, DC, July 17, 2001.
  143. M. F. Iskander, “Asian Telecommunication Study—Microwave Technologies and Propagation Models for Wireless Communication Systems,” International Technology Research Institute Workshop, Washington, DC, July 17, 2001.
  144. M. F. Iskander, Z. Yun, and Z. Zhang, “Outdoor/Indoor Propagation Modeling for Wireless Communications Systems,” 2001 IEEE AP-S International Symposium and URSI Meeting, Boston, Massachusetts, July 8–13, 2001.
  145. Z. Zhang, Z. Yun, and M. F. Iskander, “New Computationally Efficient 2.5D and 3D Ray Tracing Algorithms for Modeling Propagation Environments,” 2001 IEEE AP-S International Symposium and URSI Meeting, Boston, Massachusetts, July 8–13, 2001.
  146. Z. Yun, M. F. Iskander, and Z. Zhang, “Development of a New Shooting-and-Bouncing Ray (SBR) Tracing Method that Avoids Ray Double Counting,” 2001 IEEE AP-S International Symposium and URSI Meeting, Boston, Massachusetts, July 8–13, 2001.
  147. Z. Zhang, M. Yeddulla, M. F. Iskander, and Z. Yun, “New Phase Shifter Designs Based on Multilayer Ferroelectric Materials Technology,” 2001 IEEE AP-S International Symposium and URSI Meeting, Boston, Massachusetts, July 8–13, 2001.
  148. R. Isom, M. F. Iskander, Z. Zhang, and Z. Yun, “Multi-Band and Broadband Coaxial CTS Array Design,” 2001 IEEE AP-S International Symposium and URSI Meeting, Boston, Massachusetts, July 8–13, 2001.
  149. V. Pathak, Z. Yun, and M. F. Iskander, “Development of an Integrated Multi-Grid 3D FDTD and Finite-Difference Heat Transfer Code to Simulate Microwave Drying in Multimode Cavities,” 2001 IEEE AP-S International Symposium and URSI Meeting, Boston, Massachusetts, July 8–13, 2001.
  150. M. F. Iskander, Z. Zhang, Z. Yun, R. Isom, M. Hawkins, R. Emrick, B. Bosco, J. Synowczynski, and B. Gersten, “New Phase Shifters and Phased Antenna Array Designs Based on Ferroelectric Materials and CTS Technologies,” 2001 IEEE MTT-S International Microwave Symposium, Phoenix, Arizona, May 20–25, 2001.
  151. M. F. Iskander, “Multimedia Assets and Interactive Modules in Web-Based Microwave Education,” 2001 IEEE MTT-S International Microwave Symposium Workshop, Phoenix, Arizona, May 20–25, 2001.
  152. Z. Yun, Z. Zhang, and M. F. Iskander, “New Ray Tracing Methods for Propagation Modeling in Wireless Communications,” 2000 National Radio Science Meeting, Boulder, Colorado, January 8–11, 2001.
  153. M. F. Iskander, Z. Yun, Z. Zhang, R. Jensen, and S. Redd, “Low-Cost Antenna Array with 2D Beam Steering Capability Using the CTS and Ferroelectric Materials Technologies,” 2000 Asia-Pacific Microwave Conference, Sydney, Australia, December 3–6, 2000.

154. M. F. Iskander, "Multimedia- and Computer-Based Education in Electromagnetics," 2000 IEEE AP-S International Symposium and URSI Meeting, Salt Lake City, Utah, July 16–21, 2000.
155. M. F. Iskander, "Advances in Technology-Based Engineering Education," 2000 IEEE AP-S International Symposium and URSI Meeting, Salt Lake City, Utah, July 16–21, 2000.
156. Deepak K. Ghodgaonkar, Om P. Gandhi and M. F. Iskander, "Complex Permittivity of Human Skin In Vivo in the Frequency Band 26.5-60 GHz," in IEEE Antennas and Propagation Society Symposium Proceedings, Salt Lake City, Utah, July 16–20, 2000.
157. T. Itoh, J. Winters, and M. F. Iskander, "Recommendations for Research Opportunities from the WTEC Study on Wireless Technologies and Information Networks," 2000 IEEE AP-S International Symposium and URSI Meeting, Salt Lake City, Utah, July 16–21, 2000.
158. Z. Yun, M. F. Iskander, and Z. Zhang, "A Fast Ray Tracing Procedure using Space Division with Uniform Rectangular Grid," 2000 IEEE AP-S International Symposium and URSI Meeting, Salt Lake City, Utah, July 16–21, 2000.
159. M. F. Iskander, Z. Yun, Z. Zhang, R. Isom, and M. Hawkins, "Antenna Designs and Propagation Models for Advanced Wireless Communications Systems," 2000 IEEE AP-S International Symposium and URSI Meeting, Salt Lake City, Utah, July 16–21, 2000.
160. M. F. Iskander, Z. Yun, and Z. Zhang, "Design of a Low-Cost 2D Beam Steering Antenna using Ferroelectric Material and the CTS Technology," 2000 IEEE AP-S International Symposium and URSI Meeting, Salt Lake City, Utah, July 16–21, 2000.
161. D. Ghodgaonkar, O. P. Gandhi, and M. F. Iskander, "Complex Permittivity of Human Skin In Vivo in the Frequency Band 26.5-60 GHz," 2000 IEEE AP-S International Symposium and URSI Meeting, Salt Lake City, Utah, July 16–21, 2000.
162. Z. Zhang, Z. Yun, and M. F. Iskander, "A New Ray Tracing Method for Propagation Models in Wireless Communication," 2000 IEEE AP-S International Symposium and URSI Meeting, Salt Lake City, Utah, July 16–21, 2000.
163. Z. Yun, M. F. Iskander, and Z. Zhang, "A Fast Indoor/Outdoor Ray Tracing Procedure using Combined Uniform Rectangular and Unstructured Triangular Grids," 2000 IEEE AP-S International Symposium and URSI Meeting, Salt Lake City, Utah, July 16–21, 2000.
164. M. F. Iskander,<sup>9</sup> "Wireless Information Technology and Networks," IT Workshop sponsored by the National Science Foundation, Cairo, Egypt, March 2000.

---

<sup>9</sup>Invited presentation.

165. M. F. Iskander,<sup>10</sup> “Technology-Based Engineering Education,” IT Workshop sponsored by the National Science Foundation, Cairo, Egypt, March 2000.
166. M. F. Iskander, Z. Yun, and Z. Zhang,<sup>11</sup> “Antenna Designs and Propagation Models for Next Generation Wireless Communications Systems,” IEEE Microwave Theory and Techniques Society Symposium on Technologies for the Communication Revolution, 2000 Sarnoff Symposium, Newark, New Jersey, March 2000.
167. M. F. Iskander, “Review of NSF Workshop on RF Micromachining and MEMS for Advanced Wireless Communications Systems,” NRL Workshop on MEMS, Arlington, Virginia, February 2000.
168. M. F. Iskander, “Role of RF Micromachining and MEMS in Advanced Wireless Communications Systems,” RF Micromachining and MEMS Workshop, Arlington, Virginia, December 1999.
169. M. F. Iskander,<sup>12</sup> “Millimeter Wave Technology for Advanced Wireless Communications,” MM-Wave Symposium, Tokyo, Japan, December 19–20, 1999.
170. M. F. Iskander,<sup>13</sup> “Multimedia- and Computer-Based Engineering Education,” 29th European Microwave Conference, Munich, Germany, vol. 2, pp. 90–92, October 5–7, 1999.
171. M. F. Iskander,<sup>14</sup> “Antenna Arrays and Propagation Models for Advanced Wireless Communications,” Brazilian Microwave Conference, Rio de Janeiro, Brazil, August 11–14, 1999.
172. M. F. Iskander,<sup>15</sup> “Technology-Based and Multimedia Engineering Education,” Brazilian Microwave Conference, Rio de Janeiro, Brazil, August 11–14, 1999.
173. M. F. Iskander, Z. Yun, R. Jensen, and S. Redd, “Design of a Low-Cost 2D Beam-Steering Antenna Using the CTS Technology,” 1999 IEEE AP-S International Symposium and URSI Meeting, Orlando, Florida, July 11–16, 1999.
174. Z. Yun, M. F. Iskander, and M. J. White, “Analysis and Design of Large Antenna Arrays Using Multi-Grid FDTD and Floquet Boundary Condition,” 1999 IEEE AP-S International Symposium and URSI Meeting, Orlando, Florida, July 11–16, 1999.
175. R. Quintero-Illera, M. F. Iskander, and Z. Yun, “Polarization and Human Body Effects on the Microwave Absorption in a Human Head Exposed to Radiation From Hand-Held Devices,” 1999 IEEE AP-S International Symposium and URSI Meeting, Orlando, Florida, July 11–16, 1999.

---

<sup>10</sup>Invited tutorial.

<sup>11</sup>Invited presentation.

<sup>12</sup>Invited presentation.

<sup>13</sup>Invited presentation.

<sup>14</sup>Invited presentation.

<sup>15</sup>Keynote presentation.

176. Z. Yun and M. F. Iskander, "Development of a New Indoor Propagation Model for Wireless Communications," 1999 IEEE AP-S International Symposium and URSI Meeting, Orlando, Florida, July 11–16, 1999.
177. M. F. Iskander, Plenary Speaker, Applied Computational Electromagnetics Society Conference, Monterey, California, March 15–20, 1999.
178. M. F. Iskander, "Multimedia and Technology-Based Engineering Education," 1998 IEICE Conference, Kofu, Japan, September 29–October 2, 1998.
179. M. F. Iskander, "Wireless Technologies and Information Networks," Global Wireless Education Consortium Conference, Dallas, Texas, August 13–15, 1998.
180. M. F. Iskander, "New Wireless Technologies," 1998 International Conference on Crossed-Field Devices and Applications (CDFA'98), Boston, Massachusetts, June 17–18, 1998.
181. J. Fabrega, S. Sanz, and M. F. Iskander, "New Software Packages and Multimedia Modules for Electromagnetic Education," IEEE AP-S International Symposium and URSI Meeting, Atlanta, Georgia, June 21–26, 1998.
182. R. Quintero, Z. Yun, and M. F. Iskander, "Multigrid Code for Calculating Microwave Absorption Pattern in Human Head Radiated by Hand-Held Antennas," IEEE AP-S International Symposium and URSI Meeting, Atlanta, Georgia, June 21–26, 1998.
183. Z. Yun, M. J White, R. Quintero, and M. F. Iskander, "Application of Multigrid FDTD to the Simulation and Design of Microwave Processing System," IEEE AP-S International Symposium and URSI Meeting, Atlanta, Georgia, June 21–26, 1998.
184. Z. Yun and M. F. Iskander, "Comparison of Ray Tracing, 3D and 2D FDTD Simulation of Propagation Models for Wireless Communications," IEEE AP-S International Symposium and URSI Meeting, Atlanta, Georgia, June 21–26, 1998.
185. M. F. Iskander, "Vision, Leadership, and Commitment to the Effective Development and Implementation of Technology-Based Electromagnetics Education—Tribute to Prof. R. E. Collin," IEEE AP-S International Symposium and URSI Meeting, Atlanta, Georgia, June 21–26, 1998.
186. M. J White and M. F. Iskander, "A New 3D FDTD Multi-Grid Technique with Dielectric-Traverse Capabilities," IEEE Antennas and Propagation Society International Symposium, Montréal, Canada, July 13–18, 1997.
187. S. Bringham, M. F. Iskander, and M. J White, "Broadband, High-Temperature Dielectric Properties Measurements of Thin Substrates Using Open-Ended Probes," IEEE Antennas and Propagation Society International Symposium, Montréal, Canada, July 13–18, 1997.
188. M. F. Iskander, A. Rodriguez-Balcells, O. de los Santos, R. M. Jameson, and A. Nielsen, "New Interactive Multimedia CD-ROM for Engineering Electromagnetics," IEEE Antennas and Propagation Society International Symposium, Montréal, Canada, July 13–18, 1997.

189. M. F. Iskander, R. M. Jameson, A. Rodriguez-Balcells, A. Nielsen, E. Pronk, and J. C. Catten, "Interactive Multimedia CD-ROMs for Education," *Frontiers in Education Conference (FIE'96)*, Salt Lake City, Utah, November 6–9, 1996.
190. O. de los Santos Vidal, R. M. Jameson, M. F. Iskander, A. Balcells, and J. C. Catten, "Interaction and Simulation-Based Multimedia Modules for Electromagnetics Education," *Frontiers in Education Conference (FIE'96)*, Salt Lake City, Utah, November 6–9, 1996.
191. A. Balcells, R. M. Jameson, M. F. Iskander, O. de los Santos Vidal, and D. Jachmann, "Practical Applications-Based Multimedia Modules for Engineering Education," *Frontiers in Education Conference (FIE'96)*, Salt Lake City, Utah, November 6–9, 1996.
192. M. F. Iskander, R. Jameson, E. Pronk, A. Balcells, A. Nielsen, and J. C. Catten, "Procedures for Increasing Interactivity in Multimedia Educational Modules," *Frontiers in Education Conference (FIE'96)*, Salt Lake City, Utah, November 6–9, 1996.
193. M. J. White, M. F. Iskander, Z. Huang, and H. D. Kimrey, "A Three-Dimensional Multi-Grid FDTD Code for Modeling Microwave Sintering of Materials," *IEEE Antennas and Propagation Society International Symposium*, Baltimore, Maryland, July 21–26, 1996.
194. S. Bringhamst and M. F. Iskander, "FDTD Analysis of Dielectric Properties Measurements Using Open-Ended Coaxial Probes," *IEEE Antennas and Propagation Society International Symposium*, Baltimore, Maryland, July 21–26, 1996.
195. J. I. Ortigosa, N. Padros, and M. F. Iskander, "Comparative Study of High Performance GPS Receiving Antenna Designs," *IEEE Antennas and Propagation Society International Symposium*, Baltimore, Maryland, July 21–26, 1996.
196. M. Subirats, M. F. Iskander, M. J. White, and J. Kiggans, "FDTD Simulation of Microwave Sintering in Large (500/4000 liter) Multimode Cavities," *Materials Research Society Spring Meeting*, San Francisco, California, April 8–12, 1996.
197. S. Bringhamst, M. F. Iskander, and M. J. White, "FDTD Simulations and Analysis of Thin Sample Dielectric Properties Measurements Using Coaxial Probes," *Materials Research Society Spring Meeting*, San Francisco, California, April 8–12, 1996.
198. M. J. White, M. F. Iskander, and H. D. Kimrey, "Development of a Multi-Grid FDTD Code for Three-Dimensional Simulation of Large Microwave Sintering Experiments," *Materials Research Society Spring Meeting*, San Francisco, California, April 8–12, 1996.
199. S. Bringhamst, M. J. White, and M. F. Iskander, "Numerical Simulation and Experimental Validation of RF Drying," *Materials Research Society Spring Meeting*, San Francisco, California, April 8–12, 1996.
200. M. J. White, M. F. Iskander, and S. Bringhamst, "FDTD Simulation of Induction Heating of Conducting Ceramic Ware," *Materials Research Society Spring Meeting*, San Francisco, California, April 8–12, 1996.



201. M. J. White, S. F. Dillon, M. F. Iskander, and H. D. Kimrey, "Finite-Difference Time-Domain Simulation of Microwave Sintering in a Variable-Frequency Multimode Cavity," Materials Research Society Spring Meeting, San Francisco, California, April 8–12, 1996.
202. A. Balcells, R. M. Jameson, J. C. Catten, A. K. Jones, M. F. Iskander, and D. Jachmann, "Practical Applications-Based Multimedia Modules for Engineering Education," International Conference on Simulation and Multimedia in Engineering Education (ICSEE'96), San Diego, California, January 14–17, 1996.
203. M. Jameson, M. F. Iskander, J. C. Catten, and A. Balcells, "Interaction and Simulation-Based Multimedia Modules for Electromagnetics Education," International Conference on Simulation and Multimedia in Engineering Education (ICSEE'96), San Diego, California, January 14–17, 1996.
204. K. Jones, D. Jachmann, J. C. Catten, R. M. Jameson, A. Rodriguez-Balcells, and M. F. Iskander, "Development of Three-Dimensional Computer-Rendered Graphics for Multimedia Presentation," International Conference on Simulation and Multimedia in Engineering Education (ICSEE'96), San Diego, California, January 14–17, 1996.
205. J. C. Catten, M. F. Iskander, R. M. Jameson, A. K. Jones, and A. Rodriguez-Balcells, "Interactive Multimedia Modules for Engineering Education," International Conference on Simulation and Multimedia in Engineering Education (ICSEE'96), San Diego, California, January 14–17, 1996.
206. M. F. Iskander, J. C. Catten, A. Jones, R. Jameson, and A. Balcells, "Interactive Multimedia Lessons for Education," 1995 Frontiers in Education Conference, Atlanta, Georgia, November 1–4, 1995.
207. M. F. Iskander,<sup>16</sup> "Interactive Multimedia Lessons for Education," SBMO/IEEE MTT-S International Microwave and Optoelectronics Conference, Rio de Janeiro, Brazil, July 24–27, 1995.
208. M.F. Iskander, Y. Yao, M. Subirats, M. J White, and J. Kiggans, "FDTD Simulation of Large-Scale Microwave Processing Systems," 30th International Microwave Power Symposium, Denver, Colorado, July 10–12, 1995.
209. M. F. Iskander, M. J White, Z. Huang, and H. Kimrey, "Simulation of Realistic Microwave Sintering Experiments using a Variable-Mesh FDTD Code," 30th International Microwave Power Symposium, Denver, Colorado, July 10–12, 1995.
210. P. C. Cherry and M. F. Iskander, "Obtaining High-Performance Time-Domain Characteristics from Calculated S-Parameters for Various Electronic Package and Interconnection Structures," IEEE Antennas and Propagation Society International Symposium, Newport Beach, California, June 18–23, 1995.

---

<sup>16</sup>Invited presentation.

211. M. F. Iskander, J. C. Catten, A. Jones, R. Jameson, and A. Balcells, "CoLoS USA—An Interdisciplinary Consortium for Conceptual Learning and Innovative Problem Solving," IEEE Antennas and Propagation Society International Symposium, Newport Beach, California, June 18–23, 1995.
212. M. F. Iskander,<sup>17</sup> "Vision, Persistence, Commitment, and Leadership: The Role of Irene in the Development of CAEME," 1995 IEEE AP-S International Symposium and URSI Radio Science Meeting, Newport Beach, California, June 18–23, 1995.
213. S. Bringham and M. F. Iskander, "Thin Sample Dielectric Properties Measurement using Open-Ended Coaxial Probes and FDTD Calculations," IEEE Antennas and Propagation Society International Symposium, Newport Beach, California, June 18–23, 1995.
214. H. D. Kimrey, J. O. Kiggans, M. F. Iskander, M. Subirats, Y. Yao, S. Bringham, M. White, and Z. Huang, "Computer Simulation of Multi-Mode Microwave Cavities for Materials Processing," Advanced Industrial Materials Program Annual Meeting, Washington, DC, June 14–16, 1995.
215. M. F. Iskander, J. C. Catten, S. McClellan, R. Jameson, and A. Jones, "Interactive Multimedia Lessons for Education," International Conference on Simulation in Engineering Education (ICSEE'95), Las Vegas, Nevada, January 15–18, 1995.
216. M. F. Iskander and J. C. Catten, "The CAEME Center for Multimedia Education," IEEE Antennas and Propagation Society International Symposium, Seattle, Washington, June 19–24, 1994.
217. S. Bringham, M. F. Iskander, and P. Gartside, "Design and FDTD Analysis of Open-Ended Coaxial Probes for Broadband High-Temperature Dielectric Properties Measurements," IEEE Antennas and Propagation Society International Symposium, Seattle, Washington, June 19–24, 1994.
218. P. J. Gartside, M. J. White, M. F. Iskander, C. J. Malarkey, and D. R. Treacy, "Numerical Modeling and Simulation of Microwave Heating Processes," IEEE Antennas and Propagation Society International Symposium, Seattle, Washington, June 19–24, 1994.
219. P. C. Cherry and M. F. Iskander, "High-Frequency Electronic Package and Interconnection Effects," IEEE Antennas and Propagation Society International Symposium, Seattle, Washington, June 19–24, 1994.
220. Z. Huang, J. Tucker, and M. F. Iskander, "FDTD Modeling of Realistic Microwave Sintering Experiments," IEEE Antennas and Propagation Society International Symposium, Seattle, Washington, June 19–24, 1994.
221. D. F. Stein, R. H. Edgar, M. F. Iskander, D. L. Johnson, S. M. Johnson, C. G. Lob, J. M. Shaw, W. H. Sutton, P. K. Tien, and T. E. Munns, "Microwave Processing—An Emerging Industrial Technology?," Materials Research Society Spring Meeting, San Francisco, California, April 4–8, 1994.

---

<sup>17</sup>Invited presentation.

222. S. Bringham, M. F. Iskander, and P. Gartside, "FDTD Simulation of an Open-Ended Metallized Ceramic Probe for Broadband High-Temperature Dielectric Properties Measurements," Materials Research Society Spring Meeting, San Francisco, California, April 4–8, 1994.
223. M. J. White, P. J. Gartside, and M. F. Iskander, "Numerical Modeling and Simulation of Electromagnetic Drying Processes," Materials Research Society Spring Meeting, San Francisco, California, April 4–8, 1994.
224. Z. Huang, M. F. Iskander, J. Tucker, and H. D. Kimrey, "FDTD Modeling of Realistic Microwave Sintering Experiments," Materials Research Society Spring Meeting, San Francisco, California, April 4–8, 1994.
225. J. Tucker, M. F. Iskander, and Z. Huang, "Calculation of Heating Patterns in Microwave Sintering using a 3D Finite-Difference Code," Materials Research Society Spring Meeting, San Francisco, California, April 4–8, 1994.
226. M. F. Iskander, S. Bringham, and P. Gartside, "FDTD Simulation of an Open-Ended Metallized Ceramic Probe for Broadband High-Temperature Dielectric Properties Measurements," Applied Computational Electromagnetics Society Conference, Monterey, California, March 21–26, 1994.
227. M. F. Iskander, P. Gartside, M. White, and C. J. Malarkey, "FDTD Simulation of RF Drying and Induction Heating Processes," Applied Computational Electromagnetics Society Conference, Monterey, California, March 21–26, 1994.
228. M. F. Iskander, "The CAEME Center—New Software and Multimedia Activities," International Conference on Simulation in Engineering Education (ICSEE'94), Tempe, Arizona, January 24–26, 1994.
229. M. F. Iskander, "The CAEME Numerical Modeling Codes," IEEE Electromagnetic Society International Symposium, Dallas, Texas, August 9–13, 1993.
230. M. F. Iskander, "Analysis and Characterization of Microwave Interstitial Antennas," IEEE Antennas and Propagation Society International Symposium, Ann Arbor, Michigan, June 28–July 2, 1993.
231. P. McArthur, M. F. Iskander, C. Catten, J. Hunsaker, D. Jensen, M. Orme, and B. Tame, "Microwave Interstitial Antennas for Arterial Plaque Ablation," IEEE Antennas and Propagation Society International Symposium, Ann Arbor, Michigan, June 28–July 2, 1993.
232. M. F. Iskander, D. Roper, L. Walsh, T. Ngo, and H. Kimrey, "FDTD Simulation of Microwave Sintering in Single- and Multimode Cavities," IEEE Antennas and Propagation Society International Symposium, Ann Arbor, Michigan, June 28–July 2, 1993.
233. S. Bringham, O. M. Andrade, and M. F. Iskander, "New Metallized Ceramic Coaxial Probe for High-Temperature Dielectric Property Measurements," IEEE Antennas and Propagation Society International Symposium, Ann Arbor, Michigan, June 28–July 2, 1993.
234. M. F. Iskander and T. Reed, "Multimedia Lessons for Electromagnetic Education," IEEE Antennas and Propagation Society International Symposium, Ann Arbor, Michigan, June 28–July 2, 1993.

235. M. F. Iskander and T. Reed, "Interactive Video Lessons for Electromagnetic Education," Applied Computational Electromagnetics Society Conference, Monterey, California, March 22–26, 1993.
236. M. F. Iskander,<sup>18</sup> "The Role of CAEME in the Stimulation and Propagation of Effective Electromagnetics Education in the U.S.A. and Abroad," 22nd European Microwave Conference, Helsinki University of Technology, Espoo, Finland, August 24–27, 1992.
237. M. F. Iskander, R. Smith, O. M. Andrade, and H. Kimrey, "Modeling and Numerical Simulation of Realistic Microwave Sintering Experiments," Materials Research Society Spring Meeting, San Francisco, California, April 28–May 2, 1992.
238. S. Bringham, O. M. Andrade, and M. F. Iskander, "Narrow- and Broad-Band High-Temperature Dielectric Properties Measurements of Sintered Ceramics," Materials Research Society Spring Meeting, San Francisco, California, April 28–May 2, 1992.
239. B. Chapman, M. F. Iskander, R. Smith, and O. M. Andrade, "Simulation of Sintering Experiments in Single-Mode Cavities," Materials Research Society Spring Meeting, San Francisco, California, April 28–May 2, 1992.
240. J. Tucker, R. Smith, M. F. Iskander, and O. M. Andrade, "Dynamic Model for Calculating Heating Patterns During Microwave Sintering," Materials Research Society Spring Meeting, San Francisco, California, April 28–May 2, 1992.
241. O. M. Andrade, M. F. Iskander, and S. Bringham, "High-Temperature Broad-band Dielectric Properties Measurement Techniques," Materials Research Society Spring Meeting, San Francisco, California, April 28- May 2, 1992.
242. R. L. Smith, M. F. Iskander, O. M. Andrade, and H. Kimrey, "FDTD Simulation of Microwave Sintering in Multimode Cavities," Materials Research Society Spring Meeting, San Francisco, California, April 27- May 1, 1992.
243. M. F. Iskander, "Reflections on CAEME Software and New Developments Towards Software Implementation in Classroom Teaching," IEEE Antennas and Propagation Society and URSI International Symposium, Chicago, Illinois, July 18–25, 1992.
244. R. L. Smith, M. F. Iskander, O. Andrade, and H. Kimrey, "FDTD Simulation of Microwave Sintering in Multimode Cavities," IEEE Antennas and Propagation Society and URSI International Symposium, Chicago, Illinois, July 18–25, 1992.
245. O. M. Andrade, S. Bringham, and M. F. Iskander, "Microwave Dielectric Measurements of Ceramic Composites at High Temperatures," IEEE Antennas and Propagation Society and URSI International Symposium, Chicago, Illinois, July 18–25, 1992.

---

<sup>18</sup>Invited presentation.

246. H. Astrain, D. R. Bridges, P. C. Cherry, G. Davis, M. L. Gundersen, K. R. Hulse, M. F. Iskander, B. M. Prestwich, R. Sundstrom, M. S. Talbot, and W. Valentine, "Development of a Generalized High-Frequency Model for Surface-Mount Microelectronic Packages," IEEE Antennas and Propagation Society and URSI International Symposium, Chicago, Illinois, July 18–25, 1992.
247. M. F. Iskander, "Reflections on the First CAEME Book and a Description of Future Directions," Applied Computational Electromagnetics Society Conference, Monterey, California, March 17–20, 1992.
248. M. F. Iskander,<sup>19</sup> "The NSF/IEEE CAEME Center, an Exciting Opportunity to Make a Difference in EM Education," IEEE Education Society Meeting, "Frontiers in Engineering Education," Purdue University, September 22–24, 1991.
249. M. F. Iskander,<sup>20</sup> "Computational Techniques in Quantifying Microwave Interactions with Materials," 93rd Annual Meeting and Exposition, American Ceramic Society, Cincinnati, Ohio, April 28–May 2, 1991.
250. M. F. Iskander, O. Andrade, R. Smith, S. Lamoreaux, C. Cheng, and H. Kimrey, "Microwave Sintering of Ceramics: Parts A and B," American Ceramic Society Meeting, Cincinnati, Ohio, April 28–May 2, 1991.
251. P. C. Cherry and M. F. Iskander,<sup>21</sup> "Finite-Difference Solutions of EM Power Deposition Pattern and Temperature Distribution Patterns from an Array of Interstitial Antennas in Inhomogeneous Sections of the Human Body," Progress in Electromagnetic Research Symposium, Cambridge, Massachusetts, July 1–5, 1991.
252. J. Butler, D. Rytting, and M. F. Iskander, "16-Term Error Model and Calibration Procedure for Wafer Network Analysis Measurements," International Microwave Symposium, Boston, Massachusetts, June 11–14, 1991.
253. M. F. Iskander,<sup>22</sup> "Review of CAEME Activities and Future Focus," IEEE Antennas and Propagation Society International Symposium, London, Ontario, Canada, June 24–28, 1991.
254. M. F. Iskander, with IBM Clinic Team (N. Aakalu, J. Barnes, R. Beard, G. Christiansen, E. Kamerath, and L. Vuu), "The Design of a Knowledge-Based System for Electronic Package Design," IEEE Antennas and Propagation Society International Symposium, London, Ontario, Canada, June 24–28, 1991.
255. M. F. Iskander, P. Cherry, H. Y. Chen, and J. E. Penner, "Calculation of Optical Properties of Impure Cloud Drops Using FDTD and Realistic Modeling of Scavenging of Carbonaceous Particles," IEEE Antennas and Propagation Society International Symposium, London, Ontario, Canada, June 24–28, 1991.

---

<sup>19</sup>Invited presentation.

<sup>20</sup>Keynote presentation.

<sup>21</sup>Invited presentation.

<sup>22</sup>Invited presentation.

256. M. F. Iskander, "Review of CAEME Activities, Software Development Projects, and Future Focus," Progress in Electromagnetic Research Symposium, Cambridge, Massachusetts, July 1–5, 1991.
257. M. F. Iskander, O. Andrade, R. Smith, S. Lamoreaux, and H. Kimrey,<sup>23</sup> "Numerical Modeling of Ceramic Sintering in Single and Multimode Microwave Cavities," Progress in Electromagnetic Research Symposium, Cambridge, Massachusetts, July 1–5, 1991.
258. M. F. Iskander, "Computer Applications in Electromagnetic Education," presented at the ASEE Rocky Mountain Meeting, Provo, Utah, April 18–19, 1991.
259. M. F. Iskander,<sup>24</sup> "The NSF/IEEE CAEME Center Activities: Progress Report, Software Projects, and Future Focus," Applied Computational Electromagnetic Society Symposium, Monterey, California, March 19–21, 1991.
260. O. Andrade and M. F. Iskander,<sup>25</sup> "Comparative Study of Broadband Dielectric Properties Measurements," International Microwave Power Institute, 25th Microwave Power Symposium, Denver, Colorado, August 27–29, 1990.
261. M. F. Iskander and T. S. Lind, "Analysis of Coupling Characteristics of Coplanar Waveguides and Microstrip Lines to Multilayer Dielectric Media," IEEE Antennas and Propagation Society Symposium, Dallas, Texas, May 7–11, 1990.
262. P. C. Cherry and M. F. Iskander, "Finite-Difference Time-Domain Analysis of Power Deposition Pattern of an Array of Interstitial Antennas," IEEE Antennas and Propagation Society Symposium, Dallas, Texas, May 7–11, 1990.
263. M. F. Iskander, "Computer Utilization in Teaching Concepts: Is it Reality or Illusion," IEEE Antennas and Propagation Society International Symposium, Dallas, Texas, May 7–11, 1990.
264. M. F. Iskander, "Computer Applications in Electromagnetics Education—The CAEME Center," CAEME Workshop held in conjunction with the IEEE Antennas and Propagation Society International Symposium, Dallas, Texas, May 7–11, 1990.
265. M. F. Iskander,<sup>26</sup> "The Role of Numerical Techniques and Computer Modeling in Quantifying Microwave Interactions with Materials," Materials Research Society Meeting in San Francisco, California, April 16–21, 1990.
266. S. Y. Limaye, P. Lohse, and M. F. Iskander, "High Temperature Dielectric Properties of the Low Thermal Expansion Materials," Materials Research Society Symposium, San Francisco, California, April 16–21, 1990.

---

<sup>23</sup>Invited presentation.

<sup>24</sup>Invited presentation.

<sup>25</sup>Invited presentation.

<sup>26</sup>Invited presentation.

267. J. Anderson and M. F. Iskander, "Apparatus and Technique for Measuring Dielectric Properties in the Frequency Range of 0.1 to 200 MHz," Materials Research Society Symposium, San Francisco, California, April 16–21, 1990.
268. M. F. Iskander,<sup>27</sup> "Computer Applications in Electromagnetic Education (CAEME)," 1990 Symposium of the Applied Computational Electromagnetics Society, Monterey, California, March 19–23, 1990.
269. M. F. Iskander, H. Y. Chen, and J. E. Penner, "Calculation of Optical Properties of Impure Cloud Drops Using Realistic Modeling of Nucleation Scavenging of Smoke Particles," American Association for Aerosol Research Meeting, Reno, Nevada, October 10–13, 1989.
270. M. F. Iskander, "Computer Applications in Electromagnetics Education," Conference on Innovation in Engineering Education, sponsored by NSF/Engineering Foundation, Mercersburg Academy, Pennsylvania, August 6–11, 1989.
271. M. F. Iskander, A. M. Tumeh, and C. M. Furse, "Evaluation and Optimization of the Electromagnetic Characteristics of Interstitial Antennas for Microwave Hyperthermia," 1989 International Microwave Symposium, Sao Paulo, Brazil, July 24–27, 1989.
272. M. F. Iskander, H. Y. Chen, and J. E. Penner, "Light Scattering and Absorption by Fractal Agglomerates of Smoke Aerosols," 1989 International Microwave Symposium, Sao Paulo, Brazil, July 24–27, 1989.
273. M. F. Iskander,<sup>28</sup> "Numerical Techniques in Electromagnetics—Comparative Review with Emphasis on Application in 3D Modeling," 1989 International Microwave Symposium, Sao Paulo, Brazil, July 24–27, 1989.
274. H. Y. Chen, M. F. Iskander, and J. E. Penner, "Electromagnetic Properties of Fractal Aerosol Agglomerates," 1989 IEEE Antennas and Propagation Society International Symposium, San Jose, California, June 26–30, 1989.
275. M. F. Iskander and T. S. Lind, "Electromagnetic Coupling of Microstrip Lines and Coplanar Waveguides to Multi-Layer Lossy Media," 1989 IEEE Microwave Theory and Techniques Society International Microwave Symposium, Long Beach, California, June 13–15, 1989.
276. M. F. Iskander, "A New Course on Computational Electromagnetics," Workshop on Computer Applications in Electromagnetics Education, IEEE Antennas and Propagation Society International Symposium, San Jose, California, June 25, 1989.
277. M. F. Iskander, "CAEME—Its Objectives, Policies, and Procedures," Workshop on Computer Applications in Electromagnetics Education, IEEE Antennas and Propagation Society International Symposium, San Jose, California, June 25, 1989.

---

<sup>27</sup>Invited presentation.

<sup>28</sup>Invited presentation.

278. M. F. Iskander, "Computer Applications in Electromagnetics Education," Conference on Innovation in Undergraduate Engineering Education, sponsored by NSF/Engineering Foundation, Mercersburg Academy, Pennsylvania, August 6–11, 1989.
279. K. Joo and M. F. Iskander, "An Extended Equivalent Source Technique for Calculating Scattering and Absorption by Electrically Long and Composite Dielectric Objects," 1989 IEEE Antennas and Propagation Society International Symposium, San Jose, California, June 26–30, 1989.
280. M. F. Iskander,<sup>29</sup> "Biological Effects and Medical Applications of Electromagnetic Techniques," Materials Research Society Meeting, Reno, Nevada, April 5–9, 1988.
281. M. F. Iskander, H. Y. Chen, and J. E. Penner (invited), "Light Scattering and Absorption by Chained Agglomerates and Coagulations of Smoke Aerosols," American Association for Aerosol Research Meeting, Chapel Hill, North Carolina, October 10–14, 1988.
282. M. F. Iskander, H. Y. Chen, and J. E. Penner, "Electromagnetic Absorption and Scattering by Aerosol Chains of Complex Geometries," Defense Nuclear Agency Workshop on Climatic Impact of Smoke Aerosols, Santa Barbara, California, April 18–21, 1988.
283. M. F. Iskander and A. M. Tumeh, "Design Optimization of Interstitial Antennas for Microwave Hyperthermia," IEEE Microwave Theory and Techniques Society International Microwave Symposium, New York, New York, May 25–27, 1988.
284. M. F. Iskander, H. Y. Chen, and J. E. Penner, "Scattering and Absorption by Long Chains of Particles of Branched Structures," URSI Radio Science Meeting, Syracuse University, Syracuse, New York, June 6–10, 1988.
285. M. F. Iskander and A. M. Tumeh, "Numerical Evaluation of Interstitial Antennas for Hyperthermia," Radiation Research Society 36th Annual Meeting, April 15–19, 1988.
286. C. M. Furse and M. F. Iskander, "Three Dimensional Electromagnetic Power Deposition in Tumors Using Interstitial Antenna Array," Tenth Annual Meeting of the Bioelectromagnetics Society, Stamford, Connecticut, June 19–24, 1988.
287. A. M. Tumeh and M. F. Iskander, "Performance Comparison of Available Interstitial Antennas for Microwave Hyperthermia," Tenth Annual Meeting of the Bioelectromagnetics Society, Stamford, Connecticut, June 19–24, 1988.
288. M. F. Iskander, H. Y. Chen, and J. E. Penner, "Scattering and Absorption by Elongated Aerosol Particles in the Resonance Frequency Range," Third International Conference on Carbonaceous Particles in the Atmosphere, Lawrence Berkeley Laboratory, October 5–8, 1987.

---

<sup>29</sup>Plenary presentation.



289. M. F. Iskander, T. V. Doung, C. Chen, and C. M. Furse, "A New Sectioning Procedure for Improving the Computational Efficiency of the IEBCM," IEEE Antennas and Propagation Society International Symposium, Blacksburg, Virginia, June 15–19, 1987.
290. M. F. Iskander, M. Morrison, and M. Hamilton, "A New Course on Computer Methods in Electromagnetics," IEEE Antennas and Propagation Society International Symposium, Blacksburg, Virginia, June 15–19, 1987.
291. M. F. Iskander and C. M. Furse, "Utilization of Sectioning Procedure to Calculate Light Scattering by Very Long and Irregularly-Shaped Aerosols," CRDEC Scientific Conference on Aerosol Research, Aberdeen Proving Grounds, Maryland, June 23–27, 1986.
292. V. Sathaseelan, M. F. Iskander, G. C. W. Howard, S. M. Crocker, and N. M. Bleehen, "Theoretically Predicted Effect of Phase and Amplitude Variation on the Electromagnetic Power Deposition Patterns for the Annular-Phased Array Hyperthermia System," VIII Meeting of European Society of Hyperthermic Oncology, Villejuif, Paris, France, September 16–18, 1985.
293. M. F. Iskander, S. C. Olson, C. H. Durney, and J. F. McCalmont, "Near-Field Absorption Characteristics of Spheroidal Models in the Resonance Frequency Range," Seventh Annual Meeting of the Bioelectromagnetics Society, San Francisco, California, June 16–20, 1985.
294. S. Rattlingourd, M. F. Iskander, C. H. Durney, and A. C. Ludwig, "Calculation of SARs from Measured Electric Field Data," Seventh Annual Meeting of the Bioelectromagnetics Society, San Francisco, California, June 16–20, 1985.
295. D. K. Ghodgaonkar, M. F. Iskander, and O. P. Gandhi, "Complex Permittivity Measurement of Biological Tissues and Human Skin *In Vivo* at Millimeter Wavelengths," Seventh Annual Meeting of the Bioelectromagnetics Society, San Francisco, California, June 16–20, 1985.
296. M. F. Iskander, S. Smith, O. P. Gandhi, and D. K. Ghodgaonkar, "Dielectric Properties Measurements at Millimeter Waves Using a Free Space Method," Seventh Annual Meeting of the Bioelectromagnetics Society, San Francisco, California, June 16–20, 1985.
297. H. Massoudi, C. H. Durney, and M. F. Iskander, "Numerical Evaluation of SAR Distributions in Biological Models: Comparison of Two Different Integral Equations and Basis Functions," Seventh Annual Meeting of the Bioelectromagnetics Society, San Francisco, California, June 16–20, 1985.
298. M. F. Iskander, S. C. Olson, and D. Yoshida, "Optical Scattering by Metallic and Carbon Aerosols of High Aspect Ratio," CRDC Scientific Conference on Obscuration and Aerosol Research, Aberdeen Proving Ground, Maryland, June 17–21, 1985.
299. M. F. Iskander,<sup>30</sup> "An Iterative Extended Boundary Condition Method for Calculating Scattering and Absorption by Elongated Dielectric Objects," URSI Annual Meeting, Boulder, Colorado, January 11–13, 1984.

---

<sup>30</sup>Invited presentation.

300. M. F. Iskander, C. H. Durney, and D. G. Bragg, "Microwave Methods of Measuring Changes in Lung Water," invited presentation in the workshop on Clinical Use of Lung Water Measurements, sponsored by NIH, National Heart, Lung, and Blood Institute, Bethesda, Maryland, June 7–8, 1984.
301. M. F. Iskander, S. C. Olson, and C. H. Durney, "Extension of the Iterative EBCM to Calculate Scattering by Low-Loss Elongated Dielectric Objects and Its Hybridization with the Geometrical Optics Approximation," International IEEE Antennas and Propagation Society Symposium and National Radio Science Meeting, Boston, Massachusetts, June 25–29, 1984.
302. M. F. Iskander and M. A. K. Hamid, "A New Strip Transmission Line as a Leaky Feeder," Conference on Electromagnetic Measurements, Delft University of Technology, Delft, The Netherlands, August 20–24, 1984.
303. D. A. Keech and M. F. Iskander, "Radiofrequency Tomographic Imaging for Monitoring Oil Seepage from Tanks," Petroleum Hydrocarbons and Organic Chemicals in Ground Water Conference and Exposition, Houston, Texas, November 5–7, 1984.
304. M. F. Iskander, P. F. Turner, and G. Knight, "On the Control and Prediction of the Heating Patterns of the Annual Phased Array Hyperthermia System," Fourth Annual Meeting of the North American Hyperthermia Group, Orlando, Florida, March 24–29, 1984.
305. M. F. Iskander, S. O. Olson, and C. H. Durney, "Calculation of the Average Resonance Absorption by Human and Animal Models," Sixth Annual Meeting of the Bioelectromagnetics Society, Atlanta, Georgia, July 15–19, 1984.
306. M. F. Iskander and S. L. Rattlingourd, "A New Electromagnetic Propagation Tool for Swept-Frequency and Time-Domain Well Logging," Society of Petroleum Engineers 59th Annual Technical Conference and Exhibition, Houston, Texas, September 16–19, 1984.
307. M. F. Iskander and S. O. Olson, "An *In Vivo* Probe for Measuring the Dielectric Properties of Low-Permittivity Tissue," Sixth Annual Meeting of the Bioelectromagnetics Society, Atlanta, Georgia, July 15–19, 1984.
308. M. F. Iskander, "New Iterative Extended Boundary Condition Method for Calculating Scattering and Absorption by Elongated and Composite Objects," CRDC Scientific Conference on Obscuration and Aerosol Research, Aberdeen Proving Ground, Maryland, June 25–29, 1984.
309. D. K. Ghodgaonkar, M. F. Iskander, and O. P. Gandhi, "Experimental Determination of Complex Permittivities of Biological Samples at Millimeter Wavelengths Using Modified Infinite Sample Method," Sixth Annual Meeting of the Bioelectromagnetics Society, Atlanta, Georgia, July 15–19, 1984.
310. M. F. Iskander and R. E. Benner, "Potential Applications of the New Iterative Extended Boundary Condition Methods in the Optical Region," CRDC Scientific Conference on Obscuration and Aerosol Research, Aberdeen Proving Ground, Maryland, June 25–29, 1984.

311. J. A. D'Andrea, H. Massoudi, C. H. Durney, and M. F. Iskander, "Microwave Radiation Absorption Within Spheres and Models of the Medium-Sized Rat: Experimental Measurement," Sixth Annual Meeting of the Bioelectromagnetic Society, Atlanta, Georgia, July 15–19, 1984.
312. M. F. Iskander, O. Khoshdel-Milani, and P. F. Turner, "Numerical Calculations of the Temperature Distribution in Cross Sections of the Human Body," Third Annual Meeting of the North American Hyperthermia Group, San Antonio, Texas, February 27–March 3, 1983.
313. A. Lakhtakia, M. F. Iskander, and C. H. Durney, "On the Use of the Iterative EBCM to Solve for Absorption by Composite Dielectric Objects—The Introduction of Mixed Basis Functions," International IEEE Antennas and Propagation Society Symposium, Houston, Texas, May 23–26, 1983.
314. A. Lakhtakia, M. F. Iskander, and C. H. Durney, "Theoretical and Experimental Evaluation of the Average SARs at and Beyond Resonance," Fifth Annual Meeting of the Bioelectromagnetics Society, Boulder, Colorado, June 12–16, 1983.
315. C. Tsai, H. Massoudi, C. H. Durney, and M. F. Iskander, "Improved Calculations of SAR Distributions in Biological Models," Fifth Annual Meeting of the Bioelectromagnetics Society, Boulder, Colorado, June 12–16, 1983.
316. M. F. Iskander and J. B. DuBow, "Time- and Frequency-Domain Techniques for Measuring the Dielectric Properties of Oil Shale," International Microwave Power Symposium, San Diego, California, July 25–30, 1982.
317. M. F. Iskander, "Electromagnetic Techniques in Medical Diagnosis," International Microwave Power Symposium, San Diego, California, July 25–30, 1982.
318. M. F. Iskander, A. Lakhtakia, and C. H. Durney, "Scattering and Absorption by Dielectric Objects," IEEE Antennas and Propagation Society International Symposium, Albuquerque, New Mexico, May 24–28, 1982.
319. M. F. Iskander, H. Massoudi, C. H. Durney, and M. Yafeh, "The Development of an RF Personnel Dosimeter," Fourth Annual Meeting of the Bioelectromagnetics Society, Los Angeles, California, June 28–July 2, 1982.
320. M. F. Iskander, C. H. Durney, and S. S. Jones, "An Improved Microwave Method for Measuring Changes in Lung Water Content," Fourth Annual Meeting of the Bioelectromagnetics Society, Los Angeles, California, June 28–July 2, 1982.
321. M. F. Iskander, C. H. Durney, T. S. Grange, and C. S. Smith, "A Microwave Radiometer for Measuring Changes in Lung Water Content," Fourth Annual Meeting of the Bioelectromagnetics Society, Los Angeles, California, June 28–July 2, 1982.
322. M. F. Iskander, A. Lakhtakia, C. H. Durney, and H. Massoudi, "Iterative Solution to Improve the Stability and Frequency Range of the EBCM," Fourth Annual Meeting of the Bioelectromagnetics Society, Los Angeles, California, June 28–July 2, 1982.

323. M. F. Iskander and P. F. Turner, "A Two-Dimensional Numerical and Experimental Evaluation of the EM Power Deposition in the Human Body," Fourth Annual Meeting of the Bioelectromagnetics Society, Los Angeles, California, June 28–July 2, 1982.
324. O. P. Gandhi, P. Wahid, and M. F. Iskander, "A Modified Infinite Sample Method for Measuring the Complex Permittivity in Millimeter Wave Frequencies," Fourth Annual Meeting of the Bioelectromagnetics Society, Los Angeles, California, June 28–July 2, 1982.
325. M. F. Iskander and P. F. Turner, "Numerical and Experimental Evaluation of the EM Power Deposition in the Human Body," Second Annual Meeting of the North American Hyperthermia Group, Salt Lake City, Utah, April 17–19, 1982.
326. M. F. Iskander and G. Nabavi, "On-Line Dielectric Probe for Process Control of Oil Shale Reporting," 1982 Symposium on Instrumentation and Control for Fossil Energy Process, Houston, Texas, June 7–9, 1982.
327. M. F. Iskander, "Physical Aspects and Methods of Hyperthermia Production by RF Currents and Microwaves," American Association of Physicists in Medicine (AAPM) Summer School, Dartmouth College, Hanover, New Hampshire, August 3–7, 1981.
328. M. F. Iskander, "Electromagnetic Power Deposition in Biological Models: Numerical Calculations and Phantom Experiments," American Association of Physicists in Medicine (AAPM) Summer School, Dartmouth College, Hanover, New Hampshire, August 3–7, 1981.
329. H. Massoudi, C. H. Durney, and M. F. Iskander, "On the Adequacy and Accuracy of the Block Models of Man in Calculating SAR Distributions," Bioelectromagnetics Society Meeting, Washington, DC, August 9–12, 1981.
330. H. Massoudi, C. H. Durney, and M. F. Iskander, "Near-Field Absorption in Models of Humans Exposed to Fields of Short Electric Dipoles," Bioelectromagnetics Society Meeting, Washington, DC, August 9–12, 1981.
331. A. Lakhtakia, M. F. Iskander, C. H. Durney, and H. Massoudi, "Scattering and Absorption of Dielectric Objects Irradiated in the Near Field of Aperture Sources," IEEE Antennas and Propagation Society Symposium, Los Angeles, California, 1981.
332. M. F. Iskander, "The Development of an Antenna System for the Personnel Microwave Dosimeter," presented in a workshop held at the Naval Aerospace Medical Research Laboratory, Pensacola, Florida, January 29, 1980.
333. D. G. Bragg, C. H. Durney, and M. F. Iskander, "Transmission Monitoring of Lung Water," 28th Annual Meeting of the Association of University Radiologists, Tucson, Arizona, March 25–28, 1980.
334. C. H. Durney, M. F. Iskander, D. A. Christensen, and A. Riazi, "Heat Induction Methods," RTOG (Radiation Therapy Oncology Group) Hyperthermia Committee Meeting, St. Louis, Missouri, January 7, 1980.
335. A. Lakhtakia, M. F. Iskander, C. H. Durney, and H. Massoudi, "Irradiation of Prolate Spheroidal Models of Humans and Animals in the Near Field of a Small Loop Antenna," 1980 URSI Symposium, Quebec, Canada.

336. M. F. Iskander, R. Maini, and C. H. Durney, "Microwave Imaging: Numerical Simulation and Results," IEEE Microwave Theory and Techniques Society International Microwave Symposium, Los Angeles, California, 1980.
337. M. F. Iskander, C. H. Durney, and D. L. Jaggard, "The Development of a Microwave Personnel Dosimeter," Bioelectromagnetics Society Meeting, San Antonio, Texas, September 14–18, 1980.
338. M. F. Iskander, R. Maini, and C. H. Durney, "A Numerical Technique for Computing the Spatial Permittivity Distribution (Imaging) of the Thorax," Bioelectromagnetics Society Meeting, San Antonio, Texas, September 14–18, 1980.
339. A. Lakhtakia, M. F. Iskander, C. H. Durney, and H. Massoudi, "Near-Field Absorption in Prolate Spheroidal Models Exposed to a Small Loop Antenna of Arbitrary Orientation," Bioelectromagnetics Society Meeting, San Antonio, Texas, September 14–18, 1980.
340. M. F. Iskander, C. H. Durney, and H. Massoudi, "Qualitative Explanation of Near-Field SAR Characteristics Based on Experimental and Theoretical Observations," Bioelectromagnetics Society Meeting, San Antonio, Texas, September 14–18, 1980.
341. M. F. Iskander, C. H. Durney and H. Massoudi, "Analysis of SARs in Small Spheroids Produced by Irradiation from an Elemental Model of a Pulsed, Phased-Array Antenna," Bioelectromagnetics Society Meeting, San Antonio, Texas, September 14–18, 1980.
342. H. Massoudi, C. H. Durney, and M. F. Iskander, "Long-Wavelength Analysis of Electromagnetic Absorption in Prolate Spheroidal Models of Man and Animals Irradiated by a Small Loop Antenna," Bioelectromagnetics Society Meeting, San Antonio, Texas, September 14–18, 1980.
343. H. Massoudi, C. H. Durney, P. W. Barber, and M. F. Iskander, "Specific Absorption Rate in a Capped Cylindrical Model of Man and Animals Irradiated by an Axially Incident Electromagnetic Plane Wave," Bioelectromagnetics Society Meeting, San Antonio, Texas, September 14–18, 1980.
344. A. Lakhtakia, M. F. Iskander, C. H. Durney, and H. Massoudi, "Absorption Characteristics of Prolate Spheroidal Models Exposed to the Near-Fields of Electrically Small Apertures," Bioelectromagnetics Society Meeting, San Antonio, Texas, September 14–18, 1980.
345. M. F. Iskander, "Near-Field Irradiation of Biological Models," NATO Advanced Study Institute on Theoretical Methods for Determining the Interaction of Electromagnetic Waves with Structure, Norwich, England, July 23–August 4, 1979.
346. M. F. Iskander, H. Massoudi, C. H. Durney, and S. J. Allen, "Measurements of the RF Power Absorption in Human and Animal Phantoms Exposed to Near-Field Radiation," 1979 Bioelectromagnetics Symposium, Seattle, Washington, June 18–22, 1979.

347. K. Han, M. F. Iskander, C. H. Durney, and H. Massoudi, "Near-Field Irradiation of Cylindrical Models of Humans and Animals," 1979 Bioelectromagnetics Symposium, Seattle, Washington, June 18–22, 1979.
348. M. F. Iskander, C. H. Durney, D. A. Christensen, and A. Riazi, "A Broadband and Compact Applicator for Deep Tissue Heating Using Focused Microwaves," Bioelectromagnetics Symposium, Seattle, Washington, June 18–22, 1979.
349. M. F. Iskander, C. H. Durney, B. H. Ovard, and D. G. Bragg, "Validation of Microwave Pulmonary Edema Detection by Isolated Lung and Phantom Measurements," 1979 Bioelectromagnetics Symposium, Seattle, Washington, June 18–22, 1979.
350. D. L. Jaggard and M. F. Iskander, "Bounding the Propagation Characteristics of TEM Modes in Tunnels of Arbitrary Shape," URSI Meeting, Seattle, Washington, June 18–22, 1979.
351. M. F. Iskander, C. H. Durney, D. G. Bragg, and B. H. Ovard, "A Microwave Method for Estimating Absolute Value of Average Lung Water Content," Open Symposium of the Biological Effects of Electromagnetic Waves, Helsinki, Finland, 1978.
352. M. F. Iskander, P. W. Barber, C. H. Durney, and H. Massoudi, "Near-Field Irradiation of Prolate Spheroidal Models of Humans," Open Symposium on the Biological Effects of Electromagnetic Waves, Helsinki, Finland, 1978.
353. M. F. Iskander, C. H. Durney, H. Massoudi, and C. C. Johnson, "Approximate Analysis of Plane-Wave Irradiation of Man Near a Ground Plane," 1978 Symposium of Electromagnetic Fields in Biological Systems, Ottawa, Canada, June 27–30, 1978.
354. H. Durney, M. F. Iskander, H. Massoudi, and C. C. Johnson, "An Empirical Formula for Calculating the SAR of Prolate Spheroidal Models of Humans and Animals Irradiated by Plane Waves," 1978 Symposium on Electromagnetic Fields in Biological Systems, Ottawa, Canada, June 27–30, 1978.
355. M. F. Iskander, C. H. Durney, D. J. Shaff, and D. G. Bragg, "Pulmonary Diagnostics Using Noninvasive Microwave Methods," International Symposium on Biological Effects of Electromagnetic Waves, Airlie, Virginia, October 30–November 4, 1977.
356. C. H. Durney, C. C. Johnson, P. W. Barber, H. Massoudi, M. F. Iskander, S. J. Allen, and J. C. Mitchell, "Radiofrequency Radiation Dosimetry Handbook, Second Edition," International Symposium on Biological Effects of Electromagnetic Waves, Airlie, Virginia, October 30–November 4, 1977.
357. M. F. Iskander, C. H. Durney, and P. W. Barber, "A Technique to Calculate the Radio-Frequency Power Absorption in Models of Man at and above Resonances," International Symposium on Biological Effects of Electromagnetic Waves, Airlie, Virginia, October 30–November 4, 1977.
358. M. F. Iskander and M. A. K. Hamid, "A New Strip-Transmission Line for Moisture Content Measurements," IMPI Symposium for Microwave Power, University of Minnesota, 1977.

359. M. F. Iskander and M. A. K. Hamid, "A Time-Domain Technique for Characterizing Leaky Coaxial Cables," IEEE Microwave Theory and Techniques Society International Microwave Symposium, San Diego, California, June 21–23, 1977.
360. M. F. Iskander and M. A. K. Hamid, "Near-Field Coupling Between Two Sectoral Horns Using the Generalized Scattering Matrix Technique," USNC/URSI Meeting, University of Illinois, Urbana, Illinois, June 3–5, 1975.
361. M. F. Iskander and M. A. K. Hamid, "An Iterative Solution for the Reflection Coefficient of a Flanged Waveguide Antenna," *Proceedings of the 5th European Microwave Conference*, Hamburg, Germany, pp. 605–609, September 1–4, 1975.
362. M. F. Iskander and M. A. K. Hamid, "Numerical Solution for the Coupling Between Two Sectoral Horns," USNC/URSI Meeting, Boulder, Colorado, October 14–17, 1974.
363. M. F. Iskander and M. A. K. Hamid, "Iterative Solution of the Waveguide-Horn Junction," IEEE/G-MTT International Microwave Symposium, *Digest*, pp. 84–86, June 12–13, 1974.
364. M. F. Iskander and M. A. K. Hamid, "Near-Field Coupling Between Two Corner Reflectors," USNC/URSI Meeting, Atlanta, Georgia, June 10–13, 1974.
365. S. S. Stuchly, M. S. Rzepecka, and M. F. Iskander, "A Lumped Element Method for Permittivity Measurements at Microwave Frequencies," Microwave Power Symposium, International Microwave power Institute, University of Loughborough, United Kingdom, September 11–12, 1973.
366. M. F. Iskander and S. S. Stuchly, "A Time-Domain Technique for the Measurement of the Dielectric Properties of Biological Substances," IEEE Conference on Precision Electromagnetic Measurements, pp. 123–125, June 25–29, 1972.